Materials Science Forum

Passivation of Metals and Semiconductors

Proceedings of the 7th International Symposium on Passivity

Editor: K.E. Heusler

TRANS TECH PUBLICATIONS

Passivation of Metals and Semiconductors

Passivation of Metals and Semiconductors

Proceedings of the
Seventh International Symposium on Passivity
Passivation of Metals and Semiconductors

Technical University of Clausthal, Germany
August 21-26, 1994

Editor:

K.E. Heusler

TRANS TECH PUBLICATIONS
Switzerland - Germany - UK - USA

ISBN 0-87849-692-0

Volumes 185-188 of
Materials Science Forum
ISSN 0255-5476

***Distributed** in the Americas by*

Trans Tech Publications Ltd
LPS Distribution Center
52 LaBombard Rd. North
Lebanon, NH 03766
USA

Phone: (603) 448 0037
Fax: (603) 448 2576

and worldwide by

Trans Tech Publications Ltd
Hardstr. 13
CH-4714 Aedermannsdorf
Switzerland

Fax: (++41) 62 74 13 79
E-Mail: ttp@transtech.ch

International Advisory Board

T. Agladze, Georgia
F. Di Quarto, Italy
R. P. Frankenthal, USA
M. Froment, France
W. Gomes, Belgium
J. B. Goodenough, USA
M. J. Graham, Canada
H. L. Hartnagel, Germany
H. Hasegawa, Japan
K. Hashimoto, Japan
K. E. Heusler, Germany
E. A. Irene, USA
M. Janik-Czachor, Poland
J. Kruger, USA
D. Landolt, Switzerland
D. L. Lile, USA
D. V. Morgan, Great Britain
R. A. Oriani, USA
V. N. Ovsjuk, Russia
N. Sato, Japan
W. Schmickler, Germany
J. W. Schultze, Germany
J. C. Scully, UK
W. E. Spicer, USA
T. Sugano, Japan
P. Victorovitch, France
H. H. Wieder, USA

Organizing Committee

H. L. Hartnagel, Darmstadt

K. E. Heusler, Clausthal

R. Kassing, Kassel

R. Kirchheim, Göttingen

G. Mende, Berlin

W. Mönch, Duisburg

W. Plieth, Dresden

G. Reinhard, Dresden

R. Rubner, Erlangen

J. W. Schultze, Düsseldorf

Seventh International Symposium on Passivity
Passivation of Metals and Semiconductors

Technical University of Clausthal, Germany
August 21-26, 1994

Preface

The First International Symposium on Passivity in Heiligenberg near Darmstadt, Germany, was organized in 1957 by the late Professor K. F. Bonhoeffer and dealt with the passivity of metals. Similar Symposia were held in Toronto/Canada, Cambridge/England, and Airlie/USA. They provided the opportunity to discuss recent progress in the fundamental understanding of the passivity of metals and the relevant experimental methods in an informal atmosphere. Technical advances in the fields of corrosion resistant metals and alloys, and also microelectronic materials depend to a large degree on a proper knowledge about passivating films. Thus, during the later Symposia in Bombannes/France and Sapporo/Japan, the scope of the symposium was widened to include the passivation of semiconductors as a new theme, and papers of technical importance were added to those of a fundamental character.

The 7th Symposium followed the format of the recent symposia. All aspects of the passivity of metallic and semiconductor materials were covered. The exchange of knowledge on fundamental problems of common interest to scientists working in the fields of passivity of metals and passivation of semiconductors was emphasized. New methods of investigation, preparation and modification, and new theoretical approaches were discussed. Advances resulted from new materials in new environments, from metals and insulating films in multilayer structures, and from the chemical side of semiconductor technology. Fundamental aspects of submicron structuring in silicon, compound semiconductors - particularly with heteroepitaxial sandwiches - and related materials were dealt with.

The Symposium was organized with the help of the International Advisory Board and the Organizing Committee. The members of these bodies proposed and selected speakers, and together with some additional reviewers reviewed the papers submitted for publication in the Proceedings.

The 7th International Symposium on Passivity was held in the Technical University of Clausthal, Germany, from August 21 to 26, 1994, under the auspices of Deutsche Bunsen-Gesellschaft für Physikalische Chemie, Electrochemical Society, Fachgruppe Angewandte Elektrochemie der Gesellschaft Deutscher Chemiker, Informationstechnische Gesellschaft des Verbands Deutscher Elektrotechniker, International Society of Electrochemistry, Japan Society of Corrosion Engineering, and Société Française de Chimie with financial support from public organisations as the German Research Organization (DFG), the State of Lower Saxony, the city of Clausthal-Zellerfeld and the Technical University of Clausthal with the Society of the Friends of the Technical University of Clausthal, from industrial enterprises as BMW and Siemens, and international bodies as the United States Navy, the Soros International Science Foundation and the International Society of Electrochemistry.

Many of the 147 participants of the Symposium from 28 different countries met during the reception given by the city of Clausthal-Zellerfeld in the evening before the official opening by the chairman of the Organizing Committee on Monday, August 22, 1994. Opening addresses were also given by the rector of the Technical University of Clausthal, Professor Dr. Dr. h. c. Klaus Marx and the incoming president of the International Society of Electrochemistry, Professor Dr. Joachim-Walter Schultze. During the scientific sessions 88 oral contributions and 65 posters were presented. By avoiding parallel sessions as much as possible one of the aims of the Symposium apparently was well achieved, namely to promote a common language among the scientists from disciplines as different materials science, electrical engineering, theoretical physics, etc.

K. E. Heusler

Contents - Survey

Table of Contents

Film Properties and their Modification

Charge Transport in Passivating Films and Electrical Breakdown

Kinetics

Introduction

Materials Science Forum Vols. 185-188 (1995) pp. 3-8

A summary of the passivity symposium

H.L. Hartnagel[1] and W.J. Plieth[2]

[1] Institut für Hochfrequenztechnik, Technische Hochschule Darmstadt, Germany

[2] Institut für Physikalische Chemie und Elektrochemie, Technische Universität Dresden, Germany

The International Symposium on the Passivity of Metals and Semiconductors was held for the 7th time in the small miners' city Clausthal-Zellerfeld and its University. The trends in research and development were reflected in the plenary and key-note lectures and in an impressive poster programme.

It was decided to attempt a summary and overview of the Symposium. This is of course a very difficult task. One of us (W.J. Plieth) concentrated on the developments of metal passivation, whereas the other one (H.L. Hartnagel) covered the semiconductor presentations.

Passivity of Metals
We try to subdivide the different presentations into the following four subsections:
The substrate, the film, breakdown - local corrosion, and the methods.

Only some examples can be mentioned of the large number of outstanding contributions. They are of course a personal selection.

THE SUBSTRATE

Looking to the different materials which were discussed during the meeting, one had the traditional discussion of

- Iron and steel
- Nonferreous metals and
- Alloys

Besides passivity problems on typical technical metals some papers looked for passivity phenomena at not-so-common systems like Tl (Petrii) or the special problems of passivity in nonaqueous Li battery systems (Rahner).

For alloys the dissolution and establishment of a kinetically controlled surface composition at high field conditions was discussed (Kirchheim). In several papers and posters the present

status of ex-situ surface-analytical methods was described (e.g. Landolt, Janik-Czachor). Other papers investigated the role of components of small concentration such as silicon in austenitic stainless steel (Ives).

Light weight materials are a very important branch of alloys. Al/Mg, Al/Ta (Ono, Hashimoto, et al.) were examples of investigations presented at the conference. New research results of amorphous alloys were presented by Hashimoto and by Akiyama. An important domain of future research are composite materials. One example discussed during the meeting was an investigation on Al/SiC (Malik, Bala, Maahn).

The Film

- Formation and growth
- Thickness

Two papers investigated the growths of the film after ablation by Laser pulses (Oltra and the Poster by Itagaki, Oltra, Vuillemin, Keddam, Takenouti). A classification of film properties in dependence of the thickness was discussed by Schultze.

- The structure
- Electronic and ionic properties
- Modification of the film

Chemical composition and composition profiles were treated by Kirchheim et al. An interesting poster discussed proton migration into TiO_2 (Blum, König).

A variety of papers described new methods to determine the structure. Some examples are given in the last section.

A theoretical paper showed results of calculations using a mixture of Hartree-Fock and Local Density Approximations (Yu and Halley).
Other papers described the modification of films for instance by incorporation of transition metals into TiO_2 (Ezak, Berera, Latanison), AC treatment (Anicai, Dima) or by various coatings (Fujisawa, Tsujikawa).

Properties of films formed in anhydrous electrolytes were discussed in several papers (e.g. Banas et al; Safonov et al; Wilinski and Flis).

Breakdown - Local Corrosion

The following topics were discussed.

- Field breakdown
- Pit formation and repassivation
- Stochastic description

The role of vacancies was treated by MacDonald. Light-induced inhibition of the breakdown was reported by Schmuki and Böhni.

Noise measurements were described by several authors (e.g. Gorse, Baroux); one example of results: The local pit distribution showed an exclusion zone similar to nucleation (Heusler).

The Methods

Improvements in a scientific area are always connected with the developments in methodology. Already classical methods are

- Optical Methods
- Photoelectrochemistry

Improvements were presented in ellipsometry (Dynamic Imaging Microellipsometry, Kruger et al.) and anisotropic ellipsometry (Michaelis). Reflectance spectroscopy was applied to amorphous metals (Huerta, Heusler). Photoelectrochemistry was used in several papers. It was discussed whether the degree of hydration can be determined (Di Quarto). Other papers described photocurrents on Al_2O_3Y (Burleigh) and intensity-modulated phase spectroscopy (IMPS, Graefe, Plieth). Papers dealing with laser photoelectrochemistry discussed spallation and laser ablation (Oltra). Also photocurrent imaging and photothermal effects were discussed (Williams, Hutton). The recent advancement in the intensity of X-rays from synchrotron radiation sources has stimulated research in EXAFS and XANES/NEXAFS (Kruger, Strehblow). A report described neutron reflectivity (Kruger).

- Electron spectroscopy (ex-situ)
- Electromechanical Methods

These methods are now indispensible investigations of passive films. Examples of methods are XPS/UPS (Landolt) or AUGER/SIMS and TOF-SIMS and (e.g. Olefjord, Wegrelius).

The most exciting new development Scanning Tunneling and Atomic Force Microscopy (STM and AFM) were presented going down to atomic resolution (Marcus; Montero; Albella, Vazques; Ryan; Fujimoto, Newman, Thompson). But the papers and the posters also demonstrated the serious problems. For instance, which atoms are seen with alloy substrates, can one distinguish between amorphous and crystalline films?

Other developments concerned
- in-situ film resistance measurement (Saario, Piippo)
- microbalance measurement (very interesting in connection with laser pit formation and with AC polarization (Efimov, Oltra and Gabrielli, Keddam, Minouflet and Perrot)
- ring/disc electrode measurement with a split ring (Flis)
- measurements with a Kelvin probe (Yamashita, Oriani)
- time resolved capacitance measurements (Hassel, Lohrengel)
- in-situ oxygen measurements using Mass Spectroscopy for detection of corrosion products (Grasjö, Hultquist, Lu, Seo)
- microcalorimetry and stress measurements

Passivity of Semiconductors
This symposium has again also been an occasion of presenting new, important research results in this stormy area of research,

particularly in connection with the imminent device and IC requirements.

The contributions can be summarized by the following headings:
Film deficiencies

A number of valuable contributions concerned porosity (Bolotin et al, Russia)
Impurity inclusions, particularly C-clusters evaluated by AFM (Welland et al, Cambridge, UK) and
breakdown quality improvement by H^*-radicals in H_2O vapour (Ohmi, Japan), where the breakdown voltage for 10nm thickness could be increased to 12 Volt

Substrate preparation

It is important to separate the situation of the nearly ideal Si-SiO_2 case from that of compound semiconductors.
For Si, useful contributions concerned the substrate roughness removal (Ohmi) and the C-cluster problem treated by ozone exposure or by avoiding exposure to air (Ohmi).
Regarding compound semiconductors, one should mention here the interface improvements by the inclusion of sulfides, selenides, fluorides, chlorides, ultrathin Si, $In(PO_3)_3$ for InP and many more concepts (numerous authors are relevant, and particularly the review by Hasegawa, Japan)

Characterization techniques

This is a field where important new contributions were reported.
Atomic-Force Microscopy (AFM) can be employed to study the interface state density N_{SS} (Welland).
Photoluminescence (PL) techniques have even been extended to evaluate N_{SS} (Hasegawa)
Scanning Tunneling (ST)-electron luminescence was shown to give µm-resolution mapping of the characteristics of thinly passivated surfaces (Horn, Germany)
Local thermal-expansion dynamics was reported as important for devices and ICs (Oesterschulze, Germany).

Film production

Here, a number of new techniques were reported, such as Ultra Violet-assisted Chemical Vapour Deposition (various groups from France).
The discussions with the metal passivators were particularly useful (anodic oxidation, optical structurization, etc.).

Nanostructuring

With reference to Si, the important problem of edge breakdown was discussed (Ohmi).
In connection with compound semiconductors, a variety of problems were covered mm and submm-electronics, optics and particularly quantum structures require special technological approaches.
In view of the difficulties of the complex situation, specific solutions for particular device requirements are systematically advanced (Kräutle, Germany)

Also here, useful discussion with metal passivators took place concerning Micromechanics (Schultze, Germany) and Semiconducting films on metals (König, Germany)

Outlook

Whereas this conference was strongly relevant for nanometric electronic structures, future conferences will have to address the passivity for room-temperature quasi single-electron electronics (Hasegawa, Japan).

Final Remarks

It can be said that the discussions of this Conference were particularly valuable since it involved again the learning of each other's language, an appreciation that indeed some new aspects in one or the other field are based on already previous experiences in the other one and in particular since many observations and models are very stimulating to the other group.

There is indeed a very stimulating overlapping between the different areas. It is the impression that the cooperation between these two communities should be continued. We look ahead to the next meeting in Canada.

Materials Science Forum Vols. 185-188 (1995) pp. 9-18

Fundamental aspects of the passivation of metals and semiconductors

K.E. Heusler

Abteilung Korrosion und Korrosionsschutz, Institut für Metallkunde und Metallphysik, Technische Universität Clausthal, D-38678 Clausthal-Z., Germany

Keywords: Passivity, history, thermodynamics, kinetics, metals, alloys, semiconductors, surface stress

Abstract

Historically, the discovery of passivity in the 18th century probably was the first example of a non-monotonous dependence of the reaction rate on the driving force. This phenomenon allowed the study of oscillating reactions and was the basis for a model of signal transmission in nerves. Conflicting theories about the nature of passivity catalyzed the development of metal optics. Passivity fostered the development of instrumentation in electrochemical kinetics and led to a deeper understanding of interfacial properties and of electrochemical reactions between multicomponent phases.

Passivity is due to a thin film separating a metal or semiconductor from the environment. Formation of a passivating film is only possible, if at least the Gibbs energy of formation of the film is provided. Full equilibrium corresponds to an equilibrium electrode potential with equilibrium chemical potentials of the film forming components, and equilibrium composition and structure of the film and of its interphases. Full equilibrium is never attained in technical systems.

The passivating film lowers the corrosion rate of a material. If there is a threedimensional film, the corrosion kinetics involves transport processes across the two interphases and within the three phases. The mobilities of ionic or electronic charges depend on the structure, in particular of the solids and their interphases, these parameters in turn being a function of rates and fields. The contribution of many parameters to the reaction kinetics is the principal reason for the complexity of the behaviour of passive materials.

Excess Gibbs energies result in large interphasial potential drops and in high fields in thin passivating films of low specific conductance. Consequently, the kinetics are governed by exponential laws relating rates to driving forces, and only rarely by the linear Ohm's law. Structures usually are far from equilibrium: There is often no long range order in the film. Or, one may have injection of vacancies or other nonequilibrium defects into the substrate and the film. Structure and composition at the interphase may depend on reaction rates. At the interphase between a semiconductor and the passivating film, chemisorption influences the concentration of surface states and their energy distribution. Selected examples will be given for various cases.

Historical Introduction

The phenomenon of passivity probably was first described by Lomonossov (1711-1765) [1]. Wenzel mentioned 1782 that iron did not corrode in concentrated nitric acid [2]. In a dilute solution of silver in nitric acid, iron dissolved rapidly and silver was precipitated. In concentrated solutions, iron dissolution soon stopped and deposited silver redissolved leaving the iron in an inert state with no changes being visible to the naked eye [3]. Passivity remained of considerable interest as the early example of a nonmonotonous dependence of the reaction rate on the driving force. Berzelius discovered that iron is passivated by anodic polarization [4]. The chemist C. T. Schoenbein [5] from Basel seems to have first used the term "passive iron" in a discussion with M. Faraday [6], who against the doubts of Schoenbein proposed that the "peculiar state" of passive iron was due to "a coat of oxide ... so thin as not to be sensible". Herschel [7] and later Hittorf [8] proposed that passivity was due to a special electric state of the metal surface. Drude [9] theoretically predicted small reflectivity changes, when a film much thinner than the

wavelength of the light was formed on a bare metal surface. Although Micheli [10] had already clearly shown that there were differences in the optical behaviour of active and passive iron, Königsberger and Müller [11] in an attempt to decide between Faraday's and Hittorf's theories were unable to detect any reflectivity changes at iron in NaOH and concluded that Hittorf was right. However, the sensitivity of their apparatus was insufficient, and iron is not readily activated in this electrolyte. Finally, Freundlich et al. [12] firmly established the presence of a film on passive iron using a method also proposed by Drude which now is called ellipsometry. Tronstadt [13] produced a wealth of quantitative measurements of thicknesses and optical film properties.

Fechner [14] detected the spreading of passivity and activity along an iron wire. This property was used by Ostwald and Lillie [15] for a nerve model based on earlier experiments of Heathcote [16]. According to Bonhoeffer et al. [17] propagation of an active zone along an iron wire in nitric acid has many properties in common with signal transmission along nerves, although as one now knows [18,19] the two electrochemical processes are of a quite different nature. In order to understand the nerve model, Bonhoeffer developed a mathematical description of oscillating reactions [20], promoted experimental and theoretical work in electrode kinetics, and fostered the production of instruments like the electronic potentiostat.

The history of the passivation of semiconductors begins with the invention of the transistor. In an early patent Derick et al. [21] proposed to passivate silicon wafers in dry oxygen or in a mixture of water and hydrogen against diffusion of As or Ga. It was observed that silicon in alkaline electrolyte can dissolve in the active and passive states [22] in which the semiconductor properties were different [23-26].

Thermodynamics of Passivity

A passivating film of the composition MX_r separating two bulk phases, the solid substrate containing M and the environment containing X, becomes thermodynamically stable, if the Gibbs energy of formation of the film is provided. For the reaction

$$M + rX = MX_r \tag{1}$$

the Gibbs energy of formation is

$$\Delta G^\circ = RT \ln a(M)\, a^r(X) \qquad (2).$$

with the activities a(M) of M and a(X) of X. In an electrochemical cell the corresponding electrode potential of formation vs the standard hydrogen electrode expressed in terms of a reversible X electrode is

$$E^\circ{}_H(X/MX_r) = E^S{}_H(X) + (RT/yF)\ln a(X)/a(X^{y-}) \tag{3}$$

with the standard potential $E^S{}_H(X)$ of X forming anions X^{y-} in the environment usually being an aqueous electrolyte. An equation analogous to (3) for the equilibrium potential $E^\circ{}_H(M/MX_r)$ holds for the other component M in the film. In complete equilibrium one has $E^\circ{}_H(X/MX_r) = E^\circ{}_H(M/MX_r)$.

Complete equilibrium requires the substrate to be saturated with X and the environment with M or M^{z+} ions according to the solubility product $L = [a(M^{z+})]^{1/z}\,[a(X^{y-})]^{1/y}$. For variable activities a(X) and a(M) the dependence of the solubility product on the composition of the film is obtained from eq.(4) [27]. Interphasial equilibrium corresponds to an equilibrium shape given by to Wulff's law. According to Gibbs's surface isotherm the composition in the interphase differs from the bulk composition depending on the crystallographic orientation of a solid. In complete equilibrium of a solid there is also an equilibrium distribution of internal mechanical stress satisfying the condition of the chemical potentials of the components being the same everywhere. Electronic equilibrium corresponds to a distribution of charges and fields providing the same Fermi level throughout the whole system.

Practically, complete equilibrium is never attained during the lifetime of a technical device. At room temperature, reaction rates at solid interphases and mobilities in the solid bulk are much too

slow. This is demonstrated by the simple case of the adsorption of a component of the fluid environment insoluble in the solid substrate [28]. The adsorption of sulphate on gold i. a. depends on the activity of sulphate in the aqueous solution and on the electrode potential. As shown in Fig.1, equilibria with respect to changes of charge and mass are established rather quickly, but the specific surface energy assumes its equilibrium value only after long times. The reason is that the approach of the equilibrium stress distribution by Herring-Nabarro creep [29] is accompanied by changes of the structure requiring the motion of particles in the bulk, e. g. changes of atomic distances parallel and perpendicular to the surface [30], and of point defects. Contrary to the general opinion [31,32], plastic and elastic contributions to the specific surface energy, i. e. "superficial energy " and "surface stress", are not independent thermodynamic variables [33]. Partial relaxation of irreversible stress may lead to structures like the one shown in Fig.2 which is schematically similar to the structure observed for the passivating film on nickel [34].

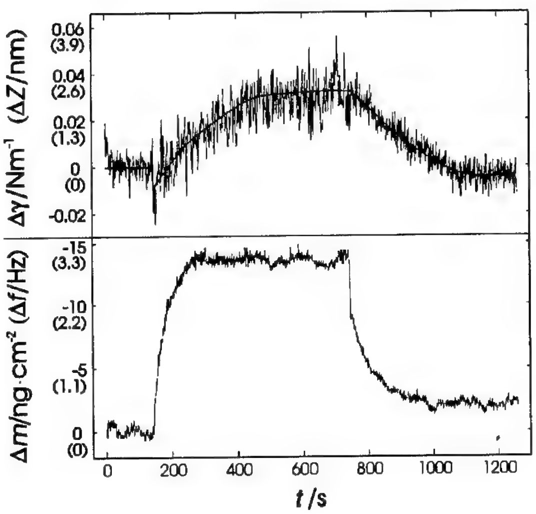

Fig.1: Dependence on time t of specific surface energy $\Delta\gamma$ (or deformation ΔZ) and mass Δm (or frequency Δf) after stepping the potential from E = -0.20 V to E = 0.05 V for Au in 0.1 M K_2SO_4, pH 3.80, 23°C [28]

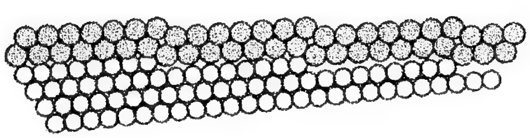

Fig.2: Schematic view of a partially relaxed solid phase boundary with 20% difference of the atomic distances

In passivating semiconductors, one wants to have a system not changing its properties with time. This requirement is usually achieved by the limiting case of zero reaction rates and not by complete equilibrium. The success of silicon technology certainly is i. a. due to the high melting points of both silicon and silicon dioxide and the correspondingly small mobilities of particles at room temperature. If one or another process is completely blocked kinetically, there is still the possibility of partial equilibria. One may have mechanical equilibrium with surface stress due to changes of the superficial energy in absence of complete chemical equilibrium. Or, there may be electronic equilibrium in absence of structural and chemical equilibrium, a behaviour exploited in the passivation of semiconductors by deposition of inert films instead of the "native" films.

Kinetics of Passivity and Passivation

Passivation often starts by chemisorption of X = OH or O on the substrate. There were long and fruitless arguments whether passivation requires the formation of a three-dimensional film or whether chemisorption of a two-dimensional film is already sufficient. A transient monolayer of OH already passivates cobalt for the dissolution of cobalt ions [35]. The monolayer later grows out to a three-dimensional film. Formation of a three-dimensional compact passivating film by a solid state reaction is possible in an environment not saturated with the film substance and often does not require nucleation. Nucleation is always observed for precipitated films.

A passivating film grows by transfer of the components into the film and by transport through the film, if an excess Gibbs energy $\Delta G = \Delta G^* - \Delta G^\circ$ is available, or if the electrode potential is positive to the equilibrium potential of formation. Usually, M is soluble in the environment and X in the substrate, or the substrate and the environment contain more than one component soluble in the film. Then, the respective transfer reactions and the transport reactions in the environment, the substrate and the film resulting in changes of the compositions at their phase boundaries must also be considered.

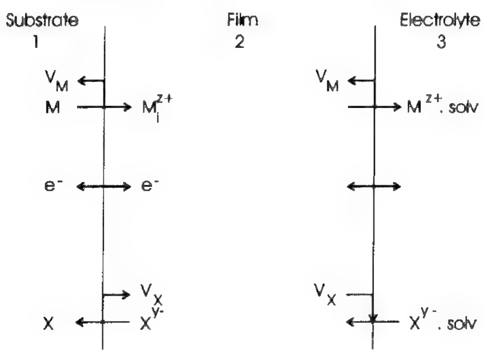

Fig.3: Scheme of processes at a substrate (1) covered by a passivating film (2) in contact with the electrolyte (3). M transferred to an interstitial site (or a metal ion vacancy) in the film may inject a vacancy into the metal. Analogous possibilities (not all of which are shown) exist for X and for transfer of M and X between film and electrolyte.

In the simple case of a pure substrate M and vanishing solubilities of X in the substrate and of M in the environment, one only has transfer of M from the substrate and of X from the environment into the film, and transport of M towards the environment and of X towards the substrate. If the transport within the film is fast compared to at least one of the transfer reactions, one expects a linear rate law for the growth of the film. Then, the excess Gibbs energy drops mainly at one or the other interphase and the rate for constant activity of X or constant electrode potential remains constant with time. In the opposite limiting case of rate determining transport and equilibrium of the transfer reactions, the rate law for film growth is exponential for large field strengths $\Delta G/d > 3RT/a$ and parabolic for small fields $\Delta G/d \leq 2RT/a$. In general, the thickness d increases at the rate

$$\partial d/\partial t = v/V = (v_o/V)\{\exp[\alpha a\Delta G/dRT] - \exp[-(1-\alpha)a\Delta G/dRT]\} \quad (4)$$

with the molar volume V of the film substance, the flux density v, the exchange rate v_o determined by the mean transport coefficients across the film, Broenstedt's coefficient α and the jump distance a. One may also use the current density $j = nFv$ with the charge number n, the exchange current density $j_o = nFv_o$ and $\Delta G = nF(E-E^o)$. The exponential law for $\exp[\alpha a\Delta G/dRT] >> \exp[-(1-\alpha)a\Delta G/dRT$ corresponds to

$$\ln (v/v_o) = \alpha a\Delta G/dRT \quad (5)$$

with the approximate dependence on time t

$$\partial \ln v/\partial \ln t \approx -1 \quad (6)$$

and the parabolic law for $v << v_o$ to

$$v/v_o = a\Delta G/dRT \quad (7)$$

with the time dependence

$$\partial \ln v/\partial \ln t = -1/2 \quad (8).$$

In the low field case when conduction follows Ohm's law, one observes coarse grained films or epitaxial growth. On the other hand, in the high field case the films usually are structurally disordered. There is often no long range order, but only short range order. In disordered films it is difficult to define vacancies and interstitials. However, there are indications that the concentration

of mobile ions grows with the field.

Both the low and high field cases can be observed in the same system depending on the conditions. The growth rate of the passivating film on iron in borate buffer at 25°C in Fig.4 follows eq.(5). At 250°C in Fig.5 it follows eq.(8). For short and long times the growth kinetics deviate from the transport limited cases. The deviation at short times in the high temperature experiments was due to a thin preexisting film. At the beginning of the experiment at low temperature there was no film. The rate remained controlled by interphasial transfer reactions until the film thickness exceeded about 1 nm. For long times, the current densities approached steady state values.

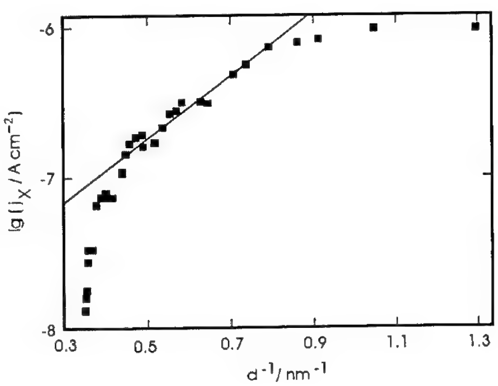

Fig.4: Growth rate j_X of an oxide film on iron in 0.4 M borate buffer, pH 7, after stepping the potential from the active range to E = -0.1 V vs the Hg/Hg_2SO_4 electrode in 1 M Na_2SO_4, as a function of reciprocal thickness d [36]

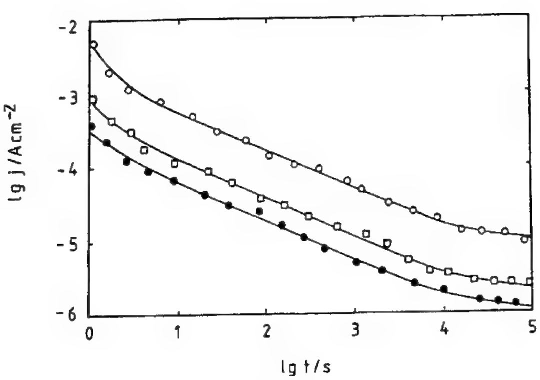

Fig.5: Anodic current density j vs time t for iron in 0.4 M borate buffer, pH 7.4 at 25°C, after stepping the potential from the free corrosion potential to the polarization ξ = 0.4 V at (•) 150°C, (□) 200°C and (o) 250°C [37]

A steady state corrosion rate different from zero is observed, if the environment is not saturated with the film substance. In the steady state, the film thickness is independent of time, and the rate determined by metal ion transfer from the film to the electrolyte is given by

$$j_s(M) = k^+(M) \cdot {}_2a(M^{z+}) \cdot {}_3[a(L)]^p \cdot \exp[\beta F \varphi_{2,3}/RT] \tag{9}$$

with the activities ${}_2a(M^{z+})$ of metal ions M^{z+} in the film and ${}_3[a(L)]$ of ligands L in the electrolyte, the reaction order p, the effective transfer coefficient ß and the potential difference $\varphi_{2,3}$ across the film/electrolyte interphase. For constant film thickness, the total current density of X is $j_s(X) = 0$, i. e. there is partial equilibrium with respect to transfer of X at the potential difference

$$\varphi_{2,3} = \varphi°_{2,3} = \varphi^*_{2,3} + (RT/yF) \ln\{a(X)/a(X^{y-})\} \qquad [10].$$

From eqs. (9) and (10) follows the dependence of $j_s(M)$ on solution composition. In the common case of oxide films, hydrolyzed metal ions are often transferred. Then, the ligand is L = X (= OH^-) and

$$\partial \ln j_s/\partial \ln a(OH^-)_{\varphi^\circ 2,3} = p - \beta/y \qquad (11).$$

In the steady state, the current due to the transfer of metal ions from the film to the electrolyte also flows through the film and through the metal/electrolyte interface. The potential drops at the substrate/film interphase and within the film adjust themselves accordingly as schematically shown in Fig.6. The relation of the steady state film thickness to the steady state current density j_s is given by eqs. (5) or (7) depending on whether v_s is, repectively, larger or smaller than v_0. For passive iron, the activation energy of ionic conduction is much larger than the activation energy of steady state dissolution. Therefore, the reciprocal steady state thickness $1/d_s$ is proportional to $\ln j_s$ at room temperature and proportional to j_s at high temperatures.

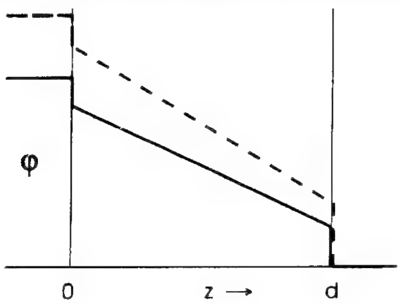

Fig.6: Schematic potential distribution at a passivating film in the steady state (——) with the anodic current density j_s and for $j > j_s$ (---)

For $j > j_s$, the film grows by incorporation of X from the electrolyte in an anodic reaction at a positive overpotential $\eta_{2,3} = \varphi_{2,3} - \varphi^\circ_{2,3}$. Then, an anodic current $j(X) > 0$ flows from the electrolyte into the film, but also the dissolution rate $j(M) > j_s(M)$ of substrate ions from the film increases with the total current density $j = j(M) + j(X)$. The total current also flows across the substrate/film interface and within the film, while the respective potential differences increase accordingly as shown in Fig.6.

Investigation of the transfer kinetics of M and X at the film/electrolyte interface requires the measurement of both partial currents. The partial derivative $\partial \ln j(X)/\partial \ln j(M)$ at constant electrolyte composition yields the ratio of the Tafel slopes. From partial derivatives with respect to the activities of reaction partners in the electrolyte at a constant value of one of the partial currents one obtains further combinations of reaction orders and transfer coefficients [38]. The film dissolves, if the anodic current is smaller than j_s. For $j = 0$ one has currentless dissolution. Then, the absolute values of the anodic current for M-ion dissolution and of the cathodic excorporation current of X-ions from the film are equal. The dependence of the currentless dissolution rate on electrolyte composition yields further kinetic information. There are always at least as many partial derivatives as one has kinetic parameters.

If the total current becomes cathodic, the film may be reduced to metal and X^{y-}. However, this process is not often observed in practice, either because other cathodic reactions proceed at potentials positive to the potential of formation of the film, or a chemical step limits the film dissolution rate such as the transfer of oxygen ions from the lattice into the chemisorbed state [27,39].

Oxygen ions at an oxide/electrolyte interphase usually are hydrated, i. e. the oxide is terminated by hydroxyl groups. Both the chemisorbed hydroxyl groups and free hydroxyl ions can participate in the ion transfer reactions. Chemisorbed or free ligands other than hydroxyl ions and water may also form complexes with metal ions during the transfer reaction. E. g. the dissolution rate of Fe(III) from passive iron is first order with respect to sulphate [40]. Sulphate and chloride are chemisorbed on the passivating oxide on iron. However, in presence of sulphate one has uniform dissolution, but in presence of chloride the oxide film dissolves locally. As a consequence, pitting occurs in a limited range of electrode potentials [41], concentrations [42] and temperatures [43]. The parallel transfer of metal ions and oxygen ions manifests itself by two additive Gaussian distributions of the probability density of intrinsic electrochemical noise [44]. During the pit initiation period this noise is greatly enhanced by chloride in a limited spectral region.

Semiconducting properties of passivating films

Electronic equilibrium is usually established within the substrate and the film and between the two phases, even if there is no electronic equilibrium between the film and the electrolyte, e. g. because of the lack of a suitable redox system. Then, the Fermi level is constant between the substrate and the interphase of the film towards the electrolyte. Since within the film there is an electric field, the chemical potentials of M and X decrease and increase, respectively, from the phase boundary towards the substrate to the phase boundary towards the electrolyte. An increase of the chemical potential of X results in an increase of r in a compound MX_r. Therefore, r is larger at the electrolyte side of the film than at the substrate side. The change of r sometimes is negligible as for SiO_2, but it can be large as for MnO_{2-x}. The electric field normal to the surface is not necessarily constant. If there is a time-independent ionic current, the field changes with the local ionic conductivity. In transient states of constant local composition of the film, a field due to space charges is superimposed. Such transient states can be observed for long times at low fields insufficient for film growth.

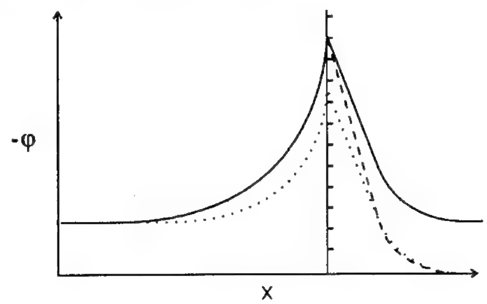

Fig.7: Potential distribution at a semiconductor/ electrolyte interphase (——) and after a cathodic shift of the electrode potential mainly in the semiconductor (···) and mainly in the Helmholtz layer (---)

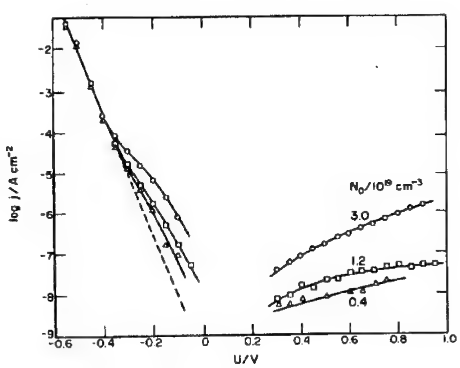

Fig.8: Current density j vs electrode potential U referred to SCE for 0.05 M $Na_3Fe(CN)_6$ + 0.05 M $Na_4Fe(CN)_6$ in 1 M $NaClO_4$ + 0.1 M sodium oxalate/oxalic acid buffer, pH 1.7, at Nb covered with Nb_2O_5 films of different donor densities N_D [45]

Constant local composition is usually assumed in studies of semiconductors. Excess charges are located in surface states or in volume states. If there are no surface states in the range of the Fermi level, any change of the potential is nearly completely accommodated in the volume of the semiconductor and only a small part drops in the Helmholtz layer due to the law of dielectric continuity [45]. If surface states are available, some part up to nearly the whole potential drop may occur within the interphase. Fig.7 shows the two limiting cases. The passivating film on niobium exhibits a behaviour close to the first case, the passivating film on titanium close to the second case. Both oxide films are n-type semiconductors. The effective cathodic transfer coefficient for electron transfer is $\alpha \approx 0.86$ RT/F at Nb_2O_5 as shown in Fig.8, but $\alpha \approx 0.55$ RT/F at TiO_2 according to Fig.9. Deviations from the Tafel line at potentials positive to the flat band potential are due to tunneling into the space charge region via surface states. These surface states can be eliminated or "passivated" by reaction of one of the two classes of hydroxyl groups on the surface of TiO_2 by reaction with hexene.

Similarly, in electronic equilibrium between a solid semiconducting substrate and a solid insulating film at constant local composition, most of the charge may either be stored in the semicon-

ductor volume resulting in a Schottky barrier of variable height, or it may be stored in surface states resulting in "Fermi level pinning". The electronic passivation of silicon by filling of surface states due to chemisorption e. g. of hydrogen during etching in HF [46,47] prior to chemical passivation by SiO_2 is analogous to the effect of chemisorption of hexen at TiO_2. Hydrogen coverage is maintained during etching according to the mechanism of Fig.10 showing the various steps of bond breaking and complexing at a kink site. Transfer of $HSiF_3$ into the electrolyte is followed by the homogeneous reaction $HSiF_3 + HF \rightarrow SiF_4 + H_2$. For etching in NaOH, F^- is replaced by OH^- [48].

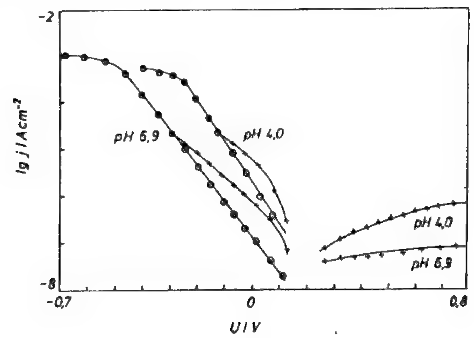

Fig.9: Current density j vs electrode potential U referred to SCE for 0.05 M $Na_3Fe(CN)_6$ + 0.05 M $Na_4Fe(CN)_6$ in 1 M KNO_3 with 0.1 M phthalate buffer, pH 4.0, or KH_2PO_4/K_2HPO_4 buffer, pH 6.9 at Ti covered with TiO_2, d = 20 nm

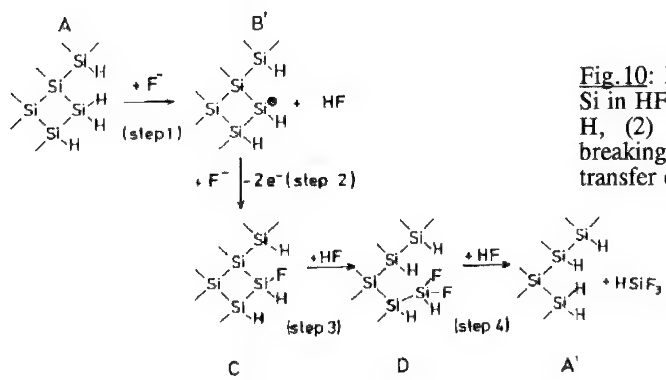

Fig.10: Mechanism of the etching of Si in HF in 4 steps: (1) desorption of H, (2) electrosorption of F^-, (3) breaking of first Si-Si bond, (4) transfer of $HSiF_3$ [47]

Transfer of ions into the film results in structural changes some of which are shown in Figs.2 & 3. One expects a relatively low activation energy for the transfer from a kink site in the substrate to an opposite kink site or surface vacancy in the film, but this situation is extremely rare with a very small entropy of activation or a small preexponential factor. More probable paths would be i) via laterally mobile atoms in the interphase, ii) transfer from kink sites of the substrate to interstitial sites in the film, or iii) transfer from any site in the substrate to any site in the film. The latter process has the largest preexponential factor, but the highest activation energy. It is the most probable path far from equilibrium. Transfer from sites other than kink sites produces surface vacancies in the substrate which will diffuse into the bulk. At a semiconductor surface, broken bonds to neighbouring atoms correspond to surface states. Vacancies diffusing from the surface into the volume may contribute to localized electronic states in the band gap.

Passive alloys

For passive compounds and alloys the ratio of the components incorporated into the film usually is quite different from their ratio in the substrate. Even if the ratio is the same, the rate constants often are vastly different. These effects result in a change of the composition at the substrate side of the inner interphase. One has speculated that due to the small diffusion rates at room temperature this change is confined to the uppermost atomic layer even at low film formation rates. However, this conclusion is wrong, because the diffusion coefficient is proportional to the vacancy concentration which increases with the corrosion rate due to the injection of vacancies [49].

The steady state corrosion of an alloy [50] proceeds at a rate different from zero, if the ratio of the partial fluxes v_i of the components to the total flux v is equal to the mole fraction y_i. The total steady state current density is given by

$$j = \sum_i (z_i F y_i) / \sum_i (y_i / k_i) \tag{12}$$

with the rate constants k_i of metal ion transfer from the film to the electrolyte. The rate constants are independent of composition, if they are are not too different, as in the case of passive FeCr alloys [54]. However, for extremely different rate constants $k_M << k_{M'}$ as during the transpassive dissolution of FeCr alloys, the rate constant of the slow component M increases exponentially with the mole fraction of the fast component M' according to the following empirical rule as shown in Fig.11 [50]:

$$k_M = k°_M \exp m y_{M'} \tag{13}$$

The steady state fluxes are the same within the substrate, from the substrate to the film, within the film and from the film to the electrolyte. Thus, depending on the relative rate constants of the transfer reactions and transport coefficients the penetration depth of the diffusion in the substrate, the compositions at the substrate side of the inner interphase and at the film interface at the outer interphase and within the film are defined [54]. The injection of defects at both sides of the solid/solid interphase apart from differences of density are also responsible for the creation of mechanical stresses which often are very large. During the growth of the passivating film on iron lateral stresses of about 60 kbar were observed [51,52]. Tensile stresses due to fast reductive dissolution of the film may mechanically remove well adhering sputtered films.

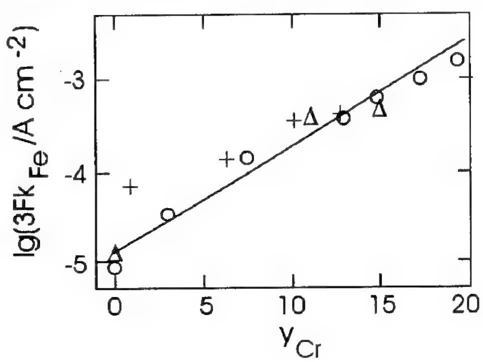

Fig.11: Rate constants k_{Fe} vs mole fraction y_{Cr} for steady state dissolution of transpassive FeCr alloys in 0.5 M sulfuric acid from data of (o) Olivier 1955 [53] and (+, Δ) Kirchheim et al. 1989 [54]. Solid line corresponds to eq.(13).

References

[1] M. V. Lomonossov, Trudy po Fizike i Khimii, Vol. 1, p. 369, Izd. Akad. Nauk SSSR, Moscow 1950
[2] C. F. Wenzel, Lehre von der Verwandtschaft der Körper, p. 108, Dresden 1782
[3] T. Bergman, Opuscula Physica et Chemica, Vol. 3, p. 84, 140, Upsala 1783
[4] W. Hisinger and J. J. Berzelius, Gilb. Ann. **27**, 275 (1807)
[5] C. T. Schönbein: *On a peculiar Voltaic Condition of Iron*, Lond. and Edinb. Phil. Mag., vol. ix, p. 53, Experimental Researches in Electricity by M. Faraday, Vol. II, p. 234, R. & J. E. Taylor, London 1844; Pogg. Ann. **37**, 490 (1836)
[6] M. Faraday, Lond. and Edinb. Phil. Mag., vol. **ix**, p. 122, Experimental Researches in Electricity, Vol. II, p. 248, R. & J. E. Taylor, London 1844
[7] J. F. W. Herschel, Ann. Chim. Phys. **54**, 87 (1833)
[8] W. Hittorf, Z. Physik. Chem. **30**, 485 (1899); **34**, 385 (1900)
[9] P. D. Drude, Ann. Phys. Chem. **38**, 481 (1890)
[10] F. J. Micheli, Arch. phys. nat. **10**, 125 (1900)
[11] J. Königsberger and W. J. Müller, Z. Elektrochem. **13**, 659 (1907); **15**, 742 (1909); Phys. Z. **6**, 847, 849 (1905); **12**, 607 (1911)
[12] H. Freundlich, G. Patscheke and H. Zocher, Z. Phys. Chem., **A128**, 321 (1927); **A130**, 289 (1927)

[13] L. Tronstadt, Z. Phys. Chem A**142**, 241 (1929); A**158**, 369 (1932); A**161**, 154 (1932); A**170**, 172 (1934) (with T. Höverstad); Kgl. Norske Vidensk. Selsk. Skr. No. **1**, 1 (1931); Kgl. Norske Vidensk. Selsk. Forhandlingar **4**, 161 (1931); Trans. Faraday Soc. **30**, 349 (1934) (with C. W. Borgmann); **31**, 1151 (1935)
[14] G. Th. Fechner, Schweigers J. **53**, 142 (1828)
[15] R. S. Lillie, Science (New York) **48**, 51 (1918)
[16] H. L. Heathcote, Z. Physik Chem. **37**, 387 (1901)
[17] K. F. Bonhoeffer, Z. Elektrochem. **47**, 147 (1941); ibid. 441 (with H. Beinert); ibid. 536 (with W. Renneberg); **52**, 29 (1948) (with E. Brauer and G. Langhammer); ibid. 60 (with V. Haase and G. Langhammer); Z. Physik **118**, 389 (1941) (with W. Renneberg)
[18] K. J. Vetter, Z. Elektrochem. **55**, 274, 675 (1951); **56**, 106 (1952)
[19] B. Sakmann, Angew. Chem. **104**, 844 (1992)
[20] K. F. Bonhoeffer, Ber. Sächs. Akad. Wiss. **95**, 57 (1943); Naturwiss. **31**, 270 (1943)
[21] L. Derick, C. J. Frosch, US Patent 2,802,760, Aug. 13, 1957
[22] M. Z. Seipt, Z. Naturforsch. A **14**, 926 (1959)
[23] S. Izidinov, T. Borisova and V. Veselovskii, Dokl. Akad. Nauk SSSR **133**, 392 (1961)
[24] V. I. Veselovskii, T. I. Borisova; A. A. Yakovleva and S. O. Izidinov, Electrochim. Acta **10**, 325 (1965)
[25] R. M. Hurd and P. T. Wrotenberg, Ann. N. Y. Acad. Sci. **101**, 876 (1963)
[26] R. M. Hurd and N. Hackerman, Electrochim. Acta**.** **9**, 1633 (1964)
[27] K. E. Heusler, Electrochim. Acta **28**, 439 (1983)
[28] G. Láng and K. E. Heusler, J. Electroanal. Chem, in print
[29] F. R. N. Nabarro, Rep. Conf. Strength of Solids, p. 75, The Physical Soc., London 1948
[30] H. Christmann, Molecular Physics **66**, 1 (1989); Progr. Surf. Sci. (1994), in print
[31] S. Trasatti and R. Parsons, Pure & Appl. Chem. **58**, 451 (1986)
[32] R. D. Meade and V. Vanderbilt, Phys. Rev. B **40**, 917 (1989); R. D. Meade, Structure and Stress of Semiconductors Surfaces, 104 pp., Diss. Harvard 1990
[33] G. Láng and K. E. Heusler, J. Electroanal. Chem. **377**, 1 (1994)
[34] V. Maurice, H. Talah and P. Marcus in: Modifications of Passive Films, p. 62, ed. by P. Marcus, B. Baroux and M. Keddam, The Institute of Materials, London 1994
[35] K. E. Heusler, Corros. Sci. **6**, 589 (1966)
[36] K. E. Heusler, Corros. Sci. **29**, 131 (1989)
[37] K. E. Heusler, B. Kusian and D. McPhail, Ber. Bunsenges. physik. Chem. **94**, 1443 (1990)
[38] K. D. Allard and K. E. Heusler, J. Electroanal. Chem. **77**, 35 (1977)
[39] K. E. Heusler and A. Grzegorzewski, Electrochim. Acta **35**, 539 (1990)
[40] K. E. Heusler, L. Jaeckel and F. Nagies in [34], p. 108
[41] R. A. Dengg and H. J. Donker, Korr. u. Metallschutz **3**, 241 (1927)
[42] H. J. Engell and N. D. Stolica, Arch. Eisenhüttenwes. **30**, 239 (1959); Z. physik. Chem. N. F. **20**, 113 (1959)
[43] F. J. Nagies, B. Kusian and K. E. Heusler, Proc. H. H. Uhlig Memorial Symposium, Electrochem. Soc., Pennington NJ, USA, in print
[44] K. E. Heusler, K. Nachstedt and H. Muscher, Bull. Electrochem. **8**, 7 (1992)
[45] K. E. Heusler and K. S. Yun, Electrochim. Acta **22**, 977 (1977)
[46] G. S. Higashi, Y. J. Chabal, G. W. Trucks and K. Raghavachari, Appl. Phys. Lett. **56**, 686 (1990)
[47] H. Gerischer, P. Allongue and V. Costa Kieling, Ber. Bunsenges. physik. Chem. **97**, 753 (1993)
[48] P. Allongue, V. Costa Kieling and H. Gerischer, J. Electrochem. Soc. **149**, 1018 (1993).
[49] J. Laurent and D. Landolt, Electrochim. Acta **36**, 49, (1991)
[50] K. E. Heusler and D. Huerta, Amorphous Metals, p. 302, ed. by H. Matyja and P. G. Zielinski, World Scientific Publ., Singapore 1986; J. electrochem. Soc. **136**, 65 (1989)
[51] K. E. Heusler, A. Grzegorzewski, L. Jaeckel and J. Pietrucha, Ber. Bunsenges. physik. Chem. **92**, 1218 (1988)
[52] L. Jaeckel, Specific Surface Energies of Solid Electrodes and Mechanical Stresses in Thin Films, Diss. Clausthal 1984
[53] R. Olivier, Passiviteit van Ijzer en Ijzer-Chroom Legeringen, Diss. Leiden 1955
[54] R. Kirchheim, B. Heine, H. Fischmeister, S. Hofmann, H. Knote and U. Stolz, Corros. Sci. **28**, 899 (1989); R. Kirchheim in [34], p. 102

The Passivation of Semiconductors

General Aspects

Materials Science Forum Vols. 185-188 (1995) pp. 23-36

Passivation and control of semiconductor interfaces by interface control layers

H. Hasegawa

Research Center for Interface Quantum Electronics and Department of Electrical Engineering, Hokkaido University, North 13, West 8, Sapporo 060, Japan

Keywords: Surface passivation, semiconductor, surface states, interface states

Abstract

A novel approach for passivation of semiconductors using an interface control layer (ICL) is presented and discussed. After reviewing briefly roles of interface, the origin of Fermi level pinning and a new PL-based interface characterization method, the concept and possible candidates of the ICL are presented. The ICL is inserted at the I–S interface, and has the role of removing the interface states by providing a coherent and smooth transition of bonds at the interface. A specific example of use of an ultra-thin silicon interface control layer (Si ICL) is then discussed in more detail. Details of interface formation and micro-structural and electronic characterization of the novel passivation structure are presented together with its applications to field effect transistor fabrication, surface passivation of quantum structures and control of metal–semiconductor and semiconductor–semiconductor interfaces.

1.Introduction

Interfaces such as semiconductor–semiconductor(S–S), insulator–semiconductor (I–S) and metal–semiconductor (M–S) interfaces are basic constituent elements of all semiconductor devices. The basic motivation for interface formation in devices is to create and utilize potential energy differences at the interface as shown in Fig.1(a). Surface "passivation" in semiconductor technologies is one of such interface technologies, and its objective is to protect devices from environmental influences by forming an I–S interface. By having insulators with large energy gap, the thick and high potential barrier at the I–S interface makes the delicate carrier motions in the device well intact against influence of the outside world. A more "active" use of the I–S interface is, of course, to utilize it as the gate dielectric of the MOS (metal–oxide–semiconductor), or more generally, MIS (metal–insulator–semiconductor) field effect transistors (FETs) which has been the key success element of the silicon planar integrated circuit technology.

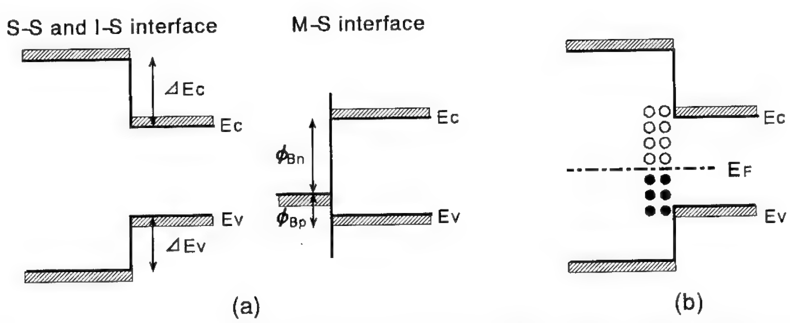

Fig.1 (a)Ideal interfaces and (b)a real interfaces with interface states causing Fermi level pinning.

The difficulty in passivation lies in the fact that formation of an I–S interface other than the Si–SiO_2 system results, in general, in creation of interface states within the energy gap as shown in Fig.1(b), leading to the so–called Fermi level pinning phenomenon. Such interface states trap carriers and cause various unwanted phenomena in devices.

Since the device feature sizes are approaching the nanometer range where quantum mechanical properties of surfaces and interfaces tend to dominate over the bulk properties, atomic–scale understanding and control of the interface becomes more and more important. Thus, the requirements for passivation will become very severe even for silicon devices. For compound semiconductors, establishment of a suitable passivation technology, or more generally, interface control technology, will become a key issue for further advances of electronic/optoelectronic devices based on known principles as well as those based on novel quantum mechanical principles.

The purpose of this paper is to present a novel approach for passivation using an interface control layer (ICL). A brief review is given first on the roles of interface, the origin of Fermi level pinning and a PL–based interface characterization method. Then, the concept and possible candidates for the ICL are presented. The ICL is inserted at the I–S interface , and has the role of removing the interface states by providing a coherent and smooth transition of bonds from one material to the other.Then, a specific example of using an ultra–thin silicon interface control layer (Si ICL) is discussed in more detail. Si ICL is formed by molecular beam epitaxy in a UHV–based growth/processing/characterization system. Details of interface formation and micro structural and electronic characterization are presented together with the applications to field effect transistor fabrication and surface passivation of quantum structures. Application of this technology to control metal–semiconductor and semiconductor–semiconductor interfaces are also discussed.

2. Roles of Interfaces and Origin of Interface States

2.1 Roles of Interfaces in Semiconductor Electronics

In Fig.2, a possible evolution of electronics from this century towards the next century is shown. In the present–day microelectronics with device feature sizes down to submicron range, S–S, I–S and M–S interfaces are utilized to provide boundary conditions for semi–classical motions of carriers so as to activate device operations or protect devices from environments. In this range, the motions of carriers are described by the semi–classical macroscopic semiconductor equations, and the boundary conditions imposed by the interfaces control the number density, movement direction, average velocity of the carriers treated as "classical particles".

In future devices with feature sizes in the nanometer range, mesoscopic nanoelectronics and single electron nanoelectronics are expected to emerge. In this quantum regime, S–S, I–S and M–S interfaces will be still utilized, but their roles will be of a more delicate nature where the quantum mechanical wave–

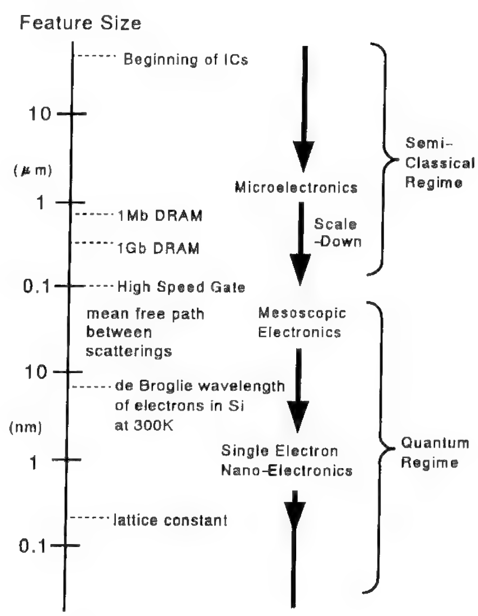

Fig.2 Evolution of semiconductor electronics with reduction of feature size.

particle duality of the electrons is precisely controlled by imposing boundary conditions to Schrödinger's equation through interfaces. Thus, the interface control will become more and more important, and the interfaces will be required to possess atomic–scale perfection in order to control, not the average motion, but the motion of individual electrons. Furthermore, not only the interface atom arrangements but also the electronic interface states should be precisely controlled.

2.2 Interface States and Their Origin

Although ideal S–S, I–S and M–S interfaces are characterized by the potential difference for electrons and holes as schematically shown in Fig.1(a), formation of real interfaces often results in additional creation of interface states within the energy gap as shown in Fig.1(b). When the density of such interface states are high, they tend to fix the position of the Fermi level at a certain equilibrium position within the energy gap, since even a slight deviation of the Fermi level from the equilibrium position produces large amounts of electrostatic charge. This phenomenon is called "Fermi level pinning" and it causes various unwanted phenomena in devices. Major adverse effects in devices caused by interface states are listed below:

(a)shielding external fields,
(b)causing unwanted carrier depletion or accumulation
(c)enhancing interface recombination,
(d)generating recombination–generation noise,
(e)causing drift and other instability phenomena
(f)adversely interacting with confined quantum states
(g)causing side–gating phenomena in planar structures.

On the other hand, one example of beneficial effects of Fermi level pinning is the strong Fermi level pinning at GaAs, M–S interfaces which has made GaAs MESFET LSIs possible.

Thus, understanding the origin of interface states is extremely important for successful control of interfaces including passivation. However, the mechanism responsible for the Fermi level pinning at semiconductor interfaces has not been well established yet, although it has been studied over 50 years since the days of the Schottky's ideal model[1] on the Schottky barrier at the M–S interface.

Recent extensive studies on semiconductor surfaces have revealed the existence of strong correlation among S–S, I–S, M–S interfaces, and based on these various models concerning the origin of Fermi level pinning have been proposed. Table 1 summarizes the major models for Fermi level pinning. It includes the Unified Defect Model by Spicer et al[2], MIGS(metal–induced gap state) model by Heine[3] and Tersoff[4], DIGS (disorder–induced gap state)model by the present author's group[5,6] and the effective workfunction (EWF) model by Woodall and Freeouf[7]. Since a detailed comparison of the models in favor of the authors' DIGS model was made previously[8], it is not repeated here.

As for the passivation technique, it is rather surprising that, in spite of numerous possible combinations of semiconducting and insulating materials, and in spite of the extremely advanced status of the semiconductor electronics, near–ideal passivation can be accomplished only in one combination of the semiconductor and insulator, i.e, silicon and silicon dioxide where the minimum interface state density, N_{ssmin}, within the range of 10^9 $cm^{-2}eV^{-1}$ can be achieved. This has led to tremendous success of silicon–based microelectronics. On the other hand, passivation of compound semiconductors still remains an unsolved technological issue because available minimum interface state density values are within the range of 10^{12}–10^{13} $cm^{-2}eV^{-1}$, causing Fermi level pinning. In this regard, it is interesting to note that the presence of an ultrathin ordered crystalline SiO_2 layer in well–behaved Si–SiO_2 interfaces, as schematically shown in Fig.3, has been reported by detailed TEM[9] and XPS[10] characterization. It strongly suggests that an ordered coherent termination of the semiconductor crystal is essential to obtain a well–behaved I–S interface, supporting the ideal of the DIGS model.

2.3 Interface State Distributions Measured by a Novel PL Technique

The shape of the distribution of the interface state density, N_{ss}, should provide important information, as is evident in Table 1. However, previous measurement techniques including high-frequency C–V (Terman's method), quasi-static C–V method, conductance method, DLTS method and ICTS method, can not determine the distribution over the entire bandgap, because filling of high density interface states causes electrostatic breakdown of the insulator film itself. Thus, it has not been clear whether the distribution has peaks as postulated by the Unified Defect Model, or it has a continuous U-shape as postulated by the DIGS model, as schematically shown in Fig.4(a).

Table 1 Major models on the mechanism of Fermi level pinning.

model	origin of pinning	N_{SS} distribution and pinning position	applicable interfaces	nature of pinning
Unified Defect Model	deep level related to stoichiometry, especially, As_{Ga}	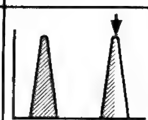	S-S, I-S, M-S	extrinsic
MIGS Model	penetration of metal wave function	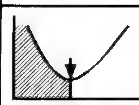 neutral level	M-S	intrinsic
DIGS Model	disorder of bonds at interface	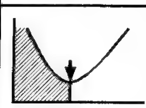	S-S, I-S, M-S	extrinsic
Effective Work Function Model	precipitation of As and P clusters at interface	pinned at E_F of metallic cluster	S-S, I-S, M-S	extrinsic

S-S : Semiconductor-Semiconductor Interface
I-S : Insulator-Semiconductor interface
M-S : Metal-Semiconductor interface

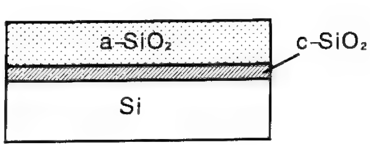

Fig.3 Recent model of Si-SiO₂ interface.

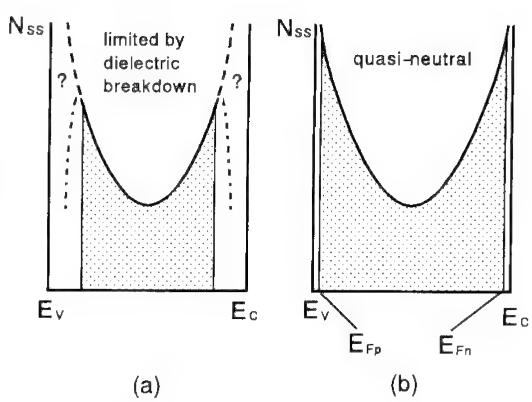

Fig.4 Determination of N_{ss} distribution (a)previous techniques limited by dielectric breakdown, (b)a PL-based new technique without breakdown problem.

This issue has been recently resolved by the novel photoluminescence surface state spectroscopy (PLS[3]) technique developed by the author's group [11]. This technique consists of a detailed measurement of excitation intensity dependence of the quantum efficiency of the band–edge PL efficiency and its subsequent rigorous computer analysis . In this technique, semiconductor surfaces are illuminated by a light source, and quasi Fermi levels for electrons and holes are swept over an entire band gap without causing dielectric breakdown as shown in Fig.4(b) owing to the quasi–neutral nature of the photo–excited surface region. The technique allows, for the first time, in-situ, non–destructive and contactless determination of surface state density (N_{ss}) distributions on the processed free surfaces of semiconductors.

Photoluminescence has been widely used for assessment of surfaces and quantum structures. However, previous PL intensity analysis has been only qualitative based on a phenomenological description of surface recombination processes in terms of a surface recombination velocity, S, and "dead" layer width, W, as schematically shown in Fig.5(a). In the new technique, a rigorous computer analysis is made of the physical situation shown in Fig.5(b), using the phenomenological semiconductor equations including SRH recombination processes through a surface state continuum. Such a computer analysis has indicated that the PL quantum efficiency and the corresponding effective surface recombination velocity exhibit three distinct regions versus excitation intensity as shown in Fig.6. At low excitation intensities, the efficiency takes a low constant value which is primarily determined by the pinning position of the surface Fermi level in the dark. On the other hand, at high excitation intensities, the efficiency approaches an intrinsic value limited by the bulk radiative and Auger recombination processes. The transition region between these two limits is related to photo–induced unpinning process where the quasi Fermi levels for electrons and holes scan the surface states within the energy gap. Thus, this region strongly reflects the N_{ss} distribution. By analyzing this region rigorously by computer, one can determine the N_{ss} distribution. Roughly speaking, the slope of the PL efficiency gives the distribution shape, being unity for discrete states.

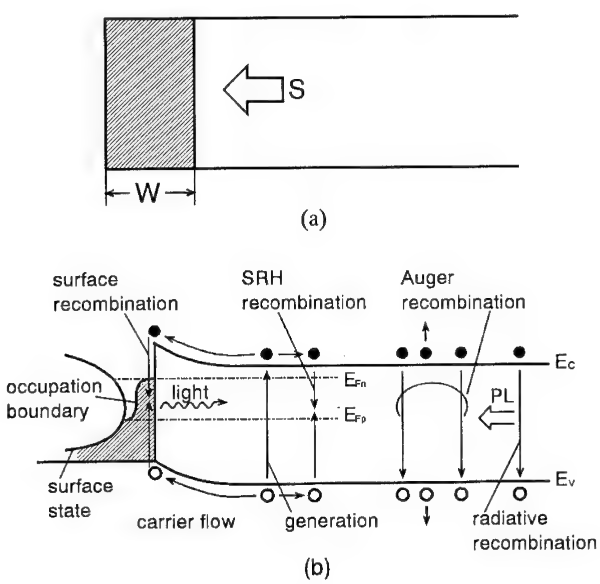

Fig.5 (a)Previous model for PL analysis and (b)the actual physical situation during measurement.

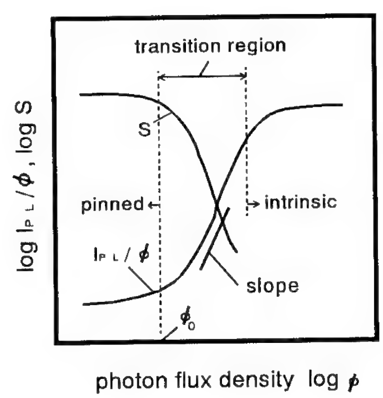

Fig.6 General behavior of PL quantum efficiency.

N_{ss} distributions were determined on as-received, freshly MBE grown, wet and dry etched, oxidized and insulator deposited surfaces of GaAs, InP, AlGaAs and InGaAs[12]. GaAs/AlGaAs and InGaAs/InAlAs S–S interfaces prepared by MBE growth interruption and regrowth were also investigated [13,14], since they are often used for fabrication of nano-structures. As schematically shown in Fig.7, all the distributions were found to be generally U-shaped with their minima occurring at the hybrid orbital charge neutral level, E_{HO}, [6], below and above which states are donor-type and acceptor-type, respectively. This is consistent with the DIGS model. E_{HO} is equivalent to the midgap energy by Tersoff[4]. E_{HO} was found to lie 0.47, 1.00 and 0.47 eV above the valence band maximum for GaAs, InP and $In_{0.53}Ga_{0.47}As$, respectively. The magnitudes of the density were found to be strongly dependent on the details of processing. Some example of the values of minimum density, N_{ssmin} measured on GaAs surfaces are summarized in the table attached to Fig.7.

3. Passivation Using Interface Control Layer

3.1 Basic Concept and Candidates for ICLs

The basic concept of the Interface Control Layer (ICL) is shown in Fig.8. ICL is inserted at the interface of two different materials. Its expected roles are the following:

(a) removing the interface states by providing a coherent and smooth transition of bonds from one material to the other.
(b) controlling the interface potential difference, or, the band discontinuity, by introducing an intrinsic dipole based on bond arrangements, or an extrinsic dipole by doping within this layer.

Thus, the ICL should provide suitable bond-matching to either side of the interface and should act as a reaction and diffusion barrier during interface formation to realize a sharp and well-defined interface. Based on the previous extensive study of the surface and interface of compound semiconductors, possible candidates of ICL are the following:

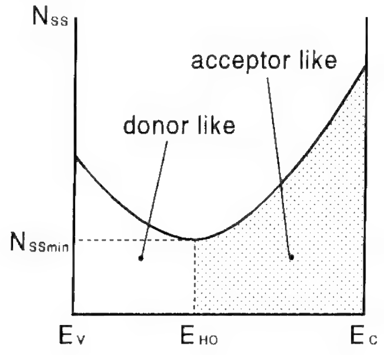

	$N_{ssmin}(cm^{-2}eV^{-1})$
as-received wafer	1.0×10^{12}
MBE growth	9.5×10^{11}
chemically etched	2.0×10^{11}
photo-CVD SiO_2 deposited	5.0×10^{11}

Fig.7 U-shaped interface state distribution with characteristic charge neutrality level E_{HO} which is generally observed by PLS[3] technique. Some measured data are given in the table.

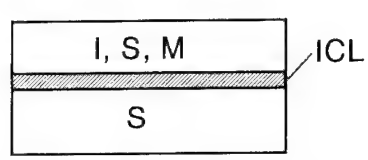

Fig.8 Concept of interface control layer(ICL).

(a) native oxides:
  $In(PO_3)_3$ for InP (Hollinger et al. 1985[15], Ishii et al. 1989[16])
  photochemical oxide of GaAs (Freeouf and Woodall 1986[17], Sawada et al. 1987[18])
(b) sulphides and selenides (Sandroff et al. 1987[19], Nannichi et al. 1988[20], Oigawa et al.1989[21], Sandroff et al. 1990[22], Kikawa et al. 1992[23])
(c) fluorides (Ishiwara et al. 1988[24], Waho et al. 1988[25])
(d) chloride (Hasegawa et al. 1988[26], Ishikawa et al. 1994[27])
(e) ultrathin silicon layer(Hasegawa et al. 1988[28], Tiwari et al. 1988[29], Fountain et al. 1988[30])
(f) ultrathin III–V epitaxial layer (Wada and Wada 1993[31])

Discussion on the applicability of the above candidates is beyond the scope of the present paper, and is not attempted here except to mention that the experiences by authors' group on the photo–chemical oxide of GaAs[18] and on sulphides [26], gave negative results. In the next section, a specific example of the use of ultrathin silicon layer as the ICL(Si ICL) is discussed in more detail.

3.2 Formation and Properties of Ultrathin MBE Silicon Layer as ICL

The basic idea for use of Si ICL for passivation is that it terminates surface bonds of the compound semiconductor by a pseudomorphic array of Si atoms which in turn make a smooth transition to an outer dielectric layer such as SiO_2 and Si_3N_4 layer[28,32]. The necessary conditions are the following:

(a) ICL should maintain pseudomorphic matching to the semiconductor,
(b) ICL should prevent direct oxidation of the semiconductor and
(c) ICL should form a good SiO_2/Si or Si_3N_4 interface.

Experiments were done using a totally UHV–based growth/fabrication/characterization system shown in Fig.9. Such a system may become necessary for fabrication of low–defect nano–scale quantum structures. Processing sequence includes the following:

(a) MBE growth of InGaAs, GaAs or AlAs
(b) MBE growth of Si ICL from a Si K–cell at a substrate temperature of 250°C
(c) thermal oxidation, photo–CVD deposition(SiO_2 or Si_3N_4) using an ArF excimer laser.

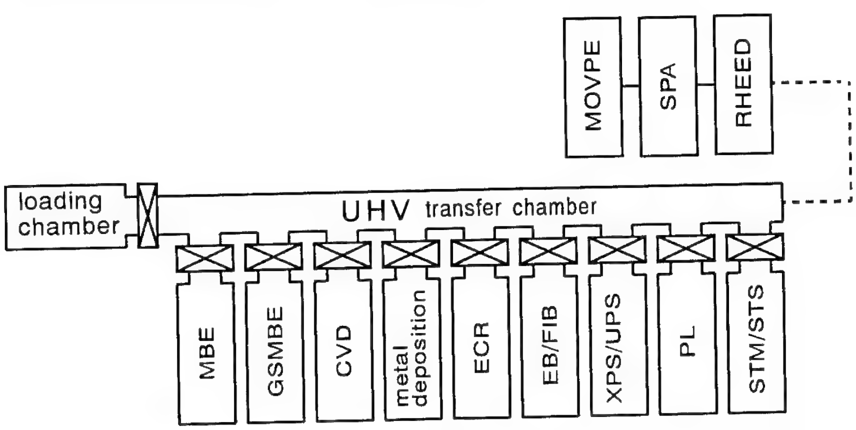

Fig.9. A schematic representation of a UHV-based fabrication/characterization system used in the present study.

The growth rate of the Si ICL was 20 Å/hour. Doping into the Si ICL was made by As and Ga both from the K–cell. The RHEED pattern quickly changed from the As stabilized (2x4) pattern to a (1x2) or (3x1) pattern during Si growth on GaAs, depending on whether the growth was done without As–supply or under the As stabilized condition, respectively.

The experiments were performed on GaAs and $In_{0.53}Ga_{0.47}As$ surfaces. When photo–CVD SiO_2 deposition is made directly onto the Si ICL, penetration of photo–excited oxygen radicals exceeds its critical layer thickness. For this reason, an improved structure involving partial thermal oxidation of the Si ICL was used[33]. The results of in–situ XPS analysis showing the improvement offered by inclusion of a thin thermal oxide layer is shown in Fig.10. Monolayer level process monitoring of suboxide components was made by in–situ XPS by separating the Si2p signal from the Ga3p signal and decomposing into suboxide components using the chemical shift data in the literature. In the case of deposition of Si_3N_4, this penetration problem has been found much less severe. An optimized process made simultaneous achievement of the above three conditions (a)–(c) possible, leading to an N_{ss0} of $1\text{–}2\times10^{11}cm^{-2}eV^{-1}$ for InGaAs with outer dielectric films of photo–CVD SiO_2 and Si_3N_4.

4. Application of Si ICL Approach

4.1 Fabrication of Field Effect Transistors

The most important device application of the passivated I–S interface is the gate dielectric of MISFETs. Particularly, depletion mode InGaAs MISFETs with a channel mobility as high as 3850 cm^2/Vs and an extremely small current drift (below 0.7 %) have been realized by UHV–processing[34].

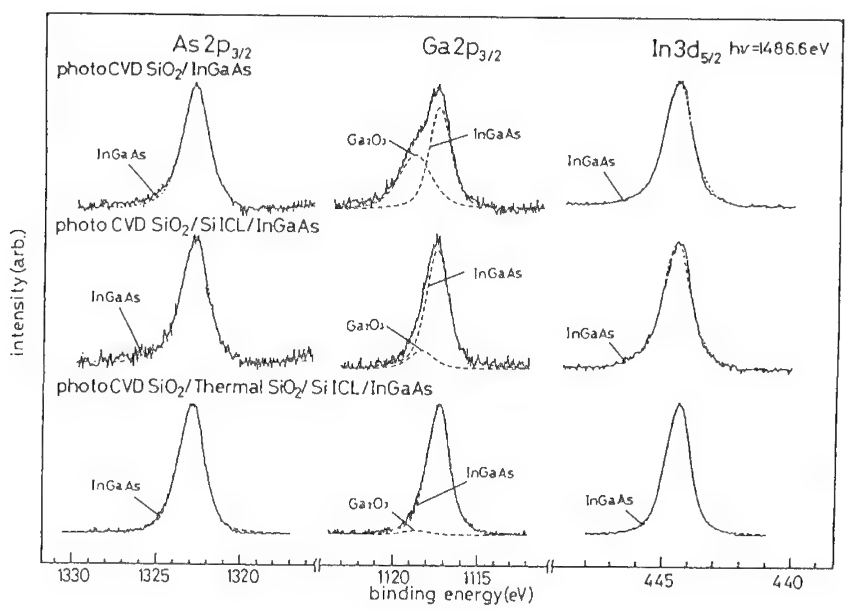

Fig.10 Effect of thin thermal oxide on the direct oxidation of InGaAs as revealed by an in–situ XPS analysis.

Such UHV–processing is not, however, compatible with the standard device processing sequence where InGaAs surface is exposed to air at a certain stage of processing. More recently, a modified Si ICL process for passivation of air–exposed surfaces has been developed, using an HF surface treatment, and successfully applied to fabrication of recessed gate InGaAs MISFET whose structure is shown in Fig.11[35].

4.2 Passivation of Near–Surface Quantum Wells

Since surfaces and interfaces play a far more important role in quantum structures than in the present–day devices, surface passivation becomes a critical issue for their successful utilization. In order to see the effect of the present Si ICL based passivation scheme on the quantum structures, it has been recently applied to near–surface $Al_{0.3}Ga_{0.7}As/GaAs/Al_{0.3}Ga_{0.7}As$ quantum wells (QW) shown in Fig.12(a).

With reduction of the top barrier thickness t_B of the $Al_{0.3}Ga_{0.7}As$ top barrier layer, the PL intensity normalized by the PL intensity from the inner reference QW is reduced [36]. According to Moison et al.[37], this is caused by interaction of confined QW states and surface states, as shown in Fig.12(b). However, remarkable recovery of PL intensity and the PL peak position was observed by application of the present passivation scheme on barrier surfaces as shown in Fig.12(c)[38], being consistent with the reduction of surface states.

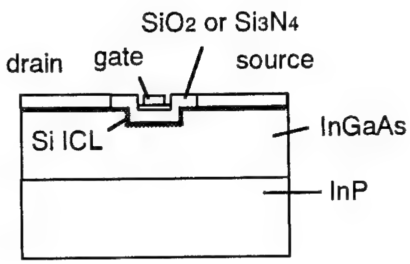

Fig.11 Structure of recessed gate InGaAs MISFET using Si ICL technique

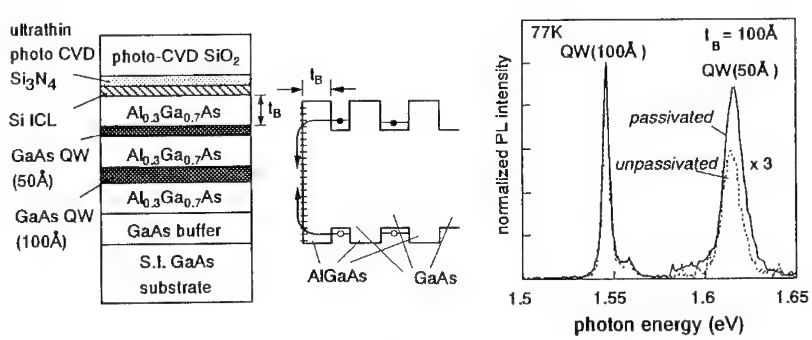

Fig.12 Passivation of near–surface quantum well by Si ICL technique: (a) sample structure, (b) band diagram and (c) effect of passivation.

4.3 Control of M–S Interface

The basic idea for control of the Schottky barrier height(SBH) using a metal/Si ICL/semiconductor structure is shown in Fig.13 [39]. It is assumed that the Fermi level is firmly pinned at the metal–ICL interface but not pinned at the ICL–semiconductor interface. For the undoped case, the band diagram becomes as shown in Fig.13(a) since the pinning at the metal–ICL interface and the band alignment at the ICL–semiconductor interface both take place at the hybrid orbital charge neutrality level E_{HO} [4][6]. When the ICL is sufficiently doped with donors, a high field resulting from ionized donors modify the SBH, as shown in Fig.13(b). The opposite takes place if it is doped with acceptors as shown in Fig.13(c).

For the doping into the Si ICL, the As, B and Ga beams supplied from K–cells were irradiated during the MBE growth of the Si ICL. The Fermi level positions before and after metal deposition were measured by XPS core level shifts and C–V/I–V analysis, respectively. Both results agreed well after taking account of the surface photovoltaic effect in XPS measurements indicating that firm pinning of the Fermi level exists even before metal deposition. It was found that As and B doping was effective but not Ga–doping. By doping As and B into Si ICL to different doping levels, SBH could be precisely controlled over about 400meV for both n– and p–type samples of GaAs and InP. The SBH value was very reproducible and the ideality factor n was close to unity (n<1.05), as long as the Si ICL was about or below the estimated critical thickness of about 10 Å.

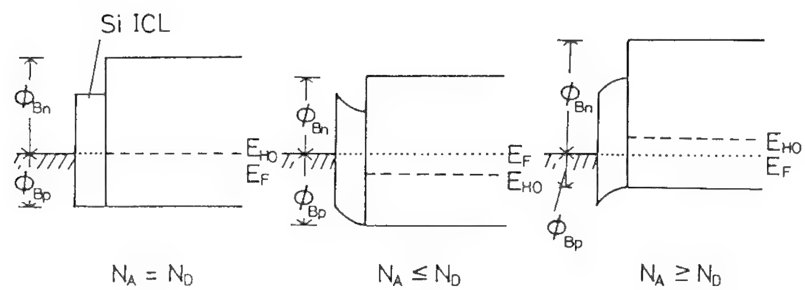

Fig.13 Principle of SBH control by Si ICL.

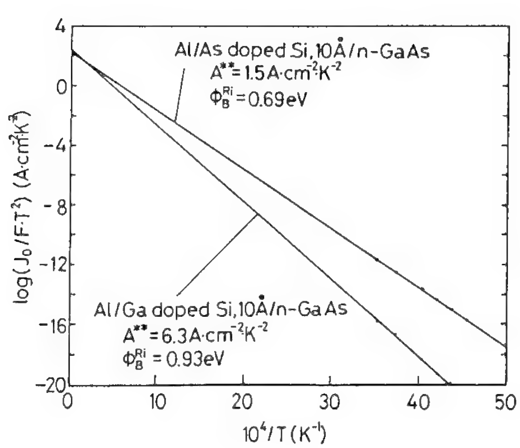

Fig.14 Modified Richardson plot of Al/Si ICL/GaAs Schottky diodes.

By a detailed analysis of the temperature dependence of C–V and I–V data, the effective Richardson constant A** of the Al/Si ICL/GaAs Schottky barrier was determined using a modified Richardson plot shown in Fig.14, where F is a correlation factor for tunneling. It was found that the values of A** was in the range 2–6 $Acm^{-2}K^{-2}$ being close to the theoretical value for GaAs of 8.2 $cm^{-2}K^{-2}$. This indicates that the Si ICL does not block the current transport.

It is obvious that control of SBH is useful to MESFETs and HEMT. Additionally, it may find important applications in the field of quantum devices. As an example, it can produce a large amplitude spatial modulation of potential over a short distance, as a result of computer simulation shown in Fig.15 indicates. If such modulation can be realized, fabrication of quantum devices becomes much easier as well as enhanced operation temperatures.

4.4 Control of S–S Interface

Feasibility of band line–up change by the ICL–induced dipole shift was recently proposed theoretically [40],[41] and verified experimentally [42]. The effect is schematically shown in Fig.16(a) and (b). In order to confirm the presence of such an effect, the effects of insertion of a Si ICL at GaAs/AlAs and InGaAs/InAlAs interfaces were investigated by XPS.

The results of XPS measurements are shown in Fig.17. Insertion of a Si ICL resulted in very large relative shifts of core levels for the GaAs–AlAs interface whose magnitudes are in excellent agreement with the data of Sorba et al [42]. Much smaller shifts were observed for InGaAs–InAlAs.

However, the following two additional effects were observed on the XPS spectra both of which were difficult to explain by the interface dipole model.

(a) anomalous increase of the energy separation between the core level (E_{CL}) and the surface valence band maxima (E_{vs}).
(b) anomalous increase of the FWHM of core level signals of the outer layer.

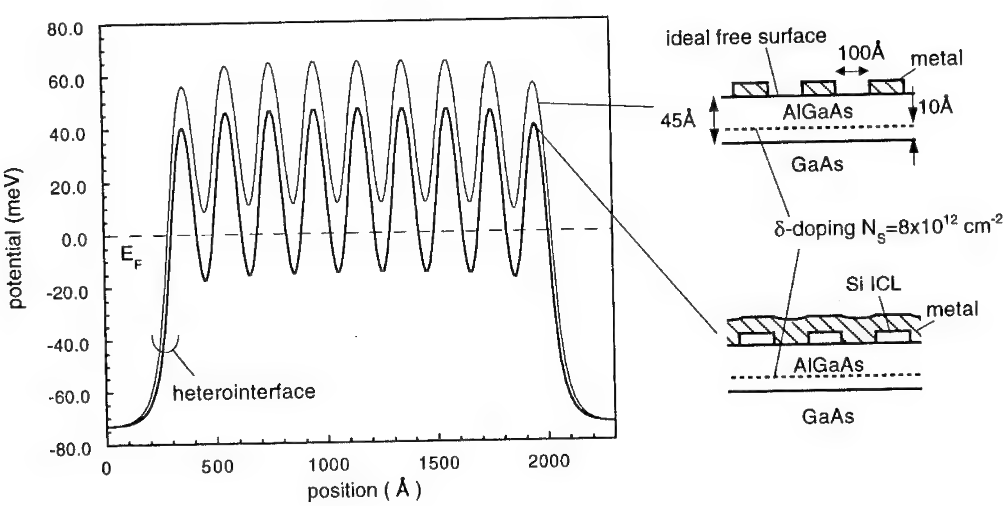

Fig.15 Expected spatial potential modulation with the use of Si ICL

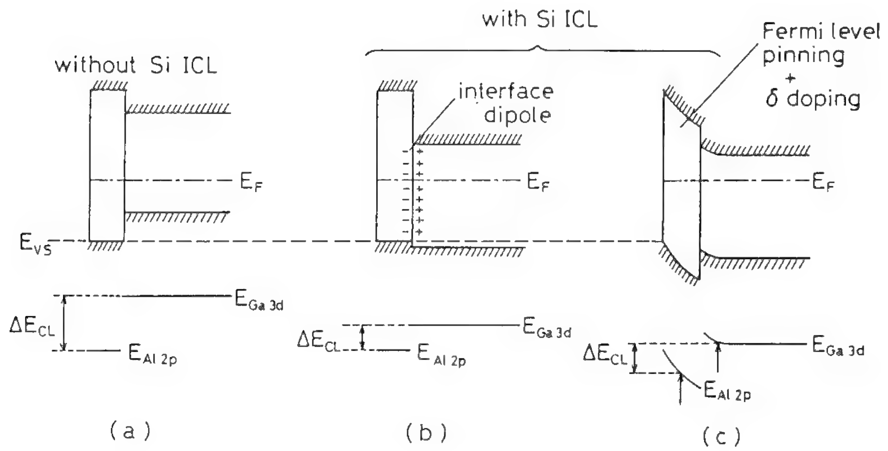

Fig.16 Schematic band diagram for interface dipole model [(a) and (b)] and δ–doped interface model [(a) and (c)] explaining apparent change of ΔE_V.

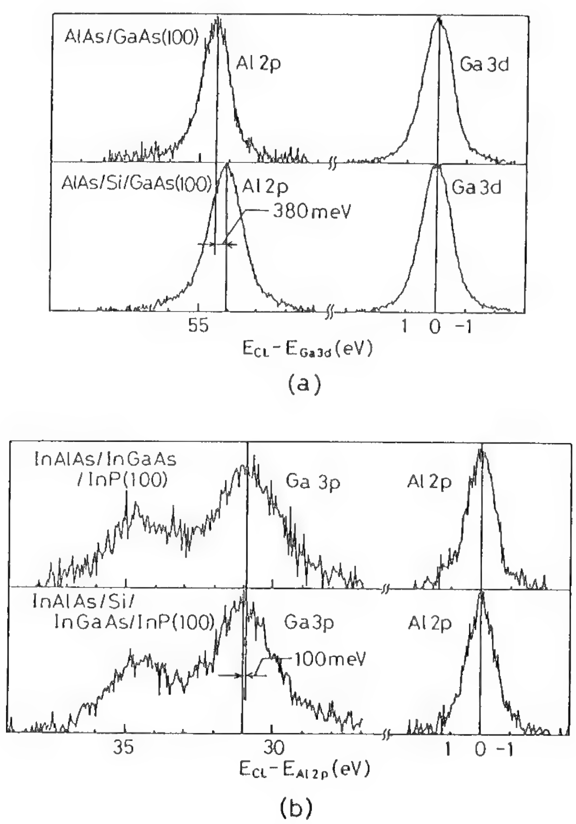

Fig.17 Observed XPS core level spectra showing Si–induced shifts, (a) AlAs/GaAs interface and (b) InAlAs/InGaAs interface.

The observed anomalous behavior was found to be quantitatively explained by the new model without modification of E_v[43]. In this model, as shown in Fig.16(c), the delta–doping effect combined with the near–midgap Fermi level pinning at the surface produces a high field within the escape depth of photoelectrons and modifies the peak position and shape of the core level spectra. By assuming reasonable parameter values for delta doping with recent reports, the observed values of ($E_{vs}-E_{CL}$) and FWHM increase can be completely reproduced on computer. One way to avoid Si diffusion may be the use of the migration–enhanced–epitaxy (MEE) growth at low temperatures which is presently being investigated.

5. Conclusions

(1) Interface control technology including passivation becomes a key issue for further advances of semiconductor electronics.

(2) ICL concept and technologies may provide acceptable solutions to the above interface issue.

References

[1] W.Schottky, Phys. Rev. **41**, 570 (1940).
[2] W.E.Spicer, I.Lindau, P.R.Skeath and C.Y.Su, J. Vac. Sci. Technol. **17**, 1019 (1980).
[3] V.Heine, Phys. Rev. **138**, 1689 (1965).
[4] J.Tersoff, Phys. Rev. Lett. **52**, 465 (1984).
[5] H.Hasegawa and T.Sawada, Thin Solid Films **103**, 119 (1983).
[6] H.Hasegawa and H.Ohno, J. Vac. Sci. Technol. **B4**, 1130 (1986).
[7] J.M.Woodall and J.F.Freeouf, J. Vac. Sci. Technol. **19**, 794(1981).
[8] H.Hasegawa, Solid–State Electron. **33**, Supplement, 201(1990).
[9] A.Ourmazd, P.H.Huoss, J.Bevk and J.F.Morar, Appl. Sur. Sci. **41/42**, 365(1989).
[10] K.Onishi and T.Hattori, Jpn. J. Appl. Phys. **33**, L675(1994).
[11] T.Saitoh, H.Iwadate and H.Hasegawa, Jpn. J. Appl. Phys. **30**,3750(1991).
[12] T.Sawada, K.Numata, S.Tohdoh, T.Saitoh and H.Hasegawa, Jpn. J. Appl. Phys. **32**, 511(1993).
[13] T.Sawada, T.Saitoh, H.Fujikura, H.Tomozawa, S.Tohdoh, and H.Hasegawa, *Int. Symp. on Gallium Arsenide and Related Compounds 1992, Karuizawa, Japan,* Inst. Phys. Conf. Ser. No. 129, (IOP Publishing, UK, 1993), pp.387.
[14] T. Saitoh, H.Tomozawa, T.Nakagawa, H.Takeuchi and H.Hasegawa, *presented at 8th Int. Conf. Molecular Beam Epitaxy, Osaka, Japan (1994)*, to be published in J. Crystal Growth.
[15] G. Hollinger, E. Bergignat, J. Joseph and Y. Robach, J. Vac Sci Technol. **A3**, 2082(1985).
[16] H. Ishii, H. Hasegawa, A. Ishii and H. Ohno, Appl. Sur. Sci. **41/42**, 390(1989).
[17] J.L. Freeouf and J.M. Woodall, Surface Science, **168**, 518(1986).
[18] T. Sawada, H. Hasegawa and H. Ohno, Jpn. J. Appl. Phys. **26**, L1871(1987).
[19] C.J. Sandroff, R.N. Nottenberg, J.–C. Bischoff and R. Bhat, Appl. Phys. Lett. **51**, 33(1987).
[20] Y. Nannichi, J.–F. Fan, H. Oigawa and A. Koma, Jpn. J. Appl. Phys. **27**, L2367(1988).
[21] H. Oigawa, J.–F. Fan, Y. Nannichi, K. Ando, K. Saiki, A. Koma, Jpn. J. Appl. Phys. **28**, L340(1989).
[22] C.J. Sandroff, M.S. Hedge, L.A. Farrow, R. Bhat, J.P. Harbison and C.C. Chang, J. Appl. Phys. **51**, 586(1990).
[23] T. Kikawa, S. Takatani and Y. Tezen, Appl. Phys. Lett. **60**, 2785(1992).
[24] H. Ishiwara, K.H. Kim, K. Tsutsui, T. Asano and S. Furukawa, *Electrochemical Society Proc. Symp. "Dielectric Films on Compound Semiconductors"*, ed. by V.J. Kapoor, **88–15**, 278 (The Electrochemical Society, Pennington, 1988)
[25] T. Waho and F. Yamanaka, IEEE Electron Device Lett. **EDL–9**, 548(1988).
[26] H. Hasegawa, H. Ishi, T.Sawada, T. Saitoh, S. Konishi, Y. Liu and H. Ohno, J. Vac. Sci. Technol. **B6**, 1184(1988).
[27] Y. Ishikawa, H. Hasegawa, H. Ishii and T. Fukui, to be published in J. Vac. Sci. Technol. **B12**, July/August issue (1994).
[28] H. Hasegawa, M. Akazawa, K. Matsuzaki, H. Ishii and H. Ohno, Jpn. J. Appl. Phys. **27**, L2265(1988).
[29] S. Tiwari, S.L. Wright and J. Batey, IEEE Electron Device Lett. **9**, 488(1988).

[30] G.G. Fountain, S.V. Hattangady, D.J. Vikavage, R.A. Rudder and R.J. Markunas, Electron. Lett. **24**, 1135(1988).
[31] Y. Wada and K. Wada, J. Vac. Sci. Technol. **B11**, 1589(1993).
[32] M. Akazawa, H. Ishii and H. Hasegawa, Jpn. J. Appl. Phys. **30**, 3744 (1991).
[33] S. Kodama, M. Akazawa and H. Hasegawa, J. Electron. Mater. **22**, 289 (1993).
[34] M.Akazawa, H.Hasegawa and E.Ohue, Jpn.J.Appl.Phys. 28, L2095(1989).
[35] Y.-G. Xie, S.Suzuki, T.Sawada and H.Hasegawa, Trans. the Institute of Electronics, Information and Communication Engineers of Japan, **J77- C-II**, 501(1993) [in Japanese].
[36] Z.Sobiesierski, D.I.Westwood, D.A.Woolf, T.Fukui and H.Hasegawa, J.Vac.Sci.Technol. **B11**, 1173(1993).
[37] J.Moison, K.Elcess, F.Housay, J.Y.Marzin, J.M.Gerard, F.Barthe and M.Bensoussan, Phys. Rev. B **41**, 12945(1990)
[38] S.Kodama, S.Koyanagi and H. Hasegawa, *presented at Int. Conf. Solid State Devices and Materials (SSDM'94), Yokohama, Japan,* to be published in Jpn. J. Appl. Phys.
[39] K. Koyanagi, S. Kasai and H. Hasegawa, Jpn. J. Appl. Phys., **32,** 502 (1993).
[40] A. Muñoz, N. Chetty and M.R. Martin, Phys. Rev. B, **41,** 2976 (1990).
[41] M. Peressi, S. Baroni, R. Resta and A. Baldereschi, Phys. Rev. B, **43,** 7347 (1991).
[42] L.Sorba, G.Bratina, G.Ceccone, A.Antonini, J.F.Walker, M.Micovic and A.Franciosi, Phys. Rev. **B43**, 43(1991).
[43] M. Akazawa, H. Hasegawa, H. Tomozawa and H. Fujikura, Jpn. J. Appl. Phys., **31,** 1012(1992).

Materials Science Forum Vols. 185-188 (1995) pp. 37-42

A comparison of the oxidation and passivation of Si, Ge and InP

E.A. Irene

Department of Chemistry, University of North Carolina, Chapel Hill NC 27599-3290, U.S.A.

Keywords: Semiconductor, passivation, films

Abstract

The electronic passivation of semiconductors is key to achieving useful electronic devices. This is usually accomplished through the growth of dielectric films on the semiconductor surfaces which not only reduces the density of surface electronic states, but also acts to support electric fields for device operation. Therefore, the dielectric film formation mechanisms and the relationship to the electronic properties of the resulting interfaces are crucial to modern device operation. This paper compares oxide growth on monatomic semiconductors (Si and Ge) with compound semiconductors (InP). It is found that the chemistry that occurs at the interface during dielectric film formation is crucial in determining electronic properties, and based on this chemistry, processes that produce electronically passive interfaces can be deduced.

INTRODUCTION

Electronic passivation is herein defined as the reduction of surface electronic states on a semiconductor surface to a level below the number of carriers that are needed for device operation. The so-called surface states arise from a number of sources, and the common progenitors are listed with the help of Figure 1. It is seen that all the features shown in the cartoon are defects which gives rise to an altered interatomic potential, which in turn yields new states that are different from the electronic states obtained from the bulk crystal crystal potential. Indeed, just the mere termination of the crystal lattice at a surface gives rise to dangling bonds which result in intrinsic surface electronic states. Other electronic states that arise due to some kind of external effect are termed extrinsic surface states.

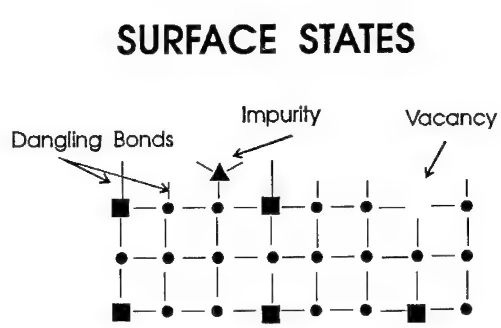

Figure 1. A pictorial representation of a variety of semiconductor surface features that can give rise to surface electronic states including unsatisfied surface bonding orbitals (dangling bonds), missing atoms (vacancies), and impurities or dopants or altered stoichiometry.

On a Si surface (and many other semiconductor surfaces) the number of intrinsic states are of the same order as the number of surface atoms, $\sim 10^{15}cm^{-2}$. Thus the density of intrinsic states can vary with the crystal orientation. It seems intuitive that the formation of a stable chemical reaction product on the Si surface would tie up the dangling bonds and reduce the number of intrinsic states. To first order this intuition is correct. However, the precise nature of the reaction and the products can influence not only the intrinsic states, but also the extrinsic states. For example reactions that are performed under energetic ion beam and/or plasma stimulation provide considerable excess energy which may also induce vacancies and/or interstitials or even other unwanted reactions producing different products than desired and extrinsic surface states. These kinds of reactions are becoming popular in microelectronics processing, because of the reduction in thermal excitation which causes interdiffusion problems such as dopant migration and the resulting loss of device junction tolerances.

Si PASSIVATION

The oxidation and passivation of Si has been studied extensively (see for example ref. [1] and references therein) during the past thirty years. The success with the electronic passivation of Si is the primary reason for the overwhelming preeminence of Si as the semiconductor in commercial applications. However, Si is not the best semiconductor in terms of electronic properties, and it would be desirable to be able to passivate Ge, InP and GaAs and other semiconductors, in order to improve device speed and versatility (opto-electronic applications). The reader desiring a more complete review of Si passivation is referred to the extensive literature (for a start see ref. [1] and refs. therein). For the present paper we review only a few salient points. First it is reasonably that a linear-parabolic rate law obtains where the time evolution of the SiO_2 thickness has linear and squared dependence and there are essentially two processes represented by two fluxes in a steady state (the linear-parabolic rate law is derived at $F_1 = F_2$) in Figure 2. One flux represents the inward diffusion of oxidant through the growing oxide film, F_1, while the other, F_2, represents the flux of oxide being produced by the interfacial reaction between Si and oxidant.

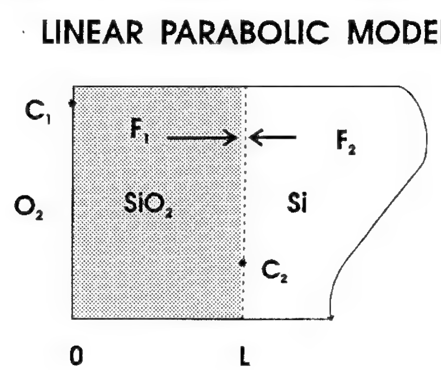

Figure 2 The linear-parabolic thermal oxidation model for Si. C_1 and C_2 are the oxidant concentrations at the outer and inner interfaces, respectively, and L is the SiO_2 thickness.

The fact that we consider only the inward flux of O is the result of $O^{18}{}_2$ tracer and other studies (see the several references to this work in ref [1]). As a result of clean thermal oxidation of high quality single crystal Si wafers, the surface electronic states are reduced from $\sim 10^{15}cm^{-2}$ to less than $\sim 10^{10}cm^{-2}$ or more than five orders of magnitude. It should be mentioned that the states resulting from film growth are no longer at the Si surface, but rather are located at a film-substrate interface and thus should be called interface states. Often both terms are used interchangeably.

We [2] and others [3] also studied the electron cyclotron resonance (ECR) plasma oxidation of Si and the kinetics are similar to thermal oxidation in that the rate of oxidation decreases with time. However, the activation energy for transport of oxidant in ECR oxidation is about 5x smaller with a pronounced substrate bias voltage effect indicating the dominance of charged atomic species, likely O^- moieties. In addition under careful processing, it is possible to obtain interfaces nearly as good electrically as those from thermal oxidation [3]. From optical measurements the same phases are present at the interface for ECR plasma oxidation as for thermal oxidation [2].

Ge PASSIVATION

For the case of the thermal oxidation of Ge, the resulting GeO_2 is thermodynamically stable at room temperature but decomposes at the GeO_2-Ge interface by a disproportionation reaction at temperatures near 500°C and higher. Si does the same but the reaction is not significant until above 900°C thereby permitting a wider thermal processing window. Also, GeO_2 is soluble in H_2O and thus degrades when exposed to atmospheric conditions. For these reasons Ge has never achieved the notoriety of Si.

We have studied both the thermal and ECR plasma oxidation of single crystal Ge [4]. A perusal of the results in Figure 3 shows that the kinetics are similar as was the case for Si mentioned above.

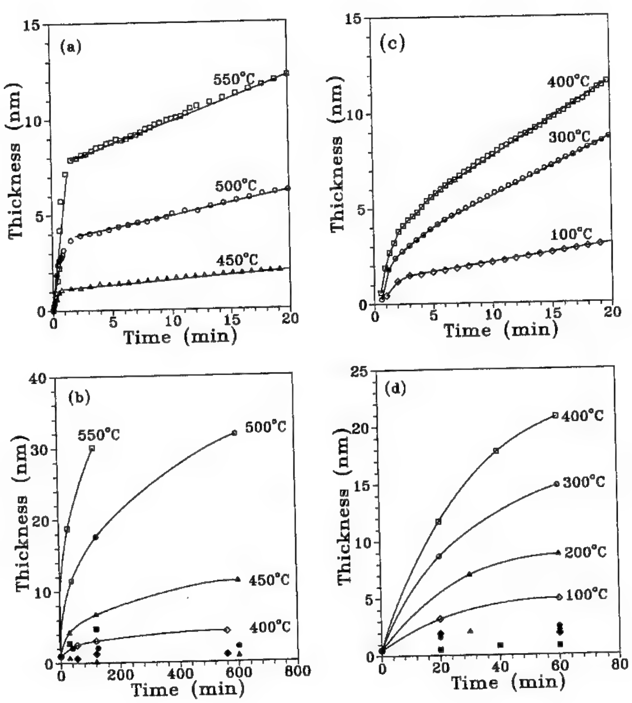

Figure 3. Oxide thickness vs oxidation time for c-Ge oxidation at different temperatures [4]. (a) and (b) are for thermal oxidation while (c) and (d) are for ECR plasma oxidation at +60V substrate bias. (a) and (c) are from real-time single wavelength ellipsometry measurements and (b) and (d) are from spectroscopic ellipsometry measurements using a two layer model. The oxide thicknesses are given by open symbols and interface layer thickness is given by solid symbols

A detailed analysis of the optical data and chemical analyses of the resulting oxidation products shows that the Ge oxidation behavior is virtually the same as for Si. Both thermal and ECR plasma oxidation of c-Ge yields a-GeO_2 with an interface or transition layer extending less than 2 nm and for optical modeling purposes consists of a mixture of a-Ge and GeO_2; the situation for Si oxidation was that the interface layer models well as a mixture of a-Si and SiO_2. While this model gives an excellent fit to the optical data and is totally in accord with XPS and IR data, the result is not totally unambiguous, because we do not have sufficient optical reference data to try to fit all other models. In fact at the outset of this study we had to commence with a detailed optical study of GeO_2 on c-Ge [5]. In progress is a study of the O^{18} diffusion into growing GeO_2 films, to confirm that the oxidation is via the inward migration of O, but until these results are available we have some reason to believe that the transport mechanism is the same as for Si.

In terms of electronic passivation, we obtain from high frequency capacitance-voltage measurements clear evidence for carrier inversion (formation of depletion region) which is a good indication of low interface state levels ($< 10^{12}$ cm^{-2}) and reasonably low levels of interface charge ($<10^{11}$ cm^{-2}) without the use of cleanroom processing or high quality materials [4]. Therefore, there is substantial reason to believe that Ge behaves much like Si, and under ideal conditions (low T and humidity) thermal oxidation would electronically passivate the Ge surface.

InP PASSIVATION

The oxidation of InP has been studied using ex-situ chemical analyses (Auger and XPS) [6] where a two layer oxide was found. We have confirmed that distinct layers form using chemical etch rate measurements and ellipsometry [7]. Essentially, it was reported that the very initial layer that forms is a stoichiometric oxide with the formula $InPO_4$. After this layer forms further oxidation yielded a mixed outer layer (In_2O_3 and $InPO_4$) over the $InPO_4$ layer with excess P in the substrate. This situation is depicted in Figure 4 [8].

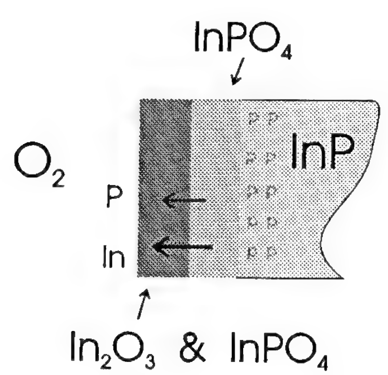

Figure 4 Schematic of the result of oxidizing InP. A two layer film is formed.

In order to further elucidate this mechanism we performed a study of thermal oxidation using $O^{18}{}_2$ as the oxidant. First oxidation was carried out in $O^{16}{}_2$ then the ambient was switched to $O^{18}{}_2$ and then SIMS analysis was done. The result was that the O^{18} containing oxide was found only at the outer oxide surface [8]. This work provided a consistent mechanism. First a stoichiometric $InPO_4$ is formed at the bare or thin oxide covered InP. However, as the oxide thickens the InP and oxidant are separated and transport must occur, in order to continue the reaction. In the InP case the In and P must migrate outward (in contrast to the Si and Ge cases).

If the In^{+3} and P^{-3} come from the substrate, then the smaller In^{+3} ion would likely migrate faster leaving excess P behind. This explanation is not yet full confirmed, but is consistent with all the data thus far produced.

On the issue of electronic passivation, the excess P would give rise to impurity states and an unpassivated InP-oxide interface which is observed upon thermal oxidation. Indeed there are many reports of high interface states for thermally oxidized InP. We commenced experiments to perform the oxidation on InP in an ECR plasma and follow the oxidation using in-situ real time ellipsometry and ex-situ XPS analyses of the oxides [9,10]. In this way we could detect the appearance of P and then try to control it. Essentially we found that for the first 2-3 nm of oxide formation, no excess P was observed. In addition if we used a shutter in between the plasma and sample, the InP surface is protected from direct ion trajectories and UV excitation, both of which have been reported to cause damage on semiconductors. Thus we oxidized briefly using real time ellipsometry and stopped the oxidation at about 3 nm. Then we covered the 3 nm film with 70 nm plasma deposited SiO_2 made in-situ without removing the oxidized InP. The high frequency C-V data is shown in Figure 5 and indicates both a low interface state density with an inverted InP surface and low charge levels. No attempt has been made to optimize this process. Our purpose here was to show how the control of interface chemistry dictates the surface state density and the final electronic properties.

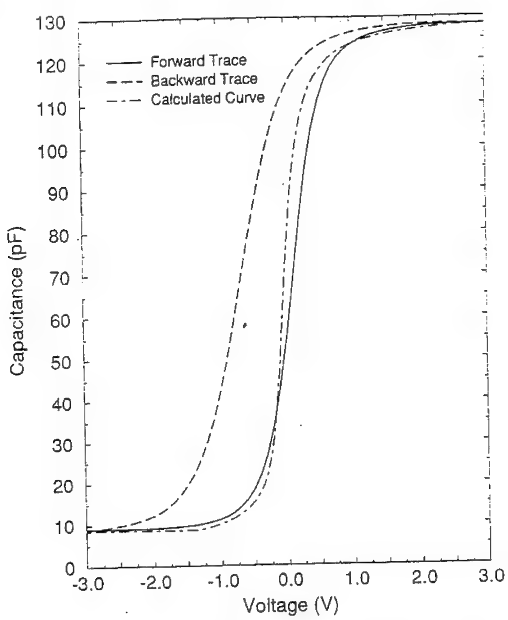

Figure 5 Typical 1 MHz C-V traces for 70 nm PECVD-SiO_2/3 nm ECR-oxide/n-InP (N_D= 2.2 x 10^{14} cm^{-3}) with Au gate (Area = 2.1 x $10^{-3}cm^2$) samples made with a shutter between the plasma and InP sample. The calculated curve is for 10 nm SiO_2 on InP.

CONCLUSIONS

It has been shown that interface electronic states at semiconductor-dielectric film interfaces are in large part controlled by interfacial chemistry. A detailed knowledge of the mechanisms of the interface formation is fundamental for the development of processes that electronically passivate the semiconductor-dielectric film interface.

ACKNOWLEDGEMENTS

The author gratefully acknowledges the support of this research by the Office of Naval Research, ONR and the National Science Foundation, NSF for support of our passivation studies and energetic processing studies, respectively. The work reported from our group was primarily due to the efforts of Profs. Y.Z. Hu, and J. Joseph and Drs. J. -Th. Zettler and X. Liu and Y. Wang.

REFERENCES

[1] E.A. Irene, CRC Critical Reviews in Solid State and Materials Science, Ed. J.E. Greene, Vol 14(2), pp 175-223 (1988).

[2] Y.Z. Hu, J. Joseph and E.A. Irene, Appl. Phys. Lett., 59, 1353 (1991); J. Joseph, Y.Z. Hu, and E.A. Irene, J. Vac. Sci. and Tech. B, 10, 611 (1992).

[3] D.A. Carl, D.W. Hess, M.A. Lieberman, J. Vac. Sci. Technol A, 8, 2924 (1990); D.A. Carl, D.W. Hess, M.A. Lieberman, T.S. Nguyen and R. Gronsky, J. Appl. Phys., 70, 3301 (1991).

[4] Y.Z. Hu, Y. Wang, M. Li and E.A. Irene, J. Vac. Sci. Technol. A., 11(4), 900 (1993); Y. Wang, Y.Z. Hu and E.A. Irene, J. Vac. Sci. Technol. A, 12, 1309 (1994).

[5] Y.Z. Hu, J.-Th. Zettler, S. Chongsawangvirod, Y.Q. Wang and E.A. Irene, Appl. Phys. Lett., 61(9), 1098 (1992).

[6] A. Nelson, K. Geib and C.W. Wilmsen, J. Appl. Phys., 54, 1108 (1983).

[7] X. Liu, J.W. Andrews and E.A. Irene, J. Electrochem. Soc., 138, 1106 (1991).

[8] X. Liu, M.S. Denker and E.A. Irene, J. Electrochem. Soc., 139, 799 (1992).

[9]. Y.Z. Hu, M. Li, Y. Wang, E.A. Irene, M.Rowe and H.C. Casey Jr., Appl. Phys. Lett., 63, 1113 (1993).

[10]. Y.Z. Hu, J. Joseph and E.A. Irene, J. Vac. Sci. Technol. B, 12(2) 540 (1994).

Materials Science Forum Vols. 185-188 (1995) pp. 43-52

Laser interferometry and SXM-techniques for thermal characterization of thin films

E. Oesterschulze, L. Hadjiiski, M. Stopka and R. Kassing

Institute of Technical Physics, University of Kassel, D-34109 Kassel, Germany

Keywords: Laser-interferometry, photo-thermal techniques, thermal characterization, scanning microscopy techniques, scanning thermal microscopy (SThM)

Abstract Photo-thermal measurement techniques are appropriate for the quantitative investigation of thermal properties of thin films and substrates. A photo-thermal interferometer set-up was designed for the detection of the thermal expansion of laser heated samples. A detection limit of 0.2 pm was achieved which corresponds to a temperature resolution of about 10^{-5} K. For the evaluation of the measurement data we used simulations based on finite element method (FEM). We successfully determined the value of the thermal diffusivity of thin films and metal substrates.

Mostly photo-thermal techniques are based on optical measurement methods limiting the lateral resolution to the optical wavelength. To enhance the lateral resolution we have replaced the laser interferometer with a scanning tunneling microscope (STM) set-up applying a miniaturized thermocouple probe instead of a conventional tunneling tip. We will present first results on silicon and diamond samples measured with the scanning thermal microscope (SThM) yielding a lateral resolution of about 100 nm.

1 Introduction

In recent years it was often shown that photo-thermal measurement techniques are capable of investigating thermal properties of materials [1, 2]. These methods are based on the optical absorption of a modulated laser beam and the subsequent investigation of the thermal relaxation processes occuring in the sample. One of the most sensitive methods is the interferometric measurement of the thermal expansion of a sample surface heated by a laser beam [3, 4]. Because of the non-contact and non-destructive detection technique it is compatible to vacuum conditions and may be used for *in-situ* characterization of deposition processes.

Owing to the optical measurement technique the lateral resolution of photo-thermal methods is restricted to the wavelength of the applied laser beam. To collect information about the thermal properties on a microscopic scale we replaced the laser interferometer with a scanning tunneling microscope (STM). We introduced a miniaturized thermocouple probe instead of the tunneling tip following the idea of Williams and Wickramasinghe [5, 6]. Using this approach it is possible to investigate the energy transport mechanisms in thin films, e.g. the influence of grain boundaries on thermal transport processes.

In this paper we will mostly concentrate on the quantitative evaluation of the thermal properties of substrates and thin metal films using the interferometer set-up. The data evaluation is done by finite element simulations of the thermal and mechanical behaviour of the samples. Finally we present thermal images of silicon and diamond samples using the scanning thermal microscope (SThM) and give a short discussion of these results.

2 Experimental

2.1 Photo-thermal Laser Interferometry

In the case of the photo-thermal laser interferometer a periodically modulated Ar^+-ion laser beam is used for optical heating of samples. The principle of this method is based on the phase sensitive

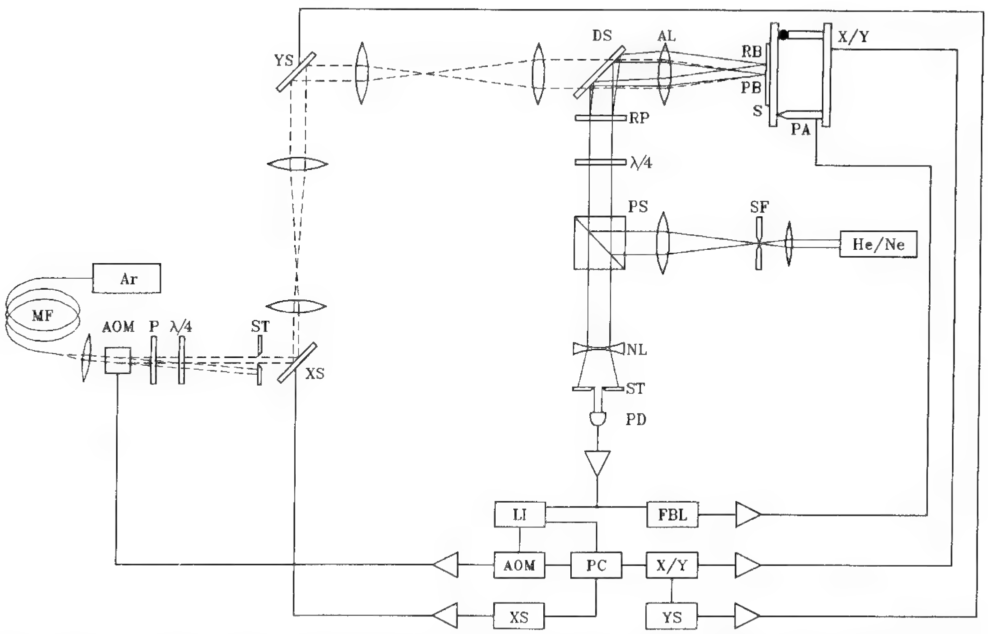

Figure 1: Photo-thermal laser interferometer set-up used for the locally resolved investigation of the thermal expansion of laser heated samples.

measurement of the thermal expansion of the sample surface as a function of the distance between the heat source and the point of detection. In Fig. 1 the set-up of the laser interferometer is shown.

The beam of the Ar^+-ion laser (AR) (Spectra Physics 164) with a wavelength of 488 nm and a maximum output power of 1 W is transmitted through an optical monomode fiber (MF). The periodical modulation of the beam is done by an acousto-optical modulator (AOM). To avoid backscattering of the beam into the plasma tube of the laser an optical isolator composed of a polarizer and a zero-order quater wave plate (P, $\lambda/4$) was installed. After passing a scanning system consisting of two afocal scanner units (XS, YS) and the dicroic beam splitter (DS), the laser beam is focused onto the sample surface (S) by an achromatic lens (AL). The scanning units are necessary to vary the distance between the Ar^+ ion laser beam and the probe beam (PB) of the interferometer on the sample surface.

For the detection of the thermal expansion of the surface a differential interferometer was designed. The interferometer employs a linearly polarized He/Ne laser beam of 633 nm wavelength and 5 mW optical power. The laser beam is spatially filtered (SF) and enters the optical path of the differential interferometer after reflection at a polarizing beam splitter (PS). A rochon prism (RP) separates the beam into two orthogonal polarized beams: one of them being the reference (RB) and the other one the probe beam (PB). A quater wave plate ($\lambda/4$) was additionally inserted to facilitate the alignment of the optical preference direction of the rochon prism. After passing the rochon prism both beams are reflected at a dicroic beam splitter (DS) and are focused onto the sample surface (S) with the acromatic lens (AL). Adjusting the center of the rochon prism to the back focal plane of the achromatic lens ensures that the optical path of the beams which are reflected from the sample surface (S), is the same for the incident beams. The reflected beams interfere while passing the polarizing beam splitter (PS) which in this case works as an polarization analyzer. The interferogram is dispersed by a negative lens (NL) and only a small part of it limited by an optical stop (ST) is finally detected with a photo diode (PD). The intensity is measured phase sensitively with a lock-in amplifier (LI) (Stanford Research Systems, SR 530).

To enhance the measurement sensitivity the detected signal is fed back to a piezo actuator (PA)

attached to the sample holder to compensate low frequency vibrations (f<10 Hz). Additionally the feedback loop (FBL) adjusts and keeps the working point of the interferometer constant. Furthermore for the locally resolved investigation of the thermal properties the sample is mounted on a motor driven stage (X/Y). The electronic equipment is controlled by an AT-compatible personal computer (PC).

2.2 Scanning Thermal Microscope (SThM)

The experimental set-up of the scanning thermal microscope is depicted in Fig. 2. It consists of a self-designed modular scanning microscope covering scanning tunneling (STM) mode as well as scanning force mode (SFM). The feedback loop is software implemented using a digital signal prozessor (DSP) and thus can be easily adapted to different kinds of sensors.

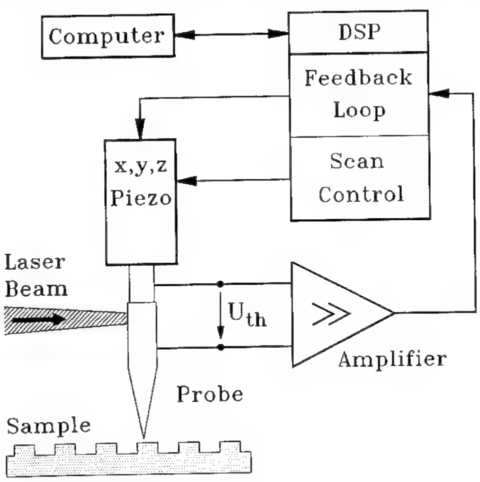

Figure 2: Set-up of the scanning thermal microscope (SThM). DSP denotes the digital signal prozessor where the feedback loop of the modular scanning microscope is implemented. The thermocouple probe is optically heated by an infrared laser diode which gives rise to a thermovoltage U_{th}.

The sensor of thermal microscope is a miniaturized thermocouple probe. It consists of a constantan wire which is electro-chemically etched to obtain a fine tip [7]. The curvature of this tip was determined by electron microscopy measurements to be less than 100 nm. After the etching procedure the tip is cleaned and covered with a thin film of epoxy resin, leaving the very tip uncoated. The epoxy resin

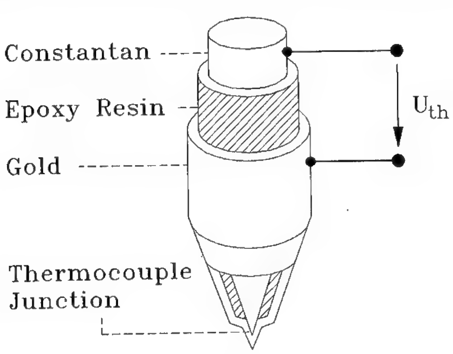

Figure 3: Thermocouple probe consisting of a gold/constantan junction at the very tip. U_{th} denotes the thermovoltage of the probe.

film serves as an electrical and thermal insulating layer. Finally the tip is coated with a thin gold layer which results in a small thermocouple sensor at the very tip. The thermal sensor is shown in Fig. 3. The thermoelectric power of the gold/constantan thermocouple junction was determined to be approximately 25 μV/K under ambient conditions.

The thermal probe was heated with an infrared laser diode 3 mm above the end of the thermocouple junction. The beam was focused to a spot with diameter of about 100 μm and an optical output power

of 3–4 mW was applied resulting in an appropriate thermovoltage. When approaching the tip to a sample surface the heat flow from the tip to the cooler sample leads to a decrease of the thermovoltage. The measurements could be done in the constant height mode mapping the thermovoltage or in the constant thermovoltage mode measuring the z-displacement of the piezo element.

3 Theory

3.1 Heat conduction in solids

To understand the signal generation process in photo-thermal experiments first of all the temperature distribution of laser heated sample has to be evaluated. This energy diffusion process is described by the 3-dimensional heat conduction equation for isotropic and homogeneous materials [8]

$$\Delta T(\vec{r},t) - \frac{\rho\, c}{k}\frac{\partial\, T(\vec{r},t)}{\partial\, t} = -\frac{S(\vec{r},t)}{k}\,, \tag{1}$$

where $T(\vec{r},t)$ denotes the scalar temperature field, k the thermal conductivity, ρ the mechanical density, c the specific heat capacity, $\alpha = k/\rho c$ the thermal diffusivity and $S(\vec{r},t)$ an external source distribution. In case of laser heating the source function of intensity I_0 in radial direction is described by a gaussian distribution of waist σ corresponding to a TEM_{00} laser mode. The laser beam is assumed to be exponentially damped in the sample with an optical absorption length β^{-1} according to the law of Lambert-Beer. The intensity of the laser beam is periodically modulated with frequency ω.

The geometry of the samples may be restricted to a stack of plane-parallel layers each consisting of homogeneous and isotropic material. At the interface between these layers two boundary conditions have to be fulfilled: the thermal flux has to be a continuous function and the energy diffusion process may be limited by a thermal resistance R_0^{th} corresponding to Newtons law [8].

Due to the axial symmetry of this problem a solution of the temperature distribution is obtained applying a special integral transform technique – the Hankel transform of zero order. Therefore the heat conduction equation is transformed to a wave equation which is solved in terms of thermal waves. A detailed description of this method is given in [9, 10].

The temperature distribution of a semi-infinite solid (index 1) in contact with a gas (index 0) is obtained applying the inverse Hankel-transform

$$z < 0: \; T_0(r,z,t) = \int_0^\infty d\rho\rho J_0(r\rho)\left[\frac{k_1 q_1 - k_1\beta_1}{k_0 q_0 + k_1 q_1(1 + k_0 q_0 R_0^{th})} e^{q_0 z}\right] \frac{I_0}{2\pi}\frac{\beta_1}{k_1}\frac{e^{-\sigma^2\rho^2/8}}{q_1^2 - \beta_1^2}\, e^{-i\omega t} \tag{2}$$

$$z \geq 0: \; T_1(r,z,t) = \int_0^\infty d\rho\rho J_0(r\rho)\left[e^{-\beta_1 z} - \frac{k_0 q_0 + k_1\beta_1(1 + k_0 q_0 R_0^{th})}{k_0 q_0 + k_1 q_1(1 + k_0 q_0 R_0^{th})} e^{-q_1 z}\right] \frac{I_0}{2\pi}\frac{\beta_1}{k_1}\frac{e^{-\sigma^2\rho^2/8}}{q_1^2 - \beta_1^2}\, e^{-i\omega t},$$

J_0 denotes the Bessel function of zero order, $q_i = \sqrt{\rho^2 - i\omega/\alpha_i}$ the wave number of the medium with index i and ρ the radial coordinate in the frequency domain. For samples revealing a more complex geometry, e. g. thin layers on a substrate in contact with a gas, the solution is given by a matrix formalism based on the same evaluation procedure described above [4, 10].

In case of the scanning thermal microscope this theoretical model may not be sufficient. This is due to the fact that microscopic effects may influence the signal generation process, e. g. evanescent optical waves may contribute to the temperature distribution. An exhaustive description and discussion of these phenomena is given in [11].

3.2 Thermal expansion of laser heated samples

The evaluation of the measured thermal expansion of the sample surface requires an additional investigation of the equation of motion. Various methods were introduced to solve this partial differential equation but all of them results in complex analytical solutions [12].

We have applied a pure numerical approach, the finite element method (FEM), to evaluate the mechanical problem as well as the temperature distribution. A detailed description of the principles and basic ideas of this technique are given in [13]. To evaluate the thermal diffusivity from measurement data they were fitted to the FEM simulations.

4 Results and Discussion

4.1 Photo-thermal Laser Interferometry

First interferometric measurements of the thermal surface expansion of laser heated samples were performed on metal substrates. Although both the amplitude and the phase distribution were collected the phase information proved to be more reliable and less affected by noise signals than the amplitude. Therefore only the phase distribution was evaluated and fitted to FEM simulation data. Figures 4 and 5 show results for a brass and copper sample for different modulation frequencies. The theoretical calculations of the phase distribution are depicted in these figures (solid lines) and show good agreement with the measurement data. The averaged value of the thermal diffusivity of the copper sample was determined quantitatively to be $(108.8 \pm 3.2) \cdot 10^{-6}\,m^2/s$ which deviates slightly from the literature value $117.0 \cdot 10^{-6}\,m^2/s$ [14]. The evaluation of the measurement data of the brass substrate results in a thermal diffusivity of $(23.6 \pm 0.5) \cdot 10^{-6}\,m^2/s$. A comparison with data from the literature was not possible because the composition of the brass material was unspecified.

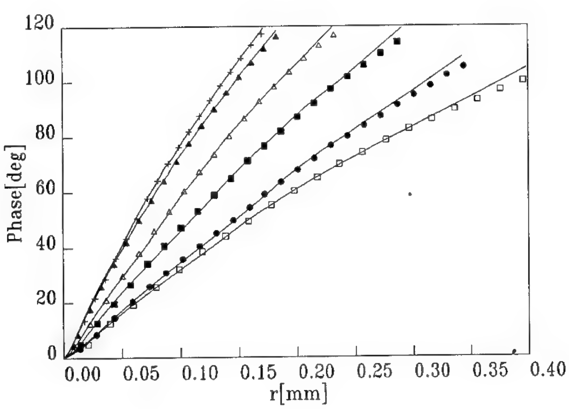

Symbol	f [Hz]	a $[10^{-6} m^2/s]$
□	539	23.1
•	1066	22.9
■	2130	23.3
△	3190	23.9
▲	4060	24.1
+	8870	24.2
		23.6±0.5

Figure 4: Radial phase distribution of the thermal surface expansion of a brass sample for different modulation frequencies f. Solid lines represent the theoretical data of FEM simulations.

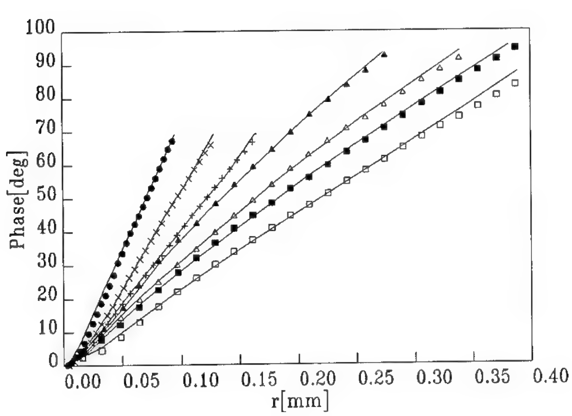

Symbol	f [Hz]	a $[10^{-6} m^2/s]$
□	545	105.1
■	1.613	103.9
△	2.150	112.4
▲	3.220	107.3
+	4.860	109.5
×	8.870	111.2
•	19.850	112.3
		108.8±3.2

Figure 5: Radial phase distribution of the thermal surface expansion of a copper sample for different modulation frequencies. Solid lines represent the theoretical data of FEM simulation.

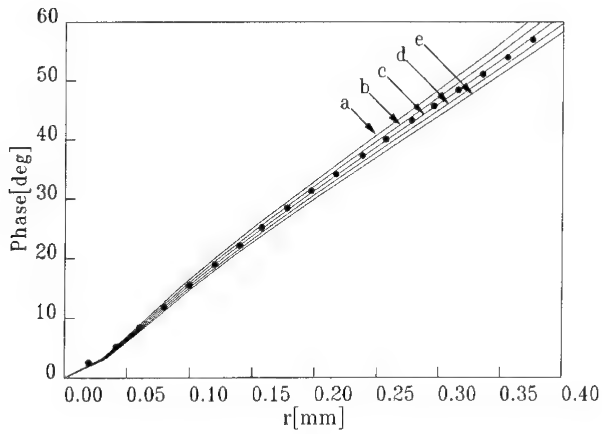

Figure 6: Radial phase distribution of the thermal surface expansion of a copper sample for a modulation frequency of 370 Hz. Curve c) represents the fitted data of the FEM simulation. Additional simulations were taken into consideration, where the thermal diffusivity was on one hand decreased by -10 % for curve a) and -5 % for curve b) and on the other hand increased by +5 % for curve d) and +10 % for curve e).

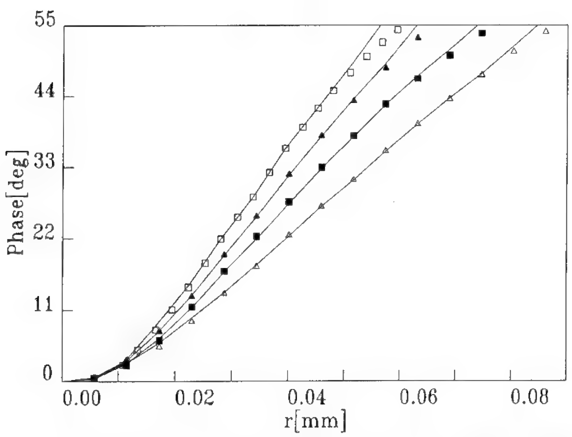

Symbol	d_1 [nm]	a_1 $[10^{-6}m^2/s]$
□	50	112.5
▲	80	102.3
■	130	95.7
△	235	107.2
		104.4±6.2

Figure 7: Radial phase distribution of the thermal surface expansion of four samples consisting of a gold layer with thickness d_1 on a tempax glass substrate. A modulation frequency of 950 Hz was used.

In the case of the copper sample the radial phase measurement was repeated applying a modulation frequency of 370 Hz (Fig. 6). After the evaluation of the thermal diffusivity of the copper sample additional simulations were done varrying this value by ±5 % and ±10 %. These calculations were also presented in Fig. 6. They reveal that the relative error for determining the thermal diffusivity may not exceed 10 % in the case of metal substrates.

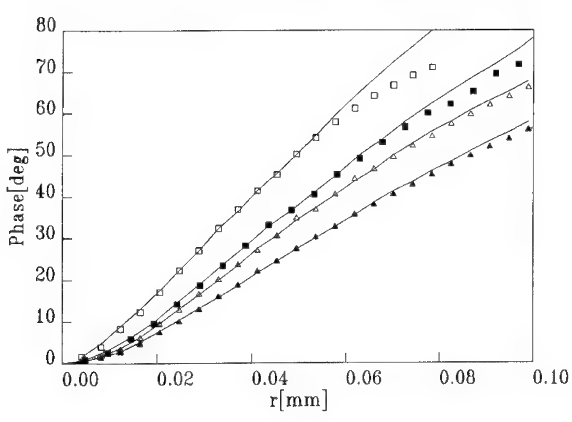

Symbol	d_1[nm]	a_1 $[10^{-6}m^2/s]$
□	100	76.7
■	270	81.7
△	300	82.8
▲	450	88.6
		82.5±4.2

Figure 8: Radial phase distribution of the thermal surface expansion of four samples consisting of a aluminium film of thickness d_1 on a tempax glass substrate. A modulation frequency of 932 Hz was used.

Furthermore the thermal diffusivity of thin metal films on glass substrates were investigated also. Figures 7 and 8 show results of the radial phase distribution for gold and aluminium films of different thickness on tempax glass. A theoretical investigation of these measurement data using the FEM approach allows again the evaluation of the thermal diffusivity of these metal films in a quantitative manner (gold $(104.4 \pm 6.2) \cdot 10^{-6}\,\mathrm{m^2/s}$ and aluminium $(82.5 \pm 4.2) \cdot 10^{-6}\,\mathrm{m^2/s}$). The thermal diffusivity of both the gold and the aluminium layers deviate from literature data for the bulk materials (gold $117.6 \cdot 10^{-6}\,\mathrm{m^2/s}$ and aluminium $80.6 \cdot 10^{-6}\,\mathrm{m^2/s}$) [14]. This is due to the fact that the physical properties of thin films depend strongly on the deposition technique and the process conditions and may thus deviate from the values of the bulk materials.

4.2 Results of Scanning Thermal Microscopy (SThM)

Initially the scanning thermal microscope was operated in the constant height mode. The thermovoltage of the sensor depends both on the topography and the local thermal properties of the sample surface.

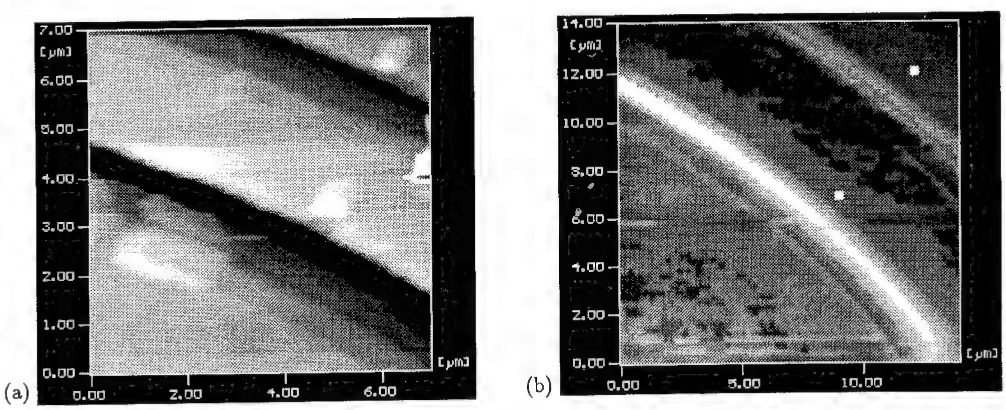

Figure 9: (a) SFM image of two trench lines on silicon produced by a reactive ion etching (RIE) technique. The trench lines are approximately 1 μm wide and deep. The distance between the lines is 4.5 μm. (b) Thermovoltage map of the same sample but different position.

To facilitate the experimental situation first of all a homogenous sample consisting of a trench line structure on a silicon substrate was investigated. The trenches were produced by reactive ion etching (RIE) technique. The width and height of these trenches are approximately 1 μm and the distance between them is 4.5 μm. Figure 9 (a) depicts the topography of the sample surface measured by a scanning force microscope (SFM). The two dark lines correspond to the trench structure. The thermovoltage map shown in Fig. 9 (b) was measured with the scanning thermal microscope at a different location. While scanning the sensor above the sample surface the thermovoltage signal has been detected. An increase of the distance between sample surface and sensor leads to decrease of the thermal flux and this results in a higher thermovoltage. In this case the trench lines should occur as bright lines on a dark background which may be obeserved in Fig. 9 (b).

A more complex experimental situation arises if the sample surface consists of different materials. Figure 10 (a) depicts a STM image of a grating structure of cromium lines on a polymethyl methacrylate (PMMA) layer which was deposited on a silicon substrate. To render tunneling on the PMMA film the surface of the sample was covered with a thin gold layer. The bright lines in the STM image correspond to the cromium lines which exhibit a width of 1 μm and a height of approximately 200 nm. The distance between each other was determined to be about 1.5 μm. In Fig. 10 (b) a thermovoltage map of the same type of sample is shown. However, in contrast to the STM measurement the surface of this sample was left uncoated. In the SThM image several dark and bright lines are observed also. In this case it is more difficult to identify the surface topography from the thermal signal because it

(a) (b)

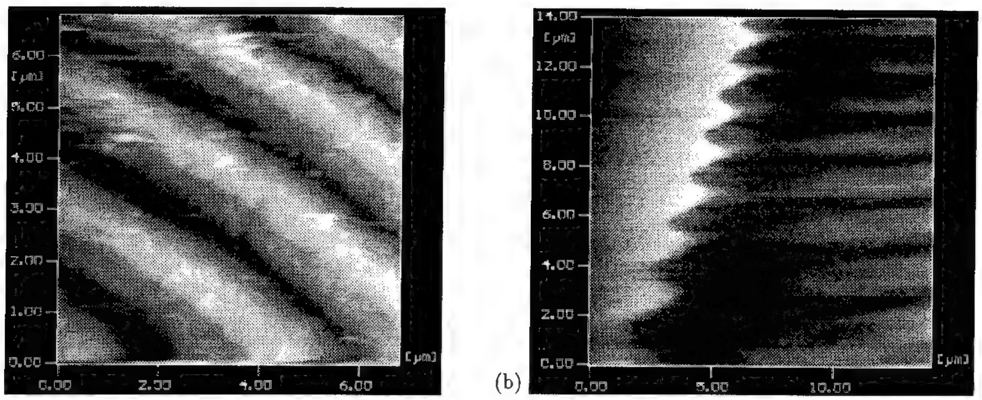

Figure 10: (a) STM image of a chromium grating structure on a PMMA layer which is deposited on a silicon substrate. To facilitate tunneling on the PMMA film the sample surface was covered with a thin gold film. (b) Thermovoltage map of a sample of the same type but without coating the surface.

is also influenced by the thermal properties.

Figure 11 (a) contains a SFM image of a thin polycrystalline diamond film on a silicon substrate. The layer consists of grains with a lateral dimension of 1–2 μm. The diamond film was deposited using a microwave CVD (chemical vapour deposition) technique. For the thermal investigation of the diamond film the feedback loop of the thermal microscope was enabled. In this detection mode the voltage of the thermocouple sensor is kept constant by controlling the z-displacement of the piezo-actuator. Figure 11 (b) depicts a map of the z-displacement measured while scanning above the diamond surface. The location differs from that of the SFM image. The structure of the SThM image resembles that of the SFM, but the thermal information is again a mixture of the topography as well as the varrying thermal properties of the diamond grains.

(a) (b)

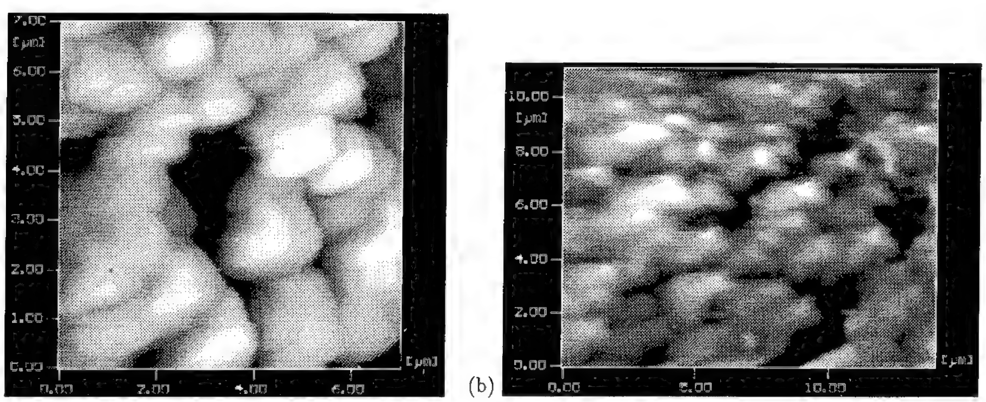

Figure 11: (a) AFM image of a polycrystalline diamond film of 1 μm thickness. (b) z-displacement obtained by scanning thermal measurement of the same sample but different scan position.

These preliminary results show that a thermal characterization on a microscopic scale is feasible with scanning thermal microscopy. The problem to separate the thermal properties and the surface topography is the most important problem to solve. It may be performed applying modulation techniques [6].

5 Summary

Photo-thermal measurement techniques are capable of investigating thermal properties of materials in a non-contact and non-destructive mode. We have employed a laser interferometric set-up for the measurement of the thermal expansion of laser heated samples. The measurement data have been compared with the results of finite element method (FEM) simulation. We were able to determine the thermal diffusivity of substrates and thin layers quantitatively. In this case the lateral resolution is limited to the optical wavelength of the excitation and detection approach.

To enhance the lateral resolution we introduced a scanning thermal microscope (SThM) based on a standard scanning tunneling microscope replacing the tunneling tip with a miniaturized thermocouple probe. First qualitative measurements on silicon and diamond surfaces were presented. They indicate a lateral resolution of about 100 nm.

6 Acknowledgement

This work is supported by the Department of Research and Technology of the Federal Republic of Germany (BMFT Project 13N6008). Only the authors are responsible for the content.

We would like to thank W. Scholz, P. Hudek and E. Schultheiß for the preparation of samples and test structures.

References

[1] F. A. McDonald. Photoacoustic, photothermal, and related techniques: a review. *Can. J. Phys.*, 64:1023–1029, 1986.

[2] J. C. Murphy, L. C. Aamondt, and J. W. M. Spicer. Principles of photothermal detection in solids. In A. Mandelis, editor, *Principles & Perspectives of Photothermal & Photoacoustic Phenomena*, chapter 2, pages 41–94. Elsevier Science Publishing Co., 1992.

[3] E. Oesterschulze, M. Stopka, M. Tochtrop-Mayr, and R. Kassing. Nondestructive evaluation of solids and deposited films by thermal-wave interferometry. *Appl. Surf. Sci.*, 69:65–68, 1993.

[4] M. Stopka, E. Oesterschulze, and R. Kassing. Photo-Thermal Characterization of Solids and Thin Films by Optical and Scanning Probe Techniques. *Microelectronic Engineering*, 24:107–112, 1994.

[5] C. C. Williams and H. K. Wickramasinghe. Scanning thermal profiler. *Appl. Phys. Lett.*, 49:1587–1589, 1986.

[6] C. C. Williams and H. K. Wickramasinghe. Thermal and photothermal imaging on a sub 100 nanometer scale. *SPIE, Scanning Microscopy Technologies and Applications*, 897:129–134, 1988.

[7] E. Oesterschulze, M. Stopka, J. Schulte, and R. Kassing. Photothermal Scanning Near-Field Microscopy. Materials Science and Engineering B (accepted for publication), 1994.

[8] H. S. Carslaw and J. C. Jaeger. *Conduction of Heat in Solids.* Clarendon Press Oxford, 1959.

[9] M. V. Iravani and H. K. Wickramasinghe. Scattering matrix approach to thermal wave propagation in layered structures. *J. Appl. Phys.*, 58:122–131, 1985.

[10] E. Oesterschulze. *Thermische Charakterisierug dünner Schichten mittels photo-thermischer Analysetechniken.* PhD thesis, Universität Kassel, Juni 1994.

[11] Jianbin XU. *Heat Transer between Two Metallic Surfaces at Small Distances.* PhD thesis, Universität Konstanz, März 1993.

[12] G. Rousset, L. Bertrand, and P. Cielo. A pulsed thermoelastic analysis of photothermal surface displacements in layered materials. *J. Appl. Phys.*, 57:4396–4405, 1985.

[13] J. N. Reddy. *Finite element analysis for engineering design.* Springer-Verlag, 1988.

[14] K. Schäfer and E. Lax. *Landolt–Börnstein, Volume II, 2/4/5/6.* Springer-Verlag, 1968.

Materials Science Forum Vols. 185-188 (1995) pp. 53-58

Determination of interface state density distribution and surface recombination velocity on passivated semiconductor surfaces by photoluminescence surface state spectroscopy

T. Saitoh and H. Hasegawa

Research Center for Interface Quantum Electronics and Department of Electrical Engineering, Hokkaido University, North 13, West 8, Sapporo 060, Japan

Keywords: Photoluminescence, surface state density, interface state density, surface recombination velocity, interface control layer

Abstract

The photoluminescence (PL) surface state spectroscopy (PLS^3) technique recently proposed by the authors allows an in–situ, contactless and non–destructive characterization of the passivated surfaces. The surface/interface state density (N_{ss}) distribution and the surface recombination velocity (S) of the device surface under any operation conditions can be determined. Various passivation processes of Si wafers are characterized in terms of the values of S under various sunlight intensities in view of solar cell applications. The technique is also applied to characterization of passivated GaAs and InGaAs surfaces, including those having silicon interface control layers.

1. Introduction

Establishment of a suitable advanced passivation technology is extremely important for development of high–performance integrated circuits and opt–electronic devices including high efficiency solar cells. Traditional figure of merits for the passivation technology has been interface state density (D_{it} or N_{ss}) or surface recombination velocity (S). The latter has been treated so far as a characteristic constant of surface[1]. However, our previous analysis [2] has shown that S is not a characteristic constant of surface, but depends on the doping density, the conduction type, the current injection level and the intensity and spectrum of the light illuminating the surface.

In this paper, it is shown that our recently proposed photoluminescence (PL) surface state spectroscopy (PLS^3) technique [3–5] allows an in–situ, contactless and non–destructive characterization of the passivated surfaces. N_{ss} distribution and the value of S under any operation conditions can be determined. As specific examples, various passivation processes of Si wafers are characterized in terms of the values of S under various sunlight intensities in view of solar cell applications. Various fabrication processes on compound semiconductors are also characterized to optimize the passivation technology.

2. Principle of PLS^3

If the surface recombination process is dominant and the surface recombination velocity does not depend on the excitation intensity, the band–edge PL intensity (I_{PL}) is expected to be proportional to the excitation intensity (ϕ). However, photo–induced unpin–

ning causes the reduction of the value of S, and this reduction leads to the increase of PL intensity. Figure 1 schematically shows the behavior of S and PL efficiency (I_{PL}/ϕ). The photo–excitation causes an intensity–dependent splitting of the quasi Fermi levels for electrons and holes, which changes the energy range of the surface or interface states contributing to recombination. Thus, the dependence of the PL efficiency on ϕ depends strongly on the distribution shape and density of surface or interface states. Determination of N_{ss} distribution becomes possible by fitting the result of computer analysis to the measurement result on I_{PL}/ϕ vs. ϕ.

3. Measurement of Surface Recombination Velocity at Passivated Si Surfaces

In this PL technique, the value of S can be determined by the calculation for arbitrary operation conditions such as current injection level and the intensity and spectrum of the light, after the determination of N_{ss} distribution. In this study, the value of S under sunlight is evaluated by the following procedure.

(1) Measurement of the PL efficiency as the function of the excitation intensity using Ar laser light (514.5nm) for the excitation source.
(2) Determination of N_{ss} distribution by computer fitting.
(3) Calculation of the value of S under sunlight by using the determined N_{ss} distribution.

Figure 2 shows the measured PL line shapes obtained from the bare Si surface, which have not been intentionally processed. As seen in Fig.2, the measured peak positions are not changed. Thus, the absence of shifts in peak position indicates that there was no excessive sample heating during the photoluminescence measurement. Figure 3 shows the measured dependence of the value of S on the sunlight intensity which is normalized the intensity of 1 sun of AM1.5 spectrum. It is seen that the value of S at Si_3N_4/Si interface formed by Plasma

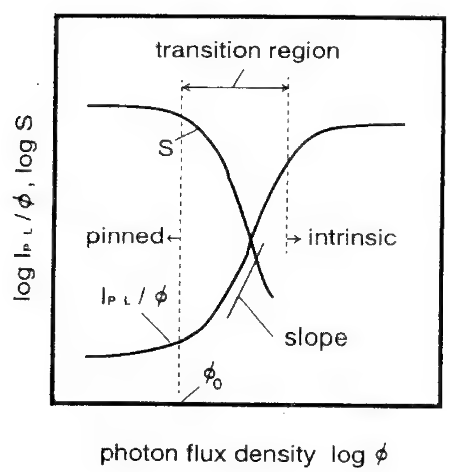

Fig.1 Principle of PLS[3]

CVD is about 30,000 cm/s under 1 sun condition, and that the best thermal oxidation process reduces the value of S by almost one order of magnitude under 1 sun condition. It is also seen that the value of S depends strongly on the excitation intensity of sunlight. This result indicates that rigorous analysis is greatly required for the measurement of S under device operation condition such as solar cells.

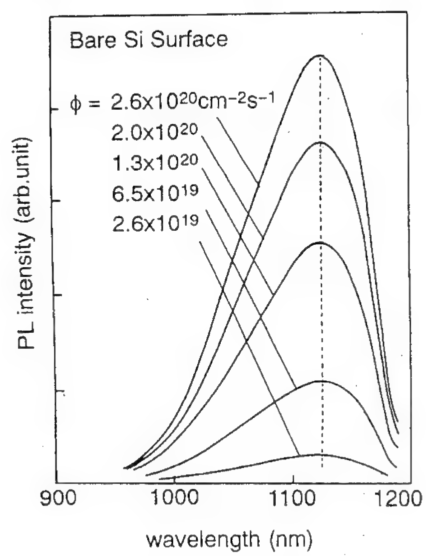

Fig.2 PL line shapes for various excitation intensity

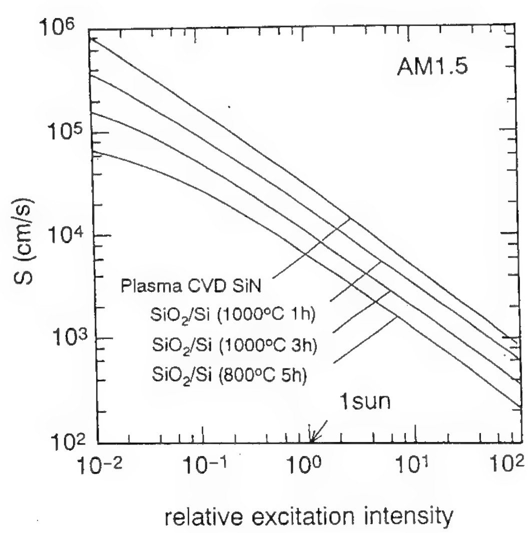

Fig.3 Dependence of S on sunlight intensity

4. Measurement of Interface State Density of Compound Semiconductor Interfaces

4.1 Passivation on GaAs and InGaAs surfaces

Photo–CVD deposition of SiO_2 on GaAs and InGaAs surfaces is performed in view of reduction of N_{ss}. Figure 4 (a) shows the measured and computer fitted dependence of the PL efficiency on the excitation intensity for passivated and unpassivated GaAs and for passivated InGaAs surface with and without Si interface control layer (ICL) [6]. It is seen that the PL efficiency of the passivated InGaAs is greatly increased by the insertion of Si ICL. Figure 4 (b) shows the determined N_{ss} distributions. All of the PL efficiency curves in Fig.4(a) could only be fitted with U–shaped distributions as shown in Fig.4(b). It is seen that the photo–CVD deposition of SiO_2 gives the minimum value of N_{ss} (N_{ss0}) of almost 10^{12} cm^{-2}eV^{-1} on both GaAs and InGaAs surfaces, and that N_{ss0} is greatly reduced by the insertion of Si ICL.

4.2 AlGaAs/GaAs heterointerfaces

Figure 5(a) shows the measured PL efficiency of continuously grown and growth interrupted AlGaAs/GaAs heterostructures and GaAs surface. These AlGaAs/GaAs samples are fabricated and characterized in a UHV–based total system consisting of MBE, EB/FIB, CVD, XPS and PL chambers connected by a UHV transfer tunnel. The growth interruption was done in UHV chamber at room temperature for 1 hour. It is seen that the PL efficiency of the continuously grown AlGaAs/GaAs heterostructure is almost 100 times as large as that of the growth interrupted AlGaAs/GaAs heterostructure. The determined N_{ss} distributions

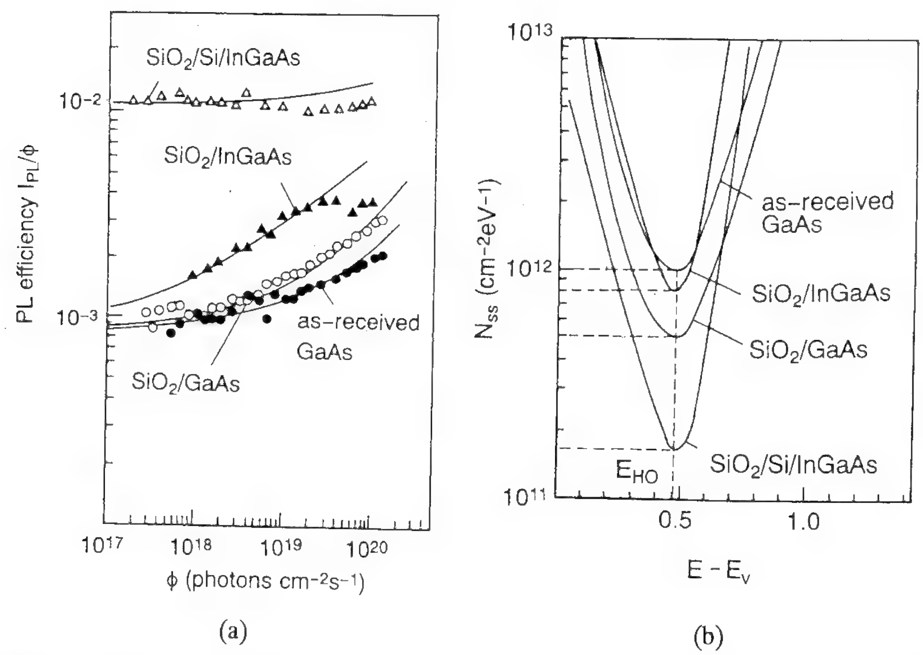

Fig.4 (a) Measured dependence of PL efficiency on excitation intensity for passivated GaAs and InGaAs, and GaAs surface.
(b) Determined N_{ss} distributions.

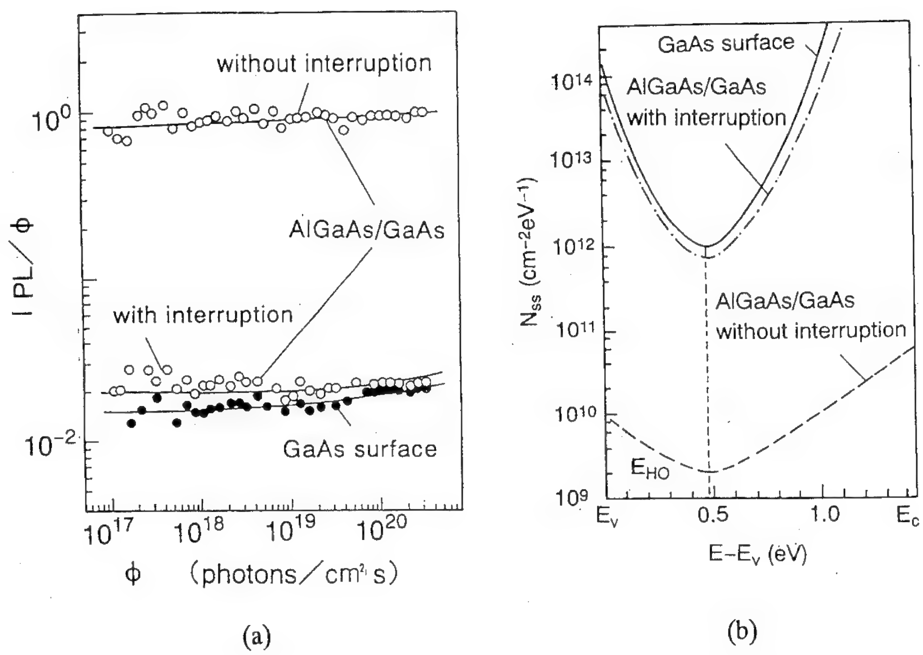

Fig.5 (a) Measured dependence of PL efficiency on excitation intensity for continuously grown and growth interrupted AlGaAs/GaAs heterostructures.
(b) Determined N_{ss} distributions.

are shown in Fig.5 (b). It is found that the interface state density of the continuously grown AlGaAs/GaAs heterointerface is quite low, and that the growth interruption causes high density of heterointerface states, although the sample is kept in the UHV chamber during the growth interruption. Thus, the growth interruption should be minimized in the device fabrication process.

5. Conclusion

Our recently proposed photoluminescence (PL) surface state spectroscopy (PLS^3) technique which allows an in-situ, contactless and non-destructive characterization of the passivated surfaces is applied to the determination of the surface/interface state density (N_{ss}) distribution and the surface recombination velocity (S) under sunlight. It is found that the value of S of passivated Si wafers greatly depends on the passivation method and condition, and on the device operation condition. The insertion of Si interface control layer to photo-CVD SiO_2 passivated InGaAs surface is found to reduce N_{ss}. This PL technique is successfully applied to the measurement of AlGaAs/GaAs heterointerface state distributions. It is found that the growth interruption process causes high density of interface states.

Acknowledgements

This work was supported by a Grant-in-Aid for Scientific Research from the Ministry of Education, Science and Culture.

References

[1] A.S.Grove and D.J.Fitzgerald: Solid–State Electron., 9 (1966) 783
[2] T.Saitoh and H.Hasegawa: Jpn.J.Appl.Phys.,29(1990)L2296
[3] T.Saitoh, H.Iwadate and H.Hasegawa: Jpn.J.Appl.Phys.,30(1991)3750
[4] T.Saitoh, Y.Nishimoto, T.Sawada and H.Hasegawa:Jpn.J.Appl.Phys.,32(1993)272
[5] T.Sawada, K.Numata, S.Tohdoh, T.Saitoh and H.Hasegawa:Jpn.J.Appl.Phys.,32(1993) 511
[6] M.Akazawa, H.Hasegawa and E.Ohue: Jpn.J.Appl.Phys.,28(1989)L2095

Materials Science Forum Vols. 185-188 (1995) pp. 59-62

Non-steady state C-V methods for determination of interface state parameters

K.L. Temnikov and I.A. Uritskaya

Herzen State Pedagogical University of Russia, St.-Petersburg, Russia

Keywords: Density of surface states, cross section, C-V characteristics, demarcation energy level, MIS structure, minority carriers

Abstract. Description of a series of simple methods to define density and cross section of surface electron states at interface dielectric-semiconductor by means of non-equilibrium C-V characteristics of MIS structures is presented.

I. INTRODUCTION

Non-steady state C-V characteristics (CVC) in metal-insulator-semiconductor (MIS) structures on Si substrate at temperatures T=50°C are observed for the bias change rate $\alpha<10$ V/s, and at room temperature $\alpha>10$ V/s. Typical low-frequency CVC for Si-SiO_2 structure are shown at Fig.1. Curve 1 there corresponds to the case when during the CVC recording there is no generation of minority carriers in the region of deep depletion (while the MIS sample is in the dark). Curve 2 is observed in case when the minority carriers appear either as a result of "turning on" of micro defect with enormously high generation rate at a certain value of V_g [1] or during short-time illumination of a sample in the end of a direct move of CVC. Both type of curves include the information on interface state parameters [2,3,4].

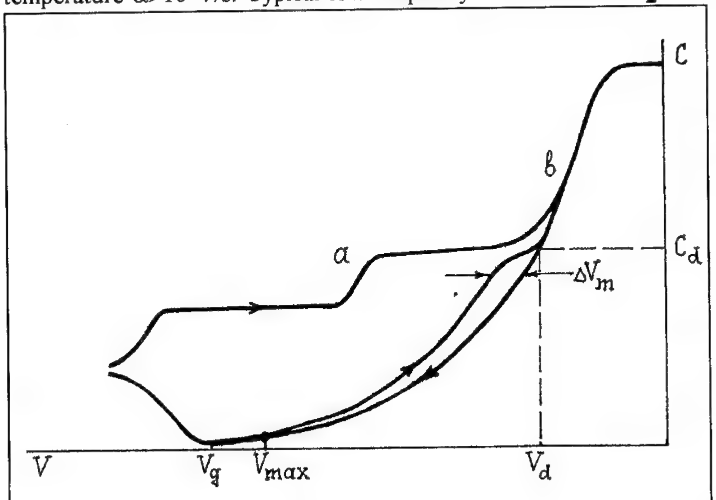

Fig.1. Typical CVC of Al-SiO_2-Si structure at 78K.

At curve 2 the portion (a-b) corresponds to simultaneous recharging of interface states situated between two demarcation levels of energy: electronic E_{dn} which is situated at conduction band when the temperature is low, and hole E_{dp},which is situated at valance band under the same conditions [2]. Curve 1 has the informative non-equilibrium portion in lower region of CVC [3]. Below methods of parameters definition of surface states are given from non-steady state C-V curves of the first type.

II. DESCRIPTIONS OF METHODS

First of the suggested methods is based on the hysteresis appearing between direct and back move in non-steady state part of CVC (curve 1 at Fig.1). According to [3] the straight direction of CVC is in equilibrium state up to a certain voltage V_d which corresponds to the crossing of Fermi level and E_{dn} level at the surface (to be more definite we describe MIS structure with semiconductor of n-type). From V_d the interface charge becomes function only time and according to data from [3] it is possible to receive the following expression for it:

$$Q_{ss}(t) = q\ N_{ss}\ kT\ \ln(1\text{-}\exp(-E_{dn}/kT))\ \exp(-v_n\sigma_nN_ct\ \exp(-E_{dn}/kT)), \quad (1)$$

where q - electron charge, N_{ss}-density of interface state, k - Boltzmann-constant, T- absolute temperature, v_n- heat rate of electron, σ_n - cross section of interface state capture, N_c - effective density of states in conduction band, t - time of system staying in non-steady state region, E_c - bottom energy of conduction band. Let us introduce the terms $\chi=E_{dn}/kT$ and $\xi=v_n\sigma_nN_ct\ \exp(-E_c/kT)$. Value ξ for Si structure at t corresponding to normal experimental times is such that with great accuracy $\exp(-\xi)=1-\xi$. That is why expression [1] could be simplified to:

$$Q(t) = qN_{ss}kT\ \ln(\xi + \exp(-\chi)). \quad (2)$$

If we introduce the time constant of interface state with energy E_{dn}-τ_d, than using expression (Eq.2) we can obtain the following expression for interface charge change for the time t from the moment when the equilibrium state was disturbed:

$$\Delta Q_{ss} = Q_{ss}(t) - Q_{ss}(0) = qN_{ss}kT\ \ln(t/\tau_d + 1), \quad (3)$$

where

$$\tau_d = 1/\ [v_n\sigma_nN_c\ \exp((E_{dn} - E_c)/kT)]. \quad (4)$$

Here E_c - is the bottom energy of conduction band.

When the minority carries are absent, as shown in [3], direct and back hysteresis is connected only with time changes of interface charge. Here the maximum value of hysteresis ΔV_m (Fig.1) is observed at the border of non-equilibrium portion. Since from the electroneutrality equation it follows that $\Delta Q_{ss} = C_o\Delta V_m$, where C_o-oxide capacity, than using (Eq.3) we obtain:

$$N_{ss} = C_o\Delta V_m/[qkT\ \ln(t/\tau_d + 1)], \quad (5)$$

According to [4]

$$\tau_d = kT\ (qN_{ss} + C_o + C_{sc}(V_d))/(C\alpha), \quad (6)$$

where $C_{sc}(V_d) = C_oC_d/(C_o - C_d)$. It is evident that using the Eq.6,7 we can define density and time constant of interface state at energy E_{dn} from experimental data, which in the depletion approximation could be calculated according to

$$E_{dn} = E_F - 0{,}5q^2\varepsilon_s\ N_D\ /(C_{sc}\ (V_d))^2, \quad (7)$$

where ε_s - dielectric penetrability of a semiconductor, N_D - donor impurity concentration. Values C_d (and correspondingly V_d and t) could be defined at the level of maximum hysteresis. If the bias change rate α is constant, the time when the structure is in the non-equilibrium state is defined from a simple formula:

$$t = (2(V_d - V_{max}) - \Delta V_m)/\alpha, \quad (8)$$

where V_{max}- maximum depletion voltage, which is less than V_g. Since the interface state time constant is connected to cross section of capture it is possible to obtain this interface state parameter using the Eq.4,7. However, due to the fact that E_{dn} in Eq.4 is included into exponent, the accuracy of defining the demarcation level should be higher than the one which could be achieved while defining C_d at the level of maximum hysteresis. It could be possible to use the recommendations of [5] where C_d is defined according to the minimum value of dC/dV from C-V curve, but this minimum is observed usually only at high interface states density. That is why in order to define the cross section it is reasonable to use the method described below. It should be mentioned that the bias change low for this method is of no relevance. For example, it is possible to use the sinusoidal voltage sweep. In this case the E_{dn} parameter should be define at the moment when the equilibrium is broken. However, it is more reasonable to use trapezoidal sweep. It allows to prolong the period of a sample stay in non-equilibrium conditions and thus to

improve the sensitivity of the method. Besides the probability of minority carriers generation is substantially lowered since it is easier to fulfill the condition $V_{max}<V_g$.
The second method is based on the dependency of demarcation value on temperature and rate of bias sweep. This dependency is described by the following expression [7]:

$$E_{dn} = E_c - kT \ln(kT\sigma_n v_n N_c(qN_{ss} + C_o + C_{sc}(V_d))/(C_o\alpha)). \qquad (9)$$

When the rate of voltage sweep is changed from α_1 to α_2 we should observe the bias of demarcation level [4]:

$$\Delta E_{dn} = kT \ln(\alpha_1/\alpha_2). \qquad (10)$$

In order to obtain Eq.10 it is necessary to neglect the change of $C_{sc}(V_d)$ when α is changed. As could be seen from the analysis carried out in [4], this is quite possible. It is also necessary to suppose that N_{ss} and σ_n change very weakly within the limit of several kT. Since the demarcation level is shifted, the non-equilibrium region of CVC is also shifted along the voltage axis for a value of ΔV_α(Fig.2). This allows use to define the surface states density according to formula:

$$N_{ss} = C_o\Delta V_\alpha/(q\Delta E_{dn}). \qquad (11)$$

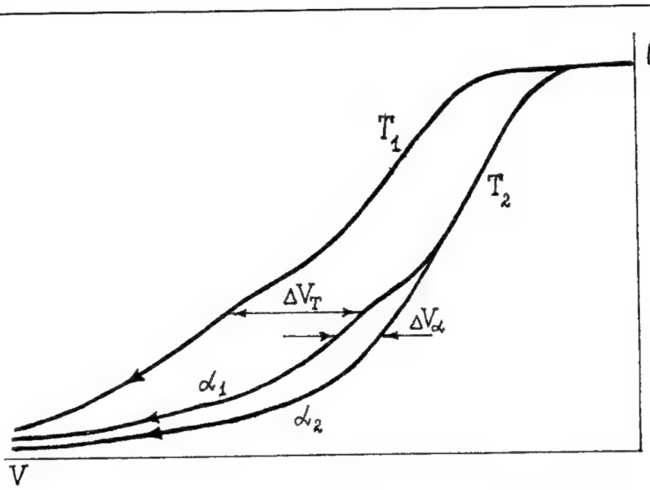

Fig.2. Influence of bias sweep rate and temperature ($T_1>T_2$, $\alpha_1<\alpha_2$) on non-equilibrium CVC.

If the temperature changes we witness the shift along the voltage axis of the whole CVC. In equilibrium region the bias is connected with temperature dependence- of Fermi level position, which is used in Gray-Brown Method [8]. In the non-equilibrium region bias ΔV_T is connected with the change of demarcation level (Fig.2). This change could be obtained by differentiating of Eq.9, if we suppose that there is no dependence on temperature of C_{sc}:

$$\frac{\partial E_{dn}}{\partial T} \cong -k \ln[\frac{kT\sigma_n v_n N_c}{C_o\alpha}(qN_{ss} + C_o + C_{sc}(V_d))] \qquad (12)$$

At small temperature change $\frac{\partial E_{dn}}{\partial T} \cong \frac{\Delta E_{dn}}{\Delta T}$, that is why it becomes possible to define from Eq.12 at given values of N_{ss} and $\Delta V_T = \Delta E_{dn} qN_{ss}/C_o$ to define the cross section of interface state:

$$\sigma_n = \frac{C_0\alpha}{kTv_n N_c(qN_{ss} + C_0 + C_{sc}(V_d))}\exp[-\frac{C_0\Delta V_T}{qN_{ss}k\Delta T}]. \qquad (13)$$

Substituting the obtained from [11,13] values of N_{ss} and σ_n into Eq.9 we can define the energy from which the interface state parameters are found.

III. INTERFACE STATES PARAMETERS SPECTRA

In both described above methods the interface states parameters are defined for energy equal to energy of demarcation level. This energy depends on the condition of experiment, that is on temperature and rate of bias voltage sweep. As was shown in [4], the sensitivity of E_{dn} to temperature is stronger than at Fermi level. That is why while changing the temperature we can obtain the spectrum of interface states parameters in broad energy range. The limiting factor here is the minority carriers generation which for Si MIS structures at $\alpha \approx 1$ V/s is noticeable already at $T \approx 220K$. However, at $\alpha > 10^3$ V/s it is possible to carry out the measurements at room temperature. The sensitivity of E_{dn} to α is small and contrary to temperature dependence is very dependent on the value of α. However changing in turn T and α it is possible nit only to broaden the range in which the spectrum of interface states is measured by using both methods simultaneously also to carry out the control concerning the absence of influence on measurements of minority carriers generation.

IV. ADDITIONAL POSSIBILITIES

The rate of charge change in non-equilibrium portion of CVC could also be used to define one of the parameters of interface state - τ_d. By differentiation of Eq.2 it is possible to obtain:

$$\frac{dQ_{ss}}{dt} = \frac{qN_{ss}kT}{\tau_d + t}, \tag{14}$$

where Q_{ss}- interface states charge. It is evident that the rate of change of interface states charge becomes to time less for the period $t=\tau_d$. In [9] it was shown that

$$\frac{dQ_{ss}}{dt} = C_0\alpha(1 - q\varepsilon_s N_d C^{-3}\frac{dC}{dV}), \tag{15}$$

where C - MIS structure capacitance. Thus using the data on C(V) and dC/dV from V measurement we can with the help of Eq.15 to define the time constant. The described method should be very sensitive to inhomogenity of MIS structures in their surface charge which reduces the rate of change of interface states charge [9], However this drawback could be used for the evaluation of structure inhomogenity degree by comparing the value τ_d, obtained by this method with the value τ_d, obtained by first method described.

REFERENCES

[1] Litovsky R.N., Mikroelektr.,16, 427, (1987).
[2] Goetzberger A., Irvin J.C., IEEE Trans. Electron. Dev.,15, 1009, (1968).
[3] Simmons J.G., Wei L.S., Solid St.Electron. 16, 53, (1973).
[4] Temnikov K.L., Semushkin G.B., Mikroelektron. 17, 141, (1988).
[5] Semushkin G.B., Temnikov K.L., Mikroelectron. 18, 297, (1989).
[6] Brown D.M., Gray P.V., J.Electrochem. Soc. 115, 760, (1968).
[7] Semushkina N.A., Semushkin G.B., Tsikin A.N., Poluprov. Elektron. 1, 88, (1974).
[8] Gray P.V., Brown D.M., Appl.Phys.Lett. 8, 266, (1966).
[9] Litovchenko V.G., Gorban A.P., "Osnovi fiziki mikroelektron. sistem MDP", Kiev, (1978).

Elemental Semiconductors

Materials Science Forum Vols. 185-188 (1995) pp. 65-72

Composition, structure and modification of passivating films on semiconductors deposited at low temperatures

M.R. Baklanov and L.L. Vasilyeva

Institute of Semiconductor Physics, 630090 Novosibirsk, Russia

Keywords: Dielectric films, deposition, reaction, porosimetry

Abstract

Dielectric films prepared by CVD are widely used in the microelectronic industry. Investigations of the composition, porous structure, kinetics and mechanism of silica film formation during the reaction of silane oxidation with O_2 at low pressure and low temperature established the real reasons for the film properties.

The problem of dielectric and passivating films is a central issue in microelectronics. Therefore, during 30 years of intensive development of microelectronics different methods of their preparation have been invented. The first method which determined the success of silicon electronics was the thermal oxidation of silicon. This method has produced the excellent composition Si-SiO_2. Later on, the technology demanded other methods of preparation based mainly upon gaseous phase deposition. Nowadays such methods of preparation of dielectric films as chemical vapour deposition (CVD), variants of plasma enhanced deposition (PECVD), RF-sputtering and some others are being widely used [1]. The use of such methods has enabled the solving of specific problems. However, today a great deal of experimental data has been collected that demonstrates there are still general problems [2,3]. Without solving these general problems it is difficult to make further progress.

In a short report it is not possible even briefly to show all the possible different methods of deposition of passivating films. Therefore, we will restrict ourselves to problems dealing with the main passivating material of microelectronics - the silica films chemically deposited from the gas phase. The main problem which today has not been solved is the question about the quality of films deposited in the low temperature region ($<250\ ^\circ$C). Nowadays it is well known that as the deposition temperature decreases and the pressure increases a significant change for the worse occur of dielectric properties [4]. The content of Si-H and Si-OH groups and quantities of adsorbed water increase.

Currently new types of semiconductors based upon A3B5 and A2B6 which have low temperature stability actively are being developed. Therefore the problem of preparing high-quality dielectric films at low temperatures arises.

It is interesting to mention that the most obvious example of the change of properties is a sharp increase of the etching rate in dilute fluoric acid. The sharp change of the etching rate takes place at about 200 $^\circ$C and it does not depend upon the methods and the country they have been received from. There is enough data to show that the increase of the etching rate is directly connected with the worsening of the dielectric and mechanical properties, and the composition and structure of the layers. It is necessary to stress that analysis of the etching rate is the most simple and convenient method of fast control [3].

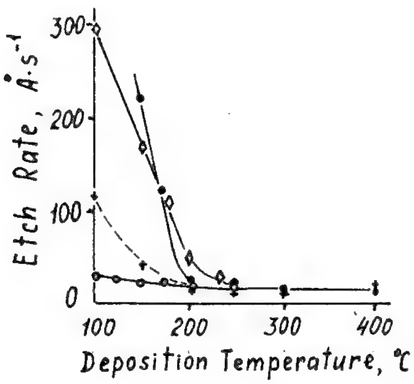

Fig.1. Dependence of silica film etching in Plyskin etchant on deposition temperature.

- • - LPLTCVD (SiH_4+O_2)
- ○ - LPLTCVD ($SiH_4+O_2+NH_3$)
- ◇ - PECVD (SiH_4+O_2)
- \+ - Photo CVD (SiH_4+O_2) [5]

The question arises: what is the reason why the layer properties become worse as the temperature decreases? Let's analyze this using the example of silane and oxygen interaction. The Brutto-equation of this reaction is well known:

$$SiH_4 + O_2 \rightarrow SiO_2 + H_2O \text{ or}$$
$$SiH_4 + O_2 \rightarrow SiO_2 + H_2$$

Actually in specific conditions from this reaction a solid product, close in composition to SiO_2 is produced. But in reality this reaction proceeds by a very complex chain branch mechanism which has not yet been understood fully. The kinetic peculiarities of this reaction have been already investigated by Shantorovitz [6] and Emeleus [7] in the thirties (Fig. 2).

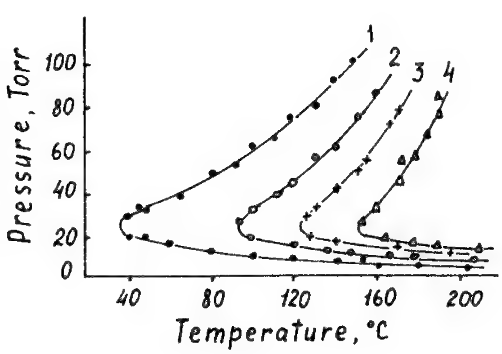

Fig.2. Self-ignition regions of silane-oxygen mixture [6].

1 - 49% SiH_4
2 - 39% SiH_4
3 - 30% SiH_4
4 - 14% SiH_4

Looking at this figure of the self-ignition region one can imagine that there is a wide region of conditions for silica film formation. But under one condition of the reaction transparent films are formed, and under another condition - the white fine grained powder (aerosyl) is produced. Microelectronics is interested only in films. To find out the conditions of the film formation several specific experiments have been conducted.

Experiments have been carried out in a tubular flow isothermal reactor at T=100-300 °C and P=0,1-1,0 Torr near the first limit of self-ignition (Fig.3a). The reactor was divided into three unequal sections. In all parts of the reactor the pressure of the gaseous mixture (P), $P(SiH_4)$, $P(O_2)$ and ratio O_2 /SiH_4 are constant. We have observed different surprising pictures in the united process [8].

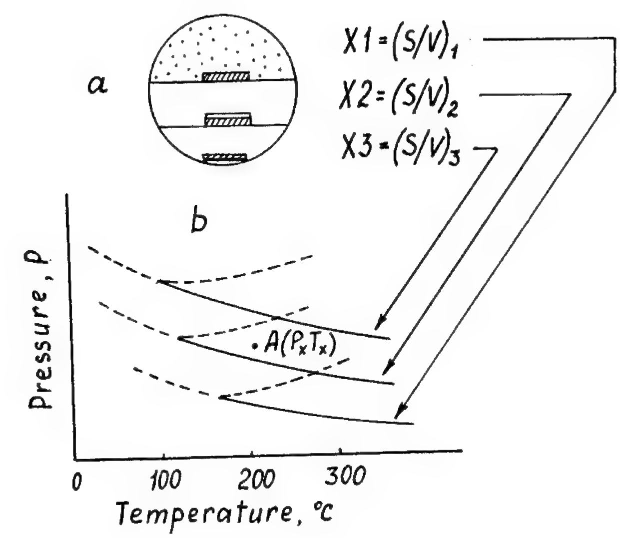

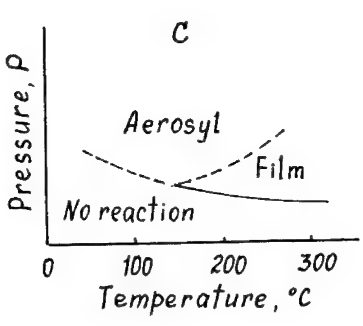

Fig.3. Cross-section of reactor (a) and peculiarities of reaction of SiH_4 with oxygen near the first limit of self-ignition (b,c).

In the lower part of the reactor - reaction does not occur, in the middle - we can see the film growth, in the upper part - the powder forms. Three above-mentioned parts of the reactor differ by the ratio $X=S/V$, where S - inner surface of reactor and V - its volume. From the theory of the chain branch reaction (CBR) it follows that the reaction rate is inversely proportional to the value of X.

In the lower part of the reactor the X value is so large that all radicals necessary for the development of the chain reaction are consumed by the walls; this means, that we are below the first limit of self-ignition. In the middle part the X-value is optimal for the heterogeneous reaction of film formation. In the upper one the intermediate concentration in the gas phase is so large that the additional channel of homogeneous reaction starts, resulting in aerosyl formation.

Therefore, inside the self-ignition region there are at least two regions differing by the products of the reaction (Fig.3c). At the X value change the first limit moves as well as the border of film formation. The position of this region was studied by means of an automatic ellipsometer which allows us to find the value of P_1 with high accuracy, when film growth begins [9]. To find the value of P_1 at the concrete conditions, the pressure was increased stepwise. During the experiment the values of the ellipsometric parameters of Ψ and Δ have been continuously recorded. For the different values of X we have received the family of curves (Fig.3b).

It is clear from the comparison of Fig.3a and Fig.3b that if the reaction takes place at the defined P_x and T_x (point A) we see the following:

- the oxidation of silane does not occur in the reactor with X3,
- the film forms in the reactor with X2,
- the aerosyl forms in the reactor with X1.

Thus we see that the value of S/V influences not only the CBR rate but also the regularity of the solid product formation (the films or aerosyl). All this is also connected with the regularities of heterophase CBR.

In our investigations it was established that the film properties worsen with decreasing temperature and increasing pressure, e.g. by shifting to the region of the aerosyl formation.

Now it is time to return to the mechanism of oxidation of the silane and try to clarify what the reasons are of powder and porous film formation. We have already mentioned that the detailed mechanism of silane oxidation has not yet been determined. Nevertheless, the efforts of experimental and theoretical workers allow us to express some definite ideas on this problem. In particular today some of radicals taking part in this reaction have been identified. They are such radicals as SiH_3, O, OH, SiO and others. In some work the possible mechanisms of silane oxidation have been analyzed. We should point out, without giving the detailed analysis of these works that the chain reaction of silane oxidation begins with the formation of the silyl radical:

$$O + SiH_4 \rightarrow SiH_3 + OH$$
$$OH + SiH_4 \rightarrow SiH_3 + H_2O$$

At the present time there is not a general consensus on the next chain transformation. Following the arguments of [2] let us consider the silyl radical, it will in future be oxidized to silanol, and later it will again take part in the development of the chain:

$$SiH_3O + SiH_4 \rightarrow SiH_3OH + SiH_3$$

Silanol is positioned to be the precursor of SiO_2. Besides the reaction of chain development, the reaction of chain termination also takes place:

$$SiH_3 + SiH_3 \rightarrow Si_2H_6$$
$$SiH_3O + SiH_3 \rightarrow (SiH_3)_2O \text{ et al.}$$

And at the end the radicals are in sufficiently high concentration to be able to actively enter the polymerization reaction.

$$SiH_3OH + SiH_3OH \rightarrow (SiH_3)_2O + H_2O$$
$$SiH_3OH + SiH_3O(SiH_2O)nSiH_3 \rightarrow SiH_3O(SiH_2O)n{+}SiH_3 + H_2$$

The last reactions result in the formation of polymer particles, including in the films, and they become porous.

For the investigation of porous structures we create the modified method of adsorption porometry. This method has been used for a long time in physical chemistry [10]. The only distinguishing feature of our method is that we have deposited the investigated films on a quartz crystal resonator. Thus we obtained the possibility to study the adsorption isotherms on thin films. It is important to mention that in the course of the experiment the following were found [3].

1. At low temperatures in silica films a large number of mesopores with diameters from 3-10 nm and with a total volume between 15-18% of the film's volume are formed. In real conditions the pores are filled by adsorptive water.

2. The concentration of pores increases with decreasing temperature of the film deposition. (Fig.4).

3. It was found that at a deposition temperature of about 200 °C the concentration of pores reaches a critical value, when in accordance with Percolation theory they become penetrated. This certainly influences the quality of the films in all ways, and this is most obvious on the curves of etching in fluoric acid. It should be stressed again that the synthesis of these layers under plasma- and photo-initiating processes does not solve the problem.

As a result there arises a natural question of how to suppress the polymerization reaction. There are some separate references in the literature that some hydride impurities of group 5 elements make a significant influence on the silane oxidation regularities. So it was shown [11] that the phosphide impurities in some specific conditions greatly increase the growth rate and to a lesser degree the coagulation of particles in the gaseous phase. Taking into account the little data available and our own intuition we decided to study the influence of small amounts of NH_3 impurities on the process of film deposition.

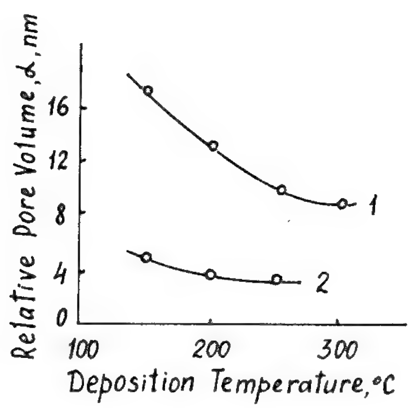

Fig.4. Dependence of relative open pore volume $\alpha = V_p/S_s$ (V_p is open pore volume, S_s is the area of film surface) of silica films 200 nm thick on the synthesis temperature:
1) Films synthesized from SiH_4 and O_2;
2) Films synthesized from the mixture $SiH_4+O_2+NH_3$.

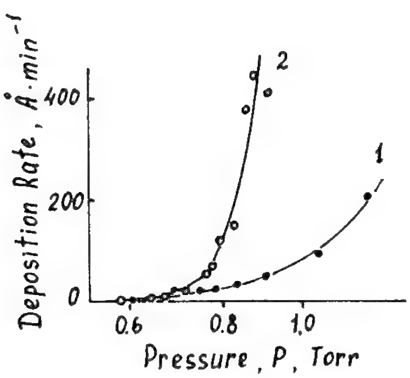

Fig.5. Dependence of deposition rate of the silica films on pressure.
1) Deposition rate without ammonia;
2) Deposition rate with ammonia;

The experiments were carried out in the temperature range from 120 to 250 °C [12]. It was found that a small ammonia addition to the gaseous phase significantly increased the growth rate of films (Fig.5). This was independent of the concentration of ammonia at least in the range from 0.05 to 0.4 Torr. By the method of Auger-spectroscopy it was found that the nitrogen concentration in the films did not exceed 1-3%. Si-N bonds were not found in the IR-spectra. Therefore the effect of the rate increase was not accompanied by a change of film composition. It was concluded after the analysis of the experimental data that the main effect of the rate increase is connected with the influence of ammonia at the stage of polymerization of the silane oxidation intermediate products. If this is so, then with an increase of growth rate there should be an increase in the film density, because there is a decrease on the part of particles which are input into the film. The experiments carried out by adsorption porometry have proved this. As it is clear from Fig.1, the films deposited with the addition of ammonia have much smaller concentrations of pores, and their etching does not produce specific features near the deposition temperature of about 200 °C [3]. These films have much better electrophysical characteristics.

That is the approximate situation with the problem of optimization of the structure and composition of passivating silica films deposited by low pressure and low temperature

chemical vapour deposition. Many details of the experimental data which were produced in our Institute recently have been omitted. The maim aim of this report was to show that there are variants in solving the problems of quality low temperature passivating layers.

Acknowledgment

The authors would like to thank L.A.Nenasheba, F.N.Dultsev, K.P.Mogilnikov, V.V.Nosov and V.N.Kruchinin for the assistance in performing experiments.

References

[1] Von G.Wahl, CVD Processes, Vacuum Technik, 38, 195 (1989)
[2] C.J.Guinta, J.D.Chapple-Sokol, R.G.Gordon, J.Electrochem.Soc., 137, 3237 (1990)
[3] M.R.Baklanov, L.L.Vasilyeva, et al., Thin Solid Films, 171, 43 (1989)
[4] I.I.Belousov, V.M.Efimov, S.P.Sinitsa, Preprint ISP, 1991.
[5] Y.Tarui, J.Hidaka, K.Aota, Jpn.J.Appl.Phys.,23, L827 (1984)
[6] P.S.Shantarovitz, Acta Physicochim, URSS, 6, 65 (1937)
[7] H.J.Emeleus, K.Stewart, J.Chem.Soc., 1182 (1935)
[8] L.L.Vasilyeva, L.A.Nenasheva, V.V.Nosov, Chimicheskaya fisika (in Russian), 11, 1399 (1992)
[9] L.L.Vasilyeva, V.N.Kruchinin, L.A.Nenasheva, V.V.Nosov, Poverchnost (in Russian), 2, 54 (1992)
[10] S.J.Gregg, K.S.W.Sing, Adsorption, Surface Area and Porosity, Academic Press, New York, 1982.
[11] A.Shintani, K.Suda, M.Maki, J.Electrochem.Soc., 124, 1771 (1977); A.Shintani, K.Suda, M.Maki, J.Electrochem.Soc., 127, 426 (1990)
[12] L.L.Vasilyeva, L.A.Nenasheva, F.N.Dultsev. Kinetika i Kataliz, (in Russian), 30, 613 (1992)

Materials Science Forum Vols. 185-188 (1995) pp. 73-82

Passivity and electronic properties of the silicon/silicondioxide interface

H. Flietner

Hahn-Meitner-Institut, Abt. Photovoltaik, Rudower Chaussee 5, D-12489 Berlin, Germany

Keywords: Nature of interface defects, chemical reactions, recombination, natural oxidation, luminescence

Abstract: With the help of the term spectroscopy one can detect and follow the development and changes of the different defect species at the interface. In addition to the known defects (strained Si bonds, Si dangling bonds (DB) with different Si-O back bonds) a new Si DB defect at midgap is discovered which is attributed to a different modification of back bonds. Each defect group has its specific chemical behaviour and affects in a distinct way stability and passivity. All bonds at interfaces have their corresponding DB defects.

The study of recombination indicates that the intrinsic Si DB (U_M-distribution) is the dominant defect determining the recombination process.

The energy distribution of interface states $D_{it}(E)$ obtained by SPV (surface photovoltage) or MCV (modulated capacitance voltage) in a contactless way allows to study etched surfaces and natural oxidation at any stage of preparation. D_{it} is a good figure of merit for the quality of the technological process including oxidation. With a good H-termination by proper chemical treatments an U-shaped distribution with midgap concentrations down to several $10^{10}cm^{-2}eV^{-1}$ may be obtained.

The luminescence of porous Si strongly correlates with the development and the changes of certain defect species at the interface.

Introduction

Passivity depends strongly upon the kind of chemical bonding in the system under consideration. Surfaces and interfaces are the prevailing systems responsible for instabilities and here again the subsystem of defects. Therefore it needs a better understanding of bonds and defects at interfaces. Most methods characterizing structure and composition are not sensitive enough to detect the relevant defects as their concentration is ranging from 10^{13} to 10^{10} cm^{-2} or even lower. And vice versa: Most defect sensitive methods do not give information about structure and chemical composition. EPR is to some extent an exception and an important link between both. The Si/SiO_2 interface offers to be a good system for studies of such problems because of the excellent quality of its technology, a wealth of experimental data, an advanced and reliable theoretical background and last not least the widespread interest in this system and therefore the possibility for a comparison of results of many groups of researchers. Great effort is done now to fill the gap of knowledge between chemical composition and electronic behaviour stimulated by new methods and new technologies as may be seen by [1,2] and this conference.

As to the defects we developed a method called "term spectroscopy" [3] which yields a correlation between electronic data (energy distribution of states etc.) and the nature of the defects [4,5]. The energy distribution of interface states at Si/SiO_2 has its origin in defects of a different chemical character. The isolated defects (with localized wave functions even for defects up to the band edges) may be separated into groups of states each group behaving differently in technological processes and stress. Each group has its characteristic spectrum, specified by its position in energy and its shape. It was shown that these features are attributed to chemical bonding and structural properties of the involved defects.

The groups of states at Si/SiO_2 interfaces are correlated to various kinds of Si

dangling bond (DB) defects differing in the surrounding of nearest neighbours (back bonds). The special shape of the related spectra is determined by the scatter in geometrical structure of the isolated defects belonging to the same group. According to the different back bonding of the defects, lattice strain will influence the structure (reconstruction) and cause de-hybridization in a degree depending on the strength of the bonds. The result is seen directly as a shift of electronic levels which determines the width of the spectrum of the group.

The results of the Si/SiO_2-interface studies are of a wider interest as the underlying model [4] even allows a unified treatment and understanding of phenomena at interfaces of semiconductors with predominant homopolar bonding. No theoretical calculations exist up to now to match the experimental observations. Thus this above mentioned semi-empirical treatment, the use of the complex band structure (which gives general correlations for the intrinsic defect behaviour) and some assumptions concerning the degree of disorder, is an important step to understanding. The chemical behaviour of the defects may be understood by the concept of their electronegativity given by their charge neutrality levels (CNL). This CNL also helps to understand Schottky barrier behaviour and Fermi level pinning [6].

After discussing the model the following sections are treating the kinetic properties of the interface states, the study of etching processes and natural oxidation as well as the correlation between luminescence of porous silicon and interface properties.

Experimental methods and results of term spectroscopy

To follow exactly the influence of treatments and stress, two contactless methods are applied. They are the long approved large signal surface photovoltage method (SPV) [7] and a newly developed modulation CV method (MCV) [8] which relies on the high sensitive detuning of a resonant circuit. In both cases an applied voltage changes the Fermi level at the surface and hence the occupation of the interface states. In the case of SPV a strong light pulse flattens the bands. The corresponding change and relaxation of the work function is measured and $D_{it}(E)$, the energy distribution of interface traps and their characteristic relaxation times are determined. MCV measures the complex impedance, which is again dependent on the position of the Fermi level at the surface, from which $D_{it}(E)$ and the relaxation spectrum are deduced. Both methods give full information as complementary pulse and spectral methods do, each with its specific advantages.

On the background of a large variety of *treatments like etching and natural oxidation, thermal oxidation, anodical oxidation, CVD-deposition, stress* (different kinds of radiation, thermal, electrical) we analysed the D_{it}-distributions and fixed oxide charges at the Si/SiO_2-interfaces received in our own or in other laboratories [9] and found that the continuous D_{it}-distributions are composed of a few *individual groups of states at the interface: band tails (U_T), symmetrical midgap states (U_M), two peaked distributions at low and high position in the gap (P_L, P_H)* [3]. These groups behave differently and may therefore distinctively be separated. The corresponding characteristic data of these groups are given in table 1.

Tab.1: Characteristics of term groups (E_t, σ_t = center, width of distribution)

Group	E_t-E_v(eV)	σ_t(eV)	kind of distribution	g_t(EPR)	Si-H bond
U_T	0,02	0,04	$N_{v,c}\exp(-\beta_{v,c}\vert E_{v,c}-E\vert)$	-	no
U_M	0,2*	0,4*	$\propto \vert dK/dE\vert$, K=Im(k)	2,006	strongest
P_L	0,4	0,12	$N_t/(\sigma_t\sqrt{(2\pi)}) * \exp-(E_t-E)^2/2\sigma_t^2$	2,003	less strong
P_H	0,7	0,08	"	?	weakest
P_{Ox}	>E_c	$\propto 0$	"	2,0008	nearly no

* values given for the donor part of the distribution

The P_{Ox}-centre is not seen in the D_{it}-distribution because of its energetic position, it contributes to the positive fixed charge like the similar E'-center. The trend in the g_t-value reflects the dehybridization from the tetrahedron-type (U_M) to the p-type wave function (P_{Ox}). The defects of each group (U_M .. P_{Ox}) have different Si-H bonding strength.

These interface state distributions show some further remarkable properties:

U_T is apparently insensitive to post oxidation treatments and stress. For at least four decades of density U_T shows at both band edges to a good approximation an exponential behaviour with $ß_v<ß_c$ ($m_cß_v \approx m_vß_c$). This exponential behaviour indicates that the accompanied isolated defects are *statistically* distributed according to a Boltzmann-distribution. No energy nor any structure is preferred in that group of states. If one knows the freezing temperature T_0 of the Si/SiO_2-system the total energy of the isolated defects may be found from their electronic position E by the relation $ß_{v,c}\,|E_{v,c}-E| = E_{tot}/kT_0$. With T_0=900°C and experimentally found values of $ß_{v,c}$ of about $40eV^{-1}$ one gets $3|E_{v,c}-E| = E_{tot}$. U_T-states have never been observed with $E_{tot} > \frac{1}{4}(E_{Si-Si})$.

The other groups of states U_M, P_L and P_H are sensitive to technological treatments and stress. All groups show a very important special feature: During all treatments only the total number of states of each group changes, the characteristic position and shape of the spectrum of each group remains unchanged. This may be described by

$$U_M = N_M u_M(E_0,E),\;\; P_L = N_L g_L(E_L,\sigma_L,E),\;\; P_H = N_H g_H(E_H,\sigma_H,E)$$

where N_M, N_L, N_H are the total numbers and u_M, g_L, g_H the corresponding characteristic shapes. u_M is approximately given by $|dK/dE|$ of the complex band structure and a disorder assumption, g_L and g_H are Gaussian distributions [3-5]. Therefore the interface is completely characterized by the numbers N_M, N_L, N_H and the fixed oxide charge.

The group U_M lies totally inside the Si-band gap almost symmetrically to midgap with a small gap left to the band edges. The total width is about $\frac{3}{4}E_g$, filling just about the space left in the gap by U_T with a small overlap. The shape is nearly symmetrical about a point E_0 somewhat below midgap. E_0 is the CNL, the states below being donors, the states above acceptors. Therefore the accompanied defects exhibit an amphoteric character. The camel-hump like shape causes several authors to believe the states in the humps being different from the states at midgap. But it could clearly be identified that the chemical character is completely equivalent, only the geometrical structure of the defects differ in hybridization.

In the next section the model which fits these properties will be described shortly.

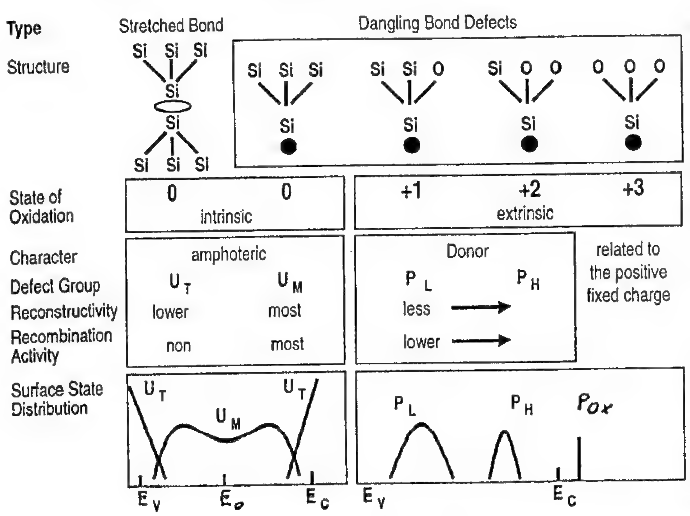

Fig.1: Defects and term groups at the Si/SiO_2 interface

Model considerations and the nature of defects

The essential features of the model are summarized in fig.1 as an excerpt of former papers [3-5] and in agreement with the results of other laboratories [9]. Many aspects of this model are supported by EPR [10-12].

As mentioned above the distributions U_T and U_M are nearly symmetrical around midgap. This suggests that their origin is determined by the complex band structure which continues the E(k)-traces of the bands into the gap where

imaginary values of k (decaying wave functions) give real values of E(k). K=Im(k) is determined by the geometrical configuration of the defect. The above mentioned scatter in geometry gives a certain N(K)-distribution of states. A δ-distribution in K-space means that all defects of the group have the same geometry. The complementary distribution to δ(K), a constant density of states in K-space means a large scatter in geometry which may be understood as disorder only governed by conditions in energy. The width of the distribution is therefore a measure of the scatter in geometry within the considered group. With the help of E(K), N(K) may be transformed to N(E). The amount of the scatter is determined by the bonds. The U_M-distribution may be calculated to a first approximation by the assumption of a complete disorder [4].

Next we consider the symmetry. Irrespective of the kind of defect each localized neutral state has a certain ionization energy and electron affinity. According to a rule of chemistry [13] the mean value of both quantities is a measure for the attraction of the electron by the neutral atom called electronegativity which is a controlling factor for binding. For the intrinsic defects both levels lie *inside* the gap. The defects are amphoteric. This is a direct consequence of the homopolar character that the intrinsic localized disturbance gives rise to a splitting from the bands into *two* levels (split Shockley-like levels [3, (1982, 1985)]. All intrinsic defects have the same mean value E_0 (fig.1, [4]) and hence the same binding behaviour. The exceptional situation for the U_M-states at E_0 (ionization energy = electron affinity) demonstrates the large ability for reconstruction of these centres. Also from these chemical considerations it is seen that E_0 is the CNL as determined by the band structure (from E_g, m_c, m_v) [4]. For the peaked distributions which are less able for reconstruction the electron affinity lies much higher (>> E_c). Therefore they have smaller electronegativities the higher their mean trap energy E_t is. By this way we understand the binding behaviour of these defects.

For large values of N_M (>10^{12}cm^{-2}) pinning of the Fermi level occurs at E_0. Metal/semiconductor contacts show this pinning or not depending on the reactivity of the metal and the creating defects. Another effect is the sensitivity of the Schottky barrier to the work function of the metal. This depends on the originated dipole at the contact given by K from the complex band structure [6]. Both effects, pinning and Schottky barrier behaviour must be distinguished which is often missed by applying the MIGS (metal induced gap states) model.

Kinetic behaviour of interface defects

Recombination and relaxation processes depend sensitively on the properties of the defects, i.e. their electronic structure. To get information about the recombination activity and the trapping behaviour of the different defects samples were prepared with a large variety of interface defect distributions especially with as large as possible different contributions of the groups to the total distribution. Fig.2 shows in the upper part D_{it}-distributions, in the lower part corresponding curves of the effective lifetime τ [14]. The different distributions (●, ○) are achieved by different oxidation stages after HF treatment. The curves for p-Si as well as for n-Si differ only by a

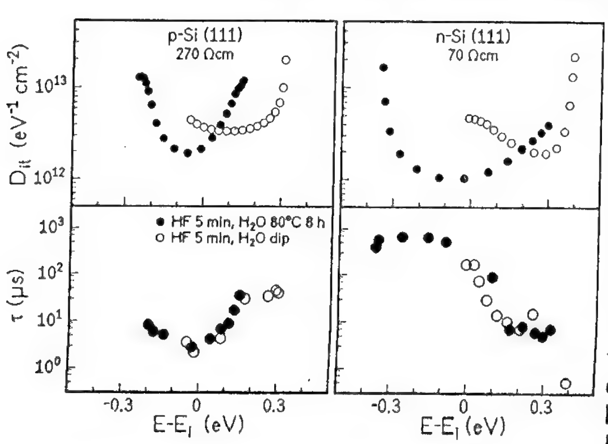

Fig.2: D_{it} and lifetime for different defect distributions

varying contribution of P_L and P_H states. Both curves (● and ○) contain the same U_M-distribution. From the lower part (τ-curves) it is seen that the peaked distributions do not influence the recombination process. It is therefore concluded that U_M is mainly responsible for recombination. The strong exchange of energy with the lattice together with the amphoteric character are determining the recombination effectiveness. It is necessary to consider in the rate equations for the Shockley-Read process not only the different occupation of states of the dangling bond [15]. One has to keep in mind that the splitting of the Quasi-Fermi levels at midgap creates both states, the ionized donor levels *and* the negatively charged acceptor levels simultaneously.

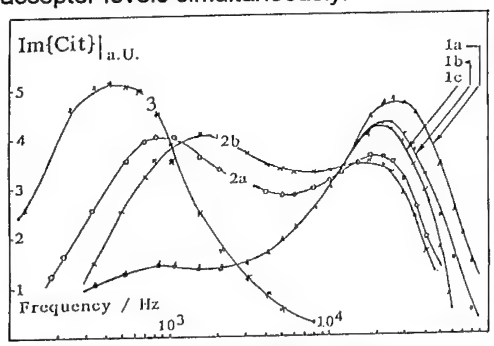

Fig.3: Relaxation spectra of etched, H-terminated and natural oxidized Si(111) surfaces

Fig.3 shows the sensitivity of the relaxation spectrum on the preparation [8]. Curves 1a-c correspond to a RCA cleaning process, curve 3 to a HF-dipped sample (nearly H-terminated), curves 2a,b to a natural oxidized stage. Contrary to the recombination process the trapping process is sensitively influenced by *all* groups. Especially with the curves 2a,b it is seen that the oxidation process which brings about peaked distributions (see below) changes the relaxation spectrum remarkably. The H-terminated surface has a tendency to lower relaxation times while the peaked distributions tend to higher frequencies. The curves labelled by a,b,c correspond to different positions of the Fermi level which enables to vary the contributions of different groups.

Study of etching and natural oxidation

The properties of etched Si-surfaces are important as they are the starting point for the preparation of thin oxides, epitaxial layers and passivation layers and since MOSFETs could be build up with natural oxides they have become of topical interest [1,2,16,17]. The new impact for research in this field stems originally from the necessity of controlling the properties of very thin oxides for getting higher degrees of integration in MOS integrated circuits. The thinner the oxides or oxinitrides as dielectric layers the higher the influences of interfaces on breakdown and instabilities. A high degree of stability means in this case to control the influence of the interface on electronic processes, i.e. electrons or holes which are going sideways and reacting with defects [1, Hot Electron Session].

Etching processes as the first step in preparation should make the surface clean and free of disturbing oxide layers. The normal etch-solutions like for example the RCA-etch leaves an interface with an oxide layer of uncontrolled structure [18]. The large progress made recently was the preparation of H-terminated surfaces, which gives an atomical flat 111-Si-surface with the saturation of the surface bonds by hydrogen [19-24]. In the early days of semiconductor surface physics such surfaces were obtained with Ge in an electrolyte solution and the surface could be terminated either by H or by OH depending on the polarity of the reaction [25]. The cleanest surfaces in the sense of the lowest concentration of surface states as could be seen by CV-measurements were prepared in this way. This is a revival of old ideas. Also for Schottky-barriers the H-termination is of influence in unpinning the Fermi-level [26,27] which may be understood by the above presented model.

We studied earlier the influence of HF and H_2O on the energy distribution of surface states at real surfaces of silicon [7]. By several cycles of HF-soak and water rinsing we succeeded in well conditioned (for that time) surfaces. Directly after a short water rinsing we observed the U_M-distribution and a large P_L-peak. This P_L-peak could be removed by a long

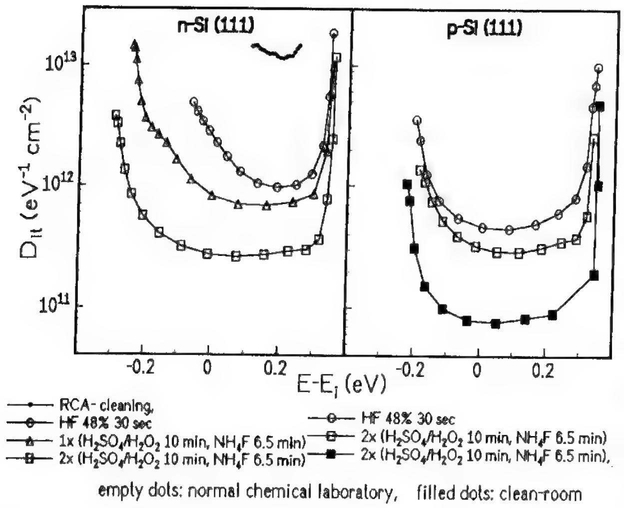

Fig.4: D_{it} for differently etched surfaces

term water rinsing (>24h at RT). Minimum term concentrations of about $10^{12}cm^{-2}eV^{-1}$ at midgap were observed. This final U-shaped distribution we called intrinsic, because a close relation to bonds of the pure silicon seemed obvious. Our recent results are in full agreement with these former ones. Now the better starting point of H-terminated surfaces brought better results.

Fig.4 shows for comparison the action of different etching processes on D_{it} up to the H-termination for surfaces of n- and p-Si. RCA-cleaning is shown for comparison and it obviously yields a poor surface. At the n-type specimen clearly an influence of P_L is seen for an incomplete preparation. Such small influences can only be seen by term spectroscopy so that this kind of control is a monitoring for a well H-terminated surface. D_{it}-values well below $10^{11}cm^{-2}eV^{-1}$ at midgap are observed, values which were up to now only received by thermal oxidation and annealing processes. The distributions are very sensitive to the pH-value of the etch which is a measure for the balance of the HF-attack to Si and the oxidizing reactions by H_2O [24].

Fig.5 shows the oxidation process in deionized water of the H-terminated surface. At the beginning a P_L-group arises, vanishes and a P_H-group arises and vanishes as well so that D_{it} for a long term oxidation in water is near to the starting D_{it} of the H-terminated surface (a). The XPS-curves indicate the corresponding changes of bonds by small peaks at the chemical shifted position (b).

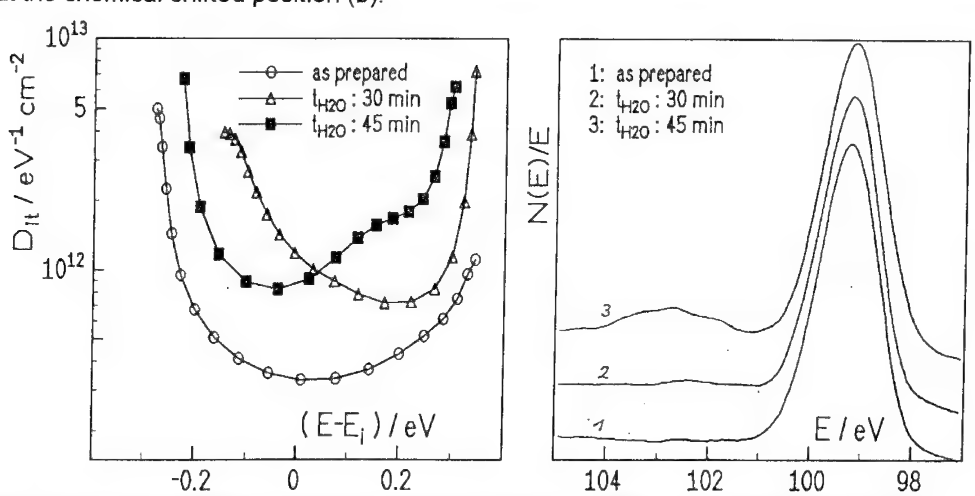

Fig.5: (a) D_{it} for H-terminated and naturally oxidized (H_2O) Si(111) surfaces, (b) correlated XPS-spectra

The oxidation in air has some other peculiarities seen in fig.6. Starting point is the HF-treated surface. During this oxidation process in air of 50% moisture a new group of states is found directly at midgap. This group arises and vanishes during the oxidation process and

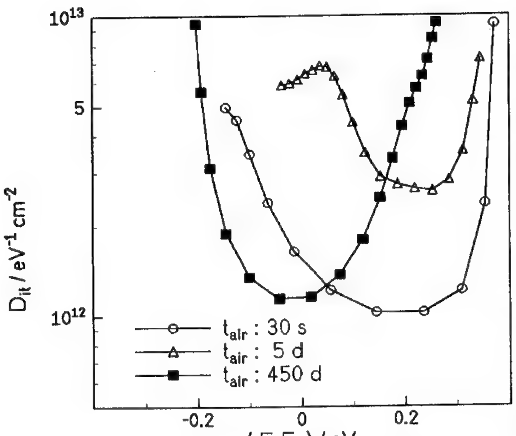

Fig.6: D_{it} for H-terminated and naturally oxidized (clean room air) Si(111) surfaces

may be attributed to the Si-DB with one Si-OH-back bond because this bond is known as being transient during the oxidation process. Further support is given to this interpretation because this bond is between P_L and P_H with respect to the dehybridisation from the tetrahedric bond to the pure p-bond. We may call this group P_M. This group may be fit into table 1 between P_L and P_H with the corresponding properties. Together with this defect all oxidation stages of the DB at the interface are present [30,31]. Even with a long duration of the air oxidation the P_H-group can not be eliminated, which indicates in this case the incompleteness of the oxidation process. This is also seen by the fixed oxide charge which has a large amount in this case. The fixed oxide charge has ist correspondence in the position of the Fermi level.

This position of the Fermi-level is a further important parameter of characterisation. Fig.7 shows the time dependence of D_{it} at midgap and the position of the Fermi-level at the surface during natural oxidation in clean room air. It is seen that there are three phases of time dependence corresponding to three different stages of the oxidation process. During the first period up to about several hours we observe a retardation of the process. The H-termination of the surface behaves passivating, which is of great importance concerning the handling of samples. This period is dominated by the growth of a monoxide-like layer which is seen in the D_{it}-picture by the P_L-development. The next period up to about one week of a faster growth is accompanied by a remarkable shift of the Fermi level from a strong n-type surface to a nearly intrinsic position. The increase of D_{it}(midgap) during the fast period and the decrease in the last period of a constant Fermi level is due to the changes of the peaked distributions. Interesting that a final situation may be obtained with the Fermi level at about midgap and an U-distribution with a low N_M (<10^{11}cm^{-2}). But this needs special effort. A comparison with the hot water oxidation above shows that different kinds of oxidation processes are performed. The completely different development of the defects gives clear hints to these differences.

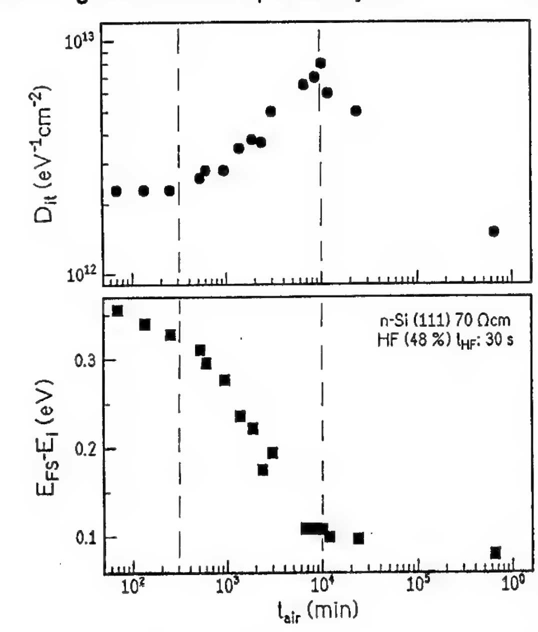

Fig.7: D_{it}(midgap) and Fermi level during natural oxidation in moist (50%) air

Fig.8 demonstrates that the retardation time is strongly dependent on the length of the HF-treatment. A too lengthy HF-treatment results in a rough surface and a poor H-termination as seen from the results above. But all HF-treated surfaces have the same time dependence of the fast oxidation period. It is the logarithmic time dependence which is known for the growth of the first layers. For p-type sam-

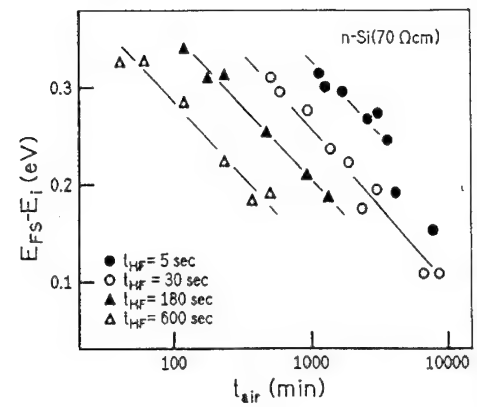

Fig.8: Influence of HF-treatment on natural oxide growth

ples the H-termination produces an inversion layer.

The existence of an n-type surface, a well known property of HF-treated surfaces, could be attributed to the existence of a P_H-group, which not in all cases is easy to be detected. This donor group above midgap (or an other group still higher in the gap and up to now not clearly detected) could give rise to this n-type surface and hence to a positive oxide charge. With a good H-termination such a group can be avoided. For applications this behaviour is very important because it is a widespread usage to produce n-type surfaces (even inversion on p-type Material) with a HF-dip. The term "fixed oxide charges" is here used in a wider sense then usually in connection with thermally oxidized surfaces. It is used more in the sense of the early slow states at etched surfaces, a species with remarkably lower cross sections [32].

Luminescence of porous silicon and its correlation to changes of interface defects

The study of porous silicon is a major topic today and many problems are not yet sufficiently resolved [33]. The luminescence is determined by the confinement of the columns [34] as well as by surface properties [35-37].

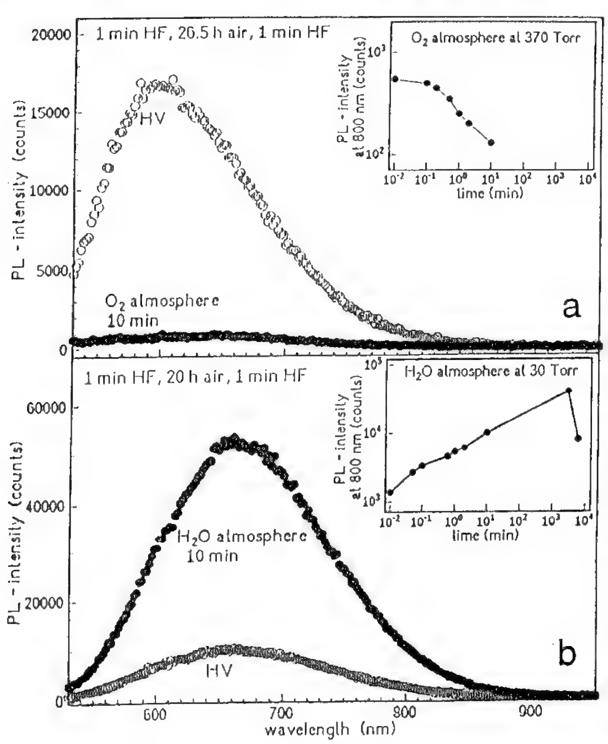

Fig.9: Influence of surface treatment and atmosphere on the photoluminescence of porous Si

Fig.9 demonstrates clearly both of these dependencies [38]. After the preparation of the porous layer by an electrochemical etching process (standard preparation: $HF:C_2H_5OH:H_2O=1:1:2$, 30mA/cm^2 anodical current) two different samples were prepared differing only in the oxidation time in air between two consecutive HF-treatments. By this way curve a with the shorter oxidation time exhibits a longer wavelength of luminescence then curve b with the longer oxidation time. The longer oxidation reduces the width of the columns of the porous silicon and therefore influences the characteristic wavelength. The time dependence of the intensity of the luminescence of the specimens exposed to dry air and to water vapour is shown in the inserts. The intensity in wet atmospheres follows the growth and decay of the P_M-group of fig.6. The intensity decay in dry O_2 corre-

sponds to the formation of U_M-type dangling bonds during the oxidation process. But one must be aware that the surface structure and therefore the reactivity differs remarkably from the flat surfaces of the previous sections.

Conclusions

A good characterization of the influence of technological processes and stress on the electronic properties of surfaces and interfaces needs experimental techniques without any further preparation which may disturb the state under examination. SPV and MCV are such methods which give full information about the energy distribution of interface states , fixed oxide charges and relaxation and recombination.

The method of term spectroscopy allows to determine very sensitively the different kinds of defects existing at interfaces. This is a reliable monitoring of the quality of the technological process. A good H-terminated surface is characterized by an U-shaped D_{it}-distribution with a low density of states (< $10^{11}cm^{-2}eV^{-1}$ at midgap). Only intrinsic defects then exist. The oxidation process may be followed by the developing of the different kinds of extrinsic Si DB defects (with Si-O back bonds). It is seen that different oxidation processes have their specific creation scheme of defects while the processes as different as they may be can always be described by these few kinds of defects, given by their respective numbers or concentrations per cm squared. An interesting case is that a properly performed natural oxidation process (in our case with H_2O) leads finally to nearly the same U-distribution as at the starting point. Such case was never observed with other oxidation processes.

A comparison between the reactions at interfaces and the time dependence of the luminescence intensity after exposing the porous Si to certain atmospheres allows the conclusion that this luminescence is strongly dependent on surface defects.

The information about the nature of the involved defects was extracted from a semi-empirical model which uses the complex band structure, assumptions about the geometrical disorder and the accompanied dehybridization and some relations known from the nature of chemical bond. Though this model is only a semi-empirical one it gives a unified description of the electronic behaviour of interfaces of semiconductors with predominant homopolar bonding. There are only a few kinds of defects at the interface. All defects are Si DB with different back bonds which determine the chemical activity and the electronic behaviour. The special conditions for the intrinsic Si DB allow a very high reconstruction of the centres which is the reason for the amphoteric character and the recombination activity of these states. At about midgap (at the CNL) even the total electron-electron interaction energy may be absorbed by the lattice. At this point the electron level of the acceptor state with two electrons is the same as that of the donor state with one electron.

Other interesting facts are the shapes of the spectra of the different defects i.e. the different groups of states. The Boltzmann-distribution of the U_T-states shows that the strain accompanying any lattice mismatch gives rise to *statistically* distributed defects. The situation that the spectrum of each defect group has its specific shape which is maintained during all reactions leads to conclusions about the dehybridisation caused by the elastic energy of the interface. Further information about the structure of the defects could be gathered by a deeper analysis of these spectra.

This paper gives a first analysis of defect reactions during natural oxidation processes. The study of defects during technological reactions in addition to the study of growth processes, bonds and structures are necessary complementary activities in this field. Finally one should not forget that Fermi-level pinning and the dipole action at metal semiconductor contacts are already well described by this model. Also band offsets are within the scope of this description whereas the CNL of the two components act like the electronegativity in bonding [3,4]. The model may be called

CAB = **c**omplex **b**and structure **b**onding model.

References

[1] Insulating Films on Semiconductors, Proc. 8th Conf., June 1993, Delft (Nd), Ed. P. Balk, J.J.M. de Nijs, Elsevier Publ. 1993
[2] Formation of Semiconductor Interfaces, Proc. 4th Int. Conf. June 1993, Jülich (D), Ed. B. Lengeler, H. Lüth, W. Mönch, J. Pollmann, World Sci. Publ. 1994
[3] H. Flietner et al: phys. stat. sol. (a) **37** 533(1976), **43** K99(1977); Phys. d. Halbleiteroberfläche **13** 157(1982), **16** 1(1985); Phys. Probl. in Microelectronics, Ed. J.Kassabov, World Sci. Publ. p.410(1985)
[4] H. Flietner: phys. stat. sol (a) **91** 153(1985); Surf. Sci. **200** 463(1988); INFOS 1991, Ed. W. Eccleston, M. Uren. Adam Hilger Publ. p.151(1991)
[5] W. Füssel et al: Nucl. Instr. & Meth. in Phys. Res. **B65** 238(1992); Proc. 11th Europ. Photovolt. Solar Energy Conf, Montreux 1992, Harwood Acad. Publ. p.746(1993).
[6] H. Flietner: phys. stat. sol. (b) **54** 201(1972), **90** K27(1978), **142** K31(1987)
[7] K. Heilig, H. Flietner, J. Reineke: J. Phys. D: Appl. Phys. **12** 927(1979)
[8] N. D. Sinh, H. Flietner in [2, p.369]
[9] P. Balk Ed.: The Si-SiO_2 System, Mat. Sci. Monogr. **32** (1988)
[10] E. H. Pointdexter, K. L. Brower, A. Stesmans, M. Stutzmann, P. M. Lenahan: Articles in. Zs. Phys. Chem. (NF) **151** 165-235(1987)
[11] P. M. Lenahan in [1, p.129]
[12] A. Stesmans, F. Scheerlinck in [1, p.139]
[13] L. Pauling: Natur d. Chem. Bindung, Vlg. Chemie, Weinheim 1968, p.91
[14] H. Angermann, Th. Dittrich, K. Kliefoth, H. Flietner in Thin Films, Ed. G. Hecht, F. Richter, J. Hahn, DGM Informationsges. Vlg. p.518(1994)
[15] M. Lannoo, D. Vuillaume, D. Deresmes, D. Stiévenard in [1, p.143]
[16] M. Morita et al: Appl. Phys. Lett. **55** 562(1989); J. Appl. Phys. **68** 1272(1990); Jap. J. Appl. Phys. **29** L2392(1990); Jap. J. Appl. Phys. **33** 370(1994)
[17] M. Hirose et al in [1, p.3]; Mat. Res. Symp. Soc. **22** 225(1991)
[18] W. Kern: Surf. Sci. **31** 207(1970)
[19] Y.Y. Chabal, G.S. Higashi, K. Raghavachari: J. Vac. Sci. Technol **A7** 2104(1989)
[20] G.S. Higashi et al: Appl. Phys. Lett. **56** 656(1990); **58** 1656(1991)
[21] M. Meuris et al in [1, p.21]
[22] T. Bitzer, M. Gruyters, H.J. Lewerenz, K. Jakob: . Appl. Phys. Lett. **63** 397(1993)
[23] Dittrich et al: phys. stat. sol. (a) **140** 463(1993); J. Electrochem. Soc.(1994), subm.
[24] Angermann et al: Appl. Phys. A: Solids and Surf. in press (1994); 2. Int. Symp. on Ultra Clean Processing of Silicon Surfaces; Bruges, Belgium, Sept. 19-21 (1994)
[25] W. H. Brattain, P. J. Boddy: J. Electrochem. Soc. **109** 574(1962)
[26] V. Yu. Aristov et al in [2, p.245]
[27] W. Mönch: Phys. Low-Dim. Struct. **4/5** 1(1994).
[28] D. Gräf, M. Grundner, R. Schulz: J. Appl. Phys. **68** 5155(1990)
[29] M. Niwano et al: Surf. Sci Lett. **301** L245(1994).
[30] F.J. Himpsel et al: Phys. Rev. B **38** 6084(1988)
[31] T. Hattori, H. Nohira, K. Ohishi, Y. Shimizu, Y. Tamura in [2, p.385]
[32] H. Flietner: phys. stat. sol. **2** 221(1962)
[33] E-MRS Spring Meeting, May 24-27, 1994, Strasbourg (F), Symposium F
[34] L. T. Canham: Appl. Phys. Lett. **57** 1040(1990)
[35] F. Koch: Mat. Res. Soc. Symp. **298** 319(1993)
[36] Y. Kato, T. Ito, A. Hiraki: Appl. Surf. Sci. **41/42** 614(1989)
[37] F. C. Rong, J. F. Harvey, E. H. Pointdexter, G. J. Gerardi in [1, p.147]
[38] Th. Dittrich et al in Thin Films, Ed. G.Hecht, F. Richter, J. Hahn, DGM Informationsges. Vlg., p.490(1994)

Materials Science Forum Vols. 185-188 (1995) pp. 83-90

Electrochemical and electronic passivation by hydrogenation of n-Si(111)

J. Rappich[1] and H.J. Lewerenz[2]

[1] Hahn-Meitner-Institut, Bereich Angewandte Physik, Abteilung Photovoltaik, Rudower Chaussee 5, D-12489 Berlin, Germany

[2] Hahn-Meitner-Institut, Bereich Physikalische Chemie, Abteilung Grenzflächen, Glienicker Str. 100, D-14109 Berlin, Germany

Keywords: Silicon, photocurrent oscillations, hydrogen-passivation, in-situ FTIR spectroscopy, surface photovoltage, density of interface states

Abstract

The surface condition of n-Si(111) exposed to an acidic fluoride solution is strongly influenced by the applied electrode potential. Some observations of electrochemical investigations are the occurrence of a hitherto unexplained dark current after oxide removal which can be used for hydrogen termination of n-Si(111) and the photocurrrent oscillations at high anodic potentials.

Photoinduced electropolishing treatments on n-Si(111) in an acidic fluoride solution followed by the dark current transient lead to a reduction of the microscopic roughness of these surfaces as investigated by in-situ Fourier transform infrared spectroscopy (FTIR) within the attenuated total reflection (ATR) mode. Furthermore, the photocurrent oscillation treatment as smoothening procedure leads to an improved passivation.

Introduction

Hydrogen-passivated and unreconstructed Si(111)-(1x1) surfaces have been prepared by chemical [1] as well as by electrochemical treatments [2-4] and result in a similar surface condition [3, 5-7]. The advantage of the electrochemical method is the control of the surface preparation by electrode potential, current and illumination [2].

Electrochemical investigations on the silicon/electrolyte interface have led to several surprising observations such as the occurrence of the dark current in fluoride containing solutions during and after oxide removal [8, 9] and the photocurrent oscillations whose physico-chemical basis could not yet be identified [10-13].

Evidence that the oscillatory behavior leads to changes in surface morphology was recently obtained with in-situ ellipsometry, scanning tunneling microscopy (STM), in-situ FTIR and combined ex-situ electrochemistry/surface analysis experiments [14-16]. In the present work we investigate the changes in surface microtopography due to photocurrent oscillations and electropolishing treatments by in-situ FTIR and ex-situ pulsed SPV measurements to get information about the chemical and electronic passivation of the silicon.

Experimentals

Infrared measurements were performed with a n-doped silicon prism (length/width/thickness: 50/20/2 mm, prism angle 45° for entrance and outlet of the IR-light at the 20 mm sides, doping level 10^{15} cm^{-3}, [111] 4° mismatch) mounted in an attenuated total reflectance (ATR) configuration as described in [17].

The electrolyte solutions were prepared from p.a. purity reagents in triply distilled water. The compositions were as follows: 1 M NH_4F (pH 4.0, adjusted with H_2SO_4) for the SPV and 1 M NaF (pH 4.0, adjusted with HF) for the FTIR experiments. The electrochemical measurements were made in a teflon or plastic cell using a platinum counter electrode, a saturated calomel electrode (SPV) or a 0.1 M KCl/AgCl/Ag electrode (FTIR) as the reference electrode. The electrode potential was controlled by a potentiostat-galvanostat (Heka model 128). The temperature of the solutions was 22 ± 1 °C.

The electrochemical oxidation of the n-Si (111) surface was performed under white light illumination (about 20 mWcm^{-2}) either at a potential of +1.3V_{NHE} or +2.8V_{NHE}, respectively (electropolishing, no oscillation was seen at this bias) or at an anodic bias of about +6.2V_{NHE} where the photocurrent oscillations occur [14, 18]. Every photooxidation treatment was followed by an etching step in the dark at a potential of +0.7 V_{NHE} to produce a hydrogen-terminated silicon surface [3, 8, 19]. This surface was then investigated by in-situ FTIR -spectroscopy and ex-situ pulsed SPV.

The sample used in the SPV experiments was phosphorus doped n-type silicon (111) with a resistivity of 6 Ωcm. The SPV measurements were carried out in the same manner as described recently [15].

Figure 1 shows a typical current-voltage characteristic of a n-silicon electrode in 1 M NaF (pH 4.0) solution under illumination (Light-intensity ≈20 mWcm^{-2}).

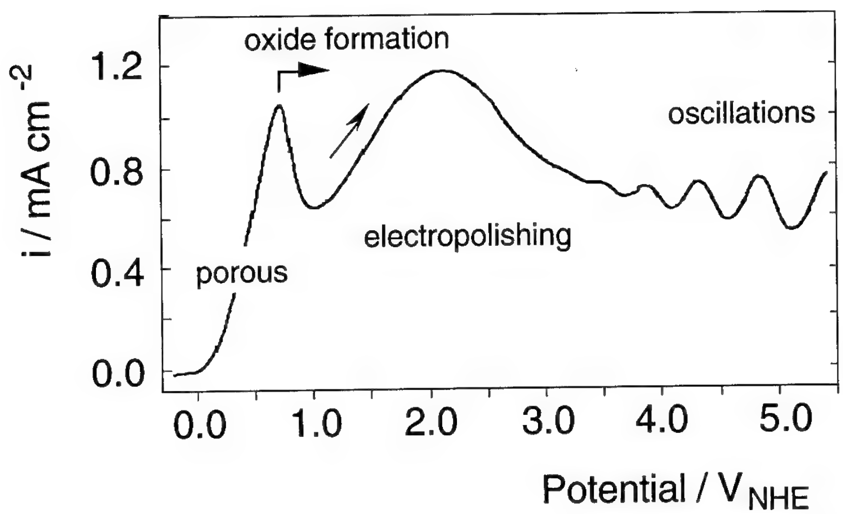

Fig.1 I/U-characteristic of a n-Si(111) electrode in acidic fluoride containing solution under illumination with white light ($\approx$20 mW cm^{-2}).

At the shoulder of the first current-peak porous silicon is formed [20-23]. After the first current-peak the oxidation of the si-surface starts and the siliconoxide is simultaneously etched back by the HF containing electrolyte (electropolishing). No SiH exists on the silicon surface at this potential region as measured by XPS and UPS. Before the experiments started, the n-Si(111) samples were first cleaned by several oxidation-etching cycles and then roughened by formation of porous silicon at about +0.4 V_{NHE} for some minutes in the same solution. The roughening (e.g. formation of steps with two dangling bonds on the [111]-surface) was recently monitored in-situ by a strongly increased IR-absorption due to the stretching mode of the SiH_2 species [16].

The time dependence of the photo- and the dark current at the electropolishing (a) and the oscillation treatment (b) is shown in Figure 2. The photocurrent oscillation starts when the light was turned on and reached a maximum of the peak amplitude with a value of 0.9 mA/cm^2 at a potential of +6.2 V_{NHE}. After some oscillations (230 s) the light was turned off and the potential was kept at +0.7 V_{NHE}. Under these conditions the etching process of the oxidized silicon surface leads to the well-known dark current transient followed by a decay [13], after which the Si-surface is hydrogen-terminated [3]. The photoinduced charge flow at the electropolishing treatments at +1.3 V_{NHE} and +2.8 V_{NHE}, respectively, was in the same order than obtained for the oscillating treatment (about 122 mC). After the dark current has reached the position indicated by the arrows in Fig. 2 (H.-term.), in-situ FTIR measurements were carried out.

The signal/noise ratio of the IR-spectra were increased by averaging 128 scans using a photovoltaic mercury-cadmium-telluride infrared detector (a process needing a period of 70 seconds). The resolution of the IR-spectra was 4 cm^{-1}.

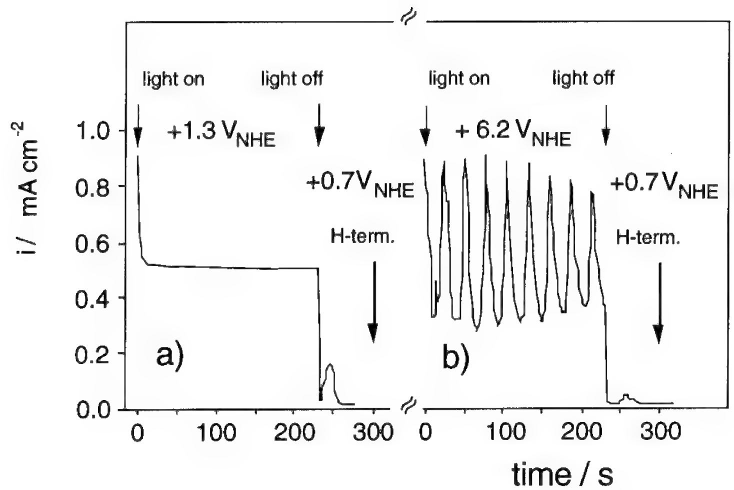

Fig.2 Time dependence of the current density of (a) the electropolishing and (b) the oscillation procedure, each followed by the dark current transient in 1 M NaF (pH 4.0).

The SPV measurements were performed after removing the sample from the electrochemical cell. The silicon was then rinsed with triply distilled water and dried under nitrogen for transfer.

For the determination of the relative change of the IR-absorption due to the SiH stretching mode at about 2100 cm^{-1} (SiH: ≈2080 cm^{-1}; SiH_2: ≈2110 cm^{-1} [24, 25]) we used the FTIR spectrum of the SiH free and oxidized surface, which was recorded at +1.3 V_{NHE} under white light illumination in the acidic fluoride solution, as our reference for all FTIR measurements.

Results and Discussion

Figure 3 shows the relative change of the IR-absorption in the region of the SiH stretching mode: (a) after interruption of the oscillating process and (b) after electropolishing treatments at +1.3 V_{NHE} and +2.8 V_{NHE} (cf. Fig.2), respectively. All photooxidation processes were followed by an etching step in the dark to obtain the hydrogen-terminated surface. The difference of curve 3(b) and 3(a), Fig. 3(d), shows an IR-absorption at 2110 cm^{-1} which indicates a larger amount of SiH_2 on the surface after the electropolishing treatment (Fig. 3(b)) than after the oscillation procedure (Fig. 3(a)). This shows that the photocurrent oscillations lead to a smoother surface than the electropolishing treatments in this electrolyte. Figure 4(a) shows the relative change of the IR-absorption in the region of the SiH stretching mode after an etching procedure using 0.2 M NaF (pH 4.5) followed by a subsequent etching step in 0.2 M NaF (pH 4.9) [26] where the Si-surface is covered with more than 90% of a monolayer SiH [3] and after the oscillation treatment, Fig.4(b).

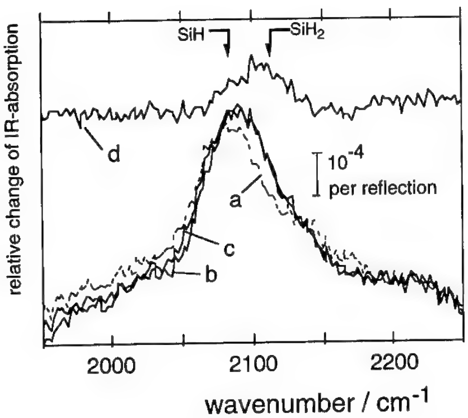

Fig.3 Relative change of the FTIR spectra with reference to the SiH free surface: (a) after the photocurrent oscillation procedure at +6.2 V_{NHE} ; (b) and (c) after electropolishing treatments in 1 M NaF (pH 4.0) at +1.3 V_{NHE} and +2.8 V_{NHE} , respectively; (d) the difference of (b)-(a); note: the difference (c)-(a) equals curve (d).

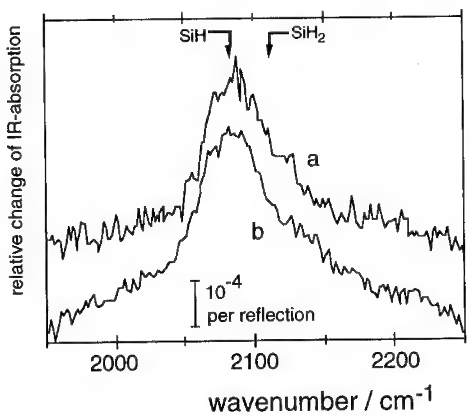

Fig.4 Relative change of the FTIR spectra with reference to the SiH free surface: (a) after an etching process at pH 4.5 followed by an etching step with pH 4.9 (each 0.2 M NaF) of an oxidized Si-surface (> 90 % SiH) and (b) after the photocurrent oscillation treatment at +6.2V_{NHE} in 1 M NaF (pH 4.0).

The IR-absorption after the photocurrent oscillation treatment is somewhat greater than that after the two step process, so that the surface must be terminated with more than 95% of a monolayer SiH. That this very good chemical passivation is accompanied by a low density of interface state is shown in Figure 5 where the dependence of the surface photovoltage, U_{ph}, is drawn as a function of the applied fieldvoltage, U_F.

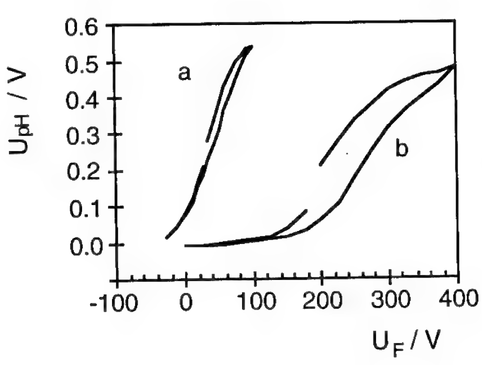

Fig.5 The U_F dependence of U_{ph}: (a) after the photocurrent oscillation procedure at +6.2V_{NHE} and (b) after an electropolishing treatment at +1.3V_{NHE} in 1 M NaF (pH 4.0).

The pulsed SPV measurements after the photocurrent oscillation treatment (Fig. 5(a)) are characterized by a stronger increase at the turning point, a smaller

hysteresis and a smaller shift on the U_F axis compared to the measurements after the electropolishing procedure $+1.3V_{NHE}$ (Fig. 5(b)). The shift on the U_F axis gives information about the fixed charge in the interface and the hysteresis results from relatively slow rechargable interface states [15]. The U_F dependence of U_{pH} allows to determine the density of interface states as described in [18, 27-29] with a value below 10^{11} $cm^{-2}eV^{-1}$ after the oscillation treatment.

These results demonstrate that the combined method based on photocurrent oscillations and dark current decay produces stable and hydrogen-terminated Si-surfaces which are chemically and electronically passivated as reflected by a microscopically smooth surface with a low density of interface states. The fact that the spatial and temporal synchronization during photocurrent oscillations obviously allows to smoothen large surfaces such as the ATR-crystall indicates the applicability of the method for wafer processing [Patent: DE 01/0394].

Acknowledgement

The authors thank Dr. T. Dittrich for measuring the surface photovoltage and enlightening discussions.

References

[1] Y. J. Chabal, Phys. Rev. Lett. **50**, 1850 (1983)
[2] H. J. Lewerenz, Electrochim. Acta **37**, 847 (1992)
[3] H. J. Lewerenz and T. Bitzer, J. Electrochem. Soc. **139**, L21 (1992)
[4] D. J. Blackwood, A. Borazio, R. Greef, L. M. Peter and J. Stumper, Electrochim. Acta **37**, 889 (1992)
[5] L. M. Peter, D. J. Blackwood and S. Pons, Phys. Rev. Lett. **62**, 308 (1989)
[6] H. J. Lewerenz, T. Bitzer, M. Gruyters and K. Jacobi, J. Electrochem. Soc.**140**, L44 (1993)
[7] T. Bitzer, M. Gruyters,H. J. Lewerenz and K. Jacobi, Appl. Phys. Lett. **63**, 397 (1993)
[8] T. Bitzer and H. J. Lewerenz, Surf. Sci. **269/270**, 886 (1992)
[9] L. Cramer, H. Duwe, H. Jungblut, P. Lange and H. J. Lewerenz, J. Phys.: Condens. Matter **3**, S77 (1991)
[10] D. R. Turner, J. Electrochem. Soc. **105**, 402 (1958)
[11] M. Etman, M. Neumann-Spallart, J.-N. Chazalviel and F. Ozanam, J. Electroanal. Chem. **301**, 259 (1991)
[12] J.-N. Chazalviel, M. Etman and F. Ozanam, J. Electroanal. Chem. **297**, 533 (1991)
[13] F. Ozanam, J.-N. Chazaviel, A. Radi and M. Etman, Ber. Bunsenges. Phys. Chem. **95**, 98 (1991)
[14] H. J. Lewerenz and M. Aggour, J. Electroanal. Chem. **8**, 2548 (1993)

[15] T. Dittrich, T. Bitzer, H. Angermann, H. Flietner and H. J. Lewerenz; J. Electrochem. Soc. in press (1994)
[16] J. Rappich, H. Jungblut, M. Aggour and H. J. Lewerenz; J. Electrochem. Soc. **141**, L99 (1994)
[17] J. Rappich, H. J. Lewerenz and H. Gerischer, J. Electrochem. Soc. **140**, L187, (1993)
[18] S. Rauscher, T. Dittrich, M. Aggour, J. Rappich, H. Flietner and H. J. Lewerenz; submitted to J. Electrochem. Soc.
[19] H. J. Lewerenz, J. Stumper, C. Pettenkofer and R. Greef, Electrochim. Acta **34**, 1729 (1989)
[20] Y. Arita and Y. Sunobara, J. Electrochem. Soc. **124**, 285 (1977)
[21] R. L. Smith and S. D. Collins, J. Appl. Phys. **71**, R1 (1992)
[22] P. C. Searson, J. M. Macaulay and S. M. Prokes, J. Electrochem. Soc. **139**, 3373 (1992)
[23] T. Unagami, J. Electrochem. Soc. **127**, 476 (1980)
[24] R. A. Venkateswara, F. Ozanam and J. N. Chazalviel, J. Electrochem. Soc. **138**, 153 (1991)
[25] P. Dumas, Y. J. Chabal and G. S. Higashi, Phys. Rev. Lett. **65**, 1124 (1990)
[26] J. Rappich and H. J. Lewerenz; submitted to J. Electrochem. Soc.
[27] Y. W. Lam; J. Phys. D: Appl. Phys. **4**, 1370 (1971)
[28] K. Heilig, H. Flietner and J. Reineke; J. Phys. D: Appl. Phys. **12**, 927 (1979)
[29] T. Dittrich, M. Brauer and L. Elstner; Phys. stat. sol. (a) **137**, K29 (1993)

Materials Science Forum Vols. 185-188 (1995) pp. 91-98

Influence of tunneling on trapping kinetics in thin layers

S. Scharf, M. Schmidt and D. Bräunig

Hahn-Meitner-Institut Berlin, Department of Applied Physics,
Glienicker Str. 100, D-14109 Berlin, Germany

Keywords: Tunneling, trapping kinetics, Si/SiO_2 interface, hole traps

Abstract

The process of trap occupation in heterostructures for example in MIS or MIM structures might be accompanied by a tunneling (detrapping) process near the adjacent contacts ($x < 5$ nm), depending on the distance, the trap energy relative to the Fermi level of the adjacent contact and the actual trap filling state. The trap parameters of thin insulating layers as capture cross section and effective trap concentration are usually determined by assuming a first order kinetic model for trapping. This procedure neglects the possibility of trap depopulation by charge transfer processes like tunneling between the adjacent contact and the traps. To investigate the influence of tunneling on trapping kinetics we analysed the hole trap occupation in thermally grown SiO_2 layers and developed a general trapping model considering the tunneling process between localized and extended states. The comparision between simulated and measured values confirms the relevance of detrapping by tunneling.

1 Introduction

The occupation of traps in heterostructures is often accompanied by a detrapping process. Traps located near to an interface may interact with the adjacent material via tunneling of electrons. A tunneling transistion depends on the distance, the potential barrier, and the occupation of both states involved.

We investigated the filling behavior of hole traps in thermally grown SiO_2 on crystalline silicon. These traps are located within several nm from the Si/SiO_2 interface. Therefore, electron transfer from silicon states via elastic tunneling is a mechanism to neutralize the trapped hole charge.

The simultaneous detrapping affects the determination of the trap parameters such as capture cross section and saturation density. The saturation value is given by an equilibrium between trapping and detrapping processes.

2 Theory

The band structure of the Si/SiO_2 system is shown in Fig. 1. Here, x is distance from the Si/SiO_2 interface and E the energy relative to the oxide valence band edge. We consider a monoenergetic hole trap level $E_T(x)$ as found in [1]. The densitiy of occupied states $N_T(x,t)$

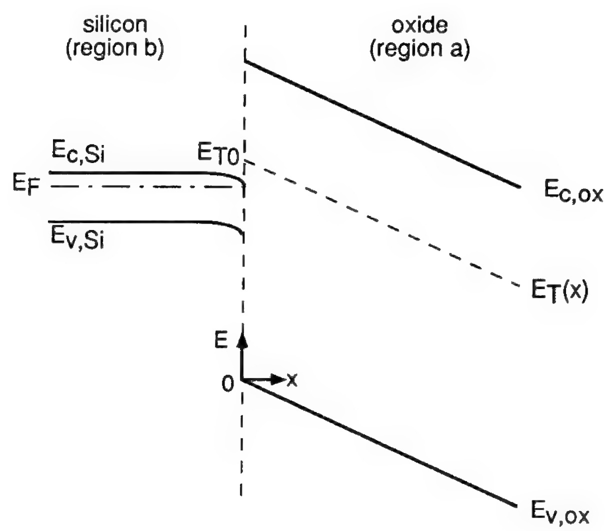

Figure 1: Scheme of the band structure of the considered heterojunction under positive oxide field.

is affected by both, trapping and detrapping. If using a first order kinetic model it is given by:

$$\frac{\partial N_T(x,t)}{\partial t} = \frac{j}{q} \cdot \sigma_t \cdot [N_{T0}(x) - N_T(x,t)] - p_{ab}(x) \cdot N_T(x,t) \tag{1}$$

The first term describes filling of the traps which is dependent on the hole current densitiy j, the capture cross section σ_t and the spatial density $N_{T0}(x)$ of the traps. The neutralization of trapped holes by electron tunneling from the silicon subtrate is considered by the second term. The electrons are tunneling from extended silicon band states into localized trap states. This transition is dependent on the tunneling rate constant $p_{ab}(E,x,T)$. Using the WKB approximation the transition rate constant is given by:

$$p_{ab}(E,x,T) = \tau_0^{-1}(E,x,T) \cdot \exp\left(2i \int_0^x k_a(E)d\tilde{x}\right) \tag{2}$$

We calculated $\tau_0^{-1}(E,x,T)$ according to Lundström and Svennson [2] and included the Fermi-distribution $f_b(E,T)$ as occupation function of the initial states and the more realistic wave vector $k_a(E)$. This leads to:

$$\begin{aligned} \tau_0^{-1}(E,x,T) &= f_b(E,T) \cdot 2\hbar k_a^2(E)\frac{m_{b,e}^*}{m_{a,h}^*} \cdot \frac{k_b(E)}{x\left(k_a^2(E) + k_b^2(E)\right)^2} \\ &\quad \cdot \left[1 - \sqrt{\frac{k_a(E)}{x \cdot k_b^2(E)}} \cdot D\left(\sqrt{\frac{x \cdot k_b^2(E)}{k_a(E)}}\right)\right] \end{aligned} \tag{3}$$

Here a denotes the insulator and b the semiconductor region. $m_{b,e}^*$ and $m_{a,h}^*$ are the effective masses of electrons and holes in the respective regions. $D(x)$ is the Dawson-integral [3]. $k_{a,b}$

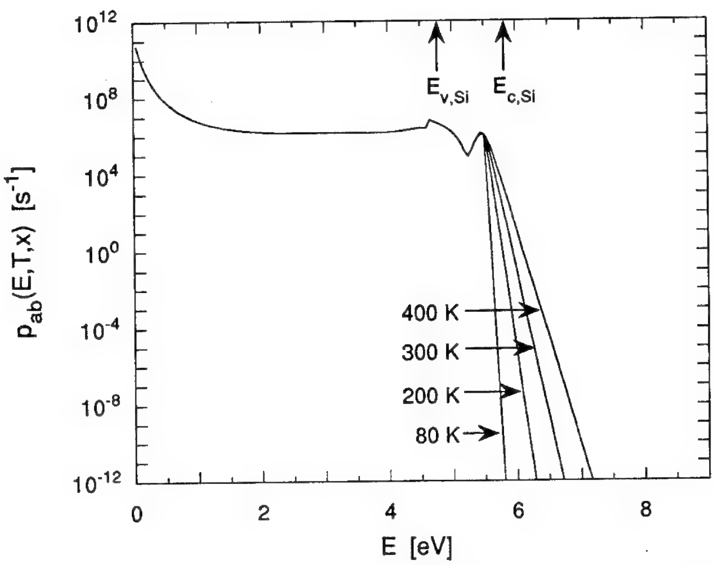

Figure 2: Tunneling rate constant versus the energy above SiO_2 valence band edge at different temperatures at a distance $x = 1$ nm from the Si/SiO_2 interface.

are the wave vectors of the electrons in the respective regions. For the exact calculation of the tunneling rate constant it is necessary to use the correct value of the imaginary wave vector inside the entire oxide gap, $k_a(E)$, given only by the two-band approximation [4]. The trap energy $E_T(x)$ relative to the initial states in the semiconductor is influenced by the applied field and the trapped charge in the oxide.

The tunneling rate constant versus trap energy for different temperatures is shown in Fig. 2. The calculations are carried out at a distance $x = 1$ nm from the interface for flatband conditions. There is an energy range where $p_{ab}(E, x, T)$ is strongly affected by the temperature. This is due to the occupation of the initial states in the semiconductor. The decharging of traps located in this energy region is dependent on the temperature.

The complementary processes of trapping and detrapping lead to a static equilibrium for the densisty of occupied states, $N_{T,sat}(x)$. The saturation density is dependent on the hole current density j as shown in Fig. 3. The region where states are filled with holes is sharply separated from the region where detrapping dominates. The transition region between both is smaller than 0.5 nm. The equilibrium position x_g is the distance from the Si/SiO_2 interface where half of the traps are occupied:

$$\frac{N_{T,sat}(x_g)}{N_{T0}(x_g)} = \frac{1}{2} \tag{4}$$

Using Eq. 1 and Eq. 2 at saturation condition this leads to the current dependence of x_g:

$$x_g = -\frac{1}{2K} \ln \left(\frac{\tau_0 j \sigma_t}{2q} \right) \tag{5}$$

with K being an average value of the wave vector inside the tunneling barrier.

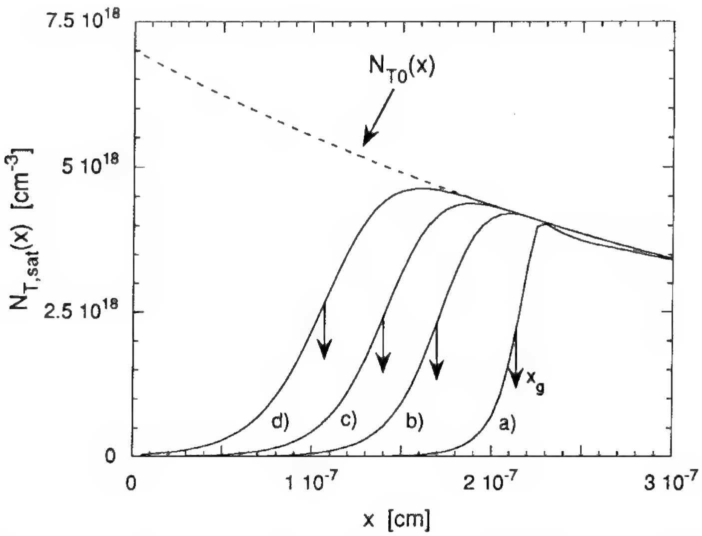

Figure 3: Density of occupied trap states in saturation for different current densities. The arrows indicate the equilibrium position x_g for the respective current density j. The current density was: a) $j = 4 \cdot 10^{-11}$ Acm^{-2}, b) $j = 4 \cdot 10^{-9}$ Acm^{-2}, c) $j = 4 \cdot 10^{-8}$ Acm^{-2}, d) $j = 4 \cdot 10^{-7}$ Acm^{-2}.

3 Experiment

The oxides were grown thermally on <100>-oriented silicon. Oxide thickness is 100 nm. The gate electrodes werde made of 10 nm thick, semitransparent aluminum. The hole current was generated by VUV irradiation with a photon energy of 10.2 eV [5]. The VUV irradiation was delivered by a hydrogen discharge lamp. The photons are absorbed in the oxide top layer. The generated electron-hole pairs are separated by an electric field. Due to the small absorption depth (10 nm) only holes are swept to the Si/SiO_2 interface if a positive oxide field is applied.

The trapped charge density was determined by C(V)-measurements. Oxide charge acts on the semiconductor capacitance like a charge sheet located at the Si/SiO_2 interface. Therefore, it is not possible to determine the spatial distribution of the charge from C(V)-measurements. The oxide charge density is calculated from the shift of the midgap voltage, ΔV_{mg}. At this condition interface states are assumed to be uncharged [6]. The relation between measured ΔV_{mg} and occupied trap density is given by:

$$\Delta V_{mg} = \frac{q}{\epsilon_{ox}} \int_0^{t_{ox}} (t_{ox} - \dot{x})\, N_T(\dot{x}, t)\, d\dot{x} \tag{6}$$

Here, q is the elementary charge, t_{ox} the oxide thickness, and ϵ_{ox} the permittivity of the oxide. The area density of the oxide charge is calculated acording:

$$\Delta N_{ot} = \frac{\epsilon_{ox}}{d_{ox} q} \Delta V_{mg} \tag{7}$$

Usually, the determination of trap parameters is examined without consideration of detrapping via tunneling. The occupation of a single trap is given by first order kinetics according:

$$\Delta N_{ot}(t) = N_\infty \left[1 - \exp\left(-\frac{j\sigma_t}{q} t\right)\right] \tag{8}$$

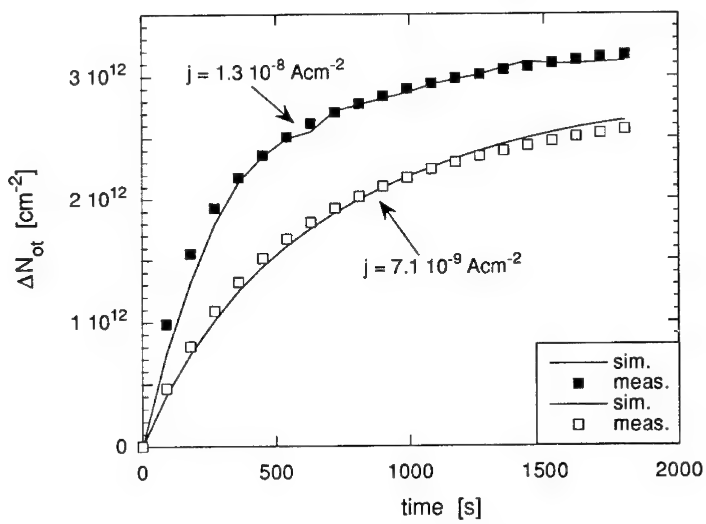

Figure 4: Measured und simulated charge buildup at the Si/SiO_2 -interface. The full lines indicate the simulation results obtained with the same set of parameters (see Table 2). The symbols are measured values. The oxide field was kept constant at +1 MV/cm.

parameter		
SiO_2 band gap	E_G	9.0 eV
Si/SiO_2 valence band discontinuity	ΔE_V	4.7 eV
SiO_2 effective electron mass	$m^*_{a,e}$	0.5 m_0
Si effective electron mass	$m^*_{b,e}$	0.92 m_0
SiO_2 effective hole mass	$m^*_{a,h}$	5.0 m_0

Table 1: Parameters of the Si/SiO_2 system used for calculations. m_0 is the electron rest mass.

To probe the validity of Eq. 8 the buildup of oxide charge for two different current densities was measured. The results are shown in Fig. 4. Both samples are from the same wafer. Therefore, the trap concentration can be expected to be equal. Contrary, we yield different values for the saturation density, N_∞, and the capture cross section, σ_t. This indicates that the detrapping by tunneling has to be considered. This is clearly demonstrated in Fig. 5 where j was varied during one experiment. The higher the hole current density j the higher is the apparent saturation value of the trapped oxide charge and vice versa. This correlates with our model where the equilibrium position x_g is shifted by variation of the current density j.

4 Simulations

To calculate the trap occupation in a more correct way Eq. 1 has to be solved. Due to the lack of an analytical solution the problem was solved in a self consistent manner. The calculations were repeated until the relative change of $E_T(x)$ was less than 1% in two subsequent loops. The free parameters of the model are the capture cross section of the traps, σ_t, and their spatial distribution, which was assumed as:

$$N_{T0}(x) = N_0 \exp\left(-\frac{x}{x_d}\right) \tag{9}$$

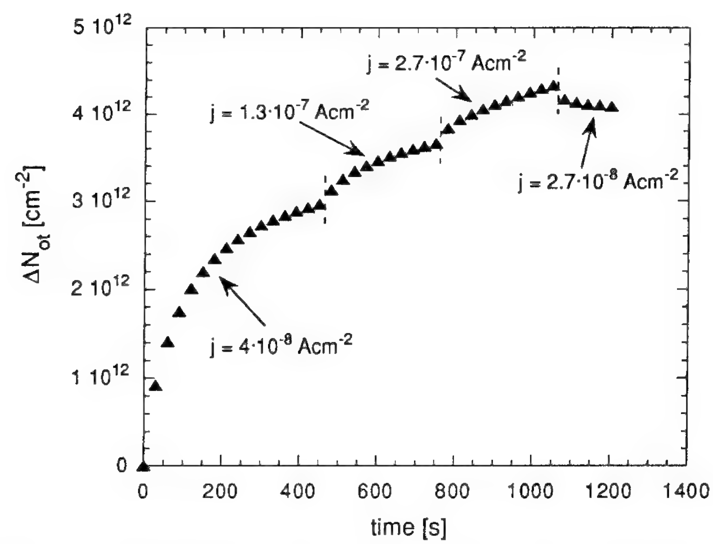

Figure 5: Buildup of trapped charge under varying injected current densities j. The applied field was kept constant at +1 MV/cm.

parameter	
σ_t	$2.7 \cdot 10^{-14}$ cm^2
N_0	$1.05(1.15) \cdot 10^{19}$ cm^3
x_d	$5.1 \cdot 10^{-7}$ cm
E_{T0}	6.25 eV

Table 2: Parameters of the simulations shown in Fig. 4. The value in brackets indicate the simulation parameter for the higher current density.

The energy level of the traps relative to the oxide valence band edge was determined in previous annealing experiments [1]. According to this the energy level used in the simulations shown here was to $E_{T0} = 6.25$ eV. The parameters of the Si/SiO_2 system used for the calculations are listed in Table 1.

The source code is written in ANSI C. Simulations are carried out on a CONVEX C240 computer.

We generated two different hole current densities by irradiating two samples from the same wafer with different VUV light intensity. The buildup of oxide charge is shown in Fig. 4. Least square fits according to Eq. 8 neglecting the detrapping process yield $\sigma_t = 4.2 \cdot 10^{-14}$ cm^2 for the lower and $\sigma_t = 4.3 \cdot 10^{-14}$ cm^2 for the higher irradiation intensity. Apparent saturation densities are $N_\infty = 2.6 \cdot 10^{12}$ cm^{-2} and $N_\infty = 3.1 \cdot 10^{12}$ cm^{-2}, respectively. The differences in the saturation densities are due to the value of x_g which is strongly dependent on j as shown in Fig. 3. If tunneling was considered a common set of parameters (σ_t, N_0, x_d, E_{T0}) was found from numerical solution of Eq. 1. Only N_0 had to be changed from $1.05 \cdot 10^{19}$ cm^{-3} to $1.15 \cdot 10^{19}$ cm^{-3} in the case of the higher intensity. The parameters for the calculations shown in Fig. 4 are listed in Table 2.

5 Conclusions

Our results show that tunneling processes must be taken into account for analysis of trap parameters. The main subject for a correct description is the energy and temperature dependent tunneling rate constant. The contrary processes of trapping and tunneling lead to a dynamic equilibrium between occupied and unoccupied traps. Both regions are sharply separated at the position x_g, which shifts towards the interface by increasing current density and vice versa.

The neglect of detrapping by tunneling yields both, too small values of effective trap concentration and too large capture cross sections. In all cases where the saturation values of effective trap densities are dependent on the current density detrapping has to be taken into account. In the Si/SiO_2 system it was shown that tunneling of electrons is the dominating detrapping process [7, 8].

References

[1] M. Schmidt and H. Koester, Phys. Status Solidi B **174**, 53 (1992).

[2] I. Lundstroem and C. Svensson, J. Appl. Phys. **43**, 5045 (1972).

[3] M. Abramowitz and I.E. Stegun, *Handbook of mathematical functions*, (Dover Publications, Inc., New York, 1972)

[4] H. Flietner, Phys. Status Solidi B **54**, 201 (1972).

[5] S. Scharf, M. Schmidt, F. Wulf, and D. Bräunig, IEEE Trans. Nucl. Sci. **41**, 460 (1994).

[6] P.M. Lenahan and P.V. Dressendorfer, J. Appl. Phys. **55**, 3495 (1984).

[7] V. Lakshmana and A.S. Vengurlekar, J. Appl. Phys. **63**, 4548 (1988).

[8] M. Schmidt and H. Koester, Phys. Status Solidi B **174**, 403 (1992).

Materials Science Forum Vols. 185-188 (1995) pp. 99-104

On the nature of the radiation-induced failure of $Si\text{-}SiO_2$ structures annealed in hydrogen

S.N. Kuznetsov and V.A. Gurtov

Petrozavodsk State University, 33 Lenin St., Petrozavodsk 185640, Karelia, Russian Federation

Keywords: MOS capacitor, ionizing radiation effect, positive charge buildup, $Si\text{-}SiO_2$ interface state generation, postoxidation annealing, capacitance-voltage method, radiation stability

Abstract

The $Si\text{-}SiO_2$ interface states and the trapped oxide charges generated by X-ray irradiation are examined for MOS capacitors with a postoxidation annealing in molecular hydrogen at high temperatures of 800 - 1300 K. The enhanced radiation response of the above parameters is observed for absorbed doses up to ~ 10 Mrad. The activation energies of the hydrogenation effect for both characteristics are nearly the same ≈ 0.7 eV, as derived from the radiation response dependence on the annealing temperature. Additional trap precursors formed by high-temperature annealing are attributed to hydrogen interaction with weak bonds at the $Si\text{-}SiO_2$ interface as well as the oxide transition region.

Introduction

As early as the '70s, Revesz [1] came to the conclusion that hydrogen is the most important impurity in $Si\text{-}SiO_2$ structures, and proper control over its content is the major problem faced by MOS technology. Discrepancy in numerous results on the role hydrogen plays in SiO_2 does not seem to be least connected with its dual behaviour in MOS structures. Hydrogen can act as a defect passivator at the interface. However, if a MOS-structure is exposed to strong stresses (i.e. radiation, high electric field, charge carriers injection from the contacts), intensive (often crucial) deterioration of electrophysical parameters of hydrogenized structures takes place. There is some evidence that the degradation rate in MOS structures under stress is governed by the hydrogen concentration: the more the concentration exceeds the optimum, the higher is the degradation rate.

In a number of papers [2,3] the correlation between hole trapping in the bulk of SiO_2 and surface state generation at the $Si\text{-}SiO_2$ interface has been found, referring to the case of ionizing irradiation as well. At present, however, the influence of hydrogen on the above correlation seems to escape the attention of the investigators dealing with the hydrogen problem in $Si\text{-}SiO_2$ structures. Instead, the primary emphasis is placed upon the role of

hydrogen at the Si-SiO_2 interface (see, for instance, [4,5]). Thus, it appears to be of certain interest to study the problems stated above in more detail, using electrophysical methods.

Experimental Procedure and Results

The results presented have been obtained for Si-SiO_2 structures with ~ 20 nm - thick dry thermal oxides formed at 1273 K on n-Si (100). Except for the reference wafer, specimens were exposed to 30-min anneal in an industrial furnace, in pure molecular hydrogen, at temperatures of 773, 1033, 1133 and 1273 K and a pressure of 10^4 Pa. Then semitransparent nickel gates were evaporated through a mask onto unheated substrates, with no following annealing, so as to avoid additional mechanical strains in the structures.

The X-ray irradiation of the MOS structures was performed in vacuum at room temperature, with the gate biased. The applied voltage resulted in the mean field value in the oxide of ~ 1 MV/cm. The gate polarity was positive, unless otherwise stated. The irradiation was conducted using an X-ray tube with a Cr anode, the absorbed dose rate being ~ 1 Mrad/h. The SiO_2 - absorbed dose D_a ranged from 1 to 8 Mrad.

The electrophysical parameters of MOS structures measured were flat band (V_{FB}) and midgap (V_{MG}) voltages deduced from the high-frequency C-V characteristics [6]. The latter is known (see, for example, [7]) to be proportional to the surface density of charge in the oxide, whereas the difference $|V_{MG} - V_{FB}|$ is proportional to the integral density of the surface states within the forbidden gap range from midgap to flat bands. Validity of such a simplified assessment has been confirmed [8].

Fig.1 shows dose dependences of V_{FB} and V_{MG} for MOS structures annealed in hydrogen at various temperatures T_a. It follows from these data that annealing at $T_a \leq 773$ K did not greatly enhance the radiation response of MOS structures, especially at moderate doses of ~ 1 Mrad. This fact is well known in the literature [8]. However, as the anneal was continued beyond the temperature mentioned above, sharp enhancement in the radiation response of the MOS structures was observed, both in charge in the oxide and in surface state concentration. It should be noted that the slope of the curves increased with dose deposition.

To quantitatively assess the effect of annealing in hydrogen, we introduced two parameters into our consideration. The first parameter refers to the accumulation rate of positive radiation-induced charge in oxide traps: $R_{ot}=\Delta V_{MG} / \Delta D_a$. The second parameter corresponds to the generation rate of surface states at the Si-SiO_2 interface:

$$R_{it} = \frac{\Delta V_{MG} - \Delta V_{FB}}{\Delta D_a}.$$

For the initial stage of the dose dependence ($D_a \leq 1$ Mrad), which is more important in practice, R_{ot}, R_{it} as a function of the annealing temperature is presented in Arrhenius

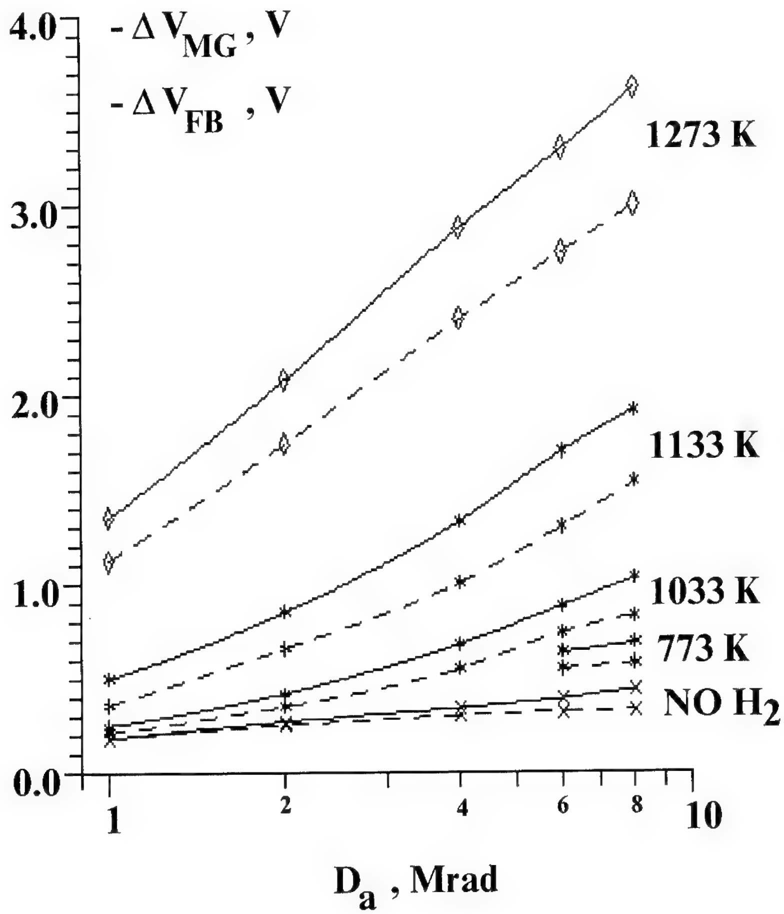

Fig.1. Absorbed dose dependences of midgap, ΔV_{MG} , and flat band, ΔV_{FB} , voltage shifts for different annealing temperatures. The dashed lines represent ΔV_{FB} .

coordinates in Fig.2. It is common practice to consider the slopes of the corresponding curves as activation energies. Thus, according to the data obtained, the activation energy of the hydrogen-induced radiation response of the oxide bulk is $E^a_{ot} \approx 0.71$ eV and that of the Si-SiO_2 interface is, similarly, $E^a_{it} \approx 0.76$ eV.

Hydrogenation enhanced asymmetry of the radiation response on inverting the gate bias polarity during irradiation. In the unhydrogenized oxide, asymmetry did not exceed 25% up to $D_a = 8$ Mrad in the field of $\pm$ 1 MV/cm, but it became sharply enhanced after hydrogenation (Fig.3). The effect observed in this case appeared to be roughly proportional regarding both the radiation-induced charge in the oxide $\Delta V^+_{MG}/\Delta V^-_{MG} \approx 2.5$ and that in surface states $\left(\Delta V^+_{MG} - \Delta V^+_{FB}\right)/\left(\Delta V^-_{MG} - \Delta V^-_{FB}\right) \approx 3.0$.

Discussion

Variation in the concentration of P_b centres in Si-SiO_2 structures during anneal in molecular hydrogen was studied by the ESR-technique [5]. The conclusion was made that the P_b concentration fall vs annealing temperature (up to the highest experimental temperature of 1100 K) can be described by the reaction:

$$P_b + H_2 \rightarrow HP_b + H \tag{1}$$

Formation of the P_b- hydrogen complex was considered as fading of the ESR signal from P_b centres (the so called passivation of P_b).

Let us discuss our results in the light of these data. It can be assumed that formation of new, HP_b- type, complexes (not only hydrogen passivation of intrinsic P_b centres) takes place at the Si-SiO_2 interface during the annealing. The complexes being formed represent precursors which can dissociate during ionizing irradiation (at room temperature), forming P_b centres, this leading to additional interface state generation. Atomic hydrogen is a by-product of decomposition, its generation in MOS structures under irradiation has been firmly established by the ESR-technique [9]. At T > 200 K, hydrogen leaves the oxide, without re-entering into a reaction.

Increase in the radiation-induced charge in the oxide during hydrogenation can be explained in the context of the above suggestion. In fact, E'- centres in the oxide look like P_b centres at the Si-SiO_2 interface. This similarity reveals itself in the ≡Si• fragment present in both types. By analogy with (1), it is possible to write down the reaction:

$$E' + H_2 \rightarrow HE' + H \tag{2}$$

Assuming, as before, that in such a way not only passivation of intrinsic E'- centres, but generation of the new E'- hydrogen complexes as well (e.g. following the reaction ≡Si-O-Si≡ + $H_2 \rightarrow$ ≡Si-H + ≡Si-OH) may proceed at high temperature, it seems possible to understand the observed variation in the radiation-induced charge in the oxide. This approach is based on the assumption that the HE'- complexes act as precursors of the hole traps in the

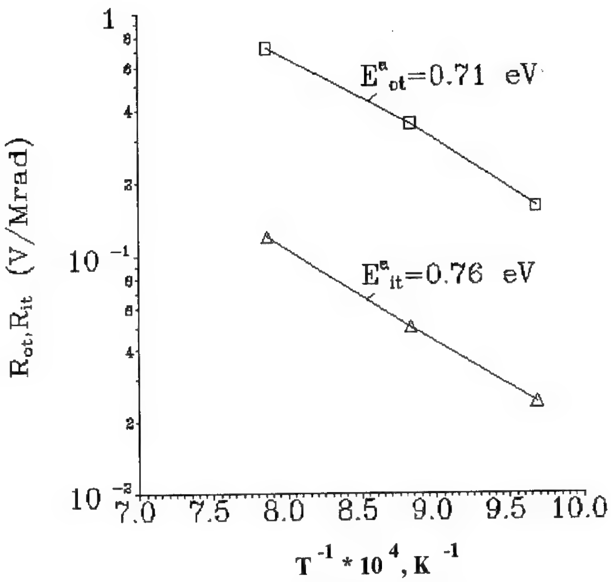

Fig.2. Arrhenius plots of the rates of interface (R_{it}) and oxide (R_{ot}) charge generation for hydrogenized MOS structures. The data are taken for the absorbed dose of ≈ 1 Mrad.

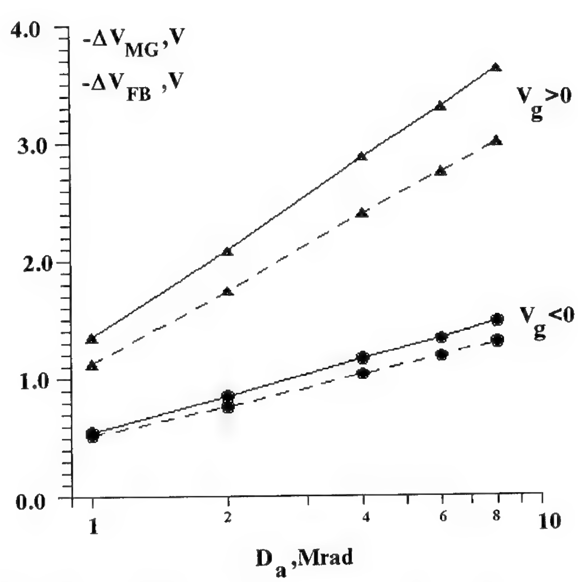

Fig.3. Radiation responses of hydrogenized MOS structure for the opposite gate polarities, V_g. The annealing temperature is 1270 K. The dashed lines show the flat band shift, ΔV_{FB} .

SiO_2 network. It should be noted that the equality of the activation energies ($E^a_{ot} \approx E^a_{it} \approx 0.7$ eV) is difficult to understand in terms of the hypothesis proposed, unless this quantity is referred to the process of molecular hydrogen diffusion in SiO_2. According to [4], however, molecular hydrogen diffusion in SiO_2 is a non-limiting stage at elevated temperatures.

Conclusions

The above results may be summarized as follows.

1. The effect of high-temperature annealing in molecular hydrogen, regarding its consequences for the stability of MOS structures, is just the reverse of that of low-temperature ($T < 800$ K) hydrogen annealing. The former leads to degradation of the radiation stability.

2. The threshold temperature of these competitive processes is about 800 K.

3. The activation energy of the hydrogenation effect with respect to the radiation response is ~ 0.7 eV in the annealing temperature range of 1000 to 1300 K.

4. Decrease in the radiation stability of Si-SiO_2 structures hydrogenized at high temperatures seems to be due to formation of HP_b- and HE'- type hydrogen complexes, that dissociate during irradiation forming surface (P_b) and bulk (E') defects.

5. The effect of radiation on hypothetical hydrogen-containing complexes appears to be indirect (i.e. not limited to the interaction between the ionizing radiation quanta and defects). This is evidenced by data on the radiation response for a hydrogenized structure at negative bias.

References

[1] A.G.Revesz, IEEE Trans.Nucl.Sci. NS-24, 2102 (1977)
[2] P.J.Winokur, H.E.Boesch, Jr., J.M.McGarrity, and F.B.McLean, J.Appl.Phys. 50, 3492 (1979)
[3] S.T.Chang, J.K.Wu, and S.A.Lyon, Appl.Phys.Lett. 48, 662 (1986)
[4] M.L.Reed, Semicond.Sci.Technol. 4, 980 (1989)
[5] K.L.Brower, Semicond.Sci.Technol. 4, 970, (1989)
[6] E.H.Nicollian and J.R.Brews, MOS (Metal-Oxide-Semiconductor) Physics and Technology (New York: Wiley, 1982)
[7] H.E.Boesch, IEEE Trans.Nucl.Sci. NS-29, 1446 (1982)
[8] K.Ohnishi and A.Ushirokawa, Japan.J.Appl.Phys. 28, 877 (1989)
[9] D.L.Griscom, J.Non-Cryst.Solids 68, 301 (1984)

Materials Science Forum Vols. 185-188 (1995) pp. 105-108

Characteristics of Si-SiO_2 systems obtained by thermal oxidation of silicon surface covered with silicon-hydrogen layers

V.Y. Uritsky[1] and B.B. Loginov[2]

[1] JSC „Svetlana", 194156, St.-Petersburg, Russia

[2] „Electron" Research & Scientific Institute, 194223, St.-Petersburg, Russia

Keywords: Silicon-hydrogen layer, Si-SiO_2 system, thermal oxidation, sulphur contents, fixed oxide charge, dissolution, silicon network

Abstract: The formation processes of silicon-hydrogen layers (SHL) at the silicon surface as well as low and high temperature oxidation of SHL in different ambient are discussed. The influence of sulphur contents in SHL on low temperature oxidation process and on generation of fixed charge in the oxide obtained by following thermal oxidation are detected and analyzed. The possibility of Si surface passivation using SHL was estimated.

I. INTRODUCTION

A native or chemical oxide is known to be formed at the Si surface. The thickness and composition of this layer depend on many heavy monitored factors. It may lead to nonreproducibility of characteristics of the oxide obtained by thermal oxidation of the real Si surface. At this point of view it seems important to form the layer with certain thickness and composition at the Si surface. It could be achieved by oxidation of Si surface covered with SHL. SHL is a product of the physical-chemical interaction between monocrystal silicon and solutions of hydrofluoric acid, which are contain certain oxidants, particularly nitrogen dioxide, nitrous acid or its salt. The characteristic feature of this interaction is the formation the SHL on the Si surface, which is more chemically active than the Si substrate[1-4].

In this work the influence of SHL formed at the Si surface on the characteristics of Si-SiO_2 structures obtained by thermal oxidation of Si wafer was investigated.

II. EXPERIMENTAL PROCEDURES

In this work the substrates of monocrystalline n-Si phosphorous-doped (N_D=5 10^{14}-10^{16} cm^{-3}) and p-Si boron-doped (N_A=10^{14}-10^{16} cm^{-3}) were used. The SHL with a thickness of 300±5 nm at the Si surface have been formed in the solution of hydrofluoric acid and natrium nitride just before oxidation [1]. The control samples (without SHL) were cleaned in a standard process including the boiling of the samples in NH_4OH-H_2O_2 and HCl-H_2O_2 solutions. The low temperature oxidation of SHL was performed in H_2SO_4 or HNO_3. The high temperature (thermal) oxidation was carried out in different conditions: in dry O_2, in O_2+HCl (1,5%), in wet O_2, in H_2O vapor at the pressure of 1 and 15 athm. The content of SHL was analyzed by IR spectroscopy, SIMS and XES techniques. The charge value in the oxide obtained was determined from high frequency C-V characteristics of Si-SiO_2 systems.

III. EXPERIMENTAL RESULTS AND DISCUSSION

The structure of a SHL obtained differs from Si crystalline structure. The SHL is penetrable for solution. The front of interaction is displaced into the Si bulk according to line-parabolic law and may reach several tens μm, while the thickness of growing SHL is no more than 1-2 μm because of dissolution of the SHL at the internal boundary. IR absorption spectra of SHL are indicated on the considerable number Si-H and Si-Si bonds, however oxygen was practically absent in the

fresh made SHL. The kinetics investigation shows that the non-dissociated molecules HF and proton-fluor groups of HF_2^- type serve as a source of hydrogen in the SHL. The penetrability of SHL follows from microlocal dissolution of Si and transpassing of Si atoms into the solution. The strong dependence between quantity of dissoluble Si atoms and quantity of Si atoms connected with hydrogen in the bulk of SHL has been established. The Si-O bonds appear in the SHL when storing the samples in the air at room temperature due to hydrolysis of Si-H bonds occurred and due to oxygen entered the silicon network

$$\text{-Si-Si-H} + H_2O \rightarrow \text{-Si-Si-OH} + H_2 \rightarrow \text{-Si-O-Si-H} + H_2. \qquad (1)$$

O O

In a similar way -O-Si-H and -O-Si-H groups are formed in consecutive order. The rate of SHL

O O

oxidation depends on humidity of the air essentially and decrease according to exponential law up to none in 3-4 month of a storage at room temperature. The SHL of 0,1-0,2 μm thickness are completely oxidized in solution of HNO_3 and H_2SO_4 at 100-200°C. After oxidation in HNO_3 or H_2SO_4 oxihydrid silicon bonds are not checked in the oxide layers, whereas the stoichiometric relationships of SiO_2 is not practically reached. The SHL oxidation rate decreases in time due to oxide layer growing and the sulphur precipitated, which is created during reduction of H_2SO_4 by Si-H bonds of the SHL, as could be seen in Fig.1. The high temperature oxidation (800°C or more) transforms SHL into oxide very fast (~1 min.). The layer obtained has a stoichiometry of SiO_2 and its IR spectrum is identical to the one of the thermal oxide. The following thermal oxidation of the SHL didn't practically influence the oxidation rate of the Si substrate. It should be mentioned that the weight density of the oxide obtained using SHL is less than the weight density of thermally grown oxide.

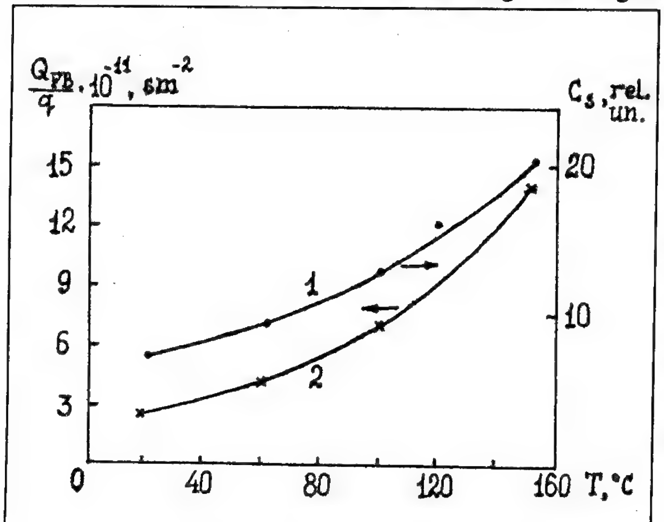

Fig.1. Sulphur contents at the Si surface after oxidation of SHL (~300nm) in H_2SO_4 C_s (1) and oxide charge Q_{fb} (2) after thermal oxidation (1050°C) in wet O_2 vs temperature of H_2SO_4

As it has been determined from C-V characteristics, the value of fixed charge in the Si-SiO_2 structures obtained by thermal oxidation of Si covered with SHL depends at the definite high temperature oxidation conditions on crystallographic orientation of Si and on low temperature oxidation condition. The Q_{fb} is considerably large in case of low temperature oxidation of Si in H_2SO_4 than in other cases (non-oxidized SHL or oxidized in HNO_3). The value of Q_{fb} depends on the time and temperature of oxidation in H_2SO_4 as well as on the thickness of SHL which covers Si surface. There is rather good correlation between surface sulphur concentration after low temperature oxidation in H_2SO_4 and Q_{fb} in the oxide after high temperature oxidation , as it is shown in Fig.1. Though this effect is observed under various high temperature oxidation conditions, it manifests itself in a different way (Table 1). It should be mentioned that usually Q_{fb} depends on crystallographic orientation. Q_{fb} increases more

Table 1.

Crystallographic orientation of Si	Oxidation ambient (1050°C)	$Q_{fb}/q \cdot 10^{11}, cm^{-2}$ after various type of Si surface treatment			
		without SHL	with SHL created	with SHL oxidized in H_2SO_4	with SHL oxidized in HNO_3
(111)	dry O_2	2,0	2,5	25,0	3,5
(111)	dry O_2+HCl	1,5	1,5	20,0	3,0
(111)	wet O_2	4,0	4,0	15,0	4,0
(111)	H_2O vapor 1 athm.	6,0	6,0	18,0	6,0
(111)	H_2O vapor 15 athm.	8,0	8,0	14,0	8,0
(100)	dry O_2	0,5	0,7	5,0	1,5

intensively when oxidation is performed in dry oxygen and less intensively in H_2O vapor at high pressure. In any case the Q_{fb} is fixed near the Si-SiO_2 interface just in the initial stage of thermal oxidation and is reduced in magnitude maintaining its localization during the whole process. That effect could be explained by interaction of silicon and sulphur at high temperature. Simultaneously the diffusion of sulphur from SHL to Si substrate occurs. That leads to the increasing of donor impurity surface concentration observed and to compensation of acceptor impurity at the lightly doped p-Si surface.

IV. CONCLUSIONS

The processes of formation, low temperature oxidation in acids and high temperature oxidation of SHL at the Si surface were investigated and discussed. SHL is formed at the Si surface as a result of interaction of Si and hydrofluoric acid containing oxidants: NO_2, HNO_2 and its salts. Due to high chemical activity of SHL, that could be connected with its high specific surface area hydrogen terminated, the rapid oxidation of SHL at 100-200°C happens in HNO_3 and in H_2SO_4. In the last case the sulphur is localized in the oxidized SHL. By the following high temperature oxidation sulphur affects the additional fixed charge creation in the oxide near the Si-SiO_2 interface. In the same time a n-doping of Si surface occurs. When SHL are not treated by low temperature oxidation or oxidized in HNO_3 only, the high temperature oxidation occurs very fast, but Q_{fb} is of the same order as Q_{fb} in the oxide obtained by thermooxidation of Si. That allows to use these SHL for the passivation of Si surface, maintaining weak surface band bending.

REFERENCES

[1] Loginov B.B., J.Prikladn. Khim., 50, 1683, (1977).
[2] Loginov B.B., Koltzov S.I., J.Prikladn. Khim., 55, 1223, (1982).
[3] Loginov B.B., Gaydaenko V.P., J.Prikladn. Spektrosk., 31, 126, (1979).
[4] Loginov B.B., Uritsky V.Ja., Poverkhnost, 3, 104, (1985).

Materials Science Forum Vols. 185-188 (1995) pp. 109-114

Passivation and depassivation of electrically active centers in the polysilicon-oxide-silicon structures

I.A. Uritskaya[1] and V.Y. Uritsky[2]

[1] Herzen State Pedagogical University of Russia, 191186, St.-Petersburg, Russia

[2] JSC "Svetlana", 19456, St.-Petersburg, Russia

Keywords: Passivation, depassivation, electrically active centers, undoped poly-Si gate, high electric field stress, C-V measurements, polySi-SiO_2-Si structure, trap density

Abstract: New aspects of hydrogen-related passivation and high electric field depassivation of electrically active centers located in the polySi-SiO_2-Si structures not only at the Si-SiO_2 but also at the polySi-SiO_2 interfaces.

I. INTRODUCTION

The polySi layers are widely used in integrated circuits (IC) as gates of different MOS elements, commutation buses, resistors and isolating layers. In the process of IC formation hydrogen and hydrogen-contained species penetrate into oxide and at its interfaces creating new and passivating initial defects. It may occur at the thermal oxidation and the following annealing if it is performed in the hydrogen-containing ambient, but it is sure to occur during postmetallization (aluminium) treatment at 400-450°C. In such treatment, even if it takes place in the inert ambient, active hydrogen is produced by the reaction of aluminium with hydrogen-containing components (H_2O, OH^-) absorbed on the IC surface [1]. The active hydrogen is also produced by interaction of aluminium and polySi due to a release of hydrogen trapped beforehand at the grain boundaries.

At IC operation high electric field may be located in the gate oxide. Moreover, the tendency to reduce MOS element dimensions (including oxide thickness) intensifies this effect. The local high fields lead to injection of charge carriers from electrodes (substrate and gate) into oxide. The following charge trapping in the oxide, a generation of electrically active centers (EAC) there and hydrogen-related electrochemical processes in the oxide explains the scientific interest to these phenomena [2, 3]. The practical interest is associated with reliability of MOS transistors, whose electrical characteristics (for example, threshold voltage, transconductance, subthreshhold current) could degrade due to the above mentioned processes.

In this work the EAC responsible for slow and fast interface traps, mobile and fixed charges in the oxide located not only at the Si-SiO_2 interface but also at the polySi-SiO_2 interface and in polySi gate as well as their hydrogen-related passivation and high electric field stress (HEFS) depassivation were studied. The interrelation between processes which take place at both internal and external oxide interfaces is also analyzed.

II. EXPERIMENTAL PROCEDURES

The polySi-SiO_2-Si structures with undoped polySi gate were used in the experiments. The were formed on n- or p-doped (N_A=N_D=8 10^{14} cm^{-3}) Si (100) wafers. Oxide layers of various thickness (40-80 nm) were thermally grown at 900°C by the direct reaction of hydrogen and oxygen in a pyrogenic system (pyrogenic oxide) or at 1000°C in dry oxygen (dry oxide). The undoped polySi layers were deposited at 620°C by thermal decomposition of silane in argon. Some samples were hydrogen-annealed (HA) at 800°C. The lithography definition of various polySi gate configuration with characteristic size of 8-640 nm (the side of the square in case of a square gate and the stripe width in case of a stripe gate were considered as a characteristic size) was performed on one half of the wafer after aluminium deposition. To reduce serial resistance an

aluminium-polySi contact was formed across the most of gate area. The postmetallization anneal treatment (PMA) of 10 min. in wet Ar at 450°C and definition of polySi gate on the other half of the wafer were performed after initial C-V measurements, HEFS and post-HEFS C-V measurements. The HEFS was performed at room temperature, during the time of (5-720)s, under gate voltage $V_g = \pm(5\text{-}60)$V. Then the comparative measurements of the structures located on both parts of the wafer were done. This sequence of procedures realized allows to detect the lateral phenomena, which could occur, if PMA takes place after the gate definition.

The use of polySi-SiO_2-Si system with lightly doped polySi gate allows to extend the possibility of C-V analysis applied to these system. Usually potential V_{fb} characterizing flat band condition at the Si-SiO_2 interface and concentration of EAC in the oxide near the Si-SiO_2 interface and in the Si surface layer may be correctly determined from C-V characteristics of MOS structure. When using weakly doped polySi gate, not only above mentioned parameters may be defined but also potential V_{fb}^g characterizing flat band condition at the polySi-SiO_2 interface, magnitude and centroid of oxide charge, concentration of EAC at the polySi-SiO_2 interface and in the polySi gate [2,3]. This possibility occurs due to influence of modulation of lightly doped polySi gate capacitance over C-V curve. The additional region of polySi surface capacitance modulation, which depends on the characteristics of EAC located in the polySi gate and at the polySi-SiO_2 interface, appears.

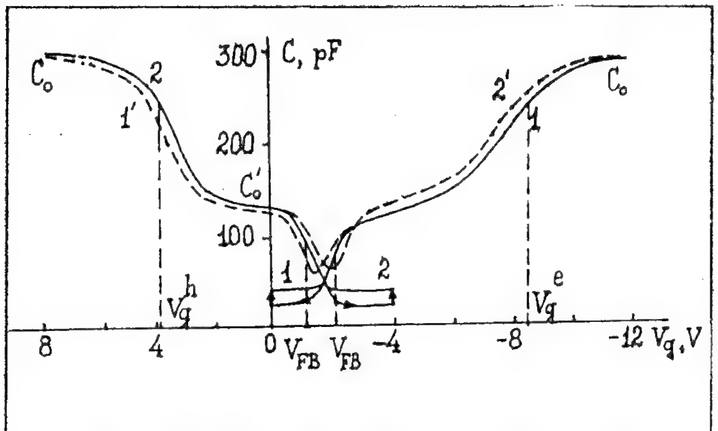

Fig.1. C-V curves of the HA, PMA treated structures. The oxide (40 nm) was formed on p-Si (1) and n-Si (2) by oxidation in dry O_2. Solid line - in the dark, dash line - under the strong illumination.

However, this approach is effective when there is no recharging of EAC in the polySi gate due to surface band bending. This situation is usually true for the shallow energy levels. If the EAC defined by the traps located at the grain boundaries in lightly doped polySi gate dominate and their energy levels are distributed across the whole polySi forbidden gap, surface band bending causes trap recharging, and so it is impossible to estimate the value of V_{fb}^g correctly. The first case is practically realized when polySi gate is deposited in hydrogen and PMA-treated at 400-450°C [4,5]. The second case occurs when lightly doped or undoped polySi gate is deposited under low pressure of SiH_4 in inert ambient [6,7], as in our case. In any case it is expedient to introduce the potentials V_e^g and V_h^g, which characterize the accumulation of holes and electrons on the polySi surface respectively. To simplify the determination of V_e^g and V_h^g it may be done in the same way as the determination of the potential V_{fb}^g in case of n- or p-Si, when N_D or N_A coincides with the concentration of EAC N_t^{gv} averaged on the maximum polySi depletion width. This situation corresponds to the minimum Co in the gate capacitance modulation region on the C-V curve, as shown in Fig.1. The total concentration of EAC in the polySi surface depletion region is given by the approximate expression:

$$N_t^g \approx C_o(V_h^g - V_e^g)/q \qquad (1).$$

However, a determination of V_h^g and V_e^g would be more difficult, if they were in the gate potential range causing inversion of the Si surface, so the high frequency capacitance would be

considerably less than the oxide capacitance. That is the reason why the C-V measurements and determination of V_h^g and V_e^g should be done only if the additional source of minority carriers is available. The presence of minority carriers can provide a restoration of quasi-equilibrium in the Si surface depletion layer and increase system capacitance until maximum value C_o' or C_o. Such a source could be provided by: i) a highly doped region with the conductivity type opposite to that of the substrate, located below the gate periphery, the outer contact to which is connected with that of the substrate; ii) a peripheral region of the substrate being under strong illumination. If the illumination is strong enough and the choice of polySi gate configuration is proper (for example, the gate which consists of narrow polySi stripes covered with "non-transparent" aluminium layer) , the capacitance of Si-SiO_2-polySi-Al structure under inversion at the Si surface reaches the value of the oxide capacitance C_o when polySi surface accumulates electrons as well as holes. This fact is proved by similarity of C-V curve segment, defined by polySi surface capacitance modulation, for both polySi-SiO_2-Si structures formed on n- or p-substrate, as shown in Fig.1.

The total concentration of EAC at the Si-SiO_2 interface may be calculated by:

$$N_t \approx C_o'(V_{inv} - V_{inv}^{th} - V_{fb})/q, \qquad (2)$$

where V_{inv} and V_{inv}^{th} are the gate voltages causing the Si surface band bending $V_S = -2\phi_B$ (ϕ_B - electrostatic potential in Si bulk), when EAC are present and in ideal case absent, respectively. In addition to C-V measurements the conductance technique and gate current measurement were used [8].

III. EXPERIMENTAL RESULTS AND DISCUSSION

The samples formed without HA have significantly high trap density at the polySi-SiO_2 interface and in the polySi gate. It results in considerable distortion of the C-V curve segment corresponding to polySi surface capacitance, as it can be seen in Fig.2, and also in frequency dispersion. Moreover, in case of p-type substrate the maximum structure capacitance in the dark is less than the oxide capacitance so V_e^g in this case is more than the permissible operation voltage (~ -40V) of this polarity (Fig.2).

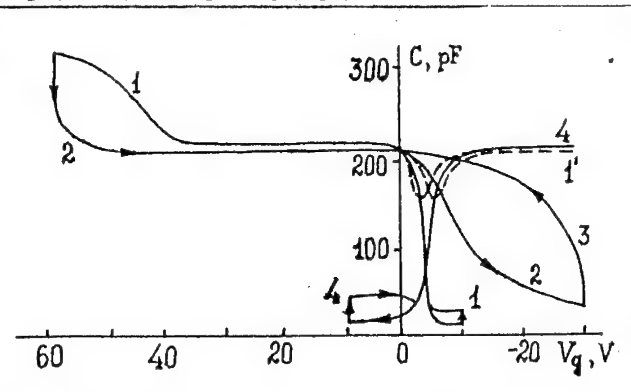

Fig.2. C-V curves of the polySi-SiO_2-Si structure with the pirogenic oxide (40 nm) formed on n-Si (1-3) and p-Si (4) before (1,4) and after HEFS (2 min,60V (2), 2 min,-30V (3)). Solid line - in the dark, dash line - under strong illumination.

When positive electric field strength during HEFS treatment exceeds 6MV/cm a generation of slow and fast traps at the Si-SiO_2 interface is observed. Generation of positive charges at the polySi-SiO_2 occurs at the same time, as it is demonstrated in Fig.2. This effect is more impressive in case of pyrogenic oxide or dry oxide annealed in hydrogen. So, the above mentioned generation of EAC at Si-SiO_2 interface may be connected with the following electrochemical effect. High electric field causes the hole injection from the polySi and electron injection from the Si substrate. Some of them are trapped near these interfaces which intensifies the field in the oxide. The other holes cause break of silicon-hydrogen bonds and then electrically non-active

centers connected with trivalent Si can lead to their electrical activation. On the contrary, electrons flux causes the neutralization of positively charged centers (H^+ or H_3O^+) drifting to Si-SiO_2 interface. Moreover, the electrons which reacted with H_3O^+ near hydrogen-passivated centers could activate the following electrochemical reaction:

$$\equiv SiH + H_3O^+ + e^- \rightarrow \equiv Si\bullet + H_2O + H_2, \qquad (3)$$

which also leads to the formation of EAC [9]. The further trapping of charge carriers on them develops the observed effect while measuring C-V curves.

HA and especially PMA before the gate definition cause the substantial reduction of the total trap density N_{tg} at the polySi-SiO_2 and N_t at the Si-SiO_2 interfaces from (5-20) 10^{12} cm^{-2} to (3-5) 10^{12} cm^{-2} and from 1.0 10^{11} cm^{-2} to (0.2-0.4) 10^{11} cm^{-2} respectively (Fig.1). The effective polySi bulk trap density N_{tgv} is also redused from 10^{18} cm^{-3} to (0.5-2.0) 10^{17} cm^{-3}. It shows that the passivation of EAC located in different regions of the structure occurs: at the Si-SiO_2 and polySi-SiO_2 interfaces as well as in the polySi gate. It means that the nature of defects, which is responsible for the traps there, was the same - the dangling silicon bond at the oxide interfaces and at the polySi grain boundaries. The traps annihilation affects the decrease of frequency dispersion of C-V curves. That fact is also proved by quasi-static C-V measurements and conductance technique.

The slow trapping in the oxide during HEFS is decreased by PMA before the gate definition. Moreover, generation, drift of the mobile charge to the Si-SiO_2 interface and the creation of fast traps occured there under positive HEFS, as may be seen in Fig.3. and Fig.4. This effect is more pronounced in case of pyrogenic oxide and HA treated dry oxide. A generation and the following drift of positive fixed charge under HEFS of positive polarity dominate in case of polySi-SiO_2 formed without HA. As it is shown in Fig.3, as a result of HEFS the substantial shift of the C-V curve segment defined by Si surface capacitance modulation is observed, whereas the shift of the segment defined by polySi surface capacitance modulation is much less. In case of polySi-SiO_2-Si structures HA-treated the above mentioned process occurs as well as the drift of positive charge activated initially by PMA. It leads to a considerable reduction of positive charge ($V_{hg} \leq 0$) in the oxide near the polySi-SiO_2 interface (Fig.4). If both time and bias voltage of HEFS increase, the distortion of C-V curve segment determined by Si surface capacitance modulation also increase. That could be explained by the fact that the mobile charges accumulated in the oxide near the Si-SiO_2 interface may operate as electron traps transforming into the neutral EAC. As can be seen in Fig.4, due to the drift of positive mobile

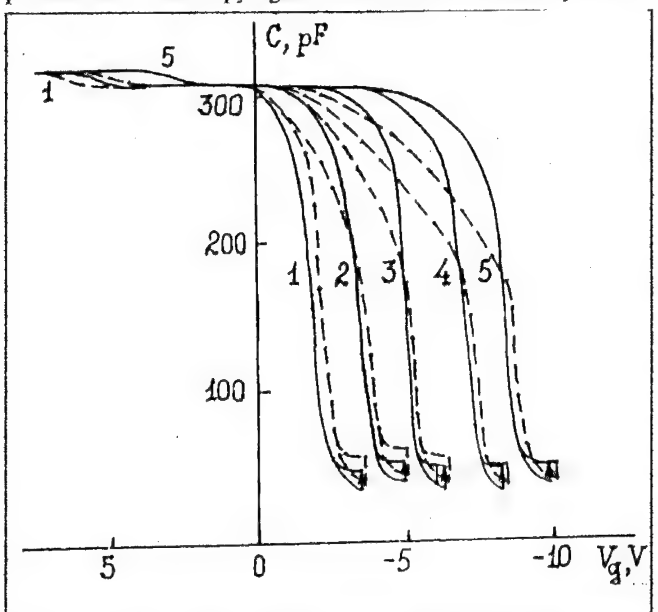

Fig.3. C-V curves of the n-Si-SiO_2 (pirogenic,40nm)-polySi-Al structure, PMA-treated before (solid line) and after (dash line) square gate definition; initial (1), after HEFS during 2 min. under +5V (2), +10V (3), +15V(4), +20V(5).

charges in the oxide from the polySi-SiO_2 to Si-SiO_2 interface, the polySi surface band bending ($V_{fb}^{s}\leq 0$) is defined by negative fixed charge dominating near the polySi-SiO_2 interface. So, the negative fixed charge in the oxide near the polySi-SiO_2 interface is the characteristic feature of this interface. The experimental data obtained as the result of investigation of Si-SiO_2 structures formed by oxidation of polySi and polySi-SiO_2-Si structure annealed in non-hydrogen ambient support it [10,11].

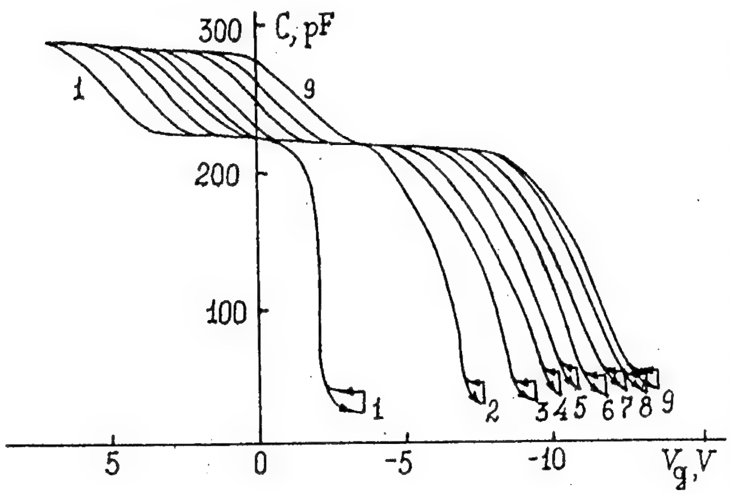

Fig.4. C-V curves of nSi-SiO_2-polySi-Al structure annealed before gate definition before HEFS (1) and after HEFS under +15V during 5s(2), 15s(3), 30s(4), 60s(5), 120s(6), 240s(7), 420s(8), 720s(9). [Pirogenic oxide HA-treated after polySi deposition].

The PMA after the gate definition causes "size"-effect which is expressed by the influence of the gate size on the above mentioned phenomena (trap annihilation and generation of mobile charge). It should be noted that in case of PMA of the structures with initially formed narrow gates a tendency of fixed negative charge dominating in the oxide at the polySi-SiO_2-Si interface and of positive mobile charge reduction at the Si-SiO_2 interface is evident. Moreover, the mobile charge isn't observed in the samples with the most narrow (8-15 μm) stripe gate (Fig.5), whereas in the samples with square gate the mobile charge is inhomogeneously distributed across the whole area is characterized by low concentration in the peripherific regions.

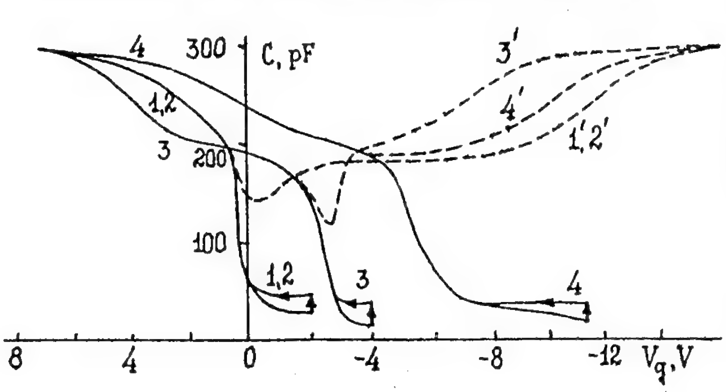

Fig.5. C-V curves of the PMA treated structures before (1,3) and after (2,4) HEFS (20V, 2 min.). Pirogenic oxide (40nm) was formed on n-Si. PMA was performed before (3,4) and after (1,2) gate definition (stripe width -8μm). Solid line - in the dark, dash line - under strong illumination.

The observed phenomena can be explained in the following way: hydrogen spread over the oxide is released from polySi during PMA and can form or activate the defects responsible for positive mobile charge. In case of the structures annealed after polySi gate definition the part of the active hydrogen depending on P/S rate (where P - gate perimeter, S - gate square) spreads

laterally and leaves the gate oxide region. It leads to the "size"-effect which results in the annihilation of surface traps at both oxide interfaces as well as in the formation of mobile charge in the oxide.

IV. CONCLUSION

The processes which take place in different regions of polySi-SiO_2-Si structure during HA and PMA treatment and result in annihilation and generation of EAC were studed. The hydrogen-related passivation of EAC during HA and PMA occurs independent of EAC localization: at the polySi-SiO_2 or Si-SiO_2 interfaces or in the polySi gate layer. It indicates to the similar nature of defects responsible for EAC located in different regions of the structure. The HEFS influence on EAC is determined by electron and atomic processes occuring in the oxide. It also leads to generation of slow and fast traps near the Si-SiO_2 interface and to accumulation of positive charge in the oxide in the result of slow hole trapping at the polySi-SiO_2 interface. The PMA causes a generation of new EAC or transformation of available ones. These EAC either directly or being activated by positive HEFS operate as positive mobile charges in the oxide. If positive mobile charges drift in the oxide from polySi-SiO_2 interface due to HEFS or leave the gate oxide during PMA by lateral diffusion, the fixed negative charge could be observed in the oxide near the polySi-SiO_2 interface. The presence of negative charge is the characteristic feature of the polySi-SiO_2 interface in contrast to Si-SiO_2 interface characterized by fixed positive charge.

REFERENCES

[1] P.Bulk, Extended Abstracts of Elrctronics Division, 14, 237, (1985).
[2] V.Ja. Uritsky, Avtorsk. Svid. 884508, (1980).
[3] G. Yaron, D. Frohman-Bentchkowsky, Solid St.Electron., 23, 433, (1980).
[4] V.Ja. Uritsky, Poverkhnost, 106, (1989).
[5] V.Ja. Uritsky, V. Gurtov, Yu. Listopadov, Mikroelektron., 19, 263, (1980).
[6] Y. Nissan-Cohen, J. Shappir, D. Frohman-Bentchkowsky, J.Appl . Phys., 57, 2830, (1985).
[7] V.Ja. Uritsky, in: Elektrichesk. Relaks.", St-Petersburg, 137, (1992).
[8] E. Nicollian, A. Goetzberger, Bell Syst. Techn. J., 46, 1055, (1967).
[9] E.N. Pointdexter, Semicond. Sci. Technol., 4, 961, (1989).
[10] V.Ja. Uritsky, R.I. Mamin, V.F. Shatalov, Poverkhnost, 149, (1985).
[11] R.I. Mamin, S.P. Prokofiev, V.Ja. Uritsky, V.F. Shatalov, Poverkhnost, 123, (1987).

Materials Science Forum Vols. 185-188 (1995) pp. 115-118

Role of electron / hole processes in the initial stage of silicon anodization

V. Uritsky

JSC „Svetlana", 194156, Saint-Petersburg, Russia

Keywords: Anodization, kinetics of oxidation, ionic current, current efficiency, hole traps density, avalanche, Si-SiO_2 interface, electrically active centers, MOS structure

Abstract: The peculiarities of n- and p-Si anodization kinetics in the initial stage under light illumination or in the dark were investigated. The anodic oxidation was carried out at constant current in a 0,04 N solution of KNO_3 in ethylene glycol. The paper presents a discussion of the correlation between an anodization kinetics in the initial stage and the hole / electron processes in the oxide, at the Si-SiO_2 interface and in the surface space charge region of silicon.

I. INTRODUCTION

The anodic oxidation of monocrystalline silicon in electrolyte attracted attention for a long period of time [1-9]. It is caused by the following circumstances: i) there is a possibility to form an oxide layer at room temperature; ii) it is easy to control the thickness of the oxide layer in anodization process directly; iii) there is a certain similarity of electronic and ionic processes taking place in the anodic oxidation of silicon and in silicon MOS structures due to the electrical field stress. These processes govern the degradation of electrical and structural characteristics of MOS structures related with defect generation [10].In the previous papers the influence of Si conductivity type and illumination (in case of n-Si) on the voltage-time curve $V_c(t)$ during the anodization was shown. Later the kinetics of oxide growth in the initial stage of oxidation of n-Si and p-Si in the dark and under illumination as well as island coalescence forming the oxide were investigated [11-13].

In this work the correlation between kinetics of the oxide growth and potential barrier in the surface space charge region governed by electron / hole processes in the initial stage of anodic oxidation of silicon was studied.

II. EXPERIMENTAL PROCEDURES

n- and p-Type (111) silicon wafers, phosphorous- or boron-doped ($N_D \approx N_A \approx 10^{15}cm^{-3}$), were anodized in the dark or strongly illuminated at a constant current J_p=0,5-0,7 mA cm^{-2}. The anodization of only one side of the sample was carried out in a 0,04 N solution of potassium nitrate in ethylene glycol at room temperature using the automatically recording of voltage-time curves. Moreover, periodically (in 15-30 s) the surface of n-Si sample oxidized in the dark was illuminated for a short period of time in order to define oxide voltage V_o and silicon surface band bending V_s. Indeed, the total voltage of the cell is given by:

$$V_c = V_o + V_s + V_R\,, \qquad (1)$$

where V_R - is the sum of the potential drops in electrolyte, in Si-bulk, at the contacts. When quasi-equilibrium keeps on in the surface space charge region (what is realized in case of p-Si) V_s is less than E_g/q, where E_g - Si band gap energy, q - magnitude of electron charge. When quasi-equilibrium is broken due to polarization current, V_s is more than E_g/q. The value of V_R can be determined from the initial value $V_c(0)$, when $V_o(0)\approx0$ and quasi-equilibrium keeps on in the Si surface space charge region, so

$$V_c(0) \approx V_R. \qquad (2)$$

The change of V_c during the silicon oxidation process until the oxide thickness d_o is reached can be obtained from the approximate expression

$$\Delta V_c(t) = V_c(t) - V_R \approx V_o(t) = \alpha\, d_o(t), \qquad (3)$$

with coefficient α = 0,55 nm V^{-1} obtained from ellipsometry measurements of the oxide thickness. When quasi-equilibrium is broken in the surface space charge region of n-Si the change of cell voltage is given by

$$\Delta V_c(t) = V_o(t) + V_s(t). \qquad (4)$$

In this case the short periodical illumination of n-Si surface used allows to determine $V_o(t)$ and $V_s(t)$. So under the strong illumination the change of V_c can be defined as

$$\Delta V_c^L(t) \approx V_o(t) \qquad (5)$$

and

$$\Delta V_c(t) - \Delta V_c^L(t) \approx V_s(t). \qquad (6)$$

III. EXPERIMENTAL RESULTS AND DISCUSSION

The typical voltage-time curves $V_c(t)$ obtained during constant current anodization of the n-Si (a) and p-Si (b) samples in the dark are shown in Fig.1. As can be seen, the initial region of the $V_c(t)$ curve differs from the linear one observed when the oxide thickness more than 30-40 nm is reached. If n-Si is oxidized under strong illumination, the voltage-time curves would be similar to those obtained for p-Si. The above mentioned procedure of short periodical illumination of n-Si surface oxidized in the dark allowed to find out some new peculiarities of silicon anodization in the initial stage. It should be mentioned that this procedure didn't influence the kinetics of oxidation because of very short light stress time. The identity of $V_c(t)$ curves obtained when using short periodical illumination of the samples oxidized in the dark and without it proves that.

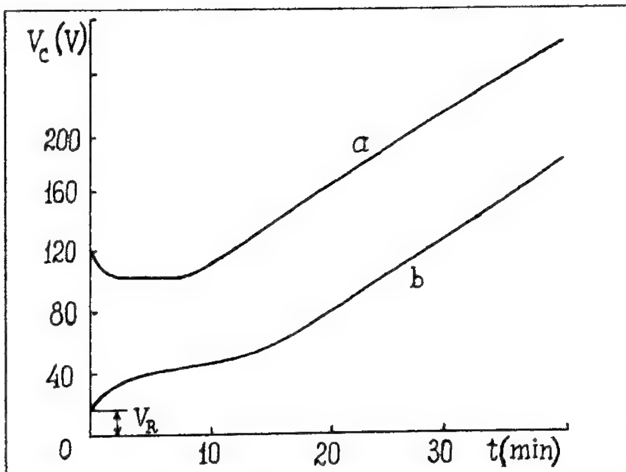

Fig.1.Voltage-time curve during the anodic oxidation (J_p=2,5 mA cm^{-2}) of n-Si (a) and p-Si (b) in the dark.

The $V_o(t)$ and $V_s(t)$ curves obtained are plotted in Fig.2. There are two different regions of the initial stage and transient region to the linear stage. The first one is an initial period of slow homogeneous oxide growth at the silicon surface. In case of illuminated p-Si oxidation or n-Si oxidation the oxide growth rate in this stage is higher than in case of n-Si oxidation in the dark. This region can be associated with the anodic reaction such as

$$Si + H_2O + zp^+ \rightarrow SiO_2 + 4H^+ + (4 - z)\, q^-, \qquad (7)$$

where $2 \leq z \leq 4$. This reaction requires the presence of holes [14].

In case of oxidation of polished n-Si wafers in the dark this first region of the initial stage transforms into the region of intensive inhomogeneous (island-type) oxide growth over the

whole surface area, when oxide thickness ~10 nm is reached. If grinded instead of polished n-Si wafers are used, the length of the first region is considerably lower. Thus the role of the first part of initial stage could be explained by destructive treatment of the wafer surface, which is necessary for the further intensive inhomogeneous oxide growth.

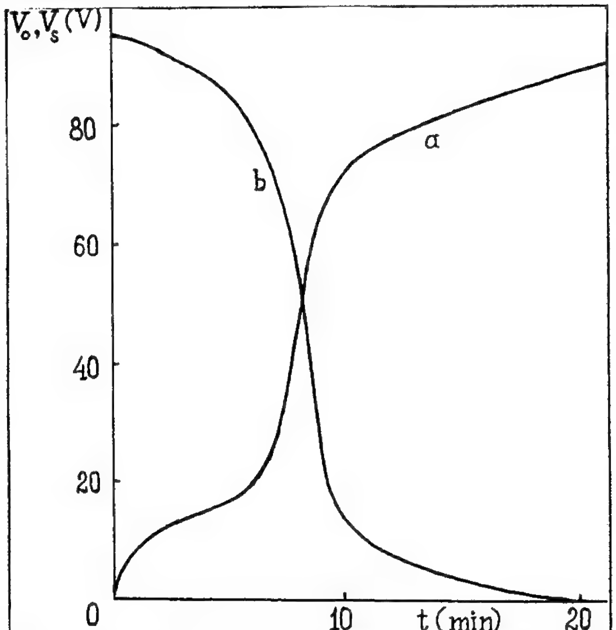

Fig.2. $V_0(t)$- (a) and $V_s(t)$- (b) during the anodic oxidation of n-Si in the dark.

The oxide growth rate in the second region of the initial stage of Si oxidation is higher than that in the following stage of linear oxide growth. It could be associated with lower hole concentration at the n-Si in the dark due to formation of wide (~10-12μm) non-equilibrium depletion layer. This leads to a decrease of tunnel hole injection into the oxide. It is this very current from the degenerate accumulation or inversion hole layer that makes the main part of the total current through the oxide, when the oxidation of p-Si or n-Si under illumination is performed. The hole current is excessive for the above reaction (eqn.7). So the current efficiency of the deposition process is very low (~1%). Contrary to this case, the portion of hole component in the total current decreases when the oxidation of n-Si is performed in the dark. To maintain the current constant the electric field strength in the oxide has to be increased in order to compensate this effect by increasing the ionic current and current of electrons coming from electrolyte. In this case the hole current through the oxide is defined by the injection of hot holes generated in wide non-equilibrium depletion layer at the n-Si surface across the Si-SiO_2 barrier (3,8 eV). Most of hot holes are thermalized due to collision (impact) with the silicon atoms and break the silicon bonds. These silicon surface atoms weakly bonded are supposed to be later transported through the oxide to its outside surface. As a result the ionic current increases and the current efficiency of oxidation 10-15% is reached. It manifests itself in a substantially higher oxide growth rate. Really, anodic polarization ($E \approx 1{,}7\ 10^7$ V cm^{-3}) of Si-SiO_2 systems with thermal oxide layers of about 150 nm resulted in high concentration of Si^+ and SiH^+ ions in the oxide as detected by SIMS technique not only at the Si-SiO_2 interface but over a region 30-40 nm long [15].

The observed rapid inhomogeneous (island-type) oxide growth all over the surface at the second part of the initial stage can be associated with the destructed surface area at the silicon wafer, which includes the centers of anomalously high generation of electron-hole pairs as well as doped regions with statistical fluctuation of concentration. Both these facts cause more intensive new local avalanches on other sites. The presence of wide (~10 μm) non-equilibrium depletion layer at the Si surface is proved by the substantial magnitude (~100 V) of V_s in Fig.2. Although V_s falls with time, the value of V_c remains weakly changed because of compensative rise of V_o. The decrease of V_s is defined by creation of EAC at the Si surface, which may be attributed to such type defects as a Si atom with dangling or broken bonds and are responsible for the thermogeneration of electron-hole pairs.

The situation, when V_s falls until the low value characterizing quasi-equilibrium at the n-Si surface, is observed since the oxide thickness 30-40 nm is reached and electron-hole pairs generation begins due to avalanche process in the oxide [16].That leads to the reduction of oxide growth rate in the area, where 30-40 nm oxide thickness has been already reached. However, the rapid oxidation extends to other sites until all the oxide growth area is oxidized till 30-40 nm.

The considerable number of charge carriers passing through the oxide and $Si\text{-}SiO_2$ interface within the anodization time must cause the generation of defects. This is supported by C-V measurements of $Si\text{-}SiO_2$ systems with high trap density ($\sim 10^{13} cm^{-2}$) in the oxide and at the $Si\text{-}SiO_2$ interface. The interface trap energy distribution is continuous and contains some peaks at the edges of the forbidden gap. The oxide charge Q_{fb} is determined by the charge of trapped carriers. It is positive in case of p-Si oxidation or n-Si oxidation illuminated as the hole trapping dominates. In case of n-Si oxidation in the dark Q_{fb} is less in magnitude and even gets negative polarity. The hydrogen anneal treatments (<500°C) passivate most of the defects; thus interface trap density can be reduced.

IV. CONCLUSIONS

The results presented here indicate that the role of electron / hole processes in the initial stage of anodic oxidation of Si has several aspects different for given n- and p-type silicon samples. First, the hole current injected from degenerated accumulation or inversion layer is excessive for the anodic reaction (eqn.7) and determines a very low efficiency of the deposition process. Second, hot holes generated in the local avalanches in a wide non-equilibrium depletion layer cause the break of surface silicon bonds. It leads to an increase of ionic current and inhomogeneous oxide growth rate accordingly. Third, the electron / hole trapping in the oxide to a considerable extent defines the total charge Q_{fb} there. Fourth, the avalanche in n-Si oxidized in the dark is reduced considerably because of two reasons: i) increase of thermogeneration velocity at the $Si\text{-}SiO_2$ interface; ii) development of the avalanche process in the oxide layer with the thickness exceeding more than 30-40 nm.

REFERENCES

[1] P.F. Schmidt, W.Michel, J. Electroch. Soc. 104, 230, (1957).
[2] P.F. Schmidt, A.O. Owen, J. Electroch. Soc. 111, 682, (1964).
[3] E.E. Duffek, E.A. Benjamini, C. Mylroie, J. Electroch. Soc. 111, 62, (1964).
[4] S.P. Maminova, L.L. Odynets, Electrochem. 1, 365, (1965).
[5] S.P. Maminova, L.L. Odynets, Electrochem. 2, 346, (1966).
[6] A.G. Revezs, J. Electroch. Soc 114, 629, (1967).
[7] P.P. Konorov, O.V. Romanov, V.Ja. Uritsky, Radiotekhnika i Elektronika, 13, 568, (1967).
[8] P.P.Konorov, J.Rychen, O.V.Romanov, V.Ja.Uritsky, Fiz. i tekhn. poluprov. 2, 840, (1968)
[9] C.R. Fritzche, J. Phys. Chem. Sol. 30, 1885, (1969).
[10] V.Ja. Uritsky, P.P. Konorov, Fiz. i Tekhn. poluprov. 8, 1622, (1974).
[11] P.P. Konorov, V.Ja. Uritsky, V.A. Melnitsky, Mikroelektron. 4, 61, (1975).
[12] A.P. Baraban, I.V. Klimov, P.P.Konorov, Vestnik LGU, (ser.4), 4, 81, (1985).
[13] I. Montero, R.J.Gomez-San Roman, J.M. Albella, A. Climent, J. Perriere, J.Vac.Si. Technol.138, 544, (1990).
[14] D.R. Turner, J. Electroch. Soc. 107, 810, (1960).
[15] J.A.Tarantov, G.F.Romanova, P.I.Didenko, V.V.Bulavinov,in "Fizik.dielektr.",128, (1982).
[16] A.P. Baraban, V.V. Bulavinov, P.P. Konorov, Pisma v JTF, 14, 806, (1988).

Materials Science Forum Vols. 185-188 (1995) pp. 119-128

Effect of structure of hydrogenated SiN_x:H films on the dissociation mechanism of Si-H and N-H bonds

E.B. Gorokhov, A.G. Noskov, V.V. Vasilyev, E.M. Trukhanov, V.N. Ovsyuk and G.Yu. Salieva

Institute of Semiconductor Physics, Academy of Sciences of Russia, 630090 Novosibirsk, Russia

Keywords: Glassy films, chemically bonded hydrogen, stress, film shrinkage, viscosity, network reconstruction

ABSTRACT

Dehydrogenation in SiN_x:H films produced by CVD and PE CVD processing from 50-800°C using an original technique of complex thermal defectometry has been studied. This technique includes an analysis of changes in film parameters (shrinkage, refractive index, mechanical intrinsic stresses and chemical composition) during annealing. The viscosity of films is determined under conditions where their chemical composition and structure vary with thermal treatment. The PECVD SiN_x:H films have been found to accumulate, during synthesis, the protons interacting with Si and N atoms as well as oxygen upon annealing. As a result, Si-H, N-H and O-H bonds are created, and the refractive index decreases. The decrease in film bulk as well as the increase in the refractive index are determined by the dehydrogenation of SiN_x:H films, which starts to proceed at annealing temperatures above 400°C. Experimental data indicate that Si-H and N-H dissociation cannot be adequately fitted by 1-st order kinetics. The qualitative models of this process, which incorporate the influence of the structure of the film and its defects are suggested. In the first model, Si-H and N-H defects are assumed to have a wide spectrum of structural modifications providing an eventually continuous spectrum of variation of the binding energy between hydrogen and silicon and/or nitrogen within 1-1.5 eV. This is due to a reduction in electronegativeness of the Si and N atoms if their bond to a hydrogen atom breaks, thus resulting in smaller dimensions of the SiN_4 tetrahedron in the silicon nitride network. The second model takes into account a pairwise interaction of H-containing defects in SiN_x:H films and a possible contribution of the other network defects. Such a contribution results in a higher order of reaction.

INTRODUCTION

An understanding of the dissociation mechanism of Si-H and N-H bonds during thermal treatment is among the key problems in studies of the effect of chemically bound hydrogen on film properties. It is known, that dehydrogenation is responsible for strong changes in the properties of SiN films is at relatively low temperatures. Dissociation of Si-H and N-H bonds in SiN_x:H layers is one of the basic stages of their formation. It begins on the growing surface of the film and continues in the bulk. The first dehydrogenation experiments were performed on Si_3N_4 layers produced at high temperatures and having a few Si-H and N-H bonds. They were annealed over the temperature range 800-1000°C. The process of hydrogen release was considered as a set of elementary acts of breaking of Si-H and N-H bonds. The dissociation energies were about 2.9 eV for SiH and about 3.1 eV for NH bonds, respectively [1,2]. The effect of the film structure on their dehydrogenation was taken into account despite an evident fact that there must be structural rearrangement in the atomic network of films during and after hydrogen elimination from Si and N atoms. The approach used suggests that the breaking of Si-H and N-H bonds as well

as structural rearrangements in the films grown under different conditions proceed identically, according to 1-st order kinetics and depend on neither the concentration of the defects nor on other specific features of the films.

However, the dehydrogenation activation energy, calculated from film shrinkage data [3], was 2.1 eV, i.e. nearly 1 eV lower. Moreover, hydrogen elimination started at lower temperatures. It seems likely that the nature of the lower activation energy is due to different levels of perfection of the film structure and also due to different concentrations of chemically bound hydrogen. The present work is aimed at studying dissociation mechanisms of Si-H and N-H bonds depending on the degree of imperfection of the structure of SiN_x:H films produced under different conditions.

EXPERIMENTAL TECHNIQUES

Analysis of the properties of silicon nitride layers was performed using various methods: IR spectroscopy, ellipsometry, double-crystal X-ray diffractometry.These methods allows one to obtain data on the changes in the chemical composition of films, thickness (d), refractive index (n), intrinsic stress (σ). A freshness of our approach is the integration of these methods into a single one called complex thermal defectometry. Its essence is that a series of annealings is performed with simultaneous IR spectra measurements as well as precision refractive index, thickness and intrinsic stress carried out on the same sample or identical ones. Complex thermal defectometry is effective in revealing the presence of various structural defects in the films (isochronal uccessive annealings with step-by-step temperature variation) and in studying the kinetics of the chemical and structural conversion rocesses (constant temperature annealing of varying duration).

RESULTS AND DISCUSSION

During annealing, Si-H and N-H bonds are reduced because of hydrogen elimination, the changes in their concentration giving rise to changes in film thickness up to 20% of the initial one. During free shrinkage, the film dimensions are assumed to change isotropically. If a film is strongly fixed to a substrate this results in non-isotropic changes of its shape and elastic-viscous deformations.

Such measurements are difficult to perform because at least two processes proceed simultaneously: film bulk shrinkage causing intrinsic stresses to increase and viscous flow of the film subjected to these stresses. There is one more factor, which complicates dynamic viscosity measurements: in the course of these processes the chemical composition of a film,its structure and mechanical properties are continuously changing.Fig.1 makes it possible to separate the component of viscous deformation from the total film deformation and to express it via the thickness variation parameters. Fig.1a illustrates the expected change in the dimensions of a free film during shrinkage.The film is not connected to a substrate and its initial dimensions l_o and d_o (the length and thickness of a film respectively) change to l_1 and d_1 due to the shrinkage (Fig.1a). It is clear that in this case an isotropic change in film size will take place, i.e. $l_1=kl_o$ and $d_1=kd_o$, where k is a certain shrinkage coefficient. Viscous deformation of a film is absent. This deformation is present in the case of the film connected with the substrate (Fig.1b), the final film dimensions are equal to l_o and d_2. Let us assume that its bulk V emains unchanged and $d_1l_1^2=V_1=V_2=d_2l_o^2$ (elastic deformation is sumed to be much less than viscous flow deformation). Hence we get $k=(d_2/d_o)^{1/3}$ and viscous deformation is equal to $\varepsilon=\Delta l/l_o=1-(d_2/d_o)^{1/3}$. Thus, to separate the actions of shrinkage (in Fig.1a) and viscous flow (Fig.1b) we come to the film produced in a real process of annealing. Knowing the magnitude

of stress (σ) causing these deformations, one can calculate the viscosity of a film by the well known formula: $\eta=\sigma\ \Delta t/\Delta\varepsilon$.

Besides, account should be taken of viscosity variation during annealing. In view of this, it is possible to measure only the average values of viscosity:

$$<\eta>=(\sigma_1+\sigma_0)\Delta t/2[1-(d_2/d_0)^{1/3}],$$

where σ_0 and σ_1 are the intrinsic stresses in a film before and after annealing respectively; d_0 and d_2 are the initial and final film thickness; and Δt is the annealing duration.

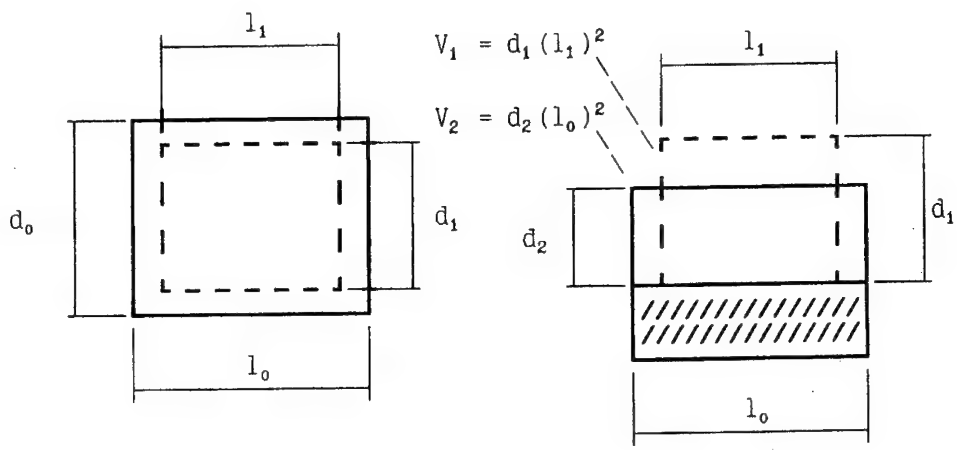

Fig.1. Schematic of film deformation due to shrinkage; (a)- isotropic deformation of the free film, (b) - non-isotropic viscosity deformation of a film connected with the substrate

For experiments we prepared films with different contents of hydrogen whose concentration usually increases with decreasing deposition temperature (T_d). We therefore used SiN_x:H films produced in the atmospheric pressure reaction of SiH_4 and NH_3 in flowing Ar at temperatures of 700 and 800°C, as well as in the PE CVD process at 50-160°C. The changes in concentrations of the Si-H and N-H bonds depends on the deposition (T_d) and annealing (T_a) temperaures as presented in the Table and in Fig.2.

For the films, a decrease in the concentration of Si-H and N-H bonds during annealing was accompanied by a decrease in their thickness and by an increased refractive index and higher intrinsic stress in the films.

TABLE
Si-H AND N-H BOND CONCENTRATIONS IN ATMOSPHERIC PRESSURE CVD SiN_x:H FILMS

Deposition temperature (°C)	Hydrogen bonds	Bond concentration ($\times 10^{21}$ cm^{-3})	
		After deposition	After annealing at 950°C for 5 h
700	Si-H	1.2	–
	N-H	7.1	2.4
800	Si-H	0.4	–
	N-H	5.3	2.8

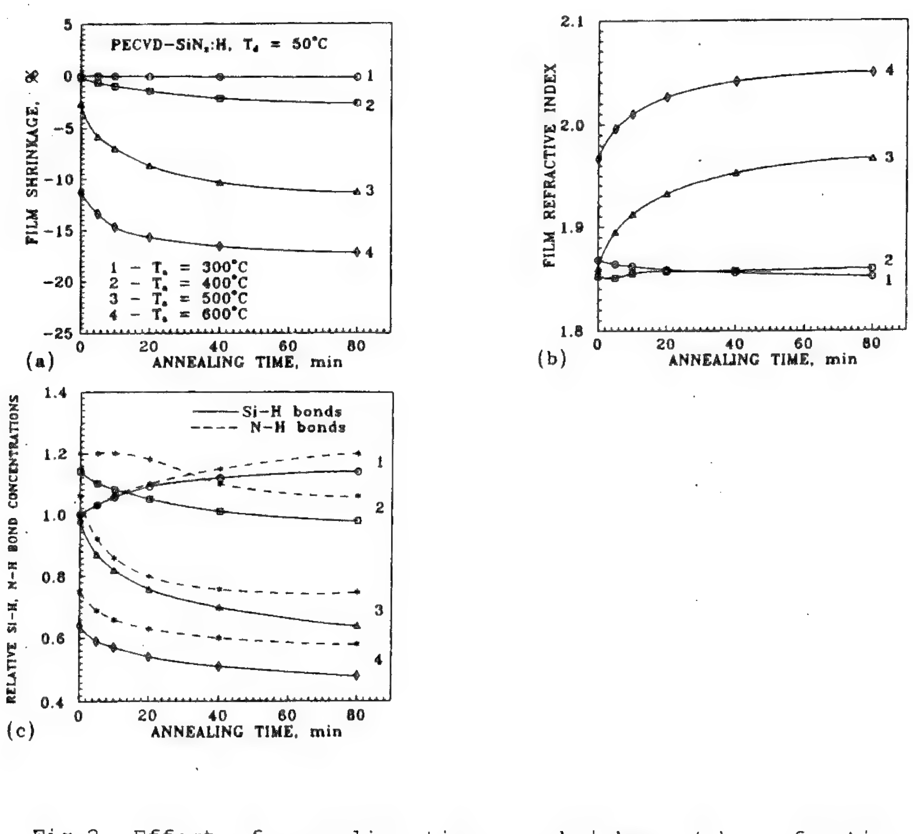

Fig.2. Effect of annealing time on shrinkage (a), refractive index (b) and relative Si-H and N-H bond concentrations (c) of the same PE CVD SiN_x:H film; after annealing at previous temperature the specimen was subjected to the subsequent one; the bond concentrations were normalized to their initial value.

The thickness and refractive index changes were also found to coincide fairly well with the kinetics of hydrogen elimination from a SiN_x:H film (Fig.3). Checking data on high-temperature film shrinkage during 850, 900 and 1000^oC annealings, the 1-st order kinetics has exhibited an incomplete correspondence of the process observed (the kinetics cannot be described by a single exponent, as it shown in Fig.4). Discrepancy between the experimental data and the model representations becomes more considerable as the amount of hydrogen in the SiN_x:H films increases with decreasing growth temperature.

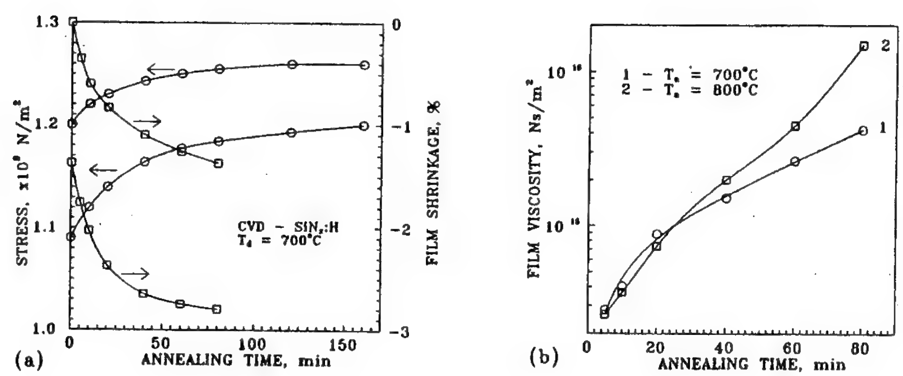

Fig.3. Effect of annealing time on stress and shrinkage (a) and film viscosity (b) of CVD SiN_x:H films; viscosity was calculated using the data presented in (a).

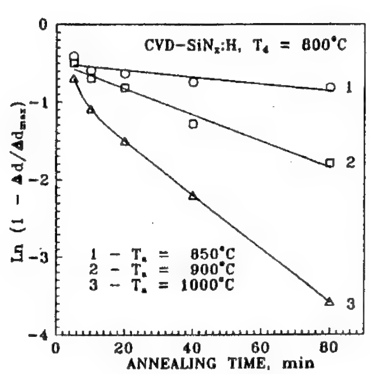

Fig.4. Effect of the annealing time on shrinkage of CVD SiN_x:H films.

Thus, for the process to be adequately described, we need a new model which is capable of explaining the following basic features:

- a decrease in the temperature at which the reaction starts to take place and a reduction of the values of the activation energy of the hydrogen-containing bond dissociation process with increasing their concentration in the bulk of the film;
- an increasing reaction rate as the annealing temperature elevates and a further deceleration of the process for longer annealing despite a high hydrogen concentration in the film.

The model must also be consistent with experimental data on changes in other properties of the film during annealing and particularly with those characterizing changes in the composition and structure: kinetics of shrinkage of the film bulk, growth of the refractive index, kinetics of intrinsic stresses and viscosity.

There are two fundamentally different ways of choosing such a model. The first way is to further develop the notion of hydrogen release from a film as an autonomous, single act of breaking of Si-H and/or N-H bonds. The second one is to admit the possibility of a pairwise interaction of Si-H and N-H defects with each other as a basic form of hydrogen release. It may be noted that in both cases it is necessary to take into consideration the dependence of the bonding energy between hydrogen and the Si and/or N atoms on the state of the atomic surrounding of these bonds in the film network.

For the first model, the assumption is made that Si-H and N-H defects may be subject to a wide spectrum of structural modifications giving rise to a virtually continuous spectrum of bond energy variations between hydrogen and silicon and/or nitrogen in the 1-1.5 eV range. Hydrogen elimination from Si-H defects is known to change the electronegativeness of a silicon atom [4], which, according to data [5], leads to shorter bond lengths between the silicon atom and the nitrogen. An elementary tetrahedron consisting of silicon atoms and nitrogen ones around them should hence become smaller in size. But since it is built in the network and is bonded to other tetrahedrons, a substantial structural rearrangement is needed. Without this hydrogen elimination may prove to be impossible in films with low concentration of structural defects. However, the more H atoms and other defect concentration in the network, the easier will be structural rearrangement, and, consequently, hydrogen release.

Two facts confirm experimentally such a model of the process:

- a sharp increas of the intrinsic stresses in the SiN_x:H films during dissociation of Si-H and N-H bonds;
- a shift to the long-wave absorption range of Si-N bonds with increasing of Si-H and N-H concentrations in the SiN_x:H films, thereby evidencing an increase in the Si-N bond length, and, hence the relaxation of its rigidity [6]. In the PE CVD SiN_x:H films under study, an opposite situation is also observed experimentally: the absorption peak of the Si-N bonds shifts to the short-wave region as Si-H and N-H bonds concentrations decrease upon annealing. It may be noted that in the same spectral region the absorption of Si-N bonds with oxygen contamination takes place. (Oxygen is in the PE CVD SiN_x:H films in noticeable amounts). In particular, this is responsible for the broadening of the IR absorption band of Si-N bonds (800-900 cm^{-1}) because the film seems to be already silicon oxynitride.

We will now turn to the second way of accounting for the observed kinetics of hydrogen release from SiN_x:H films.First of all, we have to analyze the possibility that the proceeding complex second-order reaction between hydrogen-containing complexes in a film are expected to approach closely to each other, at distances when the Si-N and Si-Si bonds can be formed and, as a result, two H atoms peel off.

We would like to mention experimental data supporting the suggested model. First, among them are the dependencies observed in the experiment and not contradicting qualitatively the model. Secondly, a direct confirmation of the model is an increase in the number of Si-N, according to fulfilled IR spectra measurements and Si-Si bonds. This is reflected in a higher refractive index of the film as is shown in Fig.2b. It exceeds the value 2 during annealing. This is usually observed in the PE CVD layers enriched by Si. The same is evidenced by a reduction of the Si-H/N-H ratio from 2.0 to 1.6 upon a 600^{o}C anneal. Thirdly, the temperature dependence of the start of the dissociation of hydrogen containing bonds on their concentration in a film is now straightforward: the longer the average distance between the defects in a film, the higher mobilities are needed to bond them to each other.

There is little likelihood that the bond Si-H (or N-H) complex is transferred in the film. However, for glassy materials, cross-linking of vacant bonds is a typical way of defect transfer[7]. This is a main atomic mechanism responsible for glass viscosity. The data on film viscosity variation during successive annealing indicate a connection between the dissociation rate of the Si-H and N-H bonds and viscosity (Figs.2,5). The higher dehydroge nation rate, i.e. the larger the number of vacant bonds on Si and N atoms, the lower is the film viscosity.

It is difficult to explain that hydrogen elimination occurs due to the transfer of the Si-H and N-H complexes and their interaction, which requires low viscosity, because a decrease in viscosity is possible only if broken bonds are created on the Si and N atoms, i.e. when the hydrogen has already left the film. According to our model, hydrogen remains bound to the network until the Si-N and Si-Si bonds, previously bonded to hydrogen, are formed. However, in this case it seems reasonable to suppose that hydrogen atom can, in principle, move over the film network in the bound state. For this we need to admit the possibility that hydrogen can transfer to the other defects in the film network. Indeed, the spectrum of the structural defects in the SiN_x:H films is not limited by the Si-H and N-H bonds; it is much wider.

For the problem under discussion, of interest, in particular, is the capability of some fraction of atoms of nitrogen bound to silicon to change their valence. This takes place due to the contribution of two unpaired p-electrons to the creation of new valent bonds [8,9]. It is clear that, to do this, some additional structural defects in the network are required when the N atom is not situated at the vertex of a usual SiN_4 tetrahedron. This defect is interesting from the viewpoint of the creation of extra bonds.

During the synthesis, the PE CVD polysilicon layers are known to trap a greate number of protons migrating in the film during thermal treatment [10]. During annealing of the PE CVD films at 200-300^{o}C, our experiments have revealed an increasing amount of bound hydrogen in the Si-H, O-H and, less reliably, N-H bonds (the absorption peak of the N-H bonds is at a wide absorption band of the hydroxyl bonds) bound to the network in various forms. This is followed by a decrease of the refractive index , a certain increase in σ and an insignificant film shrinkage (Fig.5). A comparison of all the data obtained allows us to conclude that it is apparent that we observe a capture of mobile protons into the vacant Si, N and O bonds arising during the synthesis. It is known that for CVD SiO_2 layers thermal treatment at temperatures higher than 300-400^{o}C leads to the elimination of the O-H groups [11] and to the formation of a greate deal of broken bonds in the film network. This also occurs in the PE CVD SiN_x:H films at 400-600^{o}C and is detected with respect to a reduction in the IR absorption intensity within 3200-3800 cm^{-1}. It is worth noting that this is the temperature

interval wherein dehydrogenation substantially accelerates (Fig.2), and hence we may relate the formation of vacant bonds upon release of O-H bonds to more intense dissociation of Si-H and N-H defects. Thus, the assumption that various defects in the film structure are involved in the process of dehydrogenation is corroborated.

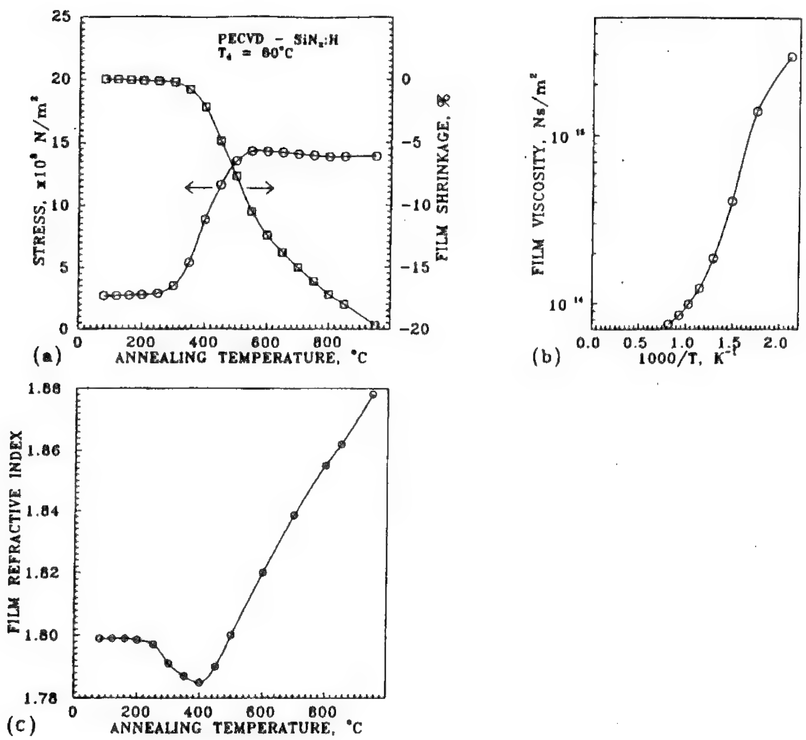

Fig.5. Effect of the annealing temperature on shrinkage and stress (a), viscosity (b) and refractive index (c) of the PE CVD film (T_d=80°C) subjected to isochronal treatments for 1 h.

CONCLUSION

Analysis of the dissociation of Si-H and N-H bonds in SiN_x:H films has shown that dehydrogenation is impossible to treat as a simple act of hydrogen elimination, without taking into account its interaction with atomic surroundings in the network. That is why the dissociation the reaction of these defects cannot be described by first-order kinetics.

Analysis of the process that takes place in the atomic network after both hydrogen release and the creation of ruptured bonds on Si and N atoms has been found to be an essential addition to the dehydrogenation. In particular, there are the changes in the electronegativeness of a Si atom and the dimensions of the elementary SiN_4 tetrahedron being a major structural union of silicon nitride.

Account should be taken of the fact that the broken bonds between Si and N annihilate upon their interaction. In turn that makes it necessary to consider various forms of mobility of structural units and related relaxation processes of the atomic network as well as to consider the material viscosity.

Viscosity variation in thermally or mechanically treated films, which is associated with a migration of vacancies in glass, is directly due, as experiments indicate, to their creation, transfer, interaction with the other network defects, and disappearance on Si and N atoms after hydrogen release. To determine the material viscosity is, therefore, an important problem whose solution could give a better insight into the nature of molecular mobility, structure and interatomic interaction in the SiN_x:H network. The paper has reported dynamic viscosity calculations for different SiN_x:H films, depending on annealing temperature and time. It should be noted that only an appropriate combination of various methods can enable us to get data on the viscosity of amorphous glassy films and on its relation to structural changes in the material. The most efficient is a complex thermal defectometry technique including ellipsometry, X-ray diffractometry and IR spectroscopy coupled with thermal treatments. As has been shown in the paper, this technique makes it possible to obtain fairly detailed information on the chemical and structural parameters of the films.

References

[1] T.P.Smirnova, V.I.Belyi and L.V. Chramova, Thin Solid Films, **74**, 287 (1980).
[2] H.J.Stein and H.A.R.Wegener, J.Electrochem. Soc. **124**, 908 (1977).
[3] A.G.Noskov, E.B.Gorokhov, G.A.Sokolova, E.M.Trukhanov and S.I.Stenin, Thin Solid Films, **162**, 129 (1988).
[4] O.I.Semenova, E.B.Gorokhov, A.G.Noskov, M.G.Sudnichenko and L.I.Rabinovich, Poverkhnost, **10-11**, 102 (1992). In Russian.
[5] G.Lucovsky, J.Vac. Sci. and Technol., **16**, 1225 (1975).
[6] R.L.Myuller, Zhurnal Prikladnoy Khimii, **28**, 363 (1955).
[7] G.M.Bartenev and D.S.Sanditov, Relaxation processes in glass-like systems.- Novosibirsk, Nauka, 1968. In Russian.
[8] C.T.Kirk, J.Appl.Phys.**50**, 4190 (1979).
[9] V.A.Nadolinny, V.V.Vasilyev and I.P.Mikhailovskii, Phys.St. Sol. A **116**,K105 (1989).
[10] S.J.Pearton, J.W.Corbett and T.S.Shi, Appl. Phys. A **43**, 153 (1987).
[11] A.Shintani, S.Sugaki and H.Nakashimi, J. Appl. Phys. **51**, 4197 (1980).

Materials Science Forum Vols. 185-188 (1995) pp. 129-142

Stress generation and relaxation in passivating films and its new application in nanolitography

E.B. Gorokhov, A.G. Noskov and V.Ya. Prinz

Institute of Semiconductor Physics, pr.Lavrenteva, 13, Novosibirsk 630090, Russia

Keywords: CVD and PECVD glassy films, controllable shrinkage, viscosity, crack formation, self-aligned nanolitographic mask

Abstract. Stress generation and relaxation processes in vitreous films grown by CVD on semiconductor substrates have been studied. Based on the results obtained, a new class of lithographic masks has been introduced, which gives a possibility of controllable and precize changing of the window sizes in masks. The change of pattern sizes can be achieved by successive shrinkage of the masking film upon its annealing and slipping on the viscous interlayer along the substrate. The proposed masks open up possibilities for the production of device elements with super-low sizes (<1 nm) not achievable yet by any know technological process. Potentialities of the technique have been demonstrated by fabrication a narrow (≈10 nm) starting window in the masks via controllable formation of crack with atomically sharp edges.

Introduction

Amorphous $SiO_x(OH)$, $SiN_x(H)$ films produced by chemical vapor deposition (CVD) or plasma-enhanced CVD (PE CVD) are widely used as passivating coatings for semiconductor devices [1]. These films are known to contain a substantial amount of hydrogen (10-20%) bound to silicon, nitrogen, or oxygen atoms [2,3]. Various physical, chemical and mechanical properties of the films are determined by the presence of chemically bonded hydrogen [2-5].

A definite relationship between variations of H and OH concentrations and those of the film volume, internal stress, and viscosity have been found when analyzing the results of comprehensive studies of $SiO_x(OH)$, $SiN_x(H)$ films grown and annealed under different conditions [2,5-8].

Some quantitative data on the values of film internal stress, shrinkage and viscosity dependent on the growth and annealing temperatures are reported. These data are of interest for practical purposes of semiconductor structure technology.

A considerable attention is given to the proposed application of controllable changing of both the film volume and internal stress permitting the production of new class of lithographic masks with controllable and self-aligned lithographic patterns for fabrication of nanoelements of electronic devices.

Controllable generation of stress in passivating films

Both dehydration and dehydrogenation of CVD and PE CVD $SiO_x(OH)$ and $SiN_x(H)$ films result in their shrinkage [5-8]. Fig.1 examplifies variation of the atomic structure of $SiO_x(OH)$, $SiN_x(H)$ films stimulated by H_2O, H_2 release which causes V_1 to V_2 decrease of the film volume. This shrinkage of the film, strictly bounded with the substrate, leads, in its turn, to the increase of internal stress in the structures [6,7]. This stress can be determined by measuring the heterostructure curvature radius with a double-crystal X-ray spectrometer.

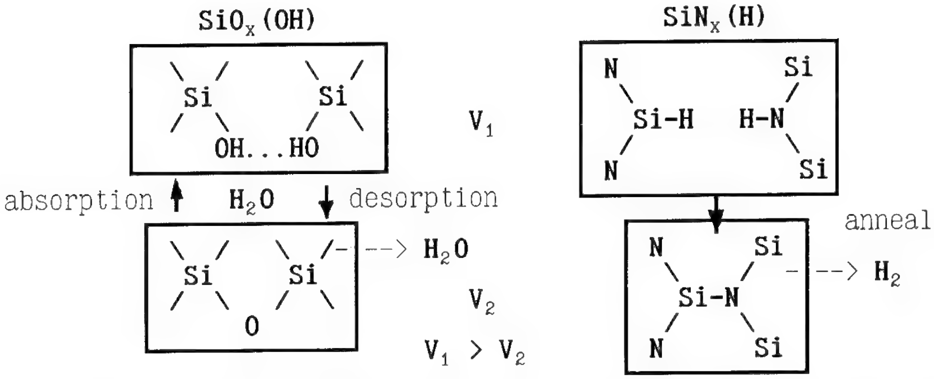

Fig.1. Variations of volume (from V_1 to V_2) of $SiO_x(OH)$ and $SiN_x(H)$ films due to structural rearrangemment.

The shrinkage of the films is determined by their defect structure, which, in its turn depends well on the deposition conditions.

Increasing of deposition temperature (T_d) at a constant growth rate of CVD $SiN_x(H)$ films (Fig.2) promotes the increase of the adsorbed radicals migration length on the surface (and, hence, the probability to occupy a more favorable site) and more rapid rupture of Si-H and N-H bonds. As a result the number of the strained Si-N bonds and various defects like Si-H and N-H ones in the film bulk, and, consequenly, the value of internal stress decreases.

The opposite is observed for $SiN_x(H)$ films grown by PE CVD at 50-120 C (Fig.3). It seemed that T_d remains an important factor for Si-H and N-H bonds rupture on the surface and in the bulk of film, but affects only slightly the surface migration of the radicals.

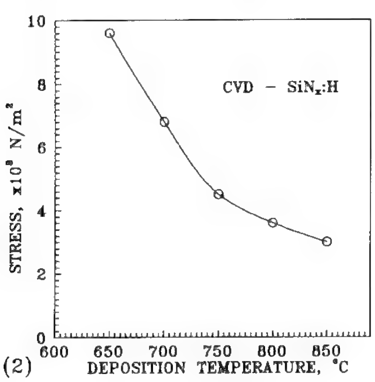

(2)

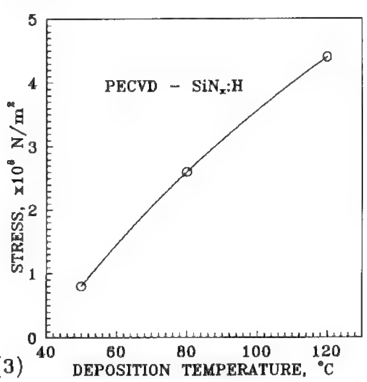

(3)

Fig.2 and 3. Dependence of internal stress on T_d in $SiN_x(H)$ layer grown on Si substrate (SiH_4+NH_3). (2) - CVD film;.(3) - PE CVD film.

The effect of power density of HF discharge on film stress is shown in fig.4 [8]. These data are consistent with those obtained for both $SiO_x(OH)$ and $SiN_x(H)$ films implanted with Ar^+,B^+,P^+ and some other high-energy ions. The latter indicate that the tensile stress drops sharply and then changes its sign at higher implantation doses (Fig.5a). Subsequent annealing leads to reconstruction of broken bonds in the lattice but in less strained configuration. Therefore, in order to achieve the initial value of stress a high-temperature treatment is needed to obtain the previous con-

centration of Si-H strained bonds by the destruction of additional Si-H and N-H complexes in the film (Fig.5b).

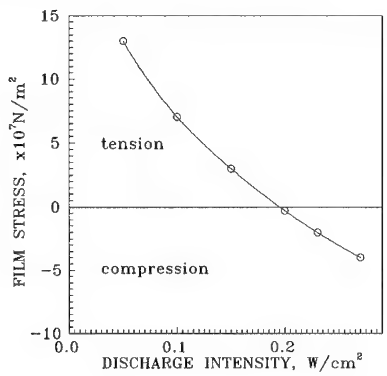

Fig.4. Dependence of stress in PE CVD SiN_x:H films on Si substrate on the power density of HF discharge. (SiH_4 + NH_3, T_d=160 C, f=136 MHz).

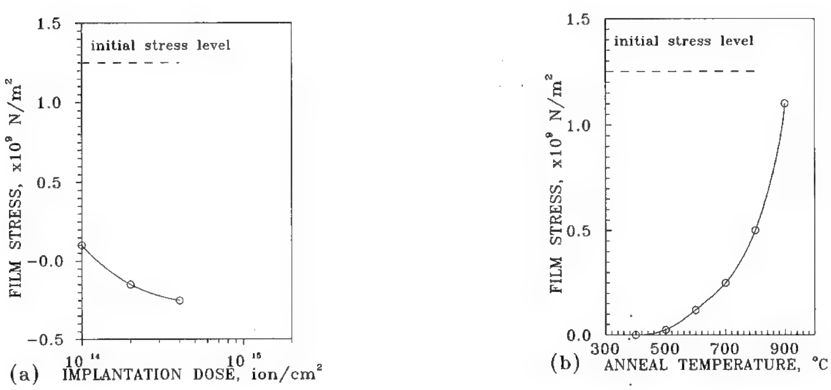

Fig.5. Effect of implantation on stress in CVD SiN_x(H) films grown on Si substrate (SiH_4 + NH_3, T_d = 700 C, h = 120 nm). (a) - dependence of σ on Ar implantation dose; accelerating voltage is 100 keV; (b) - recovery of stress after implantation in the course of isochronal annealing in films implanted with the dose of $2x10^{14}$ ion/cm^2.

There exist two possibilities of changing stress in as-grown SiO_x(OH) films: 1. Annealing and growth of tensile stress during the film shrinkage stimulated by water's desorption; 2. Expansion of the film volume due to adsorption of water from atmosphere with possible σ conversion from tensile to the compressing ones (Fig.6). Normally the duration of water absorption in CVD SiO_x(OH) films drops from 1 - 1.5 hours down to 5 - 20 minutes with the decreasing of deposition temperature.

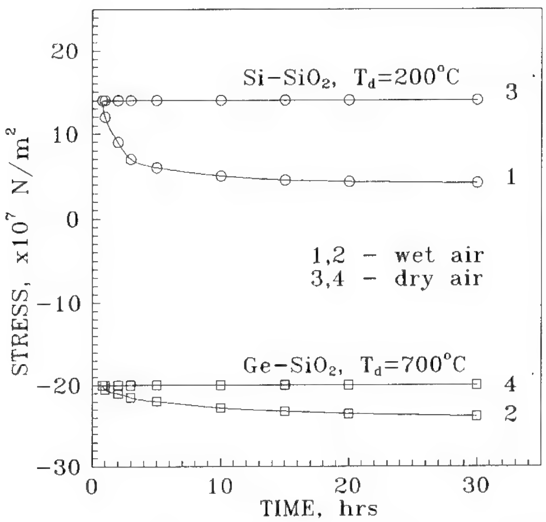

Fig.6. Variations of stress in CVD $SiO_x(OH)$ film due to water absorbtion at T = 20 C. Curves 1,3 - reaction SiH_4+O_2; curves 2,4 - pyrolysis TEOS.

Thus, in this part of the present work we have shown that it is possible to obtain 6 values ranging from positive to negative ones in $SiO_x(OH)$ and $SiN_x(H)$ films grown by CVD and PE CVD on various semiconductor substrates at relatively low T_d < 100-300 C. A rather wide range of the stress values under control is available: 0 to 1.5×10^9 and 0 to 1×10^9 N/m^2 for tensile and compressive stresses, respectively.

Formation of cracks.

Formation of cracks occurs at a certain critical thickness of the film. Experimental results indicate that the critical thickness of cracking depends on the synthesis conditions of CVD $SiN_x(H)$ $SiO_x(OH)$ films and lies in the 100-500 nm range. Formation of cracks is attributed, first of all, to the action of high values of tensile stress brought about by the volume shrinkage. Traditional concepts of the destruction mechanism are based on the following hypotheses presented by Griffith in his work [9]: 1) equilibrium propagation of fully opened crack is determined by the balance between the released mechanical energy of the elastically strained material and the energy of newly arizing surfaces; 2) such cracks start from the microcracks in the strained material. Mathematical formalism based on these assumption is a good tool for predictions and provides information as to the geometry of the critical crack, energetic or force criteria of brittle fracture, and mechanical stress distribution in the vicinity of the crack tip. Howerer, there arise difficulties concerned with description of physical processes proceeding in the very tip of crack, with the use of linear equations of elastic continuum, bringing about to singularities in the case under consideration. Firstly, the mechanism of the material cut with the propagating crack is essentially non-linear one. In the second, owing to small sizes of regions of ceramic materials wherein the non-linear processes proceed (<1 nm), it becomes necessary to take into account the discrete nature of the material when describing the fracture process.

Qualitatively new approach in revealing the nature of the brittle fracture of ceramic materials, to which both $SiO_x(OH)$ and $SiN_x(H)$ films can be assigned, was presented rather recently in [10,11]. These works, howerer, consider only bulk materials and, in the first place, siliceous glasses. The description of brittle fracture is found on the representation of crack as a narrow slit limited in the tip by nonlinear linking spring of the atomic sizes [10]. Propagation of such an atomically sharp crack occurs via successive ruptures of the bonds between atoms. Mathematical models based on this approach enable to establish a correlation between the atomic structure of glass and its stability in technical applications. This description has given impetus to understanding and prediction of the following important interaction phenomena in the crack tip: 1) chemical promotion of slowly growing cracks, 2) existance of viscous zones in the crack tip.

Our study of cracking in CVD $SiO_x(OH)$ and $SiN_x(H)$ films shows that the velocity of crack propagation is about 1 mm/s that is several orders lower than the sound velocity in the glass and, besides, depends on the gas environment of the sample. In particular, the crack propagation velocity in $SiN_x(H)$ layers grown on Si substrate was ≈ 10 times decreased when the crack passes a drop of vacuum oil on the film surface. Experiments in a vacuum chamber carried out on both Si-$SiN_x(H)$ and Ge-$SiN_x(H)$ samples at T = 20 C showed a strong dependence of crack propagation velocity on both the O_2 pressure and presence of water vapor. It follows herefrom that this cracking is not of brittle type and of the corrosion one. Furthermore, in the case of film systems one should take into

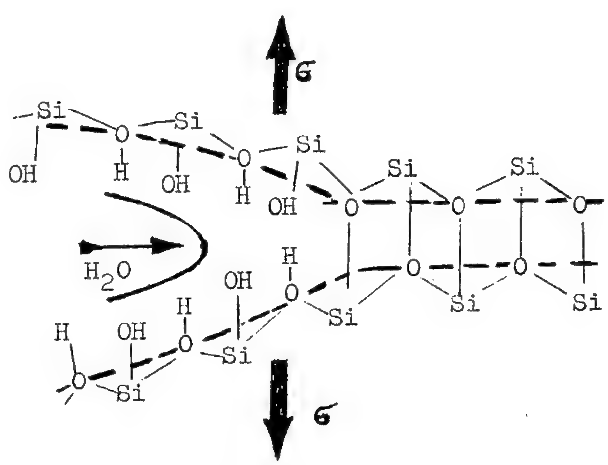

Fig.7. Crack tip, in which interaction of H_2O molecules with the strained Si-O bonds occurs, resulting in the formation of hydrated edges of the crack.

account also the role of the substrate, into which the crack can propagate, rather more chemically active with respect to water vapor or oxygen then $SiO_x(OH)$ and $SiN_x(H)$ (Fig.8). According to some data, to this point the orientation of cracks along the substrate crystallographic directions is related (Fig.8).

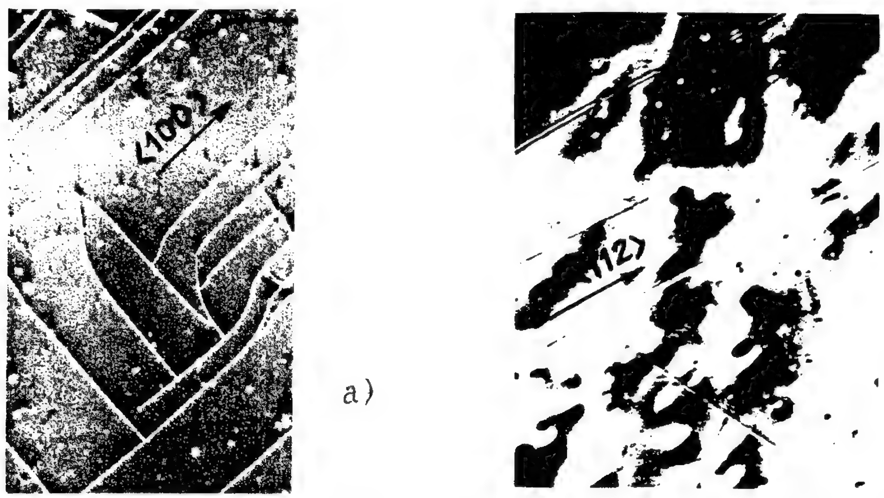

Fig. 8. Cystallogphic cracks in systems: (a) CVD SiN_x(H) film on (001) Si substrate; scanning electron micrograph of Si surface after the film removal; (b) CVD SiO_x(OH) film on CdHgTe substrate; optical micrpgraph of the film.

Indeed, the direction of crack propagation does not coincide, as a rule, with any main crystallographic direction being the characteristic one for physicomachanical and eletrophysical anisotropic parameters of semiconductors (Table). The direction of crystallographically oriented cracks on the substrate surface was found to coincide usually with the directions of projections of the anisotropic chemical oxidation vector in the near-surface regions of the semiconductor crystal.

Table. Effect of substrate orientation on the crack orientation.

Structure	Substr. orient.	(100)	(110)	(111)	(112)	(130)
SiN_x (H) SiH_4+NH_3; T_d=750° C; h_{cr}~300 nm	Crack orient.	<100>	<100> <551>	<112>	<113>	<100> <130>
SiO_x(OH) pyrol. TEOS T_d=680° C; h_{cr}~800 nm	Crack orient.	<100>	<100>	<112>	--	--

As a result, the cracks grow in the following way. The oxidant molecules penetrate toward the substrate through a pore in the strained film. A stress concentrator appears, which gives rise to local redistribution of tensile stress in the film so that the rupture of the film in the direction of higher oxidation becomes advantageous. When moving, the atomically clear surface of substrate is being opened in the crack tip and undergoes oxidation in the conditions of limited access of oxidant (see Fig. 7). A similar

mechanism operates in Si (111) - CaF_2 epitaxial system covered with PE CVD SiN_x:H film (h = 100 nm).

The cracks produce high shear stress in the substrate without giving rise to plastic deformations at low temperatures. At high temperatures (T_d and T_a) the crack edges generate dislocations in the substrate. A most drastic change of crack generation character is observed when the interlayer of a material possesing low viscosity and plasticity (i.e., Si-Al-SiO_x(OH), Ge-GeO_2-SiN_x(H), Si-GeO_2-SiN_x(H) and other systems) is introduced between the film and the substrate [12]. If the interlayer has the viscosity $\eta \approx 0$, the film should freely shrink. At the easily available ratio $l/h \approx 10^4 - 10^6$ (l and h are the length and h thickness of film, respectively) the interlayer with a very small η should prevent the film shrinkage. Thus, despite the fact that stress relaxation in systems "semiconductor - vitreous film" is as yet imperfectly investigated, qualitative understanding of its mechanism allows one in some cases to choose properly the synthesis regime and parameter of subsequent treatments of the film in order to obtain a desirable result of the relaxation process.

Viscous flow.

The characteristic time of the brittle fracture of solid body and that of the viscous flow differ considerably from one another thus giving the possibility to realize the conditions when only one process proceeds. If the duration of the tensile stress rise is large, the viscous flow process can proceed in heterostructures with films under study.

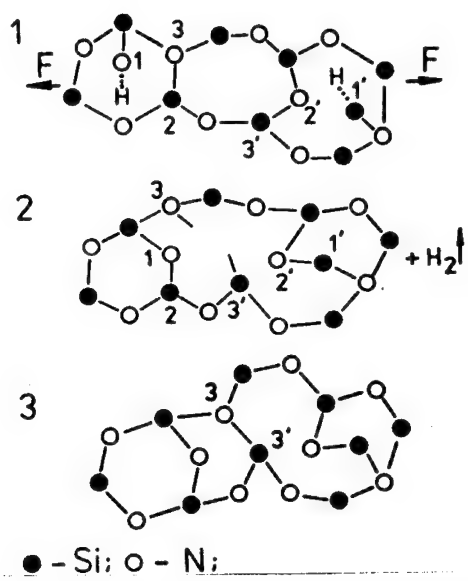

Fig. 9. Scheme of elementary atomical processes proceeding during the viscous flow of SiN_x(H) films under dehydration.
1. Initial stage; 2. Formation of vacant bonds at Si^1 and N^1 atoms after dissociation of corresponding Si^1-H and N^1-H groups and vacancy motion via cross-linking of the atomic bonds (from atoms Si^1 and N^1 towards Si^3 and N^3 ones);
3. Interlinking of vacant bonds of Si^3 and N^3 atoms with the formation of a new Si^3-N^3 bond.

The viscous flow was experimentally found in CVD SiN_x:H films, with structural scheme (Fig9) being proposed and description given in terms of Maxwell's model of viscoelastic body [7]. It is shown that for CVD SiO_x(OH) films the onset temperature of the viscous flow lies within the range 550 to 600 C, while the viscous flow in thermally-grown SiO_2 is normally observed at ≈ 900C [6]. According to theory of Muller [13], the viscosity of glasses and, hence, of vitreous layers of SiO_x(OH), GeO_2, SiN_x(H), etc., is determined by the appearance of dangling bonds in the lattice, which migrate via permanent switching from one atom to another. Simultaniously the most highly strained atomic bridges dissapear (Fig.9) and new ones, less strained, are generated. The more such broken bonds exist in the film, the lower is its viscosity and faster and easier are its structure changes. In the other words, the viscosity of film is in direct proportion with the defect content of the material lattice.

Fig.10 shows the results of an experimental study of heat-treated SiO_x:OH and SiN_x:H films. It is seen that as the annealing temperature rises, the films become more densificated due to structural rearrangements, which result in a decrease of film thickness and etching rate. Though the shrinkage of the film volume is continued at temperatures above 500 C and has to result in further increasing of the internal stress, in reality a sharp decrease of

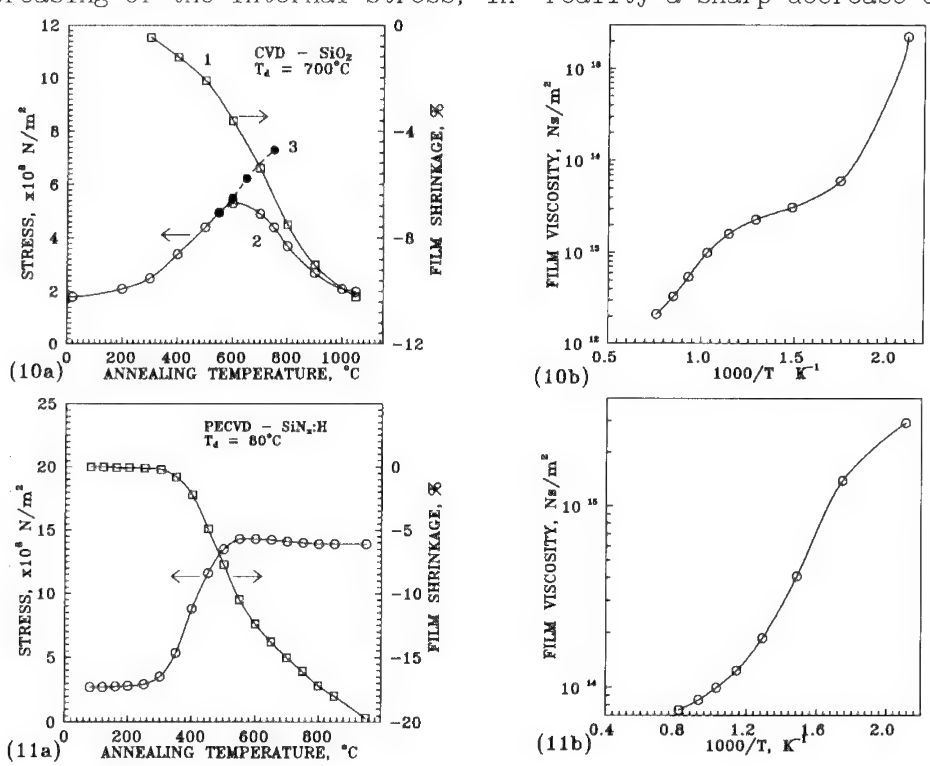

Fig.10 and 11. Effect of the T_a on shrinkage, stress, and viscosity of film: (10) CVD SiO_x:OH (pyrolysis TEOS) and (11) SiN_x:H. (10a) curve 1-film shrinkage; curve 2-films kept in the air after synthesis; curve 3 -films kept and annealed in vacuum (b) _ mean values of viscosity calculated from the data of figs.10a and 11a.

the latter is observed (for SiO_x:OH). It points out to drastic change in mechanical properties of the films within a narrow temperature interval 550 < T < 600 C with the onset of viscous flow.

Due to their porosity just after synthesis CVD SiO_x(OH) films absorb the water molecules from the air. The bonds with different binding energy are being produced between these molecules and the film lattice. During annealing H_2O molecules and OH-groups escape, the vacant sites being remained in the SiO_x(OH) lattice instead. When moving, they also break the atomic bonds, the viscosity decreasing. So, the shrinkage begins and viscous flow originates (Fig.10). In the absence of the condensed moisture (when the synthesized and annealed films are kept in a vacuum), the viscous processes in the films proceed at higher stress as compared with the films having been kept in the air (Fig.10a, curve 2).

Our investigations show that shrinkage of CVD and PE CVD SiN_x:H films (Fig.10) occurs due to interaction of Si-H and N-H defects with each other with the production of Si-N and Si-Si bonds after hydrogen's going away. The onset temperature of the reaction depends on the mean separation between these defects in the lattice and can be lowered down to 350-400 C at concentrations of defects of $\sim 10^{21}$ at/cm^3. The higher Ta, the more Si-H and N-H-groups react forming Si- and N- dangling bonds responsible for the viscosity decrease (Fig.10d). Further, these dangling bonds interlink with the formation of Si-N and Si-Si bonds, the concentrations of Si-H and N-H groups being decreased. The rate of the reaction and, hence, the generation rate of new vacant Si- and N-bonds drops. As a result, the viscosity of the film increase.

Arising the annealing temperature stimulates the release of the absorbed water more strongly bound with structure of SiO_x(OH) film and rupture of Si-H and N-H rest bonds in SiN_x:H layers with releasing of the H_2. It results in a new initiation of the viscous flow with subsequent transition of the film parameters to steady constant values. The degree of film restructuring depends on the generation level of dangling atomic bonds and their mobility.

Application of stress generation and relaxation phenomena in vitreous films for fabrication of nanolithographic masks.

Realization of recent physical concepts in devices of nanometer size range requires further progress in technology of lithographic masks and nanometer elements. The necessity of development of new technological methods stems from the fact that when approaching the nanometer sizes the available methods of electron and ion lithography have faced with some limitations. Among them are insufficient focusing and scattering of electron and ion beams, effect of reflection from the substrate, and diffraction phenomena. Low accuracy of mask-to-wafer alignment (~100 nm) is a most important one, which requires alternative methods of nanotechnology employing the self≠alignment technique.

Both SiO_x(OH) and SiN_x(H) films are frequently used for the protection of semiconductor surface under various tech- nological treatments such as etching, ion implantation, evaporation (spattering) or epitaxial growth in deliberately opened windows. Potentialities of the controllable changing of the film volume, in- ternal stress in films, viscosity and crack formation allow to propose new class of lithographic masks.

Let us consider a simpliest one involving the main (SiO_x(OH) or SiN_x:H) layer and an additional one with the reduced viscosity(for example, GeO_2), located between the main layer and the substrate.

Let the mask contain a pattern produced by means of conventional lithography, that opens the substrate surface (Fig.12). This mask possesses a specific feature which consists in the following. A possibility of controllable decreasing or increasing of the pattern size exist based, for example, on shrinkage of film upon its anneal and slipping on the viscous interlayer along the substrate, or on the volume expansion of masking areas causing by water absorption.

The possibility of controllable changing of the window size in mask by ΔL enables one to obtain a device element with the size value of ΔL by using self-alignment technique.

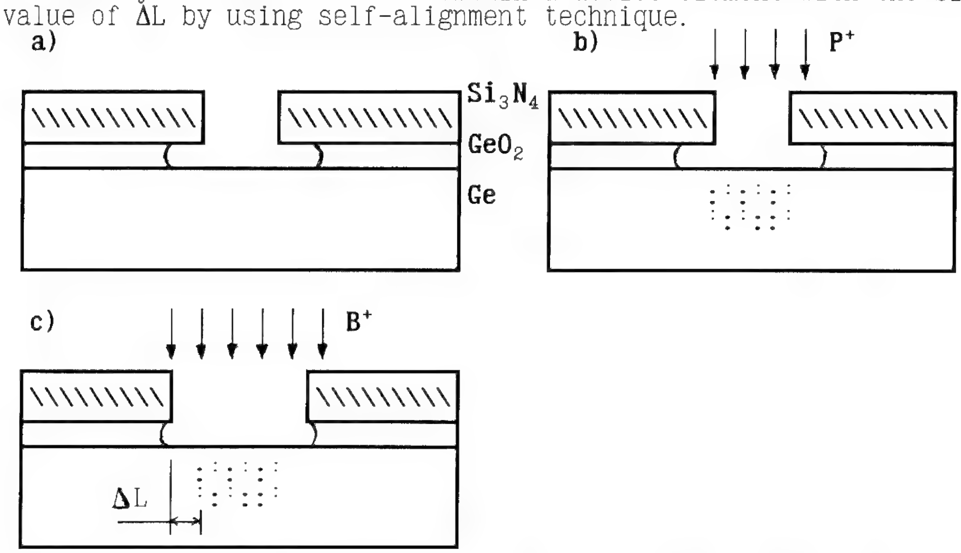

Fig.12. Scheme illustrating application of double-layer masks for the formation of a device element. (1) Opening a window in the Si_3N_4 layer; (2) Removing the GeO_2 layer and performing the first ion implantation; (3) Shrinkage of film causing the change of window width by L, and performing the 2-nd ion implantation.

With the proper choice of the conditions of synthesis and thermal treatment the edge of a 1 micrometer long masking area can be shifted by 0.1 to 250 nm. Successive external action on the top layer of mask giving rise to step-by-step sub- and nanometer shifting of its edges permits repeated employment of the mask when fabricating elements of solid-state devices.

Potentialities of masks with the size control can be unveiled completely when invoking the concept of controllable cracking. As investigations show, it is possible to choose the conditions of brittle fracture at a certain place on the film, at which the crack width does not exceed several nanometers, the appearing cracks having atomically sharp edges. It opens a unique possibility to produce the device elements of extremely small sizes.

Let us consider the above-described double-layer masking film, in which 50-150 micrometers wide strips are photolithographically etched out as shown in Fig.13. In the areas where the formation of narrow holes - slits is to be performed, special recesses are made in the strips. The recesses distort the stress field of the strips thus playing the role of stress concentrators. As a consequence the strip appears to be perforated and its ruptures at the stress rising should arise during annealing at narrow places.

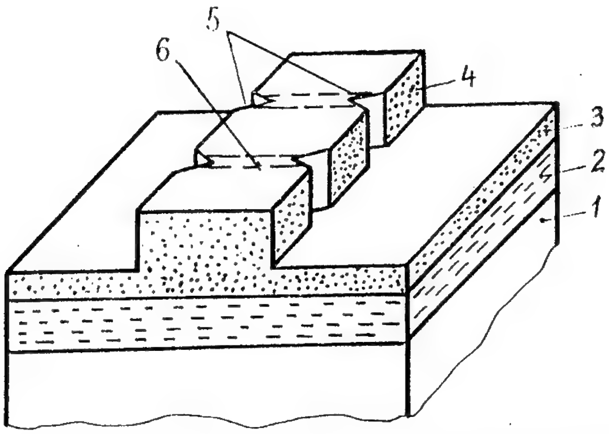

Fig. 13. Scheme of production of self-forming narrow windows in a double-layer mask with the use of controllable cracking. 1-substrate; 2-viscous interlayer; 3,4-main masking layer; 5-stress concentrators; 6-cracks.

Investigations of the controllable cracking were initiated on the single and double layer structures. A positive result has been obtained. The crack width was within the 0.15-0.3 micrometer range (Fig. 14).

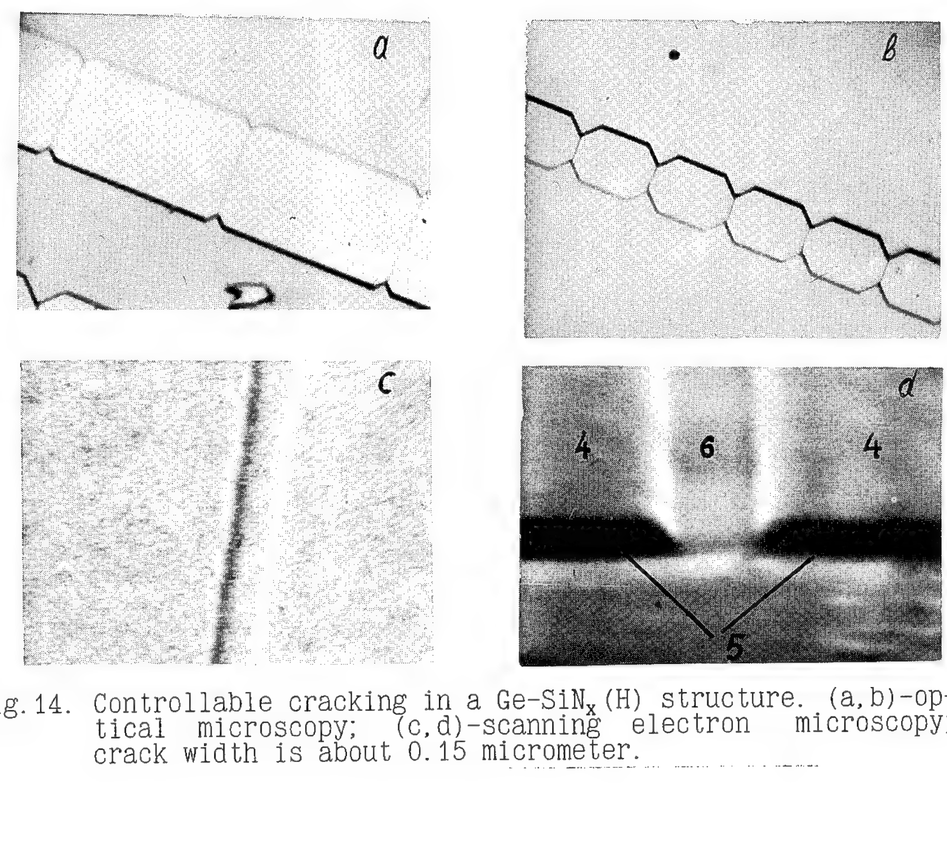

Fig. 14. Controllable cracking in a Ge-SiN_x(H) structure. (a,b)-optical microscopy; (c,d)-scanning electron microscopy; crack width is about 0.15 micrometer.

Maximum displacement of the crack edges amounted 1mm, which is illustrated fig.15.

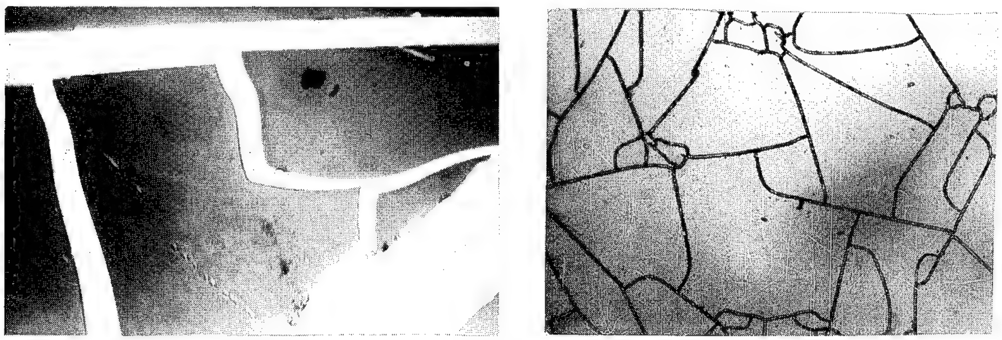

в a

Fig.15. The formation of non-oriented cracks in the double-layer masking film with a low-viscous interlayer. (a) Ge-GeO_2-SiN_x(H); (b) Si substrate; Conformal change of the island sizes due to the displacement of crack edges at 20 C.

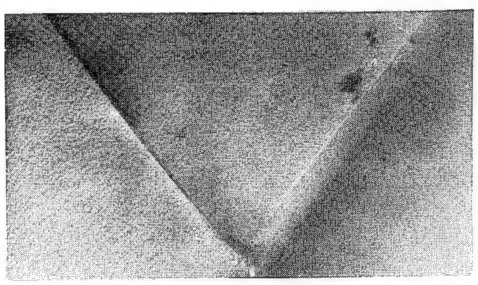

Fig.16. Transmission electron micrograph of a crack in Si-SiN_x(H) system. Crack width ≈ 10 nm.

Analysis of the advantages of the above method shows that: 1.The crack width can be brought to several nanometers (Fig.16); the critical thickness of cracking amounts to 15 to 100 nm within the T_d range from 200 to 800 C. 2. Extremely sharp edges of cracks can be obtained with the roughness at monoatomic level being not available by any other means. 3. Methods of both the film formation and stress concentrator production are simple enough and rather technological. Concentrators of б formed by means of ordinary photolithographic and chemical techniques permit the production of complicated patterns of cracks and holes in the mask. 4. The masks employed for the crack production are re-usable and permit fabrication of a number of self-aligned device elements with controllable displacement of mask edges. 5. After fabrication of device elements the whole mask or its separate regions can serve as passivating coatings.

References

[1] W.Kern, Semiconductor International, **8**, 121 (1985).
[2] A.Shintani, S.Sugaki, H.Nakashima, J.Appl.Phys.**51**,4197(1980).
[3] T.P.Smirnova, V.I.Belyi, and L.V.Chramova, Thin Solid Films, **74**, 287 (1980).
[4] W.J.Kapoor, R.S.Bailey, and H.J.Stein, J.Vac.Sci.Technol. A**1**, 600 (1983).
[5] W.A.P.Claassen, W.G.J.N.Valkenburg, M.F.C.Willemsen, and W.M.Wijgert, J.Electrochem.Soc. **132**, 893 (1985).
[6] E.B.Gorokhov, A.G.Noskov, G.A.Sokolova, S.I.Stenin, and E.M.Trukhanov, Poverkhnost, **12**, 25 (1982). In Russian.
[7] A.G.Noskov, E.B.Gorokhov, G.A.Sokolova, E.M.Trukhanov, and S.I.Stenin, Thin Solid Films, **162**, 129 (1988).
[8] O.I.Semenova, E.B.Gorokhov, A.G.Noskov, M.G.Sudnichenko, and L.I.Rabinovich, Poverkhnost, **10-11**, 102 (1992). In Russian.
[9] A.A.Griffith, Phil.Trans.Roy.Soc. **221**, 163 (1920).
[10] B.R.Lawn, J.Am.Cer.Soc. **66**, 83 (1983).
[11] T.A.Michalske, and S.W.Freiman, Nature, **295**, 511 (1982).
[12] E.B.Gorokhov, I.G.Kosulina, S.V.Pokrovskaya, and I.G.Neizvestny, Phys.Stat.Sol. **101**, 451 (1987).
[13] R.L.Muller, in book: Vitreous state, 60 (1960). In Russian.

Compound Semiconductors

Materials Science Forum Vols. 185-188 (1995) pp. 145-154

High resolution surface characterisation using STM light emission techniques

J. Horn[1], N. Marx[1], B.L. Weiss[1,3], H.L. Hartnagel[1], M. Stehle[2,4], M. Bischoff[2] and H. Pagnia[2]

[1] Institut für Hochfrequenztechnik, TH Darmstadt, Merckstr. 25, D-64283 Darmstadt, Germany

[2] Institut für Angewandte Physik, TH Darmstadt, Schlossgartenstr. 7, D-64289 Darmstadt, Germany

[3] Permanent address: Department of Electronic and Electrical Engineering, University of Surrey, Guildford, Surrey GU2 5XH, UK

[4] Present address: Institut für Festkörper und Werkstofforschung Dresden, PO Box, D-01171 Dresden, Germany

Keywords: Scanning tunneling microscopy, luminescence, semiconductor, GaAs

Abstract

In this paper we discuss the simultaneous measurement of integral photon intensity maps (using all emitted photons) and conventional scanning tunneling microscope (STM) topographs of GaAs surfaces. Furthermore we present first results of time-resolved photon emission using STM excitation for the measurement of the minority carrier lifetime in the active layer of a specially tailored GaAs sample. This technique was also used to demonstrate the strong influence of surface recombination processes on STM stimulated light emission. STM induced wavelength-resolved luminescence spectra of GaAs (100) surfaces, which reveal near-bandgap recombination processes, are also reported here.

I. Introduction

Since its development 1982 by Binnig and Rohrer [1], the scanning tunneling microscope (STM) and related scanning probe techniques have become important tools for high-resolution studies of surface and subsurface properties. In 1988, Gimzewski et al. reported the first experimental observation of photon emission from nanometer areas stimulated by an STM [2]. They demonstrated the possibility of local luminescence studies with an STM, allowing many experimental parameters to be varied. The subsequent studies concentrated mainly on light emission from thin metal films, where the photons result from the decay of surface plasmons. So far only a few publications have discussed STM stimulated luminescence (STL) from semiconductors, which is the topic of this paper. The main point of interest is the use of STL for the characterization of nanoscale devices, since the ongoing miniaturisation towards mesoscopic structures requires a spatial resolution which exceeds that of photoluminescence (PL) and even cathodoluminescence (CL) techniques. The much higher resolution of the STL method results from the fact that the extremely narrow electron beam produced by the tip, in combination with the low electron energy, means that the tunneling electrons penetrate, and thus analyse, only a very small volume of the sample. Assuming that the diffusion length of the injected carriers is not too large, this leads to an extremely high spatial resolution in the nm range.

The first STL measurements of semiconductors were obtained by Gimzewski et al. [2], who measured the emission of ultraviolet photons from Si (111)7x7 surfaces.

Abraham et al. [3] obtained luminescence from the interface region of cleaved (110) GaAs/AlGaAs heterostructures with nanometer resolution. This work was extended by Alvarado et al. [4], who were able to determine the conduction band energy of bulk material and the band bending at the surface. They also presented a method to measure the diffusion length of injected minority carriers. Renaud and Alvarado [5] reported a new technique based on STM-induced luminescence that allows the conduction band edge discontinuity and the band-bending profile at the interface to be measured directly with nanometer resolution. The first spectrally resolved luminescence results were obtained by Berndt et al. [6] from a cleaved CdS (1120) surface. A more detailed analysis of the injection luminescence from CdS (1120) surfaces is given in [7]. Montelius et al. [8] measured luminescence spectra from p-type InP (110) at low temperatures. The strong local character of these spectra was demonstrated by measurements at two different sample positions, which were only 10 nm apart. Near bandgap recombination was observed at both positions, whereas an acceptor-related emission was only found at one position. Recently, Samuelson et al. [9] reported on experiments using a large bandgap degenerately doped semiconductor (GaP) tip, which is very interesting as it enables carriers of a well defined energy to be injected into the sample. In experiments with a GaAs/AlGaAs sample containing both quantum wells and quantum wires, they were able to excite luminescence and spectrally as well as spatially resolve the signals from the quantum well and the quantum wire. In addition Wenderoth et al. [10] have reported light emission from Au passivated surfaces. Also, luminescence maps of technological relevant GaAs (100) surfaces after different surface treatments have been reported by Horn et al. [11,12].

The outline of this paper is as follows: in section II some theoretical aspects of STM induced luminescence (STL) from semiconductors are briefly discussed. In section III we present a photon map and the corresponding topography image of a GaAs (100) surface. In sections IV and V we discuss the results obtained from both time-resolved and wavelength-resolved injection luminescence, respectively and section VI contains the conclusions.

II. Theory

In STL experiments on semiconductors, two different mechanisms can lead to light emission. They are firstly the injection of minority carriers from the tip into the semiconductor, where they diffuse and recombine radiatively, and secondly impact ionisation, where the STM is operated in the field emission regime and hot electrons create electron-hole pairs. This mode is very similar to ordinary CL and the main difference is that in CL the energy of the injected electrons is ~keV whereas for STL it is ~eV.

In the following, we assume the case of minority carrier injection, since we use this mode for the acquisition of photon maps. For a p-type semiconductor, electrons from the tip tunnel into the conduction band of the sample and recombine with holes from the valence band. In the case of GaAs, the bands bend downwards at the surface due to the Fermi level pinning, resulting in a depletion region of width L_D. With a negative voltage V_t applied to the tip, tunneling is possible when $eV_t > E_C-\beta$, where E_C is the conduction band edge energy and β is the amount of band bending. Luminescence can be obtained for $eV_t > E_C$, since only in that case do the injected electrons have enough energy to cross the depletion region and enter the bulk material [5]. This enables one to determine E_C by measuring the onset of luminescence as a function of the applied voltage. However for the study of n-type semiconductor samples, electrons from the valence band of the semiconductor tunnel into free states of the metal tip, leaving holes which radiatively recombine with electrons from the conduction band.

As has been explained above, luminescence usually results from injected minority carriers and therefore it is interesting to determine the magnitude of this component of the tunneling current. The starting point is the well-known Schottky-type metal-semiconductor contact, which is similar to the tip-semiconductor region in the STM except that in the STM the tip and the semiconductor surface are separated by the tunnel gap. Current versus voltage (I/V) curves obtained with the STM exhibit the typical diode behaviour [13]. The influence of a thin insulating layer between the metal and the semiconductor surface in planar Schottky-contacts has already been investigated by Card and Rhoderick [14] and it is useful to see if their theory can be used to describe the characteristics of the tip-sample system.

For a planar forward biased ($eV > 3k_BT$) Schottky-contact with a thin insulating layer of thickness δ on a n-doped semiconductor, the majority current is usually described by :

$$I_n = FA_n^* T^2 \exp\left(-\frac{4\pi}{h}\sqrt{2m_n^*\chi_n}\,\delta\right)\exp\left(-\frac{e\Phi_{B0}}{k_BT}\right)\exp\left(\frac{eV}{nk_BT}\right) \tag{1}$$

where F is the contact area, A_n^* is the Richardson constant, χ_n is the average tunnel barrier height, m_n^* is the electron effective mass, T is the sample temperature, Φ_{B0} is the Schottky barrier height at zero bias, V is the applied voltage and n is the ideality factor. The minority carrier current in ideal metal-semiconductor contacts can be neglected, since nearly all states in the metal with an energy close to the valence band (VB) edge of the semiconductor are filled. An insulating layer presents the possibility of shifting the metal and semiconductor energy bands with respect to each other since a part of the applied voltage is dropped across the insulating layer. Thus, for a high enough voltage, valence electrons can tunnel from the semiconductor into free states of the metal tip. This mechanism can also be described as an injection of holes into the semiconductor. With the assumption that $V > \xi_p$, Card and Rhoderick [14] have shown that this minority current is given by :

$$I_p = F\frac{e^2A_p^*}{2k_B^2}\exp\left(-\frac{4\pi}{h}\sqrt{2m_p^*\chi_p}\,\delta\right)(V-\xi_p)^2 \tag{2}$$

where A_p^* is the effective Richardson constant for holes, m_p^* is the hole effective mass, χ_p is the average barrier height for tunneling holes and ξ_p is the energy difference between the semiconductor Fermi level and the VB edge in the absence of band bending. Equation (2) shows, that for an n-type semiconductor the minority carrier current is a quadratic function of the applied voltage. The minority carrier injection ratio, which is defined as $\gamma = I_p/I_p + I_n$, is obtained by combining equations (1) and (2).

The integral luminescence intensity I_L, which is proportional to the excess minority carrier concentration $\Delta\rho$, the majority carrier concentration N and the material constant B, is given by :

$$I_L \propto BN\Delta\rho \tag{3}$$

and combining equations (2) and (3) shows that the luminescence intensity is a quadratic function of the applied voltage V.

III. Photon Maps

In our experimental setup, a Beetle-type STM is operated in a high vacuum chamber. The tip sample region is placed at one focus of an ellipsoidal mirror and the photomultiplier is mounted with its photocathode at the second focus. The solid angle of detected light is about 3.5 sr.

The photomultiplier tube (Hamamatsu 943-02), which is sensitive up to wavelengths of ~ 880nm, has a dark count rate of 10 cps at T = 253 K and a detection efficiency for 1.43 eV photons of ~1%. The experiments are performed at a pressure of 10^{-5} mbar at room temperature.

The surface topography and the photon map of an n-type (N_D~$5x10^{18}$ cm^{-3}) GaAs (100) surface are shown in Figure 1. Both images have been acquired simultaneously, using the constant current mode with a tunneling current of 10 nA and a sample bias of -2.8 V. The topographic image shows three surface defects, from which the photon emission is strongly decreased, as can be seen in the photon map. The spatial resolution of these images is about 10 nm, which is several orders of magnitude better than can be achieved using PL or CL techniques. Similar results have also been obtained on InP (100) surfaces.

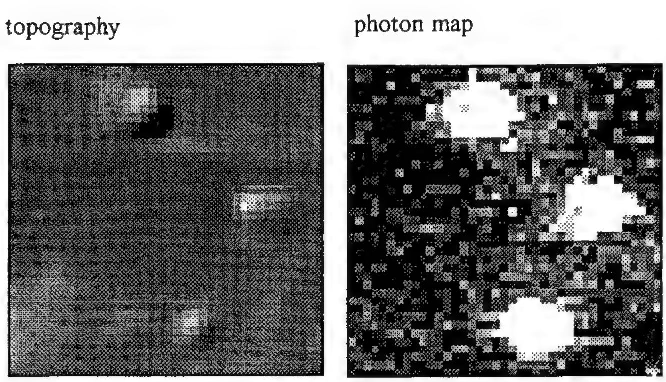

Fig. 1: STM surface topography and photon map of a GaAs (100) surface (n-type with N_D~$5x10^{18}$ cm^{-3}). Scan area: 320x320 nm^2. Tunnel current I_t=10nA, sample bias -2.8V. Regions with surface defects reveal a decreased luminescence intensity.

IV. Time-resolved Luminescence

In time-resolved luminescence experiments using the STM, the thermal equilibrium of minority carriers in a semiconductor is disturbed by carrier injection from the tip and equilibrium is restored by recombination processes. From the transient decay of luminescence, the "lifetime" of nonequilibrium minority carriers can be determined. This carrier lifetime is important as it determines the characteristics and performance limits of a variety of modern high-frequency electronic and optoelectronic devices, such as HBTs and laser diodes. Since these measurements use low energies, the material analysed is very near to the sample surface and therefore its properties are strongly influenced by the surface states. Thus this new technique may be used to evaluate the local surface state density.

The decay of the luminescence intensity $I_L(t)$ after pulse excitation can be described by :

$$I_L(t) = I_L(0) \exp(-t/\tau_{min}). \tag{4}$$

The minority carrier lifetime τ_{min} , which depends on the carrier lifetime in the bulk material τ_B and the lifetime due to nonradiative recombination processes τ_S, which includes surface recombination, is given by :

$$\frac{1}{\tau_{min}} = \frac{1}{\tau_B} + \frac{1}{\tau_S} \tag{5}$$

Therefore, from the transient decay of luminescence after pulse excitation one is able to derive detailed information about the dominant recombination mechanisms. The instrumentation used for the time-resolved measurements is shown schematically in figure 2. The output of a pulse generator is added to the constant tunnel bias V_T, which is chosen so that no light emission occurs, although stable tunneling is still possible. A trigger signal, which is synchronised with the voltage pulse, starts a voltage ramp in the time-to-pulse-height-converter (TPHC). When the first photon after the trigger signal is detected by the photomultiplier tube (PMT), the ramp stops. The stop signal is generated in the constant-fraction- discriminator (CFD), which ensures that the stop signal does not depend on the amplitude of the photomultiplier output signal. After each pulse the TPHC output voltage, which is proportional to the time difference between the pulse and the first detected photon, is fed into a multichannel analyzer (MCA), where the signal is digitized and the corresponding channel is incremented. The radiative recombination rate of the injected minority carriers is so low that the first detected photon is emitted at a random time after the excitation pulse. Thus, after a large number of photons have been detected, one is able to obtain the decay time of the luminescence intensity.

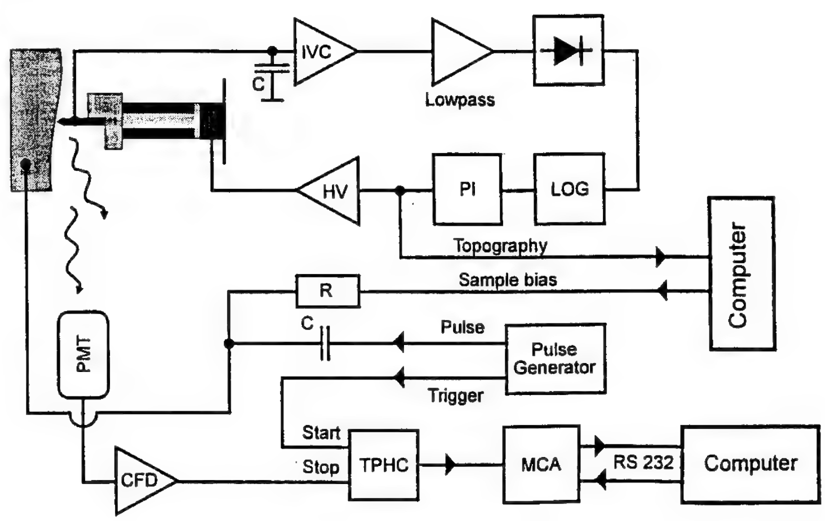

Fig.2: Experimental setup for STM stimulated time-resolved luminescence measurements.

In this study, the samples were cut from a wafer with an epitaxially grown n^+-n-n^--n^+ structure on a GaAs (100) substrate. We observed that the integral luminescence intensity of this wafer was about two orders of magnitude higher than that of highly doped (~$5x10^{18}$ cm^{-3}) bulk GaAs samples. An explanation of this behaviour is that the diffusion potential drives the injected holes towards the low doped region, which reduces the nonradiative surface recombination.

The assumption, that the emitted photons which originate from recombination in the low doped layer, as shown in figure 3, should lead to a high minority carrier lifetime. Figure 4 shows the measured decay of the time-resolved photon emission. During the voltage pulse, the luminescence remains almost constant. The initial peak results from nonideal characteristics of the voltage pulse and a nonideal transmission of the pulse from the generator to the STM tip. After the excitation pulse has finished the luminescence decays exponentially with a time constant τ_{min} of ~ 250 ns. This time constant can be used to estimate the doping concentration of the active layer. The minority carrier lifetime in the bulk material is given by :

$$\frac{1}{\tau_B} = B \cdot N \tag{6}$$

where N is the majority carrier concentration and B is a material constant. For GaAs the B is about $2*10^{-10}$ cm^3s^{-1}. If surface recombination and photon recycling processes [15] are neglected, these experiments show that the doping concentration of the active layer is ~$2*10^{16}$ cm^{-3}, which corresponds very well with the measured doping profile of the material used. This result also indicates that the assumption that the recombination takes place in the low doped region is valid here. We confirmed this interpretation by removing the highly doped top n^+-layer using etching, after which the emitted photon intensity was reduced by about two orders of magnitude. This shows that the n^+-layer is required to prevent the injected holes from undergoing nonradiative recombination near the sample surface.

Time-resolved photon emission measurements on GaAs bulk samples result in a sudden decrease of the luminescence after the voltage pulse has stopped. The time-constant of the decay is below 5 ns, as it is dominated by surface recombination, and could not be resolved accurately with the current instrumentation.

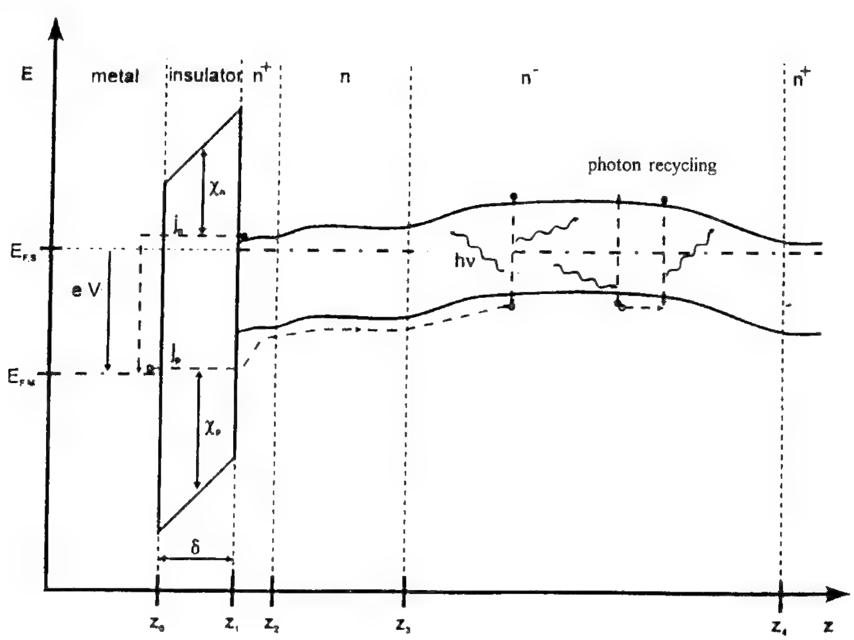

Fig. 3: The n^+-n-n^--n^+ GaAs doping profile provides a confinement of the injected holes in the low doped n^--region, where they can recombine with electrons from the conduction band.

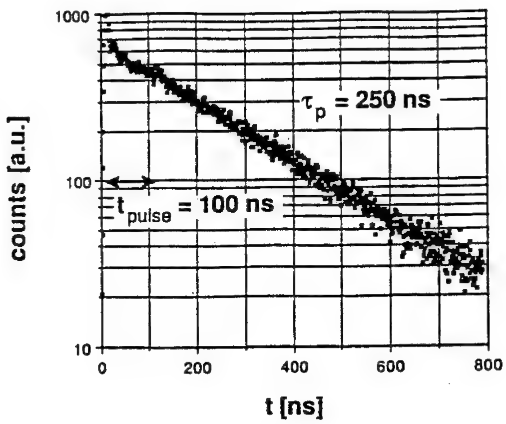

Fig. 4: Decay of luminescence after a pulse excitation. Sample bias -1.4 V, tunnel current 3 nA, voltage pulse -2.5 V, pulsewidth 100 ns, repetition rate 20 kHz.

V. Spectrally Resolved Luminescence

Spectrally resolved luminescence measurements give access to the transition energies, which are responsible for the observed luminescence. Very impressive results have been published already by Montelius et al. [8], who used large STM currents of up to 60 μA to obtain useful spectra from InP samples, and Samuelson et al. [9], who used lower currents of about 800 nA to obtain spectra from AlGaAs/GaAs samples containing both quantum wells and quantum wires. These large tip currents suggest that the lateral resolution, which they have demonstrated to be < 300 nm [9], can still be improved using significantly lower tunneling currents to produce the luminescence. Consequently we measured photon emission spectra with excitation currents in the range of 10-300 nA, which are more realistic conditions for STM operation than those reported previously [8,9]. These conditions have also been used to obtain the photon maps discussed above. Figure 5 shows an STL spectrum of the n^+-n-n^--n^+ GaAs structure, which reveals a peak at about 860 nm due to bandgap recombination in the low doped n^--layer. In contrast to the results of Montelius et al. [8], increasing the tip current above 1 μA does not produce higher photon intensities here. A possible explanation of this effect is that, for such high currents, the metal tip is already in contact with the semiconductor surface and we have a Schottky contact between the tip and the semiconductor surface. If this were the case, then the insulating layer between the metal and the semiconductor would not exist and only a negligible minority carrier current, which is required for the production of the luminescence, is produced here.

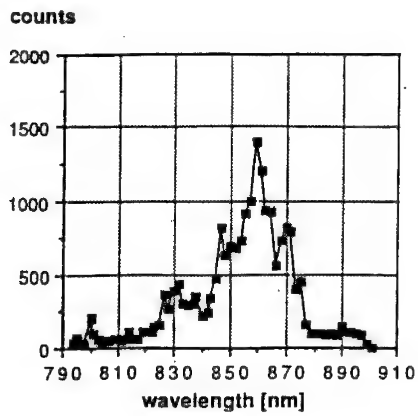

Fig.5: Luminescence spectrum of GaAs obtained using a STM for excitation.

VI. Conclusions

The results presented above show that STM induced luminescence is a useful tool for the characterisation of material on a nm scale. Clearly such characterisation techniques are essential for the development of future devices with the trend towards smaller devices well into the submicron range. In particular, we have shown that the STM may be used to determine the minority carrier lifetime using time resolved luminescence techniques and that spectrally resolved luminescence may be used to characterise structures on a scale which is about two orders of magnitude lower than that which can be obtained by photoluminescence.

Acknowledgements

The authors acknowledge the financial support of the DFG.

References

[1] G. Binnig and H. Rohrer, Helv. Phys. Acta **55**, 726 (1982)

[2] J.K. Gimzewski, B. Reihl, J.H. Coombs and R.R. Schlittler, Z. Phys. B **72**, 497 (1988).

[3] D. L. Abraham, A. Veider, Ch. Schönenberger, H. P. Meier, D. J. Arent and S. F. Alvarado, Appl. Phys. Lett. **56**, 1564 (1990).

[4] S. F. Alvarado, Ph. Renaud, D. L. Abraham, Ch. Schönenberger, D. J. Arent and H. P. Meier, J. Vac. Sci. Technol. B 9, 409 (1991).

[5] Ph. Renaud and S.F. Alvarado, Phys. Rev. B, **44**, 6340 (1991)

[6] R. Berndt, R.R. Schlittler and J.K. Gimzewski, J. Vac. Sci. Technol. **B** 9, 573 (1991)

[7] R. Berndt, J.K. Gimzewski, Phys. Rev. B, **45**, 14095 (1992)

[8] L. Montelius, M. E. Pistol and L. Samuelson, Ultramicroscopy **42-44,** 210 (1992).

[9] L. Samuelson, J. Lindahl, L. Montelius and M. E. Pistol, Inst. Phys. Conf. Ser. No. **135,** 51 (1994).

[10] M. Wenderoth, M.J. Gregor and R.G. Ulbrich, Solid State Commun.**83**, 535 (1992)

[11] J. Horn, R. Richter, H. L. Hartnagel, C. A. Sprößler, M. Bischoff and H. Pagnia, Mat. Sci. & Eng. B **20**, 183 (1993).

[12] J. Horn, M. Stehle, M. Bischoff, H. Pagnia and H. L. Hartnagel, Inst. Phys. Conf. Ser. No **135**, 73 (1994).

[13] W. J. Kaiser, L. D. Bell, M. H. Hecht and F. J. Grunthaner, J. Vac. Sci. Technol. A **6**, 519 (1988).

[14] H. C. Card and E. H. Rhoderick, Solid State Electronics **16**, 365 (1973).

[15] P. Asbeck, J. Appl. Phys. **48**, 820 (1977).

Materials Science Forum Vols. 185-188 (1995) pp. 155-164

Passivation of semiconductors by the remote plasma technique

W. Kulisch, F. Kiel, M. Schiller, S. Reinke and R. Kassing

Institute of Technical Physics, University of Kassel, Heinrich-Plett-Str. 40,
D-34109 Kassel, Germany

Keywords: Remote plasma technique, III/V-passivation, plasma diagnostics, SiO_2 deposition, integrated photoluminescence

Abstract The deposition of passivating and insulating films on III/V semiconductor surfaces calls for a low temperature, but also 'soft' deposition method. We emphasize the suitability of the Remote PECVD technique for this purpose. Plasma diagnostic measurements (Langmuir probe, retarding field energy analyzer, optical emission spectroscopy) show that under remote conditions the number of ions impinging on the substrate, and their mean energy are much lower compared to direct plasmas. A remote SiO_2 deposition process is presented yielding highly insulating SiO_2 films on silicon substrates at temperatures as low as 120°C. Application of this process to InP was prevented by poor film adhesion to the InP substrates. However, this problem can be overcome by slightly rising the temperature to 180°C, still yielding films with low interface state densities. Accompanying integrated photoluminescence measurements demonstrate on the one hand the suitability of this technique as a tool to judge *in situ* the influence of every process step on the electronic quality on III/V surfaces. On the other hand they show that the remote SiO_2 process does not degrade the InP surface.

1 Introduction

The deposition of passivating and insulating films onto III/V semiconductor surfaces is still a major problem to be overcome in the course of developing a III/V technology, despite of nearly 20 years of research in this field [1, 2, 3]. This is due to the volatility of the group V elements, and also the sensitivity of the III/V surfaces. First of all, the passivation of III/V semiconductors (especially that of InP and related materials) requires deposition at low temperatures. This requirement suggests the use of a plasma assisted method; but on the other hand, the exposure of III/V semiconductor surfaces to a plasma is not compatible with the sensitive nature of these surfaces, therefore resulting in a drastic degradation of the electronic quality of the surface by impinging energetic particles from the plasma [4, 5].

This dilemma can be overcome by applying the remote plasma technique (R–PECVD) [2, 4, 6, 7, 8] in which the surface to be coated is not directly exposed to the plasma but spatially separated from it. This results in the first advantage of the R–PECVD, a drastic reduction of the number of ions reaching the substrate. The main problem then to be overcome is to develop deposition processes resulting in high quality passivating films despite the lack of energy supply by either temperature or particle bombardment. This requires a careful choice of source compounds and deposition parameters. At this point, however, one can make use of the second great advantage of the R–PECVD: In the remote technique, only one of the reactants (excitation gas) is excited by the plasma whereas the other gases (source gases) are introduced outside the plasma (Fig. 1). This results in a more controlled reaction chemistry as has been discussed in detail in [7, 8, 9].

In this paper we will, however, mostly concentrate on the first advantage of the R–PECVD, namely the reduced particle bombardment. We will first present plasma diagnostic measurements (retarding field energy analyzer and Langmuir probe) in order to quantify the ion flux onto the substrate and the ion energy distribution under remote plasma conditions. We will then describe a remote plasma process for the deposition of SiO_2 films on silicon and InP surfaces, and discuss the problem of film adhesion to the InP substrates. Finally, we will show by means of integrated photoluminescence measurements that this deposition process does not degrade the electronic properties of the InP surface, in agreement with electrical measurements performed with SiO_2/InP MIS capacitors.

2 Experimental

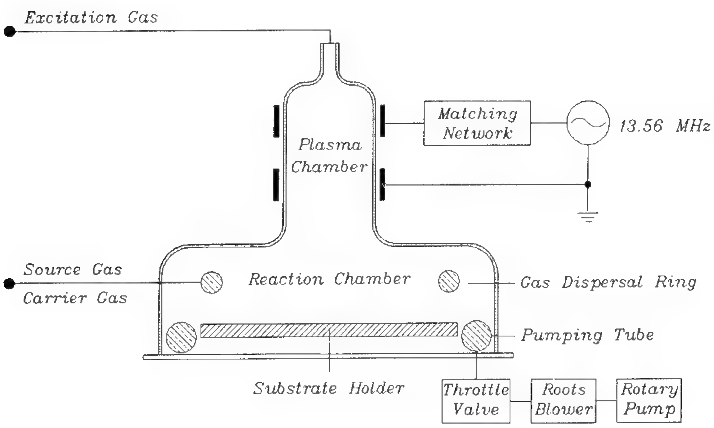

Figure 1: Remote PECVD set–up used for the plasma diagnostic measurements.

Measurements in order to characterize the remote plasma technique have been carried out in a remote plasma reactor shown schematically in Fig. 1 which has been described in detail in [8, 10]. A retarding field energy analyzer (RFEA) was used to measure the total ion current onto the substrate holder respective the resulting ion energy distribution. The plasma density and the electron temperature as a function of vertical distance from the sample holder for a variety of parameters were determined by Langmuir double probe measurements (LP). Details of the RFEA and LP (hardware design, evaluation software, and experimental procedure) will be described in another paper [11]. The results of these investigation are compared with optical emission spectroscopy (OES) measurements published earlier [12].

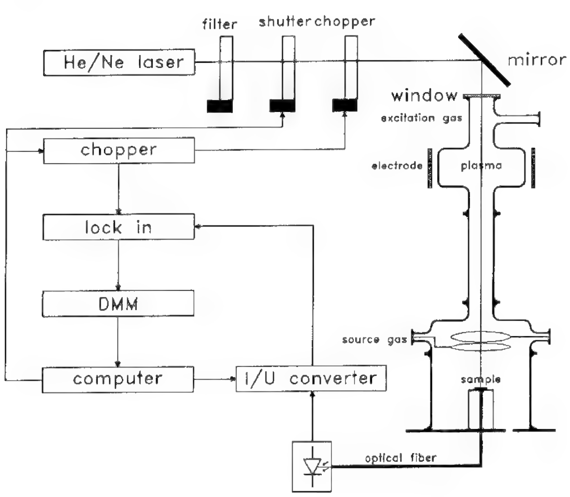

Figure 2: Remote PECVD set–up used for the deposition of SiO_2 on Si and InP substrates, and for *in situ* PL measurements. Owing to the geometrical arrangment, the 'remote character' of this reactor is even more pronounced compared to the one shown in Fig. 1.

The deposition experiments and the accompanying photoluminescence measurements were carried out in a slightly modified remote reactor which is shown schematically in Fig. 2. Details of the reactor set–up, the PL measurement arrangement, and the experimental procedure have been described in [13, 14].

SiO_2 films were deposited by means of a TEOS/O_2 (TEOS = tetraethoxy silane, $Si(OC_2H_5)_4$) discussed in detail in [13, 14]. The major process parameters and some results of this process are

Process Parameters		Results	
source gas	TEOS	growth rates	5 – 10 nm/min
excitation gas	O_2	refractive index	1.445 – 1.455
carrier gas	N_2	carbon content	$\leq 0.5\%$
pressure	$7 \cdot 10^{-2}$ mbar	contaminations	SiOH, OH
substrate temperature	$\geq 120°C$		
rf power	≤ 10 W		

Table 1: Major process parameters and results of the remote SiO_2 process used for the passivation of InP [14].

summarized in Tab. 1. Either Si(100) or InP(100) have been used as substrates. Si samples were prepared by organic cleaning only, whereas InP samples were subjected to a final HF dip. Details of sample preparation can be found in [14].

The deposited SiO_2 films were characterized by means of ellipsometry (thickness, refractive index), AES (stoichiometry, contaminations) and FTIR (film structure) [14]. Al/SiO_2/Si respective Al/SiO_2/InP MIS capacitors were used to determine the electrical properties of the insulator/semiconductor interface.

3 Results and Discussion

3.1 Characterization of the Remote Plasma

Since the first publication of Meiners [6] recommending the remote plasma for the passivation of III/V semiconductor surfaces, this technique has always been assumed to yield a drastically reduced ion current onto the substrate surface [4, 7, 15]. However, direct evidence for this is scarce in the literature, at least for the 13.56 MHz reactors most commonly used. Most of the plasma diagnostic investigations of the R–PECVD technique were restricted to spectroscopic techniques such as OES or mass spectrometry [12, 16, 17] yielding indirect evidence only. Moreover, to our knowledge there [illegible] study in the literature investigating the dependence of the most decisive quantities, the ion satura[illegible] current $J_{i,s}$, and the average ion energy respective the ion energy distribution, on the major process parameters.

We therefore investigated the ion current onto the substrate holder of the reactor shown in Fig. 1, and the resulting ion energy distribution by means of RFEA. Furthermore, Langmuir Probe measurements were carried to determine the plasma density n_e alongside the vertical axis of the reactor as a function of the distance from the rf electrodes.

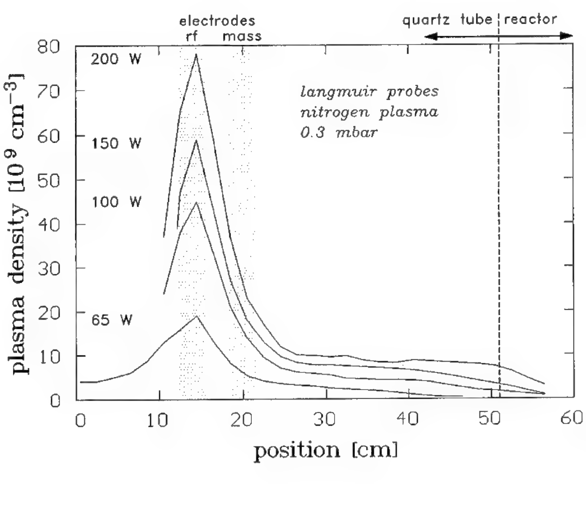

Figure 3: Langmuir probe measurements: plasma density along the vertical axis of the reactor as a function of rf power for a 0.3 mbar nitrogen plasma. The dotted areas mark the regions of the rf electrodes (cf Fig. 1). The dashed line marks the end of the plasma chamber.

Probe measurements Fig. 3 shows the plasma density along the vertical axis of the reactor as a function of the rf power P_{rf} for a 0.3 mbar nitrogen plasma. The positions of the rf ring electrodes and the end of the plasma chamber respective the begin of the reaction chamber (cf Fig. 1) are also indicated in the figure by the marked areas and the dashed line, respectively. It can be seen that irrespective of the rf power applied the plasma density is highest at the position of the powered electrode. It then decreases rapidly towards the plasma chamber reaching a relatively constant low level roughly at the end of the area of the grounded electrode. A further decrease is observed at the end of the plasma chamber which continues inside the reaction chamber.

The main effect of the rf power is an overall increase of the $n_e(x)$ curves described above as is to be expected. However, a closer examination of the curves in Fig. 3 reveals an interesting detail. Within the resolution of the figure, the plasma density inside the reaction chamber is essentially zero for the 65 W curve. For higher rf powers it is still low but distinct. This effect becomes more clearly from the probe data shown in Fig. 4. They stem from measurements inside the reaction chamber just above the sample holder. It can be seen that for $P_{rf} \leq 80$ W the plasma density is nearly constant at a very low level (compare the axis in Figs. 3 and 4). For higher powers, n_e increases linearly with P_{rf}. In this power range, a plasma can be seen burning even in the reaction chamber. We may therefore conclude that here the plasma is no longer confined within the plasma chamber but reaches into the reaction zone. Therefore, the conditions of a remote plasma are no longer fulfilled, and we have to deal with a 'direct plasma'. Further evidence for this transition which has also been observed by [8, 12, 17] is provided by the RFEA and OES measurements discussed below.

It should be mentioned that the power level at which the transition between the remote and the direct plasma takes place depends on various parameters among which the pressure is most important. However, the geometrical arrangement and even the excitation gas used also play a role. A detailed analysis of these influences is presented in [11]. It should also be pointed out that within the plasma chamber in the region of the powered electrode, i.e. the region of the highest plasma densities, n_e increases rather continuously with P_{rf} (Fig. 3); here the two regions can hardly be distinguished.

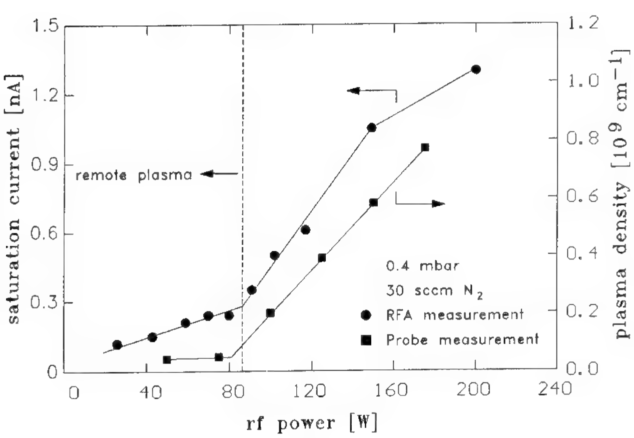

Figure 4: RFEA measurements: Saturation current onto the substrate holder as a function of the applied plasma power (left axis). Also shown is the plasma density in the reaction chamber above the sample holder according to probe measurements (right axis).

RFEA measurements Let us return to Fig. 4 and discuss the ion saturation current $J_{i,s}$, i.e. the total ion flux onto the substrate surface irrespective of the ion energy. The figure shows $J_{i,s}$ as a function of the rf power for an N_2 plasma at 0.4 mbar. As in the case of the probe measurements presented above, two regimes can be distinguished in this curve which can again be assigned to the remote plasma region and the direct plasma region discussed in the last section. Moreover, the transition between them occurs at nearly the same P_{rf} value.

From the effective area of our retarding field analyzer, the saturation current density in the remote plasma case was determined to ≈ 20 nA/cm^2. In the direct plasma case, the current is higher by

nearly one order of magnitude as can be seen from Fig. 4. For a typical parallel plate reactor under similar conditions, values of $J_{i,s}$ in the order of 0.1 to 1 mA/cm^2 are common.

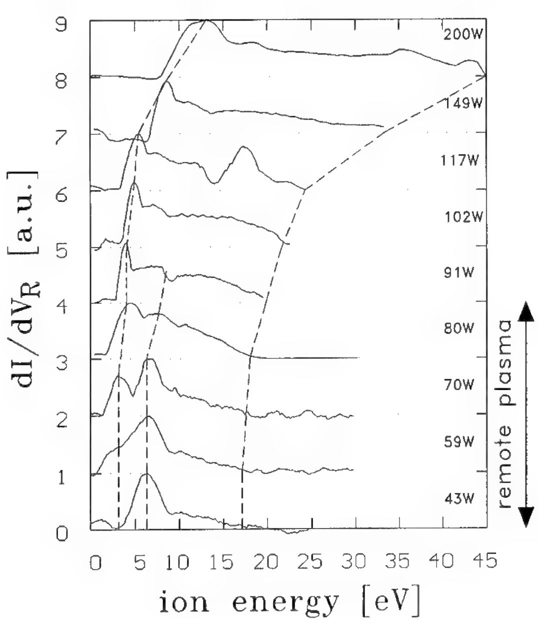

Figure 5: RFEA measurements: Ion energy distribution as a function of the rf power. Each spectrum is normalized to the its maximum.

Fig. 5 shows ion energy distributions as a function of rf power for the same N_2 plasma. It can be seen that in the low P_{rf} range, i.e. for a remote plasma, the peak ion energy is below 10 eV, and the ion current is essentially zero for $E_i > 20$ eV. If the rf power is increased, i.e. if the mode is switched to the direct plasma, the peak ion energy increases. In addition, there is a steadily increasing tail of higher energy ions reaching up to ≈ 45 eV for $P_{rf} = 200$ W. If comparing the remote and the direct plasma case, one has further to take into account that according to Fig. 4 the total ion current increases by nearly one order of magnitude.

Therefore, the results of these RFEA measurements relevant to our discussion can be summarized as follows: In the remote plasma case, the total ion current is as low as 20 nA/cm^2; the mean ion energy is below 10 eV and the maximum ion energy below 20 eV. At higher powers (i.e. a direct plasma), the ion current increases by nearly on order of magnitude, the peak ion energy increases, and there are more and more ions with energies between 20 and 45 eV.

These Langmuir probe and RFEA measurements correlate well with OES investigations which were performed in the same remote plasma reactor and which has been reported in a previous paper [12]. The most important result in the context of this discussion is the following: the intensity of ion related lines declines strongly to almost zero on transition from the direct to the remote mode in those spectra taken in the reaction chamber (cf Fig. 1). The intensity of lines related to radicals and metastables also decreases but to a distinct lower level only. This in fact opens up the very advantage of remote plasma deposition: The concentration of ions in the reaction zone is indeed very low whereas those of radicals and metastables is somewhat lower than in the direct plasma mode but still on a high level. Therefore, chemical reactions with these radicals and metastables will take place at relatively high rates whereas the detrimental effects of ions are almost suppressed. In other words, one makes use of plasma chemistry avoiding physical effects of the plasma. It should be mentioned that there are of course many applications where physical effects in PECVD are of advantage or even unindispensable as has been discussed in [8]. Nevertheless, as has been pointed out above, in those cases where a soft deposition technique or a controlled chemistry is required, the remote technique offers this very advantage over standard plasmas. The passivation of III/V semiconductors represents such a case, obviously.

We finally like to mention that the OES measurements showed again that the rf power at which the transition direct plasma $\longrightarrow$ remote plasma occurs depends on parameters such as pressure, reaction gases, and gas flows. Therefore the condition of a remote plasma has to be established for each process.

3.2 Low Temperature R–PECVD Deposition of SiO_2

3.2.1 Deposition on silicon substrate

Deposition experiments were carried out in a modified remote reactor (Fig. 2). Owing to the geometrical arrangement, the 'remote character' of this set–up is even more pronounced compared to that used for the diagnostic measurements (see Figs. 1 and 2) despite the low pressure used for these experiments. Although this assumption had not been verified experimentally yet it is in agreement with theoretical considerations [14] and also confirmed by the results described below.

With this set–up, a process for the deposition of SiO_2 from TEOS and O_2 has been developed (Table 1) which is described in detail in [14]. In this context, we like to emphasize only one but most important feature:

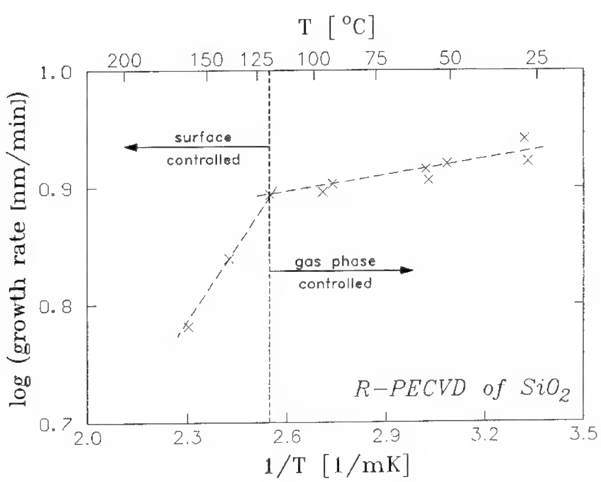

Figure 6: Growth rate as a function of substrate temperature (arrhenius plot).

Fig. 6 shows an arrhenius plot of the growth rate as a function of the substrate temperature. It is evident that two regions can be distinguished: At low T_s, the rate is approximately constant. Above a transition temperature T_t, however, the rate decreases with $ln(R) \propto 1/T$. This temperature dependence of the growth rate of TEOS/O_2 deposition processes has been observed previously by many authors. It is explained by a transition from a gas phase controlled to a surface controlled process; the latter is dominated by thermally activated desorption processes leading to the linear arrhenius plot shown in Fig. 6. It is also evident from literature that one has to work in the surface controlled region in order to obtain high quality SiO_2 films from a TEOS/O_2 process.

authors	reference	method	T_t [°C]
Secrist et al.	[18]	remote	290
Bourreau et al.	[19]	direct	230
Kulisch et al.	[20]	direct	220
Frenck	[10]	remote	200
This work		remote	120

Table 2: Transition temperatures T_t reported in the literature for the transition from gas phase to surface controlled deposition of SiO_2 from TEOS and O_2.

The most important point in Fig. 2 is the low transition temperature of $T_t \approx 120°C$. As can be seen from Table 2, this is much lower than the values previously reported for T_t. The reason for this low transition temperature for the process under discussion is not clear. It is not due to the use of the remote technique as is evident from Table 2. The low working pressure of $7 \cdot 10^{-2}$ mbar, and also the low growth rates may play a role. These aspects are discussed in detail in [14]; for the present discussion it is sufficient to state that according to Fig. 6, the deposition of highly insulating SiO_2 films should be possible at temperatures as low as 120°C.

Indeed, films deposited on silicon substrates at $T_s \geq 120°C$ were found to be stoichiometric SiO_2 without significant carbon contaminations but with some residual silanol (SiOH) groups. The SiOH concentration, however, is very small compared to the polymer–like $(SiOH)_x$ films reported by other authors for $TEOS/O_2$ processes at these low temperatures [21]. Moreover, it does not affect the insulating properties of the SiO_2 films. From I/V measurements, the resistivity could be estimated be to higher than 10^{16} Ωcm; sufficient for the performance of MIS devices.

3.2.2 Deposition on InP substrates

On transfering the process described above to InP substrates, the somewhat surprising result was obtained that the insulating properties of the SiO_2 films are very poor in contrast to the good insulating behaviour of the same films on silicon substrates. The leakage currents of MIS capacitors, for example, are higher by orders of magnitude.

In search of the cause for these differences found with the two substrate materials, we first investigated possible differences in film composition, film structure, and other film properties. Especially, we tried to clarify:

- whether there are comtaminations within the films on InP. Therefore we looked for impurities at the interface due to the different surface preparation methods. Also, a possible phosphorus contamination was investigated because phosphorus diffusion from the InP into the oxide has previously been found to degrade the insulating properties of SiO_2 films; however, these experiments had been carried out at much higher temperatures [4].
- whether the structure of the SiO_2 is influenced by the nature of the different substrate materials.

However, by SIMS and AES measurements no differences in film composition were found; also, the films on InP substrates do not contain any additional contamination, neither at the interface nor in the SiO_2 bulk. With infrared spectroscopy similarly no differences in film structure were found. Especially, the FTIR measurements show that the SiO_2 on InP is not porous.

Also, most of the other film properties investigated (refractive index, growth rate) were almost identical on both substrates, with one but most important exception: Whereas on silicon substrates the oxide films were rather hard and well adherent, those on InP could be easily removed by scraping with tweezers. Therefore, it was concluded that poor adhesion to the InP substrate is the reason of the poor insulating quality of these films (via damaging the samples during mechanical contacting). Since differences in the stress of the films could be ruled out, the true adhesion between SiO_2 and InP must be responsible.

In order to overcome these adhesion problems, several possible solutions were investigated: Adhesion of a thin film on a substrate surface will be determined by the nature of surface and film, respectively, and by the interaction between them. Since we would not change the nature of the film owing to the good results on silicon substrates, we tried to change the nature of the substrate surface, and the interaction between surface and film forming species, by the following means:

- *In situ* cleaning of the InP surface by various remote plasma chemistries.
- Creation/deposition of an interface layer.
- Rising the substrate temperature.

Care had also to be taken that the measures applied to improve film adhesion do not degrade the electronic properties of the InP surface (e.g. application of an ion bombardment to create a mixed zone at the interface is out of discussion). Therefore, these investigations were accompanied by *in situ* PL measurements (see below).

All steps undertaken to modify the InP surface by either cleaning the InP substrate *in situ* by remote plasma etching or by depositing a thin interface layers, however, failed. For the etching approach, among others H_2, HF, CH_4/H_2 and NH_3 plasmas were investigated whereas a thin native plasma oxide and a PSG (phosphoro silicate glass) layer were tried as interface layer. In non of these cases, an improved film adhesion was observed, whereas some of them results in a severe degradation of the electronic properties on the InP surface. It is beyond the scope of this paper to discuss the

reason for this failure. It should be pointed out, however, that most of the remote plasma etching approaches did not result in a cleaning of the surface but rather in a contamination. Therefore, it seem that remote plasma etching at these very low temperatures is not possible due to the lack of energy supply by either temperature or ions. For a more detailled discussion of these experiments we refer to [14].

Owing to the failure of the measures discussed above, we tried to increase adhesion by rising the substrate temperature. This would result in a reduction of the growth rate (Fig. 6) and also in an enhanced surface migration of film forming species. Both effects will enable these species to find an appropriate 'growth site' on the InP surface thus improving the interaction of substrate and film. Indeed, with increasing T_s an improved adhesion and, alongside, a reduction of the leakage current was observed. A temperature of $T_s \approx 180°C$ presents a good compromise between sufficient adhesion/insulating quality on the one hand, and a still high electronic quality of the InP surface on the other hand. C(V) measurements with MIS capacitors produced at 180°C revealing interface state densities of $\approx 1 \cdot 10^{11}$ cm^{-2}eV^{-1} only. This result is in agreement with the PL measurements presented in the next chapter.

3.3 Photoluminescence Measurements

The integrated photoluminescence signal (PL) of a III/V semiconductor surface can be regarded as a measure of its electronic quality [13, 22, 23, 24] with high PL signals corresponding to high quality surfaces. Since PL is an optical method, it is compatible with almost all deposition set-ups. In addition, PL measurements if carefully conducted, do not interfere with the deposition process. Therefore, PL measurements are a powerful tool to judge *in situ* the influence of any single process step, or that of a complex sequence of technological steps (such as a deposition process) on the electronic properties of III/V semiconductor surfaces.

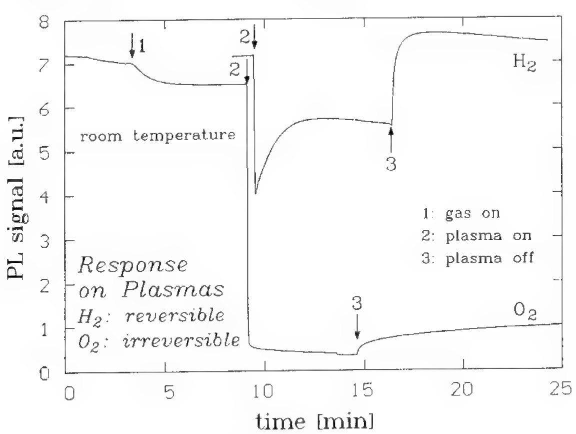

Figure 7: PL response to the exposure of an InP surface to a remote H_2 respective O_2 plasma.

On the other hand, every single technological step influences the PL signal since it influences the semiconductor surface. In the past, the effect of exposure of InP surfaces to various gases [13, 25], heat [24, 26] and plasma treatments [14, 24] as well as to different wet [23, 24] and dry etch processes [14] has been investigated. An example is given in Fig. 7 where the PL response to the exposure of InP surfaces to a remote H_2 respective O_2 plasma is shown.

The figure shows that on igniting the plasma, in either case the PL signal drops drastically. There are, however, marked differences between O_2 and H_2. In the case of O_2, the drop is far more pronounced. More important, however, is the fact that after stopping the plasma treatment the PL signal remains at a very low level. In contrast, in the case of H_2 the PL signal reaches almost its starting value after some time of relaxation. From these measurements the conclusion can be drawn

that both, O_2 and H_2 treatment, affect the InP surface. In the case of H_2, however, this interaction is reversible whereas the oxygen plasma treatment damages the surface irreversibly.

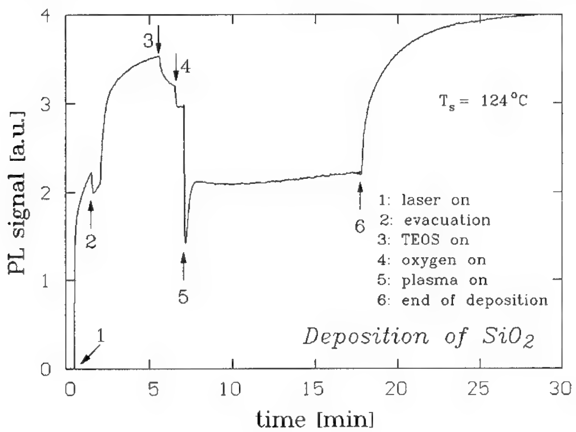

Figure 8: Developement of the PL signal during the deposition of a SiO_2 film by the remote process described above. Note that the PL signal at the end of the process reaches the value at the start of the deposition.

In situ PL measurements were also used to investigate the complete sequence of events of a typical deposition process. An example is shown in Fig. 8. First of all, the figure shows again that every single step of the deposition sequence (such as evacuation, inlet of the various gases etc.) influences the PL signal. But the most important observation is the following: On igniting the plasma, the PL signal immediately drops and remains at a relatively low level during the deposition. However, at the end of the process after some relaxation time the signal increases again and reaches finally the starting value. This indicates that the InP surface has not been degraded by the deposition process, and agrees well with the low interface state densities obtained by this process (see above).

If, however, any process step was introduced which degrades the surface, or if deposition parameters detrimental to the InP surface were used, the PL signal at the end of the process was always found to be considerable below the starting value. In each case this low PL end value corresponds to increased interface state densities and/or to anomalies in the C(V) characteristics of the respective MIS capacitors [14].

Therefore, these results show again that the PL technique is a powerful method to judge *in situ* the influence of deposition processes on the electronic properties on an InP surface. From Fig. 8 it is further evident that the remote SiO_2 process described above is compatible with the sensitive nature of this surface and does not degrade its electronic quality.

4 Conclusions

The deposition of insulating and passivating films on InP substrates by means of the remote plasma technique has been discussed under several aspects: By direct measurements of the ion flux and its energy distribution it was shown that under remote conditions the ion current as well as the mean ion energy is much lower than in the direct plasma case. Then, a remote process for the deposition of SiO_2 films at temperatures down to 120°C was presented. On silicon substrate this process yields highly insulating films; on InP substrates, however, these good electric properties are degraded due to poor film adhesion. Since all measures to overcome this problem by changing the nature of the substrate surface failed, the only solution was to rise the substrate temperature to 180°C. Finally, PL measurements show that this deposition process does not degrade the electronic properties of the InP surface, in agreement with low insulator state densities measured with MIS capacitors.

Acknowledgements

Part of this work was financially supported by the Deutsche Bundespost/TELEKOM which is gratefully acknowledged. We also like to thank Dr. Kräutle from the Research Center of the TELEKOM at Darmstadt for his support.

References

[1] D. L. Lile. In C. W. Wilmsen, editor, *The Physics and Chemistry of III–V Compound Semiconductors*, chapter 6, page 327. Plenum Press, New York, 1985.

[2] W. Kulisch. PhD thesis, University of Kassel, 1988.

[3] P. Viktorovitch, M. Gendry, G. Hollinger, S. Krawczyk, and J. Tardy. In *Fourth International Conference on Indium Phosphide and Related Materials*, page 51, Newport, RI, USA, April 21–24 1992.

[4] W. Kulisch and R. Kassing. *J. Vac. Sci. Technol.*, B5:523, 1987.

[5] W. Kulisch, F. Kiel, A. Bock, H.J. Frenck, and R. Kassing. In *Third International Conference on Indium Phosphide and Related Materials*, page 571, Cardiff, Wales, UK, April 8–11 1991.

[6] L. G. Meiners. *J. Vac. Sci. Technol.*, 21:655, 1982.

[7] G. Lucovsky and D. V. Tsu. *J. Vac. Sci. Technol.*, A5:2231, 1987.

[8] W. Kulisch. *Surf. Coat. Tech.*, 59:193, 1993.

[9] G. Lucovsky and R.J. Tsu, D. V. Markunas. In S.M. Rossnagel, J.J. Cuomo, and W.D. Westwood, editors, *Handbook of Plasma Processing Technology — Fundamentals, Etching, Deposition and Surface Interactions*, chapter 16, page 387. Nayes Publications, Park Ridge, NJ, 1989.

[10] H. J. Frenck. PhD thesis, Kassel, 1991.

[11] W. Kulisch, M. Schiller, and S. Reinke, 1994. Paper Submitted to Surf. Coat. Tech.

[12] W. Kulisch, M. Witt, H. J. Frenck, and R. Kassing. *Mat. Sci. Eng.*, A140:715, 1991.

[13] F. Kiel, W. Kulisch, and R. Kassing. In *Fourth International Conference on Indium Phosphide and Related Materials*, page 347, Newport, RI, USA, April 21–24 1992.

[14] F. Kiel. PhD thesis, University of Kassel, 1993.

[15] J. F. Wager and C. W. Wilmsen. *J. Appl. Phys.*, 53:5789, 1982.

[16] D. V. Tsu, G. N. Parsons, and G. Lucovsky. *J. Vac. Sci. Technol.*, A6:1849, 1988.

[17] D. V. Tsu, G. N. Parsons, G. Lucovsky, and M. W. Watkins. *J. Vac. Sci. Technol.*, A7:1115, 1989.

[18] D. R. Secrist and J. D. Mackenzie. *J. Electrochem. Soc.*, 113:914, 1966.

[19] C. Bourreau, Y. Catherine, and P. Garcia. In *2nd International Conference on Plasma Surface Engineering (PSE 90)*, Garmisch–Partenkirchen, September 1990.

[20] W. Kulisch, T. Lippmann, and R. Kassing. *Thin Solid Films*, 174:57, 1989.

[21] N. Selamoglu, J. A. Mucha, D. E. Ibbotson, and D. L. Flamm. *J. Vac. Sci. Technol.*, B7:1345, 1989.

[22] K. Mettler. *Appl. Phys.*, 12:75, 1977.

[23] R. R. Chang, R. Iyer, and D. L. Lile. *J. Appl. Phys.*, 61:1995, 1987.

[24] H. J. Frenck, W. Kulisch, and R. Kassing. In R. Singh and L. J. Messick, editors, *First International Conference on Indium Phosphide and Related Materials for Advanced Electronics and Optical Devices*, page 250, Norman, OK, March 20–22 1989. Proc. SPIE 1144.

[25] H. Nagai and Y. Noguchi. *Appl. Phys. Lett.*, 33:312, 1978.

[26] R. Iyer, R. R. Chang, and D. L. Lile. *J. Crys. Growth*, 83:290, 1987.

Materials Science Forum Vols. 185-188 (1995) pp. 165-170

AES study of the GaAs-germanium oxynitride interface

D. Jishiashvili, R. Dzhanelidze, Z. Shiolashvili and I. Nakhutsrishvili

Institute of Cybernetics, Academy of Sciences of the Georgian Republic,
Euli str. 5, 380086 Tbilisi, Georgian Republic

Keywords: Oxynitride, interface, germanium, AES, film, profile, pyrolysis, hydrazine, GaAs

ABSTRACT

The distribution of elements through the thickness of germanium oxynitride (GeO_xN_y) films deposited onto GaAs is investigated by the method of Auger Electron Spectroscopy (AES). The experiments are carried out to explain the reasons of perfect formation of the GeO_xN_y-GaAs interface. Pyrolytic deposition of GeO_xN_y in hydrazine (N_2H_4) vapor is realized by the following sequence of processes: in situ etching of the GaAs surface, deposition of a thin Ge Interface Control Layer (ICL) followed by formation of a connective oxynitride film with nonuniform distribution of elements and finally a stable nonstoichiometric GeO_xN_y dielectric film. Low surface state densities at the GaAs-Ge ICL and Ge ICL-GeO_xN_y interfaces result in good operating parameters of the GaAs/GeO_xN_y/Al MIS structure.

INTRODUCTION

One possible approach to solve the problem of the surface passivation of GaAs is the application of new dielectric materials and the development of new deposition technologies. Recently it was found, that pyrolytic Ge oxynitride deposited in the presence of hydrazine vapor creates a high quality interface with GaAs [1]. A capacitance-voltage (C-V) characteristics of this MIS structure measured at 1 MHz is represented in fig. 1a. The capacitance changes stepwise with a well-defined inversion region. The frequency dispersion is weak (1 - 1000 kHz) and the hysteresis does not exceed 0.1 - 0.2 V. The calculated surface state density is 3×10^{10} cm^{-2} eV^{-1} and the dielectric strength is greater than 10^6 V/cm. A comparison of theoretical and experimental curves indicates that the inversion capacitances in the two curves coincide. Thus, deep depletion of the GaAs surface is reached. Fixed negative charge mainly contributes to the surface state density. All this

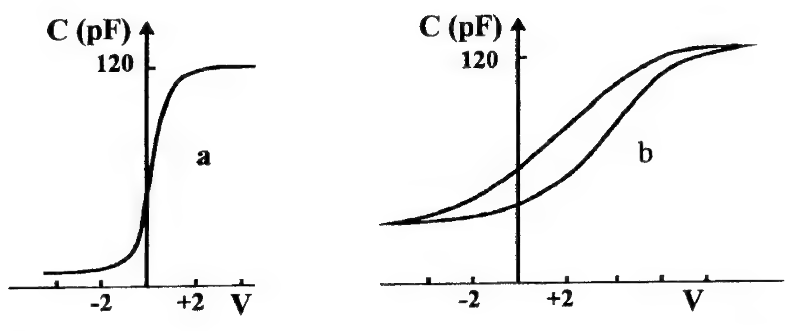

Fig.1: 1 MHz C-V curves of n-GaAs/pyrolytic/Al devices. $n = 1\times10^{11}$ cm^{-3}, voltage sweep rate 0.5 V/s, Al contact diameter 0.05 cm. GeO_xN_y deposition temperature: a) 300°C, 0.1 V hysteresis width not shown; b) 400°C

proves that the Fermi level E_F is not pinned at the GaAs surface and high quality MIS devices can be fabricated on the basis of the dielectric film chosen.

To explain this nontrivial result the following problems must be clarified:
1. What happens with the native oxide of GaAs during the process of deposition?
2. Is the formation of the high quality interface caused by the transformation of the GaAs surface to GaN in the presence of active N_2H_4 vapor?
3. What is the role of oxygen incorporated into the oxynitride film during the processes of interface formation, since it is well known even a fraction of a monolayer of oxygen causes Fermi level pinning at the GaAs surface?

The purpose of this work was to analyze the reasons of the creation of such a perfect interface by investigating the distribution of elements through the thickness of the dielectric film and through the thin GaAs oxynitride transition region.

EXPERIMENTAL

Amorphous Ge oxynitride thin films were deposited pyrolytically in hydrazine vapor at 300°C and 400°C on n-GaAs ($n = 1x10^{15}$ cm^{-1}). The composition and the distribution of elements through the thickness of the films were determined by the method of Auger electron spectroscopy. Special care was taken to avoid destruction of the films during electron and ion beam irradiation. For quantitative analysis standard films of Ge oxynitrides were used, the composition of elements in which was calculated by the method of Rutherford Back Scattering. The accuracy of quantitative analysis was ±5 at%.

RESULTS AND DISCUSSION

To study the question concerning the native oxide, the Ge oxynitride films were deposited onto the surface of GaAs not only in the presence of its native oxide (reactive ion-plasma method), but also after its removal in hydrazine vapor (pyrolytic method). In both cases the composition of oxynitride films were nearly identical.

The distribution of elements through the thickness for the structure GeO_xN_y/native oxide/GaAs is shown in Fig.2. An enrichment of oxygen and carbon at the interface is observed. The presence of carbon is due to adsorption of carbon containing compounds during the exposure of the sample to air just before film deposition. The bulk of the oxynitride film is free from carbon. Near the GaAs surface first disappears Ge and then, after passing through a maximum, the oxygen content decreases. The isolated position of the oxygen peak makes possible to differentiate the regions of oxynitride film and native oxide layer. It is obvious that the interface is formed by the native oxide layer. The C-V characteristics of this MIS structure shows the presence of surface states at high density.

A totally different profile is observed for the pyrolytic oxynitride film. In this process, before the deposition in situ etching of GaAs native oxide takes place in the vapor of such an active reducing agent as hydrazine.

Fig. 3 shows the Auger depth profiles of a pyrolytic oxynitride film with a thickness of about 70 nm deposited at 300°C. The C-V characteristics of the corresponding MIS structure is illustrated by Fig. 1a. Three regions can be clearly defined on the profile:

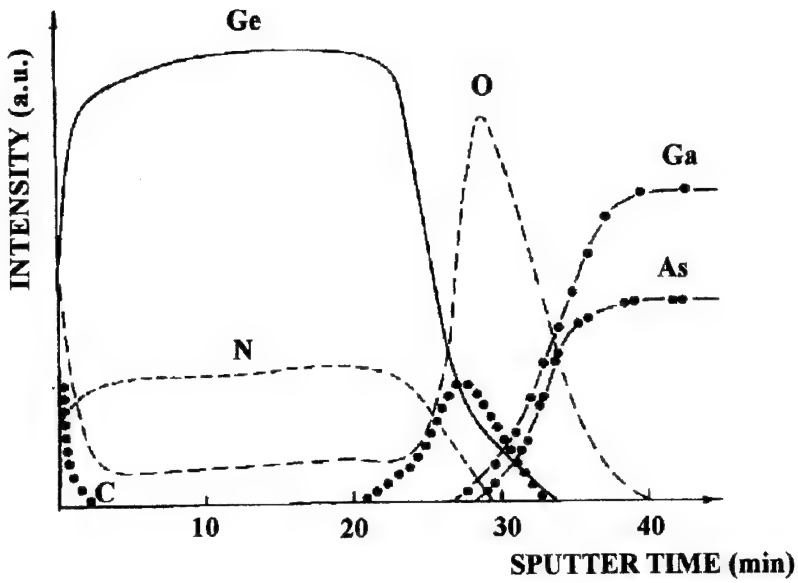

Fig.2: AES depth profile of reactive ion-plasma deposited GeO_xN_y film on GaAs. The native oxide was not etched away before deposition.

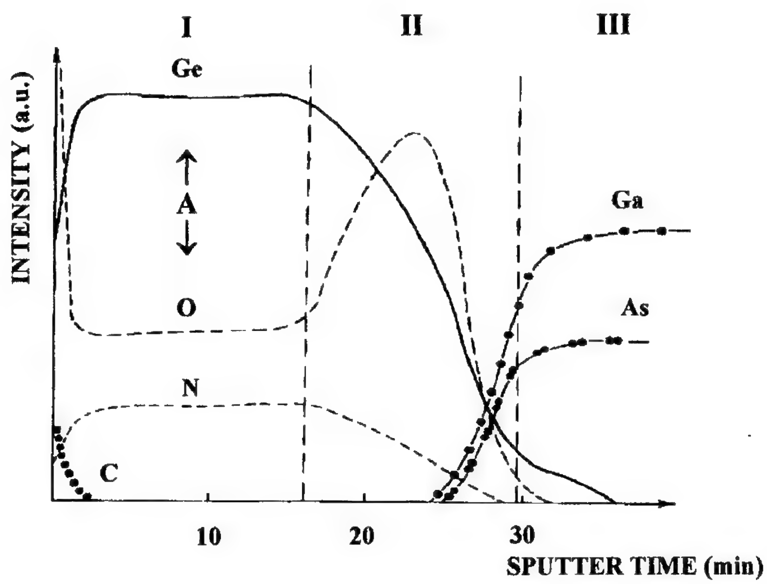

Fig.3: AES depth profile of a 70 nm thick pyrolytic GeO_xN_y film deposited on GaAs at 300°C

I. The bulk of the oxynitride film with uniform distribution of elements. At the point marked "A" the calculated concentrations of the elements are: Ge 54 at%, O 22 at%, N 24 at%. According to these data, the composition of Ge oxynitride can be described by the formula $Ge_3N_{1.3}O_{0.2}$. Comparing this result with the stoichiometric formula ($Ge_3N_{4-x}O_{1.5x}$) of the oxynitride we can conclude that the film corresponds to nonstoichiometric Ge oxynitride.

II. This region is characterized by a nonuniform distribution of elements where the concentrations of Ge and N gradually decrease and the oxygen content passes through a maximum. At the point of this maximum the concentrations of the elements are: Ge 36 at%, O 50 at%, N 14 at%.The form and the character of the curves show that in this case, in contrast to the structure with native oxide, the oxygen peak is not isolated and the oxygen is incorporated in the Ge oxynitride matrix. The absence of carbon in this region confirms the removal of the native oxide by the NH_3 vapor before the deposition of the dielectric.

III. The third region is immediately adjacent to the GaAs surface. As it is illustrated in Fig.3, there is no nitrogen in this region. So, the possibility of GaN formation on the GaAs surface can be excluded. The Ge and O contents gradually decrease but oxygen disappears before Ge. Taking into account the fact that the sensitivity of Auger spectroscopy for oxygen is nearly 4 times higher than for Ge we can conclude that the thin film containing Ge (or mostly Ge) is in close contact with the surface of GaAs. It is obvious, that this Ge film controls the interfacial properties. Its thickness is estimated at 2 to 4 nm.

However, for the formation of a high quality interface the composition of the second region connecting the Ge film with the bulk of the oxynitride is not less important.This is confirmed by the comparison of the profiles corresponding to oxynitride films deposited at 300°C and 400°C. The corresponding curves are shown in Figs.3 and 4. The comparison indicates that the concentration of elements in the bulk is negligibly changed, as well as the composition of the third region. In second region of the film deposited at 400°C, the concentration of oxygen was decreased from 50 at% to 36 at%. This change affects also the interface properties as illustrated by Fig.1b. As a result, the C-V curve is seriously stretched out, a large hysteresis appears and the surface state density is increased.

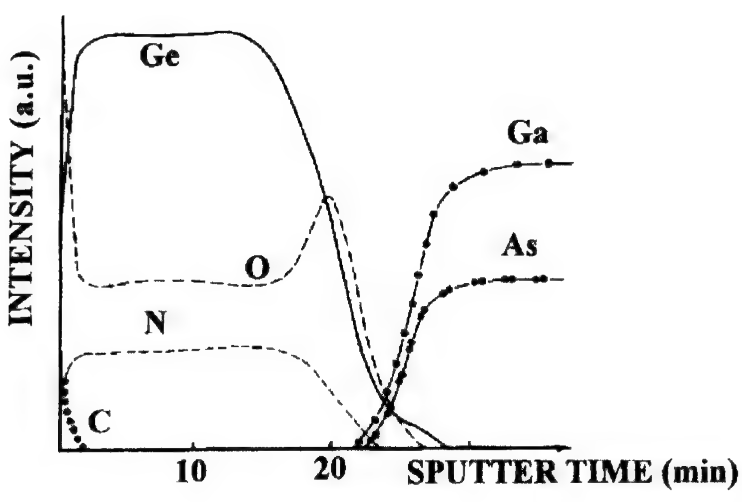

Fig.4: AES depth profile of pyrolytic GeO_xN_y film deposited on GaAs at 400°C

Summing up the experimental results, the following mechanism of pyrolytic deposition of Ge oxynitride can be proposed: In the initial stage in situ etching of GaAs native oxide occurs in the hydrazine vapor, then a thin film of Ge is deposited followed by an oxynitride film with nonuniform distribution of the elements. In the final stage the nonstoichiometric Ge oxynitride film with uniform distribution of elements is formed. All these processes take place in sequence during one closed technological cycle.

The structure obtained is analogous to the well known MIS structure on GaAs with interface control layer type Me/SiO_2/Si/GaAs which was proposed and discussed in [2,3]. The C-V characteristics of these structures, however, are not satisfactory. As the SiO_2-Si interface is nearly ideal, the main problem in this case arises at the Si-GaAs interface.

For GaAs from this point of view, Ge is one of the most suitable materials for an ICL as even a Ge film 0.6 nm thick forms a perfect interface with minimal lattice mismatch and unpinned E_F [4]. This is due to the negligible differences in the lattice constants of Ge and GaAs, the thermal expansion coefficient and the electron affinity. However, for the creation of a high quality MIS structure a new problem arises: the connection of the Ge ICL and the dielectric film with minimal surface state density at their interface. The results of our work reveals that this problem can be solved by using a pyrolytic oxynitride film with a special composition.

It must be noted that pyrolytic GeO_xN_y forms a high quality interface not only with GaAs, but also with Si, Ge and InP. The surface state densities for the corresponding interfaces are in the range of 10^{10} cm^{-2} eV^{-1}.

CONCLUSIONS

On the basis of experimental results the following conclusions can be drawn:

1. Removal of the native oxide layer being a necessary step for the formation of a perfect interface on GaAs occurs in hydrazine vapor before the deposition of the dielectric.
2. For pyrolytically deposited GeO_xN_y the interface with GaAs is formed and controlled by a thin (2 to 4 nm) Ge layer.
3. For the creation of a high quality MIS structure it is also important to optimize the composition of the thin transition region connecting the Ge ICL with the bulk of the GeO_xN_y film.
4. Low surface state density and unpinned E_F makes possible to recommend the pyrolytic GeO_xN_y film for the fabrication of high quality MIS devices on GaAs.

REFERENCES

[1] D.Jishiashvili, R. Dzhanelidze, Z. Shiolashvili, I. Nakhutsrishvili, Bull. Acad. Sci. Georgian Rep. **150**, 86 (1994)

[2] H. Hasegawa, M. Akazawa, K. Matsuzaki, H. Ishii, H. Ohno, Jpn. J. Appl. Phys. **27**, L2265 (1988)

[3] J. M. Woodall, P. D. Kirchner, J. L. Freeouf, A. C. Warren, Solid State Electron. **38** Suppl., 53 (1990)

[4] A. D. Katnani, P. Chiaradia, H. W. Sang,jr., R. S. Bauer, J. Vac. Sci. and Technol. **B2**, 471 (1984).

Materials Science Forum Vols. 185-188 (1995) pp. 171-178

Passivation studies of Se/GaAs interface using x-ray photoelectron and photoluminescence spectroscopy

B.A. Kuruvilla[1], A. Datta[2] and S.K. Kulkarni[1]

[1] Centre for Advanced Studies in Materials Science, Department of Physics, University of Poona, Pune-411007, India

[2] Alchemie Research Centre, P.B.No. 155, Thane Belapur Road, Thane-400601, India

Keywords: X-ray photoelectron spectroscopy, photoluminescence, passivation, semiconductors

ABSTRACT

The capability of group VI elements in passivating GaAs surfaces has been a topic of considerable interest for the last few years. Compared to unpassivated GaAs surface, S, P, Se and Te treated GaAs surface exhibits improvement in the electronic properties of GaAs. We have investigated the chemical interaction of S and Se with GaAs (100) using X-ray photoelectron spectroscopy. In-situ as well as ex-situ deposition of Se on GaAs were carried out at room temperature. The in-situ deposition was done in ultra high vacuum while the ex-situ deposition was done using a liquid medium. Considerable changes were observed in the surface electronic structure of GaAs. Our results indicate that Se is capable of making bonds with both Ga and As even at room temperature. It is observed that the interface reaction depends on the overlayer thickness. The As_2Se_3 phase responsible for the improved electronic properties is found to be formed at a higher thickness of selenium. It was also observed that the ex-situ treatment of GaAs with a solution of SeS_2 in CS_2 gives similar results. To investigate the protective nature of the terminating layer, Au was deposited on the Se covered GaAs surface. The results indicated that the Se layer is capable of protecting the substrate surface to a limited extent.

INTRODUCTION

Achieving unpinned surfaces and interfaces involving GaAs remains a difficult task in spite of years of efforts in the area of passivation of III-V compound semiconductors. There is a high density of states in the band gap for GaAs. This in general leads to the pinning of the fermi level, reduction in photoluminescence (PL) intensity, insensitivity of Schottky barrier height to metal work function etc. Hence the efficient use of GaAs in electronic devices makes it necessary to have a passivating layer which can make the exact termination of the bulk possible and thereby enhance the PL intensity and improve other electronic properties. GaAs passivation has been achieved to some extent using lattice matched heterojunctions, plasma treatments, chemical treatments etc. The simplest chemical method of passivation started [1] with the use of aqueous treatment using sodium sulfide. This treatment was found [2] to remove the native oxides from the surface and terminate the surface with S-GaAs bonds. The structural and electronic features desirable in a passivating overlayer are thus provided by the terminating phase. Although sodium sulfide treatment improve the electronic properties of GaAs surface it was observed [3-6] that the effect of sulfur treatment decayed rapidly.

The chemical instability of the sodium sulfide treated surfaces led to an active research on the passivation using other sulphides like $(NH_4)_2S$, H_2S, P_2S_5 etc. Recently many investigations are aimed [7] at using other elements in the VI group either in solution form or by evaporation for the purpose of passivation. Although Te has not been satisfactory, use of selenium has been found to be useful [6-10]. Se

finds many uses in electronics as well as solid state applications and resembles sulfur in many respects. The option of in-situ passivation is an additional advantage of using Se. The use of Se in solution for passivation was reported by Sandroff et al [6]. Their study showed that elemental Se does not give rise to any improvement in the electronic properties of GaAs. But the subsequent conversion of elemental Se into various oxidation states, led to a complex interface which improved the electronic properties. The formation of an As_2Se_3 phase on the surface was also shown. Though sulfur was involved in the treatment, no sulfur was detected on the surface. Hence the improved quality was considered to be entirely due to the As_2Se_3 deposited on the surface. We have also found that by dissolving SeS_2 in a suitable solvant like CS_2, it is possible to obtain a passivated GaAs surface similar to what has been reported by Sandroff et al [6]. Some preliminary work was reported earlier [11]. The possibility of in-situ deposition of Se, in high vacuum gave rise to many important results, regarding the passivation mechanism. Investigation on the surface atomic geometry of the passivated surface using X-ray photoelectron diffraction [12], photoelectron spectroscopy [9,13] RHEED and STM [14,15] also shed light on the mechanism of passivation . These studies suggest that there is a replacement of As atoms by Se, up to a few monolayers and the surface is probably terminated with selenium.This is possibly due to the comparable covalent radii of As (1.18A^o) and Se (1.14A^o). This can make the incorporation of selenium into the anion lattice site easier.

In the present case we have studied using photoluminescence and X-ray photoelectron spectroscopy, passivation due to SeS_2 dissolved in CS_2. These results are compared with other sulfide and phosphorous passivations of GaAs as performed by us. Aging studies also have been made. Further SeS_2 passivation has been compared with in-situ selenium deposition studied by photoelectron spectroscopy. To investigate the efficiency of the passivating layer we have deposited gold on in-situ as well as ex-situ deposited selenium. The PL and XPS data substantiate the effectiveness of Se as a passivating agent.

EXPERIMENTAL

All the experiments were performed on n-GaAs(100) wafers. Comparison of different passivation schemes was made using aqueous solutions of Na_2S, $(NH_4)_2S$, NH_4OH, P_2S_5, PCl_5 and SeS_2. For Na_2S treatment 1M solution of Na_2S was prepared in double distilled water. P_2S_5 and PCl_5 solutions of 0.04 M were prepared in NH_4OH. Selenium sulfide treatment was made using a 0.4M solution of SeS_2 powder dissolved in CS_2 solution. $(NH_4)_2S$ and NH_4OH solutions with pH ~ 12 were used. Samples were first degreased in trichloroethylene (TCE), acetone and methanol. These are 'as received' samples in the subsequent discussion. Before passivating the GaAs (100) samples by any of these passivating solutions, they were etched in a 4:1:1::H_2SO_4:H_2O_2:H_2O solution for 3 seconds. Passivation treatment consists of dipping the substrates in the above described passivating solution and then thoroughly washing (except selenium treated sample) with deionized water (18MΩ). The substrates are completely dried before carrying out the photoluminescence (PL) experiment.

Photoluminescence (PL) spectra were recorded using Perkin-Elmer LS-50 model using Xenon lamp. Excitation wavelength used in all the PL experiments was 578 nm. For the PL experiments freshly prepared etchants and passivants were used and PL spectra were recorded immediately after passivation at room temperature. Passivated samples were then stored in laboratory atmosphere and used later for aging studies.

X-ray photoelectron spectroscopy (XPS) analysis of the passivated samples was performed using ESCALAB MKII system supplied by VG Scientific England. Alk$_\alpha$ (hv = 1486.6eV) used as a source of radiation and concentric hemispherical analyser (CHA) yield a resolution of 1.0 eV. Au 4f $_{7/2}$ at 83.7± 0.1 eV served as an external source of reference. Vaccum ~ 10^{-9} torr was maintained throughout the experiments.

For in-situ selenium deposition experiment substrates were introduced into the ESCALAB system and further cleaning was performed by ion etching and heating to 550^{o}C. Selenium deposition was made by evaporating it from a tantalum cone heated by electron bombardment. The deposition rate was 1A^o/min. A quartz-crystal microbalance was used for thickness monitoring. Deposition of gold also was carried out

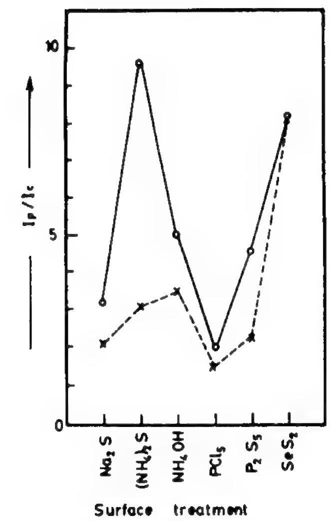

Fig. 1. Ratio of photoluminescence intensity of passivated GaAs (100) surface (Ip) to that of as received (Ic) sample.

on Se covered substrate. For this high purity gold was evaporated from a tungsten basket.

RESULTS AND DISCUSSION

Use of sulfur, selenium and phosphorous in liquid or gas phase has been tried by many. Although all methods show initial improvement in electronic properties of the passivated surface, it is essential to assess the passivation on the basis of their stability. For example the initially reported aqueous passivant viz. Na_2S showed [1,16,17] dramatical improvement in the electronic properties of the GaAs (100). However the surface was observed to be oxidized and fast decay occured [3-6] in its electronic properties. Similar is true for [6,18] other sulfides. Unlike sulfide passivants, selenium however showed better stability as illustrated in fig.1. In each case ratio of PL intensities of 'as received' sample are compared with the passivated sample surface. Although $(NH_4)_2S$ treatment yielded the best results, its long term chemical stability turned out to be poor. Same has been true for Na_2S, PCl_5, and P_2S_5 treated samples. However SeS_2 treated GaAs (100) exhibited best results.

A set of freshly passivated samples was introduced in ESCALAB for X-ray photoelectron spectroscopy studies. Here we illustrate Ga $2p_{3/2}$ and As $2p_{3/2}$ spectra. We recorded Ga 3d and As 3d core levels also, but the shifts and other information were same as for $2p_{3/2}$ core levels. Therefore we show here in fig.2 only Ga $2p_{3/2}$ and As $2p_{3/2}$ core levels. Note that all the passivated surfaces showed the same binding energy for Ga $2p_{3/2}$ i.e. 1117.3 eV except for NH_4OH treated surface. For the oxide free GaAs surface same value results for Ga $2p_{3/2}$. Except for $(NH_4)_2S$ treated surface the Ga$2p_{3/2}$ peaks are symmetric, indicating that there is no oxide or sulfide (at least detectable with the present resolution) bond with Ga on these surfaces. However some [19,20] found weak Ga-S bond and strong Ga-S bond was suggested by others [21,22]. Ga-S bond is found to be thermally more stable than As-S bond [21]. As $2p_{3/2}$ core level for each passivated surface is however different. This indicates that the nature of the surface film might be substantially different in each case. In all these cases there appear two peaks. The peak close to ~ 1323.0 eV can be attributed to As bonded with Ga as in the GaAs bulk crystal. Another peak appears on high binding energy side. For NH_4OH and PCl_5 treated samples strong peaks appear at ~ 1326.0 eV which can be attributed to As_2O_3 [6]. The shoulder in case of P_2S_5 treated sample as well as strong peaks at ~1325.5 eV in case of $(NH_4)_2S$ and Na_2S can be attributed to AS_2S_3 [6].

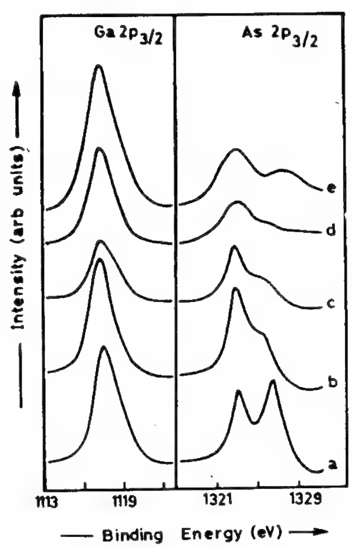

Fig. 2. XPS spectra of (a). NH_4OH (b). Na_2S (c) $(NH_4)_2S$ (d) P_2S_5 and (e) PCl_5 treated surface.

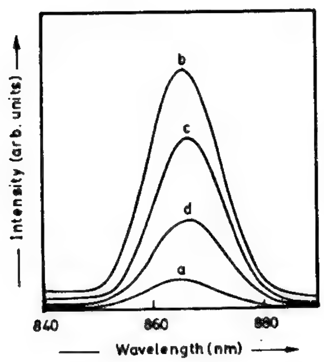

Fig.3. PL intensity of GaAs treated with SeS_2 for various timing (a) as received (b) 2 sec (c) 5 sec (d) 10 sec.

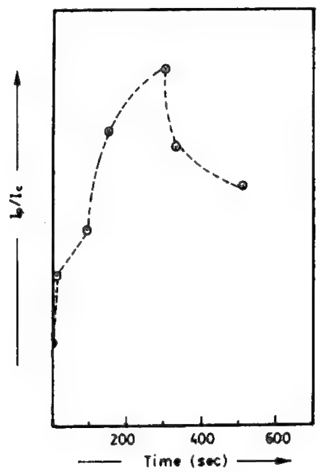

Fig.4. Ratio of PL intensity of SeS_2 passivated surface (Ip) to that of as received sample surface (Ic) with dissolution of thick film.

Thus sulfide treatments protect the surface to some extent from getting immediately oxidized, whereas other treatments like NH_4OH or PCl_5 turn out to be ineffective in this respect.

Sandroff et al [6] have shown that it is possible to use a solution of Na_2Se in NH_4OH to obtain a thin film of elemental selenium. This however does not enhance the PL intensity. It is necessary to convert this film into a selenide which imparts desirable electronic properties to the GaAs (100) surface by forming strong bonds with the surface. We have shown [11] that by using SeS_2 dissolved in CS_2 also one directly obtains the improved surface.

Although no quantitative measurements of selenium film thickness on GaAs surface by SeS_2 treatment are made here, it is observed that it is necessary to have a thin film on the surface. In fig.3, PL spectra for GaAs substrate dipped for various timings in SeS_2 solution have been shown. There is a large enhancement in the PL intensity for the sample dipped for just two seconds in SeS_2 solution. With increasing time in passivating solution, the PL intensity reduced drastically. Thus for the sample dipped in SeS_2 for 10 seconds the PL intensity was reduced by one third as compared to the best intensity shown here, although this intensity was larger than that of the 'as received' sample.

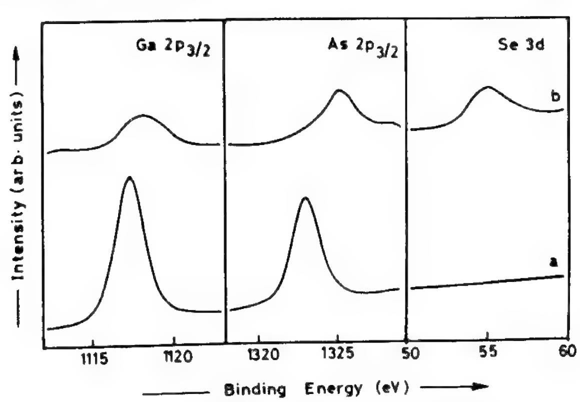

Fig.5. XPS spectra of (a) clean and (b) SeS_2 treated GaAs (100).

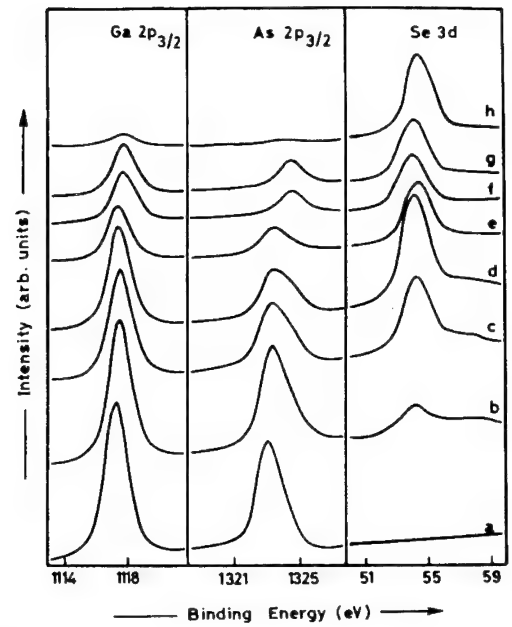

Fig. 6. XPS core level spectra of $Ga2p_{3/2}$, As $2p_{3/2}$ and Se 3d of GaAs (100) for (a) clean GaAs and (b) 1A° (c) 5A°, (d) 10A° (e) 25A° (f) 35A° (g) 41A° and (h) 43A° thickness of Se.

Thick selenium film (here 10 sec SeS_2 treated) can be partially dissolved in CS_2 solution. This enhances the PL intensity again which is shown in fig. 4. However after five minutes in CS_2 the intensity slowly started reducing. But even by dipping it in CS_2 for about sixty minutes it was not possible to completely remove the selenium on GaAs. This means that selenium which forms a thick amorphous film on the surface possibly dissolves into CS_2 solution. However, selenium directly bonded to GaAs surface or incorporated in the anion sites may not be displaced easily. This give rise to good PL intensity for the substrate.

Fig. 5 illustrates the Ga $2p_{3/2}$, As $2p_{3/2}$, and Se 3d levels for SeS_2 treated sample alongwith the in-situ cleaned GaAs (100) sample. It is observed that Ga $2p_{3/2}$ peak is located at 1118.2 eV and As $2p_{3/2}$ at 1325.0 eV. The clean sample Ga $2p_{3/2}$ is at 1117.3 eV. Thus there is a shift of ~ 0.9 eV for Ga $2p_{3/2}$ peak which is slightly larger than the band bending shift of ~ 0.62 eV expected [7-9] for selenium passivated surface. The band bending shift was determined to be ~ 0.5 eV for the in-situ deposition experiments described later. It is therefore likely that Ga $2p_{3/2}$ peak is showing chemical shift of ~ 0.2 eV indicating Ga - Se bond. Due to close electronegativity values of As and Se Ga-Se bond is not expected to show considerable shift in the binding energy. The peak at 1325.0 eV is clearly due to As_2Se_3 phase[6].

The structural quality of the interface created also determines the efficiency of passivation. A junction of excellent structural quality and low density of dangling bonds at the interface is capable of passivating the surface while disordered interface gives rise to increased defect state density leading to significant band bending and Fermi level pinning. Hence the growth of interface is of particular importance. Though various methods have been used to deposit Se on GaAs surfaces, all the treatments gave rise [7-9] to a considerable reduction in the band bending. In the present case, we have also therefore performed in-situ Se deposition on GaAs so as to compare it with SeS_2 treated surface. Deposition of selenium was started with a thickness as low as 1A°. The $Ga2p_{3/2}$, As $2p_{3/2}$ and Se

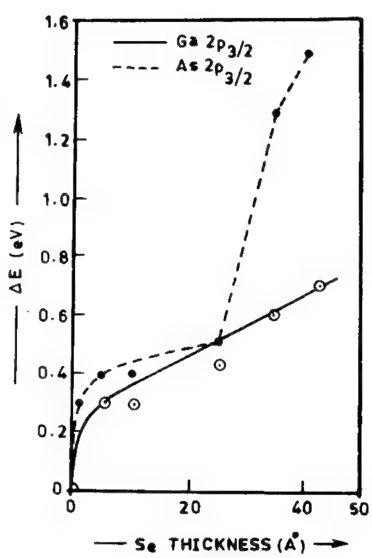

Fig. 7. Variation in the Ga2p and As 2p binding energies with increasing Se thickness.

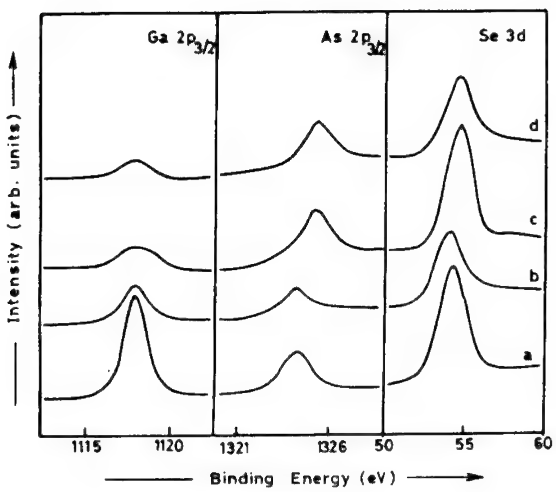

Fig. 8. XPS core level peaks of Se deposited and SeS_2 treated GaAs surface before and after Au deposition. (a) Se treated (in-situ) (b) after Au deposition (c) SeS_2 treated (d) after Au deposition.

3d core levels of the cleaned as well as Se deposited GaAs are shown in fig. 6. The substrate is kept at room temperature throughout the experiment. The absence of oxygen in the sample was ensured before and after each deposition. As shown in fig. 6a and b, clean GaAs shows $Ga2p_{3/2}$ and $As2p_{3/2}$ at 1117.3 and 1323.0 eV respectively, indicating the absence of any oxides. As shown, less than 5A^o thickness of Se gave rise to a broad peak with binding enegy varying from 53.0 to 59.0 eV. This kind of a broad peak suggesting Se in multioxidation states has been observed earlier [6] during the aqueous deposition of Se. Se 3d peak in fig.6(c) shows considerable changes as the coverage increases. The broad peak at low thicknesses gradually decreases in its FWHM on further deposition and as the thickness increases above 10A^o, the FWHM decreases to less than 3.0 eV. Se 3d shows a narrow peak at 54.3 eV when the thickness increases above 20 A^o. The $Ga2p_{3/2}$ and $As2p_{3/2}$ do not show any substantial changes in the peak shape but peak positions of $Ga2p_{3/2}$ and $As2p_{3/2}$ change gradually towards the higher binding energy. The As $2p_{3/2}$ binding energy increases from 1323.0 eV for cleaned sample to 1323.4 eV at a selenium thickness of 10 A^o. On further deposition upto 35 A^o the binding energy reaches 1324.3eV which remains stable on further deposition. This peak corresponds to As_2Se_3 [6,11] which is analogous to the As_2S_3 phase formed after sulfide treatments.

In fig. 7 we plot binding energy shifts for Ga $2p_{3/2}$ and As $2p_{3/2}$ with selenium deposition. With deposition of Se binding energy of both Ga $2p_{3/2}$ and As $2p_{3/2}$ keep on shifting rigidly within an accuracy of 0.1eV upto a Se thickness of 25 A^o. Fermi level shift by 0.5 eV can thus be deduced from the present experiments. This value is very close to the value, reported for the band bending by Takatani et al [9] for Se covered GaAs (001) surface at 600^{o}C using As 3d and valence band maximum. Thus the Fermi level is located at ~ 1.2 eV above the valence band maximum i.e. close to the conduction band minimum at room temperature. The Ga/As ratio of cleaned sample is ~ 2.0 which increases further. Our results thus suggest that there is a possibility of Se diffusion to a few monolayers replacing some of the As atoms. This may result in to a Ga_2Se_3 phase which has a zinc blende crystal structure. It has a lattice constant of 5.43 A^o close to that of GaAs. Structural coherence is maintained by Se deposition. It has been proposed earlier that liberated As reacts with some amount of selenium forming As-Se compound which may evaporate due to its high vapour pressure. However presence of As_2Se_3 phase needs to be taken into account. Ga_2Se_3 structure is then terminated at selenium monolayer. There are no Ga dangling bonds on the surface. STM pictures supports this.There is thus an indication of binding between Ga-Se but binding energy shift is very small. At a coverage of 35 A^o a sudden shift in As has been observed. The binding energy of As $2p_{3/2}$ at 1324.3 eV suggest the presence of As_2Se_3 phase.

In any passivation scheme, along with the formation of a terminating passivating layer, it is equally important to preserve the passivation. Selenium passivated surface was found to be covered with SeO_2

by Sandroff et al. [6]. Since any semiconductor device involves metal - semiconductor contact for interconnections it is worthwhile to check the stability of the passivating layer on metal depostion. Deposition of Palladium on a Se/GaAs interface has shown that the interface remains stable upto a thickness of 3 A^{o} [23]. Metal depositions can also be useful in preventing the disadvantages caused by oxidation. Deposition of an Al overlayer was useful [24] in this regard. Fig.8 shows the XPS core level spectra before and after gold deposition. Each surface was found to have As_2Se_3 as the terminating phase. Although reduction in the intensity of $Ga2p_{3/2}$ and As $2p_{3/2}$ was observed due to Au coverage ratio of Ga/As shows some increase. Thus there may be some outdiffusion of Ga in this case. Further work on the aspect of stability of selenium covered GaAs is in progress.

CONCLUSIONS

1. Passivation due to selenium and its long term stability has been found to be better than sulfide or phosphorous chemical treatments.

2. There is an indication of As_2Se_3 phase as well as Ga-Se bond formation with SeS_2 treated GaAs (100) surface.

3. Selenium deposition on n-GaAs (100) gives rise to a shift in the Fermi level position, close to the conduction band minimum.

4. There may be some outdiffusion of gallium when gold is deposited on selenium treated surface of n-GaAs (100).

ACKNOWLEDGEMENT :

SKK would like to thank the University Grants Commission and Beena Kuruvilla CSIR, India, for financial support.

REFERENCES :

[1] C.J. Sandroff, R.N. Nottenburg, J.C. Bischoff and R. Bhat, Appl. Phys. Lett. **51**, 33, (1987).

[2] C.J.Sandroff, M.S.Hegde, L.A.Farrow, C.C.Chang and J.P.Harbison, Appl. Phys. Lett. **54**, 362, (1989).

[3] M.S. Carpenter, M.R. Melloch and T.E. Dungan, Appl. Phys. Lett. **53**, 66, (1988).

[4] C.M. Wilmensen, P.D. Kirchner and J.M. Woodall, J. Appl. Phys. **64**, 3287, (1988).

[5] E.Yablonovitch, T.J. Gmitter and B.G.Bagley, Appl. Phys. Lett. **57** ,224, (1990).

[6] C.J. Sandroff, M.S. Hegde and C.C.Chang, J. Vac. Sci. Technol. **B7** ,84,. (1987).

[7] C.J.Sandroff, M.S.Hegde, L.A.Farrow, R.Bhat, J.P.Harbison and C.C.Chang., J. Appl. Phys. **67**, 586, (1990).

[8] S.A.Chambers and V.S.Sundaram, Appl. Phys. Lett **57**, 2342, (1990).

[9] Shinichiro Takatari, Takeshi Kikawa and Masatosh Nakazawa, Phys. Rev. **B45**, 8498, (1992).

[10] T.Scimeca, Y.Watanabe, F.Maeda, R.Berrigan and M.Oshima., Appl. Phys. Lett. **62**, 1667, (1993).

[11] Beena Annie Kuruvilla, S.V.Ghaisas, A. Datta, S.Banerjee and S.K.Kulkarni, J. Appl. Phys. **73**, 4384, (1993).

[12] S.A.Chambers and V.S.Sundaram, J. Vac. Sci. Technol. **B9**, 2256, (1991).

[13] T.Scimeca, Y.Watanabe, R.Berrgan and M.Oshima, Phys. Rev. **B46** ,10201, (1992-II).

[14] H.Shigekawa, T.Hashizume, H.Oigawa, K.Motai, Y.Mera, Y. Nannichi, T.Sakurai., Appl. Phys. Lett. **59,** 2986, (1991).

[15] D.K. Biegelsen, R.D. Bringans, J.E. Northrup and L.E. Swartz, Phys. Rev. **B49,** 5424, (1994).

[16] R.N. Nottenburg, C.J. Sandroff, D.A. Humphrey, T.H. Hollenbeck, and R. Bhat, Appl. Phys. Lett. **52,** 218, (1988).

[17] B.K. Skromme, C.J. Sandroff, E. Yablonovitch and T. Gmitter, Appl. Phys. Lett. **51**, 2022, (1987).

[18] C.M. Wilmensen, P.D. Kirschner, J.M. Baker, D.T. McInturff, G.D. Pettit and J.M. Woodall, J. Vac. Sci. Technol. **B6,** 1180, (1988).

[19] B. A. Cowans, Z. Dardas, W.N. Delgass, M.S. Carpenter and M.R. Melloch, Appl. Phys. Lett. **54** , 365, (1989).

[20] M.S. Carpenter, M.R. Melloch B.A. Cowans, Z. Dardas and W.M. Delgass, J. Vac. Sci. Technol. **B7** , 845, (1989).

[21] C.J. Spindt, D. Liu, K. Miyano, P.L. Meissner, T.T. Chiang, T. Kendelewicz, I Lindaw and W.E. Spicer, Appl. Phys. Lett. **55,** 861, (1989).

[22] H. Hirayama, Y. Matsumoto, H. Oigawa and Y. Nannichi, Appl. Phys. Lett. **54**, 2565, (1989).

[23] Rebecca Berrigan, Yoshio Watanabe, Tom Scimeca and Masaharu Oshima., Jpn. J. Appl. Phys. **31**, 3523, (1992).

[24]. T.Scimeca, K.Prabhakaran, Y.Watanabe, R.Berrgan and M.Oshima, Appl. Phys. Lett. **63,** 1807, (1993).

Materials Science Forum Vols. 185-188 (1995) pp. 179-184

Passivation of GaAs with sulphur surface treatment and UVCVD silicon nitride cap layer

H. Sik, J.L. Courant and B. Sermage

France Télécom, Centre National d'Etudes des Télécommuniations / PAB, Laboratoire de Bagneux, 196 Avenue Henri Ravera, F-92225 Bagneux Cedex, France

Keywords: GaAlAs/GaAs heterojunction bipolar transistor (HBT), sulphur passivation, silicon nitride, ultra-violet chemical vapour deposition (UVCVD)

Abstract: We have investigated the effects of the sulphur treatment ($(NH_4)_2S_x$ solution) on p-GaAs, and the influence of UVCVD silicon nitride deposition temperature on the as-treated surfaces. Ageing experiments have been performed on samples either untreated or S-treated, covered and not covered with UVCVD silicon nitride. The optimised deposition process (from 150°C to 240°C) does not change the minority carriers lifetime (210 ps), and this value is not affected after more than a year at room atmosphere. HBTs passivated in such conditions exhibit a 2-fold increase of current gain which does not degrade either with time or under electrical stress.

INTRODUCTION

GaAlAs/GaAs HBTs are widely studied for their potential application for ultrahigh speed logic and microwave power devices. But the reduction of dimensions, necessary for higher switching speed operation, leads to a drastic loss of DC current gain. The uncontrolled excess leakage base current results from the high level of electron-hole recombinations at the extrinsic base surface (fig.1).

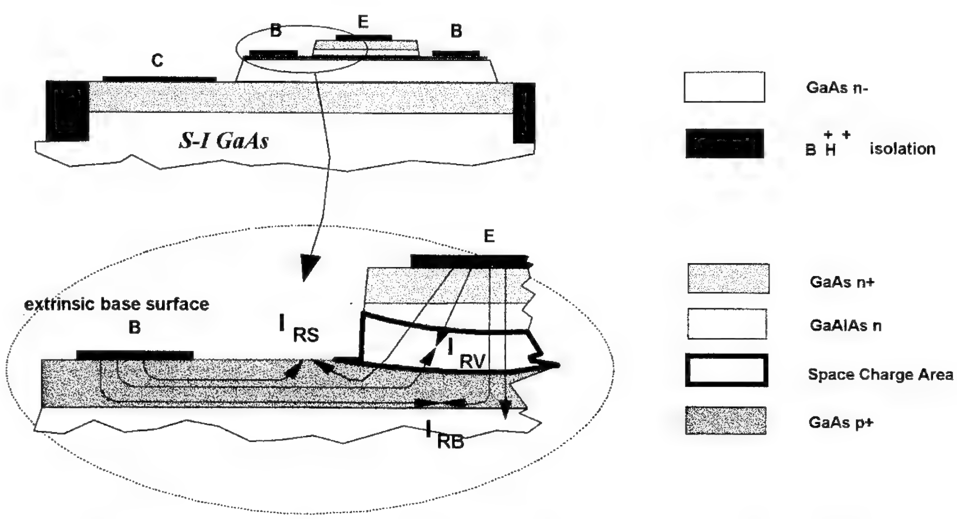

fig.1: Heterojunction bipolar transistor structure. Electron-hole recombinations have to be reduced by appropriate passivation on extrinsic base surface.

The passivation of III-V semiconductors with sulphur has already been studied and results in good electronic properties: enhancement of photoluminescence level, improvement of electrical characteristics of MIS diodes [1,2]. The reason of such behaviour is generally attributed to a reduction of interface trap density or a pinning of the Fermi level far from midgap, but the question is still being debated. However, the stabilisation of such a treatment is difficult to obtain, essentially due to the high reactivity of the treated surface. As the sulphured surface is extremely fragile, it is necessary to use a soft dielectric deposition technology in order to encapsulate it.

The ultraviolet chemical vapour deposition (UVCVD) is a low temperature (from room temperature to 240°C), ion bombardment free technique, which responds to these objectives and has already been used with success on fragile III-V semiconductors such as InP, GaInAs [3].

The purpose of this work is to show that the passivation of small dimensions HBTs, using S treatment, encapsulated with an UVCVD technique, permits to obtain the two essential characteristics for a passivation process : (1) reduction of the electron-hole recombination, and (2) stability of this effect with time.

EXPERIMENTS:

The samples used to investigate the passivation effect were p type GaAs layers grown by Chemical Beam Epitaxy on p+ doped GaAs wafers. GaAs layers were 1 μm thick and doped at $2.10^{17}cm^{-3}$. The sulphur treatment was achieved in a controlled solution of $(NH_4)_2S_x$ and deionized water. The solutions were fabricated by mixing primary commercial solutions of $(NH_4)_2S$, controled amounts of elementary sulphur and deionized water. The preparations have been characterised by UV absorption spectrometry. Using a simple gaussian fit model for the absorbance of the different species present in the solutions, the mean chain length of polysulfides was obtained by the following relationship (Eq. 1).

$$< x > = \frac{[HS^-] + \sum_{i=1}^{n} i[S_i^{2-}]}{[HS^-] + \sum_{i=1}^{n} [S_i^{2-}]} \tag{1}$$

where i is the number of sulfur atoms in the polysulfide's chain. The concentration of polysulfides is deduced from the Beer's law.

UVCVD silicon nitride was deposited from SiH_4 and NH_3 gas mixture. The gaseous go through a bubbler to add a small amount of Hg to the mixture. A photosensitised reaction is obtained with a low pressure Hg lamp emitting mainly at a wavelength of 254 nm. This technique permits a deposition process at very low temperature (from room temperature to 240°C) without ion bombardment of the semiconductor surface.

The composition of sulphurized surfaces was analysed by X-photon spectrometry. The composition of silicon nitride layers was investigated by Auger electron spectrometry for oxygen contamination and infra-red transmission (FTIR) for hydrogen contamination using the method introduced by W.A. Lanford and al. [4] based on absorption of Si-H and N-H vibrations localised at about 2200 cm^{-1} and 3370 cm^{-1} respectively. The minority carrier lifetime was measured by time resolved photoluminescence with a YAG laser to characterise the stabilisation of the passivation effect The photoluminescence intensity is measured for a He-Ne laser excitation. The diameter of the spot is 2 μm and the power of the laser is 5mW.

Application to GaAlAs/GaAs HBT was achieved to demonstrate the positive effect of S-passivation on device. Ageing experiments were made to charaterise the stability of this effect on the transistor current gain.

RESULTS

Fig.2 shows the evolution of the mean value of polysulfide chain length versus the excess sulphur added in the different commercial solutions. We report on these curves the optimal excess of sulphur necessary to get a maximum improvement of the photoluminescence intensity. It is possible to make a correlation between the mean length of the sulphide chains and the maximum of the photoluminescence intensity. The corresponding optimum length of polysulfides in the solution, was close to 1.8, for every optimal preparation of the mixture.

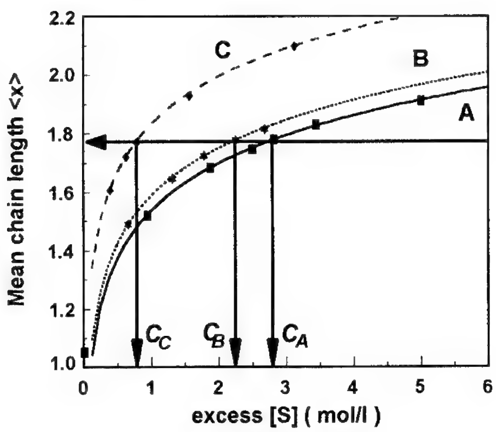

fig.2: Variation of mean chain length of sulfides with added sulfur for different preparations A, B, and C. Measurements of photoluminescence intensity on passivated p-GaAs show a maximum for excess [S] concentrations C_A, C_B and C_C. These optimal concentrations correspond to a mean chain length <x>=1.8.

It is known that ageing of the mixture has a strong influence on the treatment of the semiconductor [5] and makes this treatment not easily reproducible. The UV-visible absorption characterisation allows to follow the ageing of the mixture and makes the treatment easier to reproduce. In all the further experiments the optimised $(NH_4)_2S_x$ solution was used.

The minority carrier lifetime was measured to increase considerably (from 50 ps to 210 ps) after sulphur treatment . However, ageing experiments show that a cap layer is essential to maintain the positive effect of sulphur passivation, the treated surface beeing extremely sensitive to oxidation. In fact,at room atmosphere without any cap layer, the lifetime drops to 167 ps after 7 days and to 85 ps after 28 days.

XPS measurements reveal that after a suitable anneal, sulphur is totaly bonded with gallium as Ga_2S. Under the anneal condition, the surface seems to be more stable against atmosphere aggressions, which can be explained by the larger heat of formation of Ga_2S compared to that of As_2S_3 present on unannealed surfaces. Nevertheless, this anneal does not provide a real stability of the passivating surface layer, which must be protected.

A relatively high temperature of the deposition process is necessary to obtain Si_3N_4 with good dielectric characteristics. At 240°C, the concentration of H contaminants, measured by FTIR, is 10^{22} at.cm^{-3}, the main peak of Si-N vibration is localised at 835 cm^{-1}, close to the LPCVD Si_3N_4 value. The ratio N/O, measured by Auger spectrometry is 8, and the refractive index at 632.8 nm is 1.910. To prevent the destruction of the surface, a lower temperature seems necessary. However, the films made at lower temperature are rich in oxygen. For a deposition at room temperature the ratio N/O is 1 and the refractive index 1.695 is low, while at 150°C, the ratio N/O is 3 and refractive index rises to 1.890.

Photoluminescence measurements was performed using surfaces encapsulated with silicon nitride deposited at different temperatures. The deposition itself does not affect significantly the minority carrier lifetime as compared to PECVD (13.56 MHz) deposition techniques. The photoluminescence intensity, with a 8 fold increase after S-treatment, is unchanged after deposition of the dielectric between room temperature and 150°C, and decreased slightly for deposition at 240°C. After annealing at 300°C for one hour in an Ar-H_2 atmosphere, the gain of photoluminescence signal drops drastically for the dielectric layer deposited at room temperature. Further experiments showed a similar behaviour for the unprotected surface exposed to oxygen of air or even encapsulated with a UVCVD SiO_2 layer deposited at 180°C. In the latter case, the destruction of the passivating effect is complete. This appears to be directly correlated with the concentration of oxygen in the encapsulation layers.

The S-treated surface is very sensitive to oxygen contamination which is very detrimental for a stabilisation of the passivation effect. Because of the larger heats of formation for the oxides, the sulfur termination is likely to be unstable in the presence of oxygen. The oxygen in air or introduced in the O rich layers during deposition leads to a destruction of the sulphurized dielectric/GaAs interface. At 150°C the oxygen concentration is low enough to prevent the oxidation of the S treated surface of GaAs. Whereas absorbance peak of SiO can be observed on FTIR spectra as a shoulder on the most intense SiN peak for room-temperature deposition. This SiO absorption is not observed for the 150°C deposition. To improve the dielectric film properties, we have chosen an encapsulating process using a gradual increase of the temperature from 150°C up to 240°C to grow the film for the HBT passivation.

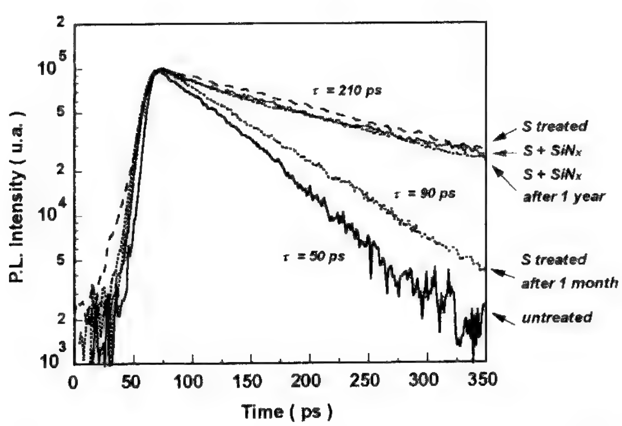

fig.3: Ageing experiments on nonencapsulated and encapsulated p-GaAs characterised with time resolved photoluminescence. Minority carrier lifetime is improved from 50 pS to 210 ps after optimised sulfur treatment, but drops drastically after 1month from 210 ps to 90 ps if not protected. UVCVD SiN_x encapsulation prevents degradation of the treated surface (no variation after 1 year).

After one year storage, it is not possible to see any difference in the minority carrier lifetime which stays at its initial value of around 210 ps. (fig.3)

PROCESSING AND CHARACTERISATION OF HBTs

The GaAlAs/GaAs HBTs were fabricated in a double mesa technology as already reported in a previous paper (ref.6). After mesa etching, samples were dipped in the optimised $(NH_4)_2S_x$ solution and encapsulated with the silicon nitride overlayer. Respectively n type AuGeNi/Ag/Au and p type Mn/Au/Ti/Au ohmic contacts were then deposited. S-passivated and unpassivated devices with various active emitter surfaces (1.5, 2 and 3x10 μm^2) processed on the same wafer were characterised electrically.

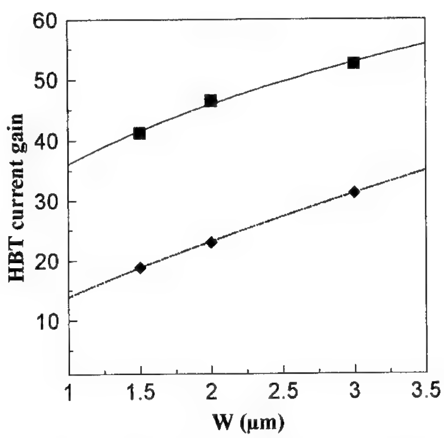

fig.4: Improvement in HBT current gain after sulfur treatment and SiN_x encapsulation. The active area length is 10µm, W is the emitter width.

Fig 4. shows the evolution of HBT DC current gain as a function of the emitter length for unpassivated and passivated devices at a collector current density of 25.10^3 A/cm^2. The curve for passivated structures shows a reduction of the current gain size effect. A 1.7-fold increase of the DC current gain was measured on 3x10 μm^2 HBT, and a 2.2-fold increase on 1.5x10 μm^2. This enhancement of the DC current gain corresponds to a reduction of the surface recombination current density by a factor 4.3 down to 2µA/µm after passivation, following the simplified relationship of Hiraoka et al. [7].

$$\frac{J_c}{\beta} = J_{B_0} + \frac{2}{w} J_{RS} \qquad (2)$$

w being the width of the emitter (i.e. 1.5, 2, 3 µm), S the emitter surface, J_{b0} the intrinsic base current density and J_{RS} the surface recombination current density.

Ageing experiments were performed on 3x10 μm^2 HBTs. An electrical stress of 4.10^4 A/cm^2 was applied for 10 hours and electrical parameters as current gain, ideality factors, leakage currents were continuously recorded. The variation of post-stressed current gain measured at 25kA/cm^2 is lower than 2%, showing the high stability of our complete passivation process. This result confirms a

previous observation of the stability of the passivating treatment after more than two years storage of the device.

CONCLUSION

We have investigated the effect of UVCVD silicon nitride on sulphurized surface of GaAs. After sulphur treatment, the samples exhibit a minority carrier lifetime rising from 50 up to 210 ps. To stabilise the passivation effect, a UVCVD silicon nitride is deposited. A high concentration of oxygen in the dielectric layer when deposited at low temperature is shown to be responsible for a degradation of the minority carrier lifetime. For deposition at 150°C the N/O ratio is 3, the H concentration is $5 10^{22}$ at.cm^{-3}, and the refractive index n=1.890. The optimised deposition process at 150°C to 240°C does not change the minority carrier's lifetime (210 ps), and this value is not affected after more than one year at room atmosphere. HBTs thus passivated in such conditions exhibit a 2-fold increase in current gain, which does not degrade after ageing under electrical stress.

REFERENCES

1) C.J. SANDROFF, R.N NOTTENBURG, J.C. BISCHOFF and R. BHAT, Appl. Phys. Lett, **51**, 1987, p.33

2)Y. NANNICHI, J.F. FAN, H OIGAWA and A. KOMA, Jpn. J. Appl. Phys., Vol. 27, **12**, 1988, L2367

3) G.POST, Y. LE BELLEGO, J.L. COURANT, A. SCAVENNEC, Materials Science & Engeneering, **B20**, 1993 , p134.

4) W.A. LANFORD, M.J. RAND, J. Appl. Phys., **49** (**4**), 1978, p.2473

5) M. PETITJEAN, Doctoral thesis, University of PARIS 6, december 1991

6) H.SIK, V. AMARGER, M. RIET, R. BOURGUIGA AND C. DUBON-CHEVALLIER,
Int. Symp. GaAs and Related Compounds, Freiburg 1993, Inst. Phys. Conf. Ser. **N°136, Chap.7**, p.473

7) Y. HIRAOKA AND J. YOSHIDA, IEEE Trans. Elec. Dev. **ED 34**, 1987, p.721

Materials Science Forum Vols. 185-188 (1995) pp. 185-190

Silicon nitride and oxide deposited by direct photolysis on sulfur treated GaAs and InP: Application to III-V passivation

N. Proust[1], E. Guillot[2], M. Petitjean[3], M. Beguet[1], J.F. Chapeaublanc[1] and J. Perrin[4]

[1] Thomson-CSF, LCR, F-91404 Orsay Cedex, France

[2] CNET Lannion, Route de Trégastel, F-22301 Lannion, France

[3] Sté Riber, 133 Bd. National, F-92503 Rueil Malmaison, France

[4] Ecole Polytechnique, Physique des Interfaces et des Couches Minces, F-91128 Palaiseau Cedex, France

Keywords: Silicon oxide, silicon nitride, UVCVD, MIS diode, passivation, sulfur, photoluminescence

ABSTRACT

We report on silicon nitride and oxide deposited by direct photolysis at 185 nm of NH_3-SiH_4 and N_2O-SiH_4 mixture.
Films are deposited at low temperature (200-300°C) under reduced pressure on GaAs and on InP. A quasi-stoechiometric insulator can be obtained for a particular composition of the gas phase. Electrical characterization is done on MIS (Metal Insulator Semiconductor) diodes. After dipping GaAs and InP in hot $(NH_4)_2S_x$ solution and after appropriate annealing procedure the density of states is significantly reduced. Good results are obtained on InP : $N_{SS} \approx 2.10^{11} eV^{-1}cm^{-2}$, a very small hysteresis and a 0.2 V flat band shift voltage are measured. After sulfur treatment on GaAs a significant improvement is observed for the C(V) curves. High resistivities ($>5.10^{15}\Omega cm$) and high critical fields ≈ 3MV/cm at $10^{-9} Acm^{-2}$ have been measured. Photoluminescence at 300°K and at 532 nm has been done on GaAs passivated samples. A significant enhancement of the signal of factor of 30 has been observed.
Sulfur treatment on III-V materials such as InP and GaAs followed by a low temperature, non aggressive, insulator deposition such as UVCVD (Ultra Violet Chemical Vapor Deposition) seems to be a good compromise for device passivation.

INTRODUCTION

Silicon nitride and oxide films have been widely studied and used for various applications such as :

- capacitor dielectrics in microelectronics ;
- TFT's gate insulator for active matrix liquid crystal displays [1] ;
- gate insulator in power field effect transistors based on GaInAs [2] on InP [3] [4] ;
- final encapsulation films for discret components or integrated circuit chips [5, 6].

In this study silicon nitride and silicon oxide are deposited at low temperature by direct photolysis of gas mixtures using the 185 nm radiation of a low pressure mercury lamp [7, 8].
We are reporting here on bulk and interface properties of both insulators. In order to lower the interface state density a sulfur treatment of InP and GaAs has been developped.
Room temperature photoluminescence enhancement at 532 nm has been measured on passivated GaAs surfaces.

DEPOSITION

Direct photolysis (without Hg atoms) of gas mixtures at 185 nm is performed in a 5 liter stainless steel chamber with a heatable substrate holder. The UV radiation emitted from a Hg lamp enters the chamber through a 10 cm diameter suprasil quartz window. A shutter located between the lamp and

the window allows good control of the photolysis initiation after lamp stabilization. At 185 nm we estimate the power density of our lamp to be 5 mW/cm2. The window substrate distance can be varied, the optimum for our experiments is 12 mm. The base pressure before deposition in the reactor is 1.3 x 10^{-4} Pa. Pressure during deposition is regulated by a throttle valve and measured by a capacitance manometer. A schematic view of the reactor is reported on Fig. 1. The temperature can be varied from 200°C to 400°C in our equipment.

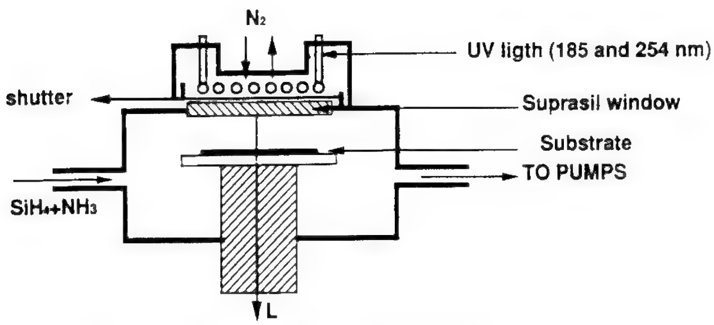

Fig. 1. Schematic diagram of the UV–CVD reactor

For nitride deposition the gas phase is a NH_3-SiH_4 mixture while for the oxide we use N_20-SiH_4. The pressure deposition is 524 Pa for Si-N-H and 655 Pa for Si-O-H. In both cases the variable process parameter R = (SiH_4)/(NH_3) or (SiH_4)/(N_2O) is varied from 1 to 10% in order to determine the best insulator from the electrical point of view.

ATOMIC COMPOSITION

Si, N, O content has been measured by Nuclear Reaction Analysis (NRA). Accuracy for Si and N is about 5% while for O it is 3%. H content has been determined by Elastic Recoil Detection Analysis (ERDA), the error in that case is about 10%. Results are reported on Fig. 2 for nitride and on Fig. 3 for oxide.

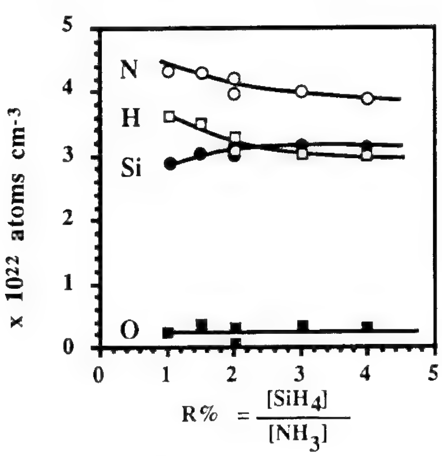

Fig 2. Atomic composition of silicon nitride films deposited at 250°C

Nitride atomic composition in atoms per cubic centimeter of the deposited films is plotted in Fig. 2 versus the injected $R = [SiH_4]/[NH_3]$ ratio. The total amount of Si and N atoms ([N] + [Si] in atoms per cubic centimeter) is found to be constant and equals to 7 x 10^{22} atoms.cm^{-3}. As the gas phase ratio R is varied from 1 to 4%, three different kinds of silicon nitride can be observed :

. For $0.5 < R < 2\%$ a nitrogen rich material is observed. Stoechiometry decreases from 1.5 for silane depletion deposition conditions to 1.33.

. For $R \approx 2\%$ the stoechiometry N/Si = 1.33 is achieved. Taking into account the hydrogen content, the global formula of the stoechiometric material is $Si_3N_4H_3$.

. For $R > 2\%$ a slicon rich nitride is deposited. N/Si varies from 1.33 (R = 2%) to 1.2 when the gas phase is silane rich (R = 4%).

The oxygen contamination 0/(Si+ N + H) is lower than 2% and mainly due to the residual pressure of the reactor. In this case we do not observe the substitution of nitrogen by oxygen as far as N+ Si remains constant with varying R. N-rich samples exhibit larger H content than Si-rich films ; this has also been observed for PECVD deposited silicon nitride.
The stoechiometry is correlated to n, the refractive index : it varies from 1.77 (R = 1%) for N-rich to 1.86 (R = 10%) for Si-rich silicon nitride. The refractive index of the low temperature deposited and stoichiometric silicon nitride is 1.80 (T_D = 250°C) which is still far from the value of 2 observed for non hydrogenated Si_3N_4 prepared at high temperature.

Oxide atomic composition is plotted in Fig. 3 versus $R = [SiH_4]/[N_2O]$. The gas phase composition is varied from 1% to 8%.

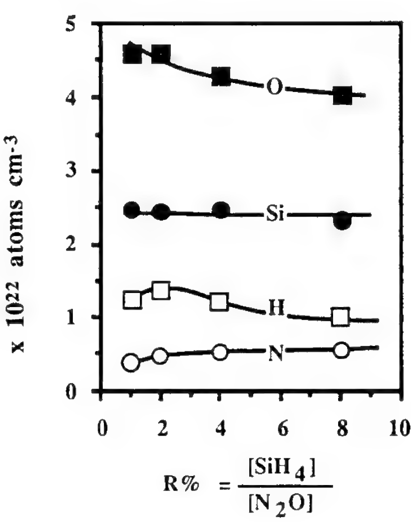

Fig. 3. Atomic composition of silicon oxide films deposited at 250°C

Si is found to be constant as R is varied, while variations are observed for O, H and N. Depending on R, the N contamination is between 4 and 7% and due to N_2O use.

. For $R < 2\%$; O/Si is increasing but the value is less than 2 ; H and N contaminations are low, respectively less than 15 and 6%.

. For R = 2%, O/Si is maximum (1.87 instead of 2 for stoechiometric silicon oxide). The hydrogen atomic concentration is also at a maximum, and of the order of 15%. The insulator chemical formula can be written as $SiO_{1.87}N_{0.20}H_{0.55}$.

. For R > 2%, the O and H atomic contents are decreasing, while nitrogen incorporation is increasing.

n varies from 1.525 (R = 0.5%) to 1.56 (R = 8%) when films are deposited at 250°C. The quasi-stoechiometric material obtained for R = 2% exhibits a refractive index of 1.535.

ELECTRICAL

Electrical properties of 800-1000 Å quasi-stoechiometric films are checked using MIS diode structures on n-type substrates or epilayers. Aluminium dots (600 µm in diameter) are evaporated onto as deposited or annealed samples.

A quasi-static I(V) method is used to determine the insulator bulk properties. We measure the capacitance of the MIS structure at 0 V, the resistivity and the "critical field" E_C corresponding to an MIS diode leakage current density of 10^{-9} A/cm^2. This E_C is very different from the breakdown field, which is measured as 10^{-3} A/cm^2.

C(V) experiments are carried out on MIS diodes at 1 MHz and at 10kHz (dV/dt = 100 mV/s) in order to characterize the interface between insulator and semiconductor. A Terman analysis can be performed to estimate the interface state density N_{SS}.
Before UVCVD deposition, InP and GaAs samples are sulfur treated in order to be deoxidized. The effectiveness of this procedure has been checked by XPS [9]. The samples are dipped for 10 minutes in a $(NH_4)_2Sx$ solution heated at 60°C or 80°C [9]. After a quick DI water rinsing they are placed in the UVCVD chamber for annealing at 350°C for 1 hour under N_2. This step is immediately followed by the insulator deposition itself.

Results of silicon oxide deposited at 200°C on InP and of silicon nitride deposited at 200°C on GaAs are reported in this paper. Generally a final thermal treatment at 300°C for one hour under N_2 is performed before electrical measurements.

- Electrical results on InP can be summarized as follows :

. From quasi-static I(V) measurements we have deduced a resistivity of 10^{15} ohm.cm and a critical field E_C (for J = 1 nA cm^{-2}) of 3.7 MV cm^{-1}, which indicates quite good bulk properties for the quasi-stoechiometric material (R = 2%).

. C(V) at 1 MHz has been performed on MIS diodes ; without sulfur passivation, N_{SS} is large and of the order of 4.10^{12} eV^{-1} cm^{-2}. S passivated InP surface is prepared by dipping in an $(NH_4)_2\ S_X$ solution. The S treatment improves the interface properties, and good results are obtained. Very small variation between C(V) at 1 MHz and 10 kHz is observed. N_{SS} determined by Terman analysis is ≈ 2.10^{11} eV^{-1} cm^{-2}. The mobile charge density deduced from the hysteresis is low, and the flat band shift voltage is small (≈ 0.2 eV) (Fig. 4).

- Electrical results on GaAs can be summarized as follows :

. From quasi-static I(V) a high nitride resistivity is obtained. $\rho = 5.10^{15}$ Ωcm cm and E_C = 4 MV cm^{-1} for the quasi- stoichiometric material (R = 2%).

. C(V) at 1 MHz has been performed on MIS diodes without sulfur passivation. A very large density of states at the interface is commonly observed and the Fermi level is pinned in the

band gap. After sulfur treatment a significant improvement is observed for C(V) curves. Hysteresis is still large ($Q_{hyst} \approx$ 8.4x10^{11} cm^{-2}) and $V_{FB} \approx$ + 3.3 V (Fig. 5) and N_{SS} is found to be in the range 6-4x10^{11} eV^{-1} cm^{-2}.

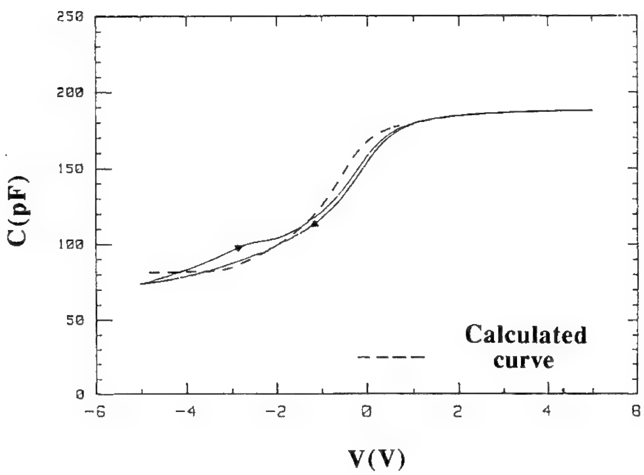

Fig. 4. C(V) at 1 MHz silicon oxide on n type InP

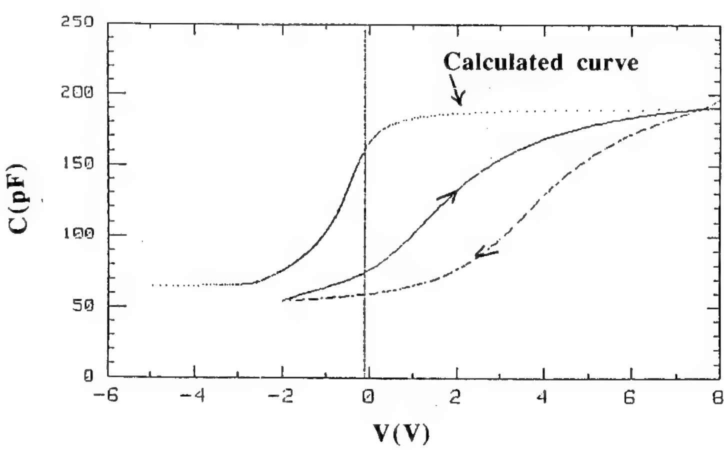

Fig. 5. C(V) at 1 MHz silicon nitride on n type GaAs

PHOTOLUMINESCENCE

Photoluminescence has been done at room temperature with a 532 nm YAG laser through insulator films deposited on GaAs. Two types of laser spot have been used. For the extended spot (SE) there are 10 mW on 350 μm diameter and for normal spot (NS) there are 10 mW on 20 μm diameter. A major difference has been observed between oxides and nitrides ; nitride photoluminescence is always stable as a function of time for ES or NS which is not true for oxide films. A comparison has been done for nitrides films having the same thickness and deposited under the same conditions on GaAs sulfur treated or not. For annealed samples an enhancement of a factor of 30 is observed for NS conditions. Without sulfur the photoluminescence pic is maximum at 871.9 nm and full width at half maximum (FWHM) ≈ 25.00 nm while with sulfur we observed a small shift in wavelength (868.21 nm) and a variation of FWHM (31.93 nm). Some more complementary experiences have to be done in order to explain what is observed here. Our results are in good agreement with those published in litterature [10].

CONCLUSION

Silicon nitride and oxide films of high quality (high resistivity and critical field) have been deposited by UVCVD at low temperature on InP and GaAs. After oxide removal by a $(NH_4)_2\,S_X$ treatment interface properties are improved which can be observed by C(V) at 1 MHz. The maximum of the room temperature photoluminescence peak is increased of a factor of 30 when GaAs is sulfur treated before nitride deposition. Preliminary encouraging results have been obtained on GaAs but complementary experiences have to be done. However sulfur treatment combined with UVCVD deposition seems to be a good compromise for device (FET's, HBT's and lasers) passivation.

ACKNOWLEDGMENT

The authors gratefully acknoledge : Dr B. Agius for RNA and ERDA measurements ; M. Champagne for photoluminescence measurements. This work has been partially supported by DRET.

REFERENCES

[1] Y. Kaneko, A. Sasano, T. Tsukada, R. Oristsuki and K. Suziki, Extended abstracts of the 18th Conf. on SSDM, Tokyo, Japan, D-11-3, 699 (1986)

[2] M. Renaud, P. Boher, J. Schneider, J. Barrier, D. Schmitz, M. Heyen and H. Jürgensen, Journal de Physique, C4, 9, **49,** 209 (1988)

[3] H. Ishimura et al., Inst. Phys. Conf. Ser. n° 106, Chapter 6, pp. 405-410, Int. Symp. on GaAs and Related Compounds, (1989)

[4] P. Saunier et al., IEEE Electron Dev. Lett., **11**, p. 48 (1990)

[5] E.Y. Chang, G.T. Cibuzar and K.P. Pande, IEEE Trans. Electron Devices, **35**, 9, 1412 (1988)

[6] N. Arnold, L. Schleicher and T. Grave, GaAs and Related Compounds, Inst. Phys. Conf. Ser., **91**, 455 (1987)

[7] M. Petitjean et al., Appl. Phys. A, **54**, 95 (1992)

[8] M. Petitjean et al., Appl. Surf. Sci., **46**, 189 (1990)

[9] M. Petitjean et al., Sensors and Actuators A, **33**, 33 (1992)

[10] S. Shikata and H. Hyashi, J. Appl. Phys. **70**, 7, 3721 (1991).

Materials Science Forum Vols. 185-188 (1995) pp. 191-198

Surface passivation of III-V compound semiconductors with chalcogen atoms

H. Oigawa, H. Shigekawa and Y. Nannichi

Institute of Materials Science, University of Tsukuba, Tsukuba, Ibaraki 305, Japan

Keywords: Surface passivation, chalcogen treatment, III-V compound semiconductor, interface state density, surface analysis

Abstract

Surface passivation of III-V compound semiconductors with chalcogen atoms (S, Se, Te) is presented in the light of electrical characteristics and data on surface analyses. The chalcogen treatment is effective for the reduction in surface/interface defect density and the effect is universal to many III-V compounds. Based on the experimental data, we propose a model to explain its effectiveness, and suggest the surface stabilization by chalcogen. Structurally, chalcogen atoms occupy the near-site of V elements on top of the surface and III-chalcogen bonds are formed. Such a structure may be stabilized through charge transfer of excess electrons into the dangling bond states.

Introduction

The apparent success of Si in electronic devices and integrated circuits depends essentially on controlling its surface/interface properties. However, those of III-V compound semiconductors remain uncontrollable to date, except for the use of heterojunctions, initially, of GaAs/AlGaAs. In particular, the presence of oxygen at the surface induces an increase in the surface recombination velocity (SRV), and degrades the performance and reliability of surface devices. In recent years, several surface treatments with sulfide solution were developed to suppress the SRV, in other words, to increase the photoluminescence (PL) intensity. The first of such is sodium sulfide ($Na_2S{\cdot}9H_2O$) treatment on GaAs reported by Sandroff *et al.*[1] Although it is recognized that Na_2S treatment produces a decrease in SRV, it is difficult to tell whether the effect is due to the reduction in the surface state density or in the capture cross section of defects caused by band bending. This is because the residual crusty film of Na_2S prevents us from fabricating the devices to measure its electronic properties. Moreover, the effect is easily lost after rinsing its film in water, and an accumulation of Na^+ ions on the surface is undesirable for the MIS devices.[2]

So we tried other chemicals and found more effective and dependable surface treatments on GaAs with ammonium sulfide ($(NH_4)_2S$) and ammonium polysulfide ($(NH_4)_2S_x$) solutions with excess sulfur. In order to clarify the difference in treatment effect of $(NH_4)_2S/(NH_4)_2S_x$ from Na_2S, we investigated the surface in both aspects of electrical characteristics and structures. We also compared the effect on various III-V compounds of GaP, (AlGa)As, InP and InAs with that on GaAs, because it is expected that the process is applicable to heterostructure devices. Electrical characteristics of Schottky and MIS structures were measured to estimate the density of surface/interface states. Surface structure was examined by using various surface analysis techniques such as Auger electron spectroscopy (AES), low-energy electron energy loss spectroscopy (LEELS), photoemission spectroscopy (PES) and reflection high-energy electron diffraction (RHEED). Based on those experimental data, we propose a model to explain the universal effectiveness of $(NH_4)_2S_x$ treatment on III-V compounds. Our model is extended to the surface treatment with chalcogen atoms other than S, that is, Se and Te. The exact position of chalcogen adsorbates in respect to the host atoms of substrate was determined by means of coaxial impact collision ion scattering spectroscopy (CAICISS), scanning tunneling microscopy (STM) and X-ray standing wave (XSW) techniques. Finally, we examined the oxidation of chalcogen-passivated surface, because the effect slowly and mildly degrades in room air.

$(NH_4)_2S_x$ treatment on III-V compound semiconductors

The procedure of $(NH_4)_2S_x$ treatment follows a simple wet process. A sample etched in a normal way is dipped into the treatment solution. We used the $(NH_4)_2S_x$ solution with 8 % of sulfur, which is readily available from venders. After taking off the sample out of solution, droplets on the surface are blown off with a dust-free jet of N_2. In this stage, a thin yellowish film of amorphous sulfur is usually observed. In vacuum at room temperature (RT), however, the surface changes its appearance from yellowish to shiny crystalline reflection because of a sublimation of amorphous sulfur. As described later more in detail, the treated surface is stabilized by heating between c. 250 °C and 520 °C in vacuum. The heat treatment is essential in obtaining a stabilized surface.

Figure 1 shows the difference in Schottky barrier height (SBH) on III-V compound semiconductors between before and after the treatment. In Fig. 1(a), it is clear that SBHs on the as-etched surfaces of GaP, GaAs and InP are almost unchanged, whereas those on the treated surfaces vary with the work function of deposited metal. According to a simple interfacial layer model, it is suggested that SBH on the treated surface approaches to the calculated value assuming no pinning traps. In other words, the $(NH_4)_2S_x$ treatment is effective for a decrease in the interface state density. This holds true also in (AlGa)As with the different contents of Al, as shown in Fig. 1(b). The similarity of these electrical properties assures the effectiveness of the $(NH_4)_2S_x$ treatment on III-V compounds, though the quantitative difference suggests the difference in effectiveness of the treatment.[3]

The reduction in the interface state density by $(NH_4)_2S_x$ treatment is also observed in the electronic properties of MIS capacitors. A significant improvement in the frequency dispersion of the MIS C-V characteristics is obtained by the treatment. Its interface state density is estimated from the 1 MHz C-V characteristics by Terman's method. In the case of GaAs, very low state density of 1 x 10^{11} $cm^{-2} \cdot eV^{-1}$ was successfully attained in the MIS structures, which were fabricated on the $(NH_4)_2S_x$-treated substrate using resistive-heating evaporated SiO_x.[4] All the results on the Schottky characteristics, the MIS C-V characteristics, and the MIS deep level transient spectroscopy (DLTS) measurement consistently indicate that the effect of $(NH_4)_2S_x$ treatment on many III-V compounds is a remarkable reduction in surface/interface defect density rather than a band bending caused by the presence of polar substances on the surface.

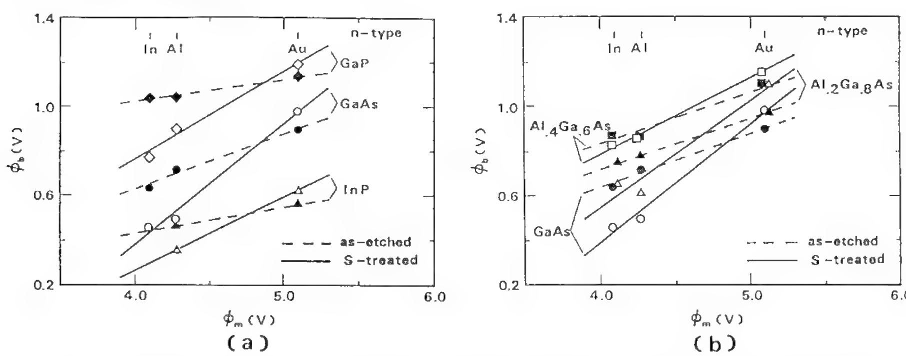

Fig. 1. Dependence of SBH on the work function of deposited metal. Schottky barriers were fabricated on the n-type (001) surfaces of various III-V compounds: (a) GaP, GaAs and InP, and (b) GaAs, $Al_{0.2}Ga_{0.8}As$ and $Al_{0.4}Ga_{0.6}As$.

A model for effectiveness of $(NH_4)_2S_x$ treatment

Combining all the surface analysis data obtained by AES, LEELS, PES, STM and RHEED, we propose a model to explain the effectiveness of the $(NH_4)_2S_x$ treatment, followed by a comparison with $(NH_4)_2S$ and Na_2S. For simplification, we explain only the case of well-studied GaAs, although our model is adaptable for many III-V compound semiconductors other than GaAs.[5] Figure 2 illustrates a model of GaAs surface with $(NH_4)_2S_x$ treatment.

The as-etched surface of GaAs is covered with a native oxide layer composed of Ga_2O_3 and As_2O_3 (Fig. 2(a)). The thickness of this layer is about 1 nm. Also observed is that cluster of elemental As, which is probably produced by a preferential formation of Ga oxide, is present in the oxide layer. We presume that interface region between oxide and GaAs is defective due to the off-stoichiometry of GaAs. When the as-etched sample is dipped into the $(NH_4)_2S_x$ solution, the oxide film is quickly etched away to reveal an oxygen-free surface of GaAs. Then the surface is instantly covered with reactive sulfur species such as S_x. This sulfurization reaction is considered not to produce the surface defects in GaAs because of the peculiarity of sulfur which nature is much different from that of other materials such as metals. For example, the sulfides of gallium and/or arsenic could form the layered structure. Since sulfides of GaAs dissolve in the alkaline solution of $(NH_4)_2S_x$, the reactions continue during a soak of the sample in it and thus the etching of GaAs layer resumes. This corresponds to the removal of surface defective layer of GaAs. The etching effect is also useful for flattening the surface. After the blown-dry process, a further precipitation of sulfur proceeds to form an amorphous layer (Fig. 2(b)). The amorphous layer of sulfur isolates the GaAs surface from the active atmosphere such as air. In vacuum, however, the amorphous layer of sulfur is so volatile that it sublimes and

disappears, leaving a monomolecular layer of sulfur on the top of GaAs. This indicates that sulfur atoms are chemically bonded with the GaAs surface.

The surface chemistry of sulfur was investigated in detail, by means of synchrotron radiation photoemission spectroscopy (SRPES).[6] On the as-treated surface of GaAs (Fig. 2(c)), some S-S bonds still remain, though most of amorphous sulfur quickly sublime in vacuum at RT. No oxygen atom is observed and As-S bonds are dominant. Ga-S bonds are barely observable or masked by the peak of As-S. By heating below 250 °C (Fig. 2(d)), S-S bonds disappear forming a monolayer of sulfur. A strong PES signal of As-S and a weak one of Ga-S are observed on the surface showing (1x1) structure. At higher temperatures above 250 °C (Fig. 2(e)), S atoms on the surface undergo the reconstruction by forming a (2x1) structure. This transition is characterized by disappearance of the dominant As-S bonds replaced by Ga-S bonds. Ga-S bonds are stable up to 520 °C. Above that (Fig.2(f)), S atoms gradually desorb to disappear from the GaAs surface.

Our interpretation for the effective surface passivation with sulfur is as follows. The etching effect of both native oxide and GaAs itself into the $(NH_4)_2S_x$ solution provide a defect-free surface, since it is considered that surface defects of the as-etched GaAs presumably concentrate at/near the interface of oxide/GaAs. Dangling bonds on this fresh/pristine surface are successfully terminated with sulfur atoms. As long as the surface is covered with sulfur, moreover, even very active oxygen is unable to chemically adsorb on GaAs. In other words, the surface of a monomolecular layer of sulfur is free from dangling bonds and so inert. According to the "advanced unified defect model (AUDM)" by Spicer *et al.*[7], this surface passivity of the sulfur-treated GaAs seems essential to the reduction in the interface state density. They have long proposed the AUDM for the origin of surface/interface states to explain the almost identical pinning position irrespective of the sort of adsorbed or deposited atoms. In their model, the pinning is introduced on (chemical) adsorption of foreign atoms or on deposition. The released energy to a substrate surface by chemical adsorption is sufficient to create the surface defects such as vacancy and antisite of As and/or Ga. Thus chemisorption of oxygen enhances in the SRV. In contrast to the chemisorption, the physicosorption may not have enough energy to create those defects. Therefore, we think that GaAs surface with sulfur is very effectively passivated and stabilized, because chemisorption to create the surface defects is prohibited on its dangling bond-free surface. This may produce the low interface state density of sulfur-passivated sample.

Another explanation could be related to the surface reconstruction. The structure of the $(NH_4)_2S_x$-treated (100) surface changes from (1x1) to (2x1) by the heat treatment.[8,9] This (2x1) diffracted pattern is due to the reconstruction of the surface involving S and Ga atoms. Furthermore, the upward band bending of n-type GaAs is relaxed by about 0.3 eV after the annealing.[6] This suggests that dominant formation of Ga-S bonds at the surface induces more decrease in the surface state density, which is consistent with the results calculated by an *ab initio* pseudopotential method. Ohno *et al.* explain this changes in surface characteristics from the results that density of antibonding states induced by As-S bond decreases with the heat treatment.[10]

Here we notice that treatment effect in our model is dependent upon the fabrication processes, *i.e.*, the degree of surface damage during the deposition. For Schottky contacts of nonreactive metals (In, Al, Au, *etc.*) with GaAs, the barrier height markedly varies approaching to the theoretical values assuming no defect density, while for reactive metals (Pd, Pt, *etc.*), the difference in SBH between as-etched and treated samples is not clearly recognizable.[11,12] Regeneration of surface/interface states might be related to the chemical reaction between metal and GaAs substrate. Moreover, the MIS structures fabricated by resistive-heating deposition are superior in electronic characteristics to those by electron-beam deposition, because the latter process involves the ion bombardment to the surface, resulting in the generation of surface defects.[4,13] We can see a similar behavior in the degradation rate of PL intensity. The as-etched surface of GaAs has a large SRV and rapidly degrades its PL intensity. On the other hand, the $(NH_4)_2S_x$-treated surface has a very slow degradation rate even after exposure to air, since its dangling-bond free surface hinders the chemisorption of oxygen, *i.e.*, oxidation.[14]

We also compare the $(NH_4)_2S$ and Na_2S treatment with $(NH_4)_2S_x$.[5] Because of the absence or a trace of the reactive sulfur species in $(NH_4)_2S$ solution, oxide removal and exposure of fresh GaAs is incomplete. Therefore, the coverage of GaAs surface with sulfur could be done only partially and the oxide could be left between GaAs and the sulfur layer. That is, the $(NH_4)_2S$ treatment is less effective. In the case of Na_2S treatment, the residue film seems to be Na_2S, as it is soluble in water. Once washed, the surface loses its improved properties. We interpret this phenomenon as follows: the Na_2S treatment leaves a polar film of $Na_2S{\cdot}9H_2O$ on the GaAs surface. The film could contain the space charge in it. The polar feature and/or space charge induce a band bending near the surface of

GaAs. In the Na_2S treatment, the defective surface layer of GaAs is left untouched, thus its real improving effect should be less significant than the $(NH_4)_2S/(NH_4)_2S_x$ treatment. In addition, once the film is washed away, the surface remains covered with the natural oxide as before the treatment. In other words, the passivation effect by the Na_2S treatment is almost founded on its polar or charged residual on the GaAs surface, though there might be a partial reduction in the defect density.

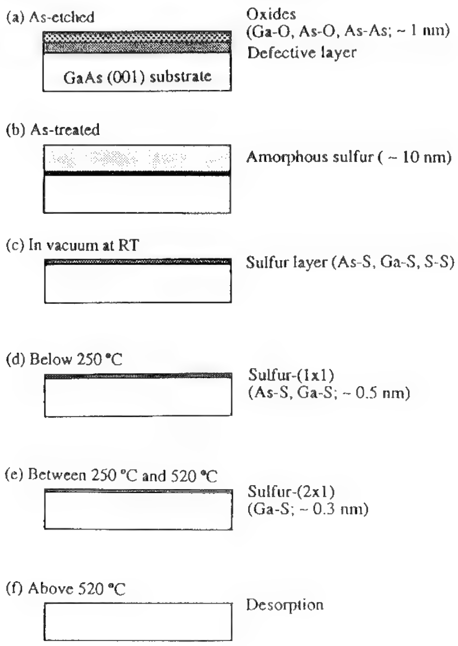

Fig. 2. Illustrative model of GaAs surface. (a) GaAs surface is covered with natural oxide, and defective layer of GaAs exists at/near the interface of oxide/GaAs. (b) Immediately after taken off the wafer out of the solution, the surface is covered with a visible, about 10 nm-thick film of amorphous S. (c) Most of amorphous S atoms quickly sublime in vacuum at RT, but some S-S bonds are observed as well as Ga-S in addition to the dominant As-S bonds. No oxygen atom is observed. (d) By heating below 250 °C, S-S bonds disappear and other bonds remain unchanged. The (1x1) RHEED pattern shows up. (e) Above 250 °C of transition temperature, Ga-S bonds become dominant on the (2x1) surface. (f) At higher temperatures above 520 °C, sulfur atoms gradually desorb to disappear from the surface. Sulfur atoms are losable by other means such as irradiation of light or electron beam.

Chalcogen treatment

We also studied on the surface passivation with chalcogen atoms (S, Se, Te). In these experiments, we used a dry process in stead of a wet process as $(NH_4)_2S_x$ treatment, due to a lack of effective solution for Se and Te treatment. An MBE technique was applied to control the molecular flux precisely and passivate the surface with chalcogen. The procedure of chalcogen treatment is as follows. The native oxide on the surface is removed with the heat treatment, and then the chalcogen flux is supplied on the clean surface at the substrate temperature of 480 °C. After shut off the flux, the substrate is cooled to RT. Schottky structures were fabricated on those surfaces at RT.

Figure 3 shows the SBH on GaAs passivated with S, Se and Te atoms. In general, SBHs of the chalcogen-treated sample have a larger dependency on the kind of metal than those of as-etched one, indicating a reduction in the interface state density. Therefore, the effect of chalcogen treatment seems quite the same on that of $(NH_4)_2S_x$ treatment, so long as a clean/fresh surface is attained prior to the treatment.

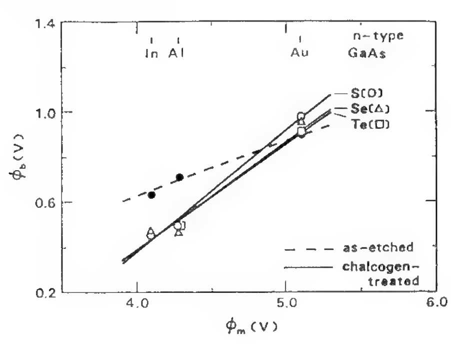

Fig. 3. Dependence of SBH on the work function of metal. The effect of Se and Te treatments is compared with that on S treatment.

Surface structure with chalcogen

Determination of the exact position of chalcogen atoms on top of the III-V surfaces is much sought after. We made observation on the various surfaces of S/InAs(001), Se/GaAs(001) and S/GaAs(111) by respective means of CAICISS, STM and XSW techniques, in order to avoid the technical difficulties in each measurement. In all those samples, however, we ascertained that the changes in bonding state of chalcogen with the heat treatment are qualitatively the same as S/GaAs(001).

The surface structure of $(NH_4)_2S_x$-treated InAs (001) was studied by CAICISS in combination with LEED and SRPES.[15] We used a sample of InAs to clearly separate the CAICISS signals between In and As, instead of GaAs with close atomic numbers. The intensity of back-scattered ions from In, As and S atoms were measured as a function of polar and azimuthal angles by using a time-of-flight (TOF) technique. In particular, we took notice of the behavior of S atoms with heat treatment and the actual displacement of S atoms involving surface reconstruction. CAICISS observations on the S/InAs(001) surface are as follows. The as-treated surface of InAs, on which exists both In-S and As-S bonds, has a less crystalline structure due to an abundance of As atoms. Based on the SRPES data that As-S bonds are predominant, this suggests that S atoms on the as-treated surface do not located on crystalline sites. On heating the sample at 380 °C, the surface morphology is gradually restored with the dominant formation of In-S bonds by the disappearance of As-S. In this condition, As atoms in the As plane of top surface are partially replaced by S atoms. The S or As atoms in the top layer form symmetric dimers lining up in the $[\bar{1}10]$ direction, resulting in the (2x1) structure. Therefore, the surface reconstruction of (2x1) is explained by the formation of dimers involving sulfur atoms. At 430 °C, sulfur atoms on the InAs surface completely desorb, since InAs has the S-desorption temperature of 400 °C comparable to 520 °C for GaAs.

More detailed study was made by use of STM. We successfully observed the surface images of Se/GaAs(001)-(2x3) and (4x1) structures at an atomic level, since RHEED patterns progressively change to (1x1), (2x1), (2x3) and (4x1) with the heat treatment. When a GaAs(001) surface with Se adsorbates is flash-heated at c. 520 °C, the (2x3) RHEED pattern appears and remains even after the sample is cooled. Elliptical protrusions ordered with 0.6 nm periodicity in the [110] direction were observed. The distance between the rows aligned in the [110] direction was about 0.8 nm. A possible explanation of the structure is to attribute the elliptical images to the Se dimers. Se dimers which result from the replacement of As atoms by Se, were found to be buckled, but the 2x-periodicity was maintained in the $[\bar{1}10]$ direction. Recent experimental results for bonding states suggest the formation of Ga-Se bonds at the Se/GaAs surface.[16] Figure 4 shows structural models for the Se/GaAs(001)-(2x3) surface.[17] Such a structure may be stabilized through charge transfer of the excess electrons into the Ga dangling bond states which appear by desorption of chalcogen atoms. Further heating at slightly higher temperature (~530 °C) produces the (4x1) surface structure of Se/GaAs(001). STM images revealed the presence of ordered arrays with regular intervals of 4x-periodicity in the $[\bar{1}10]$ direction (1.6 nm) lining up in the [110] direction. In a closer view, we also found that the 4x structure is formed by closely placed double rows. Although mechanisms to explain the formation of 4x-structure are under consideration, the reconstruction such as dimer paring may be caused by the partial replacement of As atoms by Se in the surface layers.

Furthermore, the coherent position of sulfur atoms were determined on the (111)A and B surfaces of $(NH_4)_2S_x$-treated GaAs by means of XSW technique.[18] The $SK\alpha$ fluorescence yields generated by the GaAs(111) standing waves were measured by a UHV goniometer system. The $SK\alpha$ fluorescence angular yield of the as-treated surface demonstrated that S atoms are located in nearly random positions on the surface, where Ga-S, As-S and S-S bonds coexist. This feature is common to both S/GaAs(111)A and B surfaces. After annealing, the S atoms substitute with top As atoms and occupy the coherent position of $0.89 \cdot d_{111}$ for (111)A and $0.00 \cdot d_{111}$ for (111)B, where $d_{111} = 3.264$ A is the spacing of the GaAs(111) planes. In other words, S atoms on the GaAs(111)A surface are located on top of the first layer Ga atoms, and bonded to the Ga atoms. This makes a sharp contrast to the (111)B surface, where the S atoms replace the first layer As atoms, and each S atom is bonded to three Ga atoms in the second layer. One may expect that the desorption temperature of S atoms on (111)A surface differs from that on (111)B, based on the idea that sulfur coordination number ranges from 1 for (111)A to 3 for (111)B. In fact, the temperature at which S atoms completely disappeared is 580 °C and 618 °C for the (111)A and B surfaces, respectively. This result was obtained by SRPES measurements.[19]

XSW technique is also useful to determine the position of interfacial atoms, though it is impossible to measure all the samples with various crystal orientations. With the help of XSW, we

investigated the structure of S atoms which exist at each interface of CaF_2-, Al- and Pd-GaAs(111)A·B.[20,21] We found that in the case of CaF_2 and Al, the interfacial S atoms are well-ordered even after the deposition, while those in Pd are rather disordered. The results observed by SRPES revealed the presence of Ca-S and Al-S bonds at the interface with CaF_2 and Al, respectively. As for Pd, however, Pd-Ga-As bonds are observed instead of Pd-S bonds. In fact, no significant difference in SBH between with and without the treatment was observed. As described before, the treatment effect is completely lost on the Pd/S/GaAs system because of the collapse of passivating S layer during the deposition.[12] In addition, the samples with (111)A have a lower coherent fraction than those with (111)B, meaning a less ordering of (111)A samples. This corresponds to the result that Ga-S bonds on (111)A are weaker than that on (111)B. Hence, we think that the existence of chalcogen-related bonds at the surface/interface provides the passivation effect on the III-V compounds.

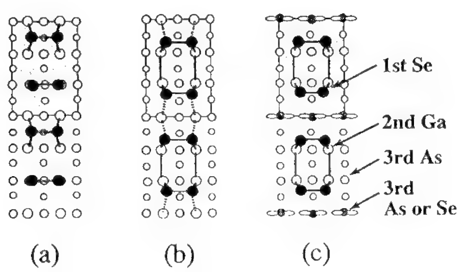

Fig. 4. Structural models for the Se/GaAs(001)-(2x3) surface.

Oxidation of chalcogen-passivated surface

The passivation effect with chalcogen is attributable to the formation of III-chalcogen bonds at the surface, in which the dangling bonds of III elements are successfully saturated. However, the chalcogen-passivated surface is not sufficiently stable against a long exposure over 10 days to air and a light irradiation. So we examined the cause of degradation observed on the air-exposed or light-irradiated surface with SRPES and positron annihilation technique.[22,23] Information obtained from the positron annihilation is about the presence of positron trapping center which has a negative charge. Among the six kinds of point defects possible in GaAs, positron is only sensitive to the acceptor-type vacancies such as V_{Ga} and/or V_{Ga}-related defects. That is, the donor-type V_{As} and antisites such as Ga_{As} and As_{Ga} have no trapping potential for positron.

In course of SRPES measurements, we found that the S-passivated GaAs surfaces which consist of 1 to 2 ML Ga-S layers comparatively protect and inhibit the surface oxidation. However, exposure to air induces the oxidation of Ga first and then As through the Ga-S layer, resulting in the degradation of surface electronic properties. This is based on that Ga oxide is thermodynamically more stable than As oxide. The preferential formation of Ga oxide is considered to generate the vacancy of Ga and excess elemental As. Nevertheless, the presence of V_{Ga} at the near-surface region could not be found by positron annihilation measurements. These results tentatively suggest an occurrence of the defect reaction; $V_{Ga} + As_{As} \rightarrow V_{As} + As_{Ga}$. This argument is founded on the theoretical calculations that enthalpy of antisite formation is much lower than that of vacancy formation.[24] An increase in the surface defects caused by the oxidation procedure results in a drastic upward band bending, approaching to the main pinning level of As_{Ga} antisite defects. Accordingly, the predominant defect at the GaAs surface might be considered to be the V_{As}-As_{Ga} complex created by the chemisorption of oxygen.

Summary

We found a very effective surface treatment of III-V compound semiconductors with the $(NH_4)_2S_x$ solution of excess sulfur. This treatment removes the natural oxide, etches III-V compounds and covers the surface with a monomolecular layer of sulfur. Moreover, the sulfur layer is so inert that the foreign atoms can not adsorb chemically. Our model suggests that these phenomena produces a well-stabilized surface and suppresses the regeneration of surface defects. In fact, the significant effect of $(NH_4)_2S_x$ treatment was observed as follows: 1) enhancement in PL intensity; 2) clear dependence of SBH on the work function of metal; 3) improvement in C-V characteristics of MIS structures. The latter two effects mean the real reduction in the surface/interface state density rather than band bending. Heat treatment of the as-treated surface is essential to stabilize

more effectively its surface. This is due to the dominant formation of III-S bonds which is stabler than V-S bonds, since III-S and V-S bonds coexist on the as-treated surface.

The effects of S-treatment were extended to those of other chalcogen (Se and Te) treatment. Similar dependency of SBH on the sort of metal was clearly observed. Therefore, we think that the effect of chalcogen (S, Se, Te) treatment is almost universal on the surface of many III-V compounds. On the as-treated surface, the V-chalcogen bonds are predominantly formed, resulting in the broken III-V bonds. Consequently, the surface indicates a less crystalline structure due to an abundance of V atoms. After annealing the samples, the partial replacement of V atoms by chalcogen and the subsequent formation of III-chalcogen bonds occur at a few layers of the surface. This behavior agrees with that III-chalcogen bonds are thermodynamically stabler than V-chalcogen bonds.

We also clarified the surface structure of chalcogen-passivated samples on an atomic scale, by the use of CAICISS, STM and XSW techniques. Chalcogen atoms occupy the near-site of V elements on top of the surface. This behavior seems to be independent of the surface orientation, although the chalcogen dimer rows are observed on the (001) surfaces. Structural models for Se/GaAs(001)-(2x3) were presented, based on the elliptical STM images corresponding to the Se dimers on the Ga layer.

Though a full understanding of the mechanism of chalcogen passivation is not reached yet, we extend that the effect and structure is qualitatively the same on the surface of III-V compound semiconductors.

Acknowledgments

We wish to thank Profs. T. Sakurai and T. Hashizume of Tohoku University, Prof. S. Tanigawa of University of Tsukuba, Dr. M. Oshima of NTT Interdisciplinary Laboratories and Dr. M. Aono of Institute of Physical and Chemical Research for their technical support.

References

[1] C. J. Sandroff, R. N. Norrenburg, J. C. Bischoff and R. Bhat, Appl. Phys. Lett. **51**, 33 (1987).
[2] Y. Nannichi and H. Oigawa, *Extended Abstracts 22nd Conf. Solid State Devices & Materials, Sendai, 1990* (Business Center for Academic Societies Japan, Tokyo,1990), p.453.
[3] H. Oigawa, J. Fan, Y. Nannichi, H. Sugahara and M. Oshima, Jpn. J. Appl. Phys. **30**, L322 (1991).
[4] J. Fan, Y. Kurata and Y. Nannichi, Jpn. J. Appl. Phys. **28**, L2255 (1989).
[5] Y. Nannichi, J. Fan, H. Oigawa and A. Koma, Jpn. J. Appl. Phys. **27** L2367 (1988).
[6] H. Sugahara, M. Oshima, H. Oigawa, H. Shigekawa and Y. Nannichi, J. Appl. Phys. **69**, 4349 (1991).
[7] W. E. Spicer, Z. Liliental-Weber, E. Weber, N. Newman, T. Kendelewicz, R. Cao, C. McCants, P. Mahowald, K. Miyano and I. Lindau, J. Vac. Sci. & Technol. B **6**, 1245 (1988).
[8] H. Oigawa, J. Fan, Y. Nannichi, K. Ando, K. Saiki and A. Koma, Jpn. J. Appl. Phys. **28**, L340 (1989).
[9] H. Hirayama, Y. Matsumoto, H. Oigawa and Y. Nannichi, Appl. Phys. Lett. **54**, 2565 (1989).
[10] T. Ohno and K. Shiraishi, Phys. Rev. **42**, 11194 (1990).
[11] J. Fan, H. Oigawa and Y. Nannichi, Jpn. J. Appl. Phys. **27**, L2127 (1988).
[12] H. Nie and Y. Nannichi, Jpn. J. Appl. Phys. **32**, L890 (1993).
[13] J. Fan, H. Oigawa and Y. Nannichi, Jpn. J. Appl. Phys. **27**, L1331 (1988).
[14] H. Oigawa, J. Fan, Y. Nannichi, K. Ando, K. Saiki and A. Koma, *Extended Abstracts 20th Conf. Solid State Devices & Materials, Tokyo, 1988* (Business Center for Academic Societies Japan, Tokyo, 1988), p.263.
[15] M. Katayama, M. Aono, H. Oigawa, Y. Nannichi, H. Sugahara and M. Oshima, Jpn. J. Appl. Phys. **30**, L786 (1991).
[16] T. Scimeca, Y. Watanabe, R. Berrigan and M. Oshima, Phys. Rev. B **46**, 10201 (1992).
[17] H. Shigekawa, H. Oigawa, K. Miyake, Y. Aiso and Y. Nannichi, Appl. Surf. Sci. **75**, 169 (1994).
[18] M. Sugiyama, S. Maeyama, M. Oshima, H. Oigawa, Y. Nannichi and H. Hashizume, Appl. Phys. Lett. **60**, 3247 (1992).
[19] T. Scimeca, Y. Muramatsu, M. Oshima, H. Oigawa and Y. Nannichi, Phys. Rev. B **44**, 12927.

[20] M. Sugiyama, S. Maeyama, T. Scimeca, M. Oshima, H. Oigawa, Y. Nannichi and H. Hashizume, Appl. Phys. Lett. **63**, 2540 (1993).
[21] M. Oshima, T. Scimeca, M. Sugiyama, S. Maeyama, H. Oigawa, Y. Nannichi and H. Hashizume, Appl. Surf. Sci. **70/71**, 496 (1993).
[22] M. Oshima, T. Scimeca, Y. Watanabe, H. Oigawa and Y. Nannichi, Jpn. J. Appl. Phys. **32**, p.518 (1993).
[23] J. Lee, L. Wei, S. Tanigawa, H. Oigawa and Y. Nannichi, Appl. Phys. Lett. **58**, 1167 (1991).
[24] J. A. Van Vechten, in *Handbook on Semiconductor*, Vol.3, edited by S. P. Keller (North-Holland, Amsterdam, 1980), p.57.

Materials Science Forum Vols. 185-188 (1995) pp. 199-208

Passivation of InP for optoelectronics

H. Kräutle

Telekom Forschungs- und Technologiezentrum, D-64295 Darmstadt, Germany

Keywords: Passivation, InP, dielectrics, deposition techniques

ABSTRACT

In modern fibre communication systems InP and related materials are of great importance. For high sensitive optoelectronic devices the passivation of the surface is essential to improve device performance. Due to the lack of ideal insulating materials on InP, compromises must be made. Depending on the device and its demands, such as reduction of inter-electronic capacitance, surface leakage currents, parasitic interaction between adjacent devices, coating of laser-mirrors, suppressing diffusion, etc., special passivating layers must be chosen. In addition, these layers should have good adhesion, low stress, should be stable and protect the surface against environment. Different materials like epitaxial s.i.InP, SiO_2, Si_3N_4, etc. deposited by different methods like CVD, PECVD, PVD, etc. are investigated. The different properties of the insulating layers and their dependence on deposition procedure will be discussed to give insight into the problematics of the passivation of InP-devices.

INTRODUCTION

The market for optoelectronic devices is fast increasing, especially in the telecommunication sector. In this field, long wavelength (1.3-1.5 μm) emitter and receiver elements [1,2] are of great importance, which are manufactured on InP based materials. One aspect is the reliability of the devices, improvement of its parameters and long time stability. Besides LEDs, lasers and photo detectors, also high-frequency electronic devices, like HBTs, FETs and HEMTs for OEIC application on InP based materials, are of great interest.

The lack of good native oxides or nitrides in the III-V compound system demands other types of surface passivation. Semiinsulating epitaxial layers seem to be ideal, however, they can be used only in some special cases. The use of photoresist and polyimid shows for some devices short time improvement [2] but stress and interface problems are observed. Chemical treatments, like sulfurisation [3,4] shows an improvement for some devices [5], however, it depends on the skill of the manufacturer. Free bonds at the surface must be saturated and excess sulphur must be avoided which otherwise diffuses rapidly and creates shallow donors in the surface layer. Another possibility is the deposition of an insulator. Great efforts have been put on the deposition of SiO_2 [5,7,8,9], PSG[6], SiN_x [10], Al_2O3 [11], BN[12], etc. Unfortunately no really compatible insulator has been found so far, so compromises must be made and the choice of the protective layer depends on the special demand of the device. Some devices allow only very low process temperatures and demand properties like high break through voltage, low leakage currents at the interface, low interface state densities, good adhesion, low stress, an expansion coefficient matched to the substrate, special dielectric constant, etc.. Some of the passivation procedures and its advantages and disadvantages will be discussed in this paper, like epitaxial overgrowth with semiinsulating layers [13,14] , passivation by ion implantation damage [12], and the deposition of dielectric layers.

In this short revue ,the most promising system SiO_2 and PSG deposited by low temperature "soft processes" like remote PE-CVD [16], modified PE-CVD [7] and photo CVD (PVD) [17] will be presented. One aspect is that InP and InGaAsP were very sensitive to elevated temperature and energetic species bombardment. For most processes a low deposition temperature degrades the quality of the insulating films concerning their electrical, chemical , optical and mechanical properties, while it preserves the semiconductor, which is very important in view of PL, leakage currents and electrical properties of the devices.

SEMIINSULATING InP

For many devices the ideal protection of an active region is a homoepitaxial layer of high resistive semiinsulating material. Also heteroepitaxial layers like InP on InGaAs can be used when the band bending (spike) does not influence the device characteristics negatively. This method has been applied with great success in laser fabrication [10]. The overgrowth of the side walls of the laser with s.i. InP forms an optical and electrical confinement. However, care must be taken to reduce etch back effects (in the CVD process), to suppress the creation of defects at the growth interface, and to avoid any influence of the compensating dopands on the active layers. Until now Fe-doped s.i. InP has been used. There is one disadvantage of Fe doped layers, the diffusion of Fe, which influences especially the Zn dopand distribution in active layers and Fe accumulates easily at the growth interface. Therefore other materials from the group of transition metals have been investigated for their use as compensating species. The diffusion has been examined on implanted and heat treated InP crystals using SIMS [18]. Some examples of Ti and Rh compared with Fe implanted in InP are presented in Fig 1a-c. It can be clearly seen that Fe diffuses very rapidly at temperatures near or above those used in epitaxial processes. Fig 1a shows that Fe diffuses towards the surface. A second peak is seen near the maximum of the original damage and a third peak at the original damage-crystalline interface. This indicates that Fe diffuses fast and segregates near defects and stressed interfaces.

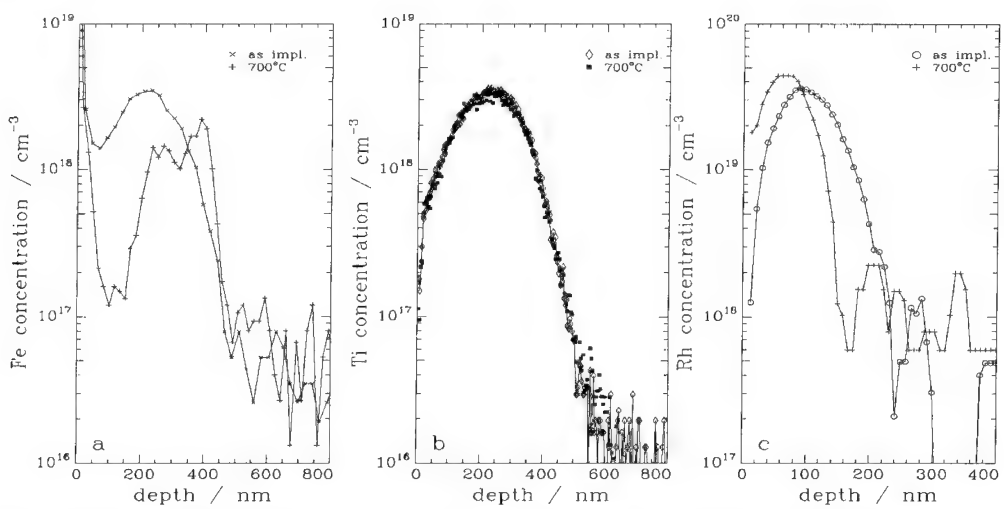

Fig 1.: SIMS Spectra of 10^{14}Fe/cm^2 (a), 10^{14} Ti/cm^2 (b), and $4*10^{14}$ Rh/cm^2 (c), as implanted with 400keV (Rh with 350keV) and after annealing at 700^{o}C for 20 min.

In contrast to this Ti ,Ru, Rh, Zr, Hf and Os do not show such pronounced diffusion and accumulation [19,20]. In general the diffusivity decreases with increasing atomic radius of the

transition metals. In contrast to Fe, which acts as deep acceptor and allows to compensate unintentionally doped InP, (which is usually slightly n-doped) Ti forms a deep donor. Therefore s.i. layers doped with Ti have to be slightly p-codoped. This might be overcome using those 4d and 5d transition metals which create deep acceptors. Very promising experiments have been carried out with Rh-doped MOCVD layers [21]. This will be applied in the future for laser passivation replacing Fe to overcome these problems which are related to diffusion.

PASSIVATION BY DAMAGE

A common process in GaAs device technology for creating an insulating region is H^+ implantation [22]. The effect is the following: the H^+ induced defects in GaAs form deep levels near the middle of the bandgap. But this damage anneals during heat treatment. Only O^+ implants show insulating behaviour, which is thermally stable [23]. For InP related devices, the method of damage insulation can be applied only in a very limited way for InGaAs. Fig 2 shows the change in resistivity of an InGaAs layer with a thin ohmic contact. After implanting H^+ or N^+ through the contact at 77 K, the resistivity of the implanted layer increases with implanted dose. Fig 2 shows also that the change in resistivity depends strongly on the doping of the material. Whereas p-InGaAs can be insulated with doses of $3*10^{13}$ H^+/cm^2, higher doses of $2*10^{16}$ cm^{-2} are necessary for n-InGaAs. Using N^+ ions a lower dose of $5*10^{14}$ cm^{-2} is sufficient to insulate the n-InGaAs layer according to the higher defect production per incident ion. This indicates that the insulating effect is due to the damage created by ion implantation. At doses of $2*10^{17}$ cm^{-2} blistering effects are seen indicating the limited usefulness of this method.

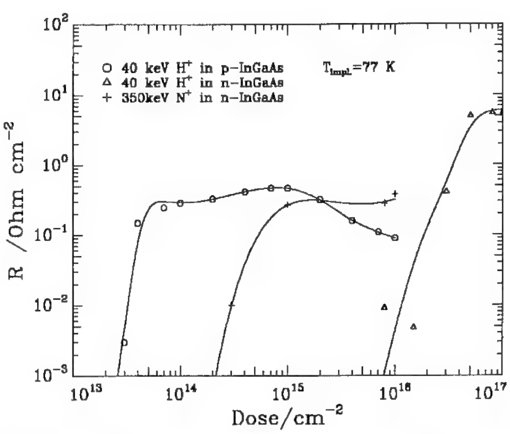

Fig. 2.: Resistivity of InGaAs implanted through the contact vs implanted dose.

H^+ ions implanted in InP create donor levels near to the conduction band. Even for low energy ion bombardment during e.g. dry etching in a RIE system (E=340 eV), an n^+ layer is formed at the surface. P-doped InP shows compensating effects within a depth of nearly 200 nm. This effect can be explained by compensation effects of hydrogen in this layer. This can be seen in Fig 3, where the carrier concentration vs depth is presented for n- and p-InP after RIE processing, measured with a chemical CV-profiler.

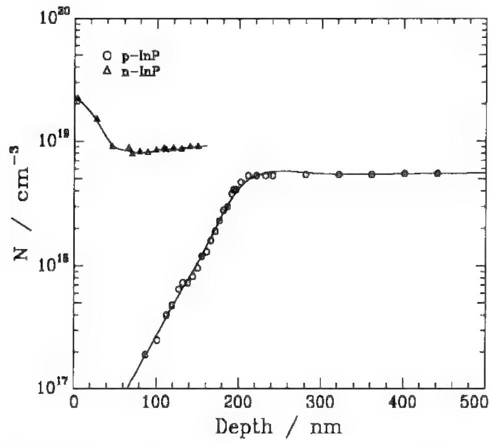

Fig 3.: Carrier concentration vs depth of InP after an RIE process (using CH_4+H_2+Ar).

DEPOSITION OF INSULATORS

a. PVD

The deposition of SiO_2, SiN_x and PSG for passivation is a well established process using e-beam evaporation, sputtering, CVD and PECVD. However, for InP and related compounds, a high interface state density and deterioration of the material is observed. Especially for optical devices a strong decrease of the PL signal and an increase of leakage currents are seen. Therefore soft deposition processes have been developed. Three of them i.e. PVD, modified PECVD and remote PECVD will be discussed. All of them have advantages and disadvantages. The PVD, like the commercial system Tylan PVD1000, uses UV light excitation, and therefore no bombardment of the surface of the wafer with energetic particles can damage the surface of the substrate. However, to initiate the chemical reaction, Hg is sensitised absorbing the Hg radiation, by which the energy for the chemical reaction. is provided

The presence of Hg could be disadvantageous, as it acts as a shallow acceptor in InP [25] when it diffuses into the substrate and it can react itself with N_2O to HgO which can be found in the dielectric layer. Calculations for the amount of molecules formed in thermal equilibrium at different temperatures are presented in Fig. 4. Comparing the calculated amount of Hg molecules with measured values (using RBS analysis [17]), it can be seen that the HgO incorporated in the SiO_2 layer coincides with the amount of HgO in the gas phase calculated for thermal equilibrium at high temperature and follows the same slope towards lower temperature. This indicates that the Hg concentration depends on the HgO concentration formed initially in the gas phase directly at the surface of the substrate and will there be spontaneously incorporated into the SiO_2 layer. This is a hint that reaction kinetic is surface controlled. This is also supported by the temperature dependence of the deposition rate regarding the Arrhenius plot. The positive slope as shown in Fig.5 indicates a surface-limited reaction, and as consequence a homogeneous step coverage can be observed. Therefore this process can be used to passivate mushroom laser structures and other devices with underetched layers.

The amount of Hg can be reduced below the detection limit of 1 ppm by increasing the SiH_4 to N_2O ratio. This is in agreement with calculations regarding the preferred formation of SiO_2. Also during annealing steps at temperatures above 400 ^oC Hg decreases below the detection limit. The expected formation of p^+ layers at the surface, due to the Hg incorporation in InP, could not be observed. The

electrical, optical and mechanical characterisation will be discussed in comparison with other deposition methods.

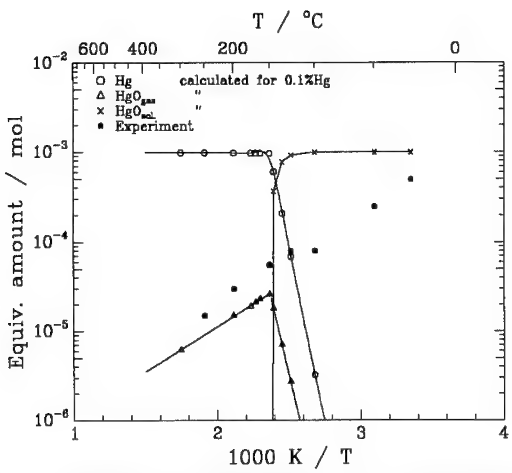

Fig. 4. Measured Hg concentration in PVD-SiO_2 vs 1/T compared with calculations for thermal equilibrium

b. Modified PECVD.

The ion bombardment of the crystal surface during insulator deposition by conventional PECVD results in a noticeably damaged InP surface. In the modified PECVD, a shield (metal mesh) has been mounted above the wafer which is in contact with the heated ground plate carrying the wafer. The wafer is now in a field free space and the ion bombardment is reduced. One advantage of the system used is the possibility to add phosphorus into the gas stream by evaporating solid phosphorous from an effusion cell into the gas line, by which the use of PH_3 is avoided. This allows to suppress the phosphorus evaporation from the InP surface and to dope the SiO_2 layer forming PSG with different phosphorus concentrations.

c. Remote PECVD.

The third method of depositing SiO_2 (SiN_x, Al_2O_3,...) at low temperature is the remote PECVD using metal organic compounds like TEOS, etc. and O_2 in N_2 [16]. Here the plasma of an inductively coupled ion source does not reach the surface of the sufficiently separated wafer. This allows an insulator deposition with a strongly reduced surface bombardment of the wafer. An equivalent process is the deposition of SiO_2 by ECR-CVD using SiH_4 + O_2 combining the remote with the shielding effect of the modified CVD. [24]. However, to obtain resonable good electrical properties, these layers has to be annealed e.g. by RTA at 500 ^{o}C.
The growth rate vs 1/T presented in Fig. 5 shows three different regimes. At low temperature the constant deposition rate indicates a gas phase controlled reaction. Due to incomplete decomposition of metal organic molecules these layers incorporate high amounts of C- and OH- groups. At higher temperature the deposition rate merges in a surface controlled regime with positive slope equal to the PVD process. Here the same kinematics has been observed indicating that a homogeneous surface and step coverage is obtained. At higher temperature the slope of the deposition rate changes to a negative value indicating an exothermal growth.

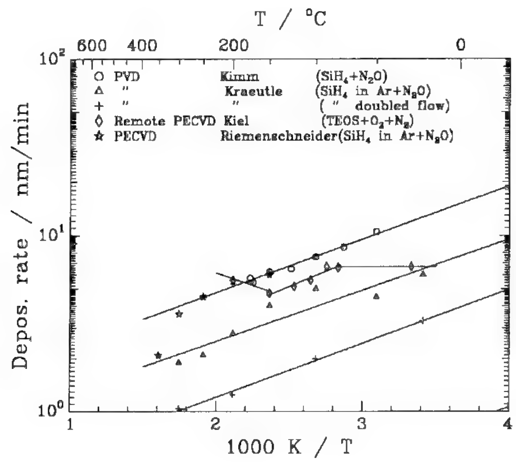

Fig.:5: Deposition rate vs (1/T) of SiO_2 layers using different techniques

ELECTRICAL CHARACTERISATION

Electrical measurements like CV, resistance, E_{br} and leakage current are summarised in Table 1.. The results of earlier publications could be confirmed. CV measurements indicate that low temperature SiO_2 incorporate mobile defects showing ion like character. The hysteresis can be quite big and at temperatures below 150 °C some CV curves show kinks [8]. The presence of OH-groups in films deposited at low temperature can be confirmed by FTIR spectroscopy. Some qualitative results of FTIR measurements are given in table 1. Incomplete reaction and the incorporation of OH- and other radicals as well as a low density of the insulators could be observed for deposition temperatures below 150 °C. Such layers can be densified during post annealing.. In the case of PVD SiO_2 deposited at RT the thickness could be reduced by more than 10% by RTA at 800 °C for 10s.

Table 1.: Data of dielectric layers deposited with different processes.

Deposition Process	dep. temp °C	dep. rate nm/min	etch.rate nm/min	n .	$R_{diel.}$ GΩcm	E_{br} MV/cm	D_{ss} $10^{11}cm^{-2}$	Si-OH (FTIR)*	O/Si .	$R_{surface}$ MΩcm	Adhesion 10^7Pa
e-beam	RT		400		34	3.7		+	1.79		
PVD	RT	7	600	1.46			10		2.3		
"	120-150	4	200-300	1.46-1.48	38	5.5-3	5-10	o	1.8-2.2	0.9-1.46	4.8
"	300	2	100			8			2.1		2.8
PECVD	300	4.5	150	1.47	<100	6.1-0.8	15	-	1.79		3.0
mod PECVD	250	4			20-30	6				1.16-1.27	5.2
PSG 2%	250	4.5	70-120	1.44-1.448	<100	8.0-5	5	-	1.72	1.04-1.67	6.6
" 14%	250	5	200	1.446		5.8-3	10		1.72	1.0	7.
R-PECVD	120	6		1.442			4-10	o			-

*** +: high, o: low, -: below detection limit**

The interface state density N_{ss} depends on surface preparation [5,26], deposition process and temperature. In contrast to GaAs, the interface state density near the conduction band of InP can be kept quite low which allows the operation of InP MIS inversion FETs with SiO_2 gate insulation [27]. Defects appearing at approximately 0.35 eV below the conduction band can be somewhat

reduced by soft deposition techniques. Surface treatment like P atmosphere during heating and P in the insulating layer influences the interface state density N_{SS} positively. Values in the order of 1-$4*10^{11}cm^{-2}$ are measured by Kulisch. Results of PVD layers deposited at the Telekom FTZ as well as of PECVD and PSG layers are published already by Hashizume et al. [28]. Actual results on improved deposition processes show values below $N_{SS}=10^{12}cm^{-2}$ [7].
The break through voltage and dielectric resistivity is relatively low for low temperature PVD SiO_2. Scavennec et al [8] showed that the resistivity can be improved by post annealing, by which H, P, In, and Hg will diffuse out of the deposited layer.
Experiments on TLM structures on s.i. InP performed, to evaluate surface currents show that first of all surface cleaning is very important and that the surface may not be deteriorated or damaged before or during layer deposition. This can be seen from the increase of surface leakage current with increasing deposition temperature for PVD layers [29]. Anyhow the leakage currents do not differ significantly for different soft deposition techniques.
The deposition process influences also the noise performance of devices. First 1/f noise measurements on TLM test structures show that PVD-SiO_2 shows pure 1/f noise like uncovered material. However, test structures deposited with PECVD SiO_2 show some deviation. From the temperature dependent noise measurements a defect level near 0.5 eV is seen, indicating that energetic particles create defects during this deposition process.

OPTICAL CHARACTERISATION

Besides FTIR measurements mentioned above, PL measurements have been carried out. InP covered with SiO_2 show different PL intensities and time response depending on the deposition process. PL of PVD-SiO_2 covered InP show high values equal those of bare crystals (Fig.6). A small decrease with deposition temperature is observed probably due to increased P-loss before SiO_2 deposition. Time resolved PL shows an increase of the PL with time. This indicates, that some interface states must be filled up firstly. The time response of the PL of InP deposited with SiO_2 using mod PECVD is fast and even decreases within a short time after the onset of the laser pulse. This quenching effect is so strong that the steady state PL intensity is very low as seen in Fig.6. Strong increase of the surface recombination velocity and defects in the crystal must be assumed to explain this behaviour. This is supported by the fact that after removing the film the PL intensity is still low.

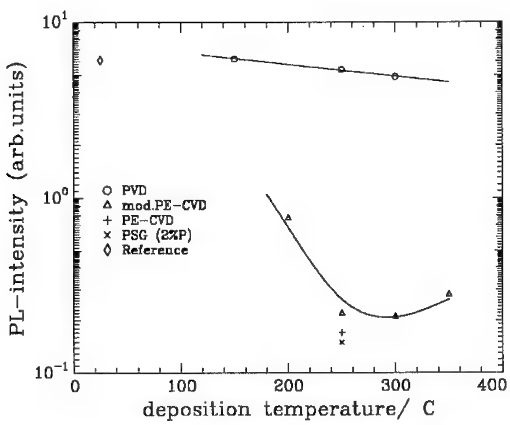

Fig.6.: PL-Intensity of InP covered with SiO_2 deposited with different techniques.

The refractive indices of different layers are shown in table 1.. Different values are published and it can easily been explained by different stochiometry and composition of the layers depending on deposition parameters. With increasing SiH_4 to N_2O ratio the refractive index increases. In addition it changes with the deposition temperature.

MECHANICAL PROPERTIES

Not at least the stress and adhesion of these dielectric layers influence the performance and lifetime of the devices. Stress free layers are quite difficult to manufacture. Sputtered, evaporated or PECVD films show usually high stress, whereas in the case of layers deposited with "soft" deposition techniques the stress is about one decade lower. Also here the stress depends on deposition temperature.

The second important mechanical property is the adhesive strength of the insulator on the crystal. Some layers peal off or show cracks. This is caused by the high stress but also by bad interfaces. Pull tests are done by gluing the wafer between two stamps and pulling until the layer or the crystal breaks. The crystal itself cracks at a power of 10^8 Pa. SiO_2 films deposited at low temperature by remote PECVD adhere not well and can easily be scratched. SiO_2 layers deposited by PVD shows

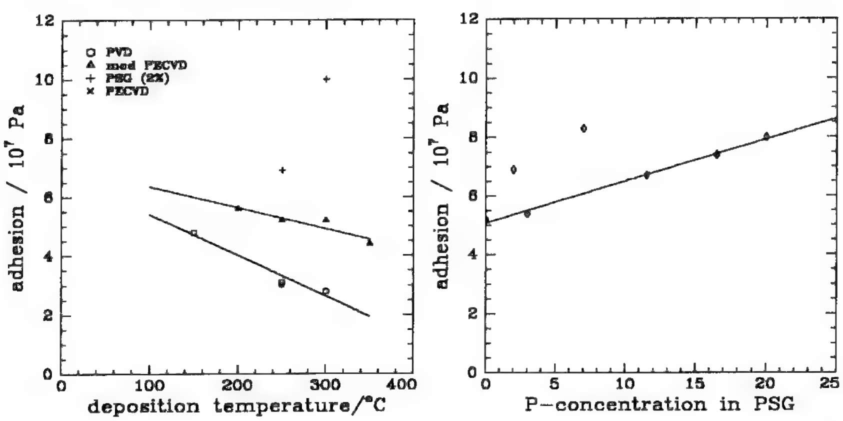

Fig.7.: Temperature dependence of the adhesion of different SiO_2 layers on InP (left), and the influence of the P concentration in PSG layers on InP on the adhesion (right).

very good adhesion. The values of SiO_2 layers deposited with mod. PECVD are even better. Fig. 7 (left) shows the adhesion vs deposition temperature. Comparing PVD and mod. PECVD layers it can be seen that the adhesion decreases with increasing temperature. For PVD the surface preparation is very important. For these experiments only an HF dip has been made before layer deposition. Soft surface bombardment in the mod. PECVD system influences the adhesion positively whereas regular PECVD, with its higher ion bombardment, lowers the adhesion due to P loss and increased InO_x formation at the interface. This is supported by experiments where P is added to the gas stream. Fig. 7 (right). shows the adhesion of PSG layers deposited with the modified PECVD vs P concentration. With increasing P concentration the adhesion improves, probably due to the reduced P loss of the InP surface.

CONCLUSION

Several promising methods of passivation have been presented. If temperatures of up to 600 ^{o}C can be allowed, a good passivation for some devices is a lattice matched, semiinsulating epitaxial layer of InP doped with low diffusive transition metals. This method which is applied very successfully for lasers cannot be applied for many other devices, e.g. devices with Zn diffused layers.
For most InP devices a soft, low temperature passivation with insulating amorphous layers (SiO_2, SiN_x, PSG, etc.) is successful. PVD, remote PECVD and some kinds of PECVD processes are successfully applied in passivating PIN diodes and transistors. A phosphorous vapour stabilises the surface and improves adhesion and lowers N_{SS} , allowing the operation of MIS-FETs. Crucial points for these processes are clean surfaces, no surface bombardment by energetic particles and a low deposition temperature in order to avoid surface degradation. To obtain not only good interfaces but also good quality insulators, the deposition rate must be low and the temperature reasonably high $T>150^{o}C$, to initiate a complete chemical reaction and to avoid the incorporation of unwanted reaction products. Still work has to be done to improve these processes.

ACKNOWLEDGEMENTS

The author wishes to thank all colleagues working in research projects of Telekom in co-operation with other research institutes who contributed actively to this passivation programme, in particular R. Riemenschneider, R. Schütz, T. Böttner and H.L. Hartnagel of TU Darmstadt, F. Kiel, W. Kulisch and R. Kassing of TU Kassel, and H. Ullrich, A. Knecht, M. Kuttler, and D. Bimberg of TU Berlin. He is indebted to colleagues of the research institute of Telekom D. Fritzsche, R. Bauchmann, H. Burkhard, H. Nickel, and R. Göbel for their contributions and discussions.

REFERENCES

[1] R.J. Deri, J. Lightwave Technol., 11, 1296 (1993)
[2] H. Nickel, and E. Kuphal, J. Opt. Commun. 4 (1983)2,63-67
[3] R. Iyer, R.R. Chang, and D.L. Lile, Appl. Phys. Lett. 53, 134 (1988)
[5] Schade, St. Kollakowski, E.H. Böttcher, and D. Bimberg, Appl. Phys. Lett. 64, 1389 (1994)
[4] D.Gallet and G. Hollinger, Appl. Phys. Lett. 62, 982 (1993)
[6] R.Kassing, W. Kulisch, S.H. Fam, I. Fernströning, and D. Fritzsche, in: Proc. 7th Europ. Conf. on Electrotechn., 581 (1986)
[7] R. Riemenschneider, N. DasGupta, R. Schütz, H.L. Hartnagel, and H. Kräutle, Appl. Surface Science 69, 277 (1993)
[8] A. Scavennec, G. Prost, P. Dimitriou, J.L. Courant, and Y. Le Bellego, Sol.-State Electron. 33,Suppl.,429 (1990)
[9] H.M. Kim, S-S. Tai, S.L. Groves,and K.K. Schuegraf, Tylan-Report
[10] A. Astito, A. Foucaran, G. Bastide, M. Rouzeyre, J.L. Leclercq, and J. Durand, J. Appl. Phys. 70, 2584 (1991)
[11] J. Saraie and S. Ngan, Jap. J. Appl. Phys. 29, L1877 (1990)
[12] W. Schmolla, H.L. Hartnagel, Sol. State Electron. 26, 931 (1983)
[13] R. Göbel, H. Janning, and H. Burkhard, in: Proc. 7th Simi-Insulating III-V Conf.,Ixtapa, Mexico, 125 (1992)
[14] P.Speier, Microelectron. Eng. 18, 1 (1992)
[15] H. Kräutle, O. Lindjörn und H. Beneking, Sol. State Electron. 26, 1033 (1983)
[16] W. Kulisch, F. Kiel, A. Bock, H.J. Frenck and R. Kassing, in: Proc. Third Int. Conf. on InP and Related Mat., Cardiff, Wales UK, April 8-11 p (1991)
[17] H. Kräutle, in:Tech. Digest 1989 Int. Conf. on VLSI and CAD,401 (1989)
[18] H. Ullrich, A. Knecht, D. Bimberg H. Kräutle, W. Schlaak J. Appl. Phys. 70, 2604 (1991)
[19] A. Knecht, M. Kuttler, H. Scheffler, T. Wolf, D. Bimberg and H.Kräutle, Nucl. Instr. & Meth. NIMB 80/81, 683 (1993)

[20] M.Kuttler, A.Knecht, D.Bimberg and H.Kräutle, in : Mat.Res.Soc.Symp.Proc.Vol.316, 179 (1994)
[21] H. Scheffler, B. Srocka, A. Dadgar, M. Kuttler, A. Knecht, R. Heitz, D. Bimberg, J.Y. Hyeon, and H. Schumann in : Mat.Res.Soc.Symp.Proc.Vol.325, 329 (1994)
[22] F. Ren, S.J. Pearton, W.S. Hobson, T.R. Fullowan, J. Lothian, and A.W. Yanof, Appl. Phys. Lett. 56, 860 (1990)
[23] H. Beneking, N. Grote, H. Kräutle und W. Roth, IEEE QE-16, 500 (1980)
[25] P.N. Favennec, H.L'Haridon, J.M. Raquais, M. Salvi, X. LeCleach, and L. Gouskov, Appl. Phys. Lett 48, 154 (1986)
[24] Y.Z. Hu, M. Li, Y. Wang, E.A. Irene, M.Rowe, and H.C. Casey, Jr., Appl. Phys. Lett, 63, 1113 (1993)
[26] W. Kulisch, Dissertation, TU Kassel (1988)
[27] D. Fritzsche, Inst. Conf. Ser. 50, 258 (1980)
[28] T. Hashizume, H. Hasegawa, R. Riemenschneider and H.L. Hartnagel, in: 1993 Int. Conf. on Sol. State Dev. and Mat., 742 (1993)
[29] R. Riemenschneider. H.L. Hartnagel, and H. Kräutle, in : Mat.Res.Soc.Symp.Proc.Vol.318, 231 (1994)

Materials Science Forum Vols. 185-188 (1995) pp. 209-216

Formation of oxide films on HgCdTe after fluorine-consist rinsing

L. Romashko, A. Myasnikov, V. Ovsyuk, V. Vasilyev and T. Zemtsova

Institute of Semiconductor Physics, Siberian Branch of Russian Academy of Sciences, 630090 Novosibirsk, Russia

Keywords: Native oxide, fluorine rinsing, surface, impurities, interface, photodiodes

ABSTRACT

Surface passivation of devices on mercury-cadmium-tellurium (MCT) is crucial to the device performance. In the case of p-type MCT the problem of finding a suitable dielectric film to passivate the surface and achieve a well-defined interface with adequate electrical properties has been rather difficult and very essential for the fabrication of high performance photovoltaic diodes. For the fabrication of the photodetector on MCT, the process of polishing the wafer with bromine etchant is used. The residue of the bromine and other impurities on the surface hinders the formation of the native oxide film in the air and adversely affect the quality of the interface.

This work was related with the investigation of influence of the removing contaminants from the surface in fluorine-consist etchant on kinetics of oxide growth in the air. The method of secondary-ion mass spectroscopy has shown the significant decrease of some impurities (Br, Cl, Ca, Na, Al, Si) on the surface after fluorine rinsing. The ellipsometric control has shown that after such rinsing the native film has been growing more rapidly and the interface between MCT and the native oxide in combination with dielectric layers of silicon dioxide and nitride has had excellent electrical properties. The main feature of the interface has been the low surface states density and practically flatband condition. Such native oxide on MCT improved the surface passivation of photovoltaic diodes implemented on p-type MCT. The diode reverse characteristics on x=0.227 has exhibited current multiplication due to tunneling at voltages near 1100mV and uniform differential resistance in the whole range. The photosensitivity of the diodes has been greater by an order than after bromine etching.

The results demonstrate that the rapid growth of oxide film after fluorine-consist rinsing made it possible to obtain the high-quality interface, minimizing the leakage current on the surface, and improve photosensitivity and uniformity of photoelectrical characteristics of photodiodes in arrays.

INTRODUCTION

The ternary alloy $Hg_{1-x}Cd_xTe$ (MCT) is an important material for the fabrication of the devices to infrared application. The MCT alloys with x=0.2-0.3 and maximum photosensitivity in the range of 3-5 and 8-12 μm are of most interest. An important problem for p-type MCT is a suitable passivation. The main requirements for it are low surface states density, good insulating properties and adhesion [1]. Usually a combination of native layers (oxides, sulfides or fluoro-oxides) and deposited dielectrics (SiO_2, Si_3N_4, ZnS) is used.

Before passivation MCT wafers are usually polished in bromine-containing etchants. This etching leaves residue of bromides which are insoluble in usual solutants (methanol, aceton or water). The presence of these bromides and other impurities on the surface leads to the increasing of surface recombination rate and decreasing of carriers lifetime and is thought to be the main cause of the degradation of the photodetectors.

The purpose of this work is the improvement of the quality of the MCT/native oxide interface. In this paper we have studied the formation of native oxide layers growing on MCT exposed to the air after bromine etching and following rinsing in fluorine-containing solution and the influence of this treatment on the device's performance.

EXPERIMENTAL METHOD

The secondary ion mass spectroscopy (SIMS) measurements were performed with MIQ-256 system (CAMECA/Riber,France) with 13-keV O^+ primary ion beam. The beam was rastered over a region 1500x700 μm and etching rate was about 1 Å/sec. To image the impurities distribution, the beam was rastered over an area 2000x3500 μm with etching rate 0.05 Å/sec.

The process of surface oxidation was controlled with ellipsometer LEF-3M with a 6328-Å laser line at 70^o angle of incidence.

For our investigation we used bulk p-type MCT wafers with x=0.22-0.23, concentration $5x10^{15}cm^{-2}$ and mobility 600 cm^{-2}/Vsec. After polishing the samples were etched in Br solution in ethanol/ethylen glycol mixture (Br- etching). Then some samples were bathed in solution containing fluorine ions (F rinsing).

Diodes arrays with test MIS-structures were fabricated for comparison of devices with different surface treatments. N-P junctions were formed by mercury diffusion from anodic oxide [2]. A layer of 700 Å SiO_2 and 500 Å Si_3N_4 was deposited as dielectric. Indium was used to form ohmic contact to n-type MCT. The diode's area was $5x10^{-5}$ cm^2 .

RESULTS

Table 1. The kinetics of polarization angles Ψ and Δ change during the air exposure after F- rinsing (1) and Br-etching (2).

time of exposure		Ψ	Δ
15 min	1	12°28'	140°48'
	2	12°25'	140°55'
30 min	1	12°36'	139°09'
	2	12°29'	140°27'
1 hour	1	12°38'	137°39'
	2	12°31'	140°06'
2 hour	1	12°41'	137°36'
	2	12°32'	139°48'
18 hour	1	12°41'	137°38'
	2	12°34'	139°06'
42 hour	1	12°42'	137°46'
	2	12°38'	137°58'
80 hour	1	12°44'	137°30'
	2	12°38'	138°06'

Table 1 gives the experimental data of polarization angles Ψ and Δ measured after studied treatments. The theoretical values of Ψ and Δ for such composition are 12°12' and 147° respectively. The angles Ψ and Δ for the first measurement, which provided through 15 minute after etching does not correspond to the sample composition. Authors [3] attribute the shift of Ψ to the influence of Te residue after Br etching and decrease of Δ to the surface roughness. This shift exists after F rinsing, too. Initial polarization angles coincide for both treatments, but the kinetics of their change when the sample was exposed to air is strictly different. After F rinsing the oxide layer grows to 40 Å during 1 hour, whereas after Br etching layer of 40 Å grows for 40 hours.

Fig.1a,b shows SIMS spectra of positive and negative secondary ions of elements on the surface after Br etching (spectrum 1) and after fluorine rinsing (spectrum 2). Comparing these spectra you can note that intensity of Si, Cl, Br, Na, K, F, Ca signals on spectrum 2 is significantly less to spectrum 1 with unchanged intensity of Cd and Te signals.

Fig.2a shows the distribution of some impurities (Na, Al, Si, K) on the sample surface after Br etching. Then a half of this sample was rinsed in fluorine solution and the picture of these impurities distribution was taken again. The conditions of the second measurement were the same but the sample was turned to a small angle (fig.2b). Note a strong decrease of Si, Na, K signal intensity and absence of changes of Al signal. The same results were obtained on spectrum (fig.1a).

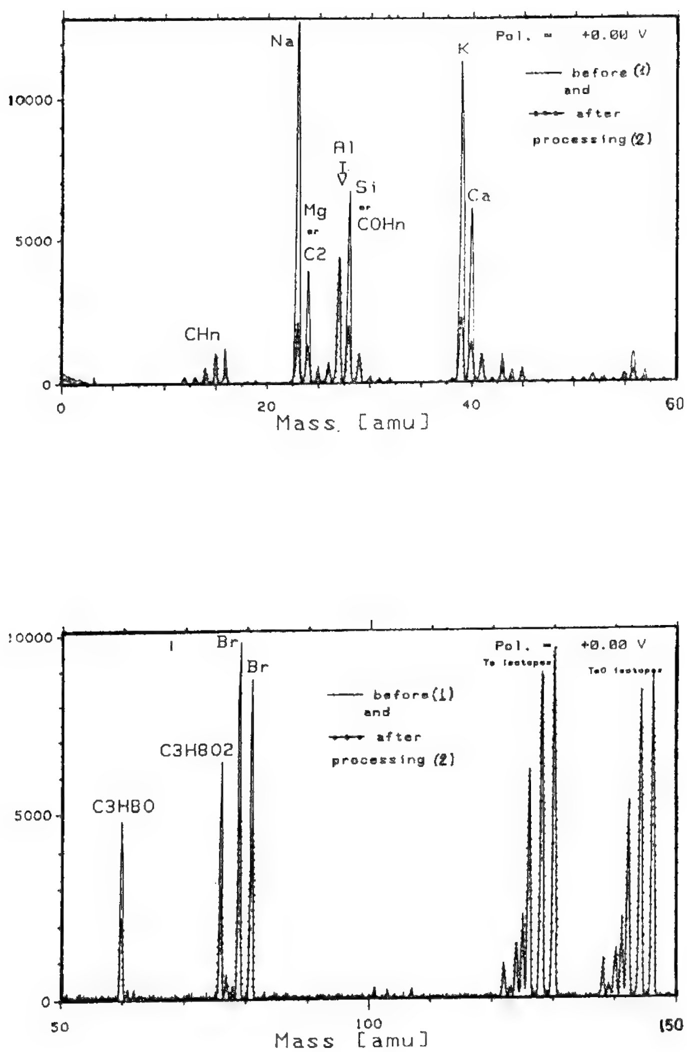

Fig.1 SIMS spectra of MCT surface after Br-etching (1) and F-rinsing (2).

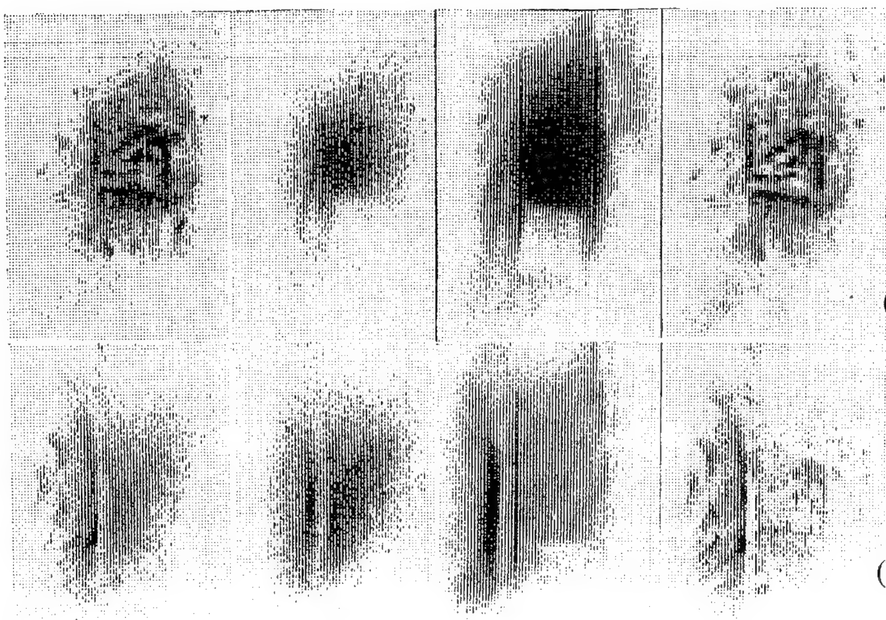

(a)

(b)

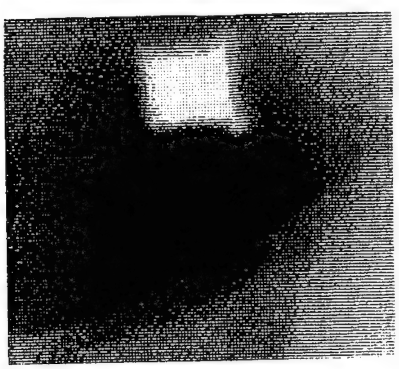

(c)

Fig.2. SIMS image of MCT surface after Br-etching (a) and F-rinsing of a right half of the sample (b). Br distribution on the surface (c) with F-rinsing of bottom part of the sample.

In contrast to these impurities Br is uniformly distributed on the surface (fig.2c) and its amount is to a great extent decreased after F rinsing.

Fig.3 shows Te, Br, Cl, F, C profiles on the depth to 400 Å. It demonstrates considerable decreasing of Br, Cl, F signals in near surface region after F rinsing. It is known [4] that C, Cl and other defects can create deep levels in bandgap and the presence of deep recombination centers significantly decreases minority carriers lifetime.

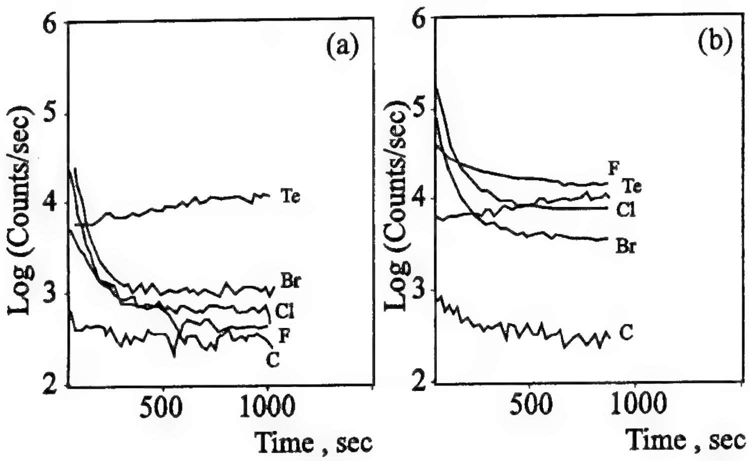

Fig.3. SIMS profiles of MCT after F-rinsing (a) and Br-etching (b).

On fig.4 shown C-V and G-V characteristics for MIS-structures with oxides grown after investigated treatments . The native oxide for both samples have a low fixed charge ($5x10^{10}$ cm $^{-2}$), calculated ignoring the work function differences and exhibit small hysteresis about 0.1V, which suggests a small amount of slow trapping effects in the interface. Note, that after F-rinsing invertion on the surface begin at greater voltages. This effect can be attributed with decreases of surface states or deep centers in bandgap near the surface after F-rinsing, which may connected with impurities or intrinsic defects of MCT.

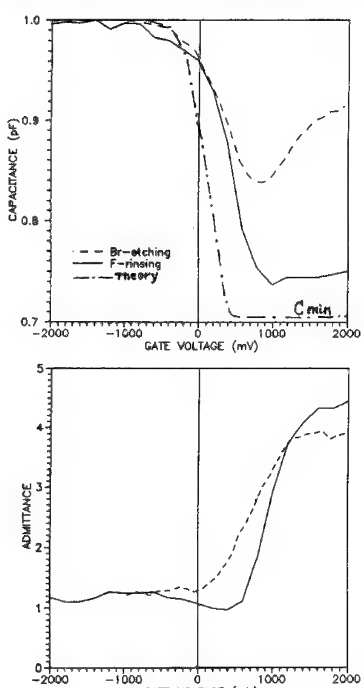

Fig.4. Capacitance - voltage and admittance-voltage characteristics of MIS structures on p-type MCT.
x=0.227
T=78K
f=1MHz

Fig.5 shows I-V characteristics of diodes in 64 element arrays fabricated with and without F rinsing. These curves demonstrate that F rinsing allows to minimize the leakage currents in n-p junction and increase photosensitivity by an order. and improve the uniformity of diode characteristics in array. Fig.6a,b demonstrates the improvement of the uniformity of dark diode currents at voltage V=-70 mV.

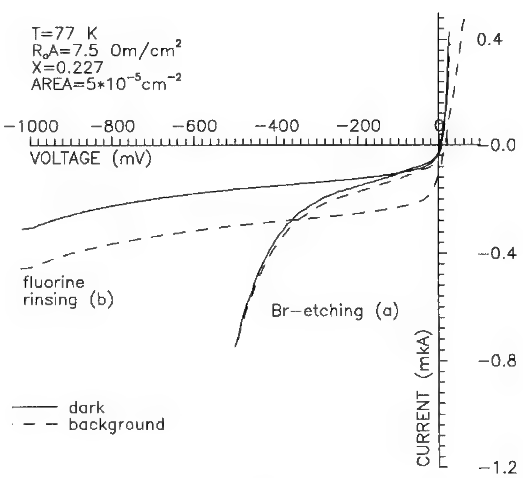

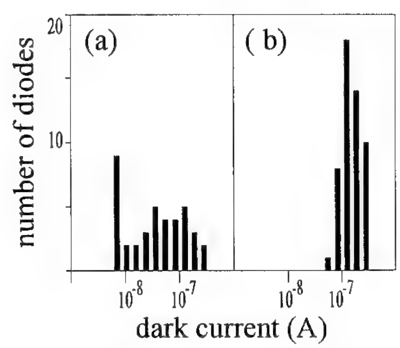

Fig.5. Current-voltage characteristics of diodes implemented on p-type MCT with x=0.227 which were Br-etched (a) and F-rinsed (b).
Fig.6. Histograms of dark diode currents after studied treatments.

DISCUSSION AND SUMMARY

Authors [5] have noted that bromine treatment leaves on the surface the bromides of Te, Cd, and Hg. Rinsing the wafer with usual solvents effectively removes the bromides of Cd and Te, but not that of Hg. The insolubility of the bromides of mercury of the reduced variety Hg_2Br_2 is supposed to be the main cause of the degradation of the photodetectors [5].

A large amount of impurities near surface after Br-etching can create deep levels and effect the leakage currents in n-p junction. And insoluble bromides covered the surface may lead to the strong decomposition of near-surface region, and prevent oxide growth, detenorate the adhesion of the capsulating dielectric.

Unlike the bromides, fluorides have an excellent solubility, that is why after fluorine rinsing the surface becomes cleaner of contaminants and (what is especially important) cleaner of bromides. Due to that oxide growth rate increases and prevents Hg evaporation. Our experiments show that fluorine rinsing permits to improve the material quality in near-surface region. Diodes with such treatment in contrast to diodes with usual etching have uniform current-voltage characteristics with uniform differential resistance and their photosensitivity higher by an order.

The authors would like to acknowledge V.I.Obodnikov for help in mass-spectra measurement.

REFERENCES

1.A.Lastras-Marines et al, J.Vac.Sci.Technol 21(1)1,157(1982)
2.N.H.Talypov, V.P.Popov, I.G.Remesnik, Z.A.Nalkina, Fisika i tekhnika poluprovodnikov, 2261,310 (1992)
3.A.S.Mardezgov, V.A.Shvets, L.L.Sveshnikova, M.G.Danylova, Poverkhost.Fisika, khimiya, mekhanika, 27 1(1989)
4.A.A.Denisov, S.G.Dorgin, V.N.Laktyushkin, U.G.Sadofyev, Obzory po elektronnoy tekhnike, 281, 7 (1986)
5.R.A.Reynolds, US patent No.3671313

The Passivity of Metals

Structure and Composition

Materials Science Forum Vols. 185-188 (1995) pp. 221-232

STM and AFM studies of passive films

P. Marcus and V. Maurice

Laboratoire de Physico-Chimie des Surfaces, Université Paris VI - CNRS-(URA 425), Ecole Nationale Supérieure de Chimie de Paris, 11, rue Pierre et Marie Curie, F-75005 Paris, France

Keywords: Surface structure, dissolution, passivation, passive films, metals, alloys, STM, AFM, high resolution imaging

Abstract: The advent of Scanning Tunneling Microscopy (STM) and Atomic Force Microscopy (AFM) has opened up new possibilities in the study of the structure of passive films. Direct imaging of the surface structure of passive metals or alloys can now be achieved with atomic resolution, providing invaluable information for the understanding of the growth, the stability and the breakdown of passive films. The published papers on near field microscopies (STM and AFM) applied to the study of dissolution and passivation of metals and alloys are reviewed. The following topics have been addressed: dissolution of metals, selective dissolution of alloys and structural analysis of passive films with emphasis on the atomic structure of passive films. STM investigation of the atomic structure of passive films is illustrated by results on nickel and chromium. On nickel single crystals (Ni(111)) the passive layer exhibits extended domains with long range order, epitaxial relationships, various structural defects and local variations of the film thickness. On chromium single crystals (Cr(110)) the STM results show the absence, in the passive film, of long range periodicity and of the associated defects, but the existence of a nanocrystalline structure. The future developments in the use of STM and AFM to investigate passive films are discussed (*in situ* investigation of localized reactions of e.g. Cl^- with passive films, local spectroscopic measurements and spectroscopic imaging).

1. Introduction

Data on the chemistry and structure of passive films are necessary to understand and predict the properties of passive films. There are now many available data on the chemical composition of passive films formed on metals and alloys. Surface analysis techniques have been, and still are, very useful to obtain such data. In sharp contrast, there is a lack of data on the structure of passive films. This is in part due to the difficulty of any structural analysis of very thin films on often rough substrates, using reflection high energy electron diffraction (RHEED) and grazing incidence X-ray diffraction. The advent of near field microscopies (STM, Scanning Tunneling Microscopy and AFM, Atomic Force Microscopy) has opened up new prospects in this field. Direct imaging of the structure with atomic resolution can now be performed in both *ex situ* (UHV or air) and *in situ* conditions.

The objective of this paper is to review the published data on *ex situ* and *in situ* STM and AFM of dissolution and passivation of metals (Ni, Cr, Cu, Fe, Al) and alloys (FeCr, FeCrMo, FeCrNi, AlTa, CuAu, AgAu), with special emphasis on atomically resolved structures, and to discuss, on the basis of the reviewed data, the questions of crystalline versus amorphous character of passive films, the nature of the defects, the relation of the structure with the available chemical information and the implications of the structural features in the stability and the breakdown of passive films.

2. Principle and Instrumentation

The principle and the instrumentation of STM and AFM are described in details in reference [1] and references therein. A brief summary is given here. The principle of STM is the tunneling of electrons through a potential barrier between two surfaces. The tunneling current I decays

exponentially with the width of this barrier (the separation s between the two surfaces). The height of the barrier is governed by the work function of the surfaces. Upon polarization of the barrier at a voltage V quite inferior to this work function, electrons tunnel from the filled electronic states of the electrode at negative bias to the empty electronic states of the electrode at positive bias. For standard values of the work function of metals, a decrease of s of 0.1 Å induces a decay of one order of magnitude of I. If one surface is a tip, the current is limited spatially to the apex of this tip because of this exponential decay. The microscope is operated by scanning the tip along the lateral X and Y axis parallel to the surface and by recording the tunneling current at each X and Y position. At each point, a feedback loop is used to adjust the vertical position along the Z axis in order to maintain the tunneling current at a constant reference value. Topographic images are then obtained by plotting the Z values versus the X and Y values. Images can be recorded at different bias voltages V between tip and surface which allow to probe filled or empty electronic states of various energies. Spectroscopic measurements can be performed by recording I vs. V curves at any X and Y point. Spectroscopic images can be obtained by recording I vs. V curves with simultaneous imaging. The main difficulty of the instrumentation is to control the tip position with respect to the surface with sub-angström precision. This is achieved by using piezoelectric tubes which can be displaced with this precision upon controlled polarization. The other requirement is to isolate the microscope from external vibrations. This is achieved by maximizing the rigidity of the microscope and by using damping systems. STM can be used to image conductive and semi-conductive surfaces in air, UHV or solution.

The operation of the AFM microscope is quite similar to that of the STM microscope. However, the basic principle is different. Here the forces between tip and surface separated by atomic distances are used. Imaging may be performed in either a repulsive regime of forces or an attractive regime of forces by varying the separation between tip and surface. The tip is mounted on a cantilever whose deflection controls the Z position of the tip with respect to the surface. The deflection is most often measured by reflection of a laser beam. AFM can be used to measure any surface in air, UHV or solution.

The operation of STM in solution with control of the electrochemical potential requires a bipotentiostat. This enables to control the electrochemical potential of the surface and that of the tip with respect to a reference electrode. The potential difference between tip and surface controls the bias voltage at which the images are recorded. The current measured on the tip is the sum of the tunneling current and of the faradic current resulting from electrochemical processes. It is then necessary to insulate the tip in order to minimize the faradic current. Details of the instrumentation of STM and AFM in solution are also given in [1] and references therein.

3. STM and AFM data on the dissolution and passivation of non noble metals and alloys

Table 1 lists in chronological order studies of dissolution and passivation which have been reported in the literature at the date of submission of the present paper. Among 22 publications listed, 14 are relative to dissolution and 8 to passivation. The review of these data is presented in the following according to this classification.

Material	electrochemical treatment electrolyte	technique conditions	References
Fe film over Al film	dissolution 0.2 mM NaCl	STM *in situ*	2
Ni	anodic dissolution and passivation 0.5 M H_2SO_4	STM *in situ*	3

Stainless Steel 304L	dissolution in 0.2M NaCl with and without NLS inhibitor	STM *in situ*	4
Cu	dissolution 10^{-4} M $HClO_4$ and 10^{-1} M $HClO_4$	STM *in situ*	5
Cu	dissolution 10^{-1} N H_2SO_4 + 10^{-2} N Na_2SO_4	STM *in situ*	6,7
Cu-25Au	selective dissolution 1 N NaCl + 10^{-2} N HCl	STM *in situ*	6,7
Fe	oxidation - reduction borate buffer	STM *in situ*	8
Al	oxidation-reduction 10^{-2} M NaCl	STM *in situ*	9
Ag-Au	selective dissolution 0.1 M $HClO_4$	STM *in situ*	10
Cu-25Au	selective dissolution 10^{-2} M H_2SO_4 + 0.99 M Na_2SO_4	STM *in situ*	11
Al Al-Ta	selective dissolution 10^{-2} M NaCl	STM *in situ*	12
Cu	anodic dissolution 0.5 M H_2SO_4	AFM *in situ*	13
Ni(111)	passivation 0.5 M H_2SO_4	STM *ex situ*	14,20
Au-25Cu(111) film on mica	selective dissolution 10^{-1} M HCl + 0.6 M NaCl	STM *in situ*	15
Cr(110)	passivation H_2SO_4	STM *in situ*	16
Fe-25Cr	passivation 10^{-1} M H_2SO_4	STM *ex situ - in situ*	17
Fe-15Cr-4Mo	passivation 0.5 M H_2SO_4	AFM *in situ*	18
Fe-17Cr Stainless Steel AISI 303	dissolution and pit formation 0.5 M NaCl	AFM *in situ*	19
Al	dissolution 0.1 M NaCl	AFM *in situ*	21

Fe	oxidation-reduction 1 M NaOH	AFM *in situ*	22
Cr(110)	passivation 0.5 M H_2SO_4	STM *ex situ*	23

Table 1: *Ex situ* and *in situ* electrochemical studies of dissolution and passivation of non noble metals and alloys by STM or AFM.

3.1. Dissolution

The first reported study is relative to dissolution. Drake et al. [2] performed real time *in situ* STM imaging of an iron film in a chloride solution. They observed topograhic changes on a lateral scale of ten nanometers within minutes of immersion. Their images suggested promising possibilities for the *in situ* investigations by STM of electrochemical processes. Lev et al. [3] were the first to investigate the possibility of *in situ* STM imaging of surface transitions induced by the electrochemical potential. They studied nickel in sulfuric acid. At rest potential and in the active region, the images were reproducible. Current versus tip-surface distance (I-s) curves showed the exponential decrease characteristic of the tunneling mechanism. When the potential was stepped in the passive region, erratic images were recorded under the same tunneling conditions. The I-s response was asymmetric and spread over large distances which is not typical of tunneling. This effect was attributed to mechanical fractures of the tip with the passive layer. Surface deposition of a nickel sulfate film resulting from the extensive dissolution produced by the potential step might also be responsible for the failure to record STM images of the passive film in this experiment. The same group applied STM to the real time study of the dissolution of stainless steel (type 304L) in aqueous chloride solution [4]. They observed that the corrosion rate was accelerated by increasing concentrations of chloride ions and by decreasing pH. The introduction of an organic corrosion inhibitor, N-lauroysarcosine (NLS) into buffered chloride solutions produced highly disordered surface structures that exhibited non ideal tunneling behaviour. This was probably caused by the strong adsorption of the non conductive inhibitor. In these 3 early studies, the aim of the authors was to test the possibility of real time observation of corrosion processes. They observed that corrosion processes occurred preferentially at the existing defects of the electrode but did not attempt to make optimal use of the high resolution capability of the STM instrument either along the Z axis normal to the surface or along the lateral X and Y axis, in order to characterize with the highest precision the observed topographic modifications.

Up to now, with only one exception, corrosion studies by means of real time *in situ* STM or AFM imaging have not been concerned with structural characterization at atomic level of the corrosion processes. This is due to the rates of mass transport of the corrosion processes which are high compared to the time of acquisition of STM or AFM images and which make it difficult to follow corrosion processes with atomic precision on the time scale of the data acquisition. The exception concerns dealloying by selective dissolution for which imaging at high resolution has been achieved thanks to slower dissolution rates of the studied alloy. The main issues of corrosion processes which have been addressed with low resolution are the amount of material consumed, localized corrosion, pitting and inhibitor effects. Copper has been the subject of 3 studies [5-7,13]. Real time STM images of dissolution in perchloric acid of different concentrations [5] have shown that more pronounced topographic changes occured with increasing acid concentrations. The local corrosion rates estimated from the localized consumption of the material were comparable to those obtained from SEM micrographs. Pickering et al. have also studied copper dissolution in perchloric acid [6,7]. Upon anodic dissolution in the Tafel region (high rate of mass transport), the copper surfaces were observed to roughen on a lateral scale of several micrometers. This was attributed to facetting as the development of facets about 1 μm across could be observed. Observation of the

evolution of these facets at a hundred nanometers scale evidenced local smoothening effects assigned to the development of low index (hkl) planes. The addition of the inhibitor K_2CrO_4 reduced the facetting rate. Upon selective dissolution of a Cu-25Au alloy, the same authors observed pronounced pitting of the surface. It was shown that STM underestimates the depth of the pits except in the initial stages of the roughening. This results from the fact that the tip may not reach the bottom of the pits because of its shape. Real time AFM imaging has also been used to study the topographic evolution of polycrystalline copper during dissolution in sulfuric acid [13]. It was shown that the evolution of the topography on the micrometer scale was dependent on the mechanical or chemical polishing pretreament of the sample and on the electrochemical potential. At low potential, dissolution removed first the perturbed layer resulting from mechanical polishing and revealed grain boundaries. At higher potential, the dissolution produced non uniform and crystallographically-etched surfaces with facets. The inhibiting effect of benzotriazole was observed. Higher anodic potentials were necessary for dissolving copper in that case and eventually produced pit-like features in the topography.

Corrosion of aluminum has been the subject of two studies [12,21]. Bhardwaj et al. [12] compared dissolution of aluminum from Al and Al-Ta samples by *in situ* STM in chloride solutions. They observed the development upon dissolution of topographic features a few nanometers high. The resulting roughening of the surface was slower for the Al-Ta sample than for the Al sample as a result of a slower dissolution rate of the alloy. Pits could be observed for a shorter time of immersion on Al than on Al-Ta. More recently, Chen et Guay [21] reported on an enhanced dissolution of Al in weakly corroding chloride solution as a result of the tip-surface interaction during *in situ* AFM imaging. They observed that hundred nanometers thick coating could be stripped during imaging and that the tip-surface interaction could be used to increase the Al dissolution rate locally. Microcavities could hence be machined at will. Iron corrosion has also been the subject of one study [19]. Gugler et al. investigated pit formation in ferritic Fe-17Cr alloys and in stainless steel (AISI 303 type) by *in situ* AFM. They could observed on the micrometer scale pit formation at nitride inclusions after potential pulse in the anodic region on the ferritic alloy in chloride solution, and the increase in the density of pit nuclei with time and potential on the austenitic alloy in chloride solution. Iron corrosion has been the subject of one study reported by Müller-Züllow et al. [22]. These authors investigated the oxidation of iron upon reduction-oxidation cycles in aqueous sodium hydroxide. The authors carried out alternatively AFM measurements in open circuit conditions and cyclic voltamograms (CV's) between the open circuit potential value and the onset of hydrogen evolution. Upon repetitive CV's they observed on the micrometer scale the overgrowth of the grinding channels resulting from mechanical polishing pretreament, the development of a uniform surface and the appearance of some crystals of well-defined polyhedral shape. They assigned the crystals to magnetite (Fe_3O_4).

Three studies of dealloying by selective dissolution have been reported [10,11,15]. Moffat et al. [11] reported on the dealloying of Cu-25Au followed by real time STM imaging. They have shown that, in a potential regime where dissolution is attributed to dissolution of Cu from sites of low coordination, roughening occurs by development of ripples on a nanometer scale. These ripples are thought to represent clustering of Au atoms at sites of extensive Cu dissolution. Ripples were observed to be mobile due to gold surface diffusion. At higher anodic potential above a critical value, the surface was observed to roughen in new regions supposedly corresponding to sites of higher coordination. Significant annealing of the roughened surface was also observed after polarization below the critical potential value. This was also attributed to surface diffusion of the gold atoms. Effects of surface atom mobility have also been observed in the dealloying of Ag-Au alloys [10]. Up to now, the only study where dissolution processes have been observed on the atomic scale is that reported by Chen et al. [15]. These authors studied the selective dissolution of Cu from Au-25Cu alloys by real time STM imaging as a function of the anodic polarization. Samples were (111) oriented films grown on mica that exhibit large terraces and atomic steps. Below the critical value of

the potential, they observed that Cu dissolution occurs by aggregation of vacancies in the first layer leading to a structure of voids that are one atom deep and grow two-dimensionally. No defects are created in the second layer during growth of these voids. Above the critical value of the potential, the growth of the voids is three-dimensional. They also observed that gold mobility was dependent of the potential and that a high mobility could annihilate second layer vacancies to maintain a layer-by-layer appearance of the dissolution process.

3.2. Passivation

The first reported STM study of passivation of non noble metals after the unsuccessful attempts of Lev et al. on Ni [3], is that of Bhardwaj et al. [8]. These authors studied by *in situ* real time STM imaging the passivation of polycrystalline iron in borate buffer. They proceeded by alternating oxidation steps at increasing anodic potentials and reduction steps at one cathodic potential. After reduction of the native oxide at the cathodic potential, relatively flat surfaces were produced supposedly corresponding to the metal substrate. Upon oxidation at anodic potential, rougher surfaces were at first produced, with patches or clusters of nanometer dimensions. These patches were observed in the first image after the oxidation step indicating instantaneous formation on the time scale of the data acquisition. Upon continuous imaging at the same oxidation potential, the surface was observed to smoothen. This was attributed to the completion of the passive layer by a fusing effect of the patches. When the potential was stepped back at the reduction value, surface roughening was first observed followed by smoothening within minutes of polarization. These topographical changes were attributed to the reduction of the passive film. The vertical dimensions of the patches produced at first by oxidation were found to increase from about 1 to about 4 nm when the anodic oxidation potential was increased. This suggested passive film of increasing thickness after completion for increasing values of the oxidation potential. This was supported by the increasing time periods necessary at cathodic potential in order to reduce completely the passive film. This study suggests that the growth process of the passive film by patches or islands fusing together is related to a nucleation and growth mechanism. The same authors performed a similar study on polycrystalline Al in sodium hydroxide [9]. They also observed that reduction of the oxide formed at anodic potentials reproduced the original substrate surface, and that when the potential is increased in the positive direction an oxide begins to grow non-uniformly as small humps or patches of nanometer dimensions, which later fuse together after longer elapsed times or at more positive potentials. As in the case of iron, it is suggested that the formation of the passive film occurs via a nucleation and growth mechanism.

Real time AFM imaging has been applied to the *in situ* investigation of passivation and oxidation in two studies [18,22]. Castle et al. [18] investigated the passivation of a Fe-15Cr-4Mo alloy in sulfuric acid. Upon polarization by a potential step in the passive region, they observed a transient phenomenon of platelets formation merging over increasing periods of elapsed time to produce eventually smooth surfaces. The platelets dimensions were in the ten nanometers range vertically and in the hundred nanometers range laterally. The authors refuted the possibility that the platelets could correspond to nucleation centers of the passive film on the basis of disturbances like breakage and lost caused by the scanning tip. They assigned the formation of these platelets to a deposit caused by the large dissolution of iron from the surface in the first instants of polarization and suggested that the platelets could owe their precipitation to the presence of Mo as no such phenomenon were observed on Fe-17Cr alloys. They did not see these platelets as structural elements of the passive film.

Ex situ STM imaging has been applied in our group to the investigation of the passive films formed on Ni and Cr in aqueous sulfuric acid solutions [14,20,23]. This was the first investigation of passive films with achievement of lateral and vertical atomic resolution. Our surface science-oriented approach has been to work with well-defined surfaces. Single crystal surfaces have been used in order to minimize the influence of substrate defects. For Ni [14,20], the (111) orientation was selected as a previous investigation had evidenced the crystallinity of the passive film formed on this

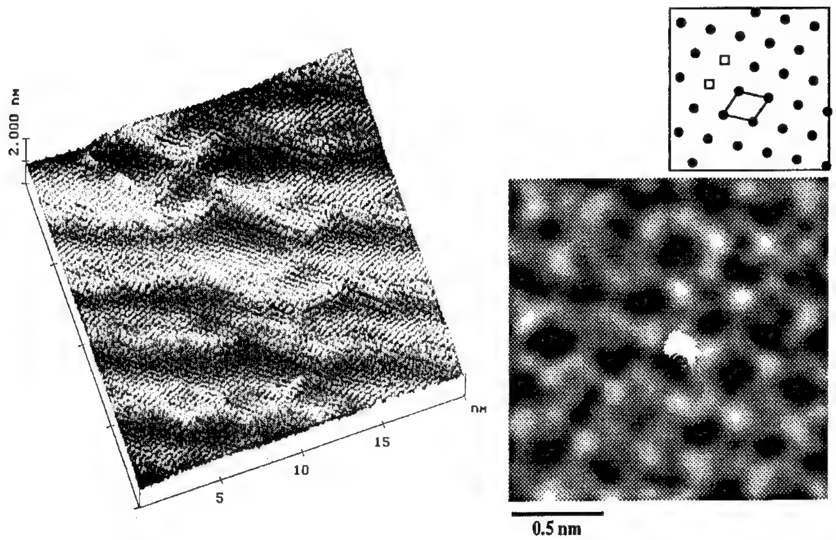

Figure 1: STM images of the passive film formed on Ni(111) in 0.05M H_2SO_4 at +750 mV/SHE. The left image shows the stepped cristalline lattice corresponding to NiO. The right image shows the lattice recorded on some terraces. The unit cell and two point defects are marked.

surface [24]. Much care was given to surface pretreaments. The samples were electrochemically polished and annealed at high temperature in a flow of pure hydrogen for several hours. These pretreaments were necessary in order to produce large atomic terraces of the substrate. The passive films were produced by potential steps from the corrosion potential value to three different values in the passive region (+550, +650 and +750 mV/SHE) after immersion in 0.05 M H_2SO_4. STM analyses were performed in air in which conditions the passive films were stable.

Modifications of the passivated Ni surfaces with respect to the non passivated ones were recorded on two different lateral scales. On a mesoscopic scale of hundred nanometers, new terraces were formed. Their size was found to decrease and their density was found to increase with increasing passivation potential. Their shape varied from trigonal contours with ledges oriented along the main crystallographic directions of the substrate, to hexagonal contours still with ledges oriented along the main crystallographic directions, and to non-symmetrical contours with non oriented ledges after passivation at +550, +650 and +750 mV/SHE, respectively. These variations have been assigned to a competition mechanism during the passivation treament between metal dissolution and formation of the passive film. The roughening effect due to dissolution increases with the potential and produces a higher density of terraces with less oriented ledges. On these submicroscopic terraces, a stepped crystalline lattice was imaged on the atomic scale. A typical image is shown in fig. 1. The lattice parameters measured on the terraces of the stepped lattice correspond to the lattice parameters of the (111) orientation of NiO, the inner component of the passive film. These lattice parameters and the step density were found to be independent of the passivation potential. The density and height of the steps correspond to an average tilt of $(8\pm5)°$ between the surface of the film and the (111) orientation of the terraces. Different epitaxy relationships with the substrate may be deduced depending on the orientation of the metal surface at the interface with the passive film. The tilt is thought to result from a relaxation of the strained epitaxy due to a mismatch of 16% between the lattice parameters of the oxide film and those of the metal substrate and/or from a relaxation of the polar NiO(111) terraces. The stepped surface of the passive film shows, from step height

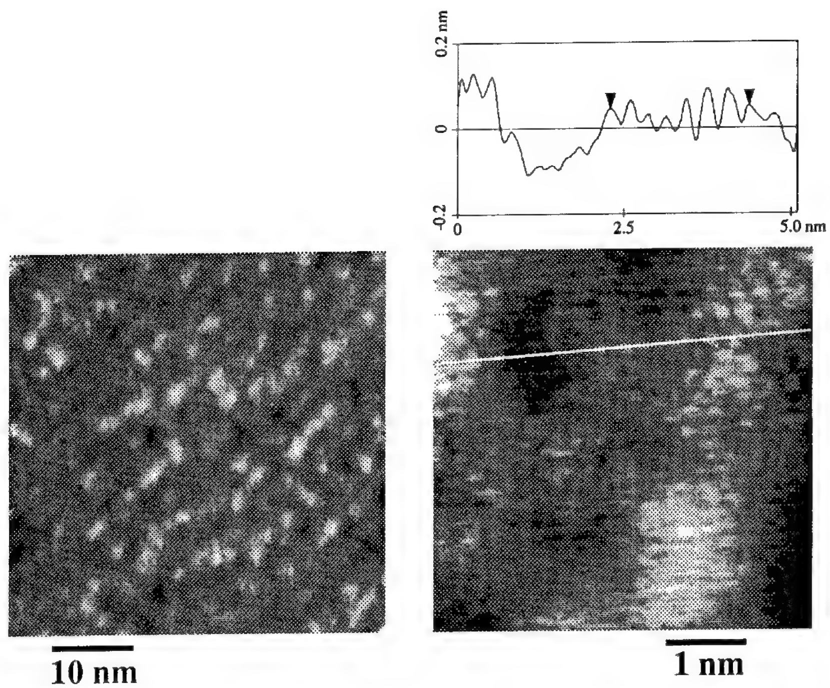

Figure 2: STM images of the passive film formed on Cr(110) in 0.5M H_2SO_4 at +500 mV/SHE. The left image shows the disordered protrusions of nanoscopic dimensions. The right image shows a small ordered domain assigned to a nanocrystal of oxide. The line profile indicates the atomic corrugations.

measurements, evidence of different chemical termination (O or Ni) of the NiO(111) terraces. In addition to steps and kinks at the surface of the passive film, other crystalline defects such as point defects possibly related to vacancies have been imaged. One example is also shown in fig. 1. The hydroxyl groups present in the outer part of the film and about one monolayer thick [25-28] could not be observed. The possible role of these groups in the tunneling mechanism is discussed below.

For Cr [23], (110) oriented single crystal surfaces were used. Pretreaments by electrochemical polishing and annealing at high temperature in hydrogen revealed, as for Ni, large atomic terraces of microscopic lateral dimensions. Passivation was also performed by potential steps from the corrosion potential to three different potentials in the passive region (+300, +500 and +700 mV/SHE) after immersion in 0.5 M H_2SO_4. Different time periods of polarization were investigated (20 minutes, 2 and 22 hours). The STM measurements were combined to XPS analysis. The XPS analysis (in UHV) showed that the passive film contains trivalent chromic species only. The oxide inner part of the film varies from dispersed 3D islands to a complete layer at most about 0.9 nm thick. The thickness of the hydroxide outer layer varies from about 0.6 to about 1.3 nm. Composition and thickness are stable upon exposure to air. STM measurements in air showed that unlike Ni, the surface is quite homogeneous on the submicroscopic scale after passivation. This is due to the quasi absence of dissolution during the passivation treament. On Cr, the surface topography is heterogeneous only on a nanoscopic scale. It is characterized by disordered protrusions of 1 to 4 nm lateral dimensions which induce vertical variations of 4 to 8 Å amplitude. A typical image is shown in fig. 2. This topography is independent of the passivation conditions. On the atomic scale, small areas of limited lateral extension are detected. This is also shown in fig. 2. These areas are characteristic of small ordered domains assigned to nanocrystals of oxide emerging at or near the film surface. The trigonal

arrangement and the distances of the corrugations may correspond to the arrangement of the O^{2-} ligands in the oxide. Larger ordered domains are observed by STM when more oxide is formed in the inner part of the film, according to XPS measurements. These ordered domains are surrounded by areas where no structural periodicity is evidenced which are assigned to the hydroxide outer part of the film. No crystalline defects are detected at the boundaries of the ordered domains. Recently Moffat et al. communicated shortly in an extended abstract [16] the results of an *ex situ* and *in situ* STM investigation of passive films formed on chromium. The authors concluded to a non-crystalline structure with small ordered domains in both conditions of investigation. This is in general agreement with our observations and tends to show that the structure is similar in *ex situ* and *in situ* conditions. Unfortunately, the absence of a more detailed report prevents a more extended comparison with our results.

On both Ni and Cr substrates, the passive film is made of an inner oxide layer at the metal interface and of an hydroxide layer in the outer part at the film surface. On Ni [25-28], the thickness of the oxide inner part is about 0.4 to about 1.2 nm and that of the hydroxide outer part is at most that of one monolayer (about 0.6 nm). No evidence of the hydroxide layer has been found in the STM images of the passive film on Ni. This can be explained if one considers two possible tunneling mechanisms. The first possible mechanism involves tunneling from the conduction band of the oxide layer to the tip (or vice versa) through the hydroxide layer. In this case the oxide layer is imaged but the hydroxide layer is not. The integrity of the hydroxide layer depends then on the width of the tunneling gap. If it is smaller than 0.6 nm, the hydroxide layer may be damaged by the scanning tip. The second possible mechanism involves electron transfer from the metal substrate to the surface hydroxyl groups and tunneling from these groups to the tip (or vice versa). In this case, the hydroxide layer can be imaged. The recorded images suggest then that the monolayer thick hydroxide layer is in epitaxy on the crystalline NiO host lattice with a (1x1) relationship, and therefore that the structure of the hydroxide monolayer duplicates the structure of the NiO host lattice. On Cr [23], the thickness of the oxide inner part varies from that of dispersed 3D islands to a complete layer at most about 0.9 nm thick, and the thickness of the hydroxide outer layer varies from about 0.6 to about 1.3 nm. The overall thickness of the film does not exceed 2.5 nm [29]. Topographic characteristics measured by STM have been assigned to this hydroxide layer on the basis of data recorded on passive films containing only dispersed islands of oxide in the inner part. It is then suggested that the tunneling mechanism on Cr is from the conduction band of the oxide and of the hydroxide to the tip (or vice versa). This difference between Ni and Cr indicates different conduction properties for the hydroxide compounds of the passive films formed on Ni and on Cr.

A comparison of the data on Ni and Cr in terms of resistance to breakdown is interesting. On Ni(111), the structure of the oxide inner part of the passive film is crystalline [14,20]. The structure of the hydroxide outer part is not observed. On Cr(110), nanocrystals with a lateral size limited to about 3 nm have been observed in the inner part. The structure of the hydroxide outer part is amorphous. This part is thicker than that formed on Ni. The defects observed for nickel are crystalline surface defects such as kinks, steps and vacancies. They are high energy defects resulting from the relaxation of the epitaxial stress with the substrate and/or from the relaxation of the polar NiO(111) terraces. The bottom of these defects correspond to sites of reduced thickness of the passive film. At these defects, there also exists sites of preferential adsorption of aggressive ions because of the lower coordination of the surface atoms. For these reasons, these sites are suspected to be preferential sites of breakdown of the film. On Cr, the topography variations of the hydroxide outer part also induce sites of variations of the film thickness. However, crystalline defects are not evidenced in these sites likely because they are cemented by the amorphous structure of the hydroxide. Therefore, they are expected to offer higher resistance to film breakdown. In addition, the amorphous structure of the hydroxide is expected to minimize the variations of coordination of the surface atoms at crystalline defects and therefore to induce a higher chemical passivity at these sites.

Hence, the nanocrystalline structure of the oxide and the role of cement played by the hydroxide would be responsible of the higher passivity of the film formed on Cr.

The only other reported STM study of passive films with atomic resolution is that of Ryan et al. [17]. These authors studied *ex situ* and *in situ* Fe-25Cr surfaces prepared by sputter deposition and passivated in a potential range where mostly Cr is expected to participate in film formation. They reported a crystalline structure *ex situ* on samples also aged *ex situ*. The periodic distance between nearest neighbour corrugations may correspond to the arrangement of the O^{2-} ligands in the oxide or to a 2D arrangement of surface OH groups. For freshly passivated samples observed *ex situ* or *in situ*, they measured only local evidence of crystalline order suggesting that ageing may be critical for the crystallinity. However, these preliminary results do not provide firm conclusions on the effect of *in situ* and *ex situ* ageing on the crystallinity of the film.

4. Discussion

Real time *in situ* STM or AFM observation of electrochemical processes is limited by the acquisition rate of the images. The acquisition rate necessary to obtain a good resolution at the atomic scale is about 1 s. per nm^2. Hence, real time observation of dynamic processes with atomic precision requires the dissolution density to be at most one atom per nm^2s, i.e. the current density should be limited to about 30 $\mu A/cm^2$. Therefore, metal dissolution processes occurring with higher current densities can only be observed with real time *in situ* STM or AFM imaging with a low resolution. The studies reviewed in the above section show that the observation of metal dissolution processes is limited to a micrometer or hundred nanometer scale. Hence, the imaging of dissolution can only reveal information on topographic evolutions versus time at surfaces. This is suitable to follow localized corrosion processes at microscopic defects and local effect of inhibitors. For example, the observation of pitting near inclusions [19] show promising possibilities for future studies of dynamic local processes at low resolution. Dealloying by selective dissolution can be observed with a higher resolution thanks to lower current densities of the electrochemical process. Vertical atomic resolution has been achieved in the real time imaging of this process [15]. However, the achievement of lateral atomic resolution in the systems investigated up to now, remains limited by the mobility of the surface atoms [10,11,15]. The future challenge in the real time observation of dealloying remains a full characterization with atomic precision of the active sites of dissolution below and above the critical potential. Passivation is a dynamic process which can be observed with relatively high precision provided the prior dissolution is quite limited. For example, this was achieved on Fe in a borate buffer [8] for which the formation of the passive film could be observed at a nanometer scale. Electrochemical systems with limited dissolution offer promising perspectives for the study of passivation with atomic resolution. The direct *in situ* observation at atomic resolution of localized reactions of aggressive ions e.g. Cl^- with passive films is among the most challenging application to be developed in future in the use of STM and AFM.

The structure of passive films has been characterized *ex situ* with lateral and vertical atomic resolution [14,16,17,20,23]. One advantage of *ex situ* investigations is to stop dynamic processes and this favours high resolution imaging. However, the drawback is having to remove the electrode from the solution environment which may cause modifications of the surface species. The extent of the modifications due to removal of the electrode depends on the stability of the electrochemically modified surface upon exposure to atmospheric pressure of air or inert gas, and/or exposure to reduced pressure (from vacuum to UHV). In principle, this stability should be analyzed in all the studies in which *ex situ* techniques are used as characterization tools. This is now becoming possible for the structure analysis by using STM or AFM. However, this is not possible for the chemical analysis. There is a gap between the chemical information which can be obtained by *in situ* techniques (e.g., Raman or infrared spectroscopic methods) and by *ex situ* techniques (e.g., XPS). More precise chemical characterization is obtained with *ex situ* techniques. This information is necessary for the interpretation of high resolution images acquired by STM or AFM. To correlate

this chemical information with the structural information can therefore be the objective of *ex situ* investigations of passive films on various substrates. It must be considered as the first step of a more complete structural investigation which should include both *ex situ* and *in situ* measurements.

A major requirement for data interpretation is a precise knowledge of the chemistry of the passive film. STM and AFM can provide the most accurate structural information only when used as a complementary technique. For example, the interpretation of the data recorded in the study of the passive films formed on Ni and Cr [14,20,23] would not have been possible without the knowledge of the distribution of the different compounds within the passive films. An additional requirement is necessary if the crystallinity of the passive films is investigated. It is then necessary to work with well-defined substrate surfaces evidenced by the observation of atomic terraces. This is in order to minimize and control the possible influence of the substrate defects on the defects of the passive film.

STM offers the possibility of performing local spectroscopic measurements (I vs. V curves). These measurements can be performed *in situ* and *ex situ*. *Ex situ* UHV conditions are however the most appropriate to ensure the non conductivity of the tunneling barrier between surface and tip. Such measurements on passive films formed on Ni and Cr should provide valuable information on the conductivity of these films. This is one promising perspective for the local characterization with high resolution of the electronic properties of these passive films. On the subject of the relation between chemistry at the atomic scale and atomic structure, the STM results on the passive film formed on Ni also show promising perspectives for further characterization. Accurate bias-dependent measurements of the terraces of the NiO oxide should provide information on their chemical termination (cation or anion). Also, such measurements should allow us to characterize the nature of point defects such as those shown in fig. 1 (i.e. cation or anion vacancy).

5. Conclusion

This review of STM and AFM studies of dissolution and passivation of metals and alloys shows that important results have been obtained by direct imaging of the surface structure, providing direct evidence on e.g. the role of surface mobility during dealloying, the crystallinity of passive films and the nature of defects. Many more results are expected to be produced, in the future, on the atomic structure of passive films, the local interactions of impurities and anions with passive films and especially with surface defects, the local conductivity of passive films derived from I-V curves at specific sites, and on chemical features derived from spectroscopic imaging. All these data should drastically improve our understanding of the relation between structure and properties of passive films.

References

[1] Scanning Tunneling Microscopy and Spectroscopy, Ed. D. A. Bonnell, VCH Publishers, Inc., New York (1993).
[2] B. Drake, R. Sonnenfeld, J. Schneir and P. K. Hansma, Surf. Sci. 181, 92 (1987).
[3] O. Lev, F.-R. Fan and A. J. Bard, J. Electrochem. Soc. 135, 783 (1988).
[4] F.R. Fan and A.J. Bard, J. Electrochem. Soc. 136, 166 (1989).
[5] X. G. Zhang and U. Stimming, Corrosion Sci. 30, 951 (1990).
[6] H. W. Pickering, Y. C. Wu, D. S. Gregory S. Geh and T. Sakurai, J. Vac. Sci.Technol. B 9(2), 976 (1991).
[7] Y. C. Wu, H. W. Pickering, D. S. Gregory S. Geh and T. Sakurai, Surf. Sci. 246, 468 (1991).
[8] R. C. Bhardwaj, A. Gonzalez-Martin and J. O' M. Bockris, J. Electroanal. Chem. 307, 195 (1991).
[9] R. C. Bhardwaj, A. Gonzalez-Martin and J. O' M. Bockris, J. Electrochem. Soc. 138, 1901 (1991).
[10] I. C. Oppenheim, D. J. Trevor, C. E. D. Chidsey, P. L. Trevor and K. Sieradzki, Science 254, 687 (1991).
[11] T. P. Moffat, F.-R. Fan and A. J. Bard, J. Electrochem. Soc. 138, 3224 (1991).
[12] R. C. Bhardwaj, A. Gonzalez-Martin and J. O' M. Bockris, J. Electrochem. Soc. 139, 1050 (1992).
[13] B. J. Cruikshank, A. A. Gewirth, R. M. Rynders and R. C. Alkire, J. Electrochem. Soc. 139, 2829 (1992).
[14] V. Maurice, H. Talah and P. Marcus, Surf. Sci. 284, L431 (1993).
[15] S .J. Chen, F. Sanz, D. F. Ogletree, V. M. Hallmark, T. M. Devine and M. Salmeron, Surf. Sci. 292, 289 (1993).
[16] T. P. Moffat, F.-R. Fan and A. J. Bard, Extended Abstracts of the Electrochemical Society Meeting (# 122), Honolulu, HO, USA 1993.
[17] M. P. Ryan, R. C. Newman, S. Fujimoto, G. E. Thompson, S. G. Corcoran and K. Sieradzki, Proceedings of the European Symposium on Modifications of Passive Films, Eds.: P. Marcus, B. Baroux and M. Keddam, The Institute of Materials, EFC 12, 1994, p. 66.
[18] J. E. Castle, X. F. Yang, J. H. Qiu and P. A Zhdan, Proceedings of the European Symposium on Modifications of Passive Films, Eds.: P. Marcus, B. Baroux and M. Keddam, The Institute of Materials, EFC 12, 1994, p. 66.
[19] G. Gugler, J. D. Neuvecelle, P. Mettraux, E. Rosset and D. Landolt, Proceedings of the European Symposium on Modifications of Passive Films, Eds.: P. Marcus, B. Baroux and M. Keddam, The Institute of Materials, EFC 12, 1994, p. 274.
[20] V. Maurice, H. Talah and P. Marcus, Surf. Sci. 304, 98 (1994).
[21] L. Chen and D. Guay, J. Electrochem. Soc. 141, L43 (1994).
[22] B. Müller-Zülow, S. Kipp, R. Lacmann and M. A. Schneeweiss, Surf. Sci. 311, 153 (1994).
[23] V. Maurice, W.-P. Yang and P. Marcus, J. Electrochem. Soc., submitted (#9405003).
[24] J. Oudar and P. Marcus, Appl. Surf. Sci. 3, 48 (1979).
[25] P. Marcus, J. Oudar and I. Olefjord, J. Microsc. Spectrosc. Electron. 4, 63 (1979).
[26] B.P. Lochel and H.-H. Strehblow, J. Electrochem. Soc. 131, 713 (1984).
[27] F. T. Wagner and T. E. Moylan, J. Electrochem. Soc. 136, 2498 (1989).
[28] D.F. Mitchell, G.I. Sproule and M.J. Graham, Appl. Surf. Sci. 21, 199 (1985).
[29] T. P. Moffat and R. M. Latanision, J. Electrochem. Soc., 139, 1869 (1992).

Materials Science Forum Vols. 185-188 (1995) pp. 233-240

Disorder and structural relaxation in passive films on Fe-Cr alloys

M.P. Ryan, S. Fujimoto, G.E. Thompson and R.C. Newman

UMIST, Corrosion and Protection Centre, PO Box 88, Manchester, M60 1QD, UK

Keywords: Corrosion, passivation, stainless steel, sputtering, percolation, scanning tunneling microscopy

Abstract

The primary passivation of Fe-Cr alloys involves selective dissolution of iron and formation of a chromium oxide [oxyhydroxide/hydroxide] layer. According to the percolation model, the passive film forms by electrochemical polymerization of the oxide network; oxygen bridging of emergent Cr ions occurs near their original spatial positions in the bcc Fe-Cr lattice. If the resulting random network is discontinuous or tenuously connected (below or near the percolation threshold), some structural relaxation can be anticipated. These predictions have now been explored using the STM. Alloys with 13-15% Cr form highly ordered passive films whose surface structure is consistent with a hydroxide monolayer on top of a Cr_2O_3 film, providing a <111> projection of the film structure. Between 15 and 21% Cr, the films are more-or-less disordered, but show crystallization in air. At 25% Cr the disordered film shows long-term structural stability. Pure Cr forms crystalline films, showing that disorder is not required for good passivity, but arises from the arrangement of Cr atoms in the alloy.

Introduction

A percolation model of alloy passivation was introduced by Sieradzki and Newman [1] and elaborated in several publications [2-5]. The model was developed for Fe-Cr, but applies to any alloy in which the passivating element can be enriched on the surface by selective dissolution, and is able to form an oxide network (i.e. it must have a valency of at least 3). The essential feature of the model is that the atoms of the passivating element form oxygen bridges to each other when they are exposed at the alloy surface, without needing to move from their original positions. In order to form a macroscopically continuous network in this manner, a site percolation condition must be satisfied by the atoms in the original alloy lattice, which is assumed to be a disordered solid solution. In the Fe-Cr system, two compositions were identified, corresponding to site percolation thresholds (p_c) for interactions up to third-nearest neighbours ($p_c\{1,2,3\}$) or second-nearest neighbours ($p_c\{1,2\}$). The values of these thresholds are about 0.10 and 0.17 respectively. At 10% Cr, atoms that are first, second or third-nearest neighbours in the alloy lattice can co-operate to form an infinitely extended oxyhydroxide network or gel [6]. This coincides with the start of Cr-like passivation, but the gel has a very open structure, contains nearly linear Cr-O-Cr linkages, and cannot prevent completely the transport of hydrated cations. True Cr-like passivity should not be achieved until around $p_c\{1,2\}$, i.e. 17% Cr. Detailed experimentation on sputter-deposited alloys showed that there were indeed vestiges of iron-like behaviour up to 16-17% Cr, where there was a sharp change in passivation kinetics [5].

No transition at the classical 13% Cr occurs for primary passivation in acid - the transitions are at 10% and 16-17%. Several other alloys were prepared by sputtering, including Fe-Al, Fe-Si, Fe-Zr and Fe-Ti, and all showed some sharp change in passivation behaviour between 16 and 20% of the solute [7].

The percolation model accounts for the passive-to-active transition with decreasing *potential* as follows: at low potentials the dissolution of Fe is less selective, so the enrichment of Cr on the surface is less marked and Cr atoms are dissolved before they have been incorporated into the network by 'finding' their Cr near-neighbours that are still covered by adjacent Fe atoms. In other words, we incorporate the reasonable chemical assumption that Cr ions with zero or one Cr neighbours (three or two hydroxides attached, respectively) dissolve faster than those that are in chains or rings as part of a network. This interpretation was extended to activation of Al-Hg [Ga,In..] anodes [4]: the mercury catalyzes dissolution by diffusing around on the surface and repeatedly occupying sites that break up an otherwise homogeneous 2-D alumina network. The resulting hydroxide-bonded Al termini dissolve more rapidly than sites that have oxygen bridges to three Al neighbours. In a sense, iron is an activator of chromium, but an inefficient one as it has little or no surface mobility. Activation can be expected in chromium alloyed with low-melting-point elements, but in much more aggressive solutions.

The above discussion provides a good starting point for an STM study of alloy passivity. The primary passive film is essentially CrOOH or Cr_2O_3, and starts life as a gel with a relatively open structure. If we need third-nearest neighbour connections (spacing 4.06Å) to complete this gel, then we can expect some permeability to hydrated cations and an incompletely passive state, as observed experimentally [5]. If we use only nearest and second-nearest Cr neighbours to form the gel, it may be permeable to water but can be shown to have a high resistance to hydrated cation transport [8]. The more loose the gel structure, the more likely is some form of structural relaxation during the passivation process. Alloys with Cr contents several percent higher than $p_c\{1,2\}$, such as Fe-25Cr, should form elastically rigid gels in which hardly any Cr ions have fewer than three Cr neighbours [6]. Such a material should show long-term structural stability at room temperature.

STM studies of passivity have been done mainly on nickel [9,10], where the passive film is crystalline and nearly epitaxial, showing minor structural changes with potential. The film on pure Cr is also crystalline [11], showing that disorder *per se* is not the reason for good corrosion performance, but rather a consequence of passivating the alloy via one component of a disordered solid solution. Ideally we would like to study the compositional dependence of Fe-Cr passivation using oriented monocrystals, but this would be a vast undertaking. Instead we use a co-sputtering technique in which flat, polycrystalline material with a range of compositions is produced in a single deposition [5,11-14].

Experimental Procedure

Fe-Cr alloy thin films with a continuous lateral variation in composition were prepared on silicon wafer substrates by ion-assisted ion-beam sputter co-deposition at Salford University (courtesy of M.C. Simmonds, H. Kheyrandish and J.S. Colligon). This technique has been described elsewhere [5,12]. The resulting flat, microcrystalline surfaces were readily imaged

in air with atomic resolution. Particular compositions could be selected for electrochemistry and STM study by cleaving small samples with their adherent substrate. For this particular research, the compositions ranged from 13.8 to 25 at.% Cr. Earlier work showed that these thin films had excellent electrochemical characteristics [5], the only difference from bulk material being an apparently lower critical current density for passivation. This may be due to a combination of low surface roughness and low-index surface orientation. A sharp change in passivation kinetics occurs around 16% Cr over a wide range of primary passivation potentials, as shown in Figure 1 for passivation at -250 mV (SCE).

The electrochemical procedures were slightly different for *ex situ* and *in situ* STM study. Specimens that were to be examined in air were passivated in 0.1M H_2SO_4 in a conventional electrochemical cell at room temperature, following a 10 min treatment at -1 V (SCE) that included 1 min at -1.5 V. The passivation potentials were -250 mV and +400 mV (SCE) and the passivation time was 5 min. Immediate rinsing with de-ionized water was followed by cold-air drying and immediate mounting in the STM. For *in situ* study the specimen was mounted in a cell designed by C.M. Vitus and the solution was changed to 0.01M H_2SO_4 to reduce corrosion under hydrogen bubbles that tended to occur during cathodic polarization in the small STM cell. The passivation times were longer, typically one hour, and were not always controllable owing to the unpredictable nature of the STM imaging process in solution. The reference electrode was Au/Au_2O_3 and the counter electrode was a platinum wire; the same passivation potentials were used as in the *ex situ* studies.

The STM was a Nanoscope II made by Digital Instruments. The tunneling tips were electrolytically etched tungsten wires, which were coated with nail polish for *in situ* work. All images were recorded in the constant height, fast-scan mode and were subject to some drift. The tip bias voltages were +400-600 mV in air and similar but negative values in solution. Tunneling currents were around 2 nA.

Results and Discussion

Figures 2a-d show *ex situ* STM images recorded in air, while Figures 3a-c show *in situ* images recorded in the 0.01M sulphuric acid solution. One possible result of the STM study would be a series of disordered passive films, which would confirm aspects of the percolation model but would provide little other useful information. The actual result was much more interesting: highly *ordered* surfaces were observed at low Cr contents, $\leq$15%, but disordered surfaces were observed at higher Cr contents. Alloys with 18 or 21% Cr showed remarkable crystallization of the initially disordered films during air exposures of up to 21 hours, as shown in Figure 2c. This result has not yet been confirmed *in situ*, and may be influenced by the change in environment and by film thickening as well as structural relaxation, but very similar behaviour occurred after applying very different passivation potentials (-250 and +400 mV SCE) for which film thickening in air would be quite different in rate and extent [13]. The crystalline surfaces invariably showed a triangular lattice of spacing 3.1Å, consistent with a <111> projection of the rhombohedral Cr_2O_3 structure, with areas where this lattice (probably composed of OH) was absent, revealing a ring-like structure, e.g. Fig. 3b centre right.

The observation of slow crystallization of the passive films around 18-21% Cr enables us

to postulate a much more rapid crystallization of the tenuously connected gel formed below 17% Cr. In other words, by the time the first image is obtained at (say) 15% Cr, the gel has already crystallized. Clearly the key experiment will be to observe the relaxation *in situ* at a composition where it takes a convenient period to occur, such as one hour. Low-drift instrumentation is now available that would enable a single area to be observed for this period of time.

The kinetics of structural relaxation in the passive films are fully in accord with the physics of random gel networks [6]. If we disregard the third-nearest neighbour connections, then below the percolation threshold (17%), there is no gel macromolecule but a series of finite clusters anchored to the alloy surface and containing many loose chains and OH termini. The material within each cluster is mobile at room temperature, and the consequent crystallization of each cluster widens the gaps between the clusters leading to further dissolution and ramification of the alloy surface. The eventual result is a porous layer containing metallic material, similar to a de-alloyed layer [2]. Around the percolation threshold, the network is infinite but still contains sparsely connected areas where continuing dissolution will produce intrusions into the alloy [3]. There is enough mobility for crystallization of such a layer to occur, but over a period of hours rather than the minutes required below p_c. Finally, several percent above p_c, the gel structure becomes elastically rigid [6] and almost every Cr atom in the original alloy becomes a member of a 5, 6 or 7-membered ring in the passive film (i.e. little or no OH is present, perhaps a few percent of the total oxygen content of the film). This structure is stable at room temperature, but admits water and oxygen to some extent, which may account for unexpected thickening of passive films on Fe-26Cr during air exposure [15].

It would be wrong to conclude from these results that the amorphous state *per se* is responsible for superior passivity [16]. Pure Cr has excellent corrosion resistance, but forms crystalline passive films [11]. The amorphous state is simply a result of the film formation mechanism in a disordered solid solution alloy.

Conclusions

1. The passive films formed on Fe-Cr alloys in acid solution are amorphous but crystallize at a rate that depends steeply on the Cr content of the alloy.

2. Very rapid crystallization of the film at low Cr contents is a result of its discontinuous nature and the availability of mobile structural elements.

3. A stable amorphous film is produced when the Cr content is several percent above the applicable percolation threshold (17%). This is in accord with the statistical physics of gel networks.

References

[1] K. Sieradzki and R.C. Newman, *J. Electrochem. Soc.* **133**, 1979 (1986).
[2] R.C. Newman, T.M. Foong and K. Sieradzki, *Corros. Sci.* **28**, 523 (1988).

[3] Q. Song, R.C. Newman, R.A. Cottis and K. Sieradzki, *J. Electrochem. Soc.* **137**, 435 (1990).

[4] Q. Song, R.C. Newman, R.A. Cottis and K. Sieradzki, *Corros. Sci.* **31**, 621 (1990).

[5] S. Fujimoto, R.C. Newman, G.S. Smith, S.P. Kaye, H. Kheyrandish and J.S. Colligon, *Corros. Sci.* **35**, 51 (1993).

[6] R. Zallen, *The Physics of Amorphous Solids*, Wiley, New York (1983).

[7] G.S. Smith, S. Fujimoto and R.C. Newman, "Passivity and percolation in metastable iron-based solid solutions", Extended Abstract #160, 183rd meeting of the Electrochemical Society (Honolulu 1993).

[8] M.P. Ryan, unpublished research.

[9] V. Maurice, H. Talah and P. Marcus, *Surf. Sci.* **304**, 98 (1994).

[10] S.L. Yao, S.R. Fan, T.P. Moffat and A.J. Bard, *J. Phys. Chem.* **98**, 5493 (1994).

[11] M.P. Ryan, R.C. Newman, S. Fujimoto and G.E. Thompson, "STM studies of passive films on Fe-Cr alloys: implications for models of alloy passivation" *Oxide Films on Metals and Alloys*, proceedings of ECS symposium, Miami, 1994, eds K. Hebert and G.E. Thompson, in press.

[12] M.P. Ryan, R.C. Newman, S. Fujimoto, G.E. Thompson, S.G. Corcoran and K. Sieradzki, in *Modifications of Passive Films*, eds P. Marcus, B. Baroux and M. Keddam, p 66, Institute of Materials, London (1994).

[13] M.P. Ryan, R.C. Newman and G.E. Thompson, "An STM study of structure and structural relaxation in passive oxide films on Fe-Cr alloys", *Philos. Mag. B* **70**, 241 (1994).

[14] M.P. Ryan, R.C. Newman and G.E. Thompson, "Atomically resolved STM of oxide film structures on Fe-Cr alloys during passivation in sulphuric acid solution", *J. Electrochem. Soc.*, submitted for publication (1994).

[15] J.A. Bardwell, G.I. Sproule, D.F. Mitchell, B. MacDougall and M.J. Graham, *J. Chem. Soc. Faraday Trans.* **87**, 1011 (1991).

[16] C.L. McBee and J. Kruger, *Electrochim. Acta* **17**, 1337 (1972).

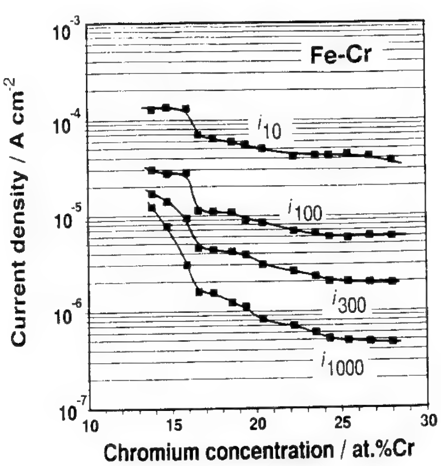

Figure 1 Current densities at various times (i_t with t in seconds) following a potential step from -1 V to -250 mV (SCE), for Fe-xCr in 0.1M H_2SO_4.

(a)

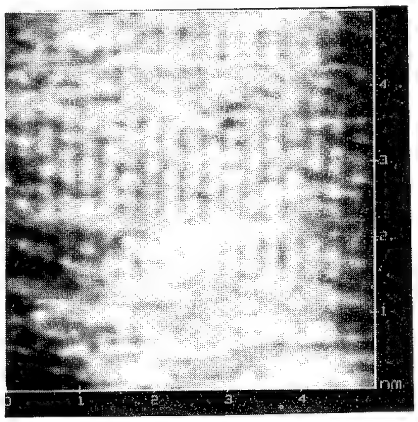

(b)

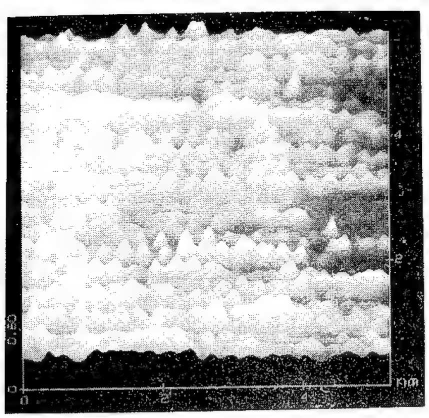

Figure 2 *Ex situ* STM images of Fe-Cr alloys passivated in 0.1M H_2SO_4 for 5 minutes at -250 mV (SCE): (a) 15% Cr [topview]; (b) 21% Cr [freshly passivated, oblique view]; (continued...)

(c)

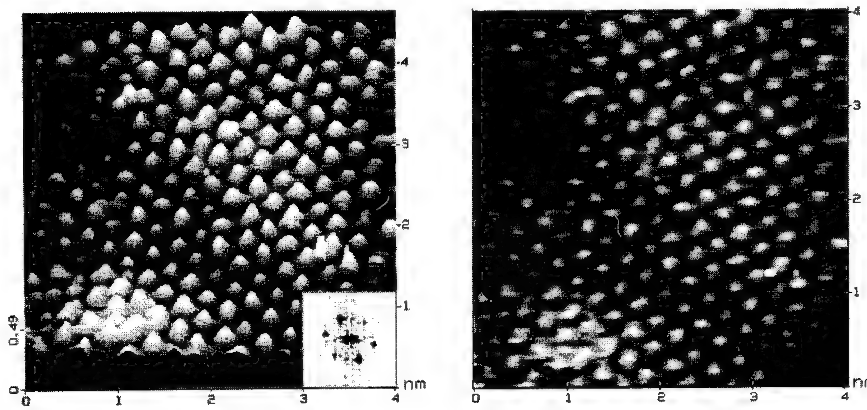

(d)

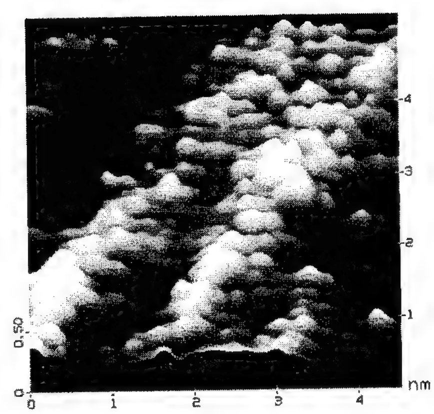

Figure 2 [continued] (c) 21% Cr (aged for 8 hours in air); (d) 25% Cr. Very similar results were obtained at +400 mV.

(a)

(b)

(c)

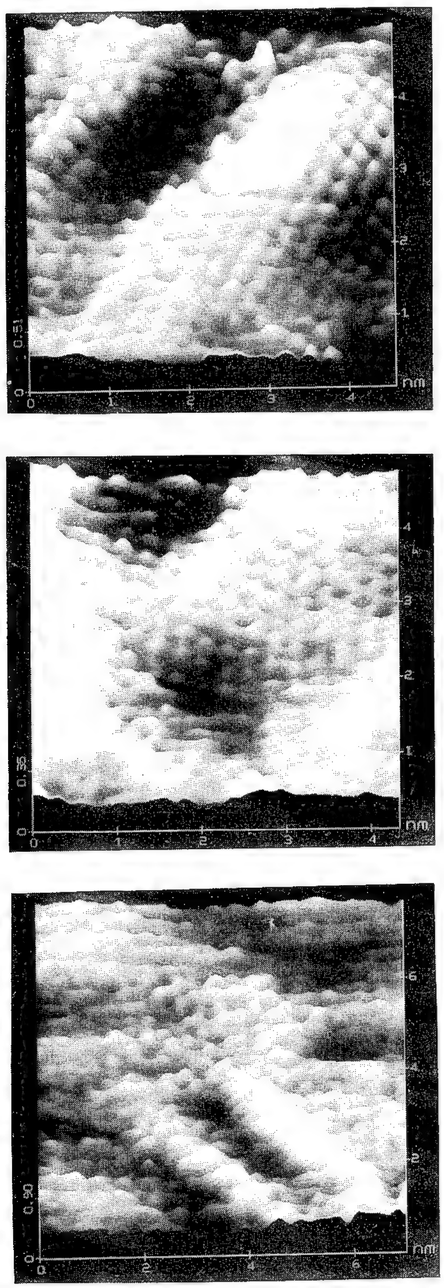

Figure 3 *In situ* STM images, recorded under potential control, for Fe-Cr alloys in 0.01M H_2SO_4 at +400 mV (SCE): (a) 13.8% Cr; (b) 14.7% Cr; (c) 16.5% Cr.

Materials Science Forum Vols. 185-188 (1995) pp. 241-250

Atomic structure and mechanical behaviour of passive film formed on stainless steels

J.M. Olive, V. Vignal and D. Desjardins

Laboratoire de Mécanique-Physique CNRS URA n° 867, Equipe Mécanique-Corrosion, Université Bordeaux I, 351 cours de la Libération, F-33405 Talence Cedex, France

Keywords: Austenitic stainless steels, passive film, mechanical behaviour, atomic structure, passivity breakdown, scanning tunneling microscopy, atomic force microscopy

Abstract: Stress corrosion cracking (s.c.c.) consists on the initiation and the propagation of brittle cracks under the combined effect of a reactive environment and a tensile stress. It's well established that passive films play an important role in stress corrosion cracking of austenitic stainless steels. One of the preponderant mechanism of crack propagation is based on successive events of film rupture, localized dissolution and repassivation.

The mechanical problem of the film rupture necessitates the knowledge of the mechanical properties of the passive film, the exterior strength induced on the film by the substrate deformation and the mechanical behavior of the interface film-substrate. The low thickness (< 10 nm) of passive films doesn't allow to measure their intrinsic mechanical properties with classical methods.

Observations ex-situ of polycrystalline austenitic stainless steel type 316 L passivated in air and in boiling $MgCl_2$ at 117°C, using scanning tunnelling microscopy (S.T.M.) are performed. Superstructure interpreted as a Moiré pattern and atomic resolution are obtained. Structural informations such as crystallinity and epitaxy give some features of mechanical behavior of passive film.

INTRODUCTION

It is well established that passive films formed on austenitic stainless steels play an important role in corrosion, stress corrosion cracking and fatigue corrosion [1]. The breakdown of passivity leads to the initiation of defects like pits, microcracks and participates to the propagation of cracks. All the electrochemical processes which occur between the metal and the aqueous medium depend on the behavior of the passive film. This film creates two interfaces; metal-film and film-electrolyte. The physical features of these interfaces and of the passive film determine the way in which the passivity breaks down. Rupture of passive films originates in several mechanisms [2-4]; action of chloride ion, high electrostatic pressure, external strength induced by plastic strain of the substrate. In fact all of these mechanisms have to be considered as acting simultaneously in situation of stress corrosion cracking.

As far as the mechanical behavior of passive films is concerned, Newman [5] remarked that few works have been done since the Vermilyea studies [6]. From impedance measurements, Keddam and al. [7] have compared, the anodic current transients produced by straining and abrasion. They have suggested that the mechanical behavior of the passive film formed on iron in sulfuric acid is ductile. It can be noted that no stress corrosion cracking was observed in this system and that a relationship between the ductility of passive film and the susceptibility to the stress corrosion cracking may exist.

Earlier, Bubar and al.[8] have studied the ductility of oxide scale and passive film. Their investigations were based on the potential dependence of the film thickness. They proposed a coefficient of ductility of 90% for a passive film formed on 304 stainless steel surface in 2 N Na_2SO_4.

Grosskreutz [9] [10] measured fracture strain and Young modulus of 3000 Angström thickness amorphous Al_2O_3 oxide scale separated from the substrate. The mechanical behaviour was perfectly brittle. When the film was adherent to the substrate, it has been shown that, for film thickness inferior or equal to 500 Angström, the film fracture occurred on the site of slip step emergence. The fracture of thicker films occurred perpendicularly to the loading direction and independently on the substrate deformation mode.

The fracture of magnetite film formed on mild steel has been observed by Mac Carthy Harrison [11]. The rupture strain reported was about 0.8 10^{-3}. Ford [12] has measured rupture strain of oxide film from straining tests at strain rate 1.5 10^{-3} s^{-1} and he ha. found 10^{-3}. However,

this value was considered too much dependent on the slip step emergence, then Ford used the values obtained by Diegle [13] which were 2 to 4 10^{-3}.

The thickness of passive film formed on the surface of stainless steels are generally between 10 and 30 AngstrÖm [14]. Thus, the classical metrology which gives the evolution of macroscopic variables as elongation and strength is inappropriate as a way of estimating the mechanical properties of passive films. During the moderately rapid straining under potentiostatic control, it has been possible to measure the strain ε_S of the sample and the corresponding stress σ_S which are associated with the appearance of an anodic current [15].

The deformation ε_S inferred from depassivation tests could be the intrinsic rupture strain of the passive film ε_f under the following hypothesis: (1) The strain tensor in the system film-substrate which is considered as a continuous media is homogeneous (i.e. without localized strain) (2) The adherence between the film and the substrate is infinite.

The thickness of the film if very inferior to the size of the elementary representative volume of polycrystalline stainless steel (grain size: 100 μm). Then, the previous hypothesis are not acceptable and the film rupture is predicted to be dependent on the emergence of slip steps. The measure of the strength during moderately straining tests have shown that the depassivation current increases during the transition elastic linear-plastic deformation. Thus the intrinsic film rupture strain is higher than the elastic limit of the substrate and the deformation ε_s is the strain of the substrate at which the film rupture occurs. Therefore, the mechanical problem of the film rupture depends on the knowledge of the exterior strength induced on the film by the slip step emergence, the mechanical properties of the film and the mechanical behavior of the interface film-substrate. Theoretical calculation of the stress state induced in the passive film by slip step emergence have been performed [16]. Quantitative assessment of film breakdown at slip steps necessites values of mechanical parameters which are unknown at present.

As far as the interface metal-film is concerned, Marcus and al. [17] have observed the passive film formed on Ni-Mo alloy in 0.05 M sulphuric acid solution. Static displacements of about 0.1 Å have been detected on the first atomic layer of the substrate in contact with the film. The authors explain this phenomenon by the possible strain induced by the film in the substrate or by the presence of a high concentration of vacancies (1%) at the interface film-substrate. This concentration of vacancies makes the adherence of the film on the substrate lower, adherence beeing one of the main mechanical parameter of the film rupture [16].

Informations about composition and shape of passive film formed on austenitic stainless steel in acidic media have been obtained by XPS [18]. A layered model of passive film has been proposed. Each layer is composed of different oxides and hydroxides of iron and chromium. Chromium hydroxide is located in the outer part of the passive layer and chromium oxide and iron oxide in inner layer. The mechanical behavior this type of film is the one of a multilayered material.

The aim of this study is to show how the use of STM can permit to give information about atomic structure of passive film. These informations are interpreted according to mechanical behavior, an amorphous film beeing more ductile and then more protective than a cristallized one.

EXPERIMENTAL

The Scanning Tunneling Microscope (S.T.M.) used in these experiments was a Nanoscope II instrument. To minimize acoustic, mechanical, electromagnetic vibrations and thermal changes, the microscope was situated on a vibration isolation table in a white room. All the images presented here were obtained in air and in the constant current mode, with a positive bias voltage (in the range of 20-40 mV) and setpoint currents between 1 and 5 nA. The residual current measured with the tip far from the substrate was approximately equal to 0,1 nA. Tips used in these studies were prepared in our laboratory by electrochemical etching of tungsten wires and then observed in Scanning Electron Microscope (S.E.M.). Moreover, to avoid loss of image quality, they were occasionally changed.

The materials observed were either a 304 L austenitic stainless steel or a 316 L austenitic steel. All the samples are polycristalline, the grains are oriented at ramdom and the average grain size is 100 μm. The chemical composition (wt %) of 304 L stainless steel used is: C: 0.021, Cr: 18.18, Ni: 10.07, Mo: 0, Si: 0.066, Mn: 1.46, S: 0.007, P: 0.026. The chemical composition (wt %) of 316L stainless steel used is: C: 0.022, Cr: 17.05, Ni: 11.15, Mo: 2.17, Si: 0.53, Mn: 1.43, S:

0.013, P: 0.025. The grains size of these polycrystalline materials is about 100 μm. First, samples (10x10x2 mm) were mechanically polished with succesive grades of emery paper and smoothed with different grades of diamond paste (6 μm, 3 μm, 0,25 μm). Then, electrochemical polishing in 90% Butoxyethanol+10% perchloric acid for 1 hour following by an etching for 30 seconds in a acid bath (20% nitric acid+10% hydrofluoric acid+70% water) were performed. Between each treatment, samples were rinsed with alcohol and distilled water. The oxide layer was formed either in air at room temperature or in a 30% aqueous $MgCl_2$ solution, at 117°C. According to these operations, atomic resolution was obtained and images were stable enough.

RESULTS AND DISCUSSION

Rougthness of the electrochemical etched surfaces and passivated in ambient air which are bright mirror finished were evaluated with long scans (STM head D) of 7000 nm. The image in Fig.1 indicates that the highest defect height is 6.2 nm. Different morphologies of defects can be seen such as: bright river lines of about 4 μm length which do not have particular orientation and large clusters of several sizes (maximum 2 nm). It can be noted the presence of very smooth zones (1.5 μm x 1.5 μm on the left hand of the image) in which the difference of level does not exceed 2 nm. The same scannings were performed on a surface passivated at open circuit potential in $MgCl_2$ solution (30 % weight) at 117°C. The image shown in Fig. 2 was obtained ex situ after immersion of 15 minutes. A very important corrugation associated with large bright oriented bands is observed. Corrugation amplitude is 120 nm and the period near of 1500 nm. The bright bands seem to be discontinuous forming lengthened small islands.

Thus, the passivation in hot chloride media leads to the appearence of a high and oriented relief. This can be attributable to anisotropic growth of passive film or anisotropic localized anodic dissolution or the both. Several mechanisms of corrugation formation can be proposed:

- Assuming that the corrugations represent thickness variations of the passive film, the substrate surface remaining smooth, the composition of the passive film should vary periodically along the surface. As it has been mentionned earlier in this paper, passive film are formed of a mixing of different metallic oxides. Several shape of passive film with different composition should be formed with their own growth kinetic and maximum thikness, forming lengthened small islands. In this case, the local thikness of the passive film would reach 120 nm. This value is very high regarding the thickness obtained on the same system by AUGER spectroscopy which gave about 10 nm [19]. If the composition of passive film is assumed to be uniform, the corrugation should be induced by the mechanism of germination and the growth of the different oxides, a corrugated external surface being then the more stable morphology.
- An other possible mechanism is based on the anisotropy and on the localization of the corrosion processes. The establishment of the passivaty state schematically consists of the mixing up of anodic dissolution and formation of oxides. Anisotropic anodic dissolution depends on the cristallographic orientation of the substrate. It is previsible that dissolution occurs favourably along traces of {111} planes. The localization of the anodic dissolution implies that all {111} planes traces are not attacked simultaneously (general dissolution) but only a few number of them. This leads to a periodic preferential anodic dissolution on oriented axes ({111} planes traces). The subsequent growth of passive film (different from the ones formed in the air before the immersion) should be then oriented along the same direction.

The relationship between corrugation orientation and cristallographic orientation of the substrate has been shown by imaging the proximity of a grain boundary.

A grain boundary on the surface of a 304 L passivated in air can be seen in Fig. 3. Oriented linear superstructure appear on important areas on both sides of the boundary making an angle of 34°. This supertstructure consists of very thin corrugations which are formed by lengthened small islands. The corrugation period is about 3 nm. This situation traduces an epitaxy with the substrate since the corrugation direction is associated with the grain cristallographic orientations of the polycristal. On the right side of the grain boubary, a lower scan of 7.5 nm has been obtained with atomic resolution (Fig.4). This image shows that lendgthened small islands of Fig. 3 are composed of an alignment of clusters containing about twenty visible atoms. A cristalloraphic order cannot be identified in these clusters.

Atomic structure of passive films formed in air at 20°C on 304L SS was clearly observed on several images. Fig. 5 shows that atoms of the oxide matrix are ordered in two directions making an angle about of 90°. Besides, the lattice constant measured is approximately 4.64 Å. Thus, we can

assume that this crystallographic structure could correspond to cubic or tetragonal systems. Two oxides have a structure near of these : FeO crystallizes in cubic system with a lattice constant a=4.3 Å and CrO_2 crystallizes in tetragonal system with the lattice constant equal to 4.41 Å. In the image illustrated Fig. 6, atoms are always ordered in two directions making an angle of 120° (rhombohedral arrangment) and the lattice constant is equal to 3.2 Å. β-NiO crystallizes in this system but this oxide is generally obtained at 275°C. Cr_2O_3 have rhombohedral structure too, but a lattice constant of about 5.36 Å which is much higher than the one observed.

Ex situ observations of surfaces of polycristalline 304 L passivated in $MgCl_2$ solution at 117°C have been realized at low scans. Image in Fig. 7 shows well-oriented superstructure forming corrugation of period 1 nm. Just like in larger scans (Fig. 3), an order exist at 15 nm scan. This denotes the high fractal character of passive films.

At this stage of the study, it is very difficult to identify the origine of these superstuctures since it doesn't exist structural models of passive films as a mixing up of oxides and hydroxides.

Few experiments have been made with a 316 L SS passivated in ambient air. An image shown in Fig.8 proove that an order exist in a long scale in the oxide. So, we can suppose that the passive film formed on 316L in air is at least partially crystallized and certainly a strong epitaxy exist with the substrate.

CONCLUDING REMARKS

These first observations could lead to make important remarks on the structure of the external part of the passive film formed on austenitic steels surfaces under different conditions :

- All these images proove the existence of an order on a significant distance suggesting that the passive film is at least partially crystallized. Even if sometimes no order seem to exist at atomic scale, for longer scans, corrugations denotes a strong epitaxy relation between the substrate and the supercial film either at atomic scale or at long scans.
- Under the same experimental conditions and for the same austenitic steel, different crystallographic systems are observed on stainless steel surface (cubic, tetragonal, rhombohedral). This constatation proove that several oxides can be present in the external layer of the passive film, even if at the present time we cannot precisely identify these oxides. Therefore, more or less important amorphous zones should exist as transition zones between these crystallographic structures.
- The strong cristallized character of the passive films suggests that their mechanical behavior is much more brittle than ductile.

These first observations were not realized in satisfactory experimental conditions. At present, we attempt to control electrochemical parameters to produce a more homogeneous film with less contamination. In this way, we use 316 L oriented single crystal and the Electrochemical STM (ECSTM) to operate in situ. The experiments are performed in a glooves box under inert atmosphere in order to control humidity and oxygen content.

Acknowledgments

The authors would like to express their gratitude to Dr H. Saadaoui, C. Daulan and Pr. J.C. Roux for their assistance with the STM experiment and for stimulating discussions.

REFERENCES

[1] R.B. Diegle, W.K. Boyd, Slow strain technique. ASTM STP 665, Eds. G.M. Ugiansky and J.H. Payer, 26 (1979).
[2] J.R. Galvele, "Passivity of metals", R.P. Frankhental and J. Kruger Eds., The Electrochemical Society, 285 (1978).
[3] M. Janik-Czachor, J. Electrochem. Soc. **128**, 513 (1981).
[4] J. Kruger, Int. Met. Rev. **33**, 113 (1988).
[5] R.C. Newman in "Embrittlement by localized crack environment", Ed R.P. GANGLOFF, AIME, 291 (1984).
[6] R.B. Diegle and D.A. Vermilyea, Corrosion **32**, 411 (1976).
[7] M. Keddam, R. Oltra, J.C. Colson and A. Desestret Corros. Sci. **23**, 4, 441 (1983).
[8] S.F. Bubar and D.A. Vermilyea, J. Electrochem.Soc **114**, 9, 882 (1967).
[9] J.C. Grosskreutz, J. Electrochem.Soc. **117**, 7, 940 (1970).
[10] J. Grosskreutz, J. Electrochem. Soc. **16**, 9, 1232 (1969).
[11] H.A. Mc Carthy Harrison, Corros. Sci. **14**, 469 (1974).
[12] F.P. Ford, EPRI report, NP 2589, (1982).
[13] R.A. Diegle and D.A. Vermilyea, Corrosion **32**, 411 (1976).
[14] P. Marcus, "Corrosion Sous Contrainte, Phénoménologie et Mécanismes" D. Desjardins et R. Oltra. Editions de Physique, 101 (1990).
[15] J.M. Olive, D. Desjardins, in "Corrosion Deformation interactions" Eds T. Magnin and J.M. Gras, 755 (1993).
[16] J.M. Olive, V. Vignal, to be published (1994).
[17] P. Marcus, J. Electrochem. Soc. **135**, 2706 (1988).
[18] E. De Vito and P. Marcus, Surf. and Interface analysis **19**, 403 (1992).
[19] C.Sarrazin, J.M. Olive, R. Karray, D.Desjardins, to be published (1994).

CAPTIONS

Figure 1: STM image of an electrochemical polishing surface of polycristalline 304L sample passivated in ambiant air.

Figure 2: Ex situ STM image of an electrochemical polishing surface of polycristalline 304L sample passivated in MgCl2 (30% weight) at 117°C.

Figure 3: Ex situ STM image of a 304 L stainless steel (S.S.) surface passivated in air at room temperature. Oriented superstructures traduce an epitaxy with the substrate. There are two orientations making an angle of 34° on both sides of a grain boundary.

Figure 4: Atomic resolution ex situ STM image of a 304 L stainless steel passivated in air at 20°C. Detail of an oriented superstructure showed in Fig. 3 at 75 nm scale. At 7,5 nm scale, clusters of atoms which form the superstructure are weakly ordered.

Figure 5: Atomic resolution of a 304 L stainless steel passivated in air at 20°C (experimental conditions : I_t=1nA, V_t=20 mV). The atomic structure should correspond to FeO (lattice constant a = 4.3 Å, cubic) or CrO_2 (a = 4.41 Å, tetragonal).

Figure 6: Ex situ STM image at atomic scale of a 304 L stainless steel passivated in air at 20°C. Rhombohedral structures are shown (lattice constant a = 3.2 Å, $2\alpha = 120°$).

Figure 7: Ex situ STM image of a 304 L stainless steel passivated in MgCl2 at 117°C. Oriented superstructure.

Figure 8: Ex situ STM image at atomic scale of a 316 L austenitic steel passivated in air at room temperature (I_t = 4.2 nA, V_t = 32mV). Important oriented rows of atoms indicating the existence of an order in a long distance.

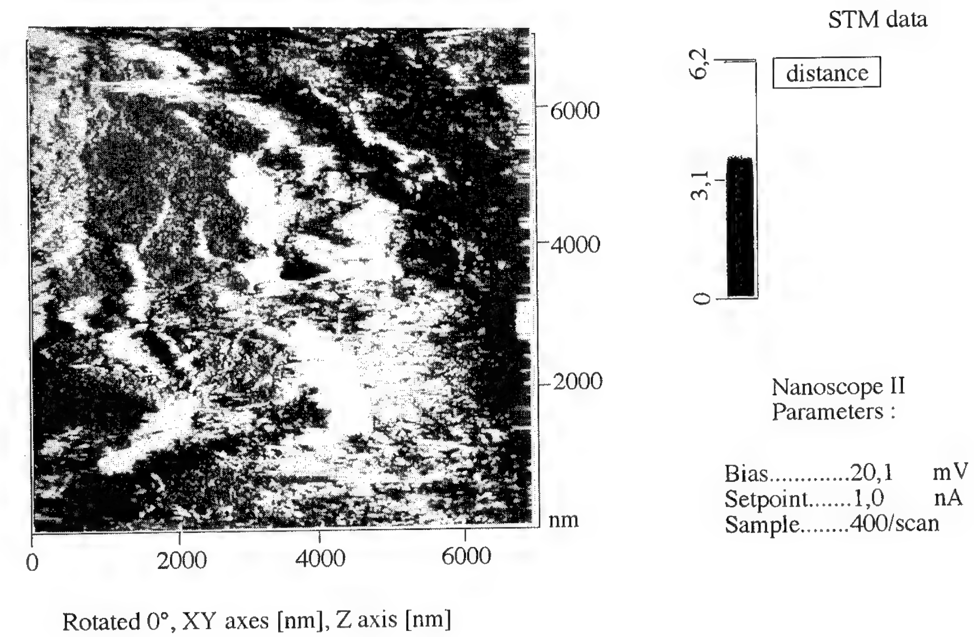

FIGURE 1

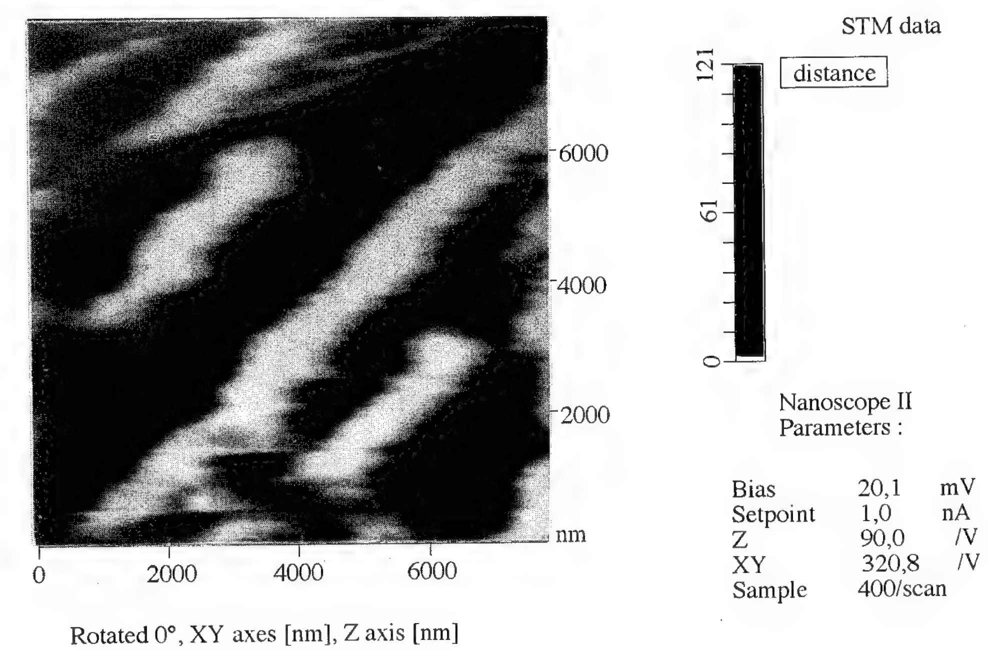

FIGURE 2

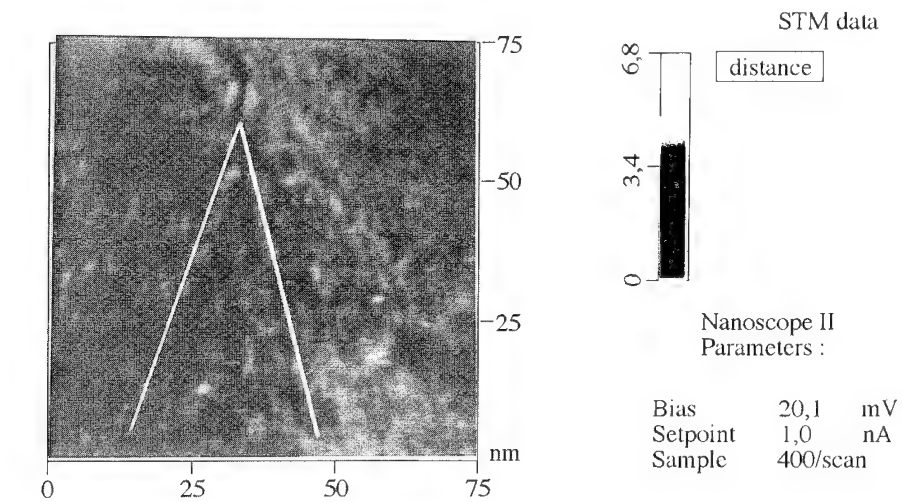

Rotated 0°, XY axes [nm], Z axis [nm]

FIGURE 3

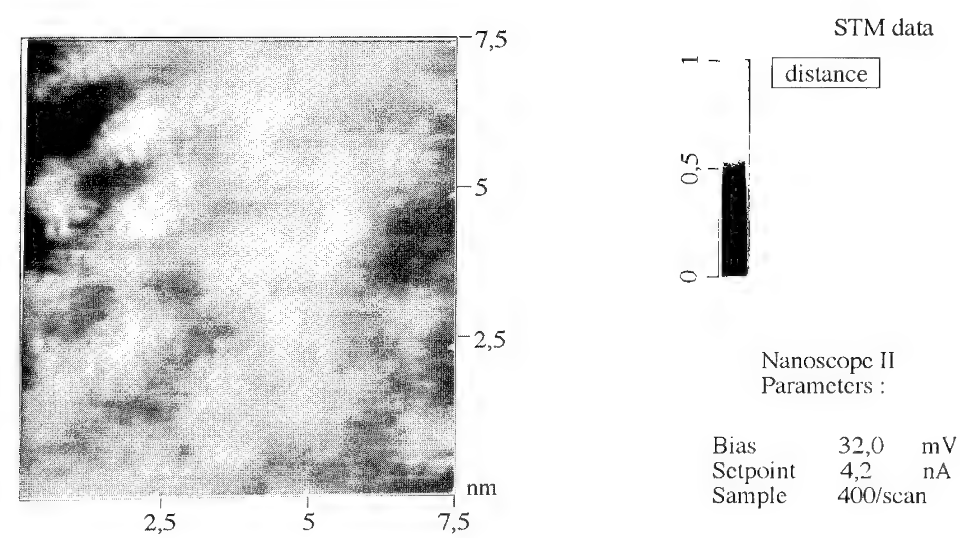

Rotated 0°, XY axes [nm], Z axis [nm]

FIGURE 4

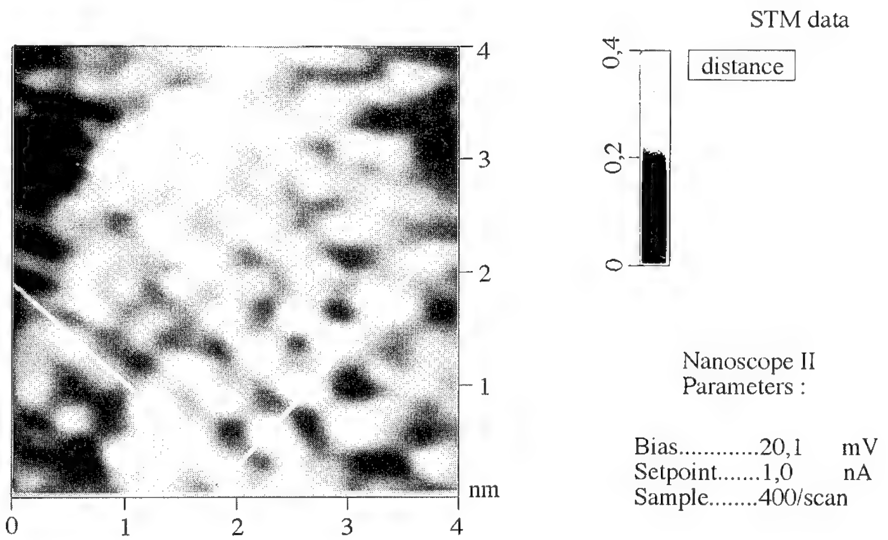

Rotated 0°, XY axes [nm], Z axis [nm]

FIGURE 5

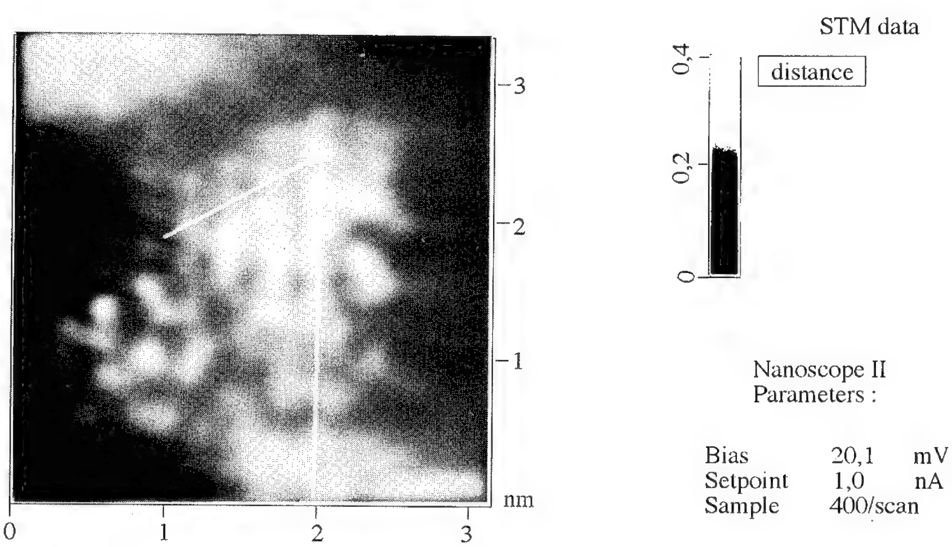

Rotated 0°, XY axes [nm], Z axis [nm]

FIGURE 6

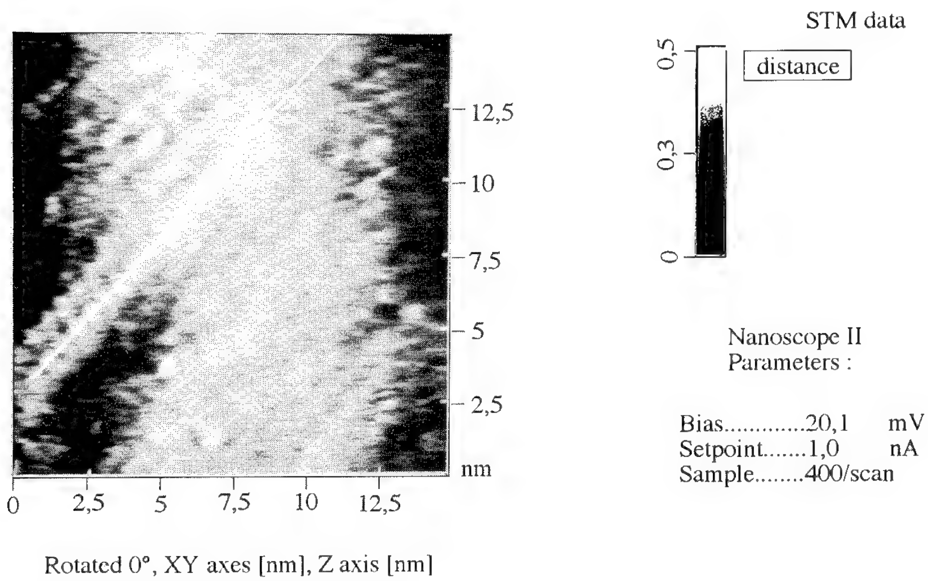

FIGURE 7

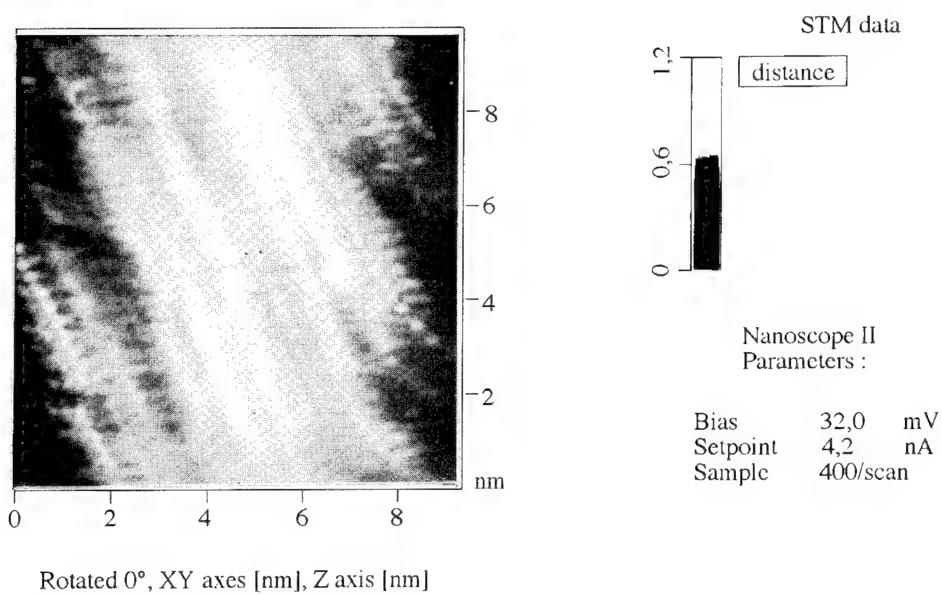

FIGURE 8

Materials Science Forum Vols. 185-188 (1995) pp. 251-260

AFM observations of the breakdown damage in anodic Ta_2O_5 films

I. Montero, J.M. Albella and L. Vázquez

Instituto Ciencia de Materiales, CSIC, Cantoblanco, E-28049 Madrid, Spain

Keywords: Tantalum oxide, anodic oxidation, breakdown, morphology, atomic force microscopy

ABSTRACT

High resolution images, at nanometric scale, of the damage produced on anodic Ta_2O_5 oxide films subjected to breakdown during anodization has been obtained by Atomic Force Microscopy (AFM). The time evolution of the breakdown damage has been followed by anodizing different samples at increasing anodization times after breakdown in galvanostatic conditions. The AFM images reveal that the breakdown is initiated in definite spots scattered all across the surface, producing a granular structure of about 100 nm diameter. Superimposed on this granular structure some protrusions of larger sizes also appear which, after further anodization, give rise to ridges and craters on the surface. They finally evolve into cracks penetrating the whole oxide thickness. The damaged areas are then propagated in the form of branches covering large regions of the oxide surface. These results have been analyzed in terms of a localized heating as a consequence of the thermal runaway produced by the avalanche currents during the breakdown process.

1. INTRODUCTION

The dielectric breakdown in anodic oxide films is a phenomenon of great interest, both from a scientific and technological point of view, since it is related to different oxide properties and applications (passivation layers, dielectric films in capacitors, gate oxide in microelectronic circuits, etc). Anodically formed films of Ta_2O_5 are amorphous when formed at voltages below breakdown, but upon heating they recrystallize to other disordered forms [1,2]. Likewise, the breakdown processes

occurring during the anodization at high voltages produce structural changes in the oxide film.

The observation of the morphology of the breakdown areas on the sample surface has traditionally been made by optical microscopy and scanning electron microscopy (SEM). However, low resolution images can be obtained by SEM due to charging effects on the insulator films. On the other hand, atomic force microscopy (AFM) provides a useful tool which allows not only direct surface observation, with tridimensional imaging at nanometric resolution, but also quantification of the surface roughness [3]. The present work has been undertaken to investigate the first stages and the evolution of the breakdown phenomenon during the anodic oxidation using this novel technique. To our knowledge, this is the first time this technique is reported in the observation of the breakdown damage.

2. EXPERIMENTAL PROCEDURE

Polycrystalline tantalum foils of 99.96% nominal purity were anodized up to the breakdown voltage in a electrolytic cell at a constant current density of 2 mA cm^{-2} in a 0.001 M H_3PO_4 solution in deionized water at room temperature. The Ta surface was first degreased and chemically polished in a mixture of concentrated H_2SO_4, HNO_3 and HF in a 5:2:2 volume ratio and finally in a buffered solution of NH_4F in HF. After this treatment the specimens were finally thoroughly washed in deionized water.

The samples were then analyzed by AFM using a Nanoscope III system (Digital Instruments) operating in the contact mode. Silicon nitride cantilevers were employed. All images were acquired at a resolution of 512 x 512 pixels. In order to obtain representative images of the surface we scanned wide areas (typically 60 μm, although sometimes we scanned 110 μm) and then we reduced the scan size. Thus, images of 60, 25, 10 and 3 μm were taken for every sample. From each image the root mean square (rms) roughness was calculated. The AFM images presented in this paper are offered in a top view (the brighter the pixel the larger the height) and in a three dimensional representation (3D).

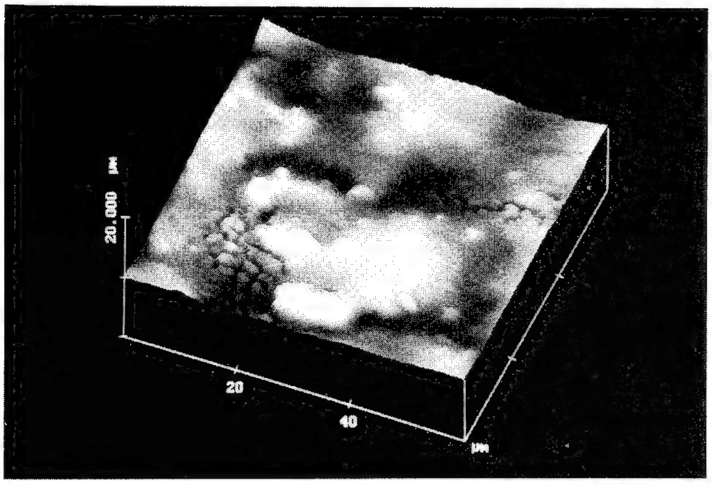

Fig. 4.- *3D AFM image (60 x 60 μm^2) of the sample of fig. 3 after reanodization at a voltage below breakdown.*

3. DISCUSSION

The above results can be explained on the light of the breakdown models during anodic oxidation. These models are generally based on the avalanche mechanisms established for insulating films flanked by metallic contacts. These avalanches are produced under the effect of the high electric field of anodization [4-6]. As a consequence of the avalanche current developed in some spots of the sample surface, there is a local heating which further increases the current, giving rise to a crystallization and finally to breakdown. The small grains observed in the flat areas of figs 1-3 can be attributed to this effect, i.e., the formation of very small crystalline grains. These small features may also develop in greater damaged areas by a cooperative effect. This is likely due to the accumulated Joule heating, which produces stresses in the films and causes the observed protrusions and ridges extended on the surface in branched structure (fig.1) [7-8]. These rough structures may finally evolve into cracks and microfissures, as observed in fig 2.

The interpretation of AFM images is often complicated by distortions resulting from the non negligible size of the probe tip. In particular, sharp angular surface features tend to be smoothed by convolution with the rounded surface of the tip. For this reason, the topography of the images tends to underestimate the sharpness and depth of the surface features. In our work this problem is only present when imaging the lateral walls of the fissures and cracks: as the fissures are very sharp the convolution with the cantilever tip geometry could be large and the surface imaged would be that of the tip rather than that of the fissure wall.

2. EXPERIMENTAL RESULTS

As it is well known, during the anodic oxidation process at a constant current density the thickness of the oxide grows almost linearly with time until the dielectric breakdown occurs. The samples prepared at voltages below the breakdown voltage present a flat surface when the oxide thickness is high enough to smooth the grain boundaries of the underlying metal. On the contrary, in the initial stages of breakdown the films offer rough spots or protrusions (around 15 nm high), encircling small valleys, which are interconnected in branches, covering wide areas of the surface. Figs. 1*a* and 1*b* are an example of this behaviour. In this case the sample was anodized at 330 V, which is somewhat higher than the breakdown voltage (V_B = 320 V). Surprisingly, no pores or microfissures are observed in fig, 1b, although small grains appear scattered on the surface with a typical size of about 100 nm in diameter and 5 nm in height. It is worth to mention that these structures, due to their small corrugation, are difficult to be observed by conventional electron microscopy.

Further anodization of the sample (V = 380 Volts) gives rise to a well defined structure of cracks and microfissures running in branches across the oxide surface, as observed in figs. 2*a* and 2*b*. The average measured depth of grooves is about 0.4 μm with a width of 1.1 μm. In the flat areas it is observed a granular structure rougher than that of previous images as it covers totally the regions between fissures as it is shown in Figure 2*b*.

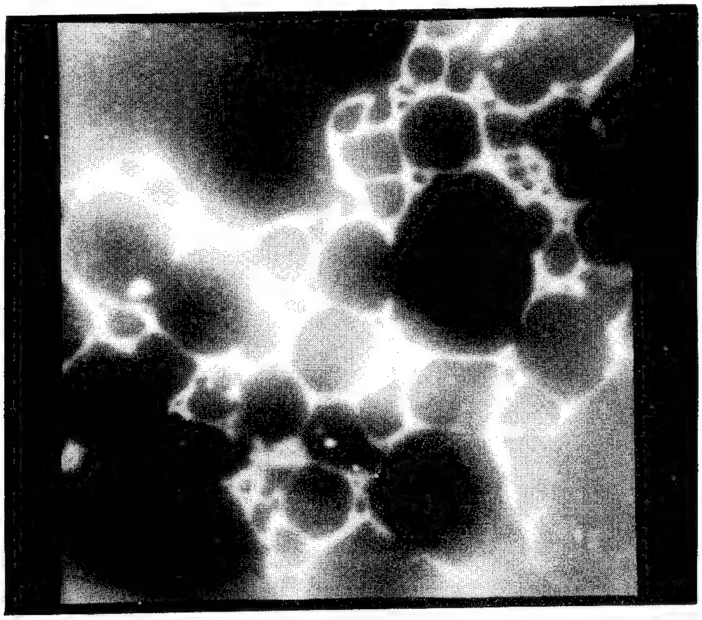

Fig. 1a.- *Top view AFM image (6.1 x 6.1 μm^2) of the sample surface at the initial stages of breakdown.*

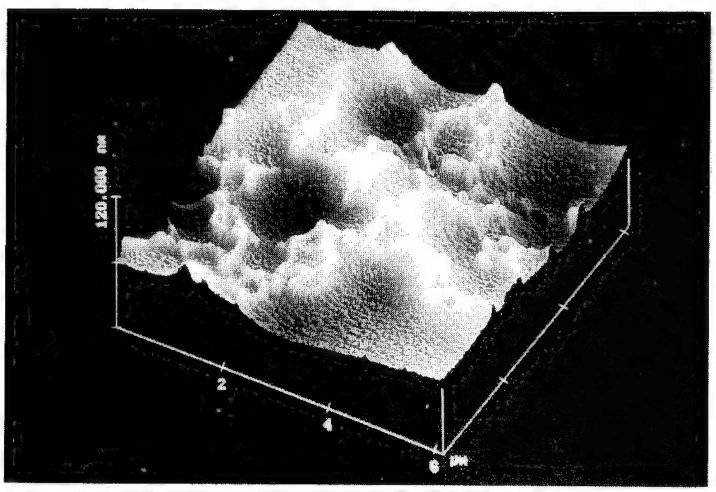

Fig. 1b.- *3D AFM image (6.1 x 6.1 μm^2) of the sample surface at the initial stages of breakdown.*

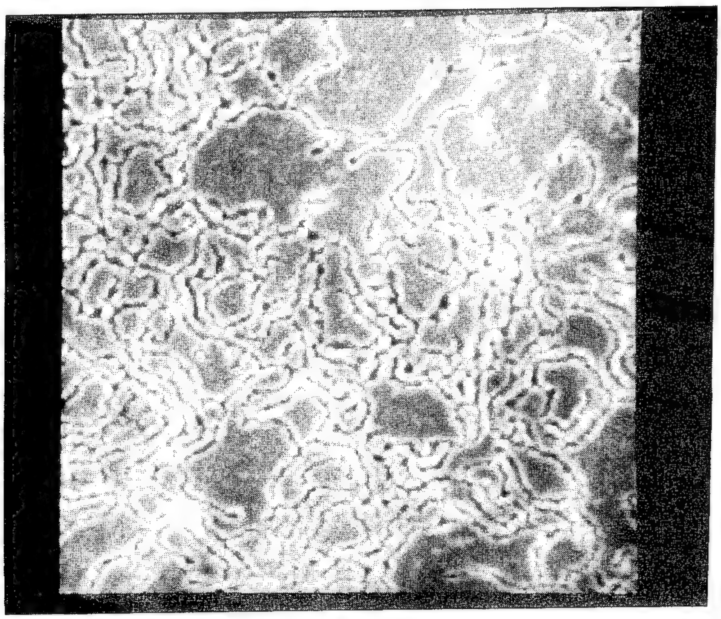

Fig. 2a.- *Top view AFM image (60 x 60 μm^2) of the breakdown damage of a sample anodized at 380 V.*

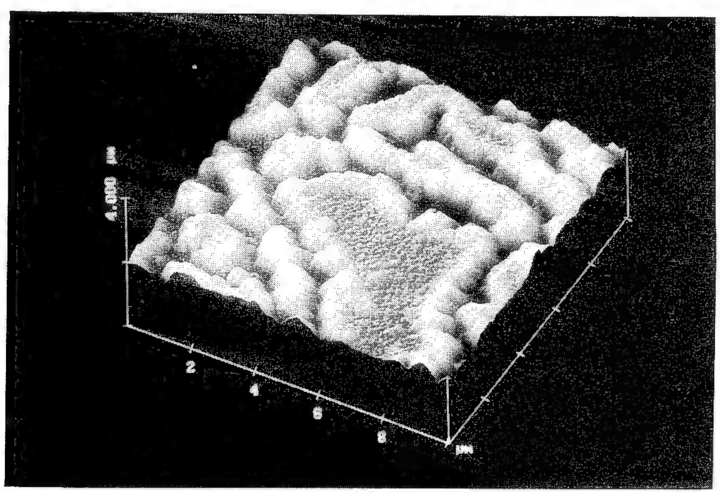

Fig. 2b.- *3D AFM image (10 x 10 μm^2) taken at higher resolution of the breakdown damage of a sample anodized at 380 V.*

Prolonged anodization after breakdown voltage produces the so-called 'grey oxide'. The sample shows in this case wider cracks and grains extended all across the surface. The greater size of the cracks (around four times larger than those of Figure 2) is likely associated to the coalescence of the multiple microfissures present in the surface (fig. 3).

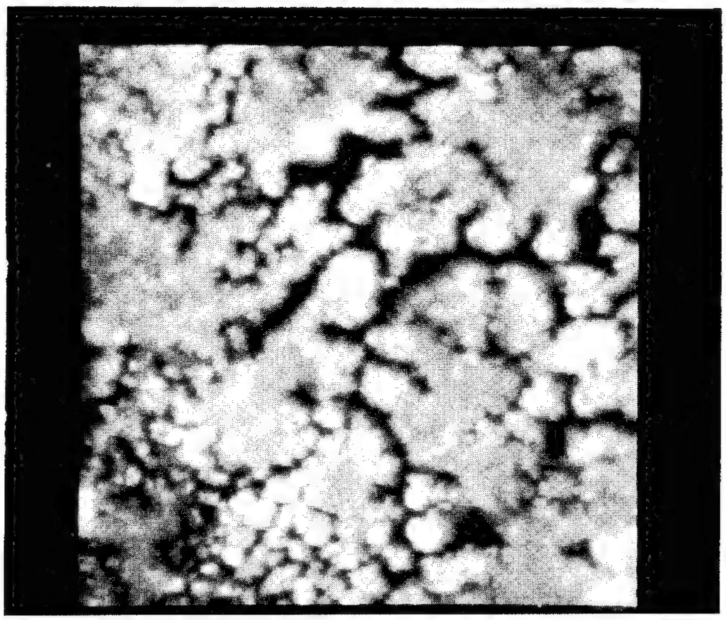

Fig. 3.- Top view AFM image (60 x 60 μm^2) of a sample subjected to prolonged anodization after breakdown, showing the characteristic 'grey oxide'.

If the sample of fig. 3 is reanodized under the same conditions but at a lower constant voltage, the surface becomes smoother again as a consequence of a healing effect of the breakdown damage. As can be appreciated in fig. 4, part of the branched microfissures have disappeared from the surface, which now shows wide flat regions.

Although some of the breakdown spots can be healed during further anodization [9], Joule heating in the brokendown spots probably increases the damage and gives the characteristic 'grey oxide' (fig. 3). The reanodization process applied on a broken down sample produces a partial healing of the damage (fig.4) in agreement with previous observations [9].

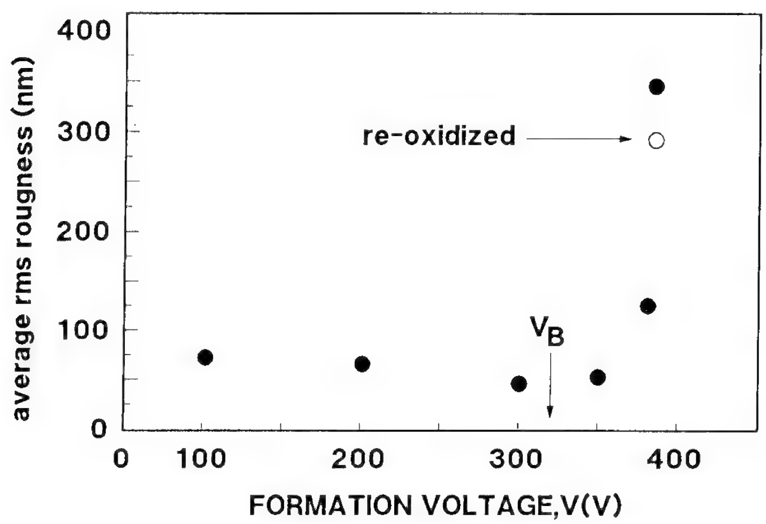

Fig. 5.- *Surface roughness at different times of anodization and breakdown.*

An assessment of the breakdown damage produced under prolonged anodization has been made through roughness measurements of the oxide surface. Fig 5 shows the roughness of the sample as a function of the anodization time, obtained from the software supplied by the AFM instrument. As can be appreciated, before breakdown the roughness of the oxide surface decreases with the formation voltage (or, equivalently, the oxide thickness) as consequence of the smoothing effect of the oxide growth. However, for voltages above breakdown the roughness suddenly increases with time, due to the surface damage produced on the oxide surface. As expected, the longer the breakdown time of the sample, the larger is the surface roughness with greater values for the 'grey oxide'. Finally the reanodization of the grey sample leads

to a smoother surface morphology (see Figure 5) where many of the fissures have been filled although the granular structure remains after the treatment.

4. CONCLUSIONS

The first stages and the time evolution of the breakdown process during the anodic oxidation of tantalum has been studied. The topography of the anodic tantalum oxide films have been examined with atomic force microscopy. This technique has proved to be an useful tool to study the evolution of the breakdown damage during prolonged anodization. The origin of the breakdown process has been associated to the electron avalanches occurring during the oxidation. Before breakdown the film growth produces a smoothing effect of the grain structure of the underlying metal. After breakdown, the oxide initially shows a rough surface which further develop into cracks and microfissures along with small crystalline grains and finally in microcrystalline powder characteristic of 'grey oxide'. Reanodization at lower voltages partially heals the brokendown areas.

REFERENCES

[1] R. E. Pawel and J. J. Campbell, *J. Electrochem. Soc.,* **111** (1964) 1230.

[2] N. C. Stephenson and R. S. Roth, *J. Solid State Chem.,* **3** (1971) 145.

[3] C.F.Quate, *Surf.Sci.*, **299/300** (1994) 980.

[4] J. M. Albella, I. Montero and J. M. Martinez-duart, *Thin Solid Films*, **125** (1985) 57.

[5] J. M. Albella, I. Montero and J. M. Martinez-duart, *Electrochim. Acta*, **32** (1987) 255.

[6] I. Montero, J. M. Albella and J. M. Martinez-Duart, *J. Electrochem. Soc.*, **132** (1985) 814.

[7] R. E. Pawel and J. J. Campbell, *J. Electrochem. Soc.,* **127** (1980) 2035.

[8] R. E. Pawel and J. J. Campbell, in "*Stress Effects and the oxidation of metals*", J. V. Cathcart, Editor, pp. 330. The matallurgical Society of AIME, New York (1975).

[9] I. Montero, M. Fernandez and J. M. Albella, *Electrochim. Acta,* **32** (1987) 171.

Materials Science Forum Vols. 185-188 (1995) pp. 261-266

STM images of material surfaces deformed by impingement of a solid ball and characterizations of their passive films

H. Nanjo[1], N. Sanada[1] and K. Koike[2]

[1] Tohoku National Industrial Research Institute, 4-2-1, Nigatake, Miyagino-ku, Sendai 983, Japan

[2] Tohoku Gakuin University, 1-13-1, Chuo, Tagajo 985, Japan

Keywords: STM, spectroscopy, tunnel current, deformation, impact, electronic property, oxide film

A study was done on the surface topography around pits which was observed with a scanning tunneling microscope(STM). The relation between tunnel current and bias voltage was measured with a tunneling spectroscope(TS).

For the pit formed in a mild steel surface by an impingement of a steel ball, the roughness in the part around pit rim was largest. On the other hand, the roughness of inner surfaces of the pit was almost as small as that of the flat surface away from the rim. In the case of a highly oriented pyrolytic graphite(HOPG), arrangement of carbon atoms was observed to be almost regular at the region from the top of the pit rim to the bottom of the pit. The atoms were not in a regular manner just at the outer region from the top. STM images such as dislocation, crack or hollow were observed with nanometer resolution.

It was possible to evaluate the electronic property of oxide film on metals at such a high bias voltage as 1 V by means of I – V spectra. In I – V spectra at the region of negative tip bias voltage to SS400 mild steel surface, the absolute values of the currents on grains generated around the pit rim were smaller than those of the flat part away from the pit rim.

1. INTRODUCTION

The properties of metal surface such as the electrical insulation and the corrosion resistance are reduced in the multiphase flow containing solid particles. Though mass loss in the flow with the particles was the same as that without them, surface topographies were apparently different from one another as shown in the Fig. 6 of appendix[1]. The difference is caused due to the breakdown of passive films on the metal; that is, the films are destroyed by the attack of solid particles and the reproduced films are formed inhomogeneously. The surface topography is not smooth and the surface conditions around the pit are different from those of flat surface. Then, the properties of passive films varies locally.

In this study, the surface topographic images around pits were observed with a scanning tunneling microscope(STM) to examine where passive films formed on metal surfaces were easily broken down by the surface deformation. The relation between tunnel current and bias voltage was measured with a tunneling spectroscope(TS) to evaluate the electronic properties of passive films around the pits. Moreover, this technique has been also used to locally characterize electronic structures of samples such as rectifying behavior[2–4] and a position of forbidden band[3,5].

2. TEST APPARATUS AND PROCEDURE

Pits on SS400 mild steel and A5056 aluminum alloy were formed by free fall of a steel ball of 1.6 mm in diameter at an impact speed of 4.4 m/s. A pit on a highly oriented pyrolytic graphite(HOPG) was made by pushing a steel needle so as not to separate layers of HOPG in impacting. The needle in cross section looked like a pentagon and the figure of the needle tip was 0.8 μm in radius. A micro hardness tester was used for pushing it. The load was 0.098 N (10 gf) and the loading period was 5 seconds. Specimen surfaces were polished with buff clothes and diamond paste of 1 μm and were washed in acetone with an ultrasonic cleaner. The specimen

surfaces were observed in air with a scanning tunneling microscope(STM). The probe tip was made of platinum and iridium[6] to reduce the effect of cleaning state of the tip[7].

Current – tip bias voltage (I–V) spectra were measured with a tunneling spectroscope(TS)[8,9]. As the representative measuring conditions, the averaging number of current was 32 at each bias voltage, the average number of I – V spectra was 16 and it took 4 seconds to obtain the final I – V spectra. The averaging[2,7,10] permitted taking a steady I – V spectrum.

3. EXPERIMENTAL RESULTS

3.1 Characteristics of metal deformation

STM image and a cross section around a pit rim of SS400 are indicated in Fig. 1. The roughness of inner surfaces of the pit was almost as small as that of the flat surface away from a pit. On the other hand, the roughness was largest in the part around pit rim and its maximum height was larger than 10 nm. The state of the roughness was not like sliding lines and was like grains as shown at the left part of Fig. 1(a). Furthermore, the roughest part was confirmed to be a pit rim in the case of A5056 aluminum alloy, too.

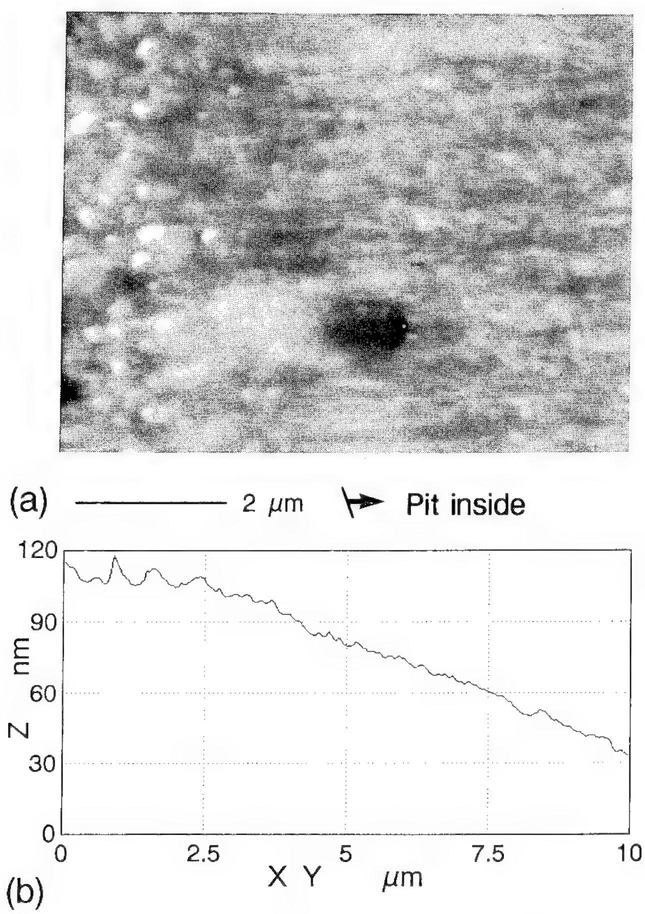

Fig. 1 (a) STM image and (b) a cross section around a pit rim of SS400 (177μm Diameter).

3.2 Characteristics of HOPG deformation

STM image and a cross section around a pit rim of HOPG are shown in Fig. 2. A swell was generated around the pit rim since the aspect ratio of depth to diameter of the pit formed by pushing the needle was fairly larger than that in the case of the steel ball. The surface from the top of the swell to the pit bottom was smooth, and the surface on the other side from the top to the outer edge of the swell was rougher.

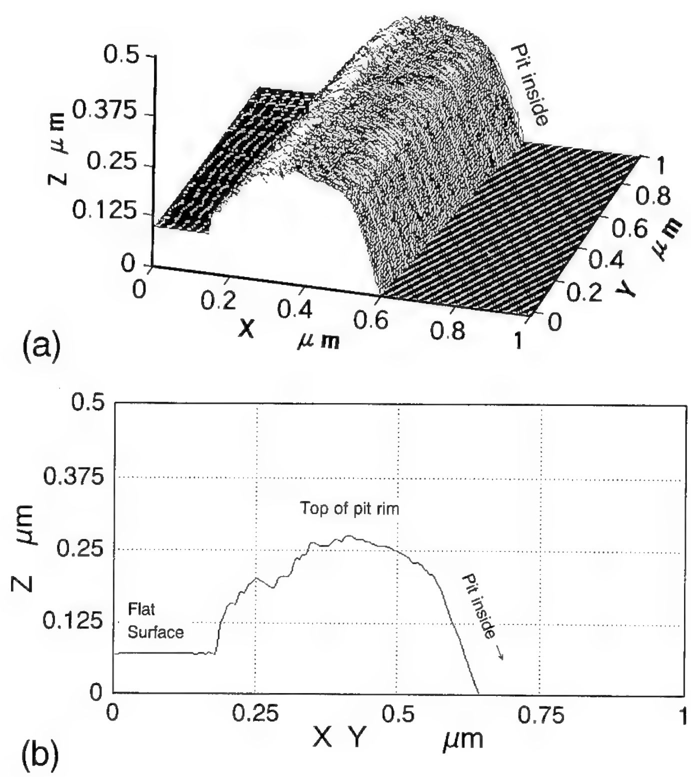

Fig. 2 (a) STM image and (b) a cross section around a pit rim of HOPG.

Figure 3 indicates STM images around the pit of HOPG. The arrangement of carbon atoms was observed to be regular at the flat surface, and the similar atomic images could be taken at the surface from the top of the pit rim to the bottom of the pit. Figure 3(b) shows the roughest part near the bottom of the pit. It was possible to observe an atomic image in spite of the roughest region. The STM image of the top of the swell is shown in Fig. 3(c). In this region the atoms were not in a regular manner just at the outer region from the top. Dislocations, cracks or hollows could be observed with nanometer resolution at the upper part of Fig. 3(c).

3.3 I – V spectra of flat surfaces and pit rims of metals

Figure 4 shows I – V spectra at the flat surfaces of A5056 aluminum alloy, SUS304 stainless steel and SS400 mild steel. In the case of a small tip bias voltage, I – V spectra of these metals

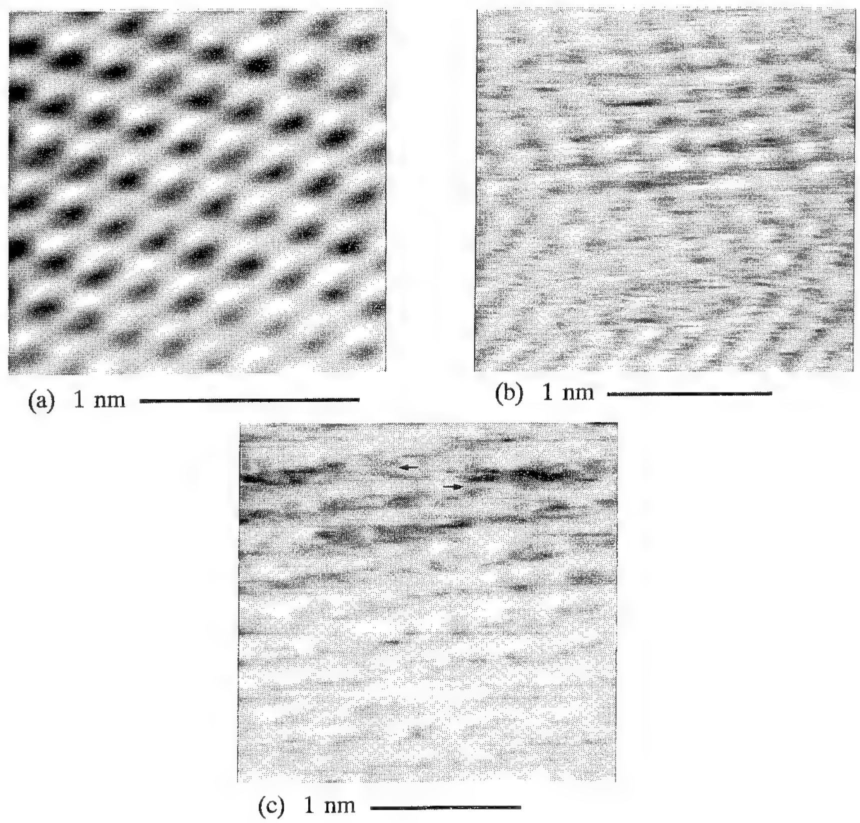

Fig. 3 STM images around a pit of HOPG : (a) a flat surface, (b) the roughest part around pit bottom, (c) a pit rim.

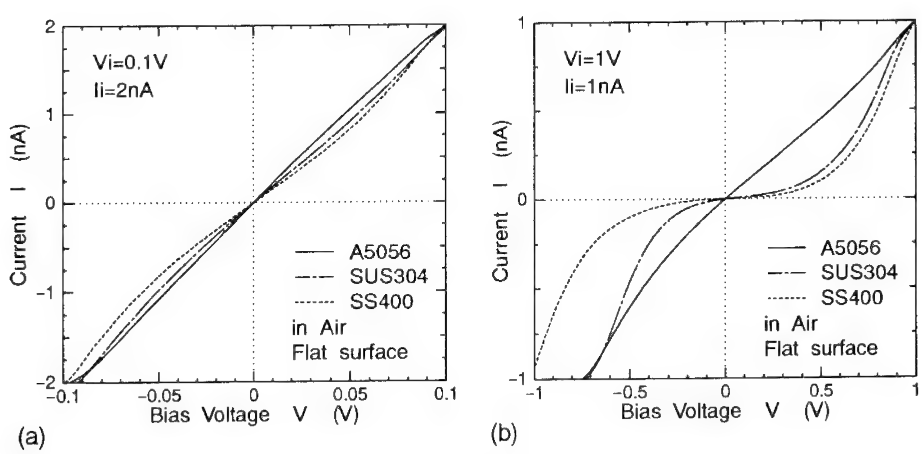

Fig. 4 I – V spectra at flat surfaces of A5056 aluminum alloy, 304 stainless steel and SS400 mild steel.

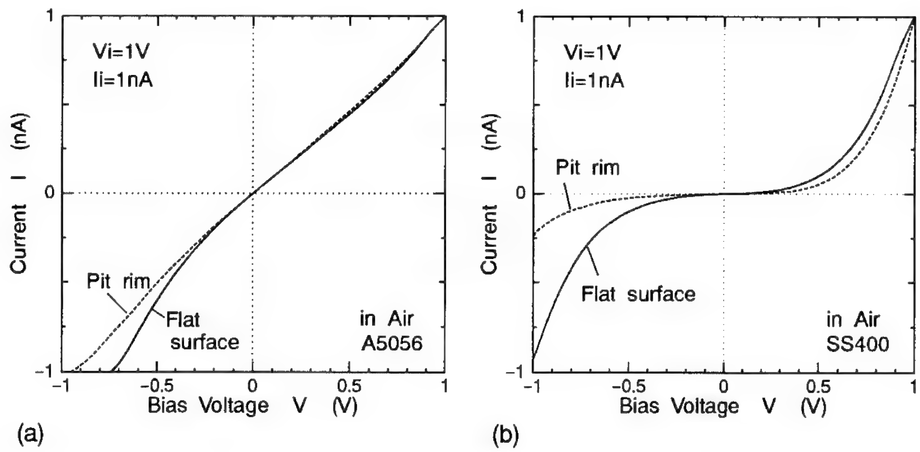

Fig. 5 I – V spectra at flat surfaces and pit rims of A5056 aluminum alloy and SS400 mild steel

were almost straight lines. When the bias voltage was higher, I – V spectrum of A5056 was also similar to a straight except for negative region. However, I – V spectra of SS400 and SUS304 were the shape of reverse S letter. It was found from this figure that it was possible to evaluate the electronic property of thin film such as a passive film.

Figure 5 indicates I – V spectra at a flat surface and a pit rim of SS400 mild steel and A5056 aluminum alloy. There was not large difference of I – V spectrum between a flat part and a pit rim of A5056. In the case of I – V spectra at negative bias voltage region of SS400, absolute values of the currents of the pit rim were smaller than those of the flat part. It was presumably because corrosion products like grains as seen in Fig. 1 were generated at the part where oxide films were broken down around the pit rim and tunnel currents were suppressed. Furthermore, the I – V spectra at the part among grains were confirmed to be similar to those at flat parts.

4. CONCLUSIONS

Surface topography around pits was observed with the scanning tunneling microscope and I – V spectra were measured to try to evaluate the film property around pits with the tunneling spectroscope. The results obtained are summarized as follows:

(1) The roughness of parts around pit rims of SS400 and HOPG were largest. On the other hand, the roughness of inner surfaces of the pit was almost as small as that of the flat surface away from the pit.

(2) In the case of a graphite(HOPG), the arrangement of carbon atoms was observed to be regular at the surface from the top of the pit rim to the bottom. The atoms were not in a regular manner just at the outer surface from the top. STM images of dislocations, cracks or hollows were taken with nanometer resolution.

(3) It was possible to evaluate the film property by I – V spectra at such a high bias voltage as 1 V. In I – V spectra at negative bias voltage region of SS400, the absolute current values on grains generated around the pit rim were smaller than those of the flat parts.

REFERENCES

[1] H. Nanjo, Y. Kurata, N. Sanada, K. Miyauchi, R. Ohshima and K. Koike, to be presented at Int'l

Conf. on Erosion by Liquid and Solid Impact, Cambridge, 1994.
[2] L. Vazquez, J. A. Martin–Gago, F. Comin and S. Ferrer, J. Vac. Sci. Technol. B, 10, 566(1992).
[3] E. T. Yu, M. B. Johnson, A. R. Powell, J. –M. Halbout and S. S. Lyer, J. Vac. Sci. Technol. B, 11, 1149(1993).
[4] G. S. Rohrer and D. A. Bonnell, J. Vac. Sci. Technol. B, 9, 783(1991).
[5] M. D. Pashley, K. M. Haberern and R. M. Feenstra, J. Vac. Sci. Technol. B, 10, 1874(1992).
[6] V. Bressler–Hill, M. Wassermeier, K. Pond, R. Maboudian, G. A. D. Briggs, P. M. Petroff and W. H. Weinberg, J. Vac. Sci. Technol. B, 10, 1881(1992).
[7] G. W. Clark and L. L. Kesmodel, J. Vac. Sci. Technol. B, 11, 131(1993).
[8] R. M. Feenstra and J. A. Stroscio, J. Vac. Sci Technol. B, 5, 923(1987).
[9] A. Schummers, H. Halling, K. H. Besocke and G. Cox, J. Vac. Sci. Technol. B, 9, 615(1991).
[10] K. Ikeda, K. Takamuku, R. Itti and N. Koshizuka, J. Vac. Sci. Technol. B, 10, 2311(1992).

Appendix

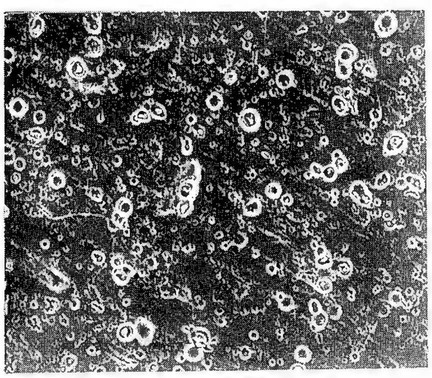

(a)

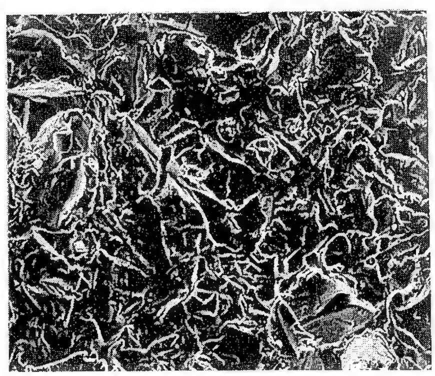

(b)

50 μm

Fig. 6 Damage patterns in multiphase flows (a) without solid particles and (b) with them. The test conditions were as follows: temperature was 390 K, flow velocity 194 m/s, volume flow rate ratio of liquid to the whole fluid 9 x 10^{-5}, mass concentration of solid particles in the whole fluid 2 mg/l, test duration 10 minutes, and mass losses of both cases 1.4 mg[1].

Materials Science Forum Vols. 185-188 (1995) pp. 267-274

Structure of galvanostatic anodic TiO_2 films: Comparison of microscopies

J-L. Delplancke, M-P. Delplancke and R. Winand

Métallurgie-Electrochimie, CP165, Université Libre de Bruxelles, 50 Avenue F.D. Roosevelt, B-1050 Bruxelles, Belgium

Keywords: Titanium, anodic films, structure, microscopies

0 Avenue

Abstract :

The galvanostatic anodization of titanium substrates at high current density (higher than 50 A/m^2 at room temperature) tends to the formation of a thin oxide film with preferential conducting channels inside a homogeneous non conducting matrix. The purpose of this paper is to compare the results obtained by different microscopies (optical microscopy, scanning electron microscopy, scanning transmission electron microscopy at high resolution with electron diffraction and atomic force microscopy) in order to identify the structure and the composition of these channels. These channels are formed by the contact of a small number (10 to 20) of submicronic (100 to 500 nm) crystals. All these crystals present the same crystallographic orientation perpendicular to the substrate. The aggregates are protruding from the relatively flat oxide surface. The different microscopies provide complementary results.

Introduction :

During the anodic oxidation of titanium substrates at high current density, thin TiO_2 oxide films are formed (1,2). These films reproduce the grain size of the underlaying titanium crystals and are then called "epitaxial" films. Depending on the crystallographic orientation of the titanium crystals, the colour produced by the anodic oxide films is changing from grain to grain for a given value of the anode potential. This is related to different oxide densities and growth rates as a function of the underlaying titanium crystal orientations (see "Ellipsometric determination of the density of TiO_2 passive films on Ti single crystals" by A. Michaelis, J-L Delplancke and J.W. Schultze - these proceedings) When the anode-to-cathode (Pt) voltage drop is higher than 10V, oxygen evolution is observed on the anode with a high current efficiency. This is related in the literature (3) to the electrical breakdown of the oxide films with possible structure modification.

Recent observations by optical microscopy (4) show, at high voltage, the formation of dark spots inside the homogeneously coloured oxide grains. Under cathodic polarization in a copper sulphate electrolyte, these spots are

preferential conducting channels and correspond to preferential nucleation sites for copper.
This paper reports the preliminary results related to the structure and the composition of these spots. The results obtained by different microscopies on the same positions of the titanium substrates are compared.

Experimental :

The commercially pure titanium substrates are chemically polished as described previously (5). The galvanostatic anodization is performed at 100 A/m^2 to 50V (anode-to-cathode (Pt) voltage drop) in a 1M sulphuric acid electrolyte (1).
After anodization, two scratches are performed in the middle of the samples, with a titanium cutter, in order to observe with the different microscopies the oxide films on the same titanium crystals.
Optical microscopy, scanning electron microscopy, transmission electron microscopy and atomic force microscopy are performed respectively with Reichert-Jung MeF3A, JEOL JSM 820, PHILIPS CM20 Ultratwin and ambient SFM BD2 Park Instrument microscopes.
For the TEM observations, the oxide films are separated from their substrates as described by Nurse et al. (6).

Results :

1) Optical microscopy :

Three main types of interference coloured oxide films are observed (see Figure 1) :
- uniform bright gold films (type A)
- pale blue films with randomly dispersed dark blue spots (type B)
- pale gold films with a high density of dark brown spots (type C)

Figure 1 : Optical microscopy of the galvanostatic anodic titanium oxide film

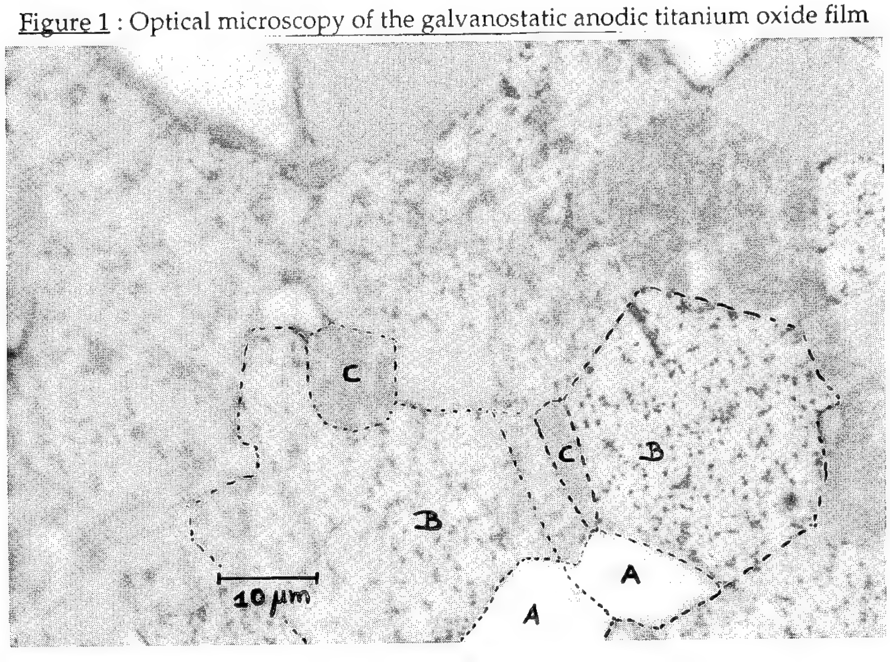

The type B films are the most commonly observed and accordingly, the sample colour is light blue. There are more type C films than type A films.
The dark blue and dark brown spots are not preferentially observed at the titanium grain boundaries.

2) Scanning electron microscopy :

The scanning electron microscopy (SEM) clearly reveals the preferential attack, by the chemical polishing solution, of the different crystals in the titanium substrate (see Figure 2). After gold metallization (due to the insulating properties of the TiO_2 films) and at high magnification, only diffuse features, that could correspond to the spots observed in the types B and C films, are visible. Otherwise, the oxide films is not observed by SEM.
A comparison of figures 1 and 2 shows that the titanium crystals producing the type B films are less attacked by the chemical polishing solution than the other crystals.

Figure 2 : Scanning electron microscopy of the galvanostatic anodic titanium oxide film (same position as Figure 1)

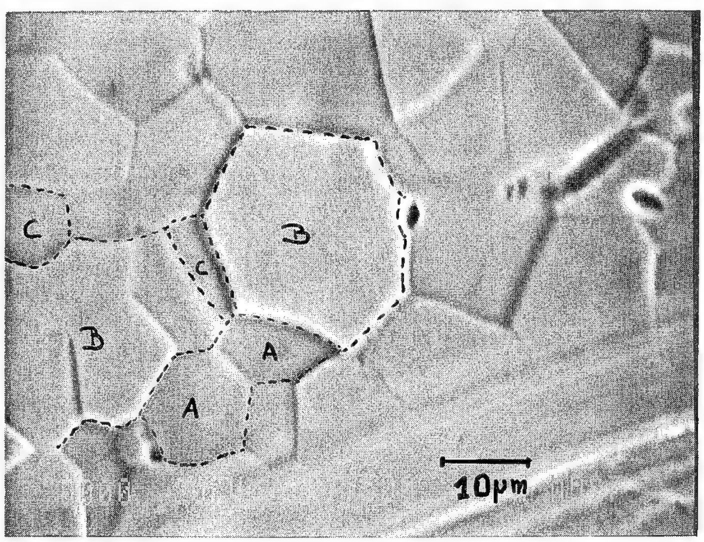

3) Transmission electron microscopy :

The transmission electron microscopy (TEM) reveals a lot of information regarding the structure of the three film types (see Figure 3) :

- the type A films correspond to the thickest oxide films. They are homogeneous but they contain few randomly dispersed very fine spots that are not observed by optical microscopy. These spots are single nanocrystals (diameter less than 100 nm).

- the type B films are the thinnest films. They are inhomogeneous : thicker areas (darker areas) are observed simultaneously with white aggregates. A close comparison between figures 1 and 3 shows that the thick areas correspond to pale gold areas inside the pale blue grains and that the white aggregates correspond to the dark blue spots observed inside these grains. At higher magnification (see Figure 4), these aggregates are identified as groups of tenths of nanocrystals.

- the type C films have an intermediate thickness between the A and B films. They contain an extremely high density of nanocrystals.

Figure 3 : Transmission electron microscopy of the anodic film after dissolution of the titanium substrate (same position as Figures 1 and 2)

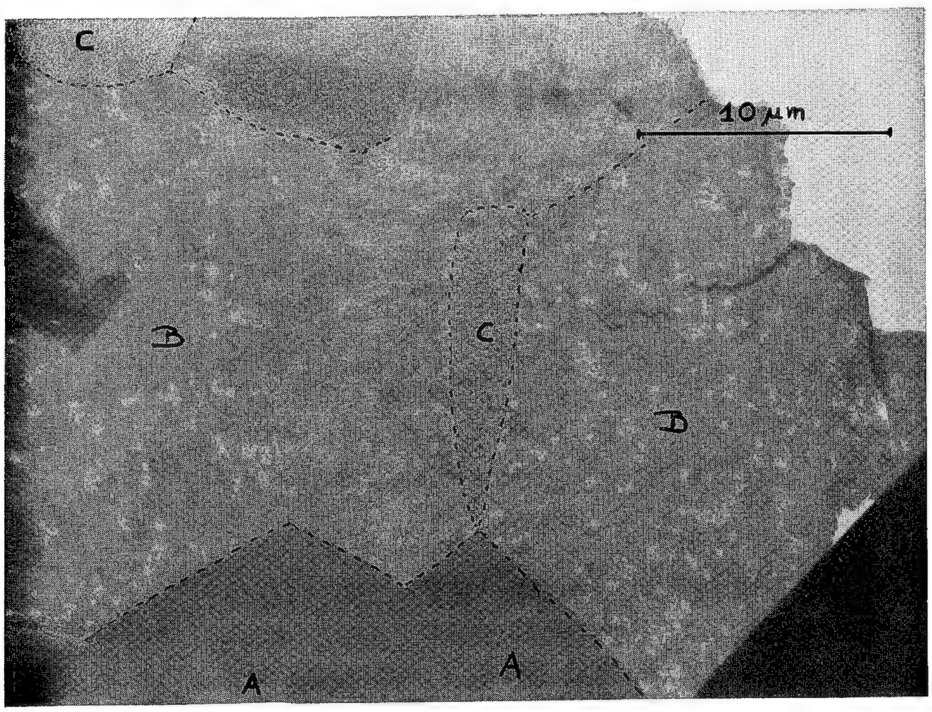

Figure 4 : High magnification TEM picture of a nanocrystalline aggregate observed in the type B oxide films

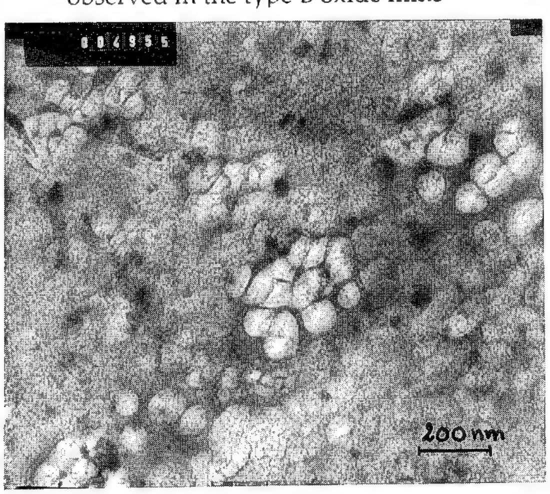

4) Atomic force microscopy :

The atomic force microscopy (AFM) reveals that the oxide surface for the three types of film is very rough (see Figure 5). The nanocrystals are protruding from the average surface. In case of aggregates (type B films), there is often a hole in the middle of the protruding nanocrystals (see Figure 6).

Figure 5 : Roughness profile by atomic force microscopy through a type C anodic film

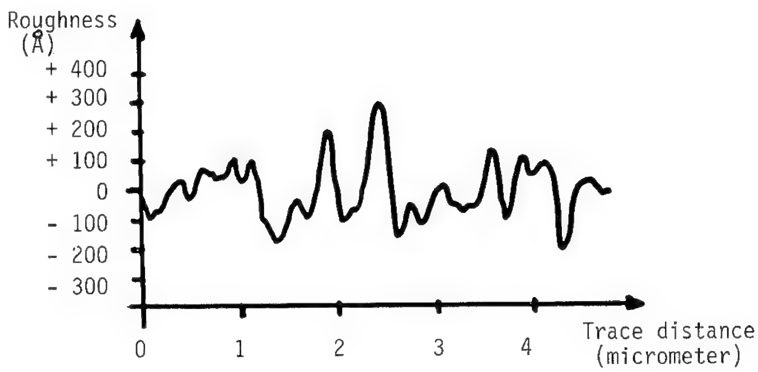

Figure 6 : Roughness profile by atomic force microscopy through a nanocrystalline aggregate observed in a type B anodic film

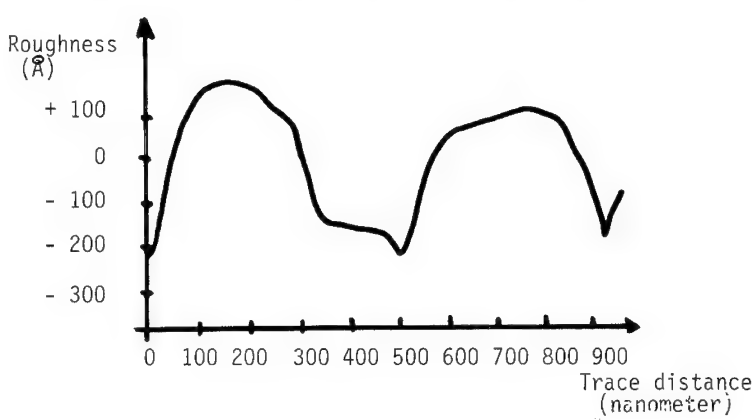

5) Transmission high energy electron diffraction :

The transmission high energy electron diffraction (THEED) shows that the B and C films are crystallized (see Figure 7). The A films do not seem to diffract the electron and are then supposed amorphous.
The matrix for the B and C films is anatase. Rutile crystals are diffracting with preferential orientations (the most intense powder diffraction peak corresponding to the (110) rutile planes is never observed). Nanodiffraction and dark field imaging are actually under way in order to correlate the nanocrystals with the rutile patterns.

Figure 7 : Transmission high energy electron diffraction in a type B film

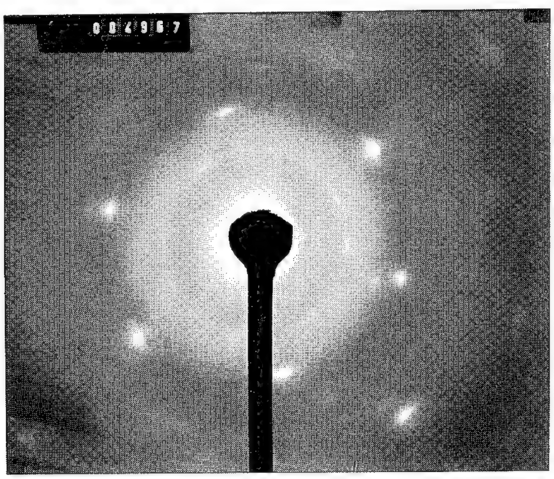

Discussion :

At high voltage and high current density, the galvanostatic anodic oxide films on titanium recrystallize in order to form rutile nanocrystals inside an amorphous or a crystalline anatase matrix. This is in agreement with the papers of Jouve et al (3, 7-8) but it is shown here that the crystallographic orientations of the underlying titanium crystals not only control the growth rate, the density and the crystallization of the covering anodic oxide film but also control the density and the structure of the rutile nanocrystals (isolated nanocrystals, nanocrystals aggregates or continuous patterns of nanocrystals). All these nanocrystals are protruding from the average oxide surface but only the nanocrystals aggregates and continuous patterns are preferential conduction channels. Further experiments are actually under way to identify the crystallographic titanium orientations leading to the formation of the A, B and C type oxide films.
On the point of view of the microscopies comparison, the STEM coupled with THEED is the most powerful technique but many complementary data are provided by AFM (surface microroughness), SEM (surface macroroughness) and optical microscopy (correlation structure defects - conducting channels (copper nucleation experiments)).

Conclusions :

By combining different analytical techniques, it has been possible to illustrate the influence of the crystallographic orientation of the titanium substrate crystals on the density and the structure of the rutile nanocrystals observed inside the oxide films grown by galvanostatic anodization at high current density. This could have important industrial consequences either for the production of insulators or for the production of (semi-) conducting electrodes (photoelectrodes , dimensionnally stable electrodes,...).

Acknowledgment :

The authors are indebted to the National Fund for Scientific Research of Belgium for its financial support.

References :

1. J-L. Delplancke and R. Winand, Electrochimica Acta, 33(11), pp1539-1549, (1988)
2. J-L. Delplancke and R. Winand, Electrochimica Acta, 33(11), pp 1551-1559, (1988)
3. G. Jouve, A. Politi, P. Lacombe and G. Vuye, J. Less-common Metals, 59, pp 175-199, (1978)
4. J-L. Delplancke, A. Garnier, Y. Massiani and R. Winand, Electrochimica Acta, 39(8-9), pp 1281-1289, (1994)
5. J-L. Delplancke, M. Degrez, A. Fontana and R. Winand, Surf. Technol., 16, pp 153-162, (1982)
6. T. J. Nurse and F. Wormwell, J. Appl. Chem., 2, pp 550-554, (1952)
7. A. Politi, G. Jouve and P. Lacombe, J. Less-common Metals, 56(2), pp 263-268, (1977)
8. A. Politi, G. Jouve, C. Servant and C. Severac, J. Microsc. Spectrosc. Electron., 3(6), pp 513-531, (1978)

Materials Science Forum Vols. 185-188 (1995) pp. 275-284

Electrochemical and surface analytical characterization of hot water oxide layers on iron-chromium alloys

F. Schneider[1], M. Herrich[1], A. John[2], J. Engelmann[1] and K. Mummert[1]

[1] IFW Dresden e.V., Institut für Metallische Werkstoffe, D-01171 Dresden, Germany

[2] IFW Dresden e.V., Institut für Festkörperanalytik und Strukturforschung, D-01171 Dresden, Germany

Keywords: Electrochemistry, iron-chromium-alloys, high temperature water, oxidation, buffer solutions, surface structure, Auger effect, scanning electron microscopy

The aim of this work is to describe the properties of hot water oxide layers in dependence on both the formation potential and the chromium content. - Oxide layers on Fe-Cr-alloys of different Cr-content (3, 6, 10, 20, 30, 40 %) were formed by electrochemical polarization both at potentials near the rest potential in oxygen free electrolyte (borate buffer of pH 8,4) and in the potential region of the anodic chromium dissolution. The electrolyte temperature was 250°C in all cases. The investigations were carried out by means of electrochemical measurements, Auger Electron Spectroscopy and Scanning Electron microscopy mainly. - The results of the investigations demonstrate a strong influence of both the formation potential and the Cr-content on thickness, morphology, chemical composition and growth kinetics.

1. Introduction

The characterization of oxide layers formed on Fe-Cr-Ni-alloys in hot water has commonly been performed by investigations at the free corrosion potential in solutions without oxygen [1,2,3]. On the other hand investigations at defined potentials or high oxygen content are rare [4] and restricted on pure iron and special alloys [5,6]. Already small amounts of oxygen are able to shift the corrosion potential of Fe-Cr-Ni-alloys to more positive values [7]. The aim of the present work is to describe the properties of oxide layers in dependence of the formation potential. Most important properties of the oxide layers are : thickness, morphology and porosity, chemical composition, growth kinetics, conductivity and on the other hand the electrochemical behaviour (current density-electrode potential curves, resistivity against localized corrosion).

2. Experimental conditions

Binary Fe-Cr-alloys with different ratios of the alloying components were selected for the investigations (Table 1). These alloys are qualified for getting correlations between Cr-content and properties of the oxide layers. - Samples of the alloys were rolled to thin plates (thickness 1 mm). Stripes of the plates (dimensions 90 mm x 5 mm) were vacuum annealed (T = 950°C, t = 1 h, vacuum cooling). These stripes were used for working electrodes (area 8 cm^2) in the electrochemical experiments.

Table 1 : Chemical composition of the investigated Fe-Cr-alloys

number	key content Cr (%)	Cr-content (%)	Fe-content (%)	C-content (%)	N-content (%)
1	3	3,1	96,9	0,0003	0,0016
2	6	5,6	94,0	0,0005	0,0025
3	10	9,4	90,6	0,0007	0,004
4	20	19,4	79,9	0,0019	0,007
5	30	29,3	70,9	0,0032	0,011
6	40	39,0	60,2	0,0015	0,014

Cuts of the stripes have been applied for the surface analytical and morphological investigations. The stripes were grinded by emery paper (quality 600) and rinsed by CCl_4

2.1. Electrochemical investigations

The oxide layers on the alloys were formed by a potentiostatic voltage pulse starting from the potential of the cathodic prereduction up to the formation potential. The conditions were :

Electrolyte: 0,3 mol/L borate buffer
pH 8,4 at room temperature (≙ pH 8,0 at 250 C [9])
Temperature: 250 C (autoclave conditions)
Internal Ni-reference electrode (U_{SHE} = -790 mV [10])
Formation potentials: U_{Ni} = +150 and +700 mV
Formation time: 24 h

Cathodic prereduction (10 s at U_{Ni} = -1600 mV) was performed to clean the metal from the oxide layer generated during heatup (4 h) of the electrolyte to 250 C.

The current-potential curves were measured with a potential scan rate of $\Delta U/\Delta t$ = 10 mV/s over 5 cycles.

2.2. Morphological investigations

Both the thickness and the morphology of the oxide layers could be obtained by means of the Ion Beam Slope Cutting Technique [11] combined with Scanning Electron Microscopy (SEM) and Backscattering Electron Microscopy (BSE). The principle of the method is shown in Fig. 1. The sample surface SF is sputtered by ion bombardement up to a sharp borderline which is the shadow projection of an oblique grinded screen SC. During the bombardement a slope arises between the bombarded region BR and the nonbombarded region SF thus producing a cutting plane through the oxide layer OL. The BSE-micrographs show the borderline BL between metal and oxide which renders it possible to estimate the thickness of the oxide layers.

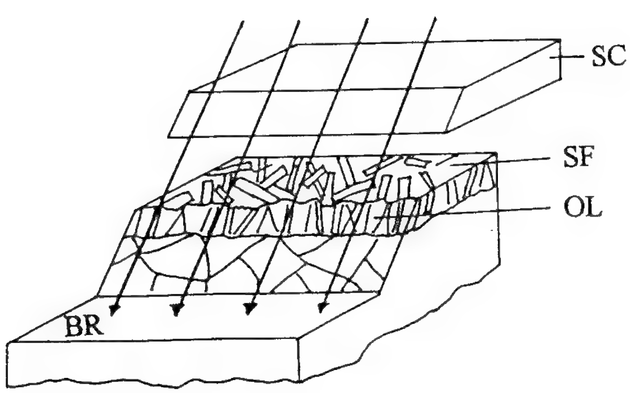

Fig. 1 : Principle of the Ion Beam Slope Cutting Technique

2.3. Auger analysis

Auger Electron Spectroscopy was performed with a Perkin Elmer PHI-660 apparatus. A primary electron current of 80 nA at 10 keV was applied. Depth profiling was performed with 4 keV Ar^+.The sputtered area was 2 x 2 mm^2.

The sensitivity factors for Cr and Fe were experimentally determined on a sputter cleaned Fe-Cr-alloy with 40 % Cr. The composition of standard samples from Fe_3O_4 and Fe_2O_3 could be reproduced with the estimated sensitivity factors of 0,230 for Fe and 0,320 for Cr.

The sputter rate was calibrated with the help of a line scan across an Ion Beam Slope Cutting (Estimation of the oxide thickness). The oxide thickness of a hot water oxide formed on 18/10 Cr-Ni-steel was compared with the sputter time for the same oxide during depth profiling. The estimated sputter rate amounts to R = 23 nm/min. The thickness of the oxides $\mathbf{D_{ox} = R \ t_0}$ is given by the sputter rate R and the sputter time t_0 resulting from the half maximum of the oxygen depth profile.

3. Interpretation of the results

3.1. Current - electrode potential curves

Fig. 2 shows a typical current-potential cycle obtained on a Fe-Cr-alloy with 30 % Cr.

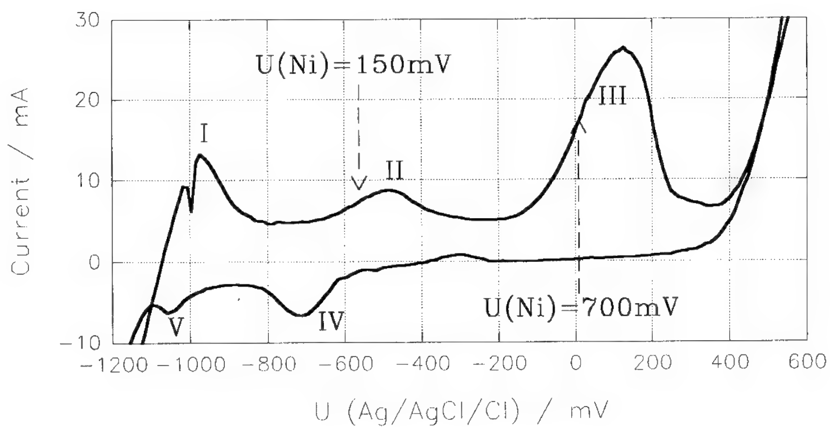

Fig. 2 : Current-electrode potential cycle of the Fe-Cr-alloy (30 % Cr) in borate buffer (pH 8,4) at 250 C

The alloys in the borate buffer solution at 250 C show five peaks. A first interpretation of the peaks should be possible by comparison with potential-pH-diagrams [12]. The peak I is thus attributed to the formation of a Cr-containing magnetite layer. But iron dissolution can't be discarded in this potential region. The inverse peak to peak I is the reduction peak V. It is superimposed to the current from the cathodic hydrogen evolution. For that reason a shoulder is visible only.
The peak II could be caused by oxidation of Fe^{2+} into Fe^{3+} within the oxide layer but oxidation of Fe^{2+} to γ-FeOOH can't be excluded [13]. The peak IV is the inverse peak to the peak II caused by the reduction of Fe^{3+} within the oxide layer into soluble Fe^{2+}.
The peak III accounts for the oxidation of chromium from the metal surface and/or from the oxide into CrO_4^{--}. There is no reduction peak corresponding to peak III because of CrO_4^{--} leaves the oxide.

3.2. Thickness and morphology of the oxide layers

The SEM-Micrographes (Fig. 3) of the oxide layers show significant differences in the morphology depending on the formation potential :

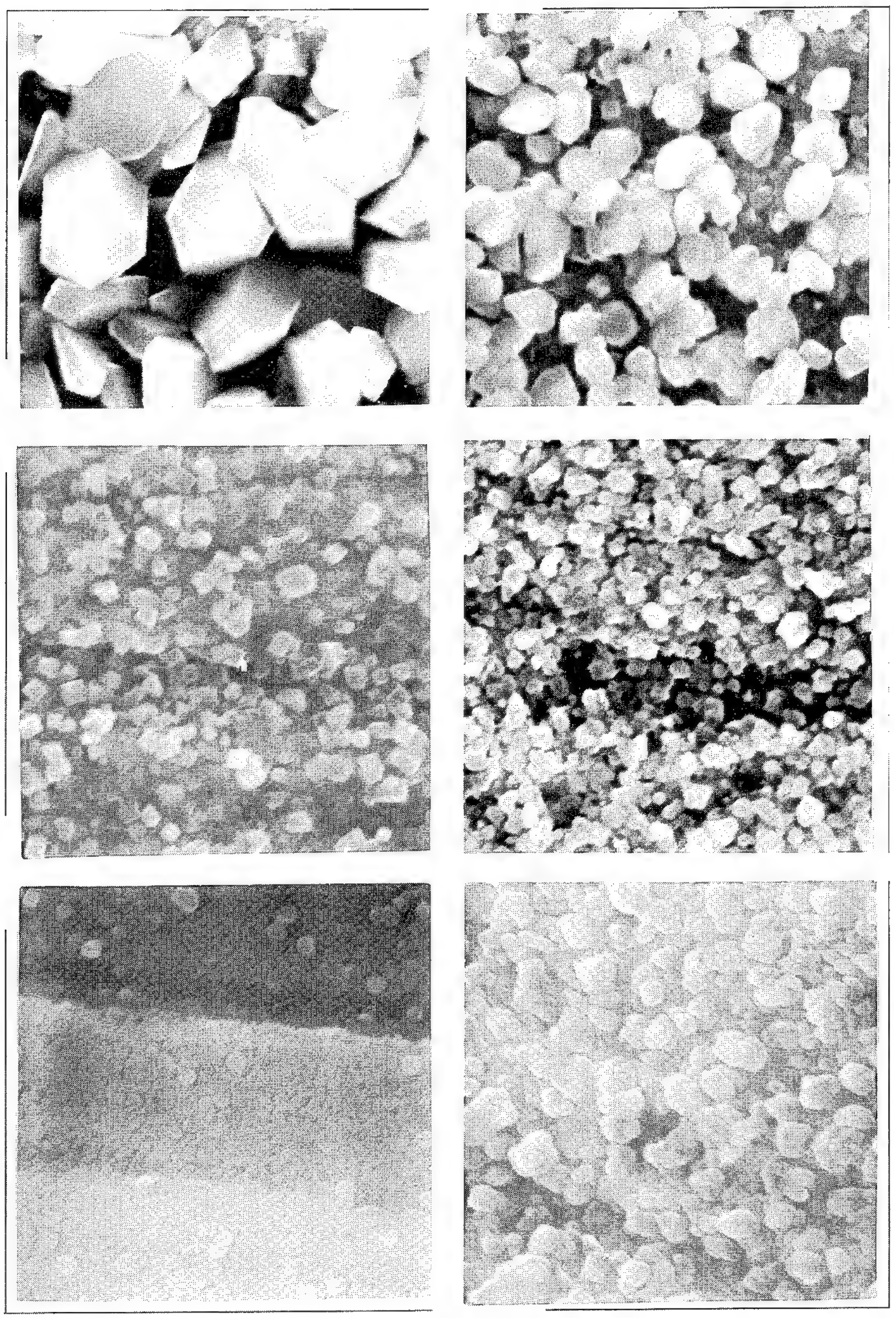

Fig. 3 : Surface morphology of oxide layers on Fe-Cr-alloys formed at 250 C at both low and high electrode potentials (M = 8000 : 1)

Low potential condition (U_{Ni} = +150 mV) :
The morphology and the thickness of the oxide layers are strongly depending on the Cr-content. The higher the Cr-content the thinner is the oxide layer (Table 2). The morphology is characterized by a sharp decrease of the crystal size especially in the region of 10 to 20 % Cr. The crystal size reduces from about 1,5 µm (3-10 % Cr) to 0,3 µm at 20 % Cr and falls down to about 0,1 µm for the 40 % Cr-alloy. The coarse grained outer surfaces of the oxide layers on alloys with 3-10 % Cr seem to be porous indeed. The Ion Beam Slope Cuttings confirm a high porosity of the outer part of these oxide layers (Fig. 4). In addition the outer crystals are very irregular indicating the possibility of mechanical stresses in the layers [14]. Imaginable the layers grow free from mechanical stresses by dissolution and precipitation of Fe^{2+}-ions during the formation at 250 C. But mechanical stresses could arise by different thermal expansion of metal and oxide during the cooling process. This may cause the localized defects in the oxide layers. On the other hand the inner part of the layers seems to grow by direct oxidation from the metal surface and not by precipitation.

Tab. 2 : Thickness of the oxide layers in µm estimated by different methods (BSE-Micrographs, Auger depth profiling, Electrical charge during layer formation)

	U_{Ni} = +150 mV			U_{Ni} = +700 mV		
Cr-cont. (%)	**BSE micrograph**	**AES depth prof.**	**Electrical charge**	**BSE micrograph**	**AES depth prof.**	**Electrical charge**
3	1,3	1,6	1,1	0,50	0,7	0,85
6	1,5	3,2	1,5	0,50	1,1	0,80
10	1,4	4,1	1,1	0,45	0.8	0,90
20	0,5	0,5	0,7	0,30	0,6	0.65
30	---	---	0,12	0,45	0,7	0,55
40	---	0,02	0,06	0,45	0,5	---

Fig. 4 : Typical SEM- and BSE-micrographs for oxide layer formed at U_{Ni} = +150 mV on Fe-Cr-alloys with 3 -10 % Cr (M = 11000 : 1)

High potential conditions (U_{Ni} = +700 mV) :
In comparison to the low potential conditions the thickness of the oxide layers is more uniform for high formation potentials. That means the oxide layers on the high chromium alloys have a considerable thickness in contrary to the low potential layers.
This result should be due to the oxidative anodic Cr-dissolution during polarization with high potentials. Because of the anodic dissolution the Cr-content of the oxide should be decreased. Accordant with the results for low formation potentials the decreasing generates more thick layers. Consequently the chromium of the oxide hinders the formation of thick layers in dependence on the Cr-concentration.
But because of the high potential the possibility of the Fe_2O_3-formation exists [12]. The formation of this oxide could reduce the growth rate too. It can be the cause of the smaller oxide thickness on low Cr-alloys in comparison to the low potential conditions.
The outer part of the oxide layers appears crystalline in the case of low chromium alloys and amorphous for high chromium alloys. The crystal size is smaller (1 μm) than for the low chromium alloys at low potential conditions. There are differences in the crystal shape, too. The oxide layers seem to be porous similiar to the thick oxide layers on low chromium alloys at low potential.

3.3. Auger analysis
Typical depth profiles of the hot water oxide layers are shown in Fig. 5. The oxygen half maximum signals are very different in dependence on both the Cr-content and the electrode potential. This behaviour reflects the thickness of the oxide layers.
Normally chromium could'nt be detected in the outer part of the oxide layers with the exception of the Fe-Cr-alloy of 40 % Cr. This alloy has a higher Cr/Fe-ratio in the oxide than in the bulk alloy at the formation potential of U_{Ni} = +150 mV.
It is difficult to detect exactly the Cr-content of the oxide for small Cr/O-ratios because both the Cr-peak and the oxygen peak in the Auger-spectra are superimposed in the case of high oxygen concentrations. However, the Cr-peak goes through a minimum with the sputter time and increases again. That should be correlated with the Cr-content. At sputter times after the minimum of the Cr-signal the Auger-spectra (Fig. 5) demonstrate higher Cr/Fe-ratios than within the bulk alloys. That indicates a Cr-enrichment near the phase boundary oxide/metal especially for the low formation potential.

3.4. The growth behaviour of the oxide layers
The growth kinetics of the oxide layers is reflected in the dependence of the current on the time. The current-time curves were taken during the potentiostatic growth at different formation potentials.

3.4.1. Growth behaviour at low formation potential (U_{Ni} = +150 mV)
The current-time curves for the low formation potentials (Fig.6) are very complex indicating several stages in the layer formation :
Probably iron dissolution caused the first flat part at the beginning of the curves. Consequently small amounts of iron have been found in the electrolyte. The highest iron dissolution rate should occur just after the cathodic prereduction at the uncovered metal surface. Precipitation of $Fe(OH)_2$ will reduce the current in a second stage. The third stage could be connected with the diffusion of Fe^{2+} and H_2O or OH^- through the pores of this layer. The selective dissolution of iron should increase the Cr-concentration of the metal surface and favor the formation of Fe-Cr-oxide below the primary $Fe(OH)_2$-layer. Therefore, the current decreases strongly during this step and eventually reaches a plateau. The height of the plateaus is depending on the Cr-content of the thin oxide layers. That means the Cr-content controls the further oxide growth which is characterized by the growth of a thick outer magnetite layer. The magnetite is generated by transformation of the adherent $Fe(OH)_2$ and more probably by field assisted migration of Fe^{2+}-ions through the thin Fe-Cr-oxide layer.

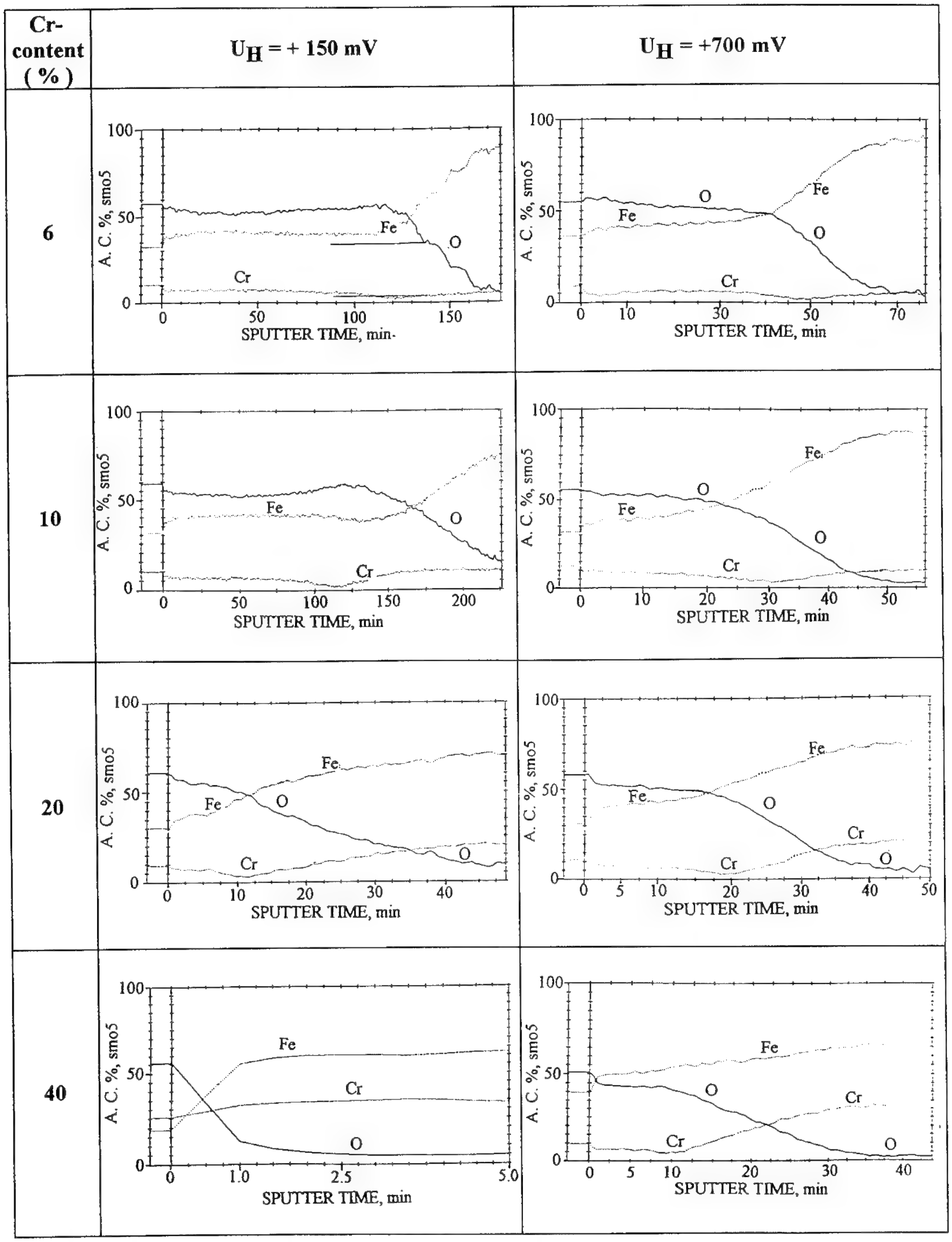

Fig. 5 : Auger depth profiles of oxide layers on Fe-Cr-alloys formed at 250°C

3.4.2. Growth behaviour at high formation potential (U_{Ni} = +700 mV)
A high formation potential generates current-time curves with 3 stages only (Fig 7). In contrast to the low potential curves there is no flat initial part. Commonly the initial slope is -1 indicating a field assisted oxidation of the surface [15]. The first stage will form Fe_2O_3 or Fe-Cr-spinell oxides. The second stage (plateau) consists in oxidative chromium dissolution from the thin oxide layers. The Cr-rich layers will be transformed to a Cr-poor oxide. Independent of the Cr-content in the bulk metal the high potential polarization generates thick chromium free layers of uniform thickness (Table 2, Fig. 5). This is in contrast to the 150 mV-situation. The difference is due to the absence of a Cr-containing thin layer which controls the growth in dependence of the Cr-content.
The formation of Fe-oxides on the top of a magnetite layer is well known for room temperature conditions. Some works [4,5] show the existence of Fe_2O_3 (and FeOOH) under hot water conditions for high potentials, too. Therefore the field assisted migration (slope -1) of ions across this layer could control the growth of a thick magnetite layer between the metal and the controlling top oxide in the third stage.

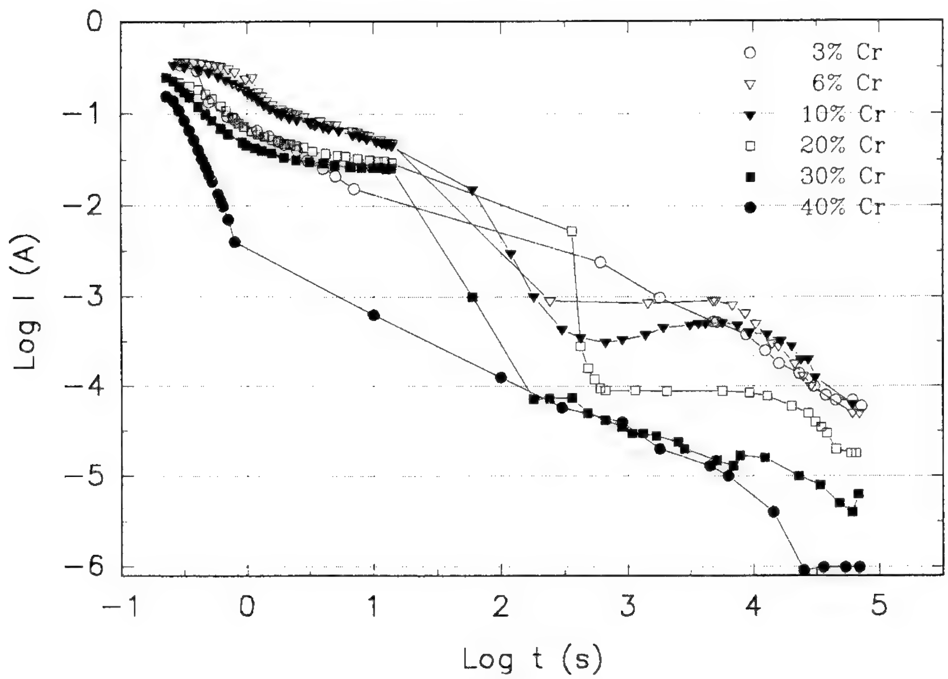

Fig. 6 : Current-time curves obtained for the potentiostatic growth of the layers at U_{Ni} = +150 mV

4. General discussion
The decrease of current density with time to very small values is the same for both potential conditions due to the formation of an unporous inner oxide during the initial time of potentiostatic growth. But the nature of the inner layer differs at different potentials because of anodic chromium dissolution at high potentials. At low potentials the Cr-content in the inner layer correlates with the Cr-content of the alloy. The Cr-content determines the field assisted migration rate of Fe^{2+}-ions across the thin oxide part and likewise also the growth rate and the thickness of the outer porous magnetite layer.
For the high potential condition a thin layer from Fe_2O_3 or more Fe^{3+}-containing magnetite should control the oxide growth. The excess Fe^{3+}-content in the magnetite reduces the migration of Fe^{2+}-

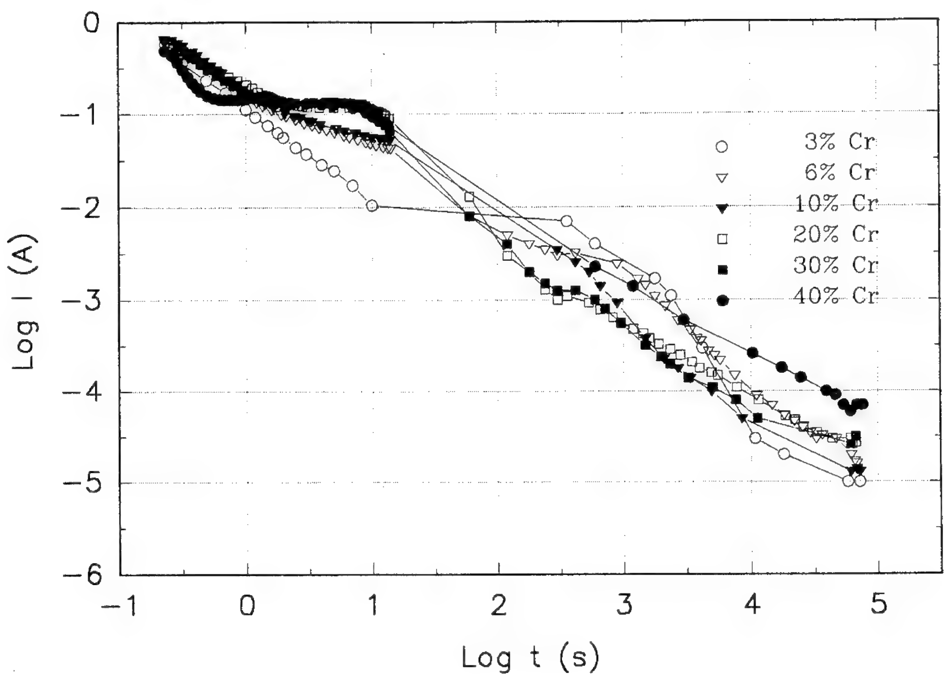

Fig. 7 : Current-time curves obtained for the potentiostatic growth of the layers at U_{Ni} = +700 mV

ions in a similar manner like the Cr^{3+} [16]. The thermodynamic data of iron oxides in contact with metallic iron [17] indicate Fe_3O_4 as the only stable oxide. Therefore Fe_3O_4 is formed additionally near the phase boundary metal/oxide by field assisted migration of O^{2-}-ions through the thin outer Fe_2O_3-layer.
The obtained results correspond with the mechanism models favouring the solid stage diffusion and migration of Fe^{2+}-ions across the oxide layer [18] as the rate controlling step of the growth.
At low formation potential the passive current, the thickness and the crystal size decrease strongly in the region between 10 and 20 % Cr-content of the alloys. This behaviour corresponds to the jump in the corrosion resistance at room temperature condition. The change of the properties is unambigous a function of the Cr-content in the inner part of the oxide layer because high potential conditions characterized by anodic chromium dissolution and no chromium in the oxide yield small changes of the properties only.

5. Conclusions

1. The results demonstrate a strong influence of both the formation potential and the Cr-content on thickness, morphology, chemical composition and growth kinetics.
2. For low formation potentials the solid state migration of Fe^{2+}-ions across a thin compact inner part of the oxide layer is the rate controlling step of the growth. The Cr-content of the thin inner part determines the growth rate.
3. For high formation potentials the Cr-content of the thin inner part is reduced by anodic Cr-dissolution. Consequently the growth rate should be determined by a thin outer Fe_2O_3-layer.

The support of this work by the Deutsche Forschungsgemeinschaft is gratefully acknowledged.

References

[1] D.W. Shoesmith, D.S. Mancey, D.C. Doern, M.G.Balley, Corrosion **45**, 149 (1989)
[2] J. Ensling, J. Fleisch, R. Grimm, J. Grüber, P. Gütlich, Corros. Sci. **18**, 797 (1978)
[3] E. Schuster, K.H. Neeb, W. Ahlfänger, R. Henkelmann, R.T. Järnström J. Nucl. Materials **152**, 1 (1988)
[4] J. Congleton, W. Zheng, H.Hua, Corros. Sci. **30**, 555 (1990)
[5] Y. Horii, K. Mabuchi, H. Konno, H. Takahasi, M. Nagayama 9th Int. Congr. on Metallic Corrosion, Toronto 1984, page 235
[6] N.S. McIntyre, D.G. Zetaruk, D. Owen, J. Electrochem. Soc. **126**, 750 (1979)
[7] W.J. Shack, T.F. Kassner, P.S. Maiya, J.Y. Park, W.E. Ruther, F.A. Nichols, Environmentally Assisted Cracking in Light Water Reactors - Annual Report October 1983 - September 1984, ANL-85-33, page 102
[8] H.H.Uhlig,, Korrosion u. Korrosionsschutz, Akademie-Verlag Berlin 1975
[9] H.C. Park, G. Gragnolino, D.D. Macdonald, Symp. on Environmental Degradation of Materials in Nuclear Power Systems - Water Reactors, Myrtle Beach (South Carolina), August 1983, published by NACE, Houston (Texas) 1984, page 604
[10] F. Schneider, A. Gebert, K. Mummert, "The Use of the Nickel-Reference-Electrode in Hot Water Application", Annual Meeting of the Working Group for Applied Electrochemistry in the Society of German Chemists, Dresden, September 1994
[11] W. Hauffe, B. Schultrich, Prakt. Metallographie **25**, 517 (1988)
[12] C.M. Chen, K. Aral, G.J. Theus, "Computer-Calculated Potential-pH-Diagrams up to 300 C", EPRI-NP 3137 (1983)
[13] M. Nagayama, S. Kawamura, Electrochim. Acta **12**, 1109 (1967)
[14] P.B. Abel, R.W. Hoffmann, J. Vac. Sci. Technol. **A4**, 2938 (1986)
[15] A.K. Vijh, Electrochemistry of Metals and Semiconductors, M. Dekker Inc., N.Y. 1973, page 129
[16] O. Madelung, Handbuch der Physik (ed. by S. Flügge), Vol. XX, Electrical Conductivity Phenomena, Springer-Verlag Berlin-Göttingen-Heidelberg, page19
[17] D.F. Taylor, Corrosion **35**, 550 (1979)
[18] J. Robertson, Corros. Sci. **27**, 443 (1991)

Materials Science Forum Vols. 185-188 (1995) pp. 285-292

Short-range order and structure of silicon dioxide and silicon nitride layers

E.A. Repnikova and V.A. Gurtov

[1] Petrozavodsk State University, 33 Lenin St., Petrozavodsk 185640, Karelia, Russian Federation

Keywords: X-raying, amorphous layers, short-range order structure, porosity

Abstract. By means of X-ray investigations structural differences in silicon dioxide and nitride amorphous layers are studied as a function of the of conditions of synthesis. Depending on the formation technique used, amorphous layers of silicon dioxides are characterized by the type of the short-range order close to the structures of α-quartz, β-crystobalite or β-tridymite. It is shown that a plasmochemical silicon nitride layer is either alloyed with excess hydrogeneous species or it is a heterogeneous system consisting of amorphous silicon nitride clusters, ordered according to the phase type α-Si_3N_4, and amorphous heterogeneous silicon clusters.

Methods. Thin layers of silicon dioxide (10^3 nm) and silicon nitride (260-780 nm) were studied by means of an X-ray investigation.

Silicon dioxide layers were obtained using both thermal oxidation of single-crystal Si (130) in various media (wet oxygen at T=1323 K resulted in a wet thermal silicon dioxide, water vapour with no oxygen added gave a hydrothermal silicon dioxide at T=1273 K and high pressure $P=10^6$ Pa) and pyrolytic monosilane precipitation at temperatures 423, 473 and 673 K.

Silicon nitride layers were precipitated in plasma from a monosilane SiH_4 and ammonia NH_3 mixture with the working pressure in the reactor ~ 60 Pa and temperatures 423 to 673 K.

X-raying of samples was performed with CuKα and FeKα monochromatized radiation.

The short-range order characteristics were calculated using the pair-functions technique [1,2]. This technique allowed to eliminate the effect of the intensity curve break on the short-range order characteristics [3]. The pair functions distribution curves D(r) were calculated from the experimental intensities. The short-range order characteristics (the number of neighbours N_{ij}, radii of coordination spheres r_{ij} and the blurring of coordination spheres σ_{ij}) were deduced by the least-squares method combined with the approximation method.

Results and Discussion. The values of N_{ij}, r_{ij} and σ_{ij} are compared with the similar parameters for crystalline modifications of α-quartz, β-crystobalite and β-tridymite [4] in Tables 1 to 3. It is evident from Table 1 that the type of the short-range order in a wet thermal oxide after annealing at 1373 K and in a vitreous silica is close to the structure of α-quartz.

In the short-range order region of a wet thermal oxide, the structure of β-crystobalite is fixed (Table 2). The difference in the short-range order for thermal wet oxides prior to and after annealing can be explained by the presence of moisture [5]. Porosity in the annealed films deduced from the data on small-angle X-ray scattering [6] is four times lower compared with that of a wet thermal oxide (Table 4). Thus, annealing of a wet thermal oxide results in a less porous film, ordered according to α-quartz of a denser type.

Table 1

The characteristics of the short-range order calculated for crystalline modifications of α-quartz, amorphous silicon dioxide layers, and vitreous silica.

neigh-bours	crystal. α-kwarz		vitreous silica			wet thermal oxide after annealing		
	r_{ij} 10^{-1}	N_i	r_{ij} 10^{-1}	$N_{ij} \pm \Delta N_{ij}$ at.	σ_{ij} 10^{-1}	r_{ij} 10^{-1}	$N_{ij} \pm \Delta N_{ij}$ at	σ_{ij} 10^{-1}
$Si\text{-}O_I$	1.61	4	1.62	4.04±0.03	0.10	1.61	4.02±0.03	0.02
$O\text{-}O_I$	2.63	6	2.65	5.83±0.03	0.16	2.63	5.95±0.05	0.28
$Si\text{-}Si_I$	3.06	4	3.02	3.86±0.05	0.17	3.02	3.9±0.10	0.18
$Si\text{-}O_I$	3.57	6	3.59	5.7±0.30	0.28	3.56	5.8±0.30	0.30
$Si\text{-}O_{II}$	3.93 4.17	4 8	4.02	11.6±0.40	0.27	4.03	11.5±0.50	0.30
$O\text{-}O_{II}$	4.15	4	–	–	–	–	–	–
$Si\text{-}Si_{II}$	4.37	6	4.38	6.05±0.50	0.12	4.40	8.0±1.0	0.10
$Si\text{-}O_{III}$	4.15	6	–	–	–	–	–	–
$Si\text{-}Si_{III}$	4.91	8	4.80	9.0±1.0	0.10	4.83	7.0±1.0	0.35

$\Delta r_{ij} = \pm(0.01\text{-}0.05)\mathrm{x}10^{-1}$ nm

Table 2

The values of r_{ij}, and N_{ij} in crystalline β-crystobalite and an amorphous film of SiO_2

neigh-bours	crystal. [4] β-crystobalit		amorphous wet thermal SiO_2 after annealing		
	10^{-1} r_{ij} nm	N_j at	$r_{ij} + \Delta r_{ij}$ 10^{-1} nm	$N_{ij} \pm \Delta N_{ij}$ at.	σ_{ij} 10^{-1} nm
$Si\text{-}O_I$	1.65-1.66	4	1.64±0.01	4.0±0.10	0.15
$O\text{-}O_I$	2.45-2.74	6	2.60±0.02	6.13±0.03	0.05
$Si\text{-}Si_I$	3.05-3.26	4	3.11±0.02	4.3±0.15	0.01
$Si\text{-}O_{II}$	3.40-3.89	6	3.60±0.02	6.2±0.30	0.10
$O\text{-}O_{II}$	4.03	3	–	–	–
$Si\text{-}O_{III}$	4.12-4.24	6	4.05±0.05	8.3±0.20	0.02
$O\text{-}O_{III}$	4.39 4.73-4.79	6 6	– 4.55±0.20	– 15.0±3.0	– 0.01
$Si\text{-}O_{IY}$	4.83-4.89	6	4.86±0.03	7.0±2.0	0.30
$Si\text{-}Si_{II}$	4.98-5.15	12	5.25±0.05	19.0±3.0	0.30
$O\text{-}O_{IY}$	5.10-5.15	9	–	–	–

In a hydrothermal amorphous film of SiO_2, the character of the atomic order in the short-range order region corresponds to the β-tridymite phase with increased lattice parameters: a=b=0,510 nm, c=0,830 nm instead of a=b=0,503 nm, c=0,822 nm (Table 3).

Table 3

The short-range order characteristics in a hydrothermal amorphous film of SiO_2 and in the β-tridymite phase

neigh-bours	β-tridymite cryst. a=0.503,c=0.822nm[4]			hydrothermal amorphous SiO_2		
	r_{ij} 10^{-1} nm	$\langle r_{ij}\rangle$ 10^{-1} nm	N_{ij} at.	$r_{ij} \pm \Delta r_{ij}$ 10^{-1} nm	$N_{ij} \pm \Delta N_{ij}$ at.	δ_{ij} 10^{-1}
$Si-O_I$	1.534 1.562	1.541	3 1	1.59±0.01	4.04±0.01	0.04
$O-O_I$	2.552		6	2.72±0.01	6.1±0.1	0.19
$Si-Si_I$	3.067 3.124	3.08	3 1	3.0±0.0	4.15±0.11	0.16
$Si-O_{II}$	3.864 3.873 3.897	3.876	4 6 3	3.77±0.0	12.17±0.05	0.33
$O-O_{II}$	4.11 4.356 4.357 4.818	4.53	2 4 4 8	4.4±0.0	21.9±0.40	0.01
$Si-O_{III}$	4.827		3	4.82±0.0	2.8±0.05	0.26
$Si-Si_{II}$	5.030 5.032	5.031	6 6	5.05±0.0	12.0±1.0	0.27
$Si-O_{IY}$	5.259 5.267 5.276	5.273	6 6 6	5.35±0.05	18.1±0.9	0.45

Table 4

The sizes of pores and porosity

SiO_2	R_{min}±0.5 nm	c_1,%	R_{max}±1 nm	c,%
Wet thermal after anneal.	20		70	0.20
Wet thermal pirolytic	40		150	0.80
T=673K	30	1.00	100	1.10
T=473K	25	1.70	165	1.77
T=423K	20	3.70	175	3.80

c_1 -porosity due to pores of minimum size,
c- total porosity

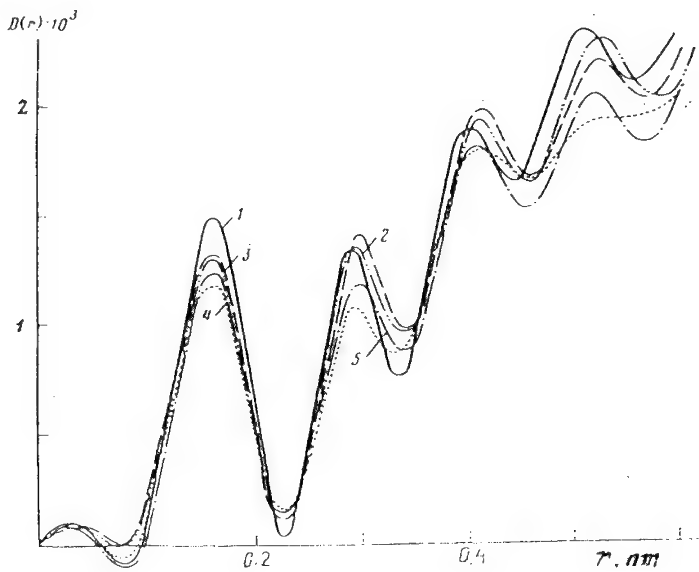

Fig 1. D(r) (in units of electrons/nm^2) for the vitreous silica (1), wet thermal SiO_2 (2); pyrolytic silicon dioxide SiO_2 (3)- 673 K, (4)- 423 K, (5)- 473 K respectively.

The formation of an amorphous structure, ordered according to β-tridymite, is favoured by the conditions of synthesis, namely, high pressure and water vapour, which act as mineralizers in tridymite phase formation [7].

Table 5

The short-range order characteristics in an amorphous pyrolytic SiO_2

neighbours	amorphous pyrolytic SiO_2					
	T=673 K			T=423 K		
	r_{ij}, 10^{-1}	$N_{ij} \pm \Delta N_{ij}$ at	σ_{ij} 10^{-1} nm	r_{ij}, 10^{-1}	$N_{ij} \pm \Delta N_{ij}$ at	σ_{ij} 10^{-1} nm
$Si-O_I$	1.64	3.98±0.02	0.18	1.64	3.96±+0.05	0.35
$O-O_I$	2.63	6.2±0.08	0.08	2.66	5.9±0.20	0.35
$SI-O_I$	3.10	4.3±0.05	0.05	3.11	3.98±0.12	0.35
$Si-O_{II}$	3.55	6.1±0.50	0.28	3.58	6.02±0.27	0.37
$Si-O_{III}$	4.02	8.0±0.50	0.01	4.02	8.4±0.4	0.02
$O-O_{II}$	4.55	20.0±2.0	0.01	4.55	18.1±1.0	0.01
$Si-O_{IY}$	4.89	7.0±1.0	0.10	4.87	6.1±0.6	0.40
$Si-Si_{II}$	5.25	20.0±2.0	0.30	5.20	16.0±2.0	0.40

$\Delta r_{ij} = \pm(0.0-0.1)\ 10^{-1}$ nm

The short-range order characteristics defined for amorphous pyrolytic oxides are given in Table 5. As the pyrolysis temperature decreases, the rate of the D(r)- curves decay grows indicating the increased degree of disordering in the films (Fig.1). The mean values of r_{ij} for the first eight coordination spheres in pyrolytic oxides SiO_2 are close to each other and correlate fairly well with the mean interatomic distances in crystalline β-crystobalite. As the pyrolysis temperature decreases, the blurring of the coordination spheres sharply increases. A marked increase in the half-width of the α(Si-O-Si) bond angle distribution curve is observed with decreasing the pyrolysis temperature (Fig.2), suggesting the enhanced atomic disordering even within a tetrahedron. The tetrahedron distortion is likely to be associated with the Si-OH type defect formation. It follows from the analysis of the IR- absorption spectra that the amount of moisture in pyrolytic oxide films SiO_2 increases by a factor of 1.5 as the pyrolysis temperature is reduced from 473 to 423 K. Forming Si-OH bonds, structural water leads to the increase in the scatter in the Si-OH interatomic distances [7]. Porosity of pyrolytic layers is larger (Table 4), increasing with the pyrolysis temperature decrease. The main contribution to porosity is due to pores (5±1)nm in diameter [6].

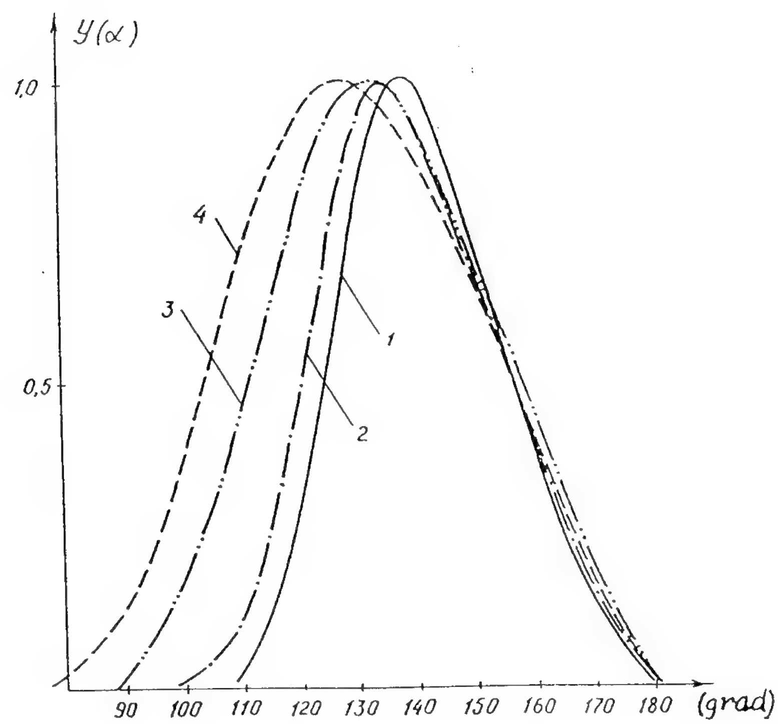

Fig.2. The bond angle distribution for Si-O-Si in (1)- a wet thermal oxide and (2,3,4) pyrolytic oxides at T=673K, 473 K, 423 K respectively.

Fig.3 shows a D(r)- curve calculated from the values of scattering intensities for pyrolytic silicon nitride. The values of N_{ij} deduced from D(r) by the least-squares method are compared with the parameters for a crystalline modification α-Si_3N_4 in Table 6. The contribution to D(r) for the seven coordination spheres calculated for the corresponding atomic pairs is presented in Fig.3.

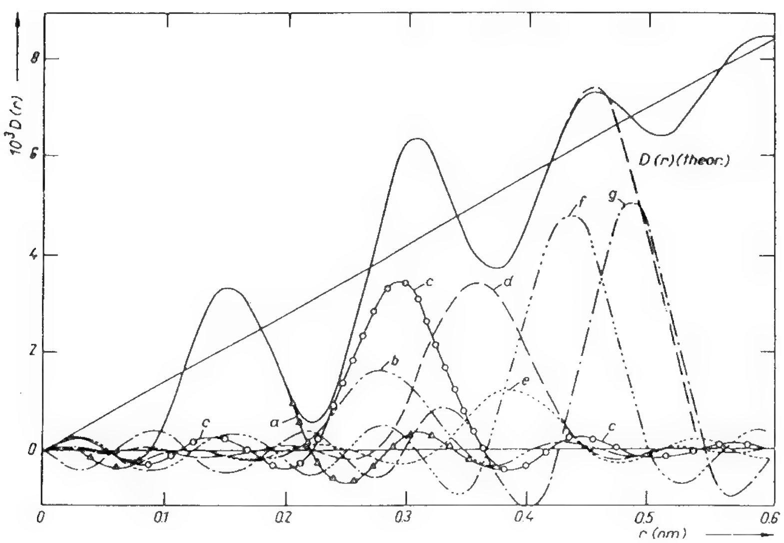

Fig.3. D(r) (in units of electrons/nm^2) and the first contributions (a) Si-N_I, (b) N-N_I, (c) Si-Si_I, (d) Si-N_{II}, (e) Si-Si_{II}, (f) Si-N_{III}, (g) Si-Si_{III} for stoichiometric pyrolytic silicon nitride. $D(r)_{(theor)}$ is the theoretical D(r) found by LSM according to $(r_{ij} - r_{7j})(N_{ij} - N_{7j})$, $(\sigma_{ij} - \sigma_{7j})$.

The first coordination number 4 suggests that pyrolytic amorphous layers Si_3N_4 are stoichiometric. The films formed by plasma chemical monosilane ammonolysis with the steam-gas ratio $[NH_3]:[SiH_4]=6.7$, turned out to be close in composition to stoichiometric silicon nitride. The short-range order characteristics calculated for the films of stoichiometric plasmochemical and pyrolytic silicon nitride are close to each other [9]. The deviation from the above ratio (6.7) to lower or higher values results in the formation of non-stoichiometric layers of silicon nitride with excess silicon content. If the above ratio increases (10; 12; 17), the first coordination number increases up to 4.5 and so does the blurring of the coordination spheres. The larger value of the first coordination number may result from the doping of the film by excess silicon atoms binding SiN_4-tetrahedra with each other. The Si-Si bond length is equal to 0.23 nm, therefore, this bond will mainly contribute to the area under the first maximum on the D(r) curve. With the ammonia to silane flow ratio amounting to 4, the coordination numbers of the first, second and fifth coordination spheres will be increased (Table 7).

Table 6

The values of r_{ij} and N_{ij} in stochiometric pyrolytic nitride and in α-Si_3N_4 crystal as well.
$<r_{ij}>$ are average, weighted values of interatomic crystal distances, N_{ij} is the total number of atoms at a distance $<r_{ij}>$

neigh-bours	pyrolytic Si_3N_4			Si_3N_4 crystal	
	r_{ij} 10^{-1} nm	$N_{ij} \pm \Delta N_{ij}$ at.	σ_{ij} 10^{-1}	$<r_{ij}>$ 10^{-1} nm	N_{ijs} at.
$Si-N_I$	1.60	4.02±0.01	0.08	1.75	4.0
$N-N_I$	2.74	11.0±0.3	0.01	2.87	11.0
$Si-Si_I$	2.98	7.9±0.2	0.36	2.99	8.0
$Si-N_{II}$	3.62	13.5±0.3	0.38	3.57	13.5
$Si-Si_{II}$	3.93	2.5±0.5	0.10	3.99	3.5
$N-N_{II}$	-	-	-	4.22	10.0
$Si-N_{III}$	4.35	15.0±0.5	0.08	4.37	10.5
$Si-Si_{III}$	4.86	11.6±0.3	0.18	4.86	12.0

$\Delta r_{ij} = \pm(0.01 - 0.05)\times10^{-1}$ nm

Table 7

The short-range order characterictics calculated for amorphous plazma-chemical silicon layers ($[NH_3]/[SiH_4]=4$)

i	neighbour	r_{ij}, 10^{-1} nm	$N_{ij} \pm \Delta N_{ij}$	δ_{ij} (10^{-1} nm)
1	$Si-N_I$	1.70	4.75±0.05	0.04
2	$N-N_I$	2.73	14.0±0.5	0.01
3	$Si-Si_I$	2.98	8.2±0.5	0.22
4	$Si-N_{II}$	3.62	14.5±0.2	0.40
5	$SI-Si_{II}$	3.96	6.8±0.5	0.40

$\Delta r_{ij} = \pm(0.01$ to $0.03)\times10^{-1}$ nm

Let us assume that the increase in the coordination numbers is due to the formation of additional Si-Si bonds. Subtracting D(r) for stoichiometric silicon nitride from D(r) for a non-stoichiometric amorphous film yields a difference curve D(r) with the maxima at r_i=0.220; 0.375; 0.450 [9]. The positions of these maxima are close to those of amorphous hydrogenized silicon (0.234; 0.383; 0.450; 0.560 nm). The values of the coordination numbers calculated from the difference curve were 1.9 ± 0.1; 2.3 ± 0.2; 4.1 ± 0.3. Thus, in this case a non-stoichiometric film of silicon nitride can be presented as a heterogeneous system consisting of the amorphous phase of stoichiometric silicon nitride Si_3N_4 and amorphous hydrogenized silicon clusters.

Conlusions

1. A method of synthesis of silicon dioxide amorphous layers has been shown to have a major effect on the character of the atomic order in the short-range order region.

2. Stoichiometry of silicon nitride amorphous layers is achieved by high-temperature pyrolysis and plasmochemical synthesis with the ammonia to monosilane flow ratio equal to 6.7.

References

[1] R.L.Mozzi and B.E.Warren,J.appl.Cryst.,2,164,(1969)
[2] R.L.Mozzi and B.E.Warren,J.appl.Cryst.,3,251,(1970)
[3] L.A.Aleshina and A.D.Fofanov,Amorphous Material X-Raying Analysis,Petrozavodsk Univ.Press,1987 (p.88)
[4] N.Nagasima,J.appl.Phys.B 43,3378,(1972)
[5] E.A.Repnikova,V.A.Gurtov,Cryst.,35,422,(1990)
[6] E.A.Repnikova,V.A.Gurtov,Inorg.mater.,25,1149,(1989)
[7] E.A.Repnikova,L.A.Aleshina,V.A.Gurtov,A.D.Fofanov,Surface.Phys.,chem.,mech.,4,65,(1989)
[8] N.V.Rumak, System silica-silicon dioxide in MOS-structure., Mn.,Sc. and Tech., 1986 (p.240)
[9] E.A.Repnikova,V.A.Gurtov,Phys.stat.sol.(a)119,113, (1990)

Materials Science Forum Vols. 185-188 (1995) pp. 293-300

Structure of aluminium oxide films and its changes due to thermal and electrochemical processes

N.M. Yakovleva and A.N. Yakovlev

Petrozavodsk State University, 33 Lenin St., Petrozavodsk 185640, Karelia, Russian Federation

Keywords: Anodic film, aluminium, short-range order, x-ray diffraction

Abstract

Anodic aluminium oxide films with thicknesses ranging from 0.2 to 80 μm were investigated by means of an X-ray diffraction modified technique. The short-range order parameters of amorphous films were calculated from the experimental scattering intensities, using the pair functions method. The influence of the conditions of film passivation, heat treatment and degradation of oxide films on the structural characteristics was studied.

Introduction

Most anodic Al_2O_3 films are amorphous [1], and much of the work has been done on morphology, phase and chemical composition of the amorphous phase. However, its structural characteristics are not yet fully understood. As to variations in the short-range order characteristics of amorphous oxides with forming conditions, there have hardly been reports on this aspect.

In the present paper, the results of calculations of the short-range order parameters for amorphous Al_2O_3 films, of both barrier and porous type, are presented.

Sample Characteristics

Amorphous and amorphous - crystalline Al_2O_3 films were studied, formed by electrochemical oxidation of aluminium (A 999) in both oxide-dissolving and non-dissolving electrolytes. Barrier-type oxide layers were obtained by oxidation in aqueous acid (boric, citric, phosphoric and adipic) solutions.

The minimum and maximum thicknesses of the compact oxides studied were equal to 250 nm and 2.5 μm, respectively. Porous Al_2O_3 films were formed by electrochemical oxidation of aluminium foil in 3% - $C_2H_2O_4$ and 5% - CrO_3 followed by etching of unoxidized Al. The stripped oxide thicknesses were 70 ÷ 100 μm and 2.5 μm, respectively.

Experimental Procedure and Data Processing

The X-ray structure analysis was the main investigation technique used. The X-raying was performed with the diffractometers DRON-3.0 and DRON-4.0 using various wave-length monochromatized radiation (Cr-, Fe-, Cu-, Mo-Kα). Scattering intensity distributions were obtained as a function of the diffraction vector $s = 4\pi\sin\vartheta/\lambda$. In the case of oxides attached to metal, scattering by the substrate contributing to scattering by an Al- Al_2O_3 system was experimentally eliminated by means of preliminary X-raying of the unoxidized metal. Besides,an asymmetrical geometry of X-raying [2] was used to reduce intensities of Bragg reflections from Al.

According to the conventional technique, corrections for scattering by air, polarization and absorption were introduced. After that, oxide film scattering intensities were converted to electronic units using Warren's method [3], followed by the elimination of Compton scattering.

The short-range order characteristics (coordination spheres radii r_{ij}, coordination numbers N_{ij} as well as blurring of coordination spheres in the amorphous materials σ_{ij}) were calculated by the pair functions method [4]. According to this method, the pair functions distribution curves D(r), characterizing the material's electronic density distribution can be derived from the experimental scattering intensities converted to electronic units. After that the short-range order characteristics were determined by the least-squares method (LSM).

The essential advantage of the pair functions method is the possibility to correctly determine the values of N_{ij}, r_{ij} and σ_{ij} for several coordination spheres using the I(s) curves obtained for a limited range of s-values [2,4].

Short-range order in barrier amorphous films

The shapes of the scattering intensity distributions for all the anodic oxide films studied indicated X-ray - amorphous materials (Fig.1). On the pair functions distribution curves D(r), there are distinct maxima at $r_1 = 0.18$ nm, $r_2 = 0.32$ nm (Fig.2). The estimation of the first coordination number with the pair functions technique yielded $N_1 \approx 5.5$ oxygen atoms around an aluminium atom.

Preliminary information on the short - range order in an amorphous material can be obtained from the comparison of the I(s) curves with Debye powder patterns for corresponding crystalline compounds. However, despite a wide variety of oxide and hydroxide crystal modifications of aluminium, the comparison of the I(s) curves with the diagrams for crystal compounds fails to give

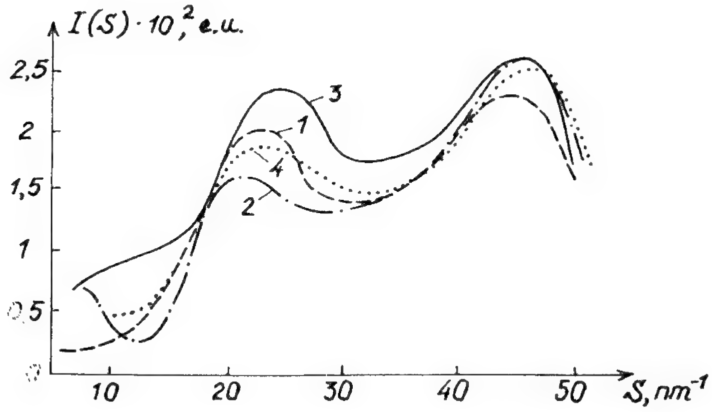

Fig.1. The curves I(s) for anodic Al_2O_3 (d = 210 nm) formed in different electrolytes : (1) adipic acid; (2) phosphoric acid; (3) citric acid; (4) boric acid

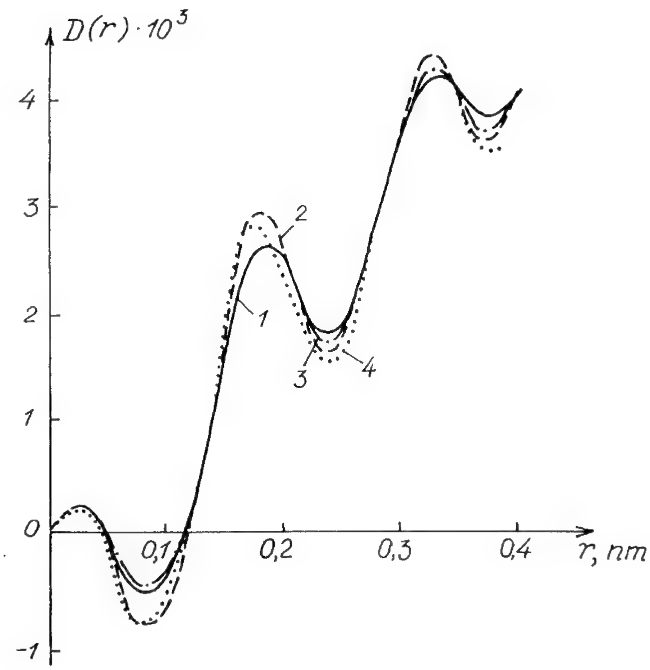

Fig.2.The pair functions distribution curves D(r) for barrier Al_2O_3 formed in electrolytes 1 to 4 (as denoted in Fig.1)

a definite answer as to what modification is indicated by the atomic arrangement in the short-range order region of

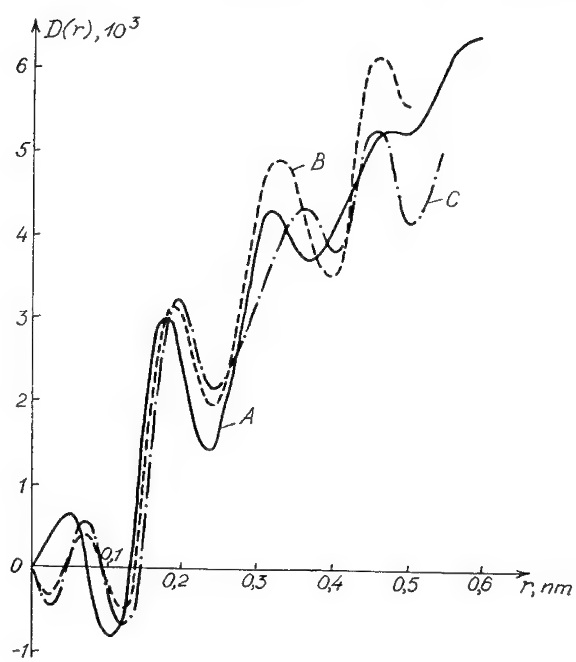

Fig.3. The D(r) curve for the amorphous oxide film formed in a boric acid electrolyte (a) and theoretical D (r) for α - Al_2O_3 (b) and boehmite AlOOH (c)

an amorphous phase. Yet, for γ - Al_2O_3 and γ' - Al_2O_3 fair correlation is observed.

The comparison of the pair functions distribution curves D(r) with the model ones calculated by the crystal lattice blurring method (Fig.3) gives all grounds to state that the atomic arrangements in crystal modifications α - Al_2O_3 and AlOOH (boehmite) are not consistent with that of the short-range order region in a barrier amorphous oxide.

The value of $N_1 \approx 5.5$ obtained correlates fairly well with the number of neighbours for Al - O in cubic crystal modifications γ-Al_2O_3 (a= 0.79 nm) and γ'-Al_2O_3 (a= 0.395 nm). However, the use of the fine-crystal model of an amorphous material for developing the amorphous oxide structure [5] revealed that with a spinel-type cell of Al_2O_3 used as "a structural unit", an additional maximum

Table 1

Coordination numbers N_{ij} and corresponding coordination spheres radii r_{ij} for crystalline γ -Al_2O_3

C_1 : C_2		type of a coordination sphere $Al-O_I$	$O-O_I$	$Al-Al_I$	$Al-O_{II}$
70 : 30	$r_{ij}\times10^{-1}$, nm	1.92	2.79	3.02	3.36
	N_{ij}, at	5.40	12.0	10.6	9.20
90 : 10	$r_{ij}\times10^{-1}$, nm	1.96	2.79	2.84	3.40
	N_{ij}, at	5.80	12.0	8.00	8.40
50 : 50	$r_{ij}\times10^{-1}$, nm	1.87	2.79	3.03	3.33
	N_{ij}, at	5.00	12.0	8.00	10.0

Note: mean-weight values are given

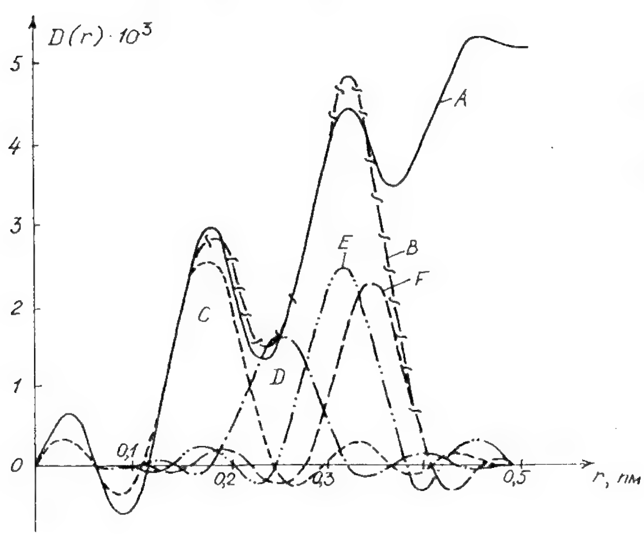

Fig.4. The D(r) curves for barrier Al_2O_3 (d = 1.5 μm) formed in a boric acid electrolyte (A), theoretical D(r) calculated by LSM (B), and the first four contributions of Al - O (C), O - O (D), Al - Al (E), Al - O (F)

appears on the theoretical curve in the range s ~ 33 to 35 nm^{-1}, which is not typical of the experimental I(s). These dependences turned out to be similar only for the crystallite size equal to that of one unit cell of γ'- Al_2O_3 [6]. The structure of γ'- Al_2O_3

is represented by a FCC lattice of oxygen ions, where Al^{3+} - ions are distributed over all the interstitial sites available in such a way that about 70% of the sites are occupied by octavoids and ~30% by tetravoids. In accordance with this, mean-weight values of coordination spheres (c.s.) radii and coordination numbers (c.n.) corresponding to the Me - O, O - O and Me - Me atomic pairs were calculated for different ratios of aluminium atoms with c.n.6 (C_1, %) and 4 (C_2, %), respectively (Table 1). It should be mentioned that there is an essential difference in the values of N_{ij} for the $C_1:C_2$ ratios indicated, at least for four c.s., while changes in the values of c.s. radii are not so pronounced. Therefore, it is impossible to draw a conclusion as to the aluminium atoms distribution in an oxide using only the c.s. radii. The values of r_{ij}, N_{ij} and σ_{ij} for the first four c.s. (Fig. 4) for barrier oxides, calculated from D(r) are given in Table 2 .

Table 2

The short-range order characteristics for barrier Al_2O_3

anodizing solution		type of a coordination sphere $Al-O_I$	$O-O_I$	$Al-Al_I$	$Al-O_{II}$
1	$r_{ij}\times10^{-1}$, nm	1.82	2.61	3.16	3.45
	$\sigma_{ij}\times10^{-1}$, nm	0.20	0.10	0.28	0.27
	N_{ij}, at	5.4±0.2	11.6±0.3	10.6±0.2	9.2±0.1
2	$r_{ij}\times10^{-1}$, nm	1.83	2.63	3.22	3.47
	$\sigma_{ij}\times10^{-1}$, nm	0.18	0.25	0.44	0.30
	N_{ij}, at	5.44±0.03	12.4±0.04	10.7±0.2	9.1±0.2
3	$r_{ij}\times10^{-1}$, nm	1.82	2.63	3.20	3.42
	$\sigma_{ij}\times10^{-1}$, nm	0.16	0.45	0.35	0.35
	N_{ij}, at	5.45±0.05	12.0±0.2	10.4±0.3	9.1±0.2
4	$r_{ij}\times10^{-1}$, nm	1.80	2.62	3.16	3.45
	$\sigma_{ij}\times10^{-1}$, nm	0.23	0.13	0.28	0.26
	N_{ij}, at	5.4±0.1	12.1±0.3	10.5±0.3	9.1±0.4
	$\Delta r_{ij}=(0.01\div0.04)\cdot10^{-1}$ nm, $\Delta\sigma_{ij}=(0.01\div0.06)\cdot10^{-1}$ nm				

The short-range order in an amorphous compact film Al_2O_3 is, thus, similar to the atomic arrangement in a distorted cubic modification γ'-Al_2O_3, where (70 ± 5)% of Al are of the octahedral coordination relative to oxygen while (30 ± 5)% are of the tetrahedral coordination [4,7].

Short-range order in porous films

According to the structural characteristics of porous oxides (Table 3) determined by the pair functions method, the short-range order in the films formed by anodization of aluminium in CrO_3 - solutions (non-aqueous and forming electrolyte anion-free) is similar to the short-range order in barrier oxide films (Table 2).

As to the porous Al_2O_3 films formed in 3% $H_2C_2O_4$, their short-range order corresponds to that of the distorted cubic modification γ'-Al_2O_3, where the ratio of aluminium atoms of the octa- and tetracoordination is $C_1:C_2$ = (45±5)% :(55±5)% .

Table 3

The short-range order characteristics for porous Al_2O_3

anodizing solution		type of a coordination sphere $Al-O_I$	$O-O_I$	$Al-Al_I$	$Al-O_{II}$
5% CrO_3	$r_{ij}\times10^{-1}$, nm	1.85	2.63	3.21	3.45
	$\sigma_{ij}\times10^{-1}$, nm	0.12	0.10	0.25	0.26
	N_{ij}, at	5.5±0.1	11.9±0.5	10.2±0.2	9.1±0.4
3% $H_2C_2O_4$	$r_{ij}\times10^{-1}$, nm	1.84	2.85	3.19	3.62
	$\sigma_{ij}\times10^{-1}$, nm	0.20	0.18	0.38	0.38
	N_{ij}, at	4.85±0.05	11.9±0.2	7.9±0.2	9.7±0.1

Marked increase in the Al-Al and $Al-O_{II}$ bond length straggling appears to be due to the disorder in amorphous films, which already enhances at distances approximately equal to the γ'-Al_2O_3 unit cell parameter (a = 0.395 nm). This fact further confirms that the correlation distance in the amorphous materials studied is extremely small (~40÷50 nm).

Electrolyte effect on the barrier film structure

For barrier-type amorphous films formed in electrolytes based on boric, citric, phosphoric and adipic acids, the shapes of the I(s) and D(r) curves are similar (Fig.1 and 2). The changes in D(r) observed are confined to blurring and insignificant shifting of the two main peaks. For all the oxides studied, the values of N_{ij}, r_{ij} (Table 2) coincide within the given values of ΔN_{ij}, Δr_{ij}, thus indicating that the character of the mutual atomic arrangement in the short-range order region remains unchanged, regardless of the anodizing solution used. However, for these films different values of σ_{ij} were obtained. For the first, third and fourth c.s.,

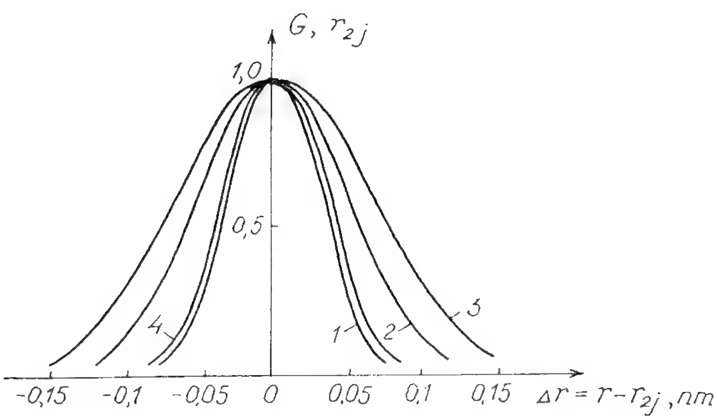

Fig.5. The distance distribution functions G (r_{2j}) for O - O_I in barrier films formed in electrolytes 1 to 4 (as denoted in Fig.1)

changes in σ_{ij} are within or slightly beyond the given values of σ_{ij}, whereas the difference in the values of the second c.s.radius blurring is rather noticeable.

This fact is illustrated by the distance distribution functions $G(r_{ij})$ taking into account the straggling in interatomic distances (Fig.5).

These marked differences suggest various degrees of the oxygen sublattice disorder in the short-range order region of compact Al_2O_3 films formed in various electrolytes. This result can be explained by the influence of the forming electrolyte anions introduced into the oxide during its formation. However,the amount of these anions [8] and, probably, the way of their introduction [9] do not appear to be sufficient to cause a change in the mutual atomic arrangement of oxygen and aluminium atoms in barrier amorphous Al_2O_3 films. The effect of the electrolyte anions is confined to its influence on the degree of oxygen sublattice disorder.

Effect of heat treatment on the oxide structure

Heat treatment of amorphous Al_2O_3 films up to the temperature of 973 K is known not to cause oxide crystallization. Little work has been done on the effect of the low-temperature heat treatment (at temperatures below the melting temperature of Al), though this aspect is undoubtedly of certain interest. The objects of the X-ray investigation were amorphous oxide films both as-grown and heat treated. Only on reaching the annealing temperature of 773 K, slight changes in the shapes of I(s) curves were observed. From the analysis of the c.n., radii and blurring calculations [10] it is possible to state that during annealing of oxide films in the temperature range 873-893 K, systematic structural changes occur, which are characterized by reduced (by 30-50 %) blurring σ_{ij} of the coordination sphere formed by Al-Al atomic pairs.

Thus, annealing of both compact and porous Al_2O_3 films results in a noticeable Al-Al bond length reduction, with no changes in the type of the short-range order.

Some traces of the crystalline component in the oxides studied were first noticed after stripped Al_2O_3 films had been annealed at 1023 K. Further increase in the annealing temperature caused transformation of amorphous Al_2O_3 into polycrystalline, represented by the cubic γ-Al_2O_3 and tetragonal δ-Al_2O_3 mixture.

Structural changes under electrophysical stress

Being exposed to such a prolonged electrophysical stress as cathodic polarization, amorphous barrier anodic oxides undergo transformation into amorphous-crystalline oxides.

This is confirmed by the presence of a number of reflections of the crystal phase on the diffraction pattern, corresponding to an oxyhydroxide of Al with the boehmite-type structure.

The comparison of the short-range order characteristics for the as-grown amorphous oxides with those for the amorphous component of the films after cathodic polarization (Table 4) shows the increased first c.n. referring to Al-O neighbours, which corresponds to the increased amount of Al cations with the c.n. 6 relative to oxygen.

Table 4

Comparison of the structural characteristics of barrier aluminium oxides (d = 210 nm) prior to (1) and after (2) cathodic polarization

		type of a coordination sphere			
		$Al-O_I$	$O-O_I$	$Al-Al_I$	$Al-O_{II}$
1	$r_{ij}\times10^{-1}$, nm	1.83	2.63	3.22	3.47
	$\sigma_{ij}\times10^{-1}$, nm	0.18	0.25	0.44	0.30
	N_{ij}, at	5.44±0.03	12.4±0.1	10.7±0.2	9.1±0.2
2	$r_{ij}\times10^{-1}$, nm	1.84	2.63	3.20	3.47
	$\sigma_{ij}\times10^{-1}$, nm	0.18	0.25	0.44	0.32
	N_{ij}, at	5.60±0.05	12.5±0.3	10.4±0.2	9.1±0.2

Formation of an aluminium oxyhydrooxide as well as the above tendency of the aluminium cations with octacoordination to increase in number, further confirm the hypothesis about "protonation" of the oxide during cathodic polarization.

References

[1] A.Despic, V.P.Parhutic, Mod.Aspects El.chem.20,401(1989).
[2] V.A.Laleko, E.A.Chupahina, N.M.Yakovleva, Petrozavodsk University, Dept. in VINITI, N 3664-B91(1991).
[3] B.E.Warren, Crystallographia. 16, 1264(1971).
[4] N.M.Yakovleva, A.D.Fofanov, Izv.AN USSR. Neorgan.mater. 21, 48(1985).
[5] N.M.Yakovleva, A.N.Yakovlev, A.D.Fofanov, Physics of oxide films. Petrozavodsk University. 74(1987).
[6] E.J.Verwey, Z.Krist. B91, 317 (1935).
[7] N.M.Yakovleva, A.N. Yakovlev, Interanod - 93, Kazan. 87 (1993).
[8] P.Skeldon, K.Shimizu, G.E.Thompson, G.C.Wood, Surface and interface analysis. 5, 252 (1983)
[9] Y.Xu, G.E.Thompson, G.E.Wood, B.Bethune, Corros.Sci. 27, 83 (1987).
[10] N.M.Yakovleva, A.N.Yakovlev, Interanod - 93, Kazan. 89 (1993).

Materials Science Forum Vols. 185-188 (1995) pp. 301-312

EXAFS analysis of passivating films

H-H. Strehblow and P. Borthen

Institut für Physikalische Chemie und Elektrochemie,
Heinrich-Heine-Universität Düsseldorf, Germany

Keywords: EXAFS, passive layers, x-ray reflectivity, grazing incidence

Abstract A short introduction is given to the EXAFS methods (Extended X-Ray Absorption Fine Structure) suitable to study thin oxide films and passive layers. Examples are given for the investigation of oxide layers on Cu, Ag and Cu50Ni alloy. For grazing incidence at sufficiently small angles (<0.3 degrees) of X-rays passive layers may be studied in the presence of the bulk metal substrate. The near range order of these passive layers indicates a more disordered structure compared to that of crystalline oxides and hydroxides

Introduction

Passive layers have only in rare cases a simple homogeneous chemical and atomic structure.Even for pure metals, usually a duplex structure is obtained as for Fe, Ni, Cu and especially for binary and more complex alloys. Many details of the chemical structure of these films are obtained from quantitative *ex situ* studies by XPS, ISS and Auger spectroscopy [1]. On the other hand, there exists only very little information about their atomic structure. Indirect conclusions are drawn from photoelectrochemical results and capacity measurements. The large concentration of donor or acceptor levels - often a consequence of the applied semiconductor model - suggest a relatively disordered structure.

Studies of passive layers by EXAFS on Fe suggest the presence of a disordered oxide which is not identical with one of the known oxides [2,3]. These studies were performed on ultra thin vapor deposited metal films which have been passivated electrochemically or chemically by redox systems like nitrite or chromate with almost all metal being transferred into oxide. One may suggest that these films are different from anodic oxides on bulk metal specimens which have been formed under potentiostatic control. The authors admit that Cr(III) as a reduction product of CrO_4^{2-} is incorporated within the films. Therefore it seems challenging to develop and apply appropriate X-ray methods to study the structure of passive layers on bulk metals which are passivated under electrochemical control.

Theoretical Aspects

The absorption of X-rays leads to the excitation of electrons from their orbitals to free electronic levels of the related atom or to the energy continuum when ionisation is achieved. The intensity of an X-ray beam travelling for a distance x through a medium with a linear absorption coefficient μ decreases according to the following simple exponential equation:

$$I = I_0 \exp[-\mu(E)\, x] \qquad (1).$$

Out of the range of the absorption edge the absorption coefficient decreases monotonously with energy. In dense media an oscillarory structure is superimposed to the smooth background of μ above the edge. These oscillations in the absorption spectrum are a consequence of the backscattering of the photoelectrons by the coordination shells of the absorbing atom, i.e. the first, second and further nearest neighbours. These features are interpreted as an interference pattern of the electron wave starting at the absorbing atom and the backscattered waves with a de Broglie wavelength $\lambda = 2\pi/k$ and the wave vector $k = [\, m/h^2\, (h\nu - E_0)\,]^{1/2}$ where E_0 is the energy of the X-ray absorption edge and $h\nu$ that of the absorbed X-rays. Thus the EXAFS modulation of μ carries the near range order information in vicinity of the central atom. μ contains a smooth part $\mu_o(k)$ decreasing continuiously with the kinetic energy of the photoelectron $E_{kin} = h\nu - E_0$ or the related wave vector k and in addition the oscillatory part $\chi(k)$.

$$\mu = \mu_o(k)\, [\, 1 + \chi(k)\,] \qquad (2)$$

The quantitative evaluation of the X-ray spectrum requires the background correction related to all other absorption processes, i.e. the pre-edge absorption, and the substraction of μ_o to obtain $\chi(k)$. $\chi(k)$ contains contributions of the coordination shells with the radii R_j.

$$\chi(k) = \Sigma\, A_j(k) \sin [\, 2\, k\, R_j + \varphi_j(k)\,] \qquad (3)$$
$$A_j(k) = S_0^2 \cdot \exp(-2R_j / \lambda) / kR_j^2 \cdot N_j\, F_j(k) \cdot \exp(-2\, \sigma_j^2\, k^2) \qquad (4)$$

The amplitude $A_j(k)$ contains an exponential damping factor due to the mean free path of the photoelectrons λ. S_0^2 takes account for a damping according to shake up and shake off events and other many body effects. The scattering power $N_j\, F_j(k)$ contains the coordination number N_j of the j-th shell and the backscattering amplitude $F_j(k)$ of the related neighbouring atoms. Finally, an exponential function takes account for the structural and thermal disorder represented by the Debye-Waller factor σ_j. A Fourier transform FT(r) of $\chi(k)$ weighted by a factor k^n to the distance space r permits to separate the contributuions of the coordination shells. As a result of an EXAFS analysis the radius R_j, the coordiantion number N_j and the Debye-Waller factor σ_j of a particular coordination shell is obtained. Disordered structures have small N_j, large σ_j and a broader spread of R_j compared to ideally ordered structures. However, even for species in solutions the data for the first coordination shell may be obtained as e.g. for the oxygen shell of a central Cu ion in alkaline CuO_2^{2-} solutions. EXAFS is a valuable tool to determine the near range order for disordered or amorphous structures where X-ray diffraction fails.

The examination of native oxides on bulk metals requires however a more surface sensitive method. If an X-ray beam hits the surface at a glancing angle Θ below the

critical value of total reflection Θ_c, one has a chance to investigate thin films without picking up (too much) signal from the substrate. Fig. 1 presents the penetration depth of X-rays at 8.6 k eV as a function of Θ for Cu and Cu_2O as obtained from the Fresnel theory. The critical angle at this energy for Cu and CuO is 6.3 and 4.9 mrad, respectively. If Θ is sufficiently small, the penetration depth is on the order of the thickness of the passive layer of some few nm.

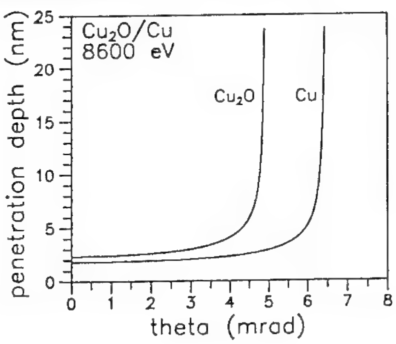

Fig. 1 Penetration depth of X-rays into media as function of the angle of incidence for a metal and its oxide at E = 8.6 keV and with the optical constants δ and β similar to Cu and Cu_2O.

oxide: $\delta = 1{,}2 \cdot 10^{-5}$, $\beta = 3.0 \cdot 10^{-7}$

metal: $\delta = 2.0 \cdot 10^{-5}$, $\beta = 4.0 \cdot 10^{-7}$

The reflectivity $R = I_R / I_0$ is related to the complex refraction index $n = 1 - \delta(E) - i\beta(E)$ and Θ by the Fresnel equations. R carries again the EXAFS oscillations as has been shown already by the work of Martens and Rabe [4]. Similar to the EXAFS evaluation one may extract the oscillations $\Delta R(k)$ of the reflectivity $R(k)$. On the other hand, $R(k)$ and $\Delta R(k)$ may be obtained by computer simulations. Starting with a first guess of the characteristic parameters R_j, N_j, and σ_j for the j-th coordination shell one obtains a first value for the oscillating part of $\beta(E)$. A Kramers-Kronig transformation gives the related value $\delta(E)$ which leads to the complex refraction index n. The Fresnel equations yield finally the simulated reflectivity $R(E)_s$. The comparison with the measured reflectivity $R(E)_{exp}$ requires a better set of data for the coordination shells for a following calculation. A computer simulation repeats the simulation till a close fit of R_s and R_{exp} and no further improvement is achieved. This briefly described procedure and the related computer programs have been developpped as a base for a quantitative evaluation of the structure of thin native films on their own substrate. Some examples for the application of this method for ex situ and in situ studies are presented below.

Experimental Procedures

The various EXAFS experiments require their specific equipment. The simplest method is EXAFS in transmission which is well suited for structural studies of bulk materials. Electrochemical reduction or oxidation processes can be studied in situ using a thin layer transmission cell (Fig.2). With this cell, structural changes as a function of the applied electrode potential have been investigated for electrochemically deposited Cu_2O layers [5,6] and $Ni(OH)_2$ films [7]. These layers are introduced as working electrodes into an electrochemical transmission cell as depicted in Fig 2. Besides layers which are formed during corrosion processes also those films may be studied *in situ* which are of interest for electrochemical energy storage as e.g. the $Ni(OH)_2$/NiOOH system [7].

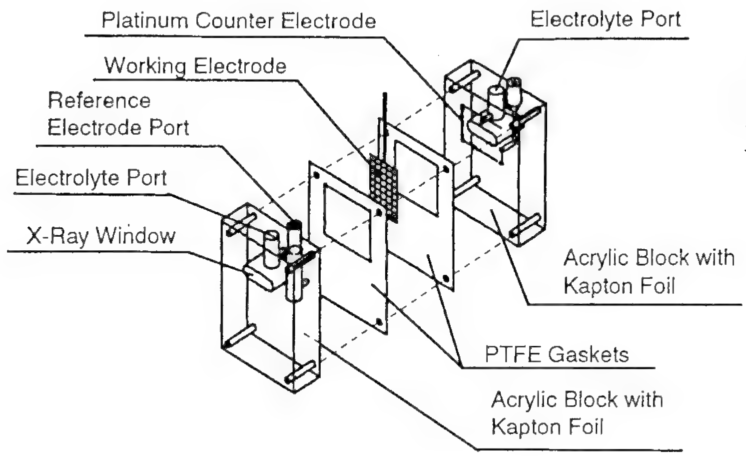

Fig.2 Electrochemical cell for in situ EXAFS studies in transmission

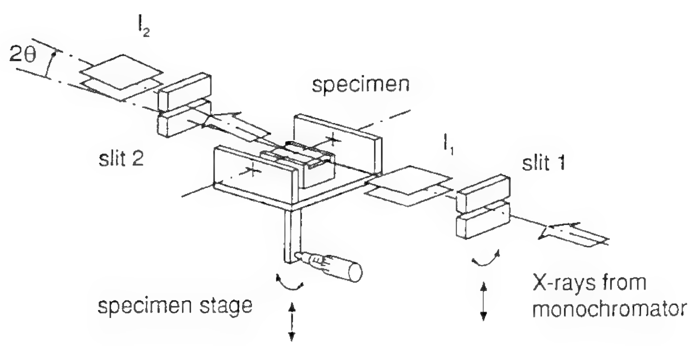

Fig. 3 Stage for EXAFS studies in reflection. I_1 and I_2 are ionisation chambers

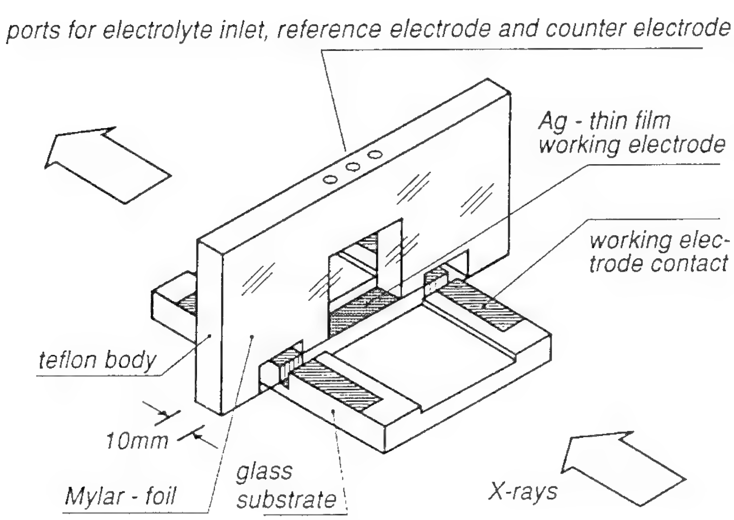

Fig. 4 Electrochemical cell for in situ EXAFS studies in reflection

EXAFS in reflection requires a more sophisticated experimental stage (Fig.3). The extremely small critical angles need a careful positioning of the specimen. With the help of a laser interferometer its position can be adjusted and reproduced quite easily. A thin entrance slit cuts out a sharp parallel beam. The incoming and reflected beam is measured by the ionisation chambers I_1 and I_2. The high brilliance and stability of a synchroton radiation source is a necessary condition to obtain good spectra. All measurements described in this paper were performed at the synchroton radiation facility DORIS III at DESY, Hamburg.

Electrochemical *in situ* experiments in reflection have still stronger requirements to the intensity and stability of the X-ray beam. In some electrochemical experiments the incident angle may be large and the X-ray fluorescence, which occurs as one of the deexcitation processes, is measured with sensitive detectors perpendicularly to the X-ray beam instead of the intensity of the reflected beam. This method is appropriate if thin films or adsorption layers of strong scattering atoms on a foreign substrate are examined. The successful studies of the structure of under-potential-deposits of heavy metal ions on noble metal substrates is one example. However, the investigation of native oxides on their own substrates requires total reflection of the beam from the specimen surface. This situation does not permit a large electrode surface covered with a thin electrolyte film whose thickness is determined by a pressed on organic foil in order to avoid reflection from this outer cover or the electrolyte surface. Therefore, a special electrochemical cell with a geometry similar to that which has been used by R. Cortes et al. [8] has been applied. The metal film was vapor deposited on float glass which was shaped mechanically to give an electrochemical cell together with an upper glued on teflon part (Fig. 4). First studies have been performed with Ag films and the growth and reduction of anodic Ag_2O- and AgO-films has been studied [9]. The high energy of the silver absorption edge of E = 25.5 keV causes only a moderate absorption within the electrolyte. Thus one can afford an electrolyte layer of ca 2 cm which in turn is good for an appropriate interaction of the X-ray beam with the substrate surface. Some results on *in situ* studies of anodic films on Ag are given in the following section. First studies with Cu electrodes in the same arrangement are also promising.

In any case the electrode surface has to be extremely flat and smooth for these reflection studies. For this purpose vapor deposited and sputtered films on float glass have been examined. In some cases thin metal foils have been glued under homogeneous pressure to float glass substrates and then mechanically polished with diamond spray and finally with 0.04 μm grain size silica. The evaluation of the reflectivity data justifies this specimen preparation which has to be done extremely carefully in order to meet the condition of total reflection of the beam with the same incident angle from all parts of the electrode surface.

Examples and Results

Cu forms passivating layers of up to a few nm thickness in weakly acidic and alkaline solutions. The continuous and poreless film contains an inner Cu_2O and an outer $CuO/Cu(OH)_2$ part if the potential is positive enough, i.e. E > 0.5 V (SHE = standard hydrogen electrode) in 0.1 M NaOH [10]. A complete reduction of the $CuO/Cu(OH)_2$ part to Cu_2O occurs at potentials E = -0.3 V. Much thicker Cu_2O films up to more than 1 μm may be prepared by additional reduction of dissolved CuO_2^{2-} in strongly alkaline

solutions. These films are also continuous and poreless because they grow by the reduction process at the oxide electrolyte interface which does not require any nucleation process compared to a direct growth on a metal substrate. They show similar electrochemical and photoelectrochemical properties as the anodic passive films [10]. Thick Cu_2O films on teflon substrates with a thin vapor deposited conducting Au film have been studied with EXAFS in transmission in a thin film electrochemical cell as described previously [6]. Fig. 5 shows a sequence of Fourier transforms during the different stages of the reduction process of thick Cu_2O layers to metallic Cu. The evaluation of the near range order of the electrodeposited Cu_2O reveals a similar structure as crystalline powder spectra with the same distance and coordination number for the first shells, especially the Cu-O and Cu-Cu distances. Also the Debye-Waller factor suggests a crystalline structure of these thick electrodeposited Cu_2O-films.

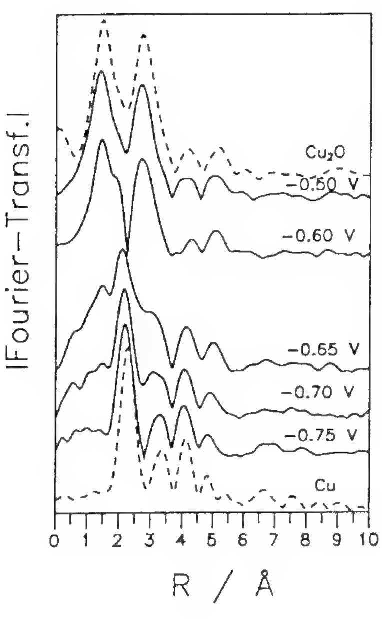

Fig.5 *In situ* EXAFS study of Cu_2O in 0.1 M borax buffer pH 9.2 at various electrode potentials, Fourier transforms for reduction of Cu_2O to Cu metal, dashed lines crystalline standards

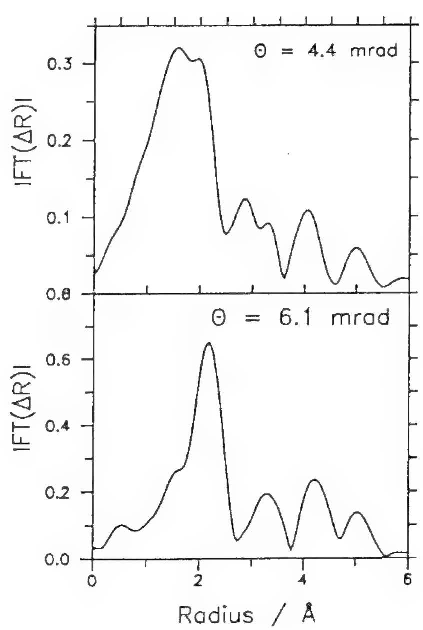

Fig. 6 Fourier Transform of reflectivity of an air oxidized Cu-film at two angles of grazing incidence

According to the calculations of Fig. 1, the reflectivity spectrum of a metal substrate covered with a thin oxide film varies strongly when the angle of grazing incidence is close to its critical value. Fig. 6 depicts the Fourier transforms of an air oxidized Cu-film on float glass. For 4.4 mrad a strong contribution due to the Cu-O coordination shell at about 0.15 nm is visible. At 6.1 mrad mainly contributions from the underlying Cu substrate are significant. Theoretical calculations suggest the presence of about 4.5 nm Cu-oxide. The weak contribution of the oxide Cu-Cu coordination shell suggests a

significantly disordered structure compared to that of crystalline Cu_2O. This example shows that structural depth profiles may be obtained from the angular dependence of the reflectivity in the range of the critical angle.

Fig 7 depicts an example of electrochemically in 1 M NaOH treated 100 nm thick vapor deposited Cu films on float glass. Fourier Transforms are presented after cathodic reduction at E - 0.6 V, anodic oxidation at 0.8 V with a duplex $Cu_2O/CuO,Cu(OH)_2$ layer and finally after reduction of the Cu(II) overlayer to Cu_2O at E = -0.3 V. The Fourier transform of the metal surface reduced at E = -0.6 V shows the structure of Cu-metal with the first four coordination shells and a slight shoulder at r = 0.16 nm attributed to 1.7 nm surface oxide which has been formed during a short air exposure. The anodic oxidation at 0.8 V causes a more pronounced peak at r = 0.16 nm attributed to the Cu-O distance within the oxide and a superposition of the Cu-Cu distance of the second shell of the oxide with the first shell of the metal substrate. The partial reduction at E = -0.3 V does not cause much changes because of the dominating presence of Cu_2O in both cases. Similar to the air formed oxide on Cu, a comparison with the simulated Fourier transform suggests a stronger disordered structure compared to that of cuprite (Fig. 7b). The Debye-Waller factor had to be changed from 0.015 to 0.02 nm for the simulation in order to get a sufficient agreement with the experimental Fourier transforms.

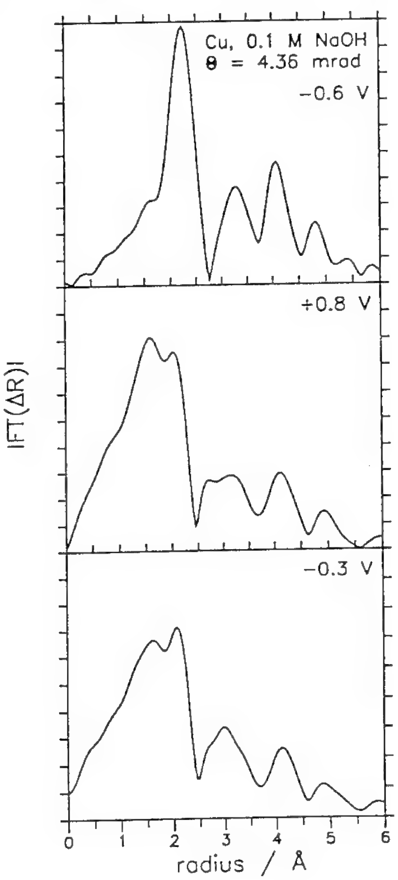

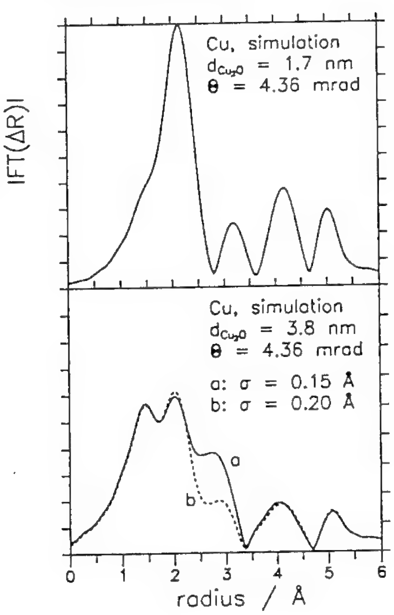

Fig. 7 Cu thin film electrochemically reduced at -0.6 V, passivated at 0.8 V and partially reduced at -0.3 V (SHE) in 0.1 M NaOH, Fourier transform of measured reflectivity (left) and computer simulated results (right)

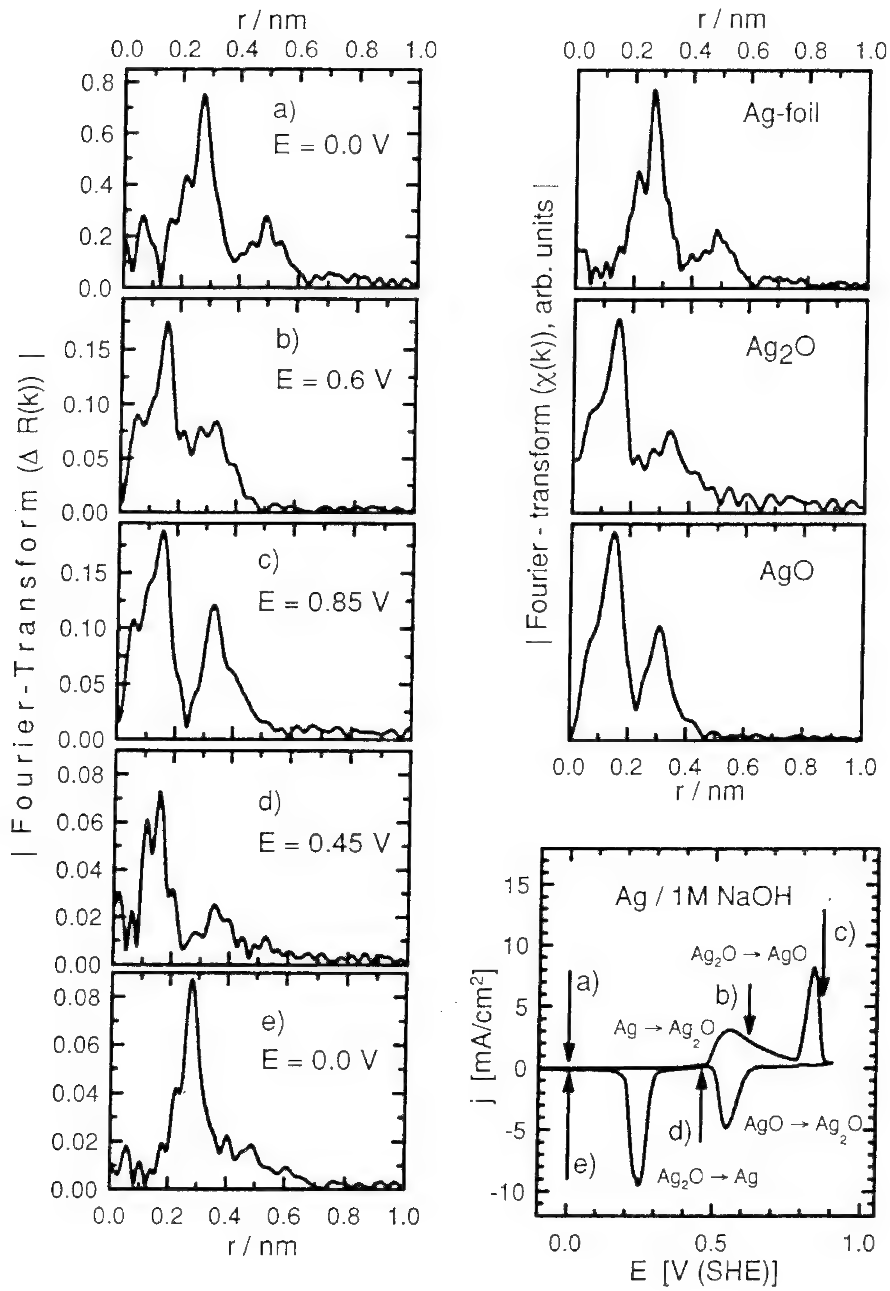

Fig. 8: Fourier-Transforms (not phase shift corrected) of the reflectivity fine structure $\Delta R(k)$ (left) and of reference compounds (measured in transmission) (upper right). Lower right: Cyclovoltammogram of Ag in 1M NAOH.

Anodic films on Ag examined in 1 M NaOH by *in situ* reflectivity spectra show Fourier transforms which are very close to those of Ag-oxide standards deduced from transmission spectra (Fig.8). One obtains the same Ag-Ag and Ag-O distances for the layers formed at appropriate potentials. Thus, the anodic formation of Ag_2O and AgO and its reduction back to Ag_2O and Ag metal respectively may be followed *in situ* with EXAFS in reflection at the appropriate potentials as indicated at the potentiodynamic polarization curve which is also depicted in Fig. 8. Fig. 8 e shows less pronounced peaks for the higher coordination shells of the Ag surface in the range of 0.4 to 0.6 nm. This can be seen as a disorder of electrodeposited Ag as a reduction product of the anodic oxides. Fig. 8 gives a good example for the study of anodic films on their metal substrate and the change of the structure by electrochemical oxidation and reduction processes. Although these films are still in the range of more than 100 nm, thinner films may be examined with this method as well. With sufficient intensity for the X-ray beam one may study films of a few nm thickness. There remains a difficulty when the absorption edge has an energy in the range of 5 to 8 keV as for Fe and Cr. For these small energies the absorption of the X-rays within the electrolyte gets too large to obtain a good EXAFS signal. One cannot decrease the thickness of the cell of Fig.4 to less than some few mm in order to have a sufficient interaction of the X-rays with the metal surface which gets smaller in the same way as the electrolyte layer. *In situ* experiments of passivated ca 4 mm broad Cu films with an absorption edge of ca 9 keV provide reflection spectra which are promising. In any case the chance to vary continuously the thickness of the oxide layer makes Ag an interesting system to improve the measurements and the experimental conditions in order to be able to study technologically more relevant metals and alloys.

Fig. 9 shows results for a passive layer on a vapour deposited Cu/Ni film on a float glass substrate. The vapour deposition was performed simultaneously from two crucibles with a subsequent annealing of the alloy films. The mean Ni content of the alloy was ca 50 wt%. After annealing and prior to the electrochemical preparation, the metal films were exposed to air thus starting the electrochemical passivation with an air formed film. Passivation was performed with two potentiodynamic polarization steps including a polarization for ca. 5 min at the final potential: (a) -0.5 V $\rightarrow$ 0.0 V, (b) 0.0 V $\rightarrow$ 1.0 V and a final reduction (c) 0.0 V $\rightarrow$ -1.0 V. After each preparation step EXAFS measurements were performed at the Ni K-absorption edge in the reflection mode at a glancing angle of 0.25 degrees (Fig. 9 left part). Calculated results obtained by computer simulation according to a procedure described already previously [11] are presented for comparison (Fig.9, right part). The refractive indices for these calculations were obtained from transmission EXAFS data with NiO-, $Ni(OH)_2$- and Cu45Ni-standards. Best agreement between the calculated and measured results were obtained for a simultion with a duplex hydroxide/oxide film with 2 nm $Ni(OH)_2$ and 2 nm NiO. Simulations with a reversed layer sequence or significantly different thicknesses of the sublayers yield much less agreement with the measured spectra. These EXAFS results are in good agreement with XPS data obtained for passivation times of more than 5 min at the same potentials [12]. Reduction at -1.0 V did not change signifcantly the observed structure of the passive layer as stated already earlier for Ni [13] and Cu/Ni alloys [12].

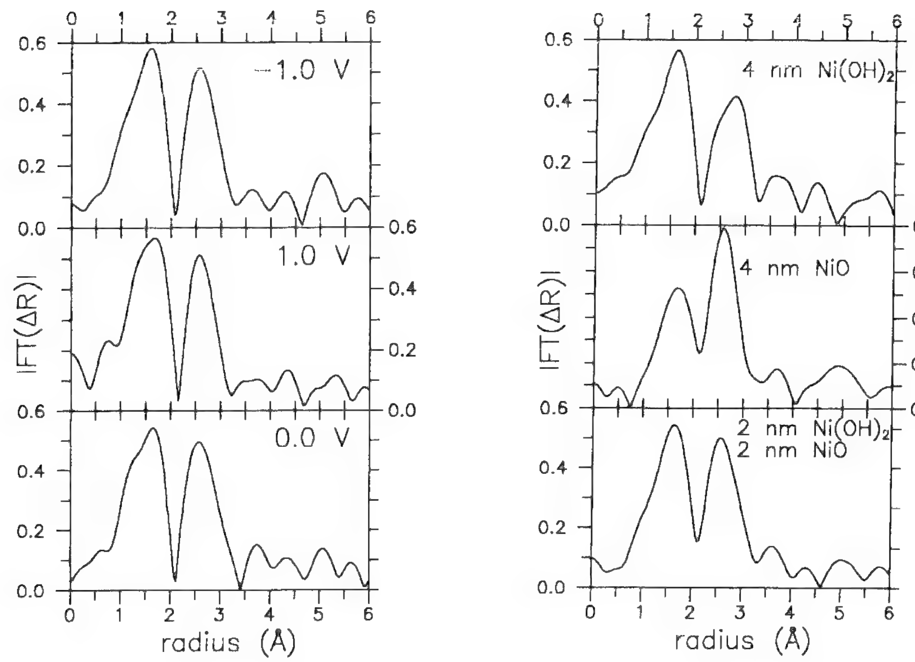

Fig. 9 Measurements and calculations for Ni K edge energy region at a glancing angle of 0.25 degrees. Left: Cu-Ni thin film consecutively potentiodynamically polarized in 1 M NaOH to the end potentials of 0.0 V and 1.0 V and including final reduction at -1.0 V. Right: Results of computer simulations for following systems: 2 nm $Ni(OH)_2$/2 nm NiO/Cu45Ni (bottom), 4 nm NiO/Cu45Ni (center) and 4 nm $Ni(OH)_2$/Cu45Ni (top). The magnitudes of the Fourier transforms peak at radii values corresponding to the first (Ni-O) and the second (Ni-Ni) coordination shell in NiO and $Ni(OH)_2$.

Conclusion

EXAFS applied to the study of the near range order of passive layers on pure metals and alloys has the advantage to examine the environment of specific atoms even when the structure of the films is amorphous, in which case X-ray diffraction would fail because it requires a long range order structure. Transmission methods are not suited for the study of the structure of the surface films because the metal substrate underneath usually dominates the spectrum. The application of ultra thin metal films in the range of some few nm and their complete oxidation during passivation is not appropriate if thin films on bulk metals are of interest. EXAFS in reflection, however, is an appropriate method for the structural studies of thin oxide layers on bulk metals. If the energy of the absorption edge is high enough and the absorption of the related X-rays in water sufficiently small it can

be applied *in situ* , but a very high beam intensity is required for a good signal to noise ratio. A simulation technique with appropriate computer methods permits a close fit of the experimental and simulated reflectivity spectra and their Fourier Transforms and an evaluation of the structural parameters like the distances and the coordination numbers as well as the Debye-Waller factors of the coordination shells. Examples are given for electrochemically formed passive layers on metals like Cu, Ag and CuNi alloys. It seems promising to examine further systems, especially also those with lower energy adsorption edges which are technologically important as i.e. Fe, Cr and Ni. Although the method needs large efforts and a synchroton radiation source it is one of the very few possibilities to get structural information on thin passivating films *in situ* .

Acknowledgement: The financial support of the Bundesministerium für Forschung und Technologie is gratefully acknowledged. We also thank P. Druska for his EXAFS data on Cu/Ni films.

References:

[1] H.-H. Strehblow, Corrosion 91, Cincinnati Ohio, NACE Houston, paper 76, (1991)
[2] G.G. Long, J. Kruger, D.R. Black, M. Kurayama, J. Electrochem. Soc. **130**, 240 (1983)
[3] M. Kerkar, J. Robinson, A.J. Forty, Faraday Disc. Chem. Soc. **89**, 31 (1990)
[4] G. Martens, P. Rabe, N. Schwentner, A. Werner, Phys. Refv. B, 17, **1481** (1978)
[5] U. Collisi, H.-H. Strehblow, J. Electroanal. CHem. **284**, 385 (1990)
[6] P. Druska, H.-H. Strehblow, J. Electroanal. Chem. 335, 55 (1992)
[7] J. McBreen, W.E. O´Grady, K.I. Pandya, R.W. Hoffmann, D.E. Sayers, Langmuir **3**, 428 (1987)
[8] R. Cortes, M. Froment, A. Hugot Le Goff, S. Joiret, Corros. Sci. **31**, 121 (1990)
[9] D. Hecht, P. Borthen, H.-H. Strehblow, J. Electroanal. Chem. (1994) in press
[10] U. Collisi, H.-H. Strehblow, J. Electroanal. Chem. **210**, 213 (1986)
[11] P. Borthen, H.-H. Strehblow, Physica B (1995) in press
[12] P. Druska, H.-H. Strehblow, Surf. Interf. Anal. (1994) submitted
[13] H.W. Hoppe, Dissertation, Heinrich-Heine-Universität Düsseldorf, 84 (1990)

Materials Science Forum Vols. 185-188 (1995) pp. 313-324

Methods to determine the composition of passive films: Recent trends in XPS, AES and SIMS

D. Landolt, P. Schmutz and H.J. Mathieu

Laboratoire de Métallurgie Chimique, Département des Matériaux, Ecole Polytechnique Fédérale de Lausanne (EPFL), MX-C Ecublens, CH-1015 Lausanne, Switzerland

Keywords: Passive film, surface analysis methods, stainless steel

Abstract

Most of our present knowledge on the chemical composition of passive films comes from surface analysis methods used ex-situ. The present paper presents an overview of the use of AES, XPS and SIMS for the study of passive films emphasizing recent developments. Typical examples from the authors laboratory and the literature are presented to illustrate the type of information obtainable. Particular points of discussion concern the interpretation of XPS spectra of passive films on iron-chromium alloys, surface imaging using SAM and TOF-SIMS, SNMS profiling using laser postionization and SIMS isotope ratio profiling.

Introduction

The study of the chemical and physical nature of passive oxide films formed on metals and alloys is a central subject of corrosion research. Indeed, our industrial civilization would not be possible without the availability of corrosion resistant alloys such as stainless steels, nickel alloys, aluminium alloys etc. All of these are thermodynamically unstable and would be rapidly destroyed by corrosion if they were not protected by oxide films of typically 2-3 nm thickness. Most of our present knowledge on the chemical composition of passive films comes from surface analysis methods used ex-situ, in particular Auger Electron Spectroscopy (AES), X-ray induced Photoelectron Spectroscopy (XPS), Secondary Ion Mass Spectroscopy (SIMS) and Ion Scattering Spectroscopy (ISS). Several reviews on the application of these methods to the study of passive films and alloy corrosion are available in the literature [1-6]. A nice overview of in-situ methods applied to the study of passive films has recently been given by Davenport [7]. The following discussion will focus mainly on the use of XPS, AES and SIMS. For the application of ISS to the investigation of passive films the reader is referred to recent papers by Strehblow [8,9]. **Fig.1** indicates different types of chemical information on passive films one may be interested in and the corresponding surface analysis techniques.

Elemental information on the average film composition can best be obtained by AES and XPS. For the study of chemical states XPS is most often applied. Of particular interest are the identification of the oxidation state of cations, hydration of oxides and incorporated electrolyte species. SIMS can in principle also give such information but often in a less straightforward way. In-depth distribution of chemical species in passive films can be obtained in a non destructive way by angle resolved XPS (ARXPS) or by angle resolved AES, but the latter method is rarely applied. ARXPS is based on the fact that the escape depth of the photoelectrons depends on the emission angle and, therefore, by changing its value the information depth can be varied. Unfortunately, for several reasons this method usually yields only qualitative in-depth information on passive films. One reason is that by limiting the acceptance angle the signal to noise ratio decreases, another that surface roughness may affect results obtained at grazing emission angle.

Most in-depth information on passsive films has been obtained by using ion sputtering in combination with AES, XPS, ISS or SIMS. Elemental AES profiles are particularly useful since they can be acquired fast and with high local resolution. Sputter profiling, however, damages the sputtered oxide film and can lead to composition changes by preferential sputtering. The influence of these effects on obtained results is not known precisely. Sputter profiling can be also used to study the distribution of oxidation states of species (XPS) and to determine isotope distributions (SIMS). Furthermore, it serves to characterize the film-metal interface (although such data are usually affected by sputter effects) and the film thickness. The spatial distribution on the surface of different species can be explored with recent high resolution imaging AES and SIMS instruments.

Thus it is in principle possible to investigate surfaces of multiphase alloys, inclusions and local adsorption phenomena. Localized depth profile analysis can also be performed. In practice there is always a trade-off between working at high lateral resolution and achieving an acceptable signal/noise ratio. In the following, particular aspects of the application of XPS, AES and SIMS to the study of passive films, in particular films formed on stainless steel type alloys, will be discussed and illustrated with specific examples from the authors laboratory and others. Recent developments and trends in the use of these methods will be stressed. For a more general introduction to the application of surface analysis methods for the study of passive films the reader is referred to a previous review by the first author of this paper [1].

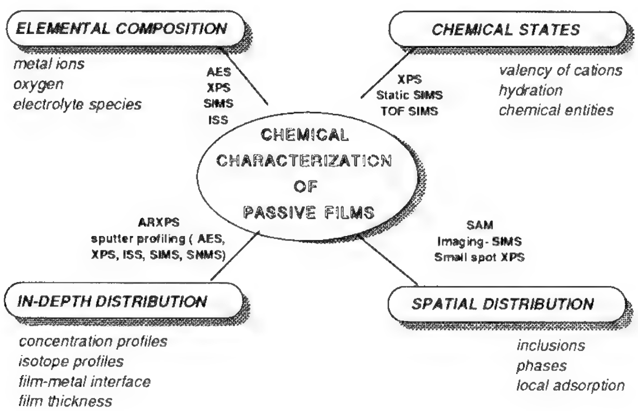

Fig. 1 Overview of surface analysis methods for the study of passive films

Investigation of passive films by XPS

XPS is the most widely used surface analysis method for the study of passive films. Recent instrumental improvements concern mostly an increase in sensitivity due to the introduction of channeltron detectors and software improvements for data handling. As a consequence routine XPS instruments use smaller areas for analysis (typically 150 micrometers) and shorter acquisition time. The use of ARXPS or of monochromators is thus facilitated. On the other hand, several physical quantities of importance for spectra interpretation are still insuffuciently understood. A typical example is the electron attenuation length (usually taken as equal to their inelastic mean free path (IMFP) which multiplied by the escape angle determines the analyzed depth.

XPS results of passive films are usually interpreted with layer type models including an exponential attenuation term associated with each layer [1]. In the simplest case, for a system consisting of a homogenous oxide layer on a metallic substrate, the intensity of the oxide signal for a given element j is given by equation (1) and that of the same element in the substrate by equation (2).

$$I_{j,ox} = K_j \; \Lambda_{j,ox} \; c_{j,ox} \; [1 - \exp(- L / \Lambda_{j,ox})] \quad (1)$$

$$I_{j,m} = K_j \; \Lambda_{j,m} \; c_{j,m} \; \exp(- L / \Lambda_{j,ox}) \quad (2)$$

In these equations K_j is a proportionality factor which depends on the ionization cross section, the primary X-ray flux and the transmission of the analyzer. L is the film thickness and $c_{j,ox}$, $c_{j,m}$ the atomic concentration of element j in the oxide and in the alloy substrate, respectively. The electron escape depth Λ (oxide or metal) is the product of the electron IMFP λ and the escape angle Θ with respect to the surface normal: $\Lambda = \lambda \cos \Theta$. It is readily apparent from these equations that by varying the angle Θ one can get in-depth information (ARXPS). Similarly, by comparing (for any angle) the signal of an element j from the substrate and the film one can deduce the film thickness L provided the electron mean free path and the respective concentrations are known.

For passive film studies the IMFP values are most often calculated by the empirical relation (3) given by Seah and Dench [10],

$$\lambda = \frac{A}{E^2} + B\ (a\,E)^{1/2} \qquad (3)$$

where a is the atomic radius and A and B are empirical constants which are different for elemental solids and inorganic compounds, respectively. By dividing λ by $a^{1/2}$ a material independent relationship between IMFP and kinetic energy E of the electrons in the solid is obtained. However, because the reported IMFP values scatter enormously the application of equation (3) introduces a considerable uncertainty. More recently, Tanuma and Powell used theoretical computations based on optical properties for establishing the IMPF [11]. These authors argued that the IMFP depends on the width of the band gap and the electron density among other and hence is materials dependent. **Fig. 2** due to Powell [12] shows IMFP values for elements corrected for atomic radius as a function of electron kinetic energy. According to this approach no universal curve is obtained and the the energy dependence to the right of the minimum is stronger ($\lambda \propto E^{0.75}$) than in equation (3). Fortunately, in the energy range corresponding to the XPS peaks of interest for many passive film studies the difference in absolute values calculated according the two approaches is relatively small. Calculated IMFP values of different peaks of interest in the analysis of stainless steels and aluminium are shown in **table 1** assuming that either an AlK_α or a MgK_α X-ray source is used for analysis.

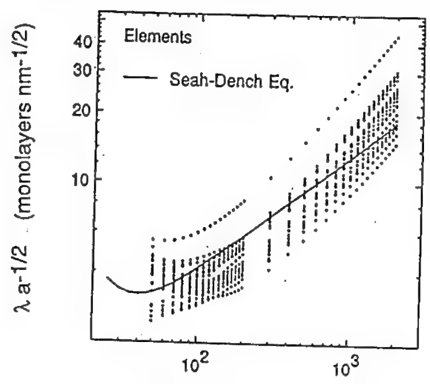

Fig.2 IMFP for elemental solids after Powell [12]

photo electron	$E_{binding}$ (eV)	E_{kin} source Al	λ S.D.	λ T.P.	E_{kin} source Mg	λ S.D.	λ T.P.
Fe $2p_{3/2}$	707	779.6	1.23	1.35	546.6	1.03	1.05
Cr $2p_{3/2}$	574.4	912.2	1.36	1.55	679.2	1.18	1.25
Ni $2p_{3/2}$	852.7	633.9	1.08	1.08	400.9	0.86	0.8
Mo $2p_{5/2}$	228	1258.6	1.81	1.96	1025.6	1.64	1.68
Al $2p_{3/2}$	73	1413.6	1.98	2.57	1180.6	1.81	2.24
Fe_20_3 $2p_{3/2}$	711	775.6	2.01	-	542.6	1.68	-
Cr_20_3 $2p_{3/2}$	576.8	909.8	2.1	-	676.8	1.8	-
Al_20_3 $2p_{3/2}$	74.4	1412.2	2.5	2.8	1179.2	2.3	2.43
O (Al_20_3) 1s	529.9-531.8	954.8-956.7	2.15	2.06	721.8-723.7	1.86	1.68

Table 1 Some IMFP values of elements and oxides calculated after Seah and Dench [10] and Tanuma and Powell [11] respectively for AlK_α or MgK_α source.

At this time, for metals the IMFP values proposed by Tanuma Powell and Penn [11] are probably the most reliable. On the other hand, for passive film oxides no values are given in the mentioned paper [11]. Palacio et al. [13,14] using a curve fitting procedure for the interpretation of oxide spectra recorded with a Mg source during in-situ oxidation of iron-chromium alloys found the following values for IMFP in the surface oxide: $\lambda = 1.9$ nm for Cr2p, 1.5 nm for Fe2p, 1.87 nm for Mo3d. Hubschmid [15] converted these values for an Al source using the energy dependency given by the Seah and Dench equation (3). Further uncertainties in measuring the composition and thickness of passive films by XPS can result from background substraction and from peak deconvolution. The influence of the latter in an apparently simple system is illustrated by **Fig. 3** [16]. It shows data from a round robin ARXPS study of oxidized aluminium samples involving four laboratories. The reported intensity ratios all show qualitatively the same variation with angle, but differ in absolute values. The differences were attributed by the authors to differences in peak fitting. Some laboratories assumed a symmetric others an asymmetric peak shape of the metal peak.

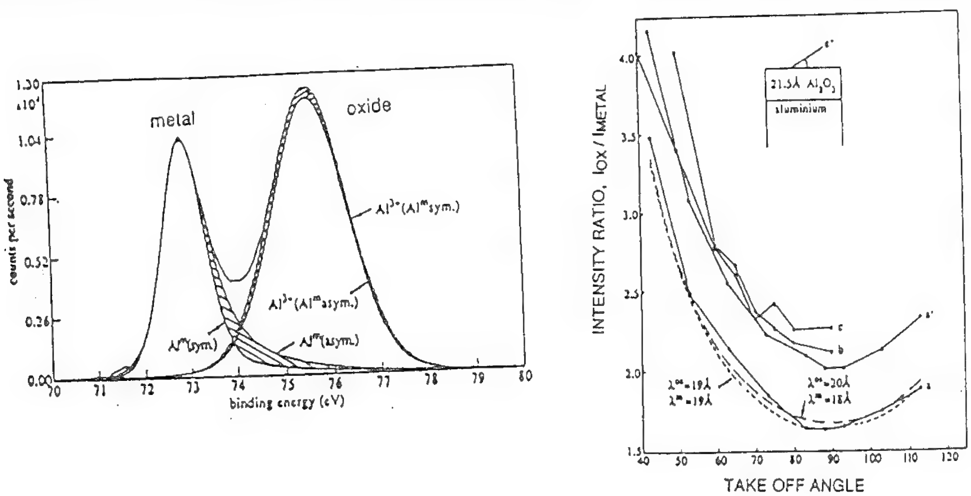

Fig. 3 ARXPS data from round robin study after Marcus et al. [16]

In case of passive films formed on stainless steel type alloys peak fitting is more delicate because more overlap occurs. To some extent, the uncertainty can be reduced using a monochromatic primary source. The use of such sources has long been hampered in practice by an insufficient signal to noise ratio, but in recent years, the transmission of monochromators and the sensitivity of detectors has been improved considerably. As an illustration **Fig. 4** shows the $Cr2p_{3/2}$ and O1s spectra of a passive film formed on Fe-25Cr in a sulfate electrolyte, a chromium oxide film produced by thermal oxidation (600°C, air) and a sputter cleaned Cr metal surface, respectively. The spectra were measured with PHI 5500 ESCA instrument equipped with a monochromator. The O1s spectrum of the passive film shows two distinct peaks associated with oxide and hydroxyde respectively, the thermally grown oxide shows only the oxide peak. The $Cr2p_{3/2}$ spectra for the passive film exhibit a metal peak and a broad oxide peak. The latter is usually fitted by assuming symmetric chromium oxide and hydroxyde peaks [17]. The present data suggest that the situation may be more complex. For a thermally grown oxide the Cr $2p_{3/2}$ exhibits a double peak which gets blurred when slightly sputtering the surface. Since no O1s hydroxide peak is visible on the thermally grown oxide the $Cr2p_{3/2}$ doublet must be due to an oxide rather than a hydroxide phase. Sputtering under the conditions of the experiment removes adsorbed impurities and probably perturbs somewhat the uppermost surface layers. This leads to a relatively broad peak comparable to that of the passive film.

Fig. 5 shows the effect of sputter cleaning the surface of a passive film on Fe-25Cr with low energy argon ions (0.2 KeV). After ten minutes the O 1s hydroxide peak has decreased to a small value indicating that it was due to adsorbed species. This conclusion is sustained by the observation that the relative peak height of O 1s oxide and hydroxyde depended much on the drying procedure used. The $Cr2p_{3/2}$ peak on the other hand does not significantly change during the

same time period. This can be interpreted by postulating that the passive films on Fe-25Cr contains essentially chromium oxide, hydroxide species being only adsorbed on the surface. SIMS and AES profile data support this hypothesis [18, 19].

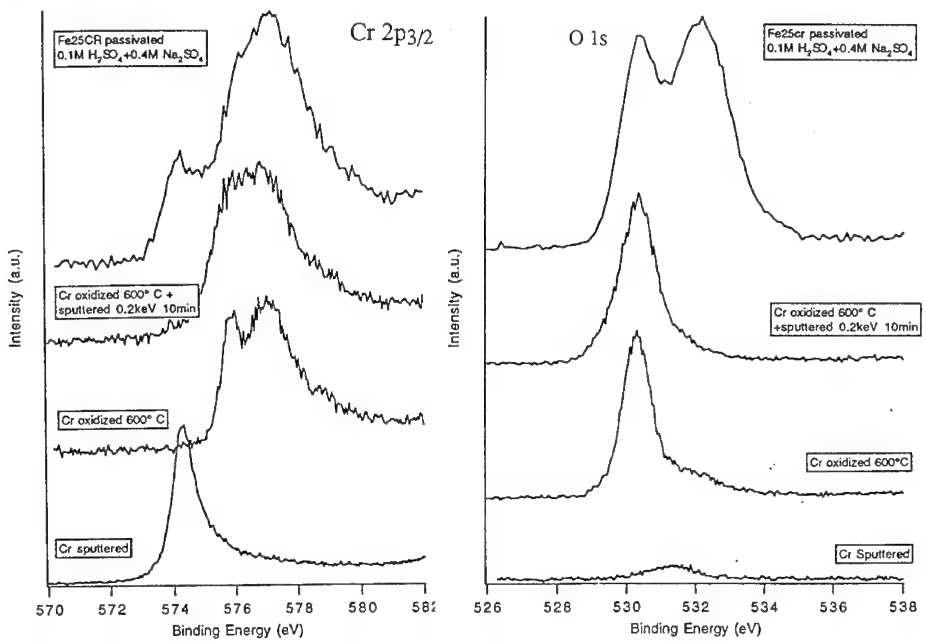

Fig. 4 Cr2p$_{3/2}$ (a) and O1s (b) peaks for (1) passive film on Fe-25Cr alloy, (2) thermal oxide on Cr, (3) a thermal oxide on Cr after sputter cleaning for 10 min at 0.2 KeV, (4) sputtered Cr surface

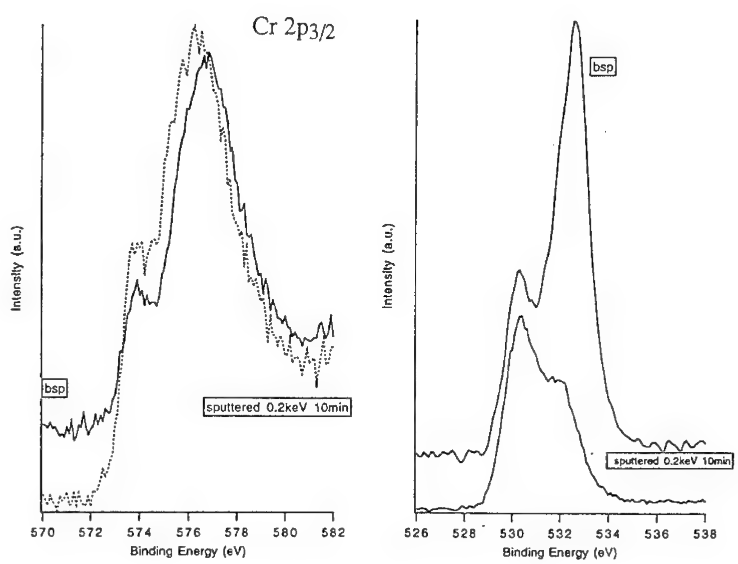

Fig. 5 Influence of sputter cleaning (0.2 KeV, 10 min) on Cr2p$_{3/2}$ (a) and O1s (b) peaks of passive films on Fe-25Cr alloy

Small area analysis by AES and TOF-SIMS

For chemcial analysis of passive films on heterogenous materials small area analysis and imaging are of interest. AES using a scanning Auger microprobe (SAM) and TOF-SIMS are the most suitable methods for high resolution studies at present, both methods offering submicrometer resolution. With XPS imaging best resolution is obtained with synchrotron radiation, but typically is in the micrometer range only [20].

Lateral resolution in SAM is essentially given by the diameter of the primary electron beam, which in modern instruments can be as small as 25 nm. The actually analyzed area is somewhat larger, however, because backscattered electrons can also induce Auger transitions in the solid and thus contribute to the measured signal. In practice, decreasing the diameter of the electron beam leads to a deterioration of the signal to noise ratio requiring long acquisition times and to increasing surface damage due to the higher primary beam energies applied. This often limits the achievable spatial resolution to values below the theoretical limit. To obtain a chemical image the primary electron beam is scanned over a given surface area while simultaneously recording the intensity of preselected kinetic energy windows. **Fig. 6** shows a Auger map of a passive surface of a Fe-25Cr11Nb two phase alloy [21]. The alloy has a chromium rich dendritic phase and a niobium rich interdendritic eutectic. The Auger map of the passive film reflects this structure. The spatial resolution of the instrument does not permit to distinguish the two constituting phases of the interdendritic eutectic though. SAM images are qualitative in nature. More quantitative information is obtained by performing local depth profiles. As an illustration **Fig. 7** shows Auger depth profiles for niobium in the passive film measured simultaneously on the dendritic and interdendritic zones. The data confirm the observation that Nb is present in significant amounts in the film formed on the interdendritic eutectic only. Separate pitting experiments showed that pitting occurred mainly in the interdendritic eutectic, but to a lesser extent than for comparable monophase Fe-Cr alloys. Local area analysis by AES has been applied to the investigation of corrosion pits by different groups [22,23].

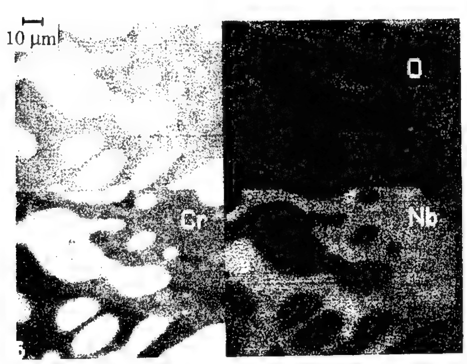

Fig. 6 Auger image of passive film on Fe-25Cr-11 Nb alloy [21]

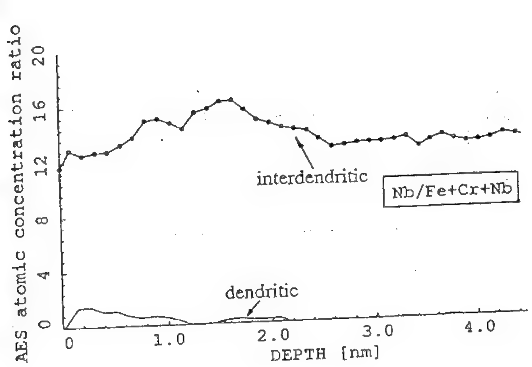

Fig.7 Auger depth profile of passive film in dendritic and interdendritic phase [21]

Chemical imaging can also be performed with dynamic SIMS (SIMS-microprobe) or with TOF-SIMS. In dynamic SIMS a well focused primary ion beam is rastered over the surface. Secondary ions are mass analyzed either by sector mass analyzer or a quadrupole mass analyzer. The ion flux is sufficiently high to cause significant sputtering. In TOF-SIMS one uses a pulsed primary ion beam and the ionic fragments are selected according to their mass/charge ratio by measuring their time of flight (which depends on mass) between the sample and the detector. **Fig.8** schematically shows a commercial instrument (Ch. Evans Ass. Redwood City, Calif.) including Cs^+ and Ga^+ ion guns, electrostatic analyzers and position sensitive detector. A complete positive or negative mass spectrum is obtained for each pulse (< ns). Measured counts are added up until an acceptable signal to noise ratio is obtained, usually within a few minutes. TOF-SIMS achieves a

mass resolution of 10^{-3} - 10^{-4} to even for high masses. The use of a pulsed primary beam minimizes surface damage on the analyzed sample. The position sensitive detectors available in modern instruments allow one to obtain a chemical image of the surface (present resolution approx. 0.2 μm using a liquid metal ion gun). **Fig. 9** shows chemical images obtained with TOF-SIMS on the same Fe-Cr-Nb sample shown in Fig. 6. It represents images of the distribution of the species Cr^+ (mass 52) and Nb^+ (mass 93), measured after 20 minutes of sputtering with gallium (estimated sputter rate 0.1 nm/min). Also shown is a line scan of Nb^+ illustrating the good lateral resolution achieved. The acquisition time of the images is 20 minutes compared to several hours for the SAM images of Fig.6. The TOF SIMS images confirm qualitatively the results of the SAM image.

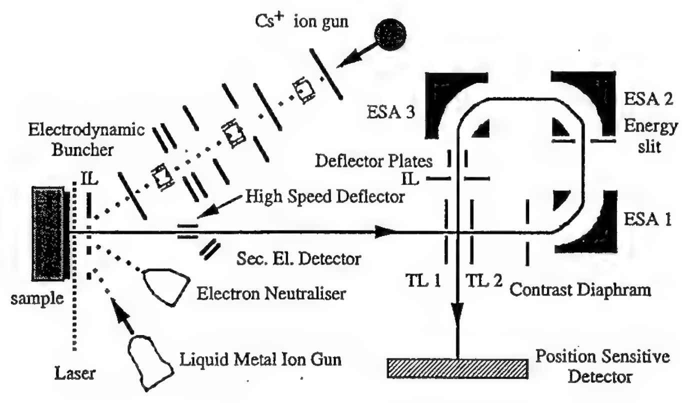

Fig. 8 Schema of TOF-SIMS apparatus

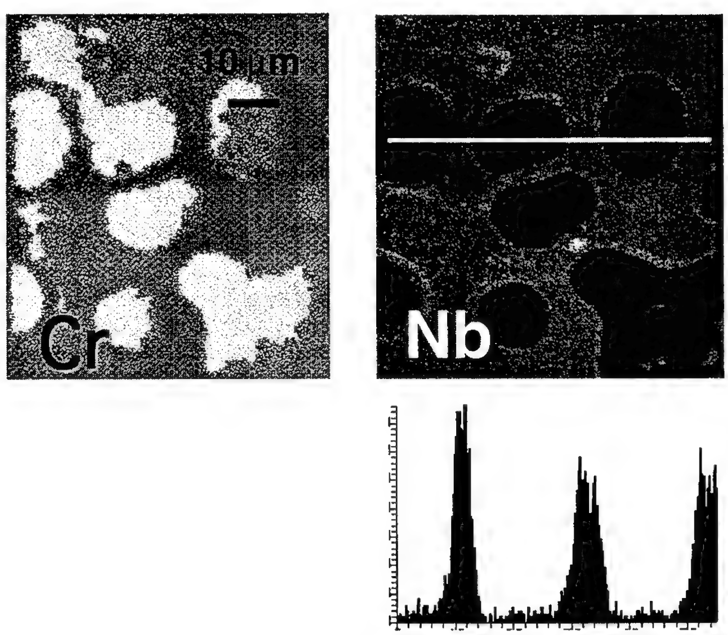

Fig. 9 TOF-SIMS image of Cr^+ and Nb^+ distribution on passive film on Fe-25Cr-11Nb alloy and corresponding line scan for Nb^+.

SIMS and SNMS Profiles

SIMS is attractive for the analysis of thin oxide films because of its high sensitivity. In our laboratory, dynamic SIMS profiling has recently been applied for the study of anion distribution in passive films [18,19] and static SIMS for the study of in-situ oxidation [25]. Pioneering dynamic SIMS studies of passive films are due to Graham and coworkers [26-28]. The most serious problem of any type of SIMS applied to the study of passive films is quantification. Indeed, only a small fraction of the emitted particles are usually ionized. Since the ionzation probability varies widely depending on the matrix the measured signal intensity for a given species changes accordingly, rendering quantitative interpretation often impossible. The best way to reduce matrix effects is to apply postionization, using a plasma or a laser to ionize the emitted neutrals. The method is known as Sputtered Neutrals Mass Spectroscopy (SNMS) or Surface Analysis by Laser Ionization (SALI).

Laser postionization was first applied to the study of thin passive oxide films by MacDonald et al [29]. Different commercial SNMS systems have since become available. **Fig. 10** shows TOF-SIMS profiles of a 30 nm tantalum oxide film measured under identical conditions (8 KeV Cs^+ ions) with and without postionization. Two ionic species were monitored, Ta^+ (mass 181) and TaO^+ (mass 197) characteristic for metallic and oxidized tantalum, respectively. Without post ionization one observes a decrease rather than an increase in Ta^+ signal intensity when sputtering through the oxide-metal interface although the atomic density of tantalum in the metal is much higher than in the oxide. The reason is that the ionization probability in the metallic phase is smaller than in the oxide. Using multiphoton post ionization with a KrF excimer laser one obtains first of all much higher count rates as shown in the figure. Furthermore, the Ta^+ signal clearly increases at the oxide-metal interface as one would expect if the signal intensity reflects the elemental concentration. In principle, TOF-SIMS with laser postionization is capable of giving quantitative results with higher sensitivity than AES and XPS. Since relatively little experience exists at this time it is still difficult to assess its practical capabilities for passive film analysis.

without postionization *with laser postionization*

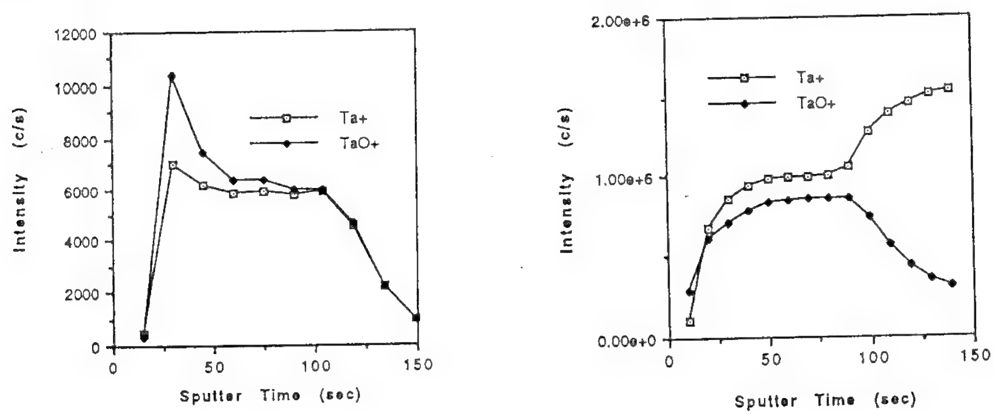

Fig.10 SIMS profiles of 30 nm tantalum oxide film and SNMS profile measured with laser postionization

SIMS Isotope Profiles

A distinctive feature of SIMS is its ability to distinguish isotopes. Isotope labelling can be used to identify the origin of oxide and other species detected in passive films. Contrary to other SIMS data, isotope ratios are not subject to the matrix effect limitations mentioned above, because all isotopes of a given element are affected the same way by the matrix. Chemical alterations during sample transfer from the electrochemical cell into the UHV analysis chamber have been studied in this way [30-33]. Indeed, a crucial question in applying ex-situ methods to the investigation of passive films is whether the analyzed film is representative for that formed in the electrolyte. The

problem has been discussed by several authors using AES and XPS (for a review see [1]) but SIMS isotope profiling has been applied to this problem only recently [30-33].

Typically, to investigate whether surface oxidation occurs during sample transfer anodic polarization is carried out in an electrolyte enriched in $H_2{}^{18}O$. The oxygen isotope ratio in the film is then compared to that of the electrolyte. Alternatively a film formed in normal water can subsequently be exposed to an atmosphere enriched in $^{18}O_2$ or it may be rinsed with $H_2{}^{18}O$ enriched water, followed by the measurement of the isotope ratio. **Fig. 11** [30] shows SIMS data obtained with a Fe-25Cr alloy passivated for one hour at 500 mV (nhe) in an acid sulfate electrolyte (0.1M H_2SO_4+0.4M Na_2SO_4). The measured ratio $^{18}O/^{16}O+^{18}O$ is shown as a function of sputter time, the sputter rate being of the order of 0.1 nm/min. The curves (I) were obtained for a sample passivated in a normal water based electrolyte, rinsed and transferred through air. The curves (II) correspond to samples passivated in an electrolyte enriched in $H_2{}^{18}O$, followed by transfer through air. Finally, the curves (III) correspond to samples passivated in a normal electrolyte placed in a glove box filled with $^{18}O_2$. They were then transferred to the UHV chamber without contact to air . The isotope ratio profiles (I) and (III) are distinctly different from (II), the latter showing an oxide enriched in the isotope ^{18}O. The data confirm that the oxygen species detected in the passive film originate from water (as required by the reaction stoechiometry) and not from atmospheric oxygen. The similarity of the curves (I) and (III) suggests that exposure of the passive film to oxygen did not lead to further oxidation. The measured ratio $^{18}O/^{16}O$ of the curves (II) at the outer oxide surface is somewhat lower than the concentration ratio $H_2{}^{18}O/H_2{}^{16}O$ of the water used for preparing the electrolyte. This behavior could be due to several factors, such as adsorption of rinsing water, incorporation of sulfate ions into the film, uncertainties in the exact $^{18}O/^{16}O$ ratio in the enriched water, or incomplete reduction of the natural oxide film during cathodic prepolarization prior to passivation.

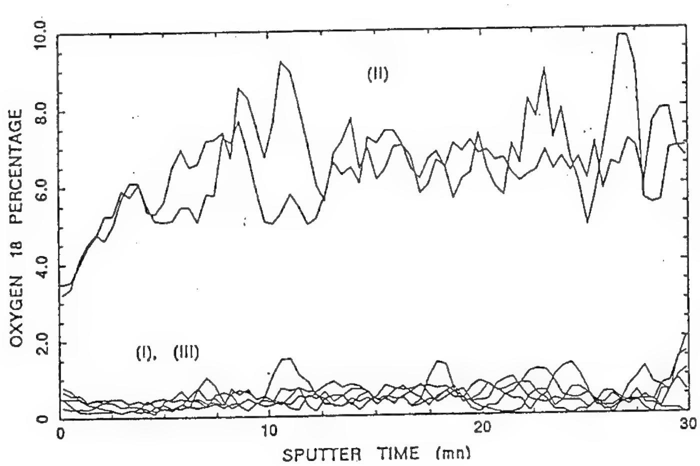

Fig. 11 SIMS isotope ratio profiles of passive films on Fe-25Cr, Courty et al. [30]

SIMS isotope profiling has been applied by Bardwell et al [33] to the study of passive film reduction during cathodic prepolarization. In acid solution the natural oxide film could be completely reduced but not in neutral solution. The authors also did a careful study of the potential dependance of post-oxidation of passive films. They found that the $^{18}O/^{16}O$ ratio in passive films formed on Fe-Cr alloys was generally lower than that of the electrolyte, the effect being most pronounced at low potentials and high pH. From the deviation of the measured from the expected isotope ratio the authors calculated an equivalent film thickness which was thought to represent the original passive film the rest being added by oxidation during transfer. **Fig. 12** illustrates the described behavior [33]. At sufficiently high potentials the difference between theoretical and

experimental film thicknesses is quite small and possibly within the error limits of such measurements (although the deviation to lower values is systematic). From the different data it is concluded that passive films formed in acid solution at relatively high potentials can be studied confidently by ex-situ methods. On the other hand films formed near the passivation potential may undergo film growth during transfer. For passive film studied in neutral and alcaline electrolytes surface preparation (film reduction) prior to passivation is a major problem affecting both in-situ and ex-situ methods.

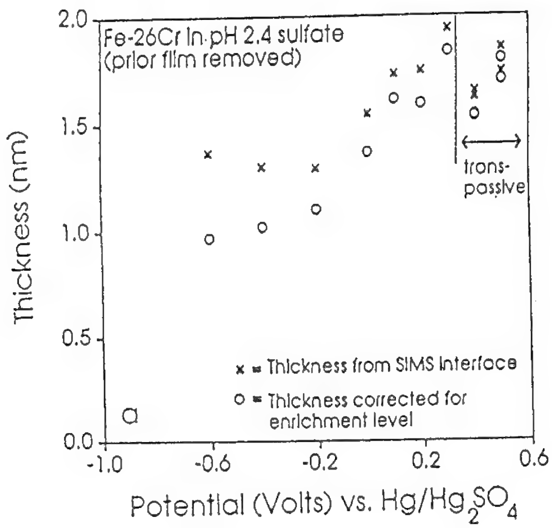

Fig. 12 Film thickness on Fe-26Cr in sulfate solution determined by SIMS isotope profiling, after Bardell et al [33]

Concluding remarks

Surface analysis methods have been around for over twenty years now, and they have contributed decisively to our present knowledge of the chemical composition of passive films. Progress in this area is intimately related to the development of improved instrumental analysis capabilities and theoretical understanding of underlying physical phenomena. In the present paper recent developments concerning both aspects were presented and remaining problems related to the use of surface analysis methods for the study of passive films were mentioned. Considerable progress has been achieved in recent years, particularly in the fields of numerical data handling, imaging and TOF-SIMS. To make full use of the new instrumental possibilities special attention must be given to the establishment of reliable procedures for sample manipulation and to further improving our understanding of the physical basis of certain effects which influence the interpretation of surface analysis data.

Acknowledgements

The authors thank Klaus Franzreb for acquisition of the TOF-SIMS images of the Fe-Cr-Nb alloy. Financial support by Fonds national suisse Bern for passive film and surface analysis studies is gratefully acknowledged.

References

[1] D. Landolt, Advances in Localized Corrosion, NACE-9, 25 (1990)

[2] D. Landolt, Surf. Interf. Anal. 15, 395 (1990)

[3] H.H. Strehblow, Surf. Interf. Anal. Vol 12, 363 (1988)

[4] J. Castle, Surf. Interf. Anal. Vol 9, 345 (1986)

[5] H. Fischmeister, U. Röll, Fresenius Z. anal. Chem. Vol 319, 639 (1984)

[6] I. Olefjord, Mat. Sci. Engr, 42, 161 (1980)

[7] A.J. Davenport, Interface Vol 2, No 3, 37 (1993)

[8] S. Haupt, C. Calinski, U. Collisi, H.W. Hoppe, H.-D. Speckmann, H.-H. Strehblow, Surf. Interf. Anal. 9, 357 (1986)

[9] C. Calinski, H.-H. Strehblow, J. Electrochem. Soc. 136, 1328 (1989)

[10] M.P. Seah, W.A. Dench, Surf. Interf. Anal. Vol 1, 2 (1983)

[11] S. Tanuma, C.J. Powell, D.R. Penn, Surf. Interf. Anal. 11, 577 (1988); 17, 911 (1991); 20, 77 (1993)

[12] C.J. Powell, Surf. Sci. 299/300 34 (1994)

[13] C. Palacio, H.J. Mathieu, D. Landolt, Surf. Sci. 214, 493 (1989)

[14] C. Palacio, H.J. Mathieu, V. Stambouli, D. Landolt, Surf. Sci. 295, 251 (1993)

[15] C. Hubschmid, Thèse EPFL No 1125 (1993); C. Hubschmid, H.J. Mathieu, D. Landolt , Proc. 12th Internatl. Corrosion Congress Houston Texas, vol. 5B, 3913 (1993)

[16] P. Marcus, C. Hinnen, I. Olefjord, Srf. Interf. Anal. Vol 20, 923 (1993)

[17] P. Marcus, I. Olefjord, Corr. Sci. 28, 589 (1988)

[18] H.J. Mathieu, A. Vogel, S. Mischler, D. Landolt, Surf. Interf. Anal. 17, 383 (1991)

[19] S. Mischler, A. Vogel, H.J. Mathieu, D. Landolt, Corr. Sci. 32 925 (1991)

[20] H. Ade, H.C. Ko, E.D. Johnson, E. Anderson, Surf. Interf. Anal. 19, 17 (1992)

[21] C. Hubschmid, H.J. Mathieu, D. Landolt Surf. Interf. Anal. Vol. 20, 755 (1993)

[22] A. Schneider, S. Hoffmann, R. Kirchheim, Werkst. Korrosion 42, 169 (1991)

[23] R. Goetz,D. Landolt, Proc. 9th ICC Toronto Vol 4, 23 (1894)

[24] D. Landolt, S. Mischler, H.J. Mathieu, Corr. Sci. 31, 431 (1990)

[25] H.J. Mathieu, D. Landolt, Surf. Interf. Anal. 14, 744 (1989)

[26] D.F. Mitchell, G.I. Sproule, M.J. Graham, Appl. Surf. Sci. 21, 199 (1985)

[27] R. Goetz, B. MacDougall, M.J. Graham, Electrochim. Acta 31, 1299 (1986)

[28] J.A. Bardwell, B. MacDougall, G.I. Sproule, J. Electrochem. Soc. 136, 1331 (1989)

[29] D.D: Macdonald, M. Ben-Haim, J. Pallix, J. Electrochem. Soc. 136, 3269 (1989)

[30] C. Courty, H.J. Mathieu, D. Landolt, Electrochim. Acta 36, 1623 (1991)

[31] J.A. Bardwell, B. MacDougall, D.F. Mitchell, M.J. Graham, J. Electrochem. Soc. 137, 3311 (1990)

[32] J.A. Bardwell, G.I. Sproule, D.F. Mitchell, B. MacDougall, M.J. Graham, J. Chem. Soc. Farad. Trans. 87, 1011 (1991)

[33] J.A. Bardwell, G.I. Sproule, M.J. Graham, J. Electrochem. Soc. 140, 50 (1993)

Materials Science Forum Vols. 185-188 (1995) pp. 325-336

XPS analysis of passive films formed on chromium in acidic solution without and with chloride ions

D. Costa, W.P. Yang and P. Marcus

Laboratoire de Physico-Chimie des Surfaces, CNRS (URA 425), Ecole Nationale Supérieure de Chimie de Paris, 11, rue P. et M. Curie, F-75005 Paris, France

Keywords: Chromium, angle resolved XPS, chlorides, passivation

Abstract Passive films were formed on chromium by polarization at +400 mV/SHE in 0.5 M H_2SO_4 for different times (30 minutes, 2 hours and 20 hours) without and with chlorides. The effect of chlorides was studied by adding NaCl to the solution before or after passivation. The chloride concentrations were 0.05, 0.3 and 1 M. The (i-E) curves recorded for Cr without and with Cl^- are similar and the addition of chlorides after passivation has no significant effect on the current recorded in the passive state. The passive films were analyzed by angle-resolved XPS (AR-XPS). The measurements performed at different take-off angles of the photoelectrons show that the films have a bilayer structure constituted of an outer hydroxide layer, $Cr(OH)_3$, and an inner oxide layer, Cr_2O_3. The thicknesses of the oxide and hydroxide layers are 3 Å and 9 Å, 6 Å and 7 Å and 6 Å and 6 Å for the films formed in 0.5 M H_2SO_4 after 30 minutes, 2 hours and 20 hours, respectively. When the chlorides are added after pre-passivation without chlorides, the inner oxide layer remains unchanged whereas the hydroxide layer thickens. Chlorides are detected by AR-XPS in the outer part of the film (hydroxide layer). The fraction of Cl^- in the hydroxide layer, expressed as $D_{Cl^-}/(D_{Cl^-}+D_{OH^-})$, is ≈3-4 at%. The passive films formed in the presence of chlorides are also thicker than that formed in chloride-free solution. In this case, both the oxide layer and the hydroxide layer are thicker. The AR-XPS measurements show that the chlorides are located mainly in the outer part of the film (i.e. in the hydroxide layer), in which the fraction of Cl^- is $D_{Cl^-}/(D_{Cl^-}+D_{OH^-}) \approx 7\%$. A small amount of chlorides is detected in the inner oxide layer. The fraction of Cl^- is $D_{Cl^-}/(D_{Cl^-}+D_{O^{2-}}) \approx 2\%$.

Introduction

Chromium is an alloying element which provides good corrosion resistance to a number of Fe-base and Ni-base alloys. The passive films formed on chromium-containing alloys are enriched in chromium oxide and this is the recognized factor for the beneficial effect of Cr on corrosion resistance.

It has been recently shown on a Fe-17Cr alloy that the resistance to pitting corrosion in chloride solution increases with increasing content of chromium oxide in the inner part of the passive film (oxide layer) [1, 2]. Fe-Cr alloys passivated in chloride-containing solutions contain Cl^- ions mainly in the outer part of the passive film [1-5]. These results suggest that the inner chromium oxide layer of the passive film constitutes a good "barrier" layer against the ingress of the chloride ions. Thus, it is interesting to test this idea by investigating the passive films formed on pure chromium without and with chloride ions.

The passive films formed on chromium have been studied by in situ techniques [6-11] and by combined electrochemical and ex-situ surface analysis techniques [12-19]. The passive layer is generally described as a Cr^{3+} oxide or oxi-hydroxide [6, 7, 9-19], which thickness varies from 3 to 20Å [13-17, 19]. Recently, a bilayer structure (oxide inner layer/hydroxide outer layer) of the passive film was evidenced [19]; the effects of passivation time [15, 16, 19] and potential of passivation [13-16, 19] have been investigated. One XPS study was reported on the passivation of chromium in chloride-containing solution; it showed that chloride ions are incorporated in the passive film [14]. The aim of this work was to investigate by Angle-Resolved X-Ray Photoelectron Spectroscopy (AR-XPS) and sputtering depth profiles the passive films formed on chromium without Cl^- and the effects of the addition of Cl^- either in the solution in which chromium is passivated or after pre-passivation in a Cl^--free solution. The chemical composition of the film, its stratified nature and the location and concentration of the Cl^- were investigated as a function of Cl^- concentration and passivation time.

Experimental method

Pure polycrystalline chromium (99.999%) was prepared at CECM, CNRS (Vitry/Seine (F)). The samples used for the electrochemical experiments had a diameter of 13 mm. For the potentiodynamic experiments ($1Vh^{-1}$), the samples were mechanically polished, washed, dried and then submitted to a cathodic reduction (2 min., -740 mV/SHE) in the electrolyte before experiment. For the potentiostatic experiments, the surface was polished mechanically, and then electrochemically in a solution of 5% perchloric acid and 95% acetic acid with a current density of 0.1 A/cm^2 for 15 minutes. This was followed by ultrasonic cleaning with acetone and doubly-distilled water and drying in air. Prior to passivation, the samples were annealed at 900°C in a flow of ultra-pure hydrogen at atmospheric pressure for about 16 hours. They were transferred under pure hydrogen at room temperature into a nitrogen-filled glove box where the electrochemical experiments were performed. The three electrode electrochemical cell was connected to a PAR 273 potentiostat. All the electrochemical experiments were carried out in deaerated solution. The electrolyte was 0.5 M H_2SO_4, prepared with reagent grade H_2SO_4 and ultra-pure water (resistivity of about 18 MΩ.cm). Pure crystallized NaCl from Merck was used. Potentiostatic measurements were carried out at +400 mV/SHE (in the passive range) for periods of 30 minutes, 2 and 20 hours. The experiments were stopped by emersion at the applied potential. The samples were then thoroughly rinsed under ultra-pure water, dried with nitrogen and transferred to the spectrometer in the transfer vessel under nitrogen to minimize any contamination or transformation of the passive layer by contact with air. All experiments were performed at least two times and the results were reproducible. The XPS analyses were performed with a VG ESCALAB Mark II spectrometer, using the Mg Kα-X-ray source (1253.6 eV) and 20 eV pass energy. The reference energies are the Au4f7/2 signal at 83.9 eV and the Cu2p3/2 signal at 932.8 eV. Characterization of the passive films was performed by means of variable angle analyses and sputter depth profiles. AR-XPS measurements were generally performed at take-off angles of 90° and 45°(angle of the surface with the direction of the analyser), and in some cases a detailed angle-dependent analysis was performed (125°, 105°, 90°, 65°, 55°, 45°, 35° and 25°). A survey spectrum was first recorded to identify all elements present at the surface, then high resolution spectra of the following regions were recorded: Cr2p, O1s, S2p, Cl2p, Na1s and C1s. The obtained spectra could be fitted, after background subtraction following the Shirley

procedure, with Gaussian-Lorentzian curves modified by a tail function. The reference XPS data used in this work are detailed elsewhere [20]. The procedure for quantitative analysis has been previously developed [20, 21]; the values of the atomic sensitivity factors were taken in [20- 22] and the attenuation lengths,λ, were estimated after [23], giving λ_{Cr}^{met} = 1.17nm, λ_{Cr}^{ox} = 1.85nm and λ_{O}^{ox} = 1.9nm. The calculations allow us to evaluate the composition and thicknesses of the passive layers. Sputtering depth profiles were performed with argon ions ($P_{Ar} = 10^{-5}$ mbar, energy: 3 kV, current: $\approx$ 1 $\mu A/cm^2$).

Results

Electrochemical behaviour

The potentiodynamic curve of Cr in 0.5 M H_2SO_4 (Fig. 1) was recorded at 1V/h after cathodic reduction and is similar to that reported in [19]. The current at the maximum of the active peak is $\approx$11 $mAcm^{-2}$ and the current recorded in the passive state is $\approx$ 3 μAcm^{-2}. In the presence of 0.3 M Cl^- and 1 M Cl^-, no pitting is observed. During the potentiostatic experiments (at +400 mV/SHE) of the samples annealed in hydrogen, the current in the passive state is $\approx$ 0.05 μAcm^{-2} after 30 min., $\approx$ 0.02 μAcm^{-2} after 2 hours and $\approx$ 0.01 μAcm^{-2} after 20 hours of polarization. In the presence of chlorides (0.05, 0.3 and 1 M) the currents in the passive state are similar than without chlorides and the addition of the chlorides after prepassivation in 0.5 M H_2SO_4 does not change the value of the current density in the passive state.

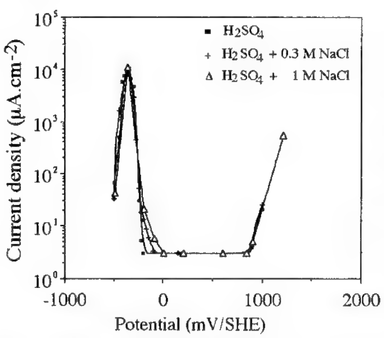

Fig. 1: Potentiodynamic curve of Cr in 0.5 M H_2SO_4 and in 0.5 M H_2SO_4 + 0.3 M NaCl and 1 M NaCl.

XPS analysis of the passive films formed in 0.5 M H_2SO_4

The survey spectra of the passivated surface showed that the elements present are chromium, oxygen, sulfur and carbon. The spectra of the Cr2p3/2 and O1s regions recorded at the take-off angle of 90° after polarization for 30 minutes, 2 hours and 20 hours at +400 mV/SHE are shown in Fig. 2. The spectra recorded in the Cr2p3/2 region could be fitted with three peaks: a first one at 574.2$\pm$ 0.1 eV corresponding to the metallic state, a second one at 576.7$\pm$ 0.1 eV corresponding to the trivalent oxide state, Cr^{3+} in Cr_2O_3, and a third one at 577.2$\pm$ 0.1 eV, corresponding to the trivalent hydroxide state, Cr^{3+} in $Cr(OH)_3$. It was pointed out in a recent paper that the Cr_2O_3 oxide may contain some amounts of CrOOH oxihydroxide, according to the higher binding energy measured for this valence state than the binding energy of thermally grown Cr_2O_3 (+0.3 eV) [19]. The O1s spectrum could be fitted with three peaks: one at 530.2 $\pm$ 0.1eV (FWHM 1.3 eV) corresponding to O^{2-} in oxide, one at 531.2 $\pm$ 0.1 eV (FWHM 1.9 eV) corresponding to OH^- in hydroxide, and a third peak at 532.2 $\pm$0.1 eV (FWHM 1.8 eV) corresponding to O^{2-} in sulfate and water [2, 20]. The S2p signal at 169.0 eV corresponds to sulfates [2]. Sulfates are adsorbed at the surface of the passive film. No sodium is detected, showing that the rinsing was efficient. Carbon is detected in the C1s region. It is due to

a

b

c

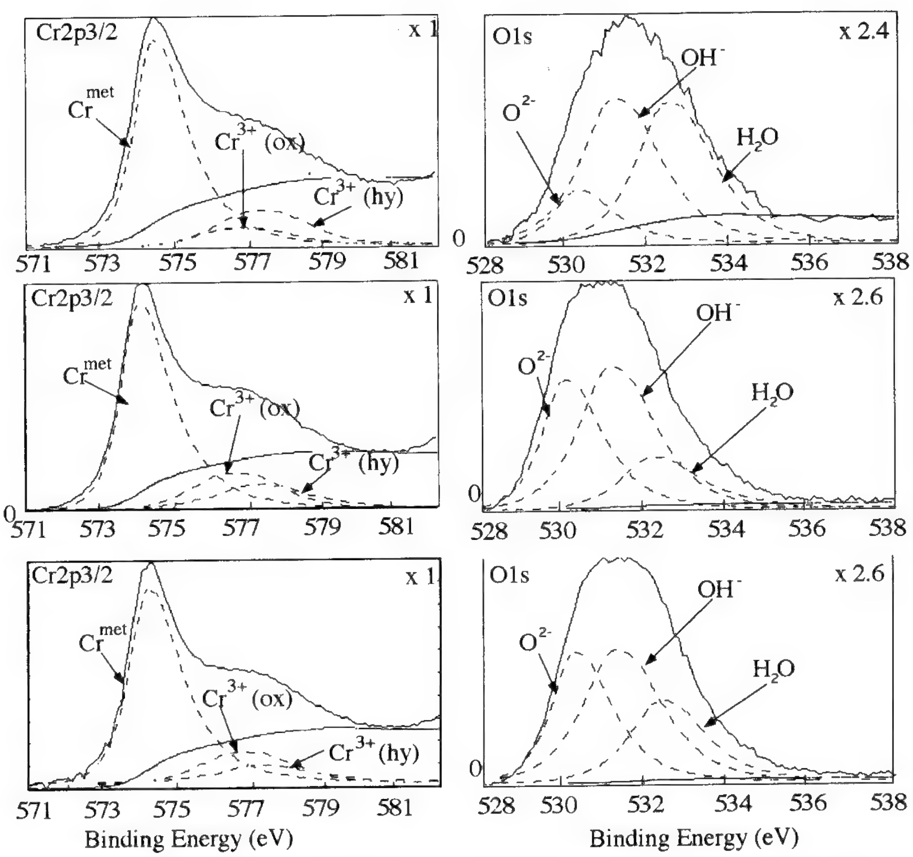

Fig. 2: XPS spectra of the Cr2p3/2 and O1s regions recorded at a take-off angle of 90° for Cr passivated in 0.5 M H_2SO_4 at +400 mV/SHE for a) 1/2 h, b) 2h and c) 20h.

contamination occuring during transfer to the spectrometer [2, 19]. Angle-dependent measurements allowed us to identify the in-depth distribution of these different species. Fig. 3a shows the spectra of the Cr2p3/2 region recorded at 6 different take-off angles (90°, 65°, 55°, 45°, 35° and 25°). Fig. 3b compares the Cr^{3+}(oxide + hydroxide) contribution to the Cr2p3/2 signals recorded at 90° and 35°. When the take-off angle decreases, the metallic contribution decreases (Fig. 3a) and the hydroxide/oxide ratio increases (Fig. 3b), showing that within the thin film formed on the metal the hydroxide is located above the oxide. This effect was not observed on a thermally grown Cr_2O_3 oxide (Fig. 3c). The angle-dependent measurements performed on the O1s region also show that in the passive film OH^- are located above O^{2-} species. The ratios of intensities $I_{OH^-}/I_{Cr^{3+}hy}$ and $I_{O^{2-}}/I_{Cr^{3+}ox}$ calculated at the take-off angle of 90° are 1.65± 0.2 and 0.75 ± 0.1, respectively, which shows, using the equations of the quantitative treatments of the intensities [20], that the stoichiometries of the layers are close to $Cr(OH)_3$ and Cr_2O_3. Therefore, it is concluded that the passive film consists of an outer $Cr(OH)_3$ layer and an inner Cr_2O_3 layer.

After 30 minutes of passivation, the thickness of the Cr_2O_3 layer is found to be 3Å (about one monolayer [19]) and that of the hydroxide layer 9Å. The ratios of the intensities

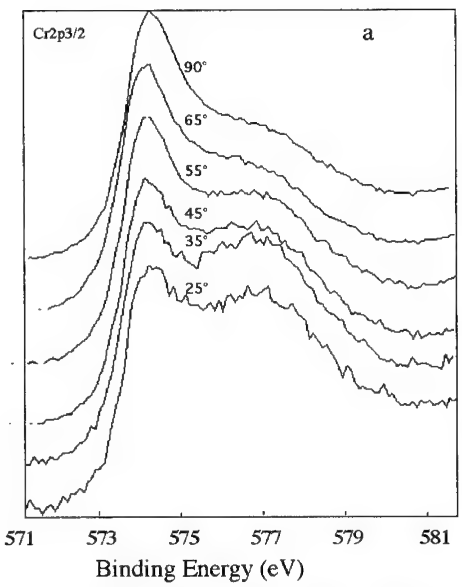

Fig. 3a): XPS spectra of the Cr2p3/2 region recorded at 6 different take-off angles for passivated Cr (0.5 M H_2SO_4, 400 mV/SHE, 30 minutes).

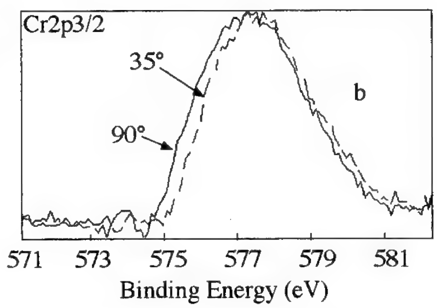

Fig. 3b): Comparison of the Cr (oxide + hydroxide) signals recorded at the take-off angles of 90° and 35°for Cr passivated in 0.5 M H_2SO_4 for 30 minutes. (Spectra obtained by subtraction of the metal contribution to the Cr2p3/2 spectrum (shown in Fig. 2a)).

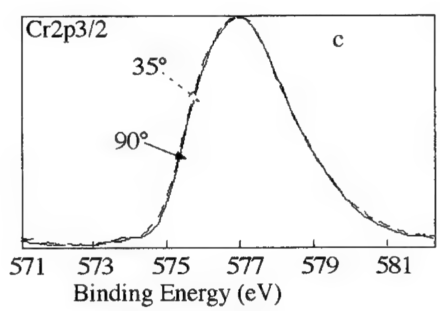

Fig. 3c): Comparison of the Cr_2O_3 signals recorded at the take-off angles of 90° and 35° for Cr after dry oxidation in the XPS spectrometer ($PO_2=10^{-6}$ mbar, 200°C, 4 min.) (spectra obtained by subtraction of the metal contribution to the Cr2p3/2 spectrum).

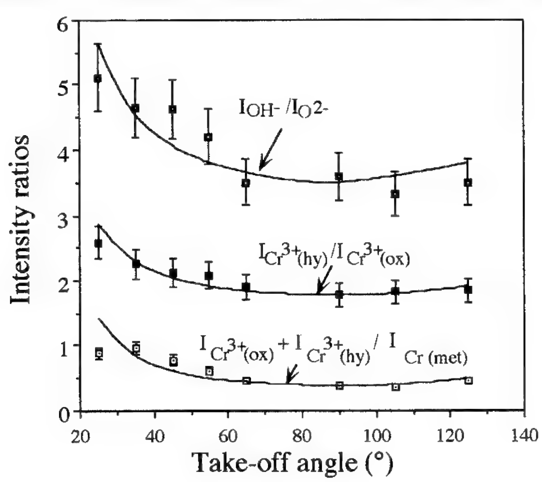

Fig. 3d): Comparison of the measured ratios $(I_{Cr^{3+}ox}+I_{Cr^{3+}hy})/I_{Cr^{met}}$, $I_{Cr^{3+}hy}/I_{Cr^{3+}ox}$ and $I_{OH^-}/I_{O^{2-}}$ as a function of take-off angle with the same ratios calculated using a stratified model of the passive film (9 Å hydroxide/3Å oxide, and the attenuation lengths from [23], $\lambda_{Cr}met$ = 11.7Å, $\lambda_{O}ox$ = 19Å and $\lambda_{Cr}ox = \lambda_{Cr}hy$ =18.5Å)(solid lines).

$(I_{Cr^{3+}ox}+I_{Cr^{3+}hy})/I_{Cr^{met}}$, $I_{Cr^{3+}hy}/I_{Cr^{3+}ox}$ and $I_{OH^-}/I_{O^{2-}}$ are plotted as a function of take-off angle in Fig. 3d. The theoretical curves calculated using the bilayer model for a 3Å oxide layer and a 9Å hydroxide layer are also reported. The good agreement between the experimental and calculated values supports the view of the bilayer structure of the passive film.

The films formed after 2 and 20 hours of polarization at +400 mV/SHE are also constituted of an inner oxide layer and an outer hydroxide layer. The thicknesses of these layers are 6Å of Cr_2O_3 and 7Å of $Cr(OH)_3$ after 2 hours and 6Å of Cr_2O_3 and 6Å of $Cr(OH)_3$ after 20 hours of polarization. Thus, the total thickness of the film remains nearly constant (12, 13 and 12 Å). The thickness of the inner oxide layer increases between 1/2 h and 2h of polarization; simultaneously, the thickness of the hydroxide layer decreases. For longer polarization time, the thicknesses of the layers do not vary. These results are in agreement with that obtained on a Cr(110) single crystal passivated in 0.5 M H_2SO_4 at +500 mV/SHE [19].

Addition of chlorides after the pre-passivation of Cr in chloride-free solution

Fig. 4 shows the spectra of the Cr2p3/2, O1s and Cl2p regions recorded after passivation of chromium for 2 hours in 0.5 M H_2SO_4 and subsequent addition of 0.3 M NaCl and further polarization for 30 minutes. The ratio ICr(hy)/ICr(ox) is higher than after passivation without Cl^- (Fig. 2b), whereas the ratio ICr(ox)/ICr(met) is unchanged, indicating an increase of the thickness of the hydroxide layer but not of the oxide layer. Chlorides are detected in the passive film. The angle-dependent measurements show that the film has a bilayer structure (outer hydroxide layer/inner oxide layer) and that the Cl^- are located mostly in the outer part of the film (hydroxide layer) (the ratios I_{Cl^-}/I_{OH^-} are 0.02± 0.01 at 90° and 0.03 ± 0.02 at 45°, whereas the ratios $I_{Cl^-}/I_{O^{2-}}$ are 0.07± 0.02 at 90° and 0.24± 0.08 at 45°); despite the low signal to noise ratio of the Cl2p signal, the variations of the ratios are significant. Considering that the Cl^- ions are located in the hydroxide layer, the $D_{Cl^-}/(D_{Cl^-} + D_{OH^-})$ fraction was calculated and found to be 3at%. The thicknesses of the oxide layer and hydroxide layer are 7 and 19 Å respectively, so the oxide layer is the same as when the film is formed in the absence of chlorides whereas the hydroxide layer is thicker. The influence of the time of prepassivation and of the Cl^- concentration added was investigated. The results (table 1) show that for all conditions of pre-polarization and Cl^- concentration added, the thickness of the hydroxide layer increases, whereas that of the inner oxide layer remains unchanged. For the same time of pre-polarization (2 hours), the increase of the hydroxide layer thickness does not vary significantly with the added Cl^- concentration in the solution. The XPS results show that chlorides are incorporated in the passive films. The angle-dependent measurements show that they are located in the outer hydroxide layer. The fractions $D_{Cl^-}/(D_{Cl^-} + D_{OH^-})$ in the hydroxide layer are ≈ 3-4 ± 1 at%. A slight dependence of the Cl^- contents in the hydroxide film with the Cl^- concentration in the electrolyte was observed, but it remains near the uncertainty limit of the measurements. This absence of significant variation with Cl^- concentration in the electrolyte may be due to the rinsing of the passive film which likely causes redissolution of non-irreversibly bonded Cl^-.

Sputter depth profiles were performed (Fig. 5). It is observed that the Cr^{3+}(hy) and OH^- signals decrease strongly after the first sputtering and this confirms the bilayer structure of the passive film. This was also observed for sputter depth profiles of passive films formed on an Fe17Cr alloy [1, 2]. It was noted in these papers that the very rapid decrease of the Cr^{3+}(hy)

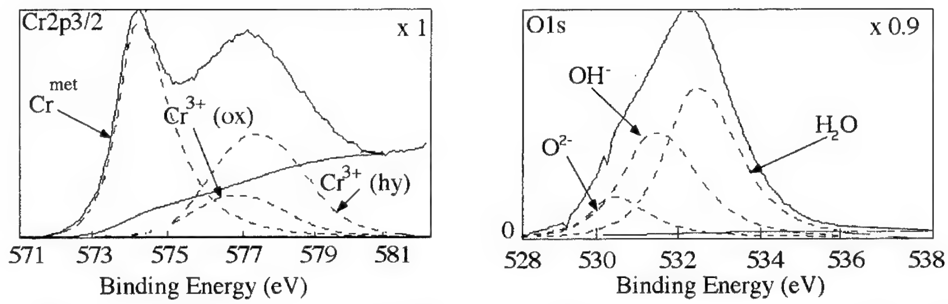

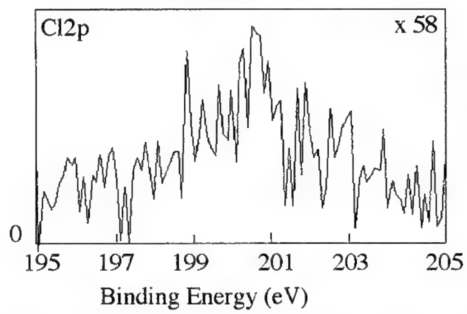

Fig. 4: XPS spectra of the Cr2p3/2, O1s and Cl2p regions recorded at a take-off angle of 90° for Cr passivated in 0.5 M H_2SO_4 at +400 mV/SHE for 2h, with subsequent addition of 0.3 M NaCl and further polarization for 1/2h.

Time of prepolarization in 0.5 M H_2SO_4	Chloride concentration added (mol l^{-1})	Oxide layer thickness (Å)·	Hydroxide layer thickness (Å)·
30 min	0	3	9
"	0.3	3	12
2 hours	0	6	7
"	0.05	7	18
"	0.3	7	19
"	1	7	16
20 hours	0	6	6
"	0.3	7	11

Table 1: Thicknesses of the inner oxide layer and the outer hydroxide layer of the passive film formed by pre-polarization in 0.5 M H_2SO_4 with subsequent addition of Cl^- and polarization for 30 minutes.

signal could also be attributed to a higher sputtering rate of $Cr(OH)_3$ than Cr_2O_3 and/or to the transformation of hydroxide to oxide during sputtering. In the present case, it is observed that after the first sputtering, the thickness of the remaining oxide (Cr_2O_3) layer is larger than the thickness calculated before sputtering, confirming the phenomenon of partial transformation of chromium hydroxide to chromium oxide during sputtering. A very small amount of Cl^- was found in the inner oxide layer ($D_{Cl^-}/(D_{Cl^-} + D_{O^{2-}}) < 1$at.%). This may be due to ion mixing effects during sputtering.

Films formed in the presence of chlorides

Fig. 6 shows the spectra of the Cr2p3/2, O1s and Cl2p regions recorded after passivation of chromium for 2 hours in 0.5 M H_2SO_4 + 0.3 M NaCl. The ratio $(I_{Cr}^{ox} + I_{Cr}^{hy})/I_{Cr}^{met}$ is

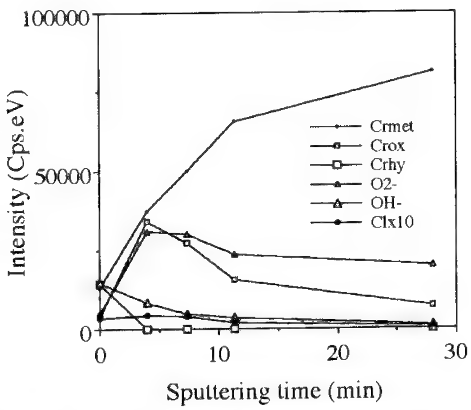

Fig. 5: Sputter depth profile for Cr passivated 2 hours in 0.5 M H_2SO_4 at +400 mV/SHE for 2h, with subsequent addition of 0.3 M NaCl and further polarization for 1/2h.

higher than after passivation without Cl^- (Fig. 2b), indicating a thicker layer. The angle-dependent measurements show that the film has a bilayer structure (outer hydroxide/inner oxide), and that Cl^- are located mostly in the outer part of the film (hydroxide layer) (the ratios I_{Cl^-}/I_{OH^-} are 0.06± 0.02 at 90° and 0.06± 0.02 at 45°, whereas the ratios $I_{Cl^-}/I_{O^{2-}}$ are 0.10± 0.03 at 90° and 0.13± 0.04 at 45°). Considering that the Cl^- ions are located in the hydroxide layer, the $D_{Cl^-}/(D_{Cl^-}+D_{OH^-})$ fraction was calculated and found to be 6 at%. The thicknesses of the oxide layer and hydroxide layer are 8 and 15Å respectively, so both the inner oxide and the outer hydroxide layers are thicker than when the film is formed in the absence of chlorides. Fig. 7 shows the sputter depth profile obtained for this passive film. The signal of the chlorides is observed until the end of the sputtering. This was also the case after passivation of the Fe17Cr in 0.5 M H_2SO_4 in the presence of 0.3 M chlorides [2]. The fraction of Cl^- found in the oxide layer during sputtering is $D_{Cl^-}/(D_{Cl^-}+D_{O^{2-}}) \approx 2$at%.

Passive films were formed at +400 mV/SHE for different times (30 minutes, 2 and 20 hours) with different chloride concentrations (0.05, 0.3 and 1 M). In every case, the passive film has a bilayer structure and contains chlorides mainly in the external part (hydroxide layer). The

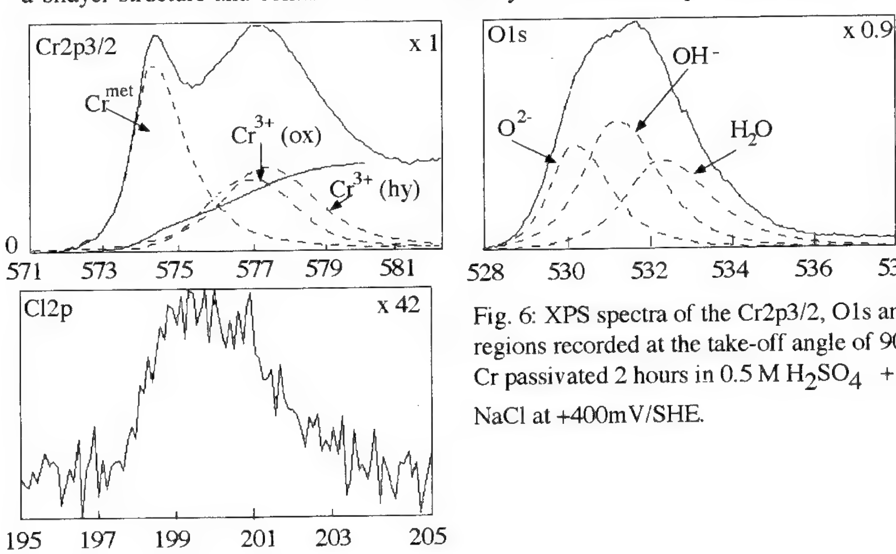

Fig. 6: XPS spectra of the Cr2p3/2, O1s and Cl2p regions recorded at the take-off angle of 90° for Cr passivated 2 hours in 0.5 M H_2SO_4 + 0.3 M NaCl at +400mV/SHE.

thicknesses of the layers are reported in Table 2. The passive film formed in the presence of chlorides is always thicker than the passive film formed without chlorides; the thicknesses of both the inner oxide and the outer hydroxide layers increase when the film is formed in the presence of Cl^-. The Cl^- fractions in the hydroxide layer were calculated and found to be $D_{Cl^-}/(D_{Cl^-}+D_{OH^-}) \approx 7 \pm 2$ at%. Here again, the observed variations of the Cl^- fractions are within the experimental uncertainty and do not allow us to evidence a dependence with the Cl^- concentration in the electrolyte or with the time of polarization.

Chloride concentration	Time of passivation	Oxide layer thickness (Å)	Hydroxide layer thickness (Å)	D_{Cl^-} (at%)
0	30 min	3	9	0
0.05	"	7	20	7
0.3	"	9	10	9
1	"	9	12	8
0	2 hours	6	7	0
0.05	"	9	15	5
0.3	"	11	16	6
1	"	11	14	7
0	20 hours	6	6	0
0.05	"	8	12	6
0.3	"	8	10	7
1	"	7	10	7

Table 2: Thicknesses of the inner oxide layer and the outer hydroxide layer and chloride ratio ($D_{Cl^-}/(D_{Cl^-} + D_{OH^-})$ (at%)) (in the hydroxide layer) of the passive films formed on Cr at +400 mV/SHE as a function of the polarization time and of the chloride concentration in the electrolyte.

Fig. 7: Sputter depth profile for Cr passivated 2hours in 0.5 M H_2SO_4 + 0.3 M NaCl at +400mV/SHE.

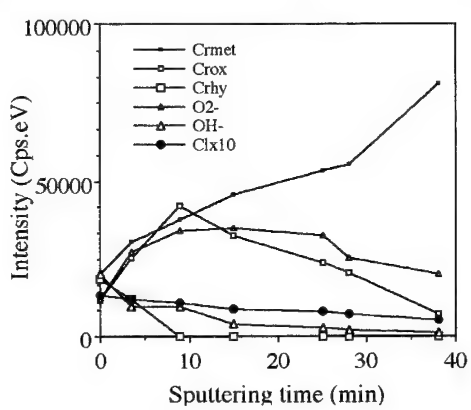

Discussion

The passive film formed on Cr in 0.5 M H_2SO_4 is composed of Cr^{3+}-oxide and hydroxide. This result is in agreement with previous findings [6,7, 9-19]. The bilayer structure was already evidenced [19] and this work confirms the presence of the outer hydroxide $Cr(OH)_3$ and the inner Cr_2O_3 layer. The thicknesses of the passive films found in 0.5 M H_2SO_4 are identical to that of the films formed on a Cr(110) single crystal [19].

The results of the present work can be compared to the results obtained on an Fe17Cr alloy

passivated under identical conditions [2] (Table 3).

	pre-polarization in 0.5 M H_2SO_4 with subsequent addition of 0.3 M NaCl		passivation in 0.5 M H_2SO_4 + 0.3 M NaCl	
	oxide layer	hydroxide layer	oxide layer	hydroxide layer
Fe17Cr (500 mV)	2%	16%	4%	16%
Cr (400mV)	-	4%	2%	7%

Table 3: Cl^- ratio ($D_{Cl^-}/(D_{Cl^-} + D_{Oxygen})$) in the outer part and in the inner part of the passive film formed on Fe17Cr [2] and on Cr [this work].

It is noteworthy that in all the conditions studied, the passive films of the Fe17Cr contain more Cl^- than the passive films formed on Cr, both in the inner part and in the outer part of the passive film. Furthermore, after prepassivation in 0.5 M H_2SO_4, the chlorides enter in the inner part of the films formed on the alloy, whereas they do not enter in the inner layer of the passive film formed on Cr.

This is observed also in solutions in which the alloy exhibit pitting corrosion: after polarization for 2h at +400 mV/SHE in 0.5 M H_2SO_4 with subsequent addition of 1M NaCl and further polarization, pitting is observed on the Fe17Cr alloy after ≈ 20 min., whereas, after 30 min., the chlorides do not enter in the inner Cr_2O_3 layer of the passive film formed on Cr. This definitely confirms the protective character of the inner Cr_2O_3 layer against the ingress of chloride ions.

Conclusion

The passive film formed on polycrystalline Cr in 0.5 M H_2SO_4 is composed of an outer $Cr(OH)_3$ layer and an inner Cr_2O_3 layer. When Cl^- are added after pre-polarization in 0.5 M H_2SO_4, they enter in the outer hydroxide layer but not in the inner oxide layer of the passive film. When Cl^- are present during the passivation, they are incorporated both in the inner oxide and the outer hydroxide layer. The incorporation of Cl^- in a layer is accompanied by an increase of thickness of this layer. The concentrations of Cl^- measured in the passive films of chromium are lower than that found in the passive film of an Fe17Cr alloy. The interaction of Cl^- with the inner Cr_2O_3 layer of the passive film formed on chromium is very small in conditions in which the Fe17Cr alloy is susceptible to pitting, showing the protective character of the inner Cr_2O_3 oxide layer against the ingress of Cl^- and thus against pitting.

References

[1] W. P. Yang, D. Costa and P. Marcus, J. Electrochem. Soc., 141, 111 (1994)
[2] W. P. Yang, D. Costa and P. Marcus, J. Electrochem. Soc., 141, 2669 (1994)
[3] C. Hubschmid and D. Landolt, in Oxide Films on Metals and Alloys, Ed. B. R. MacDougall, R. S. Alwitt and T. A. Ramanayaran, Proc. 92-22, The Electrochem. Soc., (1992), p 487
[4] C. Hubschmid, H. J. Mathieu and D. Landolt, in Proceedings of the 12th International Corrosion Congress, NACE Int. Ed., Houston Sept. 19-24, 1993, p 3913
[5] C. Hubschmid and D. Landolt, in "Modifications of Passive Films", Eds. P. Marcus, B. Baroux and M. Keddam, The Institute of Materials, EFC 12, 1994, p 1
[6] M. A. Genshaw and R. S. Sirohi, J. Electrochem. Soc., 118, 1558 (1971)
[7] N. Hara and K. Sugimoto, J. Electrochem. Soc., 126, 1328 (1979)

[8] P. C. Searson and R. M. Latanision, Electrochim. Acta, 33, 445 (1990)
[9] J. H. Gerretsen and J. H. W. de Wit, Corros. Sci., 30, 1075 (1990)
[10] L. Björnkvist and I. Olefjord, Corros. Sci., 32, 231 (1991)
[11] C. A. Melendres, M. Pankuch, Y. S. Li and R. L. Knight, Electrochim. Acta, 37, 2747 (1992)
[12] M. Seo, R. Saito and N. Sato, J. Electrochem. Soc., 127, 1909 (1980)
[13] G. Bouyssoux, M. Romand, H. Polaschegg, J. Calow, J. Electron. Spectrosc., 11, 185 (1977)
[14] L. Björnkvist and I. Olefjord, in Eurocorr'87, Proceedings of the European Corrosion Meeting, The European Federation of Corrosion, Karlsruhe 1987, p 325
[15] S. Haupt and H. H. Strehblow, J. Electroanal. Chem., 228, 365 (1987)
[16] S. Haupt and H. H. Strehblow, Corros. Sci., 29, 163 (1989)
[17] T. P. Moffat and R. M. Latanision, J. Electrochem. Soc., 139, 1869 (1992)
[18] B. Stypula and J. Banas, Electrochim. Acta, 38, 2309 (1993)
[19] V. Maurice, W. P. Yang and P. Marcus, J. Electrochem. Soc., 141, 3016 (1994)
[20] E. De Vito and P. Marcus, Surf. Interf. Anal., 19, 403 (1992)
[21] P. Marcus and J. M. Grimal, Corros. Sci., 33, 805 (1992)
[22] J. M. Herbelin and P. Marcus in the Application of the Surface Analysis Methods to Environmental/Material Interactions, Eds. D. Baer, C. R. Clayton, G. D. Davis, The Electrochemical Soc., Proceedings 91-7, (1991) p. 222
[23] M. P. Seah and W. A. Dench, Surf. Interf. Anal., 1, 2 (1979)

Materials Science Forum Vols. 185-188 (1995) pp. 337-346

Ageing of passive films on stainless steels in sulfate solutions - XPS analysis

A. Rossi[1] and B. Elsener[2]

[1] Dipartimento di Chimica e Tecnologie Inorganiche e Metallorganiche, Università di Cagliari, Via Ospedale 72, I-09124 Cagliari, Italy

[2] Institute of Materials Chemistry and Corrosion, Swiss Federal Institute of Technology, ETH Hönggerberg, CH-8093 Zürich, Switzerland

Keywords: Passivation, ageing, stainless steel, chromium, molybdenum, x-ray photoelectron spectroscopy, XPS, passive film, pitting resistance

Abstract

The passivation of stainless steels 1.4301 (18% Cr and 8% Ni) and 1.4529 (20% Cr, 25% Ni and 6% Mo) was studied in neutral 1 M Na_2SO_4 solutions as a function of polarization time (ageing) at two passivation potential in the passive range by electrochemistry and XPS analysis. The passive current density decreases with time according to a power law indicating higher stability of the passive film after ageing. XPS analyses show that the integral Cr^{3+} content in the passive films of the two stainless steels is similar, a slight increase in total film thickness and constant overall composition of the passive film with passivation time is found. ARXPS measurements indicate a bilayer structure and pronounced changes within the passive layer during ageing: Fe^{2+} becomes gradually eliminated at longer passivation times. A different ageing behaviour of the 1.4301 (without Mo) and 1.4529 SS (with 6% Mo) is found: the conventional 1.4301 steel shows a more pronounced bilayer structure after 24 h of passivation, but a lower content of hydroxide in the outer layer. On the contrary the passive film of the 1.4529 SS becomes progressively more hydrated during ageing, the amount of Cr(hy) and of OH^- increases with time. The higher pitting resistance of the 1.4529 SS might be explained by the formation of more hydrated (thus more amorphous and flexible) Cr(III)hydroxide passive film, the presence of Mo^{6+} and the lower Fe^{3+} content in the passive film (reducing pit initiation) together with the marked nickel enrichment at the interface (favouring pit repassivation).

Introduction

It is well known from literature that ageing (prolonged exposure to electrolyte at a potential in the passive range) can influence the stability of the passive film and the pitting resistance [1-6]. Okamoto concluded that the composition of the passive film depends on the condition of formation, especially the potential and the time of passivation [1]. The effect of exposure time to oxygenated water on

passive film composition of ferritic [2] and austenitic [3] stainless steels was studied by Olefjord showing an enrichment of Cr^{3+} in the passive film. Studies on pit initiation on ferritic Fe-16 Cr steels have shown a reduction in pit initiation probability after ageing at the rest potential [4] and after prolonged passivation at a potential below the pitting potential [4, 5]. XPS measurements on a Fe-17 Cr steel have shown that ageing in the passive range results in a slight increase in total film thickness, a more pronounced bilayer structure and a dehydration of the passive film [5]. Recent work on 1.4301 SS [6] in neutral chloride solutions showed a reduction of the number of metastable pitting events but an increase of the charge of the single transients and a decrease of the pitting potential with longer ageing time (up to 120 h). Fotoelectrochemical studies on stainless steels showed no changes of the mobility gap energy with time of passivation at a potential of +0.3 V SCE (pH 6) [7].

The composition of the passive films on 1.4301 and 1.4529 stainless steels have been reported in a previous work [8] after constant time of passivation of 1 h. In neutral sulfate solutions (pH 6) the cationic mass fraction of Cr^{3+} ions of the two steels is similar and decreases gradually with increasing potential, the thickness of the passive films increases linearly with increasing potential. These results are in good agreement with *in situ studies* using ellipsometry and potential-modulated UV visible reflection spectroscopy on high purity Fe-Cr alloys and Fe-Cr-Ni alloys [9].

The aim of this work was to investigate by X-ray photoelectron spectroscopy (XPS) the effect of the passivation time (ageing) on thickness, composition and chemical states of the species constituiting the passive films formed on stainless steels 1.4301 and 1.4529 with 6% molybdenum in neutral solutions at a low and a high potential in the passive range. The results are discussed with respect to the influence of ageing time, potential and the role of molybdenum related to the different corrosion behaviour and pitting resistance of the two stainless steels.

Experimental

Materials and solutions

The composition of the two stainless steels is given in table 1. The solutions were prepared from analytical grade $Na_2SO_4 * 10H_2O$ and bidistilled water and adjusted with sulfuric acid to pH 5.8. They were stored in a glass reservoir of 2L volume and deaerated with argon gas for at least 4 hours prior to the experiment. After mechanical polishing in ethanol p.a. to 1 μm diamond paste the samples - already fixed on the XPS sample holder - were mounted on the electrochemical cell (150 mL) and the deaerated electrolyte was filled in under argon pressure. The samples were hold 15 min at the open circuit potential, then polarized in one step to the passivation potential (-0.1 V SCE and +0.2 V SCE) and hold there for 10 min up to 24 hours, removed from the cell under applied potential, rinsed with bidistilled water, dried with nitrogen and transferred under a nitrogen stream to the spectrometer immediately.

Table 1: Composition of the stainless steels (weight %)

	Fe	Cr	Ni	Mo	Mn	S	P	other
1.4301	bal	18.1	8.7	0.06	1.3	0.003	0.029	N -
1.4529	bal	20.8	24.9	6.42	0.82	0.002	0.016	N 0.16

XPS analysis
XPS analysis were performed on an ESCALAB MkII spectrometer (Vacuum Generator Ltd., U.K.) using a MgKa (1253.6 eV) x-ray source run at 20 mA and 15 kV. The residual pressure in the spectrometer during data acquisition was always lower than 5.10^{-7} Pa. The unexposed surface of the sample was masked with a gold ring to allow the analysis of only the polarized surface (0.78 cm^2). The spectra were obtained in the digital mode with a constant energy of 20 eV set on the electron analyzer. The details of operation and calibration of the instrument are given in ref. [10]. The dependance of the analyzer transmission function on electron energy was calibrated by the procedure of Seah [11]. To compensate for sample charging during the analysis all the binding energies were referred to the carbon 1s signal at 284.75 eV. Acquisition of reference spectra is given in [8]. The model for the quantitative evaluation of XPS data used is given in the Appendix of ref. 8.

Results

Electrochemistry
The open circuit potential of all the samples tested decreased with time of exposure to the deaerated solution. After 15 minutes a value of -400 ± 20 mV was reached for the 1.4301 steel at pH 5.8. For the 1.4529 steel values of -280±20 mV were found. The current during potentiostatic polarization at both potentials decreased with time according to the expected power law (figure 1). Steady state current density has not been reached after 24 h of passivation.

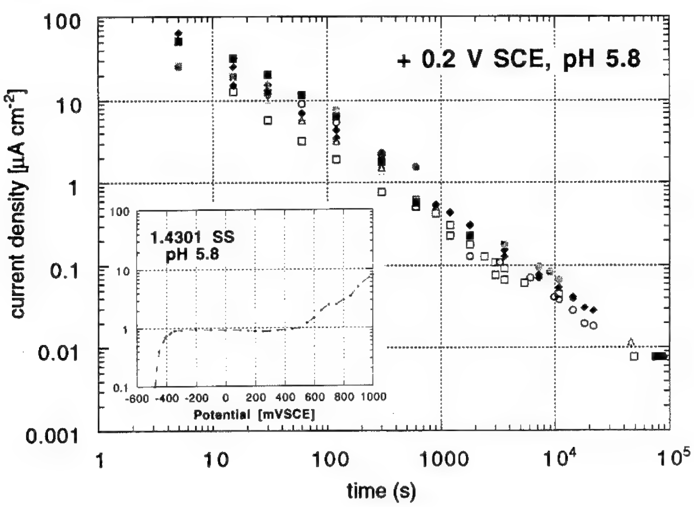

Figure 1: Current density vs time plot for the potentiostatic passivation of 1.4301 SS and 1.4529 SS at -0.1 V and +0.2 V SCE in 1 M Na_2SO_4 solution (pH 5.8). Insert: current density potential curve.

XPS results
The reference data for the pure metals and their oxides and for the alloys after ion etching are given in table 2. The detailed XPS spectra of 1.4529 stainless steel after 10 min, 1 hour and 24 h of polarization at +0.2 V SCE in 1 M Na_2SO_4 solution (pH 5.8) are given in Fig. 2 after background subtraction [12]. The spectra of all the alloy constituents show contributions from oxide and hydroxide states in the passive film and the metallic state immediately beneath the film. The Cr 2p3/2

Table 2: Binding Energies (E_B) of the different chemical states.

Sample	Chemical State		$E_B \pm 0.1$ (eV)	Ref.
Iron (ion etched)	Fe°	2p3/2	706.9	this work
Oxidized Iron	Fe^{2+}	2p3/2	709.8	[19]
	Fe^{3+}	2p3/2	710.8	[19]
Chromium (ion etched)	Cr°	2p3/2	574.0	this work
Chromium oxide (Cr_2O_3)	Cr^{3+}	2p3/2	576.6	[19]
Chromium hydroxide	Cr^{3+}	2p3/2	577.2	[19]
Nickel (ion etched)	Ni°	2p3/2	852.7	this work
sat			859.2	
Oxidized Nickel (NiO)	Ni^{2+}	2p3/2	854.8	[8]
sat 1			856.0	
sat 2			861.5	
Nickel hydroxide $Ni(OH)_2$	Ni^{2+}	2p3/2	856.2	[8]
sat 1			857.2	
sat 2			862.5	
Molybdenum (ion etched)	Mo°	3d5/2	227.9	this work
	Mo^{4+}	3d5/2	229.8	[13]
	Mo^{4+}	3d5/2	231.0	[13]
Molybdenum oxide (MoO_3)	Mo^{6+}	3d5/2	232.4	[8, 13]
1.4301 SS (ion etched)	Fe^{met}	2p3/2	706.7	this work
	Cr^{met}	2p3/2	574.0	
	Ni^{met}	2p3/2	852.8	
1.4529 SS (ion etched)	Fe^{met}	2p3/2	706.8	this work
	Cr^{met}	2p3/2	574.0	
	Ni^{met}	2p3/2	852.8	
	Mo^{met}	3d5/2	227.8	

spectra has been fitted with a Cr^{3+}(ox) component at 576.6 eV and Cr^{3+} (hy) at 577.2 eV in addition to the Cr^{met} at 574.0 eV. The Fe 2p3/2 spectra were fitted with Fe^{met} at 706.8 eV and Fe^{2+}(ox) at 709.8 eV and Fe^{3+}(ox+hy) at 710.8 eV lying between the binding energy values of Fe^{3+}(ox) and Fe^{3+}(hy) reported in [5]. The Mo3d spectra show contributions of the metallic signal Mo^{met} from the substrate at 227.8 eV and three oxidized species: Mo^{6+} at 232.4 eV, Mo^{4+}(ox) at 229.8 eV and Mo^{4+}(hy) at a binding energy of 231.0 eV [13]. The Ni2p region shows the typical satellite structure for both the metallic and oxidized nickel, the binding energy of Ni^{2+}(ox) 2p3/2 remains constant at 855.8 eV. The O1s signal is not a single peak, the curve fitting always shows three components attributed to M-O-M (530 eV), M-OH (531.5 eV) and adsorbed H_2O (532.9 eV). In the survey scans the elements carbon (contamination) and very weakly Na and S were detected.

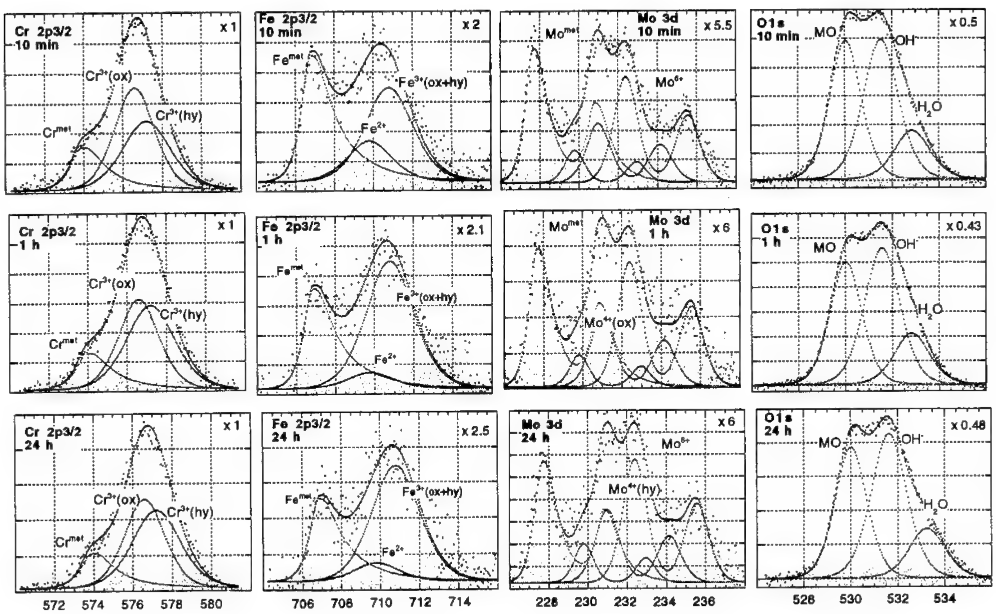

Figure 2: XPS spectra of 1.4529 SS after background subtraction [12], angle 0 deg respect to the surface normal. Passivation in 1 M Na_2SO_4 solution pH 5.8 at +0.2 V SCE, time of passivation: a) 10 min, b) 1 h and c) 24 h

The total *thickness of the passive film* (table 3) calculated according to the three layer model (ref. 10 and appendix) increased only slightly with passivation time (ageing). At lower potentials and on the high alloyed stainless steel 1.4529 the passive film thickness is lower in agreement with previous work [8]. The integral *composition of the passive film* does not change with polarization time (figure 3), the same result is found for the lower potential -0.1 V SCE. The dependance on the passivation potential is in agreement with previous work [8]. The integral Cr^{3+} content in the film is nearly the same for the two stainless steels studied, the content of oxidized iron is higher for the 1.4301 SS. About 8 % of Ni^{2+} and 12 % of oxidized molybdenum (Mo^{6+} and Mo^{4+}) is incorporated into the passive film on the 1.4529 independant of passivation time.

The *substrate* immediately beneath the passive film is strongly enriched in metallic nickel for both alloys (about twice the bulk content) and depleted in iron and to a minor extent in chromium. Molybdenum in the 1.4529 SS is present in the same concentration as in the passive film (about 12 %) but enriched compared to the bulk composition.

Table 3: Thickness of the passive film with time of ageing (nm ± 0.2 nm)

steel	potential	10 min	1 h	3 h	6 h	12 h	24 h
1.4301	-0.1 V	-	2.2	2.2	2.4	2.4	2.4
	+0.2 V	-	3.0	3.2	3.3	3.2	3.3
1.4529	-0.1 V	1.8	1.8	1.9	1.9	2.0	2.2
	+0.2 V	2.2	2.3	2.4	2.5	2.5	2.6

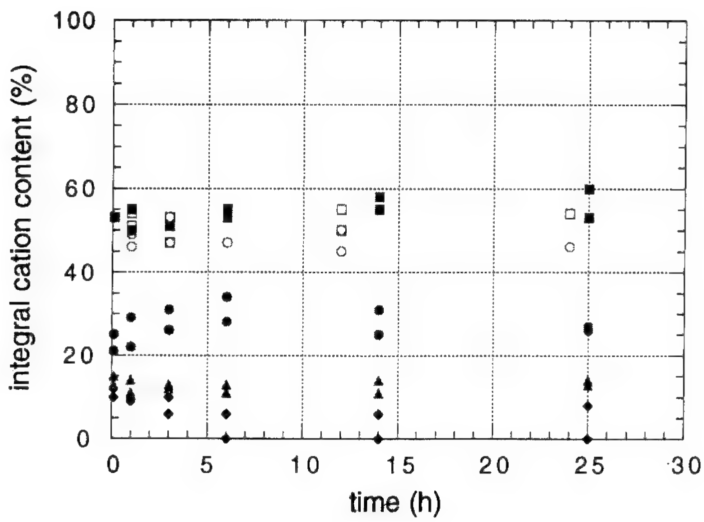

Figure 3: Integral composition of the passive film formed on 1.4301 (open symbols) and 1.4529 SS (closed symbols) in 1 M Na_2SO_4 solution (pH 5.8) at +0.2 V SCE
❑■ Cr(ox), ○● Fe(ox), ◆ Ni(ox) and ▲ Mo(ox)

Angle resolved XPS

Angle resolved XPS measurements allow to get an insight in the depth distribution of the different species in the passive film. Figure 4 shows the intensity ratios of Cr(hy) / (Cr(hy) + Cr(ox)), OH^- / (OH^- + MO) and Fe^{2+} / (Fe^{2+} + Fe^{3+}) for the passive films formed on both stainless steels at -0.1 V SCE and +0.2 V SCE after different times of passivation (from 10 min to 24 h).

- o The *films formed at the lower potential* (-0.1 V SCE) contain Cr^{3+} mainly as hydroxide (ca. 80 - 90%) independant of the type of steel and passivation time (fig. 4a). The OH^- intensity ratio (fig. 4b) shows more pronounced differences between the two angles at longer passivation times, the 1.4301 SS having a lower OH^- content. Pronounced changes occur in the Fe^{2+} intensity ratio (fig. 4c): after 10 min a high Fe^{2+} content is found that decreases with passivation time for both steels, the percentage present after 24 h is heigher on the 1.4301 SS.
- o *Passive films formed at the higher potential* (+0.2 V SCE) show more changes with type of steel and passivation time: The Cr(hy) intensity (fig. 4a) increases on the 1.4529 SS with passivation time whereas it remains constant on the 1.4301 SS. Variations with the angle of measurements indicate chromium(III) hydroxide mainly in the outer part of the passive film, a more pronounced bilayer structure is observed on the 1.4301 SS. Similar trends are observed in the OH^- intensity ratio (fig. 4b), again the passive film on the 1.4529 SS becomes more hydrated with time of passivation. The Fe^{2+} content is lower in the passive film of both steels and on the 1.4529 SS disappears completely after 24 h (fig. 4c).

Summarizing the 1.4529 SS containing 6% of Molybdenum becomes more hydrated (more Cr(hy) and more OH^-) and contains less Fe^{2+} with prolonged time of ageing, the 1.4301 SS in comparison is less hydrated and has a more pronounced bilayer structure.

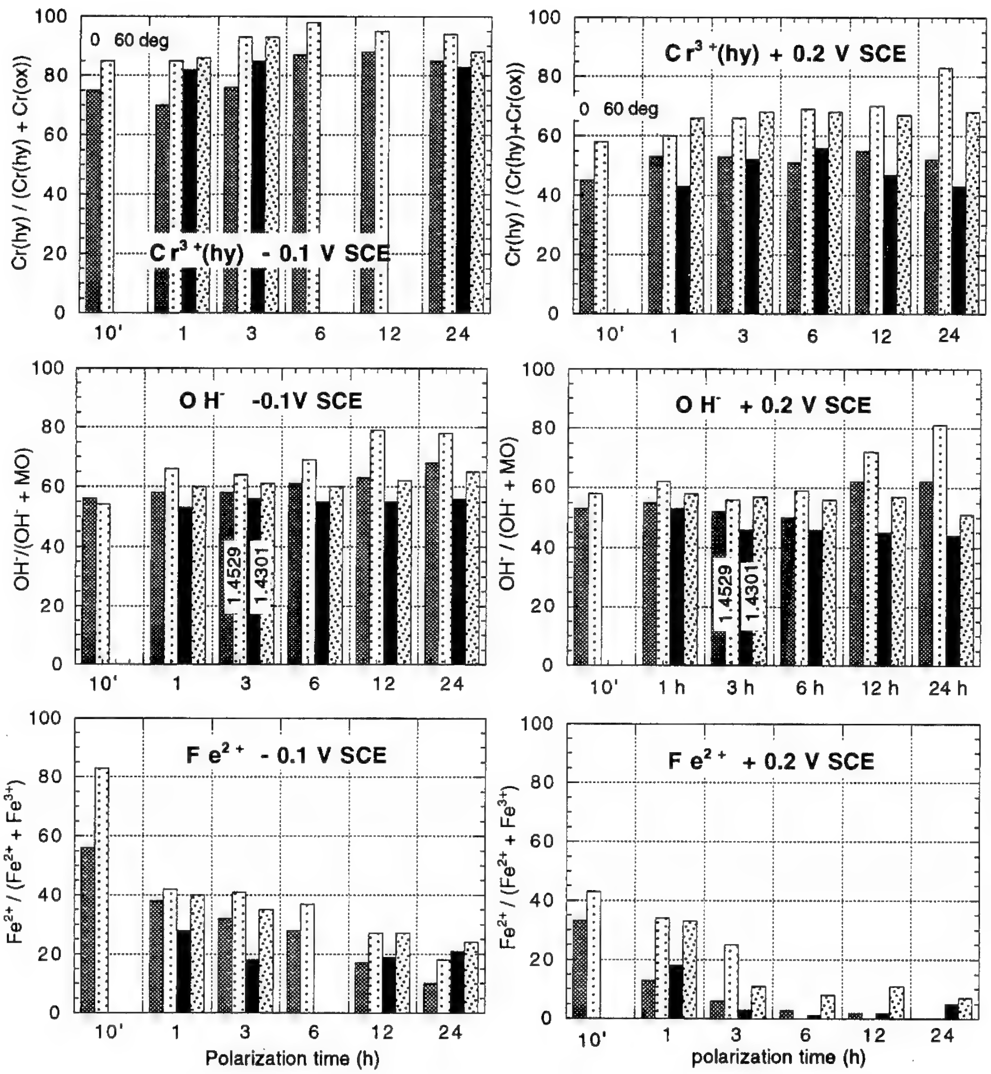

Figure 4: Results from ARXPS measurements at angle 0 and 60 deg. a) ratio of Cr^{3+}(hy) to total Cr^{3+}, b) ratio of OH^- to MO + OH^-, c) ratio of Fe^{2+} to (Fe^{2+} + Fe^{3+}) in the passive films for 1.4301 and 1.4529 stainless steel in 1 M sulfate solution of pH 5.8

Discussion

The conventional 1.4301 and the high alloyed 1.4529 stainless steel show huge differences in electrochemical behavior and pitting resistance in laboratory experiments [6, 15] and in practical conditions [15] despite a very similar chromium content in the alloy. XPS analysis of the passive films in this (fig. 3) and previous work [8] have shown that the integral Cr(III) oxy-hydroxide content is similar for both stainless steels. The main parameters that determine the chromium content of the passive film are the passivation potential and the pH of the solution [8, 16]. These results are

in good agreement with "in-situ" results obtained on the alloy Fe-20Cr-25Ni [9] at different pH in sulfate solutions.

Ageing of the passive film is known to affect the stability of the passive film and the resistance to localized corrosion [1 - 6]. At longer passivation times the passive current density becomes lower (fig. 1), indicating a higher stability of the passive film and the number of metastable pit initiation events decreases [4, 6]. The potential for pit growth after ageing was reported to increase [4, 5] as well as to decrease [6] after ageing. XPS measurements on a Fe-17Cr alloy have shown an increase of the Cr^{3+} concentration in the inner (oxidic) part of the passive film with ageing time [5]. On the stainless steels studied in this work, the total thickness of the passive film increased only slightly with ageing time (table 3) and the overall composition of the passive film remained constant (fig. 3) despite the fact that the passive current density still decreased after 24 h of passivation. Thus the enhanced stability of the passive layer must be attributed to transformations *within* the passive film, e.g. to changes in the Cr^{3+}(hy), the OH^- and the Fe^{2+} intensity ratio (fig. 4). The presence of gradients in the film revealed by ARXPS measurements (fig. 4) may imply that the "true" concentration in the outermost layers are higher then the integral values reported in fig. 3. Further work to include a bilayer structure of the passive film in the quantitative evaluation is in progress.

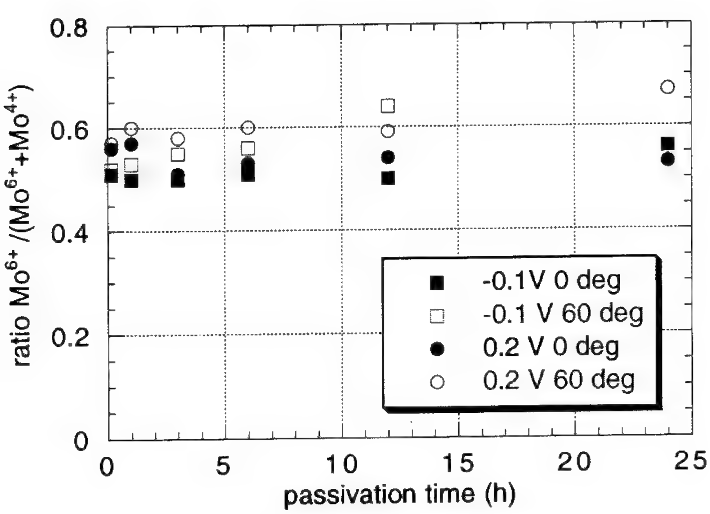

Figure 5: Time dependance of the ratio Mo^{6+} to (Mo^{6+} + Mo^{4+}) in the passive films of 1.4529 stainless steel in 1 M sulfate solution of pH 5.8 at angle 0 and 60 deg.

The two stainless steels 1.4301 (without Mo) and 1.4529 (with 6% Mo) show a different ageing behaviour:

o the conventional 1.4301 steel shows a more pronounced bilayer structure after 24 h of passivation, is less hydrated (fig. 4a, b) and contains more oxidized iron (Fe^{2+} + Fe^{3+}) in the film (fig. 3). The amount of Fe^{2+} in the oxide layer decreases with time, at the more positive passivation potential of +0.2 V SCE it is lower. Thus the 1.4301 SS behaves similar to a ferritic Fe-17 Cr alloy in NaCl solution of pH 6 [5] where the beneficial effect of ageing was attributed to an increase of the inner chromium enriched oxide layer thickness.

- o the high alloyed 1.4529 stainless steel with 6% Mo contains Ni^{2+} (10%) and oxidized molybdenum (12%) in the passive film independant of ageing time (fig. 3). In contrast to the ferritic [5] and the 1.4301 SS the passive film during ageing becomes more hydrated, the amount of Cr^{3+}(hy) and of OH^- increases with time of ageing. This effect is especially marked in the outer layer of the film (fig. 4).

The beneficial effect of molybdenum in promoting more hydrated passive films with lower thickness has been reported earlier based on XPS measurements after a constant time of passivation (1 h) [8]. Here experimental evidence is given for the progressive hydration of the passive film on Mo contaning stainless steels with ageing time (fig. 4). In the light of the basic concepts of passivity proposed by Okamoto [1] and Kruger [16], the passive film on the 1.4529 SS becomes more flexible and amorphous with ageing time, explaining the increased resistance against metastable pitting events (pit initiation) [6]. In addition, the presence of Mo6+ in the outer part of the surface layer (figure 5) may induce ion selective properties of the passive film as proposed to explain the higher pitting resistance of Fe19Cr9Ni2.5Mo alloy in 0.1 M HCl [17]. Another at least equally important reason for the much higher resistance against localized corrosion is the pronounced enrichment of nickel (ca. 50%) at the metallic interface beneath the passive film [3, 8, 18]: the high content of nickel and the presence of molybdenum (forming intermetallic Ni-Mo bonds with high stability [18]), cause a strong shift of the anodic polarization curve towards more noble potentials [20, 21] and reduce the (local) dissolution current during pit propagation, favouring repassivation of the pit embryo.

Conclusions

Prolonged passivation (ageing) of 1.4301 and 1.4529 SS in neutral sulfate solutions results in a slight increase in passive film thickness, changes in the passive film composition are revealed only by angle rexolved XPS measurements. The effect and the consequences of ageing can be summarized as follows:

1. Ageing results in a marked decrease of the Fe^{2+} content in the passive film
2. The two stainless steels behave differently during ageing: the passive film on the 1.4301 SS after 24 h shows a more pronounced bilayer structure, is less hydrated and contains more Fe^{3+} in the inner layer, the 1.4529 SS with 6% Mo instead becomes progressively more hydrated (more Cr(hy) and OH^-) with time of ageing
3. A strong nickel enrichment (about 50 %) is found in the alloy underneath the passive film of the 1.4529 SS stainless steels for all passivation times.

The increasingly higher degree of hydration with ageing, the presence of Mo^{6+} and the lower Fe^{2+} content in the passive film together with the marked nickel enrichment at the interface might explain the higher pitting resistance of the 1.4529 SS compared to that of the 1.4301 SS.

Acknowledgements

The work was financially supported by the Italian National Research Council (Comitato Tecnologico and Progetto Finalizzato di Chimica Fine e Secondaria).

References

[1] G. Okamoto, *Corrosion Science* **13** (1973) 471

[2] I. Olefjord, *Corrosion Science* **15** (1975) 697

[3] I. Olefjord and B. O. Elfström, Proc. 6th EUROCORR, London 19.-23.9.1977, The Society of Chemical Industry London (1977) p. 21 - 28

[4] B. Baroux, Proc. 11th Int. Corr. Conf. Florence 2.-6.4.90 p. 5.469 - 5.476

[5] W.P. Yang, D. Costa and P. Marcus, in "Oxide Films on Metal and Alloys, B.R. MacDougall, R.S. Alwitt and T.A. Ramanarayanan (eds), Proc. Vol. 92-22 p. 516 - 529, The Electrochmical Society, Pennington NJ (1992) and references quoted therein

[6] R. Morach, Zur Entstehung lokaler Korrosionsangriffe auf passiven Metallen, PhD Thesis No. 10677, Swiss Federal Institute of Technology ETH Zurich (1994)

[7] A. Allwart, Diplomarbeit IBWK ETH Zurich (1992)

[8] B. Elsener, D. DeFilippo and A. Rossi, *Modifications of Passive Films*, ed. P. Marcus, B. Baroux and M. Keddam, The Institute of Materials London (1994) p. 6 - 11

[9] N. Hara and K. Sugimoto, *J. Electrochem. Soc.* **138** (1991) 1594

[10] Rossi A. and Elsener B., *Surf. Int. Anal.* **18** (1992) 499

[11] M.P. Seah, *Surface Interface Analysis* **20** (1993) 243

[12] P.M.A.Sherwood, *"Practical Surface Analysis"*, ed. Briggs and M.P.Seah, Appendix 3, p.445, J. Wiley N.Y. 1983

[13] Olefjord I. And Brox B., Passivity of Metals and Semiconductors, Ed. M. Froment, Elsevier Science Publishers, Amsterdam (1983)

[14] H. Haselmair, R. Morach and H. Böhni, High alloyed Steels and Nickel Alloys for Fastenings in Road Tunnels, Corrosion NACE 50 (1994) 160

[15] B. Elsener and A. Rossi, presented at 5th Int. Symp. on Electrochemical Methods in Corrosion Research, EMCR 94, Lissabonn, Sept. 1994. To be published in Materials Science Forum

[16] J. Kruger, Nature of anodic passive films, Proc. 9th ICC Toronto 3.-7-6-1984, p. 79 - 88

[17] C.R. Clayton and Y.C. Lu, *J. Electrochem. Soc.* **133** (1986) 2465

[18] Olefjord I. and Clayton C.R., *ISIJ International*, **31** (1991) 134

[19] S. Haupt, PhD Thesis, University of Düsseldorf (1986)

[20] Newman R.C., *Corrosion Science* **25** (1985) 341

[21] Kolotyrkin Ya.M, Freiman L.I., Reformatskaya I.I. and Panshin E.A., *Protection of Metals* **30** (1994) 391 - 400

Materials Science Forum Vols. 185-188 (1995) pp. 347-356

Dissolution and passivation of stainless steels exposed to hydrochloric acid

L. Wegrelius and I. Olefjord

Department of Engineering Metals, Chalmers University of Technology, S-412 96 Göteborg, Sweden

Keywords: Stainless steel, dissolution, passivation, molybdenum, nitrogen, chloride, ESCA, electrochemistry

Abstract

Three high alloyed austenitic stainless steels (Fe20Cr20Ni, Fe20Cr20Ni6Mo and Fe20Cr20Ni6Mo 0.2N) were polarised in 0.1 M HCl + 0.4 M NaCl at room temperature. The surface compositions were determined by ESCA after polarisation of the samples to potentials in the range -375 mV to 800 mV(SCE) . The aim of the work was to study the influence of Mo and N on the dissolution and passivation of stainless steels.

Potentiodynamic polarisations of the steels show that Mo lowers the current in the active region. The current at low potentials in the passive region is independent of the Mo content. At higher potentials instable pits are formed on the Mo-free alloy; above 550 mV(SCE) stationary growth of pits occurs. During the virgin polarisation of the steel, N does not influence on the current in neither the active region nor the passive region.

Angle dependent ESCA analysis shows that the passive film formed during passivation for short time at -75 mV consists of Cr-rich oxide and Cr-rich hydroxide. The concentration of hydroxide decreases with the potential. The oxide is formed by deprotonation of hydroxide. At 500 mV the film consists of an inner oxide and an outer hydroxide with a diffuse interface. Molybdenum occurs in its four and six valence states. The Ni^{2+} content in the oxide is low. The thickness of the passive film formed on this type of alloy at low potential in the passive range is independent of the Mo- and N-content. Chloride is uniformly distributed throughout the oxide products at -75 mV (SCE). The Cl^--content is about 50% higher on the surface of the Mo-free alloy compared to the Mo-containing alloys.

Nickel is enriched on the surface in its metallic state during passivation. Chromium and Mo are depleted during polarisation due to formation of Cr- and Mo-rich oxide products. The depletion of Cr is less for the Mo-alloyed stainless steel than for the Mo-free alloy. It is suggested that the higher composition of the alloying elements enhance repassivation of initiated pits. Nitride is formed during passivation. It does not seem to influence on the dissolution rate during the primary passivation of the alloy.

Introduction

Stainless steels are passivated in aqueous solutions by formation of Cr- rich oxide products on their surfaces. The composition and thickness of the passive film is due to the composition of the alloy, the composition of the environment, the surface potential and the temperature [1-30]. Exposure of the steel to chloride or other halogen ion containing aqueous solutions may break down the passive film and thereby initiate localized corrosion attack. In order to improve the properties of Cr- steel the alloying elements Ni, Mo and N are added. Today, superaustenitic stainless steels have been developed. These steels allow high working temperature in relatively high concentrations of HCl or HF [31].

ESCA-measurements [2,7-20,28-30] have shown that the passive film formed on stainless steel in acid solutions at relatively high potentials in the passive range consists of an outer hydroxide layer and an inner oxide layer. The primary formed product is hydroxide, which has relatively low protecting properties. In the case of Cr-alloyed steels the hydroxide is deprotonated to anhydrous oxide, which gives the characteristic barrier properties of the passive film. For stainless steel the film consists mainly of Cr-products [7,10-19,28-30]. The Ni-content in the passive layer formed in acids is low. Molybdenum is enriched in the oxide products in its four (barrier layer), five [17,20] and six (outer layer) valence states. Iron is mainly present in the inner oxide products [25].

It has been proposed [13,32] that the presence of four and six valence Mo in the passive film lowers the defect density of the film and thereby the film becomes less able to be penetrated by aggressive ions. It has also been suggested [17,20] that molybdate is formed and acts a cation selective species which enhances the deprotonation of the hydroxide layer and favours formation of the barrier- oxide layer.

During anodic dissolution and passivation Fe is selectively dissolved. Thereby the alloying elements Cr, Ni and Mo are enriched on the surface [7-13,28] in their metallic states. The enrichment of the alloying elements lower the dissolution rate of the alloy and enhance the passivation [7,13]. The increased pitting corrosion resistance of Mo-alloyed austenitic steels in Cl^--containing environments is suggested [7-13], at least to some extent, to be due to the enrichment of the alloying elements in the surface region. Repassivation of an initiated pit is facilitated by the anodic segregation of the alloying elements.

Nitrogen increases the resistance to pitting corrosion markedly [33]. A strong synergistic effect between N and Mo has been demonstrated [33,15,19]. It has been suggested in [19] that an interaction between Mo-Ni-N occurs.

The aim of this work is to study the influence of Mo and N on the electrochemical behaviour of stainless steel. Attention will be focused on the influence of the alloying elements on the dehydration process, incorporation of Cl^--ions into the passive film, enrichment of the alloying elements in their metallic and oxide states during passivation.

Experimental

The composition (in weight %) of the steels studied are given in table 1. The samples (circular ϕ11 mm, thickness 2 mm) were polarised in deaerated 0.1 M HCl + 0.4 M NaCl at room temperature. The electrolyte was made of pro-analysi chemicals and deionized water. The polarisations were performed in an electrochemical cell directly connected to the ESCA instrument. All potentials in this

paper refer to the saturated calomel electrode. Two different ESCA instruments have been used, HP 5950A and PHI 5500. The X-ray radiation was AlK_{α}, 1486.6 eV.

The samples were pre-treated by grinding on emery paper down to 600 grit and then by diamond-paste polishing down to 1 μm followed by ultrasonic cleaning in ethanol. The samples were activated at the cathodic potential -700 mV for 15 min, and then the potential was swept 1 mV/s in the anodic direction. The potential of the samples prepared for ESCA-analysis was applied by stepping the potential from the activation potential to the desired potential. The potential was kept constant for 1 h when the samples were polarised in the potential range -375 to -275 mV and for 10 min when they were polarised to the potentials -75 , +500 and +800 mV. The polarisations were interrupted by pouring either acetone or isopropanol through the cell, and the samples were rinsed with methanol before they were transported into the ESCA system. Angle dependent ESCA-measurements were performed in order to obtain the in depth distribution of the elements.

Alloy	Composition, weight %										
	Fe	Cr	Ni	Mo	N	C	Si	Mn	P	S	W
FeCrNi	bal.	20.12	20.18	0.01	0.011	0.004	0.08	0.18	<0.003	22 ppm	0.02
FeCrNiMo	bal.	19.86	19.98	5.99	0.011	0.006	0.08	0.20	0.010	21 ppm	0.03
FeCrNiMoN	bal.	19.74	19.96	5.96	0.19	0.005	0.09	0.14	0.009	22 ppm	0.03

Table 1. *The chemical composition of the alloys in weight %.*

Results

Fig. 1 shows polarisation curves of the three steels exposed to deaerated 0.1 M HCl + 0.4 M NaCl -solution. The arrows in the figure mark the potentials to which the samples were polarised before surface analysis. The figure demonstrates that the polarisation behaviour of the steels is strongly dependent on the Mo content in the alloy. Nitrogen, on the other hand, does not influence on the polarisation. In the active region the maximum current of the FeCrNi-alloy is three times higher than the maximum current of the two Mo-alloyed steels; 67 and 22 μA/cm², respectively. After passivation of the alloys, the passive current at -75 mV is about the same for all three materials. It appears that the current on the FeCrNi sample fluctuates in the range 0 mV to 550 mV showing that pits are initiated and repassivated. At 550 mV the current increases dramatically as a result of stationary growing pits. The FeCrNiMo-steels with and without nitrogen are passive, without pitting, up to their transpassive regions.

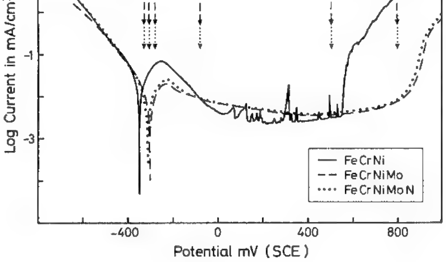

Figure 1. *Polarisation curves of the alloys exposed to deaerated 0.1 M HCl + 0.4 M NaCl at room temperature. Sweep rate was 1.0 mV/s. The arrows mark the potentials to which the samples were polarised before surface analysis.*

ESCA spectra recorded after passivation at -75 mV, from the FeCrNi alloy and the FeCrNiMoN alloy are illustrated in Fig. 2. The N-"free" (N-cont. 0.011 wt.%) alloy, gives about the same spectra (besides for the N-region) as the N-containing alloy. Fig. 2 shows that both the oxide and the metallic states of Ni, Fe, Cr and Mo are detected. In the case of Ni, the intensity of Ni^{2+} is very low. Apart from the metallic state, Fe is present in its di- and tri-valence states. The Cr-signal is divided into three peaks representing the metal phase and Cr^{3+} ions bound to O^{2-} and OH^- ions in the passive film. The oxygen signal is split into three peaks representing oxygen in O^{2-}, OH^- and H_2O. The signal from N 1s overlap the Mo $3p_{3/2}$ signal. The two N-signals represent N in nitride and ammonium or ammonia [19]. Carbon is present in contamination compounds adsorbed on the surface. The Mo-signal is split into four peaks, representing the metal phase, two four-valence states corresponding to MoO_2 and an oxyhydroxide [34], the fourth peak corresponds to the six-valence state of Mo. The Cl^--signal is relatively strong, representing Cl^--ions incorporated in the oxide products. No sodium signals were detected from any of the samples, showing that salt is not present during the analysis.

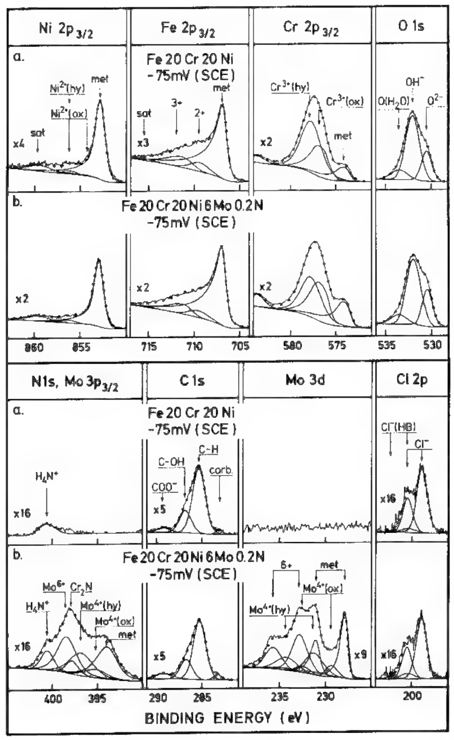

Figure 2. ESCA spectra recorded from the Fe20Cr20Ni alloy and the Fe20Cr20Ni6Mo-0.2N alloy after passivation at -75 mV(SCE). The take-off angle was 45º, monochromized AlKα was used.

Fig. 3 shows angle dependent ESCA spectra of the N 1s and Mo $3p_{3/2}$ signals recorded after polarisation of the FeCrNiMo and the FeCrNiMoN samples to -75 mV(SCE). The take-off angles (angles between the surface and the lens-axis of the spectrometer) are 30º, 45º and 90º. The N-bearing steel shows pronounced signals from a nitride-compound at BE=397.5 eV. The angle dependent intensity ratios, N^{3-}/Mo^{6+} and N^{3-}/Mo^{met}, indicate that the nitride phase, probably Cr_2N, is located at the metal/oxide boundary. The intensities of the N-signals representing ammonium are independent of the N-content of the alloy. It has been assumed [35] that the origin of this compound is N-containing impurities in the water used. The figure does not show any angle dependence for neither the $N(H_4N^+)$-signal nor the Mo^{ox}-signals showing that the ammonium ions and the Mo^{ox}-ions are uniformly distributed through the oxide products at -75 mV.

The composition and the thickness of the oxide products can be determined from the measured intensities. Details about the quantification are given elsewhere [25]. Fig. 4 shows the intensity ratios, OH^-/O^{2-}, at -75 mV and 500 mV(SCE) for the take-off angles 30º, 45º and 80º. The data points are connected by thin solid lines. The dashed lines show the average values. The OH^-/O^{2-} ratio obtained at -75 mV is about twice as high as the ratio obtained at 500 mV showing that the hydroxide content is larger at the low potential than at the high potential. It appears that the spread

in data obtained at -75 mV is very high compared to the deviation at 500 mV. At the higher potential no influence of the alloy composition can be noted. The ratios obtained at -75 mV seem to be dependent on the composition of the alloy; the highest OH^-/O^{2-} ratio is obtained from the Mo-free alloy (FeCrNi) while the Mo-containing alloys give lower ratios. This result indicates that the amount of hydroxide is dependent on the Mo-content. The thick solid lines show expected intensity ratios from a hydroxide/oxide layer-model assuming the thicknesses in the figure. The measured data can not easily be interpreted with the hydroxide/oxide layer model. Instead, the data indicates that at least the passive film formed at -75 mV consists of not well defined layers of oxide and hydroxide products. Even at 500 mV the hyroxide/oxide layer model is not perfectly satisfied. The angle dependence is less than expected indicating hydroxide/oxide layers with a diffuse interface.

The overall cation content of the oxide products formed on the steels at -75 mV is shown in Fig. 5. The thick horizontal lines show the average values and the white areas are the standard deviations. At least 4 measurements have been performed on each steel. Chromium and Mo are markedly enriched in the passive films while the Fe-and Ni-contents are less than their bulk concentrations. The measured average Fe^{ox}-concentration ($Fe^{ox}=Fe^{2+}+Fe^{3+}$) in the oxide products of all three alloys is 15.5 at.%. This value is slightly higher than the Fe^{ox}-content of the oxide formed on the FeCrNi-alloy. Thus, it seems that alloying with Mo and N gives somewhat higher Fe^{ox}-content in the oxide. The Cr^{3+}-contents of the oxides formed on the Mo and the Mo-N-bearing steels are significantly lower than the Cr-content of the oxide formed on the FeCrNi-steel.

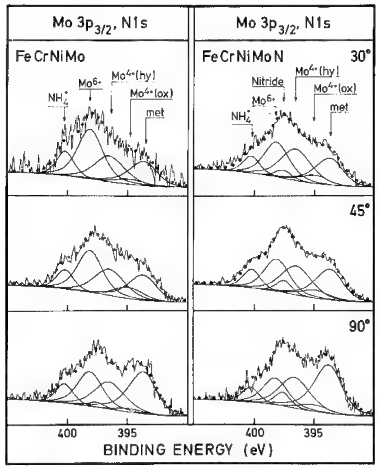

Figure 3. *Angle dependent ESCA-measurements of the N1s and $Mo3p_{3/2}$ signals recorded from the FeCrNiMo alloy and the FeCrNiMoN alloy after passivation at -75 mV(SCE), non-monochromized AlKα was used.*

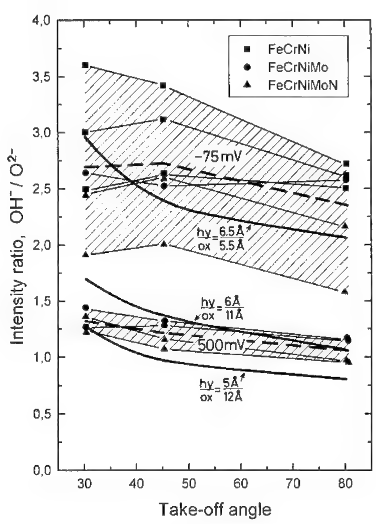

Figure 4. *The measured intensity ratios OH^-/O^{2-} at the take-off angles 30^0, 45^0 and 80^0 after passivation at -75 mV and 500 mV(SCE). The thin solid and dashed lines interconnect the measured data points and their average values, respectively. The thick solid lines are expected ratios from the hydroxide/oxide layer-model.*

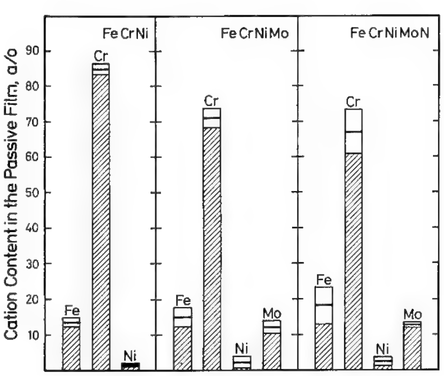

Figure 5. *The cation content in the passive film formed at -75 mV(SCE).*

Fig. 6 shows the thickness of the passive layer versus the potential. It shows that the thickness of the passive layer increases with the potential. At -75 mV the average thickness of the passive films formed on FeCrNi, FeCrNiMo and FeCrNiMoN alloys are 13.1±2.0, 12.1±1.3 and 11.0±1.2 Å, respectively. Thus, it seems that the thickness of the oxide formed is almost independent of the Mo and the N contents of the steels. At the potentials +500 and +800 mV, the thickness of the passive layers formed on the Mo and Mo-N containing steels are 17.5 and 22 Å, respectively.

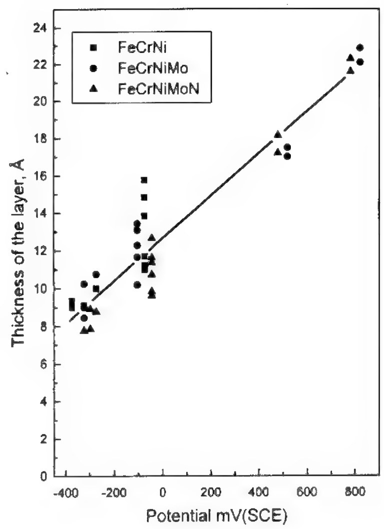

Figure 6. *The thickness of the total passive film.*

The Cl^--content in the passive film is in the range 3 to 4.5 % of the total ion content, Fig.7. The figure indicates that the Cl^--content in the film formed on the Mo and the Mo-N bearing steels are somewhat lower than in the film formed on the FeCrNi alloy.

From the angle dependent ESCA-measurements the distribution of the Cl^- in the surface products was searched. The solid lines in Fig.8 show the expected intensity ratios between the chloride signal and the total oxygen signal, $Cl^- * 100/(O^{2-}+OH^-)$, for four different distributions of Cl^--ions marked in the figure. The symbols, connected with the thin lines, show the individual measured ratios from samples polarised at -75 mV. The spread in the data is large. The dashed line connects the average values obtained. The angle dependence of the average values can be interpreted in such a way that Cl^--ions are uniformly distributed throughout the oxide products. The other models, adsorption of Cl^- on the surface and distribution of Cl^--ions only in the outer layer or in the inner layer, seem not to satisfy the measured data.

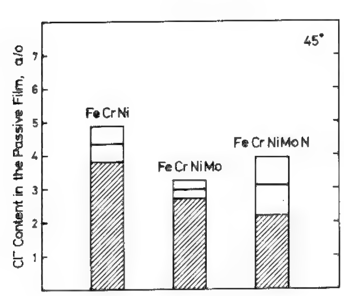

Figure 7. *The chloride content in the passive film formed at -75 mV(SCE).*

The potentiodynamic polarisation curves, Fig.1, show that the potential -325 mV is in the active range of the alloys. During potentiostatic polarisation at this potential these high alloyed steels become passivated. The film formed is about 9 Å thick, Fig.6. Due to the fact that the film is very thin it is possible to get relatively accurate information about the composition of the metallic state underneath the oxide. Figure 9a shows the apparent composition of the metal calculated from the measured intensities considering the attenuation of the photoelectrons [25] in the oxide layer. The term "apparent" is used because the distribution of the elements in the surface region is not taken into account. The dotted lines in the figure mark the compositions of the alloys. The apparent Fe-content is markedly lower than the Fe-content in the alloy. From the fact that the cation content of Fe^{ox} in the oxide is also lower than the concentration of Fe in the alloy follows that Fe is selectively dissolved during passivation. The apparent Cr-content decreases from 21 at.% in the bulk to about 15 at.%. The measured Ni-concentration is noticeably higher after polarisation than before showing that Ni is enriched at the metal/oxide interface. The measured Mo-content is slightly lower than in the bulk of the alloy.

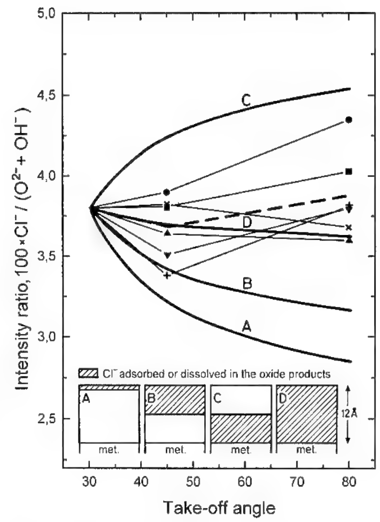

Figure 8. *The intensity ratios $Cl^-/(O^{2-}+OH^-)$ measured at take-off angles 30°, 45° and 80° after passivation at -75 mV(SCE). The thin solid and dashed lines interconnect the measured data points and their average values, respectively. The thick solid lines are expected ratios from the four different models shown in the figure.*

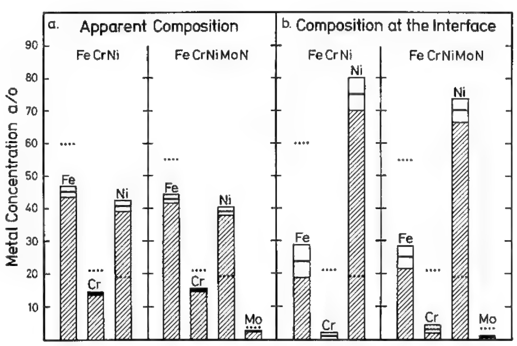

Figure 9a. *The apparent composition of the metal phase underneath the oxide phase formed during polarisation for 1 h at -325 mV(SCE).*

Figure 9b. *The estimated concentration of the elements in the outermost atomic plane of the metal phase underneath the oxide formed during polarisation for 1 h at -325 mV(SCE).*

It is obvious that the composition of the metal phase changes during dissolution and passivation of the steels. It is very easy to show that the change of the composition must take place over more than one atomic plane. The assumed concentration profile is an ERF-function with concentration changed over three atomic planes [12, 13]. Fig. 9b shows the estimated concentration of the elements in the outermost atomic plane of the metal phase underneath the oxide. It appears that for both alloys the Fe-content has decreased from 60 to about 25 at.%. The Cr-content of the FeCrNi-alloy is almost zero. (If less than three layers is chosen the Cr-content should be negative.) For the Mo-N alloyed steel the Cr-content in the outermost layer is noticeably above the zero level. The Ni-content is between 70 and 80 at.%. Due to the enrichment of Mo in the passive film the Mo content in the first plane of the metal is below the Mo-content of the bulk.

Discussion

As shown earlier [1-30] the dominating cation in the passive film formed on the surface of stainless steel is Cr^{3+}. During polarisation for short time of Fe20Cr20Ni and Fe20Cr20Ni6Mo (with and without N) at - 75 mV in 0.1 M HCl + 0.4 M NaOH the cation contents of Cr^{3+} in the films become 85 at.% and 70 at.%, respectively. The Fe-content (about 15%) is slightly higher in the oxides formed on the Mo and the Mo-N alloys in spite of the fact that these steels contain less Fe than the Mo-free alloy. The Mo-content of the oxides formed on the two Mo-containing alloys are about 12 at.%. It is not possible to determine any influence of N on the concentration of Mo or of any other of the alloying elements.

In this work it is demonstrated that polarisations for short time does not give any characteristic hydroxide/oxide layer structure, at least not at -75 mV. Even at +500 mV the ESCA measurements does not give the expected angle dependence. It is therefore suggested that a diffuse layer exist at the hydroxide/oxide interface. The content of hydroxide formed at -75 mV is larger than the hydroxide content at higher potentials. Thus, the hydroxide, which is the first reaction product formed, is transformed to oxide by deprotonation more slowly at low potential than at high potential. It was also discovered that less hydroxide is present on the surface of the Mo-containing alloys. The deprotonation rate of the hydroxide seems to be dependent on Mo in agreement with Sakashita and Sato [36] model. They have suggested that Mo^{6+} present as molybdate-ions act as a cation selective species. The acceleration of deprotonation of hydroxide by molybdate has previously been discovered by Clayton et al [17]. However, separation between Mo^{6+} dissolved in the oxide products and present as molybdate in the film is difficult.

The average thicknesses of the oxide products formed on the three alloys at -75 mV are in the range 11 to 13 Å. The standard deviation of the measurements are too large to allow a statement about the influence of Mo and N on the oxide thickness. In agreement with this results it has earlier been pointed out [10,24] that the oxide thickness is not dependent on the Mo-content.

The angle dependent ESCA-measurements show that Cl^--ions are distributed throughout the oxide at -75 mV. It was found that the Cl^--concentration in the oxide products depends on the Mo-content of the alloy. The oxide formed on the Mo-free alloy contains about 50 % more Cl^--ions than the oxide formed on the others. The influence of Mo on the Cl^--concentration in the film has been reported earlier by Mischler et al. [24]. They found that the distribution of Cl^--in the film is influenced by Mo and that Cl^- present or absent in the electrolyte does not significantly change the cation concentration in the film. Further, as shown in this paper Cl^--ions have only a minor effect on the film thickness. Chloride ions, present in the film, probably substitute O^{2-} and OH^--ions, weaken the bonding between the cations and oxygen and thereby facilitate initiation of localised corrosion attack. Molybdenum forms a series of oxychloride complexes. Some of them are soluble in acids while other complexes are stable. No attempt has been done to clarify which complexes are formed. In this respect the role of Mo could be twofold: the lower Cl^--content is obtained due to formation of water soluble oxychloride complexes; the remaining Cl^--ions could be bound in insoluble Mo-chlorohydroxide complexes. Thus, the passive film contains of less amount of weakly bound Cl^--ions. The resistance for initiation of pitting of the steel is thereby increased.

The polarisation diagram, Fig.1, shows that initiation and repassivation of pits occur on the FeCrNi-alloy. The Mo and Mo-N-containing alloys are passive up to the transpassive potential. The passivation current of the Mo-free alloy is three times higher than on the others. On the other hand the current in the passive range is about the same for all three alloys. Thus, Mo and N do not influence on the current at low potentials in the passive range. This behaviour can be understood

from the fact that the composition and the thickness of the oxide products are almost the same. As speculated above, it is possible that the passive film formed on the Mo-containing alloy is more stable because it contains less amount of Cl^--ions. Earlier, it has been proposed [7-13] that the main role of the alloying elements is that they are enriched on the surface during anodic dissolution and thereby lower the dissolution rate and enhance the passivation. For these very high alloyed steels it was not possible to keep the active state, instead the alloys passivated and formed very thin oxide layer. The analysis shows that the Cr-content under the film formed on the Mo-free alloy is almost zero. Thus, the event leading to break down of the passive film requires dissolution of the alloy before repassivation. If pitting is initiated on the Mo-alloyed steel it is more easily repassivated because the Cr-content on the surface of the metal phase is relatively high. During the early state of pitting the alloying elements is enriched on the surface by selectively dissolution of Fe. Thereby, the dissolution rate decreases and the steel is repassivated.

From the results above it is clear that N does not modify the composition of the passive film even if it is possible to detect nitride under the film. The nitride does not seem to influence on the primary passivation mechanism. Instead it has been shown [35] that the positive effect obtained by alloying stainless steel with N is that the repassivation ability is enhanced. During the primary passivation, as studied here, the dissolved volume is too small to give an enrichment effect on N.

Conclusions

Electrochemical and surface analyses of the steels Fe20Cr20Ni, Fe20Cr20Ni6Mo and Fe20Cr20Ni-6Mo0.2N exposed to 0.1 M HCl + 0.4 M NaCl show that:

- The dissolution rate in the active potential range is lower for the Mo-containing steels.
- The current at low potentials in the passive region is not influenced by neither Mo nor N.
- Initiation and repassivation of pits occur on the Mo-free alloy up to the pitting potential.
- N does not influence on the primary passivation behaviour of the steel. It enhance repassivation.
- The thickness of the film formed in the passive range is independent of Mo and N.
- Mo lower the Cl^--concentration in the oxide products.
- Cl^- ions are uniformly distributed throughout the passive film formed at -75 mV.
- The passive film consists of Cr^{3+}-rich oxide and hydroxide.
- Deprotonation of hydroxide is accelerated at -75 mV on the Mo-containing alloys.
- The deprotonation rate of the hydroxide increases with the potential.
- The Cr-content underneath the passive film is higher on the Mo-containing alloys than on the Mo-free alloy. It is suggested that the repassivation property of Mo-bearing steels thereby is enhanced.

Acknowledgements

The Research Council for Engineering Sciences (TFR) is gratefully acknowledged for financial support.

References

[1] H. Fischmeister and I. Olefjord, Monatshefte für Chemie, **102**, 1486 (1971).
[2] I. Olefjord and H. Fischmeister, Corros. Sci., **15**, 697 (1975).
[3] J. E. Castle and C. R. Clayton, Corros. Sci., **17**, 1 (1977).
[4] K. Sugimoto and Y. Sawada, Corros. Sci., **17**, 425 (1977).
[5] K. Hashimoto, K. Asami and K. Teramoto, Corros. Sci., **19**, 3 (1979).
[6] K. Hashimoto and K. Asami, Corros. Sci., **19**, 251 (1979)
[7] I. Olefjord, Materials Sci. and Eng., **43**, 161 (!979).
[8] C. Leygraf, G. Hultqvist, I. Olefjord, B.-O. Elfström, V. M. Knazheva, A. V. Plaskeyev, and Ya. M. Kolotyrkin, Corros. Sci., **19**, 343 (1979).
[9] M. Seo and N. Sato, Trans. Japan Institute of Metals, **21**, 805 (1980).
[10] I. Olefjord and B.-O. Elfström, Corros. NACE, **38**, 46 (1982).
[11] I. Olefjord and B. Brox, Proc. 5th Passivity of Metals and Semiconductors (ed. M. Froment), Elsevier Science Publishers, Amsterdam (1983).
[12] B. Brox and I. Olefjord, Proc. Stainless Steel 84, Göteborg, The Institute of Metals, p.134 (1984).
[13] I. Olefjord, B. Brox and U. Jelvestam, J. Electrochem. Soc., **132**, 2854 (1985).
[14] R. Kirchheim, B. Heine, H. Fischmeister, S. Hofmann, H. Knote and U. Stolz, Corros. Sci., **29**, 899 (1989).
[15] Y. C. Lu, R. Bandy, C. R. Clayton and R. C. Newman, J. Electrochem. Soc., **130**, 1774 (1983).
[16] A. R. Brooks, C. R. Clayton, K. Doss and Y. C. Lu, J. Electrochemical Soc., **133**, 2459 (1986).
[17] Y. C. Lu, C. R. Clayton and A. R. Brooks, Corros. Sci. **29**, 863 (1989).
[18] C. R. Clayton and K. G. Martin, Proc. High Nitrogen Steels (Eds. J. Foct and A. Hendry) Inst. of Metals, London, p. 256 (1989).
[19] R. D. Willenbruch, C. R. Clayton, M. Oversluizen, D. Kim and Y. C. Lu, Corros. Sci., **31**, 179 (1990).
[20] Y. C. Lu, M. B. Ives and C. R. Clayton, Corros. Sci., **35**, 89 (1993).
[21] J. E. Castle and J. H. Qiu, Corros. Sci., **30**, 429 (1990).
[22] A. Schneider, D. Kuron, S. Hofmann and R. Kichheim, Corros. Sci., **31**, 191 (1990).
[23] D. Landolt, S. Mischler, A. Vogel and H.J. Mathieu, Corros. Sci., **31**, 431 (1990).
[24] S. Mischler, A. Vogel, H. J. Mathieu and D. Landolt, Corros. Sci., **32**, 925 (1991).
[25] I. Olefjord and L. Wegrelius, Corros. Sci., **31**, 89 (1990).
[26] I. Olefjord and C. Clayton, ISIJ International, **31**,134 (1991).
[27] L. Wegrelius and I. Olefjord, Preceedings, 12th Int. Corrosion Cong., NACE International, Houston, **5B**, p3887 (1993)
[28] P. Marcus and J Grimal, Corros. Sci., **33**, 805 (1992).
[29] P. Marcus and I. Olefjord, Corros. Sci., **28**, 589 (1988).
[30] W. P. Yang, D. Costa and P. Marcus, J. Electrochem. Soc., **141**, 111 (1994).
[31] B. Wallén, M. Liljas and P. Stenvall, Werkstoffe und Korrosion, **44**, 83 (1993).
[32] M. Urguidi and D. D. MacDonald, J. Electrochem. Soc., **132**, 533 (1985).
[33] K. Osozawa and N. Okato, Passivity and its Break Down on Iron and Iron Base Alloys,USA-Japan Seminar, NASE, Houston Texas, p.135 (1976).
[34] B. Brox and I. Olefjord, Surf. and Interface Anal., **13**, 3 (1988).
[35] L. Wegrelius and I. Olefjord, To be pulished in J. Electrochem. Soc.
[36] M. Sakashita and N. Sato, Corros. Sci., **17**, 473 (1977).

Materials Science Forum Vols. 185-188 (1995) pp. 357-364

Study of corrosion protective layers on iron surfaces by x-ray photoelectron- and Mössbauer-spectroscopic methods

F.H. Kármán[1], Cs. Vértes[2] and E. Kálmán[1]

[1] Central Research Institute for Chemistry, Hungarian Academy of Sciences, POB 17, H-1525 Budapest, Hungary

[2] Department of Physical Chemistry and of Nuclear Chemistry, Eötvös University, H-1518 Budapest, Hungary

Keywords: Mössbauer spectroscopy, photoelectron spectroscopy, mild steel corrosion, mechanism of inhibition

Abstract - The influence of inhibitor molecules (1-hydroxy-ethane-1,1-diphosphonic acid, (HEDP) sodium benzoate (NaBz) and $NaNO_2$ on mild steel surface has been examined. Surface analytical methods (Mössbauer spectroscopy, and X-ray photoelectron spectroscopy) have been used to investigate the composition of the surface layer. Various Fe^{2+}, Fe^{3+}, and FeOOH compounds and metallic, state of Fe were identified in the surface layer in all cases. It was found that the ratio of metallic state of Fe to different oxygen containing iron compounds was increased by increasing HEDP concentrations. Very thin passive layer was detected in the presence of NaBz and $NaNO_2$ on the surface film. It was also observed that the passive state of iron in sodium nitrite solution was destroyed by HEDP and NH_3 was detected in the surface layer.

INTRODUCTION

A large number of investigations deals with the corrosion behaviour of mild steel in near-neutral aqueous solutions.
It is known that various inorganic compounds (nitrites, chromates) and organic compounds (benzoates, phosphonates) are able to prevent the corrosion of mild steel under given conditions. An important field of the corrosion sciences is the investigations of the metal-water interface. The corrosion protection ability is determined by the interphase between corrosion protective layers and metals. The aim of this study was to examine the composition of the surface film formed on mild steel in aqueous solutions in the presence of the following inhibitor molecules:
1-hydroxy-ethane-1,1-diphosphonic acid (HEDP), sodium benzoate (NaBz) and sodium nitrite ($NaNO_2$). The influence of the inhibitor molecule (HEDP) was investigated at different concentrations.
In the present paper the following methods of surface analysis were applied to the investigations of mild steel surface . Mössbauer spectroscopy (MS) is a useful technique for studying corrosion processes, as it provides qualitative and quantitative phase analysis of corrosion products of iron. [1-3] X-ray photoelectron sepctroscopy (XPS) and X-ray induced Auger electron spectroscopy (XAES) give the possibility for identification of different chemical states of the constituents of corrosion protective layers on metal surfaces.[4-5]

The main advantages of MS in corrosion research are as follows: 1) the non-destructive character of the technique; 2) possibility for qualitative and quantitative phase analysis; 3) usefulness in identification of poorly crystallized or amorphous corrosion products.

During the Mössbauer experiments, either the gamma rays or the conversion electrons should be detected. The conversion electron Mössbauer spectroscopy (CEMS) which is a special Mössbauer technique is based on the detection of the conversion electrons. The information depth (~ 200-300 nm) of this method is well suited for examinations of surface layers [1].

X-ray photoelectron spectroscopy involves bombarding the sample with X-rays. The ejected core electrons have an energy characteristic of the element from which they were expelled.

Generally the X-ray photoelectron spectroscopy studies have been performed proving that solid-state and atomic and molecular contributions can be separated in the measured electron spectra by using adequate evaluation methods.

The analytical information can be obtained on the composition of the very thin surface film, is restricted to depths of less than 10 nanometers.

EXPERIMENTAL

Mössbauer spectra of the samples were recorded at room temperature with a constant acceleration spectrometer using a ^{57}Co/Rh source. All isomer shifts were referred to α-iron. A standard least squares minimization routine was used to fit the spectra as a superposition of Lorentzian lines. The calculation of the thickness of the γ-FeOOH layer was carried out on the basis of the theory and computer software developed by F.Salvat et al. [2].

X-ray Auger electron spectroscopy (XAES) and XPS experiments were conducted by using ESA-31 XPS/XAES instrument built in ATOMKI, Debrecen.

The spectrometer based on a 180^0 hemispherical analyser with a working radius 250 mm floatable up to 10 kV, a multielement zoom input lens and a maximum 30 kV/30 mA dual anode (Al, Mo) X-ray source. FRR (fixed retardation ratio) working mode was used with 1:20 retarding ratio. During measurements the vacuum level was better than 10^{-7} Pa. Energy calibration of the electron spectrometer was performed in the XPS region by measuring polycrystalline copper and silver samples using the Cu $2p_{3/2}$ and Ag $3d_{5/2}$ binding energy values obtained by Seah et al. [6]. Peak intensities were determined from the areas under the respective photoelectron as Auger-electron lines. The evaluation was carried out by using the EWA 2.23 evaluation program [7].

The following model components were fitted to the respective electron spectrum:

Tougaard background [8] and Voigt function line shape. The background parameters were fixed while the peak parameters were let to change freely during the fitting procedure.

The amount of the adsorbed inhibitor was characterized by the P KLL signal.

Samples and preparation

Disc shaped samples were cut from a polycrystalline Fe plate of 0.25 mm thickness (composition: Fe 99.57%, Si 0.05%, C 0.05%, Mn 0.30%, S 0.01%, P 0.02%). The samples were cleaned by electropolishing in aqueous solution containing 75% (by volume) acetic acid and 20% perchloric acid for 2.5 min, and rinsed in deionized distilled water. Inhibitor adsorption was accomplished by immersing the samples in an aqueous solution of 50 cm^3 for 24 hours in the case of the MS, and for 30 min in the case of the XPS investigations. The test solutions were buffered by adding a small amount of NaOH, the pH value was adjusted to 7.0.

The following test solutions were used: (1) 10^{-4} mol dm^{-3} HEDP; (2) 3 10^{-4} mol dm^{-3} HEDP; (3) 3 10^{-4} mol dm^{-3} $ZnSO_4$; (4) 10^{-3} mol dm^{-3} HEDP; (5) 10^{-2} mol dm^{-3} HEDP; (6) 10^{-2} mol dm^{-3} $NaNO_2$; (7) 10^{-1} mol dm^{-3} NaBz. All pretreatment were carried out in solutions (with deionized distilled water) which were open to the air.

RESULTS AND DISCUSSION

Mössbauer experiments

The spectra in Fig.1. a), c) and e) consist of two components. Besides the sextet of α-iron, a doublet appears with the parameters characteristic of an Fe(III) compound. The isomer shift ($\delta \approx 0.40$ mm/s), the quadrupole splitting ($\Delta \approx 0.85$ mm/s) and the relatively high half width values of this doublet all suggest the existence of an amorphous FeOOH layer on the surface of the samples. The presence of iron-HEDP complexes cannot be excluded.

Due to some earlier studies [3] it seems very likely, that in our case a precursor state of γ-FeOOH can be assumed as a passivating layer. The thickness of this layer, that was calculated on the basis of the Mössbauer line area fractions with the help of a computer software (mentioned earlier) reached up to 80 ± 10 nm in case 3 x 10^{-4} mol dm^{-3} HEDP test solution (Fig.1.a).

The surface layer that was formed due to a 10^{-3} mol dm^{-3} HEDP test solution treatment (Fig.1.g), remained under the detection limit of this method, it was less than 2-3 nm. Similar result was obtained with treatment of 10^{-2} mol dm^{-3} HEDP solution.

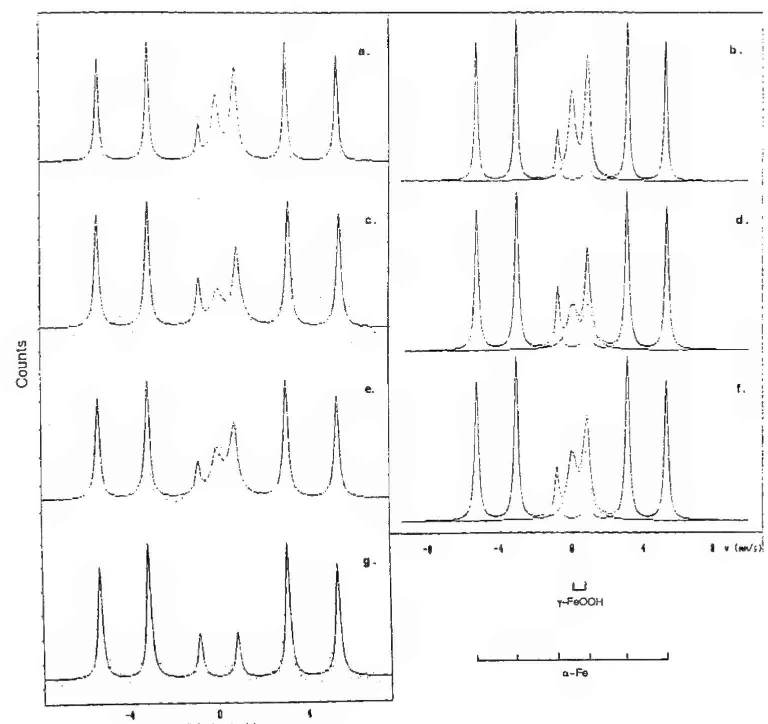

Fig.1. Conversion electron Mössbauer spectra of the mild steel sample recorded after the treatment in different solutions: 10^{-4} M HEDP (a)/subspectra (b); in 3x10^{-4} M HEDP + 3x10^{-4} M Zn^{2+} (c)/subspectra (d); in 3x10^{-4} M HEDP (e)/subspectra (f); and in 10^{-3} M HEDP (g).

The passive layer that formed due to the treatments in $NaNO_2$ and in NaBz solutions remained under or just reached the detection limit of CEMS. It is doubtful, drawing any qualitative information from the measured data (Fig.2).

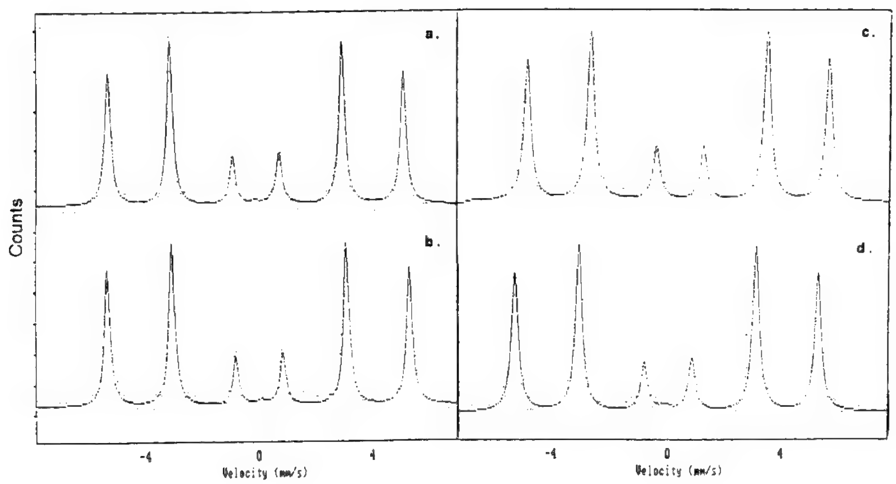

Fig.2. Conversion electron Mössbauer spectra of the mild steel sample recorded after the treatment in 10^{-2} M $NaNO_2$ (a); in 10^{-2} M $NaNO_2$ + 10^{-3} M HEDP (b); in 10^{-1} M Nabenzoate (c); and in 10^{-1} M Nabenzoate + HEDP (d).

Photoelectron Spectroscopy Analysis

Test solutions with different concentrations of HEDP and 10^{-2} mol.dm^{-3} $NaNO_2$ were used in deionized distilled water.

The composition of the surface films formed on mild steel surface in 10^{-4}, 10^{-3} and 10^{-2} mol.dm^{-3} of HEDP solutions were determined by XPS method.

Beside the metallic state of Fe, various Fe^{2+}, Fe^{3+} and FeOOH compounds were observed on the electropolished iron surface in our previous study. [4]

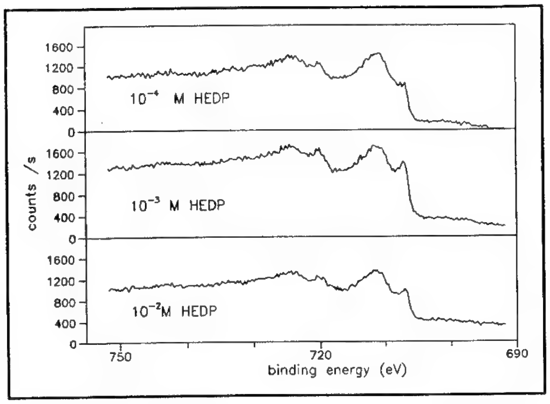

Fig.3. Fe 2p spectra of mild steel samples treated in HEDP test solutions with different concentrations

During the treatment with HEDP solution at different concentrations the composition of surface films were changed. The obtained layers contain metallic state of iron and different iron compounds too. The ratio of metallic state of Fe to different oxygen containing iron compounds was increased by increasing HEDP concentrations (Fig. 3.). Oxygen signals were decreased by increasing HEDP concentrations (Fig. 4.).

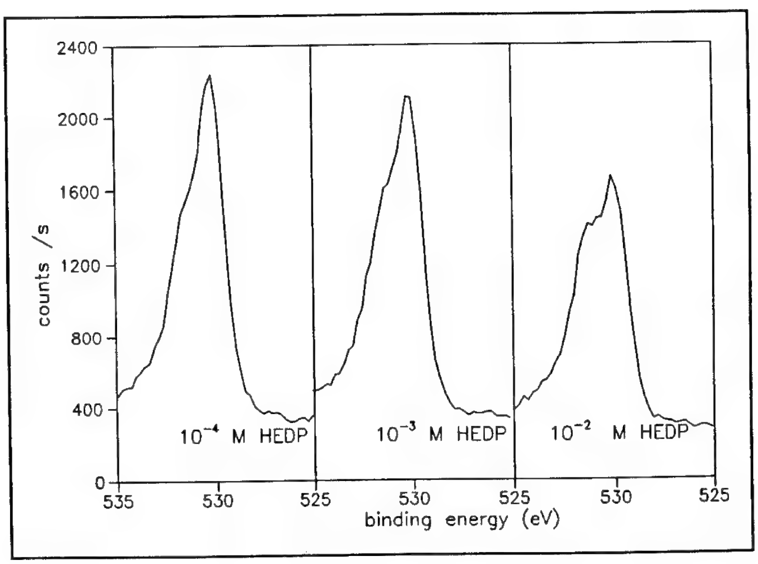

Fig.4. O 1s spectra of mild steel samples after treatment with different HEDP test solutions

Fig. 5. shows the time dependence of the Fe 2p spectra in the presence of the 10^{-2} mol dm^{-3} HEDP test solutions. The ratio of metallic state of Fe to oxygen containing iron compounds was increased with time.

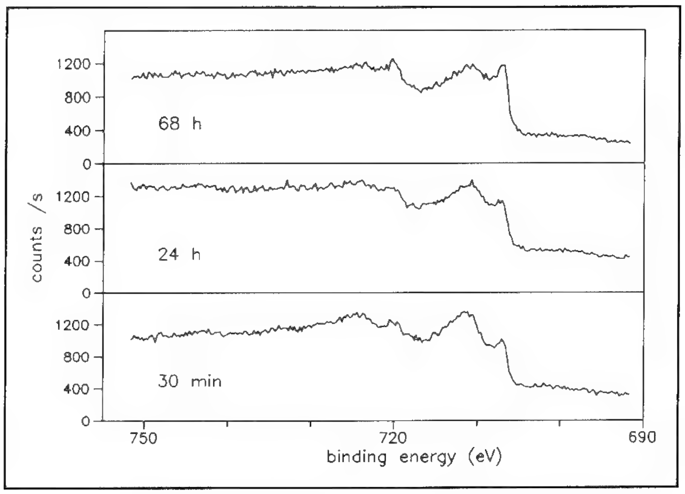

Fig. 5. Fe 2p spectra of mild steel samples treated in 10^{-2} M HEDP solutions at different immersion times

The oxygen containing compounds were decreased with time treated in 10^{-2} mol dm^{-3} HEDP.

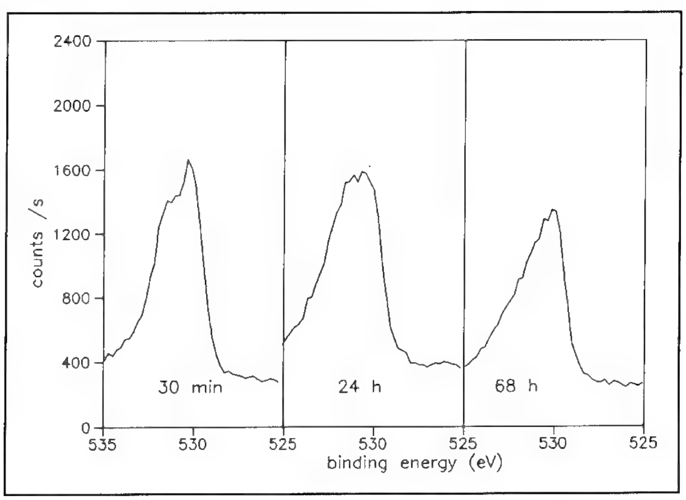

Fig. 6. O 1s spectra of mild steel samples treated in 10^{-2} M HEDP solutions after different immersion times

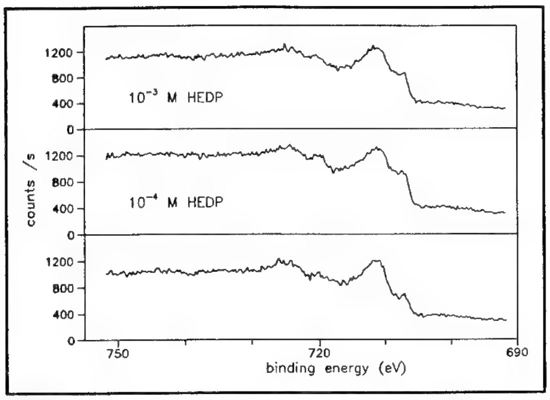

Fig.7. Fe 2p spectra in (a) 10^{-2} M $NaNO_2$; after passivation the samples was immersed in (b) 10^{-4} M HEDP; in (c) 10^{-3} M HEDP

As in Fig. 7. the Fe 2p spectra show in the presence of $NaNO_2$ in 10^{-2} mol dm^{-3} a thin passive layer formed on the metal surface. The signal of the metallic iron is small and the oxide layer is represented by a higher peak.

After passivating the samples by 10^{-2} mol dm^{-3} $NaNO_2$ for 68 hours, the mild steel was immersed into HEDP solutions at different concentrations for 30 minutes. The signal representing the metallic state of Fe was increased by the treatment with HEDP test solutions independently from their concentrations.

The signal of the oxide state was broadened comparing with the passive state.

Based on the O 1s spectra the ratio of different iron oxide can be predicted. The $FeOOH/Fe_2O_3$, Fe_3O_4 ratio increases with increasing HEDP concentrations. We conclude that because of the HEDP treatment the ratio of the different iron oxide forms changes.

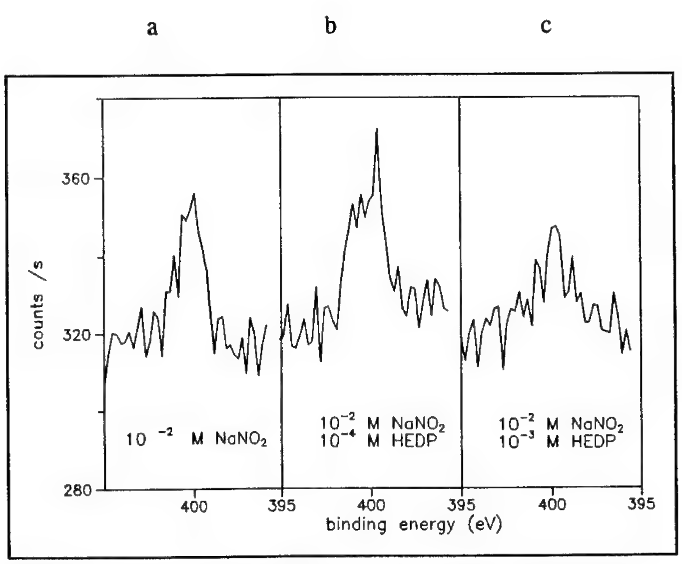

Fig.8. N 1s spectra in (a) 10^{-2}M $NaNO_2$; after passivation the samples was immersed in (b) 10^{-4}M HEDP;in (c) 10^{-3}M HEDP

On the basis of the N 1s spectra, NH_3 and its compounds were detected. The quality of the N-compounds were not changed through the HEDP treatment. Because nitrite could not be detected on the surface we can conclude the following passivation mechanism:

$$NO_2^- + 8H^+ + 6e^- = NH_4^+ + 2H_2O \tag{1}$$

$$6Fe(OH)_2 + NO_2^- = 3Fe_2O_3 + NH_4^+ + 3H_2O + 2OH^- \tag{2}$$

Table 1.

Sample	P KLL intensity
10^{-4} M HEDP/30 min	517
10^{-3} M HEDP/30 min	573
10^{-2} M HEDP/30 min	730
10^{-2} M HEDP/68 h	758
10^{-2} M $NaNO_2$ 68 h/10^{-4} M HEDP 30 min	541
10^{-2} M $NaNO_2$ 68 h/10^{-3} M HEDP 30 min	774

The P KLL signals in the surface layer were increased by increasing the HEDP concentration in the test solutions.
Further studies are in progress.

Acknowledgement - The authors thank for Dr. I. Cserny for the XPS measurements, the technical help of Dr. I. Bakó and Mrs. E.V. Király and the useful discussions of Dr. I. Cserny, Prof. A. Vértes, Prof. G. Pálinkás.
The supports of OTKA No. B 011082, JOULE E.C. programme No. 0501 and Copernicus E.C. programme No. CIPA-CT93-0120 are gratefully acknowledged.

Film Properties and their Modification

Materials Science Forum Vols. 185-188 (1995) pp. 367-376

Passivity of metals and alloys and its breakdown - New results from new non-electrochemical techniques

J. Kruger[1], L.A. Krebs[1], G.G. Long[2], J.F. Anker[2,3] and C.F. Majkrzak[2]

[1] The Johns Hopkins University, Baltimore, MD 21218, U.S.A.

[2] National Institute of Standards and Technology (NIST), Gaithersburg, MD 20899, U.S.A.

[3] Currently at The University of Missouri, Rolla, MO 65401, U.S.A.

Keywords: Passivity, breakdown of passivity, Fe, FeCr alloys, AlTa alloys, x-ray absorption spectroscopy, neutron reflectivity, dynamic imaging microellipsometry (DIM)

Abstract

In recent years a number of new techniques have been applied to the study of the solid-liquid interface. Some of these relatively new techniques have been applied to the study of the passive film and its breakdown. These non-electrochemical tools can carry out investigations of the formation, dissolution, and properties of passive films during growth and breakdown. The following techniques are considered:

(1) *Spin Polarized Neutron Reflectivity* - Using thermal neutrons as probes, the thickness of passive films, the interfacial roughness, and film magnetic properties can be measured. Spin polarized neutrons were used to in an attempt to determine whether the passive film on Fe is ferromagnetic (Fe_2O_3) or not ($\gamma FeOOH$).

(2) *X-ray Absorption Spectroscopic (XAS) Techniques* - These techniques can examine the pre-edge, near-edge (NEXAFS or XANES), or post-edge (EXAFS) regions of the x-ray adsorption edge of an element relevant to a passivity study. XAS at the chlorine K-edge was applied in an *ex situ* study of the breakdown of passive films on Fe and FeCr alloys.

(3) *Dynamic Imaging Microellipsometry (DIM)* - DIM acquires *in situ* ellipsometric data on thickness and optical constants of surface films at a spatial resolution of around 20μm using a radiometric full-field approach. The DIM study investigated the formation of passive films on microstructural features present in AlTa alloys that affect breakdown.

The real voyage of discovery consists not in seeing new landscapes but in having new eyes.
Marcel Proust

Introduction

Recent years have seen the application of a number of new non-electrochemical techniques (see [1]) to studies of passivity — a phenomenon the great British scientist, Michael Faraday, referred to as "a peculiar condition of iron" and characterized as "this very beautiful and important case of voltaic condition presented to us by the metal iron" [2].

This paper will describe the application of three relatively new techniques ("new eyes") to studies ("voyage[s] of discovery") of passivity and its breakdown. Some, but not all, of these non-electrochemical tools can be used to carry out in-situ studies of the formation, dissolution, and

properties of passive films during growth or breakdown.

The first of these techniques is spin polarized neutron reflectometry which we have recently applied in an in-situ study of the passive film on Fe [3]. In this technique thermal neutrons are used to probe the nuclear and magnetic scattering density profiles of the passive film and the substrate upon which it grows to establish parameters for the metal-film and film-solution interfaces. The thickness of the passive layer, interfacial roughness, and film magnetic properties are some of the parameters that can be measured. A study employing spin polarized neutrons to characterize the passive film on iron will be described.

The next technique, actually a group of techniques, considered is x-ray absorption spectroscopy. These techniques can examine the pre-edge, near-edge (NEXAFS or XANES), or post-edge (EXAFS) regions of the x-ray absorption edge of an element relevant to a study of a passive film. An ex-situ study of the breakdown of the passive films on Fe and an FeCr alloy at the Cl K-absorption edge will be discussed.

The last technique to be considered is dynamic imaging microellipsometry (DIM). This technique acquires ellipsometric data on the thickness and optical constants of surface films at a spatial resolution of around 20μm using a radiometric full-field approach [4]. This capability provides the opportunity to carry out ellipsometric studies on individual microstructural features on a metal or alloy surface. A DIM investigation of the formation of passive films on the microstructural phases that are present in AlTa alloys was performed in an attempt to obtain a better understanding of the superior resistance to breakdown exhibited by sputter deposited AlTa alloy films.

Spin Polarized Neutron Reflectivity

The neutron reflectometry technique enables the study the passive film at the film surface and the film-metal interface, both in-situ and ex-situ. Using this technique it is possible to obtain information on the characteristics of the passive film thickness, surface and interfacial roughness, and profiles of the nuclear and magnetic scattering densities. X-ray reflectivity measurements can be employed to complement the neutron reflectivity data.

The use of spin-polarized neutrons to probe the scattering densities of the passive layer allows the determination, for example, of whether the film is ferromagnetic. One x-ray absorption spectroscopic study [5] suggests that the passive layer on iron is Fe_3O_4 or, more likely, γFe_2O_3 (ferromagnetic), while another [6] points to γFeOOH (not ferromagnetic). This is an important issue because if the magnetic nature of the passive film on iron were determined, it would provide an important basis for deciding which of the many possible models of the passive film on iron (for example, the models described by Cohen [7]) more closely reflect the structure and composition of the film on iron. By collecting data on the native oxide, the in-situ passive film, and the same film ex-situ, neutron reflectivity measurements can also be used to explore changes in films that are removed from solution and dried after passivation.

The equations governing neutron reflectivity are similar to those for electromagnetic optics. Descriptions of neutron reflectivity theory and techniques are available from several sources [8-11].

Experimental

A neutron beam can travel through materials such as single crystal silicon with a negligible amount of attenuation or small angle scattering. The samples and electrochemical cell were

designed to take advantage of this fact, allowing the attenuation and increased background signal resulting from inelastic and incoherent scattering in an aqueous medium to be minimized. The specimen consists of a 12 nm layer of iron sputter-deposited onto a 10 cm-diameter single crystal Si wafer and the neutron beam enters from the back of the crystal.

The iron surface with its native oxide intact provided the starting point for study. First x-ray, then spin-polarized neutron reflectivity data were taken for this case. Next, neutron reflectometry was performed on the passivated surface in-situ. Finally, the sample was removed from the cell, rinsed with purified water, and dried quickly in a stream of N_2 gas for the ex-situ passive film data collection, using first neutron, then x-ray techniques. The native oxide and the ex-situ passive film were both exposed to the ambient environment for the duration of the data collection, roughly 12 hours for each neutron reflectivity scan.

The sample was clamped to a polytetrafluoroethylene cup fitted with a Pt counter electrode and a saturated calomel reference electrode (SCE) to form the body of a sealed electrochemical cell approximately 100 ml in volume. Ex-situ data were collected on the air-formed oxide, using the technique described below, before the cell was filled with the solution. The solution was a pH 8.2 borate buffer, made oxygen-free by bubbling water-saturated N_2 gas through the holding vessel before transferring the solution to the cell. After cathodically reducing the native oxide film on the surface for seven minutes (a time found sufficient in earlier studies to reduce the film while avoiding any significant entry of hydrogen into the iron) at -1.0V, the system was stepped to a passivating potential of + 0.750V. Neutron reflectivity data were collected after the initial film growth phase was completed, as indicated by the leveling off of the current density at a suitably low value (about 0.1 μA/cm2). Data collection continued over a period of roughly 12 hours while the system was held under potentiostatic control.

Data were taken on the BT-7 polarized neutron reflectometer [12] at the National Institute of Standards and Technology (NIST) Research Reactor in Gaithersburg, MD. The details of the experimental procedure for the acquisition of spin polarized neutron reflectivity data are given elsewhere [3]. X-ray reflectivity scans were also performed using a stationary anode x-ray machine. X-rays of wavelength 1.54Å were used to examine the iron surface with its native oxide. The identical examination was performed again on the ex-situ passive layer after the neutron reflectivity scans were completed. While x-rays and neutrons scatter from electrons or atomic nuclei respectively, the data sets can be handled in the same fashion, resulting in complementary scattering density profiles for the sample in the ex-situ cases. These data are especially helpful in confirming layer thickness and interfacial roughness parameters.

Results and Discussion

Figs. 1 and 2 show the most recent data for the electrochemically produced in-situ passive film. The results from the rinsed and dried ex-situ passive film on the iron are almost identical to the in-situ data. The data are given in terms of the momentum transfer Q versus the reflected intensity on a logarithmic scale. Q is related to the incident angle θ by the expression, $Q = 2k_0\sin\theta$, where k_0 is the incident wavevector magnitude. During all neutron measurements the sample was exposed to a magnetic field of 225 G parallel to the plane of the surface. The two plots indicate the reflectivities of neutrons polarized parallel to the applied magnetic field, or "spin-up" (Fig. 1), and those polarized anti-parallel, or "spin-down"(Fig. 2). The air-formed film (not shown) differed from the passive film.

Using the reflectivity modelling program developed by Ankner and Majkrzak [12], models were constructed for three data sets. The sample was first examined in its "as received" condition to

obtain values for the iron layer thickness, the air-formed film thickness, and the interfacial roughness. These data, which were independent of any magnetic moment in the sample, were used to complement the spin-polarized neutron reflectivity data of the same surface film. The models based on these data were used to characterize any features of the sample and substrate that were not expected to change during or participate in passivation (e.g., interfacial mixing at the Si/Fe interface). Next, the oxide was reduced and a passive film was grown. In-situ neutron reflectivity data for the two spin-states were then collected, and are discussed below.

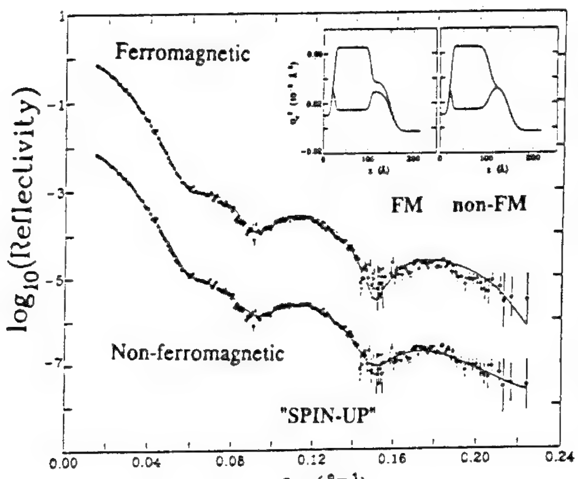

Fig. 1. Spin polarized neutron ("spin-up") reflectivity data (points) compared to data from the models for ferromagnetic and nonferromagnetic oxide films (solid lines) shown in the inset in upper right corner for in-situ passive films on a 100 Å Fe substrate layer deposited on Si.

Although the parameters describing the silicon crystal and the iron layer had the expected values, an interesting problem arose in fitting a model to the passive film. After exhaustive attempts at fitting the data by adjusting the value of the nuclear and magnetic scattering densities of the passive film, two acceptable models emerged, and are shown in Figs. 1 and 2. By examining these figures, one can see that both models appear to give good fits to the data. By observing the density profile insets, however, the difference in the two models becomes clear. In the left-hand inset (FM) of Fig. 1 or 2 the passive film has a magnetic moment associated with it, while in the right-hand inset (NFM) the film is modelled without a moment. The parameters for these models are compared in Table 1.

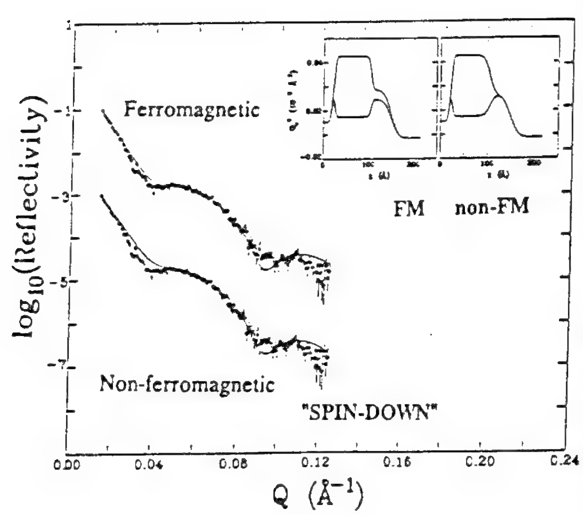

Fig. 2. Same as Fig. 1 but "spin-down".

We see that the Q_c, the Q value that is characteristic of a given medium when $\theta = \theta_c$, for the passive film is closer in value to that of Fe_3O_4 for the ferromagnetic model and halfway between the Fe_3O_4 and $\gamma FeOOH$ values for the non-ferromagnetic model. While this may indicate a somewhat less dense spinel-type (Fe_3O_4 or γFe_2O_3) composition for the passive film, the question of magnetic scattering density has not been definitively resolved.

Table 1. Passive film model parameters based on spin polarized neutron reflectivity data. Q_c^2 is directly proportional to the combined nuclear and magnetic scattering density, ρ. ($Q_c^2 = 16\pi\rho$)

	Ferromagnetic Model	*Non-Ferromagnetic Model*
Thickness	44.5 Å	43.6 Å
Surface Roughness	29.2 Å	30.4 Å
Interfacial Roughness	9.0 Å	20.1 Å
Q_c^2, "spin-up"	$3.75\text{x}10^{-4}$ Å^{-2}	$3.26\text{x}10^{-4}$ Å^{-2}
Q_c^2, "spin-down"	$2.95\text{x}10^{-4}$ Å^{-2} *"different"*	$3.26\text{x}10^{-4}$ Å^{-2} *"same"*
Fe_3O_4 Q_c^2, "spin-up"	$4.24\text{x}10^{-4}$ Å^{-2}	
Q_c^2, "spin-down"	$2.77\text{x}10^{-4}$ Å^{-2} *"different"*	
γFeOOH Q_c^2, "spin-up"		$2.364\text{x}10^{-4}$ Å^{-2}
Q_c^2, "spin-down"		$2.364\text{x}10^{-4}$ Å^{-2} *"same"*

Based on the theoretical models for γFe_2O_3 and γFeOOH films on Fe, and on the models that were directly fit to the data, the in-situ passive film on iron seems to have a scattering density close to that of a spinel-like oxide (Fe_3O_4 or γFe_2O_3). However, a magnetic scattering density could neither be confirmed nor ruled out by the fit to the data. While a measurable magnetic moment in the passive film would have been an definite indication of a ferromagnetic oxide, a lack of magnetic moment in the film may mean many things.

Water incorporated in the film would reduce the overall scattering density, which may account for the film having a scattering density less than that of Fe_3O_4. This may also affect our ability to measure a small magnetic moment that may be present. Finally, it has been observed by Brett and Graham [13] that γFe_2O_3 becomes superparamagnetic when it is very thin (~16 Å), but we do not believe the passive film is less than 30 Å thick.

We conclude that although the data hints at a somewhat less dense Fe_30_4-like oxide for the passive film, an γFeOOH-type structure cannot be ruled out. Thus, despite examination by an extremely sensitive in-situ technique, it has not been possible to carry out a complete characterization of the passive film on iron.

X-Ray Absorption Spectroscopy

XAS offers a direct surface-sensitive measurement of the structure, composition, and electronic properties of passive films on alloys. A description of the application of the technique to ex-situ studies of passive films and their breakdown is given elsewhere [14]. We measured the x-ray fluorescent and the electron total yield signals at the Cl-K edge on the passive films on Fe and a Fe-24%Cr alloy up to the end of the induction period and at the onset of breakdown. The Cl-edge is more relevant to breakdown than the O-edge used earlier in a study using the reflEXAFS technique [15].

Experimental

Two samples of each passivated metal were prepared, one which had been exposed until

just before breakdown occurred and one for which the passive film was removed from the solution just after the onset of breakdown. In both cases the specimens were carefully rinsed in deionized water after removal from the solution containing chloride ions. The films were grown on Fe and an Fe-24%Cr alloy by potentiostatic anodic oxidation in a deaerated borate-buffer solution (pH 8.4) at a potential of 0.750V (SCE) for 3-5 hours. The spectra obtained from these passive layers were then compared to the spectra for the same films exposed to borate-buffer solution, to which Cl^- ions were added after passivation. The final concentrations of the Cl^- were 0.005M for Fe and 0.009M for the FeCr alloy. The passivated surface was held at 0.750V, a potential above the breakdown potential for all of the metallic surfaces studied. The specimens were removed from the solution and rinsed as soon as possible either after a slight rise in current signaled the end of the induction period for breakdown (spectra labeled "End of Induction") or after the current increased ten-fold after the end of the induction period (spectra labeled "Breakdown of Passivity").

The samples were examined by using x-ray fluorescence and total electron yield above the chlorine K-edge. We believe that as the chloride ions attack first the passive film and then the metal itself, its bonding and coordination change and these changes are reflected in the measured spectra. By comparing our data with spectra from known materials, we can obtain electronic bonding and coordination information.

Results and Discussion

Fig. 3 compares the spectra obtained at the Cl K-edge for the passive film on Fe exposed up to end of the induction period and directly after breakdown. Exposure to chloride ions affects the Cl K-edge spectra of the films differently during and after the induction period when the onset of breakdown has occurred. Fig. 4 shows the same measurements made on a passive film on the FeCr alloy where the same general effects were observed but to a lesser extent for the films on the alloy. This agrees with earlier ellipsometric studies by McBee and Kruger [16].

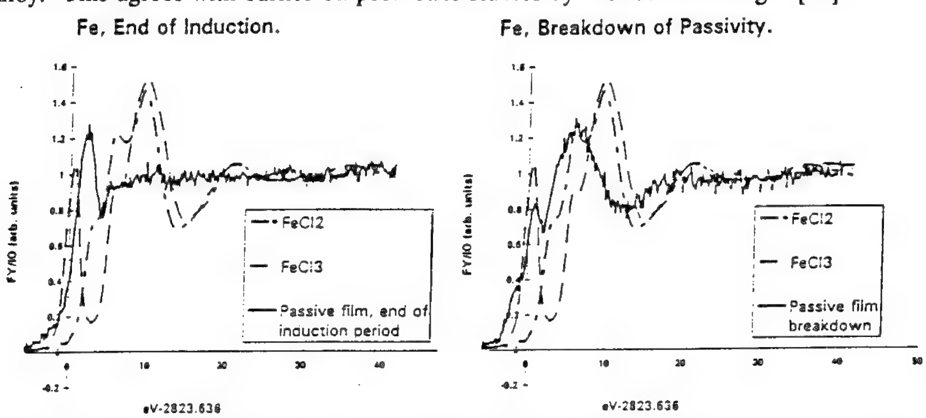

Fig. 3 NEXAFS spectra at the Cl K-edge for the passive film on Fe undergoing breakdown in a borate-buffer (pH 8.4) solution containing 0.005M Cl^- at 0.750V (SCE) compared to the spectra of the model compounds $FeCl_2$ and $FeCl_3$.

A comparison of the passive film data and the relevant standards is also given in Figs. 3 and 4. These figures show the spectra for the induction period and breakdown conditions for passive films on Fe and the FeCr alloy compared to those for $FeCl_2$ and $FeCl_3$. Although $CrCl_2$ and $CrCl_3$ were also measured, the results showed that the iron chlorides are the relevant standard compounds for the breakdown of the passive film on the FeCr alloy.

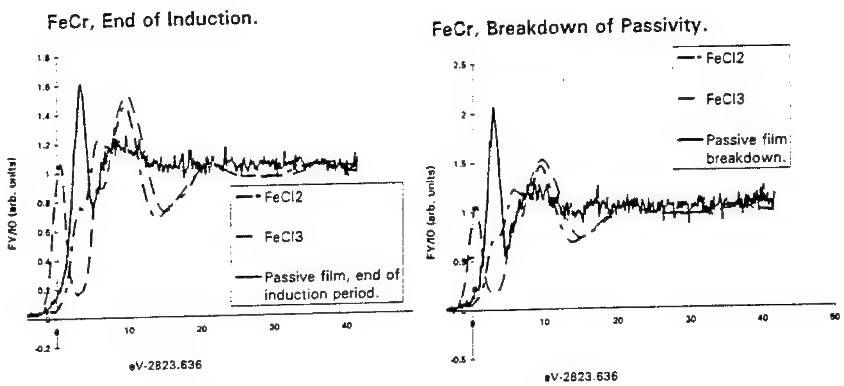

Fig. 4 NEXAFS spectra at the Cl K-edge for the passive film on Fe24Cr undergoing breakdown in a borate-buffer (pH 8.4) solution containing 0.009M Cl^- at 0.750V (SCE) compared to the spectra of the model compounds $FeCl_2$ and $FeCl_3$.

Looking at the first peak, induction period film on Fe has a peak closer to $FeCl_2$ than to $FeCl_3$. At the onset of breakdown this peak shifts towards $FeCl_3$. The same effects were also observed for the films on the FeCr alloy. There appears to be no useful data after the first peak for the passive film on Fe prior to breakdown, whereas the film on Fe after breakdown and the films on FeCr, both before and after breakdown, have spectra that exhibit oscillations after the first peak. These data are currently being modeled to determine the coordination of the chloride ion in these films to order to decide whether the Cl^- is on or in the passive film during the induction period that leads to breakdown.

Dynamic Imaging Microellipsometry (DIM)

Since it has been shown in recent years by, for example, Shaw et al. [17] that sputter deposited solid solution aluminum transition metal (Cr, Mo, Ta, W and others) alloy films have dramatically higher values for the pitting potentials, E_{pit}, the objective of this study was to try to gain a better understanding of the origins of the enhanced passivity and resistance to breakdown that leads to the initiation of pitting exhibited by these nonequilibrium materials. There have been a number of suggested mechanisms [18-20] proposed to explain this effect. Missing from these proposed mechanisms is the role of the oxide film, that forms on the matrix and precipitate materials in the initiation of pits and this, then, was the purpose of this study.

This paper describes the application of an in-situ technique, DIM, [4], to a study of the effect of a microstructural feature (the Al_3Ta precipitates that form in Al-Ta alloys) on passive film formation and breakdown. (A more detailed description of the application of this technique to studies of the Al-Ta system is given elsewhere [21].) While these precipitates are not observed in the presumably solid solution sputtered alloy films, exceedingly small precipitate nuclei may serve as the sites where pits are initiated. This paper seeks to examine the role, if any, played by Al_3Ta precipitates in the pitting process using DIM. To do this bulk Al-Ta alloys with large precipitates have been used.

Experimental

The technique used in this study, DIM, was developed to overcome the drawback of traditional ellipsometry which is a surface averaging technique and is limited in its ability to study localized corrosion processes such as the effects of microstructure on passive film growth and breakdown. Cohn et al. [4] developed DIM in order to overcome the above limitation.

To use DIM to examine *in situ* passive film formation and breakdown processes at a resolution level of the microstructures existing in an Al-Ta alloy, it was necessary to prepare an alloy that contained Al_3Ta precipitates whose size was within the detectability of DIM, 20 μm. An Al-1.5 a/oTa alloy was prepared that provided two of the microstructural features existing in Al-Ta alloys that are relevant to the study of localized passive film formation and breakdown, Al_3Ta and the dealloyed region adjacent to the A_3Ta precipitates.

Results and Discussion

Fig. 5 plots the change in film thickness vs. applied potentials. Note that at 0.0 volts the thickness of the passive film on the precipitate is approximately twice that of the matrix, at around 1.0 V the thicknesses are approximately equal and at 2.0 V, however, the film thickness over the matrix is greater than that over the precipitate. It would have been expected that the precipitates form thinner films at all applied potentials owing to enrichment by a highly protective Ta_2O_5 in the passive layer and, indeed, thinner films do form on the precipitate at higher potentials (2.0 V and above) but not at low potentials (below 0.0V). At present this is not understood.

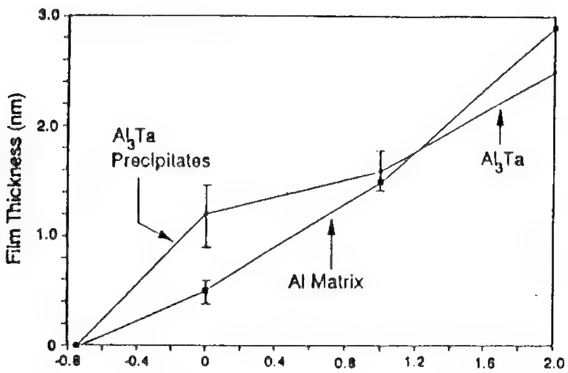

Fig. 5 Change in barrier-layer thickness vs. applied potential for the Al_3Ta precipitate and the Al matrix. Note that the thicknesses become equal at around 1.0 V. From [21]

In order to relate the experimental results to sites where breakdown leading to pit initiation takes place, the Al-1.5Ta alloy containing large Al_3Ta precipitates used in the DIM study was polarized potentiostatically to two potentials, 0.0V SCE (where the thickness of the film on the precipitate differed from that on the dealloyed region) and 1.0V (where the precipitate and matrix films were nearly equal in thickness) for 15 minutes to form barrier layer passive films. After the polarization the alloy was open-circuited and returned to E_{corr}. This took approximately 15 minutes. The samples were then removed from a buffered borate (pH 7.2) solution and immersed in an identical solution containing 0.1M NaCl and the alloy was polarized to -0.5V (approximately 0.25V above the pitting potential) to allow pits to initiate and propagate.

At the 0.0V (thicknesses unequal) it is likely that an incoherent interface exists between the two films that is susceptible to localized attack [23]. Local strains or flaws such as dislocations at the interface may promote the Cl^- adsorption or ingress that leads to breakdown. This hypothesis is supported by Fig. 6. This micrograph clearly shows the preferential dissolution of Al around a Al_3Ta precipitate. When, however, the barrier layers are nearly equal at 1.0V, approximately half of the pits were located at the interfaces between the matrix and the Al_3Ta (Fig. 7), suggesting

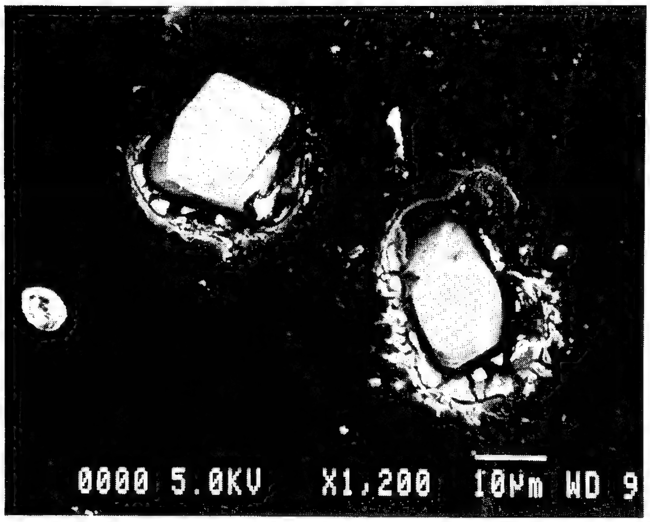

Fig. 6 SEM photomicrograph of the preferential dissolution of Al around Al_3Ta precipitates after 48 h immersion in aerated 0.1 M NaCl, pH 5, at E_{corr}, a potential that is < 1.0 V SCE at which the films on the Al_3Ta and Al have unequal thicknesses. The bright white "specks" are the result of charging and not additional precipitates or impurities. From [22]

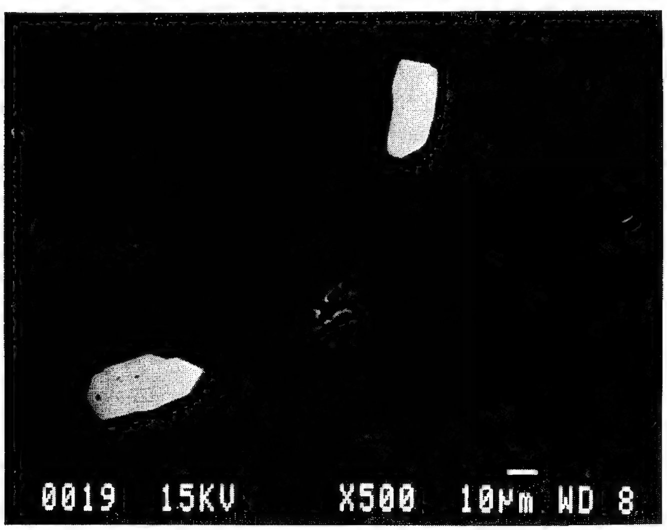

Fig. 7 SEM photomicrograph of pitted sample held at 1.0 V SCE, a potential at which the films on the Al_3Ta and Al have equal thicknesses. Pitting occurs in the Al matrix at sites away from the precipitates. From [21]

that the flaw density at the precipitate/matrix interface is probably lower for the film sample polarized at 0.0V.

This study suggests that the role played by the nonequilibrium structure of AlTa alloy films on promoting superior resistance to breakdown is to inhibit the formation of Al_3Ta precipitates. Breakdown initiates at defects in the passive film formed at the precipitate/matrix boundary. This is so because the film thickness of the film on the precipitate differs from that on the matrix. At potentials where the films have equal thicknesses, breakdown usually occurs at sites away from the precipitate/matrix interface.

Acknowledgments

The authors are grateful to the National Science Foundation, the Office of Naval Research, and the National Institute for Standards and Technology who supported this research.

References

[1] J. Kruger, Nature of Surface Films in "Synchrotron Techniques in Interfacial Electrochemistry", Proceedings of NATO Adv. Res. Workshop, Funchal Madiera, Portugal, Dec. 14-18, 1992, C.A. Melendres and A. Tadjaddine, Editors, Klewer Acad. Pub., Amsterdam, 1994, pp. 33-66.
[2] M. Faraday, "Experimental Researches in Electricity", Vol. 2, London, 1844, p. 250.
[3] L.A. Krebs, J. Kruger, G.G. Long, J.F. Ankner, C.F. Majkrzak, S.K. Satija, D.G. Wiesler, Proc. 12th Int. Cong. on Corr., Nat. Assoc. Corr. Engr., Houston, Vol. 5B, 1993 p.3863.
[4] R.F. Cohn and J.W. Wagner, Appl. Opt., 28, 3187 (1989).
[5] G.G. Long, J. Kruger, J. Kuriyama, M. Black, E. Farabaugh, D.M. Saunders, and A.I. Goldman, in Proc. 9th Int. Cong. on Met. Corr., Nat. Res. Council, Ottawa, Vol. 3, 1984, p. 419.
[6] J. Robinson, in "X-Ray Methods in Corrosion and Interfacial Electrochemistry", Davenport and Gordon, Eds., Electrochem. Soc., Pennington, NJ, Vol. 92-1, 1992, p. 239.
[7] M. Cohen, in "Passivity of Metals", Frankenthal and Kruger, Eds., Electrochem. Soc., Pennington, NJ, 1978, p. 533.
[8] C.F. Majkrzak and G.P. Felcher, Mater. Res.Soc. Bull., 15, 11, 65 (1990).
[9] J. Penfold and R.K. Thomas, J. Phys. C, 2, 1369 (1990).
[10] T.P. Russell, Mat. Sci. Rep., 5, 171 (1990).
[11] C.F. Majkrzak, Physica B, 173, 75 (1991).
[12] J.F. Ankner and C.F. Majkrzak, in "Neutron Optical Devices and pplications," Vol. 1738, SPIE Conference Proceedings, in press.
[13] M.E. Brett and M.J. Graham, J. Magnetism & Mag. Mat., 60, 175 (1986).
[14] G.G. Long and J. Kruger, Surface X-ray Absorption Spectroscopy. EXAFS and NEXAFS, for the In-situ Study of Electrodes, Chapt. 4 in Techniques for the Characterization of Electrodes and Electrochemical Processes, R. Varma and J.R. Selman, Editors, John Wiley & Sons, New York, 1991, pp. 167-209.
[15] J. Kruger, G.G. Long, Z. Zhang, and D.K. Tanaka, Corrosion Sci., 31, 111 (1990).
[16] C.L. McBee and J. Kruger, in "Passivity and its Breakdown", Staehle and Okada, Eds., Nat. Assoc. Corr. Engrs., Houston, 1976, p.131.
[17] B.A. Shaw, T.L. Fritz, G.D. Davis and W.C. Moshier, J. Electrochem. Soc., 137, 1317 (1990).
[18] P.M. Natishan, E. McCafferty and G.K. Hubler, J. Electrochem. Soc., 135, 321 (1988).
[19] G.D. Davis, W.C. Moshier, T.L Fritz and G.O. Cote, J. Electrochem. Soc., 137, 422 (1990).
[20] Z. Szklarska-Smialowska, in "Critical Factors in Localized Corrosion", Frankel, and Newman, Eds., Electrochem. Soc., Vol 92-9, Pennington, NJ, 1992, p. 311.
[21] C.C. Streinz, P.J. Moran, J.W. Wagner, and J. Kruger, J. Electrochem. Soc., 141, 1132 (1994).
[22] R.S. Lillard, Ph.D. Dissertation, The Johns Hopkins Univ., Baltimore, MD, 1993.
[23] W. Ostwald, Z. Phys. Chem., 34, 495 (1900).

Materials Science Forum Vols. 185-188 (1995) pp. 377-388

Microscopic modification of passive films on metals: Preparation of defined profiles and their analysis

J.W. Schultze

AGEF e.V., Institut an der Heinrich-Heine-Universität Düsseldorf, D-40225 Düsseldorf, Germany

Keywords: Modification, defined profile, thickness gradient, concentration gradient, grain boundaries, ion implantation

Abstract

Passive films can be characterized by profiles of their properties P(x,y,z) depending on lateral (x,y) or normal (z) coordinates. Thus, lateral (dP/dx) and normal (dP/dz) gradients can be obtained. Modification consists of the preparation of intended, specific profiles. A new challenge is given by the microscopic preparation of defined profiles within the range of micro- or nanometers.

As a first example, profiles of layer thickness l and the dimensionless gradients dl/dx are discussed. They range from 10^{-6} to 10^{3}. Natural gradients at grain boundaries or pit edges are compared with artificial gradients which can be prepared in the same order of magnitude.

Concentration profiles can be prepared in direction of x and z. While normal concentration gradients can easily be prepared up to 10^{30} cm^{-4}, the production of lateral profiles is limited to microscopic dimensions yielding gradients up to 10^{25} cm^{-4}.

1. Introduction

Many problems of passivity arise from inhomogeneity of their properties: layer thickness l, concentrations c, resistances R or others change due to substrate structures, impurities, or inhomogeneous passivation. Describing a special property P by its dependence on coordinates lateral (x,y) and normal (z) to the surface, passive films may be described by profiles P(x,y,z) or their gradients dP/dx or dP/dz. Modification of passive films consists of a preparation of defined values of P and dP. This is important for problems of corrosion protection in macroscopic dimensions. For advanced studies, fundamental research or high tech systems, a microscopic or even nanoscopic defined preparation is of great value. Limitations are caused by the resolution of the preparation technique and that of the analysis of the film as well.

Inspite of a large number of investigations and great experimental progress /1-5/, there is no straightforward description of such modifications. Therefore, in this paper the definition, preparation and analysis of defined profiles will be discussed and explained by various examples. The influence of these profiles on the electrochemical behaviour of such films, i.e. ion (ITR) and electron (ETR) transfer reactions is only briefly illustrated. Microscopic modifications are emphasized. In general, we have to distinguish non-modified (or original) passive films from artificial, modified films.

2. Thickness profiles and gradients

At first, lateral profiles of layer thickness l(x) will be described. Fig. 1a shows some typical examples of thickness profiles l(x). l (or z) may depend on the local properties of the substrate, environment or the preparation, respectively. Thickness gradients dl/dx may occur in systems with temperature or concentration gradients, flowing systems etc. They are dimensionless and may be in the order of magnitude between 10^{-6} and 10^{3}.

2.1 Analysis of thickness profiles

The determination of thickness is possible with various electrochemical, spectroscopic and other methods. The resolution in depth (z) is often very good, since even monoatomic layers can be detected. The lateral resolution (x), however, is much smaller. Fig. 1b shows a rough survey. Coulometry is only applicable for the whole electrode, while advanced techniques as the Kelvin probe or the Scanning Electro Chemical Microscope SECM allow an analysis in microscopic dimensions. Optical signals can be focussed down to the um range. In general the resolution is given not only by the diffraction limit of about 1 μm, but also by intensity, geometric conditions and others. The resolution of microellipsometry is excellent in depth, but low in direction of x, about 50 μm. That of reflectometry is better in x, (10 μm), but less in depth. Due to the good focussing, laser analysis is possible down to 1 μm. A detailed description is given in /6/. With electronic techniques, e.g. the Scanning Electron Microscope, SEM, the Atomic Force Microscope AFM, and the Tunneling Microscope, STM, a resolution in the nm range is possible. These methods refer, however, to the surface topography but not to the real layer thickness.
Correspondingly, the determination of thickness gradients is limited, too. While typical differences of l are only in the nm range, the resolution of optical or spectroscopic measurements is in the μm range. Hence, for dl/dx a value of 10^{-2} is an upper value which can be determined by optical techniques. A higher thickness gradient of passive films up to 1 can be analysed by new SXM techniques, e.g. STM. The SEM allows the determination of gradients up to 10^{3}, e.g.in the cross sections of porous oxide films.

2.2 Non modified passive films

Traditional treatments of passivity presume homogeneous films with a thickness independent of x, i.e. dl/dx = 0. In practical corrosion systems, however, even small changes of pH, temperature, potential, flow rates etc. may cause correspondent changes of l, at least some nm/mm, i.e. dl/dx = 10^{-5} or more. Small visible thickness gradients often occur at the electrolyte/air interface, while large thickness gradients may exist at the edge of pits.
An important case refers to grain boundaries. For example, on various grains of polycrystalline titanium, film thicknesses were determined by microreflectometry (Fig.2) /6/. They differ from grain to grain by about 30 nm. Since the grain boundary may influence the passive film in a region of some 100 nm, gradients up to 0.1 could be expected. Thickness gradients revealed by the microreflectometry, however, are below 10 nm / 10 μm, i.e. dl/dx = 10^{-3}. This means, that the apparent gradient may be limited by the resolution of the analytical method. On various grains the photocurrent differs, too, which can also be seen in Fig.2. The transients at the grain boundaries have a similar sharpness as the l(x) curves. $i_{ph}(x)$ yields a similar information as l(x), but with a more qualitative character, since i_{ph} depends on the thickness as well as electronic properties of the oxide.

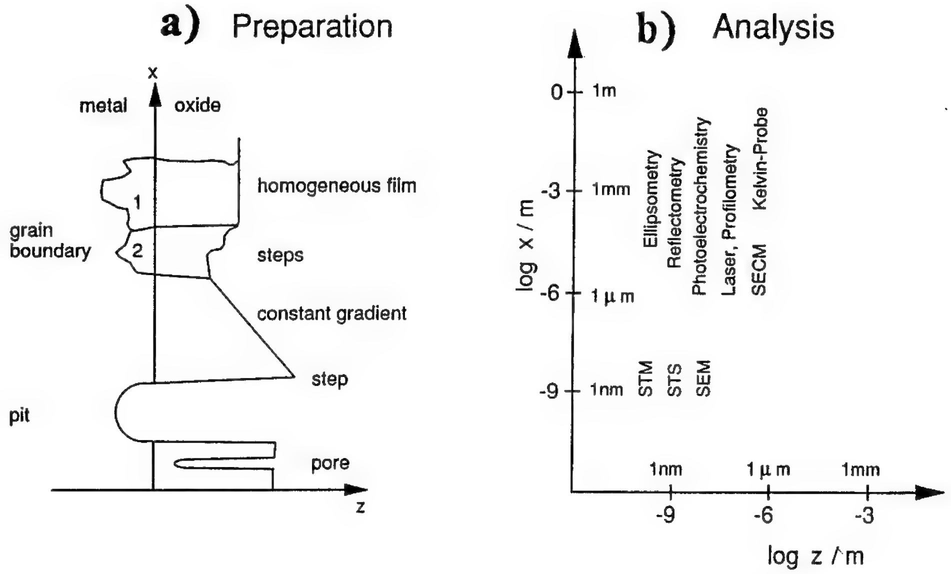

Fig. 1 Thickness profiles: a) Preparation: schematic representation of systems with various thickness profiles and gradients. b) Analysis: double logarithmic plot of lateral (x) and normal (z) resolution of various methods

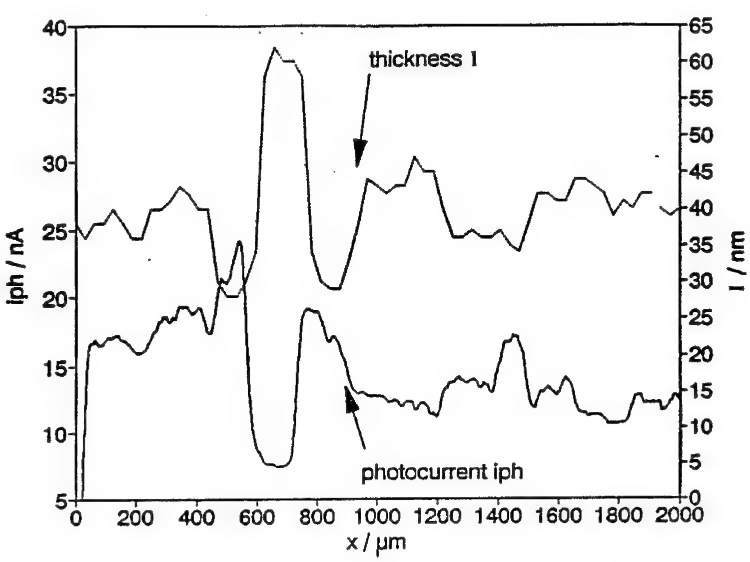

Fig. 2 Laser scanning photocurrent $i_{ph}(x)$ curve across a Ti grain-structure. Potential during the measurement 2 V, average oxide thickness 40 nm, laser power 1 mW, wavelength 257 nm, scan rate 1 μm/s. Local thickness obtained by scanning over the same grain structure with reflection spectroscopy. /6/

Very high thickness gradients should exist in porous oxide films as shown in Fig. 1a. The porous oxide film on Al with $dl/dx \approx 10^3$ /7,8/ can be given as example. The sharpness of the pore walls is given by the special film forming corrosion process. The gradients up to 10^3 can be measured in the SEM. Due to the high aspect ratio, such films can be used for regular nanostructured heterosystems /9/.
Titanium dioxide prepared by chemical oxidation of titanium in NaOH and H_2O_2 is an example of a more statistical porous film of non defined pores in the nm region. A film of a titanium suboxide is formed /10/ which gives an excellent substrate for nickel deposition in the microgalvanic processes, e.g. the Liga process.

2.3 Artificial thickness profiles

In the precious metal industry changing colours are produced on titanium by interference colours, and very small thickness gradients of about 100 nm/cm, i.e. $dl/dx = 10^{-5}$ are obtained.
The local film thickness determines also electrochemical reactions, e.g. galvanic deposition or photoreactions. Hence, for the optimization of processes, the defined preparation of very small gradients is of interest. These can be prepared for example by pulling an partially dipped electrode out of the solution with a defined velocity at simultaneous increase of the potential. In case of Ti, a pulling rate of 10^{-6}m/s at $dU/dt = 10$mV/s yielded a thickness gradient of about $2 \cdot 10^{-5}$. This was necessary to optimize the layer thickness for deposition of Ni /11/.
For microscopic modifications, laser induced oxide growth may be used to prepare definite changes of the local oxide thickness /12-14/. For example experiments with constant laser radiation at increasing potential with a simultaneous shift of the radiated site yielded an increase of film thickness in dependence on the absorption site for various metals. The microscopic picture is shown in Fig. 3 for a Ta electrode. From the interference coulors, thicknesses from 100 to 900 nm were obtained. The gradients are in the order of 0.1 to 2 μm / 100 μm. The upper value of $dl/dx = 2\ 10^{-2}$ was limited by the laser focussing as well as lateral hole diffusion /12,13/.
Fig. 4 shows an AFM profile measured across a laser induced oxide spot on titanium /11/. A gradient of $dz/dx = 0.02$ can be derived from Fig.4. This, however, refers only to the outer profile, the real thickness may be larger by a factor of 2.
Similar experiments were carried out with n-Si which is at anodic potentials only oxidized during simultaneous illumination /15/. The results of reflectometry and laser profilometry are shown in Fig.5. Obtained thickness gradients are in the range of 10^{-3}. The difference to the optimum values of 10^{-2} to 10^{-1} are due to lateral hole diffusion.
Another type of experiment can be carried out by a localized electric field in thin water films condensed from air /16/. Recent experiments with the oxide growth induced by a cathodically polarized tunnel tip yielded a titanium surface modified by oxide formation in the nm region with gradients up to 10^{-1} /16/.

3. Concentration profiles and gradients

In that case again we have to distinguish between artificial and natural concentration profiles c(x,y,z) and gradients dc/dx and dc/dz. Normal concentration profiles have been discussed for some special passive films. For passive iron, for example, the assumption of an inner layer Fe_3O_4 /17/ and an outer layer of Fe_2O_3 corresponds to a concentration gradient $dc_O/dz = 10^{30}cm^{-4}$ of oxygen. This concentration gradient is typical for all passive films on iron. In this paper we will mainly discuss artificial concentration gradients which are determined by the preparation

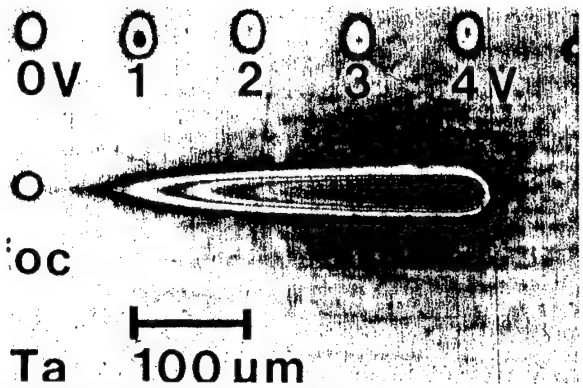

Fig. 3 Localized oxide modification induced by focussed laser light in a locodynamic experiment (0V < $U_{lit}(x)$ < 4V) at mechanically polished Ta/Ta_2O_5 (d_{ox} = 10 nm) in 0.5 M H_2SO_4, P = 3 mW /13/. Interference coulors show that the thickness of the laser induced oxide reaches 900 nm at 4 V.

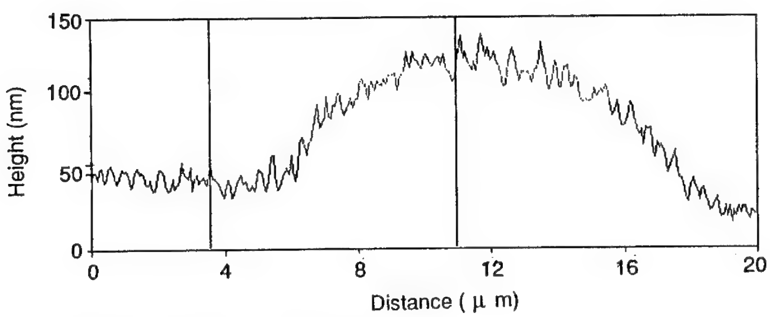

Fig. 4 AFM height profile across a laser modified passive film on Ti.

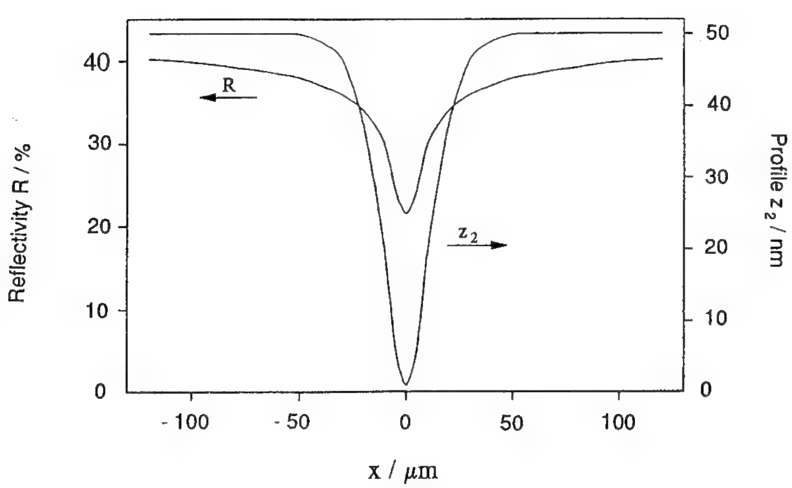

Fig. 5 Ex-situ laser profilometry of laser induced oxide grown on n-Si at 50V. The profile z_2 refers to the outer surface. The reflectivity changes simultaneously /15b/.

technique. In the research on passivity traditionally vertical concentration profiles are intended, while in semiconductor production also lateral concentration profiles are very important. The intended profiles may include sharp steps or weaker profiles broadened by diffusion.

3.1 Analysis

There are various methods of analysis of perpendicular profiles. Chemical analysis is usually not sensitive enough. If the surface film can be reduced, oxidized or corroded, electrochemical methods may be useful. On the other hand, depth profiling by sputtering and simultaneous UHV analysis, especially XPS, is well established for the nm range. Due to preferential sputtering and ion mixing during the sputter process, however, the results are only semiquantitative. Angular resolved XPS improves the resolution. In general concentration profiles up to 10^{30} cm^{-4} can be detected. Rutherford backscattering can be applied for thicker films (> 50nm) and lower gradients.
Lateral profiles may be detected by their chemical or electronic and optical properties. Hence in addition to methods described above, other laterally resolving methods may be applied which are sensitive to such profiles. The resolution of the method, however, is often not as good as the real profile, e.g. the scanning laser photoelectrochemical analysis with its resolution in the um range cannot resolve gradients exceeding 10^{26} cm^{-4}. STM and STS may detect gradients up to 10^{30}, but until now there is no example for passive films.

3.2 Vertical concentration profiles

At first we want to discuss the preparation of normal profiles, i.e. in the z-direction. Artificial profiles can be prepared e.g. by implantation of ions. Since the penetration depth increases with the implantation energy, defined profiles may be obtained which yield interesting layer properties.
As an example, schematic and calculated profiles are shown for the palladium implantation into TiO_2 in Fig. 6 /14/. While the pure TiO_2 film is insulating or n-type semiconducting, the layer becomes conducting at high concentrations of Pd. From a theoretical point of view we may prefer a rectangular profile with a constant concentration of palladium in the total oxide film ("tot" in Fig. 6). Interesting subsystems are represented by a modification only at the inner or outer part ("in" and "out" in Fig. 6). Thus, the film "out" may have interesting ctalytic properties, while the inner layer is an insulator. For a reference in these experiments the non-modified film ("0") and the film radiated without deposition within the film ("through") represent limiting cases. In practice such theoretical profiles can be approached e.g. for 40 nm TiO_2 films by palladium implantation energies ranging from 10 to 200 keV /14/. The passivation was realized at first, then the film was implanted by different energy profiles shown in the lower part of Fig. 6.
Such artificial concentration profiles should yield electrode properties differing with respect to all electronic properties, e.g. in capacity, electron transfer reactions ETR and photoelectrochemistry. For example, the electrodes were investigated in 1 N H_2SO_4 with the redox system Fe^{2+}/Fe^{3+}. The most obvious effect refers to the increase of anodic ETR, but the cathodic ETR is also enhanced. The anodic current densities are extremely small for the unimplanted film (0), greater on the film implanted outside (out), and highest for the totally implanted film (tot). Fig. 7a shows the Tafel plot for the redox reaction. The energetic diagram in Fig. 7b shows a schematic interpretation by the energetic and local distribution of implanted

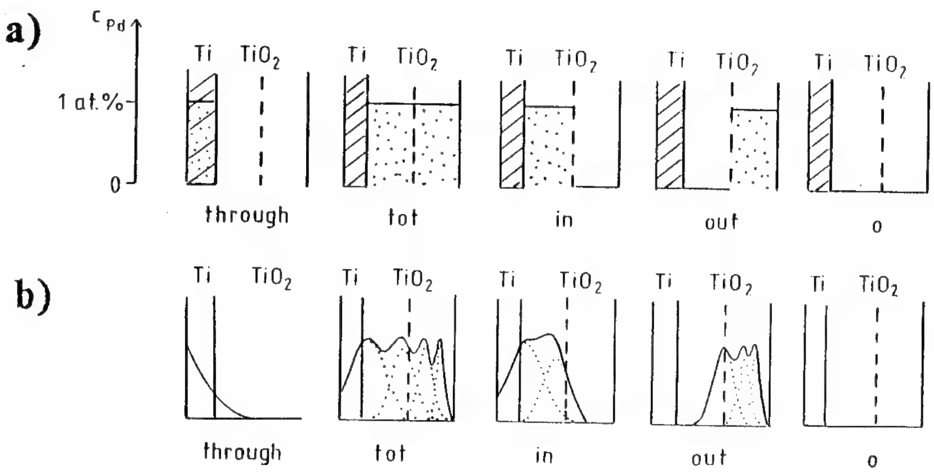

Fig. 6 Various concentration profiles prepared by Pd-ion implantation. (a) Schematic and (b) calculated palladium distributions in a 40 nm TiO_2 film (shown in Fig.7). /14/

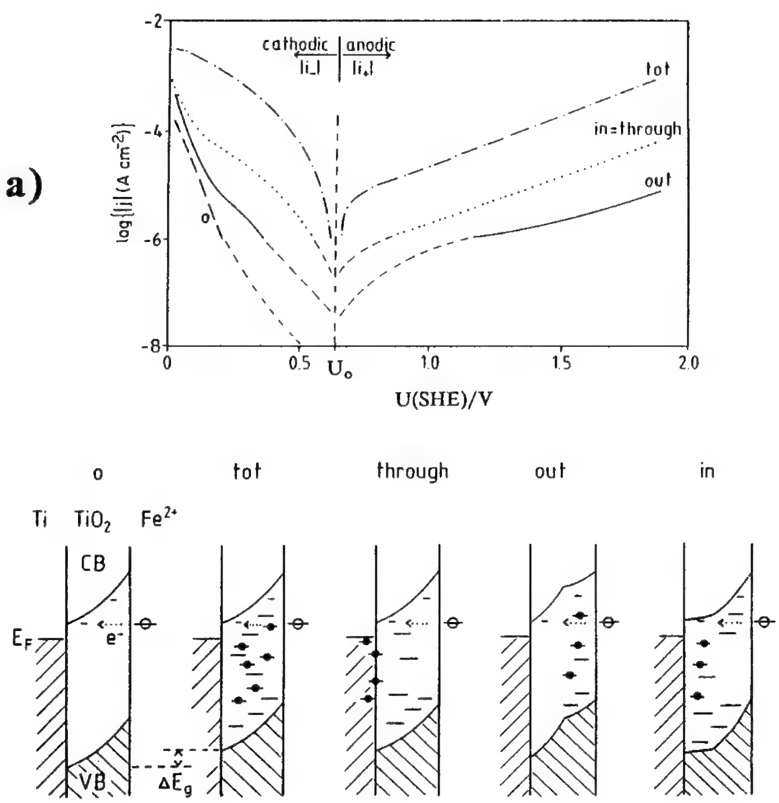

Fig. 7 Influence of concentration profiles on ETR: a) Tafel curves of the Fe^{2+}-Fe^{3+} redox reaction (0.05 N) in 1 N H_2SO_4 on TiO_2 electrodes (cathodic sweep; sweep rate dU/dt = 10 mV s^{-1}). b)Energetic diagram of ETR through the modified passive film. /14/

ions which produce electron terms of Pd and defects, respectively, in the band gap of TiO_2. They allow resonance tunneling processes from the electrolyte to the metal and vice versa. For details of this modification yielding different types of electrocatalysis see ref. /14/.

Another example of a modification of an oxide film is shown in Fig. 8. Nickel was passivated in neutral solutions in absence or presence of the inhibitor Pentylaminobenzimidazol PAB /18/. Experiments were carried out with the Ni oxidation state 2 and 3, but here only the NiOOH (3) experiments are described. The intended profiles and molecular models are shown in Fig. 8a. Without PAB the film "3 0" is prepared, a later addition yields "3 out", while a presence of PAB during the passivation yielded the concentration profile "3 tot". The experimental determination of the concentration profiles was achieved by XPS analysis of sputter profiles which confirmed the intended profiles qualitatively as can be seen in Fig.8b.
This modification of the passive film of nickel has, of course, a strong effect on the electronic properties of the film and on the total film thickness, too. In contrast to the Pd implantation described above, however, it is an inhibiting effect. The organic molecules represent barriers for ITR and ETR. Moreover the adsorption and production of intermediates at NiOOH are hindered by the inhibitor. Hence, the anodic oxygen evolution at modified nickel oxide films decreases from the reference film 3.0 to 3 out and 3 tot (Fig. 8c).

3.3 Lateral concentration profiles

Natural concentration gradients lateral to the surface sometimes occur in inhomogeneous corroding systems, e.g. at the interface electrolyte/gas where the salt concentration may decrease or increase drastically. Artificial concentration gradients can be prepared by various techniques. A simple method consists of an electrolyte wetting only parts of the electrode. For example iron electrodes could locally be inhibited by a partial dipping into a solution with an inhibitor. Such artificial concentration gradients on the same sample are very useful for investigations, if locally resolving methods are available, e.g. the Kelvin probe. An example of such an investigation is described in /19/. While the visual inspection of the sample shows a comparatively sharp interface, the Kelvin probe proofs that the concentration step only extends over 0.1 mm. Even sharper boundaries can be produced by ion implantation techniques described in detail in /13/. Visual as well as photoelectrochemical and other experiments proof that in such cases the concentration step only extends over 1 to 2 μm. Thus, such samples can be used as artificial grain boundaries. In fact various special reactions could be detected at such local inhomogeneities of the passive film.

For nanotechnology, the preparation of sharp gradients in the nm range will become decisive, but there are not yet enough successfull experiments.

4. Conclusions

The stability of passive films strongly depends on the local microscopic properties of the film. To simulate that, passive films with defined profiles were prepared. Thus, it was possible to simulate grain boundaries by a chemical modification, e.g. implantation techniques. Such systems can be used as test samples for further investigations or high tech systems. In many cases the accuracy of the analytical methods, however, is not better or even worse than the prepared profile.

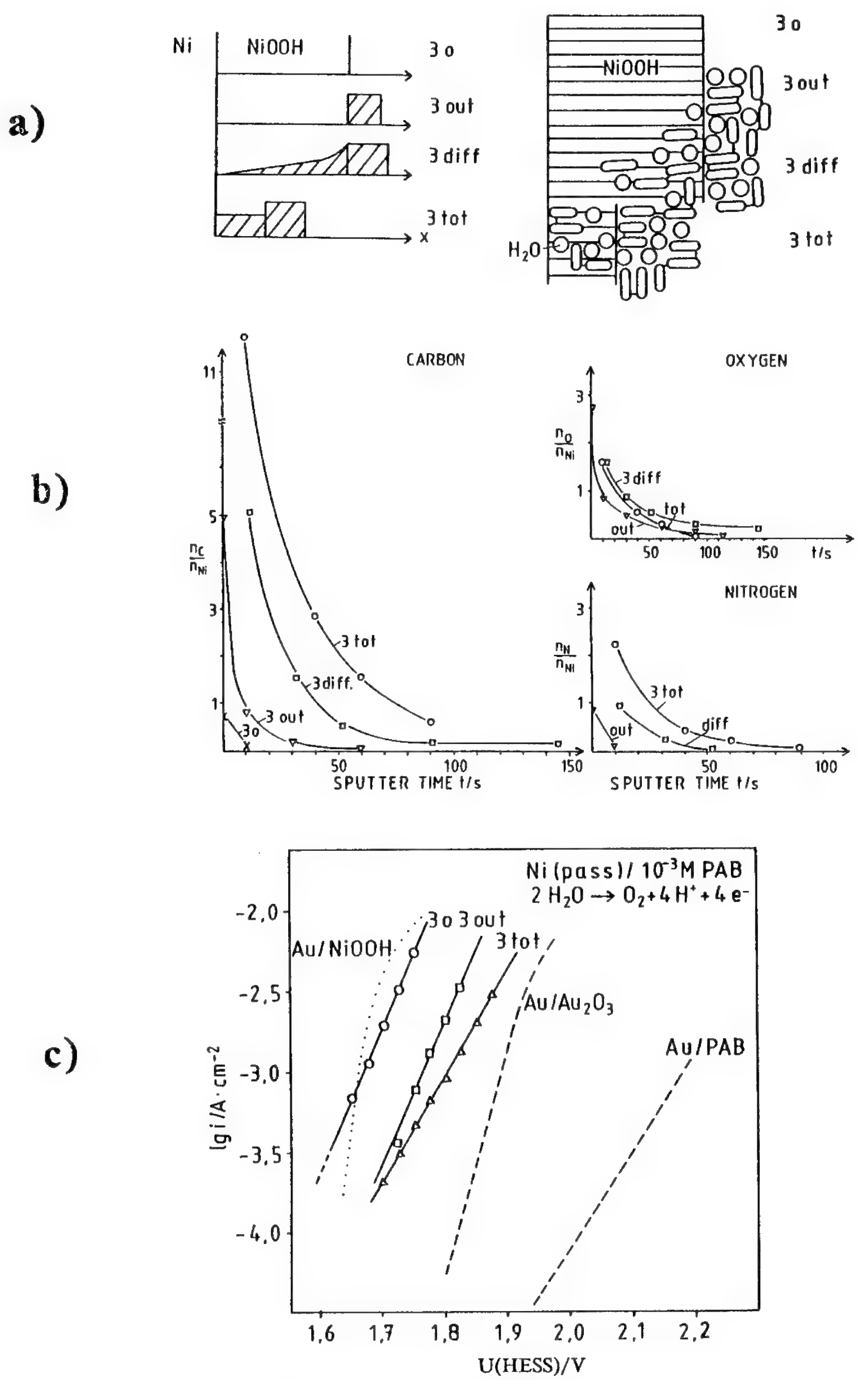

Fig. 8 Passive films on Nickel (NiOOH) modified by an inhibitor: a) Schematic concentration profiles of PAB and molecular structure at 1.76 V as concluded from the electrochemical measurements. b) XPS sputter profiles for various elements. c) Tafel plot of anodic oxygen evolution for non-modified and modified passive films on Ni. d = 20 nm (3o, 3out), d = 2,5 nm (3tot). Experiments with gold for comparison /18/.

While there is a long tradition and experience for the vertical profiles with an almost step-like stoichimetric change, the preparation of lateral profiles is much more difficult. With all of the optical and spectroscopic techniques we are limited by the diffraction of light. This refers to the lateral sensitivity (x-direction), but in the vertical (z-) direction the sensitivity is sufficient, even for monomolecular layers, e.g. with the ellipsometry. In the atomic scale we now have very sensitive methods with the STM, STS, and other techniques. The results strongly depend on the properties of the substrate. They yield, however, mainly geometric (AFM) or electronic (STM) properties of the outermost layer.

While the artificial thickness gradients can be changed from 10^{-5} to 1, natural thickness gradients often are in the range of 10^{-3} to 10^{-1} and in few cases to 10^{3}.
The artificial preparation techniques yield macroscopic, microscopic or nanoscopic gradients ranging from 10^{-6} to 10^{-1}. Passive films formed naturally even show a larger spectrum, since nanopores or pit edges may have very steep boundaries, while on the other hand inhomogeneous technical systems yield very low gradients. Future research in passivity may probably concentrate on the role of grain boundaries and their physics.

Acknowledgement:

The support of this work by the Wissenschaftsministerium des Landes Nordrhein-Westfalen and the Fonds der Chemischen Industrie is gratefully acknowledged.

References:

/1/ C. Guzman, G.K. Wolf, R.P.M. Procter (Eds.)
Mat. Sci. Eng. A115 (1989)

/2/ N. Sato, K. Hashimoto (Eds.)
Corr. Sci. 31 (1990)

/3/ P. Marcus, B. Baroux, and M. Keddam (Ed)
Modifications of Passive Films, European Federation of Corrosion Publications Number 12. The Institute of Materials 1994.

/4/ J.W. Schultze, L. Elfenthal
J. Electroanal. Chem. 204 (1986) 153

/5/ J.W. Schultze
Mat. Chem. Phys., Special Issue, 22 (189) 417

/6/ A. Michaelis, J.W. Schultze
Ber. Bunsenges. Phys. Chem., 97 (1993) 431,
and ref. /3/, page 246

/7/ T.P. Hoar, J. Yahalom
J. Electrochem. Soc., 110 (1963) 614

/8/ D. Ebling, J.W. Schultze
Metalloberfläche, 44 (1990) 491

/9/ J.W. Schultze, K.G. Jung
Electrochimica Acta, in press

/10/ A. Michaelis, J.W. Schultze, A. Thies, W. Bacher, R. Ruprecht
Dechema-Monographien 125 - VCH Verlagsgesellschaft 1992

/11/ O. Karstens, Thesis, Düsseldorf, 1995.

/12/ K. Leitner, J.W. Schultze
Ber. Bunsenges. Phys. Chem., 92 (1988) 181,
J.W. Schultze, L. Elfenthal, G. Hansen, T. Patzelt, B. Siemensmeyer, J. Thietke
Corr. Sci., 31 (1990) 213

/13/ K. Bade, O. Karstens, A. Michaelis, J.W. Schultze
Faraday Discussion, 94 (1992) 45

/14/ J.W. Schultze, L. Elfenthal, K. Leitner, O. Meyer
Mat. Sci. & Eng., 90 (1987) 253

/15/ G. Mende, F. Fenske, H. Flietner, M. Jeske, J.W.Schultze
Electrochim. Acta 39 (1994) 1259
M. Kirchhoff, Thesis, Düsseldorf 1995

/16/ H. Sugimura, T. Uchida, N. Kitamura, and H. Masuhara
J. Phys. Chem. 98 (1994) 4352

/17/ K.J. Vetter
Z. für Elektrochemie 62 (1958) 642

/18/ M.M. Goledzinowski, D. Rolle, J.W. Schultze
Werkst. u. Korr., 36 (1985) 381

/19/ K. Saurbier, J.W. Schultze, J. Geke
Electrochim. Acta 39 (1994) 1171

Materials Science Forum Vols. 185-188 (1995) pp. 389-396

Electronic structure of the passivation layer: New computational methods and results

N. Yu and J.W. Halley

School of Physics and Astronomy, University of Minnesota, Minneapolis, MN 55455, USA

Keywords: Electronic structure, rutile, surfaces, defects

We describe a new semiempirical approach to the self-consistent study of the electronic structure of the passivation layer. We treat correlations at short distances empirically and interactions at large distances in the Hartree Fock approximation. We demonstrate with results on surfaces and point defects in rutile. We find a small gap at the 110 surface, consistent with a recent first principles study. Very large charge rearrangments are found to occur at surfaces, accompanied in some but not all cases by a modification of the surface density of states, relative to bulk, We illustrate the utility of these results with a simple model calculation of the electron transfer rate at several crystal faces. We also report results on vacancies and interstitials in rutile. We find that a model in which the induced screening charge, rather than the potentials, arising from defects are linearly superimposed gives a reasonable representation of a system with multiple defects. Using this model, we can predict the self consistent state density of samples with very high densities of defects.

1. Introduction.

It is well known that the difficulties associated with a theory of the electronic structure of the passivation layer arise because one must simultaneously take account of spatial disorder and strong electron- electron interactions. Neither of these effects can be ignored and each is known in bulk to cause metal insulator transitions. We seek a theoretical framework in which both of these effects can be studied in a materials specific way, yet which is sufficiently simple to allow a wide variety of situations to be studied. For this we choose a semi-empirical modelling approach, in which some parameters are obtained from experiment or from ab initio theoretical calculations on small clusters. Our approach, described below, takes account of the short range correlations which are believed to be very important in oxides, through an empirical approach using data from atomic physics, and uses the Hartree Fock approximation to describe longer range interactions. In the next section we briefly describe the method. Section 3. applies it to rutile surfaces and Section 4. describes recent results on point defects in rutile. Section 5. is a conclusion.

2. Description of the Method.

We start [1] , with the general variational principle with respect to the density $n(\vec{r})$:

$$\delta E(\{n(\vec{r}\})/\delta n(\vec{r}) = 0 \tag{1}$$

where $E(\{n(\vec{r}\})$ is the expectation value of the energy in the ground state. The energy contains three terms, kinetic energy T, a one electron potential energy V_1 and the electron-electron coulomb interaction energy V_2. These are expressed as

$$T = \int d\vec{r} \lim_{\vec{r}\rightarrow\vec{r}'} \frac{\hbar^2}{2m} \nabla_{\vec{r}} \cdot \nabla_{\vec{r}\,'} \rho_1(\vec{r};\vec{r}\,') \tag{2}$$

$$V_1 = \int d\vec{r} \rho_1(\vec{r};\vec{r}) v_1(\vec{r}) \tag{3}$$

$$V_2 = \left(\frac{1}{2}\right)\int d\vec{r}d\vec{r}\,'\rho_2(\vec{r},\vec{r}\,';\vec{r},\vec{r}\,')\frac{e^2}{|\vec{r}-\vec{r}\,'|} \tag{4}$$

Here $\rho_1(\vec{r};\vec{r}\,')$ and $\rho_2(\vec{r},\vec{r}\,';\vec{r},\vec{r}\,')$ are one and two body density matrices defined as

$$\rho_1(\vec{r};\vec{r}\,') \equiv \int d\vec{r}_2 ... \int d\vec{r}_N \Phi_N^*(\vec{r},\vec{r}_2,...\vec{r}_N)\Phi_N(\vec{r}\,',\vec{r}_2,...,\vec{r}_N) \tag{5}$$

$$\rho_2(\vec{r},\vec{r}\,';\vec{r},\vec{r}\,') \equiv \int d\vec{r}_3 ... \int d\vec{r}_N \Phi_N^*(\vec{r},\vec{r}\,',\vec{r}_3,...\vec{r}_N)\Phi_N(\vec{r}\,',\vec{r},\vec{r}_3,...,\vec{r}_N) \tag{6}$$

in which $\Phi_N(r_1,...,r_N)$ is the ground state wave function. (In these expressions, the integrals are meant to include sums over the discrete spin variable.)

We express the energy in terms of eigenfunctions $\psi_\lambda(\vec{r})$ of the one particle density matrix, expressed as an integral operator:

$$\int \rho_1(\vec{r},\vec{r}\,')\psi_\lambda(\vec{r}\,')d\vec{r}\,' = n_\lambda \psi_\lambda(\vec{r}\,') \tag{7}$$

It is not hard to show [2]in general that $0 \leq n_\lambda \leq 1$. Here we assume, as in Hartree Fock and LDA approximations, that the n_λ are either equal to 1 or to 0 and are interpreted as occupation numbers of one electron orbitals. We use a tight binding basis and expand the $\psi_\lambda(\vec{r})$ as

$$\psi_\lambda(\vec{r}) = \sum_{i,\nu} \phi_{i,\nu}(\vec{r}) < i\nu \mid \lambda > \tag{8}$$

where $\phi_{i,\nu}(\vec{r})$ is orbital ν localized at site i. The $\phi_{i,\nu}(\vec{r})$ are orthonormal. The terms T and V_1 then become

$$T + V_1 = \sum_{i,\nu;j,\nu'} Q_{i,\nu;j,\nu'}(t_{i,\nu;j,\nu'} + v^{(1)}_{i,\nu;j,\nu'}) \tag{9}$$

in which

$$Q_{i,\nu;j,\nu'} = \sum_\lambda n_\lambda < i,\nu \mid \lambda >< \lambda \mid j,\nu' > \tag{10}$$

and

$$t_{i,\nu;j,\nu'} = \int d\vec{r}\phi^*_{i,\nu}(\vec{r})\left(\frac{-\hbar^2\nabla^2}{2m}\right)\phi_{j,\nu'}(\vec{r}) \tag{11}$$

$$v^{(1)}_{i,\nu;j,\nu'} = \int d\vec{r}\phi^*_{i,\nu}(\vec{r})v_1(\vec{r})\phi_{j,\nu'}(\vec{r}) \tag{12}$$

The sum

$$Q_i \equiv \sum_\nu Q_{i,\nu;i,\nu} \tag{13}$$

can interpreted as the number of electrons at site i. We introduce approximations for the calculation of term V_2 by separating intersite from intrasite terms in the expansion of ρ_2 in the tight binding basis. For intersite terms, we assume that the Hartree Fock approximation is adequate, while we assume that intrasite terms contribute an energy of the form $\sum_i E_i(Q_i)$ depending only on the total number of electrons on the site. We determine the $E_i(Q_i)$ from experimental ionization potentials. The energy then becomes

$$E = \sum_i E_i(Q_i) + \sum_{i\neq j,\nu,\nu'} Q_{i,\nu;j,\nu'}(t_{i,\nu;j,\nu'} + v^{(1)}_{i,\nu;j,\nu'}) + (1/2)\sum_{i\neq j}\frac{e^2Q_iQ_j}{\vec{R}_{ij}} \tag{14}$$
$$-(1/2)\sum_{i\neq j,\nu,\nu'} \delta_{\sigma_{nu},\sigma_{\nu'}}\frac{e^2Q^2_{j,\nu';i,\nu}}{R_{ij}}$$

assuming in the Hartree and exchange integrals that overlaps between the localized orbitals on different sites can be neglected and that the integrals

$$\int\int d\vec{r}d\vec{r}\,'\frac{|\phi_{i,\nu}|^2|\phi_{j,\nu'}|^2}{|\vec{r}-\vec{r}\,'|} \tag{15}$$

may be approximated as

$$\frac{1}{|\vec{R}_i - \vec{R}_j|} \equiv 1/R_{ij} \tag{16}$$

where $\vec{R}_i$ and $\vec{R}_j$ are the positions of sites i and j respectively.

The effective one electron equation is obtained by varying $\psi_\lambda = \sum_{i,\nu} \phi_{i,\nu}(\vec{r}) < i,\nu \mid \lambda >$ through variation of the coefficients $< i,\nu \mid \lambda >$ assuring normalization in the usual way through addition of a term $-\sum_\lambda \epsilon_\lambda \int \mid \psi_\lambda(\vec{r}) \mid^2$ to the energy functional. The result is

$$\left(\frac{\partial E_k}{\partial Q_k} + \sum_{j\neq k} \frac{e^2 Q_j}{R_{kj}}\right) < k\mu \mid \lambda > + \sum_{i\neq k,\nu} \left(t_{k,\mu;i,\nu} + v^{(1)}_{k,\mu;i,\nu} + (1-\delta_{i,k})\frac{e^2}{R_{ki}}\delta_{\sigma_\nu,\sigma_\mu} Q_{k,\mu;i,\nu}\right) < i,\nu \mid \lambda > \tag{17}$$

$$= \epsilon_\lambda < k,\mu \mid \lambda > - \mu < k,\mu \mid \lambda >$$

Intersite exchange is taken into account in this equation through the last term on the right hand side (though these terms are not included in the numerical calculations reported here). Intrasite exchange and correlation are taken into account empirically through the term $\frac{\partial E_k}{\partial Q_k}$. To obtain an expression for this term we use the experimentally determined ionization potentials of the relevant ions. When the ion has integer numbers of electrons, E_l is taken to be a constant minus the sum of the relevant ionization potentials. For noninteger numbers Q_l of electrons, we use a spline fit or a linear interpolation between ththe integer values. The results for $\frac{\partial E_k}{\partial Q_k}$ for the ions of interest in rutile are given in reference 2. $\frac{\partial E_k}{\partial Q_k}$ is nearly linear in Q_k. In a Hubbard model, $\frac{\partial E_k}{\partial Q_k}$ would be precisely linear and the slope would be the Hubbard U. Interpreted in this way , one finds effective U's in the range 10 to 20 eV for rutile. In our calculations we use the functions determined from ionization potentials , except that a constant is added empirically as discussed in the next section. (The empirical constant may be regarded in part as compensating for the errors made in the approximation (16) .) In general, the calculational procedure using this approach is to choose a set of initial values of Q_l and $Q_{l,\kappa;j,\nu}$, solve the one electron problem represented by (17). Using the eigenfunctions, the Q_l and $Q_{l,\kappa;j,\nu}$ are then recalculated using (13) and (10) and the procedure is iterated to self consistency.

In the calculations reported here, we will neglect the intersite exchange term $-\delta_{\sigma_\nu,\sigma_\mu}\frac{e^2 Q_{k,\mu;i,\nu}}{R_{ik}}$ as well as the terms of form $v^{(1)}_{k,\mu;i,\nu}$. Empirical estimates of the hopping integrals $t_{l,\kappa;j,\nu}$ for rutile were obtained from Vos [3]We use a tight binding model for rutile which contains five d states per titanium site and three p states and one s state per oxygen site. The diagonal energies of the orbitals are calculated self-consistently as described in the previous section, using Ewald techniques[4] to obtain the Coulomb energy in equation (17) . With this parametrization, as discussed in reference 2 , we find that the calculated optical gap is not in agreement with the experimental one. We compensate for this discrepancy, which may result from violations of Koopmans' theorem[5] or from errors in the approximation (16) by adding an empirically determined constant to the diagonal parameters of the model For the uniform system, this empirical model predicts a system slightly more covalent than predicted by a self-consistent Hartree-Fock calculation [6]. (The Hartree Fock calculation predicts an optical gap of 10eV compared to the experimental one of 3eV.). At self-consistency, the (electronic plus nuclear) charge on the titanium atom is +2.18 $\mid e \mid$ and that on the oxygen atom is -1.09 $\mid e \mid$. Some other details of the comparison of the electronic structure predicted by our model for stoichiometric rutile without surfaces appear in reference 2 where they are compared with other calculations and with experiment.

3. Results on Rutile Surfaces

These are clearly of interest for understanding the passivation layer. Here we report self consistent results for the 100, 110 and 001 surfaces of rutile. Though we have done some preliminary relaxation

studies, in the results reported here we do not allow the atomic positions to relax from the structures shown. Such relaxation is important and will be studied in the future. The samples used for calculation are shown in Figure 1.

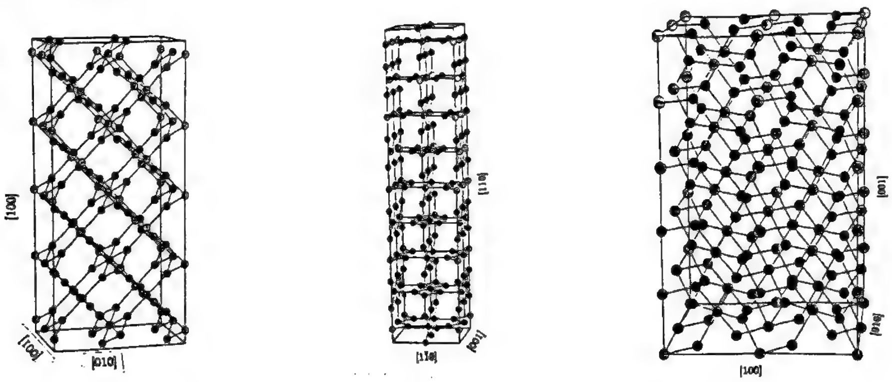

Figure 1. Calculational cells for the 100, 110 and 001 surfaces of rutile, respectively.

We show self consistent state densities from our calculations in Figure 2 . An extensive discussion appears in reference 2. Strictly speaking, the state density is only significant below the Fermi energy.

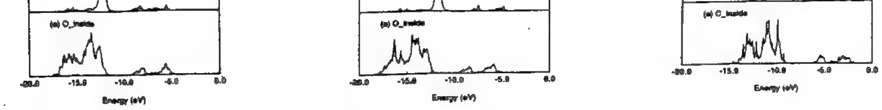

Figure 2. Self Consistent Densities of States for the Three Surfaces.

Note the particularly large rearrangement of states which occurs on the surface in the 110 surface. This results in a very small gap for this surface, consistent with the work of reference 7.

4. Point defects.

We first studied a cluster of (3 × 4 × 4) rutile unit cells, of 289 atoms, with one titanium interstitial, located in the cell at the middle of the cluster. Periodic boundary conditions are applied in all three dimensions. Self-consistent solution of this system indicates that the conduction band edge of the host lattice is little altered by the introduction of the interstitial. However, two impurity states appear below the conduction band edge, at 0.19 eV and 0.80 eV below the conduction band edge. Fig. 3(a) shows the density of states projected on the titanium interstitial and its 6 octahedral neighbors, obtained by broadening the levels with a lorentzian of width 0.1 eV.

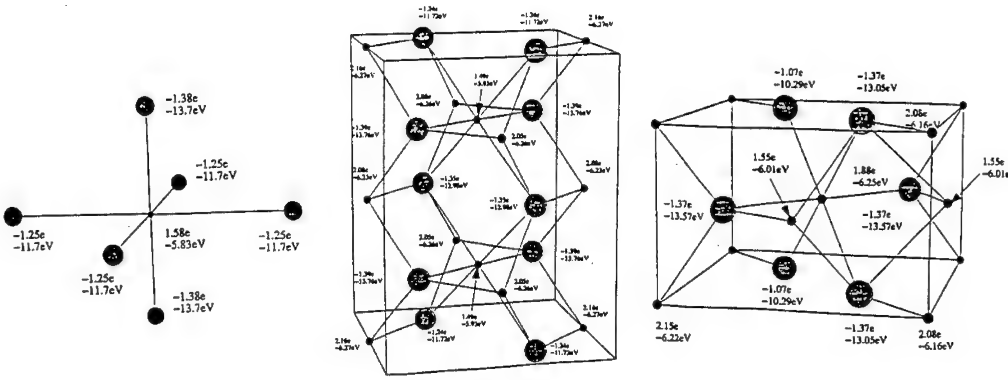

Figure 3. (a) A single interstitial (b).(c) Two configurations of near neighbor interstitials

The wave function of the impurity state 0.8 eV below the conduction band edge has little component on the six nearest neighbor oxygen atoms around the titanium interstitial. Transitions from this occupied state to the bottom of the conduction band would account well for the position of the experimentally observed peak in infrared absorption. We find that strong interference between the interstitials occurs only if the octahedra surrounding two interstitials share common oxygen atoms. This can happen only in two cases: When the two interstitials are on neighboring as shown in the next two Figures. which also show the self consistently calculated charges and orbital energies associated with the various atoms around the defects. The good local screening of the impurity charge suggests that the interference between interstitials far apart is small. We studied clusters with various numbers of impurities, and found that as long as the interstitials are far apart so that they do not share oxygen atoms as nearest neighbors, the electronic structure is close to a simple superposition of that of individual interstitials. For example, putting 4 interstitials on a square 5 $\mathring{A}$ on each side produced three levels at 6.99 eV and one at 7.01 eV, compared with one level at 6.98 eV for the single interstitial case. Examination of the charges also confirms there is little interference between the interstitials. The charges on the interstitials, for example, are 1.55 $|e|$ in both cases.

Our model for an oxygen vacancy is obtained similarly, but there is an additional uncertainty in the model for the oxygen vacancy, arising from the need to characterize the energy of the orbitals on the vacancy itself. We model an oxygen vacancy as an oxygen site characterized by an s orbital with the same hopping integrals between the orbitals on the vacancy and on other sites as the s orbital had when the site was occupied by oxygen. The diagonal energy of the orbital associated with the vacancy site is self-consistently determined through the Coulomb potential at the site plus an empirically determined constant. The constant is taken to be 9.0 eV. This value was selected so that self-consistent calculations yield a donor energy level 0.7 eV below the conduction band edge consistent with the position of the observed infrared absorption. From the local density of states on the vacancy, its nearest neighbor titanium atoms, and some of their oxygen neighbors, it is seen that the impurity state 0.7 eV below the conduction band edge mainly consists of a titanium 3d component, and some component on the vacancy. We find that strong interaction between the oxygen vacancies occurs only if the two vacancies share a titanium atom as common nearest neighbor. As examples, we studied two such pairs of vacancies, one in which the two vacancies occupy opposite vertices of the octahedron surrounding a titanium atom, and another in which the two vacancies share an edge of an octahedron. Fig. 4(b) shows the two oxygen vacancies occupying the opposite vertices of an octahedron and their titanium nearest neighbors. Another pair of vacancies is shown in Fig. 4(c) where the two oxygen vacancies share an edge of the octahedron around one titanium atom.

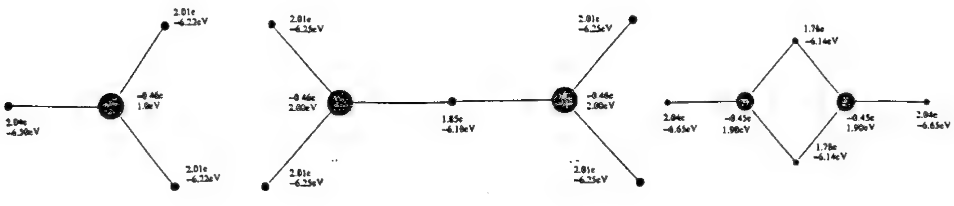

Figure 4a. Single vacancy b., c, vacancy pairs.

The above analysis indicates that the charge redistribution is restricted to the nearest neighbors of the oxygen vacancies and suggests that oxygen vacancies which do not share a titanium neighbor will behave essentially independently with regard to their electronic structure. We find this to be approximately correct in practise. For example, a self-consistent calculation for two oxygen vacancies 4.95 Å apart produces two impurity states around 0.7 eV below the conduction band, separated in energy by about 0.04 eV.

Since the first infrared absorption experiments [8] on on reduced rutile, it has generally been assumed that oxygen vacancies are responsible for the impurity band 0.7 eV below the conduction band edge, despite evidence from various diffusion experiments showing the importance of the titanium interstitials. In the model used here, titanium interstitials at low concentrations produce a band of states leading to an absorption peak very close in position to the experimental absorption peak. We now consider possible origins of the observed width of the infrared absorption band around 0.7eV below the conduction band edge. The observed width is very substantial (of order 1eV). This may seem to be in contradiction with our results, because single defects have a very sharply defined level in this calculation and, at the defect levels reported in reference 8 , only one of every 10^3 oxygen atoms is missing in the crystal. Thus if the defects were completely randomly distributed without correlation in the crystal, then the concentration of pairs and higher order clusters would be completely negligible and broadening effects due to such clusters could not account for the width observed. We suggest two possible origins for the width: 1) Charge fluctuations may result in fluctuations in the local self consistent potential (the diagonal matrix elements in our calculation) leading to a distribution of energies of the local donor levels and/or 2) the distribution of defects may not be random, leading to more clusters than the assumption of uncorrelated randomness in the distribution would predict. We discuss these possibilities in turn.

With regard to the first possibility, we illustrate the effect with a calculation on a larger sample (8x8x8 unit cells or 3072 atomic sites) in which we make the approximation suggested above : We assume that the screening charges due to multiple defects are, at each site, just the sum of the screening charges due to each defect alone in the crystal. We showed[2] that this approximation works quite well for pairs of vacancies in the last section, but its validity for hundreds of vacancies (as in this application) has not been determined and we expect that it will exaggerate the extent of charge fluctuation. We make the calculation of the total density of states in this case using the equation of motion techniques described in reference 2. This method is restricted to quite large defect concentrations and we show the results for 0.5 %, 1 % and 5 % of oxygen vacancies in Figure 5. We see that the charge fluctuation effect results in very significant broadening of the levels, even at 1 % concentrations. It appears,

however, that this is not sufficient to account for the observed width, since the calculation for 0.5 % vacancies gives a smaller impurity band width than that measured in the experiments. Furthermore, this approximation may exaggerate the width of the impurity band, because it fails to take account of possible screening of large length scale charge fluctuations.

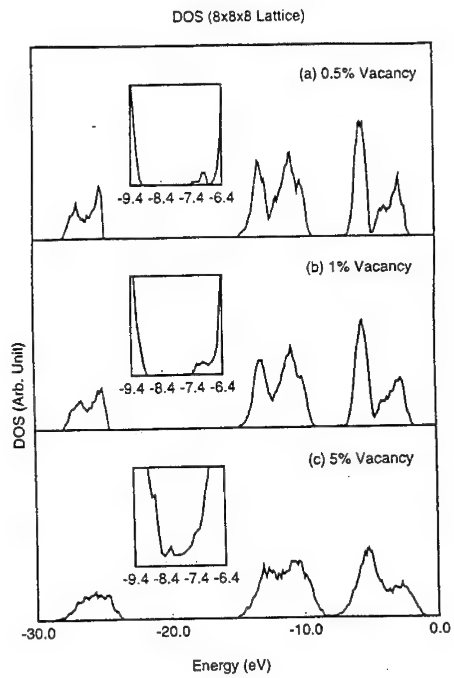

Figure 5. Density of states for rutile with large numbers of oxygen vacancies.

The second possible contributing origin of the observed width is correlations in the spatial defect distribution. It is known [9- 11] that the stable phases of reduced rutile are Magneli phases which may be regarded consisting of ordered arrays of planar defects. We think it likely that reduced samples such as those used in the infrared absorption experiments of reference 8 may be partly phase separated into regions of stoichiometric rutile and partially formed planar defects which may be regarded as clusters of interstitials and vacancies. This possibility has been extensively discussed by others [12-14] in the context of the interpretation of structural and diffusion measurements and by use of empirical modelling of interatomic forces. In such a model, significant broadening of the infrared peak might result, arising from the electronic donor levels associated with these various defect clusters. To model such a structure, one would need to include correlations in the distribution of point defects, thus increasing the number of clusters, relative to the number expected in an uncorrelated random distribution.

5. Conclusions.

Though we have gained considerable insight from this model and can begin to make useful calculations with it, thus elucidating the origin of infrared absorption features for example, nevertheless for many purposes we must include atomic motion in these calculations. Thus remains a task for the future.

6. Acknowledgements.

This work was supported in part by the Minnesota Supercomputer Institute by US Department of Energy grant DE-FG02-91-ER45455 and by Sumitomo Metal Industries.

References

1. P. Hohenberg and W. Kohn, Phys. Rev. 136, B864 (1964)
2. N. Yu and J. W. Halley, Phys. Rev. B (in press)
J. W. Halley et al, Phys. Rev. B41, 10165 (1990)
3. K. Vos, J. Phys. C10, 917 (1977)
4. D. M. Heyes, M. Barber and J. H. R. Clarke, J. Chem. Soc. Fara. Trans. **2:73**, 1485 (1977)
5. T. Koopmans, Physica 1, 104 (1933)
6. B. Silvi, N. Fourati, R. Nada and R. A. Catlow, J. Phys. Chem. Solids 52, 1005 (1991)
7. D. Vogenhuber, R. Podloucky, A. Neckel, S. G. Steinmann
and A. J. Freeman, Phys. Rev. B49, 2099 (1994)
8. D. C. Cronemeyer, Phys. Rev. 113, 1222(1959)
9. S. Anderson and A. Magneli, Naturwissenschaften 42, 495 (1956)
10. L. A. Bursill and B. G. Hyde, Prog. Solid State Chem, 7, 177 (1972)
11. R. F. Bartholomew and D. R. Frenkl, Phys. Rev. 187, 828 (1969)
12. A. N. Cormack, C. M. Freeman, C. R. A. Catlow and R. L Royle, Advances in Ceramics, **23**, 283: Nonstoichiometric Compounds, 283 (1987)
13. M. G. Blanchin, L. A. Bursill and D. J. Smith, Proc. Roy. soc. (London)Sect. A 391, 351 (1984)
14. L. A. Bursill, G. J. Shen, D. J. Smith and M. G. Balanchin, Ultramicroscopy 13, 191 (1984)

Materials Science Forum Vols. 185-188 (1995) pp. 397-406

Physical concept of single electrode potential

N. Sato

Corrosion Research Group, School of Engineering, Hokkaido University, Sapporo, 060 Japan

Keywords: Absolute electrode potential, single electrode potential, electronic energy level, ionic energy level, electron transfer, ion transfer

Abstract: The single electrode potential is defined in terms of the energy level of electrons or ions in the electrode. The electronic electrode potential corresponds to the real free energy of electron at the Fermi level and the ionic electrode potential to the real free energy of potential determining-ion in the electrode. Provided that the electrode has both electronic and ionic energy levels, these two electrode potentials are in the same scale with different zero levels and hence either can be applied. Only the ionic electrode potential can be applicable to the electrodes that have no electronic energy level in the range of practical interest, such as ionic solid electredes and electronically non-conductive polymer membrane electrodes.

Introduction

The single electrode potential, which is of fundamental importance in electrochemistry, has recently appealed to the interest not only of electrochemists but also of semiconductor physicists. Trasatti [1] has summarized the recent discussion on what is called the absolute electrode potential. It is generally accepted that the electrode potential is a relative measure of the electron energy at the Fermi-level rather than the electrostatic potential of the electrode [2,3,4,5,6]. The alternative approach to the single electrode potential may also be made based on the energy level concept of potential-determining ion in the electrode. This article discusses the ionic and the electronic energy level concepts for the single electrode potential of ion transfer and electron transfer electrodes.

Electron Energy Level in Metal and Aqueous Solution

The electronic energy level in metal M may be defined by the real free energy $\alpha_{e(M/V)}$ of electron, which is the electronic energy difference between the Fermi-level in the metal and the electronic level at the point just outside the metal close to its free surface, i.e. at the point of the outer potential ϕ_M of metal. Energy $\alpha_{e(M/V)}$ is equal to the negative work function of the metal, which is the minimum work to extract an electron from the Fermi-level of uncharged metals. As shown in Fig. 1 [7], $\alpha_{e(M/V)}$ consists of the chemical potential $\mu_{e(M)}$ of electron in the metal and the electrostatic energy $-e\chi_{M/V}$ due to the surface potential difference $\chi_{M/V}$ across the free metal surface (metal/vacuum interface).

$$\alpha_{e(M/V)} = \mu_{e(M)} - e\chi_{M/V} \tag{1}$$

where e is the elemental charge of an electron. Note that the Fremi-level $\varepsilon_{F(M)}$ of charged metal is equivalent to the electrochemical potential of electron $\bar{\mu}_{e(M)} = \varepsilon_{F(M)} = \alpha_{e(M/V)} - e\phi_M$.

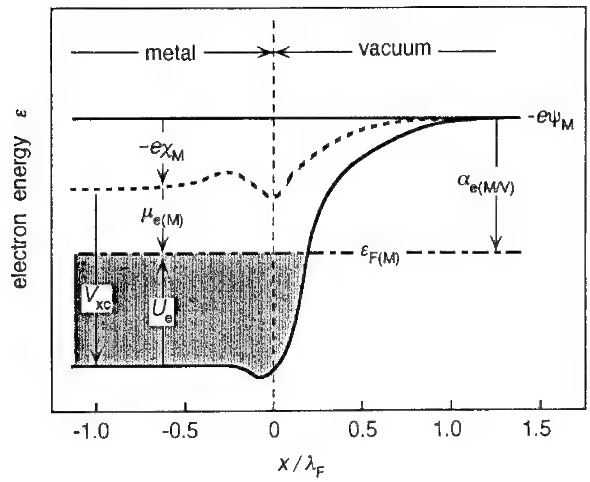

Fig. 1

Electron energy profile across free metal surface: x=distance from the metal surface, λ=Fremi-wavelength, [7].

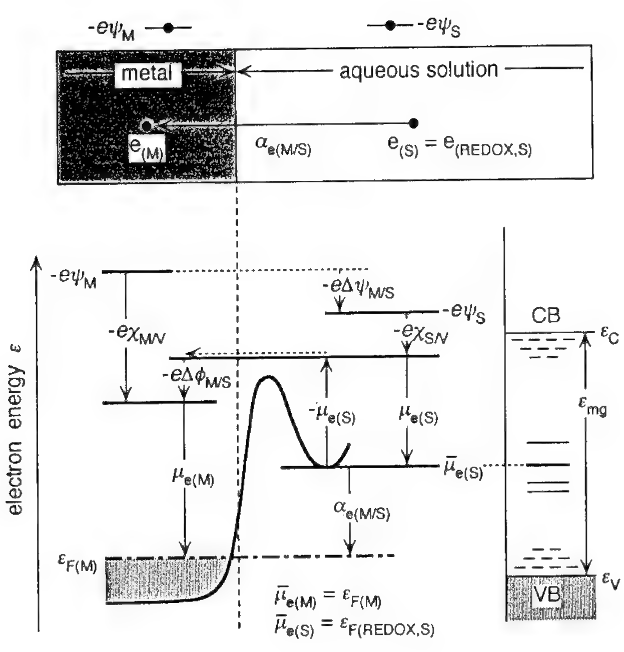

Fig. 2

Electron energy schema across metal/aqua-solution interface and Fremi-level of redox-electron in the mobility gap ε_{mg} of water: ε_c= conduction band (CB) edge, ε_v=valence band (VB) edge.

In a similar way the energy level of electron in aqueous solution S may also be defined by the real free energy $\alpha_{e(S/V)}$, which is composed of the chemical potential $\mu_{e(S)}$ of electron in the solution and the energy $-e\chi_{S/V}$ associated with the surface potential difference term.

$$\alpha_{e(S/V)} = \mu_{e(S)} - e\chi_{S/V} \tag{2}$$

The electronic energy levels in aqueous solutions of practical interest are those of reduction-oxidation electrons $e_{(REDOX,\,S)}$ localized at hydrated redox particles, which are located within the mobility gap ε_{mg} (>8 eV [8]) between the conduction band and the valence band of water, i.e. $\alpha_{e(S)} = \alpha_{e(REDOX,\,S/V)}$, as shown in Fig. 2. Note that the electrochemical potential $\bar{\mu}_{e(REDOX,\,S)}$ of redox electron is equivalent to what is called the Fermi-level $\varepsilon_{F(REDOX,\,S)}$; $\bar{\mu}_{e(REDOX,\,S)} = \varepsilon_{F(REDOX,\,S)} = \alpha_{e(REDOX,\,S/V)} - e\psi_S = \mu_{e(REDOX,\,S)} - e\psi_S - e\chi_{S/V}$.

The real free energy $\alpha_{e(M/S)}$ for electron transfer across the metal/solution interface consists of the energy to overcome the chemical potential well $-\mu_{e(S)}$, the electrostatic energy due to the interfacial potential difference $-e\Delta\phi_{M/S}$, and the chemical potential of electron $\mu_{e(M)}$ inside the metal, as shown in Fig. 2.

$$\alpha_{e(M/S)} = -\mu_{e(S)} - e\Delta\phi_{M/S} + \mu_{e(M)} \tag{3}$$

where $\Delta\phi_{M/S} = \phi_M - \phi_S$ is the inner potential difference between the metal and the solution. Note that the outer potential difference $\Delta\psi_{M/S} = \psi_M - \psi_S$ shown in Fig. 2 is called in physics the contact potential difference between the metal and the solution.

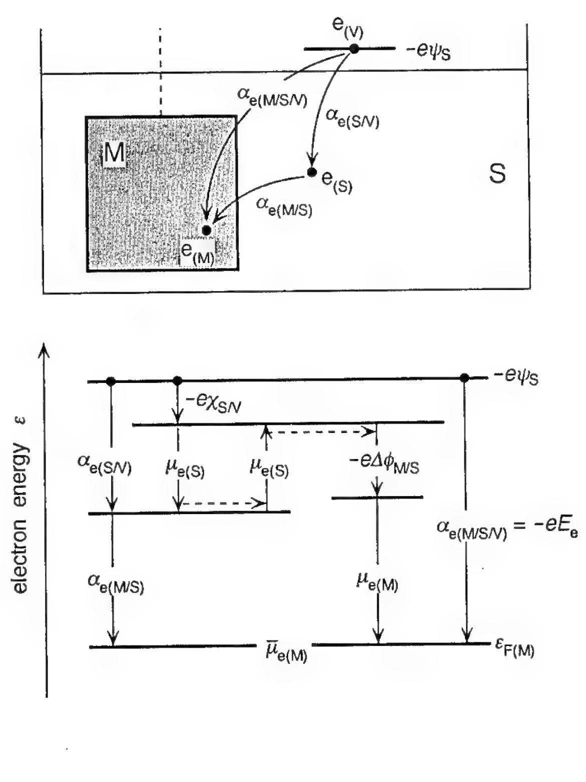

Fig. 3

Electron energy schema to define the electronic electrode potential: $\Delta\phi_{M/S} > 0$.

Electron Energy Level in Electrode (Electronic Electrode Potential)

As shown in Fig. 3, the real free energy $\alpha_{e(M/S/V)}$ of electron in the electrode relative to the energy level at the point of the outer potential ψ_S is represented by the sum of $\alpha_{e(S/V)}$ and $\alpha_{e(M/S)}$.

$$\alpha_{e(M/S/V)} = \alpha_{e(S/V)} + \alpha_{e(M/S)} = \mu_{e(M)} - e\,\Delta\phi_{M/S} - e\,\chi_{S/V} \tag{4}$$

This equation is valid no matter what energy level the electron occupies in the solution.

It has been recommended [1,5,6] to define the single electrode potential E_e (frequently called the absolute electrode potential) in terms of the real free energy of electron in the electrode, as follows;

$$-e\,E_e = \alpha_{e(M/S/V)} = \mu_{e(M)} - e\,\Delta\phi_{M/S} - e\,\chi_{S/V} \tag{5}$$

This definition can be applied whether or not the electron transfer at the electrode interface is in equilibrium. The single electrode potential thus defined based on the electron energy level is called the electronic electrode potential.

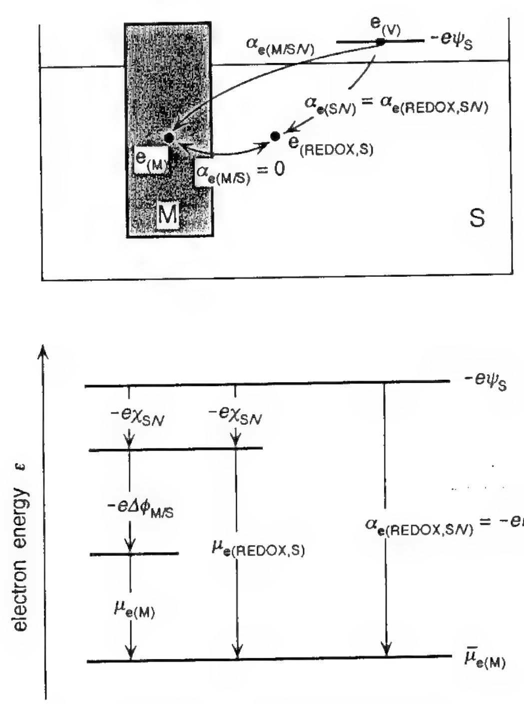

Fig. 4

Electron energy schema of electron transfer equilibrium electrode: $e_{(REDOX,S)}$ = redox electron in solution.

Electronic Equilibrium Electrode Potential

With the electrodes where the electron transfer is in equilibrium between the electrode and the hydrated redox particles ($OX_{(S)} + e_{(M)} \Leftrightarrow RED_{(S)}$), the real free energy $\alpha_{e(M/S)}$ of electron transfer between the electrode and the solution is zero, as shown in Fig. 4. Therefore, one obtains

$$-e\,E_{e(eq)} = \alpha_{e(M/S/V)} = \alpha_{e(S/V)} = \alpha_{e(REDOX,S/V)}$$
$$= \mu_{e(REDOX,S)} - e\,\chi_{S/V}\,. \tag{6}$$

The electronic equilibrium electrode potential thus corresponds to the real free energy $\alpha_{e(REDOX,S/V)}$ at the Fermi-level $\varepsilon_{F(REDOX,S)}$ of redox electron in the solution. Therefore, $E_{e(eq)}$ does not depend on the nature of the electrode, though the interface potential difference $\Delta\phi_{M/S}=(\mu_{e(M)}-\mu_{e(S)})/e$ does depend on the electrode material. Redox reaction equilibrium $\alpha_{e(REDOX,S/V)}=\alpha_{RED(S)}-\alpha_{OX(S)}$ leads to $-eE_{e(eq)}=\alpha_{RED(S)}-\alpha_{OX(S)}=\Delta G_{(REDOX,S/V)}$, which represents the free enthalpy change of the following reaction,

$$OX_{(S)}+e_{(V)}\rightarrow RED_{(S)},\quad \Delta G_{(REDOX,S/V)}=\alpha_{e(REDOX,S/V)}=-eE_{e(eq)} \tag{7}$$

where $e_{(V)}$ denotes electrons in the gaseous standard state at the point of the outer potential ψ_S with the electron energy level of $-e\psi_S$.

Ionic Energy Level in Ion Transfer Electrode (Ionic Electrode Potential)

With the metal electrodes where metal ion transfer takes place across the electrode interface, the energy level of metal ion M^{z+} in the electrode may be represented in terms of the real free energy $\alpha_{M^{z+}(M/S/V)}$ of metal ion in the electrode, which is the energy change for the metal ion transfer from the point of the outer potential ψ_S to the point inside the metal electrode passing through the solution, as shown in Fig. 5.

Energy $\alpha_{M^{z+}(M/S/V)}$ is the sum of the real free energy $\alpha_{M^{z+}(S/V)}$ of hydrated metal ion and $\alpha_{M^{z+}(M/S)}$ for metal ion transfer across the electrode interface,

$$\begin{aligned}\alpha_{M^{z+}(M/S/V)} &= \alpha_{M^{z+}(M/S)}+\alpha_{M^{z+}(S/V)}\\ &= \mu_{M^{z+}(M)}+ze\,\Delta\phi_{M/S}+ze\,\chi_{S/V}\end{aligned} \tag{8}$$

where $\mu_{M^{z+}(M)}$ is the chemical potential of metal ion in the electrode.

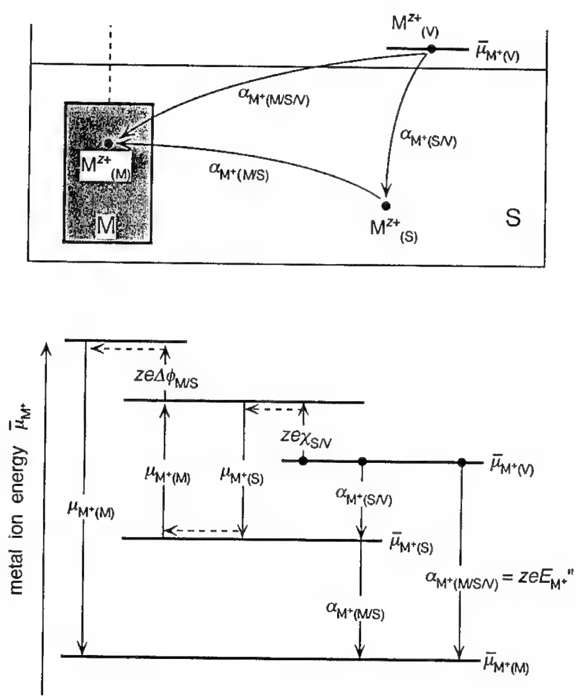

Fig. 5

Metal ion energy schema to define the ionic electrode potential: $\Delta\phi_{M/S}>0$.

One may define the single electrode potential $E_{M^{z+}}$ in terms of the ionic energy level $\alpha_{M^{z+}(M/S/V)}$ in the electrode, relative to the energy level $(\mu_{M^{z+}(V)} + z\,e\,\psi_S)$ of the ion in the gaseous standard state at the point of the outer potential ψ_S, as follows ;

$$e\,E_{M^{z+}}" = \alpha_{M^{z+}(M/S/V)} = \mu_{M^{z+}(M)} + z\,e\,\Delta\phi_{M/S} + z\,e\,\chi_{S/V}\ , \qquad (9)$$

which may be called the ionic electrode potential in contrast to the electronic electrode potential. This ionic electrode potential concept can be applicable whether or not the ion transfer at the electrode interface is in equilibrium. Note that the reference zero energy level $(\mu_{M^{z+}(V)} + z\,e\,\psi_S)$ is not the same but varies with different potential-determining ions, because of their different chemical potentials $\mu_{M^{z+}(V)}$ in the gaseous standard state.

Relation between Electronic Electrode Potential and Ionic Electrode Potential

The electronic electrode potential concept can be applied even to the case of ion transfer electrodes. Accordingly, one obtains from Eqs. (5) and (9) the following relation between the ionic and the electronic electrode potential;

$$z\,e\,(E_{M^{z+}}" - E_e) = \mu_{M^{z+}(M)} + z\,\mu_{e(M)} = \mu_{M(M)} \qquad (10)$$

where $\mu_{M(M)}$ is the chemical potential of metal atom in the metal electrode, relative to the energy level of metal ion and electrons at the point of the outer potential ψ_S.

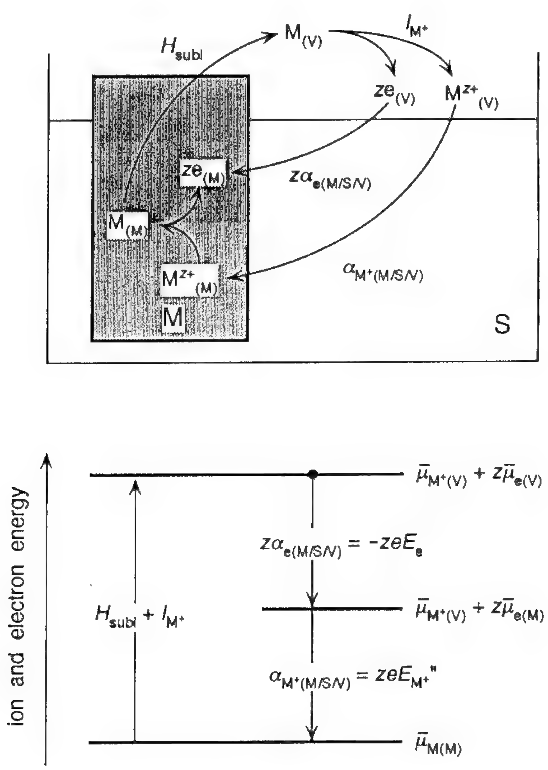

Fig. 6

Energy schema to correlate the electronic and the ionic electrode potential.

It follows from the energy balance in the cyclic process shown in Fig. 6 of metal ion and electrons that $\mu_{M(M)}$ is represented by the sum of the negative free enthalpy of sublimation H_{subl} and the negative free enthalpy of ionization $I_{M^{z+}}$ for metal atom, metal ion and electrons in the gaseous standard state.

$$z\,e\,(E_{M^{z+}}{}'' - E_{e}) = \mu_{M(M)} = -(H_{subl} + I_{M^{z+}}) \tag{11}$$

Therefore, one may use either the ionic or the electronic electrode potential to define the single electrode potential of ion transfer electrodes, provided that the electrode has both ionic and electronic energy levels in the range of practical interest. The numerical value of electrode potential, however, differs in the electronic and the ionic electrode potentials, as shown in Fig. 6.

With ionic electrodes possessing no electronic energy level, such as ionic solid electrodes and membrane electrodes with no electron conductivity, one can use only the ionic potential concept to define the single electrode potential.

Ionic Equilibrium Electrode Potential

With a metal electrode where metal ion transfer $M^{z+}{}_{(M)} \Leftrightarrow M^{z+}{}_{(S)}$ is in equilibrium, energy $\alpha_{M^{z+}(M/S)}$ is zero and hence energy $\alpha_{M^{z+}(M/S/V)}$ becomes equal to energy $\alpha_{M^{z+}(S/V)}$, as shown in Fig. 7. Therefore, the ionic electrode potential corresponds to the real free energy of hydrated metal ion $\alpha_{M^{z+}(S/V)}$ in the solution.

$$z\,e\,E_{M^{z+}}{}''_{(eq)} = \alpha_{M^{z+}(M/S/V)} = \alpha_{M^{z+}(S/V)} \tag{12}$$

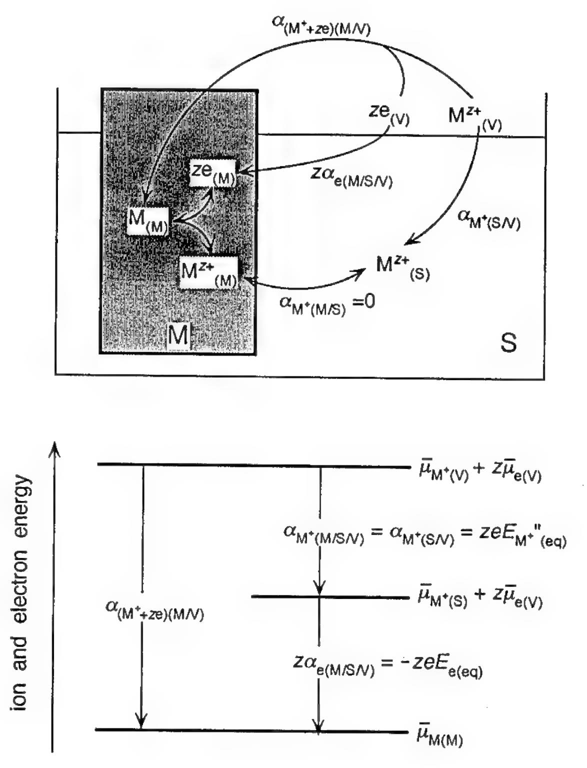

Fig. 7
Energy schema of metal ion and electron for metal ion transfer equilibrium electrode.

Energy $\alpha_{M^{z+}(M/S)}$ is in fact the metal ion hydration energy $\Delta G_{M^{z+}(M/S)}$; $M^{z+}_{(V)} \rightarrow M^{z+}_{(S)}$. Note that the equilibrium potential difference $\Delta \phi_{M/S}$ at the electrode interface is given by $z e \Delta \phi_{M/S} = (\mu_{M^{z+}(S)} - \mu_{M^{z+}(M)})$.

The electronic electrode potential $E_{e(eq)}$ of the above electrode can be written as follows;

$$-eE_{e(eq)} = \alpha_{e(M/S/V)} = \mu_{e(M)} - e\Delta\phi_{M/S} - e\chi_{S/V}$$

$$= \mu_{M^{z+}(M)} + z\mu_{e(M)} - \mu_{M^{z+}(S)} - ze\chi_{S/V} = \mu_{M(M)} - \alpha_{M^{z+}(S/V)} \qquad (13)$$

where $\mu_{M(M)} = (\mu_{M^{z+}(M)} + z\mu_{e(M)})$ is the chemical potential of metal atom in the electrode as referred in Eq.(11). Eq.(13) implies that the electronic electrode potential corresponds to the free enthalpy change $\Delta G_{M/M^{z+}(M/S/V)}$ of the following reaction;

$$M^{z+}_{(S)} + e_{(V)} \rightarrow M_{(M)}, \quad \Delta G_{M/M^{z+}(M/S/V)} (= -zeE_{e(eq)}) \qquad (14)$$

which is the formation of metal atom in the electrode from hydrated metal ion in the solution and gaseous z electrons at the point of the outer potential ϕ_S.

Equilibrium Hydrogen Electrode Potential

With the equilibrium hydrogen electrode shown in Fig. 8, one obtains from Eq. (6) the electronic electrode potential $E_{e(HE)}$, which represents the real free energy $\alpha_{e(HE,S/V)}$ of electron at the Fremi-level $\varepsilon_{F(HE,S)}$ of hydrogen redox electrons $e_{(HE,S)}$ $(2H^+_{(S)} + 2e_{(HE,S)} = H_{2(G)})$ in the solution;

$$-eE_{e(HE)} = \alpha_{e(HE,S/V)} = (1/2)\alpha_{H_2(G)} - \alpha_{H^+(S/V)} \qquad (15)$$

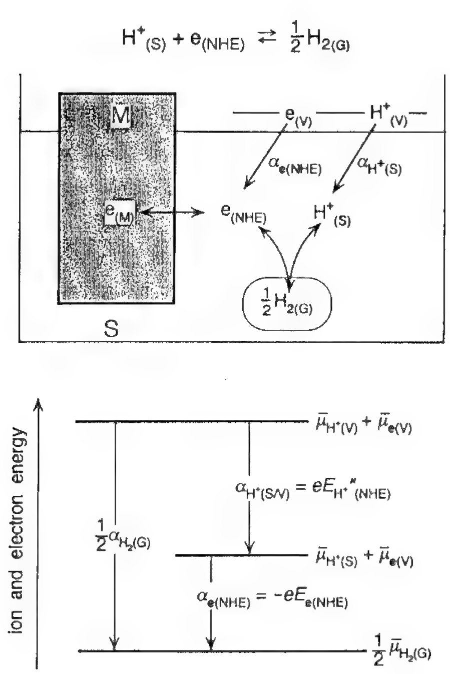

Fig. 8

Energy schema for hydrogen electrode.

Further, this electronic electrode potential corresponds to the free enthalpy change $\Delta G_{(HE)}$ of the following reaction;

$$H^{+}_{(S)} + e_{(V)} \rightarrow (1/2)H_{2\,(G)}\ ,\quad \Delta G_{(HE)}(= \alpha_{e\,(HE,\,S/V)} = -\,e\,E_{e\,(HE)}). \quad (16)$$

The hydrogen electrode may also be regarded as an ionic electrode in which hydrogen ion transfer is in equilibrium between the gaseous state of hydrogen molecule and the hydrated state of hydrogen ion in the solution. Referring to Eq. (12), one can derive the ionic electrode potential of HE as follows;

$$e\,E_{H^{+}}{}''_{(HE)} = \alpha_{H^{+}(G/S/V)} = \alpha_{H^{+}(S/V)} \quad (17)$$

where $\alpha_{H^{+}(G/S/V)}$ and $\alpha_{H^{+}(S/V)}$ are the real free energy of hydrogen ion (proton level) in the gaseous state of hydrogen molecule and that in the hydrated state in the solution, respectively, relative to the energy level of hydrogen ion in the gaseous standard state at the point of the outer potential ψ_S.

It follows that $E_{H^{+}}{}''_{(HE)}$ corresponds to the free enthalpy change for proton hydration from the gaseous standard state to the hydrated state in solution;

$$H^{+}_{(V)} \rightarrow H^{+}_{(S)}\ ,\quad \Delta G_{H^{+}(S/V)}(= \alpha_{H^{+}(S/V)} = e\,E_{H^{+}}{}''_{(HE)}). \quad (18)$$

The schematic energy diagram of electron and hydrogen ion is shown in Fig. 8.

From the thermodynamic data reported in the literature one can estimate, for the normal hydrogen electrode at room temperature, the electronic electrode potential at 4.5 V [9], 4.44 V [2] and around these values, and the ionic electrode potential at −11.30 V [10], −10.98 V [11] and around these values.

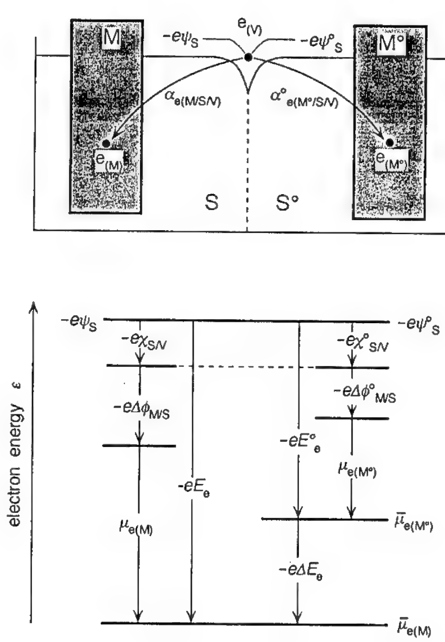

Fig. 9

Electron energy schema for relative electronic electrode potential: M=test electrode, M° = reference electrode, ψ_S the outer potential of solution.

Electrode Potential Relative to Reference Electrode

To measure the electronic electrode potential, a reference electrode is needed for an electrochemical cell, which provides the same reference level of electronic energy at the point of the outer potential ψ_S, as shown in Fig. 9.

The relative electrode potential can then be given by the difference ΔE_e between the electronic electrode potential E_e of the test electrode and that E_e^0 of the reference electrode, as follows;

$$-e\,\Delta E_e = -e\,(E_e - E_e) = \alpha_{e\,(M/S/V)} - \alpha_{e\,(M^0/S/V)}\,. \qquad (19)$$

Since the outer potential ψ_S of the solution for the two electrodes is identical, the relative electrode potential represents the difference in the electrochemical potential $\bar{\mu}_{e\,(M)}$ of electron and hence in the Fermi-level $\varepsilon_{F\,(M)}$ of electron in the two electrodes.

$$-e\,\Delta E_e = \bar{\mu}_{e\,(M)} - \bar{\mu}_{e\,(M^0)} = \varepsilon_{F\,(M)} - \varepsilon_{F\,(M^0)} \qquad (20)$$

where $\bar{\mu}_{e\,(M)}\,(=\varepsilon_{F\,(M)} = \alpha_{e\,(M/S/V)} - e\,\psi_S)$ is the electrochemical potential of electron in the electrode.

Conclusions

(1) The single electrode potential is defined by the real free energy $\alpha_{e\,(M/S/V)}$ of electron at the Fremi-level in the electrode relative to the energy level of electron in the gaseous standard state at the point of the outer potential of the solution. This is called the electronic electrode potential.

(2) The single electrode potential of ionic electrodes can also be defined by the real free energy $\alpha_{ion\,(M/S/V)}$ of potential-determining ion in the electrode, which may be called the ionic electrode potential.

(3) In cases where the electrode has both electronic and ionic energy levels, such as metal and semiconductor electrodes, the ionic and the electronic electrode potential can be correlated to one another. Accordingly, one can use the electronic electrode potential concept even in the case of ionic electrodes where no electron transfer takes place across the electrode interface.

(4) However, only the ionic electrode concept can be used in the case of ionic electrodes possessing no electronic energy levels in the range of practical interest, such as ionic solid electrodes and electronically non-conductive membrane electrodes.

REFERENCES

[1] S. Trasatti, Electrochimica Acta, **35**, 269(1990).
[2] S. Trasatti, Pure Appl. Chem., **58**, 956(1986).
[3] A. Frumkin and B. Damaskin, J. Electroanal. Chem., **66**, 150(1975).;
[4] J. Bockris, J. Electroanal. Chem., **36**, 495(1972).
[5] S. Trasatti, J. Electroanal. Chem., **139**, 1(1982).
[6] N. Sato, "Electrodic Chemistry ", Vol. **1**, p.71~93, p.147~173, Japan Technical Service, Tokyo, (1993).
[7] N. D. Lange and W. Kohn, Phys. Reviw, **B1**, 4555(1970); **B3**, 1215(1971).
[8] T. Watanabe and H. Gerischer, J. Electroanal. Chem., **122**, 73(1981).
[9] F. Lohman, Z. Naturforsh., **22a**, 843(1967).
[10] A. Matsuda, J. Inst. Catalysis, Hokkaido Univ., **27**, 101, 167(1979).
[11] R. Gomer and G. Tryson, J. Chem. Phys., **66**, 4413(1977).

Materials Science Forum Vols. 185-188 (1995) pp. 407-418

Stress generation during anodic oxidation of tungsten

S.-I. Pyun[1], J.-D. Kim[1] and R.A. Oriani[2]

[1] Department of Materials Science and Engineering, Korea Advanced Institute of Science and Technology, #373-1 Kusong Dong, Daejon 305-701, Korea

[2] Corrosion Research Center, University of Minnesota, 112 Amundson Hall, 221 Church Street S.E., Minneapolis, MN 55455, USA

Keywords: Stress generation, anodic tungsten oxide film, beam deflection technique, applied current density, oxide growth kinetics

Abstract - Stresses generated during the anodic oxidation of tungsten in 0.1M H_2SO_4 solution were measured as a function of applied current density and potential step by using a beam deflection technique. The stresses which amounted to a few GPa were developed in the oxide film and were separated into the volume-generated stress and electrostrictive stress by measuring the transients in deflections upon interrupting the applied current densities. The deflection due to electrostriction was compressive. From the estimation of the magnitude of electrostrictive force, it was found that the magnitude and sign of the stresses developed during the oxide growth are critically dependent upon the volume-generated stress. As the oxide film grew at low and high applied current density, compressive and tensile deflections due to the volume-generated stress were encountered, respectively. On the other hand, the transition from compressive to tensile deflection occurred with growing oxide film at medium current densities. The results are discussed with respect to the relevant reactions occurring at the metal/oxide interface and oxide/electrolyte interface during the oxide growth. Positive potential steps imposed upon the anodic oxide film on tungsten produced instantaneous tensile deflections followed by deflections in a compressive direction. These results are well explained in terms of the formation of oxygen vacancies at the metal/oxide interface and their subsequent annihilation by inward movement of oxygen.

1. Introduction

The application of anodic current or anodic potential to a number of metals results under suitable conditions in the formation of a continuous and protective surface oxide layer, known as barrier oxide or passive film. These oxide films are of commercial importance as well as scientific interest because of their dielectric and semiconducting behaviour applicable to electronic components such as capacitors, MOS devices and small area displays, etc.[1-3].

When metals are anodically oxidized to form barrier oxide films, growth of these films is generally accompanied by a development of internal stresses in the oxide films. The stresses are often quite large and may exceed the strength of the film resulting in cracking or delamination[4]. The problems become evident under the service conditions and make an otherwise attractive process nonviable. Therefore, a thorough quantitative understanding of the stresses produced during anodic oxidation of metal is of growing importance.

The stresses were related by Pillings and Bedworth[5] to the ratio of the molar volume of the oxide and the molar volume of the metal (Pillings Bedworth Ratio: PBR). However, the changes in the stresses are not simply attributed to PBR as previous works[6-8] showed that the magnitude and sign of the stresses are crucially determined by anodic oxidation conditions such as applied current density and anodic oxidation time. Bradhurst and Leach[6] showed that in the early stages of anodic oxidation of Al in sulphuric acid the growth stresses were tensile and later became compressive Further work[7] showed that when Al was anodically oxidized in ammonium citrate

solution at low current densities, the stresses were compressive while at higher current densities the stresses were tensile.

A mechanism to account for the effect of applied current density upon the stress behaviour may be based upon the work of Davies et. al[9] who developed a sensitive method of determining the transport number of metal ions. These workers showed that, at low current densities, oxygen migration was predominant in the anodic oxide film on Al. In contrast, at higher current densities, Al ion movement was more significant. Nelson and Oriani[8] have extended this work and used it to explain the changes in the sign and magnitude of stresses in terms of the combined effects of the PBR of metal and the transport number of ions through the oxide layer.

By considering the fact[9] that the cationic transport number increases with increasing applied current density, they suggested[6-8] that cation vacancies formed at the metal/oxide interface are important in determining the stresses in the anodic oxide film of metals. However, according to Chao et.al[10], the formation of oxygen vacancies and their movements are mainly responsible for the growth of anodic oxide film on iron. So, it is relevant to consider the role of oxygen vacancies formed at the metal/oxide interface in the stress generation of metals.

Tungsten is one of valve metals which are distinguished by their ability to form highly protective oxide films upon anodic polarization in many aqueous solutions. Having a number of interesting optical and electrical properties, the anodic oxide film of tungsten has been investigated for the purpose of its potential use as a construction material in electric display devices[2,3]. Di Quarto et al.[11] found that a mechanical breakdown of the anodic oxide film occurs during the anodic oxidation of tungsten in 0.1M H_2SO_4 solution and attributed it to the generation of high surface stresses owing to a very high PBR of 3.4. It was reported[3] that the availability of the anodic tungsten oxide films for electrochromic devices is seriously restricted by the high stresses developed during cycling process.

In this respect, it is important to investigate the surface stresses generated during the growth of the anodic oxide film of tungsten, in order not only to improve its corrosion resistance and availability for electrical devices, but also to understand the kinetic behaviour of the anodic oxide film of tungsten.

Vermilyea[12] measured the tensile stresses during the anodic oxidation of tungsten at an applied current density of 2 $mA\cdot cm^{-2}$ in a borate-containing bath. However, he did not take the relevant interfacial electrochemical reactions responsible for generation of surface stresses in the anodic oxide film into account[10]. Moreover, the stress measurement was made on as-received tungsten specimen which would have residual stresses in itself. We infer that such stresses are relieved during the anodic oxidation and are overlapped with surface stresses generated by the anodic oxidation of tungsten. So it is questionable that Vermilyea's work provides reliable data of the genuine surface stresses in the anodic oxide film. Therefore, accurate measurement and analysis of the real surface stresses in the anodic oxide film of tungsten are still necessary with respect to oxide film growth-related interfacial reactions.

In the present work, the surface stresses generated during the anodic oxidation of tungsten were determined as a function of applied current density and anodic oxidation time by using a beam deflection technique. Additionally, potential steps were applied to the anodic oxide film in an attempt to understand the relation between transients in current and deflection. The experimental results obtained have been discussed in terms of the growth kinetics of anodic oxide film on the basis of point defect model proposed by Chao et al.[10].

2. Experimental

Samples were cut from a 50 μm thick tungsten foil of 99.99 % purity into strips with dimensions of 2.5 mm x 100 mm. The strips were lightly rolled between a clean ground glass stopper and a sheet of glass to smooth the burrs produced by the cutting. In order to remove

residual stresses, the specimens were annealed at 1310 °C for 1h in an evacuated and sealed quartz tube, followed by furnace-cooling.

The samples were degreased and then electropolished at 6V in 2 wt.% NaOH solution for 15 min.[13]. After this treatment, the specimens were washed in distilled water and dried. The specimens were then coated on one side with a fast drying enamel to make that side inert. After the paint had dried, a small mirror of silvered mica was attached to the painted side near the free end to be used in measuring deflection.

Anodic oxide films of tungsten were galvanostatically formed in 0.1M H_2SO_4 solution at room temperature by applying anodic currents ranging from 0.02 to 0.65 mA cm^{-2}. Positive and negative potential steps of 2 to 4V(SCE) within the passivation range are applied to the specimen. The currents and potentials were controlled by EG&G Model 273 potentiostat and the deflection associated with the formation of the anodic oxide films were recorded on a strip chart recorder. A standard calomel electrode (SCE) with a Luggin capillary and a platinum wire were used as the reference electrode and counter electrode, respectively.

The technique used for stress measurement was based upon the method developed by Stoney[14], later modified by Nelson and Oriani[15]. Having measured the deflection of strip specimen, the surface stress, σ, was calculated from

$$\sigma = \frac{E_M t^2 z}{3(1-\nu_M{}^2)l^2 d} \tag{1}$$

where E_M is the modulus of elasticity of the specimen, t is the thickness of the specimen, z is the deflection measured at a distance *l* from the clamped end of the specimen, ν_M is Poisson's ratio for the specimen, and d is the thickness of the stressed layer. In order to distinguish the electrostrictive stress from total stress measured, deflection measurements were made at an open-circuit potential by interrupting the applied current density and allowing the tungsten strip to come to rest under the influence of other stresses in the film.

3. Results and Discussion

Deflections produced by the galvanostatic oxidation of tungsten

Figs.1 to 3 show the changes in potential and deflection as a function of time for anodic oxidation of tungsten at various applied current densities of 0.02 to 0.65 $mA\cdot cm^{-2}$. The potentials first rose sharply and then increased linearly with anodic oxidation time at applied current densities of 0.02 and 0.10 $mA\cdot cm^{-2}$. At 0.65 $mA\cdot cm^{-2}$, the linear relation was observed from the beginning of anodic oxidation. These results are similar to those found in previous work[16] on the anodic oxidation of tungsten.

As for the deflection-time curves, it is remarkable that the transition from compressive to tensile deflection occurred during the oxide film growth at an applied current density of 0.10 $mA\cdot cm^{-2}$(Fig.2), whereas compressive and tensile deflections were observed at a relatively lower current density of 0.02 $mA\cdot cm^{-2}$ (Fig.1) and at a comparatively higher current density of 0.65 $mA\cdot cm^{-2}$ (Fig.3), respectively. The transition was also observed during the anodic oxidation at an applied current density of 0.05 $mA\cdot cm^{-2}$. The time at which the transition from compressive to tensile deflection occurs was shifted to a lower value with increasing applied current density.

According to Howes' work[17], the rate of deflection produced by the anodic oxidation of Zr is linearly dependent upon the rate of potential rise and the sign of deflection is not varied with time under galvanostatic film growth condition. However, our experimental results with tungsten demonstrate that the rate and sign of deflection change with the growth of the oxide film, indicating that the rate of stress generation is not simply related to the rate of oxide growth.

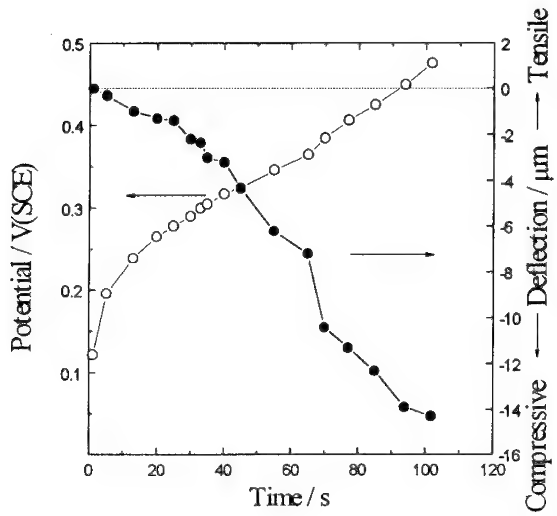

Fig.1. Changes in potential and deflection produced during anodic oxidation of tungsten at an applied current density of 0.02 mA· cm^{-2}. Dotted line represents the zero position of deflection.

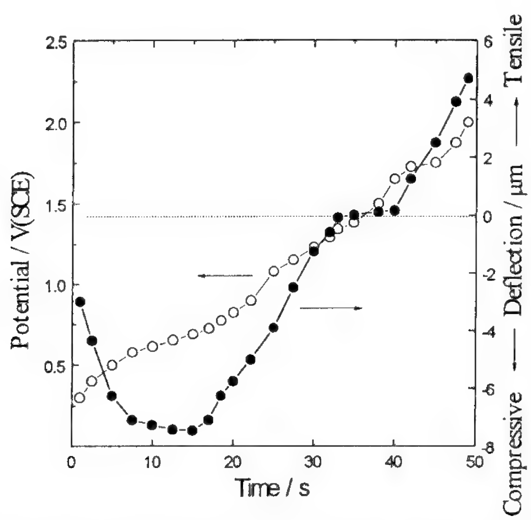

Fig.2. Changes in potential and deflection produced during anodic oxidation of tungsten at an applied current density of 0.10 mA· cm^{-2}. Dotted line represents the zero position of deflection.

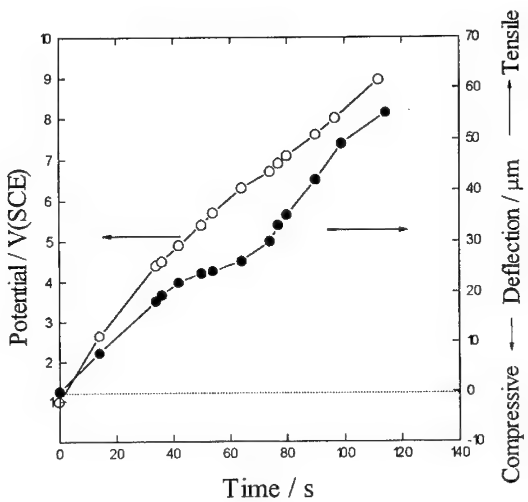

Fig.3. Changes in potential and deflection produced during anodic oxidation of tungsten at an applied current density of 0.65 mA· cm^{-2}. Dotted line represents the zero position of deflection.

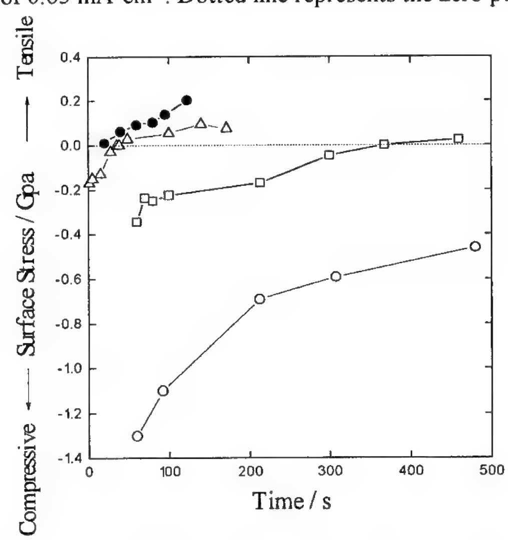

Fig.4. Changes in surface stresses with time for anodic oxidation of tungsten strip specimen at applied current densities of : ○, 0.02mA·cm^{-2} ; □, 0.05mA·cm^{-2}; Δ, 0.10mA·cm^{-2}; ●, 0.65mA·cm^{-2}. Dotted line represents the zero position of stress.

Fig.4 shows the changes in surface stress with time calculated from the measured deflections produced during the anodic oxidation of tungsten at various current densities of 0.02 to 0.65 mA·cm^{-2} by using eq.(1). Taking the thickness to potential ratio as 1.8 nm V^{-1}[12] and the following values[18]: E_M=3.78 x 10^{11} Pa and ν_M = 0.33, the magnitudes of surface stresses were calculated to be from 0.1 to a few GPa.

The thickness of the stressed layer was assumed to be the thickness of the anodic oxide film. The stresses developed during the anodic oxidation of tungsten are not homogeneously distributed

across the thickness of the anodic oxide film. Notwithstanding, it seems plausible to regard the whole thickness of the anodic oxide film as the thickness of the stressed layer owing to the fact that, in the low film thickness range investigated, the stresses are developed over the entire thickness of the anodic oxide film even though a larger proportion of stresses should be developed at the region near the metal/oxide interface relative to the region near the oxide/electrolyte interface.

The stress-time curves exhibit two characteristics to be noticed. One is that the stresses move increasingly in a tensile direction, as the applied current density increased. The other is that more compressive stresses are built up at the earlier stage of anodic oxidation and become less compressive at the later stage. These results imply that the modes of stress generation are closely dependent upon the growth kinetics of the anodic oxide film of tungsten.

According to the point defect model[10], the formation of oxygen vacancies occurs at the metal/oxide interface and the incorporation of the oxygen ions occurs at the oxide/electrolyte interface during the growth of the anodic oxide film on Fe. It was reported[19] that the activation energy for the diffusion of oxygen ions through the anodic oxide film on Fe substrate increases with increasing oxide film thickness. Thus, at very low film thickness, the oxygen vacancies formed at the metal/oxide interface can be easily eliminated by the inward diffusion of the oxygen ions formed at the oxide/electrolyte interface. Consequently, a compressive deflection occurs at the metal/oxide interface in the initial stage of the anodic oxidation of tungsten(Fig.1).

However, as the film grows, it is expected that it becomes harder for the oxygen vacancies to be eliminated due to the increase in the activation energy for the diffusion of oxygen ions through the anodic oxide film. A larger number of oxygen vacancies would build up at the metal/oxide interface with increase of the thickness of the anodic oxide film, leading to the transition from compressive to tensile deflection(Fig.2). This expectation is borne out by the present results(Figs.1 and 2) that the transition time is lowered and at the same time, the degree of movement in a tensile direction is raised with increasing applied current density. Therefore, we suggest that the changes in the sign and magnitude of the stresses generated during the anodic oxide film of tungsten are crucially determined by how fast the oxygen vacancies formed at the metal/oxide interface are annihilated by the oxygen ions which move from oxide/solution interface toward the metal/oxide interface.

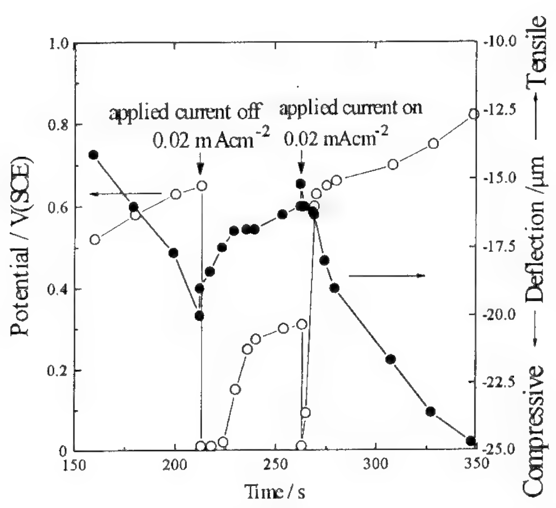

Fig.5. Responses of potential(○) and deflection(●) to current interruption during anodic oxidation of tungsten strip specimen at an applied current density of 0.02 $mA{\cdot}cm^{-2}$.

Fig. 5 shows open-circuit transients in voltage and deflection recorded during anodic oxidation of tungsten at a current density of 0.02 $mA\cdot cm^{-2}$. After interrupting the applied current density, the relaxation of electrostriction as the potential dropped produced an instantaneous tensile movement followed by a further tensile movement which declined to the steady state. The instantaneous tensile movement indicates that an electrostrictive force acts as a compressive stress component during the oxide growth.

The further tensile movement is attributed to the relaxation of elastic stress of the tungsten/anodic tungsten oxide film system[20]. As soon as the current density was reapplied, the potential and deflection decreased instantaneously and retraced their original transients. This result indicates that the anodic oxide film of tungsten does not dissolve at zero applied current density. The electrostrictive stresses were estimated from eq.(1) from the measured deflections to be 0.01 to 0.1 GPa. These values are below 10% of total stresses. These results indicate that the magnitude and sign of the stresses generated during anodic oxidation of tungsten are determined mainly by the stresses caused by the oxide growth.

The instantaneous potential drops produced by switching on and off the applied current density are expected to involve the problem of the response of the recorder used. Nonetheless, it is certain that tensile deflections are associated with the potential decreases both after interruption and after reapplication of the applied current density.

Deflection transients produced by potential steps

Fig. 6 shows the transients in current density and deflection produced by jumping up the potential from 2 to 3V(SCE), and after maintaining the applied potential constant, dropping down from 3 to 2V(SCE) upon the anodic oxide film previously formed at 2V(SCE). The upward jump of potential produced a current spike followed by a decay to a steady state(Fig.6(a)). Considering that the charge and time involved are larger than those necessary for the double layer charging[21], the current transient represents the characteristics of the oxide growth.

We expected that the upward potential jump would cause the specimen to move in a compressive direction due to the increase in electrostrictive force. However, the upward potential jump actually produced a sharp tensile movement followed by a fast deflection in the compressive direction. The compressive deflection slowed subsequently into a steady state region as the current declined to the steady-state value(Fig.6(b)). A downward potential drop to 2V(SCE) did not produce any changes in current density and deflection. From the results, it is inferred that the current-producing processes are closely related to the stress generation.

Jumping-up the applied potential upon the anodic oxide film previously formed at 2V(SCE) raises instantaneously the driving force for the reactions of oxygen vacancy formation at the metal/oxide interface and of oxygen ion incorporation at the oxide/electrolyte interfaces. The resulting electrons are removed by the potentiostat and are recorded as an anodic transient current shown in Fig.6(a). An increasing rate of oxygen vacancy formation is accompanied by an increasing rate of oxygen ion transport toward the metal/oxide interface from the oxide/electrolyte interface so that the thickness of the anodic oxide film increases and the subsequent decay of the anodic current appears.

So, it is easily expected that the instantaneous increase in anodic current density due to the upward potential jump represents the instantaneous increase in the rate of the reactions of oxygen vacancy formation and of oxygen ion incorporation. Both the instantaneous build-up of oxygen vacancies at the metal/oxide interface and the instantaneous incorporation of oxygen ions from the electrolyte into the outermost lattice layer of the anodic oxide film on tungsten would generate an instantaneous increase in a tensile deflection(Fig.6(b)). The resulting tensile deflection decreases as

the oxygen vacancies formed at the metal/oxide interface are subsequently annihilated by the inward diffusion of oxygen ions toward the metal/oxide interface.

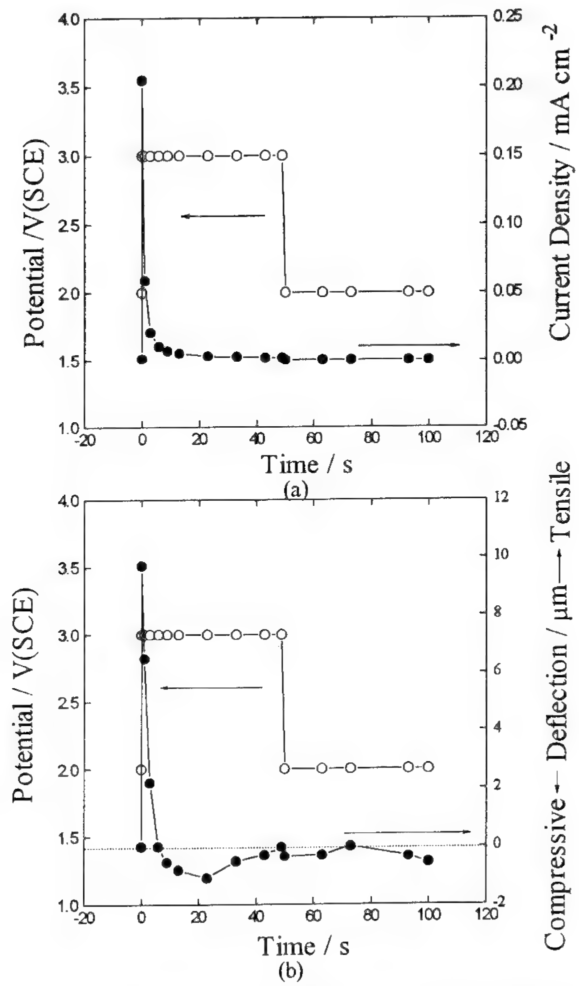

Fig.6. Transients in current density(●)(a) and deflection(●)(b) that take place with an anodic oxide film on tungsten previously formed at 2V(SCE) in 0.1M H_2SO_4 solution upon stepping the potential(○) up from 2 to 3V(SCE) and, after maintaining the applied potential constant for 50s, down from 3 to 2V(SCE). Dotted line indicates the zero position of deflection.

Fig. 7 presents an overall view of transients in current and deflection produced by jumping from one constant potential to another value upon the anodic oxide film previously formed at 3 V(SCE). In contrast to the result of Fig.6, we did not find any responses of current and deflection to the upward potential jump from 2 to 3 V(SCE). These results indicate that the influence on stress generation of potential jumps not causing oxide growth is negligibly small.

However, after steady state was attained, a subsequent potential jump from 3 to 4 V(SCE) produced the same type of current transients as shown in Fig.6, with the decay characteristics of new oxide growth and instantaneous large tensile deflection followed by a compressive deflection.

These results support the idea that the stress generation in the anodic oxide films of tungsten is considerably influenced by the growth kinetics of the anodic oxide film.

For the anodic oxide film on tungsten formed at 2V(SCE)(Fig.6), a shorter time is needed for oxygen ions to cross the anodic oxide film toward the metal/oxide interface, resulting in the cancellation of the tensile stresses(Fig.6(b)). But for the thicker anodic oxide film on tungsten formed at 3V(SCE)(Fig.7), a longer time is needed for oxygen anion transport across the film. Hence the oxygen vacancies generated at the metal/oxide interface, and therefore also the tensile stresses persist for a longer time(Fig.7(b)).

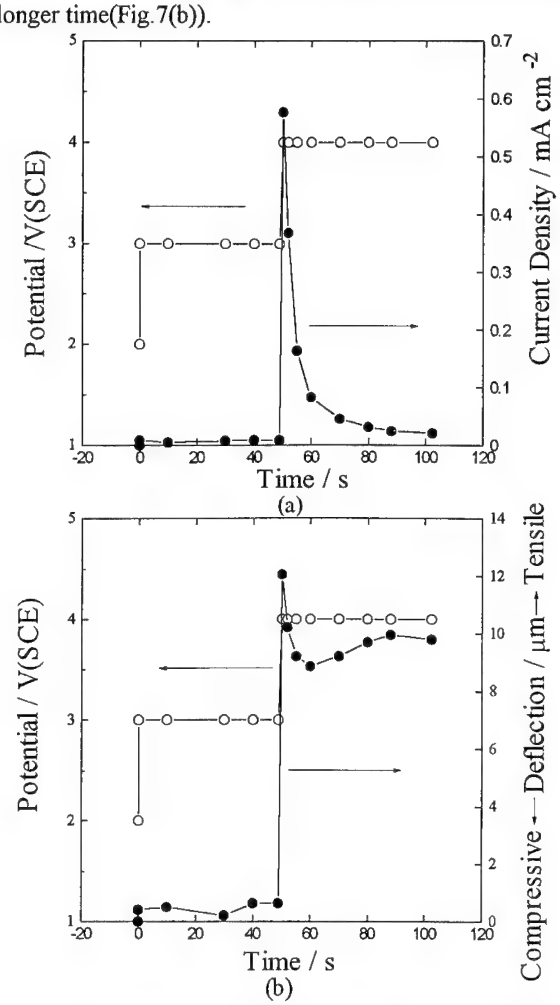

Fig.7. Transients in current density(●)(a) and deflection(●)(b) that take place with an anodic oxide film on tungsten previously formed at 3V(SCE) in 0.1M H_2SO_4 solution upon sequential jumping up the potentials(O) from 2 to 3V(SCE) and, after maintaining the applied potential constant for 50s, up from 3 to 4V(SCE).

Nelson and Oriani[15] found that upward and downward steps of potential of equal magnitude upon the anodic oxide film on nickel substrate produce equal changes of deflection of opposite signs. They attributed this to the valence changes in the nickel ions of the anodic oxide film

and hence the resulting changes in O^{2-}/OH^- ratio induced by potential steps upon the anodic oxide film on nickel[15,21]. However, in the case of the anodic oxide film on tungsten, the downward potential drop produced no cathodic transient current and no deflection in a compressive direction, indicating that the deflection responses to the potential steps are not related to the valence changes in the tungsten ions of the anodic oxide film.

4. Conclusions

Stresses developed during the anodic oxidation of tungsten in 0.1M H_2SO_4 solution at various applied current densities and potential steps have been investigated. The results are summarized as follows:

1. Compressive and tensile deflections were observed at a low(0.02 $mAcm^{-2}$) and a high applied current density(0.65$mAcm^{-2}$), respectively, whereas the transition from compressive to tensile deflection occurred with growing oxide film at applied current densities of 0.05 and 0.10 $mA \cdot cm^{-2}$.

2. Positive potential steps produced a sharp tensile movement followed by a fast deflection in the compressive direction which slowed as the current declined to the steady-state value.

3. The changes in the sign and magnitude of deflection are fairly well accounted for in terms of the combined effects of oxygen vacancy generation at the metal/oxide interface and inward diffusion of oxygen ion from the oxide/electrolyte interface.

Acknowledgment- The present work has been carried out under the auspices the joint program of Korea Science and Engineering Foundation(KOSEF) and National Science Foundation(NSF) 'Passivation and Repassivation Mechanism of W and Al by Using a Beam Deflection Technique and an Abrading Electrode Method". The authors(S.-I. P. and J.-D. K.) gratefully acknowledge the receipt of research grants 1994/96 from KOSEF and one of the authors(R. A. O.) acknowledges NSF/INT-9307995.

References

[1] H. L. Hartnagel, "Oxidation of semiconductor surfaces", in oxides and oxide films , vol.6, Ashok K. Vijh(ed.), Marcel Dekker Inc., New York(1981), p.85.
[2] P. Delichere, P. Falaras, M. Froment and A. H. Le Goff, Thin Solid Films 161, 35(1988).
[3] P. Delichere, P. Falaras, and A. H. Le Goff, Thin Solid Films 161, 47(1988).
[4] J. S. L. Leach and B. R. Pearson, Corrs. Sci. 28, 43(1988).
[5] N. B. Pillings and R. E. Bedworth, J. Inst. Met. 29, 529(1923).
[6] D. H. Bradhurst and J. S. L. Leach, Trans. Br. Ceram. Soc. 62, 793(1963).
[7] D. H. Bradhurst and J. S. L. Leach, J. Electrochem. Soc. 112, 675(1965).
[8] J. C. Nelson and R. A. Oriani, Corros. Sci., 34, 307(1993).
[9] J. A. Davies, B. Domeij, J. P. S. Pringle and F. Brown, J. Electrochem. Soc. 112, 675(1965).
[10] C. Y. Chao, L. F. Lin and D. D. Macdonald, J. Electrochem. Soc. 128, 1187(1981).
[11] F. Di Quarto, A. Di Paola and C. Sunseri, J. Electrochem. Soc. 127, 1016(1980).
[12] D. A. Vermilyea, J. Electrochem. Soc. 110, 345(1963).
[13] G. Petzow, Metallographic Etching, American Society for Metal, U. S. A. (1978)p.54.
[14] G. G. Stoney, Proc. Roy. Soc. A82, 172(1909).
[15] J. C. Nelson and R. A. Oriani, Electrochim. Acta 37, 2051(1992).
[16] M. R. Arora and R. Kelly, J. Electrochem. Soc.124, 1493(1977).
[17] V. R. Howes, Corros. Sci. 14, 491(1974).
[18] R. W. Hertzberg, Deformation and Fracture Mechanics of Engineering Materials, 2nd ed., John Wiley and Sons, New York(1983)p.8.

[19] N. Sato and M. Cohen, J. Electrochem. Soc. 111, 512(1964).
[20] J. L. Ord, J. C. Clayton and K. Byudzewski, J. Electrochem. Soc. 129, 908(1978).
[21] J. C. Nelson and R. A. Oriani, Electrochim. Acta 35, 1719(1990).

Materials Science Forum Vols. 185-188 (1995) pp. 419-424

Physical-mechanical and electrical properties of aluminium anodic films

L. Dima and L. Anicai

Research & Design Institute for Electrical Engineering,
Splaiul Unirii 313, RO-74204 Bucharest, Romania

Keywords: Aluminium anodization, anodic oxide films, electrical properties

ABSTRACT

Mechanical, thermal and electrical properties of aluminium anodic films obtained by continuously anodization of Al wires of 4.5 mm diameter and Al sheets of 40 x 0.2 mm (Al min.99.5% purity), using an electrolyte based on oxalic acid, citric acid, boric acid, isopropilic alcohol, were investigated.

The thickness of Al anodic oxide layers was $5 \pm 1\mu$, $10 \pm 1\mu$, for Al sheet, respectively $5 \pm 1\mu$, $10 \pm 1\mu$, $15 \pm 1\mu$, for Al wire. To establish the influence of anodic film formation on mechanical parameters, measurements of breaking strength and relative elongation at break for anodized and non-anodized Al conductors, were made. In order to electrically characterize the anodic films, the breakdown voltage for different curvature radii of the conductor, between 50 - 12.5 mm, were measured. The influence of the layer thickness, as well as of the cracking during its bending, was established, too. To test the thermal resistance of the insulating anodic films, the Al conductors were subjected to 1 - 5 cyclic thermal shocks at 500°C.

After the experimentals were done, it was found that Al anodic films of $5 \pm 1\mu$ may assure a breakdown voltage of minimum 200 V, for coils having a curvature radius greater than 12.5 mm and operating temperatures up to 500°C. From mechanical point of view, anodic oxide film determines a relatively reinforcing of Al conductor, but it doesn't influence its functional properties.

INTRODUCTION

When Al metal is anodically oxidized, an oxide film is produced, that usually may be non-porous(barrier type) or porous, depending on the involved electrolyte and operating parameters. For example, for certain types of electrolytes at relatively high temperatures and voltages, cristalline barrier-type aluminium anodic films were formed[1,2]. Except its great chemical inertia, that determines a high anticorrosive and mechanical resistance, anodic oxide films have good electrical properties, too[3,4,5,6,7].

This quality was for the first time used to make aluminium foil electrolytic capacitors, when dielectric is a very compact anodic oxide layer of 0.3 μ, having a great dielectrical rigidity.

For some applications that needed working temperatures greater than 250°C, enameled copper conductor or with other organic insulations, to make coiils, proved to be totally unsuitable.

In order to solve this problem, the possibility of performing Al conductors electrically insulated by an anodic oxide layer, was chosen. Practically, the coils made of this kind of conductor are able to be used up to the Al melting point (660°C), because the insulating aluminium anodic oxide film melts at 2050°C.

With such kind of conductors, induction heating coils and electromagnets to manipulate heat laminated sheets or profiles, that frequently work at temperatures of 400 - 500°C, were obtained.

From these special applications, Al anodically oxidized conductors began to be used in common applications, too, in order to replace enameled copper conductors. The most spectacular advantage of this replacement is coils weight diminishing of about 50%.

The present paper deals with some aspects regarding electrical, tharmal, mechanical properties of anodic films, obtained on aluminium wires and sheets conductors, using a newly elaborated electrolyte, that may assure a very good electrical insulation, that was applied on a continuous flow equipment.

EXPERIMENTAL

In order to characterize Al anodic films, a previously elaborated and studied anodization electrolyte [8,9], having the following composition: 50 g/l oxalic acid, 50-100 g/l citric acid, 50-100 ml/l isopropilic alcohol, was used.

Aluminium conductor anodic oxidation was performed using an installation in continuous flow for sheets and wires. The technological flow contains the following steps: (a) reeling off; (b) alkaline degreasing-pickling, (c) rinsing, (d) drying, (e) anodic oxidation, (f) rinsing, (g) drying, (h) reeling.

The following operating parameters for anodic oxidation phase, are possible to be performed, using this equipment:

- anodic oxide layer formation : 0.3μm/A.dm^2.min.;
- driving rate of conductor: 0.5 - 10 m/min.;
- diameter range of anodized Al wires: 1 - 6 mm;
- sizes of anodized Al sheets: breadth - max. 100 mm, thickness - 0.05 up to 1.5 mm;
- anodic oxidation current density: up to 30 A/dm^2;
- forming voltage of anodic oxide film: 75±10 V.

During passing of anodized Al conductors through installation, they are subjected to several bendings at curvature radii of more than 50 mm.

On this equipment, Al sheets of 40 x 0.2 mm, at thicknesses of anodic oxide layer of 5±1 μm, 10±1 μm and Al wires of 4.5 mm diameter at thicknesses of 5±1 μm, 10±1 μm, 15±1 μm, were anodized. Al sheet conductor was anodized at a thickness of 5 μm, using a driving rate of 1.3±0.1 m.min., a current density of 7.6 A/dm^2 and a temperature of electrolytr of 55±10°C. In order to obtain anodic oxide layers of 10 μm on Al sheet, a driving rate of 0.65±0.1 m/min. was used, the applied current density and electrolyte temperature remaining at the same values as mentioned above.

Al wire conductor was anodized at a thickness of 5μm using a driving rate of 3±0.1 m/min., at a current density of 15 A/dm^2 and an electrolyte temperature of 50±10°C. For a thickness of 10 μm, Al wire was anodized using a driving rate of 2±0.1 m/min., at a current density of 20 A/dm^2 and an electrolyte temperature of 50±10°C. In order to obtain a thickness of 15μm, Al wire was anodized using a driving rate of 1.5±0.1 m/min., a current density of 30 A/dm^2, while the electrolyte temperature remains the same.

The breakdown voltahe of oxide insulation was mesured for different curvature radii, to establish the influence of anodic film thickness and its cracking during bending. Thus, Al anodized conductors samples were bent at various curvature radii and then introduced in a vessel containing bearing balls of 1.5 - 2 mm diameter; the voltage increasing rate was of 50 V/s.

To test thermal resistance of insulating layer, Al anodized conductors specimens were subjected to 1 and 5 cycles of thermal shock. One cycle of thermal shock consists in a rapid heating at 500°C for 30 minutes, followed by a cooling at room temperature for 30 minutes. Then, the breakdown voltage was mesured again, at the same values of curvature radii.

The breakdown voltage at a temperature of 250°C, after 30 minutes from thermostating, was also determined.

To establish the influence of anodic oxide layer formation on mechanical parameters of Al conductor, measurements of breaking strength and relative elongation at break, for anodized and non-anodized samples, were performed.

The experimentals were done using a FP-10/1 type dynamometer, for Al conductor samples of 300 mm length, the distance between catching pieces being of 200 mm and advance rate of 5 mm/s.

RESULTS AND DISCUSSION

Variation of breakdown voltage, as a function of anodic oxide layer thickness, for different curvature radii, at room temperature and after 1 and 5 cycles of thermal shock, is presented in Tables 1 and 2, for Al sheet and Al wire respectively.

TABLE 1 - Breakdown voltage values for different anodic oxide layer thicknesses at different values of curvature radius, in the case of Al sheet conductor

Oxide layer thickness, μm	Bending way - curvature radius, mm	The breakdown voltage, V		
		initial	1 cycle of thermal shock	5 cycles of thermal shock
5±1	r = 50	330-380	300-360	340-360
	r = 25	320-380	300-360	280-340
	r = 12.5	310-360	260-340	270-320
10±1	r = 50	340-400	340-380	350-380
	r = 25	300-380	320-360	340-360
	r = 12.5	280-300	300-320	280-320

Generally, breakdown voltage is increasing with anodic oxide layer thickness; because of its glossy character, during thickening, a slight decrease of breakdown is noticed due to anodic film cracking.

In accordance with the data presented in Tables 1 and 2, for anodized Al conductors at thicnesses of 5±1μm, the breakdown voltage doesn't significantly modify as a function of curvature radius.

In the case of anodic oxide films thickness of 10±1μm, the value of breakdown voltage begins to decrease when a lower curvature radius is applied. Thus, a value of curvature radius of 12.5 mm determins a breakdown voltage decreasing of about 25%, while for anodic oxide insulations of 15±1μm, a decreasing of more than 50% was noticed.

The breakdown voltage decreasing for thicker anodic layers as a function of curvature radius, is due to micro-cracks within the insulating Al oxide film appearance, that are the more and deeper so as a greater thickness and a lower value of curvature radius are involved.

From thermal resistance point of view, according to the experimental obtained data, as it was shown in Tables 1 and 2, no significant modifications of breakdown voltage as a function of curvature radius were found to appear, after 1 and 5 cycles of thermal shock at 500°C, for all Al conductors types. Thus, the breakdown voltage value was kept in the same range, respectively of 200-380 V.

Additional experimentals that were done for the same Al conductor types at a temperature of 250°C, showed the same constancy of breakdown voltage, for oxide layer thicknesses of 5±1μm, 10±1μm, 15±1μm and curvature radii between 50 - 12.5 mm.

This facts have proved that electrical insulation properties of anodic oxide film remain unmodifyed, till a temperature of 500°C.

TABLE 2 -Breakdown voltage values for different oxide layer thicknesses at different values of curvature radius, in the case of Al wire conductor.

Oxide layer thickness, μm	Bending way - curvature radius, mm	The breakdown voltage, V		
		initial	1 cycle of thermal shock	5 cycles of thermal shock
5±1	r = 50 r = 25 r = 12.5	340-380 300-380 280-340	340-360 280-340 210-300	340-360 240-260 230-250
10±1	r = 50 r = 25 r = 12.5	350-400 300-340 280-300	320-380 240-320 240-280	320-380 300-370 320-330
15±1	r = 50 r = 25 r = 12.5	600 300-380 250-300	- - -	- - -

It was also noticed that the shape of Al conductor (sheet or wire) doesn't affect the performances of the anodic oxide electrical insulation.

Taking into account both the high values of breakdown voltage even at relatively small values of anodic oxide thickness, of 5±1 μm and its good thermal resistance as well, one can appreciate that this may be an optimum anodic oxide electrical insulation, that assures a breakdown voltage of min. 150 200 V, considered as suitable to perform various industrial applications in electrical engineering field, having working temperatures up to 500°C.

Variation of mechanical parameters, respectively of breaking strength and relative elongation at break, is presented in Table 3. Measurements of the above mentioned parameters, for Al conductors in non-anodized state and after anodic oxidation at different values of anodic oxide layer thickness, were performed.

TABLE 3 - Mechanical parameters of non-anodized and anodized Al conductors

Type of conductor	sheet 40 x 0.2			wire 4.5		
Anodic oxide film thickness,μm	0	5±1	10±1	0	5±1	10±1
Breaking strength, daN/mm^2	6.54	6.83	6.92	6.76	6.92	7.08
Relative elongation at break, %	18.5	12	11.5	39.0	30.0	25.5

It may be noticed that anodic oxide film formation on Al conductor surface determines an increase of breaking strength and a decrease of relative elongation. A relative reinforcing of Al conductor, similar to a rigidity of surface after wire drawing or lamination occurs, but without any influence on its utilization properties.

CONCLUSIONS

As a result of the performed experimentals, it may be concluded that:

- Al conductors having an anodic oxide electrical insulation obtained by anodic oxidation in the above mentioned electrolyte, at thicknesses of 5±1 μm assure a breakdown voltage value of minimum 150 - 200 V per layer that also offer a very good thermal resistance, up to a temperature of 500°C, that are suitable for industrial applications belonging to electrical engineering fielld;

- applying of small curvature radii is not recommended, because they lead to cracking appearance that may diminish breakdown voltage value;this fact is due to the glossy character of anodic oxide film ;

- Al conductors having anodic oxide electrical insulation may be used both to replace enameled copper conductors and for special applications in the field of electrical equipment that need working temperatures of maximum 500°C;

- nevertheless, there are some limitations in use of these Al anodized conductors, as it follows:(a) because of aluminium weak mechanical resistance, it is difficult to obtain wires with diameters smaller than 1 mm - this fact introduces a first limitation, the use only for great and medium power equipment where conductors having relatively high sections are involved;(b) aluminium oxide is a cristalline substance, having a glossy aspect, that is cracking during conductor bending, the more so as the insulating layer is thicker; that is why is recommendable to apply oxide thicknesses up to
10 μm, that assures a breakdown voltage between two joined wires of 300 - 400 V; this fact introduces the second limitation, only for relatively low voltage equipment;(c) because insulating layer is cracking the more so as bending radius during coiling is smaller, such kind of conductors may be used only for coils having relatively high sizes and simple forms.

Because the obtained results have proved to be attractive for many electrical applications, further studies are to be done in order to get more detailed information on such Al anodic oxide films.

REFERENCES

[1] S.Ono, N.Masuko, Corros.Eng.,**41**, 579 (1992).
[2] S.Ono, H.Ichinose and N.Masuko, J.Electrochem.Soc.,**139**(9), L80 (1992).
[3] S.Wernick, L.Pinner, "Les Traitements de Surface et la Finition de l'Aluminium et des ses Alliages", Editions EYROLLE, Paris, 1962.
[4] E.Palibroda, Electrochim.Acta, **23**,833 (1976).
[5] Russ.Patent, No.956631 (1982).
[6] Russ.Patent, No.827614 (1981).
[7] Russ.Patent, No.767239 (1980).
[8] L.Dima, G.Climovici, L.Anicai, Rom.Patent, No.98631 (1989).
[9] L.Anicai, L.Dima, Naional Conference on Chemistry and Chemical Engineering, Bucharest, vol.4, oct.1994.

Materials Science Forum Vols. 185-188 (1995) pp. 425-434

Laserphotoelectrochemical investigation of TiO_2 passive films

H. Gräfe and W. Plieth

Technische Universität Dresden, Institut für Physikalische Chemie und Elektrochemie, Mommsenstr. 13, D-01062 Dresden, Germany

Keywords: Titanium dioxide, passive layers, IMPS, photopotential transients, photocurrent transients

Abstract

LET (laser induced Electrical Transients) and IMPS (Intensity Modulated Photocurrent Spectroscopy) offer new possibilities to investigate oxide films as demonstrated with thin anodically formed TiO_2 passive layers. These nonstationary methods yield information about the semiconductor properties and especially about the kinetic processes followed by interaction with light.
From LET measurements we obtain a maximum photovoltage at t=0 corresponding to the breakdown of the electrical field across the oxide film. At sufficiently high light intensities this photovoltage marks the potential drop across the film in the dark.
The decay is dominated by a recombination current and an external photocurrent. Recombination, a nonlinear process, is observed at different passive layers. Mechanisms are given to explain two examples of the decay. The external photocurrent was determined by the electrolyte resistance and the capacitance of the oxide film.
These processes can also be observed by IMPS. In addition, slower processes can be observed. A theory is given to explain the intensity modulated photocurrent spectra.

1. Introduction

Photoelectrochemistry offers an additional method of investigating oxide films, complementing the usual electrochemical investigations [1]. With lasers working in the ultraviolet region of the spectrum, new possibilities arise [2,3]. The photoelectrochemical investigations are comparable with other electrochemical methods (Table 1) They are used to investigate semiconductors like Si, GaAs and InP [4-6]. The transients (LET) and spectra (IMPS) deliver the space charge capacity and information about charge transfer. In addition to these common electrochemical parameters, data of the recombination kinetics of excited charge carriers can be determined. This recombination process, often nonlinear, is obtained by LET measurements whereas with IMPS additional slow processes can be observed.
Information on the structure can be obtained from Raman spectroscopy [7-9].

excitation	potential U	light intensity I
stationary methods	current -potential measurement	photocurrent- potential measurement
nonstationary methods: <u>linear</u> response	impedance spectroscopy 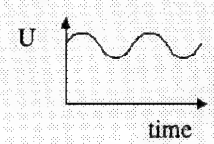	intensity modulated photocurrent spectroscopy 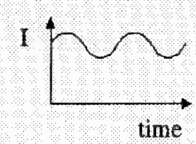
nonstationary methods: linear and <u>nonlinear</u> response	chrono amperometry 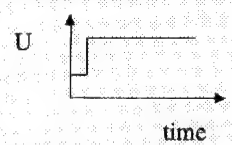	laser induced electrical transients 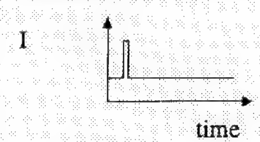

Table 1: Comparison of electrochemical and photoelectrochemical methods.

2. Experimental

The phototransients und the IMP spectra were measured with the experimental set up shown in Fig. 1 [2].
The illumination was carried out with an Excimer Laser (LET, wavelength 308 nm, pulse duration 20 ns, intensity up to 25 mJ/cm^2) and an argon ion laser (IMPS, wavelength 360 nm, intensity up to 50 mW/cm^2).
The constant intensity of the argon ion laser is modulated by an opto acoustic modulator M (Döhrer, type MT25) to yield light with an AC amplitude of 10 - 20% of the DC component. A lot of

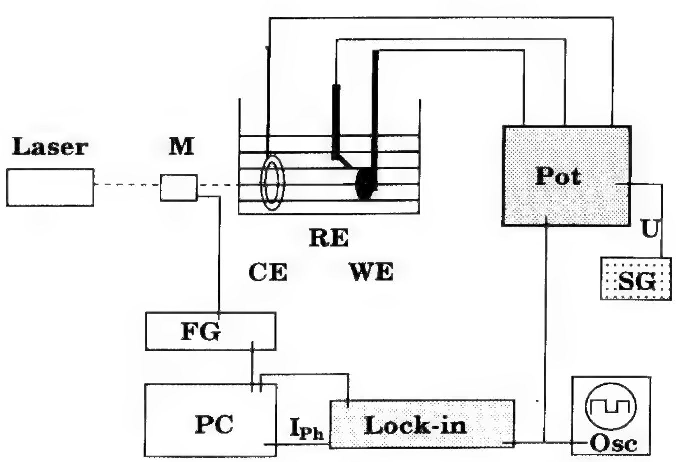

Fig. 1 Experimental set up; M: modulator, CE: counter electrode, POT: potentiostat, WE: working electrode, FG: frequency generator, RE: reference electrode, SG: voltage scan generator, PC: computer, Osc: Oscilloscope, I_{ph}: photocurrent, U: potential

experiments were carried out without a potentiostat POT. Then, the working electrode WE was polarized vs. the counter electrode CE with a DC power supply. The current was measured at an external load resistance. In order to observe the recombination at high field conditions, the external current must be supressed by a large external load resistance R_L.The stationary potential was measured by a digital voltmeter.
A frequency generator FG, a lock in amplifier (in case of IMPS measurements) and an oscilloscope Osc (in case of LET measurements) is controlled by the computer PC.
The chemical system includes an anodic (often up to 5.1 V) oxidized titanium electrode (99.99%, Good fellow) mostly in borate buffer(pH=8.4).

3. Results of the laser induced electrical transient measurements

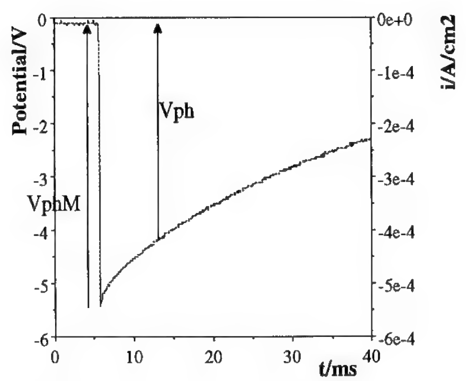

Fig. 2 Photopotential transient, titanium, pH 8.4; applied and formation potential U=5.1V, R_L =38 kΩ.

3. 1 Basic measurements of the maximum photopotential

A photopotential transient is shown in Fig.2. After the laserpulse,the photopotential V_{ph} rises to a maximum value V_{phM} and with increasing time we observe the decay of this value. Under these conditions it is obvious that this maximum is in the same range as the applied potential (U=5.1V).
The maximum photopotential depends on the laser intensity I (Fig.3). This was already observed in former investigations [3].
From the initial slope of Fig. 3a one can calculate an external quantum efficiency of 5%. The limiting value of the maximum photopotential is mainly explained by the potential drop across the layer in

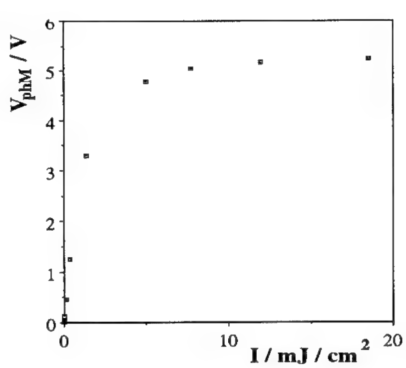

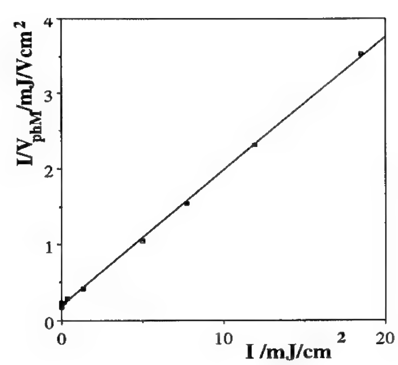

Fig. 3 a Dependence of the maximum photopotential V_{phM} on the intensity I; applied and formation potential U=5.1 V, R_L = 286 kΩ.

Fig. 3 b Intensity I / V_{phM} ratio vs. intensity (Langmuir-like behavior).

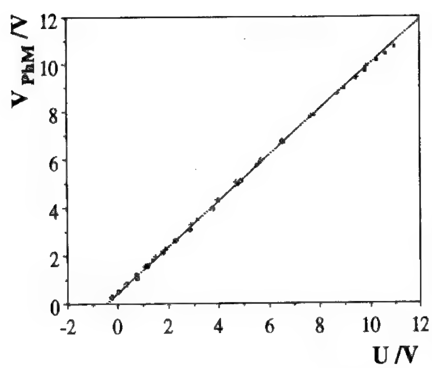

Fig. 4 Maximum photopotential V_{PhM} in dependence of the applied potential, formation voltage:
■ U = 11.2 V,
+ U = 10.0 V,
o U = 6.5 V.

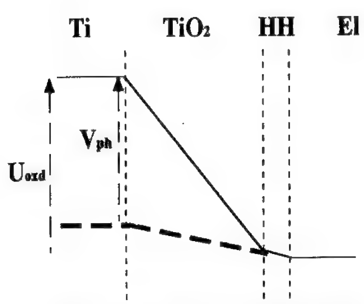

Fig. 5 Potential across the TiO_2-layer
HH : Helmholtz layer
El : electrolyte

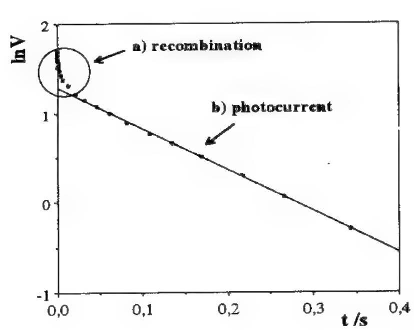

Fig. 6 Ti in borate buffer;
U=5.1V; R_L= 286 kΩ.

the dark. If one plots I / V_{phM} vs. I a linear relation is obtained as usually observed in the case of Langmuir adsorption isotherm.

The dependence of the maximum photopotential V_{PhM} on the applied potential at high light intensities is shown in Fig. 4. The results are obviously independent of the thickness of the oxide film. This could be proven by titanium dioxide films formed up to different formation potentials. The slope of the line is nearly one. The intercept with the x- axis is about U=-0.55V corresponding to the flatband potential at pH 8.4 [10]. This behaviour of the maximum photopotential leads to a simple explanation:

The first step, the excitation and subsequent separation of the charges, is a fast reaction usually impossible to observe (exception: detrapping described in 3.2.3).

The maximum photopotential V_{PhM} marks the breakdown of the electric field. Due to charge separation a photopotential V_{Ph} is build up opposite to the direction of the field in the dark. The remaining potential in the oxide is given by:

$$U_{ox} = U_{oxd} - V_{Ph} \qquad (1)$$

with

U_{ox} potential drop across the TiO_2 layer (between Helmholtz layer HH and titanium)

U_{oxd} U_{ox} in the dark.

At sufficiently high intensities saturation is achieved when the photoelectrons and photoholes are no longer separated and therefore no longer contribute to the build-up of a photoelectrical signal.

3. 2 Photopotential transient

A photopotential transient is shown in Fig 6. In the semilogarithmic presentation one can see that there are at least two processes.

The first process, which is nonlinear, belongs to the recombination, the second process is dominated by the external current.

3. 2. 1 Recombination

In the past, the recombination reaction was investigated at different semiconductors, for example GaAs. In the

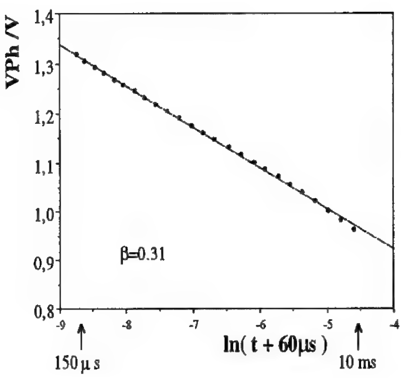

Fig. 7 Ti in borate buffer
pH = 8.4; U = 1.1V;
high external resistance R_L.

case of GaAs, with light sources of low intensity, a first order rate law was found. In the case of n-semiconductors one can assume a constant concentration of the majority charge carriers leading to a pseudo first order rate law (Eq. 2)

$$\frac{d[h^+]}{dt} = k\,[e^-]\,[h^+] = k^*\,[h^+] \qquad (2)$$

Passive layers on iron exhibit a second order recombination rate law. Due to the high intensity more photoholes and photoelectrons are generated than majority carriers are present and the pseudo first order rate law merges into a second order rate law.
In the case of high polarized passive layers one finds a different rate law. A plot of the photopotential vs. ln(t) shows a linear behaviour in the recombination region. To explain this kinetics we assume an auto inhibited reaction with an exponential influence of the inhibition. Here we also have to take into account the strong dependence of the transient on the applied potential. With $[h^+] = [e^-] = Q_{Ph}$ (photocharge) one obtains:

$$\frac{dQ_{Ph}}{dt} = -\,k_1\,Q_{Ph}^n \qquad (3)$$

$$C = \frac{Q_{Ph}}{V_{Ph}} \qquad (4)$$

$$k_1 = k_0 \exp\left(-\frac{E_A}{RT}\right) \qquad (5)$$

$$E_A = E_{A0} + \beta\,(F\,U_{ox}) \qquad (6)$$

with

C	integral capacity
n	order of reaction
E_A	potential dependent activation energy,
E_{AO}	activation energy at zero field (U_{ox}=0),
β	transfer coefficient, describing the influence of the field on the recombination,
$\beta(FU_{ox})$	potential dependent part of the activation energy

For long prepolarization times, a potential independent capacity C is obtained (Eq.4). It is assumed that in the slowest reaction of the total recombination process the charge carriers have to move against the electric field so that the activation of this process is influenced by the field (Eq. 5,6) which is strongly changing with time.
An approximate solution (Eq. 7) is obtained by neglecting the term Q_{Ph}^n which has only a small influence compared with the exponential term. In Fig. 7 the constants t_0, β and **const** are first determined by curve fitting to.

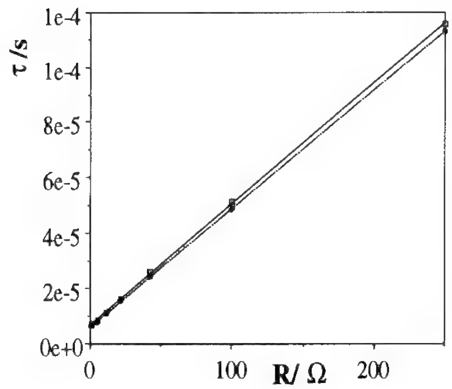

Fig. 8 Time constant τ vs. external resistance R_L different intensities I
□ $I = 12.3\ mJ/cm^2$,
● $I = 2.5\ mJ/cm^2$.

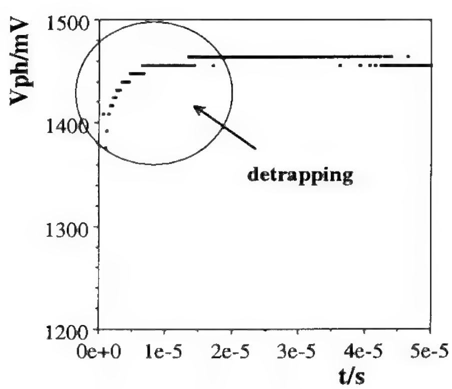

Fig. 9 Photopotential V_{Ph} vs. time t; detrapping is initally dominating; $I = 0.5 mJ/cm^2$, $R_L = 167\ k\Omega$.

$$V_{Ph} = \frac{R\,T}{F\,\beta} \ln (t - t_0) + \text{const} \qquad (7)$$

with

$$t_0 = \frac{R\,T}{\beta\,F} \exp\left(\beta \frac{F}{R\,T}\left(U_{oxd} - V_{PhM} + \frac{E_{ao}}{\beta\,F}\right)\right)$$

Eq. 7 is valid during a time from 100 µs up to 10 ms. At times less than 100 µs Eq. 4 is proven to be not valid. After 10 ms the recombination is hindered so strongly by the field that the external current is going to dominate the transient.

3. 2. 2. External current

The dependence of the time constant on the external resistance is measured in Fig. 8 according to Eq. 8. From the slope, the capacity of the oxide layer is obtained. The intercept with the x- axis corresponds to the electrolyte resistance.

$$\tau = C_{SC} (R_{el} + R_L) \qquad (8)$$

The time constants were determined during the first microseconds of the transients. Eq. 8 is valid up to ca. 10 kΩ. Then the internal oxide resistance R_{SC} is of the same order of magnitude. Recombination dominates the transient.

3. 2. 3. Detrapping

Titanium passive layers polarized for short times show an additional reaction. The maximum photopotential is build up only after ten to twenty microseconds (Fig.9). This should be caused by a resistance to charge carrier separation.
We assume that the layers contain traps in the band gap. Charge carriers captured by traps require an additional time to escape.

4. Results of IMPS measurements

With IMPS, in principle, one obtains similar information as with LET. However, especially processes with large time constants can be studied more easily with IMPS, because the LET signals are very small

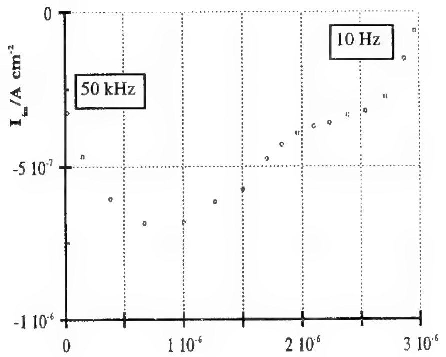

Fig. 10 Nyquist plot of IMPS measurements, Ti in borate buffer; f= 10Hz - 50kHz, U=5.1 V, prepolarization U=18 V,

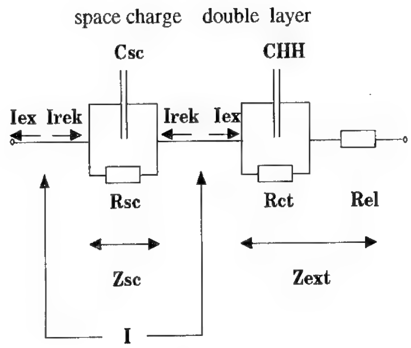

Fig. 11 Equivalent circuit of the oxide film for IMPS and LET measurement.
Z_{SC} : impedance of the space charge(determined by C_{SC} and R_{SC})
Z_{ext}: external impedance $Z_{ext} = R_{el} + Z_{DL}$
Z_{DL}: impedance of the double layer (determined by C_{HH} and R_{Ct})
I_{ex} : external current
I_{rek} : recombination current

at longer times. In Fig. 10 an IMPS plot in the Nyquist presentation is shown. Two time constants can be observed. The first one at high frequencies is identical to the process described in chapter 3b. The second one represents a process with a much larger time constant.
To explain such a result, we assume a simple equivalent circuit shown in Fig. 11. The excited charges are very quickly separated by the electrical field. For the analysis, the current I is divided into the recombination I_{rek} and external currents I_{ex}, (Eq. 9a) which are controlled by their impedances (Eq.9b).

$$I = I_{rek} + I_{ex} \tag{9a}$$

$$I_{rek} * Z_{SC} = Z_{ext} * I_{ex} \tag{9b}$$

$$H = Z_{sc} / (Z_{sc} + Z_{ext}) \tag{10}$$

The transfer function obtained (Eq. 10, normalized form) exhibits two time constants corresponding to the two capacities C_{SC} and C_{HH}. From the theory two kinds of IMPS plots (Fig. 12a and b) corresponding to the theoretical conditions are obtained (given in Eq. 11a and b).
A high semiconductor resistance R_{SC} leads to a dominating first term, as observed for oxide layers. A small space charge capacity C_{SC} (in comparison to the Helmholtz capacity C_{HH}) delivers a plot with one semicircle in the first and one in the fourth quadrant (Fig. 12 b), usually observed for semiconductors. The high frequency semicircle corresponds to the space charge capacity, the second semicircle is caused by the Helmholtz capacity. For the second semicircle other explanations are possible, for example surface states which can cause a higher AC photocurrent at low frequencies.
The analysis of the IMPS plots measured with Ti at higher frequencies shows an additional semicircle in the third quadrant (Fig.13). A reaction preceding the process discussed earlier may explain this behaviour. The time constant for this process, identical to the detrapping process described in chapter 2c,was calculated at $t_D = 20$ µs.

$$\frac{R_{sc} + R_{ct} + R_{el}}{R_{sc}} < \frac{C_{HH} + C_{sc}}{C_{HH}} \qquad (11a)$$

$$\frac{R_{sc} + R_{ct} + R_{el}}{R_{sc}} > \frac{C_{HH} + C_{sc}}{C_{HH}} \qquad (11b)$$

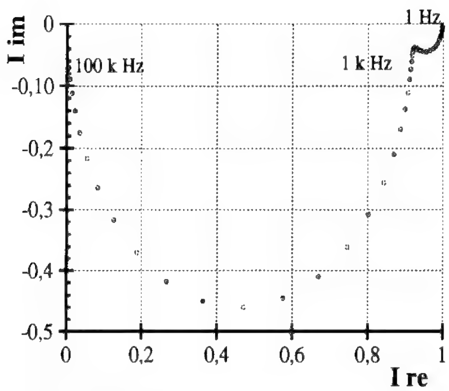

Fig. 12a Theoretical Nyquist IMPS plot, calculated fromEq.10 corresponding Eq.11a

$R_{el} = 15\ \Omega$ $C_{HH} = 16\ \mu F$
$R_{ct} = 200\ \Omega$ $C_{sc} = 1.6\ \mu F$
$(R_{sc} = 100\ k\Omega)$

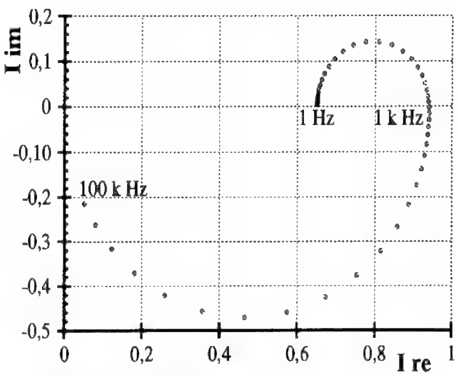

Fig. 12b Theoretical Nyquist IMPS plot, calculated fromEq.10 corresponding Eq.11b

$R_{el} = 15\ \Omega$ $C_{HH} = 16\ \mu F$
$R_{ct} = 200\ \Omega$ $C_{sc} = 0.5\ \mu F$
$R_{sc} = 400\ \Omega$

5. Discussion

Both methods, IMPS and LET, allow the analysis of the recombination kinetics. The electrical parameters obtained are identical to capacities and resistors determined by other methods like impedance spectroscopy. At sufficently high laser intensities the recombination kinetics can be observed, even if the applied potential is very high. In the case of titanium we observe an autoinhibited kinetics due to the field dependence of the activation energy of recombination. In addition the detrapping process can be observed. With IMPS slower processes are accessible.

IMPS yield informations in three quadrants whereas impedanc spectroscopy exhibits time constants only in the first quadrant. This facilitates the interpretation of the spectra.

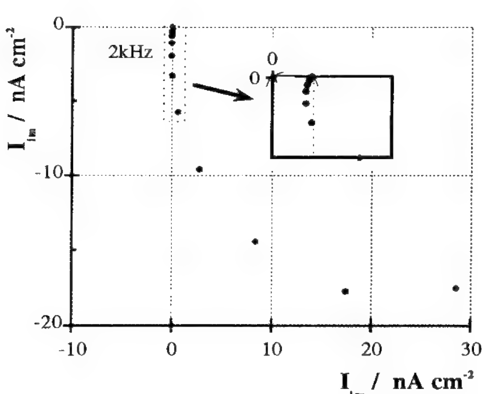

Fig. 13 Nyquist plot of an IMPS measurement, Ti in borate buffer, U = 5.1V; $t_D = 20\ \mu s$; $R_L = 5 k\Omega$;

6. References

[1] U. Stimming, Electrochimica Acta, 31, 415 (1986).

[2] W. Plieth, H.-J. Rieger, Corrosion Sci., 29, 267 (1988),
H.-J. Rieger, W. J. Plieth, Werkst. u. Korr., 39, 603 (1989).

[3] W. Plieth, A. Felske, "Grundlagen von Elektrodenprozessen", Ed. J.W.Schultze, DECHEMA-Monographien, Bd. 102, p.21, Verlag Chemie, Weinheim,1986
A. Felske, W. J. Plieth, J. Opt. Soc. Am. B3, 815-820 (1986).

[4] J. Schefold, J. Electroanal. Chem., 341, 111 (1992).

[5] L. M. Peter, Chem. Rev. 90, 753- 769 (1990).

[6] F. Willig, Ber. Bunsenges. Phys. Chem. 92, 1312- 1319 (1988).

[7] A. Hugot-Le-Goff, Thin Solid Films, 142, 193 (1986).

[8] T. Ohtsuka, J. Guo, N. Sato, J. Electrochem. Soc., 133, 2473 (1986).

[9] Lj. D. Arsov, C. Kormann, W. Plieth, J. Electrochem. Soc., 138, 2964 (1991) .

[10] H. O. Finklea, "Semiconductor electrode concept and terminology",
ed. Harry O. Finklea, Elsevier Science, (1988)

Materials Science Forum Vols. 185-188 (1995) pp. 435-446

A photoelectrochemical study of passivating layers on nickel

C. Sunseri, S. Piazza and F. Di Quarto

Dipartimento di Ingegneria Chimica dei Processi e dei Materiali, Università di Palermo, Viale delle Scienze, I-90128 Palermo, Italy

Keywords: Nickel oxides, photoelectrochemistry, passive films

ABSTRACT - The photoelectrochemical behaviour of passive films grown on bare nickel in alkaline solutions has been investigated in electrode potential ranges where the formation of Ni(II) and Ni(III) oxyhydroxides are expected. Regardless of the electrolytic solution duplex films are formed in the thermodynamic region of existence of Ni(II) with a p-NiO layer underlying a partially hydrated oxide. For anydrous oxide an optical band-gap of 3.45 ± 0.1 eV and a flat-band potential around 0.3 V/SHE at pH = 8.9 were determined. A lower optical band-gap (3.00 ± 0.05 eV) has been attributed to the hydrated oxide. The red-shift of the light absorption edge at very cathodic potentials is discussed in terms of onset of a direct electron photoemission process from the underlying metal into the solution. The photoelectrochemical data obtained in the region of Ni(III) are presented and shortly discussed.

The electrochemical behaviour of nickel has been widely investigated owing to its numerous technological applications. In fact Ni electrodes are used in energy conversion systems (secondary batteries, fuel cells), water electrolyzers, organic synthesis and electrochromic devices. Nickel is also extensively used for fabrication of alloys with high resistance to corrosion. In almost all these applications the nickel electrode is covered by an oxide film whose nature and composition usually change as function of aging time and operating conditions. Therefore the elucidation of the electrochemical behaviour of nickel electrodes needs reliable correlations between these aspects. From this point of view the major difficulties arise from: i) the existence of oxides having different oxidation numbers of nickel (+2,+3,+4), and different hydration degree, ii) the formation of surface phases constituted usually from a mixture of oxyhydroxides.

Such difficulties are revealed by the large number of formulas proposed for the nickel oxides. At the lowest oxidation state of Ni two forms of $Ni(OH)_2$ can exist in alkaline solutions [1]: a hydrated α-$Ni(OH)_2$ form and an anhydrous β-$Ni(OH)_2$ one. The real composition of the α form may be represented as $Ni(OH)_2 \cdot xH_2O$ (with $0.5 \le x \le 0.7$) [2] or $3Ni(OH)_2 \cdot 2H_2O$ [3]. In both the cases the oxidation state of Ni is +2. An alternative formulation for α-$Ni(OH)_2$ is (0.125 $NiO_2 \cdot 0.875\ Ni(OH)_2) \cdot 0.67\ H_2O$, whereas β-$Ni(OH)_2$ is also described as (0.9 $NiOOH \cdot 0.1\ Ni(OH)_2) \cdot 0.21\ H_2O$ [4]. In this case both α and β-$Ni(OH)_2$ have the same oxidation states of 2.25 but they differ for the water content. Oxidation states of Ni higher than 2 account for the p-type behaviour of these oxides.

Similarly Ni(III) oxides formed in alkaline solutions are collectively designated as NiOOH, but their real composition is much more complicated. An extended list of formulations can be found in ref. [2,4,5].

The reaction scheme for nickel oxide electrodes firstly proposed by Bode et al. [1] has been confimed by other authors [6]. Thus the α-$Ni(OH)_2$ can be reduced to Ni under cathodic polarization and converted to β-$Ni(OH)_2$ or γ-NiOOH under anodic polarization. β-$Ni(OH)_2$, once formed, is stable also at very cathodic potentials, but it can be oxidized to β-NiOOH. Conversion of β-NiOOH to γ-NiOOH can occur at more positive potentials.

The existence domain of $Ni(OH)_2$ at pH 14 is between -0.72 and 0.07 V/SHE[1] [7], but the

[1] All potentials are with respect to SHE unless otherwise stated

oxidation process of Ni(II) hydroxide is not well characterised in terms of redox potential and literature data are abundant but often conflicting [4-5,7,9-10].

The dehydration process originating the transition from α to β form in alkaline solution can occur either by aging α-$Ni(OH)_2$ for 24 hours [5] or by cycling Ni electrodes from -0.95 to -0.18 V in 0.1 M NaOH [8]. In this last case the conversion is reported to be complete when the electrode is polarized at about 0.55 V whilst at lower potentials both forms coexist. The existence of α-$Ni(OH)_2$ up to 0.1 V was also revealed by SNIFTRS [9], at variance with other results indicating that the α -> β transition occurs by polarization of Ni electrodes at potential of about -0.7 V [2].

A large number of photoelectrochemical investigations have been performed to get information on the semiconducting properties of nickel oxides. All the results confirm that Ni(II) oxides, in hydrated or anydrous form, behave like p-type semiconductors, whilst phases with Ni at higher oxidation states behave like n-type semiconductors.

Dare-Edwards et al. [11-12] proposed a band scheme for NiO single-crystal with an indirect transition at 3.58 eV and a direct one at 3.9 eV. Moreover they determined a flat band potential, V_{FB}, of 0.8 V in 0.5 M H_2SO_4. After correction for the pH shift typical of oxide semiconductors this V_{FB} value is almost coincident with the value of 0.35 V obtained by Koffyberg et al. at pH = 9.2 [13]. These last authors settled for bulk p-NiO single-crystal an indirect optical band gap at 3.47 eV although they did not exclude direct optical transitions at higher photons energy. For thick layers of Ni hydroxides in 35% (w/o) KOH Madou et al. [14] determined a V_{FB} value of 0.06 V from the photocurrent onset potential and a slightly more positive value (0.1 V) from the Mott-Schottky plot. For the reduced form of Ni hydroxide deposited on Ni Carpenter et al. [15] estimated a band gap of 3.9 eV, from absorbance measurements on trasparent films, and a value of 3.6 eV from the onset of photocurrent in the photoaction spectrum. They accepted both these values by comparing them with the 3.7 eV value assumed for p-NiO. A V_{FB} value of 0.15 V was obtained in 1 M KOH from the photocurrent onset in the photocurrent vs. potential curve. For Ni(III) hydroxide they estimated a band gap value of 1.7-1.8 eV from absorbance spectrum and a V_{FB} value less than 0.55 V. Chaojiang Zhang et al. [5] characterised the Ni hydroxide phases by near normal incidence reflectance and they concluded that in 1M KOH bulk α-$Ni(OH)_2$ and β-$Ni(OH)_2$ present identical optical absorbance spectra. On the contrary different spectra were obtained for β-NiOOH and γ-NiOOH.

Passive films grown on Ni by anodization in borate solution (pH = 8.4) at 0.85 V show both n-type and p-type photocurrents in dependence of electrode potential [16]. The authors attributed the cathodic photocurrents to p-NiO whilst n-type photocurrents were explained in terms of further Ni oxidation by photogenerated holes. The inversion photocurrent potential, U_E = 0.40 V, was assumed as the flat band potential. Based on such work a direct optical band-gap value of 3.4 eV was estimated by Stimming [17] for nickel passive films whilst the hypothesis of an indirect optical band gap at 2.2 eV was discarded without comments. More recently optical band gaps values of oxides films formed on Ni in different experimental conditions have been reported by Dagan et al. [18]. In particular for p-type films electrochemically grown they reported different band gap values as a function of electrode potential.

The present work is aimed to get a deeper insight on the origin of such a dependence as well as to try to better characterise the nature of passivating films on nickel in different conditions and electrode potential ranges. With this aim passive films on nickel were grown anodically at fixed potentials and their photoelectrochemical behaviour was investigated under experimental conditions where the existing phases are well characterised in terms of chemical composition, or Ni oxidation state. In this way it was possible to correlate the band gap values of passive films to their chemical composition. These preliminary results confirm furtherly a previous hypothesis [19-20] about the possibility to get information on the different hydration degree of the oxides by their photoelectrochemical response.

EXPERIMENTAL

Nickel electrodes were prepared from a 5 mm diam rod of 99.99% purity (Goodfellow Metals, Cambridge). Samples were degreased and sealed with a cold-curing epoxy resin (Torr-seal, Varian, Palo Alto Ca). Before each experiment the electrode surface was abraded with a 1200 grade

emery paper, washed with distilled water, and cleaned in ultrasonic bath.

Experiments were carried out in a three-electrode cell with a standard Hg/HgO (E°=0.098V vs. SHE) or standard calomel reference electrodes. In the following all electrode potentials will be referred to SHE. Immediately before each experiment air-formed oxide film was reduced by cathodic polarization at -1.5 V for 15 min in 0.5 M H_2SO_4, then the solution was changed and electrodes were passivated by polarization in one step from -1.5 V to different final voltages.

Photoelectrochemical experiments were performed using a 150 W xenon lamp equipped with a feed-back control unit of the output light power. The lamp was coupled to a grating monochromator (Kratos) and photocurrents were detected by a dual phase lock-in amplifier, mechanical chopper system. The frequency of the chopper was 10 Hz and the exit slit width was set to 3 mm in order to reduce the wavelength dispersion. For improving the photocurrent resolution in potentiostatic measurements a 450 W xenon lamp was used. The photocurrent action spectra were corrected for the photon emission of the light source. Data were acquired by an A/D interface (Hewlett Packard 7090) and transferred to a desk computer to be processed.

All experiments were carried out at room temperature in aerated solutions.

RESULTS

The passive films on Ni were grown by keeping electrodes at the formation potential, U_f, for times longer than 30 minutes. During this time the presence of photoeffects was checked. After the growth of the films photoelectrochemical measurements were done at the formation potential, then the films were held at the same potential for 12 hours for improving the quality of the photolectrochemical signal (higher signal/noise ratio). The photoelectrochemical response of the passive films at electrode potentials different from the formation one was investigated by changing the electrode potential, U_E, in cathodic or anodic direction by steps of 0.20-0.25 V with an arrest of 0.5 h at each potential.

Ni electrodes immersed in 0.25 M Na_2HPO_4 solution (pH = 8.9) showed p-type

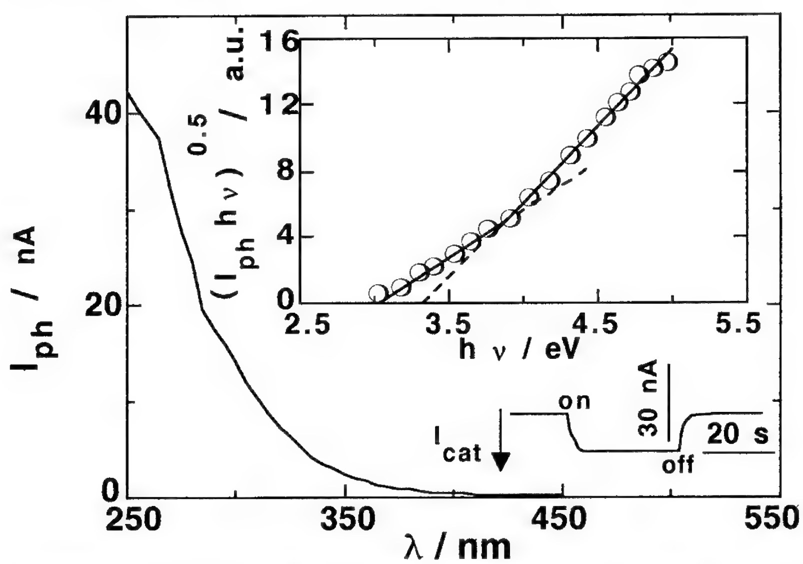

Fig. 1 - Photocurrent action spectrum and total current in the dark and under illumination (λ=300 nm) vs. time at U_E = -0.35 V for a film grown in 0.25 M Na2HPO4 at the same potential. <u>INSET</u>: determination of the optical band gap.

photoeffects soon after polarization at -0.35 V. Fig. 1 shows the photocurrent action spectrum along with the plot of the total current vs. time in the dark and under monochromatic illumination. The optical band gap, E_g^{opt}, of the passive films has been obtained according to the equation:

$$(Iph\ h\nu)^{n/2} = const\ (h\nu - E_g^{opt}) \qquad (1)$$

where hv is the energy of incident photons. The validity of this equation for both crystalline and amorphous semiconductors has been discussed elsewhere [21]. The plot of Eq. 1 for n = 1 (see inset of fig.1) gives a value of E_g^{opt} equal to 3.35 eV. The tail at lower energies in the photocurrent spectrum allows a second extrapolation giving an optical band gap at around 3.0 eV. The fitting of experimental points in the hypothesis of direct optical transitions was discarded because only very few points were matched. We like to stress that both the shape of the photocurrent spectra and the E_g^{opt} values practically do not change with the polarization time (> 24 h at -0.35 V). To check a possible modification of surface composition as effect of repeated Ni(II)/Ni(III) oxidation-reduction processes, passive films formed at -0.35 V were cycled in the interval -0.35 V $\leq U_E \leq$ 0.9 V. It was observed that also after 35 cycles at 0.02 V/sec the photoelectrochemical behaviour at -0.35 V was identical to that one of fresh films formed at the same potential.

Electrodes polarized in the region of Ni(II) at potentials more anodic than -0.35 V show identical photoelectrochemical response. On the contrary some modification in the shape of the photocurrent spectra is observed when the electrode potential is moved from -0.35 V in cathodic direction. In particular at U_E < -0.6 V a shift of the light absorption edge toward lower energies occurs so that lower optical band-gap values relative to the spectra tails ($(E_g^{opt})_2$ in Table 1), are determined. The origin of light absorption shift could be attributed to the formation of more hydrated phases having lower band-gap values, as previously reported for chromium oxyhydroxides [19], or to the onset of a process of direct electron photoemission from metal into the solution due to an increase of electric field at the metal/oxide interface under conditions of space-charge width larger than film thickness. These hypotheses will be taken into account below for explaining the results obtained in 1 M KOH, where this effect is more evident.

Table 1 - Optical band gap values of passive films on nickel as function of electrode potential in the region of Ni(II). According to Eq. 1 $(E_g^{opt})_1$ and $(E_g^{opt})_2$ are relative to the $(Iph\ h\nu)^{0.5}$ extrapolation at high and low energies respectively.

0.25 M Na_2HPO_4 pH = 8.9			buffer borate pH = 8.5			1M KOH		
U_E V (SHE)	$(E_g^{opt})_1$ eV	$(E_g^{opt})_2$ eV	U_E V (SHE)	$(E_g^{opt})_1$ eV	$(E_g^{opt})_2$ eV	U_E V (SHE)	$(E_g^{opt})_1$ eV	$(E_g^{opt})_2$ eV
0.10	3.43	3.03	0.00	3.48	3.00	-0.35	3.37	3.15
-0.10	3.43	3.09	-0.25	3.48	3.00	-0.60	3.40	3.04
-0.35	3.35	3.05	-0.50	3.37	3.00	-0.85	3.51	(2.85)
-0.60	3.38	3.05	-0.75	3.38	(2.83)	-1.10	3.21	(2.57)
-0.85	3.33	(2.83)	--	--	--	-1.25	3.31	(2.45)

Films formed at -0.35 V and stabilized at this potential for 13 hours were brought to 0.3 V in one step and then polarized up to -0.85 V by diminishing the electrode potential step by step (each step about 0.25 V). The photocurrent values measured at different wavelengths after 0.5 h of polarization at each potential are reported in fig. 2. From this plot a zero photocurrent potential near to 0.3 V can be estimated. The shape of curves of fig. 2 is typical of p-type semiconductors under depletion conditions. The sharp decrease in the photocurrent values, when the electrode potential is moved in anodic direction, can be attributed to recombination effects of photogenerated minority carriers due to the band bending lowering. The potential of zero photocurrent onset, at about 0.3 V, is in very good agreement with the flat band potential determined for p-NiO by Koffyberg et al.[13]. A saturation effect at very cathodic potentials is evidenced in the curve of fig. 2 at 260 nm. By taking into account that at this wavelength the photons energy is much higher than the estimated optical gap and then that the incident photons are strongly absorbed by the oxide film it is tempting to attribute the onset of photocurrent saturation to the existence of a depletion region covering all the film thickness.

The photoelectrochemical response of films polarized at potentials higher than 0.3 V is

completely different. Films formed at -0.35 V and polarized at 0.9 V (see fig. 3) show a n-type

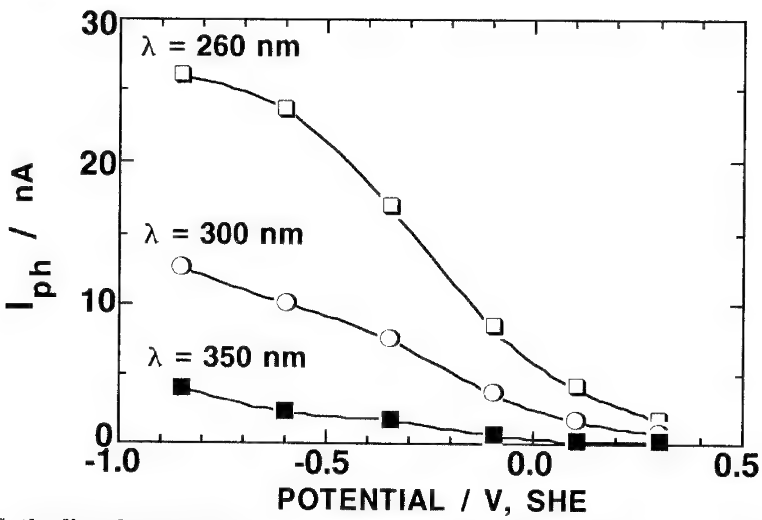

Fig. 2 - Cathodic photocurrent vs. electrode potential for a film grown in 0.25 M Na_2HPO_4

photoeffect and an indirect optical gap E_g^{opt}= 2.65 eV. A further difference is that at this potential the photoeffects can be detected only after very long polarization time (60 h). For films formed at 0.9 V

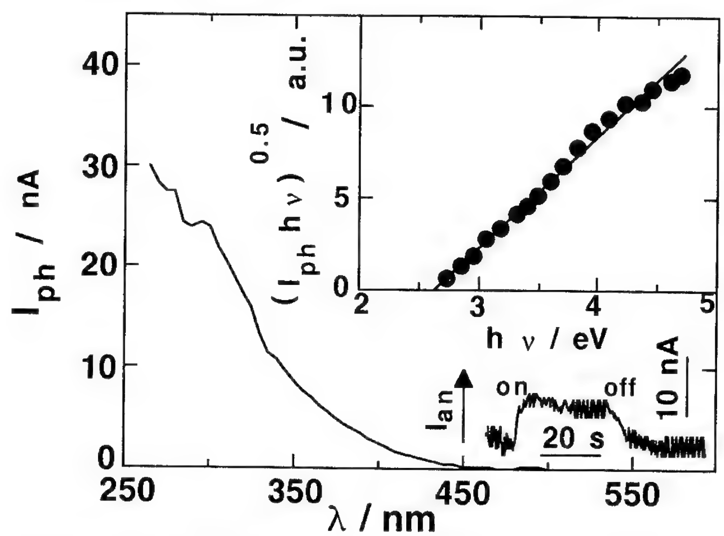

Fig. 3 - Photocurrent action spectrum and total current in the dark and under illumination (λ=300 nm) vs. time obtained at U_E = 0.9 V for a film grown in 0.25 M Na_2HPO_4 at U_f = -0.35 V. <u>INSET</u>: determination of the optical band gap.

identical photoelectrochemical results were obtained. It is noteworthy that films grown at 0.9 V and polarized at -0.35 V behave immediately like the films formed at this last potential.

To evidence a possible influence of the nature of anions on the properties of passive films, Ni electrodes were also passivated in buffer borate solution at pH = 8.5. The electrodes were prepared

and polarized following the identical procedures used for passive films grown in Na_2HPO_4. Fig. 4 shows the cathodic photocurrent spectrum at U_E = -0.25 V for a film formed in borate solution at the same potential. Two optical transitions at 3.48 eV and 3.0 eV, obtained according to Eq. 1, are reported in the inset of Fig.1. From the data of Table 1 it is evident that in borate solution, like in Na_2HPO_4, two values of E_g^{opt} can be determined in the electrode potentials region where the existence Ni(II) oxyhydroxides is allowed. The highest E_g^{opt} value is practically independent from the electrode potential, whereas the other one remains almost costant up to -0.5 V, then it decreases to 2.83 eV at -0.75 V (see Table 1). The photocurrent vs. potential curves for films formed in borate solution do not show any saturation effect and the photocurrent continously increases when the electrode potential is moved in cathodic direction. Films polarized at 0.85 V in borate solution show n-type photoeffects and E_g^{opt} = 2.5 eV after 70 hours of polarization, regardless of the initial formation potential. This E_g^{opt} value is about 0.15 eV lower than that one determined in Na_2HPO_4 solution under identical conditions

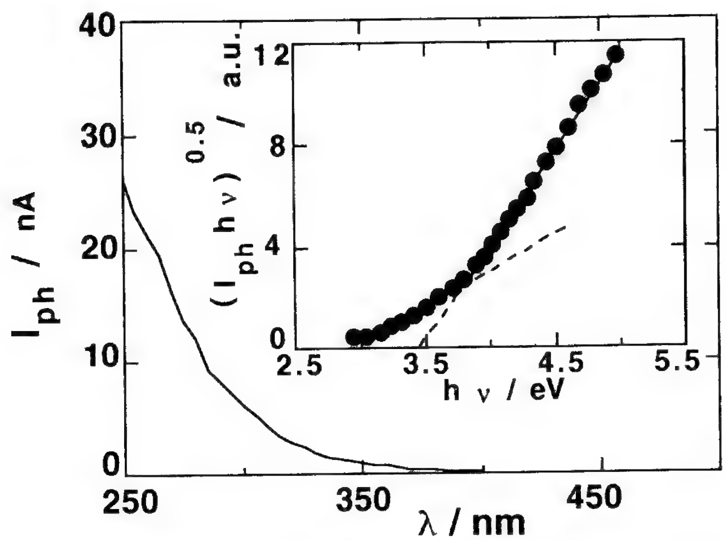

Fig. 4 - Cathodic photocurrent action spectrum at U_E = -0.25 V for a film grown in buffer borate solution (pH = 8.5) at U_f = -0.25 V. <u>INSET</u>: determination of the optical band gap.

Films grown in 1M KOH and investigated in the same solution show a photoelectrochemical behaviour quite similar to that of films grown at pH = 8.9. Films formed at -0.35 V and polarized at this potential display cathodic photocurrent spectra allowing to get optical transitions at 3.37 eV and 3.15 eV. By decreasing the electrode potential, the $(E_g^{opt})_1$ value at around 3.40 eV remained constant within ±0.1 eV up to -0.85 V whilst a monotonic decrease in the $(E_g^{opt})_2$ value was observed (see Table 1). The red-shift of the light absorption edge is clearly evidenced in fig. 5 where the photocurrent spectra at three different potentials are reported for films grown in 1 M KOH solution.

In order to explain the monotonic decrease of the threshold energy for the cathodic photocurrent onset the hypothesis of a direct electron injection process from the metal into the solution was taken into account. This phenomenon can occur when the electrode surface is oxide-free or covered from a very thin oxide film (D_{ox} < 3 nm). In this last case the electron injection in solution occurs by tunnelling through the surface oxide. The photoemission current in dependence of both photon energy, hv, and electrode potential, U_E, can be obtained according to the equation:

$$(I_{ph})^n \propto (h\nu - h\nu_0 - eU_E) \qquad (2)$$

where $h\nu_0$ is the photoelectric threshold at $U_E = 0$ in the electrochemical scale. For n = 0.4 Eq. 2

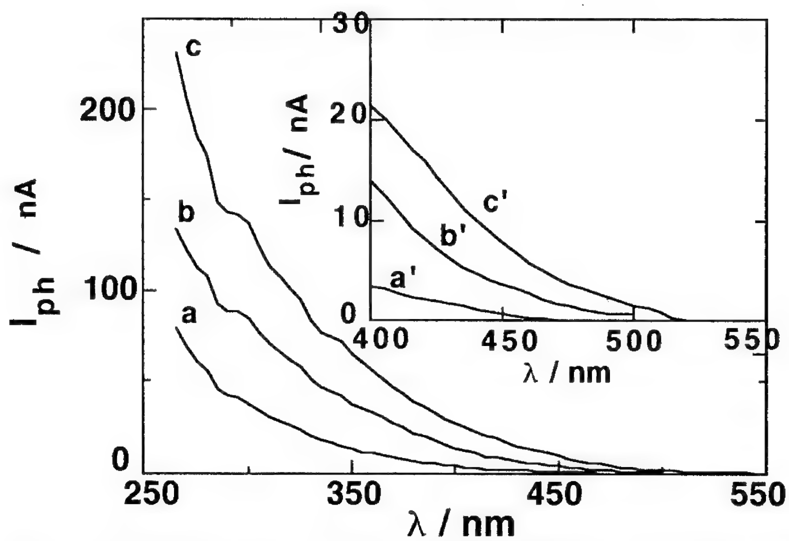

Fig. 5 - Spectral dependence of the photocurrent at different electrode potentials for a film grown in KOH at U_f = -0.35 V. a: U_E = -0.95 V; b: U_E = -1.20 V; c: U_E = -1.35 V. <u>INSET</u>: a', b',c': magnification of spectra tails obtained at the same potentials with yellow filter inserted.

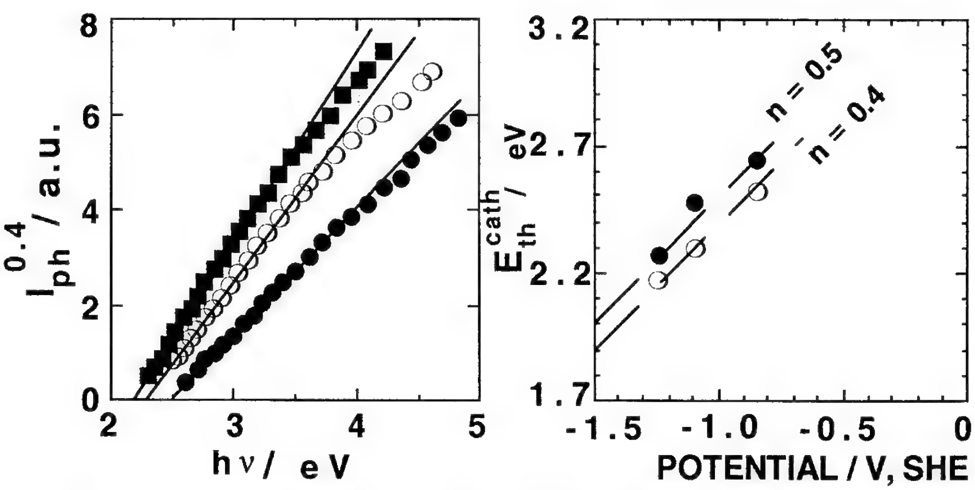

Fig. 6 - Passive film grown in KOH at -0.35 V. <u>LEFT</u>: $Iph^{0.4}$ vs. photon energy at different electrode potentials: ● U_E = -0.85 V; ○ U_E = -1.10 V; ■ U_E = -1.25 V. <u>RIGHT</u>: Cathodic threshold energy as a function of the electrode potential determined according to Eq. 2 for different values of n.

coincides with the so-called "5/2 power law", and for n = 0.5 with the "Fowler equation". The validity of this equation and its applicability with different values of n has been discussed elsewhere

[22-23]. From the extrapolation of $I_{ph}^{0.4}$ vs. hν plots the energy threshold for direct photoemission current into the solution was obtained, as shown in fig. 6 (left) for films formed at -0.35 V and polarized at -0.85 V, -1.1 V and -1.25 V. In fig.6 (right) we report the E_{th}^{cath} values determined according to Eq. 2, for both n = 0.4 and n = 0.5, as a function of electrode potentials along with the interpolating theoretical straight-lines having unitary slope. At U_E = -1.5 V the interpolating straight-lines intercept the y-axis at 1.9 eV (n = 0.4) and 2.0 eV (n = 0.5). These energy threshold values will be used to locate the conduction band edge of liquid water (see below).

The photocurrent vs. potential plots of fig. 7 parallels the analogous curves obtained in borate solution showing a supralinear increase of the photocurrent with increasing cathodic potential. In order to locate the potential of zero photocurrent, measurements were done at potential more anodic than -0.35 V. The results are not reported in fig. 7 because at -0.15 V the photoeffect is very low and the photocurrent values are poorly reliable, while at potentials more anodic than -0.15 V no photoeffects were detected even after very long (> 60 h) polarization time. Thus it can be concluded that the zero photocurrent occurs at a potential of about -0.15V. After correction of 0.06 V/pH this value is not too much distant from the corresponding potential measured in phosphate solution.

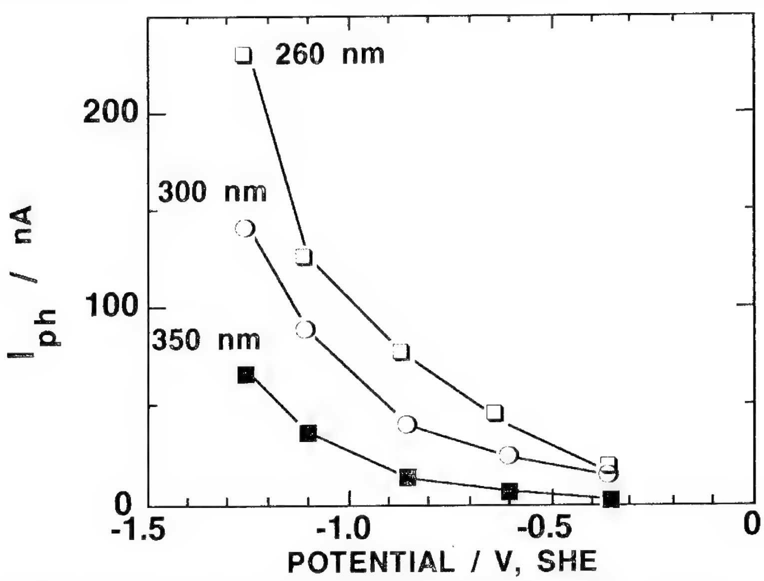

Fig. 7 - Cathodic photocurrent as a function of the electrode potential at different wavelengths for a film grown in KOH at -0.35 V

DISCUSSION

The photoelectrochemical response of passive films grown on Ni metal in the region of existence of Ni(II) indicates that the metal is covered by a film that behaves like p-type semiconductor with an indirect optical band gap of 3.45 ± 0.1 eV ($(E_g^{opt})_1$ in Table 1). This value is practically independent from both electrode potential and nature of solution. For p-NiO the literature data give band gap values ranging between 3.47 and 3.6 eV [11-13,15]; therefore the observed transition at 3.45 ± 0.1 eV can be associated to the presence of this compound. This attribution agrees also with the results of Dagan et al. [18] for air-formed NiO, which is reported to have a direct optical absorption edge at 3.7 eV. In fact in the hypothesis of indirect optical transitions a value of 3.42 eV was obtained by us, as optical band gap, by replotting the data reported in ref. [18]. The value obtained in ref. [17] on the basis of the data of Wilhelm et al. [16] is misleading because it pertains to films grown at higher potential (0.6 V/SCE) where Ni(III) compounds are likely to be formed.

The explanation of the lower values of optical band gap is more complex. In this case it is necessary to distinguish among the different electrolytic solutions; moreover for each solution the

variation of the transition threshold with the electrode potential must be analyzed. In this frame we observe that in all the solutions a second gap value around to 3.05 eV is obtained. In 1 M KOH this value was determined at -0.35 V and at -0.6 V, while in 0.25 M Na_2HPO_4 and in borate solution, pH = 8.5, it was determined in the intervals 0.1 V ÷ -0.6 V and 0.0 V ÷ -0.5 V respectively (Table 1). These results suggest that another Ni compound with a band gap of 3.0 ± 0.05 eV can exist on Ni along with NiO. This hypotheses agrees with the duplex film model by Hoppe et al. [24]. According to this model the passive films on Ni consist of an innner NiO layer linearly growing with the electrode potential and an outer $Ni(OH)_2$ part that remains almost constant in the passive range and even decreases to some extent when the potential approaches the transpassive range. The attribution of the 3.0 eV band gap to an hydrated form of NiO is also supported from the results obtained with other metals [19-20], indicating that the band gap of semiconducting or insulating oxides decreases when their hydration degree increases by keeping constant the cation oxidation state.

The identification of p-NiO as principal component of passive films grown on Ni in the existence region of Ni(II) is furtherly supported by the good agreement between the zero photocurrent potential of passive films in phosphate solution and the flat band potential of p-NiO reported by Koffyberg et al. [13].

The good agreement between the optical band gap values of passive films and the value of E_g^{opt} reported for single-crystal NiO (3.47 eV) suggests that NiO passive films are probably crystalline. This suggestion should agree with the STM results reported by Maurice et al. [25].

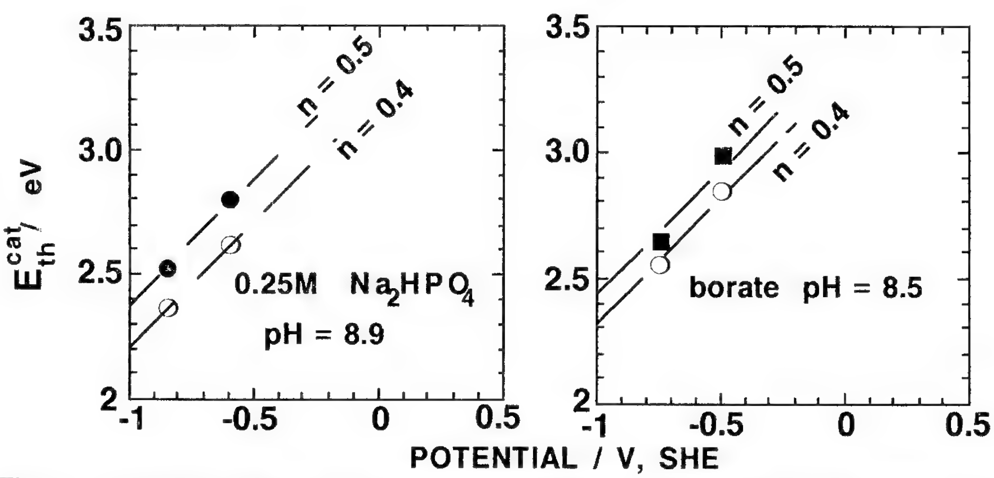

Fig. 8 - Cathodic threshold energy as a function of the electrode potential for passive films grown on nickel in different solutions.

The optical transitions at lower energies observed at very cathodic potentials can be attributed to direct photoemission of electrons from metal into the solution. This phenomenon is better evidenced in KOH solution where the most negative potentials were approached. The results reported in fig. 6 (rigth) indicate that at potentials below -0.35 V the behaviour of the interface is in full agreement with the theoretical expectations of Eq. 2. Moreover, it is possible to locate the conduction band mobility edge of liquid water, in the vacuum scale, at which electron photoemission into solution occurs. By assuming the energy level for SHE at -4.45 eV [26] the data of fig. 6 allow to locate the "conduction band" of liquid water at -1.05 eV (n = 0.4) or -0.95 eV (n = 0.5) in the vacuum scale . Both these values are in good agreement with the value of -1.0 ± 0.1 eV below the vacuum level previously reported [22,27-28]. The same calculations for the other electrolytic solutions can be done on the basis of the data reported in fig. 8 but in a shorter range of electrode potentials. For passive films formed in Na_2HPO_4 solution the theoretical unitary-slope straight line intercepts the y-axis at 2.21 eV (n = 0.4) and 2.38 eV (n = 0.5) at U_E = -1 V, whilst in borate solution at the same electrode potential the intercept value is 2.33 eV (n = 0.4) and 2.45 (n = 0.5) respectively. These data allow to

-1.04 eV (n = 0.5) depending on the extrapolation law. Both these values are not too far from the previous ones and in quite good agreement with the literature data on the conduction band location of liquid water. Thus one can conclude that also in 0.025 M Na_2HPO_4 and in borate buffer solution a direct electron photoemission process is operating at very cathodic potentials when the space-charge region extends over the whole film thickness.

Films polarized in the region of Ni(III) show n-type photocurrents with band gap values of 2.64 eV in Na_2HPO_4 and 2.5 eV in borate solutions. Such a difference could be attributed to the fact that even after very long time of polarization the noise level is so high that the resolution of the light absorption edge is rather difficult and then subjected to some errors. Moreover, it is not possible to find any support from the literature data because the semiconducting properties of the anodic Ni(III) oxides have not been widely investigated. The indirect band-gap value of 2.2 eV estimated by Stimming for passive films [17] as well as that one (1.7-1.8 eV) reported by Carpenter et al. [15] differs considerably from the values of the present work so that the differences in the optical gap values probably reflect differences in the films composition and they deserve more investigations.

CONCLUSIONS

The photoelectrochemical study carried out on passive films grown on bare nickel at electrode potentials within the existence region of Ni(II) allows to overcome some discrepancies in the literature data pertaining to the chemical composition of the films. The experimental results indicate that regardless of the electrolytic solution duplex films are formed on Ni in weakly and strongly alkaline solutions with an innner p-NiO crystalline layer having optical band-gap of 3.45 ± 0.1 eV and flat-band potential around 0.3 V at pH = 8.9, and an outer part constituted by a more hydrated compound with optical band-gap of 3.00 ± 0.05 eV. The exact stoichiometry of this Ni(II) compound is now under investigation in the frame of a research aimed to correlate the decrease of the optical band-gap of the oxides anodically grown on different metals to their hydration degree. The other aspect investigated in the present paper pertains to the red-shift of the light absorption edge with the cathodic potential observed with very thin passive films on Ni. The detailed analysis of the photoelectrochemical behaviour of such films indicates that this shift could be attributed to the onset of an electron photoemission process from metal into the solution. This effect is operating in all the solutions at very cathodic potentials where the space-charge region width reaches the metal/oxide interface. These results confirm the importance of a careful study of the different processes involved in the photoelectrochemical behaviour of thin passive films/electrolyte interfaces. Further studies are still necessary to correlate the photoelectrochemical behaviour of passive films on nickel, at higher oxidation states, to their compositions.

This work is supported financially by MURST (60% funds)

REFERENCES

[1] H. Bode, K. Dehelmet, and J. Witte, Electrochim. Acta **11**, 1079 (1966)
[2] J. McBreen in "Modern Aspects of Electrochemistry", Vol. 21, Ralph E. White, J. O'M. Bockris, and B.E. Conway, Editors, Plenum Press, New York, (1990) p.29
[3] H. Bode, Angew. Chem. **73**, 553 (1961)
[4] R. Barnard, C.F. Randall, and F.L. Tye, J. Appl. Electrochem. **10**, 109 (1980)
[5] Chaojiang Zhang and Su-Moon Park, J. Electrochem. Soc. **136**, 3333 (1989)
[6] D. Berndt, in "Maintenance-Free Batteries", Research Studies Press LTD, Taunton (1994), p.70
[7] M. Pourbaix, "Atlas of Electrochemical Equilibria", Pergamon Press, Inc., Elmsford, NY (1966)
[8] F. Hahn, B. Beden, M.J. Croissant and C. Lamy, Electrochim. Acta **31**, 335 (1986)
[9] B. Beden and A. Bewick, Electrochimica Acta **33**, 1695 (1988)
[10] R. S. Schrebler Guzman, J. R. Vilche, and A. J. Arvia, J. Appl. Electrochem. **8**, 67 (1970)
[11] M.P. Dare-Edwerds, J.B. Goodenough, A. Hamnet, and N.D. Nicholson, J. Chem. Soc. Faraday Trans. 2 **77**, 643, (1981)
[12] A. Hamnet, J.B. Goodenough, and M.P. Dare-Edwerds, J. Electrochem. Soc. **129**, 2879 (1982)
[13] F. P. Koffyberg , and F. A. Benko, J. Electrochem. Soc. **128**, 2476 (1981); idem, ibidem

129, 2880, (1982)
[14] M. J. Madou, and M. C. H. McKubre, J. Electrochem. Soc. **130**, 1056 (1983)
[15] M. K. Carpenter, and D. A. Corrigan, J. Electrochem. Soc. **136**, 1022 (1989)
[16] S. M. Wilhelm, and N. Hackerman, J. Electrochem. Soc. **128**, 1668 (1981)
[17] U. Stimming, Electrochim. Acta, **31** 415 (1986)
[18] G. Dagan, W.M. Shen, and M. Tomkiewicz, J. Electrochem. Soc. **139**, 1855 (1992)
[19] F. Di Quarto, S. Piazza, and C. Sunseri, Corr. Science **31** 721 (1990)
[20] F. Di Quarto, S. Piazza and C. Sunseri, in "Trends in Electrochemistry", S.G. Pandalay Editor, Council of Scientific Research Information, Trivandrum (India), in press
[21] C. Sunseri, S. Piazza, A. Di Paola, and F. Di Quarto, J. Electrochem. Soc. **134**, 2410 (1987)
[22] S. Piazza, A. Splendore, C. Sunseri, and F. Di Quarto J. Electrochem. Soc. **140**, 3146 (1993)
[23] F. Di Quarto, G. Tuccio, A. Di Paola, S. Piazza, and C. Sunseri, The Electrochemical Society Proceedings Series, Pennington, NJ (1994), in press
[24] H.W. Hoppe and H.H. Strehblow, Corros. Science **31**, 167 (1990)
[25] V. Maurice, H. Talah, and P. Marcus, in "Modification of Passive Films, P. Marcus, B. Baroux, and M. Keddam, Editors, The Institute of Materials, London 1994, p.62
[26] H. Reiss and A. Heller, J. Phys. Chem., **89**, 4207 (1985)
[27] T. Watanabe and H. Gerisher, J. Electroanal. Chem., **122**, 73 (1981)
[28] D. F. Feng and L.Kevan, Chem. Rev. **80**, 1 (1980)

Materials Science Forum Vols. 185-188 (1995) pp. 447-456

Photoelectrochemical analysis of the hydroxide surface films on aluminum and its alloys

T. D. Burleigh

Materials Science and Engineering Department, University of Pittsburgh, 231 Benedum Hall, Pittsburgh, PA 15261 USA

Keywords: Photoelectrochemistry, aluminum, bandgap, photospectrum, hydroxide film

Abstract

Photoelectrochemistry (PEC) was used to probe the properties of the surface films which formed on aluminum and its alloys after exposure to different voltages and electrolytes. Boiled pure aluminum exhibited an indirect bandgap energy of 3.6 eV, which was higher than that found on the native aluminum or anodized aluminum, both of which were 2.4 eV. In sulfates and in chlorides, different alloys exhibited different indirect bandgap energies, which increased as a more negative voltage was applied. All measured values of the indirect bandgap energy were within the envelope defined by native (2.4 eV) and boiled (3.6 eV) aluminum.

The passive film on aluminum is a duplex layer, with an inner Al_2O_3 film and the outer hydroxide film [1, 2]. The photocurrent is postulated to be generated in the outer hydroxide layer which is believed to range from gelatinous boehmite on native aluminum, to crystalline boehmite on boiled aluminum. The inner Al_2O_3 is believed to have a bandgap greater than 6 eV, thus is not visible with the current PEC apparatus. Photoelectrochemistry could be useful for measuring the hydration of aluminum's surface, which affects the long term adhesion of organic coatings.

Introduction

Photoelectrochemistry is a useful method to study the surface films on metals [3-5]. Several previous researchers have used light to study the oxides which form on the surface of aluminum. Goodman (1970) produced "plasma-grown" Al_2O_3 and studied its photoconduction by shining light through distilled water and onto the oxidized surface. He reported cathodic photoemission of electrons from the base Al into the Al_2O_3 starting at 2.0 eV. At higher energies, the photocurrent was anodic with electrons hypothesized being excited from the valence band to the conduction band of the Al_2O_3. This anodic photocurrent had a threshold of 3.1 eV. Goodman added these two threshold values (2.0 eV cathodic and 3.1 eV anodic) to obtain 5.1 eV as the bandgap of Al_2O_3 [6].

Nazar and Siddiqi (1981) reported photoconduction in α-Al_2O_3 using UV vacuum techniques and vapor-depositing a spot of Al on the oxide surface for electrical contact. They reported that the bandgap of α-Al_2O_3 was 4.6 eV, with two additional peaks at 3.8 and 4.5 eV due to electron traps [7]. Nazar and Jamil (1983) reported on the photoconduction in anodic Al_2O_3 films. They reported an optical bandgap of 5.52 eV, with peaks at 3.2 and 3.8, and minor peaks at 3.5, 4.5, and 5.34 [8].

Strel'tsov et al (1985) used PEC to measure the anodized films on Al (99.999% pure) and on alloys similar to 1230, 5454, 3003, and 2024. Only the 2024-type alloy showed no photopotential after anodizing. The other anodized alloys all exhibited the same photospectrum starting near 400 nm (3.1 eV) and peaking at 310 nm (4.0 eV). The photopotential was measured by illuminating the alloy with a flash lamp. The AC anodized alloys showed a negative photopotential while the DC anodized

alloys exhibited a positive photopotential. Strel'tsov reported the bandgap of anodized Al was 5.8 eV [9].

Menezes et al (1989) used PEC to analyze the oxide films on aluminum alloys 1100, 7075, and 3003 in 0.5 M NaCl solutions, and on 1100 in 0.5M Na_2SO_4 and 0.25M Na_2MoO_4. They reported that the 'pseudo-flatband' potential shifted positive with increased susceptibility to pitting corrosion. The 1100 and 3003 had an optical band edge of 3.5 eV at -0.81 V (in aerated NaCl), but the band edge increased with increasing voltage [10].

Shukla and Stimming (1989) reported cathodic photocurrents on aluminum (in 1M $NaClO_4$ solutions) for photon energies from 2.7 to 6.2 eV [11].

Di Quarto et al (1991) studied the anodic aluminum oxide films. They found a threshold energy 3.15 eV at +8.5 V, but 2.0 eV at -1.8 V [12]. They agreed with Goodman's model [6] and added the cathodic and anodic values to obtain a mobility gap for anodized aluminum of 5.1, or about 6 eV if they took into account the effect of the image force [12].

Sukamto, McMillan and Smyrl (1993) examined thin galvanostatically grown non-porous Al_2O_3 films and found both anodic and cathodic photocurrents [13]. They endorsed Goodman's (1970) model [6] as being the explanation for the system.

Arakawa and Williams (1968) used vacuum ultraviolet methods (not electrochemistry) and found the onset of absorption of light (optical bandgap edge) to occur at 6.8 eV for anodized aluminum (γ-Al_2O_3) but at 8.5 eV for corundum (α-Al_2O_3) [14]. The different researchers [6-14] do not agree as on the value of the bandgap of the oxide on aluminum.

A model for how light can generate a cathodic photocurrent is shown in Fig. 1. The light excites electrons into the conduction band, where they flow in the electric field caused by the band bending (the Schottky barrier). If there is no band bending (flatband) the excited electron would recombine with the hole, and there would be no photocurrent.

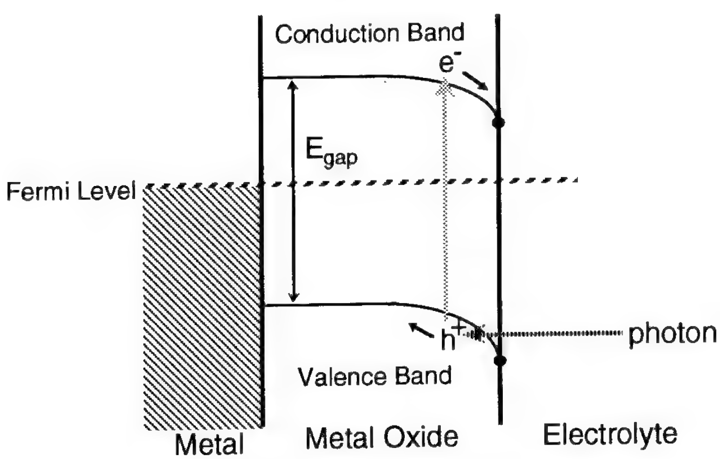

Fig 1: Photons create hole-electron pairs which are separated by the Schottky Barrier at the oxide/electrolyte interface.

Experimental Procedure

In this study, the metal sample was immersed in the electrolyte and a voltage was applied to it. The corrosion current decreased when the metal was illuminated with a bright light. The light-induced change in the current is the so-named "photocurrent," whose magnitude varies with the applied voltage and the wavelength (color) of the illuminating light. The response of the photocurrent can carry information about the oxide surface film.

The photoelectrochemical apparatus is shown in Fig. 2. The light shines from the xenon arc lamp (150 watt), and is chopped into 13.6 Hz pulses by the light chopper. The pulses of light shine through the McPherson GM 252 Czerny-Turner grating monochromator where a narrow wavelength band (±3 nm) is selected. The pulsed monochromatic light shines through a quartz window, through the electrolyte, and strikes the immersed aluminum sample. This generates a photocurrent which is measured by the potentiostat. The pulsing light causes a cyclic addition to the dark current. The lock-in amplifier separates the cyclic photocurrent from the dark current.

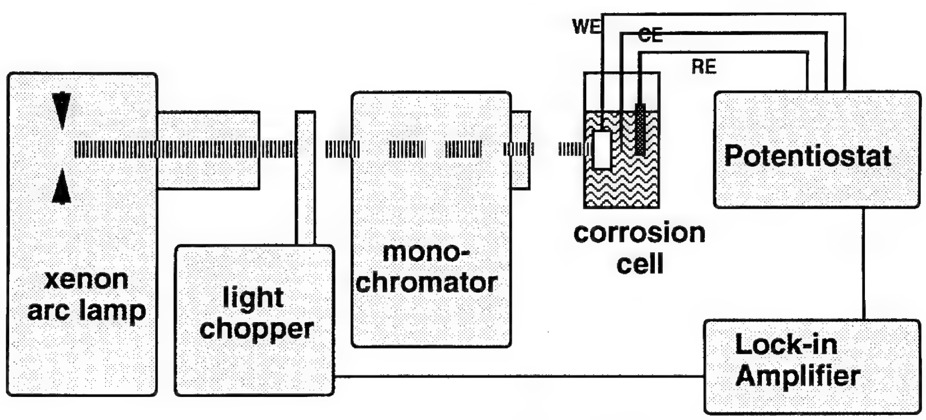

Fig. 2: Photoelectrochemical Apparatus.

The quantum efficiency (Φ) is the number of electrons detected per photon striking the sample. The quantum efficiency was calculated by dividing the photocurrent by the power of the incident light, and converting to electrons per photon. The square root of the quantum efficiency ($\Phi^{0.5}$) may be plotted against the photon energy (hv) and extrapolated to zero efficiency to determine the indirect bandgap energy. The author found $\Phi^{0.5}$ vs. hv gave the best fit to the data for aluminum.

Two neutral electrolytes were used in these experiments. The chloride solution (3.5% NaCl) and the sulfate solution (0.5M Na_2SO_4) were made with deionized water. The test solutions were deaerated by bubbling purified nitrogen gas through the solution.

The alloys studied were pure aluminum (99.999%) and binary alloys containing Cu, Li, Zn or Ge whose compositions are shown in Table 1. The alloys were all cast and solution heat treated at 505°C (940°F) for 1 hour and cold water quenched and then naturally aged at room temperature. The polished microstructures all showed precipitated second-phases after two months room temperature aging.

Table 1:	Compositions.
Al-Cu	2.32 wt. % Cu
Al-Zn	2.27 wt. % Zn
Al-Li	0.32 wt. % Li
Al-Ge	2.30 wt. % Ge

The anodized aluminum was pure Al anodized at 20 V in a boric acid solution. The boiled aluminum was pure Al boiled in deionized water for one hour, and dried in lab air for one day.

Results

Light shining on the surface of the aluminum can decrease the dark current density. Fig. 3 shows the effect on Al-Cu of 13 sec. pulses of monochromatic light. These changes in current are so distinct that they could be measured directly. Unfortunately many times the photocurrent is very small, and the dark current is very noisy. An example is shown in Fig. 4 for boiled Al in the sulfate solution, where the lock-in amplifier was needed to measure the photocurrent. Generally, the photocurrent measured with chopped light and the lock-in amp agreed with the photocurrent measured with a constant monochromatic light.

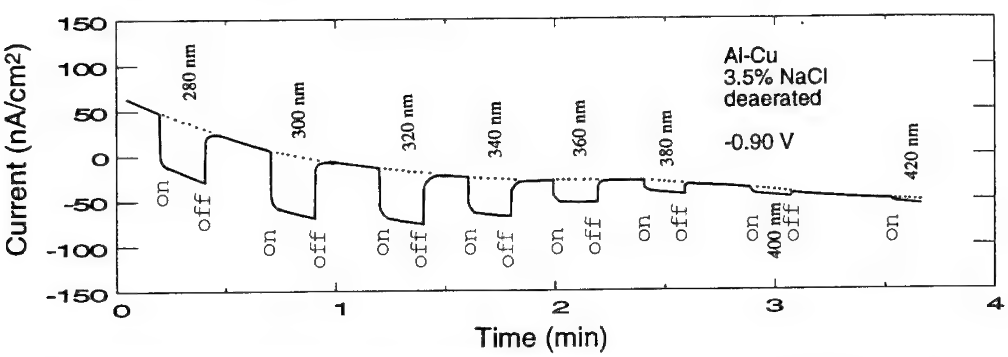

Fig.3: Pulses of monochromatic light decreased the dark current on Al-Cu immersed in saltwater.

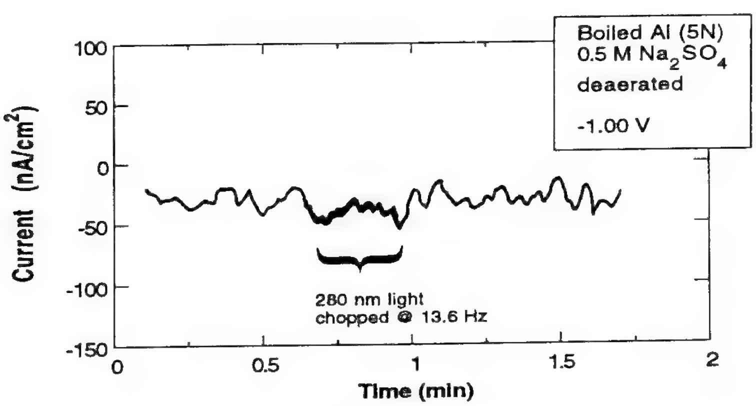

Fig. 4: The 13.6 Hz light pulses added an additional signal to the noisy dark current.

A typical cyclic voltammogram for pure Al in the sulfate solution (0.5M Na_2SO_4) is shown in Fig. 5. The aluminum was very passive, and the photocurrent was cathodic for the entire range from -1.6 to -0.3 V_{SCE}. (Menezes et al [10] showed that the photocurrent became anodic above potentials of -0.4 V_{SCE}, but this experiment did not go far enough anodic to see this change).

A typical cyclic voltammogram for Al-Cu in chlorides is shown in Fig. 6. The photocurrent is cathodic and decreasing as the voltage goes noble. There is no change in the photocurrent at the

pitting potential, which implies that there is no direct relation between the photocurrent and the corrosion current.

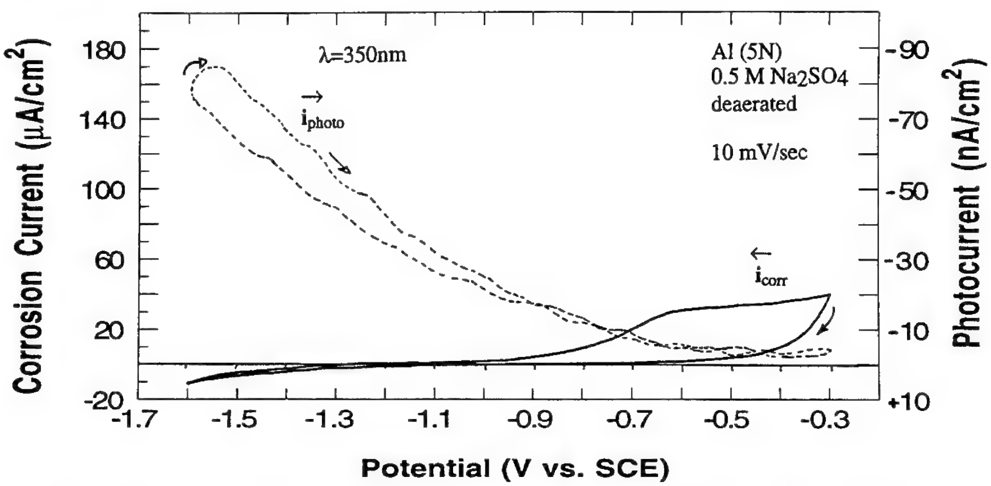

Fig. 5: Cyclic Voltammogram of photocurrent (dashed line) and dark current (solid line).

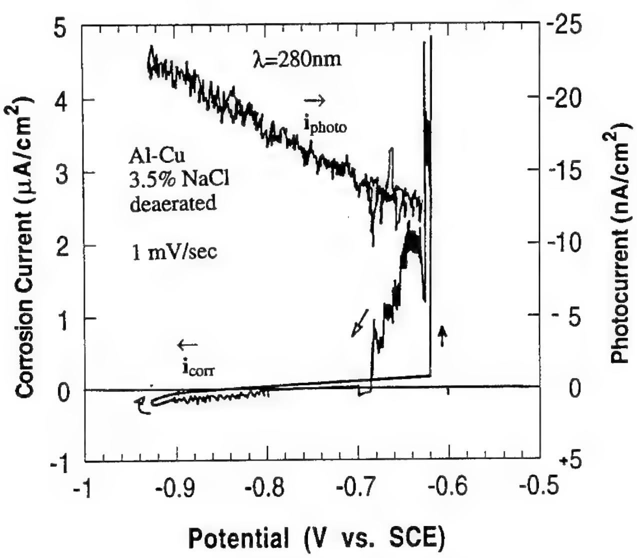

Fig. 6: The photocurrent shows no change as it approaches the pitting potential in NaCl.

The photospectra are shown in Fig. 7 for the different aluminum samples. The photospectrum for pure aluminum anodized in boric acid at 20 V shows an indirect bandgap of 2.4 eV. The anodized film is reported to be γ-Al_2O_3 (Wefers [2]). The anodic photospectrum is identical to non-anodized pure Al. The author postulates that the photocurrent is generated in the outer hydroxide (AlOOH), rather than in the barrier oxide (γ-Al_2O_3), or at the metal interface.

The photospectrum for pure aluminum boiled in deionized water is also shown in Fig. 7. This boiled aluminum should form crystalline boehmite, γ-AlOOH (Wefers [2]), and it exhibits a different photospectrum from the anodized or native films of aluminum.

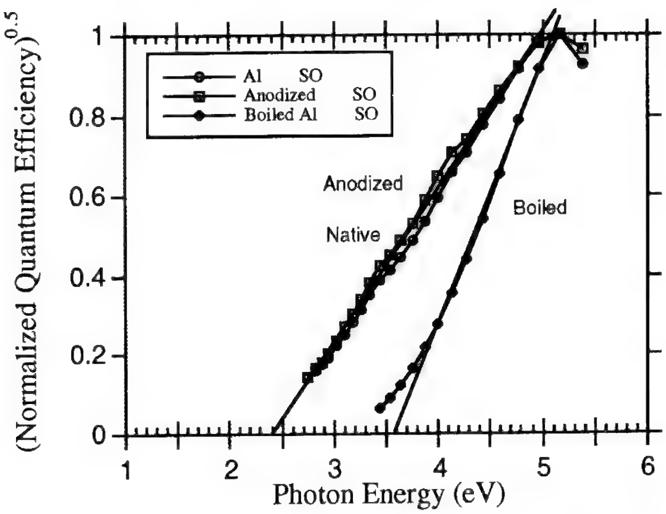

Fig. 7: Photospectra of the Native, Anodized, and Boiled surfaces in the sulfate solution.

The photospectra of the aluminum's surface layers were measured at different voltages. Fig. 8 (boiled aluminum in sulfates) and Fig. 9 (native Al film in chlorides) illustrate that the photospectra shift with applied voltage, which suggests that the surface film composition or structure varies with depth into the surface film.

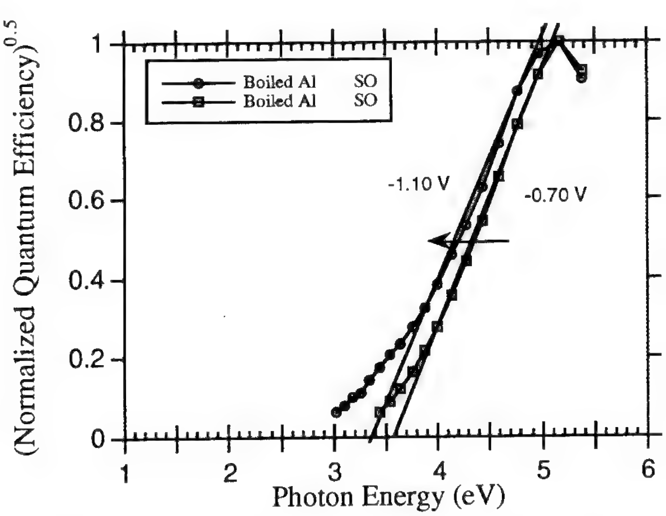

Fig. 8: Photospectra of boiled Al shift at different voltages.

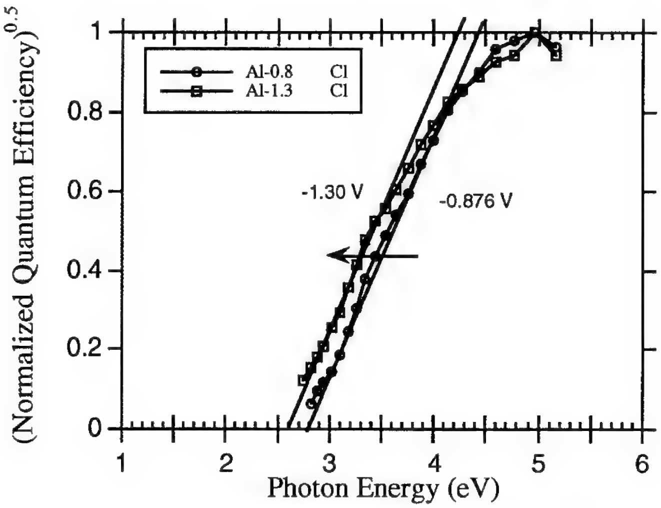

Fig.9: Photospectra for the native film shift at two different voltages.

Fig. 10 shows the photospectra for Al, Al-Ge, and Al-Zn, immersed in 3.5% NaCl. The absorption slope are different and the indirect bandgap varies from 2.6-2.8 eV.

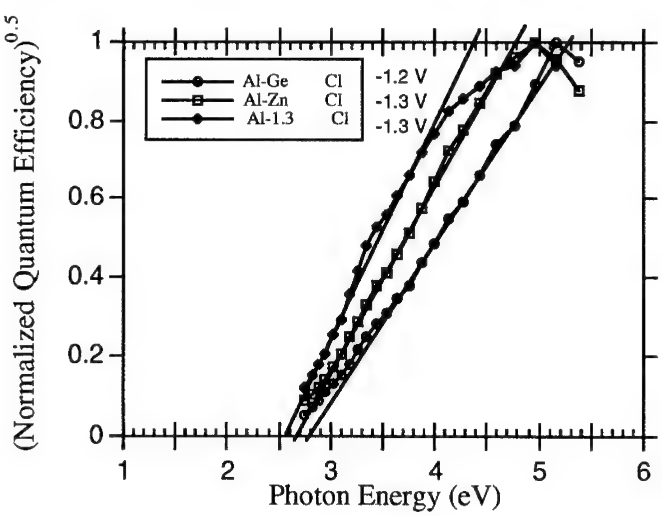

Fig. 10: Photospectra for three alloys in 3.5% NaCl.

In Fig. 11, pure Al was compared in NaCl and in Na_2SO_4 solutions, and exhibited the same indirect bandgap (2.6 eV), although the absorption slopes differ.

Fig. 12 is a composite plot showing many of the spectrums of the alloys, electrolytes and voltages. The two extremes of anodized aluminum (E_{gap}=2.4 eV) and boiled Al (E_{gap}=3.6 eV) provide an envelope enclosing all the photospectra measured on these aluminum alloys.

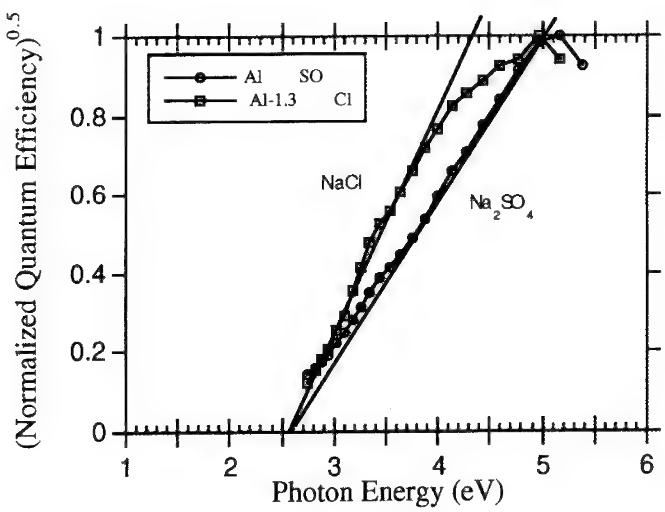

Fig. 11: Photospectra for pure Al in NaCl vs. Na_2SO_4.

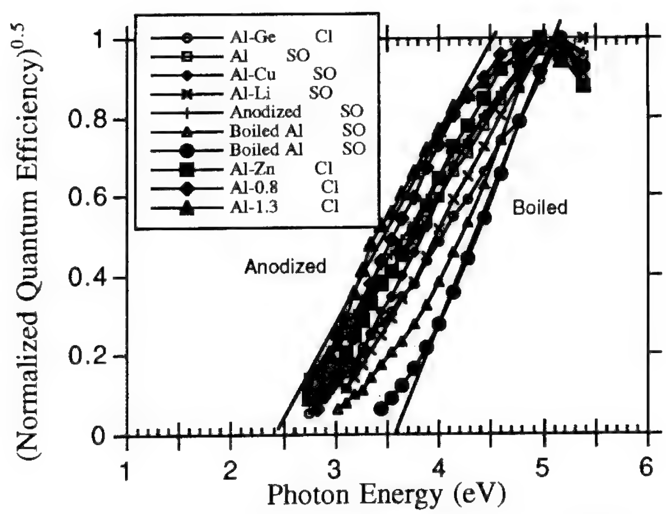

Fig. 12: The different surfaces are within the envelope defined by boiled and anodized Al.

In several experiments, no photocurrents were detectable. This occurred under four different conditions:

1) The freshly wet polished pure aluminum showed no photocurrent before cycling.
2) The sputtered deposited Al-19%Si "stainless aluminum" showed no photocurrent.
3) Pure Al tested in concentrated nitric acid showed no photocurrent over a 1.3 V range.
4) Cathodically polarized aluminum (-1.4 V for 2 hr) showed no photocurrent at -1.0 V.

Any model used to explain the photocurrents must also explain why there was no detectable photocurrent under certain conditions.

Discussion

Photoelectrochemistry can probe the properties of the oxide-hydroxide film on the surface of aluminum. Figs. 5 and 6 illustrate that there was not a direct relation between the photocurrent and the corrosion current. The author postulates that the oxide layer which controls the corrosion resistance is not the same layer which provides the photocurrent. The photocurrent is postulated to be generated in the outer hydroxide layer (the inner Al_2O_3 would have a bandgap greater than 6 eV and be invisible with the current PEC apparatus). In other words, the inner oxide adjacent to the metal controls the corrosion resistance, but the outer hydroxide layer provides the photocurrent. Fig. 13 illustrates the layers for anodized and boiled aluminum. The other alloys and conditions would range between these two extremes.

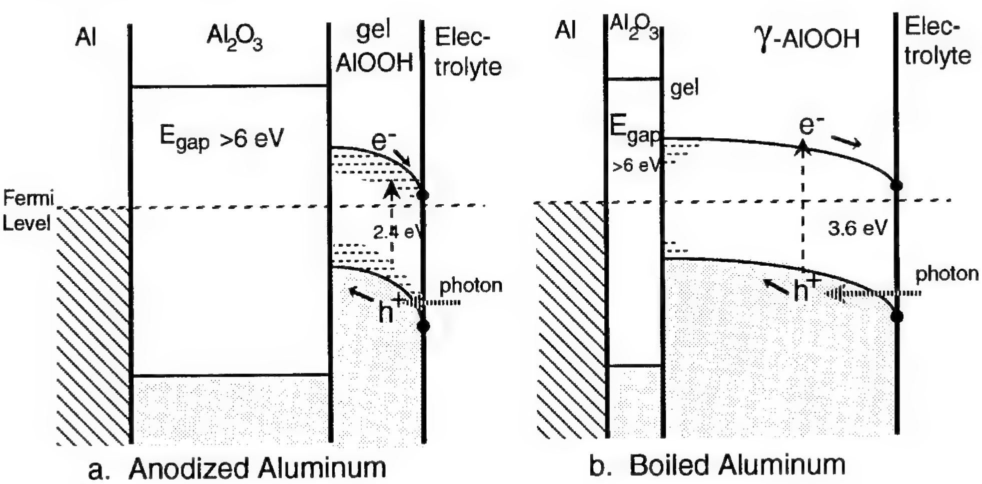

Fig. 13: Postulated model of the photocurrents being generated in the hydroxide film on aluminum.

The Al_2O_3 would be invisible in the PEC experiments because the fused quartz windows and lenses cut off light with energy greater than 6 eV. According to Arakawa, the bandgap of γ-Al_2O_3 is 6.8 eV, and α-Al_2O_3 is 8.5 eV [14].

It was shown in Fig. 12 that the bandgap of the hydroxide changed with voltage, electrolyte, and alloy composition. This implies that the hydroxide layer structure or composition can change with depth into the hydroxide. The hydroxide could vary from gelatinous (amorphous) AlOOH with a bandgap of 2.4 eV, to crystalline boehmite (γ-AlOOH, E_{gap}=3.6 eV) for boiled aluminum. (The crystalline boehmite is formed by a dissolution-precipitation reaction at the solution interface. If the samples had been aged for several days, bayerite (α-$Al(OH)_3$ could also have formed [1].)

In the cases where no photocurrent was detectable, there might not have been enough outer hydroxide on the surface to provide a photosignal. The inner oxide layer was present and provided the corrosion resistance, but was not discernible due to its bandgap being greater than 6 eV. This inner oxide could be γ-Al_2O_3 [2] or α-Al_2O_3 [15] although it is often considered amorphous [1, 2].

Voltage would have the following effect on the hydroxide layer: Near -0.4 V is flatband, and no photocurrent. At -0.7 V, there would be slight band bending at the outer edge where the bandgap was wider. Any photocurrent generated at this voltage would have a higher onset energy. At -1.1 V

there is greater band bending progressing further inward to where the bandgap is narrower. Thus as the voltage goes further negative, the bending occurs at the narrower bandgap, thus absorbing lower energy photons. The anodic photocurrents occur at potentials more noble than -0.4 V, because the bands bend upward at the electrolyte interface, reversing the electron flow. This model differs from the previous model of Goodman [6, 11-13], but can explain the data in a consistent manner.

Although the PEC apparatus used herein may not detect the oxide layer, it appears to detect the hydroxide. Therefore PEC could be useful for measuring the hydration of the aluminum's surface oxide, which determines the long-term adhesion of paints, epoxies and other polymer layers [16].

Summary

This paper reports the literature and the photospectra for films which formed on the surface of aluminum alloys exposed to different voltages, and electrolytes, and have different alloying elements. The surface of aluminum is a duplex structure with an inner oxide layer and an outer hydroxide layer [1, 2]. The inner Al_2O_3 layer is believed to have a bandgap greater than 6 eV, and the outer hydroxide layer is believed to range from gelatinous AlOOH (E_{gap}=2.4), to crystalline boehmite (γ-AlOOH, E_{gap}=3.6 eV) for boiled Al. Although PEC does not appear to carry information on the inner oxide, it could provide information on the hydration of the surface.

Acknowledgments

Special thanks to Alcoa Technical Center for the donation of the PEC apparatus and aluminum samples, and to Prof. Fred Pettit, Mr. Hiro Katayama, and Dr. Karl Wefers.

References

[1] R.K. Hart, Trans. Faraday Soc., 53, 1020-1027 (1957).
[2] K. Wefers and C. Misra, "Oxides and Hydroxides of Aluminum," Technical Paper #19, Revised, Alcoa Laboratories, (1987).
[3] U. Stimming, Electrochim. Acta., 31, 4, 415-429 (1986).
[4] L.M. Peter, Ber., Bunsenges. Phys. Chem. 91, 419-426 (1987).
[5] T. D. Burleigh, Corrosion, 46, 6, 464-471 (1989).
[6] A.M. Goodman, J. Appl. Phys. 41, 5, 2176-2179 (1970).
[7] F.M. Nazar and S.A. Siddiqi, Inst. J. Electronics, 51, 3, 205-209 (1981).
[8] F.M. Nazar and M Jamil, J. Mat. Sci. Letters 2, 10, 570-572 (1983).
[9] E.A. Strel'tsov, G.L. Shchukin, and V.V. Koleda, Zashchita Metallov, 21, 1, 116-118 (1985).
[10] S. Menezes, R. Haak, G. Hagen, and M. Kendig, J. Electrochem. Soc. 136, 7, 1884-1886 (1989).
[11] D. Shukla and U. Stimming, Corro. Sci. 29, 11/12, 1379-1382 (1989).
[12] F. Di Quarto, C. Gentile, S. Piazzo, and C. Sunseri, J. Electrochem. Soc., 138, 6, 1856-1861 (1991).
[13] J.P. H. Sukamto, L.S. McMillan, W. Smyrl, Electrochimica Acta, 38, 1, 15-27 (1993).
[14] E.T. Arakawa and M.W. Williams, (1968), J. Phys. Chem. Solids, 29, 735-744 (1968).
[15] G.D. Davis, W.C. Moshier, G.G. Long, and D.R. Black, J. Electrochem. Soc. 138, 11, 3194-3199 (1991).
[16] S. Wernick, R. Pinner, P.G. Sheasby, "Surface Treatment and Finishing of Aluminum and Its Alloys," 5th Edition, Vol. 1, ASM International., Metals Park, OH (1987).

Materials Science Forum Vols. 185-188 (1995) pp. 457-464

In-situ ellipsometric studies of the passivation of Fe-Cr-Ni steel in acid solution

W. Kozlowski

Institute of Physical Chemistry, Polish Academy of Sciences,
Kasprzaka Str. 44/52, PL-01-224 Warsaw, Poland

Keywords: Ellipsometry, passivation, stainless steel, anodic films

Abstract

An *in-situ* automatic ellipsometry was applied to characterize optical properties of anodic films formed on Fe-18Cr-11Ni austenitic stainless steel (SS), on the basis of the three parameters ($\delta\Delta$, $\delta\Psi$, $d I / I_0$). The complex refractive indices and thickness of the film were found, assuming that the films were homogeneous and optically isotropic. Measurements were performed in a de-aerated solution of 0.5 M H_2SO_4 (pH = 0.5) at 25 ^{0}C, during the potentiodynamic anodic polarization.
The electrochemical and ellipsometric results demonstrate that the optical constants of the anodic films changed with the electrode potential. This effect was particularly pronounced in the active and active-passive transition regions. In the active region, the anodic films were probably formed by Fe and Cr salts and hydroxides. In the active-passive transition region, the content of chromium in the film increased. Chromium was probably present mainly as Cr(III) hydroxide. At more noble potentials, the passive film was probably composed mainly of Cr(III) oxyhydroxide.
The changes of the chemical composition of the anodic films are explained by selective dissolution of iron and dehydration of the film.

Introduction

Passivating films on stainless steels have been studied by a number of workers [1-23]. An extensive investigations have been carried out using *ex-situ* techniques, as Auger Electron Spectroscopy (AES), X-ray Photoelectron Spectroscopy (XPS), and Secondary Ion Mass Spectrometry (SIMS). Studies with these techniques have shown that the passive films are enriched in chromium [1-15], and that nickel content in the surface films is very low [6,9,13,15-17].
According to Hashimoto et al. [7,8], one-layer passive films formed on the Fe-19Cr and Fe-30Cr alloys in HCl, consist mainly of hydrated chromium oxyhydroxide $CrO_x(OH)_{3-2x}{\cdot}nH_2O$, where x and n depend on the alloy composition and the condition of the film formation.
On the other hand, a duplex structure of the passive films formed on ferritic and austenitic SSs was suggested [3,13,15,18]. According to this model, an outer layer is more hydrated than an inner one. These discrepancies can probably be explained by the effects of alloy and electrolyte composition, conditions of the film formation, and / or by the application of the *ex-situ* techniques.

Among a few techniques that can be available for *in-situ* studies of the surface films, of importance is particularly ellipsometry, modulation spectroscopy, Raman spectroscopy, and photoelectrochemical method.

For example, two parameter ellipsometry has been applied to study the passivation films on SSs in various environments [16,19-23]. In majority of cases, ellipsometry was used to determine optical constants and thickness of passive films during the steady-state growth stage. It was found that the thickness of a one-layer passive film decreased with increasing chromium content of the alloy [19,20,23]. However, effects of potential and time of anodic polarization were not observed.

The aim of the present work was to characterize optical properties and thickness of anodic films formed on austenitic stainless steel as a function of the polarization potential and time, using *in-situ* three parameter ellipsometry and electrochemical technique.

Experimental

Measurements were made on Fe-18Cr-11Ni austenitic stainless steel (Cr: 17.6, Ni: 11.2, Mn: 1.65, Si: 0.75, C; 0.030, P: 0.026, S: 0.012 wt%). Specimen of Fe-18Cr-11Ni SS was mechanically polished with emery papers finishing with 800 grit, and with diamond sprays of 3, 1, and 1/4 μm grain size. Subsequently it was ultrasonically cleaned several times in absolute ethanol.

The specimen surface, before measurements,was cathodically pretreated at -1.05 V(SCE) for 10 min. Then the potential was increased up to -0.4 V(SCE) for 2 min. The electrode was kept under argon to remove hydrogen bubbles accumulated on the surface. After the cathodic pretreatment, the specimen was passivated potentiodynamically at scan rates of 0.01 and 0.05 $V \cdot s^{-1}$.

Measurements were performed in a solution of 0.5 M H_2SO_4 of pH = 0.5, prepared from bi-distilled and deionized water and Analytical Reagent grade chemical. The electrolyte was de-aerated with argon in a reservoir over 12 h prior to the experiments. All measurements were made at 25 ^{0}C. Electrode potentials were measured and reported relative to a saturated calomel electrode (SCE).

In-situ ellipsometric measurements were carried out with a Rudolph Automatic Ellipsometer RR 2000. The arrangement of optical elements was PSA (polarizer, sample, analyzer). The angle of incidence was 70.00 ^{0}.

Majority of measurements were performed at a wavelength of 546.1 nm. Ellipsometric measurements during potentiodynamic sweeps at a scan rate of 0.01 $V \cdot s^{-1}$ were made for wavelengths of 400 to 650 nm, at 50 nm intervals.

Changes in ellipsometric parameters $\delta\Delta = \Delta - \Delta_o$ (Δ is the phase difference), $\delta\Psi = \Psi - \Psi_o$ (Ψ is the amplitude ratio), and $dI / I_o = (I - I_o) / I_o$ (the relative intensity change) were measured. The Δ_o, Ψ_o, and I_o correspond to the bare substrate.

These three parameters, measured with an accuracy of 0.02 ^{0}, 0.01 ^{0}, 0.01%, respectively, were used for calculations of the complex refractive index $\hat{n} = n - k \cdot i$, where n is refractive index, k is extinction coefficient, $i = \sqrt{-1}$, and thickness of surface film d. An assumption was made that the films were homogeneous and optically isotropic. The values of n, k, and d were determined numerically by applying Newton's approximation. However, for the thinnest films an unambiguous solution has not been obtained. This may have been due to instabilities in the light source and the possible presence of nonuniform films.

Results

The average complex refractive index of cathodically pretreated Fe-18Cr-11Ni SS surface was 2.48 – 3.93i. This value is comparable with values obtained for Fe-26Ni- xCr SS (x = 5 to 28 wt%) after cathodic reduction in borate buffer : (2.30 to 2.44) – (3.93 to 4.32)i [19], and Fe-20Cr-25Ni SS after the film removing treatment in a bromine-methanol solution : 2.43 – 4.19 i [16].

Anodic polarization curves and the relative intensity changes (dI/I_0) for Fe-18Cr-11Ni SS measured at scan rates of 0.05 and 0.01 $V{\cdot}s^{-1}$ are shown in Fig. 1. A distinct relation between the anodic current density and dI/I_0 are seen. The active region corresponds to a relatively large drop in the intensity, especially for $dE/dt = 0.01\ V{\cdot}s^{-1}$. The minimum in the relative intensity change corresponds to the current peak at about –0.18 to –0.20 V(SCE). In the potential range from –0.20 V to about 0.20 V(SCE) the values of dI/I_0 increased significantly, whereas at more noble potentials they changed slightly.

Fig.2 shows changes of ellipsometric parameters $\delta\Delta$ and $\delta\Psi$ as a function of potential during anodic sweeps at scan rates of 0.05 and 0.01 $V{\cdot}s^{-1}$. These plots show that the $\delta\Delta$ values decreased rapidly in the active region to about –0.18 V(SCE). In the second potential region, up to about 0.20 V(SCE), they increased slightly. At more noble potentials the change in $\delta\Delta$ was very small.
The $\delta\Psi$ values increased with the electrode potential, especially in the regions from –0.25 V to about –0.18 V(SCE) and then from 0.0 V up to about 0.20 V(SCE) for $dE/dt = 0.01\ V{\cdot}s^{-1}$. The increase was less pronounced in the potential regions from about –0.18 V to 0.0 V(SCE) and at potentials above about 0.2 V(SCE).

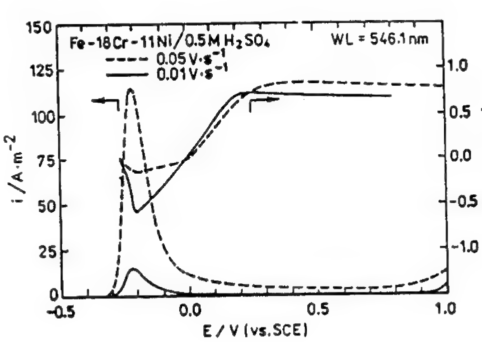

Fig. 1. Anodic polarization curves in 0.5 M H_2SO_4 and changes in relative intensity for Fe-18Cr-11Ni SS at scan rates of 0.05 and 0.01 $V{\cdot}s^{-1}$.

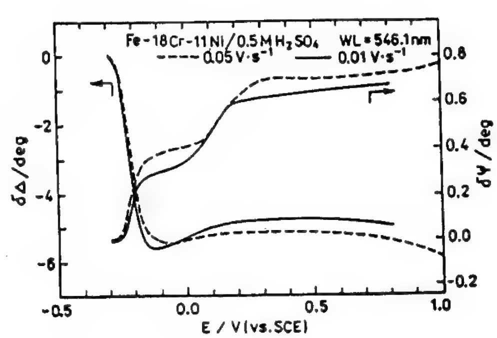

Fig. 2. Changes of ellipsometric parameteters during potentiodynamic sweeps at rates of 0.05 and 0.01 $V{\cdot}s^{-1}$ for Fe-18Cr-11Ni SS in 0.5 M H_2SO_4.

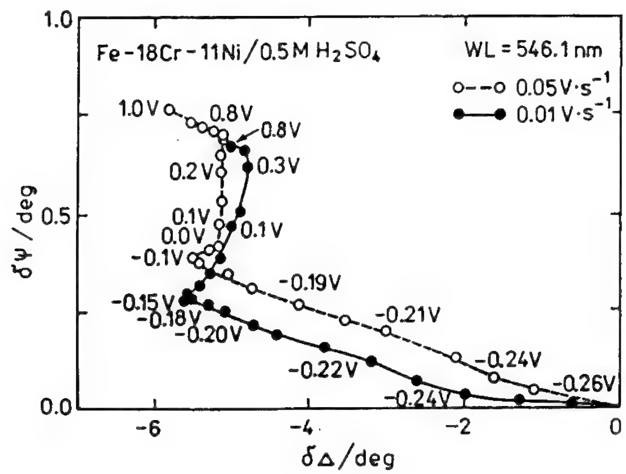

Fig. 3. Relationship between ellipsometric parameters δΔ and δΨ during anodic potentiodynamic sweeps at 0.05 and 0.01 $V \cdot s^{-1}$ for Fe-18Cr-11Ni SS in 0.5 M H_2SO_4.

Fig. 3 shows changes of δΔ vs δΨduring potentiodynamic sweeps at 0.05 and 0.01 $V \cdot s^{-1}$. The δΔ decreased significantly in the active potential region to about −0.18 V(SCE). At nobler potentials δΔ decreased slightly. The δΨ increased significantly in the entire potential region. Changes of δΔ and δΨ were for both sweep rates comparable.

The results of calculations of refractive indices (n), extinction coefficients (k) and film thickness (d), using the three parameter method, are shown in Fig. 4 and Fig. 5. Fig. 4 shows the potential dependence of n, k, and d obtained for wavelength of 546.1 nm (dE / dt = 0.05 and 0.01 $V \cdot s^{-1}$). Anodic polarization curves are also shown in this Figure.

Fig. 5 shows changes of n, k, and d with potential for different wavelengths from 400 to 650 nm at 50 nm intervals.

Refractive indices (n) and extinction coefficients (k) exhibit larger values at the potentials of the active-passive transition range. In the potential region from about −0.20 V to about 0.20 V(SCE) the optical constants decreased significantly. At more noble potentials they changed less. Values of n obtained for a sweep rate of 0.01 $V \cdot s^{-1}$ increased slightly at potentials positive to about 0.20 V, whereas those for d E / d t = 0.05 $V \cdot s^{-1}$ were practically constant in this potential region (Fig. 4).

The film thickness increased with the potential in the active-passive transition region. At about 0.20 V for sweep rate of 0.01 $V \cdot s^{-1}$ the film thickness exhibited a maximum, and at more noble potential it decreased distinctly. For the higher sweep rate, the thickness of anodic films increased slightly at more anodic potentials to about 0.20 V(SCE).

As shown in Fig. 5 the optical constants n and k are dependent on wavelength. However, they changed similarly with potentials. It can be seen in Fig. 5, that the k values are higher for a wavelength of 500 nm (2.48 eV) for films in the passive range.

The changes of the film thickness with the wavelength were neglible and remained within the experimental error.

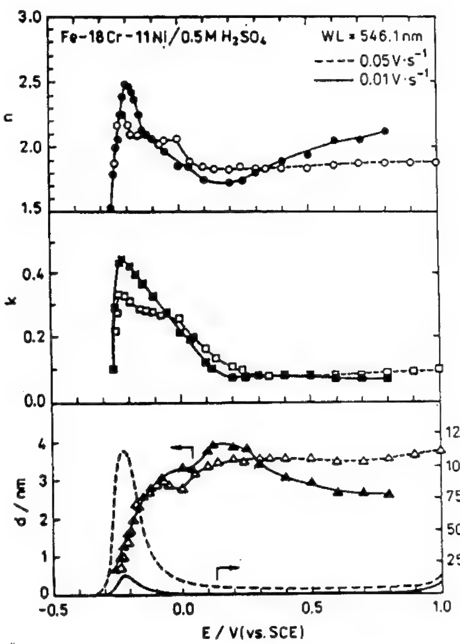

Fig. 4. Potential dependence of refractive index (n), extinction coefficient (k) and thickness (d) of anodic films formed on Fe-18Cr-11Ni SS in 0.5 M H_2SO_4 during potentiodynamic polarization at scan rates of 0.05 and 0.01 $V{\cdot}s^{-1}$; wavelength of 546.1 nm.

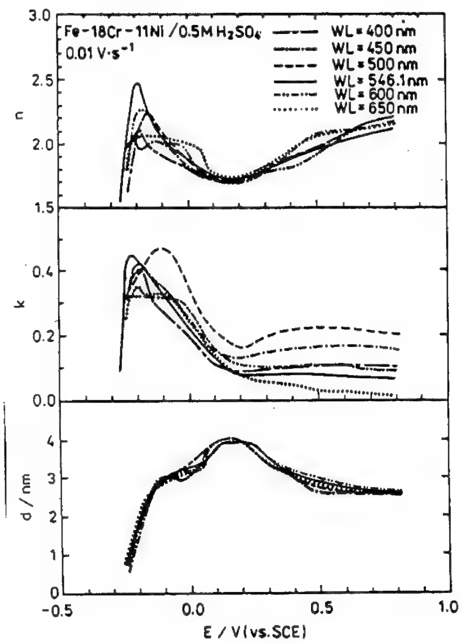

Fig. 5. Changes in refractive index (n) extinction coefficient (k), and thickness (d) of anodic films grown on Fe-18Cr-11Ni SS at a sweep rate of 0.01 $V{\cdot}s^{-1}$; wavelength of 400 to 650 nm.

The refractive index (n) and extinction coefficient (k) spectra are given in Fig. 6. They were obtained for different potentials during potentiodynamic polarization. For potentials in the active range (−0.22 V and −0.20 V), the refractive index n and extinction coefficient show a maximum at about 2.25 eV (550 nm). For the higher potential in the active-passive transition region (−0.10 V), only the extinction coefficient exhibits a maximum at about 2.5 eV (500 nm). The passive films at nobler potentials (0.20 V and 0.60 V), are characterized by two k maxima, at about 2.07 eV (600 nm) and at 2.5 eV (500 nm).

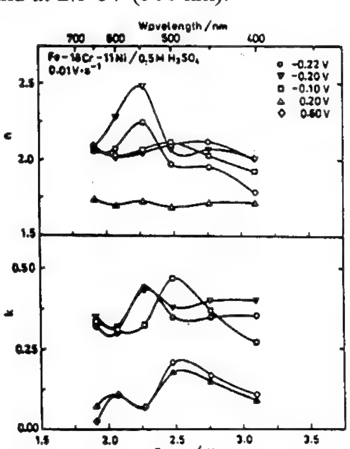

Fig. 6. Refracitve index (n) and extinction coefficient (k) spectra of anodic films formed on Fe-18Cr-11Ni SS at different potentials during anodic polarization at a scan rate of 0.01 $V{\cdot}s^{-1}$.

Discussion

The changes of ellipsometric parameters $\delta\Delta$, $\delta\Psi$, and d I / I_o with potential (Figs 1 – 3) suggest that the optical properties of anodic films formed potentiodynamically are potential dependent. The largest changes of n and k occured in the active and active-passive transition regions.

In order to examine the changes in the film composition, the optical constants of anodic films formed on Fe-18Cr-11Ni SS were compared with those of iron, chromium and nickel compounds. Comparison of the n and k values (Figs 4 and 5) of the anodic films with the literature data suggests that in the active region the initially formed films were probably composed of Fe and Cr salts and hydroxides (for Fe, Cr and Ni sulphates n = 1.47 to 1.81; for $Fe(OH)_2$ n = 1.76; for FeOOH and Fe_2O_3(hydrated) $\hat{n}$ = (1.95 to 2.58) – 0.05i ; and for $Cr(OH)_3$ n = 1.62 [24-27]).

With increasing potential in this region, the ratio of Cr / Fe in the film increased and the film consisted probably of iron hydroxides , oxyhydroxides, and chromium hydroxides. The enrichment of the film in chromium can be explained by the selective dissolution of iron [2, 10, 15, 28]. The formation of such a film with the higher Cr / Fe ratio explains the decrease in the anodic current and in the film growth rate (Figs 4 and 5). The selective dissolution of Fe continues in the nobler potentials (up to 0.2 V). The increase in the chromium content in the film can be responsible for lower n and k values. At these potentials the films are probably composed predominatly of chromium hydroxide.

As the chromium enrichment increased, the growth rate decreased. The passive film becomes thinner and more compact.

At the higher potentials in the passive region for a sweep rate of 0.01 $V \cdot s^{-1}$ the n values increased and the film thickness decreased. This effect can be explained by dehydration of the passive film. The passive film can be composed mainly of chromium oxyhydroxide (for CrOOH n = 2.00 [29]).

These changes were not observed for a sweep rate of 0.05 $V \cdot s^{-1}$.

According to Okamoto [2], the amount of water in the passive film formed on Fe-18Cr-11Ni SS in 0.5 M H_2SO_4 is relatively higher in the lower potential region. Other workers [8, 12] have reported that Cr enrichment of the surface layers on SSs increases with the nobler potential.

The results of measurements at different wavelengths have shown that the films formed in the active region exhibit an absorption peak at about 2.25 eV (550 nm). The comparison of this peak with the absorption spectra obtained for α Fe_2O_3 [30] and for anodic films on Fe [31–34] suggests that this peak can be assigned to Fe^{3+} ion in the layer. At the potential of –0.10 V only one peak appears at about 2.5 eV(500 nm), and at the higher potentials in the passive region the additional small peak exists at about 2.07 eV (600nm).

According to the literature data, Cr_2O_3 shows absorption at 2.07 ,2.70 and 3.50 eV in the visible region [35,36]. These absorptions are assigned to Cr^{3+} in the oxide.

However,anhydrous Cr_2O_3 does not form probably on Cr in acid solutions [37]. At low pH values the passive film on Cr consists of a poorly hydrated oxide Cr_2O_3 with the bandgap value of about 3.3 eV. Lower values of bandgap energy should be assigned to more hydrated films, e.g. about 2.5 eV for $Cr(OH)_3$ [37].

On the other hand , the reflection spectra obtained for the surface films formed on pure Fe, Cr, and Fe-Cr alloys did not show peaks at about 2.07 eV and 2.2 eV [38].

Conclusions

The three parametrs ellipsometry was applied to characterize the optical properties and the kinetics of passivation of Fe-18Cr-11Ni austenitic stainless steel in 0.5 M H_2SO_4 (pH = 0.5).

During the potentiodynamic polarization three potential regions were distinguished:
(a) – active region,
(b) –low anodic potential region between the critical passivation potential and about 0.20 V(SCE), and
(c) – passive region above 0.20 V (SCE).

In the active and low anodic potential regions anodic films are probably composed mainly of iron and chromium compounds. With the increasing potential, the anodic film is enriched in Cr(III) in the both regions. This effect can be explained by a selective dissolution of iron to the electrolyte. The increase in the Cr / Fe ratio in the film decreases anodic currents and SS is passivated.
In the passive region of low anodic potentials passive film is probably composed mainly of chromium hydroxide.

At the higher potentials of the passive region the passive film is probably dehydrated to chromium oxyhydroxide.

References

[1] J. B. Lumsden and R.W. Staehle, Scr. Metall. **6**, 1205 (1972).
[2] G. Okamoto, Corros. Sci. **13**, 471 (1973).
[3] I. Olefjord and H. Fischmeister, Corros. Sci. **15**, 697 (1975).
[4] A. E. Yaniv, J. B. Lumsden, and R. W. Staehle, J. Electrochem. Soc. **124**, 490 (1977).
[5] M. da Cunha Belo, B Randot, F. Pons, J. Le Hericy, and J. P. Langeron, J. Electrochem. Soc. **124**, 1317 (1977).
[6] H. Ogawa, H. Omata, I. Itoh, and H. Okada, Corrosion **34**, 52 (1978).
[7] K. Hashimoto, K. Asami, and K. Teramoto, Corros. Sci. **19**, 3 (1979).
[8] K. Hashimoto and K. Asami, Corros. Sci. **19**, 251 (1979).
[9] K. Asami and K. Hashimoto, Corros. Sci. **19**, 1007 (1979).
[10] K. Leygraf, G. Hultquist, I. Olefjord, B. Elfstrom, V. M. Knyazheva, A..V. Plaskayev, and Ya. M. Kolotyrkin, Zashch. Metallov **15**, 395 (1979).
[11] I. Olefjord and B.-O. Elfstrom, Corrosion **38**, 46 (1982).
[12] R. Goetz and D. Landolt, Electrochim. Acta **29**, 667 (1984).
[13] I. Olefjord, B. Brox, and V.Jelvestam, J. Electrochem. Soc. **132**, 2845 (1985).
[14] R. Kircheim, B. Heine, H. Fischmeister, S. Hofmann, H. Knote, and V. Stolz, Corros. Sci. **29**, 899 (1989).
[15] P. Marcus and J. M. Grimal, Corros. Sci. **33**, 805 (1992).
[16] K. Sugimoto and Y. Sawada, Corros. Sci. **17**, 425 (1977).
[17] I. Olefjord, Mat. Sci. Eng. **42**, 161 (1980).
[18] A. R. Brooks, C. R. Clayton, K. Doss, and Y. C. Lu, J. Electrochem. Soc. **133**, 2459 (1986).
[19] S. Silverman, G. Cragnolino, and D. D. Macdonald, J. Electrochem. Soc. **129**, 2419 (1982).
[20] N. K. Goswami and R. W. Staehle, Electrochim. Acta **16**, 1895 (1971).
[21] K. Sugimoto and S.Matsuda, J. Electrochem. Soc. **130**, 2323 (1983).
[22] S. Matsuda, K. Sugimoto, and Y. Sawada, J. Japan Inst. Metals **39**, 848 (1975).
[23] K. Sugimoto and S. Matsuda, Mater. Sci. Eng. **42**, 181 (1980).
[24] J. O' M. Bockris, M. A. Genshow, V. Brusic, and H. Wroblowa, Electrochim. Acta **16**, 1859 (1971).
[25] E. Posnjak and H. E. Mervin, Am. J. Sci. **47**, 311 (1919).

[26] Gmelins Handbuch der Anorganischen Chemie, **Vol 52**, part B, Verlag Chemie, Weinheim (1962).
[27] Hanbook of Chemistry and Physics, 72 nd Edition, 1991 - 1992 (Ed. D. R. Lide), CRC Press Inc., Boca Raton, Florida (1991).
[28] G. Hultquist, C. Leygraf, and D. Brune, J. Electrochem. Soc. **131**, 1773 (1984).
[29] M. A. Genshow and R. S. Sirohi, J. Electrochem. Soc. **118**, 1558 (1971).
[30] C. - T. Chen and B. D. Cahan, J. Opt. Soc. Am. **71**, 932 (1981).
[31] C. - T. Chen and B. D. Cahan, J. Electrochem. Soc. **129**, 17 (1982).
[32] D. Wheeler, B. D. Cahan, C. - T. Chen, and E. Yeager, in Passivity of Metals, R.P. Frankenthal and J. Kruger, Editors, p. 546, The Electrochemical Society, Princeton, N J (1978).
[33] W. Hopfner and W. J. Plieth, Werkst. und Korrosion **36**, 373 (1985).
[34] V. Jovancicevic, R. C. Kainthla, Z. Tang, B. Yang, and J. O' M. Bockris, Langmuir **3**, 388 (1987).
[35] B. Karlsson and C. G. Ribbing, J. Appl. Phys. **53**, 6340 (1982).
[36] R. E. Kirby E. L. Garwin, F. K. King, and A. R. Nyaiesh, J. Appl. Phys. **62**, 1400 (1987).
[37] C. Sunseri, S. Piazza, and F. Di Quarto, J. Electrochem. Soc. **137**, 2411 (1990).
[38] N. Hara and K. Sugimoto, J. Electrochem. Soc. **126**, 1328 (1979).

Materials Science Forum Vols. 185-188 (1995) pp. 465-470

Passivation of $(Fe_{1-z}Cr_z)_{83}B_{17}$ glassy metals studied by ellipso-reflectometry

D. Huerta and K.E. Heusler

Abteilung Korrosion und Korrosionsschutz, Institut für Metallkunde und Metallphysik, Technische Universität Clausthal, D-38678 Clausthal-Zellerfeld, Germany

Keywords: Glassy metals, passivation, ellipso-reflectometry, passivating films

Abstract

Relative reflectivity changes ΔR/R were measured for three azimuths of a rotating analyzer after reflection of linearly polarized light at a mirror of glassy metal used as the working electrode in a quartz cell. By comparing reflectivities of the passive and active electrode the film thickness, its refractive index and absorption coefficient were determined.

The effect of chromium substitution z on the passivity of glassy alloys with the composition $(Fe_{1-z}Cr_z)_{83}B_{17}$ was studied. On the spontaneously passivating alloy with $z = 0.15$ a thin film with a steady state thickness $d = 0.4$ nm and a complex refractive index $\mathbf{n_2} = 2.26 - 1.15i$ was formed. On the not spontaneously passivating alloy with $z = 0.10$ the film at first grew to a large thickness of 5.8 nm. After about 70 minutes the thickness decreased to $d = 0.4$ nm. During this time, the refractive index changed from $n_2 \approx 2.4$ to 1.8 and the absorption coefficient from $k_2 \approx 3.2$ to 5.8. The optical parameters indicate severe roughening during the transition to the steady state.

Introduction

In order to understand the role of chromium substitution on the passivation of $(Fe_{1-z}Cr_z)_{83}B_{17}$ glassy metals, an optical analysis of the film was performed in-situ using the method of ellipso-reflectometry [1,2]. In the three-phase model used it is assumed that a light absorbing planar film of uniform thickness d_2 and isotropic refractive index $\mathbf{n_2} = n_2 - ik_2$ separates two phases, the transparent electrolyte with the refractive index n_1 and the absorbing metal with the refractive index $\mathbf{n_3} = n_3 - ik_3$.

Traditional ellipsometric techniques suffer from the disadvantage that that from two experimental parameters, the relative amplitude (Ψ) and the phase retardation (Δ), three unknown parameters, the thickness, the refractive index and the absorption coefficient of the film, must be determined. In ellipso-reflectometry, relative reflectivity changes ΔR/R of incident plane polarized light are measured at three azimuths of the reflected light.

Experimental

Monochromatic light with the wavelength $\lambda = 500$ nm leaving the prism monochromator was split by a semitransparent mirror into a reference beam and a measuring beam. The incident sam-

ple beam was polarized by a polarizer at the azimuth P = 35° and specularly reflected at an angle of incidence Φ = 55° from the working electrode in the center of a cylindrical quartz cell of 0.1 dm^3 volume with walls of optical quality. The reflected light was polarized by the analyzer. The intensities of both light beams were measured by a silicon photodiode connected to two lock-in amplifiers at different frequencies of the light choppers. The electrical signals from the sample beam and the reference beam were fed to the inputs of a dividing amplifier. Relative reflectivity changes appearing at the output were recorded and displayed continuously during the experiments at three azimuths of the analyzer A = 0°, 45° and 90°. The azimuths were set by a stepping motor operated by a pulse generator and microcomputer which was also used for storing the experimental data, for data processing and for plotting the results. Further details of the apparatus are described elsewhere [1,3].

The optical parameters of the substrate and the film were calculated by the Newton-Raphson method of successive approximation from Fresnel's and Drude's equations with the refractive index n_1 = 1.339 of the electrolyte solution using the procedures explained earlier [1,2,4-6].

Melt-spun ribbons of $(Fe_{1-z}Cr_z)_{83}B_{17}$ glassy metals with 25 μm thickness, 0.7 mm width and 20 mm length were used as the working electrodes. The samples were polished mechanically with 600 and 1200 grit SiC abrasive paper and fixed to PTFE insulated platinum wires by spot welding. The Pt wire and the contact points were insulated with a vinyl lacquer. A specularly reflecting surface of the glassy metal was obtained by polishing with 0.25 μm diamond paste. After rinsing with ethanol in an ultrasonic bath, washing in distilled water and drying under a stream of nitrogen, the working electrode was transferred to the cylindrical quartz cell.

The working electrode was adjusted to the optical axis of the cell. A platinum counter electrode was used. The saturated calomel reference electrode (SCE) was connected to the cell by a PTFE capillary. The electrolyte with pH 1.8 was was a mixture of 0.5 M sodium sulphate solution with 0.5 M sulphuric acid solution both prepared from triply destilled water and analytical grade chemicals. The electrolyte deaerated by a stream of nitrogen was kept at 22°C during the measurements.

The measurements were started immediately after filling the cell with electrolyte. With the fresh surface, two sets of measurements at the free corrosion potential were performed within 19 minutes to test for reproducibility of the reflectivity changes and to determine the complex refractive index of the substrate. The value $\mathbf{n}_3$ = 1.904 - 2.626i was used for the calculations of the film properties. Later on, the electrode was passivated at E = 0.3 V vs SCE. The relative releflectivity changes were measured continously at the azimuths 0°, 45° and 90° of the analyzer.

Results

Steady-state polarization curves of $(Fe_{1-z}Cr_z)_{83}B_{17}$ with z = 0.10, 0.15 and 0.25 in a sodium sulphate solution, pH 1.8, are shown in Fig.1. The critical passivation potential of the glassy metal with z = 0.10 was E = -0.4 V vs SCE. The passivation potentials shifted to more negative values with higher chromium contents. The alloys with z > 0.12 passivated spontaneously [7]. The steady-state corrosion rates of the passive alloys decreased with the chromium content. At E = 0.3 V the steady state current density of the alloy with z = 0.10 was one decade higher than the current density of the alloy with z = 0.25.

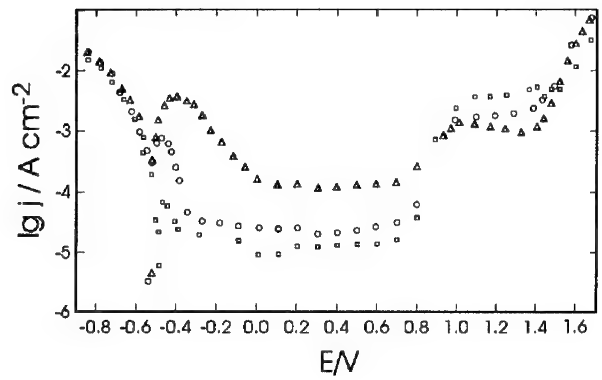

Fig.1: Steady-state polarization curves of the glassy alloy $(Fe_{1-z}Cr_z)_{83}B_{17}$ in 0.5 M sodium sulphate, pH 1.8, at 298 K for different degrees z of substitution. (Δ) z = 0.10 ; (o) z = 0.15; (□) z = 0.25

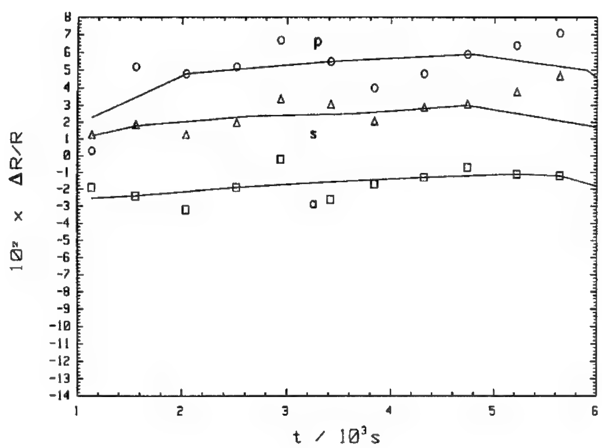

Fig.2: Relative reflectivity changes ΔR/R for incident light of the wavelength λ = 500 nm polarized at P = 35° with the angle of incidence Φ = 55°, measured at the azimuths (o) A = 0°; (□) A = 45° and (Δ) A = 90° as a function of time t during the passivation of the glassy alloy $(Fe_{1-z}Cr_z)_{83}B_{17}$ with z = 0.10 at E = 0.3 V vs the SCE in 0.5 M sodium sulphate solution, pH 1.8

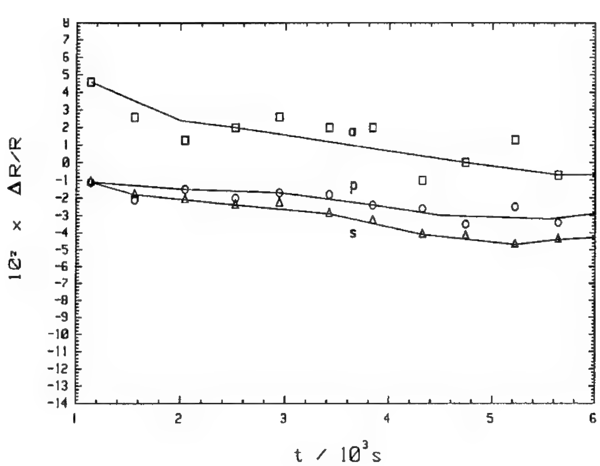

Fig.3: Relative reflectivity changes ΔR/R for incident light of the wavelength λ = 500 nm polarized at P = 35° with the angle of incidence Φ = 55°, measured at the azimuths (o) A = 0°; (□) A = 45° and (Δ) A = 90° as a function of time t during the passivation of the glassy alloy $(Fe_{1-z}Cr_z)_{83}B_{17}$ with z = 0.15 at E = 0.3 V vs the SCE in 0.5 M sodium sulphate solution, pH 1.8

Fig.2 shows the reflectivity changes ΔR/R relative to the reflectivities at the free corrosion potential for the azimuths A = 0°, 45° and 90° during passivation at E = 0.3 V of the not sponta-

neously passivating alloy with z = 0.10, and Fig.3 the same dependence of the spontaneously passivating alloy with z = 0.15. The relative reflectivities changed quickly immediately after the potential step. With the alloy of the degree z = 0.10 of substitution they stayed nearly constant for about 6000 s after passivation and later decreased rapidly. The reflectivities of the spontaneously passivating alloy with z = 0.15 decreased monotonically. With the glassy metals, measurements usually could not be extended to times larger than $\approx$7000 s because of crevice corrosion.

Figs. 4 and 5 show the changes with time of the thickness d and the optical constants of the passivating films on the glassy alloys passivated at E = 0.3 V. On the alloy with z = 0.10 at first a film with a relatively large thickness of 5.8 nm was formed which at long times decreased to 0.4 nm. Simultaneously, the absorption coefficient rose from k_2 = 3.2 to k_2 = 5.8 and the refractive index decreased from n_2 = 2.4 to n_2 = 1.8. The film on the glassy alloy with z = 0.15 approached a steady state thickness d = 0.4 nm after 2000 s with the complex refractive index $\mathbf{n_2}$ = 2.26 - 1.15i.

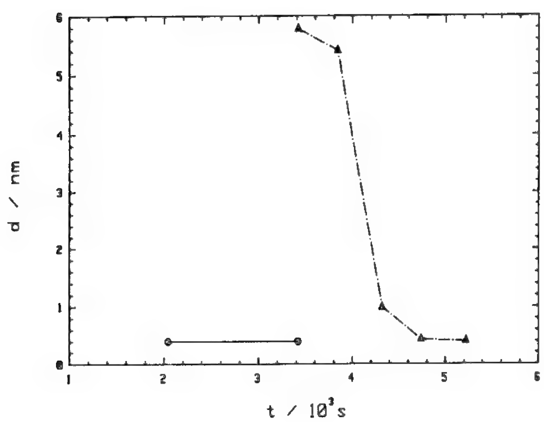

Fig. 4: Thickness d of the film as a function of time t during passivation of the glassy metals with (Δ) z = 0.10 and (o) z = 0.15 at E = 0.3 V vs SCE in 0.5 M sodium sulphate solution, pH 1.8

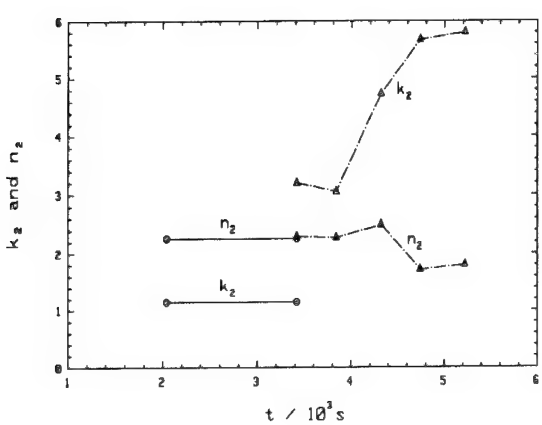

Fig. 5: Refractive index n_2 and absorption coefficient k_2 as a function of time t during the passivation of the glassy metals with (Δ) z = 0.10 and (o) z = 0.15 at E = 0.3 V vs SCE in 0.5 M sodium sulphate solution, pH 1.8

Discussion

The refractive index $n_2 = 2.3$ of the passivating film on the alloy with $z = 0.15$ is close to the value $n = 2.5$ for Cr_2O_3 given in the literature [8]. Thus, the film seems to be enriched in chromium. The relatively large apparent absorption index may be due to the influence of changes of the optical properties of the metallic phase upon passivation, since the Debye length of the space charge in the metal is comparable to the film thickness. Some roughening may also be involved.

The film initially formed on the non-spontaneously passivating alloy with $z = 0.10$ also has an refractive index close to the one of Cr_2O_3. The relatively large thickness may be caused by changes of the alloy composition at the interface due to selective corrosion in the active state which does not occur at the spontaneously passivating alloy. The large increase of the absorption coefficient with time indicates severe roughening.

References

[1] T. Ohtsuka and K. E. Heusler, J. electroanal. Chem. **100**, 319 (1979)
[2] K. E. Heusler and T. Ohtsuka and K. E. Heusler, Surface Sci. **101**, 194 (1980)
[3] N. B. De Cristofaro, D. Huerta and K. E. Heusler, Electrochim. Acta **35**, 69 (1990)
[4] B. D. Cahan, J. Horkans and E. Yeager, Surface Sci. **37**, 559 (1973)
[5] J. Horkans, B. D. Cahan and E. Yeager, Surface Sci. **46**, 1 (1974)
[6] F. B. Hildebrand, Introduction to Numerical Analysis, McGrawHill, New York, 1956
[7] K. E. Heusler and D. Huerta, J. Electrochem. Soc. **136**, 65 (1989)
[8] D'Anx Lax, Taschenbuch für Chemiker und Physiker, Vol. 1, 3rd ed., Springer-Verlag, New York 1958

Materials Science Forum Vols. 185-188 (1995) pp. 471-480

Ellipsometric determination of the density of TiO_2 passive films on Ti single crystals: Combination of ellipsometry and coulometry

A. Michaelis[1], J.L. Delplancke[2] and J.W. Schultze[1]

[1] Institut für Physikalische Chemie und Elektrochemie, Heinrich-Heine-Universität Düsseldorf, D-40225 Düsseldorf, Germany

[2] Faculté des Sciences Appliquées, Université Libre de Bruxelles, B-1050 Bruxelles, Belgium

Keywords: Ellipsometry, coulometry, density, TiO_2

Abstract

An entirely ellipsometric determination of layer densities for nonabsorbing films is presented. For this, the direct proportionality between the ellipsometrically obtained refractive index n and the density ρ described by Drudes formula is applied. The densities as well as the layer thicknesses d can be used for the evaluation of coulometric measurements. This allows the separation of the different contributions to the measured total charge q_{tot} (e.g. the corrosion charge q_{corr}). As an example the system Ti/TiO_2 was chosen. The measurements were carried out on Ti single crystals to ensure that homogeneous areas were investigated. For this reason the anisotropy of the system must be regarded.
The experimental results show that the density of the TiO_2-layers depends on both the crystallographic orientation of the substrate and the conditions of layer formation (e.g. potentiodynamic sweep rate). Although the measured total charge is nearly equal on different crystal surfaces (2.86 mC V^{-1} cm^{-2}, electrolyte 0.5 M H_2SO_4, sweep rate 50 mV/s) the layer thickness as well as the corrosion charge varies from orientation to orientation. On the (0001) and $(01\bar{1}1)$ orientation, no corrosion took place during anodization, whereas the contribution of q_{corr} to q_{tot} was about 8 % for an (xxx0) orientation.

1 Introduction

Coulometric analysis during anodic passivation of Ti allows the determination of layer thicknesses Δd using eqn. (1).

$$\Delta d = \frac{M}{zF\rho}\Delta q_{ox} \tag{1}$$

with: M = molar mass; F = Faraday constant, $z = 4$ (Ti^{4+}), q_{ox} = oxide formation charge.
Usually, the density ρ of the crystalline TiO_2 modifications (e.g. anatase) is chosen, but some reports [1, 2, 3] show that thin anodic films (up to 50nm) are amorphous. Moreover, microscopic investigations show that Ti surfaces are heterogeneous, which is indicated by a large variety of interference colours on different single Ti grains (diameter about 20 μm). Hence, on macroscopic electrodes just an average layer thickness is determined assuming an uniform density not checked by an independent experimental method.
If Δd is determined by ellipsometry and Δq_{tot} by coulometry, the layer density can be evaluated using eqn.(1). For this, the assumption $q_{tot} = q_{ox} + q_{corr} + q_{O_2} \approx q_{ox}$ is required (neglection of the corrosion charge q_{corr} in a region without O_2-evolution).
In this study, we present an independent, purely ellipsometric determination of ρ, which avoids the above assumption and allows therefore the separation of q_{corr}. In order to rule out heterogeneous effects, the measurements were carried out on single crystal surfaces. The results can be transferred to the properties of single Ti grains in technical material, because each grain behaves like a small crystal.

For such homogeneous areas, the optical anisotropy of the Ti substrate becomes important, which considerably complicates the mathematical evaluation of ellipsometric data. Moreover, this affects the experimental procedure. All ellipsometric measurements must be carried out in dependence on the azimuth angle α, which describes sample rotation around the surface normal (Anisotropy-Ellipsometry). This is demonstrated by fig. 1, which shows the ellipsometrical Δ and Ψ-values in dependence on α for two different crystal orientations. In the case of the optical axis (c-axis) being perpendicular to the surface normal (xxx0), a strong variation of Δ and Ψ with α occurs, since the rotation changes the angle between the c-axis and the ellipsometric plane of incidence. This angle is constant for rotation of the (0001) surface, i.e. no variation occurs for this orientation (c-axis parallel to surface normal).
It is evident that this effect is very useful as it allows the determination of crystallographic information, e.g. the orientation of the optical axis. The detailed analysis of anisotropy-ellipsometry, along with the complete mathematical formalism [4, 5, 6], will be published elsewhere (see e.g. [7, 8]).

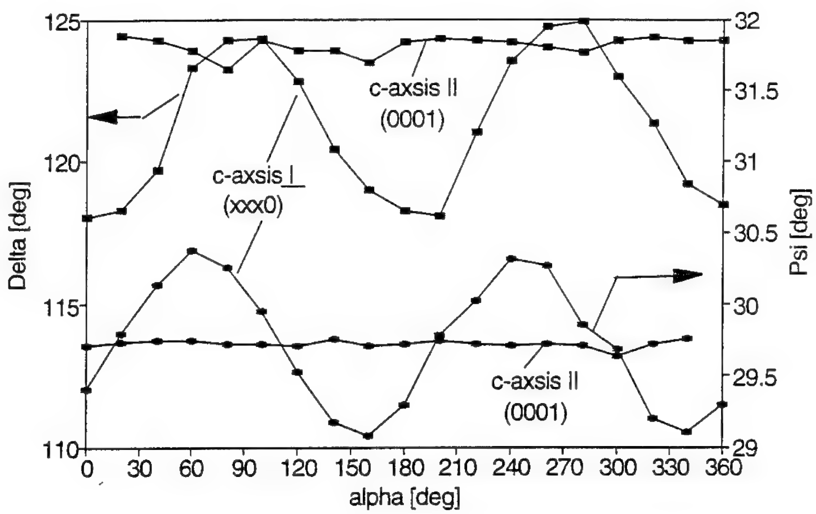

Figure 1: Anisotropy-Ellipsometry. Δ and Ψ as a function of the azimuth angle α for two different crystal orientations (optical axis parallel (0001) and perpendicular (xxx0) with respect to the surface normal). The Ti-crystals are layered by the natural passive film of about 3 nm.

2 Experimental

For ellipsometry, an automatic rotating analyzer device shown in fig. 2 (AFE Sentech) with a HeNe laser as light source was used (λ = 632.8 nm). The angle of incidence was 70 deg. In order to allow sample rotation around the surface normal a special in-situ cell was constructed. For this, the windows were mounted on the ellipsometer arms using an alignable connector and simply dipped into the electrolyte. Therefore, rotation of the whole cell was possible without affecting the window alignment.
The electrochemical measurements were carried out in 0.5 M H_2SO_4 (pH 0.3, 25 °C). Potentials are given with respect to the standard hydrogen electrode (SHE). The Ti single crystals were delivered by L & K company, Geilenkirchen - Germany. Three different orientations (0001), ($01\bar{1}1$), and (xxx0) shown in fig. 3 were investigated ((xxx0) refers to any surface parallel to the c-axis). Ti crystallizes in the hcp-lattice and therefore is optical birefrigent. In this case, the permittivity number $\epsilon(\omega)$ becomes a permittivity tensor containing the ordinary (o) and extraordinary (ao) optical constants. Analysis of the anisotropy-ellipsometric data yielded as optical constants for the substratum Ti:

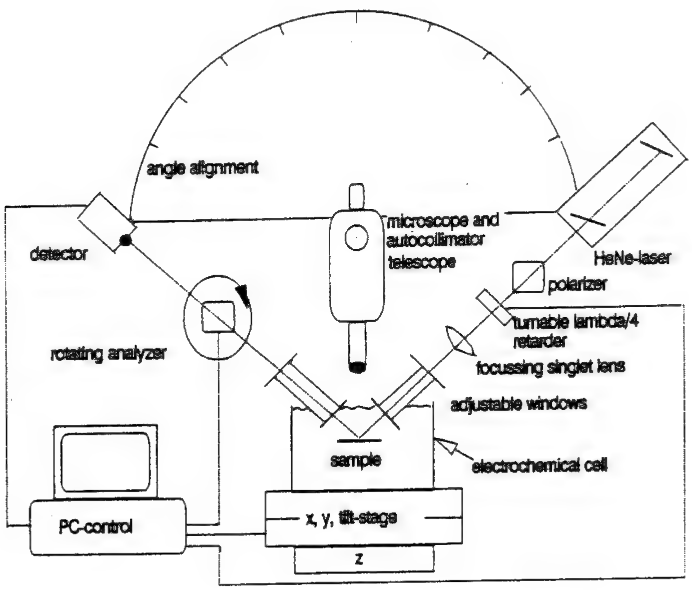

Figure 2: Schematic ellipsometer setup

$\tilde{n}_o = 2.9 + i3.8$ $\quad\tilde{n}_{ao} = 2.62 + i3.38$. The real part refers to the refractive index n, the imaginary part to the absorption coefficient k. These substrate constants were used for all ellipsometric evaluations throughout this paper.
The crystalline TiO_2 modifications are optical anisotropic, too, but the thin layers investigated here were amorphous, i.e. they can be described by isotropic constants.

3 Results

Fig. 4 shows the cyclovoltammograms (cv) measured on the different crystal surfaces (sweep rate 50 mV/s). Although the oxygen evolution starting at about 3 V ($i_{tot} = i_{ox} + i_{corr} + i_{O_2}$) is very different for the orientations, the current density in the coulometrically evaluable region ($i_{O_2} = 0$) between 0 and 3 V is nearly equal. In this region a total charge of about 2.9 mC V^{-1} cm^{-2} results. Applying eqn. (1), it might be concluded that the layer thickness or the growth factor ξ given by

$$\Delta d = \xi \cdot U \tag{2}$$

is identical for the different crystal surfaces. This is contradicted by ellipsometric measurements during the potentiodynamic sweep, which show a thickness depending on the crystal orientation as well as on the conditions of layer formation (sweep rate). This fact

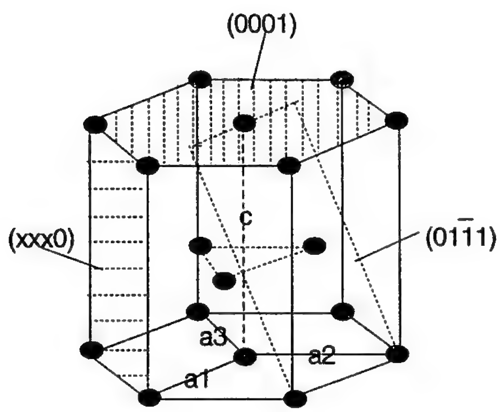

Figure 3: Bravais-lattice of Ti. The investigated surfaces are indicated, c defines the optical axis.

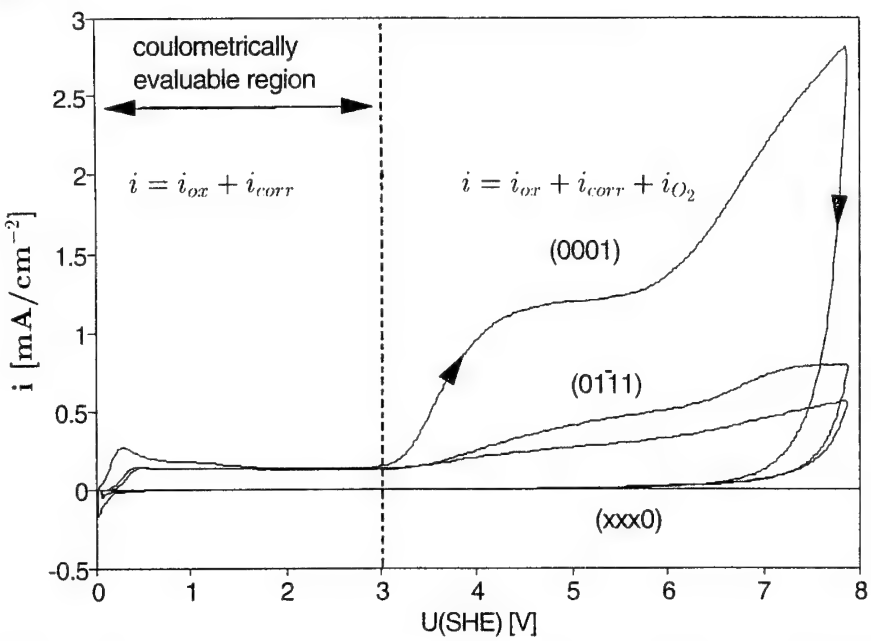

Figure 4: Cyclovoltammogramms on different Ti-crystal surfaces (0.5 M H_2SO_4, 50 mV/s).

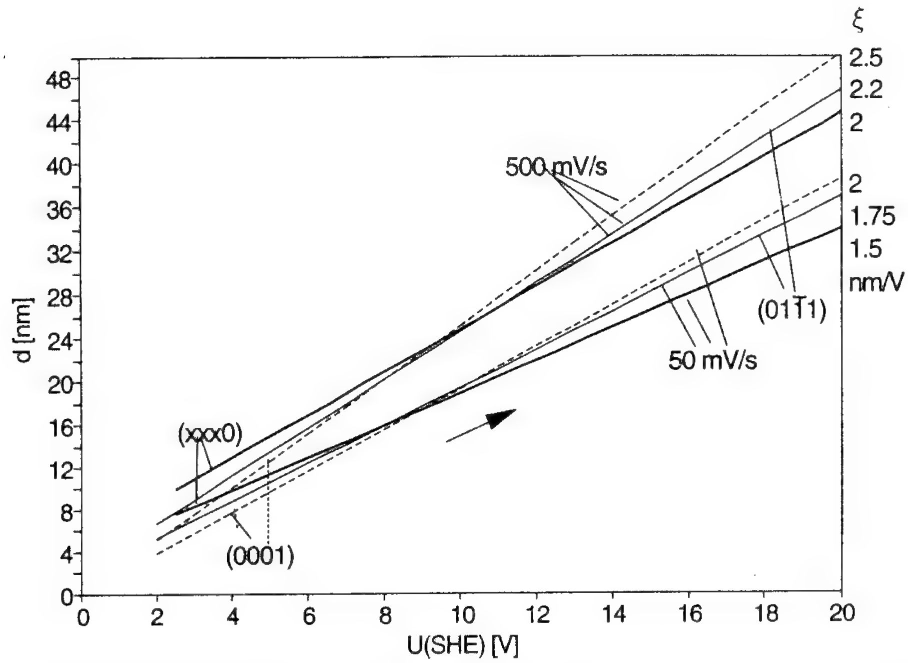

Figure 5: Ellipsometrically determined thickness d during the cv of fig. 4. The slopes of the curves yielding the growth factors ξ are shown on the right side of the figure (this is not a second ordinate).

is shown by fig. 5. The slopes of the d(U)-plots yield the growth factors ξ which are indicated, too.

In fig. 6, the layer growth factors ξ as well as the values for the refractive indices n of the layers as a function of the sweep rate are shown. The absorption coefficients k of the films were 0 in all cases. From the experimental result of fig. 6 it can be deduced that

$$\frac{n_1}{n_2} \approx \frac{\xi_2}{\xi_1}. \tag{3}$$

This relationship can be explained theoretically starting from the well known Drude equation (see textbooks of theoretical electrodynamics), which describes the correlation of the refractive index n and the electron density N_e for nonabsorbing layers. Expanding this relation into a Taylor series stopped at first order yields

$$\begin{aligned} n \approx \sqrt{\epsilon(\omega)} &\approx 1 + \frac{2\pi N_e e^2}{m} \sum_j \frac{f_j}{\omega_j^2 - \omega^2 - i\gamma\omega} \\ &= 1 + \text{const} \cdot N_e \end{aligned} \tag{4}$$

with: f_j = oscillator strength, ω_j = resonance frequency, m = electron mass, γ = damping constant.

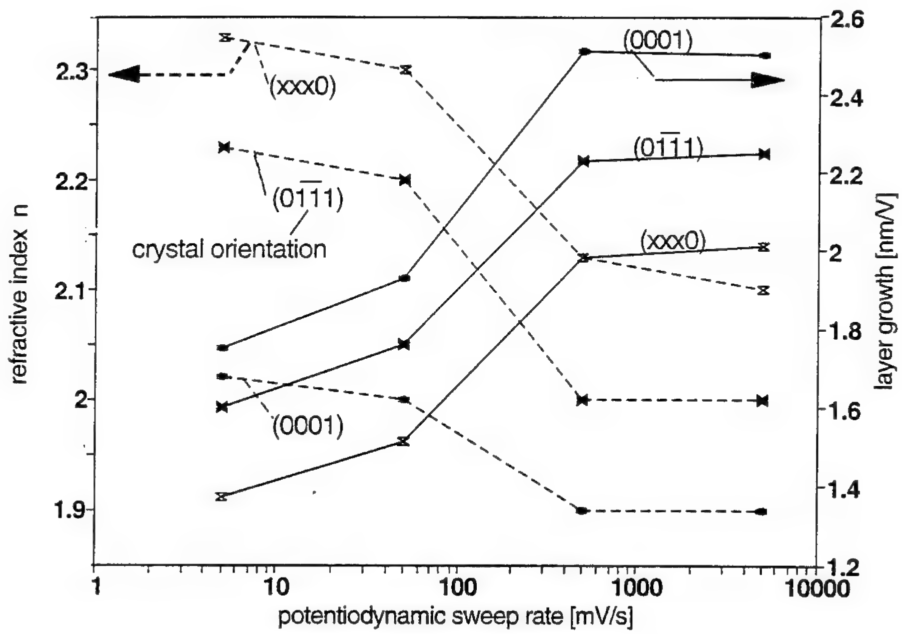

Figure 6: Variation of the TiO_2 refractve indices n and the layer growth factors ξ with the sweep rate for different crystal orientations.

This expansion holds despite of the large n-values (> 2) of the TiO_2 layers. It is reasonable to assume a proportionality between the electron density N_e and the density ρ of the medium, yielding:

$$\boxed{(n-1) \sim \rho}. \tag{5}$$

Along with eqn. (1), (2) and $q_{ox} \sim \Delta U$ this yields:

$$\boxed{\xi \sim \frac{1}{\rho} \sim \frac{1}{n-1}}, \tag{6}$$

which can be rewritten as

$$n_1 \cdot \xi_1 = n_2 \cdot \xi_2 + \Delta\xi. \tag{7}$$

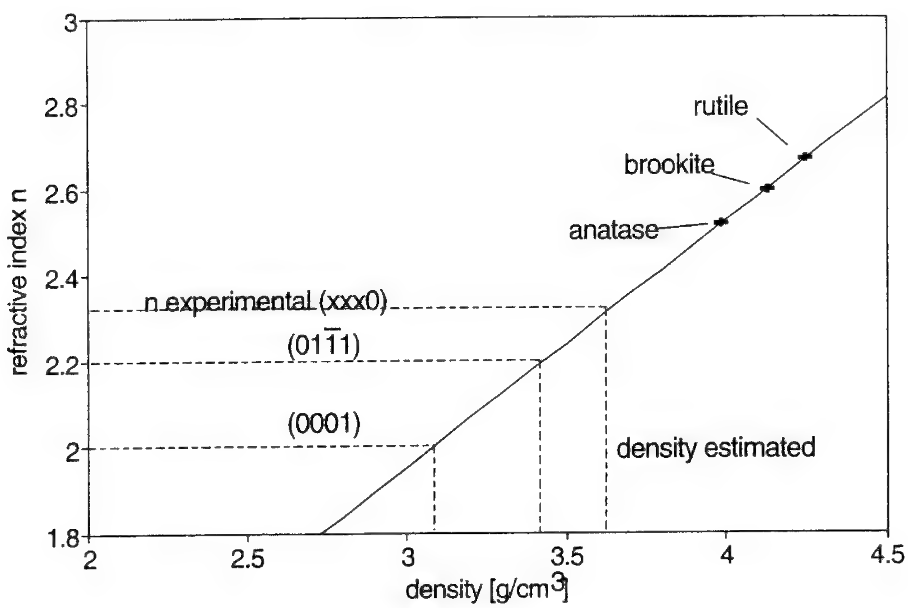

Figure 7: Extrapolated $n(\rho)$-line. The values of the crystalline TiO_2-modifications are indicated. Dashed lines indicate experimental n-values for the different orientations.

Tab. 1 Ellipsometric determined layer formation constant ξ, density ρ as well as measured charge q_{tot} and determined corrosion charge q_{corr} for different Ti-crystal orientations (electrolyte 0.5 M H_2SO_4, sweep rate 50 mV/s, $q_{O_2} = 0$ for U < 3).

	(0001)	(xxx0)	(01$\bar{1}$1)
ξ [nm V^{-1}]	1.93	1.51	1.76
ρ [g cm^{-3}]	3.1	3.65	3.45
q_{tot} [mC V^{-1} cm^{-2}]	2.86	2.86	2.86
q_{corr} [mC V^{-1} cm^{-2}]	0	0.12	0

Neglection of the small part $\Delta\xi := \xi_2 - \xi_1$ leads to the experimental result of eqn.(3). Therefore the application of eqn.(5) is experimentally justified leading to the major point of this paper.

The proportionality between refractive index n and density ρ of the anodic TiO_2-layers allows an estimation of ρ by simply measuring n. For this, a calibration curve $n(\rho)$ is needed which can be obtained by using the well known data for the crystalline modifications anatase, brookit, and rutile. According to theory, these values show a nearly linear

relationship. The resulting linear function can in first approximation be extrapolated by regression yielding the calibration curve shown in fig. 7. If n is measured ρ can be determined directly from this line.
Along with the ellipsometrically determined ξ-values, the passive layer formation charge q_{ox} can be computed applying eqn. (1). This charge can then be compared with the measured one q_{tot}, enabling the separation of q_{corr} applying the equation $q_{tot} = q_{ox} + q_{corr}$ in the coulometrically evaluable region. The results for the different crystal orientations are summarized in tab. 1. During passivation, corrosion occurs on the (xxx0) orientation only. The (0001) and (01$\bar{1}$1) surfaces show greater resistivity to corrosion. This is in agreement with elder investigations by Green et al. [9, 10]. There also the corrosion resistance of the (0001) surface is emphasized.
It shall be pointed out that the measured charge q_{tot} for the (0001) surface can exactly be reproduced by the ellipsometrically determined values d and ρ. This is an important test for the validity of the method for density determination presented here.

4 Conclusions

Both layer thicknesses and densities of TiO_2 layers can be independently determined using ellipsometry. This allows separation of the different contributions (as e.g. the corrosion charge q_{corr}) to the experimentally obtained total charge q_{tot} . Measurements were carried out on three different Ti crystal orientations. On the (0001) and (01$\bar{1}$1) surfaces no corrosion took place, whereas the contribution of q_{corr} to q_{tot} is about 8 % for the (xxx0) surface. The application of micro-ellipsometry will enable to determine q_{corr} on single Ti grains. Hence, the effect of the substrate-texture on the corrosion behaviour can be investigated. Future investigations will deal with this subject.
Although the coulometrically measured total charge is equal for different crystal orientations, the corresponding layer thicknesses as well as the densities vary in a way that the product of ρ times d is almost constant. This means that on surfaces covered by thinner passive layers, higher densities are observed and vice versa. It is important to note that the layer densities on different crystal orientations show unexpected large variations from 3.1 to 3.65 g cm^{-3}. All densities determined are much lower than the ones known for the crystalline modifications. This gives evidence for the amorphous structure of thin TiO_2 passive layers. In consequence, the commonly used coulometric assumption of uniform densities close to the bulk crystalline ones appears doubtful and should not be further

applied for thin TiO_2 films.

Acknowledgments

The financial support of the Bundesministerium für Forschung und Technologie is gratefully acknowledged.

References

[1] J.S.L. Leach and B.R. Pearson, Corr. Sci., 28 (1988) 67

[2] G. Blondeau, M. Froelicher, M. Froment, A. Hugot-Le Goff, M. Brien, R. Carlson, P. Larroque, J. Microsc. Spectrosc. Electron. 2 (1977) 27

[3] D.J. Blackwood, L.M. Peter, Electrochem. Acta 34 (1989) 875

[4] D.W. Berreman, T.J. Scheffer, Phys. Rev. Lett., 25 (1970) 577

[5] D.W. Berreman, J. Opt. Soc. Am., 63 (1973) 1374

[6] D.J. De Smet, Surf. Sci., 56 (1976) 293

[7] A. Michaelis, Dissertation, Heinrich-Heine-Universität Düsseldorf, Verlag Shaker Aachen ISBN 3-8265-0239-6 (1994)

[8] A. Michaelis, J.W. Schultze, Thin Solid Films, 233 (1993) 86

[9] J.A.S. Green, R.M. Latanision, Corr., 29 (1973) 386

[10] J.A.S. Green, Corr., 30 (1974) 175

Materials Science Forum Vols. 185-188 (1995) pp. 481-488

Potential modulated ellipsometric measurements on the Fe17Cr alloy in sulphuric acid

L.C. Jacobs, H.P. De Vogel, K. Hemmes, M.M. Wind and J.H. De Wit
Delft University of Technology, Laboratory for Materials Science, Division of Corrosion Technology and Electrochemistry, PO Box 5025, NL-2600 GA Delft, The Netherlands

Keywords: Ellipsometry, iron chromium alloys, passive, potential modulation

Abstract

Ellipsometric measurements on the Fe17Cr alloy have been performed combined with electrochemical measurements in order to study the passive film as a function of the electrode potential. The ellipsometric parameters Ψ and Δ change with varying potential, due to the formation of a passive film or to changes in the composition and thickness of the film.
It is shown that it is possible to determine a range of physically acceptable values for the refractive index of the passive film for thicknesses between 1.5 and 2.5 nm. The values found for the imaginary part; about 2 to 3, indicate the strongly degenerate semiconductive character of the film. At this stage it is not possible to conclude whether the passive film grows with the electrode potential. The composition of the film in the passive region from -600 mV to +450 mV (SSE) hardly changes. In the transpassive region film growth and considerable change in composition were observed.

Introduction

The corrosion resistance of iron chromium alloys is controlled in a wide potential region by the physical and chemical properties of the passive film. Several analytical techniques using electron diffraction[1], Auger electron spectroscopy[2, 3] and XPS[4-8] have given quite detailed information on the chemical composition and the structure of the passive film.
It was shown by McBee and Kruger[1] that as the chromium content increased the oxide films were generally less able to sustain an epitaxial relationship with the substrates. The structural characteristics for the passive oxide films on iron chromium alloys were found to be mainly amorphous.
Ellipsometric studies[9] have established that the passive films formed on the alloys would have thicknesses at least 1.5 nm thick within two hours after initiation of growth.
Yaniv et al.[2] revealed an enrichment of chromium in the film with a corresponding depletion of iron at -150 mV (vs. SHE) and + 60 mV (vs. SHE) both in a sulphuric acid solution ($pH \approx 3$) and a sulphuric acid-1 M NaCl solution ($pH \approx 3.45$). For a NaOH ($pH=14$) solution the opposite was found: in every case a depletion of Cr was observed in the films. In the transpassive region at + 1250 mV (vs. SHE) in the sulphuric acid-1 M NaCl solution a depletion of chromium for all the alloys and an enrichment of iron relative to the chromium depletion was found. At a cathodic potential, - 1150 mV (vs. SHE) the composition of the films on the alloys was the same as resulting from the polarisation in the transpassive region.
It was found by Asami et al.[6] that the chromium content in the passive film formed both at +340 mV (vs. SHE) and + 740 mV (vs. SHE) showed a steep increase when the alloy contains ca 13 at% of Cr. It was seen that the compositions immediately underneath the passive film are exactly the same as those of the bulk alloys, despite the remarkable chromium enrichment in the passive film on the alloys with 13 at% Cr or more. This result suggests that the enrichment of chromium in the passive film is caused by preferential dissolution of iron into the solution.
From recently obtained XPS results by Norgren[8] it was shown that the passive film on the Fe17Cr alloy was enriched by Cr cations over the entire potential region remaining almost constant in the passive region, between + 760 mV and + 1160 mV (vs. SHE). In the transpassive region the content of Cr cations decreased to about 28% of the total cation concentration. The concentration of Cr in the substrate, immediately underneath the film was comparable to that in the bulk alloy.
Furthermore from reported results of other XPS measurements[10-15], γ spectrometry[16] and ellipsometry[17, 18] it can be seen that the thickness of the passive film on iron chromium alloys varies from about 1.5 to 2.5 nm in the passive region. Also electrochemical measurements such as cyclic voltammetry[19] and electrochemical impedance spectroscopy[20, 21] have provided information on the composition and the electrochemical properties of the passive film. From results of the last two techniques it was deduced that hydrogen evolution plays an important role in the corrosion mechanism of the Fe17Cr alloy. From Dobbelaar[20] it was shown that Cr^{2+} is formed during the corrosion reaction, which can occur by direct dissolution of chromium from 'active' sites without the aid of water. However, the dissolution is most likely to occur in two steps, namely

through the formation of Cr^{2+}_{ad} which can diffuse over the surface and then dissolves as Cr^{2+}. The formation of the passive film can occur at the terrace and at the kink and ledge sites. In the passive region Cr still dissolves slowly as Cr^{2+}, which gives rise to the passive current in this region. Furthermore hydrogen is evolved, both at the bare metal surface and at the film- electrolyte interface, between +360 mV and 660 mV (vs. SHE).
Castro et al.[21] found semiconductive character of the passive film on iron and Fe12Cr having donor concentrations of $1.7*10^{20}$ cm^{-3} and $1.2*10^{22}$ cm^{-3}, respectively.
Sugimoto et al.[17] investigated the passive and the transpassive films on iron chromium alloys in 1 M Na_2SO_4 using in situ ellipsometry combined with electrochemical measurements. The optical constants of the films on these alloys were determined. Dielectric values for the optical constants of the passive and the transpassive films were found, i. e. the imaginary part of the refractive index of the film (k_1) is in the order of about 0.4. Furthermore the thickness was reported to increase from about 1.4 nm to about 1.9 nm in the passive region and from about 2.0 nm to 3.0 nm in the transpassive region.
We have reason to believe that the passive layer on iron chromium alloys is a reasonably good electronic conductor: repassivation of the iron chromium alloys, after local breakdown, is extremely fast, which is only possible if the cathodic reaction at the passive film (reduction of oxygen and the electron transfer reaction) is fast. Therefore electrons must be able to travel through the passive film. Moreover Marichev et al.[22] used a new technique, Contact Electric Resistance (CER), in order to investigate the electric resistance of passive films on stainless steels. They found evidence that these films have a low electric resistance, in the order of 1-10 $\mu\Omega$. In other words the passive film on these materials is a good electronic conductor and therefore has a semi metallic character. In Gaussian or ESU units the conductivity σ_1 is related to the complex refractive index of the film $N_1=(n_1-ik_1)$ by [23, 24]

$$2n_1(\omega)k_1(\omega) = \frac{4\pi\sigma_1(\omega)}{\omega} \tag{1}$$

where ω is the angular frequency. Therefore we believe that k_1 must be larger than the values found by Sugimoto et al.[17]. However the mechanism of formation and breakdown of the passive film is not yet entirely clear. Therefore more information can be obtained if electrochemical measurements are combined with e. g. XPS or ellipsometry[7, 17, 19, 25-28].
In this work we monitored the passivation and breakdown of the passive film using ellipsometry during an anodic potential scan. In this way we were able to observe in situ the changes of the optical parameters and the current density as a function of potential.
For the interpretation of our ellipsometric measurements we used the homogeneous film model as shown in figure 1[29, 30] . Here it is assumed that a homogeneous film (medium 1) has parallel-plane boundaries of separation d and is sandwiched between an ambient (medium 0) and a (metal) substrate (medium 2).

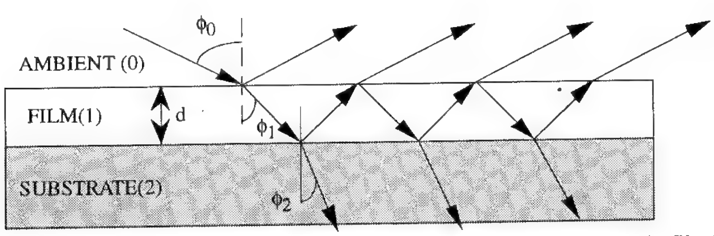

Fig.1. Reflection and transmission of a plane wave by an ambient(0)-film(1)-substrate(2) system, with parallel-plane boundaries. d is the thickness. ϕ_0 is the angle of incidence in the ambient and ϕ_1, ϕ_2 are the angles of refraction in the film and substrate respectively[29, 30].

Polarised light incident at an angle ϕ_0 will be partly reflected and transmitted by the 0-1 interface. This process is described by the Fresnel reflection and transmission coefficients[29]. The transmitted light waves suffers multiple internal reflections at the 1-2 and 1-0 interfaces and

refractions at the 1-2 interface. The general equation of reflection ellipsometry for the homogeneous film model is

$$\rho = \frac{R_p}{R_s} \frac{r^p_{01} + r^p_{12} e^{-2i\beta}}{1 + r^p_{01} r^p_{12} e^{-2i\beta}} * \frac{1 + r^s_{01} r^s_{12} e^{-2i\beta}}{r^s_{01} + r^s_{12} e^{-2i\beta}} = \tan \Psi \, e^{i\Delta} \qquad (2)$$

where R_p and R_s are the complex-amplitude reflection coefficients for the parallel and perpendicular polarisations, r the Fresnel reflection coefficients, Ψ and Δ the relative amplitude diminution and the relative phase retardation respectively and where β is called the film phase thickness which is dependent of the refractive index and the thickness of the film. The function ρ is an implicit function of the thickness d of the passive film, because β is a function of the film thickness d. For many systems of practical interest, e. g. the passive film on iron chromium alloys, the film thickness is much smaller than the wavelength of light, i. e. $d \ll \lambda$ or $|\beta| \ll 1$. It then is permitted to linearise eq. (14). This results in

$$\rho = \rho(0) \left\{ 1 - 2i\left(\frac{2\pi}{\lambda}\right) d \, \frac{(N_1^2 - N_0^2)(N_1^2 - N_2^2) N_0 \cos\phi_0 \sin^2\phi_0}{N_1^2 (N_2^2 \cos^2\phi_0 - N_0^2 \cos^2\phi_2)} \right\} \qquad (3)$$

in which $\rho(0)$ is the ρ function of the bare substrate.
The ellipsometric coefficient, as given by the homogeneous film model, eq. (3), is determined by eight parameters: N_0, $N_1=(n_1-ik_1)$, $N_2=(n_2-ik_2)$, ϕ_0, d and λ. Of these N_0, ϕ_0 and λ are well known. N_2, the refractive index of the substrate, is often quite sensitive to the system parameters, e. g. impurities, morphology etc. Therefore it is customary to obtain N_2 for the system under consideration from a measurement of a bare (i. e. film free) substrate. We have followed this procedure by measuring Δ and Ψ at a very high cathodic potential (-1200 mV vs. Saturated Sulphate Electrode, SSE, +660 mV vs. Standard Hydrogen Electrode), where it is assumed that the substrate is free of any (oxide) film. These film free quantities will be denoted by $\bar{\Delta}$ and $\bar{\Psi}$. We are left with three unknown parameters, $N_1=(n_1-ik_1)$ and d, to be determined from the two ellipsometric angles

$$\Psi = \tan^{-1} |\rho(N_0, N_1, N_2, d, \phi_0, \lambda)| \qquad (4)$$

$$\Delta = \arg [\rho(N_0, N_1, N_2, d, \phi_0, \lambda)] \qquad (5)$$

The film thickness d is known to be small for the passive film on iron chromium alloys, typically less than about 3 nm. Therefore the most convenient next step to solve eqs. (4) and (5) is to select a value for d in the indicated range. Numerical values for the two different solutions for N_1 are then obtained by applying an iterative procedure, using different seeds. Finally the values thus found values for d, n_1 and k_1, have to be carefully checked for physical relevance. It is worth noting that the fact that N_1 has two solutions in the correct half plane ($n_1>0$), follows directly from the fourth order nature of the thin film expansion, eq. (3). In most cases one solution represents an absorber ($k_1>0$), the other an amplifier ($k_1<0$). Occasionally both, or even rarer neither, of the solutions are absorbers. Amplifiers ($k_1<0$) are excluded and also too large values for N_1 ($n_1>5$ or $k_1>5$) are rejected.

Experimental methods
The electrodes for the measurements were made by cutting chips with a thickness of about 5 mm from a rod of a Fe17Cr alloy with a diameter of 12 mm. The composition, determined by means of Electron Probe Micro Analysis (EPMA), is shown in table 1. The alloy was polished to 0.25 µm with diamond paste for the measurements. The experiments were performed in 0.5 M H_2SO_4, which was deaerated. The potentiostat used was an ECO PGStat 10. Potentials were measured

against a saturated mercury sulphate electrode (SSE; 660 mV vs. SHE) using a capillary. All potentials are given with respect to this electrode.

Table 1.Composition of the Fe17Cr alloy used for the potential controlled ellipsometric measurements.

Specimen	%Cr	%Fe	%Mo	%Ni	%Mn	%C	%N	%O	%Si
Fe17Cr	16.47	83.42	0.01	0.03	0.01	0.06	nihil	nihil	0.002

The experiments were performed in a cylindrical teflon vessel with quartz windows fixed at an angle of approximately 70° with respect to the electrode.
The ellipsometric measurements were done with a Hazebroek-Holscher interferometric ellipsometer with HeNe laser (with wavelength 632.8 nm), schematically shown in figure 3. A full description is given in[31, 32].

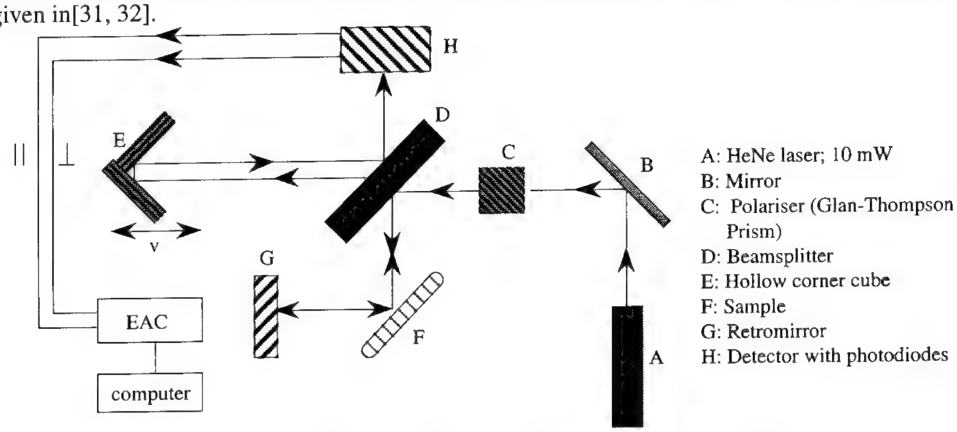

Fig. 3. A schematic view of the Hazebroek-Holscher ellipsometer[31, 32].

The signals coming from the detector enter the Ellipsometric Analyser Controller (EAC) and are stored in a computer (HP Vectra 286).
This computer evaluates the amplitude ratio ($V_{p,\,max}/V_{s,\,max}$) and the phase difference (δ_p-δ_s) of the two sinewaves. To be able to determine the amplitude ratio and the phase difference caused by the sample only, first a so called 'reference'measurement (retromirror positioned between the sample and the beamsplitter) is performed, followed by the actual 'sample'measurement. The ellipsometric parameters characteristic for the sample only are calculated from

$$\Psi_{sample} = \arctan\left[\frac{(V_{p,\,max}/V_{s,\,max})_{sample}}{(V_{p,\,max}/V_{s,\,max})_{reference}}\right]^{\frac{1}{2}} \tag{6}$$

$$\Delta_{sample} = \frac{1}{2}(\Delta_{sample} - \Delta_{reference}) \tag{7}$$

Before performing potential controlled ellipsometric measurements the Hazebroek-Holscher interferometric ellipsometer was tested on reproducibility. This was done by performing five measurements at three different angles of incidence on a smooth gold surface in air. Each measurement consists of five cycles of sinewaves. After each measurement the sample was removed and cleaned with alcohol. After drying the sample, the sample was inserted in the equipment again and after aligning a new measurement was performed. From reproducibility tests it was found that the deviation of Δ was about 0.05° and the deviation of Ψ was about 0.03°.
For the Fe17Cr alloy the cathodic pretreatment was at a potential of -1400 mV during 60 sec. and the bare substrate parameters were measured at -1200 mV. The potential was then quickly and automatically stepped to -600 mV, where the actual scan started. The potential was scanned up to 1000 mV. The scan rate was 0.5 mV/sec. The bare substrate parameters $\bar{\Delta}$ and $\bar{\Psi}$ were measured at -1200 mV. During potential scanning the ellipsometric parameters Δ and Ψ and the current density

were measured at intervals of 50 mV. The angle of incidence during these measurements was 63° and the refractive index of the medium (N_0) was taken as 1.33.

Results

In figure 4 the polarisation curve of the alloy is given and in figure 5 the changes in the optical parameters as a function of potential is shown. In figure 6 the Δ vs. Ψ curve for both the passive and transpassive region is shown, In figures 6 A refers to the clean substrate, while the other characters stand for the potentials, indicated in fig. 4 at which a range of refractive indices was calculated at thickness of 1.5 nm, 2.0 nm, 2.5 nm and 3.0 nm for both the passive and the transpassive region.
The range of the real and imaginary part of the refractive index of the passive film and transpassive film on the alloy is plotted in figure 7.
The values for the bare substrate parameters, $\bar{\Delta}$ and $\bar{\Psi}$, are 131.05° and 29.90°, respectively, leading to a refractive index of the substrate of 2.80-3.38i.

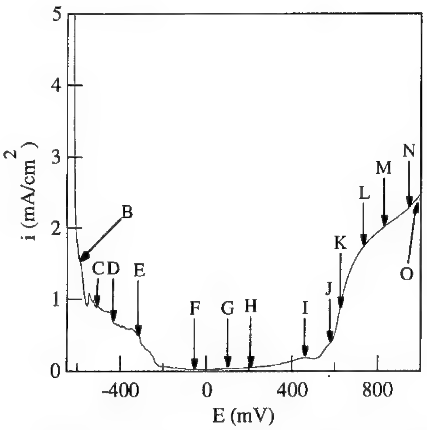

Fig.4. The polarisation curve of the Fe17Cr alloy in 0.5 M sulphuric acid. The scan rat was 0.5 mV/s. The characters denote the potentials at which a range of refractive indices of the film is calculated.

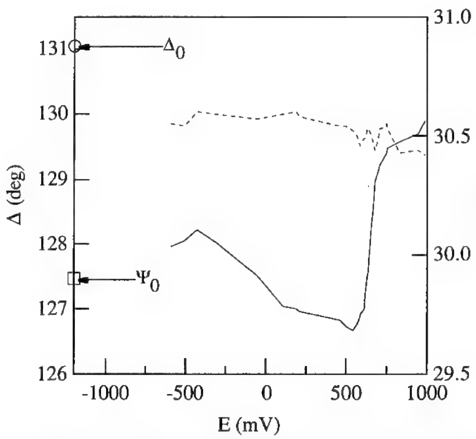

Fig.5. The relative amplitude diminution (Ψ) (dashed line) and the relative phase retardation (Δ) (solid line) as a function of the potential. Δ_0 and Ψ_0 are the bare substrate parameters.

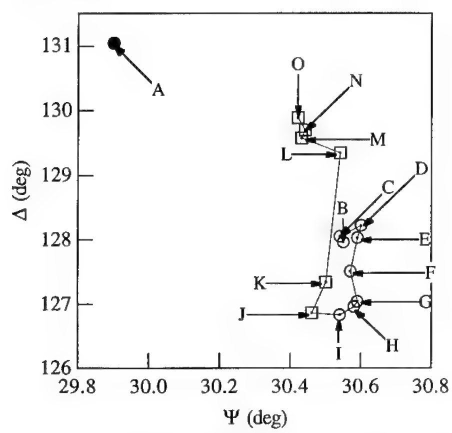

Fig.6. The experimental Δ vs. Ψ curve in the *passive* (circles) and in the *transpassive* region (squares).

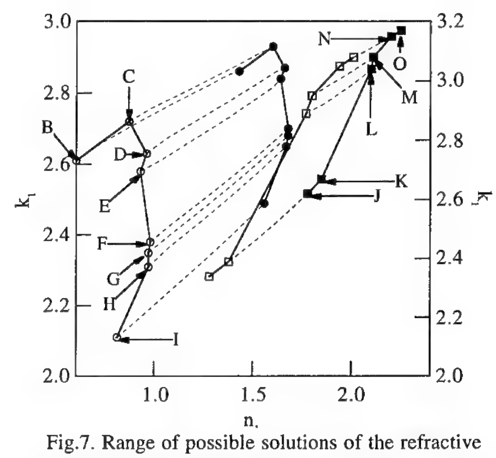

Fig.7. Range of possible solutions of the refractive index of the passive and transpassive film. ¤: 1.5 nm; □:2.5 nm (passive region); ●: 2.0 nm; ■: 3.0 nm (transpassive region).

In the passive region (-600 mV to +450 mV) the variations in Δ and Ψ are moderate and at the passive-transpassive transition at about 500 mV, as the current density starts to increase, Δ starts to increase and Ψ decreases slightly. In the transpassive region Ψ fluctuates, while Δ still increase. The values of the experimental values of both Δ and Ψ and the refractive indices of the film on the Fe17Cr alloy are summarised in table 2.

Table 2. Physically acceptable combinations of refractive indices of the film at thickness 1.5, 2.0, 2.5 and 3.0 nm for both the passive and transpassive region on the Fe17Cr alloy.

Point	E (mV)	Δ (deg)	Ψ (deg)	d=1.5 nm	d=2.0 nm	d=2.5 nm	d=3.0 nm
			PASSIVE REGION				
A	-1200	131.05	29.90	-----	-----	-----	-----
B	-593	127.96	30.55	0.81-2.16i	1.26-2.38i	1.57-2.54i	1.77-2.65i
C	-509	128.05	30.54	0.85-2.19i	1.30-2.53i	1.60-2.56i	1.80-2.68i
D	-430	128.22	30.60	0.84-2.32i	1.30-2.53i	1.59-2.66i	1.79-2.76i
E	-313	128.03	30.57	0.79-2.22i	1.25-2.44i	1.55-2.58i	1.76-2.70i
F	-55	127.51	30.57	0.66-1.97i	1.10-2.22i	1.43-2.39i	1.66-2.52i
G	+106	127.04	30.59	0.53-1.80i	0.95-2.07i	1.29-2.24i	1.52-2.38i
H	+207	126.96	30.58	0.52-1.76i	0.93-2.03i	1.27-2.21i	1.52-2.35i
I	+461	126.83	30.54	0.53-1.70i	0.93-1.97i	1.26-2.15i	1.52-2.29i
			TRANSPASSIVE REGION				
Point	E (mV)	Δ (deg)	Ψ (deg)	d=1.5 nm	d=2.0 nm	d=2.5 nm	d=3.0 nm
J	+582	126.86	30.46	0.59-1.67i	0.99-1.93i	1.33-2.10i	1.58-2.26i
K	+622	127.34	30.50	0.67-1.86i	1.11-2.11i	1.44-2.28i	1.67-2.43i
L	+734	129.35	30.54	1.35-2.89i	1.71-2.99i	1.92-3.05i	2.06-3.12i
M	+828	129.58	30.43	1.59-2.92i	1.89-3.02i	2.07-3.08i	2.18-3.13i
N	+944	129.70	30.44	1.63-3.00i	1.92-3.08i	2.09-3.14i	2.20-3.17i
O	+985	129.89	30.42	1.73-3.10i	1.99-3.16i	2.15-3.20i	2.25-3.23i

Discussion

From the measurements performed on a smooth gold surface in air we can conclude that the values of Δ and Ψ are reproducible within about 0.05°. Without removing and cleaning the sample, but immediately repeating the measurement a reproducibility of the same order was found.

The bare substrate parameters of the Fe17Cr alloys is measured and calculated directly after the pretreatment at -1400 mV. This leads to a value of the refractive index of 2.77-3.37i. These values are different from the value found in literature[19].

In literature[17, 19, 26-28, 33, 34], there is a great discrepancy between the values found for the refractive index of the bare substrate of pure chromium and the iron chromium alloys. These large differences can be attributed to either different chemical composition or morphology, or to the different pretreatments that have been applied. For example heat treatment is known to affect the structure like grains and grain boundaries, which could affect the optical response. E. g. annealing of a Fe25Cr alloy at 850°C leads to sensitisation, i. e. the amount of chromium at the grain boundaries will be lowered due to the formation of chromium carbides[20]. If no heat treatment is applied large internal strains will arise[20]. The effect of grains and grain boundaries on the refractive index of the substrate is yet unknown. Surface roughness also affects the optical (ellipsometric) response of the system and therefore the apparent value of the refractive index of the substrate. After polishing the substrate is always slightly rough and chemical or electrochemical pretreatment may increase the surface roughness. Hydrogen development during cathodic electrochemical pretreatment may lead to the absorption of H_2 into the substrate. We have studied the influence of the cathodic pretreatment on the surface roughness. Gerretsen[19] has applied a cathodic pretreatment at -1700 mV during 600 sec. This pretreatment may cause an increase of the surface roughness and also take up of hydrogen in the metal lattice. These reasons may account for the differences between the values of the refractive index of the substrate found in literature. By Differential Interference Contrast Microscopy we found that after polishing at 1 μm the surface is optically smooth, except for scratches of maximally 20 nm thick. Cathodic pretreatment both at -1400 mV during 60 sec. and at -1700 mV during 600 sec. did not increase the surface roughness very much.

When the results of the electrochemical and ellipsometric measurements are compared in the passive region it can be seen that Ψ remains almost constant and Δ decreases from -500 mV to 0 mV, see fig. 5. The decrease in Δ is about 1°. The passive film, which is formed, contains Cr^{2+} and will be present as an amorphous Cr(II)oxide/hydroxide[19, 20]. Going to more anodic potentials

this passive film is further oxidised to Cr(III) oxide/hydroxide[19, 20]., i. e. the composition of the film has changed. n_1 decreases from about 0.85 to 0.5, when d=1.5 nm and from 1.6 to 1.3 in case of d=2.5 nm. k_1 decreases from ±2.2 to ±1.8 in case of 1.5 nm and from ±2.6 to ±2.2 in case of d=2.5 nm. It is possible that both the composition and the thickness of the passive film has changed. An alternative explanation could be the increase of the sub microscopic roughness which has also been observed for the passive film on nickel by Marcus et al. [35]. Between 0 mV and +500 mV n_1 remains almost constant (0.5 at 1.5 nm and 1.3 at 2.5 nm). k_1 decreases from 1.8 to 1.7 at 1.5 nm and from ±2.2 to ±2.1 at 2.5 nm. In the transpassive region the current density increases and also the changes in the ellipsometer signals are larger than in the passive region. The major change in this region is that some chromium dissolves as chromate thus increasing the relative Fe content. At these potentials Cr(III) in the film can be oxidised to Cr(IV) or Cr(VI), which could account for the change in the refractive index of the film[19]. n_1 starts to increase to ±1.7 at 990 mV when d=2.0 nm and to 2.2 when d=3.0 nm. k_1 starts to increase to ±3.2 when both d=2.0 nm and 3.0 nm. The decrease in n_1 could possibly be due to an optically less dense oxide film, while a lower value of k_1 could possibly be ascribed to a less semi metallic character of this film. For the Fe17Cr and for all thicknesses we find a value larger than 1 for k_1, i. e. the film has a more semi metallic character than a dielectric one. In literature[28, 36-39] some values of some iron (hydr)oxides and chromium (hydr)oxides are given. These values of refractive indices are bulk values having values of k_1 smaller than 1, i. e. have a more or less dielectric character. Furthermore it can be seen that k_1 of the iron (hydr)oxides have a larger value than those of the chromium (hydr)oxides. Sugimoto et al.[17] also calculated the refractive index of the passive film on iron chromium alloys. They found an imaginary part of the refractive index of the film smaller than 1. Marichev et al.[22] found evidence that passive films on stainless steels have a low electric resistance, i. e in the order of about 1-10 $\mu\Omega$. In other words the passive film on these materials is a good electronic conductor and therefore has a semi metallic character. Therefore we have reasons to believe that our values found for the imaginary part of the refractive index of the passive film are in good agreement with this semi metallic character.

Conclusions

It was shown that potential controlled ellipsometry is a very sensitive in situ measuring technique to study thin (passive) films. Using single wavelength ellipsometry no exact values of the refractive index and the thickness can be obtained. However, realistic value ranges and order of magnitudes can be given. From our calculations we find that the real part of the refractive index of the passive film is in the range of 0.5 (assuming d=1.5 nm) to 1.7 (for d=2.5 nm), while the range of the imaginary part is about 2 to 3. To obtain exact values of the refractive indices and thicknesses of the passive film more information is needed, e. g. measurement at other wavelengths or at other angles of incidence.

Furthermore it was shown that the value of the refractive index of the substrate has a great effect on the values for the refractive index of the passive film. Also surface roughness has a great influence on the refractive index of the substrate and therefore on the refractive index of the film. It was shown that after polishing and cathodic pretreatment the surface roughness is in the order of maximally 20 nm.

While anodic scanning takes place the oxide film, containing Cr(II), is gradually transformed into an oxide film containing Cr(III). The composition of the film in the passive region from about -600 mV to +450 mV hardly changes, since the ellipsometric parameters hardly change.

In the transpassive region it is likely that the film starts growing to a thickness in the order of about 3.0 nm at 990 mV while considerable modifications of the composition takes place.

Acknowledgement

The authors wish to thank the Koninklijke/Shell Lab. , Shell Research B. V. Amsterdam for the donation of the Hazebroek-Holscher interferometric ellipsometer to our laboratory and Dr. W. Visscher, W. M. Visser and P. F. Colijn for their assistance.

References

1. C. L. McBee and J. Kruger, Electrochim. Acta., **17**, 1337 (1972)
2. A. E. Yaniv, J. Lumsden and R. W. Staehle, J. Electrochem. Soc., **124**, 490 (1977)
3. H. Ogawa, H. Omata, I. Itoh and H. Okada, Corrosion (Houston) **34**, 52 (1978)
4. K. Sugimoto, K. Kishi, S. Ikeda and Y. Sawada, J. Jpn. Inst. Met., **38**, 54 (1974)
5. K. Asami, K. Hashimoto and S. Shimodaira, Corrosion Sci., **16**, 387 (1976)
6. K. Asami, K. Hashimoto and S. Shimodaira, Corrosion Sci., **18**, 151 (1978)

7. B. S. Norgren, M. A. J. Somers, W. G. Sloof and J. H. W. de Wit, in proceedings of the 12th Scandinavian Corrosion Congress and Eurocorr'92 (1992)
8. B. S. Norgren, M. A. J. Somers, W. G. Sloof and J. H. W. de Wit, to be published
9. J. R. Ambrose and J. Kruger, unpublished work
10. I. Olefjord and B. Brox, in "Passivity of Metals and Semiconductors", ed. M.Froment, Amsterdam 561 (1982)
11. M. Knote, S. Hofman, H. F. Fischmeister and Z. Fresenius, Anal. Chem., **329**, 292(1987)
12. J. H. Gerretsen, "Passivation and breakdown of passivity of Stainless Steels Constituents, Thesis, Delft University of Technology, The Netherlands (1990)
13. R. Kirchheim, B. Heine, H. Fischmeister, S. Hofman, H. Knote and U. Stolz, Corrosion Sci., **29**, 899(1989)
14. P. Marcus and I. Olefjord, Surf. and Interface Anal., **11**, 569 (1988)
15. T. P. Moffat and R. M. Latanision, Trans. Tech. in Corr. Sci. and Eng. Corr. Div. of the electrochem. Soc. inc., Proc. **89-1** (1989)
16. C. Leygraf, G. Hultquist, I. Olefjord, B.-O. Elfstrom, V. M. Knyazheva, A. V. Plaskeyev and J. M. Kolotyrkin, Corrosion Sci., **19**, 343 (1979)
17. K. Sugimoto and S. Matsuda, Mat. Sci. Eng., **42**, 181 (1980)
18. Go Okamoto, Corrosion Sci., **13**, 471 (1973)
19. J. H. Gerretsen and J. H. W. de Wit, Corrosion Sci., **30**, 1075(1990)
20. J. A. L. Dobbelaar, E. C. M Herman and J. H. W. de Wit, Corrosion Sci., **33**, 765 (1992)
21 E. B. Castro and J. R Vilche, electrochim. Acta, **38**, 1567 (1993)
22. V. A. Marichev, T. Saario and V. V. Molokanov, ICC **93**, Houston Texas
23. B. Bleaney and B. I. Bleaney, Electricity and Magnetism, **1**, 3rd edition, Oxford University Press, 1976
24. R. E. Hummel, Optische Eigenschaften von Metallen und Legierungen, Springer-Verlag Berlin (1971)
25. S. Haupt and H. H. Strehblow, J. Electroanal. Chem., **228**, 365 (1987)
26. M. Seo, R. Saito and N. Sato, J. Electrochem. Soc., **127**, 9, 1909 (1980)
27. H. T. Yolken and J. Kruger, J. Opt. Soc. Am., **55**, 842 (1965)
28. M. A. Genshow and R. S. Sirohi, J. Electrochem. Soc., **118**, 7, 1558 (1971)
29. R. M. A. Azzam and N. M. Bashara, Ellipsometry and Polarized Light (1989)
30. R. J. Archer, Manual on Ellipsometry (Gaertner Scientific Corp. Chicago, 1968)
31. H. F. Hazebroek and A. A. Holscher, J. Phys. E: Sci. Instrum., **6**, 822 (1973)
32. H. F. Hazebroek and W. M. Visser, J. Phys. E: Sci. Instrum., **16**, 654 (1983)
33. J. H. Weaver et al., Physics Data, the optical properties of metals, the transition metals, **1**.,
34. K. N. Goswami and R. W. Staehle, Electrochim. Acta, **16**, 1895 (1971)
35. P. Marcus, H. Talah and V. Maurice, 12th International Corrosion Congress, **38** (1993) p. 2105
36. C. E. Leberknight and B. Lustman, J. Opt. Soc. Am., **29**, 59 (1939)
37. A. B. Winterbottom, J. Iron Steel Inst., **165**, 9 (1950)
38. J. O'M. Bockris, M. A. Genshow, V. Brusic and H. Wroblowa, Electrochim. Acta, **16**, 447 (1971)
39. Handbook of Chemistry and Physics, Chemical Rubber Co., Cleveland, Ohio, 56th ed., 1975, p. B87

Materials Science Forum Vols. 185-188 (1995) pp. 489-496

Analysis of electrochemically coloured aluminium anodic films by diffuse reflectance spectra

L. Anicai[1], A. Meghea[2], C. Sirean[1] and L. Dima[1]

[1] Research and Design Institute for Electrical Engineering, Splaiul Unirii 313, RO-74204 Bucharest, Romania

[2] Faculty of Industrial Chemistry, „POLITEHNICA" University, Calea Grivitei 132, RO-78122 Bucharest, Romania

Keywords: Aluminium colouring, electrochemical colouring, anodized aluminium

ABSTRACT

The experimentals in order to analyse the electrochemically coloured aluminium anodic films in electrolytes based on $CuSO_4$, using alternative current, were presented. Anodization of Al foils in 15% H_2SO_4 and 7.5M HNO_3 electrolytes were done, followed by an electrochemical treatment in a.c, using electrolytes containing $CuSO_4$, for different colouring times and values of a.c voltage. A characterization of the existent species in the coloured anodic film, by means of diffuse reflectance spectra in visible and near infrared domain(400-1200 nm) revealed the existence of Cu^{2+}, Cu^{o}, whose ratio is dependent on the colouring time. Colouring process strongly depends on initial anodization electrolyte; this fact was also visually noticed, by means of a different colours domain appearance.

INTRODUCTION

A great advance has been made in recent times in the use of coloured anodized aluminium, having excellent anticorrosive properties and good colour fastness. Because of aesthetic and technical reasons the use of organic colouring agents have often proved to be unsuitable.

Aluminium integral colouring process was a considerable advancement in technology, because coloured oxide films can be obtained in one step, but these procedures produce oxide layers only in a restricted colour range(gold-bronze, gray-black).

Taking into account these points of view, electrochemical colouring of aluminium anodic oxide films, using a.c electrolysis, proved to be the most suitable procedure. There are several studies dealing with technological improvement of a.c electrochemical colouring. According to this method, Al is subjected to an initial anodization, usually done in sulfuric acid electrolyte, followed by an a.c. electrolysis in a metallic salt solution (e.g. Cu, Ni, Sn, Fe, etc.), when as counterelectrode, the corresponding salt metal is involved [1,2,3,4]. To characterize the formed coloured anodic film, several techniques were used, such as: SEM, TEM [5], Mossbauer spectroscopy [6], IR spectroscopy and X-ray diffraction [1], etc. All the studies revealed the existence of metallic species as Me^{o} within coloured anodic film.

The present paper intends to analyse, from the existent species point of view, the electrochemically coloured aluminium anodic films in electrolytes based on $CuSO_4$, using alternative current., by means of electronic diffuse reflectance spectra, that proved to be a sensible method, in order to optically characterize the colour and chemical structure of solid materials [7,8].

EXPERIMENTAL

Samples of aluminium foils (Al min.99,5% purity), with a thickness of 0.2 mm, of 100x40 mm, having a constant working surface of 0.4 dm^2, were used. They were subjected to a surface treatment,as it follows: (a) alkaline degreasing in 2-5 g/l NaOH, 50-100 g/l $Na_2CO_3.10\ H_2O$, 50-100 g/l $Na_3PO_4.12\ H_2O$ solution, at 60-80°C, for 1-5 min.; (b) hot water rinsing; (c) chemical pickling in 30% HNO_3 at room temperature for 30 s; (d) cold water rinsing.

The Al specimens were anodized in the two following electrolyte types:

A - 15%(wt) H_2SO_4 solution, usually recommended as the initial stage of electrochemical colouring of anodic films;

B - 7.5M HNO_3 solution, recommended to obtain porous anodic films that may offer a better absorption capacity in electrochemical colouring phase, according to our own recent researches[11,12].

For electrolyte A, anodization was performed at a current density of 5 A/dm^2, a bath temperature of 20-25°C, for 5, 15, 30 minutes.

For electrolyte B, anodic oxidation was done using current densities of 2 A/dm^2 and 5 A/dm^2, at a bath temperature of 20-25°C, for 2, 5 and 20 minutes.

Electrochemical colouring was effected using a copper counterelectrode and an electrolyte with the following composition: 30 g/l $CuSO_4.5\ H_2O$, 10 g/l H_2SO_4, in alternative current, at different values of a.c voltage(10, 20, 30, 40 V), for different colouring durations(1, 2, 5, 10, 20, 30, 45 minutes), at a temperature of 25°C.

All experiments were done in stationary electrolysis conditions(non-stirred).

To examine the colour and ascribe it to the chromophoric species in the coloured anodic film, electronic diffuse reflectance spectra in the range of 400-1200 nm were recorded, using a VSU-2 type spectrophotometer equiped for reflectance. Because in all cases a.c. electrochemical colouring occurs over the anodic oxide film, recording of electronic spectra was made using Al foils anodized in 15% H_2SO_4, respectively 7.5 M HNO_3 for calibration, so that only the contribution of coloured layer is revealed. Because Al samples are not transparent, the light transmission is negligible; thus, the reflected light (R) is complementary to the sample absorbed light (A). So, absorbance A = 100-R (%) against incident radiation wavelength, was recorded in order to highlight the absorption electronic bands.

RESULTS AND DISCUSSION

Figures 1 and 2 show the colour changes vs. colouring time for anodized Al samples in 15% H_2SO_4 and 7.5M HNO_3, at different values of a.c voltage.

For an initial anodization in 15% H_2SO_4 (Fig.1), electrochemical colouring in $CuSO_4$ solutions produces red-purple coloured films. The colour becomes darker if colouring duration is increased, so that, after 30 minutes, the anodic films are black. An adherent, uniform, glossy, without blemishes coloured anodic layer, is obtained.

Variation of applied a.c colouring voltage determines a darkening of colour, from light purple at 5-10 V a.c, till black, at 20-30 V a.c.

When initial anodization is performed in 7.5M HNO_3, the subsequent electrochemical colouring in the same above mentioned electrolyte, produces another colour range, from grey, grey-green, up to dark brown-red, as it is shown in Figure 2.

A small value of anodization current density, for example 2 A/dm^2, develops during colouring stage,gray tones; if anodization duration is increased (e.g. 20 min.),the coloured anodic film has green tones(grey-greeny, green-reddish).

A greater value of anodization current density, respectively of 5 A/dm^2,determines an uniform colouring, with less blemishes, but also a colour darkening, up to mat reddish. It may be

remarked that anodization in nitric acid electrolytes determines mat layers formation, because of uniform porous structure of oxide film.

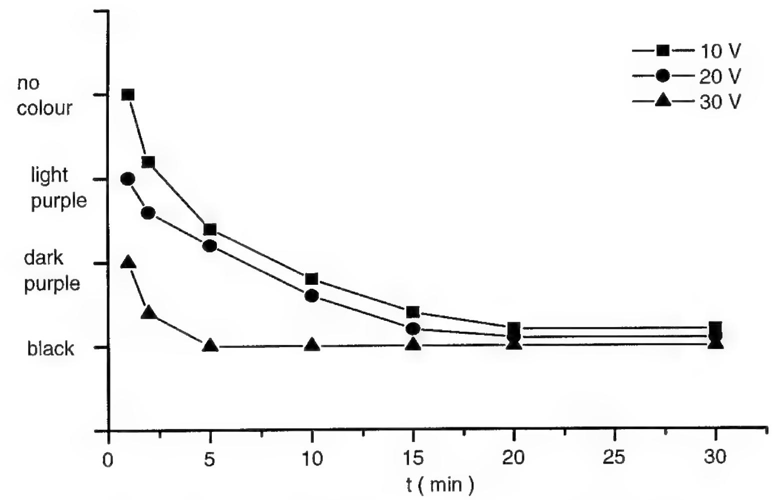

Fig. 1.Change of colour gradation measured with the eye *vs.* colouring time at different a.c. voltages, for Al initially anodized in 15% H_2SO_4.

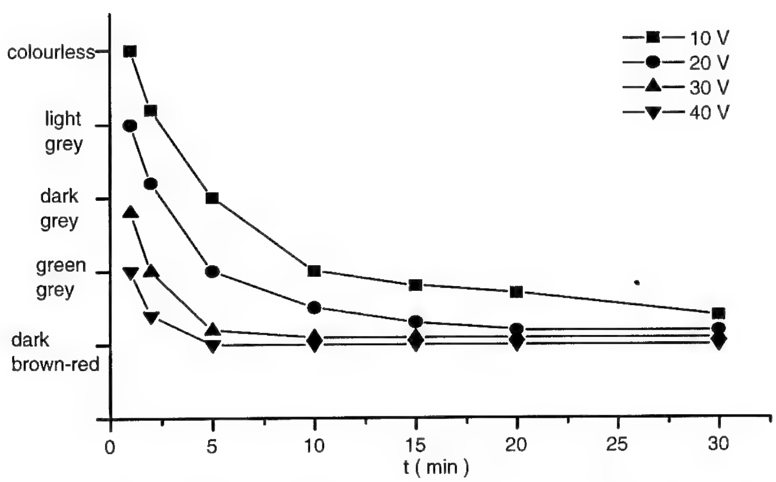

Fig. 2. Change of colour gradation mesured with the eye *vs.* colouring time at different a.c. voltages for Al initially anodized in 7.5M HNO_3 at a dc of 5 A/dm^2 for 2 min.

Moreover, because the initial anodic film is porous, the coloured layer is not totally adherent to substrate, so that a supplementary hot water sealing phase, must be introduced. Increasing of

sealing time from 5 minutes to 30 minutes leads to a better pores compactness, with uniform maintenance of the obtained colour.

Nevertheless, a slight modification of colour appears during sealing, respectively from brown-red to green-blue tones, probably due to a possible hydration of copper ions that are present in the anodic oxide film.

A modification of colour range, from light grey to dark reddish is also noticed, as a function of a.c colouring voltage, respectively from 10-20 V a.c up to 40 V a.c.

Great values of a.c voltage lead to some flaws appearance in the coloured layer, that are probably due to scintillation or sparking phenomena that are usually characteristic to anodic films formed at high voltages.

Electronic diffuse reflectance spectra

Figures 3(a) and (b), 6(a) and (b) present the electronic absorption spectra, for some of the studied ellectrochemically coloured Al anodic films.

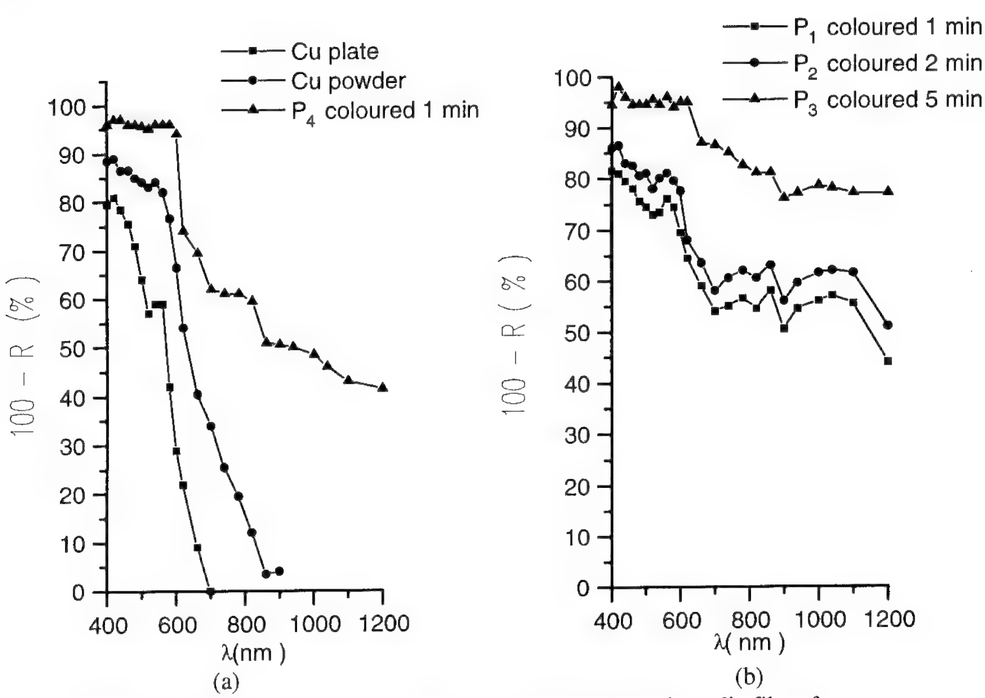

Fig.3. Recorded electronic absorbtion spectra for Al coloured anodic films for different values of colouring time - initial anodization in 15% H_2SO_4, for 5 min (b) and 30 min (a), colouring at 10 V a.c. in $CuSO_4$ solution, against metalic Cu specimens.

Grey tones correspond to a relatively uniform absorption on the whole visible range(400-700 nm); this fact was noticed in the case of coloured anodic oxide films that were initially anodized in electrolyte B, at small colouring times.

Predominant absorption in a certain domain of visible spectra determines the sample specific colour through reflected complementary radiation, according to Table 1.

Table 1 - Reflected complementary colour vs.absorbed radiation

Absorbed radiation (nm)	400-450	450-500	500-560	560-580	580-595	595-650	650-750
Reflected complementary colour	yellow	orange	red	violet	indigo	blue	green

The anodized specimens in 15% H_2SO_4, at different values of colouring time, according to Figure 3 (a) and (b), with red-purple tones, have a preponderent absorption in the range of 400-600 nm, with a well defined maximum at 580 nm, that leads to this colour. It is ascribed to the existence of metallic copper and is confirmed by the obtained spectra both for electrolytic copper plate and copper powder tablet samples against a tablet of magnesium oxide, according to Fig.3 (b).

It comes out that the two standard samples of metallic copper have similar electronic spectra, with absorption maxima at 420 nm and 580 nm, corresponding to electronic transitions between valence band and conduction band of metallic copper.

Quantitative evaluation of absorbance at 580 nm for coloured samples shows systematic variations of colour intensity vs. anodizing and colouring time (Figures 4 and 5). Obviously, in this case, anodization process determines more powerful effects than electrochemical colouring one.

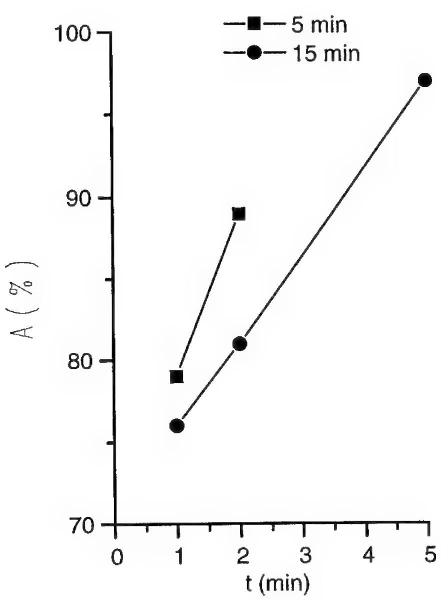

Fig.4 Absorbance *vs.* colouring time for Al initially anodized in 15% H_2SO_4 at different anodization times; λ = 580 nm

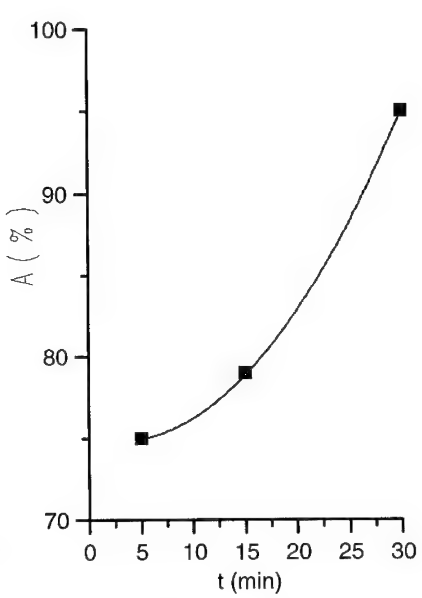

Fig.5 Absorbance *vs.* anodization time for Al initially anodized in 15% H_2SO_4 and electrochemically coloured for 1 min; λ=580 nm

Electronic spectra for samples P5-P10, that are initially anodized in 7.5M HNO_3, according to Figure 6 (a) and (b), are different from those anodized in 15% H_2SO_4 and are very sensible to anodization and colouring time. This fact shows a different composition of coloured anodic films, as a result of some different colour formation mechanism.

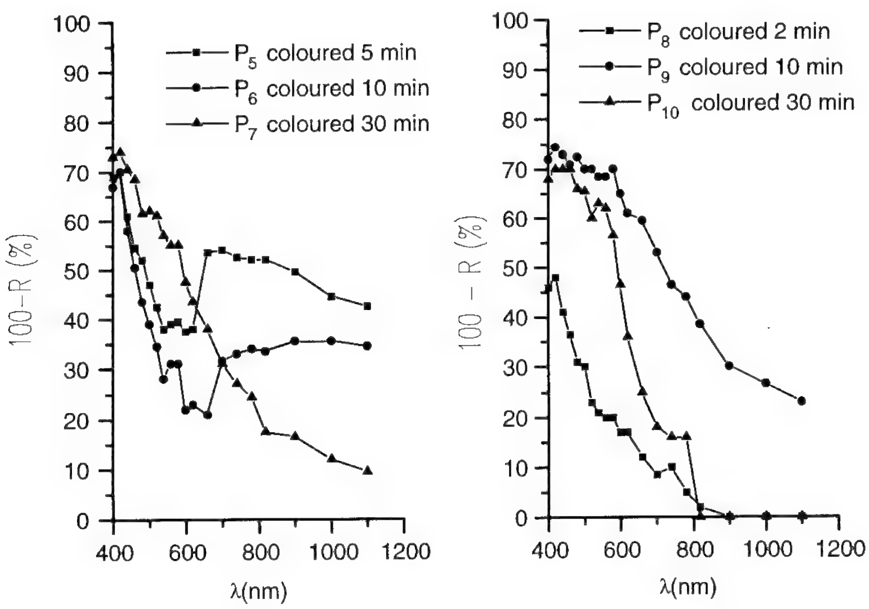

Fig. 6. Recorded electronic absorbtion spectra for Al coloured anodized films for different values of colouring time; initial anodization in 7.5M HNO_3, cd of 5 A/dm^2, for an anodization duration of 2 min (a) and 20 min (b); 10 Va.c. for electrochemical colouring -

Thus, except predominant absorption at 400-600 nm, two bands are developing: one centered at 660 nm that determines a blue tone, specific to hydrated-hexacoordinated Cu^{2+} ion and another between 700-800 nm that determines a greenish tone, specific to tetra- or penta-coordinated Cu^{2+} ion [9,10].

Therefore, in this case, both colour and the nature of component species for coloured anodic films are to be analysed using two diagnosis bands, respectively λ_1 = 580 nm for Cu^o and λ_2 = 700 nm for d-d transitions of Cu^{2+} for different compounds.

The existence of Cu^{2+} ion was also revealed by means of EPR spectra, both for samples initially anodized in 15% H_2SO_4 and 7.5 M HNO_3 electrolytes, that were subjected to a.c. electrochemical colouring in $CuSO_4$ - H_2SO_4 solutions; these experiments are to be subsequently presented in further papers.

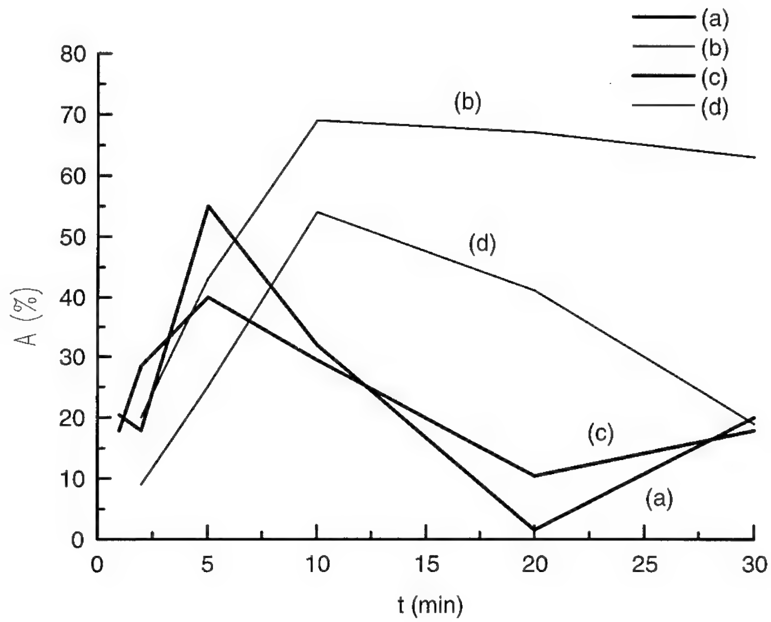

Fig.7 Absorbance *vs.* colouring time for Al samples initially anodized in 7.5 M HNO_3 at different anodization durations for 2 diagnosis bands: (a) 2min, $\lambda_2 = 700$ nm; (b) 20 min, $\lambda_1 = 580$ nm; (c) 2 min $\lambda_1 = 580$ nm; (d) 20 min, $\lambda_2 = 700$ nm

Figure 7 presents the dependence between absorbance and colouring time for the two selected diagnosis bands and the two initial anodization durations (20 min. and 2 min.), for the obtained coloured anodic films.

Curves (b) and (d) from Figure 7 show the evolution of these two bands intensity vs. colouring time, after an initial anodization in 7.5 M HNO_3, for 20 minutes.

Firstly, it may be noticed the higher value of absorbance at 580 nm, comparatively with that obtained at 700 nm, which determines a reddish shade of greenish coloured films. An increase of colouring time determines a predominant, practically constant content of metallic Cu, while the existent Cu^{2+} species presents a maxima after 10 minutes.

For colouring times greater than 30 minutes a decrease of the both species content is observed, probably due to coloured film deterioration.

Initial anodization in 7.5 M HNO_3 for shorter duration, of only 2 minutes, according to Figure 7-curves (a) and (c), shows a modification of colour against colouring time, from a predominant greenish to reddish tones; the two curves cross and invert their maxima. This behaviour suggests an initial adsorption of Cu^{2+} ions and formation of some compounds on Al surface; after that, reduction processes to Cu^0 become predominant. This fact is also visually confirmed,when, for colouring times over 20 minutes the coloured Al anodic film appears as a matted deposition of metallic copper.

Thus, one may conclude that the anodization electrolyte type determines a modification of colouring mechanism; this is also visually highlighted by means of the two colour ranges existence, as it was mentioned above.

Colouring duration takes action on chromophoric species ratio, respectively Cu^{2+}, Cu^{o}, that coexist in the coloured anodic film and implicitly produces different colour tones.

CONCLUSIONS

After the experimentals were done, it was found out that:

- the type of electrolyte used for initial anodization strongly influenced the colour range of subsequently electrochemically coloured anodic film in $CuSO_4$ based electrolytes;

- dark shades obtaining is facilitated either by higher values of a.c voltage or of colouring time; there is a critical limit of these two parameters, over that, coloured anodic films with flaws, were noticed;

- electronic diffuse reflectance spectra revealed the existence of chromophoric species: Cu^{2+}, Cu^{o} in the coloured anodic film, whose content depends on colouring duration; further experiments are to be done, in order to get more information and to better understand this electrochemical colouring process;

- when initial anodization takes place in sulfuric acid type electrolyte, subsequent electrochemical colouring mainly determines the existence of Cu^{o} (metallic) in the coloured film;

- an initial anodization in 7.5 M HNO_3 leads during electrochemical colouring to a different colour formation mechanism, consisting in an initial adsorption of Cu^{2+} and formation of some compunds on Al surface, followed by reduction processes to Cu^{o}, that finally, become predominant.

REFERENCES

[1] Edith Lichtenberger-Bajza, F.Domolki,I.Imre-Baan, Metal Finishing, **72**, 50 (1973).
[2] S.A.K.Hsieh, Metal Finishing, **79** (10), 21 (1981).
[3] M.Wrzecian, Galvano-Organo, **499**, 781 (1979).
[4] Y.Itoi, A.Hasumi, E.Sato, K.Tachihara, Electrochim.Acta, **25**, 1297 (1980).
[5] T.Kawaguchi, S.Ono, T.Sato and N.Masuko, J.of Surf.Finish.Soc.Japan, **41**, 6, 690 (1990).
[6] R.L.Cohen, Ch.J.Raub and T.Muramaki, J.Electrochem.Soc.,**125**(1), 34 (1978).
[7] F.E.Godic, B.F.Orment, Fiz.Tverd.Telo.,**2**,3017 (1960)
[8] W.D.Wright, "The Measurement of Colour ", 3rd ed., Hilger & Watts Ltd., London, 1964.
[9] Russell S.Drago, "Physical Methods for Chemists", 2nd ed.,Sounders College Publishing, 1992.
[10] A.B.P.Lever, "Inorganic Electronic Spectroscopy", 2nd ed.,Elsevier, New York, 1984.
[11] L.Dima, Liana Anicai, Rom.Pat.No.98 547,(1989).
[12] Liana Anicai, L.Dima, T.Visan, M.Buda,"Aluminium Anodization in Nitric Acid Solutions", in Studia Universitatis Babes- Bolyai, Series Chemia, in press (1994).

Materials Science Forum Vols. 185-188 (1995) pp. 497-504

Strong acid- and alkali-resistant ZrO_2-TiO_2 composite oxide thin films formed by low-pressure MOCVD

S. Kikkawa, N. Hara and K. Sugimoto

Department of Metallurgy, Faculty of Engineering, Tohoku University, Sendai, Japan

Keywords: ZrO_2-TiO_2 composite film, MOCVD, corrosion resistance, aqua regia, sodium hydroxide, ellipsometry

Abstract

In order to obtain composite oxide films with corrosion resistances against both aqua regia and concentrated NaOH solutions, ZrO_2-TiO_2 films were formed on Pt and Si substrates by low pressure CVD techniques using zirconium-tetra-isopropoxide ($Zr(O\text{-}i\text{-}C_3H_7)_4$) and titanium-tetra-isopropoxide ($Ti(O\text{-}i\text{-}C_3H_7)_4$) and oxygen. The films obtained were composed of composite oxides of which the in-depth composition was uniform. The changes in the corrosion resistance of the films were investigated as a function of film composition. The corrosion resistance of the films in aqua regia increased with increasing cation fraction of Ti, but that in $10 kmol{\bullet}m^{-3}$ NaOH increased with increasing cation fraction of Zr. The highest corrosion resistance against both aqua regia and $10 kmol{\bullet}m^{-3}$ NaOH was obtained at a cation fraction of Zr of *ca.* 0.7. The films with such composition have homogeneous amorphous structures.

1. Introduction

Composite oxide films having corrosion resistances against highly corrosive solutions over a wide pH range have been synthesized by metalorganic chemical vapor deposition (MOCVD) technique using mixed precursors for oxides with different corrosion characteristics. For example, Amano and Sugimoto [1] synthesized Ta_2O_5-ZrO_2 composite films having corrosion resistances against both aqua regia and $10 kmol{\bullet}m^{-3}$NaOH from precursors of tantalum pentamethoxide ($Ta(OCH_3)_5$) and zirconium-tetra-isopropoxide ($Zr(O\text{-}i\text{-}C_3H_7)_4$). Although the corrosion resistance of the films is extremely high, the weakness is the high price of the reagent $Ta(OCH_3)_5$.

The purpose of present study is to synthesize economically advantageous composite films having corrosion resistances against both strong acid and strong alkali solutions. Amano and Sugimoto [2] reported that ZrO_2 films formed at 573 K by low pressure CVD using $Zr(O\text{-}i\text{-}C_3H_7)_4$ hardly dissolve in $10 kmol{\bullet}m^{-3}$ NaOH at 298 K. Toyoda and Sugimoto [3] also reported that TiO_2 films formed at 573 K by ambient pressure CVD using titanium-tetra-isopropoxide ($Ti(O\text{-}i\text{-}C_3H_7)_4$) were close to no dissolution in $2 kmol{\bullet}m^{-3}$ HCl at 298 K. The price of the reagent $Ti(O\text{-}i\text{-}C_3H_7)_4$ is much lower than that of the reagent $Ta(OCH_3)_5$. Therefore, it is thought that the objective composite films should be obtained by CVD using $Zr(O\text{-}i\text{-}C_3H_7)_4$) and $Ti(O\text{-}i\text{-}C_3H_7)_4$ as precursors. In the present study, the synthesis of ZrO_2-TiO_2 composite films were performed and corrosion resistances of the films were examined in aqua regia and $10 kmol{\bullet}m^{-3}$ NaOH.

2. Experimental

2.1. Synthesis of ZrO_2-TiO_2 composite films

ZrO_2-TiO_2 composite oxide films were made by MOCVD technique. $Zr(O\text{-}i\text{-}C_3H_7)_4$ and $Ti(O\text{-}i\text{-}C_3H_7)_4$ were used as vapor sources and heated at 443 K and 318 K, respectively. N_2 was used as a carrier gas. The total flow rate of carrier gases for each vapor source was kept constant at a value of $16.67\times10^{-6}m^3{\bullet}s^{-1}$. O_2 was used as a reaction gas and mixed with the source gases just before the introduction into a CVD cell. The flow rate of O_2 was kept constant at a value of $6.67\times10^{-6}m^3{\bullet}s^{-1}$. The formation of composite films was performed at substrate temperatures of 573, 623, and 723 K.

A polycrystal Pt plate and a single crystal Si(100) plate in dimensions of 25mm×15mm×0.5mm were used as substrates. The surface of the Pt plate was finished with 1 μm-diamond paste and degreased ultrasonically in acetone. Surface oxide films on Si(100) were removed by dipping in 2 mass% HF at 298 K just before the experiment. KBr disks were also used as substrates for films which were used for transmission electron microscopic observation and electron diffraction.

Figure 1 shows the schematic of the MOCVD system. Each source was heated in an oil bath and the source vapor was carried into a mixing cell by the carrier gas. Source gases and O_2 were mixed in a mixing cell and then introduced into a CVD cell. The total pressure of the CVD cell was kept at 2.0 kPa. The substrate was attached on a holder having a heater within. A cover with a small slit and a porous partition was set on the substrate to get homogeneous gas flow. The composition of the films was controlled by the flow rate of the carrier gas. The thickness of the films was adjusted to *ca.* 60 nm by controlling the deposition time.

2.2. Ellipsometry

The thickness and optical constants of the films were determined by ellipsometry. A rotating analyzer type automatic ellipsometer, which has the conventional polarizer-compensator-specimen-analyzer configuration, was used. Monochromatic light of wavelength 546.1 nm was used for the measurements. The angle of incidence of the monochromatic light was 60.00°. The polarizer was fixed at an angle of 45°. The analyzer was rotated at an angular velocity of $360°s^{-1}$. The intensity of light through the analyzer was measured by a photodiode and recorded with a computer as a function of rotation angle.

The quantity measured by an ellipsometer is the ratio ρ of the complex-amplitude reflection coefficient R_p and R_s for the p- and s-polarization, respectively, given by the equation [4]

$$\rho = R_p \bullet R_s^{-1} = \tan\psi \bullet \exp(i\Delta) \qquad (1)$$

where Δ is the relative phase retardation and ψ is the arc tangent of the relative amplitude reduction. The thickness and optical constants of deposited films were determined using a theoretical Δ *vs.* ψ curve which fits the experimental ellipsometric data (Δ, ψ) with minimal error. Theoretical Δ *vs.* ψ curves were calculated using Drude's exact optical equations which start from the Eq.1.

2.3. ICPS analysis

The chemical composition of composite oxide films was determined by chemical analysis: films were dissolved in 10^{-5} m^3 of 98 mass% H_2SO_4 at 473 K and then the solution was diluted to 10^{-4} m^3 by adding distilled water. This diluted solution was analyzed by inductively coupled plasma-emission spectroscopy (ICPS), which gave the content of the Zr and Ti in the films, W_{Zr} and W_{Ti}. The cationic mass fraction of Zr and Ti, X_{Zr} and X_{Ti}, of the films were calculated from W_{Zr} and W_{Ti}, for example, $X_{Zr} = W_{Zr} \bullet (W_{Zr} + W_{Ti})^{-1}$; $X_{Zr} + X_{Ti} = 1$.

2.4. AES analysis

In-depth composition profiles of composite oxide films were obtained by Auger electron spectroscopy (AES) in combination with Ar ion sputtering. The Si(100) was used as substrates of specimens and composite oxide films of *ca.* 50 nm thickness were deposited on it. The measurement

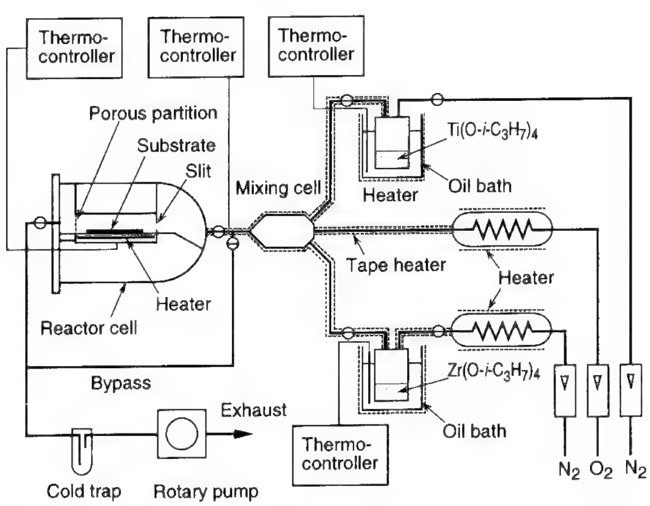

Fig.1 Apparatus for MOCVD.

of the spectra was carried out under a pressure of 1.2×10^{-7} Pa. The applied voltage for the acceleration of primary electron was 3 kV and the current was 0.5 μA.

2.5. TEM observation

Micro- and crystal structures were examined by transmission electron microscopy (TEM) and electron diffraction (ED), respectively. Composite oxide films of *ca.* 100 nm thickness were deposited on KBr disks and then the disks were dissolved by distilled water to separate the films. The separated films were picked by Cu mesh (180 mesh) and served for observation.

2.6. Corrosion test

The corrosion resistance of composite oxide films was tested in aqua regia (HNO_3 : HCl = 1 : 3) and 10kmol•m^{-3}NaOH at 298K. Si(100) substrates were used for specimens tested in aqua regia and Pt substrates were used for those tested in 10 kmol•m^{-3} NaOH. The thickness of composite oxide films was adjusted to 50-60 nm. The decrease in film thickness was measured by ellipsometry after the corrosion test in each solution.

3. Results

3.1. In-depth composition profile

Figure 2 shows an AES composition profile for a composite oxide film of X_{Zr}=0.30, which was formed at 623 K. The ratio of Zr to Ti was approximately constant except for the interface region between the film and the substrate. The same composition profiles were obtained for other composite films of different X_{Zr} values. Therefore, the composition of the composite films formed by the MOCVD process was thought to be homogeneous.

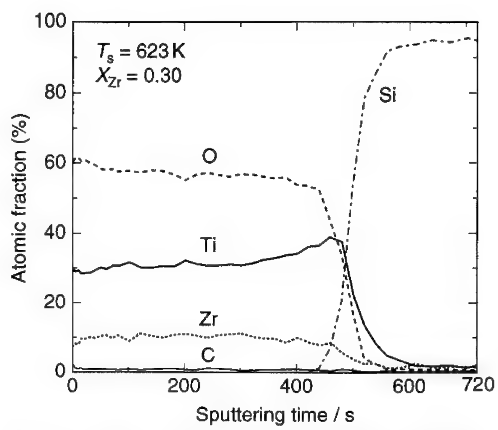

Fig.2 Depth profile of composite film with X_{Zr}= 0.30 formed at 623 K.

3.2. Micro- and crystal structures

Figure 3 shows transmission electron micrographs and electron diffraction patterns for composite films of different X_{Zr} values, which were formed at 623 K. The TiO_2 film (X_{Zr}=0) and the ZrO_2 film (X_{Zr}=1) have fine crystal grains. However, composite films (X_{Zr}=0.27 and 0.45) have no crystal grains and show homogeneous structures. The TiO_2 film and the ZrO_2 film have an anatase and a tetragonal structure, respectively. On the other hand, composite films (X_{Zr}=0.27 and 0.45) have amorphous structures. The same results were obtained for the other composite films of X_{Zr}=0.05 and 0.90. That is, the composite films of X_{Zr}=0.05 - 0.9 were all amorphous and homogeneous. Imashita *et al.* [5] also reported that ZrO_2 -TiO_2 films of X_{Zr}=0.1 - 0.9, which were formed at 623 K, were amorphous, although they used different source materials for CVD. The crystallization should be suppressed by compounding ZrO_2 and TiO_2.

3.3. Corrosion resistance against aqua regia

Figure 4 shows changes in ellipsometric parameters, Δ and ψ, with time for a composite film of X_{Zr}=0.94 in aqua regia. The film was formed at 623 K. Theoretical Δ - ψ curves for films with different optical constants, $N_2=n-ki$, which show changes in Δ and ψ with the change in film thickness, are also given in Fig.4. The experimental Δ - ψ locus moves from a theoretical curve for a high optical constant, N_2=1.78 − 0.00i, to that for a low optical constant, N_2=1.64 − 0.00i, with increasing time, t. This decrease in the optical constant might be due to an increase in the surface roughness of film with the progress of dissolution. In this case, the theoretical curve for the optical constant of N_2=1.74 − 0.00i was approximately selected as the best fit curve through the whole test duration. The film thickness at a given time was determined by drawing a perpendicular to the theoretical curve from the experimental curve.

The decrease in film thickness as a function of time for composite films of X_{Zr}= 0 - 1 is shown in Fig.5. Every film dissolves linearly with time except for the early stage of dissolution. The dissolution

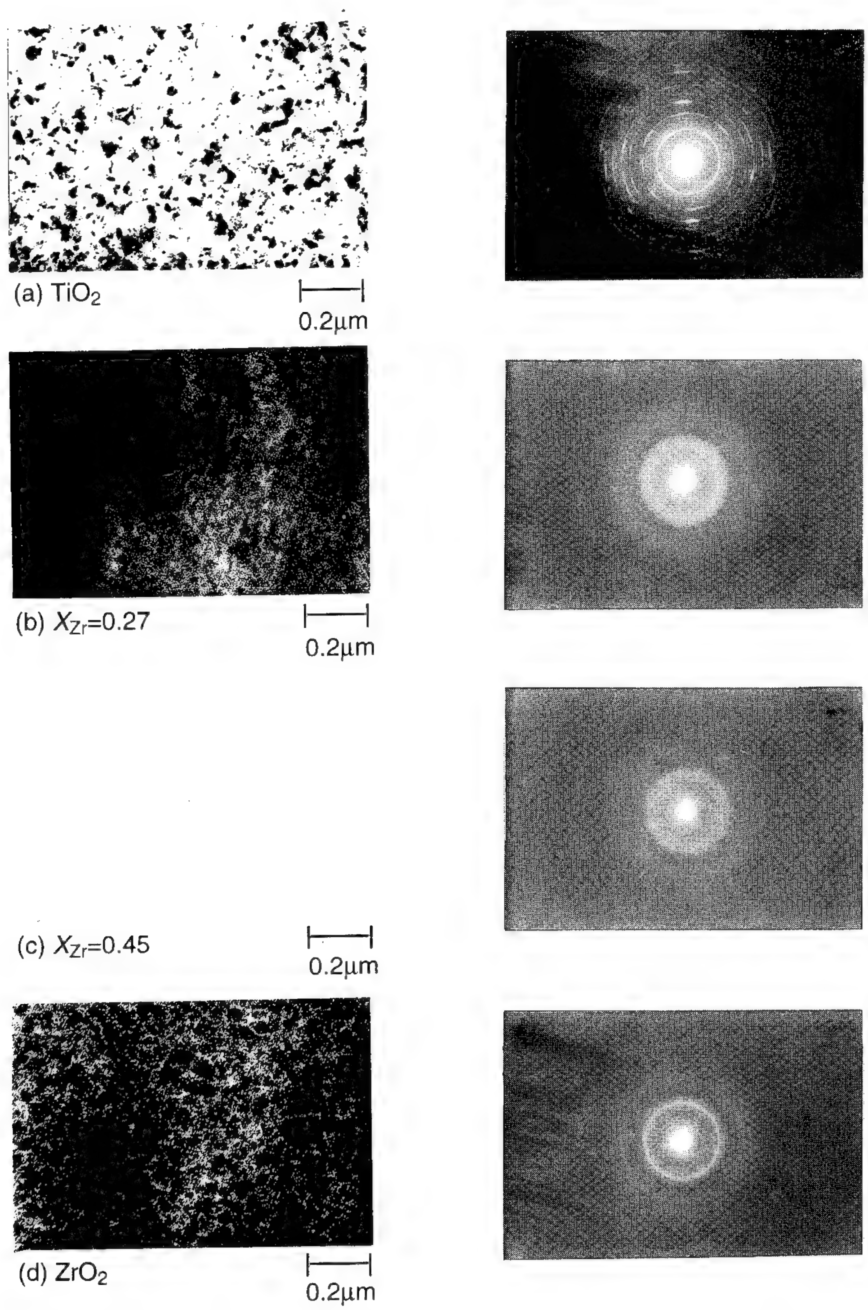

Fig.3 Transmission electron micrographs (left) and electron diffraction patterns (right) for TiO_2 (a), composite films having X_{Zr}=0.27(b), 0.45(c), and ZrO_2(d) formed at 623 K.

rate of films, that is, the decrease rate of film thickness, $-\Delta d \cdot \Delta t^{-1}$, can be determined by the gradient of Δd *vs.* Δt curves.

The decrease rates of film thickness thus obtained are given in Fig.6 as a function of X_{Zr} for composite films formed at 573, 623 and 723 K. The decrease rate of film thickness in aqua regia increases with increasing X_{Zr} vale for films formed at any temperature. The rate at a given X_{Zr} value, however, decreases with increasing film-formation temperature. The films formed at 623 and 723 K show the rates of lower than 3.5×10^{-6}nm$\cdot$s^{-1} up to X_{Zr} values of 0.7 and 0.8, respectively.

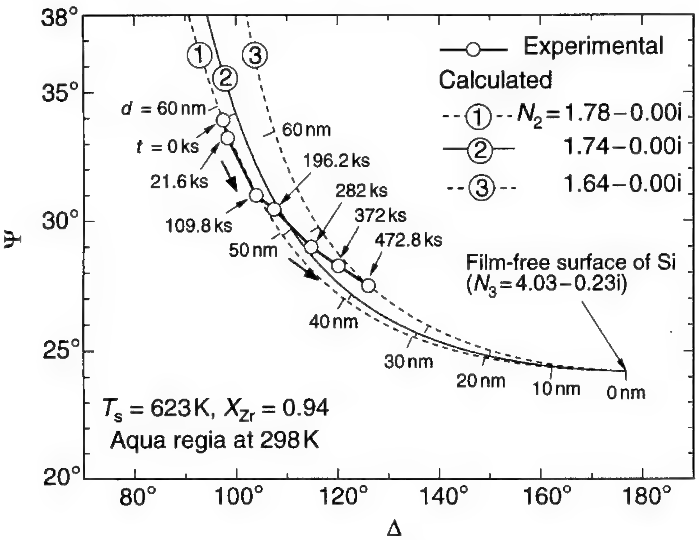

Fig.4 Experimental Δ - ψ locus for dissolution of composite film of X_{Zr}=0.94 , which was formed on Si substrate at 623 K, in aqua regia and theoretical Δ - ψ curves for films with optical constants of N_2=1.64−0.00i, 1.74−0.00i and 1.78−0.00i.

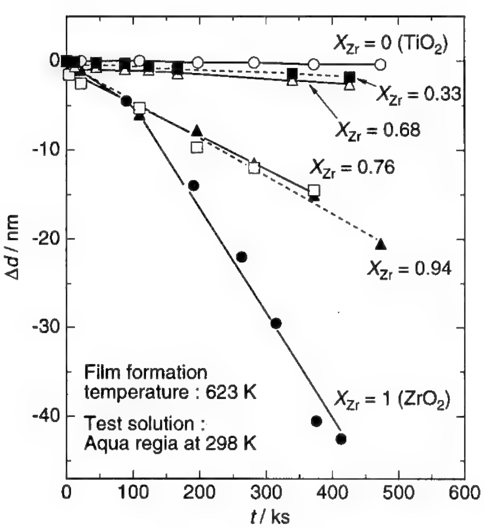

Fig.5 Decrease in film thickness, Δd, as a function of time, t, for composite films in aqua regia at 298 K.

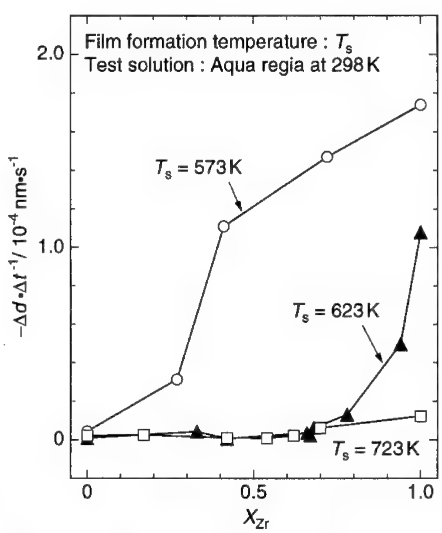

Fig.6 Decrease rate of film thickness,$-\Delta d \cdot \Delta t^{-1}$, as a function of cationic fraction of Zr, X_{Zr} , for composite films in aqua regia at 298 K.

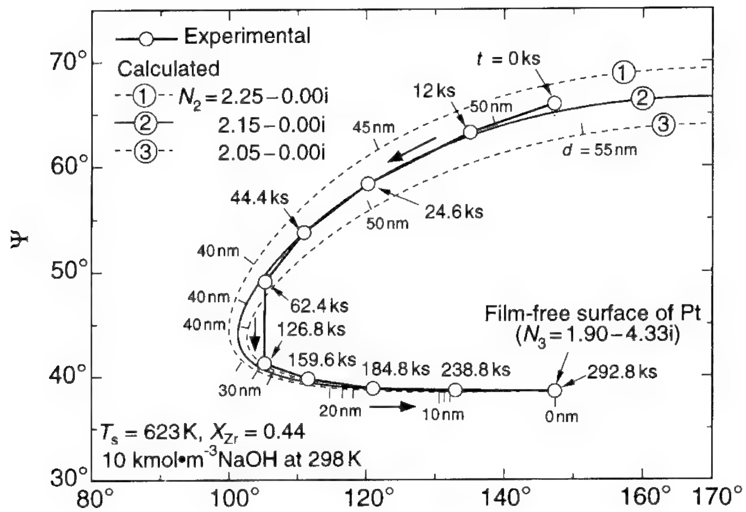

Fig.7 Experimental Δ - ψ locus for dissolution of composite film of X_{Zr}=0.44 , which was formed on Pt substrate at 623 K, in 10 kmol•m^{-3} NaOH and theoretical Δ - ψ curves for films with optical constants of N_2=2.05−0.00i, 2.15−0.00i and 2.25−0.00i.

3.4. Corrosion resistance against 10 kmol•m^{-3} NaOH

Figure 7 shows changes in ellipsometric parameters, Δ and ψ, with time for a composite film of X_{Zr}=0.44 in 10 kmol•m^{-3} NaOH. The film was formed at 623 K. Theoretical Δ - ψ curves for films with different optical constants of N_2=2.25−0.00i, N_2=2.15−0.00i, and N_2=2.05−0.00i are given in Fig.7. The experimental Δ - ψ locus fits well the theoretical curve for the optical constant of N_2=2.15 −0.00i. This means that general and homogeneous dissolution of the composite film proceeds through the whole test duration. The film thickness at a given time was determined from an experimental point on the theoretical curve.

The decrease in film thickness as a function of time for composite films of X_{Zr}= 0 - 1 is shown in Fig.8. Every film dissolves linearly with time from the early stage of dissolution. The decrease rate of film thickness, $-\Delta d \bullet \Delta t^{-1}$, was determined by the gradient of Δd *vs.* Δt curves.

The decrease rates of film thickness obtained are given in Fig.9 as a function of X_{Zr} for composite films formed at 573, 623 and 723 K. The decrease rate of film thickness in 10 kmol•m^{-3} NaOH increases with increasing X_{Zr} value up to an X_{Zr} value of 0.3 and then decreases with increasing X_{Zr} value up to an X_{Zr} value of 1 on films formed at any temperature. The rate at a given X_{Zr} value decreases with increasing film-formation temperature. The films formed at 623 and 723 K show the rates of lower than 2.65×10^{-5}nm•s^{-1} at X_{Zr} values larger than 0.7. A slight increase in the rate at X_{Zr}

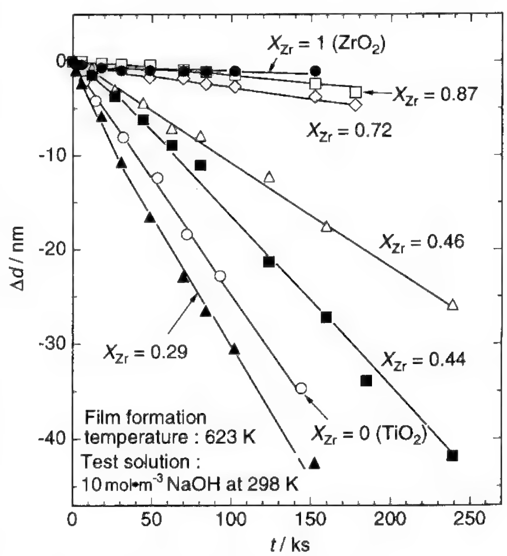

Fig.8 Decrease in film thickness, Δd, as a function of time, t, for composite films in 10 kmol•m^{-3} NaOH at 298 K.

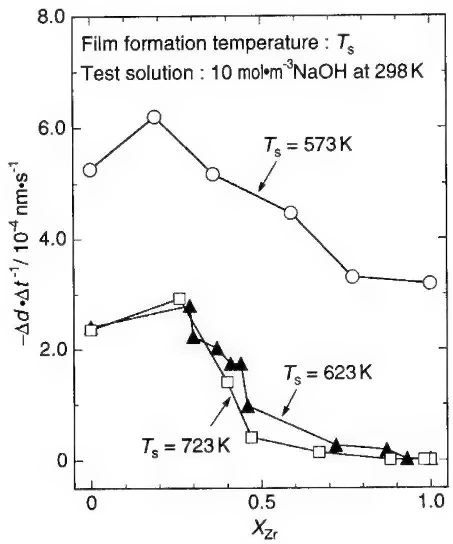

Fig.9 Decrease rate of film thickness, $-\Delta d \cdot \Delta t^{-1}$, as a function of cationic fraction of Zr, X_{Zr}, for composite films in 10 kmol•m^{-3} NaOH at 298 K.

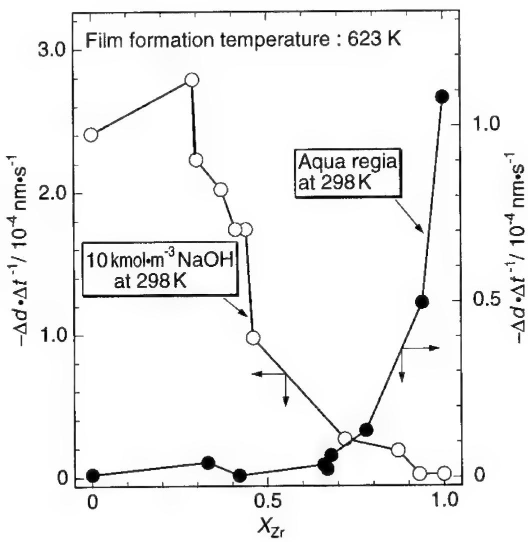

Fig.10 Decrease rate of film thickness, $-\Delta d \cdot \Delta t^{-1}$, as a function of cationic fraction of Zr, X_{Zr}, for composite films in aqua regia and 10 kmol•m^{-3} NaOH at 298 K.

values smaller than 0.3 might be due to the low density amorphous structure of ZrO_2-TiO_2 films with low ZrO_2 content.

3.5. Composite films resistant to both strong acid and alkali

Figure 10 summarizes the decrease rates of film thickness as a function of X_{Zr} for composite films in aqua regia and 10kmol•m^{-3} NaOH at 298 K. The films were formed at 623 K. From this figure, it is seen that the films with X_{Zr} values of around 0.7 have high corrosion resistances against both strong acid and alkali solutions. At a film formation temperature of 723 K, the corrosion resistant region enlarges between X_{Zr} values of 0.5 and 0.8 (see Figs.6 and 8).

4. Conclusion

(1) ZrO_2-TiO_2 composite films were formed by MOCVD using Zr(O-*i*-$C_3H_7)_4$ and Ti(O-*i*-$C_3H_7)_4$ as source gases.
(2) The composite films, which were formed at 623 K and had X_{Zr} values between 0.05 and 0.90, showed homogeneous amorphous structures.
(3) The composite films with an X_{Zr} value of about 0.7, which was formed at 623 K, exhibited high corrosion resistance against both aqua regia and 10kmol•m^{-3} NaOH at 298 K.
(4) On films formed at 723 K, the corrosion resistant region for both strong acid and alkali enlarges between X_{Zr} values of 0.5 and 0.8.

References

[1] K.Amano and K.Sugimoto, J. Japan Inst. Metals, **56**, 1192 (1992).
[2] K.Amano and K.Sugimoto, *ibid.*, **56**, 204 (1992).
[3] M.Toyoda and K.Sugimoto, *ibid.*, **54**, 925 (1990).
[4] R.M.A.Azzam and N.M.Bashara, "Ellipsometry and Polarized Light", North-Holland, New York (1977).
[5] K.Imashita, H.Funakubo, N.Kieda, M.Kato, and N.Mizutani, J. Chem. Soc. Jpn, **1990**, 1395 (1990).

Materials Science Forum Vols. 185-188 (1995) pp. 505-514

Passive rust layer on low-alloy steel exposed in atmospheric environment

M. Yamashita[1], H. Miyuki[1], H. Nagano[1] and T. Misawa[2]

[1] Research and Development Center, Sumitomo Metal Industries, Ltd., 1-8 Fusohcho, Amagasaki-660, Japan

[2] Materials Science and Engineering, Muroran Institute of Technology, Muroran-050, Japan

Keywords: Passive rust layer, ferric-oxyhydroxide, low-alloy steel, atmospheric corrosion, long-term transformation of rust

Abstract

The passive rust layer formed on a low-alloy steel after a long-term exposure to an atmospheric environment has been examined. It was shown that the passive rust layer was composed of densely aggregated fine-particles of α-ferric-oxyhydroxide containing a considerable amount of Cr. The characteristic feature of synthetic α-ferric-oxyhydroxides containing various amounts of Cr suggests that the coexistence of Cr in the passive rust crucially affects the protective ability of the passive rust against atmospheric corrosives. It was also found that the nature of the Cr-containing oxyhydroxide was dependent upon the Cr content in the rust matter.

1. Introduction

It has been believed that the atmospheric corrosion behavior of low-alloy steels is strongly affected by the characteristics of the rust layer formed on the steel surface. During the last several decades, weathering steel, which is a low-alloy steel containing Cr, Cu and P, has been designed to spontaneously form a passive and protective rust layer by exposure to an atmospheric environment.

Because of this barrier effect of the passive rust layer, weathering steels have been widely employed as various kinds of structural materials usually used outdoors and have shown significant performance even without protective coatings. However, as will be mentioned later, the structure and property of the passive rust layer have remained ambiguous. The difficulty in understanding the characteristics of the passive rust may arise from a long-term aging which is indispensable for the formation of the passive rust outdoors.

The authors have been aware that the rust constituents vary with time of exposure for several decades [1], and pointed out that the final stable passive rust is composed mainly of α-ferric-oxyhydroxide[2,3]. In this work, further characterization of the α-ferric-oxyhydroxide passive rust was performed.

2. Model for passive rust layer

It is generally accepted that the rusts formed on steels exposed in an ordinary atmosphere are mainly composed of ferric oxyhydroxides, magnetite and amorphous substance. The amount and distribution of these rust constituents influence the protective ability of the rust layer.

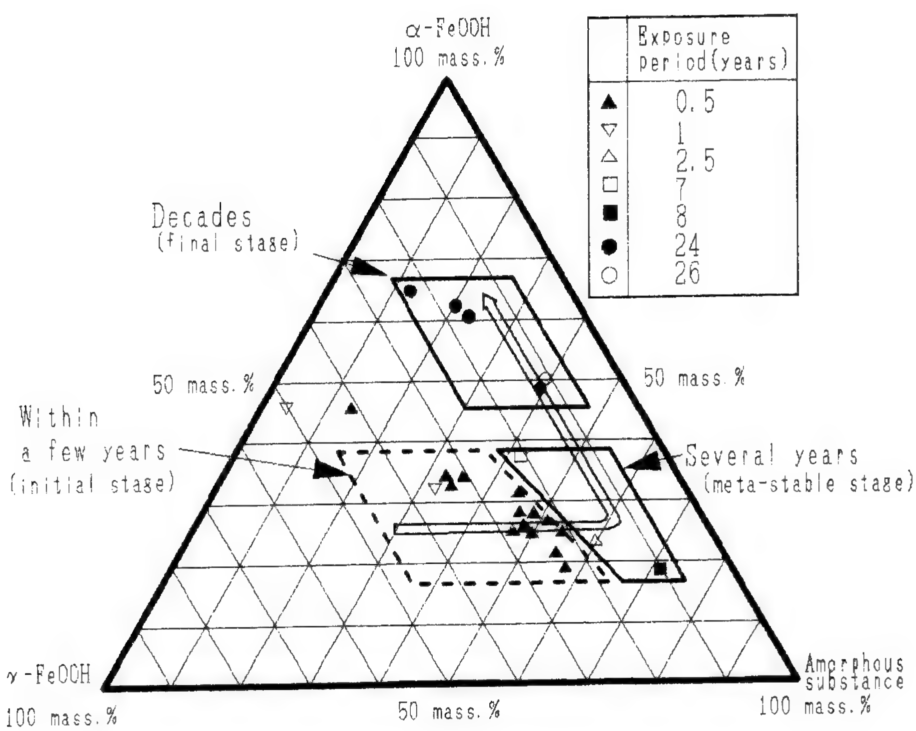

Fig.1 Change of the fractions of rust constituents formed on low-alloy steels by atmospheric corrosion with exposure time [1].

It has been thought that the protective rust on the weathering steel forms as bilayers consisting of the outer and inner layers. Okada et al. [4] and Kihira et al. [5] reported that the inner amorphous spinel type oxide containing alloying elements possesses a higher ability for protection of low-alloy steels. Misawa et al. [6-8] pointed out that the amorphous ferric oxyhydroxide acts as a protective rust against atmospheric corrosion of steels. According to Keiser and Brown [9], the protective rust was identified to be mainly composed of δ-FeOOH with 10-20% γ-FeOOH and a small proportion of α-FeOOH. More recently, Townsend et al. [10] suggested the importance of the formation of the thin outer layer of hematite and magnetite in the mechanism of protective rust formation on weathering steels.

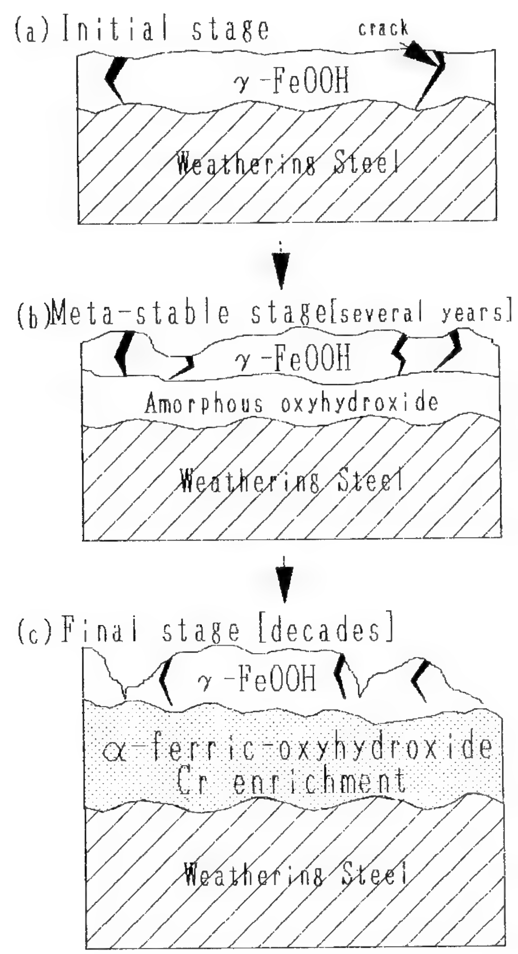

Fig.2 Schematic illustration of the progress of growth of passive rust layer formed on low-alloy steel in an industrial region [2,3].

As briefly reviewed above, no completely satisfactory model has been proposed to understand the characteristics of the passive rust layer. This may be due to the difficulty of monitoring rust growth for many years.

In order to assess the variation of the rust constituents on the weathering steel with exposure period, we have examined the rusts of a number of low-alloy steels corresponding to a weathering steel exposed to the weather for various periods up to 26 years. It was found that the main constituent of the rust layer formed on the low-alloy steels continuously changed with exposure period from γ-FeOOH to amorphous substance, and finally to α-ferric-oxyhydroxide for a few decades, as shown in Fig.1 [1]. The final passive rust layer of α-ferric-oxyhydroxide is the compact inner layer containing a considerable amount of Cr underlying a porous outer layer of γ-FeOOH. The formation process of this passive rust layer is schematically illustrated in Fig.2 [2,3]; γ-FeOOH as an initial rust layer is transformed into the final passive rust layer, probably via amorphous substance, during atmospheric corrosion and aging for a few decades.

In this paper, a more detailed feature of the passive rust layer of α-ferric-oxyhydroxide is examined employing both the well-matured passive rust formed on a weathering steel exposed for 26 years and α-oxyhydroxides of Fe synthesized in the presence of various amounts of Cr ions.

3. Experimental

3.1. Passive rust layer

Plates of a weathering steel containing 0.12mass%C, 0.49Si, 0.50Mn, 0.149P, 0.020S, 0.57Cu, 1.19Cr and 0.49Ni were exposed in the industrial region in Amagasaki, Japan at an angle of 30 degrees facing south for 26 years in order to spontaneously obtain the passive rust layer. After the exposure of the specimens, the rust formed was removed by a razor until the steel surface appeared. It was found that the rust was composed of the outer porous layer and that the inner dense layer was responsible for the protection from a corrosive environment [2]. The removed rust was then ground into powder and stored in a desiccator for a week.

3.2. Synthesis of α-ferric-oxyhydroxides

Synthesis of α-ferric-oxyhydroxide was carried out in the absence or presence of various amounts of Cr. First of all, a 4 mass% NaOH solution was added to 2.5×10^{-4} m^3 of a N_2 saturated 0.6 kmole/m^3 solution of $FeSO_4(NH_4)_2SO_4\cdot6H_2O$ until the pH reached 13.0-13.5. Then, the solution was left for 30 hours for hydrolysis at ambient temperature [11]. Ammonium chromium(III) sulfate was then added into the solution to make a mole ratio of Cr^{3+}/Fe^{2+} to be between 0 and 1.0. In addition, a deionized water was added to make the

amount of the solution $1x10^{-3}$ m^3 and the room air was introduced in the solution at a flowing rate of $1.4x10^{-3}$ m^3/min. for 18 hours. Then, the oxide precipitated in the solution was matured for 30 days. Thereafter, the solution was stirred and left for a while and only the solution was discarded. By repeating this procedure, the oxide formed was roughly rinsed. Finally, the residual solution was filtered and the residue was rinsed with a deionized water until phenol phthalein became insensitive. The synthetic α-ferric-oxyhydroxides were dried in a desiccator for more than a week. The amount of Cr in the α-ferric-oxyhydroxides was chemically analyzed.

3.3. TEM observation and X-ray diffraction characterization

The spontaneous and synthetic rust powders were examined using a TEM (transmission electron microscope:JOEL JEM200CX) and an analytical TEM (Hitachi HU-700H). The rust powders were adhered onto an acetyl cellulose film and carbon-deposited. Then, after the acetyl cellulose film was dissolved, the powders on the carbon film were employed for TEM observation using Mo mesh.

The rust powders were also subjected to X-ray diffraction characterization using Rigaku RU200 with CoKα radiation. The scanning rate was adjusted to be 2 degrees/min..

4. Results and discussion

Typical examples of the TEM observation of the two main constituents in the rust formed spontaneously by exposure to environmental atmosphere for 26 years are shown in Fig.3. It is to be noted that the crystal size of the α-ferric-oxyhydroxide in the passive inner rust layer (Fig.2c), shown in Fig.3a, is only a few tens of nm whereas that of γ-FeOOH in the outer rust layer is apparently much larger. It was found by analytical TEM inspection that approximately 3 mass% of Cr was present in the inner α-ferric-oxyhydroxide whereas Cr was not present in the outer rust. The electron diffraction pattern of the Cr-containing inner rust layer suggests that Cr exists in the oxyhydroxide lattice as a substitutional alloying constituent since only α-FeOOH is identifiable from the diffraction patterns. This is also supported by the result obtained by Schwertmann and Cornell [12] who showed that Cr is the substitutional element for α-FeOOH.

In order to clarify the effect of Cr, the crystal morphology of the synthetic α-ferric-oxyhydroxides is compared with that of the spontaneous passive rust layer, as shown in Fig.4. The pure α-FeOOH is composed of large acicular crystals a few hundreds of nm long, as can be seen in Fig.4a. However, the appearance of the α-ferric-oxyhydroxide precipitated with the addition of Cr ions indicates that the presence of Cr yields rather small crystals. The crystal size of the α-ferric-oxyhydroxide tends to be reduced with increasing amounts of Cr.

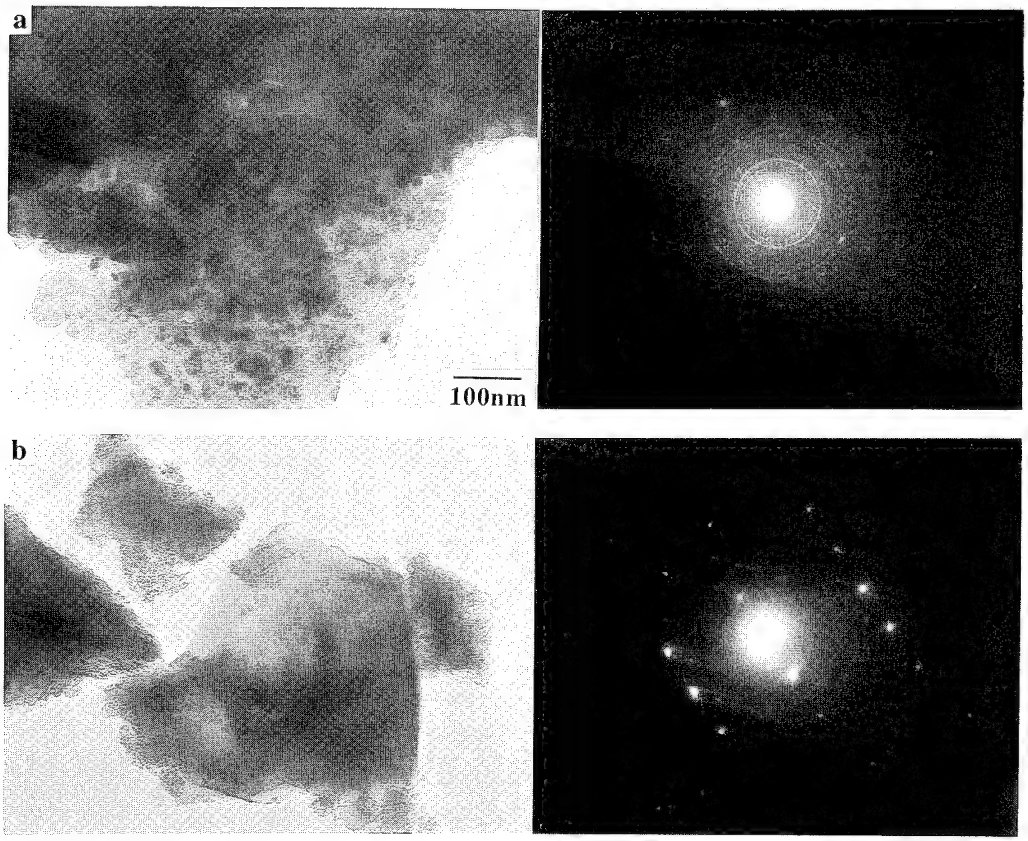

Fig.3 Transmission electron micrographs of the inner passive (a) and the outer (b) rust layers formed on the low-alloy steel by exposure to environmental atmosphere for 26 years.

The Cr content in the α-ferric-oxyhydroxides evaluated by chemical analysis is shown against the mole ratio of Cr^{3+}/Fe^{2+} in Fig.5. It is said that the Cr content is directly proportional to the mole ratio added. Therefore, the decrease in crystal size of the α-ferric-oxyhydroxide is obviously due to the coexistence of Cr.

It is also pointed out that α-FeOOH is the only crystal constituent identified by the electron diffraction pattern of the Cr-containing α-ferric-oxyhydroxide. This suggests that Cr substitutes the lattice point of α-FeOOH, as was also pointed out in the spontaneous passive rust layer. Another striking feature in the morphology change with Cr content in the α-ferric-oxyhydroxide is that the crystals tended to agglomerate with increasing Cr content.

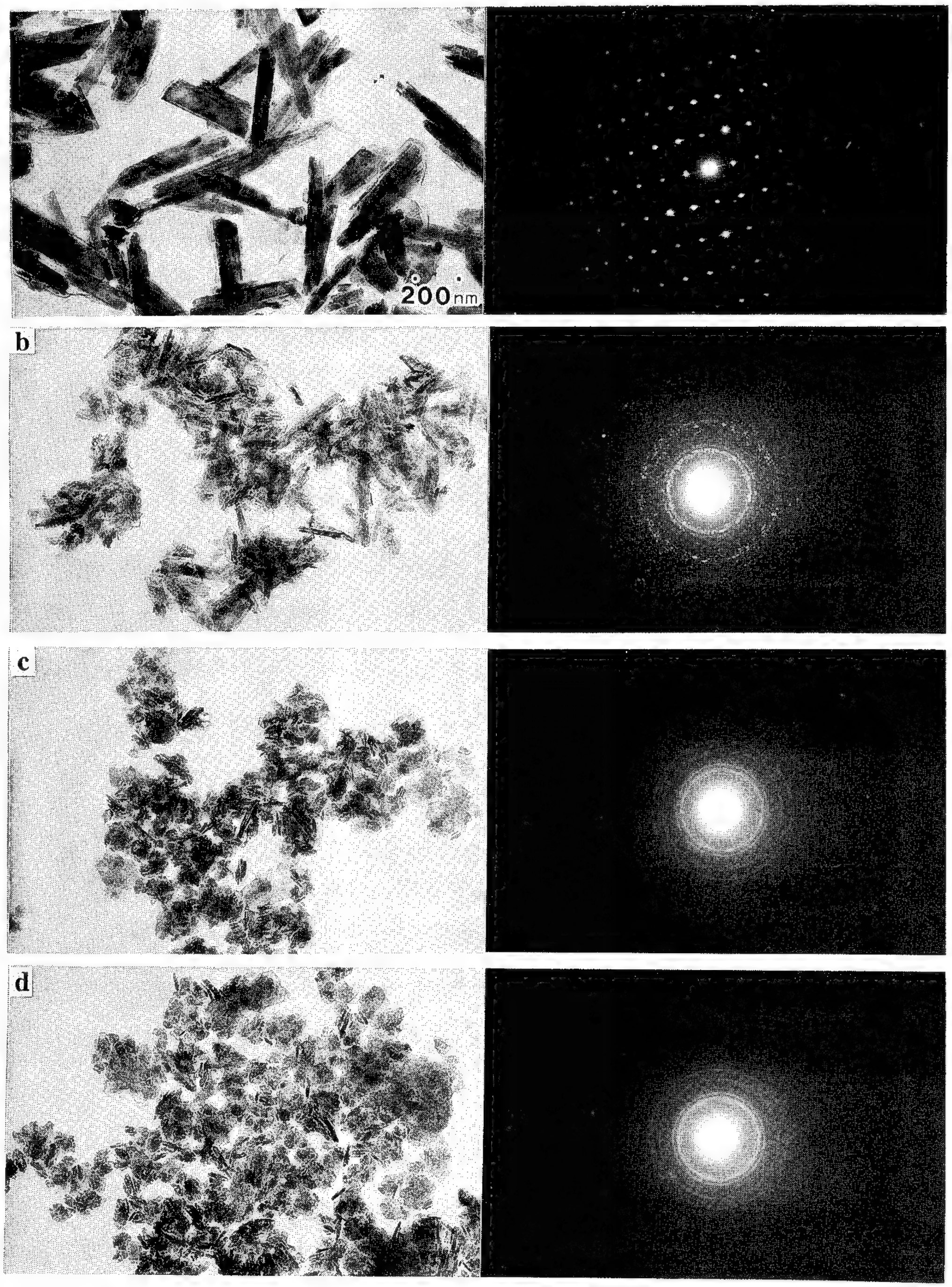

Fig.4 Transmission electron micrographs of the synthetic α-ferric-oxyhydroxides. The mole ratio of Cr^{3+}/Fe^{2+} added is 0 (a), 0.1 (b), 0.5 (c) and 1.0 (d), respectively.

Figure 6 shows the X-ray diffraction patterns of the α-ferric-oxyhydroxides containing various amounts of Cr. It is confirmed that the diffraction peaks are identified as those of α-FeOOH. While the peak widths are almost the same in the α-ferric-oxyhydroxides for Cr addition in the range of 0 to 0.1, the patterns become broader for Cr addition of 0.5 and 1.0. These results support that the crystal size of the α-ferric-oxyhydroxide becomes extremely small with increasing the Cr content and that the crystal probably contains lattice defects such as substitutional Cr ions.

The characteristic feature of the synthetic α-ferric-oxyhydroxides, showing a decrease in crystal size and crystal agglomeration with increasing Cr content, is consistent with the observed fact that the passive rust layer found after long-term exposure outdoors is comprised of densely aggregated fine-particles of α-ferric-oxyhydroxide containing a considerable amount of Cr. The morphology change (Fig.4) of the synthetic α-ferric-oxyhydroxide with Cr content implies that the characteristics, therefore the protective ability, of the passive rust layer on a weathering steel is to be associated with the amount of Cr itself.

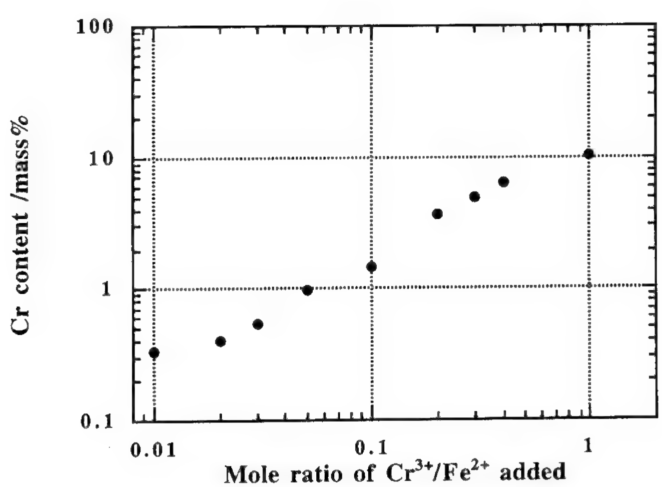

Fig.5 The Cr content in the α-ferric-oxyhydroxides against the mole ratio of Cr^{3+}/Fe^{2+} added.

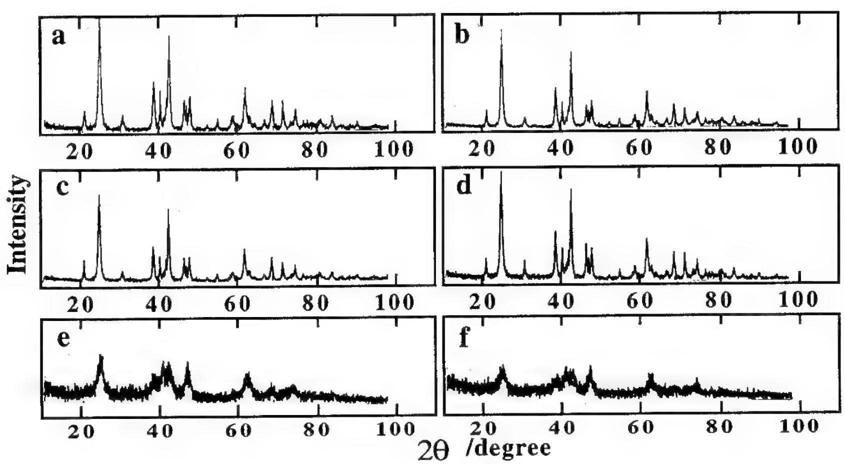

Fig.6 X-ray diffraction patterns of the α-ferric-oxyhydroxides containing various amounts of Cr. The mole ratio of Cr^{3+}/Fe^{2+} added is 0 (a), 0.02 (b), 0.05 (c), 0.1 (d), 0.5 (e) and 1.0 (f), respectively.

It can be concluded that the passive rust layer of a low-alloy steel is the dense rust layer containing Cr, probably substituting a lattice point, producing very fine α-ferric-oxyhydroxide crystals of α-$(Fe_{1-x}, Cr_x)OOH$. We infer that the coexistence of Cr in the passive rust provides the fine particles of the α-ferric-oxyhydroxide of α-$(Fe_{1-x}, Cr_x)OOH$ which yield the retardation effect for both metal dissolution and oxygen reduction due to the strongly aggregated rust particles.

5. Conclusion

The characteristic nature of the passive rust layer formed on low-alloy steel after long-term exposure to environmental atmosphere and that of the synthetic α-ferric-oxyhydroxides containing various amounts of Cr has been examined. It is found that the passive rust layer responsible for protection from atmospheric corrosives is an aggregation of α-ferric-oxyhydroxide fine-particles containing a considerable amount of Cr. By examining the synthetic α-ferric-oxyhydroxides, it is shown that the α-ferric-oxyhydroxide becomes agglomerated and smaller in size with increasing Cr content. The amount of Cr in the passive

rust layer is considered to be one of the key factors controlling the property of the passive rust layer.

References

[1] M.Yamashita, H.Miyuki, H.Nagano and T.Misawa, Corrosion Engineering, **43**, 43(1994).

[2] T.Misawa, M.Yamashita, Y.Matsuda, H.Miyuki and H.Nagano, J. Iron Steel Inst. Japan, **79**, 69(1993).

[3] M.Yamashita, H.Miyuki, Y.Matsuda, H.Nagano and T.Misawa, Corros. Sci., **36**, 283(1994).

[4] H.Okada, Y.Hosoi, K.Yukawa and H.Naito, J. Iron Steel Inst. Japan, **55**, 355(1969).

[5] H.Kihira, S.Ito and T.Murata, Corros. Sci., **31**, 383(1990).

[6] T.Misawa, K.Hashimoto and S.Shimodaira, Corros. Engng Japan, **23**, 17(1974).

[7] T.Misawa, K.Asami, K.Hashimoto and S.Shimodaira, Corros. Sci., **14**, 279(1974).

[8] T.Misawa, Corros. Engng Japan, **32**, 657(1983).

[9] J.T.Keiser and C.W.Brown, Corros. Sci., **23**, 251(1983).

[10] H.E.Townsend, T.C.Simpson and G.L.Johnson, *Proc. 12th Int Corrosion Cong.* NACE, Houston, **2**, 624(1993).

[11] K.Inoue, Y.Taki and K.Kaneko, Corros. Engng Japan, **33**, 446(1984).

[12] U.Schwertmann and R.M.Cornell, *Iron Oxides in the Laboratory,* VCH, Weinheim, (1991).

Materials Science Forum Vols. 185-188 (1995) pp. 515-524

Kelvin probe measurements of the corrosion potential of low-alloy steels in dry-wet cycles

M. Yamashita[1,3], H. Nagano[2], F. Guillaume[1] and R.A. Oriani[1]

[1] Corrosion Research Center, Department of Chemical Engineering and Materials Science, University of Minnesota, 221 Church Street, 112 Amundson Hall, Minneapolis, MN 55455, USA

[2] Research and Development Center, Sumitomo Metal Industries, Ltd., 1-8 Fusohcho, Anagasaki-660, Japan

[3] on leave from Iron and Steel Research Laboratories, Sumitomo Metal Industries, Ltd., 1-8 Fusohcho, Amagasaki-660, Japan

Keywords: Atmospheric corrosion, corrosion potential, thin electrolyte layer, low-alloy steel, rust layer, Kelvin probe

Abstract

Corrosion potentials of a mild steel and low-alloy steels containing Cr have been examined under humidity films and under very thin electrolyte layers using the Kelvin probe technique. It was found that the corrosion potential was strongly affected by the thickness of the electrolyte layer due to the very large effect of the transport kinetics of the oxygen reduction reaction. Addition of Cr to the mild steel influenced the corrosion potential probably due to the change in the quality of a corrosion product which affects both the anodic and the cathodic reactions.

1. Introduction

It is well recognized that the corrosion rate of a low-alloy steel decreases with dry/wet cycling during exposure to an outdoor atmosphere. This decrease in the dissolution rate of the steel is caused by the formation of a protective rust layer on the surface of the steel [1]. The formation process and the quality of this corrosion product are affected strongly by the characteristics of the thin electrolyte layer covering the steel surface from rain fall and dewing and the subsequent dry/wet cycles.

Although the importance of the process of wetting by a thin electrolyte layer and its drying out has been frequently pointed out in the field of atmospheric corrosion, it is so difficult to apply the conventional electrochemical techniques for examining the corrosion behavior under the electrolyte

film that little information is available to discuss the corrosion process during the dry/wet transitions. Experimental work using the Kelvin probe technique [2], usually used for measuring the work function has recently been directed towards the understanding of corrosion behavior of metals covered by thin electrolyte films [3-6]. However, only a relatively small number of experiments for the study of the corrosion of metals in corrosive atmospheres have been carried out.

The objective of the present study is to examine the corrosion potential of low-alloy steels under thin electrolyte films and after subsequent dry to wet transitions, using the Kelvin probe technique. In this paper, preliminary results of the effect of Cr addition to a mild steel on the corrosion potential variation during the dry/wet cycles are reported.

2. Experimental

2.1. Kelvin probe apparatus

The principle of the Kelvin method and the details of our experimental setup have been presented elsewhere [4]. The Kelvin probe reference material used in this experiment was a 2mm diameter silver wire (AESAR 99.999% purity) coated with a film of AgCl deposited according to a technique described in a previous publication [7]. The Kelvin probe signal was demodulated by a Stanford Research SR850 digital lock-in amplifier and read by a Keithley 2001 digital multimeter. Both instruments were connected to an AT 486-DX PC computer via an I.E.E.E. 488 bus. Temperature and relative humidity inside the Kelvin probe chamber can be monitored by a 12 bit data acquisition system. The noise level on the Kelvin probe reading was typically $1mV_{RMS}$. All electrical connections between instruments and the Kelvin probe chamber were twisted pairs. A combination of inductive, capacitive shielding and active guarding kept the magnitude of pick-up and secondary Kelvin effect down to 85 dB of the Kelvin signal for a 2 V sample to probe polarization.

It has been established [4] that the null-current reading of the Kelvin apparatus in mV, Vkp, can be converted to the corrosion potential, Ecorr, through the linear relation,

$$\text{Ecorr} = \text{Vkp} + \text{const.} \quad (1),$$

when the specimen is under an electrolyte film. In the present investigation, the Ag/AgCl reference probe used has been calibrated against the redox system of a Ag/AgCl, saturated KCl solution. The Vkp can be converted to the corrosion potential by

$$\text{Ecorr} = \text{Vkp} + 5 \quad \text{mV vs SCE} \quad (2).$$

The advantage of using the Ag/AgCl reference probe is that the Vkp is insensitive to the relative humidity of the atmosphere. The stability of the probe against a change in the relative humidity has been confirmed [7]. It was found by measuring the Vkp with respect to the redox systems of different humidities that the variation in the constant of Eq.2 with a change of the relative humidity between 40 and 96% was within 3mV.

2.2. Preparation of the specimen

Table 1 summarizes chemical compositions (in mass%) of the steels tested. A mild steel and two low-alloy steels containing 2% and 5% Cr respectively were employed. Two types of specimens were prepared from each steel. One with the dimensions of 10 x 10 x 3mm^3 was employed for measurement under the extremely thin electrolyte film established in a humid air with 95.5±0.5% relative humidity. The other was for the test using a thin electrolyte with the thickness of hundreds of μm; this specimen was machined as a dish 45mm in inner diameter and 2mm wall thickness.

The specimens were mechanically polished with emery papers and alumina paste and then rinsed with distilled water.

Table 1 Chemical compositions of the steels tested in mass%.

C	Si	Mn	P	S	Cu	Ni	Cr	sol.Al
0.054	<0.01	0.003	<0.001	0.0001	0.001	<0.01	0.002	0.001
0.054	0.01	0.001	<0.001	0.0001	0.001	<0.01	1.98	0.001
0.053	0.01	0.002	<0.001	0.0003	0.001	<0.01	4.64	0.001

2.3. Humidity test

Sodium sulfate crystals were uniformly deposited on the specimen surface at 1×10^{-4} mole/m^2 by pouring upon it and quickly drying a measured volume of 1×10^{-3} molar solution before the experiment. The temperature inside the Kelvin probe chamber was controlled to be 25±0.5°C. In the beginning of each experiment, air of 0% humidity was flowed through the specimen chamber. Then, the humidity inside the chamber was increased by flowing humidified air, so that the final stable relative humidity was controlled to be 95.5±0.5%. In this humidity, the specimen became covered with an extremely thin sodium sulfate solution (humidity film) after which the corrosion potential can be measured. From the measured relationship between the vapor pressure of water over an aqueous solution of sodium sulfate and the concentration of the salt, the concentration of sodium sulfate in the humidity film can be calculated to be 1 molar. From the known area of the specimen surface and the concentration, the mean thickness of the humidity film is calculated as about 0.1μm. After measuring the corrosion potential, the air inside the chamber was dried out by simply flowing dry air. This dry/wet cycle was subsequently repeated. The air used in this study is an artificial mixture of 20.7% oxygen and 79.3% nitrogen from commercial gas tanks.

2.4. Thin electrolyte test

This experiment was performed by pouring 1×10^{-3} molar sodium sulfate solution into the dish-shaped specimen, so that a solution layer of approximately 250 μm average thickness was formed on

the specimen. Therefore, the corrosion potential can be measured from the beginning of this experiment. The temperature inside the Kelvin probe chamber was controlled to be 25±0.5°C. The solution layer was then thinned by the evaporation of water caused by dry air flowing through the chamber. After the specimen surface was completely dried, the specimen was removed from the chamber, rinsed with distilled water and another layer of $1x10^{-3}$ molar solution was deposited on the specimen. The rinsing was done to avoid the accumulation of sodium sulfate at the specimen surface during the subsequent wet/dry cycles. This procedure was repeated in order to examine the effect of the wet/dry cycling.

3. Results and discussion

3.1. Corrosion under humidity film

Figure 1 shows typical examples of the variation in the Vkp for several dry to humid cycles. Before the first humidification, the surfaces of the specimens were covered with both dry sodium sulfate and pre-formed oxides. It should be noted that the Vkp measured for the dry specimen is merely the work function of the dry surface and should not be converted to a corrosion potential since such a conversion has no physical basis. The magnitude of the Vkp for the dry state depends on the characteristics of the oxides which cover the specimen surface, the distribution of sodium sulfate crystals upon the oxides and so on. The drop in the Vkp immediately after introducing the humid air is due to the adsorption of water molecules on the sodium sulfate and the oxides. At some time the humidity over the specimen surface reached the deliquescent point of the sodium sulfate, and therefore it dissolved to produce an almost saturated extremely thin solution layer which thickened and became less concentrated as the relative humidity increased. At the end of the humid stage, the relative humidity reached 95.5±0.5% and the Vkp reached a steady state, at which the concentration of the sodium sulfate solution film can approximately be estimated at 1 molar. Then, the Vkp can be converted to a corrosion potential.

3.1.1. Mild steel

As shown in Fig.1, the corrosion potential at the first humidification was +130mV(SCE). This value is much higher than approximately -600mV(SCE) [8] measured by a conventional electrochemical technique in a large amount of solution of sodium sulfate. This difference can be understood as showing that the oxygen reduction rate is not transport controlled in the extremely thin electrolyte, whereas it is in the bulk electrolyte. The higher corrosion potential prevents any reduction of ferric to ferrous ions that was shown by Stratmann et al. [9] to occur under relatively thick electrolyte layers (see subsequent section). The drying period produces a Vkp representing the work function of the sodium sulfate covered surface. Subsequent humidification causes a slight anodic

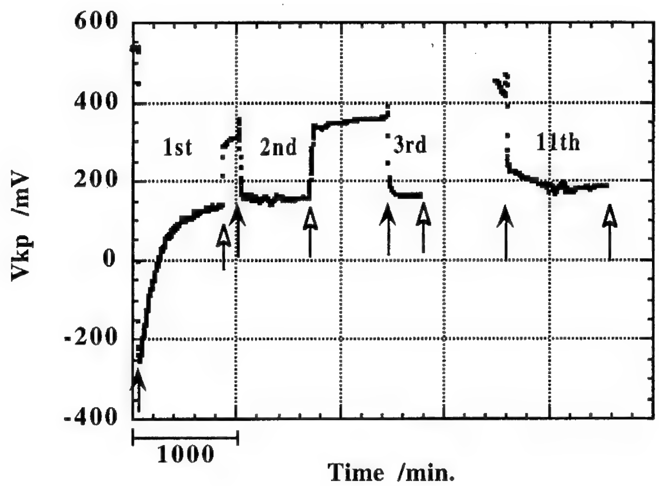

Fig.1 Variation in the Vkp value with time in the 1st, 2nd, 3rd and 11th humid/dry cycles of the mild steel. The open and solid arrowheads indicate the introducing of the dry and humid air respectively. It should be noted that the Vkp can be converted to the corrosion potential (SCE) only when the specimen is under an electrolyte film.

shift from cycle to cycle. This is probably due to a retarding effect of the corrosion product on the metal dissolution.

3.1.2. Low-alloy steels

The corrosion potential variations of the Cr-containing steels with the number of dry to humid cycles were similar to those of the mild steel in that the corrosion potential increased somewhat with increasing number of cycles in the early stage of the experiment. Figure 2 shows the corrosion potentials against the Cr content under various dry to humid cycles.

It can be pointed out that the corrosion potential of the 2%Cr steel is much lower than that of the mild steel whereas that of the 5%Cr steel is mostly higher. This result may possibly be interpreted by a competitive relation between the oxygen reduction rate and the metal dissolution rate in each alloy.

It is difficult to consider that the corrosion rate of the 2%Cr steel is higher than that of the mild steel since an addition of Cr to steels reduces the corrosion rate [1] as a consequence of the formation of densely packed corrosion product adhering to the steel surface. Therefore we infer that the low

corrosion potential of the 2%Cr steel is mainly due to the retardation of the oxygen reduction rate because the oxygen reduction rate is controlled by the corrosion product and is kinetically slow. Furthermore, the decrease in the real surface area of the corrosion product due to the more dense packing of the oxide results in a decrease of the oxygen reduction rate.

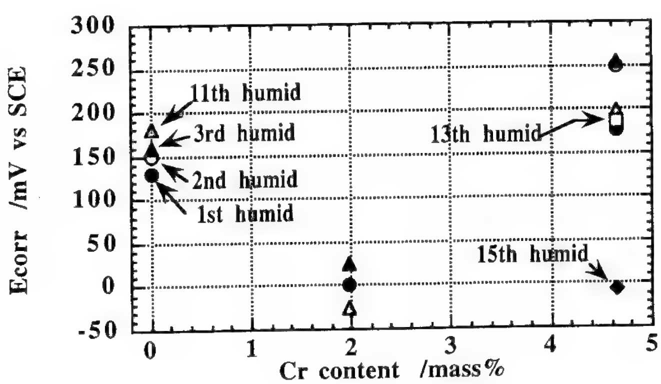

Fig.2 Corrosion potential, Ecorr, against the Cr content under 1st , 2nd 3rd and 11th humidity films.

Although the retardation of the oxygen reduction is also likely to occur at the surface of the 5%Cr steel, the corrosion potential in the first, second and third humidifications of this steel was higher than that of both the mild and 2%Cr steels. We can only infer that the metal dissolution rate is much more suppressed than is the oxygen reduction rate, probably due to the higher protecting ability of the oxide layer formed on the 5%Cr steel surface. It has been pointed out [10] that the densely aggregated oxide layer which contains a considerable amount of Cr possesses a superior ability for the protection of steel against atmospheric corrosion. The corrosion potential of the Cr steels decreased reversely in the subsequent humidification. This fact suggests that the further retardation of the oxygen reduction occurred at the corrosion product on the Cr steels.

3.2. Corrosion under thin electrolyte layers

3.2.1. Mild steel

Figure 3a shows the progress of the Vkp during the first drying of the sodium sulfate solution which was initially 1×10^{-3} molar and about 250 μm in depth. Underlying the solution is the air-

formed oxide film on the steel, presumably composed of tri-valent iron oxide and hydrous oxide. During the drying, caused by the flow through the Kelvin chamber of dry air, water evaporates causing the salt concentration to increase and the solution depth to decrease. The initial Vkp stayed at a fairly constant -200mV, representing a corrosion potential of about -200mV(SCE). This value is lower than that obtained under the humidity film, discussed above. Since the electrolyte layer is some 2500 times thicker than the humidity film, partial transport control of the oxygen reduction can be expected for the layer but not for the humidity film. This is consistent with the observed difference between the corrosion potentials in the two cases.

Because the initial corrosion potential is comparable to the potential for equilibrium between magnetite and ferric-oxyhydroxide [11] at a neutral or slightly alkaline environment in the thin sodium sulfate solution, there is a driving force for the generation of ferrous ions on the surface of the steel, which increase the rate of oxygen reduction on the oxide [9]. This, plus the decreasing impediment to oxygen transport due to the evaporative thinning of the electrolyte layer, causes the sharp rise of the corrosion potential at about 250minutes seen in Fig.3a. Then, the corrosion potential stayed at approximately 0mV for a while, corresponding to the corrosion potential of the steel covered only with the wet corrosion product without the solution layer. At this secondary plateau, the corrosion product may partly convert to α-ferric-oxyhydroxide [11]. With increasing time of drying, The Vkp becomes the work function of the metal covered by the completely dry corrosion product containing salt crystals.

Figure 3b shows the Vkp-time behavior of the same specimen during drying of the second electrolyte layer that was deposited on the specimen after rinsing off the salt remaining after the experiment of Fig.3a. Again the initial corrosion potential is about -200mV(SCE), showing that the quality of the corrosion product under this second electrolyte layer was almost the same as that formed under the first electrolyte layer. Further drying produces nearly the same Vkp history as that shown in Fig.3a.

Subsequent wettings (Fig.3c,d) produce initial higher or lower corrosion potential values that probably depend on the change in the characteristics of the corrosion product, which suppresses both the oxygen reduction and the metal dissolution. The suppression of metal dissolution by the increasing thickness of oxide is probable. The only reason that we can infer to interpret the decrease in the initial corrosion potential between the second and third wettings of about 150mV is based on the degree of conversion of ferrous to ferric ion that occurs during the secondary plateau observed in the first and second wettings. As was pointed out above, ferrous ion can be converted to α-ferric-oxyhydroxide at the corrosion potential of the secondary plateau and α-ferric-oxyhydroxide is the final stable product in an usual atmospheric environment [1]. Therefore, once ferrous ion is converted to ferric ion as the α-ferric-oxyhydroxide, the absence of ferrous ion in the corrosion product causes the retardation of the oxygen reduction [9]. It is supposed that this retardation was

greater than the suppression of metal dissolution in the third wetting, so that the initial corrosion potential was lowered to approximately -350mV(SCE) in the third wetting. This is also suggested by

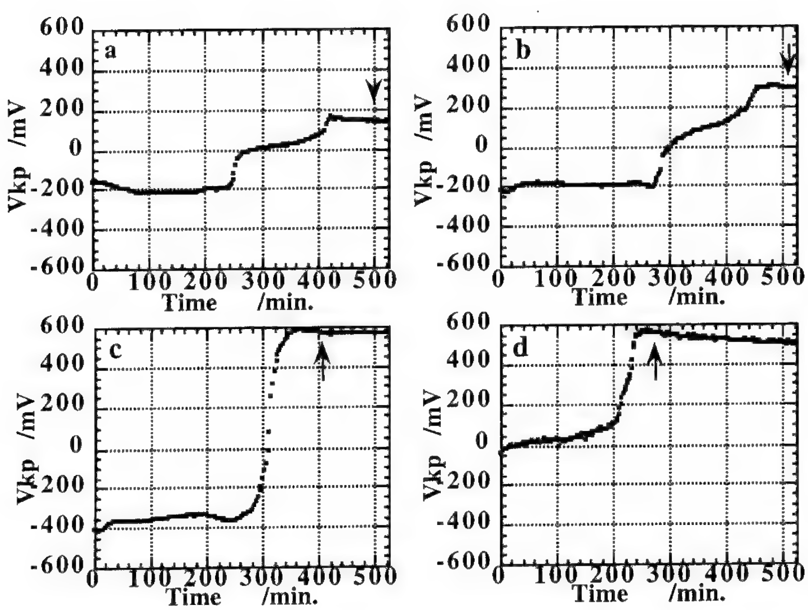

Fig.3 Progress of the Vkp during the 1st(a), 2nd(b), 3rd(c) and 10th(d) drying of the sodium sulfate solution in the mild steel. The specimen was completely dried up at the points indicated by arrows.

the rise of the corrosion potential following the evaporative thinning of the electrolyte layer at about 250minutes in the third wetting being much smaller than those observed in the first and second wettings.

The increase in the corrosion potential in the subsequent wettings (Fig.3d) may be due to the combination of the larger suppression of the metal dissolution by the increasing thickness and denser packing of the corrosion product and the acceleration of the oxygen reduction at the surface of the corrosion product. The latter was caused by the thinness of the solution layer above the thicker oxide into which most of the deposited solution penetrates.

3.2.2. Low-alloy steels

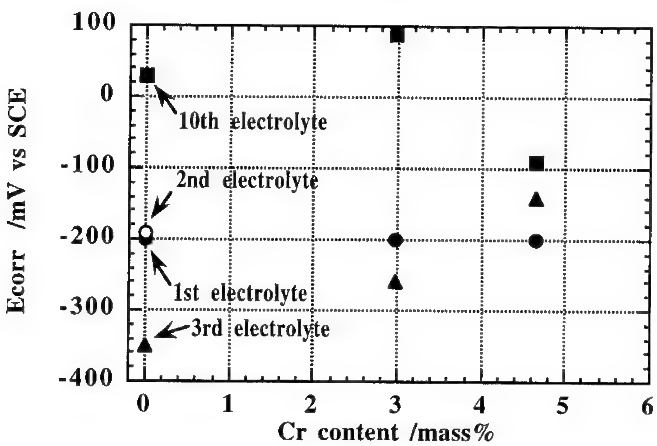

Fig.4 Corrosion potential, Ecorr, against the Cr content under 1st, 2nd 3rd and 10th thin electrolyte layers.

The behavior of the initial corrosion potential of these alloys in each drying of the electrolyte was similar to that of the mild steel mentioned above. The change in the corrosion potential of each alloy as a function of the number of wet to dry cycles is shown in Fig.4. The variation in the initial corrosion potential of the 2%Cr steel can also be interpreted in terms of the quality and thickness of the corrosion product formed, as was discussed above for the mild steel. However, the corrosion potential drop between first and third cycles of the 2%Cr steel was approximately 60mV, which is smaller than that of the mild steel. This smaller drop suggests that the corrosion product formed on the 2%Cr steel suppresses the metal dissolution more than on the mild steel.

In contrast with the result obtained in the mild and 2%Cr steels during first, second and third drying of the electrolyte, the decrease in the corrosion potential with increasing number of wet to dry cycles was not observed in the 5%Cr steel. The retardation of the oxygen reduction is also probable in the 5%Cr steel in the wet to dry transitions. However, it is supposed that the metal dissolution rate in the Cr steels was much more suppressed even in the early stage of corrosion by the formation of densely aggregated rust layer. As has been pointed out previously [9], the Cr ions formed by dissolution of a Cr steel can become a constituent of a rust layer and make the rust layer more dense so that the protective ability of the rust layer is increased. If it is assumed that the corrosion products

formed on the 2% and 5%Cr steels during wet to dry transitions contain a certain amount of Cr, it is probable that the corrosion products are more protective than those formed on the mild steel. It is possible to interpret the increase in the corrosion potential of the 5%Cr steel with the number of wet to dry transitions in terms of the larger suppression of the metal dissolution. In addition, the corrosion potential, approximately -90mV(SCE), of the 5%Cr steel under the 10th thin electrolyte layer, which is lower than those of the mild and 2%Cr steels, suggests the further retardation at the corrosion product on the 5%Cr steel.

4. Conclusion

Kelvin probe investigation of the corrosion of mild steel and of low-alloy steels under humidity films and under very thin electrolyte layers has demonstrated the very large effect of the variation of the transport kinetics of the oxygen reduction reaction caused by varying electrolyte thickness. Addition of Cr to an iron-carbon alloy produces an oxide that affects both the anodic and the cathodic reactions with the balance between the two depending on composition. Although the results of this preliminary study using sodium sulfate electrolytes to simulate the atmospheric corrosion of steels exposed to an industrial environment are interesting, this knowledge cannot be directly used to make inferences about corrosion in various atmospheres because atmospheric air has in it corrosive compounds absent in the present experiments. The effect of normally occurring pollutants on the corrosion potential of steels exposed to humid air is a matter for future work.

References

[1] e.g., M.Yamashita, H.Miyuki, Y.Matsuda, H.Nagano and T.Misawa, Corros. Sci., **36**, 283(1994).
[2] L.Kelvin, Phil. Mag., **46**, 82(1898).
[3] M.Stratmann and H.Streckel, Corros. Sci., **30**, 681(1990).
[4] S.Yee, R.A.Oriani and M.Stratmann, J. Electrochem. Soc., **138**, 55(1991).
[5] J.Wang and T.Tsuru, *Proc. JSCE Corrosion `93*, **A306**, 93(1993).
[6] O.Albani, S.-M.Huang and R.A.Oriani, Corrosion NACE, **50**, 331(1994).
[7] R.T.Atanasoski, S.-M.Huang, O.Albani and R.A.Oriani, Corros. Sci., In press.
[8] e.g., H.Okada, Y.Hosoi and H.Naito, J. Iron Steel Inst. Japan, **56**, 277(1970).
[9] M.Stratmann, H.Streckel, K.T.Kim and S.Crockett, Corros. Sci., **36**, 715(1990).
[10] M.Yamashita, H.Miyuki, H.Nagano and T.Misawa, Corrosion Engineering, **43**, 43(1994).
[11] T.Misawa, Corros. Sci., **13**, 659(1973).

Charge Transport in Passivating Films and Electrical Breakdown

Materials Science Forum Vols. 185-188 (1995) pp. 527-534

Dielectric breakdown processes in anodic films under high electric fields

J.M. Albella, I. Montero and J.M. Martinez-Duart

Inst. Ciencia de Materiales, CSIC, and Dept. Física Aplicada, Universidad Autónoma, C-12, Cantoblanco, E-28049 Madrid, Spain

Keywords: Valve metals, anodization, anodic oxides, avalanche, impact ionization, breakdown, electrolyte/oxide interface

ABSTRACT

The breakdown characteristics during anodization of valve metals are first analyzed. It turns out that the breakdown properties are mostly determined by both the solid state properties of the oxide and the nature of the contacting electrolyte used in the anodization process. The breakdown mechanism is examined in terms of the avalanche theories developed for a similar system, i.e. insulating films contacted with metallic electrodes. On discussing the existing avalanche models adapted for the case of electrolytic contacts, major emphasis is placed on the injection mechanism of the primary electrons through the electrolyte/oxide interface, since this is the critical step controlling the breakdown voltage. It is shown that all the models predict a similar equation for breakdown voltage although not definite answer can be given on the prevailing injection mechanism for the primary electron current.

1. INTRODUCTION

Anodic oxides films of valve metals has been traditionally the subject of intensive research due to its interesting technological applications: passive and decorative coatings [1], dielectric layers for electrolytic and thin film capacitors [2] and more recently gate oxide in thin film transistors and MOS structures [3]. It has been shown, for instance, that anodic SiO_2 layers, once they have been annealed, can withstand higher breakdown voltages than the corresponding thermal oxides [4]. Other applications as diffusion masks in semiconductors and passivation layers for III-V and II-VI compounds have been also envisaged [5]. In this regard, the possibility of low-temperature growth offered by the anodic oxides (i.e. below 90 °C) seems to be an attractive alternative with respect to thermal oxidation.

In all these cases, the anodic oxide is grown from the parent metal by the cooperative movement of oxygen (and in some cases electrolyte) anions and/or metal cations in opposite directions through the already formed oxide under the influence of the applied electric field. When the oxidation is carried out under well controlled galvanostatic conditions and no other lateral reactions occur, the oxide grows linearly with time following Faraday's laws, giving rise to a parallel increase of the applied voltage. The ionic movement is an activated process which has been well studied in the literature, being characterized by an exponential relation between the ionic current and the applied electric field [6].

One of the striking features of this process, apparently succeeding under steady-state conditions (i.e. with constant electric field and ionic current) is the sudden appearance of instabilities in the form of minute discharges when the applied voltage reaches a critical value. These discharges are evenly scattered through the oxide surface and are characterized by small voltage pulses in the voltage-time curve. Generally, they are also accompanied by copious gas evolution and additionally by the emission of visible sparks. This phenomenon, usually known as *scintillation* or *electrolytic breakdown*, gives rise to an abrupt deviation of the linear growth as well as a degradation of the oxide characteristics, with the formation of pores, cracks and microcrystalline powder. In some oxides, such as anodic zirconium oxide, mechanical failure due to internal film stresses may also appear in conjunction or even before the electrolytic breakdown [7].

Much of the research work on anodic oxides has been addressed to the understanding of this problem since it imposes a limit to the final oxide thickness. The final goal is to investigate the cause of the instabilities in order to improve the breakdown characteristics. Most of the approaches are based on the avalanche theories developed for insulator films flanked by metallic contacts, which also exhibit similar breakdown events. In this review we shall be concerned mostly with the breakdown in some anodic oxides, like Ta_2O_5, Al_2O_3, Nb_2O_5, etc., which under certain conditions may exhibit nearly ideal anodization characteristics. Among the proposed avalanche models, the major differences are found in the source of the primary electron current. In fact, the identification of the injection mechanism for the primary electron current is critical, since this step can be considered as the main cause initiating the breakdown.

2. THE BREAKDOWN CHARACTERISTICS

The breakdown is a complex phenomenon which can be characterized by a large variety of processes. Due to its complexity we shall refer here to nearly ideal systems in which the anodization takes place uniformly with almost 100 % efficiency, i.e., not showing other lateral reactions (oxide dissolution or oxygen evolution). Tantalum, niobium and aluminum oxides, anodized in certain electrolyte solutions are good

examples of this behaviour. In this context, we shall discard the mechanical breakdown offered by some metal oxides, like zirconium or tungsten oxide, which can be attributed to internal stresses generated during film growth [8].

We can summarize the main breakdown features in these 'quasi-ideal' systems as follows: i) In well characterized metal surfaces (i.e. free of impurities and defects), the breakdown voltage is mostly determined by both the nature of the metal and the composition of the contacting electrolyte. This fact implies that the breakdown voltage, instead of being only an "intrinsic" oxide property, is also controlled by the electrolyte/oxide interface. ii) Furthermore, for a given oxide/electrolyte system, the breakdown voltage, V_b, depends linearly on the logarithm of the electrolyte resistivity, ρ, according to the well known empirical law [9]:

$$V_b = A + B \cdot \log \rho \qquad (1)$$

with A and B constants, characteristic of the electrolyte and oxide. iii) Successive anodization experiments applied on the same sample changing the electrolyte resistivity (concentration) show that the final breakdown voltage is exclusively determined by the last electrolyte, regardless the previous anodization processes carried out on the sample.

Generally, it is established that the breakdown appears during the anodization in galvanostatic conditions when the growing film reaches a critical thickness, x_b, although no quantitative evaluation of x_b has been made. This fact tries to remark the electronic avalanche aspects of the breakdown process associated to a similar system: insulator films flanked by two metallic electrodes (*filamentary breakdown*). In fact, some of the breakdown models for the anodic oxidation (thermal breakdown, impact avalanche multiplication, etc.) were previously postulated for semiconductors and insulators subjected to high electric fields. However, it is very important to emphasize the differences between both systems: i) In the anodization system the contacting electrode is a liquid electrolyte with a limited capacity to supply electrons to the oxide conduction band. ii) The interfaces between the oxide and contacting electrodes are not fixed, since new oxide layers are continuously being formed at each interface. iii) During anodization, the oxide lattice is not at rest because of the positive and negative ion movement in opposite directions. iv) The anodic oxides generally present a relatively high proportion of electrolyte species (very often oxyanions) incorporated in the oxide lattice, which may act as impurity centers in the oxide band gap. v) We should also consider that under galvanostatic conditions the average electric field across the oxide, F, is constant and determined by the current imposed during the anodization. Typical values of F are in the range of 10^6 to 10^7 Vcm^{-1}. Similar electric fields are found in the case of filamentary breakdown, although in this case the breakdown tests are performed at increasing electric fields.

3. BREAKDOWN MODELS.

Any theory of the breakdown processes during anodic oxidation must account for the above mentioned experimental facts. Earlier works on breakdown emphasized the role of the electrolyte as well as the solid state properties of the oxide [10,11]. The above-said idea of a 'critical thickness' for breakdown led to different authors to postulate the avalanche process as the basic mechanism of breakdown [12]. In these models, the breakdown is produced by the electrons injected by the electrolyte into the oxide conduction band, where they are accelerated and multiplied in avalanche by the high anodization field. If the oxide thickness is large enough, the avalanche current may reach a critical value to produce a local heating and finally the breakdown.

The first attempt to give a quantitative model for the breakdown during anodization was put forward by Ikonopisov [13], on the basis of the theory developed by Forlani and Minnaja for filamentary breakdown in insulating films [14]. The model assumes that the primary electron current, j_o, is injected either from the electrolyte by a Fowler-Nordheim (tunnel) or a Schottky (activated) mechanism. The electrons are then accelerated until they reach enough energy, E_i, to produce an avalanche current by impact ionization of the lattice atoms. The avalanche multiplication produces an exponential growth of the electronic current along the oxide thickness, i.e.: $j_e(x) = j_o \cdot \exp(reFx/E_i)$, giving rise to breakdown when the avalanche current (and therefore the thickness) reaches a critical size, j_b. In Ikonopisov's model the breakdown voltage is given by the equation:

$$V_b = (E_i/re)\,[\ln (j_b/j_o)] \qquad (2)$$

(where e is the electron charge and r a recombination factor). In this result, the breakdown voltage directly depends on the solid state properties of the oxide (through the constants E_i, r and j_b) and also on the injecting properties of the electrolyte (through the constant j_o). The model further assumes for the primary electron current, j_o, a dependence on the electrolyte resistivity according to an inverse power law, i.e.:

$$j_o = a_e\,\rho^{-n} \qquad (3)$$

(with a_e and n constants, determined by the electrolyte composition). Curiously, this hypothesis is based on experimental results obtained for the electrical conductivity of some anodic oxide films contacted by electrolytes with different resistivities [15]. When the value of j_o is substituted in eq. 2, a logarithmic dependence of V_b on the electrolyte resistivity is obtained, in agreement with eq. 1.

The conductivity results used in Ikonopisov's model were questioned by Lalèko *et al.* [16] and lately by Albella *et al.* [17]. In addition, the hypothesis about the origin

of the primary electron current was also revised by Odynets *et al.* [18] who assumed that the electronic charge comes from chemisorbed -OH radicals on the surface of the anodic oxide. These radicals give rise to surface electronic levels from where the electrons may tunnel to deep trap levels into the oxide. Although the origin of these trap levels in the oxide is not certain, they have been detected by conductivity measurements in the electrolyte/Ta_2O_5/Ta system which shows a Poole-Frenkel mechanism of conduction.

Kadary and Klein [19] also accepted the avalanche model as the main cause of the breakdown and they took into account the effect of the positive charge left behind by the electrons after the ionizing collisions as well as the localized nature of the avalanches, which occur in a stochastic process. By measuring the rate of breakdown events in the form of light sparks and current pulses they were able to calculate the ionization coefficient, α, the mean free path of the electrons, λ, and the avalanche size, showing a reasonable fit with the experimental results.

In the above models (Ikonopisov and Kadary *et al.*) the role played by the electrolyte anions remains uncertain, and no definitive account is given about their influence on the anodization and breakdown processes. This problem was explicitly considered by Albella *et al.* [20,21], by assuming that the primary electrons are originated at the electrolyte/oxide interface from the electrons released from the electrolyte species once they get incorporated into the oxide. As stated above, the electrolyte species may act as impurity centers in the oxide forbidden band, being able to release electrons by a Poole-Frenkel mechanism as a consequence of the high electric field. In this model, the primary electron current j_o is considered to be only a fraction η of the current consumed in the incorporation of the oxyanions, j_2. This current, j_2, is also assumed to be a certain proportion, γ, of the anodization current, j_1, so that: $j_o = \eta j_2 = \gamma\eta j_1$. Under these hypothesis, the breakdown voltage results:

$$V_B = (F/\alpha) \ln (z/\gamma\eta) \tag{4}$$

(with z = constant). When appropriate values of the parameters are substituted in eq. 4, the resulting breakdown voltage is $V_b \approx 370$ V for anodic T_2O_5 grown in phosphoric acid electrolyte, which is in agreement with the experimental results reported in the literature [21]. Moreover, it has been found for Ta_2O_5 anodized in phosphoric or oxalic electrolytes a correlation between the coeffient γ and the electrolyte concentration according to a power law:

$$\gamma \approx aC^b \tag{5}$$

Using this correlation, eq. 4 predicts a logarithmic dependence of the breakdown voltage on the electrolyte anion concentration, similar to eq. 1.

One important aspect of this model is its ability to give an easy explanation to the successive anodization experiments mentioned above [22]. In effect, from the above equation for γ we can obtain for j_o:

$$j_o = a\eta j_1 C^b \tag{6}$$

Thus, when an oxide is first grown until breakdown in a concentrated electrolyte, the primary electron current, j_o, is that corresponding to this concentrated electrolyte. If the sample is then reanodized in a dilute electrolyte, j_o is reduced to a new value and hence the avalanche current is also reduced, thus allowing for the oxide to grow further until a new critical breakdown voltage is reached, i.e. the one corresponding to the last electrolyte.

Recently, DiQuarto *et al.* [23], on the basis of Odynets *et al.* model [18], have assumed that the injection of the primary electrons at the electrolyte/oxide interface arises from the oxidation reaction of the -OH radicals chemisorbed on the surface, according to the scheme:

$$\text{M-OH} = \text{M-O} + H^+ + e^- \tag{7}$$

These authors further assumed that the primary electron current j_o is influenced by the double layer potential at the interface, which is in turn determined by the electrolyte concentration, C, through an equation of the type:

$$j_o = K j_{O_2} C^{(\alpha'/z)} \tag{8}$$

where K, z and α' are parameters dependent on the electrolyte characteristics and j_{O_2} is the current consumed in the oxygen evolution under galvanostatic conditions in absence of the double layer effect. Using eq. 2, they obtained the following expression for the breakdown voltage:

$$V_b = (E_i/re)[\text{constant} - \ln j_{O_2} - (\alpha'/z)\ln C] \tag{9}$$

which reflects the well-known logarithmic dependence of V_b on the electrolyte concentration, (or equivalently the resistivity). The model is also able to explain some other experimental findings such as the practical independence of the breakdown voltage on the electrolyte pH.

5. COMPARISON BETWEEN THE EXISTING MODELS

The essential aspects of Ikonopisov's model about the avalanche formation during anodization and breakdown have been generally accepted among the researchers.

Within this general approach, it follows from the above discussion that the main differences between this and later models refer to the origin of the primary electron current. The direct injection of electrons from the electrolyte postulated by Ikonopisov has been questioned but, at present, there is no quantitative assessment on the validity of the hypothesis put forward by Odynets *et al.* [18] and DiQuarto *et al.* [23] on one side (injection from the $-OH$ radicals chemisorbed on the surface) and Albella *et al.* [20] on the other (electron emission at the surface from the incorporated electrolyte species). Although both models are established on different theoretical basis, they predict for the primary electron current a similar dependence on the electrolyte concentration (compare eqs. 6 and 8). This variation of the primary electron current also coincides with that of eq. 3, established by Ikonopisov on empirical basis. This fact implies that j_o is determined ultimately by the nature and concentration of the electrolyte. Interestingly, all these authors also give an equation for the breakdown voltage which can be considered similar since the first coefficient in eqs. 2 and 9 is practically the same as in eq. 4), and in all cases the equation shows a logarithmic dependence of V_b on C, in agreement with abundant results in the literature. Unfortunately, the final expression of V_b contains adjustable parameters, so it is very difficult to ascertain in a definite way the validity of one or another model.

One of the main conclusions derived from Albella *et al.* model is that electrolytes having lower incorporation rates into the oxide should be the best candidates for obtaining higher breakdown voltages. Although we need experimental evidence to support this assertion, this has proved to be true in some cases, such as citric and oxalic acid electrolytes in tantalum anodization [21]. Furthermore, it is a current practice in the capacitor industry to use high anodization temperatures which lead to a decrease of the anodization field for a given current and hence to a reduction of the incorporation of electrolyte anions. Recently, it has been found that basic electrolytes (such as sodium and potassium hydroxides), which result in very pure oxide films, yield high breakdown voltages during aluminium anodization [24]. Similar results for the filamentary breakdown in SiO_2 has been obtained using pure water and very low current densities during anodization [25]. In any case, more experiments are needed to elucidate this question.

REFERENCES

[1] C.G.GRANQVIST, *J. Appl. Phys.*, **51**, 3359 (1980).

[2] F.MECA and K.JONSCHER, *Thin Solid Films*, **59**, 201 (1979).

[3] J.A.BARDWELL, K.B.CLARK, D.F.MITCHELL, D.A.BISAILLION, G.I.SPROULE, B.MACDOUGALL and J.GRAHAM, *J. Electrochem. Soc.*, **140**, 2135 (1993).

[4] G.MENDE, E.HENSEL, F.FENSKE and H.FLIETNER, *Thin Solid Films*, **168**, 51 (1989).

[5] R.R.CHANG, T.HWANG, K.M.GEIB and W.WILSEN, *J. Electrochem. Soc.*, **134**, 1243 (1987).

[6] C.J.DELL'OCA, D.L.PULFREY and L.YOUNG, in *"Physics of Thin Films"*, vol. 6, Academic Press, N.Y. (1971).

[7] F.DiQUARTO, S.PIAZZA AND C.SUNSERI, *J. Electrochem. Soc.*, **131**, 2901 (1984).

[8] L.C.ARCHIBALD and J.S.L.LEACH, *Electrochim. Acta*, **22**, 15 (1977).

[9] D.A.VERMILYEA, in *"Advances in Electrochemistry and Electrochemical Engineering"*, vol. 3, Interscience, N.Y. (1963).

[10] G.C.WOOD and C.PEARSON, *Corrosion Sci.*, **7**, 119 (1967).

[11] R.S.ALWITT and A.K.WIJH, *J. Electrochem. Soc.*, **116**, 388 (1969).

[12] A.K.WIJH, *Corrosion Sci.*, **11**, 411 (1971).

[13] S.IKONOPISOV, *Electrochim. Acta*, **22** 1077 (1977).

[14] F.FORLANI and MINNAJA, *Phys. Stat. Solidi*, **4**, 311 (1964).

[15] S.IKONOPISOV and N.ELENKOV, *J. Electroanal. Chem.*, **86**, 105 (1978).

[15] V.A.LALEKO, L.Ya.BEREZIN, T.I.MEDVEDEVA, V.P.MALINENKO, L.L.ODYNETS and L.V.SMIRNOVA, *Elektrokhimiya*, **20**, 1266 (1984).

[17] J.M.ALBELLA, I.MONTERO and J.M.MARTINEZ-DUART, *J. Mat. Sci.*, **26**, 3422 (1991).

[18] L.L.ODYNETS, E.Ya.KHANINA and S.CHEKMASOVA, *Elektrokhimiya*, **19**, 204 (1983)

[19] V.KADARY AND N.KLEIN, *J. Electrochem. Soc.*, **127**, 139 (1980) and **128**, 749 (1981).

[20] J.M.ALBELLA, I.MONTERO and J.M.MARTINEZ-DUART, *Thin Solid Films*, **125**, 57 (1985).

[21] J.M.ALBELLA, I.MONTERO and J.M.MARTINEZ-DUART, *Electrochim. Acta*, **32**, 258 (1987).

[22] J.M.ALBELLA, I.MONTERO, M.FERNANDEZ, C.GOMEZ-ALEIXANDRE and J.M.MARTINEZ-DUART, *Electrochim. Acta*, **30**, 1361 (1985).

[23] F.DiQUARTO, S.PIAZZA and C.SUNSERI, *J. Electroanal. Chem.*, **248**, 99 (1988).

[24] P.SKELDOM, G.E.THOMPSON and G.C.WOOD, *Thin Solid Films*, **148**, 333 (1987).

[25] T.F.HUNG, H.WONG, Y.C.CHENG and C.K.PUN, *J. Electrochem. Soc.*, **138**, 3747 (1991).

Materials Science Forum Vols. 185-188 (1995) pp. 535-542

Study of the anodic silicon oxide transformation during the breakdown process

O. Najmi, I. Montero, L. Galán and J.M. Albella

Instituto de Ciencia de Materiales, CSIC, and Departamento de Física Aplicada, C-XII. Universidad Autónoma de Madrid, Cantoblanco, E-28049 Madrid, Spain

Keywords: Silicon oxide, anodic oxidation, breakdown, IR, XPS, SEM, EDX

ABSTRACT

In the anodic oxidation technique, the dielectric breakdown process has an important significance since it establishes a limit for the maximum thickness attainable by the film. In this work we have studied the breakdown process during the galvanostatic anodic oxidation of single-crystal silicon. The oxidation kinetics of silicon change from a fast linear voltage increase to a saturation regime after the breakdown process. The silicon oxide modification during the breakdown process has been analyzed using Infrared Spectroscopy (IRS), X-ray Energy Dispersion (XED), X-ray Photoelectron Spectroscopy (XPS) and Scanning Electron Microscopy (SEM) techniques. After the breakdown process an important change in the morphology and composition of the silicon oxide film is observed. Apart of the IR Si-O stretching band, located at 1054 cm^{-1}, new infrared bands due to the presence of carbon groups into the silicon oxide film appear. In agreement with this results, XPS analysis indicate that the composition of the silicon oxide film change from SiO_x to SiO_yC_z after breakdown due to the incorporation of carbon species from the electrolyte. Finally, after long breakdown times a thin carbon-rich layer is formed covering the SiO_yC_z compounds. However, we can observe by means of XED technique that the concentration of carbon is not uniformly distributed in the material. This results can be associated to the stochastic distribution of breakdown points over the silicon oxide surface.

INTRODUCTION

Silicon oxide films grown at room temperature under high electric fields by anodization technique have several advantages with regard to thermal silicon oxide.

For instance, no redistribution of dopant impurities occurs during the anodization process and an accurate thickness control of the oxide layer is possible [1-4].

In the anodization process the gradual addition of oxide layers requires an increase in the applied voltage across the oxide until a maximum cell voltage is reached. This critical voltage is accompanied by sparking and copious oxygen evolution. Generally, the oxide films affected by breakdown are nonuniform containing deep grooves and cracks on the surface.

Different studies of anodic oxide films under electrolytic breakdown were previously reported for valve metals. A theoretical model dealing with the electron injection and avalanche mechanisms which give rise to the initiation of the breakdown of the oxide during the anodization has been developed in our laboratory [5-8]. In some metals, like aluminum and tantalum, it was found that the breakdown of anodic films is associated to a crystallization process, whereas, in other metals a crater-like morphology with polycrystalline grains was revealed [9-11]. However, the structure and the composition of anodic silicon oxide films under breakdown process had not been studied. Thus, the purpose of this work is to analyze the breakdown precess and the transformation of the oxide layers formed once the breakdown occurs.

EXPERIMENTAL DETAILS

Oxide layers were grown on two-side-polished p-type <111> oriented silicon wafers by anodic oxidation under galvanostatic conditions. Before oxidation, the substrates were cleaned, etched in 10% HF solution, rinsed with deionized water and dryed with N_2. The anodization was performed in a 0.04 M solution of KNO_3 in ethylene glycol at room temperature with a current density of 17 $mAcm^{-2}$.

The voltage-time curves were recorded by a data acquisition system using a microcomputer that has been described previously [12]. The analytical characterization of the silicon oxide films was carried out by IR, XPS, EDX and SEM techniques. The IR spectra were recorded in the 4000 - 400 cm^{-1} range using a Hitachi spectrophotometer, mod. 270-5. X-ray photoelectron spectroscopy (XPS) analysis were performed with a VG ESCALAB 210 instrument using non monocromatic Mg K_α X-ray radiation and 20 eV analyzer pass energy (0.3 eV resolution). The overall composition and The morphology of the samples were also studied by the energy-dispersive X-ray spectroscopy (EDX) and the scanning electron microscopy (SEM) using a Philips XL-30 microscope. In this last case, the samples were metallized using a thin layer of Au.

RESULTS AND DISCUSSION

Figure 1 illustrates a typical anodization voltage-time curve, V(t), corresponding to a sample anodized in the KNO_3 electrolyte at 20ºC. Two regions can be distinguished in the V(t) curve: In the first one, the cell voltage increases linearly with time until a critical voltage is reached, and in the second region, an abrupt decrease of the slope with small fluctuation was observed. This change in the slope of the V(t) curve was reported in the oxidation of different valve-metals as characteristic of the breakdown. The slope change could be used to define the breakdown potential, V_b, being in this case V_b = 540 V. This point can also be used as the origin for breakdown time, t_b (see Fig. 1).

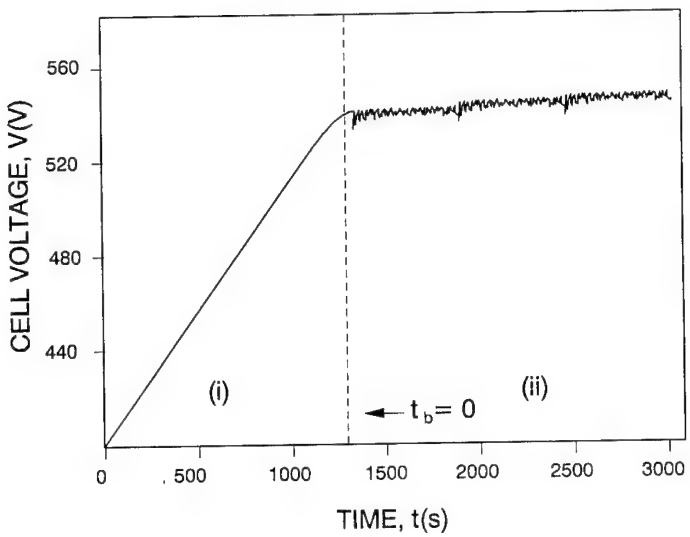

Figure. 1.- Cell voltage as function of the anodization time.

The IR absorption spectra obtained from silicon oxides prepared at different breakdown times, t_b, are reported in Fig.2. Before the breakdown process the IR spectrum of the silicon oxides films (curve a) only exhibits three absorbance peaks located at about 1060, 803 and 450 cm^{-1}, corresponding to the asymmetric stretching, bending and rocking transverse optical modes. The asymmetric stretching mode (ASM) presents a shoulder towards high wave numbers [13]. After the breakdown process, the IR spectra show other absorptions bands located at 3600, 3350 and 2340 cm^{-1} attributed to Si-OH, H-O-H and Si-H stretching modes, respectively. These bands have also been observed in the silicon oxide films obtained with a higher water

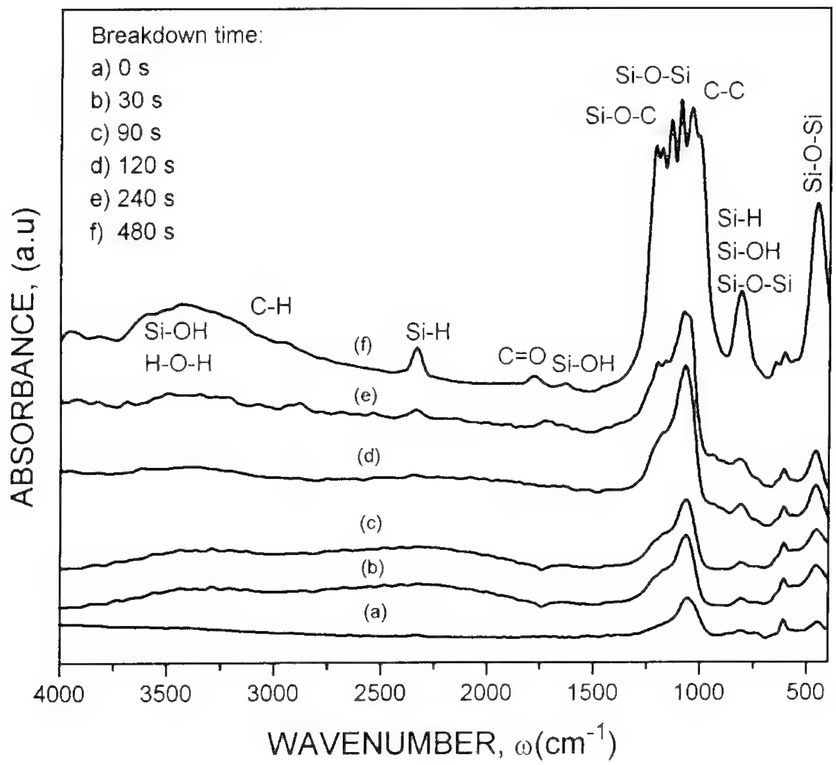

Figure. 2.- ***IR spectra corresponding to the anodic silicon oxide obtained at different breakdown times.***

concentration in the electrolyte [14-15]. An increase in the FWHM and amplitude of the high-frequency shoulder of the Si-O ASM were observed as a function of the breakdown time. This particular shoulder in the vicinity of the Si-O stretching mode is identified as due, to the Si-O-C modes located at 1190 cm^{-1} [16]. Furthermore, the IR spectrum of the oxide film with a long breakdown time, (curve f), show also an intesity increase in the side of low wave-numbers associated to a band centered at 1012 cm^{-1}. This band must be attributed to the presence of C-C bonds in the sample. Also, new absorption bands around 2312 and 1784 cm^{-1} were observed in the spectra. These peaks are associated to C-H and C=O bonds present in the oxide film, respectively [17]. These results indicate that carbon species from the electrolyte are incorporated into the silicon oxide during the breakdown process.

More detailed information on the chemical transformation of the silicon

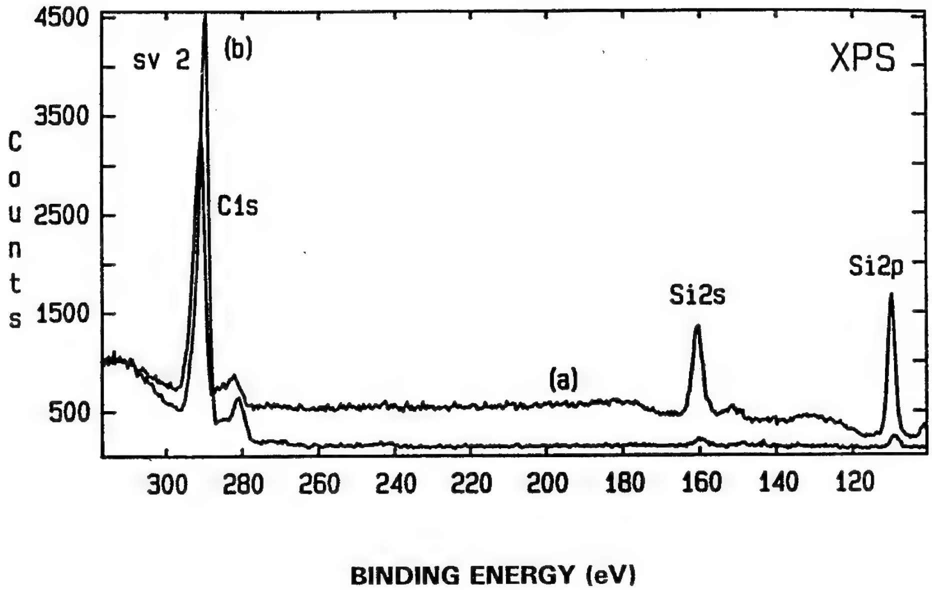

Figure. 3.- *XPS spectra of two anodic silicon oxide films formed at different breakdown times: a) 90 min, b) 120 min.*

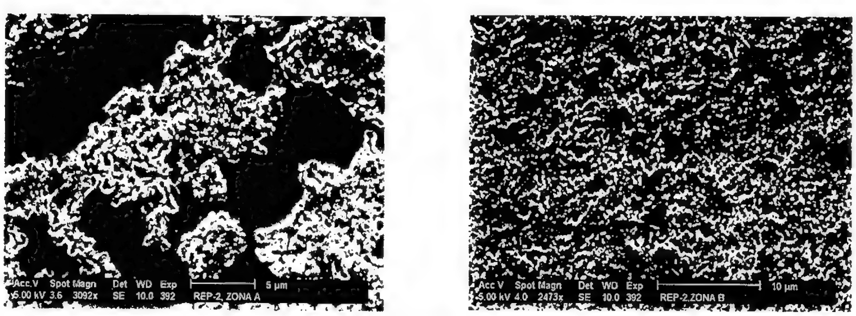

(a) (b)

Figure 4.- *SEM micrographs of silicon oxide film: (a) t_b = 5 min and (b) t_b = 100 min.*

oxidefilms during the breakdown process was obtained by XPS analysis. Figure 3 illustrates XPS spectra of two samples formed at different breakdown times (90 and 120 min). Photoelectron lines of Si, O (not shown in the Figure) and C were observed in both films. A quantitative analysis of the XPS spectra indicate the formation of SiO_xC_y compounds. The average x and y values were found to depend on the breakdown time, being x = 2.8 and y = 2.7 for t_b = 90 min., while for the samples obtained at t_b = 120 min. (curve b) the x and y values are 10.1 and 33.7 respectively. Thus, during the breakdown process the relative intensity of the Si 2p signal decrease as a consequence of the incorporation of carbon species in the surfaces layers of the silicon oxide.

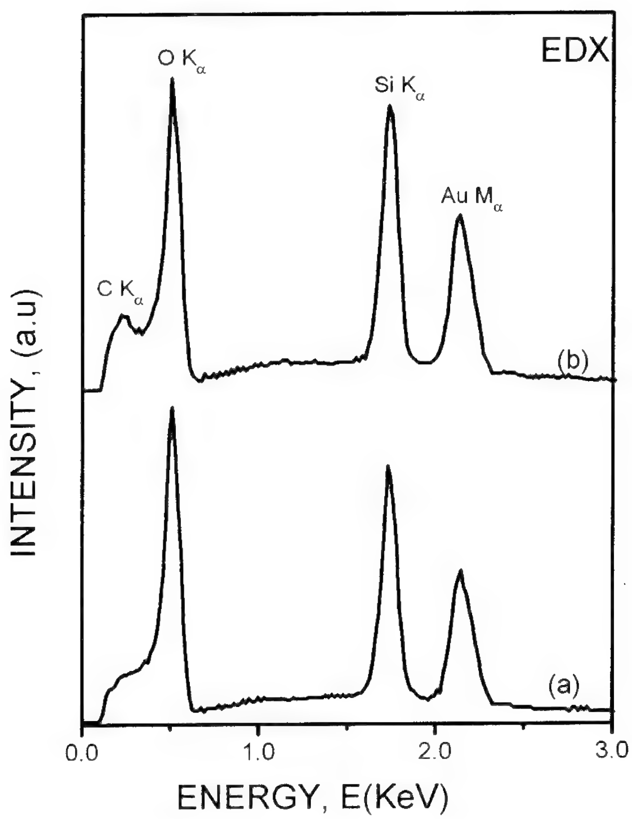

Figure. 5.- ***EDX spectra corresponding to two regions of the anodic silicon oxide after the breakdown process.***

The surface morphology transformation during the breakdown process has been

observed by SEM technique. The analysis was carried out for two specimen obtained at short and long t_b values. Figure 4-a shows the backscattered electron image for t_b = 5 min. In this case, the surface of the oxide exhibit two different zones, with and without breakdown damage. We can observed the presence of some island-type breakdown zone composed of pores, cracks and microfissures. Whereas, for long breakdown times, t_b = 100 min. (Fig. 4), the smooth zones disappears and the breakdown zones cover completely the surface of the sample. In this regard, the fluctuations observed in the second region of V(t) kinetic curve, Fig. 1, can be attributed to the irregular growth of the oxide layers during the breakdownprocess. EDX analysis was obtained at different points of the surface of the sample with and without breakdown damage, for t_b = 10 min. Figure 5-*a* shows that on the flat areas, only silicon and oxygen are detected, whereas on the roughest surface an emission peaks of silicon, oxygen and also carbon were detected, Fig. 5 *b*. An quantitative analysis was carried out in an area of 4 μm^2. It was found that the x = O/Si ratio in the smooth surface is 1.9. However, in the zone with breakdown damage, SiO_xC_y compounds were detected, with x = 2.6, and y = 4.8. The small carbon concentration of the film obtained in bulk EDX analysis compared with the XPS results indicate that the incorporation of carbon is in the outer layers of the silicon oxide film.

CONCLUSIONS

The kinetics of the electrochemical anodization of silicon in a electrolyte composed of KNO_3 solved in ethylene glycol follows a quasi-linear law until the irreversible process of the breakdown is initiated, then the V(t) curve shows a saturation. During the breakdown process important modifications in the structure and composition of the silicon oxide film are produced. From IR spectra, it is concluded that the silicon oxide film after the breakdown process contain large amounts of carbon compounds in the form of C-H, C=O, Si-O-C and C-C groups. This is due to the incorporation of the electrolyte into the silicon oxide. XPS studies indicate the presence of the SiO_xC_y in the oxide. The quantitative analysis of the spectra show that the carbon incorporation increases toward the surface of the sample. EDX combined with SEM analysis evidence that the carbon is not homogeneously distributed on the surface. Thus, the carbon presence is in island-type zones of the surface affected by the breakdown process.

REFERENCES

[1] E. F. Duffek, E. A. Benjamin and Mylroie, *J. Electrochem. Soc*, **3**, 75 (1965).

[2] E. Shmidt and W. Michel, *J. Electrochem. Soc*, **104**, 230 (1957).

[3] M. J. Madou, W. P. Gomes, F. Fransen and P. Cardon, *J. Electrochem. Soc*, **129**, 2749 (1982).

[4] G. Mende, H. Flietner and M. Deutsher, *J. Eslectrochem. Soc*, **140**,188 (1993).

[5] J. M. Albella, I. Montero, and J. M. Martinez-Duart, *J. Electrochem. Soc*, **131**, 1101 (1984).

[6] J. M. Albella, I. Montero and J. M. Martinez-Duart, *Thin Solids Films*, **58**, 307 (1979).

[8] I. Montero, J. M. Albella and J. M. Martinez-Duart, *J. Electrochem. Soc.*, **132**, 814 (1985).

[9] J. Yahalom and J. Zahavi, *Electrochem. Acta*, **15**, 1429 (1970).

[10] V. Kadary and N. Klein, *ibid.*, **127**, 139 (1980).

[11] S. Ikonopisov, *Electrochim. Acta*, **22**, 1077 (1977).

[12] J. M. Albella, I. Montero and J. M. Martinez-Duart, *J. Electrochem. Soc*,., **131**, 1101 (1984).

[13] I. Montero, L. Galán, O. Najmi and J. M. Albella, *Physical Review B*, **50**, (1994).

[14] I. Montero, L. Galán, E. de la Cal, J. M. Albella and J. C. Pivin, *Thin Solid Films*, **193** (1990) 325.

[15] O. Najmi, I. Montero, L. Galán, J. Perrière and J.M. Albella, *App. Surf.Science*, 70/71, 217 (1993).

[16] C. Charles, P. Garcia, B. Grolleau and G. Turban, *J. Vac. Sci. Technol*, **A 4**, 1407, (1992).

[17] N. B. Colthup, L. H. Daly, S. E. Wiberley *"Introduction to Infrared and Raman Spectroscopy"*, Third Edition "London", p. 358 (1990).

Materials Science Forum Vols. 185-188 (1995) pp. 543-552

Basic laws of electrical breakdown of thin dielectric layers

V.A. Gurtov, N.Yu. Ershova and P.A. Raikerus

Department of Solid State Physics, Petrozavodsk State University,
33 Lenin St., Petrozavodsk, 185640, Karelia, Russian Federation

Keywords: Thin dielectric layer, anodic film, thermal and electrical breakdown

Abstract Electrical breakdown in thin dielectric layers, including Ta_2O_5, Nb_2O_5, Al_2O_3, SiO_2 and Si_3N_4, under static, dynamic and pulse conditions was inverstigated. The experiments were carried out with an automated setup, using Au and Pt wire electrodes. To analyze the experimental results, Weibull statistics was used. Field and temperature dependences of the time lag to breakdown τ_{br} were obtained in the range of 10^{-6} - 10^{3} s. A dependence of the breakdown voltage V_{br} on the ramp rate in the dV/dt range of 10^{-2} - 10^{5} V/s was identified. Dependences of τ_{br} on the applied voltage pulse duration and off-duty factor were determined. Kinetic dependences of the pre-breakdown current were studied. The main breakdown-determining processes were defined.

Introduction At present, a wide variety of experimental data on breakdown in solid dielectrics is available. However, studies of electrical breakdown in thin dielectrics layers lack a complex and unified approach to interpretation of the results. For this reason, the present work is of topical interest. It aims at a systematic experimantal investigation of the electrical breakdown in silicon oxide and silicon nitride, as well as anodic oxides of valve metals under static, dynamic and pulse conditions. A universal breakdowm model for thin dielectric layers is expected to be developed as a result of these studies.

Experimental Oxides of valve metals (Ta_2O_5, Nb_2O_5, Al_2O_3) as well as silicon dioxide and silicon nitride were used in the present work. Metal oxides were obtained by anodizing annealed elect-

ropolished foil of the corresponding metals (Ta, Nb and Al) using the conventional technique. Silicon dioxide SiO_2 was formed by thermal oxidation of silicon in dry oxygen at T = 1323 K. Silicon nitride was synthesized by ammonolysis of monosilane at 933, 1033, 1103, 1143 and 1288 K.

The thicknesses of the dielectric layers under study were in the range of 30 - 300 nm.

Experimental studies of dielectric strength are rather laboursome because of statistical nature of this phenomenon. To facilitate measurements, an automated setup was created, allowing to use the main techniques, namely: static (V_{br}=const), dynamic (dV/dt=const) and pulse voltage conditions.

The main technical characteristics of the device are:

- the working voltage range of 0 ÷ 256 V;
- the time of the build-up of the high-voltage amplifier's transient characteristics of $1.5x10^{-5}$ s;
- the working temperature range of 293 ÷ 573 K;
- the accuracy of maintaining temperature of 0.5 K;
- the measured time range of 10^{-6} ÷ 10^3 s.

To connect a computer to the apparatus, a system CAMAC is used, comprising both standard and original specialized modules [1].

A programme package was created, allowing to perform the experiment in all conditions mentioned, followed by statistical treatment of the results obtained. The technique used was described in detail [1].

The results were treated with Weibull statistics and extreme-value statistics. For the analysis of the experimental data we used mean values of the logarithm of the time lag to breakdown τ_{br} and breakdown voltage V_{br}, deduced from a set of N = 30 - 50 values, as well as the values of τ_{br} and V_{br} corresponding to the probability P_s=0.63 in Weibull distribution.

Thin Au (or Pt) wire ~ 0.15 mm in diameter was used as a gate, allowing to perform up to 10^4 breakdown events on various spots of the oxide surface area of 1 cm^2 and, thus, to investigate both field and temperature dependences of the time lag to breakdown on one specimen.

Results and discussion Fig.1 shows experimental field dependences of the time lag to breakdown $\tau_{br}(V)$ at room temperature for systems with Ta_2O_5, Nb_2O_5, Al_2O_3, SiO_2 and Si_3N_4 (gate positive). For all the structures under study, common features are observed on the $\tau_{br}(V)$ curves, namely: two regions referring to large values of τ_{br} and low fields (the first region) and to small values of τ_{br} and high fields (the second one). The decrease of τ_{br} with increasing voltage is slower in the first region than in the second. The intersection of these regions usually lies in the range $\tau_{br}>10^{-2}$ s.

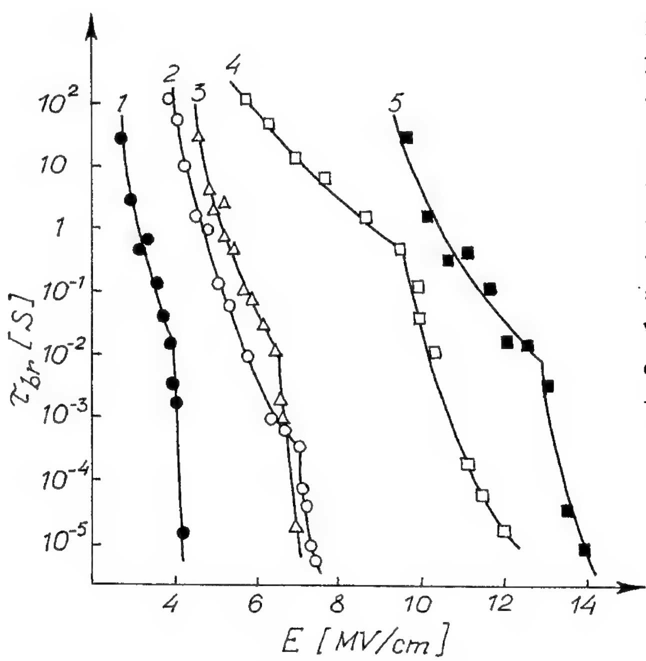

Fig.1. The time lag to breakdown vs applied voltage.
1 - Nb_2O_5, d_{ox}=240 nm,
2 - Al_2O_3, d_{ox}=190 nm,
3 - Ta_2O_5, d_{ox}=180 nm,
4 - SiO_2, d_{ox}=100 nm,
5 - Si_3N_4, d_{ox}=100 nm.
$V_G>0$. The tests were carried out at room temperature.

For systems with Al_2O_3 and Si_3N_4, the $\tau_{br}(V)$ plot at $V_G<0$ is similar to that at $V_G>0$ (Fig.2 and 5). For Al_2O_3, asymmetry in the characteristics is observed: the values of τ_{br} at $V_G<0$ are larger than at $V_G>0$. Rapid decrease in the time lag to breakdown with increasing breakdown voltage is typical of the systems with oxides Ta, Nb and Si at $V_G<0$ (τ_{br} changes by six orders of magnitude at V = 1 - 3 MV, see Fig.2). For Nb_2O_5 the plot is similar to that of Ta_2O_5.

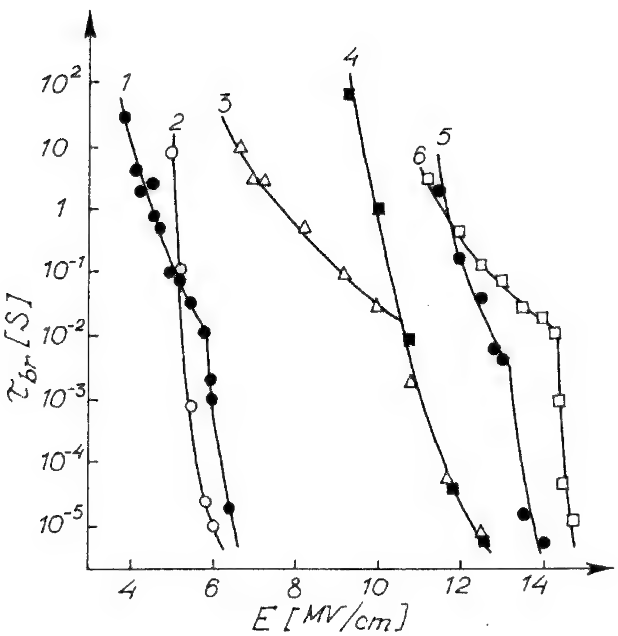

Fig.2. The time lag to breakdown vs applied voltage.
1,2 - Ta_2O_5; 3,4 - SiO_2; 5,6 - Si_3N_4 (p-Si).
1,3,5 - $V_G>0$. 2,4,6 - $V_G<0$.

For MNOS structures with Si_3N_4 formed at various temperatures of the synthesis on both n-Si and p-Si substrates, the $\tau_{br}(V)$ curves are similar at $V_G>0$ and $V_G<0$ (Fig.3). As T_{syn} decreases, a parallel shift of the functional dependence $\tau_{br}(V)$ is observed to low fields, which may be due to reduced depth of the trapping centres in the bulk of Si_3N_4 and, consequently, to the increase in the structure conductivity [2].

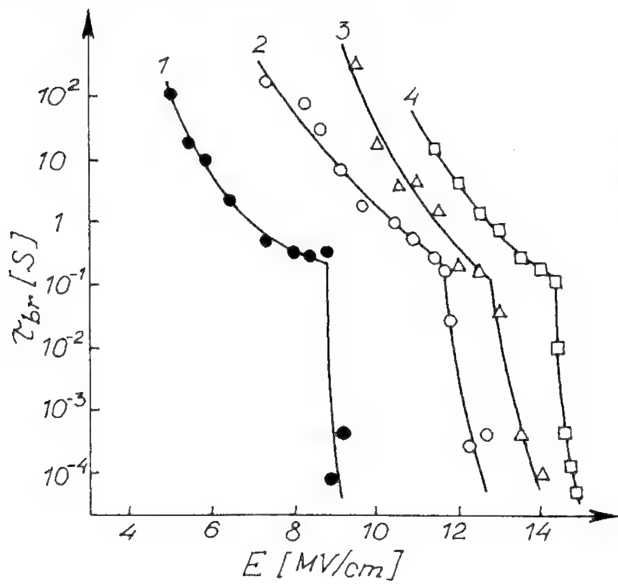

Fig.3. The time lag to breakdown vs applied voltage at various synthesis temperatures of Si_3N_4 films.
1 - 933 K, 2 - 993 K, 3,4 - 1143 K.
1,2,3 - Si_3N_4 (n-Si), 4 - Si_3N_4 (p-Si). $V_G>0$.

The $\tau_{br}(V)$ plots at room and elevated temperatures for systems with Ta_2O_5, Si_3N_4 (for Nb_2O_5 the plot is similar) and Al_2O_3 are shown in Figs.4 and 5. As the temperature increases, the values of the tme lag to breakdown reduce and the plot's appearance remains unchanged. The effect of the temperature on dielectric strength of the valve metal oxides is qualitatively similar to that of the temperature of silicon nitride synthesis.

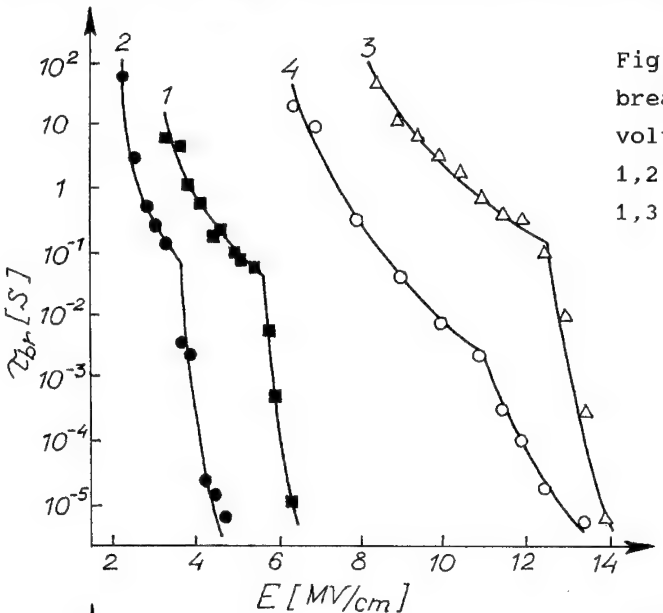

Fig.4. The time lag to breakdown vs applied voltage. $V_G>0$.
1,2 - Ta_2O_5; 3,4 - Si_3N_4.
1,3 - 293 K; 2,4 - 473 K.

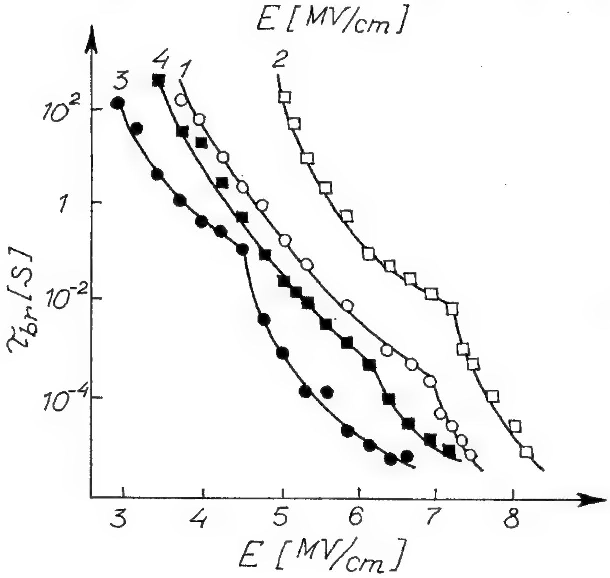

Fig.5. The time lag to breakdown vs applied voltage for an Al_2O_3 oxide film with the oxide thickness of 190 nm.
1,2 - 293 K; 3,4 - 416 K.
1,3 - $V_G>0$. 2,4 - $V_G<0$.

It has been esperimentally established for SiO_2 that the breakdown mechanism responsible for the first region on the $\tau_{br}(V)$ plot is temperature-dependent, while the one responsible for the second region is temperature-independent (Fig.6). These two mechanisms work in parallel, therefore, at each particular value of E_{br} and T the determining mechanism will be that with the minimum time lag to breakdown. As the temperature increases, the temperature-dependent mechanism becomes more important leading to expansion of region 1 to higher fields. In region 2, the values of τ_{br} for various temperatures coincide. These data are interpreted fairly well in terms of the hot carries-induced breakdown model [3,4].

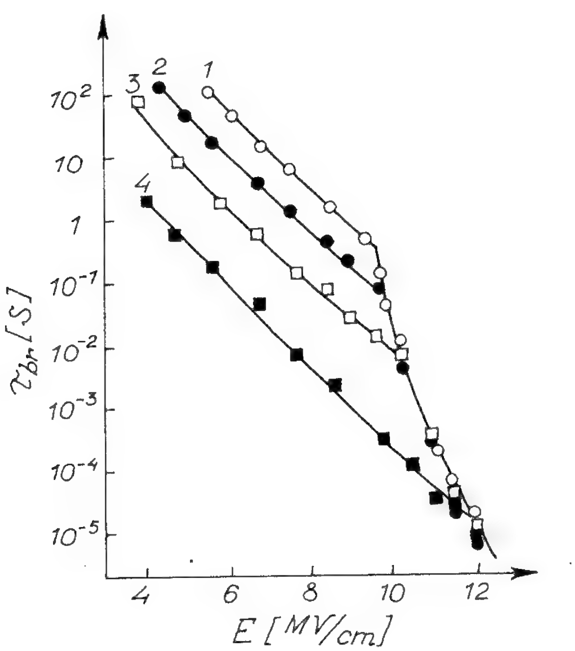

Fig.6. The time lag to breakdown vs applied voltage for a silicon oxide film with the oxide thickness of 100 nm at various temperatures. $V_G>0$.
1 - 293 K, 2 - 333 K, 3 - 373 K, 4 - 435 K.

The breakdown voltage V_{br} as a function of the ramp rate dV/dt obtained in the range $dV/dt = 10^{-2} \div 10^5$ V/s at $V_G>0$ for structures with Ta_2O_5 and Si_3N_4 is given in Fig.7a. For $V_G<0$, V_{br} is independent of dV/dt. In Fig.7b, the same dependence is replotted in t(V) coordinates which are more convenient for comparison with the field dependence of τ_{br}.

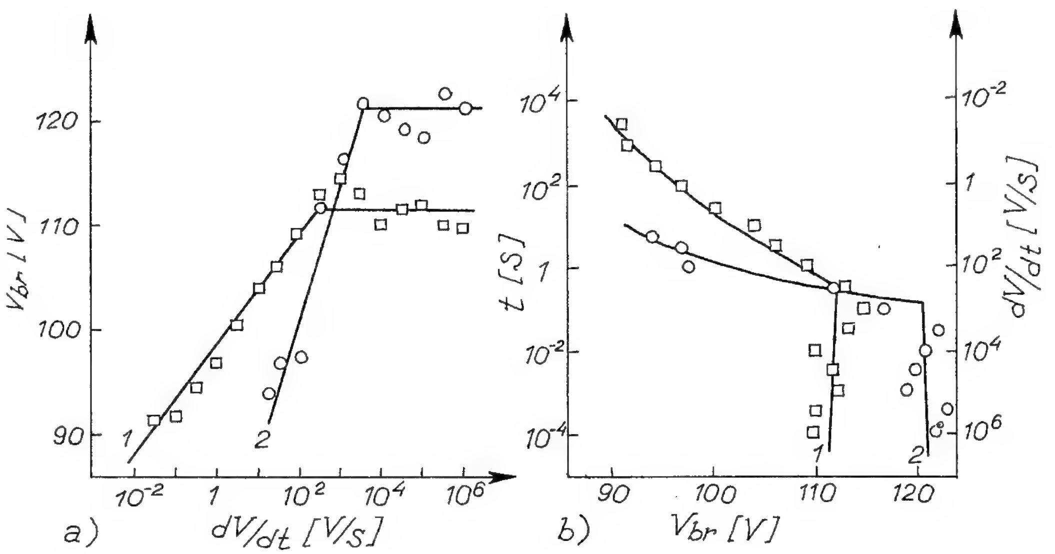

Fig.7. a) The breakdown voltage V_{br} as a function of the ramp rate. b) The time lag to breakdown as a function of V_{br}. 1 - Ta_2O_5, 2 - Si_3N_4.

Note that the two regions of the V_{br}(dV/dt) plot correspond to the two regions of the field dependence of $\tau_{br}(V)$: the region of the breakdown voltage increase with the ramp rate is similar to region 1 of the $\tau_{br}(V)$ relationship, where $\tau_{br}>10^{-2}$ s, and the region with the dV/dt - independent breakdown voltage is identical to the region of the field dependence, where voltage remains nearly constant while τ_{br} changes by several orders of magnitude.

In Fig.8 the results on dielectric strength for a Au-Ta_2O_5-Ta structure under pulse conditions are presented. Three regions can be distinguished on the total time lag to breakdown vs applied voltage pulse duration with the off-dute factor S = 2 (Fig.8, curve 1): the first region lies in the pulse duration range t_p = $3x10^{-7} \div 2x10^{-5}$ s, where τ_{br} is independent of the pulse duration (Weibull's parameter a = 0.90 $\pm$ 0.09); the second region is in the ranges of $2x10^{-5} \div 10^{-3}$ s, where τ_{br} decreases with increasing t_p (a = 0.83 $\pm$ 0.04), and the third is in the range t_p = $10^{-3} \div 10^2$ s, where the total time lag to breakdown is independent of t_p and coincides with τ_{br} during breakdown at constant field (the va-

lue of V_{br} under pulse conditions equals to that of V_{br} at constant field), $a = 0.50 \div 0.02$ in this case. The latter is in good agreement with the results obtained earlier for Ta_2O_5 while studying dielectric strength at constant field. The above three regions characterized by various values of the parameter a indicate different breakdown mechanisms in the ranges of t_p considered. With the off-duty factor S = 5 (Fig.8, curve 2), the $\tau_{br}(t_p)$ relationship shifts to the right along the X-axis. The first region expands up to $t_p = 10^{-3}$ s in this case, while the third one is not registered in the pulse duration range studied.

The experimental results obtained during investigation of dielectric strength of Ta_2O_5 under pulse conditions are treated in terms of electronic breakdown models. In [5], however, a similar dependence of the total time lag to breakdown on pulse duration was obtained and two regions were distinguished on the $\tau_{br}(t_p)$ plot, corresponding to regions 2 and 3 in Fig.8, curve 1 of our paper. But the authors of [5] suggested that in the range of $t_p > 10^{-3}$ s breakdown is due to thermal processes. That is why we considered it necessary to conduct an experiment confirming our point of view.

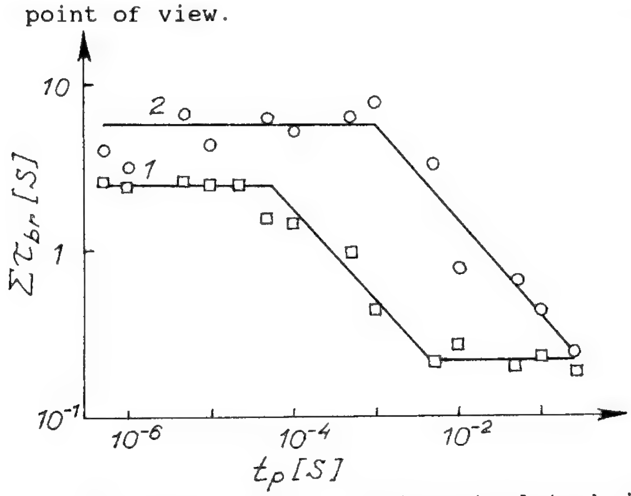

Fig.8. The time lag to breakdown vs applied voltage pulse duration for a Ta_2O_5 oxide film with the oxide thickness of 68 nm. The off-duty factor S=2 (1) and S=5 (2).

The permanent current control technique used in our experiments allowed us to conduct "step-by-step" breakdown of the specimen. Constant voltage was applied to the Ta-Ta_2O_5-Pt system and at the program-given current level the breakdown process was inter-

rupted. After a pause, the duration of which varied, voltage was re-applied to the system. Such interruptions were made repeatedly, with the overall time to breakdown remaining constant within the statistical scattering. Each time the pre-breakdown current started to increase from that very value where the breakdown process had been interrupted (Fig. 9). The above experiment could hardly be interpreted in terms of purely thermal breakdown. Instead, the electronic breakdown model approach in terms of dielectric localization and memory track could be used for interpreting the results obtained [6].

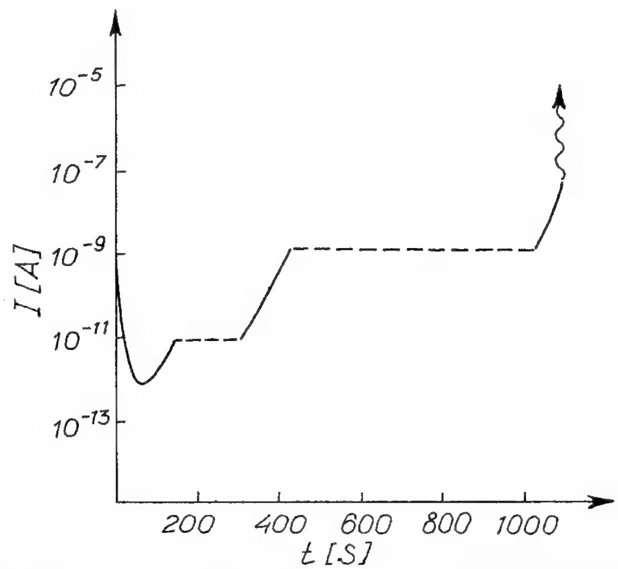

Fig.9. "Step-by-step" breakdown for a Ta-Ta_2O_5-Pt system.

In conclusion, the main processes which may have effect on breakdown in thin dielectric layers have been identified nowadays. They are: injection of charge carriers, their mobility in electric field, the resulting thermal effect, space charge formation, impact ionization and other effects, that are often considered separately, thus failing to reveal the whole picture of breakdown. Besides, models are usually developed with no particular object of study referred to or, on the contrary, only for some particular materials and for interpretation of some separate experimental de-

pendences, disregarding the wealth of the accumulated experimental data.

Therefore, the need for developing a universal model able to explain the main experimentally found laws of breakdown in thin film systems is quite evident. However, difficulties arise, for the experimental data available, required for developing a model, are incomplete. To cope with the problem, it is necessary not only to gather sufficient statistical information on every aspect of breakdown, but also to consider data on conductivity of the materials under study and, perhaps, structural changes in high electric fields.

References

1. Laleko V.A., Kozhevnikov S.V., Naumov V.G., Dragan I.I., Shavkera V.L., Petrozavodsk University, Dep. in VINITI, N 2284-B92 (1992).
2. N.Yu.Ershova, O.N.Ivashenkov Proc.Conf.Physics of Oxide Films, June 1994, Petrozavodsk University Publ.Unit.
3. M.V.Fischetti, D.J.Di Maria, S.D.Brorson, T.N.Theis, J.R.Kirtley Phys.Rev.B, 31, 12, 8124 (1985).
4. T.V.Shmidt, V.A.Gurtov, V.A.Laleko, J. "Mikroelektronika", 17, 3, 244 (1988).
5. N.Klein and E.Burstein, J.Appl.Phys., 40, 7, 2728 (1969).
6. A.K.Jonscher, J.Phys.I: Appl.Phys., 13, 143 (1980).

Materials Science Forum Vols. 185-188 (1995) pp. 553-562

A new model of ionic and electronic processes during anodic oxidation of valve metals

L.L. Odynets

Petrozavodsk State University, 33 Lenin St., Petrozavodsk,
185640, Karelia, Russian Federation

Keywords: Anodic oxide films, anodic oxidation, ionic and electronic current

Abstract

A new model has been proposed for mechanisms of ionic and electronic processes during anodic oxidation of valve metals. In amorphous oxide films ionic transport is determined by single charged non-coordinated oxygen (MO^-) and metal (MO^+) atoms (broken bonds) at the metal/oxide and oxide/electrolyte interfaces. Total ionic current flowing during anodic oxidation includes currents of oxide formation and oxide dissolution, determined by the corresponding processes on Helmholtz layer at the oxide/electrolyte interface and essentially dependent on the charge on the inner surface of Helmholtz layer (IHL).

The analytic lgI-F dependence for the oxide formation current is similar to Young's well-known empirical equation. The equation for the ionic dissolution current is of the same form. Electron injection takes place from the surface of the OH-groups chemisorbed at the oxide/electrolyte interface (IHL), but the electronic current through an oxide film is bulk-controlled and independent of the electrolyte nature, concentration and pH.

INTRODUCTION

A number of kinetic laws, which have been proved experimentally for the last twenty years, operate during anodic oxidation of valve metals:

a) During ionic defect migration, the order of the metal and oxygen atoms remains unchanged and each atom is displaced by an elementary distance close to the Me-O bond distance in the short-range order of an anodic oxide film (AOF).

b) New oxide layers are formed at the metal/oxide and oxide/ electrolyte interfaces.

c) Migration of ionic defects of both signs takes place, their transport being interdependent (co-operative transport).

d) The $j \sim E$ relationship is nonlinear and can be fitted by an empirical formula [1]:

$$j=j_0 \exp\left(-\frac{W}{kT}\right)\exp\frac{ze}{kT}(\alpha-\beta E_{0X})E_{0X} \quad , \qquad (1)$$

where α and β are the constants.

It is evident that any theoretical model should answer these laws as well as provide a noncontradictory explanation of other ionic and electronic processes occurring during anodic oxidation.

<u>Ionic defects in AOF.</u> X-ray amorphous thin oxide films are generally formed during anodic oxidation of aluminium, tantalum

and niobium. Bonds in these oxides are of a mixed type, i.e. ionic-covalent, with ionicity of 50-60%. In the amorphous oxide structural network, regions can be distinguished, where the short-range order similar to that of the crystalline oxide structure is still retained. These regions, analogs of an elementary cell in a crystal, are referred to as "structural units". In amorphous AOF, as well as in compact single-component oxide glasses, the probability of formation of Frenkel-Schottky-Vagner ionic defects is negligible and the simplest point defects will be represented by the single charge non-coordinated oxygen (MeO^-) and metal (MeO^+) atoms or, in other words, single vacant (broken) bonds possessed by oxygen and metal atoms in the oxide network. Such defects migrate by means of switching of a vacant bond with the adjacent atoms possessed by the Me-O-Me brige (Fig.1).

On such switching, atoms are displaced from their equilibrium states by distances not longer than the Me-O bond distance. A series of such accumulative directed displacements lead to the atomic transport process. Thus, it can be stated that transfer of a fractional part of the composition takes place during directed bond switching (contrary to experiment (a)).

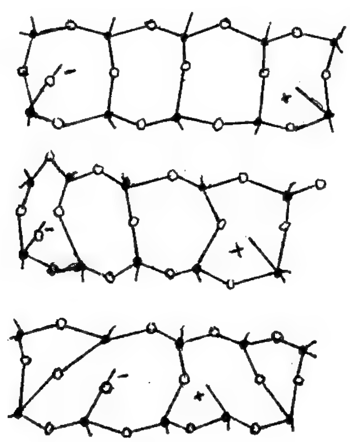

Fig.1 Schematic bond switching in the amorphous oxide network [2].

The broken bond concentration in the bulk of the oxide is very low since the energy of the Me-O bond disruption in the Me-O-Me bridge is very high. Hence, it can be assumed that defects are formed not in the bulk but at the metal/oxide and oxide/electrolyte interfaces.

ANODIC OXIDATION

<u>Reactions at the metal/oxide interface.</u> A transition layer (t.l.) consisting of the lower oxides exists at the metal/AOF interface. This is the case not only for transition metals but for aluminium, too. At the interface (x=0), the reaction of oxygen removal from the adjacent oxide layer takes place, accompanied by formation of a vacancy bond on the oxygen atom and a new oxide molecule in the transition layer

$$Me/MeO_{x=0} \rightarrow MeO^+_{x=0+\delta} + MeO_{t.l.} + e_{Me}, \qquad (2)$$

$$Me_{Me} + \frac{1}{2}O_2 \rightarrow MeO_{t.l.} \qquad (3)$$

Field-assisted migration of the MeO^+ "vacancies" formed to the outer interface takes place, wich act as adsorption centres (main Lewis centres) on the AOF surface.

The current j_+ of positive defect transport and of new oxide layer formation at the metal/AOF interface corresponds to the above reactions. It is shown in [2] that the current-controlling barrier at the Ta/Ta_2O_5 and Nb/Nb_2O_5 interfaces does not exceed 1.2 eV, which is two times lower than the barrier for anodic oxidation [1].

Reactions at the oxide/electrolyte interface. In contact with an aqueous electrolyte, dissociative adsorption of water occurs on the surface centres MeO^+

$$MeO^{+}{}_{X=X+\delta} + H_2O \rightarrow Me\text{-}OH_{X=X+\delta} + H^{+}{}_{sol.}, \qquad (4)$$

followed by dissociation of chemisorbed OH groups and formation of noncoordinated oxygen atoms (metal "vacancies"), MeO

$$Me\text{-}OH_{X=X+\delta} \rightarrow MeO^{-}{}_{X=X+\delta} + H^{+}{}_{sol.} \qquad (5)$$

Besides, the H^+ - ion from the solution may join the MeO-group

$$MeOH_{X=X+\delta} + H^{+}{}_{sol.} \rightarrow MeOH^{+}{}_{2X=X+\delta} \qquad (6)$$

In addition to this, adsorption of the electrolyte ions - K^+-cations and Al_xO_y - anions - can take place:

$$MeOH_{X=X+\delta} + K^{+}{}_{sol.} \rightarrow MeO\text{-}K^{+}{}_{X=X+\delta} \qquad (7)$$

and, for example,

$$MeOH_{X=X+\delta} + SO_4^{2-}{}_{sol.} \rightarrow MeSO_4^{-} + OH^{-}{}_{sol.} \qquad (8)$$

Chemisorption of the SO_4^{2-} or PO_4^{3-} anions will result in displacement of a chemisorbed OH-group.

During anodic polarization, surface defects formed, MeO^-, can join the MeO^+ bond possessed by the Me-O-Me bridge in the underlying oxide layer, forming a new oxide molecule:

$$MeO^{-}{}_{X=X+\delta} + (Me\text{-}O\text{-}Me)_{X=X-\delta} \rightarrow MeO^{-}{}_{X=X-\delta} + MeO_{X=X+\delta} \qquad (9)$$

The MeO^- defect formed in the oxide layer adjacent to the electrolyte will migrate to the metal/oxide interface and recombine there. The current j_- of migration of MeO^- defects and formation of new oxide layers at the outer interface of AOF corresponds to reaction (9). Reactions (2), (3), (4)-(9) result in the new oxide layers formation at both interfaces, wich is fully consistent with experiment (b).

If pH of the solution is larger than pH_{zpc} (zero point charge), reactions (6) and (8) will prevail. The former, together with reaction (9), will determine the growth of an oxide layer at the outer interface, whereas the latter will be responsible for the electrolyte anion introduction into the outer part of this layer.

Applying conventional methods of chemical thermodynamics to reactions (6) and (8), it is possible to define the value of charge σ at IHP, formed by chemisorbed MeO^- and $MeSO_4^-$ ions.

$$б^{0} = - eN_X\Theta_0\left[\Theta_c a_{H^+} K_- + \left(a_{SO_4^{2-}} a^-_{H^+}\right)_{sol} K_a\right]\exp\varphi_{IHP/sol}/kT \qquad (10)$$

Here N_X is the total number of adsorption centres per oxide surface unit, Θ_0 is the relative density of chemisorbed OH^- groups and Θ_c is the equilibrium relative density of chemisorbed "+"- and "-" - groups in zpc. The quantities K_- and K_a are the equilibtium constants of reactions (6) and (8) respectively, while a_{H^+}, a_{OH^-} and $a_{SO_4^{2-}}$ represent H^+-; OH^- - and SO_4^{2-} - ions' activities in solution.

The charge б will essentially contribute to the field strength in HL. Since the relation

$$\varepsilon_{ox}E_{ox} = \varepsilon_X E_X = \varepsilon_H E_H + \frac{б}{\varepsilon_0}, \qquad (11)$$

is valid, where ε_{ox}, ε_X and ε_H are the dielectric constants of the oxide layer and the HL, respectively; E_{ox}, E_X and E_H are the electric field strengths in these layers.

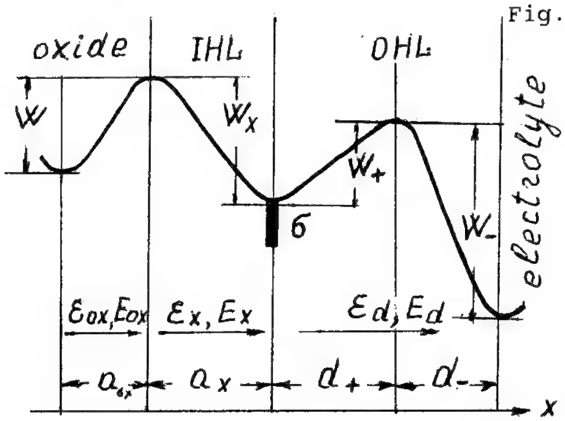

Fig.2. Energy diagram for the double layer at the oxide/electrolyte interface [4].

From Fig.2 and eqs. (6) and (8), current of oxygen transport across the oxide/electrolyte interface [3]:

$$j_- = eN_X\Theta_0\frac{\nu_+}{\nu_-}\nu_X a_{H^-}\exp\left(-\frac{W_A}{kT}\right)\exp\frac{e}{kT}\left(d_H E_H + a_X E_X\right) \qquad (12)$$

Since stoichiometry of the AOF surface can be considered unaltered during anodic oxidation, surface concentrations of the MeO^+ and MeO^- defects should remain constant. Under this condition, the current j_+ of the MeO^+ defect transport from the metal to the outer interface should compensate the defects subsidence resulting from reactions (4)-(6),(8),(9) followed by the current j_- of the MeO^- defect migration from the outer interface to the metal. Thus, the currents j_+ and j_- of the MeO^+ and MeO^- defect migration and, hence, of the new oxide layer formation turn out to be non-interdependent, contrary to experiment (c).

As the currents j_+ and j_- are non-interdependent, it can be assumed that $j_+=cj_-$, where c=const. Then the total current of anodic oxidation $j_A=j_+ + j_- =(1+c)j_-$.

Assuming that the anodic oxidation current-controlling barrier is at the oxide/electrolyte interface, using eq.(12) and taking (11) into account for the current j_-, we have:

$$j_A = j_0 \exp\left(-\frac{W_A}{kT}\right) \exp\frac{e}{kT}\left(a\ E_{0x} + \frac{d_H}{\varepsilon_0 \varepsilon_H}|\sigma|\right) \qquad (13)$$

$$a = \varepsilon_{0x}\left(\frac{a}{\varepsilon_x} + \frac{d_H}{\varepsilon_H}\right), \quad \text{where } W_A = (W_x - W) + (W_+ - W_-)$$

where a is the width and W_A is the height of the barrier at the oxide/electrolyte interface determining the MeO^- defect transport into the bulk of the oxide; d_H is the width of HL and ε_x is the dielectric constant of the inner HL ($\varepsilon_x \approx \varepsilon_{0x}$). This equation is similar to eq.(256) in Dignam's paper [4], but the author disregards the term including the charge σ, through it is not quite reasonable. Indeed, if we assume $\sigma = 10^{-2}$ Cm^{-2}, the field generated by this charge $\sigma/\varepsilon_0 \approx 1.2\times10^9$ Vm^{-2}, i.e. it is of the same order as the fields in HL. The influence of the electrolyte composition and concentration on the rate of anodic oxidation is determined by variation of the charge value σ resulting from adsorption of the electrolyte anions on the AOF surface and by variation of pH.

Many authors ascribe the increase in the field strength during anodizing in higher concentration electrolytes to the reduced oxygen ion mobility in the anion-containing layer, compared with a stoichiometric oxide. A simple experiment is known that does not correlate with the above explanation but is quite understandable in terms of our model. If a specimen is first anodized in a lower concentration electrolyte followed by anodization in a higher concentration electrolyte, the field strength will "jump" upon changing electrolytes. In reverse order of anodization, the result will be the same. With any variation of the experiment, the field strength at a constant current density will be determined only by the electrolyte the specimen is in at the moment (Fig.4).

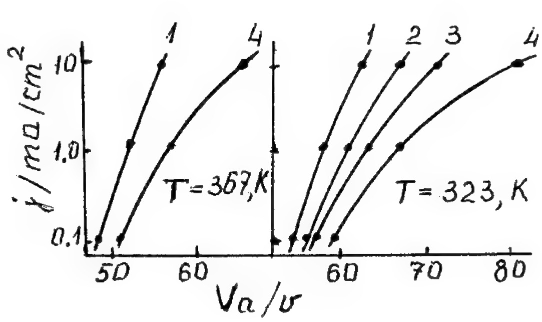

Fig.3. lgj as a function of V or E, with the same film thicknesses of 350 nm, in H_2SO_4 solutions of various concentrations: mass.%: 1-1; 2-50; 3-60; 4-70; [1]

If the equilibrium field of anodization is considered to be dependent on the adsorption charge σ (10), then, as follows from (13), this rule is quite clear.

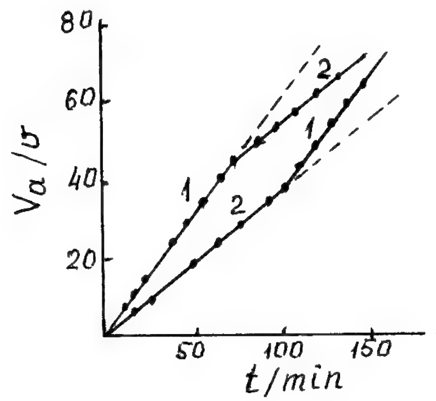

Fig.4. Overvoltage V vs time t for successive oxidation of tantalum in two H_3PO_4 solutions with the concentrations M: 1-14.7; 2-0.33 [3].

It follows from Young's experimental data [1] (Fig.3) that, being a positive one, the first derivative $d\sigma/dE$ must decay with increase in the electrolyte concentration and its decreased temperature, i.e. the second derivative $d^2\sigma/dE^2$ must be negative. It follows from (1) and (13)

$$\frac{d\lg j}{dE_{ox}} = \frac{q}{kT}\left(\alpha-2\beta E_{ox}\right) = \frac{e}{kT}\left(a_x + \frac{d_H}{\varepsilon_H\varepsilon_0}\times\frac{d|\sigma|}{dE}\right), \tag{14}$$

$$\frac{d^2\lg j}{dE^2_{ox}} = -\frac{q}{kT}2\beta E_{ox} = \frac{e}{kT}\times\frac{d_H}{\varepsilon_H\varepsilon_0}\times\frac{d^2|\sigma|}{dE^2_{ox}}, \qquad \frac{d^2|\sigma|}{dE^2} < 0 \tag{15}$$

These equations suggest that the $\sigma(E)$ dependence should be of the form

$$\sigma(E) = \sigma^0 + a_\sigma E_{ox} - 1/2\times bE^2_{ox} \tag{16}$$

It is evident from comparison of eq.(16) with (13) that

$$a_\sigma = \varepsilon_{ox}\frac{d_H}{\varepsilon_H} \qquad \text{and from (12)} \qquad \sigma^0 \sim \exp\frac{e\varphi^0_{x/sol}}{kT}$$

Formally, the quantity a may be included in a_x, and the latter may be considered as the effective activation distance for the MeO^- - defect transport from IHP into the oxide bulk. It also follows from (16) and (13) that the absolute value of the equilibrium field of anodization E_{ox} at ~ j=const will be increased with increase in the electrolyte concentration.

Young's results treated by Dignam as well as similar data by E.Khanina [5] allow to obtain the value of $d\sigma/dE_{ox}$ and the relationship between σ and E_{ox}, as well as the dependence of σ on the electrolyte concentration. The charge σ turned out to be negative in accordance with eq.(10), with its absolute value increasing with increase in the electrolyte concentration (see the Table).

Electrolyte	0.1 M H_2SO_4	0.33 M H_3PO_4	14.7 M H_3PO_4
$\sigma\times10^2$ Coul/m^{-2}	- 13.8	- 15.1	- 17.5

The above analysis of the processes at the oxide/electrolyte interface indicates that Young's non-linear relationship represents a specific case of non-linear kinetic relationships characteristic of a number of electrochemical systems.

DISSOLUTION OF ANODIC OXIDE FILMS

Generally, two types of dissolution of anodic oxide films are distinguished: chemical dissolution, the rate of which is independent of whether the electrode is polarised or not, and polarization-dependent dissolution which can be called as "electric field-assisted dissolution". In most cases, on analysing dissolution processes an oxide is treated as an ionic crystal, the dissolution of which is diffusion controlled. We do not consider this mechanism to be well-founded since, practically, there are no free ions in amorphous AOF. In amorphous materials with a large portion of covalent bonds, the dissolution rate must be controlled by heterogeneous surface reactions and the process cannot be a diffusive one [6,7]. Let us use these notions for describing the process of dissolution of AOF with barrier-type AOF on aluminium taken as an example, since their dissolution has been studied well enough. Dissociative adsorption of water takes place on the surface vacancy bonds on the aluminium ($AlO^{+}_{2/2}$) and oxygen ($AlO^{-}_{4/2}$) atoms, and the bonds will be neutralized by the H^{+} and OH^{-} ions, i.e. the surface of AOF turns out to be one-side hydrated. With the adsorption of water going on, hydration of separate surface areas will enhance. Hydration of separate surface structural units cannot be discounted either.

As a result of hydration, surface aluminium and oxygen atoms as well as separate surface structural units acquire additional energy and turn out to be activated complexes. Once the energy of such a complex is higher than the energy of a chemical bond keeping it on the AOF surface, the complex proceeds into the solution dissociating into a hydrated ion of aluminium and water. Since vacancy bonds on the noncoordinated metal and oxygen atoms take part in the initial hydration process, equivalent amounts of these atoms proceed to the solution. Once the process is completed, similar vacancy bonds will be available on the surface remained and the dissolution process will go on. This process can be considered as a monomeric reaction and the dissolution rate will be determined by the equation [8]

$$V = -\frac{1}{S}\times\frac{dn_S}{dt} = n_S \nu \frac{F_a}{F_S}\exp\left(-\frac{W_a}{kT}\right), \qquad (17)$$

where n_S is the surface adsorption centres concentration (since the AOF surface is electroneutral on the whole, the surface concentrations of the $AlO^{+}_{2/2}$ and $AlO^{-}_{4/2}$ centres are equal); ν is the frequency of the activated complexes dissociation, F_a and F_S are the sums of the states of activated and chemisorbed particles, W is the activation energy for dissolution. According to Golubev's data [9], the activation energy for dissolution of Al_2O_3 AOF in aqueous acids is in the range of 67-71 kJ/mole and is slightly different from the W_a values found during dissolution of other oxides.

At anodic polarization of a metal, two reactions take place: the oxide layer formation and its dissolution. During field-assisted dissolution, as in the case of chemical dissolution, transfer of the aluminium ions to the solution and their hydrati-

on will take place on separate surface areas of AOF (4). But, unlike for chemical dissolution, vacancy bonds on the oxygen atoms, $AlO^{-}_{4/2}$, will remain on the surface in this case, and these will be transported by field to the metal/oxide interface and recombine there. This dissolution reaction will be compensated by new oxide layer formation at the metal/oxide interface resulting from "vacancies" ($AlO^{+}_{2/2}$) formation, similar to reactions (2) and (3) compensating removal of such defects from the AOF surface as a result of the hydration and dissolution reactions. Consequently, under the steady-state conditions, the thickness of the undissolved part of AOF will remain unchanged. Ionic dissolution current

$$j_{sol} = j_{sol}\exp\left(-\frac{\Delta H}{kT}\right)\exp\frac{3ed_H}{kT}\left(\frac{\varepsilon_{ox}}{\varepsilon_H}E_{ox} + \frac{|\sigma|}{\varepsilon_0\varepsilon_H}\right) \qquad (18)$$

where ΔH is the heat of the dissolution reaction.

The dependence of the dissolution rate on the average field strength, or on the variation of the polarization potential of the aluminium /AOF/ electrolyte system, correlates fairly well with the data by Goroch et al. provided in semilog coordinates (Fig.5).

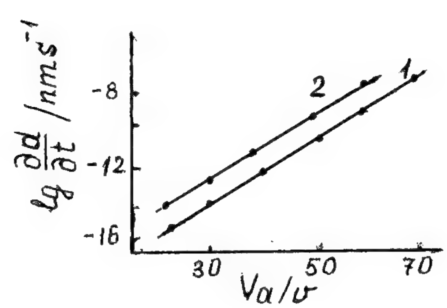

Fig.5. The rate of dissolution (thickness variation) of an anodic Al_2O_3 film during anodization in the oxalic acid as a function of anodizing potential φ_A. Acid concentration: (gm×ion×l^{-1}) 1-0.04; 2-0.1 [10].

The total current j flowing through an Al/AOF/electrolyte system will be represented by the sum of the oxide layer formation and dissolution currents, $j=j_A \times j_{sol}$. It has been established by Thompson [10] that there exists a limiting value of the anodization current above which the rate of the AOF formation is practically not influenced by the dissolution of AOF. This seems to be valid at $j_{sol} \ll j_A$. It follows from (13) and (18):

$$\frac{j_{sol}}{j_A} = \left[1 + \mathrm{const}\times\exp\frac{e}{kT}\left(a_x E_{ox} + \left(3\frac{\varepsilon_{ox}}{\varepsilon_H}d_H E_{ox} + \frac{2d_H}{\varepsilon_0\varepsilon_H}|\sigma|\right)\right)\right]^{-1}. \qquad (19)$$

It is evident from the equation that the limiting current condition may be reached by increase in an average field E_{ox} and must be dependent on the HL structure at the AOF/electrolyte interface as well as, through E_{ox}, on the absorption properties of the oxide and the electrolyte composition and concentration.

Electronic current in a metal/oxide/electrolyte system. As stated in [12], electron injection in anodic layers is determined

by desorption of OH^- - groups chemisorbed at IHP.

$$2MeOH_{ox} \rightarrow MeO_{ox} + 1/2 \times O_2 + H_2O_{sol} + e_{ox} \qquad (20)$$

The electron level on a chemisorbed OH^- - group may be determined from a simple thermodynamic cycle: let us transfer an OH^- - group from IHP to uncharged vacuum. Then the work would be equal to the heat of chemisorption ΔH_{OH} . If we detach an electron from a free OH^--ion, the work would be equal to the electron affinity ζ of an OH-molecule. Let us transfer this molecule back to the oxide surface. The energy released in this case would be equal to the heat of physical adsorption ΔH_{ads} of the OH-molecule on the oxide surface. If we transfer an electron from vacuum to the bottom of the oxide conduction band, the energy χ_{ox} of the electron affinity of the oxide would be released.

The electron level on a chemisorbed $MeOH_{ox}$-group seems to be:

$$\varphi = \Delta H_{OH} + \zeta - \Delta H_{ads} - \chi_{ox} \qquad (21)$$

Rough estimation of φ from (21) for a Ta_2O_5/electrolyte system [13] has shown that the electron level on a chemisorbed OH-group is 1.34 eV lower than the bottom of the oxide conduction band, i.e. the oxide/electrolyte contact is a blocking one and electron injection occurs only by tunneling into local levels in the forbidden band of the oxide. For more detailed consideration of the mechanism of electronic conduction in a metal/oxide/electrolyte system see [12].

CONCLUSION

The three processes, namely, anodic film formation, its dissolution and electron injection in an oxide layer, depend on the structure of HL at the oxide/electrolyte interface and on the processes going on in this layer.

REFERENCES

[1] L.Young, Proc.Roy.Soc., Lond., A258, 496 (1960)
[2] L.Odynets, Fizika okisnych plenok (Oxide Films Physic.) Part.I., Petrozavodsk Univ., 1979
[3] L.Odynets and V.Orlov, Anodnye oksidnye plenki (Anodic Oxide Films), "Nauka", Leningrad, 1991
[4] M.Dignam Oxide and Oxide Films, M.Dekker, Ink., N 4, 1, 91 (1978)
[5] E.Ya.Kchanina, Anodnye okisnye plenki (Anodic Oxide Films), Petrozavodsk Univ., 138 (1978)
[6] R.MБller, Chimia tverdogo tela (Solid State Chemistry), Leningrad Univ., 9 (1965)
[7] S.Repinski, Uspechi chimii (Success of Chemistry), 52, 922 (1983)
[8] S.Glastone, K.J.laidler, H.Eyring, Die Theorie der Ratenprozesse, McGraw-Hill, Book Co., N4, 1941
[9] A.I.Golubev, Anodnoe okislenie alyuminievych splavov (Anodic Oxidation of Aluminium Alloys), Izdat.Akad.Nauk USSR, 1961

[10] V.F. Surganov, G.G.Goroch, Journal prikladnoy chimii (J.of Applide Chemistry), 16, 156 (1968)
[11] Thompson, Y.Xu, P.Skeldon, S.H.Han and G.C.Wood, Phys.Mag. B.55, 661 (1987)
[12] L.L.Odynets, E.Ya.Kchanina, S.S.Tchekmasova, Sov.Electrochem., 19, 181 (1983)
[13] V.A.Laleko, L.L.Odynets - this Journal, p.

Materials Science Forum Vols. 185-188 (1995) pp. 563-572

Kinetic electronic phenomena in metal oxide dielectric films

S.D. Khanin

GIRICOND Scientific & Research Institute, 10 Kurchatov Street,
St. Petersburg, 194223 Russia

Keywords: Anodic oxide layers, hopping conduction, polarons, low carrier mobility, localized states

Abstract. The picture of charge transport in amorphous tantalum and niobium oxides is worked out and a number of experimental techniques for investigating the electronic properties of disordered dielectrics are suggested.

Wide application of amorphous metal oxides in various fields of modern technology caused intensive investigations of their fundamental electronic properties. We investigated and described the nature of the kinetic electronic phenomena in amorphous tantalum and niobium oxides (a-Ta_2O_5, a-Nb_2O_5) in different and widely varying environments and the influence of structural defects on the electronic properties of the materials under study.

The experiments were performed on anodic oxide layers of high uniformity with a nearly stoichiometric composition in model capacitor structures prepared using a laboratory process. It has been specially shown that transport processes in such layers are determined by the bulk properties of the oxide dielectric.

An analysis of electronic kinetic phenomena has shown that the charge transport in a-Ta_2O_5 is of a non-Boltzmann type as attested in particular by the following experimental evidence [1- 3]:

(i) A temperature dependence of static conduction with an activation energy slipping with decreasing temperature and described by the $T^{-1/4}$ Mott law in the low temperature region (Fig. 1).

(ii) A field dependence of d.c. conductivity exhibiting a section where γ decreases with increasing E prior to exponential increase in γ (Fig. 2).

(iii) A non-activation behavior of low-temperature conductivity in strong field and its field dependence obeying the $E^{-1/4}$ Shklovsky law (Fig. 3).

(iv) An nth power frequency dependence of a.c. conductivity in lower frequency range (Fig. 4) where the conductivity due to transport of free charge carriers should be frequency-independent.

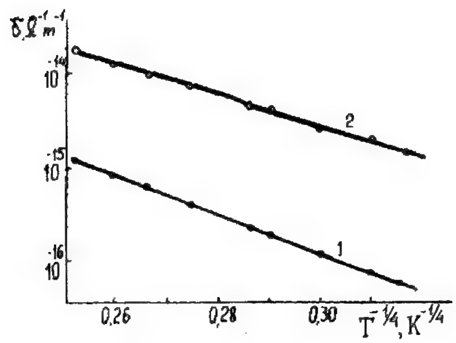

Figure 1 Temperature dependence of static conduction in amorphous tantalum (1) and niobium (2) oxides for lower-temperature region.

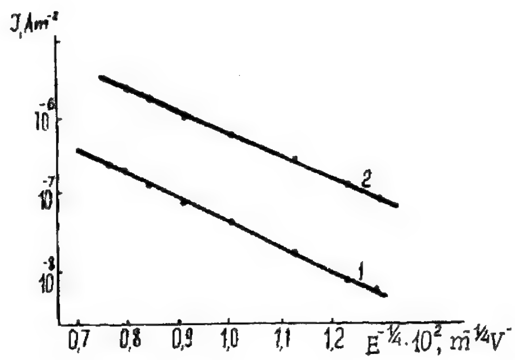

Figure 3 Field dependence of the static conductivity of tantalum (1) and niobium (2) oxides for temperature 150 K.

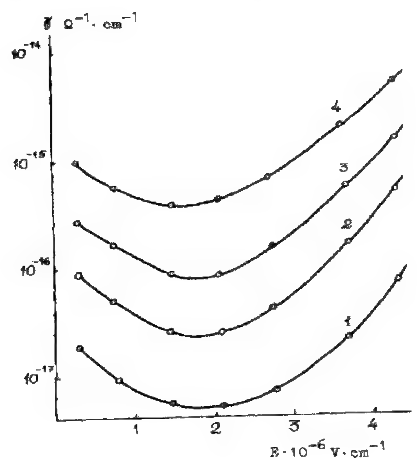

Figure 2 Tantalum oxide conductivity vs. field strength for different temperatures: 298 K (1), 323 K (2), 343 K (3), 363 K (4).

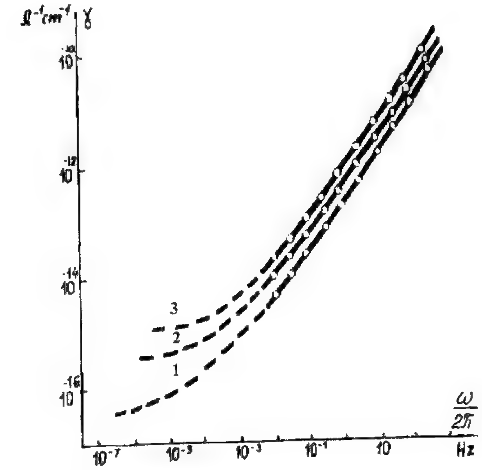

Figure 4 Frequency dependence of a.c. conductivity for amorphous tantalum oxide film without bias for different temperatures: 298 K (1), 325 K (2), 353 K (3).

The experimental results obtained have led to the assumption of a hopping mechanism of the conduction in amorphous metal oxide dielectric. Electron transitions here are phonon-assisted jumps of charge carriers between localized states. In a range of relatively high temperatures, charge transport is effected on the energy level corresponding to the maximum density of localized states whereas in a lower temperature range, near the Fermi level, which accounts for the observed changes in the behavior of conductivity with decreasing temperature.

The effect of a decrease in conductivity with increasing field is due to a change in charge transport paths and is inherent in disordered systems with strong electron-phonon interaction[4].

D.c. hopping transport in disordered systems is effected along one-dimensional, optimum (regarding the least resistance) paths which interconnect the electrodes. In the ohmic voltage range, there are returns in current paths where charge carriers move in the direction opposite to that determined by an external field. In the strong field range, the probability of jumps in a counter-field direction in disordered dielectrics with strong electron-phonon interaction drastically decreases because of an increase in the potential barrier for a jump. The former current paths cease to be optimum and rearrange themselves so as to exclude returns. This comes about through the closing of current paths` dead ends. Both of the factors cause a decline in conductivity with increasing field strength. With a transition from an isotropic to a directed flow, a decrease in the potential barrier for charge carriers` jumping in the direction determined by an external field becomes the factor that governs the field dependence of conductivity.

In systems with strong electron-phonon interaction (small-radius polarons), the probability of a site-to-site jump is given by

$$P = P_0 \cdot \exp\left(-\frac{E_a}{kT} + \frac{e \cdot E \cdot R}{2kT}\right) \qquad (1)$$

where E_a = energy of a site-to-site polaron jump, R= jump length, T= temperature, k = Boltzmann`s constant, $P_o = I^2/(\pi\ E_a\ kT)$ in a non-adiabatic regime (I= resonant integral), P_o = frequency of optical phonons in an adiabatic regime. Using the cluster technique [4], it has been shown that the field and temperature dependence of conductivity is here of the form

$$\gamma(E,T) = \gamma(0,T) \cdot f(E/T) \qquad (2)$$

where γ (0,T) = ohmic conductivity of the material,

$$f(E/T) = \exp\left[-2\alpha R_c\left(\frac{e\cdot E}{\alpha kT}\right)^{1/v'} + \frac{eR_cE}{3kT}\right] \qquad (3)$$

Herein α^{-1} = radius of the localization of electronic states, R_c = critical jump length, v`= scaling parameter.

Using the data obtained, the density N of localized states in tantalum oxide and the radius of electronic states localization α^{-1} have been restored to be of the order of 10^{19} cm^{-3} and 0,1 nm, respectively, the latter estimate having been obtained from independent experiments in determining the low temperature conductivity and the field strength corresponding to the minimum non-ohmic conductivity in the range of relatively high temperatures. Also, the scaling parameter has been estimated at 1.2 to 1.4 that agrees with numerical calculations.

The behavior of the non-stationary conductivity of oxide is explicable in the framework of a model of hopping transport within clusters of limited size [4]. With decreasing a.c. signal frequency, or, which is equivalent, with increasing d.c. voltage duration, the size of a cluster of states involved in transport increases, a transition to the regime of multiple jumps (the so-called multiplet hopping conduction) takes place and, for the longest times, where it comes to the least probable, critical hopping in the current path, which hopping closes the interelectrode space static conduction sets in.

In agreement with those concepts are the experimental evidences of an enhancement of the voltage, temperature and field effect on the non-stationary conductivity of oxides with increasing duration of the indicated factors[5].

A theoretical analysis of the non-stationary conduction in amorphous metal oxides has enabled the picture of charge transport to be worked out in detail and a number of experimental techniques for investigating the kinetic properties of disordered high-resistance materials to be suggested including the determination of dynamic hopping conduction regimes, strong electron-phonon interaction and low carrier mobility.

Consider the a.c. conductivity of a disordered dielectric with a strong electric field applied from a field range where the conductivity decreases with increasing E[6]. In the lower frequency range where the size of the cluster of states involved in transport is large enough, the above strong-field effects are preserved. They take place up to a boundary frequency where the cluster size becomes too small for strong-field-induced changes in current flow to affect essentially the non-stationary conductivity.

Because $\gamma(\omega,E) < \gamma(\omega,0)$ for $\omega < \omega_o$ and $\gamma(\omega,E)= \gamma(\omega,0)$ for $\omega>\omega_o$ the frequency dependence of $\gamma(\omega,E)$ is enhanced as compared to that of $\gamma(\omega,0)$ and becomes superlinear.

It is reasonable to assume that, in the presence of a d.c. bias in a frequency range where the cluster size is large enough, the a.c. conductivity may be given by

$$\gamma(\omega,E) = \gamma(\omega,0)\cdot g\left(\frac{e\cdot E\cdot L}{kT}\right) \qquad (4)$$

Herein, g = dimensionless function of barometric parameter $x = eEL/kT$, where L = state cluster size within which hopping transport is effected in a non-stationary regime, $g(x) \to 1$ for $x \to 0$.

The boundary frequency ω_o is then determined from the equation

$$\frac{c\cdot e\cdot E\cdot L(\omega_0)}{kT} = 1 \qquad (5)$$

(c = numerical factor).

Considering the L vs. ω dependence for multiplet hopping conduction [4], we arrive at the analytical expression for the frequency ω_o

$$\omega_0 = P_c\cdot\exp\left[\alpha\cdot N^{-1/3}\cdot\left(\frac{c\cdot e\cdot E\cdot N^{-1/3}}{kT}\right)^{2/l}\right] \qquad (6)$$

Herein, P_c = probability of a critical jump in an endless cluster, which probability determines the static conduction, N = density of localized states, l= index equal to 1 in the effective medium approximation and to 2ν or $2\nu - \beta$ in scaling theory (ν=0.9 and β=0.4 are the critical indices of the correlation length and power of an endless cluster, respectively).

The expression obtained shows in particular that the temperature dependence of boundary frequency is determined by that of critical jump probability. In the case of strong electron-phonon interaction where P_c increases with T following the activation law for a high activation energy, this factor may become predominant and ω_o may increase with T. It follows from the above that the direction of a shift in ω_o with varying temperature provides an indication of the presence of strong electron-phonon interaction in a disordered dielectric.

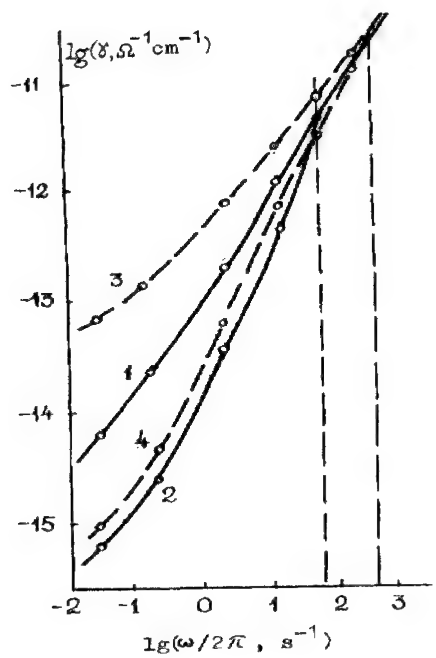

Figure 5 Frequency dependence of a.c. conductivity for tantalum oxide film, 170 nm thickness, without bias (1,3) and with 50 Vd.c. (2,4) for different temperatures: 298 K (1,2), 358 K (3,4).

Starting from the above, the following experimental technique has been suggested. The frequency dependencies of the a.c. conductivity of a disordered dielectric are determined with and without a d.c. bias in the range where the non-ohmic conductivity decreases with increasing field. The boundary frequency is found at which these dependencies are coincident. The measurements are made at different temperatures. And the presence or absence of strong electron-phonon interaction is judged by the direction of the shift of the boundary frequency with varying temperature.

The experimental results obtained for amorphous tantalum oxide point to the presence of strong electron-phonon interaction (Fig. 5).

The technique suggested for determining the low mobility of charge carriers in disordered dielectrics is based on the photo memory effect experimentally discovered in amorphous tantalum oxide[7]: optical excitation of the dielectric gives rise to a maximum in the frequency dependence of the loss tangent in the infrasonic range, which maximum increases in magnitude and shifts toward lower frequencies with time (Fig. 6). To explain this effect, a model has been developed which takes into account the non-uniformity of optical excitation, i.e. the generation of non-equilibrium charge carriers in the surface layer of thickness d_l, which results in a non-uniform conduction in the dielectric[8]. This non-uniformity accounts for the fact that the frequency dependence of tgδ exhibits an extremism. The observed evolution of this dependence with time is associated with the propagation of charge carriers into the bulk of the specimen.

For the value of tgδ at a maximum, the expression $(tg\delta)_{max} = A\, d_l/d$ has been obtained [8]. Herein, d = the width of the specimen, factor A obtains from the conductivity distribution function for the charge-carrier-enriched region of the dielectric, $f(x/d_l)$, as $A = \int_0^\infty dz \cdot \frac{f}{f^2 + c^2}$

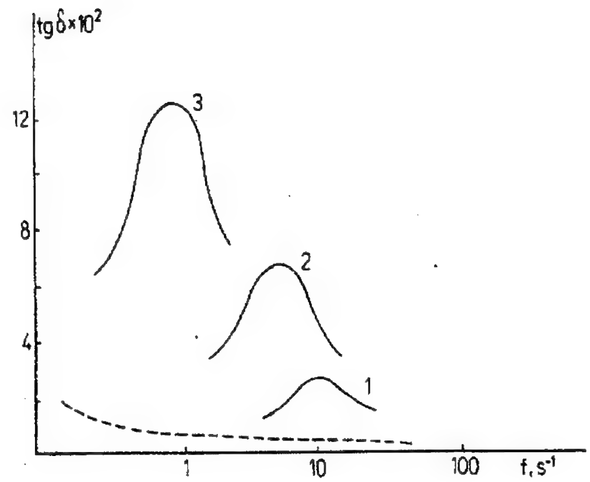

Figure 6 Frequency dependence of tg δ for amorphous tantalum oxide at few observation times after irradiation: t=0 (1), 30 min (2), 17 hours (3). The dashed line represents the frequency dependence of a "shadow" tg(d).

And the value of c is determined from the equation

$$\int_0^\infty dz \cdot \left[f \cdot \left(f^2 - c^2\right) / \left(f^2 + c^2\right)\right] = 0$$

In the model of a two-layer dielectric wherein f(z) is a step function (f(z) is equal to 1 for z<1 and to 0 for z>1), A=1/2 with certain limits set on the parameters [8].

Because $(tg\delta)_{max}$ is proportional to the width d_l of the region enriched in non-equilibrium charge carriers, it is possible to determine the charge carrier mobility from the slope of a linear section of the curve representing $[(tg\delta)_{max}]^2$ as a function of time elapsed after injection of an electronic packet.

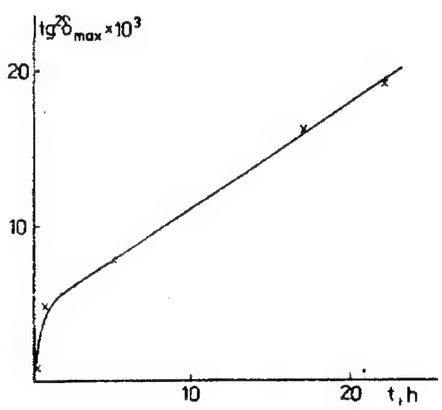

Figure 7 $tg^2\delta_{max}$ vs. time for amorphous tantalum oxide.

The mobility thus evaluated for tantalum oxide at room temperature (Fig. 7) is of the order of 10^{-15} $cm^2/V.s$. Also, the mobility has been found to increase with temperature obeying an activation law. The data obtained agree with the other results of the work on hopping transport in amorphous tantalum oxide, including long-term relaxation of an electret state due to the screening of the surface charge of injected carriers by intrinsic charge carriers [9].

The ultralow mobility in $a\text{-}Ta_2O_5$ is closely related to the very small radius of localization of carriers, which is of 1 A . The resonance integral I, determined by the overlap of the wave functions of the adjacent centers, is proportional to $\exp(-\alpha R)$ and the mobility is in turn proportional to I^2. At such low values of the localization radius the nature of the temperature dependence of the hopping electrical conductivity may be influenced by

the dependence of the resonance integral on the amplitude of the lattice vibrations [10].

A calculation of the hopping electrical conductivity was made using the model of small polarons and allowing for the influence of thermal lattice vibrations on the resonance integral (ultrasmall polarons). The result of this calculation is

$$\ln\left(T^{3/2}\cdot\gamma\right) = A - E_a/kT + kT/\varepsilon \qquad (7)$$

where $\varepsilon = kT/2\alpha^2\overline{\rho^2}$, $\overline{\rho^2}$ = root-mean-square displacement of atoms, A = temperature-independent term. The obtained refinement of the temperature dependence of conductivity is essential on condition that $\alpha^2\overline{\rho^2}\geq 1$, i.e. for a very small localization radius (ultrasmall polarons).

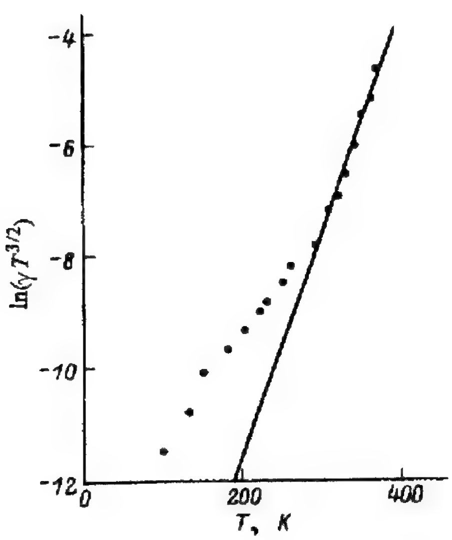

Figure 8 Dependence of ln(γ $T^{3/2}$) on temperature for amorphous tantalum oxide film. The parameter ε is estimated from the slope of the continious straight line.

The experimental temperature dependence of conductivity for a-Ta_2O_5 is adequately represented by the foregoing equation (Fig. 8), α^{-1} being estimated from experimental data at about 2A.

For the purpose of identifying the nature of electronic states through which hopping transport is effected, experimental and theoretical studies on the energy spectrum of electronic states in amorphous tantalum oxide have been undertaken [11-13]. As the result of the studies performed, models of the electronic structure of a-Ta_2O_5 have been suggested which relate the electronic states in the forbidden band (mobility gap) of amorphous metal oxide to the structural defects characteristic of the material studied. Among such defects are:

(i) Short-range fluctuations, i.e., local regions with a larger metal-oxygen interatomic spacing and a lower metal coordination number as compared to the matrix. It follows from the results of the cluster modeling of the electronic spectrum that the presence of structural defects of this type (micro-heterogeneity) gives rise to the occurrence, in the mobil-

ity gap of a metal oxide, of metal's electronic states whose density increases as the bulk concentration of regions with rarefied atomic structure increases [12].

(ii) Defects due to oxygen deficiency non-stoichiometry in oxide composition. X-ray photoelectron spectroscopy and electronic spectrum modeling show that, in this case, states relating to a metal in a non-ultimate oxidation state occur in the mobility gap [11, 13].With increasing concentration of the metal's low-valent cations, the conductivity of amorphous tantalum oxide increases exponentially (Fig. 9).

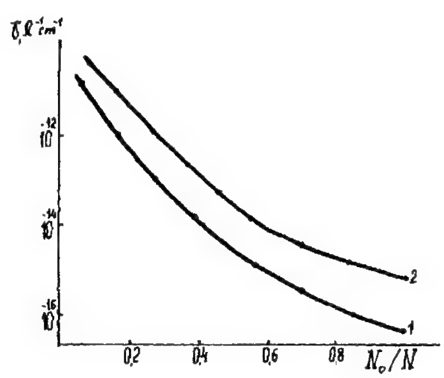

Figure 9 Effect of non-stoichiometric defects on static conductivity of tantalum (1) and niobium (2) oxides.

Starting from the above the following approaches to improving the insulating properties of tantalum oxide films has been suggested: (i) ordering (densification) of the structure of amorphous oxide and (ii) stabilization of higher metal oxidation degrees.

A general result of this study consists in the establishment of the mechanisms of the electronic processes of charge transport in amorphous tantalum oxide, which opens up new means for improvements in capacitors and for an analysis of the kinetic properties of a large class of disordered dielectrics.

References

[1] V.V.Bryksin,M.N.Dyakonov, and S.D.Khanin,Fiz.Tverd.Tela 22, 1403 (1980) [Sov.Phys.Solid State 22, 818 (1980)].

[2] V.V.Bryksin, A.V.Goltsev, S.D.Khanin, A.V.Novotelnova, and A.N.Vasilev, Phys.Status Solidi B 161, 771 (1990).

[3] S.D.Khanin, Problems of the Electrophysics of Metal Oxide Capacitor Dielectrics, Reviews of Eleectronic Technology, 5, 1 (1990)

[4] H.Böttger, and V.V.Bryksin Hopping Conduction in Solids, Akademie Verlag, Berlin (1985),p.398.

[5] V.V.Bryksin,M.N.Dyakonov,V.M.Muzhdaba, and S.D.Khanin, Fiz. Tverd. Tela, 24,2682 (1982).

[6] V.V.Bryksin, L.G.Karpukhina, and S.D.Khanin, Fiz.Tverd. Tela 32, 3564 (1990).

[7] M.N.Dyakonov, L.G.Karpukhina, V.M.Muzhdaba, and S.D.Khanin, Pisma Zh.Tekhn.Fiz. 8, 1186 (1982).

[8] V.V.Bryksin, A.V.Goltsev, and S.D.Khanin , Phil.Mag. B64, 91 (1991).

[9] V.V.Bryksin, S.N.Dorogovtsev, M.S.Morgunov, and S.D.Khanin, Fiz. Tverd. Tela 33,2031 (1991).

[10] V.V.Bryksin and S.D.Khanin, Fiz.Tverdogo Tela 35, 2266 (1993) [Sov. Phys. Solid State 35, 1126 (1993)

[11] Yu.P.Kostikov, D.V.Kostrov, G.F.Tomilenko, and S.D.Khanin, Zh.Tekhn. Fiz. 53,2189 (1983).

[12] A.L.Gubsky, and S.D.Khanin, Fiz.Tverdogo Tela 32, 2278 (1990).

[13]S.D.Khanin and A.L.Ivanovskii, Phys.Status Sol. B174, 449 (1992).

Materials Science Forum Vols. 185-188 (1995) pp. 573-580

Structure inhomogeneities of the oxide dielectric and the properties of tantalum capacitors

S.D. Khanin

GIRICOND Scientific & Research Institute, 10 Kurchatov Street, St. Petersburg, 194223 Russia

Keywords: Structural defects, conductivity, dielectric spectroscopy, loss tangent, excess noise, injection current

Abstract. The paper presents a number of experimental techniques for detecting in amorphous tantalum and niobium oxide films structural defects, which accelerate film destruction processes in a strong electric field and thus are potentially dangerous under prolonged thermoelectric stresses applied to capacitor structures.

In the bulk of the dielectric anodic film and in the vicinity of the interface between the same and the tantalum (niobium), there are structural defects which create channels of increased conductivity and effect the leakage current of tantalum capacitors. The nature, concentration and electrical activity of the structural defects of an anodic film are determined by the composition and structure of the surface layer of the tantalum, the conditions of formation of the oxide layer, the material and the method of formation of the cathode material.

In the course of electrothermal loading of tantalum capacitors, under certain conditions, biographic structural defects of the oxide layer develop, which, in addition to an integrated increase in the conductivity of the dielectric and the occurrence in the same of additional leakage channels, results in irreversible loss of the films electrical insulation properties and in a failure of the capacitor.

Presented below are a number of experimental techniques for detecting, in an amorphous oxide dielectric, structural defects which accelerate film destruction processes in a strong electric field and thus are potentially dangerous under prolonged thermoelectric stresses applied to capacitor structures. These techniques are based on structure-sensitive electrical phenomena in amorphous metal oxide dielectrics.

The kinetics of the processes of electrical destruction determines the reliability of oxide dielectric capacitors. The processes of electrical destruction take place in one of the two forms, viz., a breakdown of the oxide dielectric in capacitor structures whose counterelectrode is constituted by a solid phase material (metal, semiconductor or solid electrolyte), or an electrically stimulated growth of metal oxide crystals in metal-oxide-electrolyte capacitor structures [1].

As a result of studying the breakdown of a highly homogeneous oxide dielectric it has been shown that such a breakdown is preceded by storage processes (dielectric aging). This conclusion is based on the following body of experimental evidence [1-3]:

(i) Breakdown development over a range of electric field strengths in a time interval determined by electric stress conditions.

(ii) Comparison of experimental data on the ramp slope dependence of the dielectric strength, E_{br} of oxide dielectrics subjected to a ramp voltage, E, to data calculated from the field dependence of breakdown development time, $\tau(E)=A\exp(BE)$, the experimental values of E_{br} being coincident with those calculated from the equation which follows from the principle of storage of disturbances.

(iii) Breakdown of an oxide dielectric subjected to a train of rectangular voltage pulses the duration of each of which is less than the breakdown development time of the dielectric in specified electric stress conditions.

Using X-ray diffractometry, structural changes have been revealed in amorphous tantalum oxide in a pre-critical state which point to partial reduction of the oxide. These changes are a decrease in the coordination number of the metal and an increase in the metal-oxygen interatomic spacing. The time dependence of current in the breakdown development process in amorphous metal oxides is similar to that previously established for titanium oxide whose aging is caused by anionic transport. A decrease in the activation energy for breakdown development as a result of thermal reduction treatment of the oxide and an accelerated growth of metal oxide field crystals in breakdown channels are obtained. The anionic transport involved in the breakdown development process leads to oxygen depletion of the oxide and, as a result, to an exponential increase in the conductivity of the dielectric and to a positive space charge arising in the dielectric region near the electrode (with uncompensated extraction of oxygen from the oxide) and creating an additional electric field. The latter may be critical for the stability of the structure of the oxide itself and for the injection of excess charge carriers into the oxide.

Analyzing the kinetics of the process of electrically stimulated metal oxide crystal growth, the paper presents the results of an experimental study of the time dependencies of the crystallinity $\eta(t)$ of oxide films and the ionic current $i(t)$ flowing in the capacitor structure as crystalline formations grow radially (Fig. 1,2) [4,5]. It has been shown that they may be described in the framework of a model for the two-dimensional growth of crystalline formations at a specified number of centers in the form

$$\eta(t) = 1 - \exp(-\pi\beta v^2 t^2) \qquad (1)$$

$$i(t) = 2\pi q v^2 t \cdot \exp(-\pi\beta v^2 t^2) \qquad (2)$$

Herein, η = area fraction of crystalline phase, β=crystallization center density at the metal surface, v = radial growth rate of crystalline formations, q = charge required to form a crystalline metal oxide at a unit surface area of the metal.

Equation (1) corresponds to general nucleation theory [4] for the above mentioned model. The observed deceleration of the process and a maximum in the time dependence of current are due to geometrical overlapping of crystalline areas.

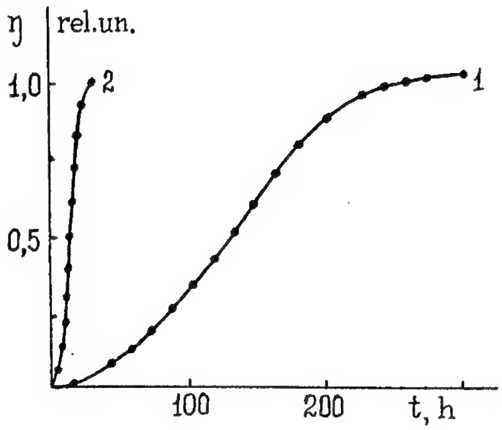

Figure 1. Time dependence of the crystallinity of tantalum (1) and niobium (2) oxide films.

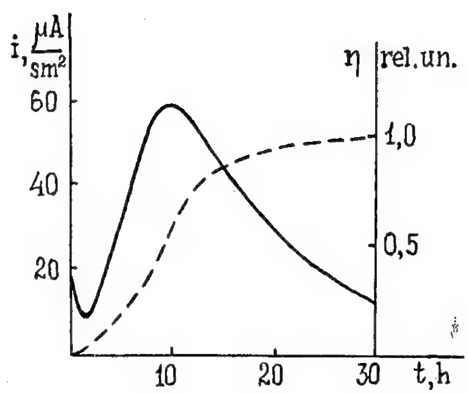

Figure 2. Time dependence of ionic current in the process of growth of oxide crystals for niobium oxide film.

Using the experimental data on $\eta(t)$, the slope of I (t) on an initial section and the coordinates of the maximum of the current for Ta_2O_5, we have obtained convergent estimates of the radial growth rate v [5].

Starting from the kinetic data obtained, experimental techniques have been developed for evaluating the stability of an oxide dielectric against destruction in a strong electric field and, accordingly, the lifetime of capacitor structures. Thus, the rate of electrically stimulated growth of metal oxide crystals may be estimated from the initial slope of the ionic current vs. time curve and the coordinates of the maximum in the time dependence of current.

The formation, in an oxide layer, of a crystalline phase and its area fraction at an early stage of electrical destruction may be checked against the electronic conductivity of the dielectric. This technique uses as the basis the experimentally established relationship between the electronic conductivity of an aged amorphous-crystalline oxide film and the concentration of the crystalline phase (Fig. 3), which relationship is described in the framework of the parallel connection model for the resistances of the amorphous and crystalline regions of the film, so that

$$I_{ac} = I_a \cdot \left[(A-1) \cdot \eta + 1 \right] \qquad (3)$$

Herein, I_{ac} = density of the current flowing through amorphous-crystalline oxide film, I_a = density of the current flowing through the amorphous region of the dielectric, A = ratio of the current densities between the crystalline and amorphous regions of the dielectric.

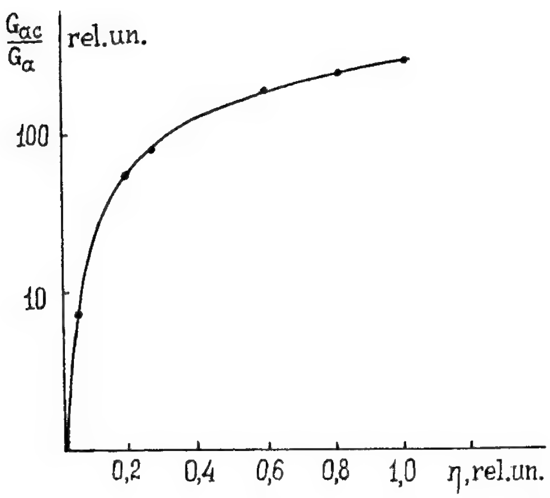

Figure 3. Crystallinity dependence of electronic conduction of amorphous-crystalline tantalum oxide.

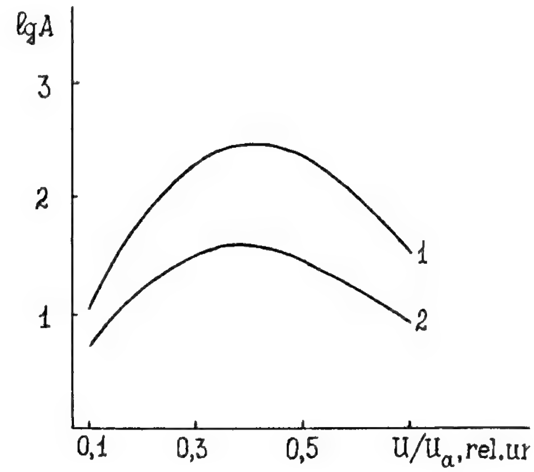

Figure 4. Voltage dependence of conductivity ratio between crystalline and amorphous oxide for tantalum (1) and niobium (2) oxides. U_a = the anodization voltage of the metal.

The ratio of the conductivities between the crystalline and amorphous oxides, i.e. the value of A, has been shown experimentally to be especially large for a voltage corresponding to the minimum in the field dependence of the non-ohmic conductivity of the amorphous metal oxide (Fig. 4). This is due to a qualitatively different behaviour of the non-ohmic conductivity of crystalline formations arising during a destruction process [6]. The field dependence of the conductivity of an amorphous oxide has a minimum whereas the conductivity of field crystals increases exponentially with increasing field in the whole voltage range. In this connection, the parameter informative for the diagnostics of phase inhomogeneity in an oxide dielectric is the value of the current flowing in the capacitor structure at an applied voltage equal to 0.3 to 0.4 of the anodization voltage U_a of the metal.

To clear up the microscopic picture of the electrically stimulated growth of metal oxide crystals, isotopic examinations were undertaken using O^{18} oxygen isotope in the formating or working electrolytes [7]. Using SIMS techniques, the in-depth concentration profiles of elements were taken separately for the amorphous and crystalline regions of an aged oxide film. The results obtained have shown that the O^{18} isotope content of the crystalline regions of an oxide is determined by that of the working electrolyte of capacitor structures. From this it follows that the process being considered practically proceeds without consumption of the

amorphous film material and is due to the reactive electrical diffusion of oxidizer particles towards the metal surface accompanied by the formation, at this surface, of a metal oxide crystalline phase.

The anionic transport process leading to the destruction of the oxide layer is structure-sensitive. This is confirmed in particular by the experimentally established fact that the growth of crystalline formations is considerably enhanced by increasing concentration of structural defects such as low-valent (underoxidized) metal cations in the amorphous oxide layer adjoining the metal. The formation of a crystalline phase may be represented in the framework of a picture involving the generation of structural defects and polycentric nucleation at the metal-oxide interface [7].

A dielectric's structural inhomogeneity such as a junction oxide layer of non-stoichiometric composition adjoining the metal results in a two-layer dielectric as regards conductivity. This inhomogeneity may be detected by means of dielectric spectroscopy. Of informative value is here the frequency dependence of loss tangent tgδ. In two-layer dielectrics this dependence has a maximum while oxide films in general feature a monotonic frequency dependence of tgδ [8].

Considering that structurally inhomogeneous sites are very likely to contain charge carrier trap centers, of interest to the diagnostics of oxide capacitor dielectrics are the measurements of tgδ at a fixed frequency with and without a d.c. voltage bias in a range where the conductivity of a disordered dielectric decreases with increasing voltage as well as data on excess noise associated with current flow through the dielectric [9,10]. It is to be expected that, in samples having potentially dangerous structural defects, tgδ considerably decreases with a d.c. field applied and the intensity of low-frequency excess noise increases.

Experiments have confirmed the reasoning presented here. Measurements of the loss tangent and the power spectral density of low-frequency excess noise in the infrasonic range make it possible to discern, at the manufacturing stage, among structures undistinguishable as regards standard capacitor fitness criteria, samples with the indicated anomalies in their properties such as a frequency dependence of tgδ having an extremum, a substantial decrease in tgδ with a d.c. voltage applied, and an increased power spectral density of excess noise as compared to that of most samples.

For an experimental verification of the usefulness of dielectric and electrofluctuation spectroscopy to find dangerous defects in amorphous tantalum oxide we prepared a series of oxide Ta samples by use of different technologies which imbed certain defects in the dielectric structure. Investigated samples were placed into an electrolyte (38% water solution of H_2SO_4). Then their electroparameters have been measured. It should be noted that the standard parameters (such as a leakage current, the capacity and tgδ at the industrial frequency) were the same for all of the samples and corresponded to the accepted norms for a capacitor dielectric. The frequency dependence of tgδ was determined in the range from 0.01 sec^{-1} to 100 sec^{-1} without and with a bias voltage. Noises of electrolytic capacitor structures were measured too. The voltage applied to capacitor electrodes was related to the minimum of the d.c. conductivity of amorphous tantalum oxide and the maximum of noise spectral density [10]. Measurements show that some of samples have the anomalies considered above that is (i) a maximum of a frequency dependence tgδ near 1 sec^{-1} (Fig. 5); (ii) strong decreasing tgδ at a fixed infrasound frequency on applying a permanent electric field to the dielectric; high density of the excess low-frequency noise (Fig. 6).

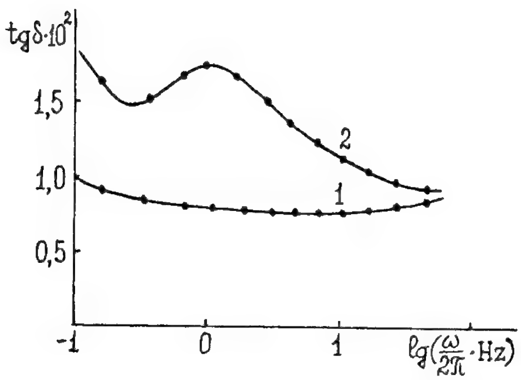

Figure 5. Normal (1) and abnormal (2) frequency dependence of tgδ for amorphous tantalum oxide.

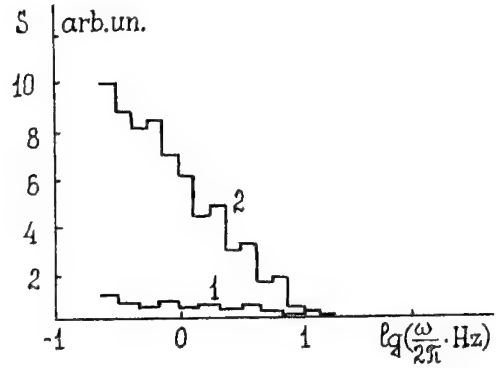

Figure 6. Normal (1) and abnormal (2) power spectral density of low frequency excess noise in amorphous tantalum oxide.

We have obtained that the anomalies have a stable relation to one of types ofstructure non-uniformities in the dielectric namely a thin transitional layer of non-stoichiometric composition lying on the interface between oxide film and basis metal. Some samples with randomly arranged structure defects within the oxide volume show such a frequency behavior of tgδ which does not possess the anomalies but have anomalously high intensity of the excess low-frequency noise. Result of long time tests of electrolytic capacitors under an electric load show that if a sample has anomalous low-frequency characteristics on the preparation stage then one possesses a tendency to increasing a leakage current with increasing time (Fig. 7). This fact results from a phase aging of the oxide film (an electrostimulated growth of the metal oxide crystals on the anode surface)[11-13].

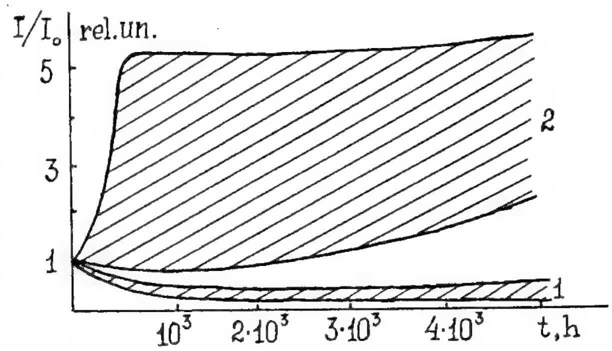

Figure 7. Leakage current regions for tantalum electrolyte capacitors under test. Capacitors with normal (1) and abnormal (2) low-frequency characteristics at manufacturing stage.

Oxide layer defects such as local thinnings where dielectric breakdown channels are very likely to form may be detected by measuring injection currents in the dielectric. This is associated with the high sensitivity of injection currents to film thickness and hence their localization at thinned sites. Electron- and proton-injection currents flow in case of cathode bias of an oxide in contact with a hydrogen-bearing counterelectrode material [14]. The passage of a proton-injection current leads to partial reduction of the tantalum and niobium oxides and, as a result, to a substantial increase in their conductivity. It has been shown experimentally that of informative value for the diagnostics of an oxide layer are the rate of current rise

with time at a sufficiently high cathode voltage of short duration or the very fact that the current increases with time at lower voltages.

In conclusion, the principles of testing the stability of oxide capacitor dielectrics have been developed and it was shown that the low-frequency dielectric and electrofluctuation spectroscopy may be considered as a perspective methods of a non-destructive control of the oxide capacitor quality.

References

[1] B.Yu. Gelikman, L.L. Kristalinsky, L.A. Stolov, and S.D. Khanin, The Principal Causes and Mechanisms of Capacitor Failures, Reviews of Electronic Technology, 8,3 (1989).

[2] S.D. Khanin, Problems of the Electrophysics of Metal Oxide Capacitor Dielectrics, Reviews of Electronic Technology, 5,1 (1990).

[3] I.V. Bei, M.N. Dyakonov, V.M. Muzhdaba, and S.D. Khanin, Fiz. Tverdogo Tela 26, 2265 (1984).

[4] P.W.M. Jacobs, Kinetics of Reactions in Ionic Systems, Plenum Press, New York, 1969.

[5] L.A. Aleshina, V.P. Malinenko, A.V. Novotelnova, and S.D. Khanin, Zh. Tekhn. Fiz. 56, 2253 (1986).

[6] V.A. Isayev, A.V. Novotelnova, and S.D. Khanin, Elektrokhimiya 27, 530 (1991).

[7] A.P. Kovarsky, A.V. Novotelnova, S.D. Khanin, and N.L.Chernius, Zh. Tekhn. Fiz. 58, 415 (1988).

[8] S.D. Khanin, Zeszyty Naukowe Politechniki Rzeszowskiej: Matematyka I Fizyka 13, 67 (1991).

[9] M.N. Dyakonov, Yu.S. Kapshin, V.M. Muzhdaba, V.A. Noskin, S.D. Khanin, and V.A.Yudin, Preprint LIYAF, Akad. Nauk SSSR,884 (1983).

[10] Yu.S. Kapshin, V.M. Muzhdaba,V.A.Noskin, M.M.Odintsova, and S.D. Khanin, Zh.Tekhn.Fiz. 56,1187 (1986).

[11] M.N. Dyakonov, V.M. Muzhdaba, I.V. Netupsky, and S.D. Khanin, USSR Inventors' Certificate, No. 762044 (1980).

[12] M.N. Dyakonov, V.M. Muzhdaba, I.V. Netupsky, and S.D. Khanin, USSR Inventors' Certificate, No.930406 (1982).

[13] M.N. Dyakonov, Yu.S. Kapshin, V.M. Muzhdaba, I.V. Netupsky, V.A. Noskin, and S.D. Khanin, USSR Inventors' Certificate, No 997113 (1983).

[14] G.M. Gusinsky, L.G. Karpukhina, V.M. Muzhdaba, G.F.Tomilenko, and S.D.Khanin, Fiz. Tverd.Tela 29, 3253 (1987).

Materials Science Forum Vols. 185-188 (1995) pp. 581-590

Preparation and properties of ultra thin anodic valve metal oxide films

A.W. Hassel and M.M. Lohrengel

Institut für Physikalische Chemie und Elektrochemie, Heinrich-Heine-Universität, D-40225 Düsseldorf, Germany

Keywords: Anodic aluminum oxides, ultra thin films, current transients, impedance spectroscopy, ionic conductivity

Abstract: Ultra thin (1-3 nm) oxide films on Al were prepared by electropolishing and investigated by different electrochemical techniques. The dielectric properties are equal, the film resistance is similar, compared with thicker films. The oxide film growth changes, due to the fact that a 1 nm film is crossed by one ion hop. Films below 1 nm are not stable.

1 Introduction

Because of the high affinity of valve metals like Al, Nb, Ta for oxygen, the surfaces are always covered by thin oxide films from air contact. The thickness of these barrier type films is in the range of some nm ($d_{0,Al}$ = 3 nm [1], $d_{0,Nb}$ = 3.6 nm [2], $d_{0,Ta}$ = 1-2 nm [3]) at room temperature. This is the lower limit of the film thickness in electrochemical investigations in neutral electrolytes. Accordingly most experiments start at potentials 0-1 V (vs. hydrogen electrode in the same solution) which corresponds to these thicknesses. Some examples are given in fig. 1: a freshly electropolished electrode (with air contact) and electrodes stored under different conditions.

The film thickness d may be increased by anodic polarization and is mainly determined by the final potential. d can be calculated from the formation factor k (typically 1-2 nm/V) and the potential U:

(1)
$$d = k \cdot U$$

The time dependence is less pronounced and often described by an inverse logarithmic growth law [4]. The anodic oxide films are homogeneous, at least up to 30 V [5]. This simplifies the interpretation of many effects. The capacity will be given as an example: In impedance investigations the oxide film behaves like an almost ideal dielectric material. The capacity C of the film is given by

(2)
$$C = \frac{\varepsilon\, \varepsilon_0}{d}$$

where ε_0 is the dielectric field constant and ε is the relative permittivity, i.e. the system behaves like a simple parallel plate capacitor.

The film is handled like the bulk oxide, i.e.

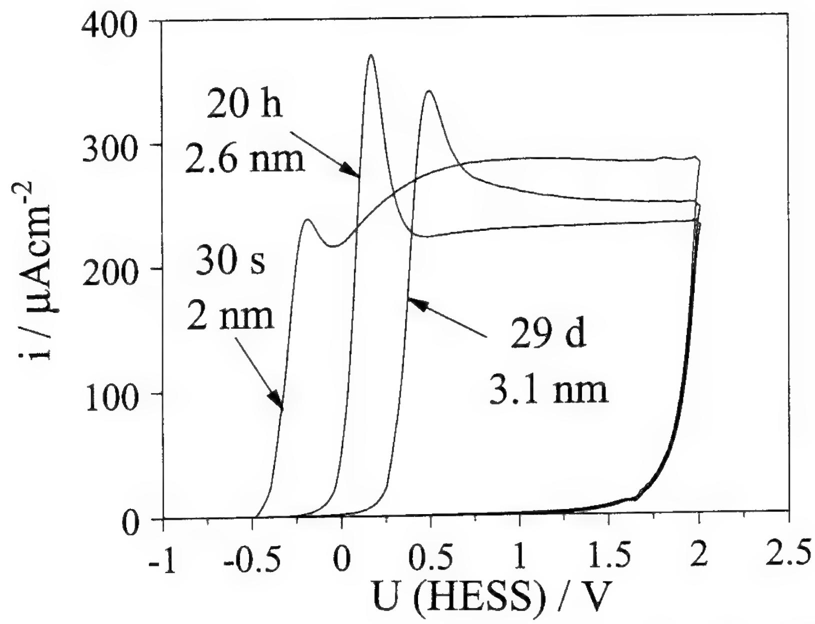

Fig. 1. Voltammograms of anodic oxide formation on a freshly electropolished Al wire (with air contact) and wires which were stored at 30 °C for 20 h or 29 d and the corresponding film thicknesses; acetate buffer, pH = 5.9, 25 °C, dU/dt = 100 mV/s, from [16].

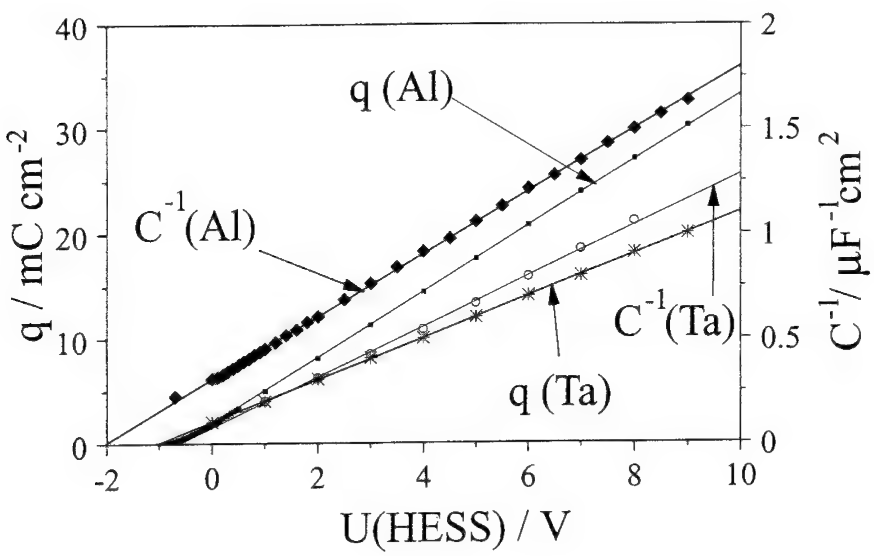

Fig. 2. Anodic charge q and inverse capacity 1/C vs. potential U of oxide films on Al and Ta at 25 °C.

- the thickness may be changed continuously, there are no effects of the lattice constant,

- the physical properties of the three different phases metal, oxide, and electrolyte change abruptly, there is no transition layer or a continuous change,

- the influence of the interfaces metal/oxide and oxide/electrolyte is negligible.

These assumptions may be true, if the film thickness is larger than the ion diameters. Obviously, no discontinuities are observed starting with film thicknesses d_0 as given above. The aim of this paper is to present preparation techniques and electrochemical investigations of films with $d < d_0$. Most experiments presented here were carried out with Al electrodes.

2 Experimental

The preparation of ultra thin oxide films was tried by different techniques. Further problems were the transfer to the electrolyte, the film stability in the electrolyte, and the determination of film thickness. We required fast in-situ techniques. Most suitable were the following methods:

(i) Determination of the potential of beginning oxide growth, e.g. in sweep experiments. The point of inflection of the increasing current was used. Thicknesses on Al were calculated from a formation factor of 1.6 nm/V and a potential of zero thickness of -1.6 V. The (logarithmic) time dependence could be neglected, as the experiments were carried out in an almost constant time range of some s.

(ii) Measurement of the anodic charge, assuming an efficiency of oxide formation of 100%. A composition Al_2O_3 and a density of 3.1 g/cm^3 [6] was used. This method requires the knowledge of the initial thickness.

(iii) The capacity of the oxide film was measured and the thickness was calculated according to eq. 2.

Results of the methods (i) and (iii) are presented in fig. 2. The anodic charge q and the reciprocal capacity $1/C$ were plotted vs. U. The experimental data depend linearly on U, as expected from the eqs. 1 and 2. The following values were taken from fig. 2:

$$\varepsilon_{Al} = 12 \qquad \varepsilon_{Ta} = 28 \qquad k_{Al} = 1.6\ \mathrm{nm/V} \qquad k_{Ta} = 1.8\ \mathrm{nm/V}$$

2.1 Preparation of Ultra Thin Oxide Films by Corrosion

A storage of electrodes in the electrolyte under potential control at very low potentials (< 0 V) yields ultra thin layers by corrosion. This requires much time, as the corrosion current (which is almost independent on the potential) in the acetate buffer used here is about 0.4 μA/cm^2 and, hence, the corrosion rate is $\approx$ 0.6 pm/s. Other undesired effects are a roughening of the electrode surface and an inhomogeneous thickness distribution. Nevertheless, this process was used in some cases.

2.2 Preparation of Ultra Thin Oxide Films by Physical Vapour Deposition

Film formation by physical vapour deposition at room temperature yielded porous layers [7]. The pores could be closed anodically or by exposure to air [8], forming a barrier layer of some nm. These films were not suitable.

2.3 Preparation of Ultra Thin Oxide Films in an Inert Gas Atmosphere

Electropolishing of the aluminum electrode wires was carried out in glacial acetic acid containing 5% of $HClO_4$ for 30 s at 200 mA/cm^2. Tantalum was electropolished in concentrated H_2SO_4 containing 7% of HF for 120 s at 100 mA/cm^2. All solutions were de-aerated by stirring with N_2. This procedure yields initial thicknesses $\approx$ 1 nm. The increase of thickness by gas oxidation depends on the partial pressure of oxygen. Therefore, all the steps of preparation, transfer, and investigation were carried out in a glove box in a nitrogen atmosphere at 25°C.

As the electropolishing process evolves some oxygen gas, an absolute oxygen-free atmosphere cannot be achieved. Nevertheless, the thickness increase of the oxide film was < 0.1 nm for a transfer within 30 s.

2.4 Electrochemical Investigations

The working electrodes, Al wires (99.999%) with a surface of 0.3 cm^2, were prepared as described above, immediately transferred and immersed under potential control. The electrolyte was an acetate buffer, pH 5.9. The electrolyte was de-aerated and stirred by nitrogen (99.999%). A gold foil (4 cm^2) was used as a counter electrode. All potentials given here refer to the hydrogen electrode in the same solution (HESS).

The oxide films were investigated by potentiostatic pulses, sweep techniques, and impedance spectroscopy. The current transients of potentiostatic pulse experiments were recorded in a wide range of current (1 μA/cm^2 $\leq i \leq$ 10 A/cm^2) and time (1 μs $\leq t \leq$ 1000 s). The sweep rate was 100 mV/s, the ac amplitude in the impedance investigations was 10 mV.

The electronic equipment consisted essentially of a fast rising potentiostat (rise time 0.3 μs), a pulse generator (for multiple pulses), a fast auto-ranging current detection system (switching time 1 μs), a nonlinear rate generator (1 MHz to 1 mHz), all in-house developments, and a Solartron 1255 frequency analyzer.

3 Results

3.1 Thickness and Dielectric Properties

If electrodes which had been anodized to a potential U_1 (yielding a film thickness d_1) are immersed into the electrolyte at a potential U_2 (which normally yields d_2), different currents may be measured:

- anodic current, i.e. $U_1 < U_2$, the film thickness increases,

- zero current, i.e. $U_1 \geq U_2$; the thickness decreases slowly by corrosion.

Hence, it is possible to prepare one given thickness in two ways: from thinner layers by oxide growth or from thicker layers by corrosion. *Kluger* [9] found that both processes yield identical films, characterized by the film capacity. The corrosion process required some ks ($i_{corr} \approx$ 0.3 μA/cm^2) in the acetate buffer used here.

Therefore it is possible to determine the thickness of the electrodes prepared as described in section 2.3. A successive immersion of the electrodes at different potentials enabled us to find out that at potentials $U_2 \geq$ -1 V the current was anodic, i.e. the preparation yielded a film thickness of 1 nm which is stable at -1 V (eq. 1). At potentials < -1 V the initial current was cathodic (hydrogen evolution). The

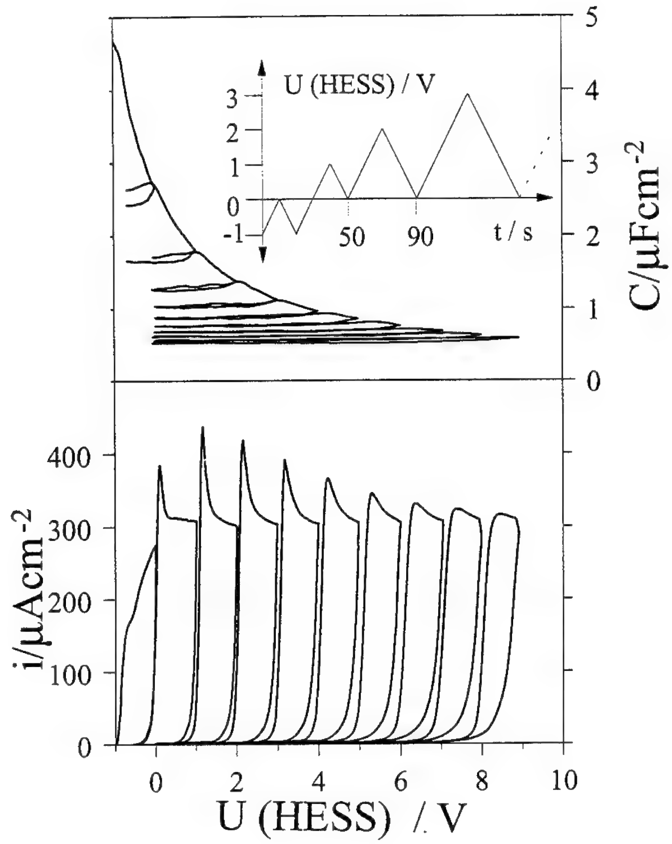

Fig. 3. Subsequent sweep experiments on Al with 100 mV/s (below), the corresponding film capacity (above), and the potential-time scheme (insert).

Fig. 4. Impedance and phase angle of an Al oxide film at -0.5 V. At a potential of -1 V the spectra become time dependent. One spectrum was recorded every 360 s. Only the phase angles are given for reasons of clearness.

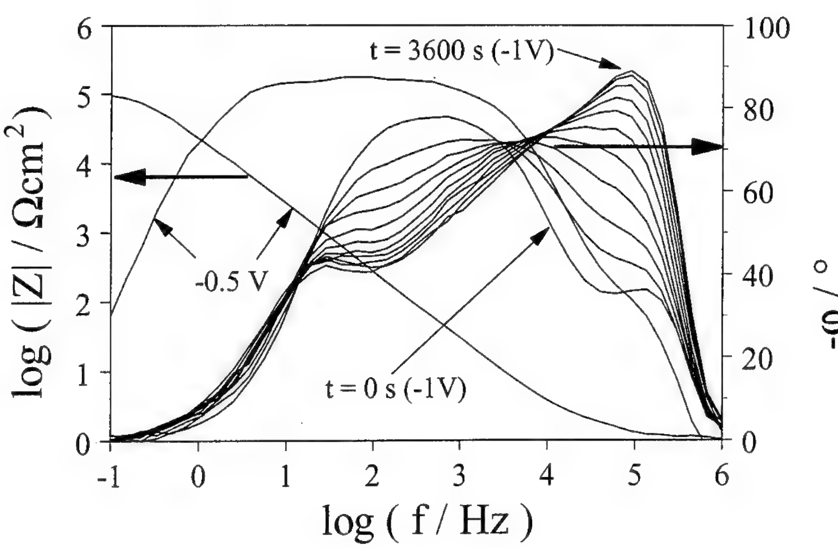

same result was obtained from successive sweep experiments (fig. 3). The anodic sweep current increases at -1 V and then remains almost constant at 300 $\mu A/cm^2$. Every sweep starts with a small peak, the so-called overshoot, which is an effect of the formation of mobile ions within the film **[10]**. The overshoot becomes more and more smeared out with increasing potential (and thickness). This is also found in current transients. The increase of thickness during the sweeps is monitored by the film capacity which is also presented in fig. 2. The slow increase of current in the first sweep (-1 V to 0 V) might be an artefact of a hindered oxide formation at low potentials or of an distribution of film thickness. More probable is an influence of cathodic hydrogen evolution. The first sweep is the sum of the anodic partial current density which is similar to the subsequent sweeps and a cathodic current increasing exponentially with the (cathodic) overpotential. This is also indicated by the remainder of the overshoot, the small hump at about -0.7 V. A moderate hydrogen evolution is possible at these thin films and a cathodic breakdown occurs at potentials < -0.8 V after long periods of time **[11]**.

The oxide film thickness was monitored by impedance spectroscopy. The simple equivalent circuit is independent of time at potentials > -0.8 V: the film capacity C, the film resistance R in parallel and, in series, the electrolyte resistance between working and reference electrode (some Ω). An example at -0.5 V is given in fig. 4. In the frequency range from 1 Hz to 10^4 Hz the impedance is dominated by C (about 5 $\mu F/cm^2$), at frequencies < 0.1 Hz only the film resistance R is measured ($\approx$ 100 $k\Omega cm^2$). Therefore, the time dependent capacity C in the sweep experiments could be taken from continuous single frequency measurements. These values are presented in the upper part of fig. 3. A plot $1/C$ vs. U (fig. 2) yields a straight line which is consistent with the eqs. 1 and 2.

So far, the ultra thin oxide films (1 nm $\leq d \leq$ 3 nm) behave like the thicker ones: The dielectric properties and the anodic film growth is identical. At potentials < -0.8 V (or thicknesses < 1.3 nm), however, the film is not stable. The impedance spectra in fig. 4 show a strong time dependence and a second time constant develops, obviously indicating the beginning cathodic breakdown **[9]**.

3.2 Transient Behaviour

The overshoot was observed in sweep experiments, e.g. fig. 3. Current transients of potentiostatic pulse experiments yield more pronounced peaks [**12, 13**]. The model of emission of mobile ions presented there predicts the moment of overshoot (peak maximum) t_{max}

(3)
$$t_{max} = \frac{\rho d}{i_0 \exp(\beta E)}$$

and the current density in the maximum i_{max}

(4)
$$i_{max} = i_0 \exp(\beta E)$$

where d is the initial thickness, ρ is the concentration of mobile ions, and β and i_0 are oxide specific constants. The electric field strength E in the oxide is calculated from the potential drop ΔU across the oxide and the layer thickness d

(5)
$$E = \frac{\Delta U}{d} = \frac{U - U_0}{d}$$

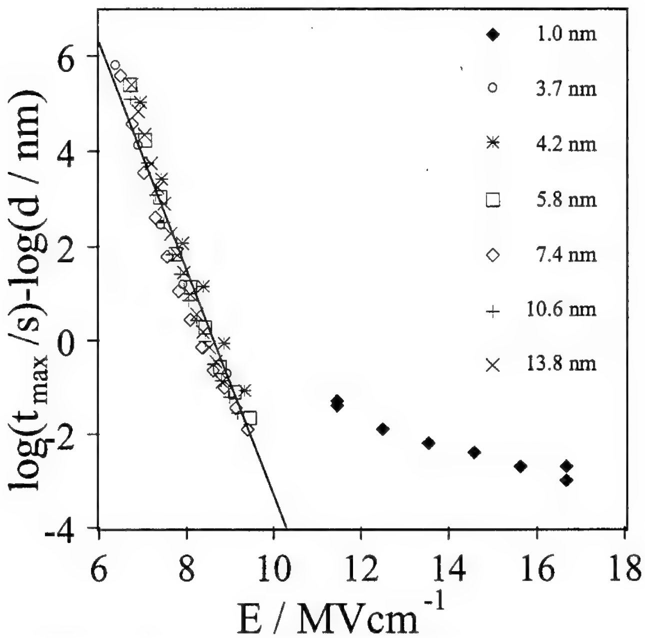

Fig. 5. Logarithm of moment of overshoot t_{max} over initial thickness d vs. electric field strength E. Films > 2 nm show a linear dependence (eq. 3); t_{max} is almost independent on E on 1 nm films.

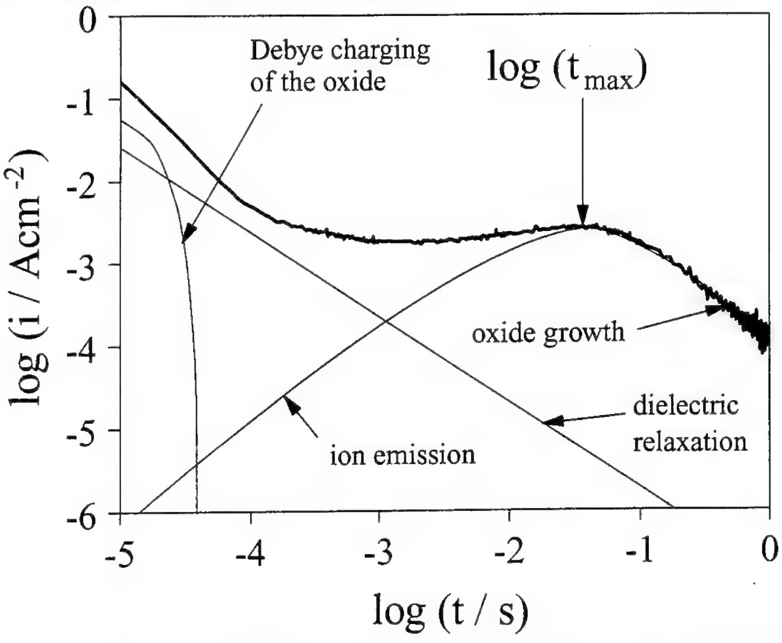

Fig. 6. Current transient of further oxide growth (initial thickness 1.8 nm) of a potentiostatic pulse (step from -0.5 to 0 V). The different processes of Debye-charging, dielectric relaxation [17], and ion emission and oxide growth are given by the full lines. The moment of overshoot t_{max} is indicated.

where U denotes the electrode potential. U_0 is the potential where the field strength is zero. U_0 (Al: $U_0 = -1.6$ V) includes the potential drops at the oxide interfaces, which depend only weakly on the current density [13]. According to eq. 3, a plot log (t_{max}/d) vs. E should yield straight lines. Some examples of thicker oxide films (> 3 nm) are presented in fig. 5 and a straight line is achieved.

The moment of overshoot of the ultra thin films, however, is much less pronounced (fig. 6) and weakly dependent on E. The emission model (eq. 3 and 4) assumes the formation of localized ionic space charges, which requires a sufficient thick oxide film. The mean jump distance a of the mobile ions was calculated from β

(6) $$\beta = \frac{\alpha a z F}{RT}$$

where α is a symmetry factor and z is the mean charge number of the ions. A value of about 0.8 nm is calculated ($z = 2.5$, $\alpha = 0.5$, $\beta = 44$ nm/V), i.e., the ions cross the oxide film with almost one hop. This is the ultimate lower limit of a hopping mechanism.

3.3 Oxide Film Resistance

The final value of the oxide film resistance R (after 10^2-10^4 s, depending on the potential) is given vs. U in fig. 7. R increases with U. R might be determined by three processes:

- the ionic conduction due to an high field transport of ions,

- an elastic tunnelling process of electrons as one step of hydrogen evolution at the interface oxide/electrolyte,

- a proton conductivity as a prerequisite of an oxygen evolution at the interface metal/oxide.

The ionic conductivity may be calculated from the high field equation

(7) $$i = i_0 \exp(\beta E)$$

and, hence, the film resistance is given by [5]

(8) $$R = \frac{\mathrm{d}U}{\mathrm{d}i} = \frac{d}{\beta i_0 \exp(\beta E)}$$

and the specific resistance R_s

(9) $$R_s = \frac{1}{\beta i_0 \exp(\beta E)}$$

which should strongly depend on the field strength E. If the film is stationary, the corrosion losses (i_{corr}) must be compensated by the ionic current of oxide formation i. i_{corr} is determined by the potential drop across the interface oxide/electrolyte [14] which depends on the pH-value, but is almost independent of the current [15] or potential. If $i = i_{corr}$, eq. 9 simplifies to

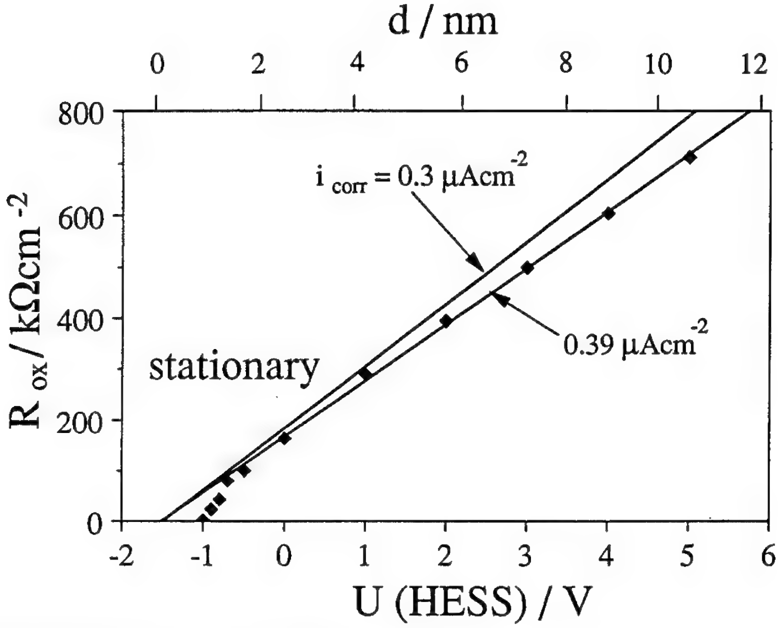

Fig. 7. Oxide film resistance R vs. potential U or thickness d (eq. 1). The straight lines are calculated from the eqs. 10 and 1. A corrosion current i_{corr} = 0.39 µA/cm^2 was calculated from the experimental data ($U \geq -0.7$ V), which is similar to the value estimated by Kluger (0.3 µA/cm^2 [9]) in the same electrolyte. Below -0.7 V the resistance is dominated by tunnelling processes.

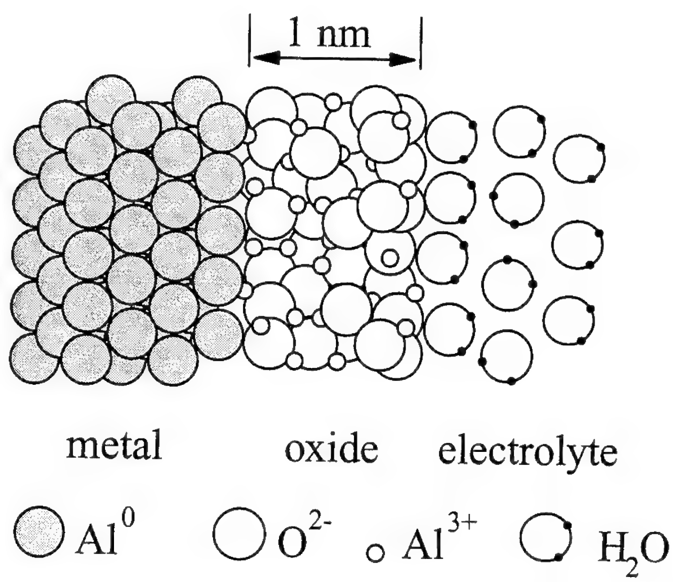

Fig. 8. Schematic representation of a cross-section of a 1 nm oxide film. The distance of ion hopping is about 0.8 nm (eq. 6).

(10) $$R_s = \frac{1}{\beta i_{corr}}$$

i.e., values of $\beta = 44$ nm/V and $i_{corr} = 3.9 \cdot 10^{-7}$ A/cm^2 yield a specific resistance R_s of about $6 \cdot 10^{11}$ Ωcm. Values of the film resistance R, calculated from R_s and eq. 1, are compared in fig. 7 with the experimental data. The coincidence is sufficient at potentials > -0.7 V. Below this potential, the experimental resistances are smaller, probably due to the parallel tunnelling process of electrons (hydrogen evolution) through oxide films of < 1.4 nm. A possible, additional influence of proton conductivity cannot be separated.

4 Summary

The preparation of anodic oxide films with thicknesses ≥ 1 nm is possible on Al by electropolishing under an inert gas atmosphere (N_2). These ultra thin films were investigated by current transients, sweep experiments, and impedance spectroscopy. The dielectric properties are equal, compared with thicker films. The film resistance is similar, but influenced by the parallel process of elastic electron tunnelling. The oxide film growth changes slightly, especially in transient experiments, due to the fact that a 1 nm film is crossed by one ion hop. This situation is illustrated in fig. 8. Films below 1 nm are not stable.

The financial support of the *AGEF e.V. Institut an der Heinrich-Heine-Universität Düsseldorf* and the *Deutsche Forschungsgemeinschaft* is gratefully acknowledged.

References

1. H. Sambe, D. E. Ramaker, *J. Vac. Sci. Technol.* A 10 (1992) 2991
2. S. Piazza, C. Sunseri, F. Di Quarto, *J. Electroanal. Chem.* 293 (1990) 69
3. M. R. Arora, R. Kelly, *Electrochim. Acta* 19 (1974) 413
   V. Macagno, J. W. Schultze, *J. Electroanal. Chem.* 180 (1984) 157
4. N. Cabrera, N. F. Mott, *Rep. Prog. Phys.* 12 (1948-49) 163
5. M. M. Lohrengel, *Mat. Sci. Eng.* R 11 (1993) 243
6. P. Skeldon, K. Shimizu, G. E. Thompson, G. C. Wood, *Surf. Interf. Anal.* 5 (1983) 247
7. R. A. Haefer, "Oberflächen- und Dünnschicht-Technologie", Springer Verlag, Berlin 1987
8. D. Diesing, S. Rüße, M. M. Lohrengel, *Proceedings of the Electroceramics IV*, Aachen 1994
9. K. Kluger, *Thesis*, Heinrich-Heine-Universität Düsseldorf 1993
10. A. W. Hassel, M. M. Lohrengel, S. Rüße, J. W. Schultze, submitted to *Bull. Chem. Technol. Macedonia*
11. A. W. Hassel, M. M. Lohrengel, *Electrochim. Acta* 39 (1994), in press
12. M. M. Lohrengel in "Electrochemical and Optical Techniques for the Study and Monitoring of Metallic Corrosion" M. G. S. Ferreira, C. A. Melendres (eds.), Kluwer Academic Publishers Dordrecht (1991) pp. 69-121
13. M. M. Lohrengel, *Ber. Bunsenges. Phys. Chem.* 97 (1993) 440
14. M. M. Lohrengel, *Electrochim. Acta* 39 (1994) 1265
15. J. Siejka, J. P. Nadai, G. Amsel, *J. Electrochem. Soc.* 118 (1971) 727
    A. J. Davenport, G. T. Burstein, *J. Electrochem. Soc.* 137 (1990) 1496
16. T. Gebauer, Diplomarbeit, Heinrich-Heine-Universität Düsseldorf 1994
17. S. Rüße, M. M. Lohrengel, J. W. Schultze, *Solid State Ionics* 72 (1994) 29

Materials Science Forum Vols. 185-188 (1995) pp. 591-600

Logarithmic kinetics of the ion charge accumulation in the SiO_2 dielectric layers

V.N. Ovsyuk

Institute of Semiconductor Physics, Siberian Branch of Russian Academy of Science, Lavrentyev ave.13, Novosibirsk, 630090 Russia

Keywords: Ionic transport, silicon dioxide layers, MIS structures

KEYWORDS: Ionic transport, silicon dioxide layers, MIS structures

ABSTRACT: The integral dynamic volt - ampere characteristic method for measurements of the ionic transport through dielectric layers in MIS structures was developed. A qualitative sensitivity of the method was less than 10^9 ion/cm^2. The absolute accuracy of $5 \cdot 10^9$ ion/cm^2 was achieved.

The method was applied to the comparative investigations of the ion charge behaviour in SiO_2 layers obtained by different ways in **Si** MIS structures with the **Al** and **Si** polycrystalline electrodes.

Logarithmic kinetics of the ion charge accumulation in "dry" SiO_2 layers was detected and its peculiarities were found.

INTRODUCTION. It is commonly supposed that an ion drift and ion charge accumulation $Q(t)$ in the dielectric SiO_2 layers are in agreement with the well known diffusion theory according to the law $Q \sim (t/\tau)^{1/2}$, where t is the time of the external bias voltage application and τ is the characteristic time constant of the process [1]. The only exception was provided by work [2] where an exponential dependence $Q \sim (1 - \exp(-t/\tau))$ was observed and explained by an ion emission from ion traps near the metal and dielectric interface.

We found [3] that ion accumulation in SiO_2 layers can follow the logarithmic law $Q \sim \ln(t/\tau)$. Main features of the phenomenon were established and the appropriate model was derived.

We used an improved modification [4] of the dynamic volt - ampere characteristic method [1,5] with direct integration of the current over the bias voltage from a certain extreme value $-V^m_g$ to the current value $V_g(t)$ that permitted us to obtain the function [6]

$$Q(V_g) = Q_d(V_g) + Q_s(V_g) \qquad (1)$$

where

$$Q_d = \int_0^d \frac{z}{d} \cdot \rho(z, V_g) \cdot dz \Bigg|_{-V_g^m}^{V_g(t)} , \qquad (2)$$

$$Q_s = \int_{-V_g^m}^{V_g} (C_d - C(V_g)) \cdot dV_g \qquad (3)$$

Q_d is the effective ion charge in the dielectric layer, the absolute value being equal to the charge induced on the semiconductor, Q_s is the change of the charge in the space charge region near the semiconductor surface, $\rho(z, V_g)$ is the charge density distribution with the coordinate **z** in dielectric layer, **d** and C_d are the thickness and the capacity of the dielectric layer, respectively, $C(V_g)$ is the low-frequency **C-V** characteristics of the MIS structure.

The second term $Q_s(V_g)$ in **Eq.1** is the weak function of temperature and therefore can be measured at room temperatures when ion displacement is negligibly small. The desired dependence $Q_d(V_g)$ can be found as the difference of the curves $Q(V_g)$ measured at a high and room temperatures.

SAMPLES. The investigated **SiO_2** films as thick as 850 ± 50 Å were prepared on **Si** (100) surfaces either by dry oxidation at 1050^0 C or by chlorine oxidation at 900^0 C with the subsequent annealing of the samples at the same temperature in the fluid of the dried argon. A part of the samples was covered additionally by the **borophosphorosilicate glass** (**BPSG**) with the thickness of 250 Å.

Two different types of material for the top electrode of the MIS structures were used. The first of them was the **Al + Si** (2%) layer obtained by the magnetron spraying. The other one was the silicon polycrystalline layer grown in the low pressure reactor chamber at 640^0 C with the subsequent doping implantation of the layer with P^+ ions at 880^0 C providing the specific layer resistance of 15 ÷ 30 Ohm/□. The ion form of the native sodium contamination was studied without special doping of the samples. The main attention was devoted to distinction of different technologies and to the ion time kinetics.

EXPERIMENTAL RESULTS. A typical set of the integral dynamic Q - V

characteristics is depicted in **Fig.1a,b** for the **Si** - **SiO_2**(dry) - **Al** structures at several temperatures.

Curve 1 at 295 K in **Fig.1a** corresponds to the practical absence of mobile ions. This curve is taken to be a zero level for the measurements of the ion accumulation from the integral **Q - V** characteristics measured at higher temperatures where this initial curve is repeated several times by the dotted lines.

One can see from the Figure that two effects develop with an increasing temperature. Firstly, the quantity of the travelling ions taken for every cycle of the bias voltage alteration increases. Secondly, the ion drift in the opposite directions from the metal electrode to semiconductor and back is unsymmetrical: ions are accumulated in the dielectric layer relatively slow for their moving from the metal electrode and return back sufficiently fast together with a transition to the negative value of the bias voltage. This effect can be attributed to existence of ion traps near the metal - dielectric interface as it was suggested in [2].

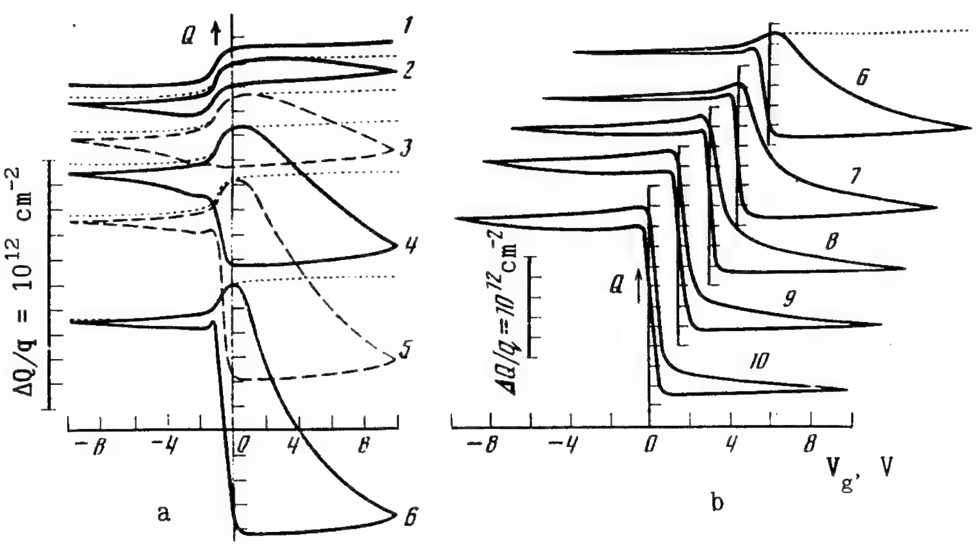

Fig.1. The integral **Q-V** characteristics of the **Al-SiO_2**- Si structure at the temperatures: **1** - 295, **2** - 341, **3** - 364, **4** - 388, **5** - 410, **6** - 434, **7** - 483, **8** - 529, **9** - 551, **10** - 575 K (f = 0.05 Hz)

At sufficiently high temperatures (**curves 9, 10** in **Fig 1**b) the ion drift velocity from the metal electrode becomes high and the integral **Q-V** characteristics turn practically into the symmetric ones.

Under the same measurement conditions the **Si-SiO_2(dry)-BPSG-Al** structures exhibit a substantially smaller quantity of the mobile ions, no more than 10^{11} cm^{-2} at 600 K. The general quantity of the ions varies over no more than 2 ÷ 3 times in different samples. The integral **Q - V** characteristics demonstrated only an approximate symmetrical slow kinetics of the ion accumulation and disappearance in these dielectric layers.

For the structures with the chlorine **SiO_2**, the ion drift was insignificant even in the absence of the protecting **BPSG** layer.

The general quantity of mobile ions for the dry **SiO_2** with the polycrystalline electrode was different appreciably for different parties of the samples which can be divided into three groups according to this parameter. The first one had a small ion drift and properties similar to those of the **SiO_2** (dry) - **BPSG** - samples. The thermoelectrical treatment did not affect the ion density. For the second group, the Q_d^m/q magnitude was $2 \div 3 \cdot 10^{11}$ cm^{-2} at 480-600 K but the quantity of the mobile ions became less by 20 ÷ 30 % than it was in measurements made for the progressive heating of the sample from the room temperature. The third group of the samples had the same quantity of the mobile ions up to 500 K followed by the drastical increase of the Q_d^m/q up to $2 \cdot 10^{12}$ cm^{-2} at 600 K. During the subsequent gradual cooling of the sample, the mobile ion quantity increased by 20-30 % at every given temperature.

As a result we may conclude that the thermoelectrical treatment of the samples with the polycrystalline electrode can lead to both increasing and decreasing mobile ion quantity for the dry **SiO_2**.

It should be also noted that the kinetic peculiarities of the ion drift were indentical for MIS structures fabricated on the **silicon-on-sapphire substrates** (SOS).

THE KINETICS OF THE CHARGE ACCUMULATION IN THE DRY SiO_2 LAYERS. **Fig.2**a shows the temperature dependence of the ion quantity travelling forward and back for single cycle of the measurement related to the three different coordinate systems for the same sample that was shown in **Fig.1** a,b. It can be seen from the Figure that the

dependence $Q_d(T)$ is not exponential (**curve 1** is not linear in the coordinate axes $\lg(Q) \sim 1/T$. On the other hand, the dependence $Q_d(T)$ may be represented approximately either by the law $A_1 + B_1 \cdot T$ (**curve 2**) or $A_2 + B_2/T$ (**curve 3**) where $A_{1,2}$ and $B_{1,2}$ are certain constants.

The measurements showed also that the effective mobile ion density Q_d^m/q was a linear function of the logarithm of the frequency of the alternating bias voltage (**Fig.2b**) and therefore it was proportional to the logarithm of the time of the electrical sweep.

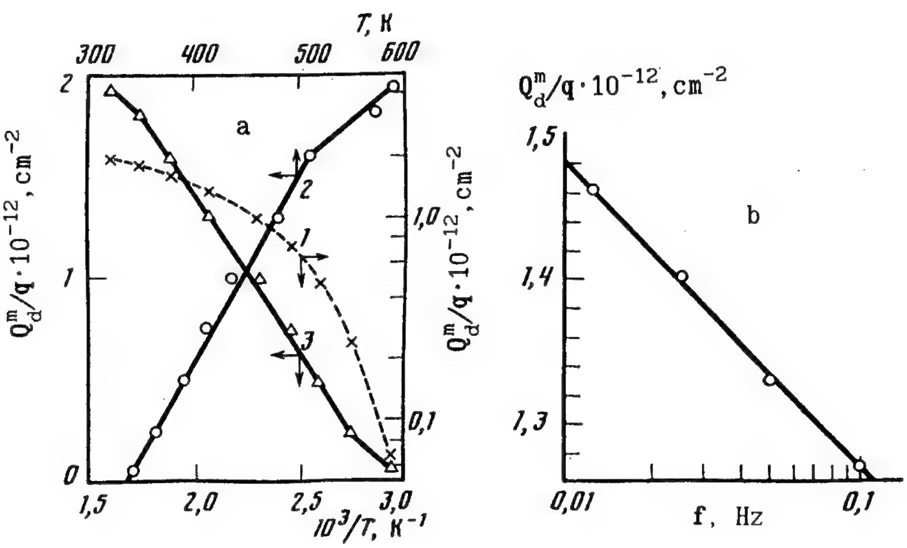

Fig.2. The dependences of the ion charge quantity for the single measurement cicle on temperature (a) in the different coordinate systems (f = 0.05 Hz) and on the frequency (b) at 410 K.

The direct relaxation curves

$$Q_d = \int_0^d \frac{z}{d} \cdot \rho(z,t) \cdot dz \qquad (4)$$

for three temperatures are shown in **Fig.3**. At the temperature as high as 485 K, the ion charge moving from the metal electrode is slower in comparison with that moving in the back direction even in the absence of the external bias voltage. It is complied with the

behaviour of the integral Q - V characteristics and forced us to let the ion displacement from the metal electrode be limited by the emission rate from the ion traps near the metal - dioxide interface. Further, the time interval between the subsequent measurements was made sufficiently large providing complete restoration of the initial ion distribution over the normal coordinate.

Fig.3.
The kinetics of the accumulation I (V_g = 10 V) and of the depletion II (V_g = 0) of the ion charge Q for the Si_{pc} - SiO_2(dry) - SOS structure at the temperatures: 1 - 326, 2 - 413, 3 - 485 K

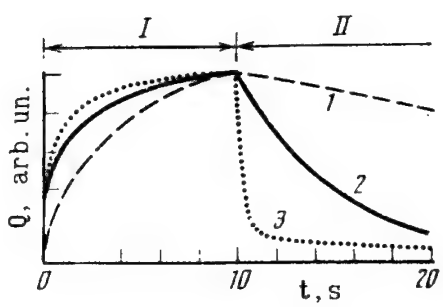

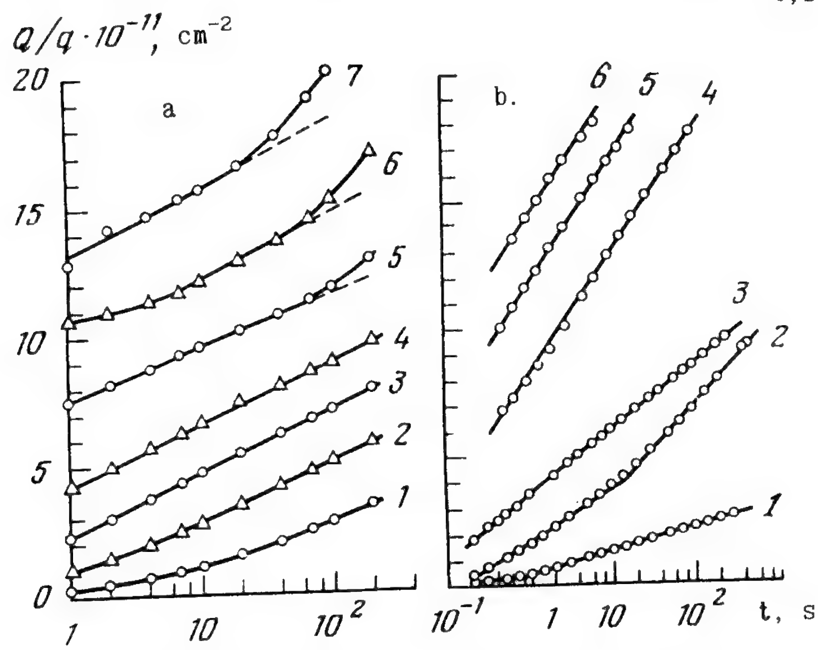

Fig.4. The kinetics of the ion charge accumulation for the Al-SiO_2-Si (a) and Si_{pc}-SiO_2-SOS (b) structures at different temperatures (a): 1 - 364, 2 - 388, 3-410, 4-434, 5-483, 6-529, 7-575 K; (b): 1-326, 2-347, 3-384, 4-413, 5-457, 6-485 K (V_g = 10 V).

The kinetic $Q(\lg t)$ dependences for different temperatures are shown in **Fig.4** a,b for two different samples. The similar dependences for several values of the bias voltage are depicted in **Fig.5** for one of the samples. It is evident from the Figures that (i) the initial parts of the $Q_d(\lg t)$ dependences become more gently sloping for law values of both temperatures and bias voltage; (ii) there is a tendency to saturating for the sufficiently high values of temperature and bias voltage; (iii) the ion charge Q_d increases with increasing temperature or bias voltage at the fixed time of ion accumulation while the $Q_d(\lg t)$ dependences are shifting monotonously along the Q axes.

Sometimes a drastic change of the slopes of the $Q(\lg t)$ dependences can be observed at certain temperatures for the samples with the **Si** polycrystalline electrode (**curve 2** in **Fig. 4**b).

THE MODEL OF THE LOGARITHMIC KINETICS OF THE ION CHARGE ACCUMULATION

Assume that there are ion traps at the interface between the SiO_2 layer and the metal electrode and the trap activation energies E are distributed quasicontinuously over the region (E_1, E_2), $E_1 < E_2$. Assume also that the ions migrate to the semiconductor surface instantly after their emission, i.e. the emission rate determines the whole kinetics of the ion accumulation in the SiO_2 layer.

The diminution of the ion layer concentration $N_I(t)$ per the energy unit will follow the law

$$N_I \cdot dE = N_{IO}(T) \cdot \exp(-t/\tau) \cdot dE \qquad (5)$$

where $\tau = \nu_0^{-1} \cdot \exp(E/k_0 T)$, $N_{IO}(T)$ is the amplitude of the initial ion distribution in the activation energies which can be a function of temperature, ν_o is the characteristic frequency and k_o is Boltzman's constant. For the sufficiently extended interval (E_1, E_2) there is a range of time values satisfied to the conditions $t / \tau(E_1) \gg 1 \gg t / \tau(E_2)$. In this case, the integration of **Eq.5** over the interval (E_1, E_2) gives the following expression for the ion quantity $N_I(t)$ escaped from the interface potential well to the moment t:

$$N_I(T) = N_{IO} \cdot k_o \cdot T \cdot \ln(\tilde{\gamma} \cdot t/\tau_1) \qquad (6)$$

where $\tau_1 = \tau_1(E_1)$ and $\tilde{\gamma} = 1.789$ is Eiler's constant.

The top border of the potential well **U(z)** may be not abrupt. In this case, a definite influence of the electric field on the activation energy and therefore on the emission rate must exist. On the assumption that the shape of the activation barrier is determined by the mirror - image efficiency, the potential well can be described by the expression $U(z) = -\mathbf{q}^2 / 16\cdot\pi\cdot\bar{\varepsilon}_o\cdot\bar{\varepsilon}_d\cdot\mathbf{z}$, where $\bar{\varepsilon}_o$ is the vacuum permittivity and $\bar{\varepsilon}_d$ is the relative permittivity of the dielectric. In this case, the above used activation energy **E** must be replaced by $E(0) - \delta E$, where $\delta E = \beta\cdot E_d^{1/2}$, E_d is the average electric field strength and $\beta = [\, \mathbf{q}^3 / 4\cdot\pi\cdot\bar{\varepsilon}_o\cdot\bar{\varepsilon}_d\,]^{1/2} = 3\cdot 10^{-23}$ $J\cdot cm^{1/2}\cdot V^{-1/2}$ for $\mathbf{SiO_2}$ at $\bar{\varepsilon}_d = 4$. The characteristic time τ may be rewritten as $\tau_1 = \tau_{1o}\cdot\exp[-\beta\cdot E_d^{1/2}/\mathbf{k}_o\cdot T]$, where τ_{1o} is related to the $E_d = 0$ condition. As a result, the relaxation law (6) is modificated to the form:

$$\mathbf{N}_I(\mathbf{t}) = \mathbf{N}_{IO}\cdot\mathbf{k}_o\cdot\mathbf{T}\cdot\left[\ \ln(\tilde{\gamma}\cdot\nu_o\cdot\mathbf{t}) - \frac{\mathbf{E}_1(0) - \beta\cdot E_d^{1/2}}{\mathbf{k}_o\cdot\mathbf{T}}\right] \tag{7}$$

We can see that (i) both **Eqs.6** and **7** describe a logarithmic kinetics of the ion accumulation in the dielectric layer; (ii) the slope of the dependence $\mathbf{q}\cdot\mathbf{N}_I[\lg \mathbf{t}]$ is proportional to the multiplication $\mathbf{N}_{IO}\cdot\mathbf{k}_o\cdot T$, (iii) the effective ion charge $\mathbf{q}\cdot\mathbf{N}_I$ increases proportionally to $E_d^{1/2}$ for fixed values of **t**.

Then with the extrapolation of (7) to $\mathbf{N}_I = \mathbf{0}$, a certain value of $\mathbf{t}^*$ connected with the characteristic time $\tau_1 = \tilde{\gamma}\cdot\mathbf{t}^*$ can be obtained. Using the dependence of $\ln\tau_1$ on the reciprocal temperature 1/T, the top boundary of the activation energy distribution $E_1[\mathbf{V}_g]$ can be found.

And at last, the intersection of the linear dependence $\lg[\tau_1(1/T)]$ with axis of ordinates gives us the characteristic frequency ν.

DISCUSSION. **Fig.6 (curve 1)** presents the dependence $\lg[\tau_1(1/T)]$ obtained for the sample shown in **Fig.5** a using the above presented algorithm. This dependence is actually linear and gives $\mathbf{E}_1 = \mathbf{1.0}$ eV (for $\mathbf{V}_g = 10$ V) and $\nu_o = 1.1\cdot 10^{13}\ s^{-1}$. The obtained magnitude corresponds to the common view of thermal atom vibrations on a

solid - state medium. Note also that the procedure for the extraction of the E_1 and ν_0 is not effected by possible temperature dependence of N_{IO}.

For the structures with the polycrystalline electrode, the temperature dependence of $\ln \tau_1$ points to an existence of the processes with the activation energies 1.0 and 0.42 eV respectively (**curve 2** in **Fig.6**). For the second value of the activation energy connected probably with an ion generating process the characteristic frequency has the drastically reduced value $\nu = 5 \cdot 10^6\ s^{-1}$.

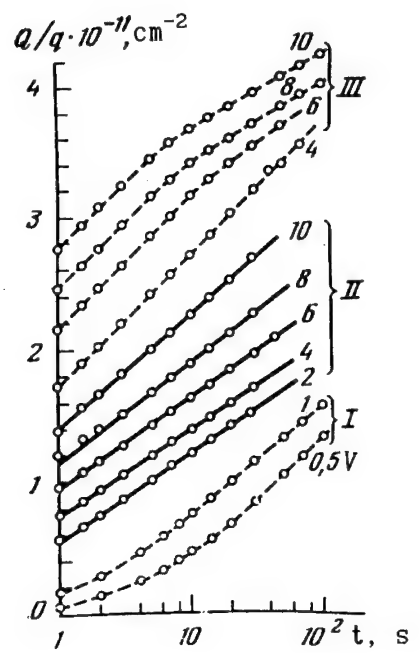

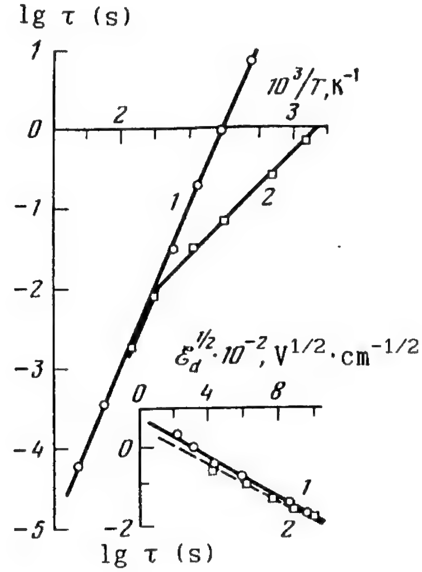

Fig.5. The kinetics of the ion charge accumulation for the Si_{pc} - SiO_2 - SOS structure for different voltages at the temperatures: I - 386, II - 413, III - 485 K.

Fig.6. The dependence of the lg τ on 1/T for the **Al** - SiO_2 - **Si** (1) and Si_{pc} - SiO_2 - **SOS** (2) structures. In the insert: **1**-386, 2-413 K.

The insert to **Fig.6** shows the experimental dependence of ln τ_1 on $E_d^{1/2}$ having a linear shape in accordance with **Eq.7**. The slope of the dependence gives the parameter $\beta = 3.1 \cdot 10^{-23}$ $J \cdot cm^{1/2} \cdot V^{-1/2}$ that is coincident practically with the theoretical value for $\bar{\varepsilon}_d = 4$. Hence we obtain the extrapolated to $E_d = 0$ value $E_1(0) = 1.2$ eV.

The experimental data do not show a remarkable temperature increase of the slopes for the dependences $\mathbf{Q_d}$(lg **t**) (**Fig.4**). The experiment indicates probably the constant values of the slopes for the investigated temperature range. This effect may be connected with existence of a slight dependence of $\mathbf{N_{IO}}$ on **T** that can be found by the following way. Using the extrapolation of $\mathbf{Q_d}$(lg **t**) to the intersection with the **x**-coordinate, we obtain the values of the multiplication $\mathbf{N_{IO}(T) \cdot E_1}$, where $\mathbf{E_1}$ was found previously. From here the $\mathbf{N_{IO}}$ magnitude for different temperatures may be found. We obtained the diminution of $\mathbf{N_{IO}}$ with temperature for the sample in **Fig.4** approximately from $3 \cdot 10^{12}$ cm^{-2} eV^{-1} at 388 K to $2.2 \cdot 10^{12}$ cm^{-2} eV^{-1} at 529 K that allows us to accept the approximation $\mathbf{N_{IO} \sim 1/T}$ which leads to the dependence

$$\mathbf{N_I} \sim \ln(\tilde{\gamma} \cdot \nu_o \cdot \mathbf{t}) - \mathbf{E_1/k_o} \cdot \mathbf{T} \qquad (8)$$

in accordance with the above presented experimental results (**curve** 3 in **Fig.4**a).

As a result it can be seen that the suggested model of the ion accumulation in the **Si** dioxide layers permits a detailed analysis of the phenomenological parameters related to the logarithmical kinetics of the process.

REFERENCES

[1] E.H.Snow, A.S.Grove, B.E.Deal et al.,Appl.Phys., **36**, 1664 (1965)

[2] S.R. Hofstein, IEEE Trans. Electron. Devices, ED-**13**, 222 (1966)

[3] B.B.Koltsov, G.N.Lutsenko, V.N.Ovsyuk et al., Microelectronica (in Russian), **16**, 259 (1987)

[4] B.B.Koltsov, G.N.Lutsenko, V.N.Ovsyuk et al., Microelectronica (in Russian), **16**, 254 (1987)

[5] N.J.Chou, J. Electrochem. Soc., **118**, 601 (1971)

[6] V.N.Ovsyuk, Electron processes in semiconductors with space - charge regions (in Russian), Novosibirsk, Nauka publ. (1984)

Materials Science Forum Vols. 185-188 (1995) pp. 6?'-610

A surface charge approach to the growth and relaxation in anodic passive films on metals

M. Bojinov

Central Laboratory of Electrochemical Power Sources, Bulgarian Academy of Sciences, 1113 Sofia, Bulgaria

Keywords: Anodic passivation, space charge, anodic oxide film, impedance spectroscop' kinetic model

ABSTRACT

A model of the kinetics of growth and of anodic passive films on metals and associated relaxation phenomena is proposed. It is based on the assumption that during the growth of the anodic layer surface charges of ionic character are formed both at the metal/film and film/solution interfaces. Within the film bulk, a quasi-uniform field is established. It is suggested that positive defects within the anodic film are responsible for its growth. A negative surface charge is built up at the metal/film interface accelerating growth and leading to a decrease of the electric field strength during anodic oxidation. A positive defect surface charge due to adsorbed anions is formed at the film/electrolyte interface accelerating the motion of negative ionic defects and presumably leading to film breakdown.Local dissolution/repassivation reactions at the film/electrolyte interface are taken into account within the frames of the model. Expressions connecting the main structural and kinetic parameters are evaluated both in steady state and transient conditions. The validity of the model is demonstrated by studying passive films on tin and bismuth in various electrolytes as representative systems.

THEORY

1.Galvanostatic anodization, steady state regime

1.1) Positive ionic defects (oxygen vacancies) are generated at the metal/oxide interface and their migration through the film bulk is the rate limiting step of the growth process.

1.2) Negative ionic defects (metal vacancies) are generated at the oxide/solution interface and participate to the formation of a negative surface charge (q_n) because the vicinity of the metal/film interface can be regarded as quasi-impermeable for them[6]. It is postulated that this surface charge has a thickness considerably greater than a monolayer, which assumption will be justified below.

1.3) This surface charge influences the motion of positive defects, increasing their migration rate. The value of the charge is a function of current density and field intensity at constant thickness, and of thickness at constant current density.

1.4) A mean defect concentration (c_0) is defined as the concentration at the reaction plane where film growth proceeds via defect annihilation. It is assumed to depend on current density.

1.5) The current density vs. field dependence is described by the De Wit equation [6] which follows from a modification of the general dielectric polarization theory of Dignam[7]:

$$i = i_o \exp[B(E + q_n/\varepsilon\varepsilon_o)] \qquad (1)$$

where i_o and B are constants, E is the field strength (E = U/L, where U is the overpotential), ε is the dielectric constant of the growing film, and ε_o is the dielectic permittivity of free space.

1.6) The thickness dependence of the background charge q_n is derived from the general theory of Fromhold[8]

$$q_n = (\varepsilon\varepsilon_o/B)\ln(1 + L/x) \qquad (2)$$

where x is the so-called space charge screening parameter, defined as follows[8]

$$x = 1/[c_o a\,(zF)^2/(\varepsilon\varepsilon_o RT)] \qquad (3)$$

where z is the charge on the positive defect and a is the half- jump distance. Combining (1) and (2) and solving for the potential we obtain $U = (L/B)\ln[i/i_o(1 + L/x)]$. The anodic film thickness L can be evaluated using Faraday's law (assuming a constant 100% current efficiency[1,2]) $L = (M/d\sigma nF)Q$, where Q is the quantity of charge passed, M is the molecular weight of the oxide, d is its density, n - the number of charges transferred per oxide molecule, σ is the roughness factor and F is Faraday number. From these starting points the resulting U vs. Q dependence is evaluated

$$U = (M/d\sigma nFB)Q \ln[i/i_o(1 + MQ/d\sigma nFBx)] \qquad (4)$$

This equation describes the galvanostatic potential vs. charge curve for a surface charge assisted film growth.

The field intensity E = U/L can be evaluated using two independent methods:

a)Using Faraday's law : $E = U(d\sigma nF/MQ)$

b) measuring the film capacitance C immediately after anodization at a sufficiently high frequency [1] $E = UC\sigma/\varepsilon\varepsilon_o$. It will be shown below that the field strength calculated by both formulae is not a constant during the anodization process.

2.Transient processes during galvanostatic oxidation and at open circuit conditions

2.1) In order to account for the superimposition of alternating current with a small amplitude, the time and field dependence of the space charge have to be evaluated. The model of De Wit *et al.* [6] is used: $dq_n/dt = iW\,(gE / W - q_n)$, where W is the cross capture section per ionic defect, and g is a field parameter depending on the ratio between the velocities of positive and negative defects. This equation predicts a middle frequency time constant including a negative capacitance in series with a negative resistance [6,7].

A modification of this treatment is developed within the frames of the present model in order to account for the space charge dissipation at open circuit conditions.

2.2) Upon opening the circuit, a dissipation of space charge begins. The field strength caused by this dissipation is in the opposite direction of the alternating current flowing through the system *eg* in an impedance experiment. This field we denote as E_{sc} : $dq_n/dt = iW\,(gE_{sc}/W - q_n)$.

When a small sine wave perturbation is passed through the system, the following expressions hold

$$i = |i| \exp(j\omega t)\ ,\quad E_{sc} = E_{sc,o} + |E_{sc}| \exp(j\omega t + \varphi_E),\quad q_n = q_{no} + |q_n| \exp(j\omega t + \varphi_q) \quad (6)$$

Here q_{no} and $E_{sc,o}$ are the dc components of the field and space charge, and $|i|$, $|q_n|$ and $|E_{sc}|$ are the complex amplitudes of current, field and space charge, respectively. As the perturbation amplitude is considered small, it is to be expected that the low-field (ohmic) transport equation is valid

$$|i| = -2i_oB\,(\,|q_n|/\varepsilon\varepsilon_o + |E_{sc}|\,) \quad (7)$$

where the physical meaning of the negative sign was explained above. After some algebra one can obtain for the complex faradaic capacitance of the system [1]

$$C_{ac} = -2i_oB/[2i_oBW/\varepsilon\varepsilon_o(gE_{sc,o} - q_{no}) + j\omega] \quad (8)$$

which corresponds to a time constant including a negative capacitance and a negative resistance.

3. Generalized impedance response during the growth and dissolution of an anodic film in steady state conditions

A scheme for the metal/film/electrolyte system [2,4] is given in Fig.1.

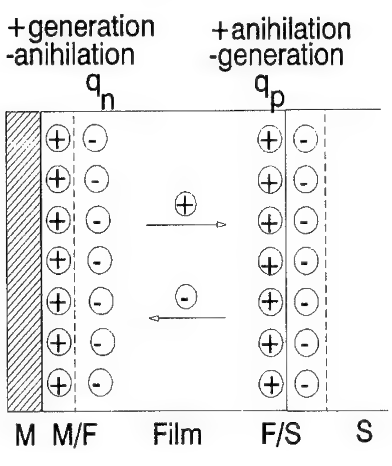

Fig.1. A simplified scheme of the metal/film/solution interface according to the extended space charge approach.

The explanation for the formation of the surface charge q_p is analogous to the one given above for q_n but related to the film/solution interface: the adsorption of negatively charged counter ions from

the solution slows down the motion of positive carriers. The main assumptions for the generalized treatment are presented below.

3.1)At the metal/film interface, generation of positive charge carriers V_o^{2+} procceds according to the reaction

$$M_m \rightarrow M_M^x + V_o^{2+} + xe^- \qquad (I)$$

3.2)These defects are annihilated at the film/solution interface by the following interaction

$$V_o^{2+} + H_2O \rightarrow 2H^+ + O_o \qquad (II)$$

It is assumed that both reactions (I) and (II) obey Tafel kinetics : $i_i = k_i\exp(b_i\eta)$, i=I,II , where η is the overpotential.

3.3)In the bulk of the film vacancies are transported by a space charge assisted high field migration. The kinetic equation is a generalized form of (1) taking into account the influence of both surface charges q_n and q_p on the vacancy motion process

$$i_b = i_b^o\exp[B(\eta/L + (q_n - q_p)/\varepsilon\varepsilon_o] \qquad (9)$$

3.4) The dissolution of the film is also potential dependent according to the suggestions of Glarum and Marshall[10]: $i_{III} = k_{III}\exp(-{}^*b_{III}\eta)$.

3.5)The impedance response of the overall system will be the sum of the impedances of the passive film, the metal/film and film/electrolyte interfaces

$$Z = Z_b + Z_{M/F} + Z_{F/S} \qquad (10)$$

If it is assumed that $q_n >> q_p$ we obtain for the impedance of the barrier film[5]

$$Z_b = \{j\omega C_b + i_b /L[B + gi_b/(i_bW + j\omega)]\}^{-1} \qquad (11)$$

where C_b is the film capacitance.

The impedance of the metal/film interface is reduced to the parallel combination of the double layer capacitance and the charge transfer resistance of reaction (I): $Z_{M/F} = (j\omega C_d + di_I/d\eta)^{-1} = (j\omega C_d + i_Ib_I)^{-1}$. Since the law of conservation of charge has to be fulfilled, at steady state $i_I = i_b = i_{II} + i_{III}$ = const. The impedance of the film/solution interface can be calculated from the expression derived by Epelboin and Keddam[11]: $Z_{F/S} = \{i_Ib_I[1 + (B_o + B_1j\omega)/(A_o + A_1j\omega + A_2\omega^2)]\}^{-1}$, where A_o, A_1, A_2, B_o and B_1 are functions of the rate constants of reactions (I)-(III)[11]. Thus the overall impedance response can be calculated.

4. Breakdown of anodic films

The dependence of the breakdown voltage U_b on the resistivity of the electrolyte ρ is given by the empirical equation of Burger and Wu[12]

$$U_b = a_b + b_b \log\rho \qquad (12)$$

In order to assess the breakdown situation, the generalized space charge approach (paragraph 3) is applied.

4.1) We postulate that negative defects motion leads to film breakdown. At the film solution/interface, the positive counter surface charge q_p accelerates the transport of negative and slows down the transport of positive charges.

4.3) The adsorbed anions react with positive defects (oxygen vacancies) forming ion-vacancy pairs

$$V^{2+}{}_{o,F/S} + A^{-}{}_{ad} \rightarrow A_{F/S} \qquad (III)$$

4.4) Breakdown takes place after a critical amount of excess charge is reached (following Chao *et al.* [13]):$(i^{-}{}_{M/F} - i_m)t = \Delta q_{cr}$, where i_m is the rate of submergence of negative defects at the metal/film interface which is considered independent from the processes at the opposite interface and $i^{-}{}_{M/F}$ is the rate of transport of negative defects[13].

4.5) For galvanostatic conditions, $i^{-}{}_{M/F}$ is proportional to the current density;

4.6) For the equilibrium of reaction (II) it is shown in [13] that $[V^{2+}{}_{o,F/S}][A^{-}] = u\exp(-\alpha U/RT)$, where u and α are constants depending on the polarizability of the film/solution interface. As for galvanostatic conditions $[V^{2+}{}_{o,F/S}]$ = const, solving for U_b gives

$$U_b = K_1 - 2.3(RT/\alpha F)\log[A^{-}] \qquad (13)$$

where $K_1 = 2.3(RT/\alpha F)\log(u/[V^{2+}{}_{o,F/S}])$ = const.

Assuming complete dissociation of the electrolyte, its concentration c is proportional to $[A^{-}]$; from the other hand, it is well established that a power dependence relates resistivity and concentration;a relation between U_b and ρ can be derived[2] as an equation of the form of (11).

EXPERIMENTAL

Disc electrodes made of 99.999%Bi and 99.99% Sn were used[1 - 5] as working ones in a conventional three electrode cell with a platinum mesh counter electrode and a saturated calomel or mercurous sulphate electrodes as reference ones. A glycol borate electrolyte (GBE, equimolar mixture of tetramethyleneboric acid and NaOH) described elsewhere [1,3] and a range of H_3PO_4 and H_2SO_4 solutions [2,4-5] prepared from p.a. chemicals and bidistilled water were employed.

Impedance measurements were accomplished using a Solartron ECI 1286 potentiostat/galvanostat and a Solartron FRA 1250 analyser[1]. Galvanostatic anodization experiments were performed on a laboratory made potentiostat/galvanostat (600 V,0.5 A)[3]. Photocurrent in potentiostatic conditions was registered with a PAR 186 A lock-in amplifier using a 100 W halogen lamp coupled to a 7300 monochromator (Applied Photophysics) as a light source[2,5].

RESULTS

I. Anodization of bismuth in non-dissolving electrolytes[1-3]

1. Steady state galvanostatic oxidation

Galvanostatic charging curves during anodization of Bi in GBE at different current densities are presented in Fig.2. The non-linearity of of the potential vs. charge dependence is well pronounced, especially at higher current densities. The excellent agreement between experiment (points) and predictions according to equation (4)(solid lines) is also presented. Table 1 summarizes the best fit parameters x, B and i_0 for the three current densities used[3].

Table 1. Best - fit values of the parameters in equation (4) as depending on the current density [3]

i / mA.cm^{-2}	i_0 / mA.cm^{-2}	B / MV^{-1}cm	x / nm
0.20	3.9	2.3	1600
2.00	11.1	2.3	120
20.0	17.0	2.5	3.2

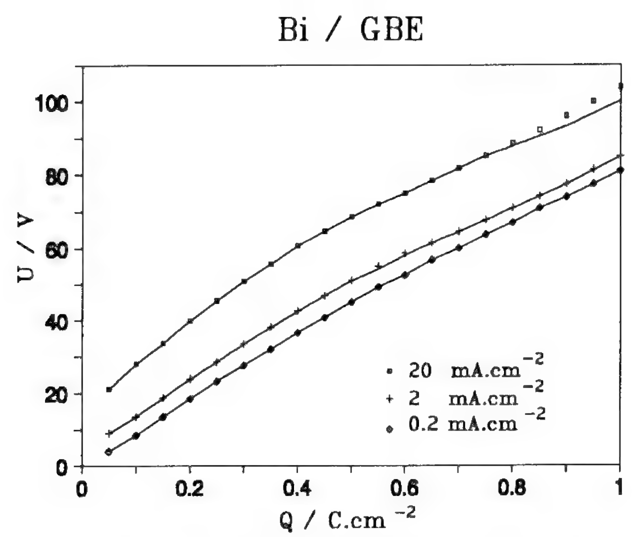

Fig.2. Anodic charging curves of a Bi electrode anodized in GBE with various current densities. Points: experiment, solid lines - best-fit calculation according to equation (4).

The average values of the electric field strength are presented in Fig.3. The model predictions are denoted with solid lines. Once again a satisfactory agreement between experiment and model approach is obtained.

2. AC impedance measurements during relaxation of the surface charge at open circuit conditions

Fig.4 presents a capacitance spectrum of the system Bi/Bi_2O_3/GBE after 10 min. of stay at open circuit following galvanostatic oxidation with 0.062 mA.cm^{-2} up to 10 V. Points are

experimental values, and the solid line is calculated using equation (8) with the ohmic resistance (R_{ohm}) and the non-faradaic capacitance (C_o) in series. A complete agreement is obtained suggesting the validity of the proposed approach for the dissipation of the surface charge at open circuit conditions.

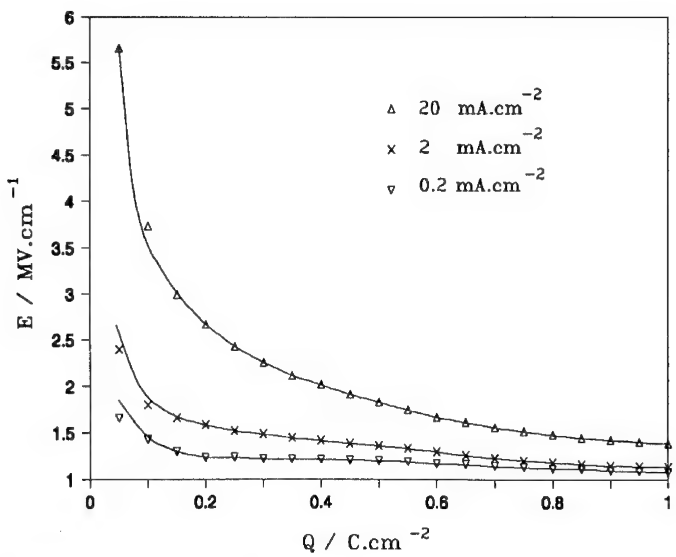

Fig.3. Average field strength in the anodic film depending on the quantity of charge passed. Points: experiment, solid lines - best-fit calculation[3].

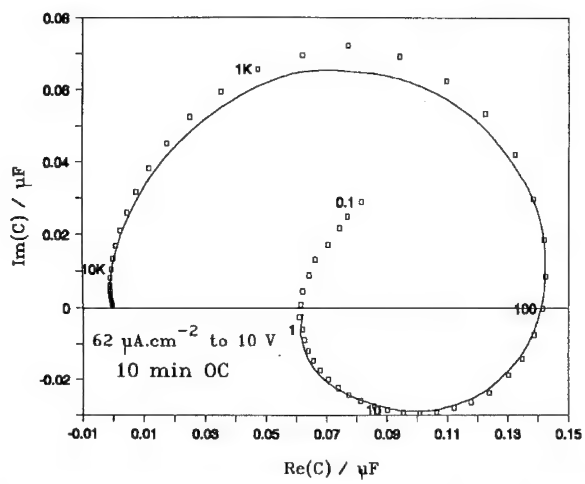

Fig.4. A complex capacitance spectrum registered at open circuit after anodization of Bi in GBE at 0.062 mA.cm^{-2} up to 10 V. Time of stay at open circuit, 10 min. Solid lines - simulation according to equation (8). The following parameters are used in the calculation: C_o = 0.13 µF, $\boldsymbol{E}_{sc,o}$= 0.1 MV.cm^{-1}, $q_{n,o}$ = 20 µC, ε = 45, W = 2.10^{-4} C^{-1}cm^2, g = 6 cm. µF^{-1}, B = 2 MV^{-1}.cm, R_{ohm} = 800 Ω.

3. Breakdown of anodic films on bismuth

In [2] the validity of the Burger and Wu's equation (12) was demonstrated for anodization of Bi in a wide concentration range of H_3PO_4 solutions. In the extended surface charge approach accounting for film breakdown (Theory section, paragraph 4), a major attention was paid to the positive surface charge q_p forming at the oxide/electrolyte interface probably as a condensed electrolyte layer. The formation of such charge would affect the conductivity of the electrolyte in the vicinity of the anode. In order to verify this assumption, electrolyte resistivity in the anodic compartment was monitored during anodization and a quasi-linear decrease up to breakdown was observed[2]. This may be caused by the formation of a condensed electrolyte layer at the barrier film/solution interface, resulting in an overall increase of the conductivity via an increase of the amount of counterions.

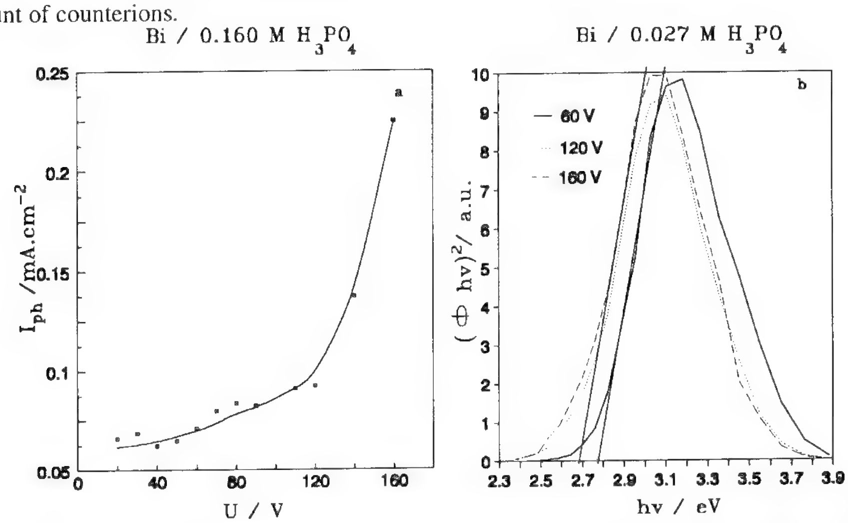

Fig.5. a) potential dependence of the photocurrent for films formed on Bi in 0.016 M H_3PO_4 up to a range of potentials; b) photocurrent spectra for films formed on Bi in 0.027 M H_3PO_4 and stabilized for 1 h at different potentials.

The dependence of the photocurrent on formation potential for films formed on Bi in 0.05 M H_3PO_4 at 5 mA.cm^{-2} is presented in Fig.5a. The photocurrent is practically constant for potentials lower than 90 V and increases sharply thereafter. It is worth mentioning that for potentials higher than 100 V potentiostatic breakdown takes place almost instantaneously(the highest voltage at which photocurrent was measured corresponds to the galvanostatic breakdown voltage). It can be suggested that the electronic conductivity of the oxide/solution interface increases sharply after potentiostatic breakdown takes place.

Photocurrent spectra for an anodized Bi electrode stabilized for 1 h at four potentials are presented in Fig.5b.For formation potentials smaller than 120 V, the estimated direct band gap of the oxide(2.8 eV) coincides well with the one reported by a number of authors [14-16]. For films stabilized at higher potentials a decrease of the estimated gap with *ca* 0.2 eV is observed. This fact

can be explained by the production of donor levels in the condensed electrolyte layer bearing the space charge q_p.

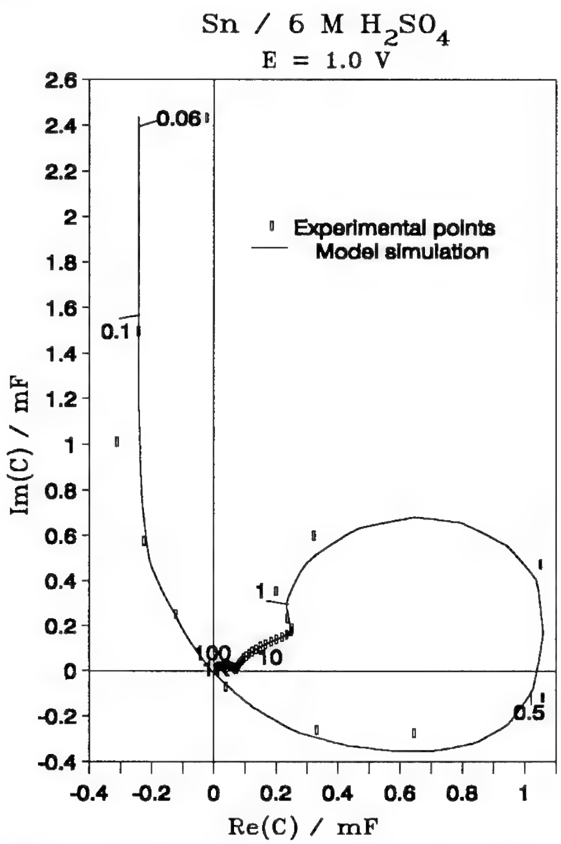

Fig.6. Impedance spectrum of the passive tin electrode in 6 M H_2SO_4 at a potential of 1.0 V vs. $Hg/Hg_2SO_4/K_2SO_{4(sat.)}$ electrode and a simulated impedance spectrum using the proposed surface charge approach (Eq.9 - 11).

II. Anodic passivation of tin in H_2SO_4 solutions[4,5]

It was demonstrated in [4,5] that tin passivates in concentrated H_2SO_4 solutions via the formation of a barrier-like layer of amorphous SnO. A locally coupled dissolution/repassivation reaction at the film/solution interface causes the electrode system to behave as a second order dynamic one[4]. At high anodic overpotentials(> 1,5 V), further oxidation of the SnO layer proceeds resulting in the formation of a film with a pronounced photoactivity [5]. Impedance spectra were found to be qualitatively the same in the whole high-potential interval. A typical spectrum recorded at a potential of 1.0 V vs. the $Hg/Hg_2SO_4/K_2SO_{4(sat.)}$ electrode is presented in Fig.6. A total of five time constants was detected in the spectrum, related to the processes occurring in the bulk of the film and the metal/film interface (in the high frequency domain) as well as to the film/solution interface interface (in the low frequency one).A complex capacitance spectrum

calculated using the procedure proposed in the Theory section, paragraph 3 (Eq.9 to 11) is presented in Fig.9 with a solid line. The simulated spectrum is able to reproduce semi-quantitatively the experimental one, which can be taken as a proof for the validity of the suggested model approach. The great number of parameters, however, furnishes some ambiguity in the calculation as there might be another set of kinetic constants representing the experimental data equally well. Thus these kinetic constant are neither given nor commented[5].

CONCLUSIONS

1) The proposed model accounts quantitatively for both steady state and transient response of the metal/oxide/electrolyte system during anodization under galvanostatic conditions;

2) The derived approach describes adequately the open-circuit relaxation of the system metal/oxide/electrolyte;

3) A generalized space charge approach taking into account the formation of a counter space charge at the film/solution interface is able to predict the impedance response of growing and dissolving anodic passive films;

4) This generalized approach is used to derive the empirically found dependence of the galvanostatic breakdown voltage on electrolyte resistivity furnishing a reasonable physical picture of electric breakdown phenomena. .

REFERENCES

1. M. Bojinov, I. Kanazirski and A. Girginov, *Electrochim. Acta* **37**, 2415(1992)
2. I. Kanazirski, M. Bojinov and A. Girginov, *Electrochim. Acta* **38**,511 (1993)
3. I. Kanazirski, M. Bojinov and A. Girginov, *Electrochim. Acta* **38**, 1061(1993)
4. M. Bojinov, K. Salmi and G. Sundholm, *J. Electroanal. Chem.* **347**, 207(1993)
5. M. Bojinov, K. Salmi and G. Sundholm, *J. Electroanal. Chem.* **358** , 177(1993)
6. H.J. De Wit, C. Wijenberg and C. Crevecoeur, *J. Electrochem. Soc.* **126**, 779(1979)
7. M.J. Dignam, in *Comprehensive Treatise of Electrochemistry*, Vol.4, J.O'M. Bockris, B.E. Conway, E. Yeager and E. White, Ed., Plenum Press, New York (1981), p.247.
8. A.T. Fromhold Jr., in Oxides and Oxide Films, Vol.3, J.W. Diggle and A.K. Vijh, Ed., Marcel Dekker, New York, 1976, p.1-271.
9. J.M. Albella, I. Montero, O. Sanchez and J.M. Martinez-Duart, *J. Electrochem. Soc.* **133**, 876(1986)
10. S.H. Glarum and J.H. Marshall, *J. Electrochem. Soc.* **132**, 2878(1985)
11. I. Epelboin and M. Keddam, *Electrochim. Acta* **17**, 177(1972)
12. F. Burger and J. Wu, *J. Electrochem. Soc.* **118**, 2039(1971)
13. C.Y. Chao, L.F. Lin and D.D. McDonald, *J. Electrochem. Soc.* **128**,1194(1981).
14. S. Ikonopisov, L. Andreeva and Ts. Nikolov, *J. Electrochem. Soc.* **120**, 717(1973)
15. M. Metikos-Hukovic, *Electrochim. Acta* **26**, 989(1981).
16. L.M. Castillo and L.M. Peter, *J. Electroanal. Chem.* **146**, 377(1983).

Materials Science Forum Vols. 185-188 (1995) pp. 611-620

Transient ionic space charges in thin oxide films: Determination of thickness distribution, temperature, and localized phenomena

M.M. Lohrengel and S. Rüsse

Institut für Physikalische Chemie und Elektrochemie, Heinrich-Heine-Universität, D-40225 Düsseldorf, Germany

Keywords: Anodic aluminum oxides, space charge layers, temperature dependent oxide growth

Abstract: The thickness distribution of thin (3 to 20 nm) anodic oxide films on Al (and Ta, Nb, Ti), the temperature dependent oxide growth and the incorporation of water were investigated by fast transient methods: current transients of potentiostatic pulse experiments (resolution some μs), combined with immersion transients (resolution 2 ms) and temperature step transients (resolution 1 K).

1 Introduction

The anodic oxide growth on Al, Nb, Ta and others yields in neutral solutions thin oxide films of the barrier type. If the electric field strength E in the oxide film exceeds 10^6 V/cm, the current density i of anodic oxide formation is given by the high field equation [1]:

(1) $$i = i_0 \exp(\beta E)$$

The ion transport is described [2] as a field supported, thermally activated hopping of ions. The constants i_o and β are given by

(2) $$i_0 = \nu \rho a \exp\left(-\frac{W}{RT}\right)$$

and

(3) $$\beta = \frac{\alpha a z F}{RT}$$

where ν is the vibration frequency of the ion, ρ is the concentration of mobile charge carriers (in C/cm^3), a is the jump distance, W is the activation energy of hopping, α is a symmetry factor, and z is the charge number of the ion. The field strength E is calculated from the potential drop ΔU across the oxide and the layer thickness d

(4)
$$E = \frac{\Delta U}{d} = \frac{U - U_0}{d}$$

where U denotes the electrode potential. U_0 is the potential where the field strength is zero. U_0 (Al: $U_0 = -1.6$ V) includes the potential drops at the oxide interfaces, which depend only weakly on the current density **[3]**.

The film thickness d is mainly determined by the final potential. d can be calculated from the formation factor (typically 1-2 nm/V). The time dependence is less obvious and often described by an inverse logarithmic growth law **[4]**. Using *Faraday*'s law, the increase of the layer thickness d as a function of the time t is given **[5]** by

(5)
$$\frac{\mathrm{d}d}{\mathrm{d}t} = \frac{i_0 M}{\rho_{ox} y F} \exp\left(\beta \frac{U - U_0}{d}\right)$$

where M and ρ_{ox} are the molecular weight and the density of the oxide, respectively, y is the number of elementary charges, and F is the *Faraday* number. Eq. 5 cannot be solved in a closed form, but must be integrated numerically to obtain $d = f(E,t)$ or $i = f(E,t)$ **[6]**.

1.1 Overshoot

For short periods of time ($t < 1$ s) the film growth is small and, therefore, the anodic formation current i should be constant (eq. 5, **[6]**). In many cases, however, the shape of experimental curves differed significantly from those predicted by the high field model (Al, Nb, Ta, and, with some restrictions, Ti). Under potentiostatic conditions a delayed oxide formation, followed by a pronounced current peak (overshoot), was observed. After this overshoot the oxide grows according to the high field model. This effect was noted for the first time by *Güntherschulze* and *Betz* **[1]** on Al and later by *Vermilyea* **[7]** on Ta and Nb. The first comprehensive investigation of the overshoot was published by *Crevecoeur* and *de Wit* **[8]**. The overshoot depended on the film thickness, field strength, temperature, pre-treatment, and electrolyte.

The mechanism of overshoot was explained in a number of recent papers **[9, 10, 11, 12, 13]**, hence, only a brief description is given. The concentration ρ (eq. 4) of mobile charge carriers (e.g. Al^{3+} and O^{2-}) is low, if the field strength is low. Mobile ions cannot be formed somewhere within the oxide, but only at the interfaces. They form intermediate space charges which migrate to the opposite interfaces. Excess charge means, according to *Poisson*'s law, local distortions of the electric field strength, which hinders further migration and oxide growth. Therefore, a macroscopic compensation by an adequate amount of mobile counter ions is required, which explains the transport numbers close to 0.5 **[14]**. The individual aspects of mobilities of different ions, e.g. volume or interaction with the lattice, are reduced to one principle, the charge. The mean concentration of mobile ions ρ is a function of E and t. The current increases until the charge carriers meet the opposite interfaces. In the maximum (overshoot) ρ reaches the final value and i_0 becomes constant. The oxide film grows. The final concentration of mobile ions ρ was estimated to 100 C/cm^3, which is close to the value of *Winkel et al.* **[15]** (Al: $8 \cdot 10^{21}$ cm^{-3}).

The model is true for Al, Nb, Ta, and, with some restrictions, for Ti. Due to the limited space we reduce to the effects on Al electrodes ($\beta = 43$ nm/V, $i_0 = 10^{-17}$ A/cm^2, $U_0 = -1.6$ V).

2 Experimental

Most of the experiments presented here were carried out as current transients of potentiostatic pulse experiments. The transients were recorded in a wide range of current (1 $\mu A/cm^2 \leq i \leq 10\ A/cm^2$) and time (1 $\mu s \leq t \leq 1000$ s). The electronic equipment consisted essentially of a fast rising potentiostat (rise time 0.3 μs), a pulse generator (for multiple pulses), a fast auto-ranging current detection system (switching time 1 μs), a nonlinear rate generator (1 MHz to 1 mHz), all in-house developments. For experimental control, data processing and graphic presentation a '486 PC was used. The special equipment for the immersion transients is described in section 3.2.

The working electrodes were aluminum wires (99.999%) with a surface of 0.3 cm^2 limited by photoresist resin. The wires were electropolished 30 s in glacial acetic acid containing 5% $HClO_4$ at 200 mA/cm^2. A gold foil (4 cm^2) was used as a counter electrode. The electrolyte was acetate buffer (pH 5.9). The solution was prepared from p.a. chemicals and de-ionized water. All potentials given here refer to the hydrogen electrode in the same solution (HESS).

3 Results

The model described in section 1.1 predicts **[16]** the moment of overshoot i_{max} (peak maximum)

(6)
$$t_{max} = \frac{\rho d}{i_0 \exp(\beta E)}$$

and the current density in the maximum i_{max}

(7)
$$i_{max} = i_0 \exp(\beta E)$$

with the final values of ρ and i_0. A combination of the eqs. 5, 6 and 7 enables the calculation of complete current transients *i(E,t)* **[6]**. Eq. 6 was developed from the model, but it was confirmed by a large number of transients and, therefore, may be also used like an empirical equation. The reproducible experimental transients and the reliability of eq. 6 encouraged us to use transients with overshoot as an analytical method.

3.1 The Distribution of Film Thickness

t_{max} varies experimentally in a wide range from μs to 10^4 s **[12, 17]**. Eq. 6 predicts a twofold dependence on the oxide film thickness *d*, a linear and an exponential, as $E = \Delta U/d$. Some examples are presented in fig. 1. Three experiments were carried out with different film thicknesses and potentials, but at a constant field strength E = 7.6 MV/cm. Therefore the values of i_{max} were equal (eq. 7). t_{max}, on the other hand, is shifted due to the different thicknesses according to eq. 6.

At a given potential U, t_{max} depends only on *d*. Fig. 2 presents a current transient and, in addition, the positions of overshoot t_{max} for different thicknesses, calculated from eq. 6. The shape of the overshoot peak is mainly determined by the emission of mobile ions, but an inhomogeneous thickness would cause an additional broadening. The shape, therefore, indicates an upper limit of such a thickness distribution. Local fluctuations of the thickness should be smaller than ± 0.2 nm.

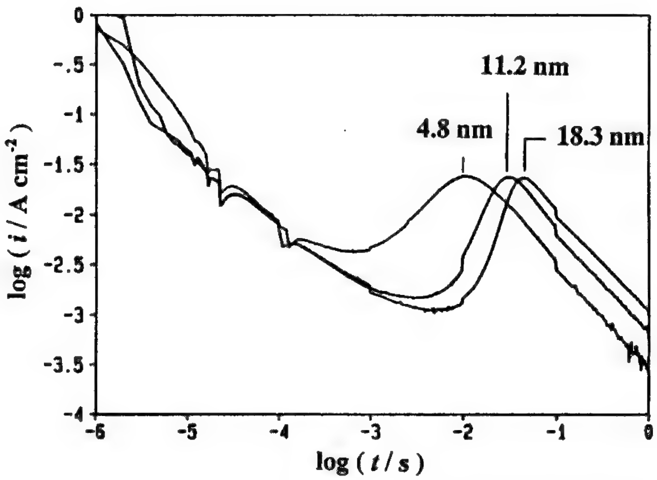

Fig. 1. Current transients of potentiostatic oxide growth at $U = 2$ V (4.8 nm), 6.95 V (11.2 nm), and 13 V (18.3 nm) on Al at 25 °C, pH = 5.9. The initial thicknesses were chosen in such a way that the initial field strength was always 7.6 MV/cm. The height of the overshoot peak is equal (eq. 7), but the position depends on the thickness (eq. 6).

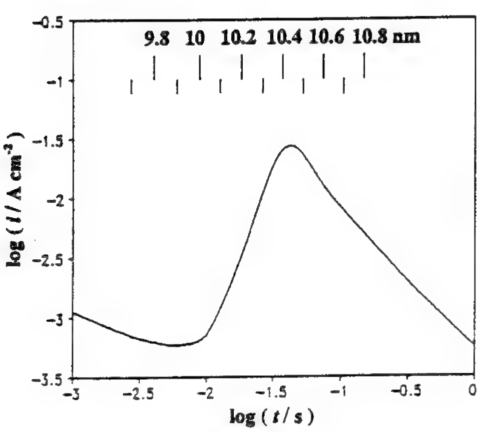

Fig. 2. Current transient of a potential step to 7 V, initial oxide film thickness 10.5 nm. Positions of the overshoot (t_{max}) for different thicknesses, calculated from eq. 6, are given in addition.

Fig. 3. Current transients of an initially terraced oxide film (2% of the surface with a thickness of 6.8 nm, 22% of 7.9 nm, 76% of 9 nm) on Al, stepped to 5 V.

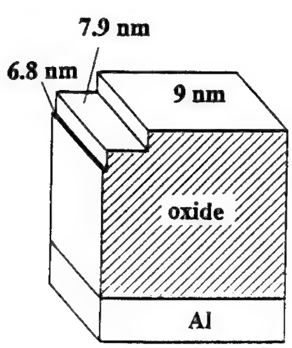

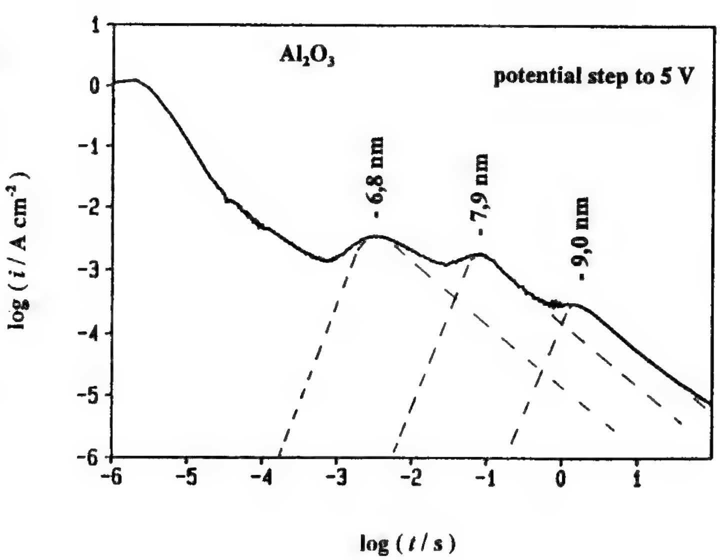

The thickness of oxide films, on the other hand, may be taken from experimental transients. This was proved by special experiments. Different oxide film thicknesses were prepared on one Al electrode. The wire was immersed by steps and the potential was decreased simultaneously. The result was a terraced structure of the film, according to the scheme in fig. 3. The subsequent transient to a higher potential is presented. The areas of different thickness behave independently, producing separate, pronounced peaks. The experimental transient is the sum of three transients with the corresponding thicknesses, multiplied with their individual degree of coverage Θ_i. It is no problem to detect small, thin fractions beside thicker, large areas, as the current depends exponentially on the field strength (eq. 1).

This means, the overshoots indicate no collective property of the complete surface, but are caused by the local ionic conductivity and, hence, local thickness.

The overshoot in potentiostatic current transients is useful to monitor the thickness distribution of oxide films. Two examples were already published: the thickness distribution in oxide films formed by vapour deposition at room temperature **[18]** (which are not dense and homogeneous **[19]**) and the evolution of pores as an initial step of the cathodic breakdown of oxide films **[20]**.

It must be pointed out that such a distribution of thicknesses cannot be investigated by other in-situ methods, e.g. impedance spectroscopy. The electrolyte and the metal electrode form equipotential surfaces and, hence, the mean capacity of the terraced surface is measured. Sweep experiments, however, indicate different thicknesses **[21]**, but the areas of different thickness must be of comparable size **[22]**. A fundamental problem of sweep experiments is the simultaneous change of time and potential, i.e. the superposition of the overshoot and potential dependent growth, which makes the interpretation difficult.

3.2 Immersion Transients

The incorporation of water from air humidity into oxide films is a well-known phenomenon. Stresses in porous layers depending on humidity were reported by *Alwitt et al.* **[23]**. They found weight losses up to 1.3% in dry air. Stress and weight loss were reversible. Accordingly, alumina films may be used as humidity sensors **[24]**. *Ebling* **[16]** monitored the water incorporation with an electrochemical quartz micro balance and reported a mass increase. *Greuel* **[25]** investigated the breakdown of thin anodic oxide films of the type $Al/Al_2O_3/Au$ and detected an influence of protons from the humidity of environment through the (obviously porous) Au film.

We investigated the incorporation of water into the thin Al_2O_3 films in contact with the electrolyte and the influence on the ionic conductivity. These experiments are limited to an exposure < 1000 s, when corrosion becomes notable and reduces the film thickness. Hence, we focussed our interest on shorter periods of time. A fast, well defined wetting procedure seemed to be necessary to obtain reproducible results. Stimulated by experiments of *Chazaviel* **[26]**, we developed a special equipment (fig. 4). The electrode wire was fixed to a vertically sliding frame. This frame was fixed to it's upper position above the electrolyte by a small permanent magnet. The frame was accelerated down by an electromagnet and dipped the electrode wire into the electrolyte. The movement of the electrode was supervised by segments at the frame which moved through an infra-red light barrier.

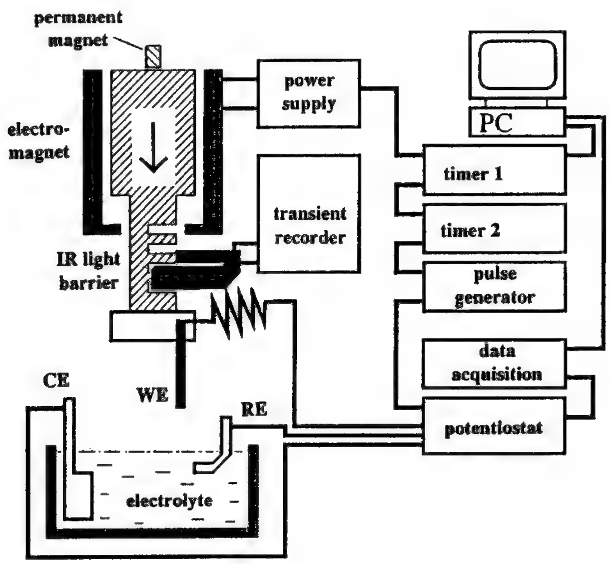

Fig. 4. Schematic representation of the immersion transient set-up. The electrode wire is mounted above the electrolyte and accelerated down into the electrolyte by an electromagnet.

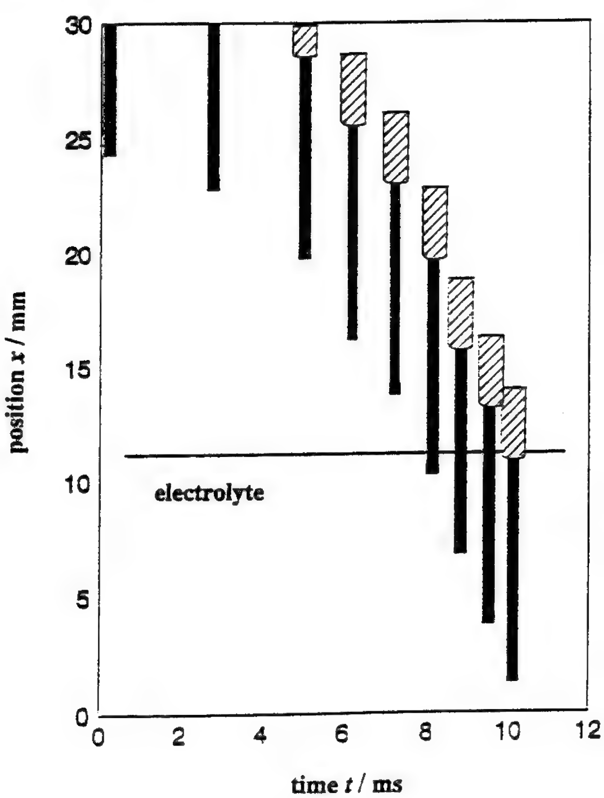

Fig. 5. Position of the electrode wire vs. time during immersion. The immersion process (and wetting) is limited to 2 ms. The wire is accelerated by 640 m/s^2, the final speed is 5.7 m/s.

The movement of the electrode wire during immersion is illustrated in fig. 5. The complete movement is about 10 ms, the actual immersion process is reduced to 2 ms. This time includes the wetting process, as the current increases to it's initial value within these 2 ms.

Fig. 6 shows current transient of oxide formation after different times of exposure t_w. The electrodes were stored about 20 h in dry air before use. The transients are almost identical for $t_{exp} < 1000$ s. At $t_{exp} = 1000$ s the overshoot is shifted to shorter periods of time due to an insignificant thinning of the oxide film by corrosion. Structural changes as a result of water content which influence the ionic conductivity were not observed.

3.3 Temperature Dependent Transients

The eqs. 2, 3 and, therefore, 6 predict a temperature dependence. Further effects may come from the temperature dependence of corrosion and structural change due to re-crystallisation or changes of composition, e.g. Water content. In the first experiments the oxide films were formed and measured at the same temperature (5° to 80°C). The resulting transients of further oxide growth are presented in fig. 7 and appear to be independent of the temperature. Obviously, different temperature effects compensate each other almost completely. This is the well-known temperature anomaly **[27]**. A separation of the different effects is possible if they occur in different time scales, therefore, the experimental procedure had to be modified.

The layers were formed at 25°C. This guarantees a reproducible initial film structure. The technique of the immersion transients (section 3.2) was used to transfer the electrodes (within 2 ms) to the electrolyte of different temperature. The electrodes were stored under potential control for different times t_w (1 ms to 1000 s), before the transients were started. The transients (fig. 8) indicate two effects: a heating period of about 100 ms (which will be discussed later), followed by a period of negligible time effects (> 10 s). For longer periods of time (100 s) the shape of transients changes again, influenced by corrosion and structural changes. This means, the film is meta-stable for some 100 s at a different temperature. Only heating effects are measured in this period, any re-structuring which influences the ionic conductivity requires ≥100 s.

Temperature dependent immersion transients yielded results as expected from the eqs. 6 (fig. 9). The activation energy of ion hopping W may be taken from such experiments **[13]**.

Obviously, the shift of t_{max} is very sensitive to the temperature with a resolution of about 1 K. Hence, we tried to monitor the heating or cooling process of the oxide film by this method. Transients in the time range < 1 s were compared with calculated transients to get the respective temperatures. These temperature transients (relative temperature change $\Delta T/\Delta T_{max}$ vs. time t) are shown in fig. 10 for a heating from 25°C up to 80°C. The inverse process of cooling down was realized by electric heating of the electrode wire to 110°C and subsequent transfer to an electrolyte of 25°C. Both processes had finished after some 100 ms and the oxide film had the same temperature as the electrolyte. It is worth mentioning that the temperature of a film of some nm is measured by these experiments; the bulk of the electrode wire and the electrolyte may have different temperatures in the same moment.

4 Summary

Thin (3 to 20 nm) anodic oxide films on Al (and Nb, Ta, Ti) were investigated by fast transient methods: current transients of potentiostatic pulse experiments (resolution some µs), combined with immersion transients (resolution 2 ms) and temperature step transients (resolution 1 K). The thickness distribution,

Fig. 6. Al electrodes with a dry oxide film were immersed (≈ 2 ms) and an anodic transient was triggered after different times of exposure t_w. No effects of a possible swelling are observed. Corrosion shifts the overshoot to shorter periods of time if t_w > 100 s.

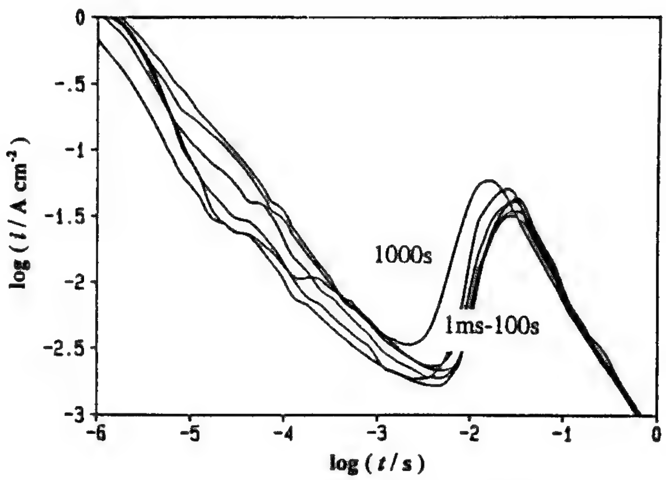

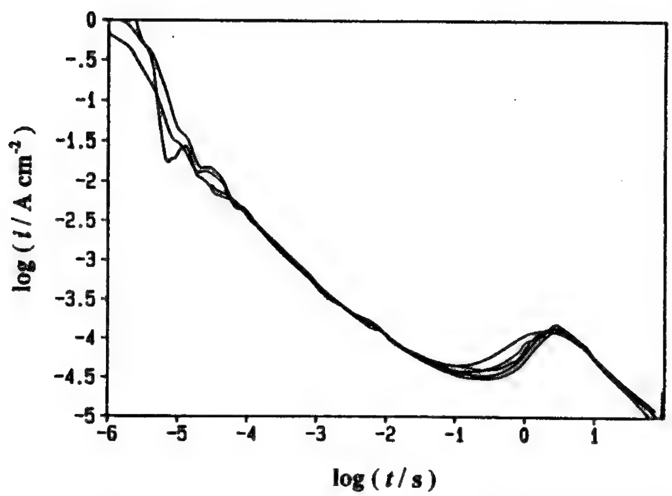

Fig. 7. Current transients (step to 9 V) at different temperatures (5 ℃ to 85 ℃). The oxide film was formed and investigated at the same temperature. The oxide growth is apparently temperature independent.

Fig. 8. Temperature dependent immersion transients. Oxide films about 15 nm were formed at 25 ℃ and immersed (within 2 ms) into an electrolyte of 80 ℃. The transients (step to 9 V) were triggered after different times of exposure t_w. The heating period of the film has finished after 100 ms, the layer is meta-stable up to 10 s, then corrosion and re-structuring takes place.

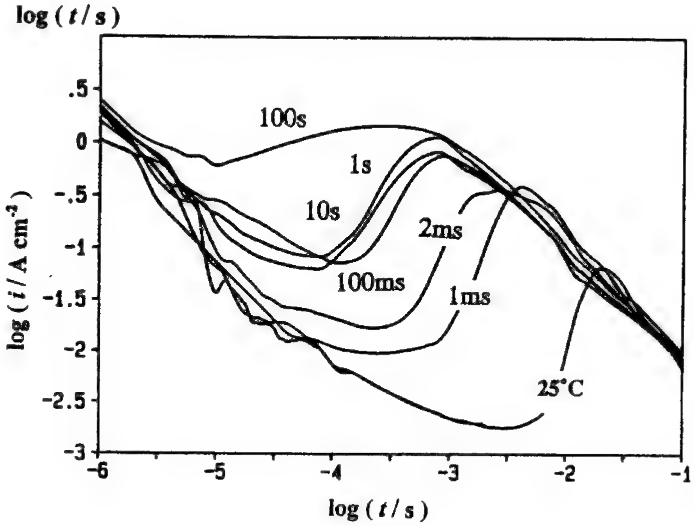

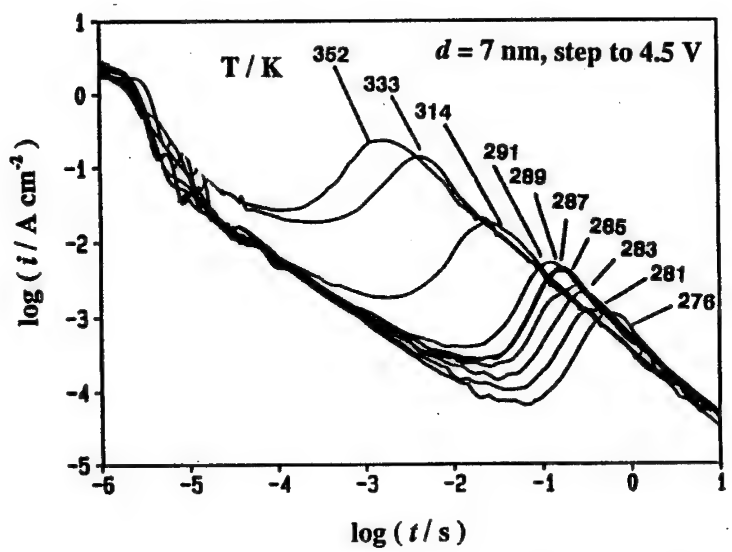

Fig. 9. Temperature dependent immersion transients. 7 nm of oxide were formed at 25 ℃, transferred to the electrolyte of different temperature, and stepped to 4.5 V. A temperature dependence due to the eqs. 2, 3, 6, and 7 is observed.

Fig. 10. Heating or cooling process of oxide films of about 15 nm on Al, taken from immersion transients. Relative temperature change vs. logarithm of time. Heating: a wire of 25 ℃ was transferred to an electrolyte of 80 ℃; cooling: a wire of 110 ℃ (electrically heated) was transferred to an electrolyte of 25 ℃.

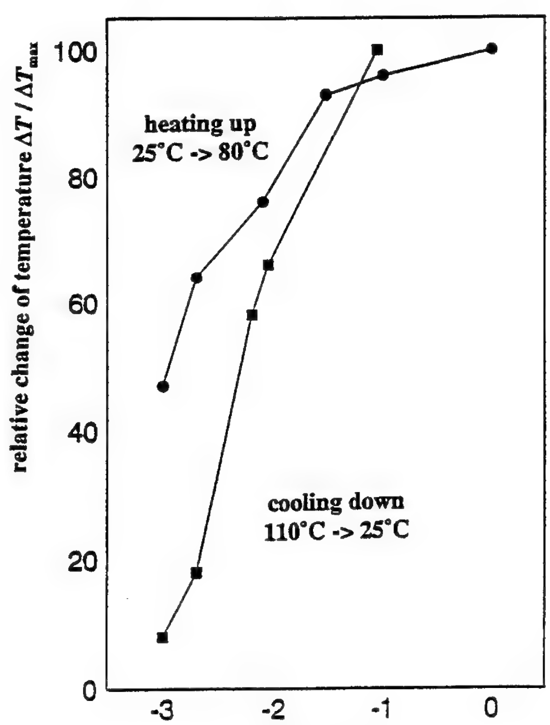

the temperature dependent oxide growth, and the incorporation of water were measured. The oxide films are very homogeneous in thickness (local fluctuations < 0.4 nm) and ionic conductivity. The temperature dependent oxide growth is given by the eqs. 1-6, deviations are observed only at longer periods of time (> 100 s), when other effects as corrosion become notable. The strong dependence of the overshoot on the temperature may be used to determine the temperature of the thin film. An incorporation of water, if possible, has no effect on the ionic conductivity.

These transients are certainly no universal in-situ, high speed ruler, thermometer, or microscope. Their use to determine the time resolved oxide film thickness distribution, the temperature changes in the film, and structural changes is limited to well defined, thin oxide films on Al, Nb, and Ta. Advantageous, on the other hand, is the analysis of the time dependent ionic conductivity, which is responsible for corrosion and breakdown phenomena. The well-known temperature anomaly (apparently temperature independent oxide growth from 5° to 80°C) is a result of the increasing growth rate and corrosion rate with temperature, effects which compensate each other almost completely.

The financial support of the *AGEF e.V. Institut an der Heinrich-Heine-Universität Düsseldorf* and the *Deutsche Forschungsgemeinschaft* is gratefully acknowledged.

References

1 A. Güntherschulze, H. Betz, *Z. Phys.* 92 (1934) 367
2 E. J. W. Verwey, *Physica* 2 (1935) 1059
3 J. Siejka, J. P. Nadai, G. Amsel, *J. Electrochem. Soc.* 118 (1971) 727
A. J. Davenport, G. T. Burstein, *J. Electrochem. Soc.* 137 (1990) 1496
4 N. Cabrera, N. F. Mott, *Rep. Prog. Phys.* 12 (1948-49) 163
5 K. J. Vetter, "Elektrochemische Kinetik", Springer Verlag, Berlin 1961
6 M. M. Lohrengel, K. Kluger, *Elektrokhimiya* 23 (1993) 89
7 D. A. Vermilyea, *J. Electrochem. Soc.* 104 (1957) 427
8 C. Crevecoeur, H. J. de Wit, *J. Electrochem. Soc.* 121 (1974) 1465
9 K. Kluger, M. M. Lohrengel, *Ber. Bunsenges. Phys. Chem.* 95 (1991) 1458
10 M. M. Lohrengel, *Ber. Bunsenges. Phys. Chem.* 97 (1993) 440
11 M. M. Lohrengel, *Materials Sci. Eng.* R 11 (1993) 243
12 M. M. Lohrengel, *Electrochim. Acta* 39 (1994) 1265
13 S. Rüße, M. M. Lohrengel, J. W. Schultze, *Solid State Ionics* (1994), in press
14 J. P. S. Pringle, *Electrochim. Acta* 25 (1979) 1423
15 P. Winkel, C. A. Pistorius, W. Ch. van Geel, *Philips Res. Rep.* 13 (1958) 277
16 M. M. Lohrengel in "Electrochemical and Optical Techniques for the Study and Monitoring of Metallic Corrosion" M. G. S. Ferreira, C. A. Melendres (eds.), Kluwer Academic Publishers Dordrecht (1991) pp. 69-121
17 T. Hurlen, S. Hornkjφl, *Electrochim. Acta* 36 (1991) 189
18 D. Diesing, S. Rüße, M. M. Lohrengel, *Proceedings of the Electroceramics IV*, Aachen 1994
19 R. A. Haefer, "Oberflächen- und Dünnschicht-Technologie", Springer Verlag, Berlin 1987
20 A. W. Hassel, M. M. Lohrengel, submitted to *Electrochim. Acta*
21 C. G. Dunn, *J. Electrochem. Soc.* 115 (1968) 219
22 A. W. Hassel, M. M. Lohrengel, S. Rüße, J. W. Schultze, *Bull. Chem. Technol. Macedonia*, submitted
23 R. S. Alwitt, J. Xu, R. C. McClung, *Electrochem. Soc. Proceed.* 92-22 (1992) p. 428
24 C. L. Cutting, A. C. Jason, J. L. Wood, *J. Sci. Instrum.* 32 (1955) 425
A. C. Jason, J. L. Wood, *Proc. Phys. Soc.* (London) B 68 (1955) 1105
25 G. Greuel, Thesis, RWTH Aachen 1994
26 J.-N. Cazaviel, *Surf. Sci.* 88 (1979) 204
27 D. A. Vermilyea, *Acta Met.* 1 (1953) 282
L. Young, Trans. *Faraday Soc.* 50 (1954) 159

Materials Science Forum Vols. 185-188 (1995) pp. 621-628

A new eletrochemical technique for in situ measurement of electric resistance and semiconductor characteristics of surface films on metals

T. Saario and J. Piippo

Manufacturing Technology, Technical Research Centre of Finland, PO Box 1704, FIN-02044 VTT, Espoo, Finland

Keywords: Electric resistance, Inconel 600, zircaloy, high temperature water

Abstract

Development of new in-situ surface analytical techniques is an area of high interest at the moment. In this paper a new Contact Electric Resistance (CER) technique is introduced. Results are presented of an investigation of the effect of TiO_2 inhibitor on the electrical properties of passive film on Inconel 600 in simulated steam generator crevice environment. In-situ monitoring of oxide growth on zircaloys in high temperature water environments is discussed based on a comparison of passive film electric resistance measurements with in-reactor test results.

CER technique

The new Contact Electric Resistance (CER) in situ technique [1] has been applied in several different fields of technology. These include e.g. investigations of passive film stability and candidate inhibitors in steam generator crevice environments [1,2], thiosulphate pitting [3] and competitive adsorption in paper mill wet end environment [4], effect of LiOH on degradation of oxides of Zircaloys [5] and characterization of semiconductor properties of GaAs [6]. The technique can be used for any conductive material and has in principal no limitations in pressure and temperature of the electrolyte.

In the CER technique an electrode is brought repeatedly into contact with the surface under investigation, and direct current is led through the contact. According to Ohms' law the electric resistance of the contact surface generates a voltage signal which is amplified and recorded. The contacting electrode can be of the same material as the material under investigation or one can choose to use a noble metal which does not have a surface film itself in the electrolyte and a range of electrochemical potentials used in the measurement.

The maximum measurement frequency is roughly one hertz, which makes it possible to follow the kinetics of most of the surface related processes, such as adsorption, passivation and film growth. The technique can also be used to differentiate between changes in the film resistance due to changes in electron or hole density and changes due to ionic movement or structural changes in the film. Figure 1 shows the CER equipment used in the high temperature and high pressure environments. This design allows the contact position displacement to be repeated with an accuracy of better than 10^{-10}m.

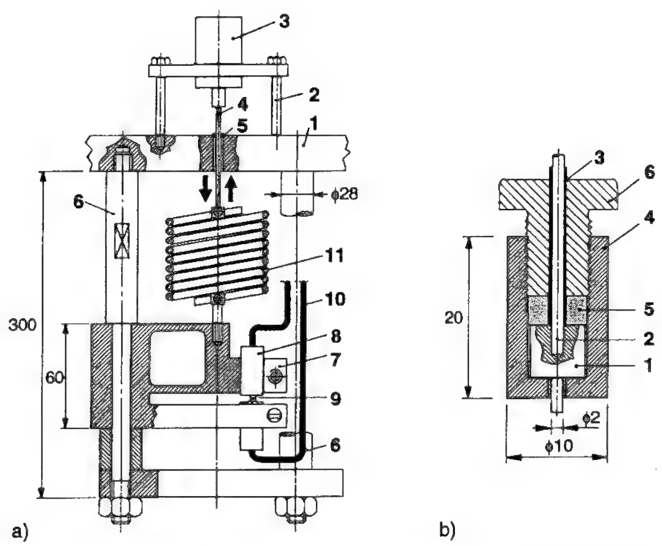

Fig. 1. Scheme of the CER equipment for high temperatures and pressures {a}. (1) autoclave head, (2) supporting frame, (3) step motor, (4) pull rod, (5) seal, (6) supporting frame, (7) stiff spring, (8) specimen holder, (9) specimen, (10) connecting wires, (11) soft spring. Specimen holder with fixed specimen {b}. (1) specimen, (2) silver connecting wire, (3) insulation, (4) Zr holder, (5) Zr-ring, (6) Zr screw.

Steam generator tube corrosion

Steam generator tubes made of Inconel 600 suffer frequently from intergranular attack (IGA) and intergranular stress corrosion cracking (IGSCC). The phenomena is proposed to be accelerated by accumulation of e.g. NaOH in crevices due to boiling. High cost of maintenance and replacement of steam generators has given impetus to research work trying to find inhibitors for IGA and IGSCC. IGA typically occurs at electrochemical potentials close to or sligthly anodic to the open circuit potential, and that the phenomena is related to the lack of a passive film on Inconel 600 in this potential range. IGSCC has been found at potentials equal or higher than the potential at which passive film formation takes place. It has been proposed that the presence of a surface film is a necessary prerequisite for IGSCC to occur.

In case of pure metals the potential at which film formation takes place can be accurately calculated based on thermodynamics. Fig. 2 shows, in the form of a Pourbaix-diagram, a comparison of equilibrium potentials of film formation determined with the CER technique and the calculated equilibrium potentials. The excellent coincidence over the whole range of pH indicates that the CER technique can be used to correctly identify the potential at which film formation takes place. Fig. 3 shows the result from a CER measurement of Inconel 600 in 1M NaOH electrolyte as a function the electrode potential at 300°C. At open circuit potential the measured resistance was close to zero, indicating that there was no film on Inconel 600. When the specimen was polarized anodically about 0.14 V the surface film resistance increased by several orders of magnitude. This indicates formation of a surface film. However, when the potential was switched back to open circuit, the film that formed at anodic potentials was reduced in a matter of minutes.

Titanate, TiO_2, is one of the candidate inhibitors considered for prevention of IGA and IGSCC in steam generators. In tests with the CER technique, introduction of TiO_2 into the 1M NaOH electrolyte resulted in formation of a film that was stable at open circuit potential. In both cases,

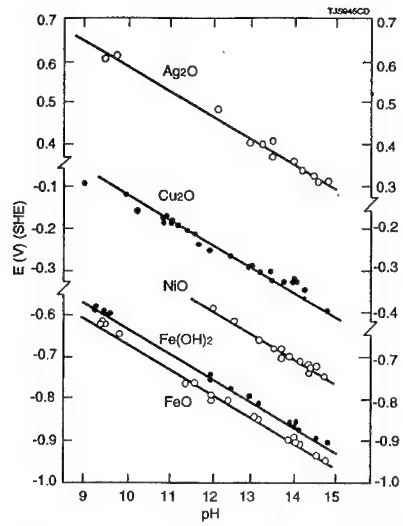

Fig. 2. Equilibrium potentials of formation of Ag_2O, Cu_2O, NiO, FeO and $Fe(OH)_2$ as measured by the CER technique (filled circles) and as calculated from thermodynamical data (solid lines).

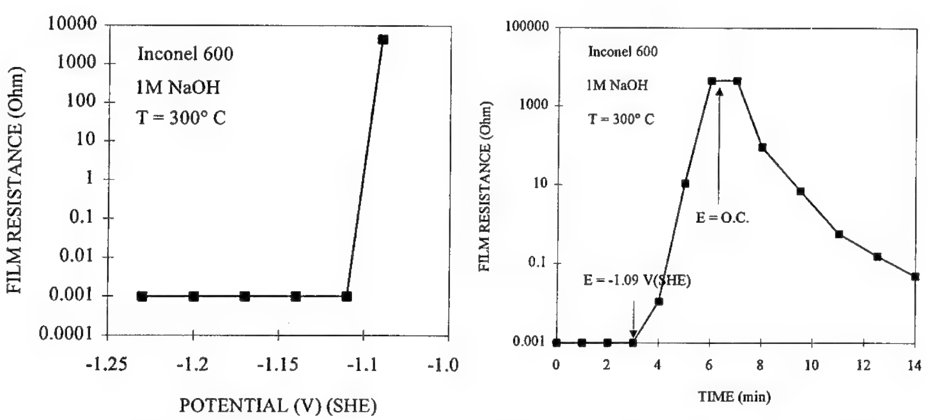

Fig. 3. (a) Surface film resistance as a function of the electrochemical potential; (b) kinetics of film formation and reduction. Inconel 600 in 4% NaOH at 300°C.

with and without TiO_2 the film on Inconel 600 was found to have n-type semiconductor characteristics. The electric resistance of such a film depends on the charge carrier density and on the potential. Polarization to negative potentials equals injecting electrons into the film. This results in immediate decrease of measured resistance of an n-type semiconductor. The converse is true when the specimen is polarized to positive potentials. According to the theory of semiconductors 9] and to the CER experiments with doped GaAs crystals the resistance of an n-type semiconductor decreases when potential is decreased until the flat band potential (E_{FB}) is reached. Further decrease of the potential causes no further change in the resistance.

Fig. 4 shows a comparison of the film resistance measured for Inconel 600 surface films formed without an inhibitor and with 10 ppm TiO_2 in 1M NaOH at 300°C. In both cases the film was formed at an anodic potential, and then the potential was switched to different potentials for about 20 seconds, after which the potential was switched back to the original one. During the short period at each potential only charge carriers with high mobility, i.e. electrons or holes, have

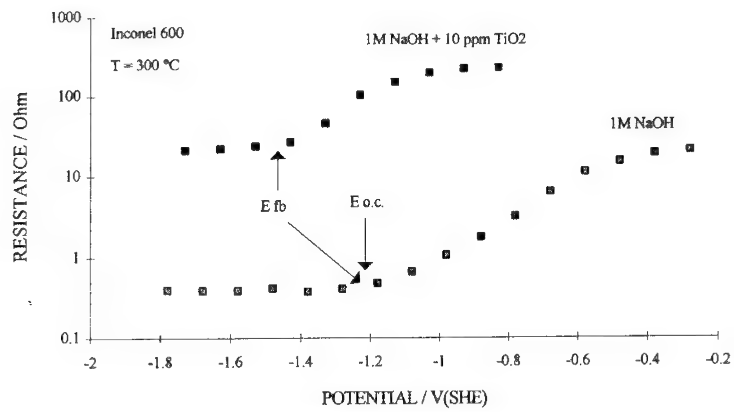

Fig. 4. Surface film resistance of Inconel 600 as a function of potential in 1M NaOH at 300°C. The films were formed at anodic potentials and had an initial electric resistance of 12 Ω and 197 Ω for films formed without and with 10 ppm TiO_2, respectively. The open circuit potential ($E_{O.C.}$) and flat band potentials (E_{FB}) are marked with an arrow.

time to react. This potential jump technique eliminates possible changes in the measured resistance due to ionic movement. In both cases the film resistance was found to decrease immediately when more negative potentials were applied, indicating n-type semiconductor characteristics. As shown in Fig. 4 the flat band potential of the film formed without an inhibitor was close to the open circuit potential, whereas the E_{FB} of the film formed with TiO_2 was about 0.2 V more negative than the open circuit potential.

The coincidence of the open circuit potential and the flat band potential of the film formed without the inhibitor indicates that the surface barrier (Schottky barrier) in this case is very low, making charge transfer through the film/electrolyte interface easy. We propose that the low barrier for charge transfer is responsible for the fact that at open circuit the passive film is not stable. As shown in Fig. 3, anodic polarization of about 0.14 V resulted in film formation. In this case the barrier needed for film formation (i.e. semiconductor band bending) was created by anodic polarization.

In the case of the film formed in the presence of the inhibitor the flat band potential was found to be about 0.2 V more negative than the open circuit potential. Also, the resistance at the flat band potential was almost two orders of magnitude higher with the inhibitor. It was also found that in the presence of the inhibitor the surface film was stable in open circuit conditions. For this film, the barrier needed for a stable film to form is created by the open circuit potential being more positive than the E_{FB}. The open circuit potential, being more positive than the E_{FB} forces the energy bands of the n-type semiconductor film to bend upwards creating a depletion layer on the surface of the film. This depletion layer has a net positive charge, which attracts OH^- anions and thereby promotes passivation.

The above presented CER results clarify the mechanism by which TiO_2 inhibits IGA. The mechanism of IGSCC of Inconel 600 in steam generator crevice environment is still under discussion, and a full treatment of the subject is beyond the scope of this paper.

Zircaloy tube corrosion

Oxides on Zircaloys are considered to be insulators, the thickness of which continues to grow during exposure to high temperature water environment. Minimizing the growth rate of the film is one of the main targets in alloy development of Zircaloys. The electric resistance of the oxide on three different Zircaloys is shown in Fig. 5 as a function of exposure time in simulated PWR water. At the beginning of each test the air borne oxides were removed by mechanical polishing. All three alloys behaved basically in a similar manner. First there is a period of instability, then steady growth of the resistance up to a certain level, after which the resistance remains rather stable. The thickness of the oxides at the end of the exposure, as measured by ex-situ surface analytical techniques, ranged from 0.6 to 0.8 µm. Concentration of hydrogen and lithium in the films was similar in all cases. These facts indicate that the large differences in the time to reach a stable level of resistance and in the absolute value of this level are not caused by differences in the oxide thickness or by incorporation of elements from the electrolyte into the growing oxide.

The structure of the oxide on Zircaloys typically consists of a protective thin barrier layer at the metal-oxide interface, while the remaining thickness of the oxide contains defects, pores and cracks, and is considered to be non-protective. The period of steady growth of resistance in Fig. 5 is proposed to result from growth of the barrier layer. The time to reach a stable level of resistance is a measure of the diffusion rate of oxygen anions from the oxide-electrolyte interface to the metal-oxide interface. The longer the time, the better the alloy is considered to be, and the smaller weight gain one would expect to have in a long term exposure.

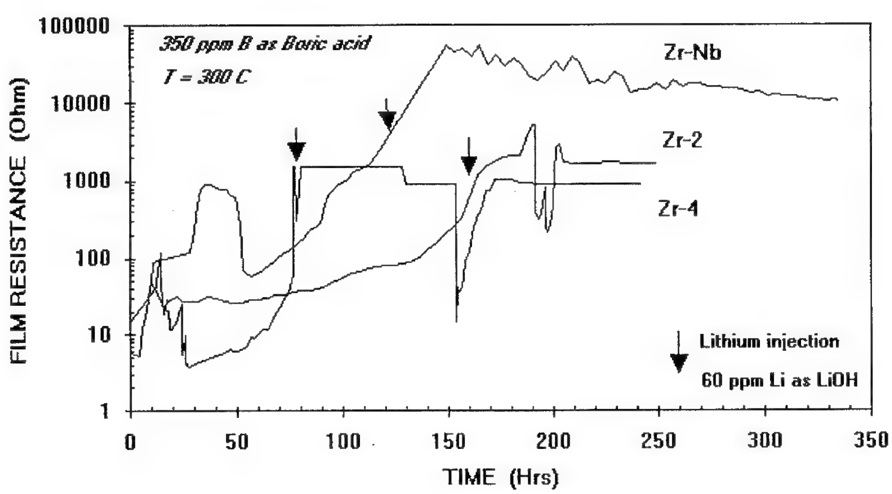

Fig. 5. Surface film resistance of Zircaloy-2, Zircaloy-4 and Zr-Nb alloys as a function of time in PWR water environment (2000 ppm H_3BO_3, 300°C).

In case of insulator type films such as the oxide on Zircaloy the rate determining step of the film growth can change from oxygen in-diffusion to transfer of electrons through the film. In such a case one would expect the alloy with the highest resistance to have the lowest weight gain. Table 1 shows ranking of the three alloys either based on the time to reach the stable level of resistance or based on the absolute level of resistance reached. Also shown is the ranking of the same alloys based on weigth gain measurements from in-reactor tests. The results from CER tests are in

excellent agreement with the in-reactor results. An additional benefit in using the in-situ CER technique to characterize Zircaloys is that the time needed for testing is roughly 10 days, in comparison with the 150 to 700 days required for the conventional weight gain tests.

Table 1. Comparison of ranking order of Zr2, Zr4 and ZrNb materials based on in-reactor experience (42 - 68 MWd/kgU) [8, 9] and CER tests.

	Ref. [7]	Ref. [8]	resistance value of stable oxide	incubation time
Zr2	1	-	2	1
Zr4	2	2	3	3
ZrNb	-	1	1	1

Conclusions

The Contact Electric Resistance, CER technique is a versatile in-situ technique for characterization of surface films on metals. The technique has been successfully applied in investigation of corrosion problems e.g. in high temperature water environment. The possibility to discern between film resistance changes due to structural changes and changes in charge carrier density in the film is one of the main advantages of the CER technique. The CER equipment has in principal no limitations regarding temperature and pressure, and the technique is applicable both in liquid and gaseous environments.

Acknowledgements

Electric Power Research Institute (EPRI), Academy of Finland, Sandvik Steel Ab and ABB Atom Ab have supported parts of this work.

REFERENCES

[1] T. Saario and V.A. Marichev, Proc. 12th International Corrosion Congress, vol. 6, pp. 4325 - 4336, NACE International, 1993.

[2] EPRI Report TR-103750, Effect of the Surface Film Electric Resistance on Eddy Current Detectability of Surface Cracks in Alloy 600 Tubes, May 1994.

[3] V.A. Marichev, T. Saario and V.V. Molokanov, NACE International, Proc. 12th International Corrosion Congress, **2**, 826 (1993).

[4] T. Salonen, T. Saario and J. Likonen, Corrosion 94, NACE, Paper No. 426.

[5] T. Saario and S. Tähtinen, IAEA Technical Committee Meeting on Influence of Water Chemistry on Fuel Cladding Behaviour, Rez, The Czech Republic, October 4 - 8, 1993.

[6] L. Charny, T. Saario and V.A. Marichev, Surf. Sci. **312**, 422 (1994).

[7] M. Limbäck, M.A. Krammen, P. Rudling, S.R. Pati and A.M. Garde, Proc. AMS Int. Topical Meeting on LWR Fuel Performance, West Palm Beach, Fl., USA, April 17-21, 1994, p. 286.

[8] G.P. Sabol, R.A. Weiner, K.R. McAtee, W.J. Leech, O.A. Correal-Pulver, R.N. Stanutz, R.J. Comstock and R.S. Miller, Proc. AMS Int. Topical Meeting on LWR Fuel Performance, West Palm Beach, Fl., USA, April 17-21, 1 (1994).

[9] S.R. Morrison, Electrochemistry at Semiconductor and Oxidized Metal Electrodes, Plenum Press, NY, USA, 153 (1980).

Kinetics

Materials Science Forum Vols. 185-188 (1995) pp. 631-640

Investigations of the anodic behaviour of iron in sulfuric medium by the electrochemical quartz crystal microbalance under ac regime

C. Gabrielli, M. Keddam, F. Minouflet and H. Perrot

CNRS, UPR 15, Laboratoire de Physique des Liquides et Electrochimie, Université P. et M. Curie, Tour 22, 4, place Jussieu, F-75252 Paris, France

Keywords: Passivation, iron, impedance, quartz microbalance

Abstract

Numerous models for dissolution and passivation of pure iron are proposed in the literature. Electrochemical impedance provides kinetic information but not an analytical one. An additional ac technique, based on the quartz microbalance, is now associated with electrochemical impedance. The background and the first application of this new technique to iron passivation are presented.

INTRODUCTION

Passivity of iron, particularly in acidic media is wellknown to obey the so called high field migration mechanism according to which the ionic current across the film is expressed by an exponential relationship :

$$i = i_0 \exp \frac{B\,(\varepsilon - \varepsilon_F)}{\ell} \qquad (1)$$

where ε is the total applied potential, ε_F is the Flade potential, ℓ is the passive film thickness and B is the high field exponent :

$$B = \frac{\alpha\, z\, F\, a}{RT}$$

α : symmetry factor of the activation barrier
a : jump distance
z : charge of mobile carriers, 3 in case of Fe^{3+}
F, R and T have their usual meaning.

A constant stationary current independent of the electrode potential is therefore associated with a potential independent electric field strength within the film, *i.e.* a film thickness proportional to the fraction of potential $\varepsilon_2 = \varepsilon - \varepsilon_F$ applied to the oxide. The potential drops at the metal/film and film/electrolyte interfaces are formally related to the Flade potential measured at a negligibly thin film.

Steady state is generally agreed to result from a migration current, Eq.(1), exactly balanced by the corrosion current i_{co} taking place at the outer boundary of the film.

Earlier, it was recognized that a much deeper insight into the mechanism of passive film growth and corrosion in the passive state can be obtained by investigating non-steady state polarization either potentiostatically or galvanostatically. Vetter and Gorn [1] and Heusler [2] showed by means of various techniques (solution analysis, ring-disc experiments) that under transient regime the corrosion rate of the passive iron electrode deviates seriously from its steady value. Kirchheim [3] attributes this deviation to a transient part η of the total applied potential ε contributing to the corrosion current i_c at the film/electrolyte interface according to :

$$i_c = i_{co} \exp \frac{\alpha_c F \eta}{RT} \tag{2}$$

and to the film growth or dissolution by displacement of the redox equilibrium :

$$i_\ell = i_{\ell o} \left[\exp \frac{\alpha_\ell^+ F \eta}{RT} - \exp - \frac{\alpha_\ell^- F \eta}{RT} \right] \tag{3}$$

(α_ℓ^+ and α_ℓ^- are positive)
The components of the electrode current obey the conservation equation :

$$i = i_c + i_\ell \tag{4}$$

It was verified that Eq.(1-4) are correctly obeyed under galvanostatic and potentiostatic regimes at acidic and neutral pH [3]. The ratio $\frac{\ell}{B}$ was estimated to 0.060 ± 0.002 V, at 1.08 V/SHE and B to $(4.5 \pm 1.0) \times 10^{-6}$ cm.V^{-1}, corresponding to an electric field ≈ 4.10^6 V.cm^{-1} and a thickness/voltage ℓ/ε_2 dependence, in the steady state, around 2.5 nm.V^{-1}.

Passive iron was also investigated by a c impedance measurements [4]. Contrasting with most of the impedance works which focused on the dielectric or Mott-Schottky characterization of the film material, emphasis was put on the low frequency response of both the ionic transfer across the film and the film thickness.

A recognised advantage of the impedance approach is to provide information on the dynamic behaviour of the sample interface at various steady states at the cost of a very small perturbation. As a first approximation the faradaic impedance of iron in the passive state was previously shown [4] to consist of a series connection of a resistance R_{HF}, displaying the response of the high field migration across the film, and a capacitance Γ standing for the charge. The latter is faradaically stored by the increment of the film thickness with respect to the electrode potential. An inductive loop observed at the middle-range frequencies is formally represented by a series (L, ρ) branch in parallel with R_{HF} as shown in Fig. 1. It can be easily established that the presence of this inductance in the impedance network is strictly equivalent to the so-called voltage overshoot reported at short times during galvanostatic transients [5].

The elementary model A, developed below and involving a frequency dependence of the overvoltage η, is unable to account for the inductive or overshooting behaviour. This paper is aimed at proposing, in terms of impedance, an advanced model of corrosion and film growth on passive iron, likely to explain the presence of an inductive response. This model is inferred from a tentative explanation of the voltage overshoot proposed by Kirchheim [5].

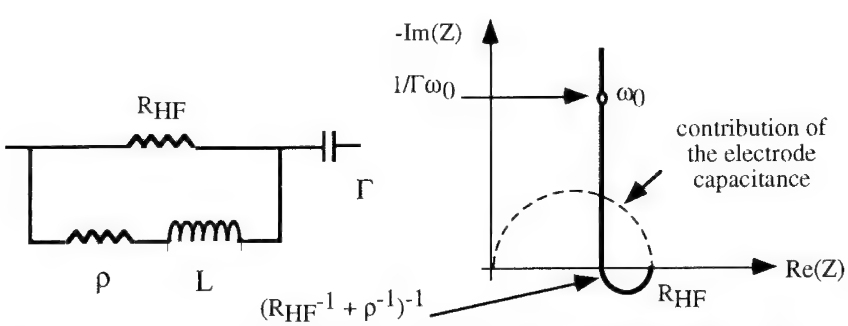

Figure 1. Equivalent circuit and Nyquist representation for electrochemical impedance.

Taking advantage of the recent development of frequency resolved EQCM (Electrochemical Quartz Crystal Microbalance) measurements, the electrogravimetric transfer functions $\frac{\Delta m}{\Delta \varepsilon}$ and $\frac{\Delta m}{\Delta Q}$ associated with the electrochemical impedance are also derived and compared with experiments. These functions appeared as particularly suitable for the investigation of the passive electrode behaviour. Indeed, they offer the unique possibility of discriminating, on the basis of their individual frequency responses, between the change of electrode mass due to metal dissolution on the one hand and relaxation of the film thickness on the other hand.

BASIC MODELS OF AC IMPEDANCE AND ELECTROGRAVIMETRIC TRANSFER FUNCTIONS

1. Corrosion and film growth controlled by potential drop at the film/electrolyte interface : model "A"

First, the derivation deals with the simplest model involving a dependence of the corrosion and film growth reactions upon the overvoltage η at the film/electrolyte interface[1]. According to Eq.(1), at any moment, the high field migration across the film is :

$$i = i_o \exp\frac{B(\varepsilon - \varepsilon_F - \eta)}{\ell} \tag{5}$$

the steady state conditions being reached for $\eta = 0$.

Differentiation of (5), (2) and (3) under small ac modulation of ε at an angular frequency ω, around steady state ε, gives :

$$\Delta i = i_p \frac{B}{\ell}(\Delta\varepsilon - \Delta\eta) - \frac{i_p B\varepsilon_2}{\ell^2}\Delta\ell \tag{6}$$

where i_p is the potential independent passive current.

$$\Delta i_c = i_{co}\frac{\alpha_c F}{RT}\Delta\eta = i_{co} P_c \Delta\eta \tag{7}$$

$$\Delta i_\ell = i_{\ell o}(\alpha_\ell^+ + \alpha_\ell^-)\frac{F}{RT}\Delta\eta = i_{\ell o} P_\ell \Delta\eta \tag{8}$$

In addition, the rate of film growth is expressed by :

$$\frac{d\ell}{dt} = \Lambda\, i_\ell \tag{9}$$

where $\Lambda = \frac{\text{molar volume of the film material}}{z_\ell F}$

---

1 All the derivations assume a unit electrode area. Volumic densities are numerically equal to surface densities.

with z_ℓ the number of elementary charges for growing a molecular unit of film ($z_\ell = 6$ for Fe_2O_3).

(i) Electrochemical impedance

Eq.(4) and (6-9) solved for the electrode impedance $Z = \frac{\Delta\varepsilon}{\Delta i}$:

$$\boxed{Z = \frac{\ell}{B\, i_p} + \frac{1}{i_{co}P_c + i_{\ell o}P_\ell} + \frac{1}{j\omega}\frac{\varepsilon_2\,\Lambda}{\ell}\frac{1}{1 + \frac{i_{co}P_c}{i_{\ell o}P_\ell}}} \tag{10}$$

Z is a series arrangement of the high frequency resistance R_{HF} and the capacitance Γ :

$$R_{HF} = \frac{\ell}{B\, i_p} + \frac{1}{i_{co}P_c + i_{\ell o}P_\ell} \tag{11}$$

$$\Gamma = \frac{\ell}{\varepsilon_2\,\Lambda}\,\frac{i_{\ell o}P_\ell + i_{co}P_c}{i_{\ell o}P_\ell} \tag{12}$$

R_{HF} contains a contribution from the high field migration in the film bulk ($\frac{\ell}{B\, i_p}$) and from the film/solution interface ($\frac{1}{i_{co}P_c + i_{\ell o}P_\ell}$). The capacitance Γ represents the charge $\frac{\ell}{\varepsilon_2\,\Lambda}$ involved in the increment of the film thickness multiplied by $\frac{i_{\ell o}P_\ell + i_{co}P_c}{i_{\ell o}P_\ell}$ a factor accounting for the relative excess of charge consumption by the corrosion process under non-steady state. Experiments in low pH sulfuric solutions [3] yielded Γ values ($\approx$ 40-50 $mF.cm^{-2}$) about ten times as great as the theoretical value for a 2.5 $nm.V^{-1}$ film thickness/voltage dependence [3].

(ii) Electrogravimetric functions

The electrogravimetric response $\frac{\Delta m}{\Delta\varepsilon}$ can be derived similarly by considering the time dependence of the electrode mass due to electrode dissolution and film growth :

$$\frac{dm}{dt} = \frac{-A_{Fe}}{zF}\, i_c + \rho_{ox}\,\frac{d\ell}{dt} \tag{13}$$

where A_{Fe} is the atomic weight of iron.

ρ_{ox} is the density of the film material considering only the participation of oxygen in the mass balance (oxidation of Fe atoms to Fe^{3+} in the film (lattice sites or mobile carriers) has no gravimetric effect).

Under a.c regime Eq.(13) becomes :

$$j\omega \frac{\Delta m}{\Delta \varepsilon} = \frac{1}{Z}\frac{1}{j\omega}\left(\frac{-A_{Fe}}{zF}\frac{\Delta i_c}{\Delta i} + \rho_{ox}\, j\omega \frac{\Delta \ell}{\Delta i}\right)$$

by substituting from Eq.(7-9) :

$$\frac{\Delta m}{\Delta \varepsilon} = \frac{1}{Z}\frac{1}{j\omega}\left(\frac{-A_{Fe}}{zF}\frac{1}{1+\frac{i_{\ell o}P_\ell}{i_{co}P_c}} + \rho_{ox}\,\Lambda \frac{1}{1+\frac{i_{co}P_c}{i_{\ell o}P_\ell}}\right)$$

or

$$\boxed{\frac{\Delta m}{\Delta \varepsilon} = \frac{1}{j\omega R_{HF} + \frac{1}{\Gamma}}\left(\frac{-A_{Fe}}{zF}\frac{1}{1+\frac{i_{\ell o}P_\ell}{i_{co}P_c}} + \rho_{ox}\,\Lambda \frac{1}{1+\frac{i_{co}P_c}{i_{\ell o}P_\ell}}\right)} \qquad (14)$$

and

$$\boxed{\frac{\Delta m}{\Delta Q} = \frac{\Delta m}{\Delta \varepsilon} Z j\omega = \left(\frac{-A_{Fe}}{zF}\frac{1}{1+\frac{i_{\ell o}P_\ell}{i_{co}P_c}} + \rho_{ox}\,\Lambda \frac{1}{1+\frac{i_{co}P_c}{i_{\ell o}P_\ell}}\right)} \qquad (15)$$

According to (14) the complex diagram of $\frac{\Delta m}{\Delta \varepsilon}$ is a semi-circle in the complex plane between the origin at infinite frequency and a low frequency limit :

$$\Gamma\left(\frac{-A_{Fe}}{zF}\frac{1}{1+\frac{i_{\ell o}P_\ell}{i_{co}P_c}} + \rho_{ox}\,\Lambda \frac{1}{1+\frac{i_{co}P_c}{i_{\ell o}P_\ell}}\right).$$

The $\frac{\Delta m}{\Delta Q}$ is a frequency independent real quantity proportional to the low frequency limit of $\frac{\Delta m}{\Delta \varepsilon}$. This real quantity displays the antagonistic contributions of the electrode dissolution and layer growth to the gravimetric response.

2. Corrosion and film growth controlled by potential drop at the film/electrolyte interface plus relaxation of charge carriers density in the film : model "B"

This derivation is based on a semi-quantitative approach proposed by Kirchheim [5] for interpreting the overshooting at short times in the galvanostatic transient. In this model it is assumed that the density of cationic vacancies, supporting the transport of Fe^{3+} towards the solution, is increased by the current flowing in excess of the steady state passive current i_p. In the present derivation it is equivalently considered that the relaxing parameter is the density of mobile Fe^{3+}. Accordingly the current balance, Eq.(4), becomes :

$$i = i_c + i_\ell + \frac{\ell\, dC}{dt} zF \qquad (16)$$

where C is the molar concentration of Fe^{3+} charge carriers.

By using Eq.(9) :

$$\frac{dC}{dt} = (i - i_c)\frac{1}{\ell\ z\ F} - \frac{1}{\Lambda\ \ell\ z\ F}\frac{d\ell}{dt} \tag{17}$$

Λ and z are defined as above.

Let introduce the new parameters : $\mu = \frac{1}{\ell\ z\ F}$ and $\kappa = \frac{1}{\Lambda\ \ell\ z\ F}$

Exactly like in the previous model :

$$i_c = F\ k_c\ C \exp\frac{\alpha_c\ F\ \eta}{RT} \tag{18}$$

$$i_\ell = \frac{1}{\Lambda}\frac{d\ell}{dt} = \frac{1}{\Lambda}\ k_\ell\ C\,(\exp\frac{\alpha_\ell^+\ F\ \eta}{RT} - \exp\frac{-\alpha_\ell^-\ F\ \eta}{RT}) \tag{19}$$

$$i = F\ k\ C \exp\frac{B\ (\varepsilon - \varepsilon_F - \eta)}{\ell} \tag{20}$$

After differentiation with respect to ε, η, C and ℓ, one has around a steady state passive current i_p ($i_{co} = F\ k_c\ Co = i_p$; $\eta = 0$; $C = C_o$) :

$$j\omega\,\Delta C = (\Delta i - \Delta i_c)\mu - \kappa j\omega\,\Delta\ell \tag{21}$$

$$\Delta i_c = F\ k_c\ \Delta C + i_p\ P_c\ \Delta\eta \tag{22}$$

$$\Delta i_\ell = \frac{1}{\Lambda}\ j\omega\,\Delta\ell = \frac{1}{\Lambda}k_\ell\ C_o P_\ell\ \Delta\eta \tag{23}$$

and assuming $\Delta\eta = \beta\Delta i$.

(i) Electrochemical impedance

By successive substitutions between Eq.(21-23) and the differential of (20) :

$$\Delta i = \frac{i_p B}{\ell}(\Delta\varepsilon - \Delta\eta) - \frac{i_p B}{\ell^2}\ \varepsilon\,\Delta\ell + \frac{i_p}{C_o}\ \Delta C \tag{24}$$

one obtains :

$$\boxed{Z = \frac{\ell}{Bi_p} + \beta + \frac{\varepsilon_2}{\ell j\omega} C_o\beta\, k\ell\, P\ell \;-\; \frac{\ell}{BC_o}\, \frac{\mu - \beta\,(i_p\, P_c\, \mu + C_o\, k\ell\, P\ell\, \kappa)}{j\omega + Fk_c\mu}} \quad (25)$$

Eq.(25) shows that the impedance obeys the electrical circuit of Fig. 1.

The series resistance :

$$R_{HF} = \frac{\ell}{Bi_p} + \beta \quad (26)$$

contains both contributions of bulk migration in the oxide layer and of the outer interface. It is connected in parallel with a (L, ρ) series arrangement generated by the third term of Eq.(25) when its numerator is positive *i.e.* the increase of charge carriers density is dominating the corrosion and film growth processes in the range of medium frequencies.

The capacitance :

$$\Gamma = \frac{\ell}{\varepsilon_2\, C_o\, \beta\, k\ell\, P\ell} \quad (27)$$

still corresponds to the relaxation of the film thickness. The weighting factor $C_o\, \beta\, k\ell\, P\ell$ reflects which part of the overall current Δi is involved in the film growth with respect to corrosion or build-up of mobile cations density in the film.

(ii) Electrogravimetric functions

By using the same assumptions as in model "A", one derives after substituting $C_o\, \beta\, k\ell\, P\ell$ by $\frac{\ell}{\varepsilon_2\Gamma}$ (Eq.27) :

$$\boxed{\frac{\Delta m}{\Delta \varepsilon} = \frac{1}{Z\, j\omega}\left[\frac{-A_{Fe}}{zF}\, \frac{1}{j\omega + F\, k_c\mu}\left(F\, k_c\mu\, \left(1 - \frac{\ell\kappa}{\varepsilon_2\Gamma\mu}\right) + j\omega\beta i_p\, P_c\, \mu\right) + \frac{\rho_{ox}\, \ell}{\varepsilon_2\Gamma}\right]} \quad (28)$$

The high frequency limit is zero and the low frequency limit :

$$\left(\frac{\Delta m}{\Delta \varepsilon}\right)_{\omega\to 0} = \Gamma\left[\frac{-A_{Fe}}{zF}\left(1 - \frac{\ell\kappa}{\varepsilon_2\Gamma\mu}\right) + \frac{\rho_{ox}\, \ell}{\varepsilon_2\Gamma}\right] \quad (29)$$

depends on the relative contribution of the electrode corrosion (first term) and layer growth (second term).

In the same way we obtain :

$$\boxed{\frac{\Delta m}{\Delta Q} = \frac{\Delta m}{\Delta \varepsilon} Z\, j\omega = \frac{-A_{Fe}}{zF}\, \frac{1}{j\omega + Fk_c\mu}\left(Fk_c\mu\, \left(1 - \frac{\ell K}{\varepsilon_2\Gamma\mu}\right) + j\omega C_o\beta i_p\, P_c\, \mu\right) + \frac{\rho_{ox}\, \ell}{\varepsilon_2\Gamma}} \quad (30)$$

Contrasting definitely with the model "A" now $\frac{\Delta m}{\Delta Q}$ is frequency dependent due to individual frequency responses of i_c and i_ℓ under the influence of the relaxation of the charge carriers density C.

The high and low frequency limits are respectively given by :

$$\left(\frac{\Delta m}{\Delta Q}\right)_{\omega\to\infty} = \frac{-A_{Fe}}{zF}\,\beta i_p\, P_c\, \mu + \frac{\rho_{ox}\,\ell}{\varepsilon_2\Gamma} \tag{31}$$

$$\left(\frac{\Delta m}{\Delta Q}\right)_{\omega\to 0} = \frac{-A_{Fe}}{zF}\left(1 - \frac{\ell\kappa}{\varepsilon_2\Gamma\mu}\right) + \frac{\rho_{ox}\,\ell}{\varepsilon_2\Gamma} = \frac{1}{\Gamma}\left(\frac{\Delta m}{\Delta\varepsilon}\right)_{\omega\to 0} \tag{32}$$

EXPERIMENTAL

1. The microbalance and electrode material

The quartz crystal microbalance (QCM) used the change of the resonance frequency of a 6 MHz "AT- cut" quartz crystal, delivered by Copelec, France. Two gold electrodes were deposited on the opposite sides of the quartz crystal : they allowed an electric connection to the oscillator circuit whereas one of the electrodes was used as the working electrode. The iron anode was prepared by electroplating [6] a 3 μm thick iron layer onto the electrode of one side of the quartz crystal. In order to remove codeposited hydrogen, the sample was annealed in argon atmosphere for one hour at 450°C. The iron surface was then mechanically polished with 0.3 μm alumina. The metal purity was checked by X-Ray fluorescence (Tracor); electrochemical behaviour of the deposited iron was similar to that of pure bulk metal.

In our study, the frequency response to an added mass could be described by the Sauerbrey equation [7]. Thus, for a 6 MHz quartz crystal, the theoretical value of the sensitivity factor is equal to - 8.1×10^7 Hz.cm^2/g. Nevertheless, a calibration process was previously performed with silver electro-deposition. According to the Faraday's law, an experimental sensitivity factor was calculated (-5.2×10^7 Hz.cm^2/g).

2. Electrogravimetric and electrochemical measurements

In order to use the QCM in ac regime, the modified working electrode was polarized and subjected to a small amplitude sinusoidal perturbation. The frequency response Δf related to the modulation of mass Δm, produced on the modified working electrode, was measured. The signal was sent to a four-channel Transfer Function Analyser (Schlumberger-Solartron 1254) which allowed the electrogravimetric transfer function to be calculated simultaneously with the impedance of iron passivated in a molar sulfuric solution. The experimental setup has already been described elsewhere [8].

RESULTS AND DISCUSSION

Electrode impedance and $\frac{\Delta m}{\Delta\varepsilon}$ electrogravimetric transmittance measured at 0.5 V/ S.S.E. are shown in Fig. 2A and 3A. The electrode impedance displays the shape represented in Fig. 1 in agreement with the previous results on bulk Johnson-Matthey iron [4]. $\frac{\Delta m}{\Delta\varepsilon}$ has a slightly depressed

semi-circular shape and exhibits a small positive real part at frequencies higher than 4 mHz. This shape of $\frac{\Delta m}{\Delta \varepsilon}$ is definitely different from that expected for a direct anodic dissolution : a pure imaginary quantity proportional to $\frac{1}{j\omega}$ [8].

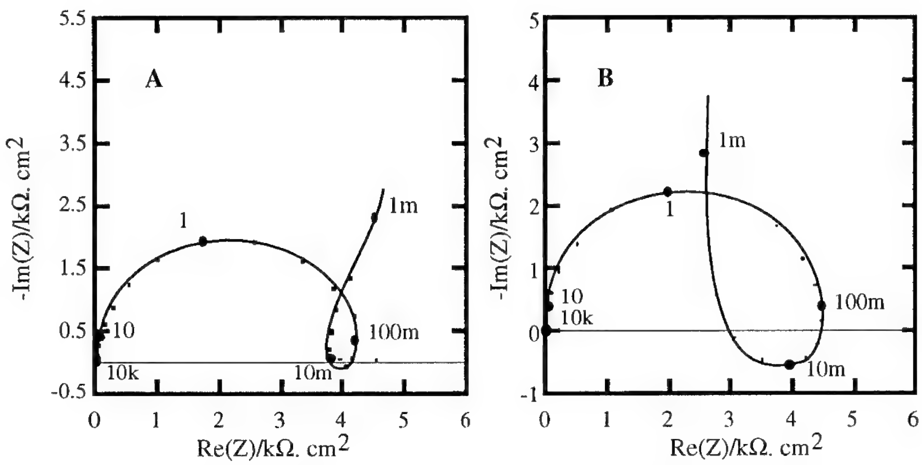

Figure 2. Experimental, A, and simulated, B, electrochemical impedances.

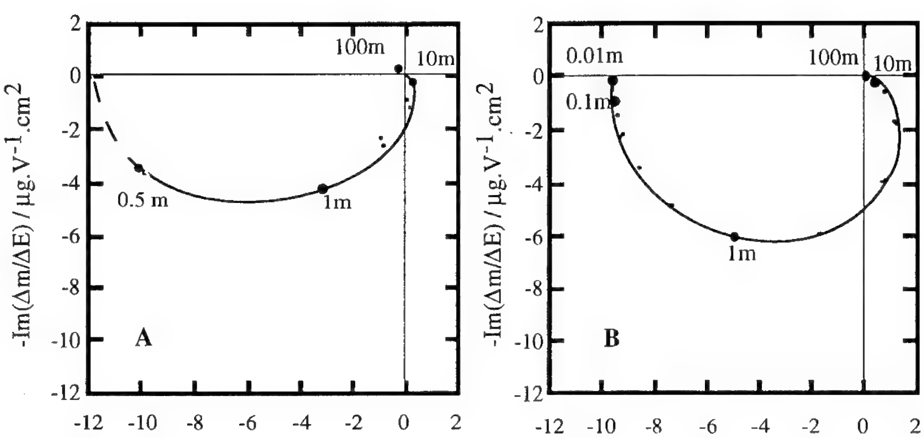

Figure 3. Experimental, A, and simulated, B, electrogravimetric transfer functions.

A rough extrapolation gives an estimate of its low frequency limit around 12 $\mu g\ V^{-1}\ cm^{-2}$. Model "A" is obviously unable to account for the inductive loop of Z. Similarly the positive real part of $\frac{\Delta m}{\Delta \varepsilon}$ at high frequencies, kinetically related to the inductance, is not predicted by this model because Eq.(14) can produce strictly a semi-circle. Therefore, results are discussed only in terms of model"B".

It is noteworthy that a restricted number of parameters are adjustable. μ and κ are straightforward from their definition. $\mu = \frac{1}{3\ell F}$. For Fe_2O_3 as a film material, a molar volume 30.5 cm^3 [3] and a film thickness ℓ = 1nm, gives μ = 34.5 C^{-1} mole cm^{-1}, κ = 6.5 10^5 mole cm^{-4}, ρ_{ox} 1.56 g cm^{-3}. Electrochemical measurements yield $i_p = 5.10^{-6}$ A cm^{-2} and $\frac{\ell}{B}$ = 0.04 V at ε = 0.5 V [3].

Numerical simulations of Z and $\frac{\Delta m}{\Delta \varepsilon}$ have been performed with the optimal set of parameters below :

$C_0 = 1.7\ 10^{-2}$ M. cm^{-3}.
$k_c = 1.2\ 10^8\ cm^{-1}\ s^{-1}$
$\beta\ P_c = 2.4\ A^{-1}cm^{-2}$
$\beta\ k_\ell\ P_\ell = 7.3.10^{-4}\ C^{-1}$ mole^{-1} cm^4

and are shown in Fig. 2B and 3B. The computed diagrams fit well the shape, size and frequency spacing of the experimental ones. The following conclusions can be drawn :

-ac impedance has been associated with electrogravimetric transmittance for investigating the electrochemistry of passive iron,

-the negative low frequency limit indicates, according to Eq.(29), that the contribution of the mass loss from the corrosion component dominates largely the mass gain due to the film growth. Consistently with the over-estimation of film/potential ratio from Γ values, 12 $\mu g\ V^{-1}\ cm^{-2}$ is about 12 times the value for 2.5 nm V^{-1} of Fe_2O_3. Both techniques conclude that the major part of the charge supplied during a transient within the passive range contributes to iron corrosion, and not to film growth.

-this fair consistency between electrochemical and gravimetric data seems to rule out any appreciable side effects on the EQCM due to mechanical stress in the film.

REFERENCES

[1] K. J. Vetter and F. Gorn, Electrochim. Acta **18**, 321 (1973).
[2] K. E. Heusler, Ber. Bunsenges phys. chem. **72**, 1197 (1968).
[3] R. Kirchheim, Electrochim. Acta **32**, 1619 (1987).
[4] M. Keddam, J. F. Lizée, C. Pallotta and H. Takenouti, J. Electrochem. Soc. **131**, 2015 (1984).
[5] R. Kirchheim, Corros. Sci. **29**, 183 (1989).
[6] V. I. Lainer and N. T. Kudryavtsev, Fundamentals of electroplating part II, U.S. Department of Commerce, p. 7, (1966).
[7] G. Sauerbrey, Z. Phys. **155**, 206 (1955).
[8] S. Bourkane, C. Gabrielli and M. Keddam, Electrochim. Acta **34**, 1081(1989).

Materials Science Forum Vols. 185-188 (1995) pp. 641-648

The use of rotating split-ring disc electrodes for the estimation of Fe(II) and Fe(III) species in surface layers on iron in borate buffer

J. Flis and J. Wilinski

Institute of Physical Chemistry of the Polish Academy of Sciences,
PL-01-224 Warsaw, Poland

Keywords: Iron, borate buffer, surface layers, Fe(II), Fe(III), RSRDE

Abstract - A rotating split-ring disc electrode (RSRDE) was used to determine the formation of Fe(II) and Fe(III) species during the anodic and cathodic potential sweeps on iron in a buffered borate solution of pH 8.4. Composition of anodic films was deduced mainly from the Fe(II)-detecting current in the cathodic sweeps. It is suggested that the passive film in the active-passive transition region can be described by a spectrum of compositions, ranging from $Fe(OH)_2$ through Fe_3O_4 to FeOOH, or by a non-stoichiometric FeOOH. The film undergoes a continuous transformation, involving a decreasing content of FeOOH and an increasing content of Fe_3O_4. The second anodic peak in the passive region can be associated with the oxidation of Fe(II) to γ-FeOOH; contrary to the passive film, the layer formed at the second peak did not transform. The peak at the most active potential of the cathodic sweeps (peak IV) can be ascribed to the reduction of Fe_3O_4 to Fe(II).

Introduction

Various models of passivity of metals have been presented at the recent conferences [1, 2], and the proposed compositions of the passive films on iron have been reviewed by Cohen [3] and Kruger [4]. It has been proposed that the films may contain Fe_3O_4, γ-Fe_2O_3, γ-FeOOH, a polymeric $[Fe(OH)_2]_x$, or cation deficient γ-Fe_2O_3; Cahan and Chen [5] have postulated that the film composition can best be characterized by a Fe(III) oxy-hydroxide, capable of existing in a relatively wide range of stoichiometry.

It has been suggested that the compounds can form a single layer or two and more layers. For iron in buffered borate solutions, a two-layer model was suggested by Cohen *et al.* [3, 6], Kruger [7], Ord and DeSmet [8] and others [9, 10]; a single-layer film was suggested in other studies [5, 11, 12].

In the passive region there can form an outer layer composed of a deposited film of γ-FeOOH [13, 14], but this layer is not related to passivity [13].

Gui and Devine [14] studied the passive film on iron in borate solution by *in situ* surface enhanced Raman spectroscopy (SERS) and found that the common constituent of all films appeared to consist of a mixture of Fe(II) and Fe(III) which was referred to as $Fe(II)(III)(OH)^{*}_{x}$. These authors expressed an opinion that the controversy regarding the identity of the passive film on iron results from the fact that there is no single passive film, but instead there is a spectrum of possible film chemistries and

structures. The formation and chemistry of a film depends on the electrochemical conditions [15].

The purpose of the present work was to evaluate the content of Fe(II) and Fe(III) species in surface films on iron in a buffered borate solution. These species were determined with a rotating split-ring disc electrode (RSRDE) during anodic and cathodic potential sweeps and potentiostatic holds.

Experimental

Measurements were performed on decarburized iron (0.010 S, 0.005 P, total metallic elements 0.07 wt.%) in the RSRDE assembly [16]. The iron disc was 5.1 mm in diam. Two half-rings were made of Type 316 steel (as in [17]), with an inner radius of 2.70 mm and an outer radius of 4.00 mm. The calculated collection efficiency for each of the half-rings was 15.7 %. A three-compartment cell was used with the Luggin capillary being placed in the disc ring plane about 10 mm from the disc center.

Measurements were carried out at 25°C in a deaerated borate buffer solution of 0.15 M H_3BO_3 + 0.0375 M $Na_2B_4O_7$ (pH 8.4), prepared from bidistilled water and reagent grade chemicals. The solution was purged with argon.

Potentials were measured with reference to a saturated calomel electrode (SCE).

The working electrodes were polished with 800 emery paper and rinsed with water. Before the measurements, the iron disc was polarized at -1.3 V (SCE) for 15 min to reduce the air-formed oxides. Potentials of the half-rings for detection of Fe(II) and Fe(III) species were 0.4 V and -0.9 V (SCE), respectively. The rotation velocity was 25 rps.

Cyclic voltammograms were measured at a potential sweep rate of 10 mV s^{-1}.

Results

Fig. 1 shows a voltammogram for iron disc (i_D) and the currents on half-rings, i_RFe^{2+} and i_RFe^{3+} of soluble Fe(II) and Fe(III) species formed on the disc, respectively. It should be borne in mind that i_RFe^{2+} and i_RFe^{3+} depend on solubilities of the Fe(II) and Fe(III) species, and hence they do not specify the composition of the products.

The voltammogram exhibited two oxidation peaks (I and II) on the sweep to nobler potentials, and two reduction peaks (III and IV) on the reverse sweep. Vertical lines in Fig. 1 mark equilibrium potentials for some possible reactions on iron in an aqueous solution of pH 8.4; the potentials were calculated from equations for the Fe-H_2O system [18]. They suggest that in the observed active region there can form $Fe(OH)_2$, Fe_3O_4, and α-FeOOH. The formation of solid products in the active region was manifested by a slight decay of current under potentiostatic conditions.

In the forward sweep, Fe(II) was detected only in the region of peak I (peak *A* of i_RFe^{2+}), whereas in the reverse sweep i_RFe^{2+} revealed two peaks *B* and *C* at potentials of peak III and IV, respectively. Peak *C* indicates that the reduction peak IV is related to the reduction of a Fe(III)-containing oxide or oxyhydroxide to Fe(II), but not of $Fe(OH)_2$ to metallic Fe°.

During anodic polarization, Fe(III) started to form at a potential of about 0.1 V nobler than that for Fe(II); i_RFe^{3+}

increased with the increasing potential through the entire active region.

Fig. 2 presents the iron disc current i_T and true currents for soluble Fe(II) and Fe(III) ($i_{Fe(II)}$ and $i_{Fe(III)}$), calculated after taking into account the collection efficiency. It has been assumed that the collection of Fe(II) and Fe(III) is not controled by a kinetic factor of reactions at the rings, but only by the collection efficiency. Fig. 2 also shows the i_F/i_D ratio, where i_F

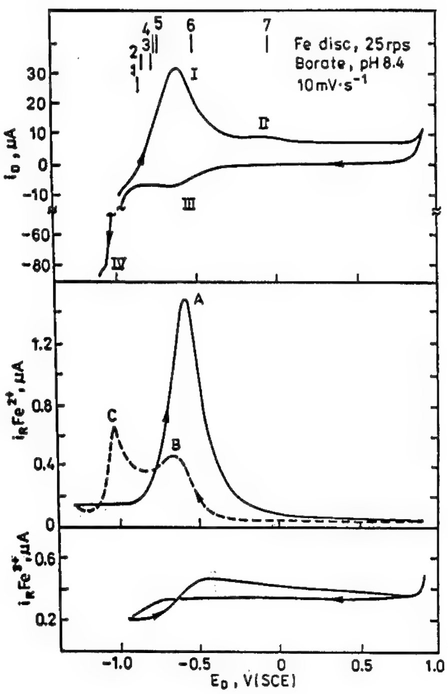

Fig. 1. Voltammogram for iron disc (i_D) and current response on half-rings ($i_R Fe^{2+}$ and $i_R Fe^{3+}$) in the borate solution.

Vertical lines refer to equilibrium potentials [18] for the couples:

Formation of $Fe(OH)_2$:

1, $Fe/Fe(OH)_2$

Formation of Fe_3O_4:

2, Fe/Fe_3O_4
3, $Fe(OH)_2/Fe_3O_4$

Formation of FeOOH:

4, $Fe(OH)_2/\alpha$-FeOOH
5, Fe_3O_4/α-FeOOH
6, $Fe(OH)_2/\gamma$-FeOOH
7, Fe_3O_4/γ-FeOOH

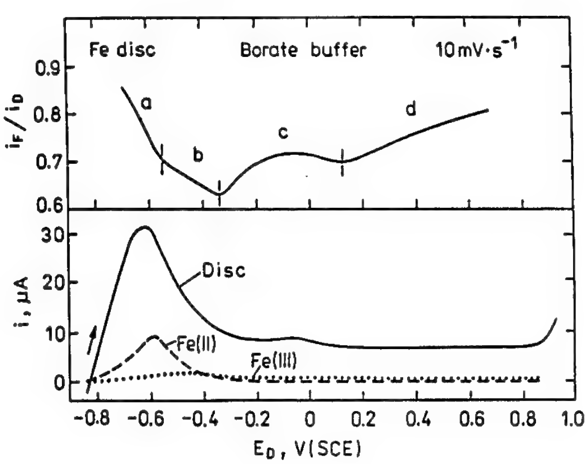

Fig. 2. Total current for iron disc, true currents of soluble Fe(II) and Fe(III) species, and fraction of the current consumed for the film formation i_F/i_D.

is the current for the film formation determined as

$$i_F = i_T - i_{Fe(II)} - i_{Fe(III)} \quad (1)$$

where i_T is the total current measured for the disc. In case of any kinetic control of the ring currents, the current for the film formation (i_F) would be overestimated.

The i_F/i_D ratio presents the fraction of current for the film formation, including the growth of solid products and/or their oxidation. Segments *a*, *b*, *c*, and *d* of the i_F/i_D curve correspond to the active, active-passive transition, peak II, and passive regions for the iron disc, respectively.

In the active region, over 70% of the total current was used for the film formation. In the potential sweep up to peak I, the i_F current corresponds to the formation of about 1.5 nm of the $Fe(OH)_2$ layer. A growth of the film in this region was also revealed in the ellipsometric studies [19-21]. The currents $i_{Fe(II)}$ and $i_{Fe(III)}$ demonstrate that the film contains Fe(II) and Fe(III) species. In the active-passive transition region, contribution of the total current to the film formation was lower than in the active region. Segment *c* can be ascribed to the electrochemical oxidation of Fe(II) to Fe(III).

Consecutive sweep-reversal cycles for iron disc and the current response on the Fe(II)-detecting half ring are shown in Fig. 3. When the reversal was made at the ascending side of peak *A* of Fe(II) species (cycle 1), the reverse sweep was similar to the forward one. This indicates that the Fe(II) species resulted from the anodic dissolution of iron. Anodic dissolution also appeared to be the source of Fe(II) after the reversal at the beginning of the active-passive region (cycle 2).

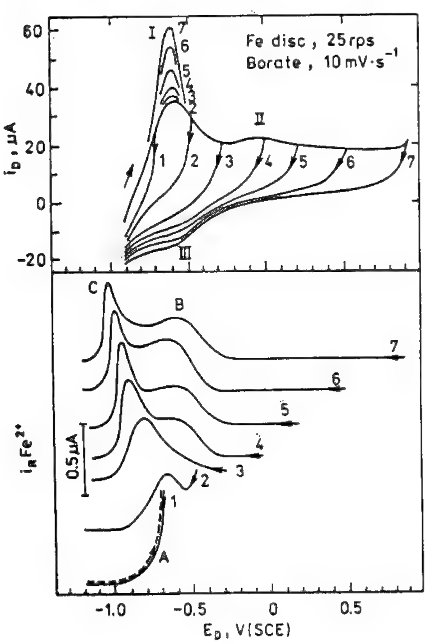

Fig. 3. Cycle sweep-reversal voltammograms for iron disc and current response on the Fe(II)-detecting half ring.

The reversals from nobler potentials resulted in the formation of the Fe(II) peaks *B* and *C* which evidently were associated with the reduction of surface layers. Peak B started to form after attaining the peak II; it grew as the potentials of the reversals became nobler, but occurred always at the same potential of about -0.45 V (SCE), coinciding with the reduction peak III. This indicated a direct relationship between peaks II, III and *B*.

Unlike peak *B*, peak *C* shifted to the negative potentials and became narrower as the reversal was made at nobler potentials. Eventually, a sharp peak *C* built up at the potential of about -1.05 V (SCE).

Peak *C* also shifted to the negative potentials with the time

of potentiostatic polarization. Fig. 4 shows consecutive sweep-reversal cycles including potentiostatic holds for various times at given potentials. Holds at -0.5 V (SCE) (active-passive region) give rise to the formation of peak *C* and its distinct shift in the negative direction. Holds at -0.2 V (SCE) (peak II) result in the appearance of peak *B* and in the rise of both peak *B* and *C*. A hold at 0.5 V (SCE) (passive region) leads to the rise of the both peaks, however, peak *C* appears to have reached its final potential and shape.

Reversal of cathodic sweeps after and before peak *C* allows to evaluate protectiveness of the film undergoing reduction at this peak. In Fig. 5 cycles 1 and 2 were made from the potential more negative than peak *C* (in this case the film was reduced); the currents in these two cycles were similar. Cycle 3 was started from the potential nobler than peak *C* (in this case the film was not reduced); in this cycle the disc and Fe(II) currents were significantly lower than in the previous cycles. This demonstrates that the film renders a considerable protection.

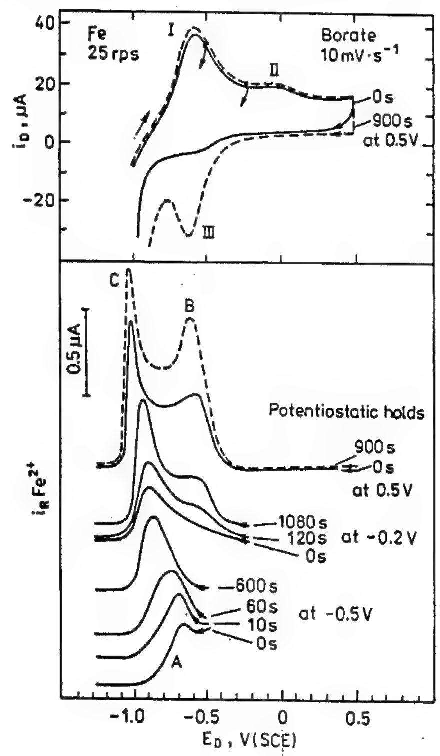

Fig. 4. Cycle sweep-reversal voltammograms for iron disc and current response on the Fe(II)-detecting half ring with potentiostatic holds in the active-passive, peak II, and passive regions.

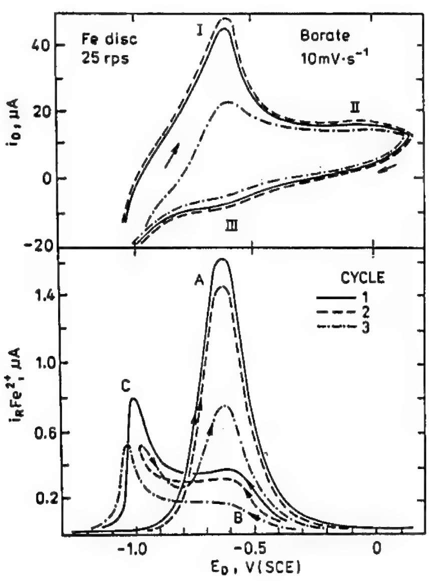

Fig. 5. Cyclic voltammograms with reversal of cathodic sweeps after and before peak *C* (cycle 2 and 3, respectively).

Discussion

The equilibrium potentials and the detected Fe(II) and Fe(III) species (Fig. 1) suggest that in the active region, $Fe(OH)_2$, Fe_3O_4 and FeOOH can form. Fe(III) species can also be in form of $Fe(OH)_3$ [18]. The presence of $Fe(OH)_2$ and/or species resembling $Fe(OH)_2$ or FeO was found in the SERS studies on iron in borate solutions [14, 22]. Presence of some Fe_3O_4 on iron in the active region was suggested in [6]; this oxide is formed in significant amounts in the active-passive transition and passive regions [6, 14].

Species $Fe(OH)_2$, Fe_3O_4, FeOOH and/or $Fe(OH)_3$ appear to play a vital role in the formation of the passive film in the active-passive transition region. Presence of Fe_3O_4, FeOOH and/or other Fe(III) components in the passive film can be ascertained with the RSRDE, especially in the cathodic sweeps. The latter sweeps suggest that the composition of the passive film can be deduced from peak *B* *C* of Fe(II) species formed during reduction of the film (Figs. 1, 3, 4).

Peak *C* appeared after polarization at potentials of the active region, when both Fe(II) and Fe(III) formed, and especially after polarization in the active-passive transition region. This indicates that the passive film starts to form in the active region, and it intensely grows in the active-passive transition region.

As the time and/or potential of anodic polarization increase, peak *C* shifts from -0.70 V (SCE) down to -1.05 V (SCE). It is supposed that the peak at -0.70 V (SCE) can be assigned to the reduction of FeOOH, whereas the peak at -1.05 V (SCE) is most probably associated with the reduction of Fe_3O_4 to $Fe(OH)_2$. This reaction is possible because the potential of -1.05 V (SCE) is by about 0.3 V more negative than the equilibrium potential for the couple $Fe(OH)_2/Fe_3O_4$ (Fig. 1).

The shift of peak *C* suggests that there is a spectrum of compositions, whose limits are determined by FeOOH and Fe_3O_4. FeOOH is the dominant component in the freshly formed films, whereas Fe_3O_4 is the dominant component in the aged films.

The spectrum may comprise a mixture of these compounds, including the modifications of FeOOH exhibiting different reduction potentials. E. g., the equilibrium potential for $Fe(OH)_2/\alpha$-FeOOH is -0.76 V (SCE), whereas for $Fe(OH)_2/\gamma$-FeOOH it is -0.50 V (SCE).

It is noted that peak *C* never split into separate peaks, as it would be expected in case of the formation of different stoichiometric compounds. The lack of a split suggests that the film is formed of a single layer; this can also be indicative for the presence of a non-stoichiometric FeOOH, in accordance with the concept of Cahan and Chen [5].

On the basis of the RSRDE results, the component of the passive film can be viewed as an intermediate between $Fe(OH)_2$, Fe_3O_4 and FeOOH, being in conformity with a non-stoichiometric FeOOH [5] and the component $Fe(II)(III)(OH)^*_x$ [14].

As manifested by the shift of peak *C*, the freshly-formed film undergoes a continuous transformation. This transformation can be easily followed by the RSRDE method.

In contrast to peak *C*, peak *B* did not shift with time and potential (Figs. 3 and 4). It grew with the polarization at potentials of peak II and above, evidently being associated with the reduction of the product formed at peak II. The lack of a shift indicated a different nature of this product in comparison to the

passive film formed in the active-passive transition region. This can be (a) a deposited layer of γ-FeOOH formed as a result of the electrochemical oxidation of Fe(II) in the solution, or (b) a part of the passive film formed by the oxidation of $Fe(OH)_2$ which accumulated on the surface in the active region.

The equilibrium potentials and the RSRDE results suggest the occurrence of the following reactions during the anodic and cathodic sweeps (Fig. 1):

Active region and peak I:

$Fe \Rightarrow Fe(OH)_2$; $Fe \Rightarrow Fe_3O_4$; $Fe(OH)_2 \Rightarrow Fe_3O_4$; $Fe(OH)_2 \Rightarrow \alpha$-FeOOH; $Fe_3O_4 \Rightarrow \alpha$-FeOOH.
Detected soluble Fe(II) (peak *A*) and Fe(III) species can be in the form of $FeOH^+$ and $Fe(OH)_2^+$ [18], respectively.

Active-passive transition region:

Growth of the passive film which can be characterized by a composition spectrum, ranging from $Fe(OH)_2$ through Fe_3O_4 to FeOOH, or by a non-stoichiometric FeOOH.
Composition and transformation of this film is reflected in peak *C* of Fe(II) in the cathodic sweeps.

Peak II:

$Fe(OH)_2 \Rightarrow \gamma$-FeOOH
This electrochemical oxidation can involve Fe(II) species present in the film and/or in the solution.
The occurrence of this reaction is reflected in the reduction peak III and in peak *B* of Fe(II);

Peak III:

γ-FeOOH $\Rightarrow Fe(OH)_2$
This reaction is manifested by peak *B* of Fe(II) species in the cathodic sweep.
Peaks II, III and *B* are directly interrelated.

Peak IV:

$Fe_3O_4 \Rightarrow Fe(OH)_2$
This reaction is manifested by peak *C* of Fe(II) species at -1.05 V (SCE).

Conclusions

Fe(II) and Fe(III) species were determined with a rotating split-ring disc electrode (RSRDE) during anodic and cathodic potential sweeps on iron in a buffered borate solution of pH 8.4. The main conclusions are as follows.

1. The passive film in the active-passive region can be described by a spectrum of compositions, ranging from $Fe(OH)_2$ through Fe_3O_4 to FeOOH, or by a non-stoichiometric FeOOH.

2. The passive film undergoes a continuous transformation in time and at nobler potentials. FeOOH is the dominant component in the freshly formed films, whereas Fe_3O_4 is the dominant component in the aged films.

3. The transformation of the film is reflected in the shift to negative potentials of the Fe(II)-detecting current in the cathodic sweeps. RSRDE method can be effectively used to follow this transformation.

4. The second anodic peak in the passive region is associated with the oxidation of Fe(II) to Fe(III), probably deposited γ-FeOOH; contrary to the passive film formed in the active-passive transition region, this Fe(III) film does not undergo a transformation.

5. The peak at the most active potential of the cathodic sweeps (peak IV) can be ascribed to the reduction of Fe_3O_4 to Fe(II).

6. The anodic film in the passive region can be composed of Fe_3O_4 and γ-FeOOH.

References

[1] R. A. Oriani and H. J. Engell (eds.), *German-American Colloquium on Electrochemical Passivation*. Corros. Sci. **29**, 117-387 (1989).
[2] N. Sato and K. Hashimoto (eds.), *The Sixth International Symposium on Passivity "Passivation of Metals and Semiconductors"*, Corros. Sci. **31** (1990).
[3] M. Cohen, in *Passivity of Metals* (Eds.: R. P. Frankenthal and J. Kruger), p. 521. Electrochem. Soc., Princeton, N. J. (1978).
[4] J. Kruger, in ref. [1], p. 149.
[5] B. D. Cahan and C.-T. Chen, J. Electrochem. Soc. **129**, 921 (1982).
[6] M. Nagayama and M. Cohen, J. Electrochem. Soc. **109**, 781 (1962).
[7] J. Kruger, in *Corrosion and Protection* (Eds.: R. P. Frankenthal and F. Mansfeld), Vol. **81-8**, p. 66. Electrochem. Soc., Pennington, N. J. (1981).
[8] J. L. Ord and D. J. DeSmet, J. Electrochem. Soc. **123**, 1876 (1976).
[9] K. Ogura and N. Hackerman, J. Electrochem. Soc. **121**, 1013 (1974).
[10] T. Tsuru and S. Haruyama, Corros. Sci. 623 (1976).
[11] N. Sato, K. Kudo and T. Noda, Corros. Sci. **10**, 785 (1970).
[12] J. O'M. Bockris, M. A. Genshaw, V. Brusic and H. Wroblova, Electrochim. Acta **16**, 1859 (1971).
[13] M. Nagayama and M. Cohen, J. Electrochem. Soc. **110**, 670 (1963).
[14] J. Gui and T. M. Devine, Corros. Sci. **32**, 1105 (1991).
[15] K. E. Heusler, in ref. [1], p. 131.
[16] J. Wilinski, J. Flis and P. Kedzierzawski, Brit. Corros. J. **25**, 184 (1990).
[17] K. E. Heusler, Berichte Bunsengesell. **72**, 1197 (1968).
[18] T. Misawa, Corros. Sci. **13**, 659 (1973).
[19] Z. Szklarska-Smialowska and W. Kozlowski, J. Electrochem. Soc. **131**, 234, 499, 723 (1984).
[20] W. Kozlowski and J. Flis, Corros. Sci. **28**, 787 (1988).
[21] W. Kozlowski and J. Flis, Corros. Sci. **32**, 861 (1991).
[22] C. Rubim and J. Dûnnwald, J. Electroanal. Chem. **258**, 327 (1989).

Materials Science Forum Vols. 185-188 (1995) pp. 649-654

Effect of bare metal surface on the repair and dissolution of magnetite film

I.H. Plonski

Institute of Atomic Physics, IFTM, PO Box MG-6, RO-76900 Bucharest - Magurele, Romania

Keywords: Magnetite film, corrosion, galvanic coupling

Abstract The potential-time dependence of magnetite layer on carbon steel with initially exposed small bare areas have been studied. As a function of the ratio of exposed metal to oxide area a falling - rising - falling wave is obtained its minimum pointing the dominance of oxide film repair over its dissolution. The experiments simulate the case of magnetite scales partially removed from surfaces in the course of chemical cleaning when coupling conditions occur with area ratios variable in time.

Introduction Magnetite is the principal corrosion product of sludge, deposits and thick oxides build up on carbon steel surfaces of heat transfer components . Acid cleaning has now become a common practice, desined to enhance the service life of steel industrial equipment, to improve heat transfer, minimize local corrosion and reduce the radiation field around nuclear power plants. For this reason many laboratory investigations have been conducted to provide understanding of magnetite dissolution together with the influence of the metal substrate on the process [1-2].

The classical galvanic coupling of spatially located magnetite and steel has also been studied in order to simulate particular situations encountered in the power plants. Short-circuited potentials and curents were measured in time for Fe_3O_4-to-Fe area ratios ranging between 0.2 and 7 . This is low enough for the resulting galvanic coupling to enter the active region of iron dissolution [3-8]. An enhanced dissolution of active steel and magnetite, as a result of the galvanic coupling was reported [6,7]. Similar studies using large Fe_3O_4-to-Fe area ratios have not yet been published. Moreover, there are distinctions between a classical external short-circuit of two spatially located electrodes and magnetite on carbon steel exposing metal surfaces, as is the actual case during the chemical cleaning when a mechanical detachment of oxide layer due to the undermining of the base metal occurs. Three are mentioned below :

- First, during magnetite dissolution and its mechanical detachment, an increasing number of alternative Fe_3O_4 and Fe surfaces characterizes this kind of single, macro-heterogeneous electrode. The external galvanic current is zero, but there are local galvanic currents which determine the electrode potential.
- Second, the chemical nature of the so-called electron sink and electron source surface is not always stable with time; under particular conditions, initially or accidentally produced bare metal is recovered by an oxide.
- Lastly, the potential drop in the solution is much lower when the electrodes are not spatially separated and can be neglected in such a case.

This paper reports a study of the behavior of the pseudo-galvanic heterogeneous electrode obtained by a controlled scratching of the magnetite layer in order that a definite small area in comparison with the oxide area is exposed at immersion time. Additional experiments on pure magnetite and carbon steel were performed, covering the real situations encountered during chemical cleaning, thus helping to define oxide on carbon steel dissolution chemistry.

Experimental For the *carbon steel* (**CS**) small cylinders of AISI 1045, exposing to the solution a 173 mm^2 lateral area, were cut from a rod, mechanically polished, etched with boiling 10% HCl for 3 min, washed with distilled water and boiled for 15 min in acetone.
For the *magnetite on carbon steel* (**CS /Fe_3O_4**) cylinders of CS prepared as above were oxidized for 21 days in LiOH aqueous solution, pH = 10.5 pressurized with D_2 in a passivated stainless steel autoclave thermostated to 333 ± 3°C. The resulting duplex layer of 2.0 ± 0.2 µm thickness consisted of an outer layer of spherical monocrystals and crystallites and a porous base layer.

Composite samples simulating pseudo-galvanic coupling between carbon steel and magnetite were obtained by mechanical removal of the oxide layer in order to expose four metal areas of roughly (mm^2) : 0.02, 0.1, 0.2, and 1.
Solutions Complex buffer solutions of 0.1M HCl and O.1M disodium citrate (Na_2HCit) were mixed to obtain pH between 1.9 and 4.8.

The experiments were performed in a 250 ml cell thermostated at 35°C under a nitrogen atmosphere.

Results and Discussions Fig. 1 shows the potential - time curves for carbon steel and magnetite on carbon steel for pH=2.4 and 4.1 at 35°C. A typical curve for Fe_3O_4 on Fe in EDTA pH 3.3 at 21°C, reported by Shoesmith [9] is superimposed. The horizontal straight lines represent the equilibrium potentials for the thermodynamically possible reactions at $a_{Fe^{2+}} = 10^{-6}$ M and $p_{H2} = 1$ atm.

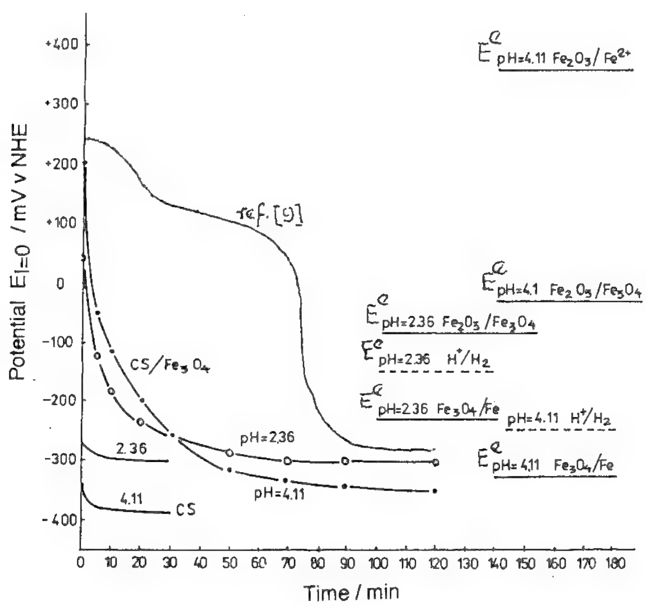

Fig. 1. The time-dependence of the open circuit potential of carbon steel (CS) and magnetite on carbon steel (CS/Fe_3O_4) in 0.1M HCl + 0.1M disodium citrate, as function of pH, at 35°C, under N_2 atmosphere. A typical curve for Fe/Fe_3O_4 electrode in EDTA pH 3.3 at 21°C, reported by Shoesmith [9] and horizontal straight lines representing the equilibrium potentials for the thermodinamically possible reactions at $a_{Fe^{2+}} = 10^{-6}$ M and $p_{H2} = 1$ atm are superimposed.

When the metallic substrate is present, the initial open circuit potential is always more negative that that of the free magnetite; this supports the Frenier and Growcock [10] idea that all magnetite layers grown on ferrous surfaces contain a number of microcracks at the base of which additonal anodic reactions take place. Rationally, this leads to the conclusion that the initial potential of the magnetite layer depend in a complex way on the metallic surface area, free or in a low oxidation state. Thus, in contrast with the partially protective magnetite grown on iron support which displays a typical sigmoid shaped curve with a potential plateau between 100 and 200 mV/NHE stabilized over at least 1 hour, for the experiments performed with CS $/Fe_3O_4$ the potential reaches immediatelly the region of sharp decrease, which lasts about 1 minute, then moves slowly

toward a value corresponding to carbon steel free corosion. This characterizes a non-protective oxide layer.
All E-t curves have a negative slope dE/ dt attesting the predominance of the local electron source reactions over the electron sink ones.

In Fig. 2, the time evolution of the open circuit potential in a solution with pH 4.1 is plotted for various initual metal-to-magnetite surface area ratios.

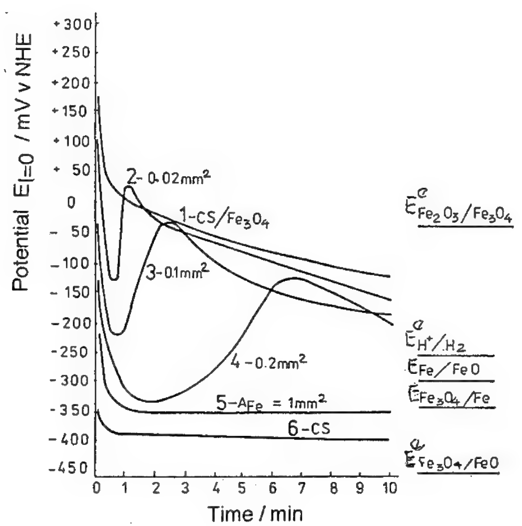

Fig. 2. The time-dependence of the open-circuit potential of the carbon steel (curve 1), magnetite on carbon steel (curve 6) and of the pseudo-galvanic coupling between magnetite and carbon steel in 0.1M HCl + 0.1M disodium citrate pH 4.1, at 35°C, under N_2 atmosphere and static condition, for various ratios between geometrical initial free metal and oxide layer areas (mm^2) : A_{Fe}/A_{Fe3O4}: curve (2) 0.02/173 ; curve (3) 0.1/173 ; curve (4) 0.2/17 3; curve (5) 1/172.

From this figure the following observations may be made .
a). At the beginning of the sharp decrease region, the mixed potential as well as the slope dE/dt are more negative the greater the free metal area.
b). For a small initial free metal area, when the initial potential is more positive than the equilibrium potential of the hydrogen evolution reaction (curves 2, 3, and 4), the potential decreases to a minimum whose value is always above the equilibrium potential of the Fe/Fe_3O_4 or Fe/FeO systems, then increases to a maximun whose value is approximately equal to the potential value which the CS/Fe_3O_4 electrode would have in the absence of the initial free metal (curve 1). The potential then slowly decreases towards the CS electrode potential. The minima and maxima in potential are more negative and delayed the greater the initial free metal area. Removal of the electrode from the solution when the potential reaches its maximum value, showed that the initial bare metal surface was again covered by a black oxide.
c). If the initial bare metal area is sufficiently large enough (curve 5) so that the potential has an initial value more negative than the equilibrium potential of the H^+/H_2 electrode, the E - t wave develops a plateau which lasts until curve 1 is reached; thereafter, the two curves proceed roughly in parallel . This may be due to the fact that as soon as the hydrogen ions are discharged on the metal, the resulting atomic and molecular hydrogen blocks the iron surface [11,12] protecting it

against reoxidation. Concomitantly, the atomic hydrogen diffuses toward the oxide increasing its dissolution through a reductive mechanism.
d). The extrapolation of the remark b) to the limit A_{Fe}^i / A_{Fe3O4}^i (i=initial) leads to the conclusion that when the initial bare metal surface is small enough, the wave turns into a monotonously decreasing E - t curve superimposing on curve 1, when porous, penetrable layer is present, and in a sigmoid curve for more compact layers. The extrapolation of the remark c), for very high values of the ratio A_{Fe}^i / A_{Fe3O4}^i again leads to the conclusion that the E - t wave turns into a monotonously decreasing E - t curve, approaching curve 6.
e). When Fe_3O_4 - on - CS enters in the region of potential sharp decrease, the time it takes to complete oxide dissolution is not much altered by the sudden presence of the bare metal; this statement is based on the fact that the final parts of all E - t curves practically coincide. It appears that the existence of the bare metal and the reactions occuring on it have no detectable influence on the opening of the pores and generally on the oxide dissolution from the covered surface.

Theoretical treatment The transient regime of the open circuit potential of a composite, heterogeneous electrode from the moment of immersion in the solution until the steady - state is reached can be approached through an equivalent electric scheme in which the equivalent capacitor of the electrode system $Fe/sol/Fe_3O_4/sol$ is charged by the time-dependent faradaic internal source which supplies the net current intensity resulted from the currents associated the electrochemical reactions occuring on both Fe and Fe_3O_4 surfaces. For simplicity, in the derivation given below, we assume that all the determining potential reactions evolving on both metal and oxide surface occur practically at the same potential, which is the same to consider the electric circuit Fig. 3.

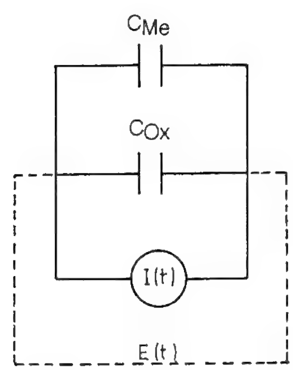

Fig.3. Equivalent electric circuit simulating the charging of the Magnetite/Solution/Iron/Solution interfaces under open circuit conditions : C_{Mc} = metal/solution capacitor, C_{Ox} = oxide/solution capacitor; G = internal source due to the net current intensity resulted from electrochemical reactions occurring on the iron and magnetite surface, respectively.

In this case, the differential equivalent capacity of the composite electrode C_{DL} is given by

$$C_{DL} = (A_{Fe}C_{Fe} + A_{Fe3O4}C_{Fe3O4}) / (A_{Fe} + A_{Fe3O4}) \qquad (1)$$

where the C_{Fe} and C_{Fe3O4} are the metal/solution and oxide/solution differential capacity , respectively, and the metal and the oxide area, A_{Fe} and A_{Fe3O4}, respectively, are time - dependent.
Consequently, the kinetic equation describing the charging of the double layer capacity concomitantly with the establishing the electrode potential, E, versus the reference potential , E_{ref}, can be written as

$$(A_{Fe} + A_{Fe3O4}) C_{DL} \cdot d (E - E_{ref}) / dt = A_{Fe} \sum I_{Fe} + A_{Fe3O4} \sum I_{Fe3O4} \quad (2)$$

where $\sum I_{Fe}$ and $\sum I_{Fe3O4}$ represent the sum of faradaic currents associated with the electrochemical reactions occuring on the metal and on the oxide surface, respectively, and t is the time. As customary in physics, when too many complex phenomena interfere, only particular situations are considered . Here, the characteristic points at minimum and maximum of the ($E - E_{ref}$) - t curve, for which obviously

$$d(E - E_{ref}) / dt \Big|_{E = E^{min}, E^{max}} = 0 \quad (3)$$

are analysed. Also, to simplify the treatment, this discussion will be confined to electrodes displaying the minimum above the equilibrium potential of hydrogen reaction so that this last process can be neglected.

Therefore, for the composite electrode the following processes are taken into account as proceeding in the region of potentials under discussion: iron dissolution and oxide formation according to reactions

$Fe \longrightarrow Fe^{2+} + 2e$ and $Fe + H_2O \longrightarrow FeO + 2H^+ + 2e$, respectively, on the bare metal surface, and the first stage of magnetite reduction [10]

$Fe_3O_4 + e + H^+ \longrightarrow Fe_3O_4H$

hypothetically assumed as the rate determining step, occuring on the oxide surface.
During this treatment, the following notations will be used:
A_{Fe}^i, A_{Fe}^{min} , A_{Fe}^{max} = bare metal area at immersion time, at minimum and maximum, respectively
A_{Fe3O4}^i = initial oxide surface area,
$k_{Fe/Fe^{2+}}$, $k_{Fe/FeO}$, $k_{Fe3O4/Fe^{2+}}$ = the electrochemical rate constant corresponding to the reference electrode potential of the above mentioned reactions, respectively, and $\alpha = F/2RT$, where F, R, and T have the usual meaning.

Because, as it results from Fig. 2, the curves which display their minima at potentials more positive than the equilibrium potential of hydrogen electrode have their maxima at times shorter than 3 min., we estimate that the metal surface changes abruptly but the oxide surface varies slowly enough to be considered approximately constant.

Thus, the faradaic current intensity associated with the above mentioned reactions is given by

$$I_F = 2FA_{Fe}^{min} (k_{Fe/Fe^{2+}} + k_{Fe/FeO}) \exp (2 \alpha E^{min}) - A_{Fe3O4}^i k_{Fe3O4/Fe^{2+}} \cdot a_{H^+} \cdot \exp (- \alpha E^{min}) = 0 \quad (4)$$

for $E = E^{min}$, and by

$$I_F = 2FA_{Fe}^{max} (k_{Fe/Fe^{2+}} + k_{Fe/FeO}) \exp (2 \alpha E^{max}) - A_{Fe3O4}^i k_{Fe3O4/Fe^{2+}} \cdot a_{H^+} \cdot \exp (- \alpha E^{max}) = 0 \quad (5)$$

for $E = E^{max}$. On combining the Eqs. (4) and (5) , one obtains

$$E^{min} = \ln[(A_{Fe3O4}^i k_{Fe3O4/Fe^{2+}} \cdot a_{H^+}) \div (2 A_{Fe}^{min} (k_{Fe/Fe^{2+}} + k_{Fe/FeO}))] \div 3\alpha \quad (6)$$

and

$$E^{max} = \ln [(A_{Fe3O4}^i k_{Fe3O4/Fe^{2+}} \cdot a_{H^+}) \div (2 A_{Fe}^{max} (k_{Fe^{2+}} + k_{Fe/FeO}))] \div 3\alpha \quad (7)$$

By substracting (6) from (7) and recalling the expression of α one may write the ratio between the bare metal area at minima and maxima of the potential - time curve.

$$A_{Fe}^{min} / A_{Fe}^{max} = \exp\ [3RT (E^{max} - E^{min}) \div 2F)] \qquad (8)$$

By substituting the experimental difference $E^{max} - E^{min}$ taken from curve 2, Fig. 2 in Eq. (8) a value $A_{Fe}^{min} / A_{Fe}^{max}$ of about 10^4 is obtained, which means that the free metal area is orders of magnitude lower at the maximum that at the minimum of the E - t curve. This result is in agreement with the experimental observation that in this region of potential on the initial free metal surface protective oxide was repaired a phenomenon by which the bare metal area continuously decreases.

Conclusions

* Magnetite layers build up on ferrous metal support in aqueus solutions are always heterogeneous electrodes initially exposing a large surface area of compact, coherent, magnetite and a small surface area of rapidly soluble thin oxide, most probably in a low oxidation state, covering the metal surface at the base of pores, cracks and other faults.

* The initial value of the open circuit potential of this heterogeneous electrode is more negative with respect to the pure magnetite potential the greater the initial ratio between the base of the faults and the compact oxide layer surface areas.

* When the compact magnetite layer is damaged to such an extent that , before the system enters the region of sharp decrease, some superficially oxidized or free metal is exposed to the solution attack, the initial value of the potential as well as the trend of the potential - time curve depends on the ratio between the metal and the compact oxide surface areas.

* If the initial open circuit potential is more positive than the equilibrium potential of the hydrogen electrode, the anodic iron oxide formation runs in parallel with iron dissolution in supplying electrons for magnetite reduction. The initial bare metal is recovered by a black oxide and the potential - time curve is wave - shaped. After the maximum of the wave, the potential declines similarly to the usual undamaged magnetite on carbon steel. From the practical standpoint, this means that the duration of a chemical cleaning is not significantly modified and there is no real condition for local corrosion in this case.

* If the initial open circuit potential of this composite electrode is more negative with respect to the equilibrium potential of the hydrogen electrode, the oxide dissolution and the increase in bare metal surface prevail and the potential - time curve is decreases monotonically similarly to the case of carbon steel electrodes.

* In order to enhance the rate of oxide dissolution by means of a galvanic coupling, the initial ration between the metal and oxide area must be high enough the initial potential enters the region below the equilibrium potential of hydrogen reaction.

References

1. I. H. Plonski, Corrosion 47 (1991) 840.
2. I. H. Plonski, J. Radioanal. and Nucl. Chem. 178, 359 (1994).
3. M. J. Pryor and U. R. Evans, J. Chem. Soc. 1259 ; ibid. 1266 (1950) .
4. H. J. Engell, Z. Phys. Chem. 7, 158 (1956) .
5. R. H. Hausler, in Corrosion / 79 NACE, Atlanta 1979, paper no. 17.
6. S. Brunet and G. Turluer, in Proceeding 5th European Symp. on Corrosion Inhibitors, Italy, Ferrara, sept. 1980, p. 513.
7. S. Brunet, G. Pinard-Legry and G. Turluer, in Proceeding 8th Int. Congress on Metallic Corrosion, Germany, Frankfurt am Main, Dechema, 1981, p. 1634.
8. G. Trabanelli, F. Zucchi and A. Frignani, Werk. und Korrosion, 30 (1979) 426.
9. D. W. Shoesmith, T. E. Rummery, Woon Lee, and D. G. Owen, Power Industry Research, 1 (1981) 43.
10. W. W. Frenier and F. B. Growcock, Corrosion, 40 (1984) 663.
11. I. H. Plonski, Corrosion, 46 (1990) 581.
12. I. H. Plonski, Ber. Bunsenges. Phys. Chem. 97, 8 (1993).

Materials Science Forum Vols. 185-188 (1995) pp. 655-666

The study of the kinetics of the passivation of nickel in high temperature aqueous solutions

T. Agladze, G. Tsurtsumia, I. Khorbaladze and T. Ekhvaia

Georgian Corrosion Center, Georgian Technical University, 380075 Tbilisi, Republic of Georgia

Keywords: Passivity, corrosion of metals, electrochemical kinetics, high temperature aqueous solution, nickel, nickel oxide film

Abstract. The kinetics of the active dissolution and passivation of nickel in the temperature range 25° to 300°C in acidified sulfuric solutions have been studied by potentiostatic technique. The effect of vanishing of the active-to-passive transition of nickel above a critical temperature, first discovered by Cowan and Staehle has been confirmed. The controversy between the improved thermodynamic stability of NiO and the loss of susceptibility to the passivation of nickel at temperatures higher than the boiling point of solvent have been explained on the basis of the assumption that direct formation of 3D oxide film, which should take place in the absence of adsorbed intermediate $Ni(OH)_{ads.}$, proceeds with significant kinetic difficulties. The desorption of $Ni(OH)_{ads.}$ and the proceeding of nickel dissolution reaction via simple consecutive charge-transfer mechanism have been deduced from the kinetic data.

Introduction. Variation in temperature alters both thermodynamic and kinetic characteristics of metal-solution system. Potential pH-diagram of nickel-water system in the temperature range 25°-300°C, constructed by Cowan and Staehle [1] displays a higher stability of nickel oxide with an increase in temperature. On the other hand the disappearance of the active-to-passive transition of nickel above critical temperature (about 120°C) takes place. It was stated in [1] that this controversy was not predicted by any theory of nickel passivity. It is surprising that such pronounced discrepancy between the thermodynamic and kinetic behaviour of nickel electrode did not attract much attention, though it seems that this effect reflects fundamental peculiarities of the process of formation of protective film on nickel. An attempt to explain the nature of this effect on the basis of the analysis of the kinetics of both dissolution and passivation processes is described in this paper.

Experimental Method

CELL DESIGN. Electrochemical measurements were carried out in a temperature region 25°-300°C in a glass cell installed in an autoclave, made of stainless steel. Schematic diagram of the experimental arrangement is shown in Fig.1. The autoclave is divided into two temperature zones. The working (1) and reference (2) (saturated Ag/AgCl) electrodes are placed in the upper part, heated by electric furnice (3). The auxiliary electrode (4) is located in the lower part, which is cooled by water cooler (5). At the temperature of the hot zone 300°C, the temperature of the cool zone

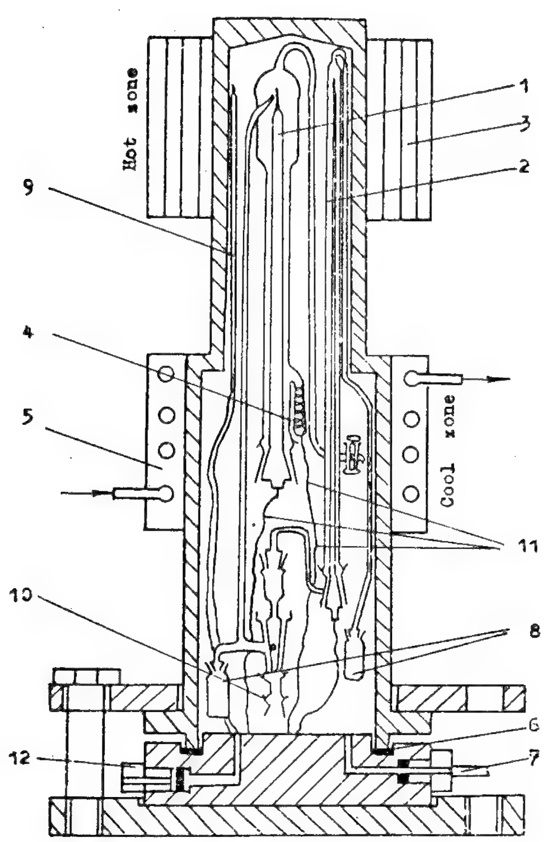

Fig.1.Schematic diagram of the experimental apparatus for high-temperature electrochemical experiments. (1) Working electrode, (2) reference electrode, (3) electrical furnace, (4) auxiliary electrode, (5) water cooler, (6) gummy sealings, (7) argon gas inlet, (8) teflon bellows, (9) thermocouple, (10) test solution inlet, (11) current feeders, (12) electrical contacts.

does not exceed 30°C. Gummy seals (6) mounted in the cool zone provide hermeticity in the autoclave. Inner pressure (6 MPa) created in the autoclave by argon is transmitted to the cell and reference electrodes by means of Teflon bellows (8) located in the cool zone. The temperature within the autoclave was measured by copper-constantan thermocouple (9) with the accuracy ±1C°. The estimated temperature gradient across the height of the working electrode compartment is less than the accuracy limit of the temperature measurement.

The combination of hermetically sealed autoclave with a convinient three-compartment electrochemical glass cell provides a number of advantages [2]. 1.The prevention of contact of solution with the atmosphere and material of the autoclave. 2.The operation of working and reference electrodes at the same temperatures. 3.Easy handling and the use of standard ground cocks, fittings, metal-glass solderings etc. 4.The possibility to carry out electrochemical measurements in the entire region from room temperature to 300°C in one cell. On the other hand the presence of hot and cool zones results in the appearance of thermodiffusion potential at the interface of the solutions with different temperatures. However, due to the equal geometry of the tubes, leading from cool to hot zones, and backward thermodiffusion potential drops in them are compensated and do not contribute to the measured potentials. Another source of possible error can arise from Sore effect. The establishment of thermodiffusion equilibrium even in thin layers of the electrolyte requires hours and even tens of hours [3]. Under test conditions, where tubes of 2-4 mm in diameter and 100-200mm in length were used and the time of keeping of the system at constant temperature was of the order of 0,5-1 hour, and the time, necessary to switch from one temperature to another was about 1-2 hours, the estimated error is negligible.

MATERIALS AND EXPERIMENTAL PROCEDURE. Test solutions were prepared from double distilled water and double recrystalized nickel salts. The solutions were thoroughly deoxiginated and under hydrogen pressure were transmitted to the electrochemical cell. Nickel electrode was prepared by cathodic deposition at preliminary pickled and degreased platinum sheet (0,12 cm^2) from 0,5 m $NiSO_4$ pH 1,2 solution, at current density 20 mA/cm^2 under hydrogen atmosphere. The auxiliary electrode was prepared from platinum sheet (8 cm^2). The results of the polarization measurements were recalculated into standard hydrogen electrode scale with an account of the temperature variation of the potential of Ag/AgCl reference electrode [4]. Polarization curves were measured at relatively fast 5 $mV \cdot s^{-1}$ and slow 0,5 $mV \cdot s^{-1}$ potential sweep rates.

Experimental Results

PASSIVATION BEHAVIOR. The anodic polarization curves of nickel measured in sulphate solutions of pH 1,3 and 3,4 at different temperatures are shown in Fig.2 and 3. The dissolution and passivation currents were time and pH dependent. Additionally it was found that at ambient temperatures nickel is more easily passivated after preliminary cathodic polarization. These effects disappear at high temperatures.

An increase in temperature up to 150°C is accompanied by an increase in anodic current density at both pH. Simultaneously the dramatic change in the shape of the anodic polarization curves, revealed in the vanishing of active to passive transition region is observed. At high temperatures current density monotonously increases with an increase of polarization until the region of anodic limiting current is reached. An increase in temperature higher than 150°C is accompanied by a slight decrease in anodic current. This effect is more pronounced at higher pH, but somewhat leveled in the region of limiting current. The later decreases with an increase in $NiSO_4$ concentration. The fractions of light green

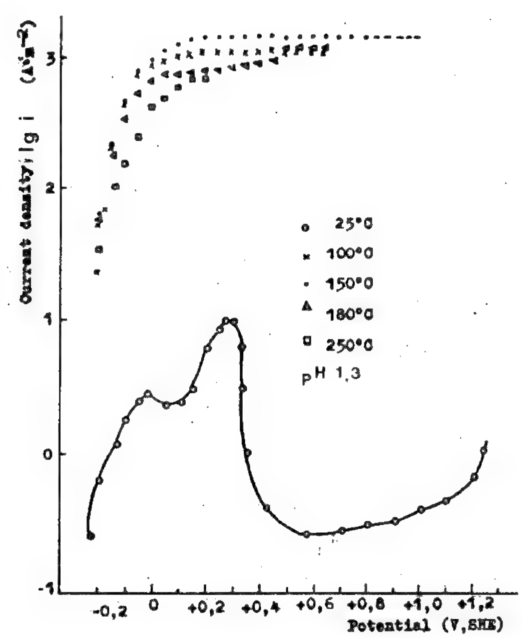

Fig.2.Anodic polarization curves of nickel in the nickel sulphate solution, pH 1,3 at different temperatures. Scan rate of 0,5 $mV.s^{-1}$.

crystalline substances were detected at the surface and in the bulk of the solution after prolong anodic polarization of nickel in $NiSO_4$ solutions at high temperatures.

If some minor discrepancies, which are apparently caused by differences in experimental procedure and in the way of preparation of test electrode are ignored it can be concluded that experimental data are in good agreement with those obtained in [1] and confirm the fact that at temperatures higher than 100-150°C nickel looses the susceptibility to passivation.

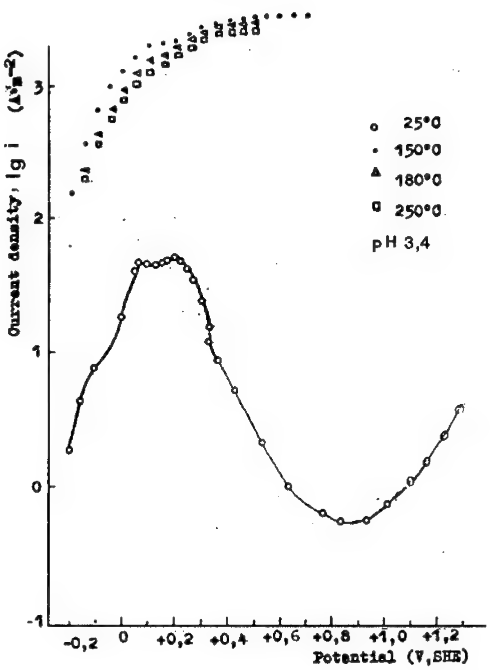

Fig.3.Anodic polarization curves of nickel in the nickel sulphate solution, pH 3,4 at different temperatures. Scan rate of 0,5 $mV.s^{-1}$.

It is obvious that above mentioned effect should be stipulated by an effect of temperature on fundamental property of metal such as its chemical reactivity in relation to solvent molecules or oxygen containing species. Some ideas on this phenomena can be deduced from the study of the effect of temperature on the equilibrium potential of the Ni/Ni^{2+} and Ni/NiO systems.

Ni/Ni^{2+} equilibrium. At room temperatures the potential of nickel electrode in aqueous solutions containing nickel salts displays extremely non-equilibrium behaviour [5-9]. There are two cases when

the transition from nonequilibrium to equilibrium state of Ni electrode takes place. The first one is when the bare surface is exposed at ambient temperatures to aqueous solutions of nickel salts [7-9]. The second one is when the temperature of nickel electrode increases higher than 100°C [5,6]. In both cases the variation of nickel electrode with temperature and activity of nickel (II) ions follows the Nerst relationship, calculated from the equation:

$$E_{eq} = E^{\circ} + (K_1 - K_2)(T - T_o) + 2,3\ RT/nF\ \ln a_{Ni^{2+}} \qquad (1)$$

where K_1 and K_2 are thermic coefficients of standard potentials of the test and reference electrodes.

Ni/NiO equilibrium. According to potential-pH diagram constructed for nickel-water system in the temperature region 25-300°C an increase in temperature affects the stability of all types of nickel oxides [1]. Taking into account the determining role of NiO in the formation of protective layer at nickel we focused on the effect of temperature on the stability of NiO ignoring details concerning other oxidation states. As follows from the potential-pH diagram shown in Fig.4 an increase in temperature results in significant improvement of thermodynamic stability of NiO. On the basis of these data an improvement of passivating characteristics of nickel electrode in acid solutions at elevated temperatures was expected, but as it was discussed earlier these expectations were not proved experimentally

There are two simple explanations of this contradiction. 1.NiO is not the actual protecting agent. 2.The formation of NiO at elevated temperatures is significantly hindered by kinetic reasons.

Proceeding from the modern understanding of the nature of passive films on nickel [10-14] the later assumption seems to be more realistic. Hence it is necessary to examine the reasons of the inhibition effect, which apparently may be linked with the hindrance of the steps of nucleation or growth of passive layers on nickel, proceeding in active, transition and prepassive regions [15,16].

Kinetics of the dissolution-deposition reactions. The overvoltage of nickel electrode significantly varies with temperature. This is mainly caused by the transition of the Ni/Ni^{2+} electrode from irreversible to reversible behaviour with an increase in temperature. Thus apparent overvoltage, determined as a difference between steady-state (rest) potential and the potential of anodically polarized electrode, coincides with the true overvoltage, determined

under the same current density in respect to the equilibrium potential, only at temperatures close 150°C, at which the behaviour of

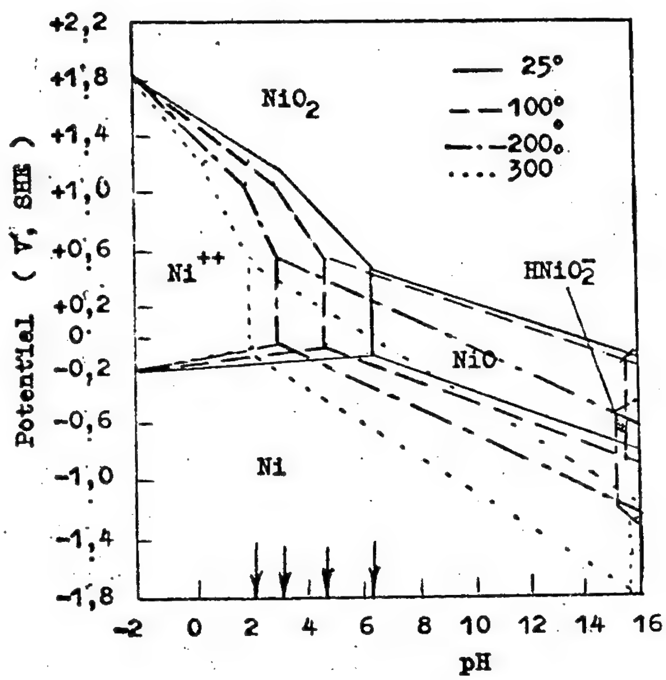

Fig.4.Potential - pH diagram of nickel-water system at different temperatures for ionic activity equal to unity [1] (for simplicity the region of stability of Ni_2O_3 and Ni_3O_4 is not shown).Note the arrows, indicating a shift of stability lines of NiO to lower pH with an increase in temperature.

Ni/Ni^{2+} electrode becomes reversible [5,6]. The anodic and cathodic pH-independent overvoltage curves at temperature 150°C shown in Fig.5. The average kinetic parameters, determined from these data: $\partial\eta/\partial \lg i_a \sim 0{,}85v$, $\partial\eta/\partial \lg i_c \sim 0{,}11v$, $\partial \lg i_o/\partial \lg a_{Ni^{2+}} \sim 0{,}6$ are at first approximation in agreement with equilibrium kinetic parameters, determined at ambient temperatures at bare nickel electrode [8,9], which leads to the simple consecutive charge-transfer mechanism of the dissolution of nickel

$$Ni \rightleftarrows Ni^{+} + e \qquad (2)$$

$$Ni \rightleftarrows Ni^{2+} + e \qquad (3)$$

with a fast parallel reaction of disproportionity of intermediate

$$2Ni^{+} \rightleftarrows Ni^{\circ} + Ni^{2+} \qquad (4)$$

Discussion. It is reasonable to assume that principal differences in passivation behaviour of nickel at ambient and elevated temperatures are connected with the difference in the mechanisms of dissolution of metal under these two conditions and more generally

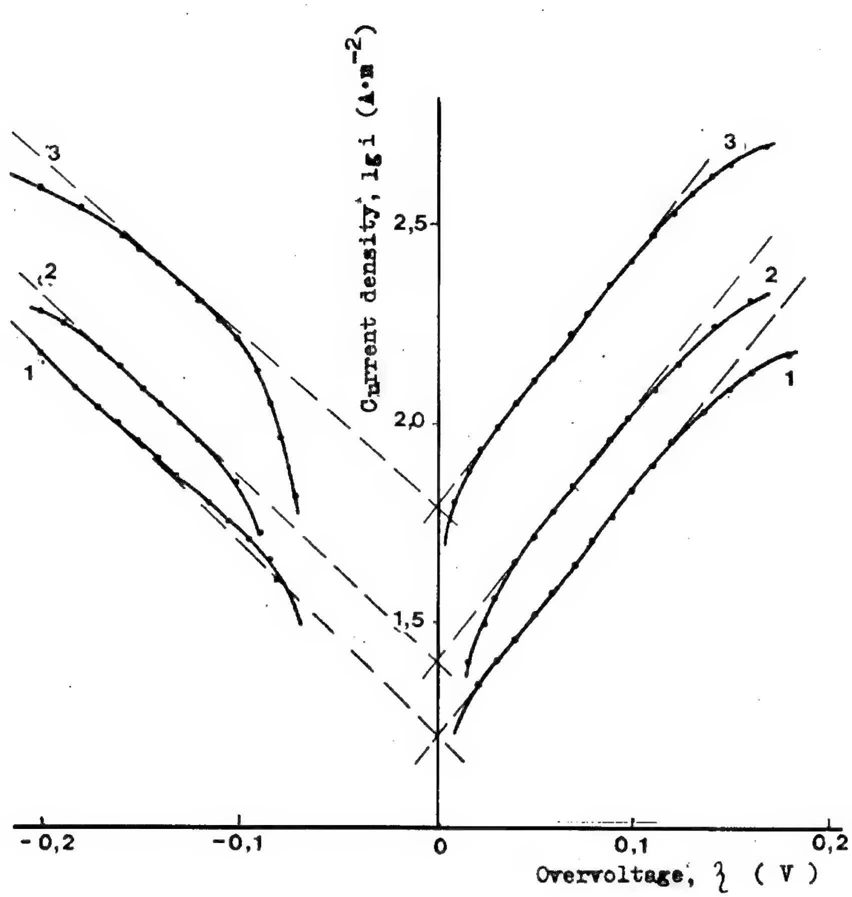

Fig.5.The cathodic and anodic overvoltage curves of nickel in $NiSO_4$, pH 1,3 solution. The concentration of $NiSO_4$, m: 0,05(1); 0,1(2) and 0,5(3).

with the reasons, which cause the differences in equilibrium behaviour of nickel electrode at lower and higher temperatures.

It is common knowledge that at ambient temperatures the active dissolution of nickel, as well as iron and cobalt, in aqueous solutions involves an intermediate, which is formed in a reaction of dissociative chemisorption of water molecules at kink sites [15-21].

$$Ni + H_2O \rightleftarrows Ni(OH)_{ads} + H^+ \qquad (5)$$

In a transition and prepassive regions the continuous dehydratation of the adsorbed intermediate and formation 2D and 3D oxide layers are assumed

$$Ni(OH)_{ads} \rightleftarrows Ni(O)_{ads} + H^+ \rightleftarrows NiO \qquad (6)$$

The blocking of active sites by $(O)_{ads}$. inhibits the active dissolution of metal in the transition range, since it is assumed that the rate constant for dissolution from kinks with $(O)_{ads}$. is much lower than that from kinks with $(OH)_{ads}$. The passive layer formation range is usually associated with phase transformation from a 2-D oxidic film to a 3-D nonporous oxidic film [15] or with two-dimensional transformation, resulting in the formation of a condensed phase of metal oxide layer at a definite potential, at which the interaction of bridge-formation energy between neighboring adsorbed hydroxide particles is higher than a certain threshold value [22]. Hence any model of the nucleation of compact protective passive layer is based on the assumption of the existence of the precursor film consisting of adsorbed intermediate. In case of nickel *in - situ* experimental evidence of the existence of such precursor adsorbed film was also obtained [23].

It was shown earlier that the formation of adsorbed intermediate $M(OH)_{ads}$ (as well as of adsorbed anions), inhibits the dissolution-deposition reactions proceeding at the bare surface of nickel [7-9]. The deviation from the equilibrium state of the Ni/Ni^{2+} system is caused by a decrease of exchange current density by more than three orders of magnitude (Fig.6). This effect defined in [9] as a "primary passivity"comparable and even higher than the inhibition effect caused by normal "secondary" passivity and cannot be ignored when the kinetics of the passivation is considered.

It follows from the present data that an increase in temperature of the nickel electrode results in the similar effect as the creation of the bare surface. It is reasonable to expect that under temperatures higher than the boiling point of the solvent the dissociative chemisorption reaction (5-6) is suppressed and

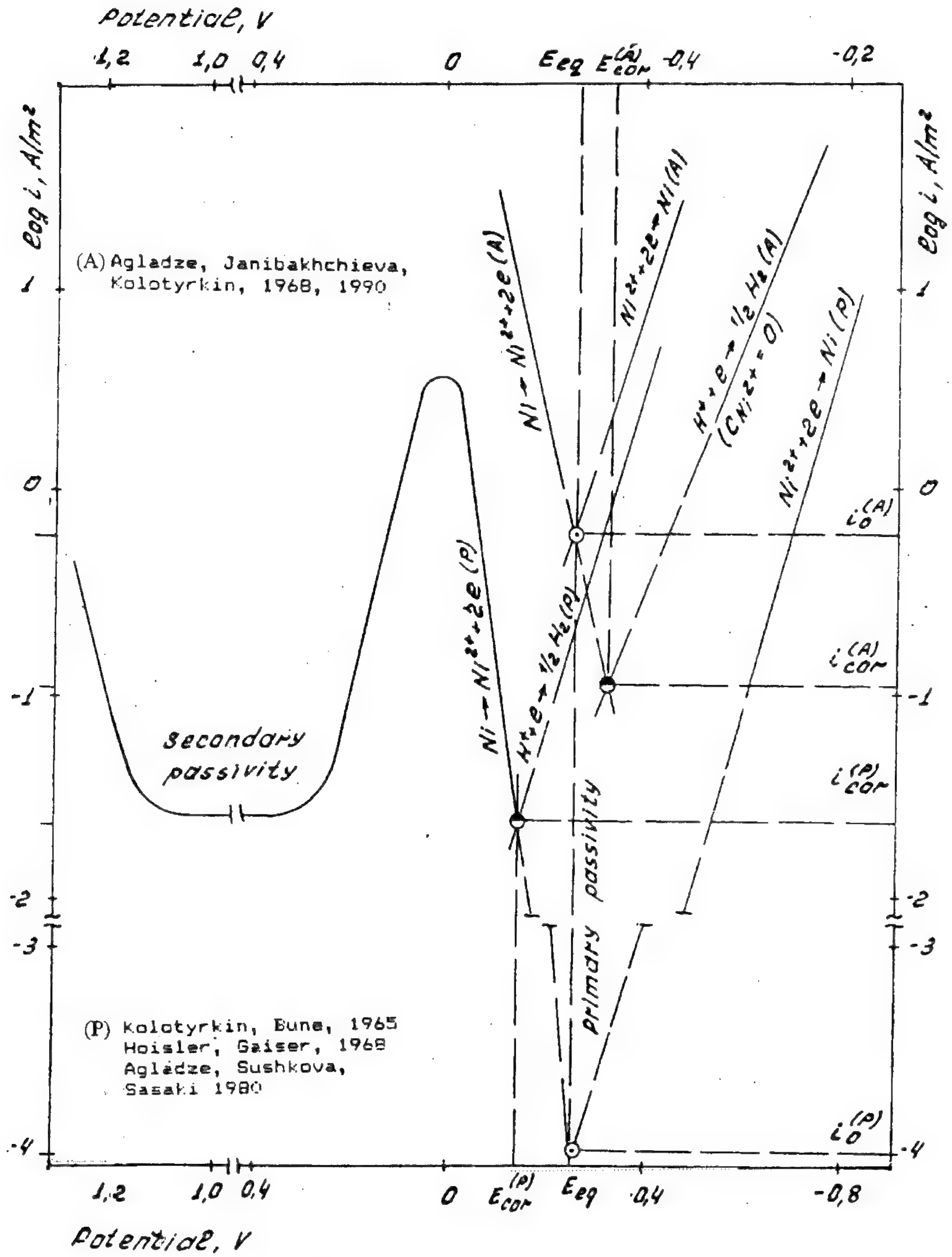

Fig.6 Polarization curves, corrosion rates and exchange current densities on passive (P) and active (A) surfaces of Ni in solution 0.5 M $NiSO_4$, pH=2.5, t=25°C [9].

surface concentration of $(OH)_{ads.}$ is vanishingly small.

The desorption of intermediate results in the fact, that the formation of protective film may proceed under new route, alternative to (5-6), involving direct nucleation of 3D nickel oxide film at metal-solution interface. However such reaction is energetically much less favorable and could in principle create anodic overvoltages higher than the tested potential limit. Kinetic hindrances in the formation of protective oxide layer in the absence of precursor $Ni(O)_{ads.}$ intermediate are apparently the major reason of the fact that in spite of improved thermodynamic stability of NiO at high temperatures nickel looses its ability to passivity.

The dissolution of metal under these conditions seems to proceed via reaction (2-4), which at high anodic overvoltages is probably determined by the diffusion of dissolution products through a non-protective porous salt layer.

Thus it can be concluded that solvent chemisorption steps play a decisive role in the mechanism of formation of passive layer at nickel. It can be expected that this phenomenon will be also critical for repassivation kinetics of nickel and nickel-based materials.

References:

[1] R. L. Cowan, R. W. Staehle, J.Electrochem. Soc., B 118, 557 (1971).
[2] V. Tsionski, L. Kriksunov, Pribory i Technika Experimenta, (Equipment and Techniques of Experiments, Moscow). 1, 224 (1988).
[3] A. S. McKie, High Temperature, High Pressure Electrochemistry in Aqueous Solutions - NACE - 4 Conference, Ed. D. G. Jones, J. Slater and R. W. Staehle, Univ. of Surray, 467 (1976), A. A. Seys, A. A. Van Haute, T. Fujii, ibid, 467.
[4] Electrochemical test-book, Ed.A. Suchotin, Leningrad, Chimia, 3 (1981).
[5] A. Vagramjan, M. Zhamagortsyants, L. Uvarov, A. Javich, Elektrokhimia, 6, 755 (1970).
[6] L. Uvarov, A. Vagramjan, M. Zhamagortsyants, G. Savchenkov, Transactions 3rd International Congress on Metal Corrosion, Moscow, v.3, 261 (1968).
[7] T. Agladze, Y. Kolotyrkin, L. Janibakhchieva, in Passivation of Metals and Semiconductors, Ed. N. Sato, K. Nashimoto, Pergamon Press, P.1, 607 (1990).
[8] T. Agladze, Y. Kolotyrkin, L. Janibakhchieva, Electrokhimia, 24, 1443 (1988).

[9] T. Agladze, L. Janibakhchieva, Zaschita Metalov (Protection of Metals), 27, 561 (1991)
[10] A. J. Arvia, D.Posada in Encyclopedia of Electrochemistry of the Elements, v.III, Ed. A.J.Bard, Dekker, N.Y. (1975) and refs. therein.
[11] K.E.Heusler, in Passivity of Metals, Ed. R.P.Frankenthal and J.Kruger, The Electrochemical Society, Princeton, N.J. 771 (1978) and refs. therein.
[12] R. Cortes, M.Froment, Hugot-Le Goff, S. Joiret, In Passivation of Metals and Semiconductors, Ed. N.Sato, K. Hashimoto, Pergamon Press, 121 (1990).
[13] H.W.Hoppe, H.H.Streblow, in Passivation of Metals and Semiconductors, Ed. N.Sato, K.Hashimoto, Pergamon Press, P 1, 167 (1990).
[14] N.Hara, K.Sagimoto, in Passivation of Metals and Semiconductors, Ed. N.Sato, K.Hashimoto, Pergamon Press, P.1 197 (1990).
[15] W. J. Lorenz, K. E. Heusler, in Corrosion Mechanisms, Ed. F.Mansfeld, Marcel Dekkar Inc., N.Y., 1 (1987).
[16] N. Sato, in Passivation of Metals and Semiconductors, Ed. N.Sato, K. Hashimoto, Pergamon Press, P.1, 1 (1990).
[17] K. E. Heusler and L.Gaiser, Electrochim. Acta, 13, 59 (1968).
[18] Ya. Kolotyrkin, G. Lopovok, and L. Medvedeva, Zaschita Met., 2, 527 (1966), 5, 3 (1969).
[19] T. Agladze, H. Sasaki, O. Sushkova, Proc. Second Japan-USSR Corrosion Seminar, Tokyo JCS, 61 (1979).
[20] T.Agladze, O.Sushkova, H.Sasaki,Electrokhimia,16,1459(1980).
[21] D. Gilroy and B. E. Conway, J.Phys. Chem., 69, 1259 (1965).
[22] G. L. Griffin, J.Electrochem. Soc., 131, 18 (1984).
[23] J. O'M. Bockris, A. K. N. Reddy and B. Rao, J.Electrochem. Soc., B 113, 1133 (1966).

Materials Science Forum Vols. 185-188 (1995) pp. 667-676

Oxide film formation studies on aluminium using the quartz crystal microbalance

J. Gnoinski[1], F.K. Crundwell[2] and S.W. Orchard[3]

[1] Anglo American Research Laboratories (Pty) Ltd., PO Box 106, Crown Mines, 2025, South Africa

[2] Department of Chemical Engineering, University of the Witwatersrand, Johannesburg, Private Bag 3, Wits 2050, South Africa

[3] Centre of Applied Chemistry and Chemical Technology, Department of Chemistry, University of the Witwatersrand, Johannesburg, Private Bag 28, Wits 2050, South Africa

Keywords: Aluminium, oxide film formation, quartz crystal microbalance, surface analysis

Abstract Oxide film formation on aluminium in an acetate buffer (pH 5.9) was investigated using the electrochemical quartz crystal microbalance and surface analytical techniques. The results suggested the formation of an oxide film consisting of at least two oxygen containing species. It was found that the outer layers of the barrier films were more hydrated than the inner film regions. Oxide film growth was explained in terms of the high field mechanism.

Introduction

Anodic oxidation of aluminium in aqueous solutions at room temperature results in the formation of amorphous oxide layers of low electronic and ionic conductivity [1]. Crystalline oxides are formed in increasing proportions at high applied temperatures and voltages [2]. The growth of these insulating layers on aluminium have mainly been described in terms of the high field mechanism, according to which the rate of ion transport depends exponentially on the applied electric field [3,4]. Studies have indicated that the oxide structure and composition has a strong effect on the oxide growth mechanism [5,6,7,8]. The composition of oxide films on aluminium has mainly been determined by *ex situ* techniques such as X-ray photoelectron spectroscopy (XPS) and secondary ion mass spectroscopy (SIMS) [9,10,11]. Only a few studies have been carried out to determine the oxide film composition *in situ*. In the present study the quartz crystal microbalance (QCM) has been used in conjunction with electrochemical techniques such as cyclic voltammetry, chronoamperometry and chronopotentiometry to elucidate the composition and the formation kinetics of thin oxide layers on aluminium. In addition X-ray photoelectron spectroscopy (XPS), secondary ion mass spectroscopy (SIMS) and Auger electron spectroscopy (AES) were used to determine the oxide film composition. The QCM technique allows the simultaneous determination of charge and mass changes thus yielding important information on the film stoichiometry and oxide growth.

Experimental

Electrochemical Measurements

The QCM instrumentation consisted of a modified Pierce-Miller circuit and a potentiostat with a grounded working electrode (WE), locally designed at Mintek. Details about the instrumentation can be found in [12]. Frequency measurements were made with a high resolution counter-timer (Keithley 775A). Planar 5 MHz AT-

cut quartz crystal disks 13.7 mm in diameter were sputter coated with high purity polycrystalline aluminium (Johnson Matthey, 99.999%) to a thickness of approximately 300 nm, while the opposite site was coated with gold (100 nm). The geometric surface area of the WE was 0.363 cm^2. The integral mass sensitivity, c_f, of the crystal was determined as 18.8 ng cm^{-2} Hz^{-1} by electrolytic deposition of a known amount of copper ions onto a gold-coated quartz crystal. Electrical contact was made to the crystal with copper wires using conductive silver epoxy. The counter electrode (CE) was a platinum flag (10 x 10 mm) which was positioned parallel to the WE at a distance of 5 nm, while the reference electrode was a saturated calomel reference electrode (SCE). All potentials in this work are referred to the SCE. The experiments were carried out in acetate buffer solutions of pH 5.9 to minimize corrosion. The buffer solutions were prepared from analytical reagent grade acetic acid, sodium acetate and deionised water (Millipore). De-aeration was accomplished by bubbling high purity nitrogen (Afrox, 99.999%) through the cell solutions. A nitrogen atmosphere was maintained above the solutions. All experiments were carried out at 25 ±0.1°C.

Prior to the measurements the air-formed oxide film was removed by immersing the electrode for 15 s in a 0.025 mol dm^{-3} NaOH solution. The aluminium-coated quartz crystals were then rinsed with deionised water and then immersed in the acetate buffer and allowed to reach steady state. Typically this was achieved after approximately 30 min. This procedure resulted in reproducible open-circuit potentials (E_{oc}). Differences in frequency from the initial reading were used to calculate the initial oxide film thickness. Potential sweep experiments were carried out by sweeping the electrode potential from E_{oc} in an anodic direction at a rate of 20 mVs^{-1} and then reversing the potential at a pre-set anodic limit. In subsequent sweeps the anodic limit was increased by 300 mV steps. Aluminium-coated quartz crystals were oxidized at 50 and 100 $\mu A\ cm^{-2}$ and the potential and frequency measured as a function of time. The potential step experiments were carried out by stepping the potential from E_{oc} to -519, -423, -340, -132, -25 mV. The average E_{oc} was determined as -1100 ±40 mV vs SCE. The charge was obtained by integration of the current, and the mass changes were determined from the observed frequency change.

Surface Analysis

The XPS analyses were performed after completion of the electrochemical oxidation of the aluminium-coated quartz crystals. The surface analyses were carried out within 5 hrs of completion of the electrochemical experiments. The XPS instrument was a VG ESCALAB MK II equipped with a hemispherical analyzer. The specimens were irradiated using the Mg *Kα* X-ray line of a magnesium anode under ultra high vacuum (UHV) (10^{-9} Torr). The acceleration voltage was 15 kV and the step size 0.05 eV. The XPS spectra were recorded in the Al 2p region to distinguish the metal from its oxide and its hydroxides. XPS spectra were also recorded in the O 1s region. The XPS spectra were fitted using a 50% mixed Gaussian-Lorentzian function and a non-linear curve fitting program.

SIMS was employed to determine the distribution of hydrogen through the oxide films. For this purpose a VG ESCALAB MK II spectrometer equipped with a quadropole SIMSLAB analyzer was used to perform the analysis. The SIMS spectra were recorded by sputtering the sample surfaces under high vacuum (10^{-9} Torr) using O^+ ions as a primary target. The ion beam current was 5 nA and the acceleration voltage 10 kV. The rastered samples had a geometric surface area of 480 x 690 μm each.

AES depth profiles were obtained by continuous argon sputtering at a rate of 5 nm min^{-1} and simultaneous AES analysis using a Perkin Elmer 595 spectrometer. For the

depth profiles the following Auger electron peak energies were used: Al(68 eV), Al(51 eV), Al(1376 eV) and O(510 eV).

Results and Discussion

Oxide Film Composition

Fig. 1 shows a typical cyclic voltammogram of an aluminium-coated quartz crystal in the acetate buffer (pH 5.9). The corresponding frequency changes are shown in Fig. 2. Similar results were obtained by Ebling *et al.*[5].

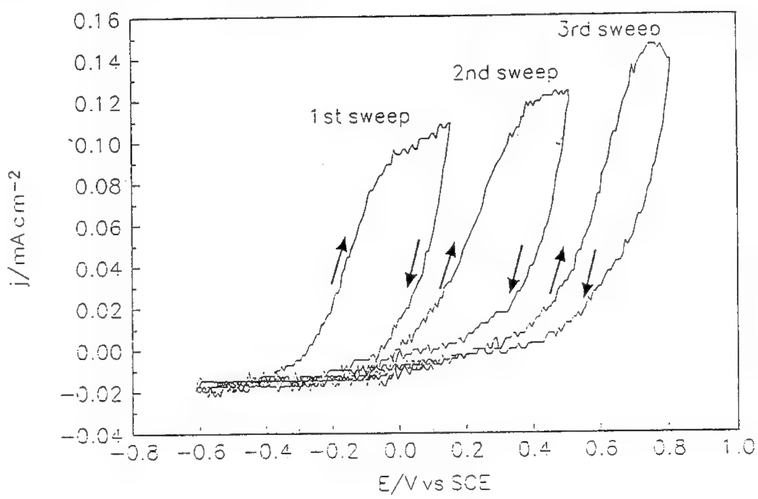

Figure 1 Cyclic voltammograms of an aluminium-coated quartz resonator in an acetate buffer (pH 5.9), sweep rate = 20 mVs^{-1}, T = 25°C.

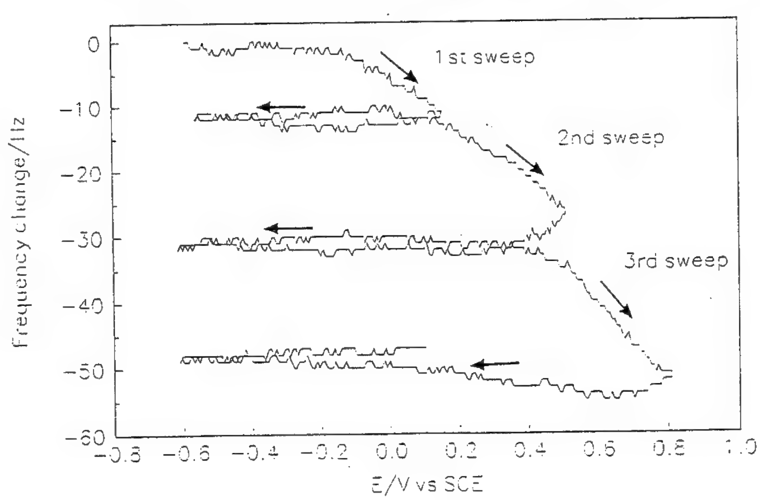

Figure 2 Frequency changes obtained simultaneously with the current response (Fig.1).

The increase in the anodic current was accompanied by a decrease in the frequency change indicating mass gain. The observed hysteresis and absence of a current peak on the reverse sweep indicated irreversible film formation and is typical of valve metals. Fig. 3 shows a typical plot of the frequency change versus the integrated anodic charge for the three forward sweeps. For each sweep an approximately linear relationship between mass and charge was obtained suggesting that the film thickness depended linearly on the electric field. Assuming a six electron transfer reaction, and only the incorporation of oxygen or water into the thin layer an apparent molar mass of 105 g mol^{-1} was determined for the first anodic sweep, 106 g mol^{-1} for the second and 116 g mol^{-1} for the third. These values may be compared to the theoretical values of Al_2O_3 (102 g mol^{-1}) and $Al_2O_3.H_2O$ (120 $gmol^1$). Although there were differences between the theoretical and experimental results, the results suggested the initial formation of Al_2O_3 and gradual hydration of the oxide film to $Al_2O_3.H_2O$ in the subsequent sweeps. The deviation from the theoretical value could also be due to the formation of a mixed oxide such as Al_2O_3 and $Al_2O_3.H_2O$ or surface roughening of the metal substrate. Examination of the oxidized surface by scanning electron microscopy (SEM) indicated no significant change compared to the original surface morphology. Reversal of the sweep direction, which corresponded to a decrease in the electric field strength, indicated a further increase in mass, which may be due to incorporation of water into the oxide film. Incorporation of water into the oxide film during the reverse sweep was observed by Ebling *et al.*[5].

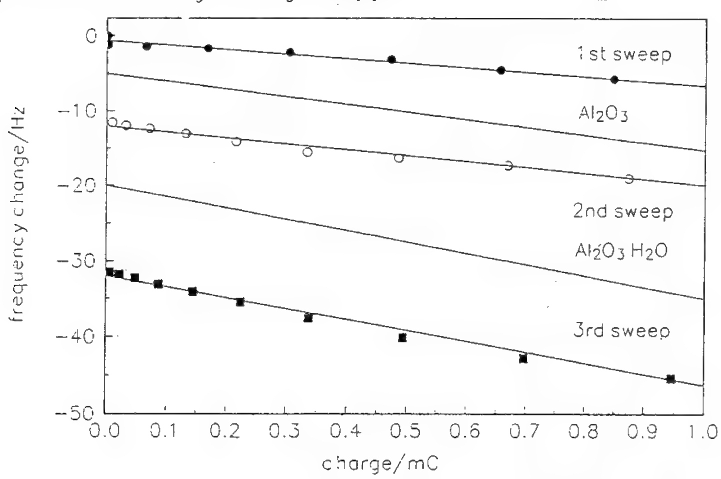

Figure 3: Plot of frequency change versus integrated anodic charge obtained for the three anodic sweeps.

In order to determine whether a barrier-type film was formed during anodic oxidation of the oxide films in the acetate buffer (pH 5.9), the aluminium-coated quartz crystals were electrochemically oxidized at 50 and 100 $\mu A\ cm^2$. Fig. 4 shows the frequency change and corresponding electrode potential as a function of time. The approximately linear increase of the potential suggested the formation of a barrier-type layer. This is consistent with the high field mechanism of oxide growth [1]. The linear decrease of the frequency with time suggested the formation of a uniform surface layer. For the oxide films formed at 50 $\mu A\ cm^2$ the mass increase per six moles of electrons passed and only the incorporation of oxygen was was determined as 99 g mol^{-1}. For the film formed at 100 $\mu A\ cm^2$ the average value was calculated as 109 g mol^{-1}. The higher 100 $\mu A\ cm^2$ is possibly due to partial hydration of the oxide layer. Roughening of the surface during oxidation seemed

unlikely as there was no visible indication of roughness when the samples were examined in the SEM.

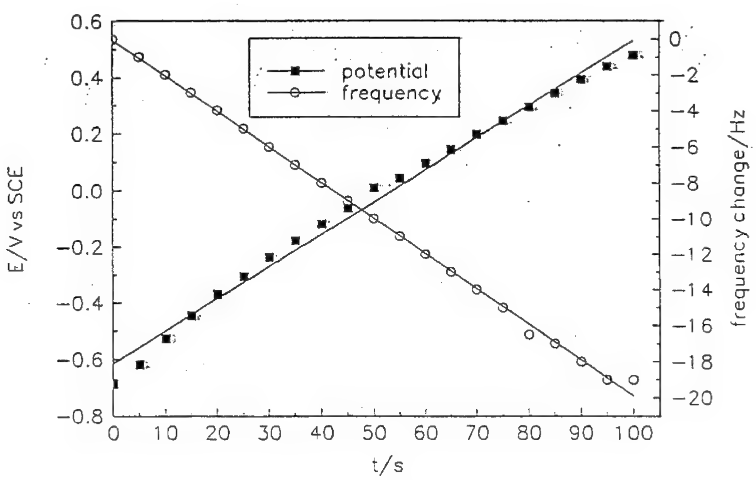

Figure 4 Electrode potential and change in resonance frequency versus time during film growth at 50 μA cm^{-2}.

The composition of the oxide layers was investigated using XPS and SIMS. Figs. 5 and 6 show the Al 2p core and O 1s spectra measured after electrochemical oxidation of the aluminium films at 50 μA cm^{-2} in the acetate buffer (pH 5.9). The Al 2p binding energy of the metal is 71.8 eV, while the binding energies of the oxides, hydroxides and oxyhydroxides are all around 74.5 eV [13]. By means of a non-linear curve fitting programme it was possible to resolve the Al 2p spectrum into two peaks. For the aluminium film oxidized in the acetate buffer (pH 5.9) the first peak was assigned to Al and the second to Al_2O_3 and Al_2O_3 and $Al_2O_3.3H_2O$. The broad O 1s peak was clear evidence of several oxygen species being present on the electrode surface. The first peak at 534 eV was assigned to SiO_2, the second at 532 eV to $Al_2O_3.3H_2O$ or $Al_2O_3.H_2O$ and the third at 531 eV to unhydrated Al_2O_3. However, considering that the binding energies of the aluminium species lie within a very narrow band width, it was not possible to identify the oxide species with absolute certainty. However, the XPS results suggested the formation of an amorphous layer involving at least two types of oxygen-containing aluminium species.

The extent of hydration of the oxide film was investigated using secondary ion mass spectroscopy (SIMS). Previous work by Abd Rabbo *et al.* [9] suggested that the degree of hydration of anodically barrier type oxide layers increased with pH and that the outer regions of the oxide film were more hydrated than the inner film regions. A typical SIMS spectrum is shown in Fig. 7.

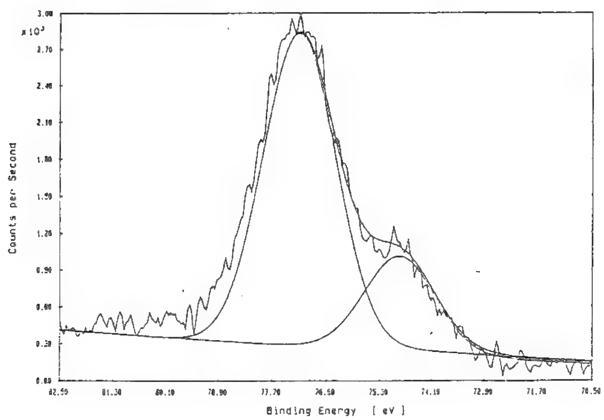

Figure 5 Experimental and fitted Al 2p spectrum obtained after electrochemical oxidation of aluminium at 50 μA cm^{-2} for 100s in a pH 5.9 acetate buffer (T = 25°C).

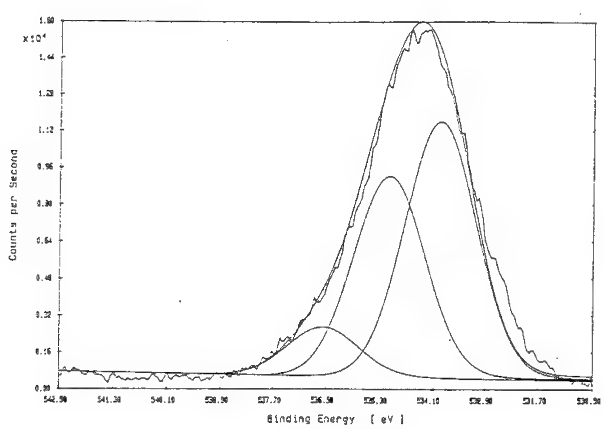

Figure 6 Experimental and fitted O 1s spectrum obtained after electrochemical oxidation of aluminium at 50 μA cm^{-2} for 100s in a pH 5.9 acetate buffer (T = 25°C).

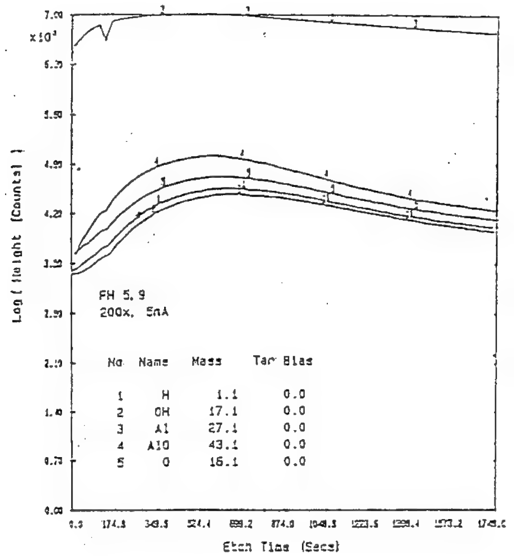

Figure 7 Typical SIMS spectrum obtained after electrochemical oxidation of aluminium at 50 μA cm^{-2} for 100s in a pH 5.9 acetate buffer (T = 25°c).

It was apparent that the OH^- and H^+ species were uniformly ejected during argon sputtering, suggesting that the oxide films formed under the experimental conditions were hydrated to some extent. Hydration in this context refers to chemisorbed water in the oxide film, rather than physisorbed water. Previous studies have shown that physisorbed water desorbs under high vacuum, while water chemically bound to the oxide structure will remain [11].

Auger depth profiles of the oxide films, which were galvanostatically formed at an anodic current density of 50 μA cm^{-2}, indicated that the uppermost region of the film enriched with oxygen with an O/Al ration of 7. The ratio was found to decrease with sputter etching to a value of 1.5 as the metal substrate was reached.

The results of the surface analysis techniques and QCM measurements may be summarized to give the following model of the structure of the oxide film formed in the acetate buffer (pH 5.9). The oxide layer is most probably amorphous and consists of an inner layer involving Al_2O_3 and hydroxide species such as $Al_2O_3.H_2O$. The outer layer has a similar chemical composition but is more hydrated. The present results are also in agreement with theories of the growth of barrier-type oxide films. According to these theories, oxide film formation involves the migration of ions such as OH^- and O^{2-} and Al^{3+} across the pre-existing oxide layer [2]. Oxide film formation thus can take place at both the metal/oxide and oxide/electrolyte interface by inward migration of ions such as OH^- and O^{2-} and Al^3 across the pre-existing oxide layer [2]. Oxide film formation thus can take place at both the metal/oxide and oxide/electrolyte interface by inward migration of O^{2-} ions and outward migration of Al^{3+}. Anodic oxide growth at both interfaces as well as the mobility of both ions has been taken into consideration in the extended high field model [1].

Oxide Film Formation Kinetics

The kinetics of film formation were investigated using potential step and mass measurements. A typical current-time transient is shown in Fig 8. Prior to these experiments the initial oxide film thicknesses were determined from the mass measurements during equilibration of the electrode in the electrolyte. The initial

oxide film thicknesses were determined as approximately 10 nm. The general feature of the current-time transients was an initial sharp increase in the anodic current density followed by a decay to a constant value. The corresponding frequency change showed an initial sharp decrease, indicating mass gain, before reaching a constant value. The changes in the resonance frequency obtained over the first twenty seconds were plotted against the anodic charge for a number of potential steps and are presented in Fig. 9.

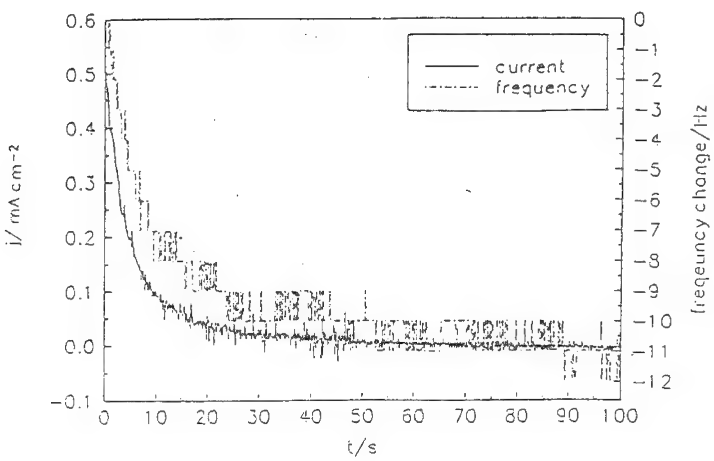

Figure 8 Current-time transient and simultaneous recorded mass changes of an aluminium-coated quartz crystal obtained in an acetae buffer (pH 5.9), stepped from -1100 mV to -500 mV.

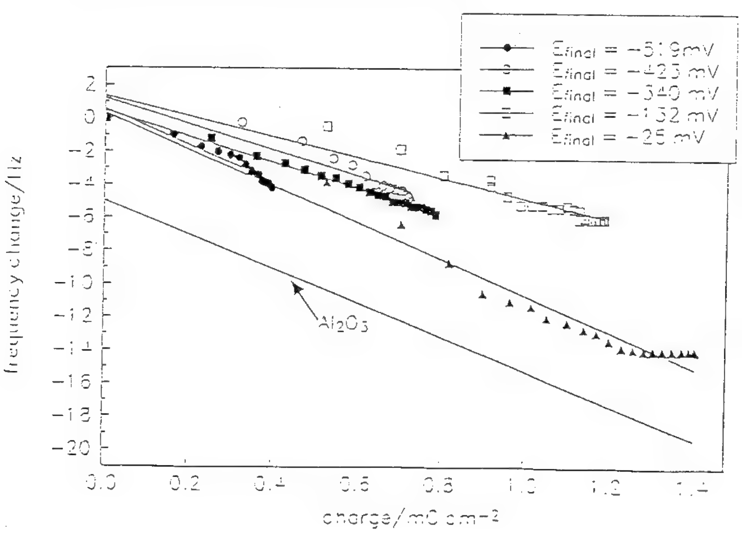

Figure 9 Plot of frequency cahnge versus integrated anodic charge obtained for the potential step experiments.

Calculation of the mass-charge ratio indicated the formation of an Al_2O_3 surface layer. The current-time transients were analyzed in terms of the high field mechanism. According to this mechanism the growth of the oxide film is characterised by a linear decay in $\log j$ with $\log t$ [1]. Fig. 10 shows a double – logarithmic plot for the current-time transient shown in Fig. 8. The average slopes of these curves were calculated as -1 confirming qualitatively the validity of the high field mechanism. In order to determine whether oxide growth occurred according to the inverse or direct logarithmic law the oxide film thicknesses were plotted against time in semi-logarithmic form (Fig.11).

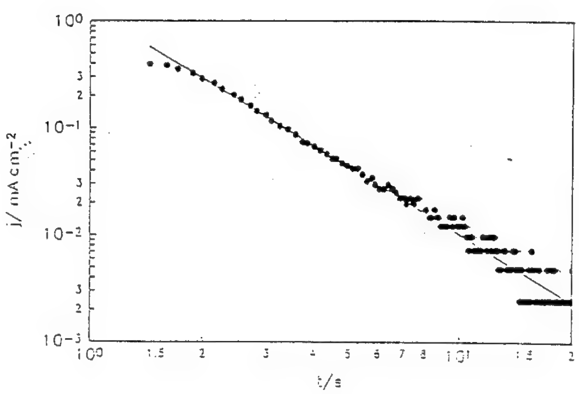

Figure 10 Typical double-logarithmic plot of current density versus time for the current transient shown in Fig. 8.

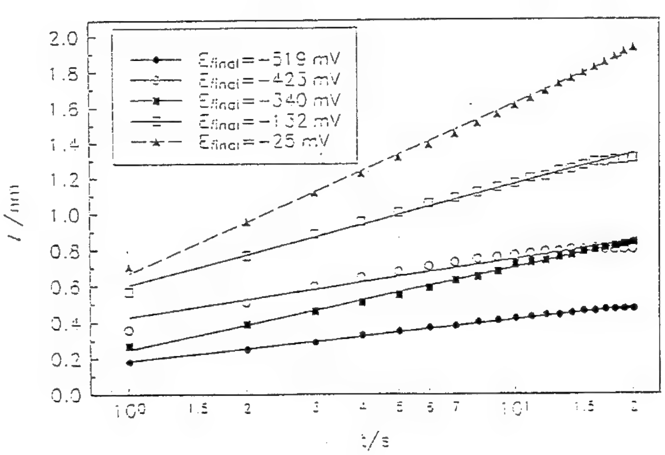

Figure 11 Semi-logarithmic plot of oxide film thickness versus time.

The results suggested that oxide film growth occurred according to the direct logarithmic law. Previous results indicated that oxide film growth occurred according to the inverse logarithmic law [1]. Considering the small changes in the oxide film thicknesses such deviation are not unexpected since both laws are approximations of the high field equation [1].

Conclusion

The results of the QCM and surface analyses suggested the formation of an oxide layer during anodic oxidation. The XPS results indicated that the oxide films consisted of at least oxygen containing species. The oxide layers consisted of an inner barrier-type layer and a hydrated outer layer. These results support a mechanism involving both the metal/oxide and oxide/electrolyte interface. This transport mechanism has been recently considered by Lohrengel [1] in the extended high field mechanism. The analysis of the current and mass change transients indicated that the high field mechanism was valid in agreement with published literature. These results demonstrate that the QCM technique is a useful technique for probing oxide film growth.

Acknowledgment

The authors would like to thank the University of the Witwatersrand and the CSIR for financial support.

References

[1] M.M. Lohrengel, Materials Science and Engineering, **R11**, 243 (1993)

[2] K. Shimizu, Corr. Science, 35, 247 (1993)

[3] N. Cabrera, N.F. Mott, Rept. Progr. Phys., **12**, 163 (1948)

[4] M.M. Lohrengel, Ber. Bunsengs. Phys. Chem., **97**, 440 (1993)

[5] D. Ebling, M.M. Lohrengel, A. Meyer, A. Thyssen, Dechema Monographie, **117**, 443 (1989)

[6] J.A. Davies, B. Domeij, J.P.S. Pringle, F. Brown, J. Electrochem. Soc., **112**, (1965)

[7] J.P.S. Pringle, J. Electrochem. Soc., **120**, 398 (1973)

[8] J.P.S. Pringle, J. Electrochem. Soc., **120**, 1391 (1973)

[9] M.F. Abd Rabbo, J.A. Richardson, G.C. Wood, Corr. Science, **16**, 689 (1976)

[10] M.F. Abd Rabbo, J.A. Richardson, G.C. Wood, Corr. Science, **22**, 1375 (1976)

[11] W.C. Moshier, G.D. Davis, J.S. Aheran, Corr. Science, **27**, 785 (1987)

[12] A.H. Gafin, S.W. Orchard, J. Appl. Electrochem., **22**, 830 (1992)

[13] D.A. Buttry, M.D. Ward, Chemical Reviews, **92**, 1355 (1993)

[14] S. Thomas, M.A. Sherwood, J. Chem. Soc. Faraday Trans., **89**, 263 (1993)

Materials Science Forum Vols. 185-188 (1995) pp. 677-686

Investigation of passive film formation by using impedance spectroscopy

M. Gaberšcek[1], S. Pejovnik[1], O. Fruhwirth[2] and G. Herzog[2]

[1] National Institute of Chemistry, Hajdrihova 19, 61115 Ljubljana, Slovenia

[2] Technical University Graz, Stremayrgasse 16, A-8010 Graz, Austria

Keywords: Impedance spectroscopy, passive film formation, zinc oxide thin film, borax solution, lithium chloride thin film, thionyl chloride, spontaneous passivation

Abstract

Impedance spectroscopy is used for detection and quantitative analysis of the process of spontaneous coverage of a metal surface with a passive film. Two passivating systems are investigated: the Zn/borax solution and the Li/$SOCl_2$ system. The time development of the impedance spectra is measured, whereby individual spectra are monitored at a high enough sampling rate in order to keep the error due to the time variability of the system below 10 % of relative error. The measured spectra are analysed by using a simple model relating the overall impedance response with the degree of metal surface coverage. The results of such analyses are presented in the form of the degree of surface coverage vs. time plots, characterised by two parameters - the mean coverage time and the rate of surface coverage. The relevance of the proposed model is verified by observing the dependence of the two coverage parameters on passivation conditions.

Introduction

In last decade electrochemical impedance spectroscopy (EIS) has become one of the most important experimental techniques in electrochemistry and corrosion science. In electrode/electrolyte systems the use of this technique has been focused mainly on investigation of the electrical properties of a system under steady-state conditions while it has rarely been used for studying time-dependent interface processes, such as the creation of double (triple) layers at the electrode/electrolyte interface, the creation of adsorbed or passive layers on a metal surface, passive layer growth and recrystallisation etc. That such studies have been avoided may be explained by the fact that the impedance response measurements are only correct if accomplished on time-invariant systems [1]. Knowing that a single impedance response measurement usually takes at least several minutes, the time-invariance requirement practically precludes investigation of the phenomena proceeding on a time-scale shorter than ca. 10-20 minutes. In this paper, however, we demonstrate that under certain experimental conditions EIS may also be used for investigation of much faster processes, such as the spontaneous coverage of a metal surface with a passive layer taking place over a time interval of 2-5 minutes.

The EIS studies of spontaneous surface coverage are presented on two model systems: a zinc/borax solution and a lithium/thionyl chloride system. The passivation process in the zinc/borax solution system has been extensively studied by Herzog [2] and Friedmann *et al.* [3,4]. However, the kinetics of the passive layer formation has only been examined in time intervals of more than 1 h [3], so nothing could have been said about the initial stage of passivation, e.g. the formation and properties of an adsorption [5-7] or oxide [7,8] precursor (prepassive) film or the formation of the passive film itself. On the contrary, in the Li/$SOCl_2$ system Moshtev *et al.* [9] studied, using the galvanostatic pulse technique, the initial coverage of a lithium electrode with a LiCl monolayer and the consequent

passive layer growth in $SOCl_2$. Their results indicate that the coverage of the lithium surface with a passive monolayer is accomplished within 20-30 minutes of the moment of immersion of the lithium electrode in $SOCl_2$. Later, Hedges *et al.* [10] found by potential sweep and step experiments at microdisc lithium electrodes that "a period on open circuit of 100 s is long enough for the formation of a film of thickness sufficient to inhibit corrosion...". Obviously, there is a discrepancy of more than one time decade between the two results and it was hoped that the use of impedance spectroscopy would give additional data to resolve this problem. Moreover, by studying two essentially different systems we tried to check if the use of EIS in monitoring the process of surface coverage is generally applicable to passivating systems.

Experimental

Impedance response and OCV measurements were performed using Solartron equipment: 1250 Frequency Response Analyser, 1260 Frequency Response Analyser and 1286 Electrochemical Interface.

Zn/borax solution system

The working electrode was a Zn rotating disc electrode (99.99%) (A = 0.5cm^2) concentrically encircled with a Pt mesh (ca. 120 cm^2) serving as a counter electrode. A Hg/HgO/0.1 M borax solution (pH = 9.2) reference electrode was connected to the cell via a salt bridge. The electrolyte was 0.1 M borax solution (pH = 9.2), except in one set of experiments where the borax concentration varied from 0.02 M to $8 \cdot 10^{-4}$ M. It was possible to bubble the electrolyte with gaseous N_2 or O_2. About 1 min before the immersion in the electrolyte the Zn electrode was ground in air with grinding paper No. 600 and the grinding residues were removed with borax-wet cellulose wadding. The rotation rate of the Zn electrode could be varied continuously from 7 to 45 r.p.s.

Li/$SOCl_2$ system

The cells were prepared and measured in Ar flushed dry boxes. The cell construction is shown in Fig.1. All electrodes were made of Li sheets (Mineral Foot, battery grade) pressed onto stainless steel screw-shaped holders. During the cell assembly the lithium sheets were tightly pressed against the teflon edges encircling the electrolyte compartment, so no contact between the stainless steel holder and the electrolyte was possible. The electrolyte was 1.5 M $LiAlCl_4/SOCl_2$ prepared as described elsewhere [9].

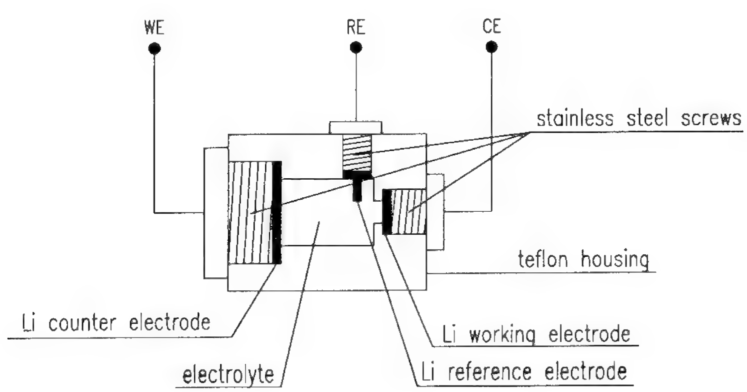

Fig.1. Three-electrode cell used for investigation of passive film formation in the Li/$SOCl_2$ system.

Results and discussion

Fig. 2 shows the time development of the open circuit voltage (OCV) between the Zn and Hg/HgO reference electrode (a), the absolute impedance at 3.5 Hz (b) and the phase angle at 3.5 Hz (c) of the Zn/electrolyte interface after the immersion of the rotating Zn electrode in 0.1 M borax solution. At each point the impedance measurements were made in such a way that no direct current flowed through the system, while the amplitude of sinusoidal excitation was 10 mV or less. A single impedance measurement took ca. 5 s. We presume that the impedance measurements did not disturb the spontaneous process(es) taking place at the Zn/electrolyte interface after the moment of immersion.

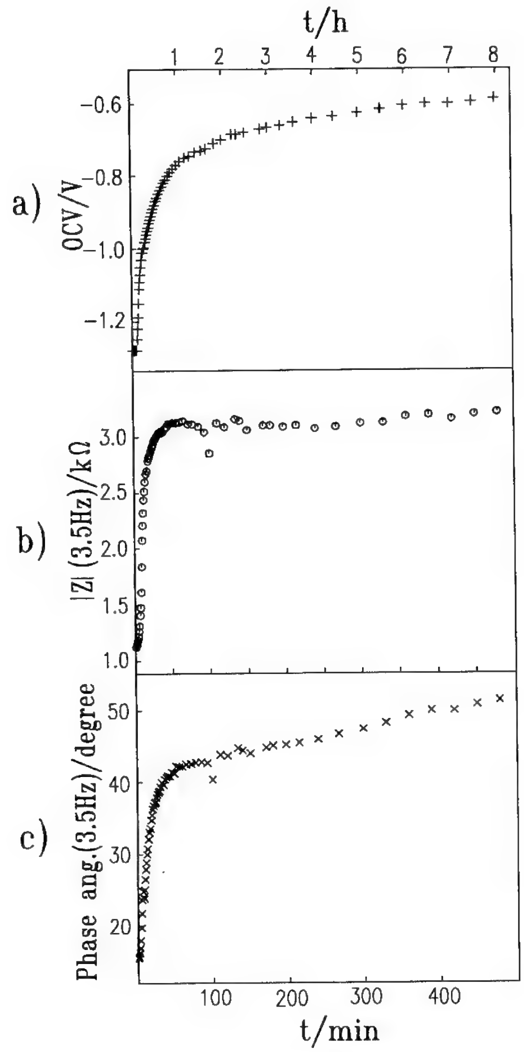

Fig.2. Time development of open circuit voltage (OCV) between Zn and Hg/HgO/0.1M borax solution reference electrode (a), and the absolute impedance (b) and phase angle (c) at 3.5 Hz for Zn/borax solution system. Time 0 corresponds to the moment of immersion of Zn electrode in borax solution in equilibrium with air. The rotation rate of Zn electrode was 7 r.p.s.

The OCV shift from ca. -1.35 V to 0.6 V versus the Hg/HgO electrode has been shown to be associated with the process of zinc passivation [2]. Fig. 2 reveals that during the spontaneous passivation of the zinc surface the impedance parameters may also change significantly. Careful inspection of the three graphs in Fig.2 reveals that the transition of the impedance curves from one to another value is even more abrupt than is the transition of the OCV curve. This particularity may indicate that the impedance technique is in a way a more sensitive method for detecting the early stages of passivation process than are the OCV measurements.

The impedance measurements presented in Fig. 2 were performed at one frequency only while normally the impedance response measurements may include a wide frequency range, e. g. from 1 Mhz to 1 mHz (the latter measurement type is highly preferred as it usually yields much more information about the measured system). The decision to start our investigation with the simpler single-frequency measurements had a fundamental background. Namely, in the initial stage of passivation (first 30 minutes after immersion) the electrical properties change with time very rapidly, so it is impossible to measure the impedance response correctly in a wide frequency range as the system will then change its electrical properties during the measurement itself. In this case the measured impedance response will not satisfy the requirement of time-invariance [1]. If the impedance measurements are to be performed rapidly enough to remain within this condition, one is forced to limit either the frequency range of measurements or the number of measured points - both cases leading to a reduced amount of information and accuracy.

Based on numerous tests we decided to follow the spontaneous passivation of zinc by measuring the impedance response in the frequency range 200 - 2 Hz, at 8-12 selected frequencies, which represents a compromise between the two limiting cases described above. Typical results are shown in Fig. 3, where the time development of the impedance response spectra of the zinc/electrolyte interface is shown in the complex plane representation. The duration of an individual impedance response measurement did not exceed 20 s. The estimated relative error due to the time variation of the system during an individual impedance response measurement was 5-10 % (the error refers to the fluctuations in the fitted value of equivalent circuit elements such as shown in Fig. 4). Up to 3 impedance response measurements per minute were possible. Care was taken that no direct current flowed through the system during the measurement.

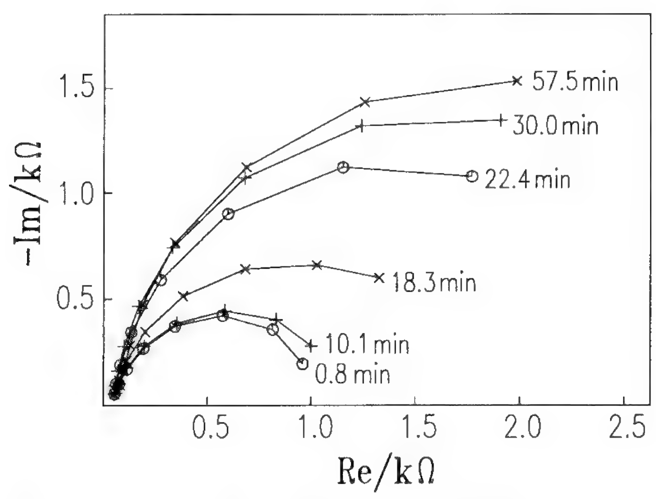

Fig.3. Time development of the impedance response of Zn/borax solution system.

The time development of the impedance at one frequency and the impedance response shown in Figs. 2 and 3 was associated with the process of coverage of the zinc's surface with a passive layer. Thus, the impedance response, measured immediately (i.e. in the first 20 secs) after immersion of the zinc in the electrolyte, was ascribed to the bare (uncovered) zinc surface in contact with the electrolyte. Within the measured range this response could be approximated with a single RC term in parallel (Fig. 4a). The impedance response, measured at 1 h after the immersion of the zinc, was ascribed to the completely covered zinc surface with a passive layer. This impedance response had to be approximated by at least 2 RC terms in order to get a satisfactory fit (Fig. 4b). Obviously, the initial and the final state correspond to 2 different equivalent circuits, *i.e.* two different impedance response functions. This essential feature cannot, by definition, be observed at single-frequency measurements or equivalent techniques (e.g. the galvanostatic pulse technique used by Moshtev *et al* in [9]).

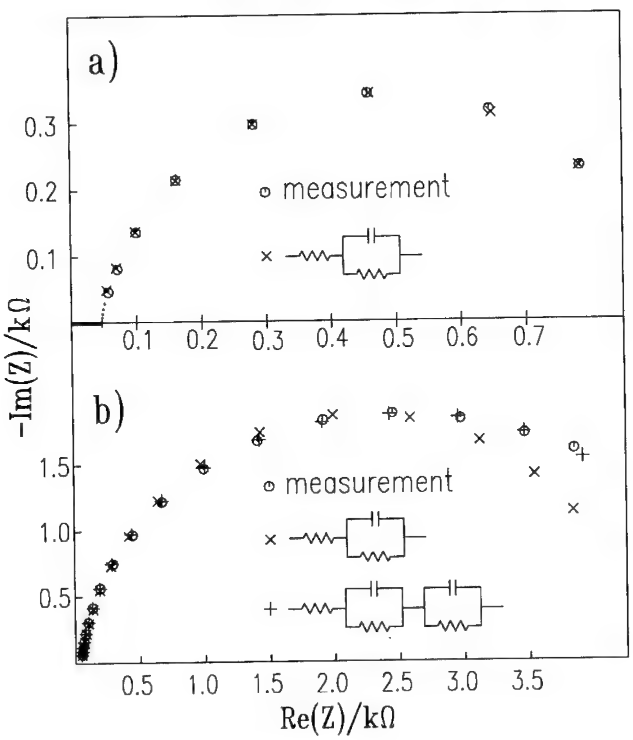

Fig.4. Impedance response before (a) and after (b) coverage of Zn surface with passive layer. Equivalent circuits and the corresponding fits are included.

Combining the results shown in Figs. 2 - 4 one may suggest the following analysis of the impedance response measurements on the zinc/borax solution interface (Fig.5):

1. The impedance responses measured before and after the typical transition in OCV or in impedance are fitted by corresponding functions which, in general, may have a different form. These impedance responses represent either an entirely bare (i.e. free of film) zinc surface or an entirely covered zinc surface, respectively.
2. The impedance responses measured during the typical transition of the electrical properties are fitted with a parallel combination of the initial and the final impedance response. These impedance responses represent a partially covered zinc surface, the degree of coverage at a

certain instant being determined by a weighting parameter Θ (a most simple weighting may be expressed by the covered A_1 and the uncovered A_2 geometric surface area of the metal, *viz* $\Theta = A_1/(A_1+A_2)$).

Quantitatively, the proposed analysis may be written as:

$$\frac{1}{h(\omega)} = \frac{1}{(1-\Theta)\cdot f(\omega)} + \frac{1}{\Theta \cdot g(\omega)} \tag{1}$$

where $h(\omega)$, $f(\omega)$ and $g(\omega)$ represent the impedance response functions corresponding to a partially covered, a bare and a completely covered metal surface, respectively, and Θ is the degree of metal surface coverage as defined under point 2. We will refer to Eq. 1 as the model of surface coverage (MSC).

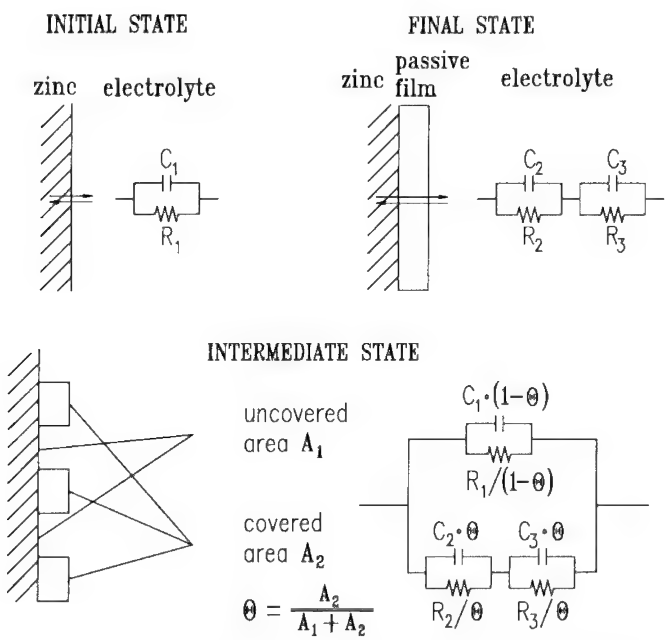

Fig.5. Schematic representation of the model of surface coverage (MSC) used in analyses of the measured impedance response spectra.

MSC implicitly assumes the following properties of the measured system:

- The transition from the initial (bare) to the final (covered) surface state is gradual.
- At all degrees of coverage Θ, each point on the surface is describable either by the initial (bare) or the final (completely covered) surface state.
- The direction of the electric field should be perpendicular to the metal surface at all surface points.

The second and third assumption probably represent an oversimplification of the real situation during the process of surface coverage. Still, if the model is fundamentally correct, its application to the impedance response measurements should provide reasonable results in the form of time dependence of the degree of surface coverage. A typical result of such an analysis is shown in Fig. 6. The obtained curve may be described by two characteristic quantities: the slope k meaning "rate of surface coverage" and the time t_0 defined as mean coverage time, i.e. the time when a half of the

metal surface has been covered with a passive layer. Both quantities are defined according to the point on the curve corresponding to 50% of coverage ($\Theta = 0.5$).

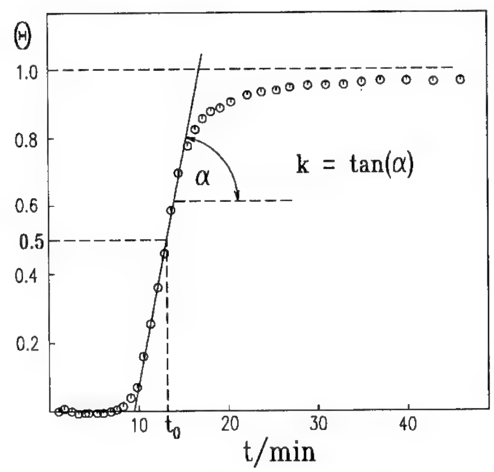

Fig.6. A typical Θ vs time curve resulting from an analysis of measured impedance spectra with MSC. The rate of surface coverage k and the mean coverage time t_0 are defined according to the point on the curve where $\Theta = 0.5$.

The relevance of the proposed analysis was verified on three sets of measurements. In the first set the impedance response was measured as a function of time at different concentrations of oxygen dissolved in the electrolyte (Table 1). The amount of dissolved oxygen was controlled by bubbling the electrolyte with gaseous N_2 or O_2 for a selected period before the immersion of the zinc electrode and the beginning of the impedance response measurements. Table 1 shows that the higher the oxygen concentration the shorter the mean coverage time and the higher the rate of surface coverage. This result is consistent with the previously observed effect of the presence of dissolved O_2 on the corrosion process in the zinc/borax solution system [3].

Table 1. Mean coverage time t_0 and rate of coverage k for a rotating zinc electrode immersed in 0.1 M borax solutions with various concentrations of dissolved oxygen. The oxygen concentration was controlled qualitatively, by bubbling the electrolyte with nitrogen or oxygen prior to immersion of zinc electrodes. The third row corresponds to the condition of equilibrium between the electrolyte and air.

Gas	*Bubbl. time/h*	*t_0/min*	*k/min^{-1}*
N_2	5.6	∞	0
N_2	1.7	13.15 ± 0.10	0.135 ± 0.005
-	-	4.08 ± 0.02	0.200 ± 0.01
O_2	5.5	2.26 ± 0.04	0.270 ± 0.01

In the second set the time dependence of the impedance response was measured at various rotation rates of the rotating zinc electrode (Table 2). The results clearly indicate that the higher the rotation rate the shorter the mean coverage time and the higher the rate of surface coverage. The observed tendency may be explained by the well-known influence of rotation rate on the mass transport to an

electrode. Hence, it seems that in our case the oxygen diffusion towards the electrode surface determines the overall kinetics of the passive film formation.

Table 2. Mean coverage time t_0 and rate of coverage k for a rotating zinc electrode immersed in 0.1 M borax solutions as a function of rotation rate.

Rot. rate/r.p.s.	t_0*/min*	*k/min*$^{-1}$
7	17.80 ± 0.20	0.094 ± 0.006
11	14.00 ± 0.05	0.135 ± 0.003
15	11.72 ± 0.00	0.142 ± 0.004
19	9.95 ± 0.05	0.163 ± 0.002

In the third set the time dependence of the impedance response was measured at various concentrations of borax (Table 3). We chose this parameter as it had been supposed that it would not affect significantly the process of coverage. The results shown in Table 3 confirm the expected behaviour. The slight fluctuations of the two parameters with borax concentration might be associated with the fact that the solubility of O_2 in borax slightly changes with borax concentration.

Table 3. Mean coverage time t_0 and rate of coverage k for a rotating zinc electrode immersed in borax solutions of various borax concentrations.

C(borax)/M	t_0*/min*	*k/min*$^{-1}$
0.02	1.25 ± 0.10	0.52 ± 0.02
0.004	1.50 ± 0.05	0.45 ± 0.01
0.0008	1.47 ± 0.03	0.44 ± 0.02

As a whole, the results shown in Tables 1-3 are expected or, at least, easy to explain, which shows that the proposed analysis by using MSC gives reasonable information about the process of zinc surface coverage with a passive layer. The obtained parameter values indicate that in the zinc/borax solution system typical mean coverage time t_0 may range from 1-20 minutes while the rate of coverage k may have values from around 10 to 50 % min^{-1}, depending on the measuring conditions.

The next system sudied was the Li/ $SOCl_2$ system. Fig. 7 shows the time development of the absolute impedance (a) and the phase angle at 15 Hz (b). Due to the specific cell configuration (all electrodes consisted of lithium) the OCV data were not considered for this system. The time 0 refers to the time when Li came into contact with $SOCl_2$ during the cell assembly. In contrast to the Zn/borax solution system, the time dependence of the impedance parameters shown in Figs. 7 a and b is much more complex, showing at least 4 different regions clearly separated from each other. In previous investigations [9, 11, 12] this feature could not be observed, as the sampling rate was in all cases much smaller than that used in this study. We assume that the observed behaviour is due to different steps in the process of lithium passivation, such as the gradual coverage of the lithium surface with a thin passive film [9], the consequent thickening of the initial film [11], the dissolution/precipitation of the passive film [13] etc. In this study we were only interested in the first step, i.e. the initial coverage of the lithium surface with a passive film. This stage was analysed in a manner analogous to the one applied to the Zn/borax solution system: i) first the measuring conditions under which the measured impedance responses remained within the 10% relative error due to the time variability were determined, ii) the impedance responses were monitored as a function of time passed from the

moment of the Li immersion into $SOCl_2$, iii) the first and the last measured impedance response in region I (see Fig. 7) were ascribed to a bare and a completely covered Li surface, respectively, iv) all other impedance responses were used for evaluation of the degree of surface coverage Θ at a certain moment using the MSC approach (Eq. 1). A typical Θ vs time curve resulting from the analysis, together with the corresponding values for k and t_0, is shown in Fig. 7c.

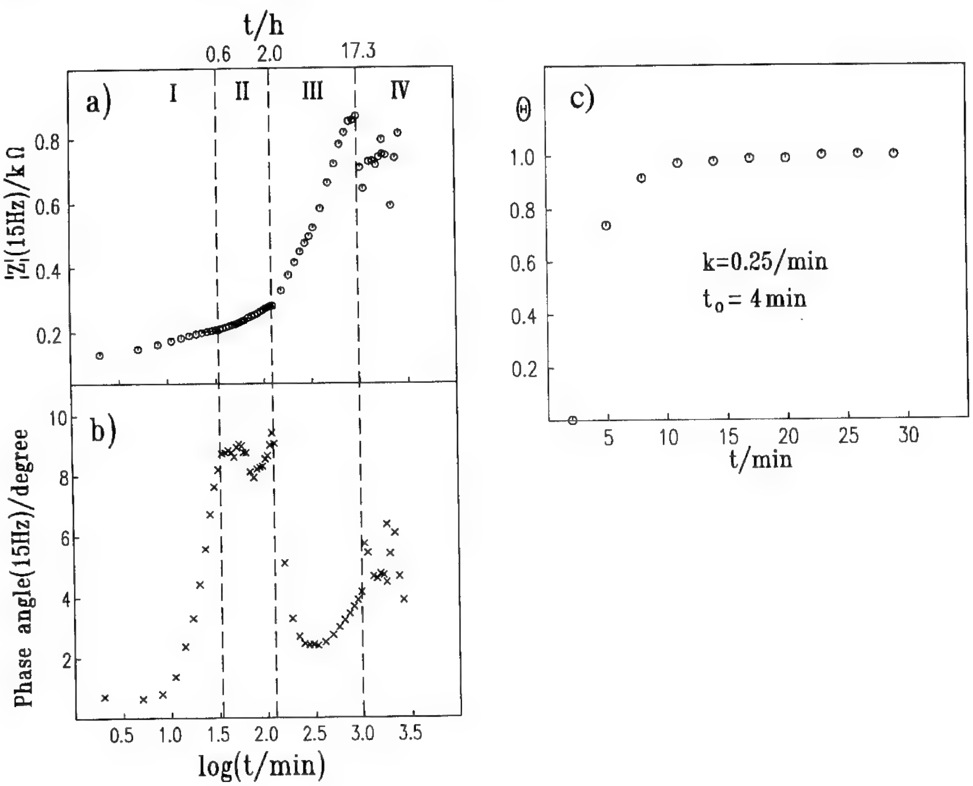

Fig.7. Time development of the absolute impedance (a) and phase angle (b) at 15 Hz for $Li/SOCl_2$ system. Time 0 corresponds to the moment of immersion of Li electrode in the electrolyte. c) Time development of surface coverage for $Li/SOCl_2$ system as obtained by analysis with MSC. The lithium electrode was not pre-treated before use.

Due to the difficulty of handling Li-electrodes and the very agressive nature of $SOCl_2$-based electrolytes, it was practically impossible to change the conditions of surface coverage in a sense comparable with that shown for the Zn/borax solution system. What we could do, however, was prepare two different types of Li surface. In the first case, i.e. the one corresponding to Fig. 8, we used an as-purchased battery-grade Li foil; in this case the Li surface was covered with a thin protective organic foil which, after immersion in the electrolyte, was supposed to be quickly dissolved. The second type of Li surface was prepared so that the working Li electrode was freshly cut immediately before being brought into contact with the electrolyte. In this case the mean coverage time t_0 reduced from 4 to about 2 min, while the rate of surface coverage k remained essentially unchanged. If both parameter values are combined one finds that in the case of the freshly cut Li electrode the process of surface coverage starts immediately after the moment of contact

between Li and the electrolyte. But it takes about 6 min before about 99% of the lithium surface is covered. It may be concluded that, unlike in previous results obtained by Moshtev *et al* [9] and Hedges *et al* [10], the use of the impedance spectroscopy gave quantitative information about the time dependence of the process of surface coverage for an $Li/SOCl_2$ system.

Conclusions

i) It was shown that during the process of spontaneous passivation in a Zn/borax solution and in a $Li/SOCl_2$ system the impedance response changes significantly. The changes in impedance response occuring within the first hour after immersion of the metal in the electrolyte were ascribed to the process of coverage of the metal surface with a thin passive film.

ii) A general model relating the measured impedance response and the degree of surface coverage with a passive layer was presented. The model was tested by changing the passivation parameters of the Zn/borax solution system in a controlled manner; in all cases expected relationships were obtained, thus confirming the relevance of the proposed model.

iii) From the results presented it follows that in both systems studied the process of metal surface coverage with a passive layer is a gradual process proceeding on a time scale of at least several minutes. This is a slow enough process to be detected and quantitatively analysed by using the impedance response measurements.

References

[1] W. Mc C. Siebert, Circuits, Signals and Systems, MIT Press, Cambridge, 1986.

[2] G. W. Herzog, Electrodeposition Surf. Treat. **1**, 175 (1972/73).

[3] J. Friedmann, O. Fruhwirth, G. W. Herzog, Electrodeposition Surf. Treat. **3**, 343 (1975).

[4] J. Friedmann, O. Fruhwirth, G. W. Herzog, Surf. Technol. **6**, 469 (1978).

[5] H. H. Uhlig, Electrochim. Acta **16**, 1939 (1971).

[6] V. M. Novakovskii, Y. M. Kolotyrkin, Zash. Met. **8**, 283 (1972).

[7] V. Brusic, in Corrosion Chemistry (G. R. Brubaker, P. B. P. Phipps, eds.) Chap. 6, ACS Symposium Series 89, American Chemical Soc., Washington, D.C., 1979.

[8] J. O'M. Bockris, A. K. N. Reddy, Modern Electrochemistry, Vol.2, Plenum Press, New York, 1970, pp. 1323-1327.

[9] R. V. Moshtev, Y. Geronov, B. Puresheva, J. Electrochem. Soc. **128**, 1851 (1981).

[10] W. M. Hedges, D. Pletcher, C. Gosden, J. Electrochem. Soc. **134**, 1334 (1987).

[11] M. Mogensen, J.Power Sources **14**, 123 (1985).

[12] M. Gaberšček, J.Jamnik, S. Pejovnik, J.Power Sources **25**, 123 (1989).

[13] E. Peled, in J.-P. Gabano (ed.), Lithium Batteries, Academic Press, New York, 1983, p. 43.

Materials Science Forum Vols. 185-188 (1995) pp. 687-692

The nature of passive films on thallium anodes in basic solutions

O.A. Petrii, G.A. Tsirlina and S. Yu. Vassiliev

Chemical Faculty, Moscow University, V-234, GSP-3, Moscow, 119889, Russia

Keywords: Thallium, passive films, basic solutions

Abstract Passivation of thallium anodes in 1 - 10 M KOH solutions was studied in potentiodynamic and potentiostatic conditions. Special attention was payed to the stationary polarization behaviour. Chronoamperometric and voltammetric data on the reduction of passive films are also presented and X-ray diffractometric results are used to discuss the film composition. The existence of a mixed-valence thallium oxide in the passive film is supposed.

Thallium anode passivity in bases had been found as early as at the beginning of the century [1, 2] in connection with attempts to develop thallium batteries. However, high and almost pH-independent rate of the thallium active dissolution makes it impossible to observe passive regions on thallium anodic polarization curves at base concentrations lower than 1 - 2 M [3 - 8]. Solubility of thallium (I) salts is lower than that of TlOH, hence the salt passivity always takes place in the presence of a supporting electrolyte [2, 4, 6]. Formation of oxide-hydroxide passive layers in concentrated bases was described [2, 4, 9-11], particularly two passive regions were observed in potential intervals of thallium (I) and thallium (III) stability, respectively [9-11].

In accordance with [10], Tl_2O and Tl_2O_3 films were formed in the above mentioned passive regions. More detailed investigation [9] with the use of both electrochemical, resistivity and X-ray diffraction measurements demonstrated a complex multilayer character of these films with the composition greatly dependent on the stationarity degree of passivation conditions. The formation of an intermediate differing from all known thallium oxides and hydroxides in the course of the partial reduction of the film corresponding to the second passive region was proposed in [9]. The existence of ohmic drops in passive films on thallium was also pointed out in this work. The purpose of the present work was to investigate in detail the difference between thallium anode passivation in bases under stationary and non-stationary conditions and to compare the nature of oxide phases growing on thallium metal with phases electrodeposited on foreign substrates from thallium(I) solutions, particularly, recently found unusual phases [12-14].

Experimental. A thallium 99.999 wire of 3 mm diameter was pressed into a PTFE tube. Before experiments, the surface was mechanically polished and washed with bidistilled water. Ohmic losses were corrected, if necessary, according to [15].

Potentials **E** were measured in relation to saturated calomel electrode (*sce*). A three-electrode PTFE-cell with divided compartments and a Pt counter electrode was used. Solutions prepared from electrolytically pure KOH and bidistilled water were deaerated by oxygen-free argon before experiments.

Potentiometric experiments under open-circuit conditions were carried out in a glass cell with a rotating (~1000 min^{-1}) thallium electrode. Before the measurements, KOH solution with the

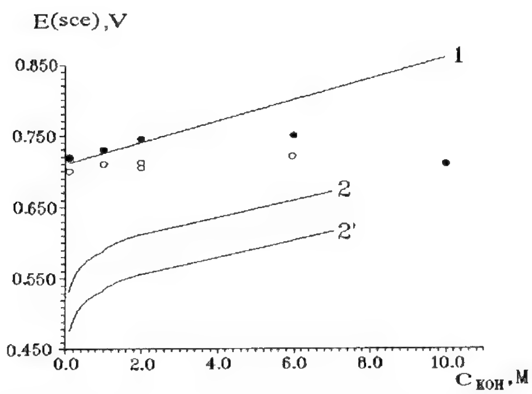

Fig. 1. Theoretical reversible potentials vs KOH concentration for redox systems Tl/Tl(I)(1) and Tl/solid TlOH(2,2') (according to [16](1,2) and [17](2')).Points — experimental $\mathbf{E_s}$ values under stirring (dark) and on stationary electrode (bright).

additives of 1 mM Tl_2SO_4 (twice recrystallized) were deaerated in the separate vessel and then it was forced over to the deaerated working electrode compartment by argon flow.

Results and discussion. When a fresh thallium electrode surface is brought into contact with a Tl -containing solution with pH 11-12 (or lower), the stationary potential value $\mathbf{E_s}$ with the accuracy ±10 mV is equal to the reversible potential of the Tl/Tl^+ redox system [16]. At higher pH, $\mathbf{E_s}$ shifts in the positive direction. One should bear in mind that in alkaline medium two other redox systems can be realized — Tl/non-dissociated TlOH and $Tl/[Tl(OH)_2]^-$ [17] (in [16] the second system was not discussed, and the first one was claimed to be essential only at pH > 14.5). For thorough calculations of the dependencies of reversible potentials on KOH concentration (Fig. 1, curve 1) we used data on hydroxocomplex stability [18]. However, it is important, that the kinetics of Tl^+-OH^--association is practically unknown, and in real systems the deviations from curve 1 are possible due to the slow complexation.

$\mathbf{E_s}$ values in 0.1 - 2 M KOH solutions coincide with calculated values (Fig. 1, curve 1) only after a short-time stirring of solution (Fig. 1, dark points). Before stirring $\mathbf{E_s}$ are more positive than reversible potentials (Fig. 1, bright points), and after interruption of stirring $\mathbf{E_s}$ begins to shift slowly in the positive direction. It should be noted that in all conditions $\mathbf{E_s}$ values remain more negative in comparison with reversible potentials of Tl/solid TlOH(Fig. 1, curves 2, 2' - calculated from data of [16] and [17] respectively). If the KOH concentration exceeds 2 M, $\mathbf{E_s}$ values always fall into the interval between curves 1 and 2(2'), independently of stirring rate and duration.

These results can be interpreted under the assumption that at the open circuit a TlOH non-continuous film is formed in the near-electrode layer, and the nature of the cathodic process taking part in the formation of stationary potential changes (reduction of solid TlOH instead of O_2 reduction). As the pH increases, the quantity of TlOH also increases and its mechanical removal from the surface becomes more difficult.

The anodic potential sweep in comparatively dilute (< 2 M) solutions could be realized only in a narrow region (150-250 mV) and produced a sharp current rise corresponding to the active dissolution (see [8] for details). Passivation in these solutions manifested itself only in a gradual Tafel-slope decrease.

In more concentrated solutions the Tafel region on cyclic voltammograms was 20 - 30 mV wide in the vicinity of $\mathbf{E_s}$, and a current maximum and a wide region of passivity were observed. The second current peak appeared at potentials 0.1 V or even more positive as compared with the reversible potential of $TlOH/Tl_2O_3$ redox system. The position of both peaks strongly depended on the scan rate (Fig. 2). The reduction of films at the cathodic sweep demonstrated two peaks at potentials where thallium(I) oxide and hydroxide are thermodynamically stable and the wave of reduction of thallium(I) to metal.

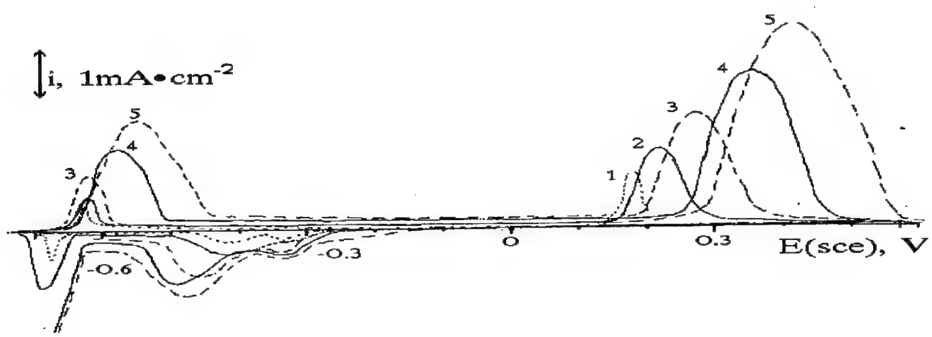

Fig. 2. Cyclic voltammogrames of thallium in 10M KOH; scan rates 0.04 (1), 0.2 (2), 0.4 (3), 1 (4), 2 (5) $V \cdot min^{-1}$.

The voltammogram discribed above differs from that given in [9]. First of all, current rise corresponding to the second maximum is observed at potentials 0.4 V more negative than in [9] where this rise was associated with oxygen evolution. Another point is the form of the passive region - the step was observed in [9], which appeared in several experiments, but was not reproducible. We also registered oscillations of current in the vicinity of the step mentioned in [9], the effect was more pronounced in 2.4 and 4 M solutions and was practically absent in 6 - 10 M KOH. Finally, the non-homogeneity of a thallium (III)-containing passive film in our experiments is evident directly from electrochemical data (bifurcation of cathodic peak), while in [9] it was found out only by diffractometry.

The instability of the anodic polarization behaviour of thallium in the region of the first maximum and at the beginning of the passive region is due to sporadic deposition of a loose layer of TlOH from the supersaturated solution layer near the electrode surface. Under certain conditions, one can visually observe the appearance of a light-yellow or white cloudiness in solution. The pronounced shifts of maxima with increase of the scanning rate (Fig. 2) can be explained by the rise of the ohmic drop when the quantity of insulating TlOH on the surface increases. The removal of TlOH rapidly forming in the process of active dissolution strongly depends on the supersaturation conditions and natural convection characteristics (both factors change with KOH concentration), to say nothing of the scanning rate; therefore, the cyclic voltammetry prooves to be a low-informative technique for studying thallium passivity.

Potentiostatic anodic polarization measurements were fulfilled with the use of an automatically controlled device [19]. The program governing the experiment shifted the potential to the next step after reaching the current value equal to the previous one with a given accuracy expressed by the value of the stationarity criterion (SC), $\% \cdot min^{-1}$(see [19] for details). The SC decrease led to the increase of the passivation in the wide potential region. In 10 M solution the first current peak disappeared, and the second one was observed only at high SC (Fig. 3a). But if repeatative measurements were fulfilled in the same solution, an increase of the second peak was observed (Fig. 4). It should be noted that in the whole potential range investigated the current growth was also observed due to the roughening of the surface, but at $-0.1 < \mathbf{E} < 0.1$ V this growth was essentially higher. Data of Fig. 4 illustrate the accumulation of thallium(I) in solution. We assume that the absence of a sharp current decrease at $\mathbf{E} > 0$ V in the forth cycle (Fig. 4, curve 4) corresponds to a sufficiently high thallium (I) concentration, which does not change strongly after the Tl_2O_3 film formation.

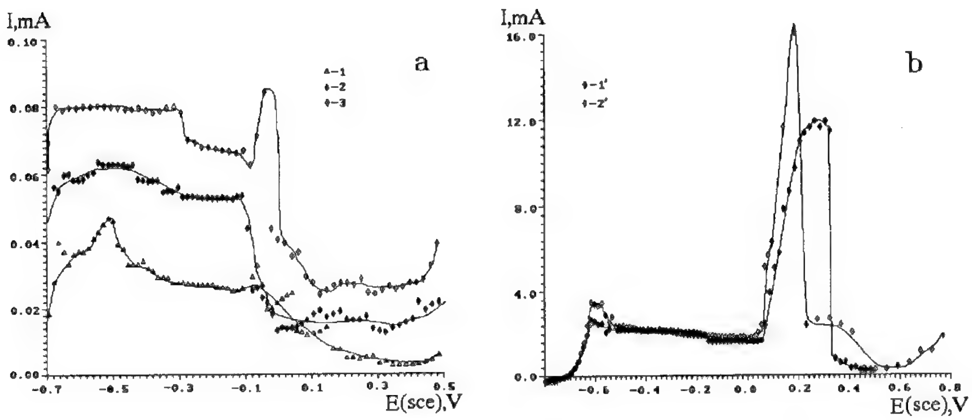

Fig. 3. Potentiostatic polarization curves of a thallium anode in 10(a) and 2.4(b) M KOH measured with SC 1(1,1'), 5(2,2'), and 10(3) % · min^{-1}.

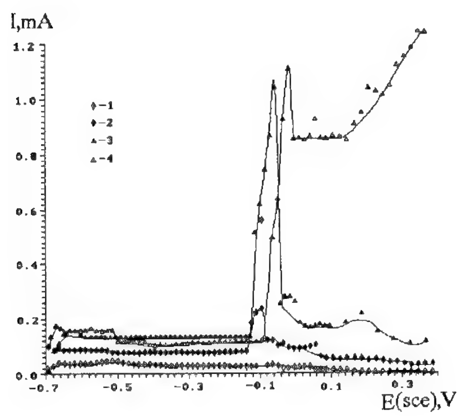

Fig. 4. Stationary polarization curves of a thallium anode in 10M KOH (SC=1% · min^{-1}) measured in subsequent cycles (from 1 to 4).

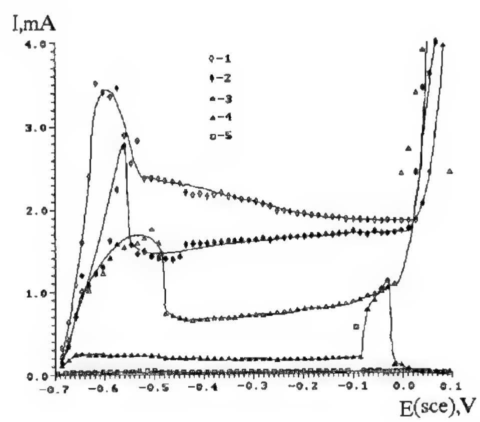

Fig. 5. Stationary polarization curves of a thallium anode (SC=1% · min^{-1}) measured in 2.4(1), 4(2), 5.5(3), 7(4), 10(5) M KOH solutions.

It is significant that the second peak under stationary conditions shifts directly to the TlOH/Tl_2O_3 reversible potential corresponding to high TlOH concentration. In the potentiodynamic regime, in the wide range of scan rates, this peak was observed at more positive potentials. It seems possible that under stationary conditions the removal of TlOH is more effective, and the problems with supersaturation and the formation of an insulating solid TlOH are diminished, i. e. the corresponding ohmic drop becomes smaller. On the other hand, the accumulation of thallium(I) in slow measurements can produce higher concentrations and, therefore, more negative reversible potentials for thallium (I/III) redox systems.

The main tendencies of the influence of KOH concentration on the anodic behaviour of thallium are the rise of currents throughout the region investigated and the shift of the second maximum towards more positive potentials with the dilution (Fig. 5, data for the first cycles in each

solution). The last fact is in agreement with pH-dependence of thallium(I/III) redox potentials. The second passive region was observed for all concentrations, but passivation potentials were strongly dependent on SC (see Fig. 3b for example).

Under stationary conditions no cathodic currents were observed on the reverse (negative) course of the curve up to $\mathbf{E_s}$. The series of chronoamperometric experiments was carried out on the reduction of films grown potentiostatically in the first and second passive regions. The last films when reduced at the potentials of the first passive region produced non-stationary cathodic currents with a simultaneous change in the film colour from black to light-gray. At $\mathbf{E} < \mathbf{E_s}$ the chronoamperograms of complex form were observed, and the change of colour corresponding to the reduction of thallium(III) took place immediately (the charge for its reduction was only few % of total reduction charge). These experiments are not informative enough because the reduction of thallium(I) from solution at $\mathbf{E} < \mathbf{E_s}$ and the thallium dissolution at $\mathbf{E} > \mathbf{E_s}$ give a large contribution to the current.

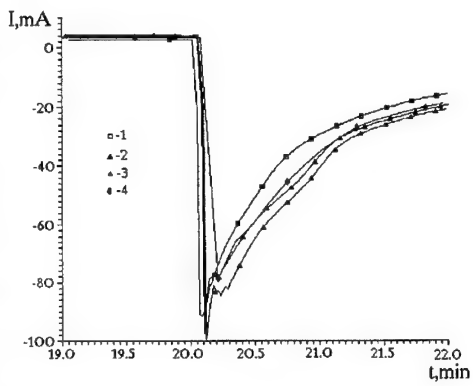

Fig. 6. Chronoamperograms measured at E=-0.78V immediately after polarization at E=0.10V (1) and after partial reduction at E=-0.40V (2-4, obtained in subsequent cycles).

Reduction at $\mathbf{E} < \mathbf{E_s}$ of the films grown in the first passive region gives a chronoamperogram with one maximum (Fig. 6, curve 1). If we form the film in the second passive region and partially reduce it at $\mathbf{E} > \mathbf{E_s}$ (up to the onset of positive currents), further reduction at $\mathbf{E} < \mathbf{E_s}$ produces the curves with two waves (or maxima), the second one increasing in the subsequent cycles (Fig. 6, curves 2-4).

X-ray analysis of the films formed in the first passive region show the presence of TlOH and Tl_2O phases (data of [20] were used as the standards). Films corresponding to the second passive region consist predominantly of Tl_2O_3, though traces of TlOH and Tl_2O are also observed. The same films after partial reduction (see previous paragraph) include not only Tl_2O, but also the second phase with X-ray characteristics identical to those of the mixed-valence oxide obtained previously by us [14].

Conclusions. Passivity phenomena (both adsorption and phase mechanisms) are studied preferentially for transition metals, whereas the corrosion behaviour of comparatively active sp-metals is preferentially known in the region of active dissolution. The last group of metals has a tendency to phase (salt or oxide-hydroxide) passivation inducing the comparatively low reproducibility of the passivation potential.

Thallium passivity in bases is very specific and shows practically no features similar with passivity of other IIIb-group elements (Al, In, Ga). The latter have no stable monovalent states in aqueous media and form non-continuous threevalent oxide-hydroxide layers at potentials close to $\mathbf{E_s}$. Moreover, it is difficult to find direct analogies with any other metal. The main feature of the first passive layer on thallium is that it is formed as a result of the solution supersaturation, and the second passive region is induced by the oxidation of the dissolution product in solution. These features are partly similar to those of copper passivity [19], but semiconducting copper oxide films

reduce sharply the rate of anodic processes even when their thickness is several nanometers, and thallium oxide films are considerably thicker.

Poorly studied bismuth and lead passivity is, probably, closest related phenomenon: two types of phase oxides can be formed on these metals in bases with respectively similar electric properties. But the stability of hydroxocomplexes for the elements mentioned is higher than that of thallium, and in concentrated bases the active dissolution with the formation of high-valency hydroxocomplexes can play a significant role.

It is interesting to recall that with respect to the active dissolution thallium shows strong similarity with alkali metals. Hence, the corrosion behaviour of this element, as well as its other numerous chemical and electrochemical features, is quite anomalous.

The work was financially supported by Russian Fond of fundamental Investigations, project no. 93–03–18053.

References

1. L. Jonas, Z. Elektrochem., **9**, 523(1903).
2. W. J. Muller-Mulhausen, Z. Elektrochem., **15**, 696(1909).
3. R. Piontelli, G. Poli, Gazz. Chim. Ital., **79**, 642(1949).
4. W. Popp, Electrochim. Acta, **8**, 361(1963).
5. M. E. Straumanis, R. C. Martin, Corr. Sci., **5**, 765(1965).
6. W. Jumes, P. J. Aragon, J. M. Johnson, J. Less Common Met., **22**, 341(1970).
7. P. C. A. Bailey, G. A. Wright, Electrochim. Acta., **16**, 865(1971).
8. S. Yu. Vassiliev, G. A. Tsirlina, O. A. Petrii, Elektrokhimiya, **31**, no. 2 (1995).
9. E. Brauer, Werk. und Korr., **21**, 717(1971).
10. F. F. Faizullin, V. A. Makarov, Elektrokhimiya, **7**, 1571(1971).
11. L. Z. Manapova, F. F. Faizullin, S. V. Kuzovenko, Elektrokhimiya, **10**, 289(1974).
12. O. A. Petrii, G. A. Tsirlina, T. V. Rakova, S. Yu. Vassiliev, J. Appl. Electrochem., **23**, 583(1993).
13. G. A. Tsirlina, S. Yu. Vassiliev, A. I. Danilov, O. A. Petrii, Elektrokhimiya, **30**, 134(1994).
14. G. A. Tsirlina, S. Yu. Vassiliev, N. V. Korzakova, O. A. Petrii, Elektrokhimiya, **30**, 185(1994).
15. S. V. Dmitrenko, A. I. Molodov, V. V. Losev, Elektrokhimiya, **17**, 933 (1981).
16. Pourbaux M. Atlas Electrochemical Equilibria in Aqueous Solutions. Pergamon Press, Cebelcor, 1966.
17. Bratsch S. G. //J. Phys. Chem. Ref. Data. **18**, 1(1989).
18. Baes C. F. , Mesmer R. E. The Hydrolisys of Cations. Wiley, NY, 1976, P. 329.
19. S. Yu. Vassiliev, G. A. Tsirlina, O. A. Petrii, Elektrokhimiya, **30**, 783(1994)
20. Powder Diffraction File. Inorganic Phases/ Ed. W. F. McClune, N. Y. : JCPDS, 1989.

Materials Science Forum Vols. 185-188 (1995) pp. 693-702

A theoretical interpretation of dissolution and passivation of titanium in acidic media

A.I. Scherbakov and T.E. Andreeva

Institute of Physical Chemistry of Russian Academy of Science,
Leninsky Prospect 31, Moscow 117915, Russia

Keywords: Titanium, dissolution, passivation, mechanism, hydride, equation of the polarization curve, rate determining step

Keywords: Titanium, dissolution, passivation, mechanism, hydride, equation of the polarization curve, rate determining step.

Abstract A new mechanism of dissolution and passivation of titanium in acidic solutions is suggested. It is based on the Themkin isotherm and hydrogen coverage linear dependence on potential. Taking into account certain experimental data the charge transport is assumed to be a fast step .It follows by the rate detemining step. The rate determining step is supposed to be the transport of titanium from hydride to adsorbed state. For the passivation process it is conceived that the passive layer coverage changes linearly with the potential. It is based on the Themkin isotherm of the passive monolayer adsorption on the titanium electrode. All polarization curves of titanium are described by parabola. Theoretic curves are in a good accordance with the experimental data.

There is no consensus of opinion among authors as to the details of the mechanism of titanium dissolution. There are two general directions in theoretical interpritation of titanium anodic kinetics. The first (E.J.Kelly [1,2]) is based on full description of the entire process by elemental steps. Unfortunately, the obtained equations are rather cumbersome for practical use. A.Caprani and Y.P.Frayret with co-authors [3-5] suggested a more simple model. It can be used for the calculation of rate constants. The model is based on the following scheme:

$$\begin{array}{l} Ti \xrightarrow[k_1^0 \cdot e^{a\varepsilon}]{-3\bar{e}} Ti(III)_{ads} \xrightarrow[k_3]{} Ti(III)_s \\ \qquad\qquad\quad \llcorner \xrightarrow[k_2^0 \cdot e^{b\varepsilon}]{-\bar{e}} Ti(IV)_{ads} \xrightarrow[k_4]{} Ti(IV)_s \end{array} \quad , \qquad (1)$$

where **Ti** is the metal substrate, $\mathbf{Ti(III)_{ads}}$ and $\mathbf{Ti(IV)_{ads}}$ are the adsorbed ter and tetravalent intermediates. $\mathbf{Ti(III)_s}$ and $\mathbf{Ti(IV)_s}$ are the soluble ter and tetravalent species. This model is described by following relationship:

$$I = \frac{F(3k_3 + 4k_2^0 \cdot e^{b\varepsilon})}{1 + \dfrac{k_3}{k_1^0 \cdot e^{a\varepsilon}} + k_2^0 \cdot e^{b\varepsilon}\left(\dfrac{1}{k_1^0 \cdot e^{a\varepsilon}} + \dfrac{1}{k_4}\right)}. \qquad (2)$$

Where **I** is a current. **F** is Faraday constant. ε is a potential. $\mathbf{k_1...k_4}$, **a**, **b** are the constants of chemical and electrochemical steps, respectively.

Eq.2 has six unknown parameters. Using the optimization method our data were calculated . The polarization curves showed a good agreement between the Eq.2 and the data, but obtained constants depended on the initial approximation. The function of the sum of the squares of deviations experimental data from the theoretical curves had many extremums. There were many sets of parameters which minimized this function. It was difficult to find the global extremum because of the rather high errors of experiment.

Moreover there are some important limitations of the model:

1. The mathematical description of the model doesn't take into consideration that the dissolution of titanium proceeds at the surface of hydride, as was shown in [6,7];

2. The model doesn't take into account high overpotential (~1V) of titanium electrode (the equilibrium potential of reaction Ti⇔Ti+3e is -1.2 V [8] and potential of active corrosion changes from -0.4 to -0.2 in acids);

3. The model ignores that the Tafel law is disobeyed for the titanium electrode. Although the appropriate conditions can be selected when it is possible (the rate constants are variously dependent on temperature, potential, environment);

4. The model doesn't take into consideration that apparent activation energy must be a function of temperature. If the process has two or more rate-controlling steps, activation energy can not be expressed by the Arrenius equation. Nevertheless, the Arrenius equation is valid for numerous experiments. Consequently, the active titanium dissolution has only one rate-controlling step;

5. If the electrochemical step is one of rate-controlling steps, the apparent activation energy must strongly depend on potential (~15 kJ at 100 mV). However, our investigations (Fig.1) show that apparent activation energy doesn't change with the potential rising in a wide potential region (from -0.7 to 0.2 V). The rate of titanium dissolution was obtained by photocolorimetric analysis of solutions.

All these limitations are inherent in the E.J.Kelly mechanism too.

Our model is free from the above-described limitation. It is based on the main experimental fact, that the step of charge transfer is not a rate-determining step. It

follows from the Fig.1. Moreover, it can not proceed before the real control step. Even though charge transfer is in equilibrium and precedes the control step, apparent activation energy will include free Gibbs energy of charge transfer as a component and will depend on potential.

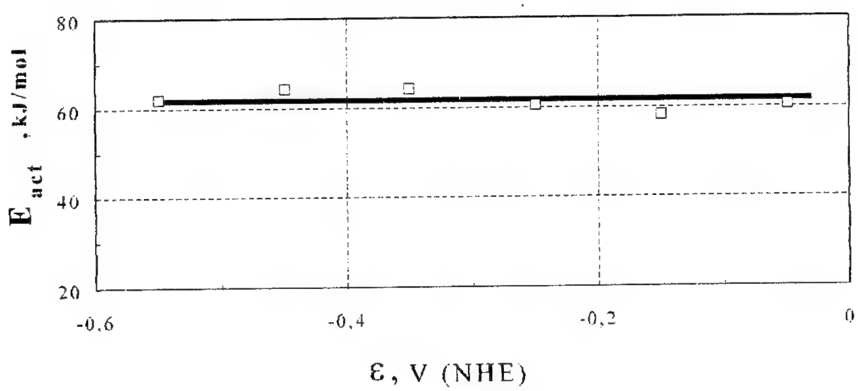

Fig.1. The apparent activation energy of titanium dissolution in 2.5*M* H_2SO_4 vs. potential

The hydride grows by the diffusion law (the diffusion is a control step) [9]. Consequently, the reaction of the hydride formation is in equilibrium. So it can be supposed, that titanium diffusion in hydride is a rate-determining step of the dissolution process. If so, the rate of dissolution would change with time (the hydride thickness changes as a square root of time [9]). However, the real dissolution rate isn't a function of potential [10,11]. Consequently, the diffusion of titanium can't be a rate-determining step. Then, rate-determing step can be only between the steps of titanium diffusion in hydride and charge transfer. Obviously, it is the step of transfer of titanium atoms throw the hydride-solution boundary.

Thus, the rate determining step of titanium dissolution is assumed to be the transfer of titanium atoms from the hydride to adsorbed state. Then, the rate of active dissolution can be described as: $\mathbf{w=kC_{Ti}}$ (in mol/m^{2}c), where **k** is a rate constant (mol/m^{2}c), $\mathbf{C_{Ti}}$ is a titanium concentration in the upper layer of hydride (in mole parts). The **k** isn't a function of the potential, but $\mathbf{w=f(\varepsilon)}$. Consequently, the titanium concentration depends on potential. Obviously, $\mathbf{C_{Ti}=1-C_H}$, where $\mathbf{C_H}$ is a hydrogen concentration in the sourface layer of hydride and proportional to adsorbed hydrogen coverage Θ. Using the Themkin assumption [12] that Θ is proportional to the adsorption energy, we can write in our case: $\mathbf{\Theta=Constant+a'\varepsilon}$. Because Θ is proportional to $\mathbf{C_H}$ and $\mathbf{C_{Ti}}$ the latter can be expressed as:

$$C_{Ti}=C_o+a(\varepsilon-\varepsilon_o), \qquad (3)$$

where **a** is a constant, ε_o is a potential, when hydride is saturated with hydrogen, C_o is a concentration of titanium under this condition. The data [13,14] corroborate the existence of the saturated hydride on the titanium surface. According to these data, the hydride growth rate increases with increasing cathodic polarization. When some polarization (5-10 mA/cm^2) is reached, the hydride growth rate is constant. Due to the diffusion law, the surface concentration of diffusing component is also constant.

So it can be written for the current of active titanium dissolution:

$$i_a=nFkC_{Ti}=nFk[C_o+a(\varepsilon-\varepsilon_o)]. \qquad (4)$$

Consequently, the current varies linearly with the potential in the active region. It should be noted that condition of the Themkin isotherm holds for the coverage up to 0.8. Obviously, this value corresponds to C_o and ε_o . It should be expected that the equation will begin to depart from linearity for the highest coverage.

In order to explain the titanium passivation, we divide the polarization curve in 4 parts (current density correspondes the rate of titanium dissolution on Fig.2).

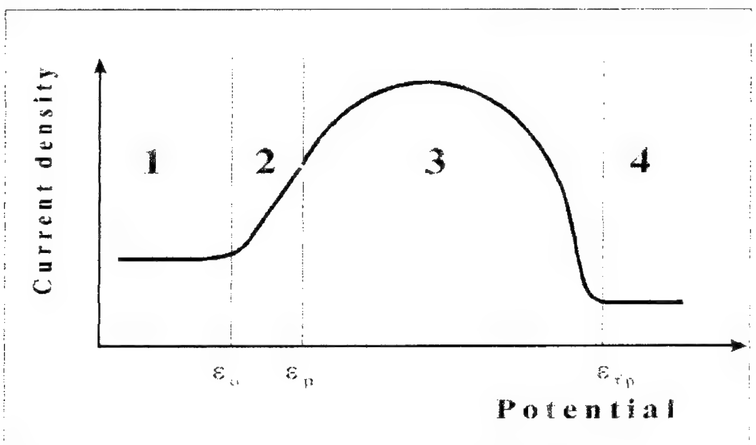

Fig.2. A schematic titanium polarisation curve.

The first one is the dissolution of titanium from the saturated hydride. The rate of dissolution is constant and almost independs on potential. The second one is the active dissolution (as described above). The rate changes linearly with the potential. The third one is deviation from a linear dependence because of passivation. The 4 is the region of full passivity.

Taking into account the monolayer mechanism of passivation and the Themkin isotherm, **N** is taken as active part of surface. (**1-N**) is the passive surface. The current is the sum of currents from active and passive parts:

$$\mathbf{I = i_a N + i_{fp}(1-N),} \qquad (5)$$

where $\mathbf{i_a}$ and $\mathbf{i_{fp}}$ are active and passive current densities, respectively. Considering that N changes linearly with potential we obtain:

$\mathbf{N=(\varepsilon-\varepsilon_{fp})/(\varepsilon_{fp}-\varepsilon_p)}$ and $\mathbf{1-N=(\varepsilon_p-\varepsilon)/(\varepsilon_{fp}-\varepsilon_p)}$,

where ε is the current potential, ε_p is the potential of the beginning of passivation and ε_{fp} is the potential of the full passivation. Then the common equation for the 3-d part is:

$$\mathbf{i=nFk[C_o + a(\varepsilon-\varepsilon_o)](\varepsilon-\varepsilon_{fp})/(\varepsilon_{fp} -\varepsilon_p) + i_{fp}(\varepsilon_p -\varepsilon)/(\varepsilon_{fp} -\varepsilon_p).} \quad (6)$$

Thus, we have a parabolic dependence. Eq.6 can be rewritten as:

$$\mathbf{i= A\varepsilon^2 +B\varepsilon+C,} \qquad \mathbf{(7)}$$

where $\mathbf{A= -nFka/(\varepsilon_{fp} -\varepsilon_p)}$,

$\mathbf{B=-nFk(C_o-a\varepsilon_{fp}-a\varepsilon_p -i_{fp}/nFk)/(\varepsilon_{fp} -\varepsilon_p)}$,

$\mathbf{C=-(nFka\varepsilon_p\varepsilon_o -nFk\varepsilon_{fp}C_o +i_{fp}\varepsilon_p)/(\varepsilon_{fp} -\varepsilon_p).}$

The coefficients **A**,**B**,**C** can be easily calculated by regression analysis of the stationary polarization curve. If $\mathbf{di/d\varepsilon=0}$ we can express maximum of the current ($\mathbf{i_m}$) and the respective potential (ε_m):

$$\mathbf{i_m =-B^2/4A+C} \qquad (8)$$

$$\mathbf{\varepsilon_m=-B/2A=-C_o/2a+\varepsilon_{fp}/2+\varepsilon_p/2+i_{fp}/nFka\ .} \qquad (9)$$

The parabola is symmetric about the ε_m. Consequently, if $\mathbf{i_{fp}}$ is less than current of the free corrosion (this is no question that it's so), then ε_p is less than the potential of free corrosion. From this, the linear part can't be found in the experimental polarization curve. Thus, entire polarization curve is described by only parabola from corrosion potential to full passivation potential . As a result, it can be detected, that polarization curves are symmetric in all famous works on the titanium electrochemistry.

In order to check the equations we obtained stationary potentiostatic polarization curves of titanium in acidic solutions. After obtaining, in open circuit, a stationary potential value, the stationary current-potential curve is plotted point by point going towards the increasing anodic potential. The electrolytes were thermostated and deoxigenated by pure argon bubbling.

The calculated current-voltage characteristic and the experimental curve in 2.5*M* H_2SO_4 are in a good agreement (Fig.3). We had a good agreement also in sulfate and chloride solutions in large regions of temperatures and pH.

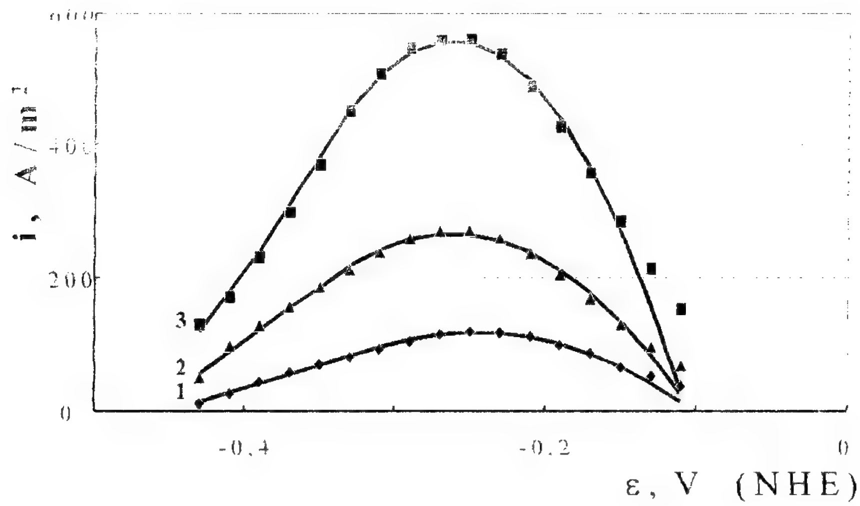

Fig.3. The experimental (symbols) and calculated (lines) stationary polarisation curves of Ti in 2.5M H_2SO_4 (1- 50°C; 2- 60°C; 3- 70°C).

Passive current is taken to be zero. Using the parabola symmetry, we supposed, that the parabola intersects the axis at the points ε_p and ε_{fp}.The calculated parameters of Eqs.6-9 under this assumption are presented in Table 1.

According to Table 1, ε_m,ε_{fp},ε_p remain virtually constant. On the contrary, **A**, **B**,**C** strongly depend on the temperature. Consequently, the **ka** strongly depends on the temperature too. This product is used, because the individual value **k** can not be calculated from the parabola parameters. This constant can be obtained from the independent data on the titanium dissolution rate, when the potential is less than ε_o.

Table 1.

The parameters of Eqs. 6-9 under various temperatures.

Temperature,°C	30	40	50	60	70
A, $Am^{-2}V^{-2}$	-910	-2200	-5600	-10300	-22800
B, $Am^{-2}V^{-1}$	-450	-1080	-2760	-5420	-11980
C, Am^{-2}	-36.9	-87.4	-222	-444	-1010
ε_m, V (NHE)	-0,247	-0,250	-0,246	-0,261	-0,262
ε_{fp}, V (NHE)	-0,105	-0,102	-0,101	-0,102	-0,106
ε_p, V (NHE)	-0,390	-0,398	-0,391	-0,422	-0,418
$\mathbf{i}_m$, Am^{-2}	18,5	47,3	118,3	265	558
ka,$molm^{-2}s^{-1}V^{-1}$	0,894	2,21	5,63	11,4	24,7

The apparent activation energy of the process (71.6 kJ/mol) was calculated from the temperature dependence of **ka** (Fig.4). Obviously, the apparent activation energy includes Gibbs free energy of the penetration of hydrogen trough the boundary and the energy of hydride formation (because of the existence of **a** in the product) in addition to activation energy of the rate determining step.

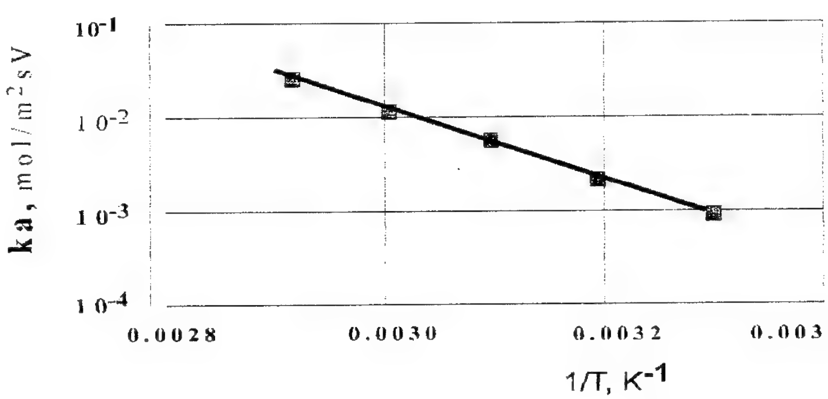

Fig.4. The product of the rate constant **k** into **a** vs. 1/T (Ti in 2.5M H_2SO_4).

In the paper [14] the dependence of titanium dissolution rate on pH was founde. It was shown[14] that the reaction order with respect to H_3O^+ is 0.5 in the sulfuric solution at the pH from 0.25 to 2. We carryed out measurements at the pH from -0.4 to 0.4 in the mixed electrolytes H_2SO_4+Na_2SO_4 at a constant sulfate-ion concentration (3.5M). The reaction order is very close to 2 (Fig.5). A decrease in the

reaction order at the highest pH is assumed to be connected with transition from the monolayer passivation to phase passivation.

As the **a** values is independent of pH a reaction order of 2 is only determined by the rate constant. Consequently, the rate determining step includes the interaction of titanium with two ions of hydroxonium when titanium passes to the adsorbed

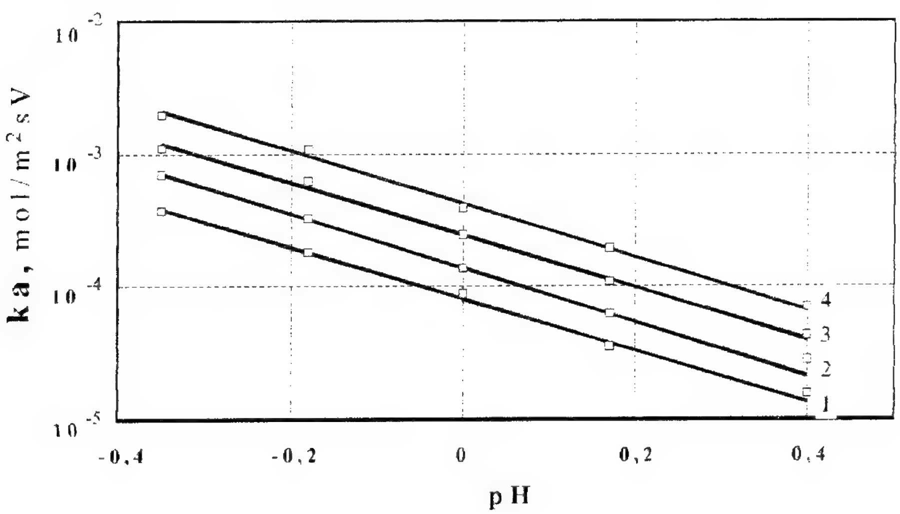

Fig.5. The product of the rate constant **k** into **a** vs. pH. Ti in 2.5*M* H_2SO_4: 50 °C (1), 60 °C (2), 70 °C (3), 80 °C (4).

state. Then, we can express two-steps process as

$$Ti_{hydr} + 2H_3O^+ \xrightarrow{k} [Ti(H_3O^+)_2]_{ads} \xrightarrow{-3\bar{e}} Ti^{3+}_{sol} + 2H_3O^+ .$$

where the first step is rate determining, and the second one is an equilibrium step.

Thus the main rate determining step is expressed by the kinetic equation $\mathbf{w = kC_{Ti}C^2_{H^+}}$ and consequently, the Eqs.4 and 6 should be corrected accordingly.

REFERENCES

[1] E.J. Kelly, in "Modern Aspects of Electrochemistry". Vol. 14, J.O'M . Bockris, B.E. Conway and R.E. White, Editors, New York ; 319 (1982) .

[2] E.J. Kelly, J. Electrochem. Soc. **126**, 2064 (1979).

[3] A. Caprani and Y.P. Frayret, Electrochim. Acta **24,** 835 (1979).

[4] Y.P. Frayret, A. Caprani , H. Luc and F. Priem , Corrosion **40,** 14 (1984).

[5] Y.P. Frayret and A. Caprani , Electrochim. Acta **26 ,** 1789 (1981).

[6] I.Ogawa and D.I. Watanabe , J. Japan Inst.Metals **18,** 523 (1954).

[7] A.M. Sukhotin and L.I. Tungusova . Zaschita metallov **4,** 8 (1968).

[8] M. Pourbaix . Atlas d'equilibres electrochimiqes (25^{o}C). Paris, Gauthier-Villars, (1968).

[9] N.D.Tomashov , V.N. Modestova, S.T. Glasunov, E.A. Borisova and V.L.Zotov, "Corrosion of Metalls and Alloys, Coll. No 1", N.D.Tomashov, Editor, p.196, N.L.L.S.T., Boston Spa, West Yorkshire, England (1964).

[10] A.I. Scherbakov, V.N.Dorofeeva, G.M.Plavnik and T.P.Puryaeva , Zaschita Metallov **28,** 364, (1992).

[11] A.I.Scherbakov, I.V. Kasatkina , N.D.Tomashov et al, Zaschita Metallov **28**, 559 (1992).

[12] M.I.Themkin , Russ. J. Phys. Chem. **15**, 296 (1941).

[13] N.D.Tomashov , V.N. Modestova, A.S.Anatol'eva , "Corrosion of Metalls and Alloys, Coll. No 1", N.D.Tomashov, Editor, p.207, N.L.L.S.T., Boston Spa, West Yorkshire, England (1964).

[14] G.N.Trusov, E.P. Gochalieva and M.F.Fandeeva , Sov. Elektrochem. **10**, 1507 (1974).

[15] N.T. Thomas and K. Nobe, J. Electrochem. Soc. **119**, 1450 (1972).

Materials Science Forum Vols. 185-188 (1995) pp. 703-712

In situ measurements of oxygen consumption and hydrogen evolution in corrosion of some metals in liquid water

L. Gråsjö[1], G. Hultquist[1,2], Q. Lu[2] and M. Seo[3]

[1] Division of Physical Chemistry, Dept. of Chemistry, Royal Institute of Technology, S-100 44 Stockholm, Sweden

[2] Division of Corrosion Science, Dept. of Materials Science, Royal Institute of Technology, S-100 44 Stockholm, Sweden

[3] Lab. Electrochemistry and Corrosion Science, Faculty of Engineering, Hokkaido University, Sapporo 060, Japan

Keywords: Aqueous corrosion, *in situ* gas analysis, oxygen consumption, hydrogen evolution, film composition, oxygen content, hydrogen content

Abstract

Mass spectrometry has been used in a virtually closed reaction chamber in continous monitoring of O_2 and H_2 concentration in the gas phase above water where different metals are immersed. The measured changes in gas composition are entirely due to corrosion of the immersed metal since the background interference is negligible. The mass spectrometer is placed in an ultra high vacuum (UHV) environment and the reaction chamber is UHV compatible. Provided the corrosion is accompanied by oxygen consumption and/or hydrogen evolution corrosion rates less than 100 Å/year can then be monitored.
The apparatus is described and results from reactions of Al, Cu, Fe, Zn, and SS 316 in pure water are presented. By combining measurements of weight increase of solid reaction product and oxygen consumption together with hydrogen evolution, determination of the hydrogen-to-oxygen ratio, z/y, in the solid reaction product $Me_xO_yH_z$, is possible. The role of O_2 is discussed as well as hydrogen uptake in the solid reaction products.

Introduction

It is well established that many metals react both with dry oxygen and with pure water vapour. Often these studies deal with characterisation of composition, microstructure and transport properties in the oxide film [1]. In mixtures of O_2 and H_2O gases, and in aqueous corrosion with water in contact with air, we should consider various reaction routes. However, extensive studies of hydrogen-containing corrosion products are still lacking [2]. The usually powerful surface analytical methods, X-ray Photoelectron Spectroscopy, (XPS), Auger Electron Spectroscopy, (AES), etc., are unable to detect hydrogen explicitly. Moreover, ultra high vacuum (UHV) may reduce the eventual water content in the oxide, thus making the analysis refer to an altered oxide. The problem with detection of hydrogen was treated recently, using *in situ* Secondary Ion Mass Spectrometry (*in situ* SIMS) [3,4].

A method for gas analysis has been developed to perform studies of oxidation, corrosion and catalysis of different materials in $H_2/H_2O/O_2$ gas mixtures, ranging from 1-1000 mbar and at moderate temperatures. Results from reaction of Cu and Fe in $H_2{}^{16}O/H_2{}^{18}O/O_2$ gas mixtures at 160-400°C gave that the metals mainly reacted with water [5,6,7]. Oxygen, O_2, was mainly consumed in reaction with H/H_2 on the metal surface.

In this work we studied the reaction of Al, Cu, Fe, Zn and a stainless steel, SS316 in liquid water with low and normal O_2 content. We will discuss the role of O_2 as well as hydrogen uptake in the metal and the oxide.

Experimental

The apparatus used in this study to monitor changes of gases during reaction of metals is shown schematically in Fig. 1. The detection, both qualitative and quantitative, takes place in the mass spectrometer placed in ultra high vacuum (UHV), with a base pressure ~2 $\cdot 10^{-10}$ mbar. For probing of the gases from the reaction chamber, the gases are lead via a leak valve, through a quartz tube directly into the ionization region of the mass spectrometer. At 5 $\cdot 10^{-7}$ mbar, which is a typical inlet in this study, the consumption of gas from the reaction chamber is ~5 $\cdot 10^{-7}$mol/100 h. Gas volumes range from 3-20 cm^3. The reaction chamber has an O_2 consumption/H_2 production rate less than 10^{-8}mol/100 h, and can hence be considered virtually closed with respect to consumption and relese of gases due to processes other than the reaction under study. The transformation of the spectrometer signals to pressures was facilitated by calibration with the respective gases.
Samples of Al (99.999%), Cu (99.996%), Fe (99.7%), Zn (99.99%) and SS 316 were 0.1 mm thick foils ground with 1200 mesh SiC paper, and cleaned ultrasonically in 99.5% ethanol, before immersion in pure water. Water volumes were 10-20 cm^3. Weight gain measurements of Al and Fe were performed after respective exposure in water by using a balance. Excess water was removed in air at room temperature. The accuracy in the measurement was estimated to be better than ± 0.05 mg.

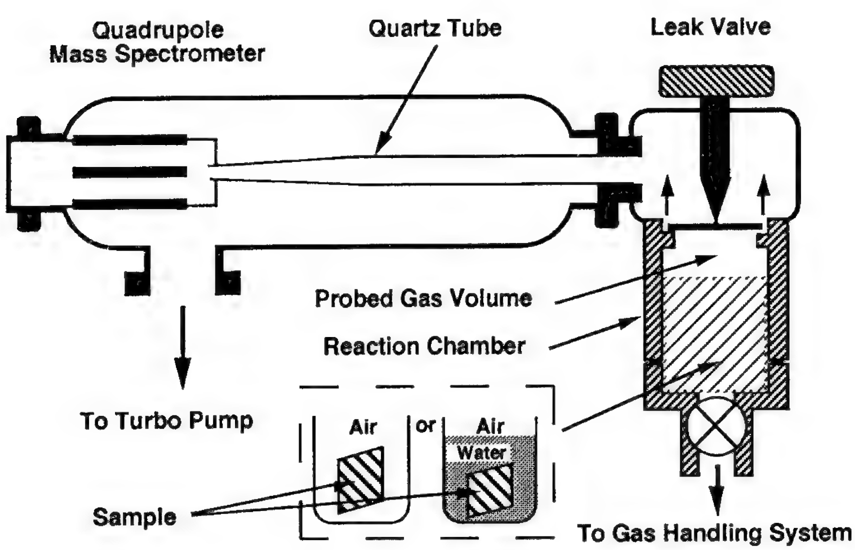

Figure 1. Apparatus used for *in situ* monitoring of the gas phase during aqueous corrosion.

Calculation of Hydrogen and Oxygen Uptake in the Reaction Product

In the present study where H_2 and O_2 gases are measured during reaction with metals, also weight gains have been determined. Since the weight measurement must wait until the experiment is interrupted, the result represents an average of the total reaction product. A combination of weight change and consumption and release of gases enables the hydrogen-to-oxygen ratio, z/y, in $Me_xO_yH_z$ to be calculated. We denote the experimentally obtained parameters :

- ***a*** [g], the weight gain due to reaction
- ***b*** [mol H_2], the amount of hydrogen gas formed during reaction
- ***c*** [mol O_2], the amount of oxygen gas consumed during reaction

The equations needed to be solved are obtained from mass and material balances [8]. The first equation relates the weight gain, ***a***, to the content of hydrogen, ***z***, and the oxygen, ***y***, in the reaction product.

$$a = 16y + z \qquad (1)$$

where ***a*** is in [g] while ***y*** and ***z*** are in [mol]. The factor 16 is the atomic mass of oxygen. The amount of oxygen in the product is:

$$y = b + \frac{z}{2} + 2c \qquad (2)$$

From equation (1) and (2) we get:

$$\frac{z}{y} = \frac{2a - 32b - 64c}{a + 2b + 4c} \qquad (3)$$

Table 1 shows the results of the calculation for Al.

Table 1. Calculation of z/y for corrosion products on Al formed in water.

O_2 pressure [atm]	***a*** [mg]	***b*** [mmol H_2]	***c*** [mmol O_2]	*z/y*
0.001	1	.01225	.000937	1.51
0.21	22	.234	.00593	1.61
0.21	29	.278	.00593	1.65

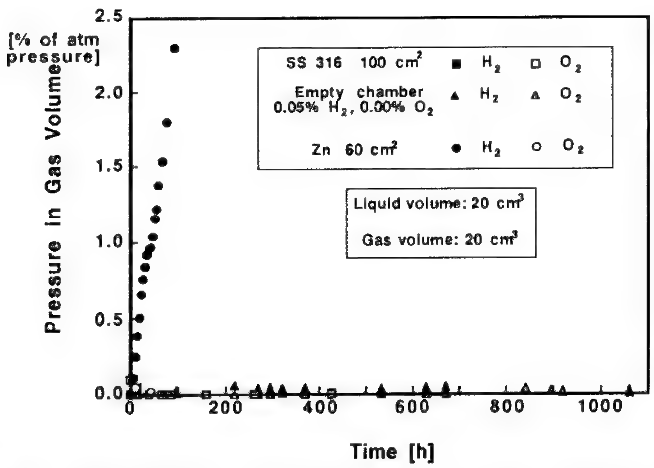

Figure 2. Composition of gases, H_2 and O_2, in gas volume during corrosion of Zn, SS 316 and "empty chamber". Deaerated solution.

Results and Discussion

Fig. 2 shows experimental results obtained for a stainless steel, SS316, Zn and the empty reaction chamber containing only 0.05 % H_2, 78 % N_2 and liquid water. Zn is included in this figure to clearly show the difference between the measurable rates and those rates considered negligible in this study. In the case of SS316 the oxygen consumption and hydrogen production is negligible compared to other metals, as can be seen in Fig. 2 where all the data for SS316 is found on the base line in the diagram. This is of course in full agreement with the fact that stainless steels are passivated, thus having a negligible corrosion rate upon immersion in pure water.

Fig.3a. shows the course of the oxygen pressure above the solution, with and without metals immersed. The "no metal" blank experiment shows how much O_2 is present in the water at start of each experiment. The increase of O_2 for "no metal" is due to equilibration of O_2 between liquid and gas after removal of O_2 from the gas phase at zero time of immersion. As clearly seen in Fig. 3a initially all the metals, Al, Fe and Zn consume the O_2 present. Fig. 3b shows the hydrogen production under the essentially oxygen free conditions described above. For Fe and Zn the corrosion proceeds at a fairly constant rate, as measured from the H_2 production. The rates, 2.2 ng H_2/cm^{2}h for Fe and 8 ng H_2/cm^{2}h for Zn is similar to results in an earlier study [9]. The constant rate is a consequence of that the product is not protective. Fe does not dissolve to the same extent as Zn, but under essentially dearated conditions the corrosion product is not tightly bound to the substrate and easily falls off. The situation for Al is quite different, and it is known that the dissolution of metal is negligible [10]. After passing an initial time period, the H_2 production rate starts to accelerate, and it increases at least a factor 100. Table 1 shows calculations of hydrogen-to-oxygen ratios, z/y, in the corrosion product, $Al_xO_yH_z$. This ratio is seen to vary between 1.5 and 1.65. Compared to AlO(OH) or $Al(OH)_3$, this is a more hydrogen rich compound. Since the calculation at this stage is a calculation of the total hydrogen and oxygen content in the "metal+film",

we cannot distinguish between hydrogen in the film and hydrogen in the bulk metal. It is hence quite possible the increased rate is due to hydrogen in the metal lattice.

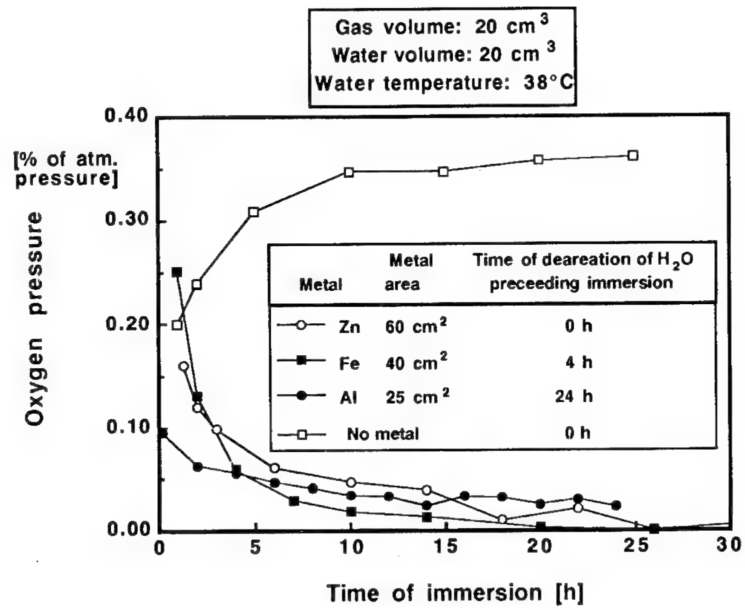

Figure 3a. O_2 pressure in gas volume during corrosion of Al, Fe, Zn in water. The blank is to show the O_2 background.

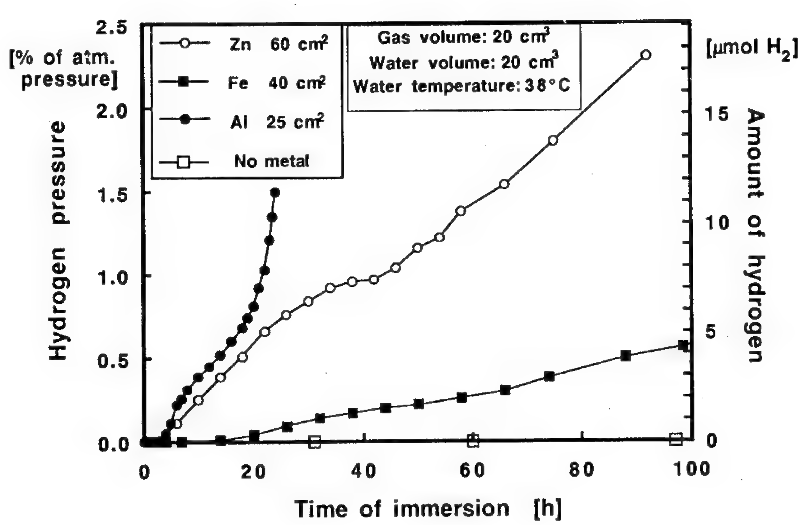

Figure 3b. H_2 evolution during corrosion of Al, Fe, Zn and a blank in deaerated water

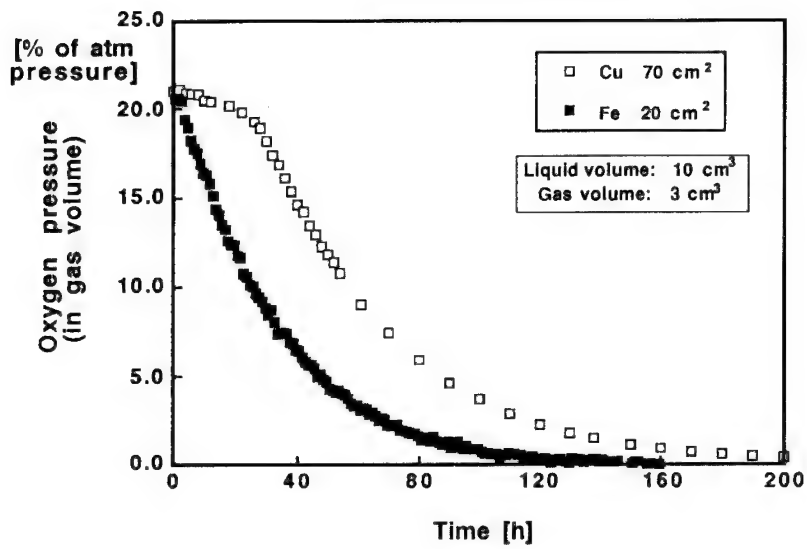

Figure 4. O_2 consumption during corrosion of Cu and Fe immersed in water.

The consumption of oxygen during corrosion of Cu and Fe immersed in water in contact with a gas phase containing normal air is shown in Fig. 4. Fig. 5 shows the normalized oxygen consumption rate versus the oxygen pressure in the gas phase. The straight lines shows that the rate expressions for O_2 consumption are simply proportional to the oxygen pressure. Such a linear relation is not obtained for the situation in which the oxygen is directly involved in, for instance, a parabolic film growth rate. However, the results in Fig. 5 is consistent with our results from gas phase oxidation, where O_2 was mainly consumed in a surface reaction with hydrogen, formed in reaction between water and metal [6,7]. Those results indicated an increased fraction of water participating in the reaction at lower temperatures and higher abundance of water in the atmosphere. H_2 is not displayed in Fig. 4. In the case of Cu no H_2 was detected due to the residual O_2 concentration.

H_2 evolution in corrosion of Fe is shown in Fig. 6. In this experiment a thicker sample, 1 mm Fe plate, was used. The H_2 pressure exceedes the O_2 pressure after about 100 h. After all the O_2 is consumed at ~160 h, H_2 increases at a fairly constant rate until it reaches 40-50%, where it levels out. The whole sample remained totally immersed during the experiment. After the experiment, both the sample and the solution were recovered for further analysis of the H and O content according to Eq. 1. Since the reaction product did not adhere to the sample, but was essentially found as a powder at the bottom of the solution, the procedure to determine the weight change, a, was slightly altered. The total weight change due to corrosion was calculated from the weight loss of the sample, 4.9 mg, and the weight of the dried corrosion product found at the bottom of the solution, 14.3 mg, see Table 2a. The total z/y ratio for the sample+product, calculated from this weight change, was 1.34. The consumption of O_2 and production of H_2 was taken from Fig. 6.

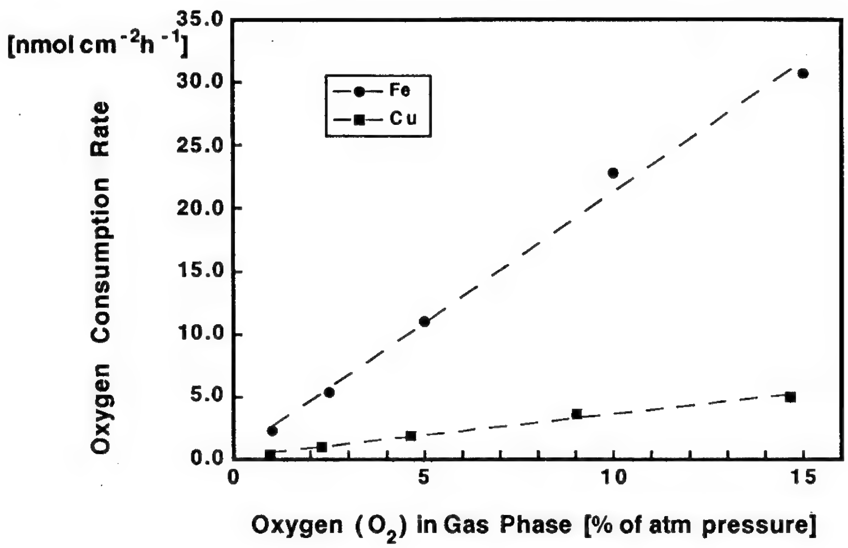

Figure 5. O_2 consumption rate v.s. O_2 pressure.

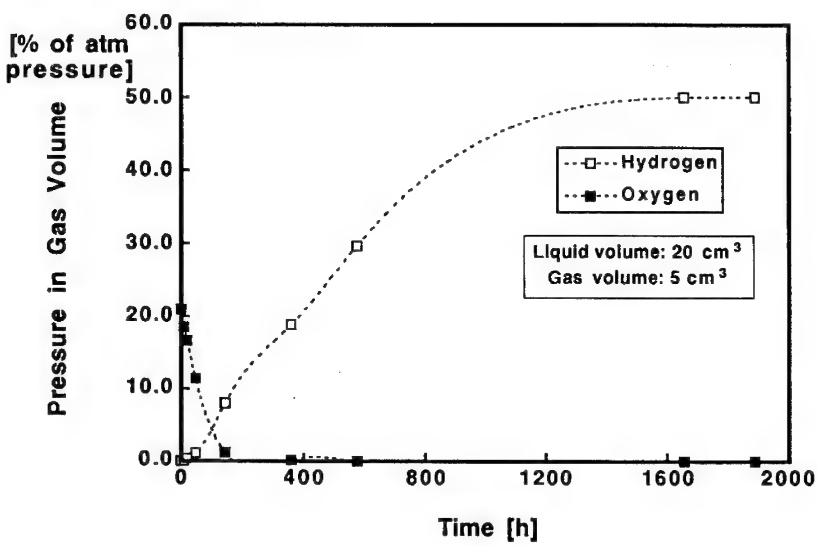

Figure 6. O_2 consumption and H_2 evolution during corrosion of Fe. The weight of the sample was 7.1 g and the surface area was 18 cm^2.

Table 2a. Calculation of z/y (tot), for "Fe+product" using Eq.1, for the corrosion of Fe. The weight change, ***a***, was obtained from the sum of Δm (sample) and Δm (prod). H_2 and O_2 were taken from Fig. 6.

	Δm (sample) [mg]	Δm (prod.) [mg]	a [mg]	b [mmol H_2]	c [mmol O_2]	z/y (tot)
Step I (corr.)	- 4.9	14.3	9.4	0.1	0.04	1.34

Table 2b. Calculation of z/y (oxid), for the corrosion product of Fe, using the corrected value for z (oxid) in Eq.1.

	Δm (sample) [μg]	H_2O [μg]	H_2 [μg]	z (Me) [mmol]	z (Oxid) [mmol]	y (Oxid) [mmol]	z/y(Oxid)
Step II (outgas)	- 367	447	40	0.05	0.67	0.53	1.20

In order to investigate eventual hydrogen uptake in the metal, the sample was polished and outgased in vacuum at 400°C, Fig. 7. The amount of hydrogen was measured to ~40 μg. When the amount of hydrogen in the metal, z_{Me},is subtracted from the total z, a value for z/y in the oxide can be calculated. In this case we obtained z/y = 1.2, Table 2b. The hydrogen is most likely to enter into the metal after the O_2 is consumed. As long as sufficient amount of O_2 is present, an efficient reaction with H/H_2 has been shown to occur [5-7], which is also the interpretation of the results in Figs. 4 and 5.

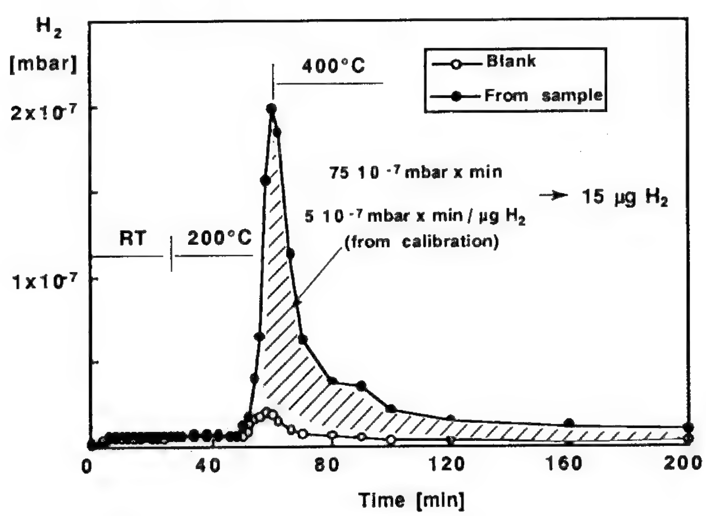

Figure 7. Outgasing of H_2 from ~1/3 of the sample in Fig. 6. Total amount of H_2 in the sample was ~40 μg.

Conclusions

In this work we have studied corrosion of some metals immersed in water by measuring changes of hydrogen and oxygen in the gas phase above the water. Both aerated and deaerated situations were studied. The following conclusions are based on the experimental results and the discussion of these results.

***In situ* gas montoring:** *In situ* monitoring of gases during reaction of metals contained in a virtually closed reaction chamber offers direct detection and quantification of gaseous reactants and products.

By noting certain parameters like the weight change and the consumption and production of O_2 and H_2 respectively, the y, z and z/y ratio in $Me_xO_yH_z$ can be calculated.

Fe: Hydrogen is released mainly under deaerated conditions in reaction with water.

Hydrogen was produced up to a pressure of about 0.5 atm.

Hydrogen diffused into the bulk metal.

Oxygen, while present, is consumed at a rate proportional to the oxygen pressure in the gas phase. This is consistent with that oxygen consumption proceeds in reaction with hydrogen on the metal surface.

The z/y in $Me+Me_xO_yH_z$ was 1.3 for the whole sample, metal+"oxide".

The z/y in $Me_xO_yH_z$ was 1.2 for the oxide.

Al: Hydrogen is produced under deaerated conditions at a rate which was the highest among the metals investigated.

After a certain period the hydrogen production rate accelerates several orders of magnitude.

The oxide film consists of a $Al_xO_yH_z$ product, with z/y = 1.5

Cu: No hydrogen was detected in the experiments where O_2 was present to ~0.2 % of atm pressure.

Oxygen, while present, is consumed at a rate proportional to the oxygen pressure in the gas phase. This is consistent with that oxygen consumption proceeds in reaction with hydrogen on the metal surface.

Stainless steel: As expected SS316 is passivated in immersion in water, judged from the negligible oxygen consumption and hydrogen production compared to the other metals.

References

[1] P. Kofstad, "Microscopy of Oxidation: Proceedings of the first international conference on microscopy of oxidation", p.2, (1991)

[2] J. Krueger, *Corros.Sci.*, **29**, 149, (1989)

[3] G. Hultquist, M. Seo, Q. Lu, G.K. Chuah and K.L. Tan, *Appl.Surf.Sci.*, **59**, 135, (1992)

[4] Q. Lu, *Oxid.Met.* , **40**, 421, (1993)

[5] G. Hultquist, Q. Lu and L. Gråsjö, "Progress in the Understanding and Prevention of Corrsion", Barcelona, p.785, (1993)

[6] G. Hultquist, L. Gråsjö and Q. Lu, *Corros. Sci.*, **34**, 1035, (1993)

[7] G. Hultquist, L. Gråsjö, Q. Lu and T. Åkermark, *Corros.Sci.*, **36**, **1459**, (1994)

[8] L. Gråsjö, To appear in Ph.D. thesis, Royal Institute of Technology, Stockholm, Sweden, Dec 1994

[9] M. Seo, G. Hultquist, L. Gråsjö and N. Sato, 10th ICMC, Madras (India), p.481, (1987)

[10] J.W. Diggle and A.K. Vijh, "Oxides and Oxide films, (IV)", Ch. 3, (1976)

Materials Science Forum Vols. 185-188 (1995) pp. 713-722

The influence of the subsequent oxidation on the passive behaviour of nitrided and nitrocarburized steels

U. Ebersbach[1], S. Friedrich[2] and T. Nghia[2]

[1] Hochschule für Technik, Wirtschaft und Kultur, PF 66, D-04251 Leipzig, Germany

[2] TU Bergakademie Freiberg, Gustav-Zeuner-Str. 5, D-09596 Freiberg, Germany

Keywords: Nitriding, subsequent oxidation, structure of layers, polarization curves, passive behaviour of nitrides, pitting potential

Abstract

The corrosion resistance of nitrided / nitrocarburized and post-oxidized steels 20MnCr5 and 45Cr2 is investigated in relation to the structure and morphology of the compound layers. The ϵ - carbonitride phase with the concentration ratio $[C/(N+C)]_\epsilon$ of 0.02 to 0.2 shows the best passive behaviour, being similar to that of the magnetite phase. By the subsequent oxidation of salt bath nitrocarburized steels this corrosion resistance can be obtained within the entire compound layer.

Introduction

Nitriding and nitrocarburizing of steel represent useful protection against corrosion, wear and cyclic loads /1/. The produced nitrided layer consists of a compound layer adjacent to the surface and a diffusion zone with embedded nitride precipitates.

Figure 1 shows schematically the microstructure of the nitrided layer of nitrided steel /2/. The compound layer on nitrided / nitrocarburized iron, unalloyed and low-alloy steels consists of the γ'- nitride (Fe_4N) and the ϵ - phase $[Fe_2(N, C)_{1-x}]$. The iron nitrides and -carbonitrides are passive in neutral solutions. An oxide layer is formed on the surface of these phases and produces useful corrosion resistance /1,3/. In the earlier paper /4/ we have shown that ϵ- and γ'- nitride layers decrease corrosion by one order of magnitude, and ϵ - carbonitride layers decrease it by two orders of magnitude in comparison to the matrix material in a 0.9 M NaCl solution.

The corrosion resistance of nitrided and nitrocarburized steels is clearly improved by subsequent oxidizing treatment. The oxidation of gasnitrided / nitrocarburized steels is carried out in a water vapour at temperatures from 450 to 550 °C /5/. On the other hand, the oxidation of salt bath nitrocarburized steels is accomplished in an oxidative cooling bath at 330 to 400 °C /6/. By this treatment the nitrides and carbonitrides on the surface are converted into oxide. When the surface is completely covered with an oxide, the released nitrogen diffuses into the compound layer under the oxide layer.

Thus, the subsequent oxidation causes a modification of the compound layer by the following processes /7,8/:

- the formation of an outer oxide layer on the surface
- the increase of the content of nitrogen under the oxide layer
- the filling of pores within the compound layer with oxide and consequently a decrease of attack areas by corrosive media.

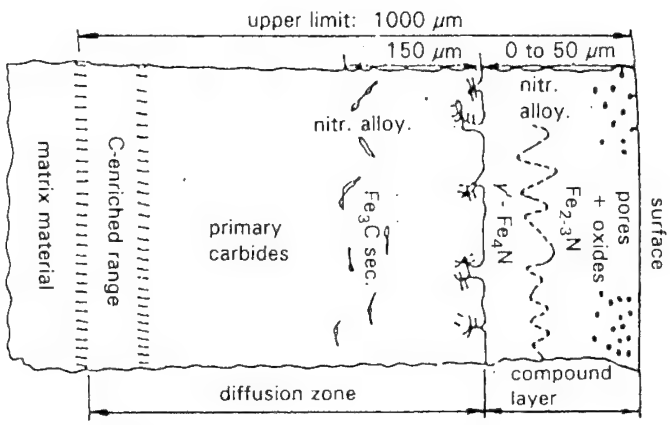

Fig. 1: Microstructure of nitrided layer (schematically) for nitrided steel [2] (nitr. alloy.: nitrides of alloying elements)

These structural and morphological changes within the compound layer by post - oxidation lead to the increase of corrosion resistance in comparison with the nitrided and nitrocarburized steels. Until now not much is known about the influence of oxidation parameters on the corrosion behaviour.
In the present work the nitrided and nitrocarburized steels were oxidized in vapour and the relation between the structure and morphology of the post-oxidized compound layers and the corrosion behaviour was investigated. Thus, the obtained corrosion data were discussed in dependence on the distance of the test areas to the outer surface of the compound layer as well as the content of interstitials in the ϵ - phase. These results of post-oxidized nitrided / nitrocarburized steels were described in comparison with the behaviour of nitrided / nitrocarburized steels.

Experimental
The material of specimens included normalized steel 20MnCr5 and quenchend and tempered steel 45Cr2. The specimens were in form of a disk (diameter 11 mm, height 5 mm). The front faces of the disks were prepared by wet grinding.
The parameters of nitriding and nitrocarburizing which are frequently applied, are shown in Table 1. By this treatment the expected compound layers of about 20 to 30 μm thickness were formed on the steels. Later the specimens were oxidized in a water vapour at a temperature of 450 °C and at a treatment time of 1 hr.. According to the method Quench Polish Quench (QPQ) /6/, post-oxidized specimens were polished and oxidized under the same conditions once again.
The structure and morphology of layers were investigated by X-Ray Diffraction, Electron Probe Micro Analysis (EPMA), Light Microscopy and Scanning Electron Microscopy (SEM). X-Ray Diffractograms recorded with Cu radiation were used for the determination of phase concentration profiles of the compound layers. Surface areas and test areas after abrasion in steps of 4 μm were measured.
Precision lattice constants were the basis for the determination of the concentration of interstitials $[N, C]_\epsilon$ in the ϵ - phase. The concentrations of nitrogen, carbon and oxygen

were obtained by means of an Electron Probe Micro Analysis. Light and Scanning Microscopy were applied to examine the morphology of the nitride layers.
Electrochemical corrosion tests at surfaces and areas after a defined surface abrasion were carried out in a 0.9 M NaCl solution to characterize the corrosion behaviour of the nitrided / nitrocarburized and oxidized steels. The corrosion data, especially the rest potential, polarization resistance, passive current density and pitting potential, were estimated on the basis of the rest potential measurements and potentiodynamic current - potential curves. Diagrams demonstrate the corrosion data in dependence on the distance of the test areas to the outer surface of the compound layer as well as the content of interstitials in the ϵ - phase.

Results and discussion

Structure and morphology of post-oxidized compound layers
Compound layers produced on the steels 20MnCr5 and 45Cr2 consist mainly of ϵ - phases. Figure 4b and 5b demonstrate the phase concentration profiles of the compound layers of salt bath nitrocarburized steels 20MnCr5 and 45Cr2. Profiles of the other remaining treated steels were shown in earlier papers /4,9,10/. The nitrocarburizing of the steel 20MnCr5 leads to a monophase ϵ - compound layer, whereas gasoxinitriding of 20MnCr5 and the treatment of the steel 45Cr2 produce γ'- nitride as well. In the direct surface range a small content of magnetite (Fe_3O_4) was dectected (Table 1). By the subsequent oxidation of nitrided / nitrocarburized steels the content of iron oxide (Fe_3O_4) increased up to 50 wt % in the surface range of about 3 μm thickness. Magnetite was found up to a depth of 8 to 16 μm for the gasnitrocarburized / gasoxinitrided and oxidized steels /11,12/. On the other hand, the salt bath nitrocarburized and oxidized steels contain magnetite in the entire compound layer (Figures 4c and 5c). The differences in the content of oxide within the compound layer is caused by the different structure of pores of nitrided / nitrocarburized steels (see below).

treatment $T / K_N / t$ [°C] [h]	steel	phase concentration in the surface range up to 3 μm depth, wt %					
		nitrided			nitrided + oxidized		
		ϵ	γ'	Fe_3O_4	ϵ	γ'	Fe_3O_4
salt bath nitrocarburizing 580 / - / 3.5	20MnCr5	96	-	4	55	-	45
	45Cr2	92	8	-	40	11	49
gasoxinitriding 590 / 3 / 6	20MnCr5	92	4	4	54	-	46
	45Cr2	94	2	4	59	2	39
gasnitrocarburizing 580 / 1.1 / 5	20MnCr5	98	-	2	72	-	28
	45Cr2	98	2	-	61	-	39

Table 1: Parameters of nitriding / nitrocarburizing and influence of the subsequent oxidation in water vapour ($T = 450$ °C, $t = 1$ h) on the phase concentration in the surface range up to 3 μm depth (K_N nitriding parameter)

The ϵ - phase has a different content of interstitials $[N, C]_\epsilon$ in dependence on the parameters of treatment and the distance of the test area from the outer surface. The concentration of nitrogen lies between 7 and 9 wt %. In the compound layers of nitrocarburized steels the ϵ - phase predominantly has carbon contents of 1 to 2.4 wt %. On the other hand, the gasoxinitrided steels have smaller values of about 0.2 to 0.6 wt % /12/. Therefore, the ϵ - phase has to be considered as ϵ - carbonitride with a C - content varying over a wide range.
Figure 2a shows the nitrogen profiles of differently treated steel 20MnCr5. As can be seen, by the subsequent oxidation the nitrogen is shifted to larger depths from the outer surface. Our "oxidation polish oxidation" treatment leads to the best effect. In agreement with the oxygen profiles showed in figure 2b, the content of oxygen increases strongly on the direct surface.

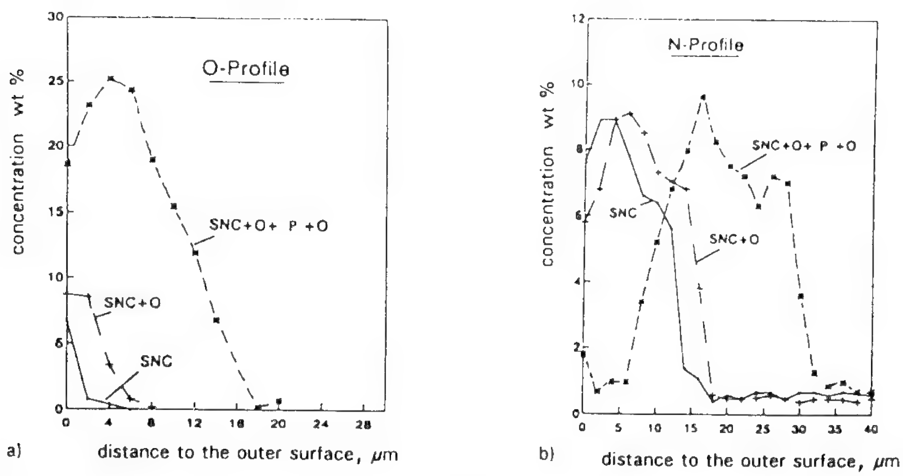

Fig. 2: Concentration profiles of nitrogen (a) and oxygen (b) of the compound layer of treated steel 20MnCr5

SNC	salt bath nitrocarburized
SNC + O	salt bath nitrocarburized and oxidized
SNC + O + P + O	salt bath nitrocarburized and oxidized and polished and oxidized

The morphology of the compound layers of treated steels is characterized by the layer thickness of about 20 to 30 μm and differences in the structure of pores caused by several nitriding procedures /4/. During treatments in gas, micropores (diameter ≤ 0.25 μm) form in the outer range of the compound layer, whereas in the salt bath nitrocarburized layers deeper reaching pores are formed additionally. The thickness of the layer with pores is estimated to be between 30 and 50 % in comparison with the thickness of the entire compound layer. In view of the corrosion behaviour the surface roughening of nitrided surfaces as a result of pore formation was calculated using a model. In this way roughness factors (fa) were obtained:

fa = 2.2 for gasoxinitriding, fa = 2.5 for gasnitrocarburizing and
fa = 5 for salt bath nitrocarburizing.

By the subsequent oxidation an oxide layer of 0.5 to 2 μm in thickness is produced

directly on the surfaces. The thickness of the entire compound layer is unchanged. By means of metallographic investigations it is proved, that the pores in the compound layer are filled partially or completely with oxide.

Electrochemical corrosion behaviour of treated steels

Electrochemical investigations in 0.9 M NaCl solution have shown that the corrosion resistance of treated steels is mainly dependent on the phase concentration, on the content of interstitials in the ϵ - phase and the porosity within the compound layer. Rest potentials of the surface and of the test areas in the outer layers of the compound layer of nitrided / nitrocarburized steels are almost 200 to 400 mV more positive in comparison with the matrix materials /4/. The noblest potentials and therefore the stablest passive layers are found on the test area of ϵ - carbonitride phase with a concentration ratio $[C/(N+C)]_\epsilon$ of 0.02 to 0.2 /9/. Especially the surfaces of salt bath nitrocarburized steel 20MnCr5 demonstrate this behaviour (Fig. 3). By subsequent oxidation as well as polish and new oxidation the surfaces of salt bath nitrocarburized steel show the most positive rest potentials (Fig. 3).

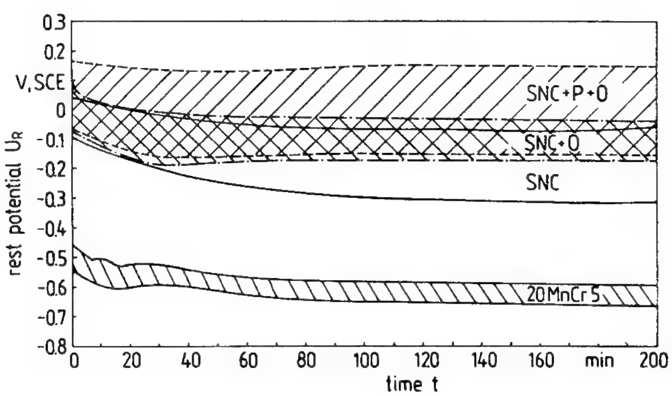

Fig. 3: Rest potential-time dependence of the surfaces of treated steel 20MnCr5 and of the matrix materials in 0.9 M NaCl solution

SNC	salt bath nitrocarburized 3.5 h or 2.75 h resp.
SNC + O	salt bath nitrocarburized 3.5 h and oxidized
SNC + P + O	salt bath nitrocarburized 2.75 h and polished and oxidized

Figures 4 and 5 demonstrate the reciprocal polarization resistance - as a measure of the corrosion rate - and phase concentration of the compound layer in dependence on the distance from the outer surface. The decrease of corrosion along the depth up to about 8 μm of salt bath nitrocarburized steels (Fig. 4a, 5a) is in agreement with the decrease in porosity and also in the roughness factors. As was expected, the non porous part of the compound layer (depths 12 to 18 μm) provides the best protection against corrosion. The corrosion rate of the monophase ϵ - carbonitride layer of salt bath nitrocarburized steel 20MnCr5 (Fig. 4a) is smaller by one order of magnitude in comparison with

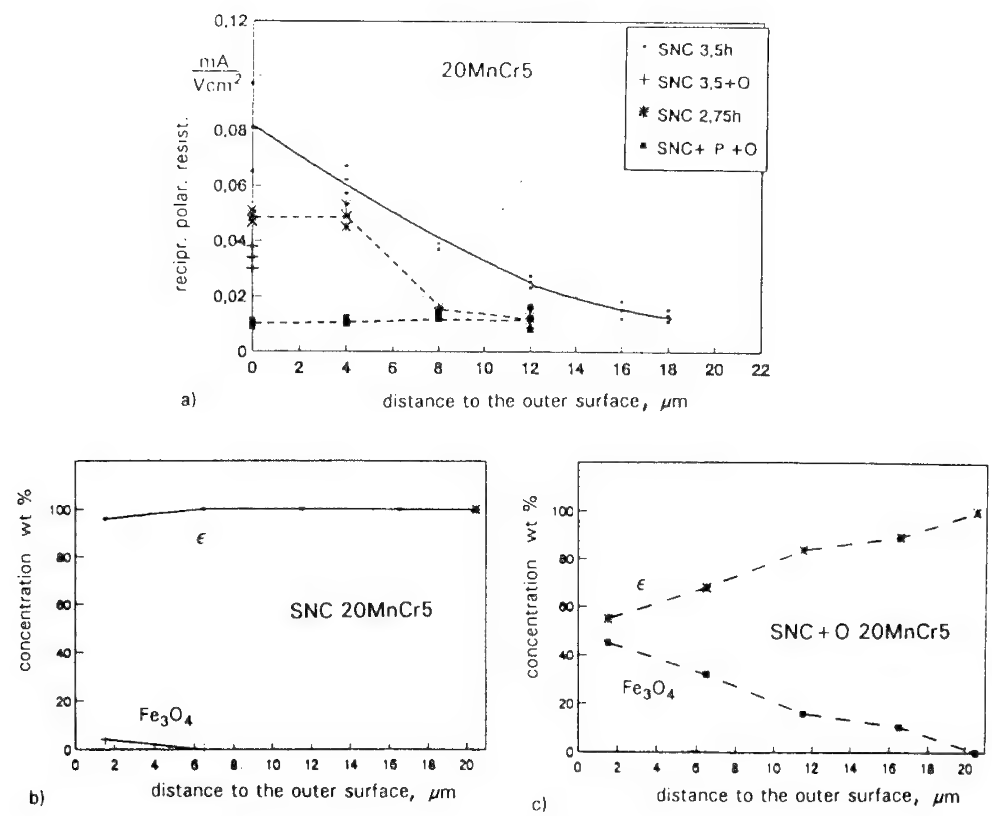

Fig. 4: Reciprocal polarization resistance in 0.9 M solution (a) and phase concentration (b, c) of the compound layer of treated steel <u>20MnCr5</u>

SNC 3.5 h — salt bath nitrocarburized 3.5 h and 2.75 h, resp.
SNC 2.75 h
SNC 3.5 h + O — salt bath nitrocarburized 3.5 h and oxidized
SNC + P + O — salt bath nitrocarburized 2.75 h and polished and oxidized

the (ϵ + γ') - compound layer of the salt bath nitrocarburized steel 45Cr2 (Fig. 5a). The stronger corrosion of treated 45Cr2 can be attributed to the selective corrosion of the ϵ - carbonitride and the less noble γ'- nitride.

The content of the interstitials in the ϵ - phase strongly influences the corrosion resistance of the ϵ- phase. The reciprocal polarization resistances of the test areas of treated steels is corrected by roughness factors fa. Figure 6 demonstrates the reciprocal resistance as a function of concentration ratio $[C/(N + C)]_\epsilon$ in the ϵ - phase. Thus, the ϵ - carbonitride with concentration ratio of 0.02 to 0.2 shows a better corrosion resistance in comparison with the ϵ - nitride or ϵ - carbonitride, which is made up of the high C - content. The measured values in the above range of 0.02 to 0.2 are found mainly on the ϵ - compound layer of salt bath nitrocarburized steel 20MnCr5.
The subsequent oxidation leads to the effective decrease of corrosion within the

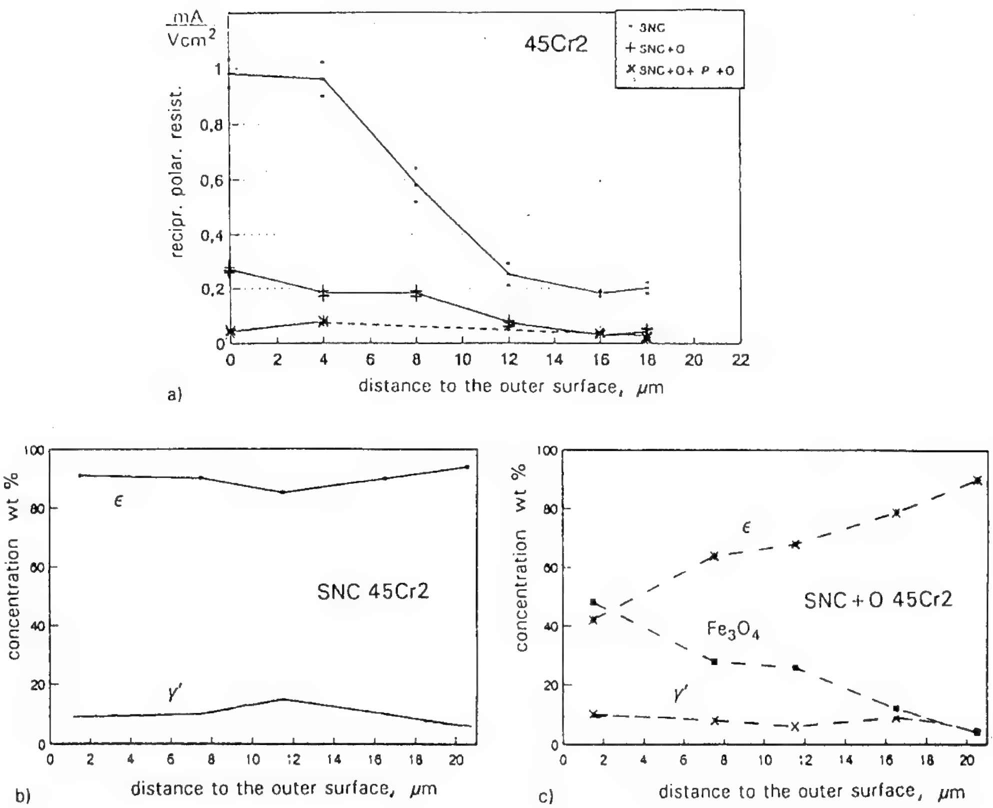

Fig. 5: Reciprocal polarization resistance in 0.9 M solution (a) and phase concentration (b, c) of the compound layer of treated steel 45Cr2

SNC	salt bath nitrocarburized
SNC + O	salt bath nitrocarburized and oxidized
SNC + O + P + O	salt bath nitrocarburized and oxidized and polished and oxidized

compound layer. The corrosion rate of salt bath nitrocarburized and oxidized steel 20MnCr5 is diminished by the filling up the pores with oxide - in agreement with the roughness factor. The decrease of corrosion of the other treated steels is additionally dependent on the phase composition. The influence of the increased contents of interstitials located under the oxide layer on the corrosion rate is presently investigated. By polishing and new oxidation a further decrease of corrosion is achieved (by the factor up to 1/50) and the corrosion rate attains constant value throughout the entire compound layer. The ϵ -carbonitride layer of salt bath nitrocarburized steels 20MnCr5 shows the stablest oxide layers by the subsequent oxidation (Fig. 4a).
Figure 7 demonstrates the anodic current density-potential curves of nitrided / nitrocarburized and post-oxidized steel 45Cr2 in 0.9 M NaCl solution in comparison with the matrix material. Whereas the matrix material dissolves actively, the surfaces of treated

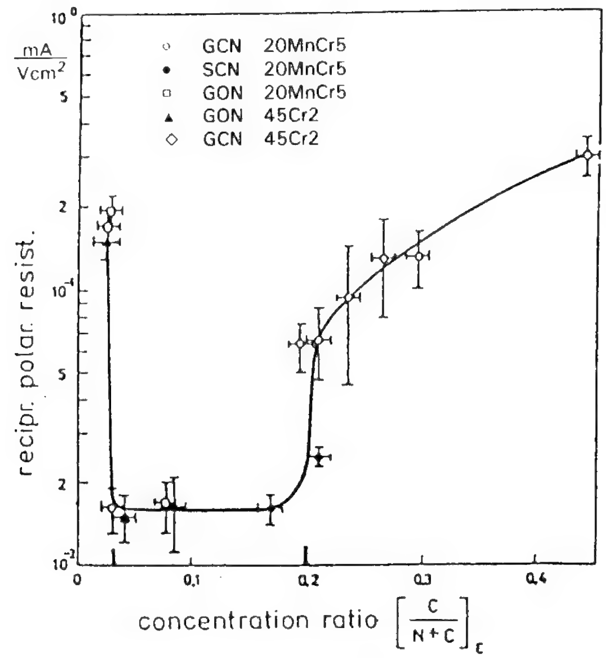

Fig. 6: Reciprocal polarization resistance of nitrided and nitrocarburized steels in 0.9 M NaCl solution in dependence on the concentration ratio $[C/(N + C)]_{\epsilon}$ in the ϵ - phase of the compound layer

steels show passive behaviour. The polarization curves of treated steel 20MnCr5 were published in the earlier paper /4/.

The passive current densities of nitrided and nitrocarburized steels differ by about one order of magnitude depending on the conditions of treatment. By the subsequent oxidation the passive current density is reduced by the factor 1/3 to 1/4, especially up to 1/50 for the salt bath nitrocarburized steel 20MnCr5. By both polishing and subsequent oxidation an additional decrease of corrosion of about 1/3 is obtained.

The pitting potentials of the nitrided and nitrocarburized surfaces are dependent on the concentration of interstitials $[N + C]_{\epsilon}$ in the ϵ - phase, as can be seen in Fig. 8. Although the treated surfaces consist only of the ϵ - phase (Tab. 1), the pitting potentials determined after anodic polarization are very different. The observed increase of the pitting potential with the concentration $[N + C]_{\epsilon}$ in the ϵ - phase can be explained by a better adaptation of the formed passive layer to the ϵ - phase in accordance with the Pilling - Bedworth ratio /13/. Pitting corrosion susceptibility by layer crack formation is diminished. The subsequent oxidation reduces the pitting corrosion susceptibility of the surfaces of nitrided and nitrocarburized steels. After recording the anodic polarization curves, only the gasnitrocarburized and post-oxidized steel 45Cr2 exhibit the pitting corrosion. For the other post-oxidized steels the potentials of the increase of current are the breaktrough potentials. By polishing and new oxidation, gasnitrocarburized and oxidized steel 45Cr2 do not show the former pitting corrosion.

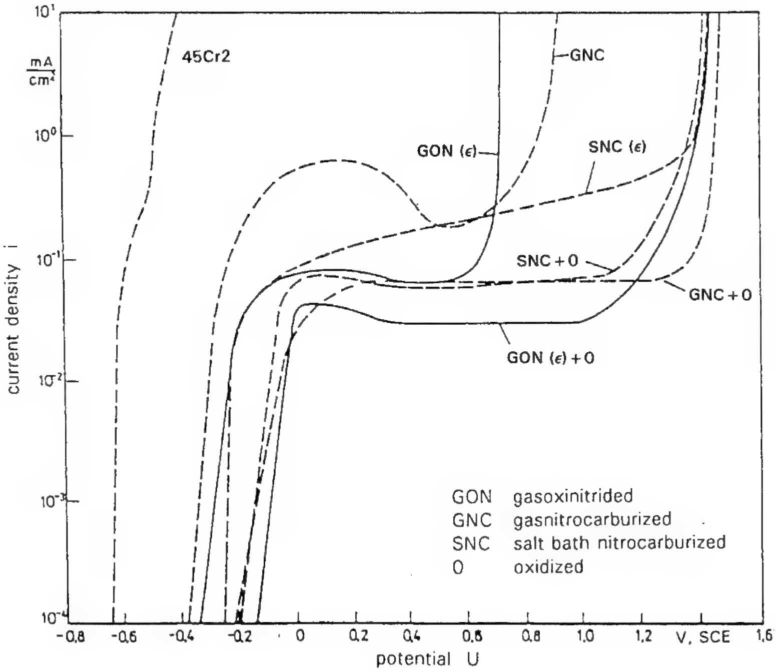

Fig. 7: Potentiodynamic anodic current density-potential curves of the matrix material, the nitrided / nitrocarburized and oxidized steel 45Cr2 in a 0.9 M NaCl solution (parameters of nitriding / nitrocarburizing see table 1; parameters of oxidation: T = 450 °C, t = 1 h)

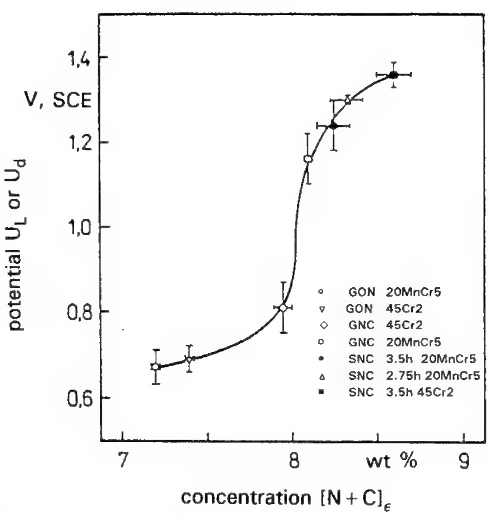

Fig. 8: Pitting potential U_L and breakthrough potential U_d, respectively, of nitrided and nitrocarburized steel surfaces in 0.9 M NaCl solution in dependence on the concentration of interstitials $[N,C]_\epsilon$ in the ϵ - phase

Summary and conclusions

Nitrided and nitrocarburized steels 20MnCr5 and 45Cr2 were oxidized in water vapour at a temperature of 450 °C and at a treatment time of 1 hr. Electrochemical investigations in 0.9 M NaCl solution have shown, that the corrosion resistance of treated steels is mainly dependent on the phase concentration, on the content of interstitials in the ϵ - phase and the porosity within the compound layer. The polarization resistance method was used to characterize the corrosion rate of treated steels in dependence on the distance to the outer surface.

The corrosion behaviour of post-oxidized steels shows:

- the most noble rest potentials (up to 300 mV)
- the decrease of the corrosion rate within the compound layer by the factor up to 1/50
- the decrease of the pitting corrosion susceptibility at the surfaces

in comparison with nitrided and nitrocarburized steels. In a range of concentration ratios $[C/(N + C)]_\epsilon$ from 0.02 to 0.2, ϵ - carbonitride provides the best passive behaviour, which is comparable to the passive behaviour of magnetite oxid layer on salt bath nitrocarburized steel 20MnCr5.

The influence of the parameters of oxidation on the corrosion behaviour will be investigated in the future to optimize the corrosion resistance of post-oxidized nitrided / nitrocarburized steels.

Literature

/ 1/ R. Chatterjee - Fischer: Wärmebehandlung von Eisenwerkstoffen: Nitrieren und Nitrocarburieren, Expert-Verlag 1986.

/ 2/ H. Oettel; S. Böhmer; H. Baum: Schmierungstechnik, 17(1986)2, S. 36-40

/ 3/ A.N. Minkewitsch: Chemisch-thermische Oberflächenbehandlung von Stahl. VEB Verlag Technik, Berlin, 1953.

/ 4/ U. Ebersbach; S. Friedrich; T. Nghia; H.-J. Spies: Härterei-Tech. Mitt. 46(1991)6, S. 339-349.

/ 5/ S. Pakrasi: Härterei-Tech. Mitt. 43(1988) S. 365-373.

/ 6/ G. Wahl: Z. wirtsch. Fertig. 77(1982)10, S. 501-106.

/ 7/ Th. Schubert; H. Oettel; D. Bergner: Untersuchungen an nachträglich oxidierten Verbindungsschichten gasnitrierter Eisenwerstoffe. Härterei-Tech. Mitt. 42(1987)6, S. 332-337.

/ 8/ H. Somers; E.J. Mittemeijer: AWT - Tagung Nitrieren und Nitrocarburieren, Darmstadt (1991), Tagungsband S. 152-162.

/ 9/ U. Ebersbach; S. Friedrich; T. Nghia: Proc. Int. Conf. on Surface Engineering Bremen (1993), S. 299-304.

/10/ U. Ebersbach; S. Friedrich; T. Nghia: 4. Wärmebehandlungstagung Chemnitz (1991), Tagungsband.

/11/ T. Nghia: Diss. TU BA Freiberg (1994)

/12/ S. Friedrich: Diss. TU BA Freiberg (1994)

/13/ J. Mittemeijer; P.F. Colijn: Härterei-Tech. Mitt. 40(1985)2, S. 77-79.

Materials Science Forum Vols. 185-188 (1995) pp. 723-730

Dissolution, passivation and composition of passive films of binary iron-nitrogen alloy

U. Kamachi Mudali[1], B. Reynders[2] and M. Stratmann[3]

[1] Indira Ghandi Centre for Atomic Research, Kalpakkam-603 102, India

[2] Max-Planck-Institute for Iron Research, D-40237 Düsseldorf, Germany

[3] Institute for Materials Science IV, Friedrich-Alexander-University Erlangen-Nürnberg, D-91058 Erlangen, Germany

Keywords: Iron-nitrogen alloy, anodic dissolution, passivity, potentiostatic transients, capacitance, surface analysis

Abstract

To understand the passivation kinetics in Fe-N model alloys, potentiostatic transient experiments were conducted with pure iron nitrided on the surface in an ammonia-hydrogen gas mixture at 810 °C for 45 minutes to yield about 0.9 wt% N. The experiments were conducted in a solution containing 0.01 M H_2SO_4 and 0.99 M Na_2SO_4 (pH = 2.8) and the potential jumps of 1 ms were applied as follows : from cathodic (-700 mV_H) to anodic (900 mV_H) region, from cathodic to active (200 mV_H for 100 to 1000 ms) and then to anodic region, and from cathodic to active (-200, -100, 0, 100, 200 mV_H for 2 s) and then to anodic region. The results indicated that with nitrogen addition the time required for passivation decreased from 295.9 ms to 34.9 ms, and also the charge required for passivation decreased from 260.45 to 25.9 mC/cm^2 for pure iron. Further, after holding in the active region the steady state current was lower, and the charge required then for passivation significantly decreased with nitrogen addition. Electrochemical impedance spectroscopic studies showed an increase in the capacitance of the films with nitrogen addition. Also XPS analysis of the films developed indicated the presence of nitrogen in two different states, and for the film developed after holding at the active potential showed more nitrogen and hydroxyl ions.

Introduction

Nitrogen as an alloying element in steels and stainless steels significantly improves the mechanical and corrosion properties. It has been reported that the passivation characteristics and the localised corrosion resistance of the Fe-based alloys improved considerably with nitrogen addition [1-4]. However, the role of nitrogen in improving the passivity is not clearly understood, though many attempts were made to explain the mechanism based on the results from the experiments conducted with steels and stainless steels containing different levels of nitrogen. In the present work with the combination of electrochemical techniques like potentiostatic transient and electrochemical impedance spectroscopy and surface analytical techniques like XPS and Auger electron microscopy an attempt is made to highlight the exact role played by nitrogen in enhancing the passivity of pure iron. For this purpose, to eliminate the effects of other alloying elements, pure iron was nitrided to get Fe-N model alloys, and the studies were conducted with them.

Experimental

Pure iron specimens of 15 mm * 5 mm * 1 mm sizes were cut and polished up to 1000 grit SiC paper prior to nitriding in ammonia-hydrogen gas mixture. The nitriding experiments were carried out at 810 °C for 45 minutes and the resultant surface was found to have about 0.9 wt% N when examined for chemical composition by electron microprobe analyser. The metallographic examination of the surface revealed a homogeneous microstructure without microvoids and nitride precipitates.

Potentiostatic Transient Experiments :

The nitrided specimens were polished on one side up to 1000 grit SiC paper and only an area of 0.04 cm^2 was exposed to the test solution of 0.01 M H_2SO_4 and 0.99 M Na_2SO_4 (pH=2.8). A modified electrochemical cell with appropriate positioning of the anode, cathode and the reference electrode was standardised through systematic experiments for obtaining reproduceable transients. A *wenking* Potentioscan POS 73 (FRG make) was used for the present investigation. The potential jumps were applied using a *Prodis* programmable function generator (UK make), and the resultant current transients were captured using a *Gould* digital storage oscilloscope (USA make). The data from the oscilloscope were recorded using a personal computer. The electrode potentials were measured against a $Hg/HgSO_4$ reference electrode and the potentials were represented in standard hydrogen scale (SHE). Potential jumps of 1 ms duration were applied from (1) cathodic (-700 mV) to anodic region (900 mV), (2) cathodic (-700 mV) to active (200 mV for 100 to 2000 ms) and then to anodic region (900 mV), and (3) cathodic (-700 mV) to active (-200, -100, 0, 100, 200 mV for 2 s) and then to anodic region (900 mV). The resultant transients were recorded and the data were analysed for the passivation time and charge for both pure iron and Fe-N alloy. From the charge values the thickness of the films was calculated using the relationship, $t = qm / nAFd$, where q - charge required for passivation, m - molecular weight of the film, Fe_2O_3, n - number of electrons, A - area of the specimen exposed, F - Faraday constant and d = 5, density of the film, considering Fe_2O_3. The passive film is considered to be consisting of mainly Fe_2O_3 and the thickness calculations were made accordingly.

Electrochemical Impedance Spectroscopy :

Impedance experiments were carried out under the same testing conditions of direct potentiostatic transient experiments (cathodic to anodic region) in order to evaluate the capacitance of the passive films. From the impedance spectra the capacitance values at 500 Hz were calculated using the relationship $C = 1 / 2\pi * f * |Z| * \sin\theta$, where f - frequency at which the phase angle is maximum, |Z| - modulus of the impedance, θ - phase angle. A *Heka* potentiostat (FRG make) connected to a frequency response analyser (NF electronic Instruments S-5720 C, Japan make) through a personal computer was used in the present investigation for conducting the experiments. From the capacitance values the thickness of the films were also estimated using the relationship, $C = D*D_o / t$, [5] where D = 12, dielectric constant of Fe_2O_3 [6], $D_o = 80.104$, dielectric constant of water.

Surface Analysis by X-ray Photoelectron Spectroscopy (XPS) and Auger Electron Spectroscopy (AES) :

The passive films of pure Fe and Fe-N alloy specimens developed at 900 mV for 30 minutes after the direct potential jump as well as after an intermittent hold at 200 mV for 2 s were

examined by XPS and AES. The measurements were carried out using a *Microlab* 310-D (VG make, UK) XPS / AES system with Mg Kα x-ray source. High resolution spectra of C (1s), O (1s), N (1s) and Fe (2p) were obtained, and their binding energy values were measured.

Results and Discussion

Figure 1 shows the current transients obtained for pure iron and Fe-N alloy when the potential jump was applied directly from cathodic to anodic region. The coressponding potential applied are also shown in an inset in the figure. From these transients the time required for passivation was found significantly lower for Fe-N alloy (34.9 ms) compared to that of pure iron (295.9 ms). Also from the integration of the current transients, charge required for passivation was calculated, and this showed a charge value of 25.9 mC/cm^2 for Fe-N alloy compared to that of 260.45 mC/cm^2 for pure iron. Thus the addition of nitrogen enhances the passivation tendency of pure iron. The thickness values of the films developed during the transient experiments were calculated for both pure iron and Fe-N alloy, and this indicated that the film developed on Fe-N alloy was thinner compared to that of pure iron (Fig.2).

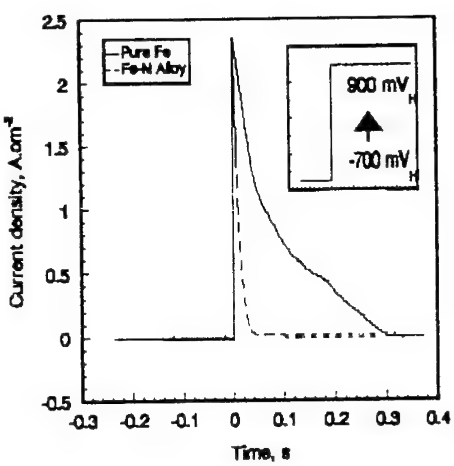

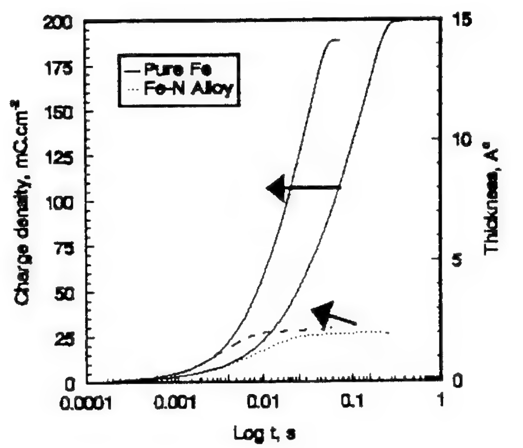

Fig.1 : Potentiostatic current transients of pure Fe and Fe-N alloy with an inset showing the potentials at which the 1 ms jump was made.

Fig.2 : Charge and thickness values obtained from the transients for pure Fe and Fe-N alloy

When the potential jump was carried out with an intermittent holding at the active potential it was found that the charge accumulated during dissolution was increasing with the increase in the hold time for pure iron and this was lower and almost constant in the case of Fe-N alloy (Fig.3a). This indicated that the addition of nitrogen slowed down the dissolution kinetics of iron. However, the charge required for passivation was about 15 mC/cm^2 for pure iron and about 7.5 mC/cm^2 for Fe-N alloy irrespective of the hold time (Fig.3b). Two important points were noticed from the shape of the current transients obtained in these experiments : prior to passivation the steady state current did not reach a stable value, and a lot of oscillations were noticed during the decay of the current transients. In the next set of experiments the hold time was increased to 2 s and the steady state current values were measured at 1.5 s where it was stable, and also the charge required for passivation for

different potentials in the active range. Figures 4 (a & b) show the steady state current values and the passivation charge for both pure iron and Fe-N alloy. Pure iron showed significant increase in the steady state current values compared to that of Fe-N alloy at all potentials. The very low steady state current values shown by Fe-N alloy at all potentials confirmed the slowing down of the dissolution of iron atoms from the surface. When chloride ions were added during the transient experiments with a hold at active potentials -100 and 0 mV it was noticed that the dissolution of Fe-N alloy was not increased significantly indicating its resistance to chloride environment. Fe-N alloy also exhibited low passivation charge values compared to that of pure iron at all potentials. The higher passivation charge values of pure iron could also account for the precipitation of ferrous hydroxide during this period.

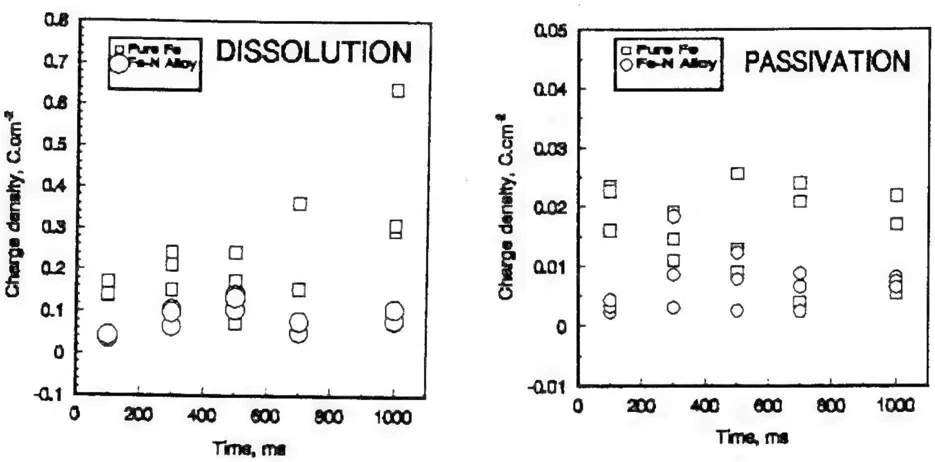

(a) (b)

Fig.3 : Charge accumulated during (a) dissolution, and (b) passivation, for pure iron and Fe-N alloy while the potential jump was applied with a hold at 200 mV for various durations.

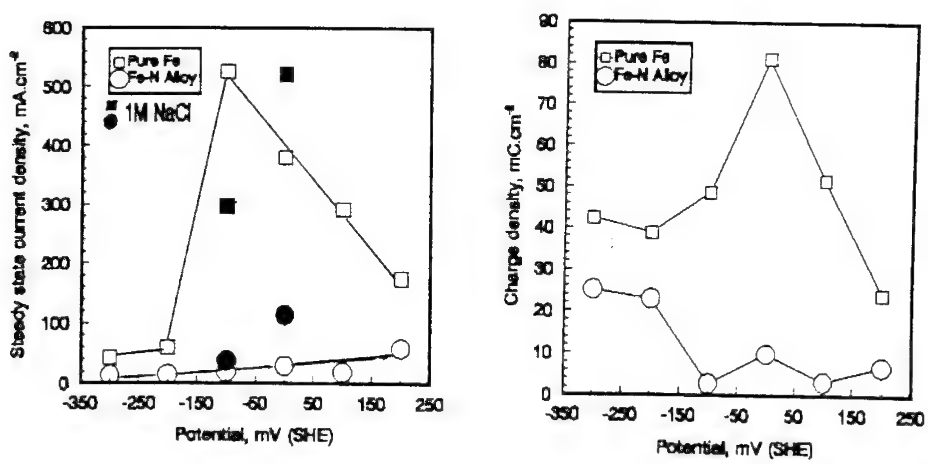

(a) (b)

Fig.4 : (a) Steady state current values, and (b) charge accumulated during passivation, for pure Fe and Fe-N alloy while the potential jump was applied with a hold at various potentials in the active region for 2 s.

The presence of oscillations during the decay of current transients during dissolution and prior to passivation for Fe-N alloy (Fig.5) could account for the following hypothesis : during active dissolution iron atoms dissolve into the solution and precipitate partially as ferrous hydroxide, and nitrogen as N^{3-} ions dissolve into the solution to form ammonium ions near the surface. The formation of ammonium ions and the subsequent consumption of protons in this process raises the near surface pH to a higher value thus decreasing the dissolution kinetics. However, the precipitated ferrous hydroxide now dissolves into the solution to increase the dissolution current, and thus we have typical oscillations indicating the competition between dissolution of ferrous hydroxide and the passivation effect due to ammonium ion formation. The overall balancing of the proton should also account for the protons that are displaced from the surface by the injection of ferrous ions from the surface, release of protons from the dissolution of ferrous hydroxide and the equilibrium between ammonia and ammonium ions. We are presently working on a model based on the above points to formulate the mechanism by which nitrogen improves the passivation tendency of pure iron.

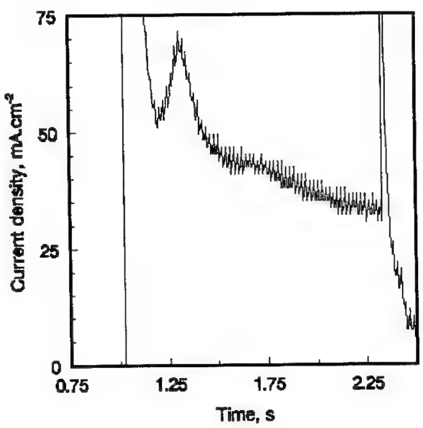

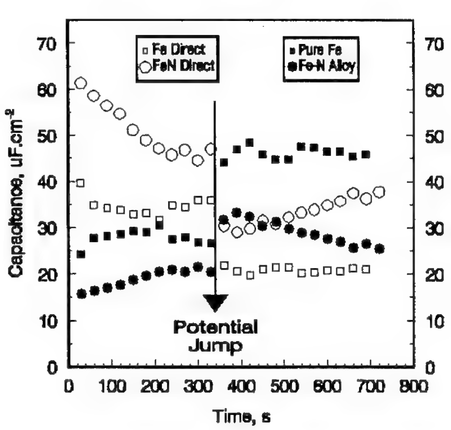

Fig.5 : Current oscillations during the active dissolution of Fe-N alloy while the potential jump was applied with a hold at 200 mV for 1300 ms.

Fig.6 : Capacitance and thickness values of pure Fe and Fe-N alloy calculated at 500 Hz while direct potential jump was made from cathodic to anodic region.

Figure 6 shows the capacitance values of pure iron and Fe-N alloy measured during the direct potential jumps, and the corresponding thickness values calculated from the capacitance of the films. Normally at the cathodic region no film is expected to be present and hence the capacitance is attributed to the double layer charging. The capacitance values of the Fe-N alloy was also higher than that of pure Fe in the anodic region followed by the potential jump. This could be due to either a thinner passive film formation or a passive film with different conducting properties to that of pure iron. Figure 6 also showed the thickness values of the films on the surface. The reduction in the thickness of the passive film developed on Fe-N alloy was clearly seen with about 45A ° for pure Fe and 25 A° for Fe-N alloy.

The results of the surface analyses of the passive films on pure Fe and Fe-N alloy grown for 30 minutes after direct potential jump and also after hold at active potential indicated that no significant change occurred with respect to Fe (2p) peaks (Fig.7a). However, the analysis of the O (1s) peaks indicated that more hydroxyl ions are present in the film after holding at the active potential compared to the film grown after direct potential jump (Fig.7b). The high

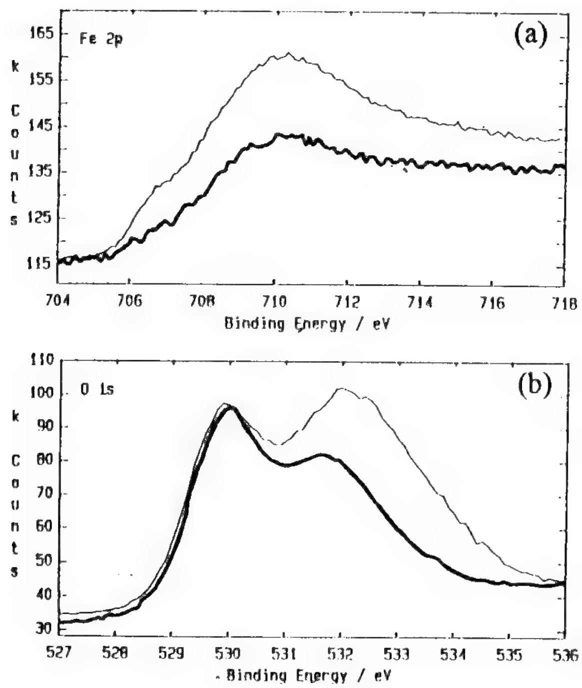

Fig.7 : XPS high resolution spectra of (a) Fe (2p) and (b) O (1s), from the passive films grown for 30 minutes after direct potential jump (▬) and potential jump with a hold at 200 mV for 2 s (—).

resolution spectra of N (1s) peaks are given in Fig.8a for both passive film conditions. The film grown after holding at the active potential showed a peak at 400.5 eV whereas the film grown after direct potential jump showed two peaks at 397.4 and 400.5 eV. The spectra after curve fitting are shown in Figs. 8b and 8c for films grown under both test conditions. A significant change in the area of the peaks was noticed being from 45 % to 62% for the peak at 400.3 eV, and from 55% to 38% for the peak at 397.4 eV for passive films grown after direct jump and after holding at active potential, respectively. The binding energy values at

397.4 eV represents nitrogen present as FeN [7], and that at 400.3 eV represents N dissolved in Fe [8]. It was clear from the present results that more nitrogen is present in the passive film when the specimen was dissolved at the active potential compared to the film grown after direct potential jump. Further, the incorporation of more hydroxyl ions in the passive film for the specimen held at active potential combined with the more availability of free nitrogen in the film suggested that the nature of the passive film was altogether different compared to the film grown after direct potential jump.

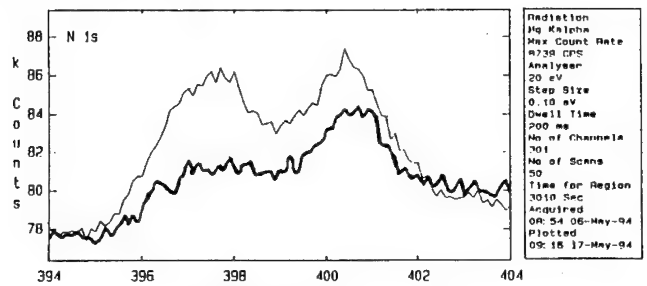

(a)

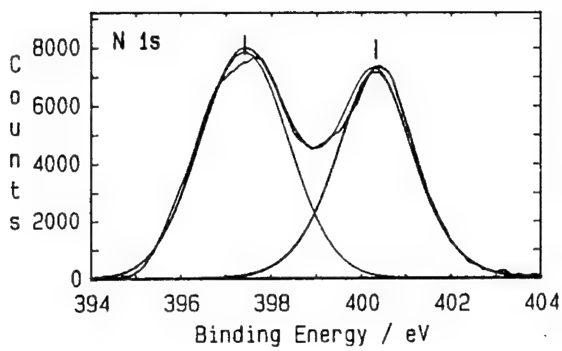

Peak	Centre (eV)	FWHM (eV)	Hght %	G/L %	Area %
	400.3	2.10	94	51	45
	397.4	2.32	103	1	55

(b)

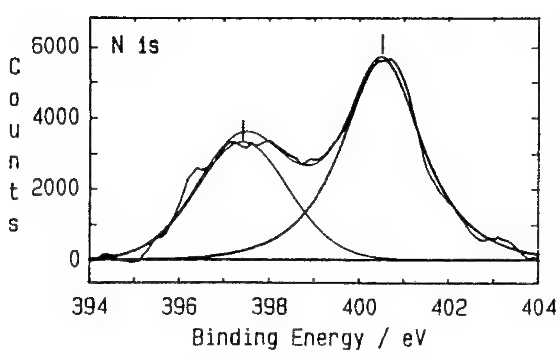

Peak	Centre (eV)	FWHM (eV)	Hght %	G/L %	Area %
	400.5	2.14	100	82	62
	397.4	2.47	59	28	38

(c)

Fig.8 : XPS high resolution spectra for N (1s) from the passive films grown for 30 minutes after direct potential jump (▬), and potential jump with a hold at 200 mV for 2 s (—), (a) as recorded, (b) curve fitted for (—) and (c) curve fitted for (▬).

Summary and Conclusions

1. From the potentiostatic transient experiments the time and charge required for the passivation of Fe-N alloy was found to be 34.9 ms and 25.9 mC/cm^2, respectively, in comparision with 295.9 ms and 260.45 mC/cm^2, respectively, for pure iron.
2. The steady state current and the charge required for passivation after holding at the active potential decreased significantly for Fe-N alloy compared to pure iron.
3. The thickness values calculated from the charge and the capacitance values indicated a decrease in the thickness of the passive film on Fe-N alloy.
4. The capacitance of the film on Fe-N alloy was higher compared to pure iron, however, the capacitance decreased for both when the potential jump was made from cathodic to anodic region.
5. The surface analyses of the films indicated that the film grown after holding at the active potential for Fe-N alloy contained more nitrogen and hydroxyl ions.

In general the dissolution kinetics was hindered and the passivation tendency improved significantly for pure iron with the addition of nitrogen. From the results of the present experiments a model by which nitrogen enhances the passivity is supported.

References

1. K. Osozawa and N.Okada, in Passivity and Its Breakdown on Iron and Iron-Base Alloys, National Association of Corrosion Engineers, Houston, USA, 135 (1976).
2. R.C.Newman, Y.C.Lu, R.Bandy and C.R.Clayton, in Proceedings of the Ninth International Congress on Metallic Corrosion, National Research Council, Ottawa, Canada, **4**, 394 (1984).
3. J.J. Eckenrod and C.W.Kovach, in Properties of Austenitic Stainless Steels and Their Weld Metals (Influence of Slight Chemistry Variations), ASTM STP 679, American Society for Testing and Materials, Philadelphia, USA, 17 (1979).
4. U. Kamachi Mudali, Studies on Pitting, Intergranular Corrosion and Passive Film in Nitrogen-Bearing Austenitic Stainless Steels, Ph.D Thesis, University of Madras, India, (1993).
5. U. König, M.M. Lohrengel and J.W. Schultze, Ber. Bunsenges. Phys. Chem., **91,** 426 (1987)
6. U. Stimming and J.W. Schultze, Ber. Bunsenges. Physik. Chem., **80**, 1297 (1976)
7 J.S.Murday and I.L.Singer, J. Vac. Sci. Tech. **17**, 327 (1980).
8 G.Principi, P. Mattenzzi, E. Ramous and G. Longworth, J. Mat. Sci. **15**, 2665 (1980).

Materials Science Forum Vols. 185-188 (1995) pp. 731-740

Effect of nitrogen on the passivity and passivity breakdown of high nitrogen austenitic steels

B. Reynders[1] and M. Stratmann[2]

[1] Max-Planck-Institut für Eisenforschung, Postfach 140 444, D-40074 Düsseldorf, Germany

[2] Friedrich-Alexander-University Erlangen-Nürnberg, Martensstr. 7, D-91058 Erlangen, Germany

Keywords: Nitrogen, high nitrogen steels, HNS, P900, P900N, P903, Fe, Fe-N, Fe-Ni, Fe-Ni-N, pitting corrosion, stress corrosion

Abstract: The corrosion behaviour of two High Nitrogen Steels (HNSs) was investigated in comparison to steels with similar composition but without or with a lower content of nitrogen. Model alloys (Fe-N, Fe-Ni-N) were investigated for comparison to pure Fe and Fe-Ni to separate the influence of nitrogen from that of other alloying elements.

1. Introduction

High nitrogen steels with a nitrogen content >0.5 wt.-% show very attractive mechanical properties, e.g. high strength at a good ductility. Moreover, it is reported by several authors, that the high nitrogen content also improves the corrosion resistance especially against pitting corrosion and also against stress corrosion cracking, intergranular corrosion and crevice corrosion [1-3]. The effect of nitrogen in these corrosion processes is not clearly understood up to now. In this study besides two complex multi-alloyed high nitrogen steels, model alloys were also investigated.

2. Investigations on high nitrogen steels

Two high nitrogen steels (P903 and P900N, Vereinigte Schmiedewerke GmbH (VSG)), which were manufactured by the PESR-process (**P**ressurized **e**lectro**s**lag **r**emelting-process) [4] at the Krupp Forschungsinstitut (KFI) were investigated in comparison to commercial steels with similar composition (Amagnit 3964, Thyssen and P900, VSG). New base materials (P903V and P900V) without any nitrogen were produced at the Max-Planck-Institute and experiments were conducted with them for comparison. The chemical composition of the materials used in this study are given in Table 1. Prior to experiments the materials were annealed at 1120°C for 2 hours followed by water quenching in order to obtain a homogenised microstructure retaining whole nitrogen in solid solution.

Several investigations have been carried out to clarify the effect of nitrogen for the different areas of application of the steels. P903 and Amagnit are mainly used in chemical industry and off-shore applications, while P900N and P900 were specially designed to manufacture retaining rings of turbine generators in power plants. Therefore investigations were done concerning the corrosion behaviour and the stress corrosion cracking behaviour of these materials in sodium chloride solutions and artificial sea water.

alloy	C	Si	Mn	Cr	Mo	Ni	V	Cu	Al	Nb	P	S	N
P900N	0.044	0.40	18.89	18.69	0.07	0.46	0.13	0.05	0.010	-	0.018	<0.001	0.90
P900	0.054	0.27	18.83	18.15	0.06	0.36	0.08	0.02	0.007	-	0.030	<0.001	0.58
P900V	0.0036	0.53	17.6	19.6	-	-	-	-	-	-	-	-	0.0075
P903	0.050	0.48	7.9	20.2	2.90	11.2	0.10	-	0.013	0.20	0.029	0.002	0.79
Amagnit 3964	0.03	0.40	5.1	20.63	3.01	15.25	-	-	-	0.19	0.012	0.009	0.29
P903V	0.0031	0.58	6.77	21.7	2.98	15.0	-	-	-	-	-	-	0.0125

Table1: Chemical composition of the experimental materials (wt.-%)

2.1. P903 - Amagnit 3964 - P903V

Potentiodynamic measurements were carried out on these steels in Ar-purged 1 and 3% sodium chloride solution and in artificial sea water at room temperature and at 60°C, and the potential was applied at a scan rate of 0.1 mV/s (Figs. 1a-c). A shift in the corrosion potential towards more cathodic potentials was noticed for these materials after the addition of nitrogen. With the increasing nitrogen content enlargement of the passive region was observed. Nitrogen improved the resistance to pitting corrosion with a shift of the pitting potential to more anodic values.

For studying the stress corrosion cracking (SCC) behaviour round tensile bar specimens (gage diameter: 3 mm, gage length: 15 mm) were strained by constant elongation rate test (CERT) in air (strain rate: $8.3 * 10^{-6}\ s^{-1}$) and in the above mentioned electrolytes (strain rate: $1.67 * 10^{-6}\ s^{-1}$) under potential control (Figs. 2a-c). The materials showed only overload rupture and no failures caused by SCC cracks or pits. The positive effect of nitrogen can be seen in the increase of the fracture stress for P903 (150 N/mm^2 higher in comparison to Amagnit 3964) [5].

a)

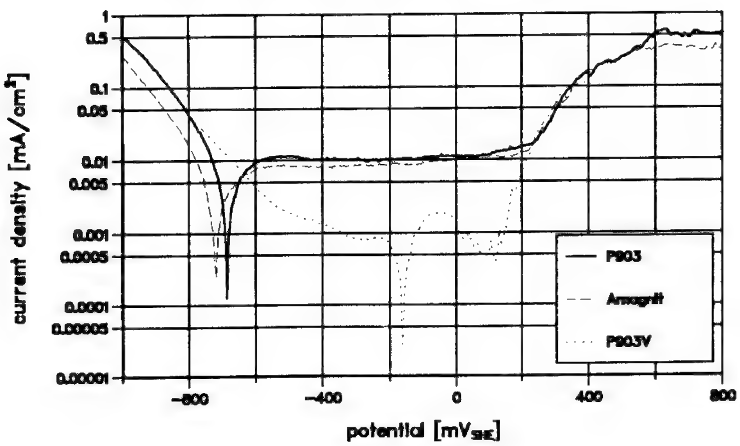

b)

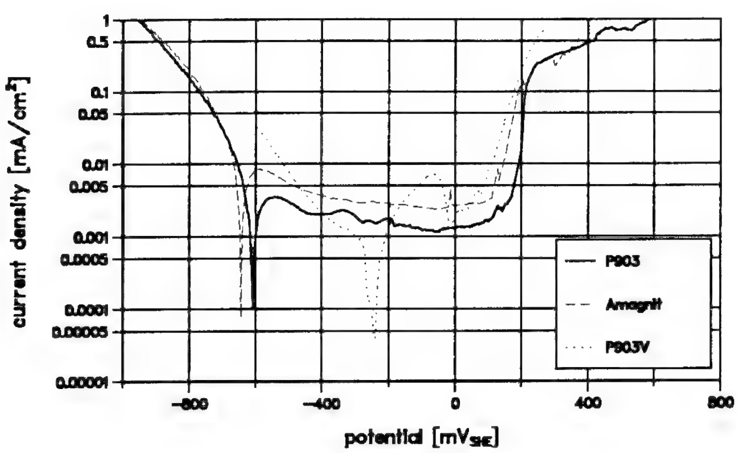

Figure 1: Current density-potential curves of
a) P903 - Amagnit - P903V in 3% NaCl solution at room temperature
b) P903 - Amagnit - P903V in 3% NaCl solution at 60°C

c)

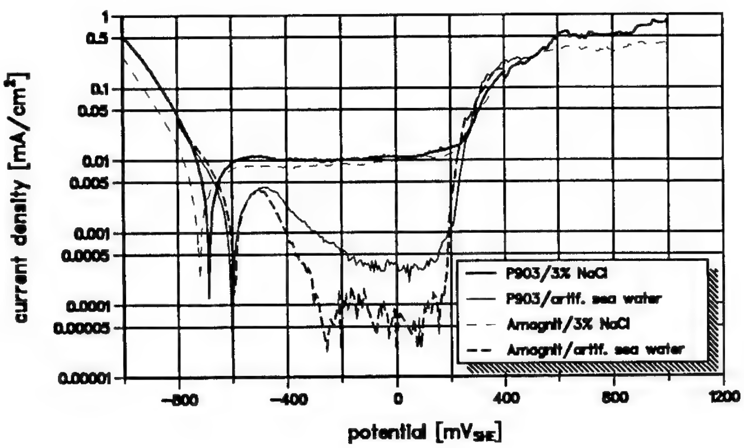

Figure 1: Current density-potential curves of
c) P903 - Amagnit in 3% NaCl solution and artificial sea water at room temperature

Figure 2: Stress-strain diagrams
a) of Amagnit and P903 in air
b) of Amagnit in electrolytes
c) of P903 in electrolytes

2a)

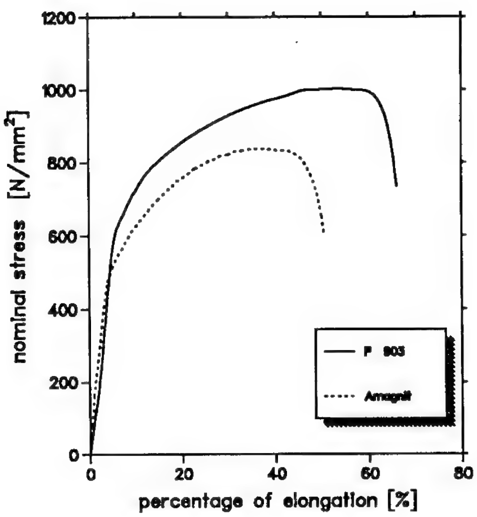

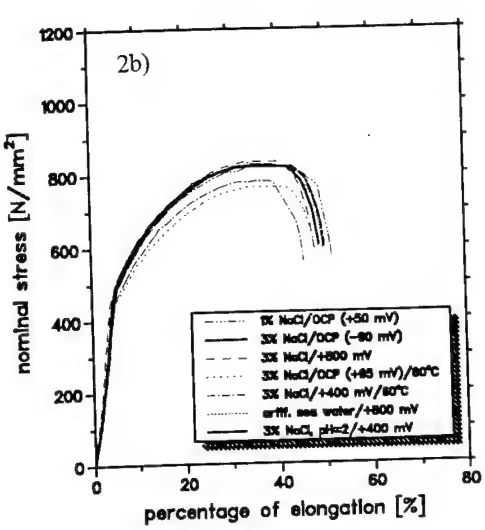

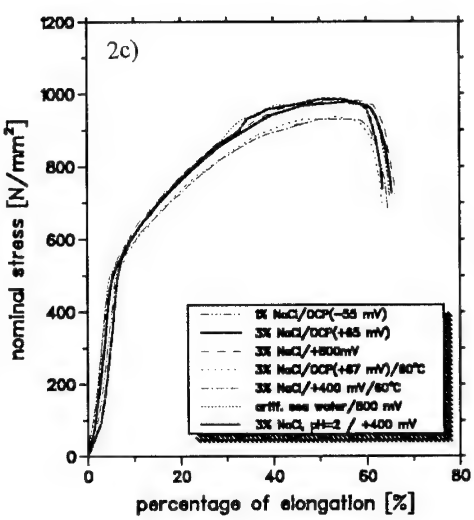

2.2. P900N - P900 - P900V

Polarization curves were obtained at a scan rate of 0.1 mV/s in de-aerated 1% NaCl solution at ambient temperature (Fig. 3). The corrosion potential was found shifted towards more cathodic potentials after the addition of nitrogen. P900 and P900N also had a wide passive plateaux with a gradual active-to-passive transition. For P900 the breakdown potential was found at 250 mV_{SHE}, while that of P900N was 320 mV_{SHE}. Pits were observed at the specimen surface after the polarization. Thus, the breakdown potential corresponds to the pitting initial potential.

Stress corrosion cracking experiments were carried out in air and 1% NaCl-solution (strain rates: see 2.1.). The stress versus percentage of elongation curves for tests in air are shown in Fig. 4. The results indicated that the strength increased with the increasing N-content, consistent with the results reported in the literature [6]. The strengthening mechanism was mainly attributed to the lattice expanding effect of dissolved nitrogen.

The results of the tests carried out in NaCl solution and the influence of the applied potential are shown in Figs. 5a and 5b. A significant reduction in tensile strength and ductility were noticed at 500mV_{SHE} for P900 and 635 mV_{SHE} for P900N, indicating the occurrence of SCC [7].

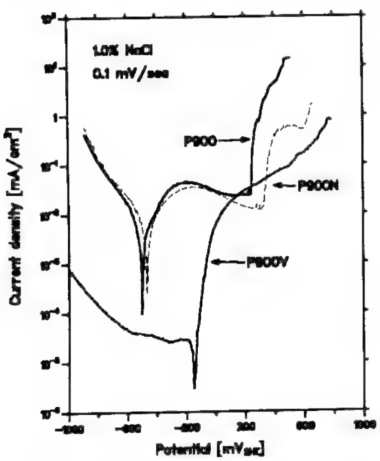

Figure 3: Current density-potential curves of P900V - P900 - P900N in 1% NaCl

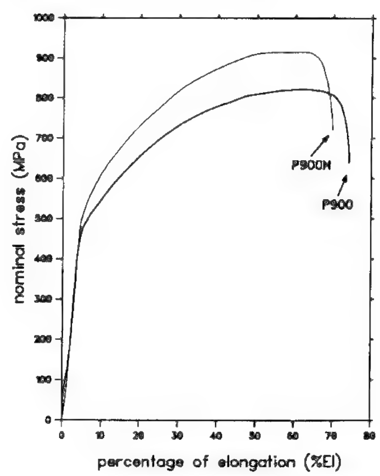

Figure 4: Stress-strain diagrams of P900 and P900N in air

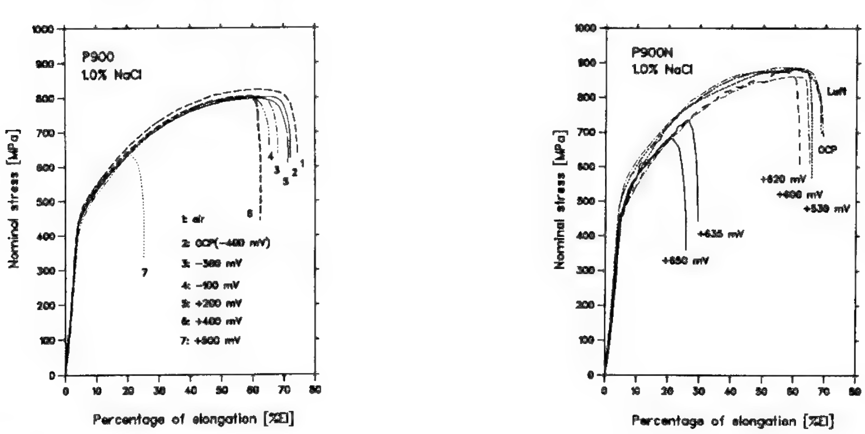

Figure 5: Stress-strain diagrams of
a) P900
in 1% NaCl solution at various potentials

b) P900N

3. Investigations on model alloys

To separate the influence of nitrogen on the corrosion behaviour of steels from that of other alloying elements model alloys (Fe-N, Fe-Ni-N) were prepared and then investigations were carried out with them. Further experiments are planned on the quaternary alloy Fe-Ni-Mo-N to elucidate the suggested synergetic effect between Mo and N [2].

3.1. Preparation of the model alloys

Iron-base alloys containing high concentrations of nitrogen can be prepared by nitriding in NH_3-H_2 mixtures, according to the reaction

$$NH_3\ (g) = N(\text{dissolved}) + 3/2\ H_2\ (g) \tag{1}$$

In NH_3-H_2 mixtures at elevated temperatures very high nitrogen activities can be achieved, corresponding to nitrogen pressures of some thousand bars. Thus high concentrations of nitrogen in the metal lattice can be obtained. To avoid the formation of nitrides, the nitriding was conducted at 810°C with a gas mixture of NH_3 - H_2, where, according to the 'Lehrer-diagram' [8], (Fig. 6) only the γ-solid solution of nitrogen in iron should be obtained. After nitriding for 24 h, Fe-N alloys were obtained with concentrations between 0.6 and 0.8 wt.-%. Quenching in oil leads to a martensitic microstructure (Fig. 7), with homogeneous nitrogen distribution as confirmed by measurements with electron microprobe analyser. The microstructure of the nitrided specimens showed pores in a surface-near region caused by the recombination of nitrogen in the lattice according to the reaction

$$2\ N\ (\text{dissolved}) = N_2\ (g) \tag{2}$$

For the investigation of localised corrosion phenomena, like pitting corrosion specimens with pores were unsuitable and hence short time nitriding (45 min.) was carried out to avoid pores. A metallographic cross section of iron after nitriding for 45 min. and subsequent quenching is shown in Fig. 8a. The nitrogen distribution was investigated by electron microprobe. The nitrogen concentration profile is given in Fig. 8b. After final preparation of the specimens for the studies a nitrogen concentration of approximately 0.9 wt.-% was present on the surface.

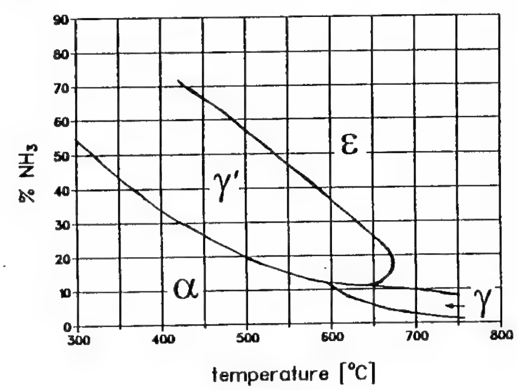

Figure 6: Phase diagram of Fe-N, showing stability ranges of phases formed in flowing NH_3- H_2 mixtures [8]

a) 

b) 

Figure 7: Metallographic cross section of iron nitrided for 24 h / 810°C
a) 50:1 b) 500:1

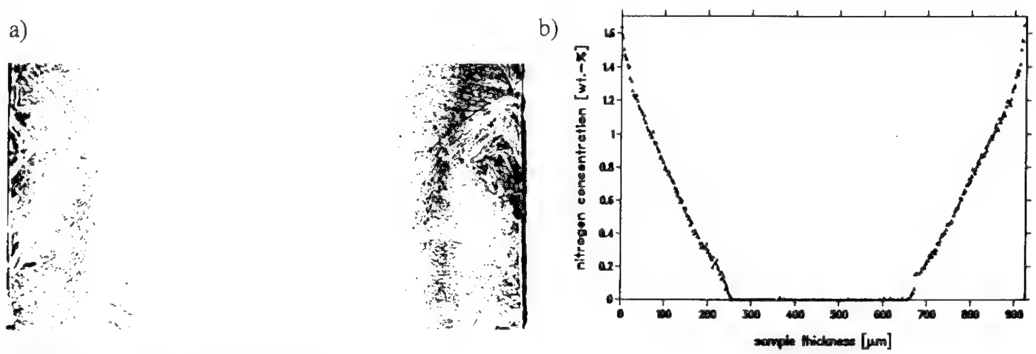

Figure 8: Iron nitrided for 45 min.
a) Metallographic cross section (100:1)
b) nitrogen concentration profile

For the preparation of the ternary Fe-Ni-N alloys, Fe-Ni-specimens (nickel content: 5, 10, 15, 20 wt.-%) were nitrided under similar conditions. The temperature was held at 810°C, so that the alloys were in the austenitic phase. In Fig. 9 the isothermal section of the phase diagram Fe-Ni-N is shown [9]. In the γ-phase the solubility of nitrogen decreases with the increasing nickel content. Therefore mainly Fe-10% Ni-alloys were used for investigations. A metallographic cross section of a Fe-10% Ni specimen nitrided for 45 min. and the nitrogen concentration profile measured with electron microbeam analyser are given in Figs. 10a and 10b. After final preparation of the specimens for the studies nitrogen concentration of approximately 0.4-0.6 wt.-% was present on the surface.

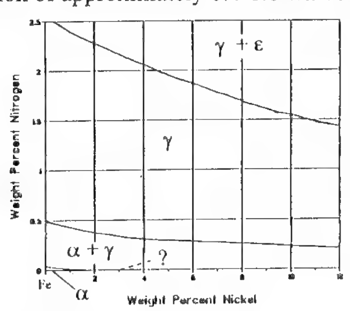

Figure 9: Isothermal section of the phase diagram Fe-Ni-N at 810°C [9]

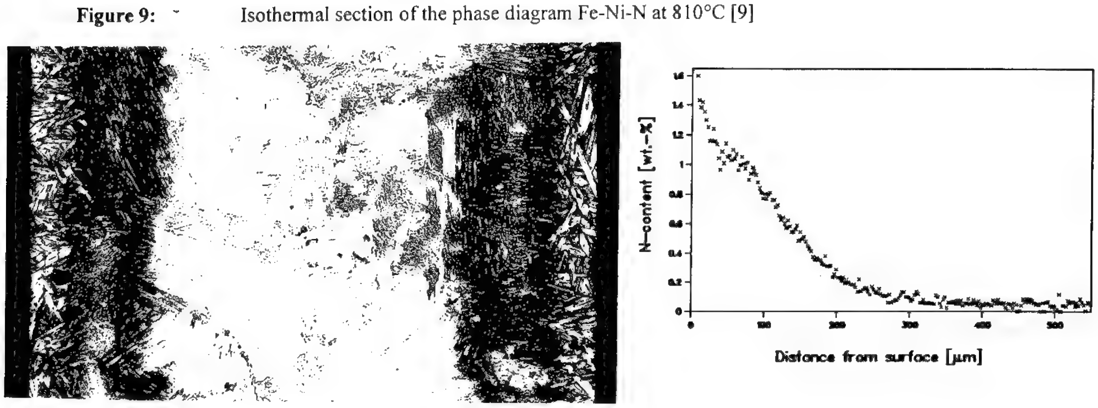

Figure 10: Fe - 10% Ni, nitrided for 45 min. at 810°C
a) metallographic cross section
b) nitrogen concentration profile

3.2. Experimental

The electrochemical behaviour of the nitrided alloys in comparison to nitrogen free specimens was investigated in solutions of sodium sulfate and sulfuric acid at constant ion concentrations (Table 2). Anodic polarization curves were measured, starting 200 mV below the corrosion potential at a sweep rate of 0.1 mV/s. The passivation kinetics was measured by recording the current density - time curves during a potential jump from the cathodic to the passive range. The Flade potential was measured after the potential jump and holding the sample in the passive range for 2 hours, and then by decreasing the potential at a sweep rate of 0.1 mV/s until reactivation occurs.

Number	Electrolyte		pH
	H_2SO_4 [mol/l]	Na_2SO_4 [mol/l]	
1	0.01	0.99	2.80
2	0.05	0.95	1.95
3	0.10	0.90	1.65
4	0.50	0.50	0.90

Table 2: Composition of the electrolytes used in this study

For testing the pitting behaviour experiments were conducted in the electrolytes 2 (Fe-N) and 1 (Fe-Ni-N) given in Table 2. Therefore after the potential jump into the passive region the electrode potential was fixed at 700, 1000 and 1300 mV_{SHE} for Fe-N and 600, 800 and 1000 mV_{SHE} for Fe-Ni-N. After adding chloride ions (NaCl; 10^{-3} mol/l for Fe-N; $5 \cdot 10^{-3}$ mol/l for Fe-Ni-N) the change in the current density with time was recorded. After reaching a current density of 10 mA/cm^2 the experiments were stopped and optical microscope investigations of the specimens were performed.

3.3. Results

3.3.1. Binary Fe-N alloys

The polarization curves for Fe and Fe-N are given in Figs. 11a and 11b. The resulting data for the corrosion potential and the corrosion density are shown in Table 3. In comparison to Fe the corrosion potential for Fe-N was shifted to more negative values and the nitrogen containing specimens showed a higher anodic dissolution rate confirmed by the higher values of the corrosion current. The higher anodic dissolution rate could be caused by an increase in the coverage of OH^- ions on the Fe-N alloy surface due to the formation of NH_3 and/or NH_4^+ during dissolution. According to Heusler [10] the dissolution of iron in acidic solutions is enhanced by the presence of OH^-.

Electroyte number	Pure Iron			Fe-N		
	E_{corr} [mV_{SHE}]	i_{corr} [mA/cm^2]	E_{Fl} [mV_{SHE}]	E_{corr} [mV_{SHE}]	i_{corr} [mA/cm^2]	E_{Fl} [mV_{SHE}]
1	-347	0.025	445	-365	0.45	493
2	-297	0.090	483	-327	1.10	526
3	-290	0.150	523	-300	1.20	566
4	-262	0.600	571	-273	2.10	620

Table 3: Corrosion potentials, corrosion current densities and Flade-potentials for pure iron and iron-nitrogen-alloys in sodium sulfate / sulfuric acid solutions of different pH

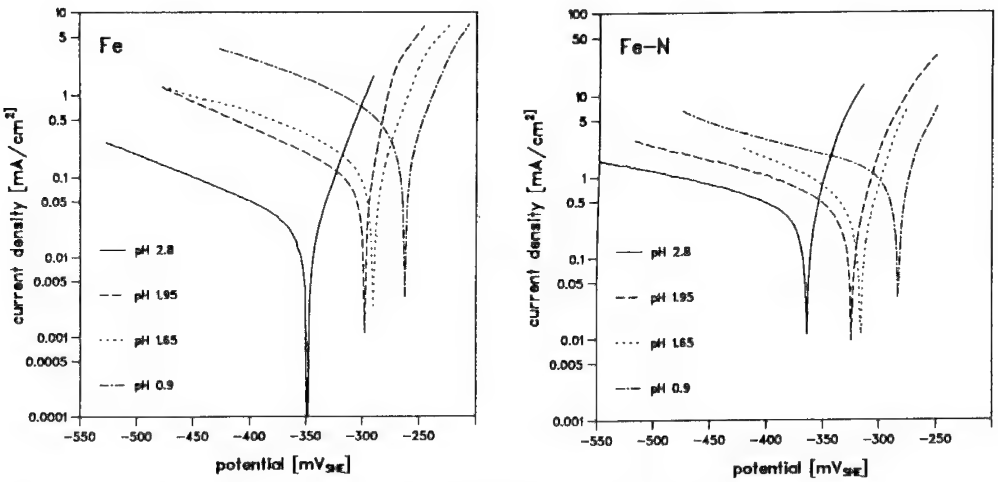

Figure 11: Current density-potential curves measured in H_2SO_4 - Na_2SO_4 solutions of different pH
a) Fe b) Fe-N

The Flade potentials obtained for Fe and Fe-N in all the test solutions are given in Table 3. The Flade potential for Fe-N alloys was about 45 mV higher than that for Fe, which means that the active range of the Fe-N alloys was markedly wider.

To study the passivaion kinetics of this alloys current density versus time curves obtained during a potential jump from -700mV_{SHE} to 900 mV_{SHE} for Fe and Fe-N were measured. The passivation kinetics is positively influenced by the nitrogen addition; a steady low passive current was noticed for the Fe-N alloy after 34.9 ms, whereas the passivation time for Fe was about 295.9 ms. More comprehensive investigations on the passivation kinetics of Fe-N compared to iron are described in [11].

Pitting corrosion experiments showed that a high nitrogen content in iron markedly suppressed pitting corrosion; the incubation time for pitting was prolonged and the extent of attack was greatly decreased [12].

3.3.2. Ternary Fe-Ni-N alloys

The addition of nitrogen caused a shift of the corrosion potential to more cathodic values and a decrease of the corrosion rate was observed. As an example the polarization curves of Fe-10% Ni - N and the nitrogen free alloy in solution 3 are shown in Fig. 12. This potential shift can be explained by the slowing down of the cathodic reaction as well as by a significant acceleration of the metal dissolution. This acceleration was presumably caused by a pH-shift by nitrogen explained above.

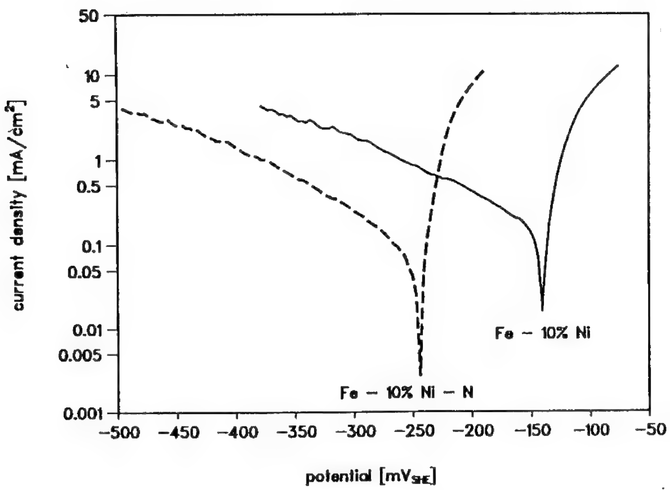

Figure 12: Current density-potential curves for Fe - 10% Ni and Fe - 10% Ni - N in 0.1 H_2SO_4/0.1 Na_2SO_4

The passivation behaviour is positively influenced by nitrogen. The nitrogen dissolved in the lattice favours the formation of a passive layer; both the passivation time and the charge were decreased by the nitrogen addition [13].
In pitting corrosion experiments (electrolyte 1 + 5 $*$ 10^{-3} m NaCl) at different potentials in the passive range the pitting incubation time was distinctly increased in case of the nitrided specimens (Table 4, Fig. 13).

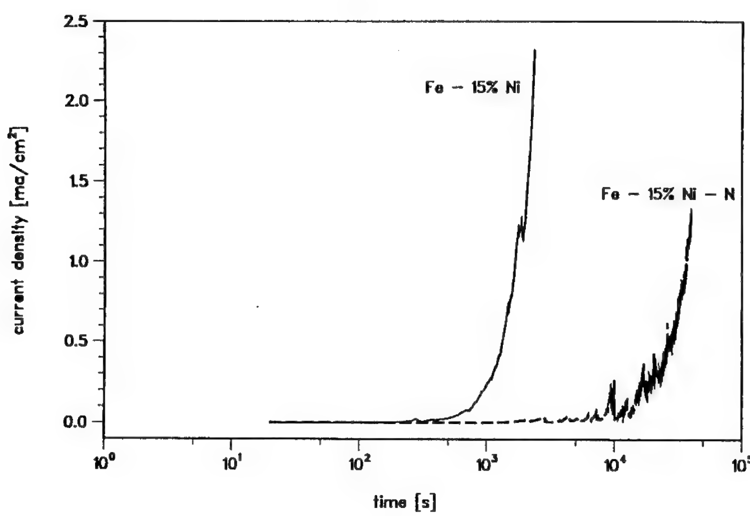

Figure 13: Current densitiy-time curves of Fe-15% Ni and Fe-15% Ni-N at 600 mV_{SHE} in 0.01m H_2SO_4 / 0.99 m Na_2SO_4 / 5 $\cdot 10^{-3}$ m NaCl

	Pitting incubation time [min]		
	600 mV_{SHE}	800 mV_{SHE}	1000 mV_{SHE}
Fe - 5% Ni	45	-	13
Fe - 5% Ni + N	266	-	16
Fe - 10% Ni	40	33	17.5
Fe - 10% Ni + N	450	78	17.5
Fe - 15% Ni	17	67	23
Fe - 15% Ni + N	350	58	60
Fe - 20% Ni	112	-	25
Fe - 20% Ni + N	250	-	72

Table 4: Results of the pitting corrosion experiments in 0.01 m H_2SO_4 / 0.99 m Na_2SO_4 / $5 \cdot 10^{-3}$ m NaCl

4. Conclusions

- Active dissolution of nitrogen-containing alloys was found to be accelerated in comparison to nitrogen free alloys. This effect can be explained by the formation of OH^- ions during active dissolution caused by the formation of NH_3 and/or NH_4^+ at the metal electrolyte interface [10].

- The pitting corrosion resistance was positively influenced by nitrogen addition. The presence of nitrogen decreases markedly the extent of pitting and prolongs the incubation time before start of pitting.

- Nitrogen improves the stress corrosion cracking resistance of High Nitrogen Steels. The fracture stress was increased by nitrogen, which can be explained by the lattice expanding effect of dissolved nitrogen. The critical potential for SCC was increased by the addition of nitrogen, similar to the shift of the pitting potential to more anodic values.

5. Literature

[1] J.E. Truman, M.J. Coleman, K.R. Pirt, British Corrosion Journal **12**, 236 (1977)
[2] R.C. Newman, Y.C. Lu, R.Bandy, C.R. Clayton, Proceedings of the 9th International Congress on Metallic Corrosion **4**, 394 (1984)
[3] U. Kamachi Mudali, Ph.D. Thesis, University of Madras, India (1993)
[4] P. Pant, P. Dahlmann, W. Schlump, G. Stein, Steel research **58**, 18 (1987)
[5] K. Gnann, Diplomarbeit, University of Erlangen (1993)
[6] M.O. Speidel, Proceedings Int. Conf. on High Nitrogen Steels, HNS 88, Lille, France, 251 (1988)
[7] W.T. Tsai, B. Reynders, M. Stratmann, H.J. Grabke, Corrosion Science **34.10**, 1647 (1993)
[8] E. Lehrer, Z. Elektrochemie **36**, 382 (1930)
[9] V. Raghavan, Phase Diagrams of Ternary Iron Alloys, Part 1, Indian Institut of Technology, Dehli (1982)
[10] K.F. Bonhoeffer, K.E. Heusler, Z. phys. Chemie N.F. **8**, 390 (1956)
Z. Elektrochemie Ber. Bunsengesellschaft phys. Chemie **62**, 582 (1958)
[11] U. Kamachi Mudali, B. Reynders, M. Stratmann, this volume
[12] S. Hirsch, Studienarbeit, Technical University Merseburg (1992)
[13] S. Hirsch, Diplomarbeit, Technical University Merseburg (1993)

Materials Science Forum Vols. 185-188 (1995) pp. 741-748

The formation and properties of a thick passive film on Fe-Cr alloys with square wave potential pulse polarisation

S. Fujimoto and T. Shibata

Department of Materials Science and Processing, Faculty of Engineering, Osaka University, 2-1 Yamada-oka, Suita, Osaka, 565 Japan

Keywords: Interference colour, pitting, XPS, TEM, ultra-microtome, stainless steel

Abstract – Extraordinarily thick passive film (0.05 μm to few μm) showing interference colour is obtained for Cr containing Fe based alloys with square wave potential pulse polarisation. Type304 Stainless steel was polarised in 0.5 or 5 kmol m^{-3} H_2SO_4 solution with the applied potential modulated as square wave. The frequency and total polarisation time were typically 5 Hz and 20 min., respectively. The thick passive film is obtained when the lower potential of the square wave, E_L, is in the active region and the higher potential, E_H, is in the passive region of Cr, respectively. Fe^{2+} and Cr^{2+} dissolve at E_L, and then Cr^{2+} ions are re–oxidised into Cr_2O_3 and/or $Cr(OH)_3$ at E_H. The film consists of mainly Cr oxide and hydroxide. This film, however, never inhibits any initiation of localised corrosion in chloride solution, and the film grows following a linear rate law. Therefore, this film seems to contain many pathways, which permit subsequent growth without any decrease in the rate and penetration of water and ions. The initial network structure of chromium oxide/hydroxide, which is formed at E_L and have many defects through which ions and water molecular pass, is preserved according to deprotonation under the high field provided by E_H. The repetition of the cycle results in further formation of the film beneath the previously formed layer.

INTRODUCTION

Passive film on stainless steel is usually very thin and consists of oxide or hydroxide layer, which is highly protective to give the superior corrosion resistance to steels. On the other hand, thick films which show interference colour can be obtained on stainless steels using some chemical procedures, such as INCO process[1,2]. The thickness of the film is 0.05–0.2 μm, that is extremely thicker compared with ordinary passive film, and is reported to be porous. The processes, that are essentially based on electrochemical reactions, can be substituted for electrolytic processes. Sone *et al.*[3] reported an alternative constant current (galvanostatic) polarisation process in a hot sulphuric acid bath containing Cr^{6+}, which are also contained in the INCO process bath. Recently, Oki *et al.*[4] introduced an alternative potential polarisation process. This square wave potential pulse method can be operated with acid or alkaline bath containing no Cr^{6+} ions. These processes are considered to be essentially based on cathodic reduction of Cr^{6+} into Cr^{3+} oxide deposition. However, we reported a similar thick film formation as an anodic process with similar square wave potential pulse polarisation[5,6]. The mechanism and preferable conditions for this process, however, are still not defined yet. In this report, the electrochemical regions for anodic and cathodic film

formation have been evaluated. The structure and properties, including pitting potential, of the film are also analysed to propose a mechanism for this extraordinarily thick anodic film formation.

EXPERIMENTAL

Materials and solution

The materials tested was a commercial bright annealed Type304 stainless steel sheet of 0.1 mm in thickness. The material was cut into coupon specimens of 10 mm x 12 mm, and attached to a connecting wire of the same material. The specimen was electrochemically polished in a phosphoric acid + sulphuric acid (7 Vol./3 Vol.) solution at a constant bath voltage of about 5V, then rinsed with distilled water. The test solution was deaerated 0.5 or 5 kmol m^{-3} H_2SO_4.

Procedure

The applied potential was modulated as square wave as shown in Fig.1. The higher and the lower potentials are described as E_H and E_L, and the width of both pulses t_H and t_L, respectively. The square wave potential pulse was applied at the same time of immersion, and was continued typically for 20 minutes. A platinum counter electrode and a Ag/AgCl/3.3 kmol m^{-3} KCl reference electrode were used for electrolysis processes.

Characterisation of films

The thickness of the film can be estimated from the colour which is derived from interference of visible light between the light reflected at the surface and that reflected at the film/substrate interface. The wave lengths, λ, of the light which is enhanced or diminished by interference are given as follows:

$$2d\sqrt{n^2 - \sin^2 i} = \begin{cases} m\lambda & \text{(enhancement)} \\ (m - 1/2)\lambda & \text{(diminution)} \end{cases}$$

where d is the thickness of the film, n is the refractive index, i is the incident angle of the light, m is the order of interference which is natural number. In this work, ultra–violet/visible reflectance spectrum was measured using spectrometer. According to the above equation, the relation between the interference wave number, that is reciprocal of wave length, $1/\lambda$, and order of the interference becomes a straight line that passes the origin as shown in Fig.2. The slope of the line gives $2d\sqrt{n^2 - \sin^2 i}$. In this work, 83 degree was employed for i. The refractive index adopted here was n=2.55, because most of reported value for iron or chromium oxide are around this number.

The film structure was characterised by XPS and TEM. Specimen for TEM observation was prepared as follows using an ultra–microtome technique[7]. The coloured specimen was mounted in resin and cross section approximately 50 nm in thickness was obtained using an ultra–microtome. The sections were examined using a transmission electron microscope.

Pitting Potential

Pitting corrosion susceptibility was measured for the Type304 steel covered with the coloured film which was produced at the following conditions: in 0.5 kmol m^{-3} H_2SO_4 at 50°C, E_H=1050 $mV_{Ag/AgCl}$, E_L=–440 $mV_{Ag/AgCl}$, t_H=t_L=0.5 s for 40 minutes. The pitting potential was measured with potentio–dynamic polarisation with the scanning rate of 20 mV $min.^{-1}$, in 3.5 wt% NaCl solution. The pitting potential without coloured film was also measured for

comparison.

RESULTS

Thickness of the Film depending on the applied potentials

The variation of thickness as functions of E_H and E_L has been reported for wide potential range. In this report, results for some specific potential region are provided, that is critical to discuss the film formation mechanism. Figures 3(a) and (b) show the variation of the film thickness formed in 5 kmol m^{-3} H_2SO_4 at 50 C for 1200 s, with t_H=t_L=0.04 s. As shown later, the film growth rate does not change with the elapse of time. Therefore, the comparison between film thickness can be regard as film formation rate. In Fig.3(a), changes in thickness for various E_L are shown for three specific E_H of 1250, 1100, and 1000 mV$_{Ag/AgCl}$, that are in transpassive, transition from passive to transpassive, and passive region of chromium, respectively. When E_H is in the transpassive region, 1250 mV$_{Ag/AgCl}$, thickness of film is fairly large and is independent of E_L. For E_H in the passive range of chromium, in contrast, film thickness decreases with increasing E_L, and no coloured film obtained above −260 mV$_{Ag/AgCl}$, which is equivalent to the lower limit of the passive range of chromium. According to Fig.3(b), when E_L is in the passive region of chromium, thick films are observed if E_H is above 1100 mV$_{Ag/AgCl}$, which is the beginning of the trans-passive region. On the other hand, for the E_L in active region of chromium, the coloured film is formed in the passive region of the chromium and gradually becomes thicker, then grows rapidly above 1100 mV$_{Ag/AgCl}$.

Film Growth

Changes in the thickness with the time elapsed is shown in Fig.4. As can be seen in this figure, the film grows linearly.

A marker test was conducted in order to discuss the film growth mechanism. Prior to deposition, gold was deposited on the stainless steel substrate by evaporation in a vacuum, then coloured film was formed as usually. The gold deposition is confirmed to affect nothing for film formation. The profile of gold distribution, which was analysed by XPS with sputtering, prove to be located only at the surface above the thick film. This means the film grows at the film/substrate interface.

Film Structure

In the present work, the authors are interest in the film formed at the condition that E_L is in active and E_H in passive region of chromium, respectively, that is, the film formed as anodic process discussed later. In the following, the results for anodically formed films are described. XPS analysis shows the chemical structure reveals no distinguished variation for films formed in various conditions. Generally, the film consists of mainly chromium oxide and hydroxide, with the cation ratio, [Cr]/([Fe]+[Cr]+[Ni]), in the range of 75–85 %.

Figure 5 is the TEM micrograph of a coloured film obtained under the condition shown in the caption to the figure. The film was formed on a stainless steels sheet which was not subjected to electrolyte polishing prior to the film formation. Although the substrate alloy is successfully sectioned thin enough to get light image, the contrast of the substrate is made dark in order to obtain clear image of the film, because the density of film is greatly smaller compared with that of substrate. The texture of the micrograph show the film is porous and consists of microstructure of approximately 30–50 A. The selected area electron diffraction pattern shows this film composes of fine crystalline.

Pitting Corrosion Susceptibility

Pitting potentials for Type304 steel with and without coloured films are described on the regular distribution plots as shown in Fig.6. No appreciable difference was recognised between these two plots. Therefore, although the films covered the stainless steel surface are very thick compared with ordinalry passive film, this film has no further effect on inhibition of localised corrosion.

DISCUSSION

Preferable Potentials for Anodic Thick Film Formation

We reported[5] the variation of film thickness for a wide range of applied potentials of the square wave, E_H and E_L. When E_H is in the transpassive region, the thick film forms for E_L in the range covering the active and the passive region of chromium. If E_H is in the passive region of chromium, on the other hand, the coloured film is only obtained when E_L is in the active region. According to Fig.3, if E_L lies in the active region of chromium, the film growth rate increases steadily with increasing E_H, and then rises abruptly at around 1100 $mV_{Ag/AgCl}$, coinciding with the onset of transpassive region of chromium. Moreover, no coloured film was obtained if both E_L and E_H were in the passive region. Alternatively, if E_L is in the passive region, coloured film is formed only when E_H lies in the transpassive region. Therefore, it is concluded that, when E_L is in the active region, the film formation mechanisms are different for E_H in the passive and in the transpassive region of chromium.

Oki *et al.*[4] reported that coloured films were obtained when E_H was in the transpassive region and E_L was in the potential range covering from the active to the passive region of chromium. They discussed that Fe^{3+} and $Cr_2O_7^{2-}$ were formed as transpassive dissolution at the higher potential of square wave, then $Cr_2O_7^{2-}$ was reduced into a chromium–enriched oxide film at the lower potential. In the present work, results which supports this are obtained indeed, that is, formation of the thick film in the case that E_H is in the transpassive and E_L in the active and the passive region of chromium. Consequently, the film obtained under this condition is formed by cathodic reduction of Cr^{6+} which is formed as transpassive dissolution. On the other hand, the film formed under the condition that E_L is active and E_H[5,6] in passive region must be ascribed to another mechanism which we mentioned previously, because cathodic reduction of Cr^{6+} is impossible under this condition. The proposed mechanism is briefly that the hydroxide which is formed as the result of active dissolution of Cr^{2+} at E_L is re–oxidised into oxide and/or hydroxide of Cr^{3+}, which then loses protons to be oxide and/or hydroxide of Cr^{3+} under the high field provided at E_H. Accordingly, this mechanism is described as an anodic film formation process. The results in this work reasonably support this idea. Therefore, it is concluded that the thick film obtained by the square wave potential pulse polarisation is formed by both anodic and cathodic mechanism depending on the applied potentials, that are, E_H and E_L.

The growth mechanism of the anodic film will be discussed in the following. As already described, this film consists of hydroxide and oxide of mainly chromium, that is similar to usually obtained passive film on Fe–Cr alloys. However, this film is extraordinarily thick, porous and non–protective (*i.e.* localised corrosion resistance is not improved). According to the TEM micrograph, the film structure is 'gel' type, and has many channels through which ions and water molecular pass. In the usual passivation process of the Fe–Cr alloys, a selective dissolution of iron leaves hydrated chromium which becomes very thin, fine, and highly protective passive film with elapsed time, at high field provided by an anodic polarisation. Alternatively, the process for the square wave potential pulse polarisation is assumed as follows. Cr^{2+} which dissolves with Fe^{2+} instantaneously forms chromium

hydroxide network at E_L, the structure of which may be fluid 'sol' like, because distribution of Cr ions is fairly sparse due to selective dissolution of Fe. Then the initial network becomes 3–dimensional 'gel' type with many diffusion paths, in which hydrated Fe^{2+} or Fe^{3+} might be trapped. At the next cycle of E_L, similar 'sol' type chromium is formed beneath the previously formed 'gel' network. In this period, newly ionised Fe^{2+} and re–activated Fe^{2+}, which is trapped in the film pass through the film to bulk solution. At the next E_H period, the 'sol' network newly formed at the film/substrate interface is converted to be 'gel' film. The 'gel' type 3–dimensional network may condense locally to be fine crystalline textures leaving many pathways linking with each others. The repetition of the cycle results in the thick porous layer of oxide/hydroxide.

The thick and porous film, showing interference colour, has similar structure and appearances to that of INCO film[2,8], which is essentially formed as cathodic process. The film obtained in the present work, however, is concluded to form according to an anodic reaction, which is similar to the ordinary passivation on stainless steels. Although the mechanism of this thick anodic film formation has been not understood in detail, the discussion on this film may give a clue for further understanding of the passivity phenomena.

CONCLUSIONS

1. The thick films showing interference colours are obtained on Type304 stainless steel using square wave potential pulse polarisation in H_2SO_4 solution.
2. The film formation mechanism is concluded to be classified into two processes according to the applied potentials. When the higher potential, E_H, of the square wave is in transpassive region and the lower potential, E_L, in passive region, the film grows as reduction of Cr^{6+}, which is formed as transpassive dissolution, into oxide or hydroxide. Alternatively, if E_L is in the active and E_H in passive region of chromium, the film is formed as anodic process.
3. The anodic type film consists of mainly chromium oxide and/or hydroxide, similar to usual passive film of stainless steel, but has many defects through which ions and water molecules pass and then non–protective. The TEM micrograph which is obtained using ultra–microtome technique reveals that this film consists of fine crystalline with the size in the range 3 to 10 nm, and has many pathways linking with each others.
4. The initial 'sol' network of chromium oxide/hydroxide, which is formed at E_L as a result of selective dissolution of iron, is preserved by de–protonese under the high field provided at E_H to be 3–dimensional 'gel' type network. The repetition of the cycle results in further formation of films beneath the previously formed film to be a thick porous anodic film.

Acknowledgement

The authors gratefully acknowledge to Dr K. Shimizu of Keio University for his helpful discussion and for collaboration of TEM observation using ultra–microtome technique. The authors also acknowledge to Research Center for Ultra–High Voltage Electron Microscopy, Osaka University for TEM observation.

REFERENCES

[1] T.E. Evans, A.C. Hart and A.N. Skedgell, *Trans.Inst.Met.Finishing* **51**, 108 (1973).
[2] R. Blower and T.E. Evans, *Sheet Metal Ind.* **51**, 230 (1974).
[3] Y. Sone, K. Shimizu, S. Kurahashi, M. Ishii, S. Hasuno and S. Suzuki, *Materials and Process* **1**, 689 (1988).
[4] B.–Z. Yun, M. Okido and T. Oki, *Hyomen–Gijutsu* **39**, 505 (1988).

[5] S. Fujimoto, T. Shibata and K. Wada, *Tetsu-To-Hagane* **77**, 1192 (1991).
[6] S. Fujimoto, T. Shibata, K. Wada and T. Tsutae, *Corros.Sci.* **35**, 147 (1993).
[7] B. Bethune, G.E. Thompson and G.C. Wood, *Corros.Sic.* **19**, 63 (1979).
[8] R.C. Furneaux, G.E. Thompson and G.C. Wood, *Corros.Sci.* **21**, 23 (1981).

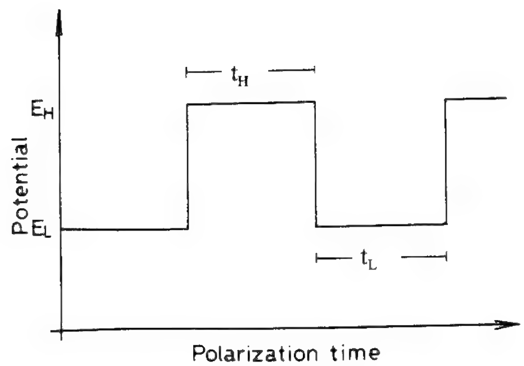

Figure 1 Potential wave form used for the square wave potential pulse polarisation.

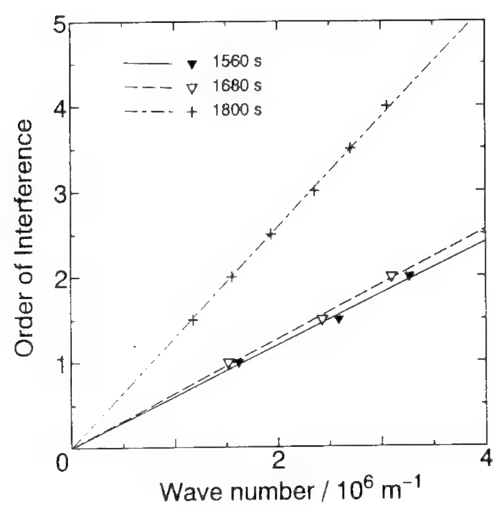

Figure 2 Relation between wave number, that is, reciprocal wave length, $1/\lambda$, and order of reflectance, *m*. Films were formed in 5 kmol $m^{-3}H_2SO_4$ at 50 C, E_H=1000, E_L=-410 $mV_{Ag/AgCl}$, t_H=0.04 s, t_L=0.02.

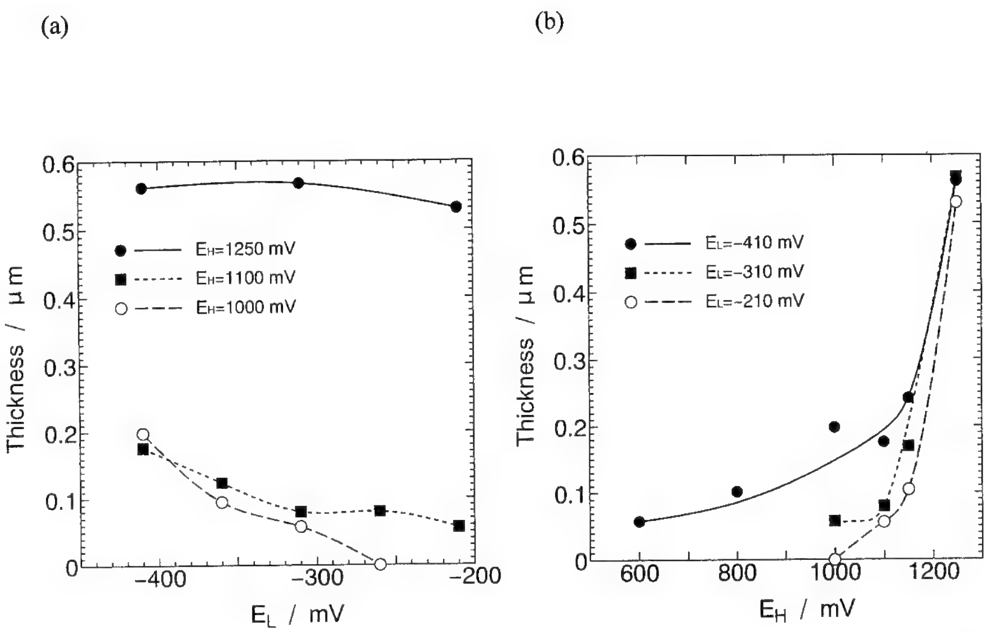

Figure 3 Variation of the thickness of the films for various applied pulse potential. The film formed in 5 kmol $m^{-3}H_2SO_4$ at 50 C, t_H=t_L=0.04 s for 1200 s.

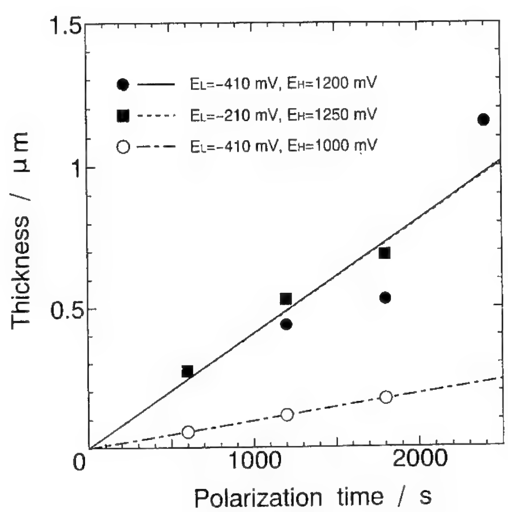

Figure 4 Change in the thickness of the films with polarisation time in 5 kmol $m_{-3}H_2SO_4$ at 50 C, t_H=0.04 s, t_L=0.02 s.

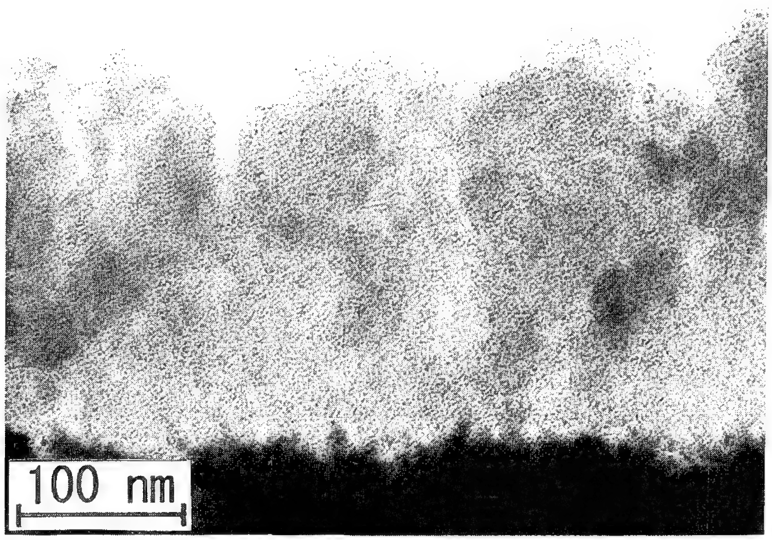

Figure 5 Transmission electron micrograph of the cross section of the film on Type 304 stainless steel. This film was formed in 5 kmol $m^{-3}H_2SO_4$ at 50 C, E_H=1100, E_L=-430 $mV_{Ag/AgCl}$, t_H=t_L=0.1 s, for 1200 s. The specimen was prepared using an ultra-microtome technique.

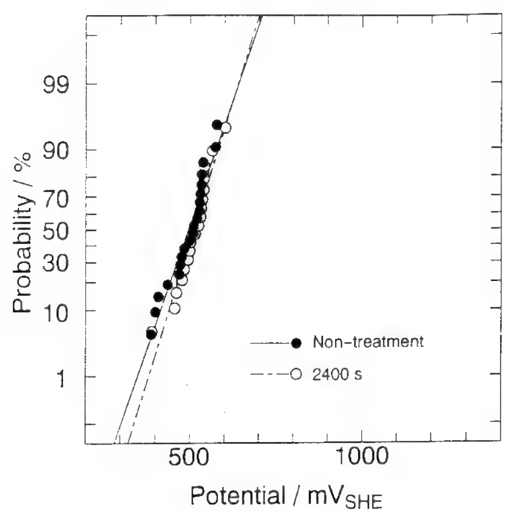

Figure 6 Normal distribution plots of pitting potentials for Type304 stainless steel with and without the coloured film measured in 3.5% NaCl using potentiodynamic polarisation with scanning rate of 20 mV $min.^{-1}$. The film was formed in 0.5 kmol $m^{-3}H_2SO_4$ at 50 C, t_H=0.1 s, t_L=0.1 s, E_H=1050, E_L=-440 $mV_{Ag/AgCl}$. The thickness of the film was *ca.* 300 nm.

Materials Science Forum Vols. 185-188 (1995) pp. 749-758

The influence of copper on passivation of Fe-Cr-Cu and Fe-Cr-Ni-Cu stainless steel

A. Mazurkiewicz[1], J. Glownia and J. Banas[2]

[1] Radom Technical University, ul. Malczewskiego 22, PL-26-600 Radom, Poland

[2] University of Mining and Metallurgy, Faculty of Foundry Engineering, ul. Reymonta 23, PL-30-059 Kraków, Poland

Keywords: Passivation, stainless steels, copper in steels

Abstract
The anodic passivation of Fe-Cr-Cu and Fe-Cr-Ni-Cu cast alloys has been investigated in 1M H_2SO_4 and 1M H_2SO_4 - NaCl solutions. The presence of copper in a solid solution (ferrite, austenite) does not influence the stability of a passive film, but the precipitation of copper as ε -phase has a detrimental effect on corrosion resistance of passive chromium-nickel steels.

Introduction

Copper stimulates active-passive transition of iron-chromium alloys and therefore is very often used as a cathodic component of high-alloyed stainless steels [1,2]. Though the effect of this metal on active-passive transition is very well known nevertheless the influence of copper on the stability of a passive film is not sufficiently recognised.

The solubility of copper in austenite is relatively high (~ 4%) [3]. This metal does not form carbides but stimulates the graphitization of high-alloyed cast iron [4,5]. As it is known, copper is one of the elements that increase the stacking fault energy (SFE) of austenite . The growth of the SFE reduces the distance between partial dislocations containing the stacking faults, reducingplanes at the same time the frequency of their occurrence. These dislocations adjoining the slip form dislocation pile-ups that testify to the increase of SFE [6,7]. The stacking fault energy of austenite is very important, because it determines the susceptibility of austenite to intercrystalline fracture during stress corrosion [4].

The solubility of copper in ferrite is low (~0.2%) [8]. Depending on the copper content and the heat treatment, the precipitation of ε-phase occurs in ferritic and ferritic-austenitic stainless steels. The small grains of this phase (< 300A) contain up to 96%Cu. The presence of ε–phase in ferrite increases the hardness of ferritic steels [9].

This work concerns the influence of copper content in chromium and chromium-nickel stainless steels on the stability of a passive film. Different alloys were taken into account: alloys with dissolved copper (austenitic stainless steels) and alloys containing dispersed inclusions of ε-phase (ferritic and duplex austenitic-ferritic steels).

Experimental

The chemical composition of alloys is shown in table 1. Table 2 presents the heat treatment and structure of the investigated cast steels. The structural investigations included the conventional metallographic analysis, analysis of the segregation of elements by means of a CAMECA MS 46 X-ray analyser and transmission electron microscope analysis with the application of a thin film technique.

Table 1

The chemical composition of alloys

No. of sample	Chemical compositioin, wt %								
	C	Mn	Si	P	S	Cr	Ni	Mo	Cu
M1	0.05	0.18	0.30	0.020	0.018	18.10	11.25	2.25	--
M2	0.05	0.21	0.028	0.020	0.019	18.40	11.65	2.20	1.20
A1	0.06	0.28	0.34	0.021	0.017	23.25	23.15	2.84	1.30
A2	0.06	0.29	0.42	0.020	0.018	22.95	22.20	2.70	3.35
F1	0.06	0.18	0.21	0.020	0.019	17.85	--	--	0.02
F2	0.06	0.15	0.19	0.023	0.018	17.05	--	--	0.73
F3	0.05	0.15	0.25	0.021	0.018	17.90	0.10	--	1.58
AF1	0.07	0.27	0.36	0.022	0.016	24.10	6.46	3.12	1.34
AF2	0.08	0.28	0.41	0.020	0.018	24.35	6.15	2.95	3.35

M1, M2 - monocrystals α
A1, A2 - austenitic cast steel
F1, F2, F3 - ferritic cast steel
AF1, AF2 - austenitic - ferritic cast steel

Table 2

The heat treatment and structure of the investigated cast steels

No. of sample	Heat treatment	Structure
M1, M2	Cast state	α – monocrystal
A1,	Cast state	γ
A2	Cast state	$\gamma+M_{23}C_6$
A1,	Solution annealing state 1050°C/w	γ
A2	Solution annealing state 1050°C/w	$\gamma+M_{23}C_6$
A1, A2	After solution annealing ageing at 700°C/8h	$\gamma+M_{23}C_6+\sigma$
F1	Cast state	$\alpha+M_3C$
F2	Cast state	$\alpha+M_3C$
F3	Cast state	$\alpha+M_3C+\varepsilon$
F3	Annealing state 850°C/1h	$\alpha+M_3C$
F3	Drawing annealing state 500°C/5h	$\alpha+M_3C+\varepsilon$
F3	Drawing annealing state 600°C/5h	$\alpha+M_3C+\varepsilon$
AF1, AF2	Cast state	$\alpha+\gamma+M_{23}C_6$
AF1	Solution annealing state 1050°C/1h	$\alpha+\gamma+M_{23}C_6$
AF1	After solution annealing ageing at 500°C/5h	$\alpha+\gamma+M_{23}C_6+\varepsilon$
AF1	After solution annealing ageing at 600°C/5h	$\alpha+\gamma+M_{23}C_6+\varepsilon$

The electrochemical measurements were performed on the mechanically polished samples (carbimet papers, diamond paste) in the deaerated aqueous solutions of 1M H_2SO_4 and 1M H_2SO_4 - NaCl at room temperature. The saturated calomel electrode has been used as a reference electrode.

Results and Discussion

Copper dissolved in austenite

Fig.1 presents the effect of Cu on the anodic polarization of monocrystals of Fe-18%Cr-11%Ni-Mo-Cu alloys in 1M H_2SO_4 - NaCl solution. Copper dissolved in austenite does not influence the stability of a passive film.

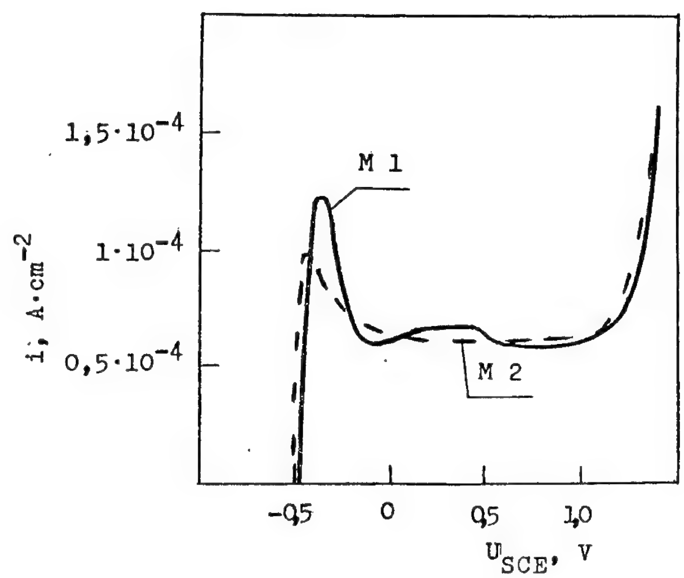

Fig.1. Anodic polarization of monocrystals M1 and M2 in 1M H_2SO_4 + 1M NaCl, at 20°C

In some circumstances high copper content promotes the precipitation of carbide phase in high alloyed steels. This effect is connected with the detrimental influence of dissolved copper on the diffusion of carbon in austenite [5]. Fig.2 presents the structure of polycrystalline Fe-22%Cr-23%Ni-3%Mo-Cu cast alloys (A1 and A2). Cast steel with high copper concentration (A2) contains inclusions of $M_{23}C_6$ carbides in the interdendritic areas (Fig.2b and 3).The carbides were also found after solution annealing . The presence of carbides in interdendritic areas and connected with it the microsegregation of elements (Cr,Ni and Mo) diminishes the stability of passive film (Fig.4). The solution annealing decreases the difference between the passive behaviour of steels with low and high copper concentration (Fig.5).

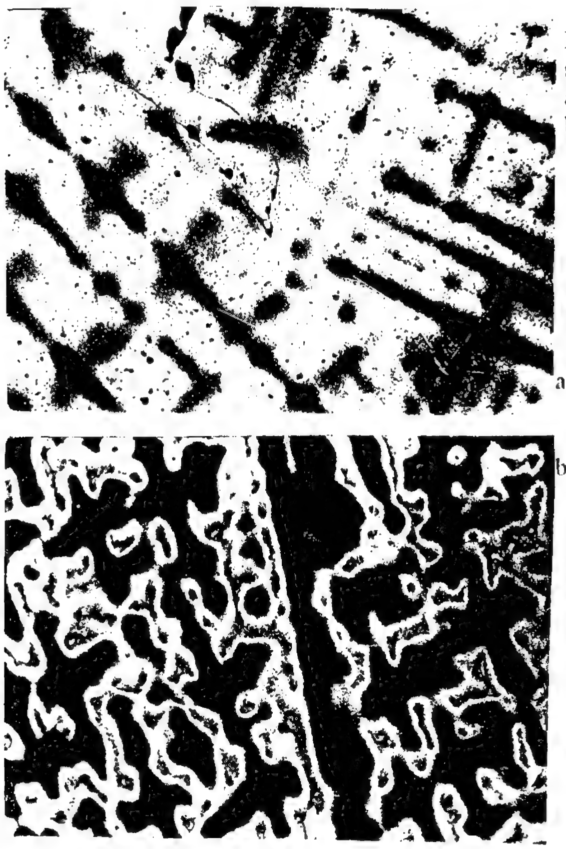

Fig.2. Structure of the austenitic cast steel;
a - cast state A1, magnification x100,
b - cast state A2, magnification x100

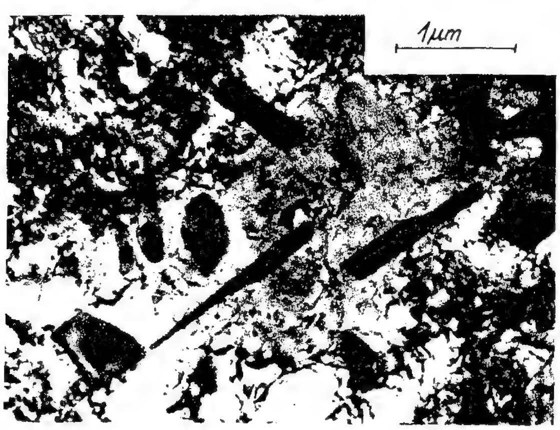

Fig.3. Structure of the austenitic cast steel A2, cast state, precipitation of the carbide phase ($M_{23}C_6$) in the interdendritic space. Electron microscope

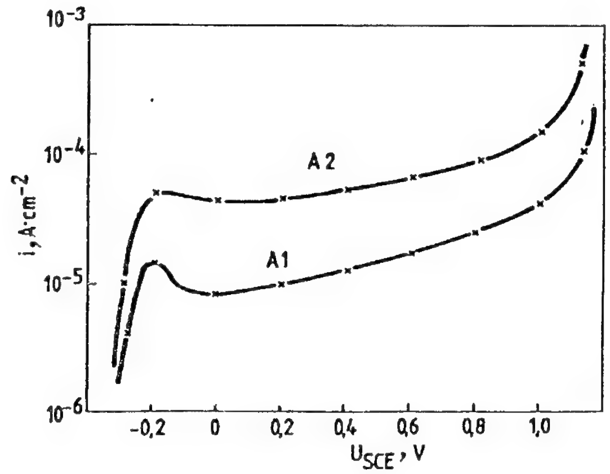

Fig.4. Anodic polarization of the austenitic cast steels A1 and A2 (cast state) in 1M H_2SO_4 + 1M NaCl, at 20°C

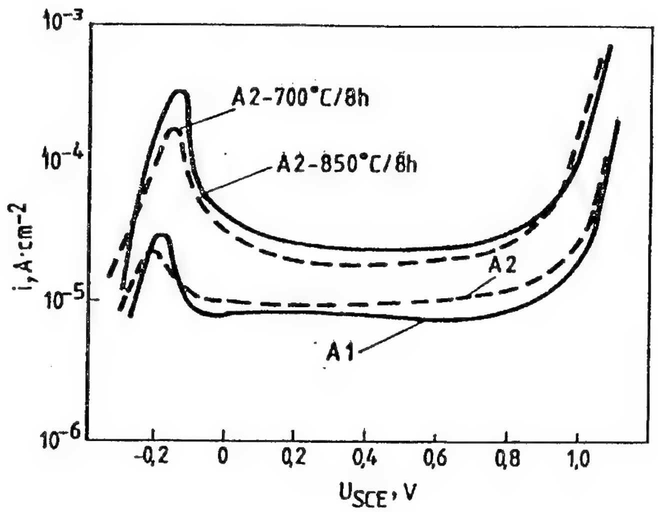

Fig.5. Anodic polarization of the austenitic cast steels (A1 and A2 - solution annealing state,; A2 - ageing 700°C and 800°C in 1M H_2SO_4 + 1M NaCl, at 20°C

Copper in ferritic steels

Fig.6 shows the microstructure of ferritic cast steel F3 .The samples as cast, without heat treatment contain carbide precipitations in ferritic matrix. The M_3C carbides were identified in alloys independent of copper content . The alloy F3 with high copper concentration contains

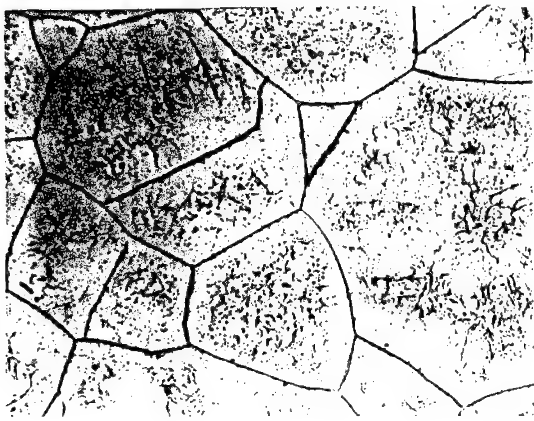

Fig.6. Structure of the ferritic cast steel F3, cast state, magnification x100

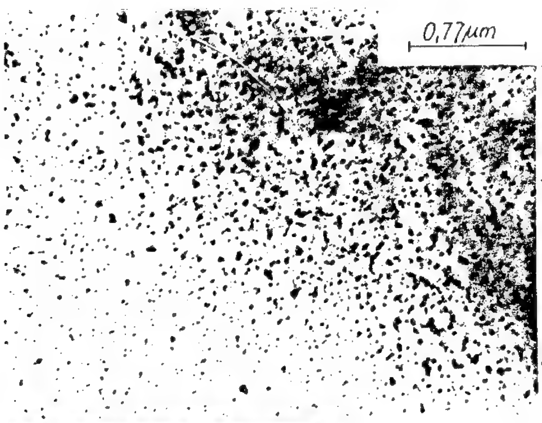

a

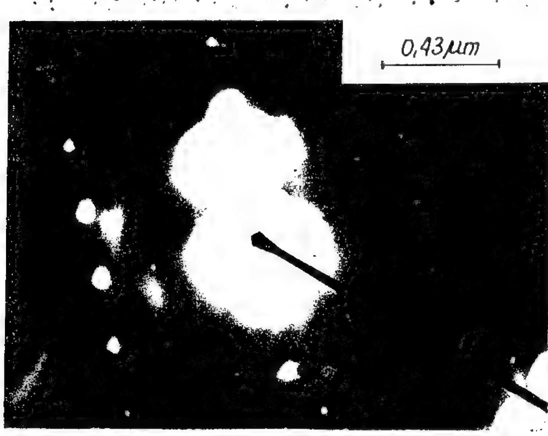

b

Fig.7. Structure of the ferritic cast steel F3 (cast state);
a - precipitation of the ε –phase dispersed in ferrite. Electron microscope;
b - difraction image (ferrite + ε–phase)

the inclusions of ε-phase (Fig.7) dispersed in ferrite. The inclusions can be dissolved in ferrite during annealing at 850°C.
The presence of ε–phase in Fe-17%Cr alloys has a negative influence on the stability of a passive film in 1M H_2SO_4 + 0.5M NaCl solutions. Fig.8 presents the anodic polarization of the investigated ferritic alloys. The alloy F3 containing the inclusions of ε–phase shows higher susceptibility to local corrosion than the alloys F1 and F2 . The annealing of F3 alloy at the 850°C and the dissolution of ε-phase increases the resistance of this alloy to pitting corrosion (Fig.9)

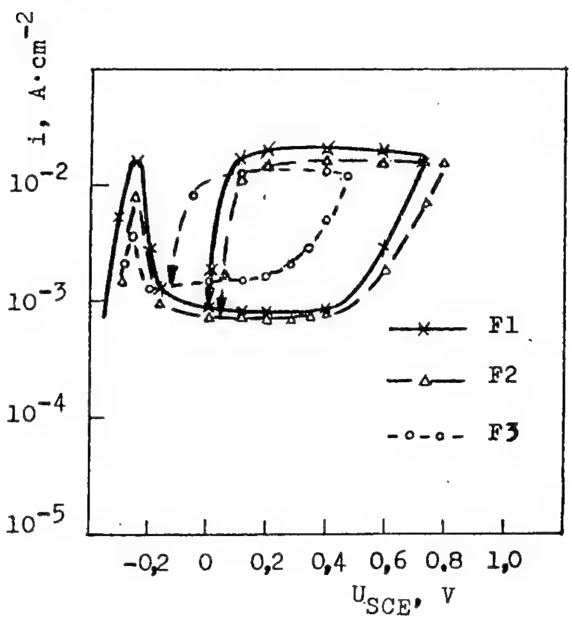

Fig.8. Anodic polarization of the investigated ferritic alloys (cast state) in 1M H_2SO_4 + 0.5M NaCl, at 20°C.

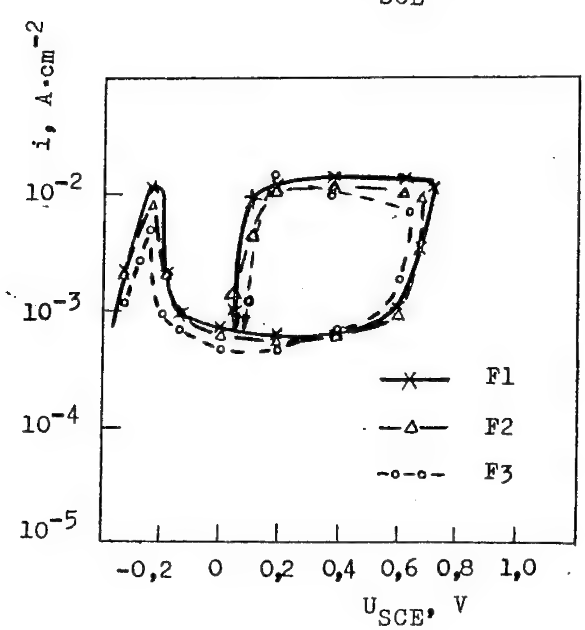

Fig.9. Anodic polarization of the investigated ferritic alloys (annealing state 850°C/1h) in 1M H_2SO_4 + 0.5 M NaCl, at 20°C

Copper in duplex austenitic-ferritic steels

The microstructures of alloys AF1 (1.34%Cu) and AF2 (3.35%Cu) are similar both as cast and after quenching at 1050°C (Fig.10). Copper, the element stabilizing the austenite, does not influence the proportion between austenite and ferrite phases in the investigated duplex steels. The lack of the structural differences between both steels AF1 and AF2 causes the lack of the differences of passive behaviour . The steels as casts and after quenching do not contain

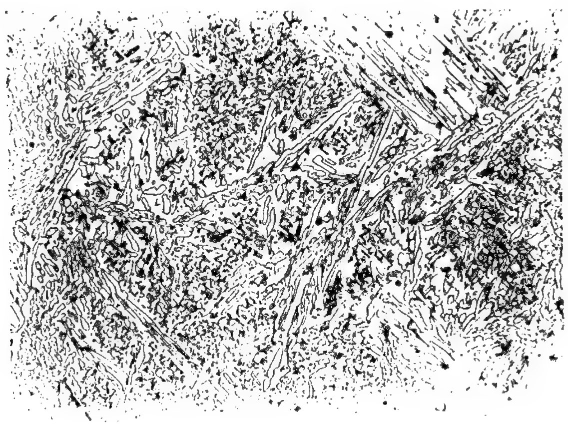

Fig.10. Structure of the austenitic - ferritic cast steel AF1, magnification x100

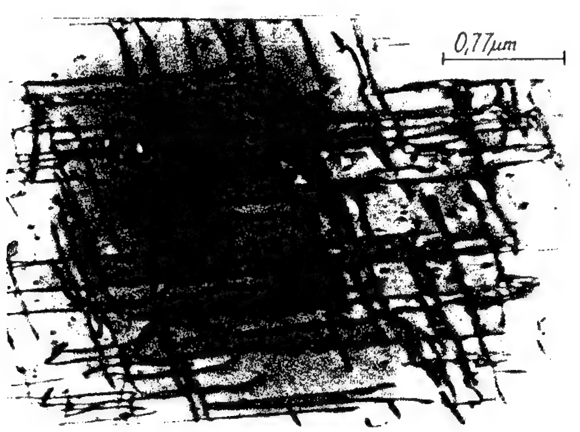

Fig.11. Structure of the cast steel AF1. Precipitation of the ε-phase dispersed in ferrite. Electron microscope

ε-phase. The presence of austenite in duplex steels, of phase with high solubility of copper, limits the possibility of precipitation of ε-phase in ferrite. The precipitation of ε-phase can be obtained after ageing at 500° and 600°C (Fig.11). The presence of inclusions of this phase in ferrite stimulates local attack of ferrite grains (Fig.12). The polarization measurements presented in Fig.13 show that the alloy AF1 after aging (ε-phase present) is more susceptible to pitting corrosion than the same alloy after quenching (ε-phase dissolved).

Fig.12. Pitting of the cast steel AF1 in 1M H_2SO_4 + 1M NaCl, U=+600mV, t=0.5h. Drawing annealing state 600°C, magnification x500

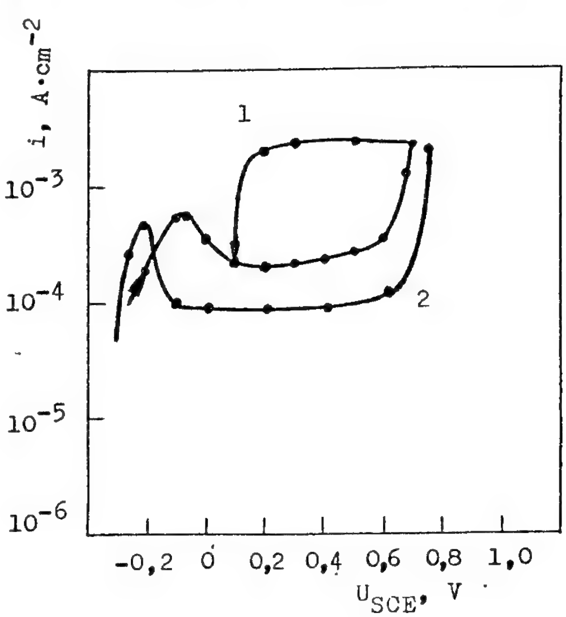

Fig.13. Anodic polarization of the austenitic - ferritic cast steel AF1 in 1M H_2SO_4 + 1M NaCl, at 20°C
1 - drawing annealing atate 600°C/5h
2 - quenching 1050°C/1h

Conclusions

Copper dissolved in austenite does not influence the stability of a passive film on austenitic stainless steels. However this element can stimulate the carbides precipitation and therefore can show an indirect effect on corrosion resistance of austenitic chromium - nickel steels.

Copper presented as ε-phase in ferritic and austenitic-ferritic steels stimulates the local corrosion of these alloys. The local attack is observed preferentially in ferrite grains. The inclusions of ε-phase dispersed in ferrite are probably the "weak points" of the surface, susceptible to local dissolution.

References

[1] L. Colombier, I. Hochmann, Stale odporne na korozję i stale żaroodporne, Wyd. Śląsk, Katowice (1964).
[2] H. Uhlig, Korozja i jej zapobieganie, WNT, Warszawa (1976).
[3] I. Le May, L. Mc. D. Schetky, Copper in Iron and Steel. John Wiley Sons. Inc. USA (1982).
[4] F. B. Pickering, Physical Metalurgical Development of Stainless Steel. Confer. Goeteborg, 1 (1985).
[5] J. Peleg, The British Foudryman, **56**, 482 (1963).
[6] I. Nutting, D. Dulieu, The Iron and Steel Institute, p.140 (1964).
[7] P. C. Gallagher, I. Metall. Trans. **1**, 2429 (1970).
[8] Metals Handbook, Metals Park, Ohio, **8** (1973).
[9] F. B. Pickering, The Metals Society (1984).

Materials Science Forum Vols. 185-188 (1995) pp. 759-768

Investigation of spontaneous passivation of stainless steels modified with ruthenium

P. Baradlai[1], J.H. Potgieter[2], W.O. Barnard[3], L. Tomcsányi[4] and K. Varga[1,5]

[1] Department of Radiochemistry, University of Veszprém, H-8201 Veszprém, Hungary

[2] PPC Technical Service, Johannesburg, PO Box 40073, Republic of South Africa

[3] Department of Physics, University of Pretoria, Pretoria 0002, Republic of South Africa

[4] Department of Physical Chemistry, University of Veszprém, H-8201 Hungary

[5] Author to whom correspondence should be addressed

Keywords: Accumulation of HSO_4^-/SO_4^{2-} and Cl^- ions, spontaneous passivation, austenitic steel, duplex steel, Ru additive, radiotracer method, AES and XPS studies

ABSTRACT

In this paper, time, potential and concentration dependence of HSO_4^-/SO_4^{2-} and Cl^- accumulations measured by an in-situ radiotracer method on surface oxide layers of stainless steels of various microstructures (austenitic or duplex) and compositions (in the presence and absence of Ru as additive) are presented and discussed. Several independent techniques such as AES, XPS and ICP Optical Emission Spectrometry are also used to characterise the complex features of the passivation phenomena of steels modified with ruthenium. The experimental results reveal that the surface excess values of bisulfate/sulfate ions are much higher (up to $\Gamma=1.5\times10^{-9}$ mol cm^{-2}) as well as their interaction with passive oxide layer is substantially stronger than those of chloride ions on all stainless steels studied. Both the extent and the strong character of bisulfate/sulfate accumulation are most likely related to the redistribution of the main alloying components (Cr, Ni, Mo) as well as the Ru in the surface oxide films formed on steels passivated spontaneously in dilute HCl and H_2SO_4.

INTRODUCTION

Although a number of investigations dealing with the surface properties of stainless steels of various structures and compositions in aggressive solutions containing Cl^- and SO_4^{2-} ions have been published, how such anions take part in the formation and breakdown of the passive oxide layer were not satisfactorily interpreted. Stainless steels normally have excellent corrosion resistance in oxidising acid media, but they are very prone to corrosion in reducing acids such as H_2SO_4 and HCl. It was found that the corrosion resistance of virtually all stainless steels against reducing acids can be remarkably increased by alloying them with small amounts of a platinum group metal (PGM). The nature of the passive films of stainless steels cathodically modified with PGM's is the subject of an ongoing discussion in the corrosion literature (see e.g. [1-4] and references therein).

It seems that PGM's can act upon corrosion in two ways. As may be seen from Fig.1, sufficient amounts of these alloying components
(i) increase the rate of hydrogen evolution, i.e., increase the efficiency of the cathodic process in order to shift the open-circuit (corrosion) potential towards more positive values,
(ii) inhibit the anodic dissolution of the alloy to which they are added.

The fact that ruthenium is the cheapest of the PGM's perpetuates the interest in the self-passivation processes of steels containing small amounts of Ru as additive ([5-8] and references therein). Very little is currently known about its precise role in the whole corrosion process.

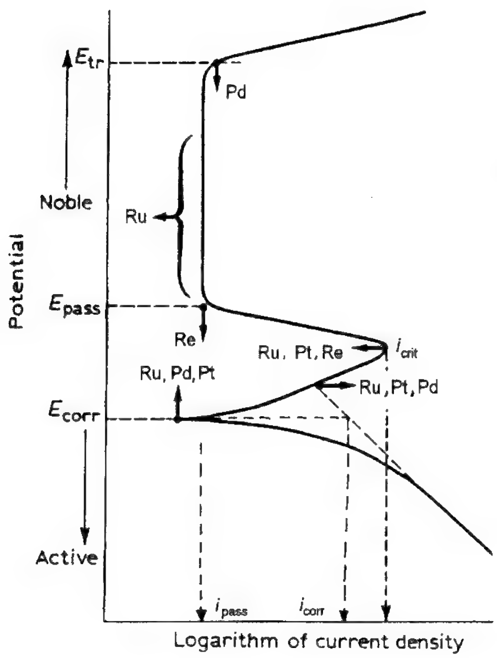

The meaning of the various symbols

i_{pass}	passive current density
i_{corr}	corrosion current density
i_{crit}	critical current density
E_{corr}	corrosion potential
E_{pass}	passivation potential
E_{tr}	transpassive potential

Fig.1. Summary of the effects of alloying additions on the polarisation characteristics of Fe-Cr stainless steel in non-oxidising acids (HCl and H_2SO_4).

In the present work, we use a combination of an in situ radiotracer method and voltammetry to get a deeper insight in the accumulation of Cl^- and HSO_4^-/SO_4^{2-} ions on surface oxide layers of stainless steels of various microstructures (austenitic or duplex) and compositions (in the presence and absence of ruthenium as alloying component) [9]. Surface properties of an austenitic (AISI 316L + O,5% Ru) and experimental duplex stainless steels with small Ru additions in non-oxidising media (in dilute sulphuric and hydrochloric acids) are compared to those of austenitic (08x18H10T (GOST5632-61)) and duplex stainless steels containing no Ru as additive. In addition, the complex features of the passivation phenomena are characterized by several independent techniques. Namely, the time dependence of the dissolution of Fe content measured by ICP Optical Emission Spectrometry in dilute acids yields further information on the rate of the surface transformation. Comparative studies with surface analytical techniques such as AES and XPS are performed on the spontaneous passivated duplex stainless steels with and without Ru additions in order to contribute to the better understanding of the role of different elements in the whole passivation process.

EXPERIMENTAL

Accumulation of HSO_4^-/SO_4^{2-} and Cl^- ions was studied on powdered steel samples by an in-situ radiotracer method. The main features of the experimental technique as well as the basic principles of the determination of surface concentration (Γ) were described in [9].

The composition of stainless steels is shown in Table 1. Some characterising data of the system studied by radioactive labelling are given in Table 2. Millipore water (Milli Q Plus), perchloric acid (AR grade, Merck) and sulfuric acid (Suprapure, Merck) were used in the preparation of the solutions. H_2SO_4 labelled with S-35 (molar activity: $1{,}8x10^9$ Bq $mmol^{-1}$) as well as HCl labelled with Cl-36 (molar activity: $2x10^7$ Bq $mmol^{-1}$) were supplied by Du Pont.

The measurements were carried out in $HClO_4$ supporting electrolyte under experimental conditions specified in details together with the experimental results.

Table 1. Chemical composition of the stainless steels studied (w%)

(A) Austenitic stainless steels

Alloy type	Fe	Cr	Ni	Mo	Ru	Mn	Si	S	P	O	Ti	C
08x18 H10T (GOS 5632-61)	rest	17.0-19.0	9.0-11.0	-	-	1.0-2.0	< 0.80	< 0.02	< 0.035	-	(5xC%)-0.6	< 0.08
AISI 316 L + 0.5% Ru	rest	16.0-18.0	9.0-12.0	2.0-3.	0.5	2.0	< 0.75	-	-	-	-	< 0.03

(B) Duplex stainless steels

Alloy		Fe	Cr	Ni	Mo	Ru	Mn	Si	S	P	O	N	C
No.	Type												
377	Fe-22%Cr9%Ni3%Mo0%Ru	rest	22.0	9.07	2.81	-	< 0.	0.070	0.01	<0.0	0.021	0.006	0.03
380	Fe-22%Cr9%Ni3%Mo0.3%Ru	rest	22.4	9.24	2.92	0.28	< 0.	0.030	0.01	<0.0	0.037	0.005	0.02

Table 2. Some characterising data of the system studied by in-situ radiotracer technique

Type of species studied	$E_{\beta max}$ (keV)	Mass-absorption coefficient μ ($cm^2\ g^{-1}$)	Characteristic dimensions of the steel samples			Range of concentration ($mol\ dm^{-3}$)
			Thickness ($mg\ cm^{-2}$)	Diameter of powder	Roughness factor	
H_2SO_4 labelled with ^{35}S	167	320*	15	< 56 μm	2.24	$5x10^{-6}$-$1x10^{-3}$
HCl labelled with ^{36}Cl	710	34	81	< 56 μm	11.19	$2x10^{-5}$-$2x10^{-2}$

**Measured value.*

The concentration of Fe dissolved from the 1 g samples of powdered steels into the supporting electrolyte was determined by ICP Optical Emission Spectrometer (type: ARL 3410). The concentration of sulfuric acid was ranged from 0 to $1x10^{-3}$ mol dm^{-3} in 0.1 mol dm^{-3} $HClO_4$.

The composition of the passive films formed on duplex stainless steels passivated spontaneously in HCl and H_2SO_4 were studied by Auger Electron Spectroscopy (AES) and X-ray Photoelectron Spectroscopy (XPS). The AES and XPS measurements were conducted in a PHI 610 and PHI 5300 instruments, respectively. Some characterising data of the pretreatment and size of steel samples studied are summarised in Table 3.

Table 3. Some characterising data of the steel samples studied by AES and XPS.

Pretreatment (spontaneous passivation after cathodic reduction)			Size of the samples (mm)
Electrolyte	Cathodic reduction	Temperature	
0.1 mol dm^{-3} HCl	5 min;-0.8 V(SCE)	25 °C	15x15x2
1 mol dm^{-3} H_2SO_4	5 min;-0.8 V(SCE)	25 °C	15x15x2

RESULTS AND DISCUSSION

Time and concentration dependence of HSO_4^-/SO_4^{2-} and Cl^- accumulations

It should primarily be mentioned that relevant literature data imply

(i) The self-passivation processes of austenitic stainless steel type AISI 316L with 0,5% Ru occurring in non-oxidising acids result in its enhanced corrosion resistance compared to ordinary austenitic grades like 08x18H10T (GOST5632-61) [2].

(ii) The experimental duplex stainless steels studied (Table 1.), which consist of ca. 50% austenite and 50% ferrite in the absence and presence of Ru as alloying component, are passivated spontaneously in the dilute HCl and H_2SO_4 [7,8].

These statements are strongly supported by the remarkably high positive values of corrosion potentials attained in present studies (see open circuit (corrosion) potential values in the text to Figs.2-5). It is to be noted that spontaneous passivation of both the duplex and austenitic steels is most likely due to not only the Ru but Mo contents. It is assumed that Mo not only retards anodic dissolution, but also increases the effectiveness of the cathode process owing to the reduced overvoltage of hydrogen on molybdenum ([2,7] and references therein).

The radiotracer studies (Fig.2-5) give illustrative examples regarding how the self-passivation processes of stainless steels are influenced by a pronounced sorption of HSO_4^-/SO_4^{2-} and Cl^- ions. Specifically, while no measurable sorption of Cl^- ions (surface excess (Γ) less than $2x10^{-11}$ mol cm^{-2}, if any[10]) on austenitic stainless steel containing no Ru was found, a small but significant accumulation of chloride was detected on AISI 316L modified with 0.5% Ru at HCl concentrations of $2x10^{-5}$-$5x10^{-4}$ mol dm^{-3} (Fig.2.a). As clearly seen in Fig. 2.b, the labelled Cl^- ions accumulated on austenitic steel containing Ru can be easily displaced by the large excess of non-labelled species, indicating that no strong embedding of Cl^- ions takes place.

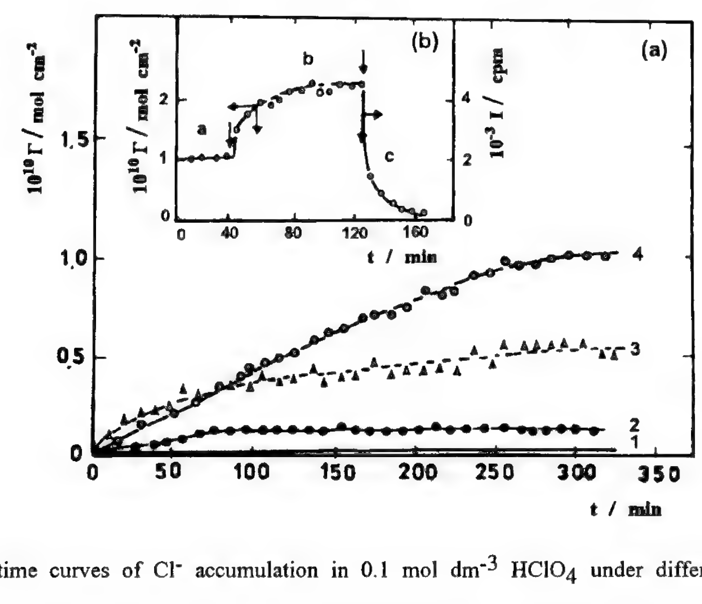

Fig.2. Γ vs. time curves of Cl^- accumulation in 0.1 mol dm^{-3} $HClO_4$ under different experimental conditions :

(a) At open circuit potential: (1) on steel type 08x18H10T at $2x10^{-2}$ mol dm^{-3} concentration of labelled Cl^- ions; (2), (3), (4) on steel type AISI 316L+0.5%Ru at Cl^- concentrations of $2x10^{-5}$, $1x10^{-4}$ and $5x10^{-4}$ mol dm^{-3}, respectively; (open circuit potentials were shifted in the range of -20 to 580 mV).

(b) Study of the mobility of labelled Cl^- ions accumulated on steel type AISI 316L+0.5%Ru from solution containing $5x10^{-4}$ mol dm^{-3} Cl^-: (a) open circuit potential; (b) 1200 mV; (c) 1200 mV, addition of $1x10^{-2}$ mol dm^{-3} non-labelled HCl.

Fig.3 shows the time dependence of Cl^- sorption measured on duplex stainless steels. The surface concentrations of Cl^- ions on both steels are small (less than $\Gamma=1x10^{-10}$ mol cm^{-2}) and do not differ basically from those found on austenitic grades (Fig.2).

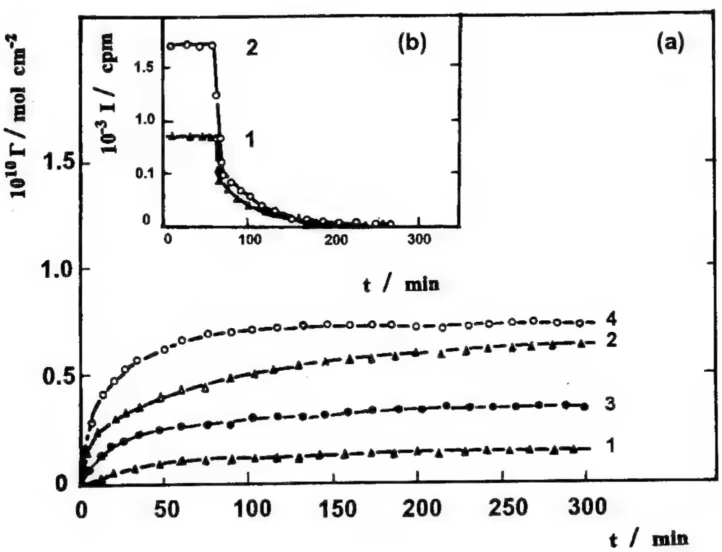

Fig.3. Γ vs. time curves of Cl^- accumulation in 0.1 mol dm^{-3} $HClO_4$ under open circuit conditions:
(a) (1) and (2) on duplex stainless steel No. 377. at Cl^- concentrations of $2x10^{-5}$ and $1x10^{-4}$ mol dm^{-3}, respectively; (3) and (4) on duplex stainless steel No. 380. at Cl^- concentrations of $2x10^{-5}$ and $1x10^{-4}$ mol dm^{-3}, respectively;
(b) Study of the mobility of labelled Cl^- ions accumulated on duplex steels Nos. 377 and 380 (curves 1 and 2, respectively) by addition of the large excess of non-labelled HCl (c = $1x10^{-2}$ mol dm^{-3}).

Γ vs. time curves of bisulfate/sulfate accumulation measured on the surfaces of austenitic and duplex stainless steels in the presence of labelled H_2SO_4 up to $1x10^{-3}$ mol dm^{-3} concentration are shown in Fig.4 and Fig.5, respectively. As may be seen in Fig.4.a and b, the surface excess values of bisulfate/sulfate ions are much higher (up to $\Gamma=1.5x10^{-9}$ mol cm^{-2}) as well as their interaction with passive oxide-layer is substantially stronger than those of chloride ions on both austenitic stainless steels studied. The latter assumption is supported by the results of the exchange of labelled HSO_4^-/SO_4^{2-} ions sorbed on AISI 316L+0.5% Ru, revealing that part of bisulfate/sulfate species is strongly bonded to the passive layer formed upon the spontaneous passivation (curve 3.b. in Fig.4.b). The peculiarity in the concentration dependence of bisulfate/sulfate sorption on austenitic stainless steel modified with Ru (Fig.4.b), that is, the decrease of the surface excess with increasing bulk concentration of labelled H_2SO_4, is probably due to the changes occurring in the state of the surface oxide-layer as it will be discussed later on.
It is obvious from the results of the radiotracer studies presented in Fig.5 that the Ru content does not exert significant effects on the sorption behaviour of the duplex steel surfaces. Moreover, the bisulfate/sulfate accumulation on both duplex steels seems to be smaller than that on austenitic grades and attains to a saturation surface concentration of about $4.5x10^{-10}$ mol cm^{-2}.

If we accept that the spontaneous passivation of the austenitic stainless steel modified with 0.5% Ru is accompanied with the selective dissolution of less-noble elements (e.g. Fe) of the alloy [1,4-5], a study of the time dependence of Fe dissolution may be considered as a direct tool for the characterisation of self-passivation phenomena. The conspicuous behaviour of HSO_4^-/SO_4^{2-} accumulations shown in Fig.4.b may be interpreted on the basis of the time dependence of Fe dissolution from steel samples at various experimental conditions (Fig.6).

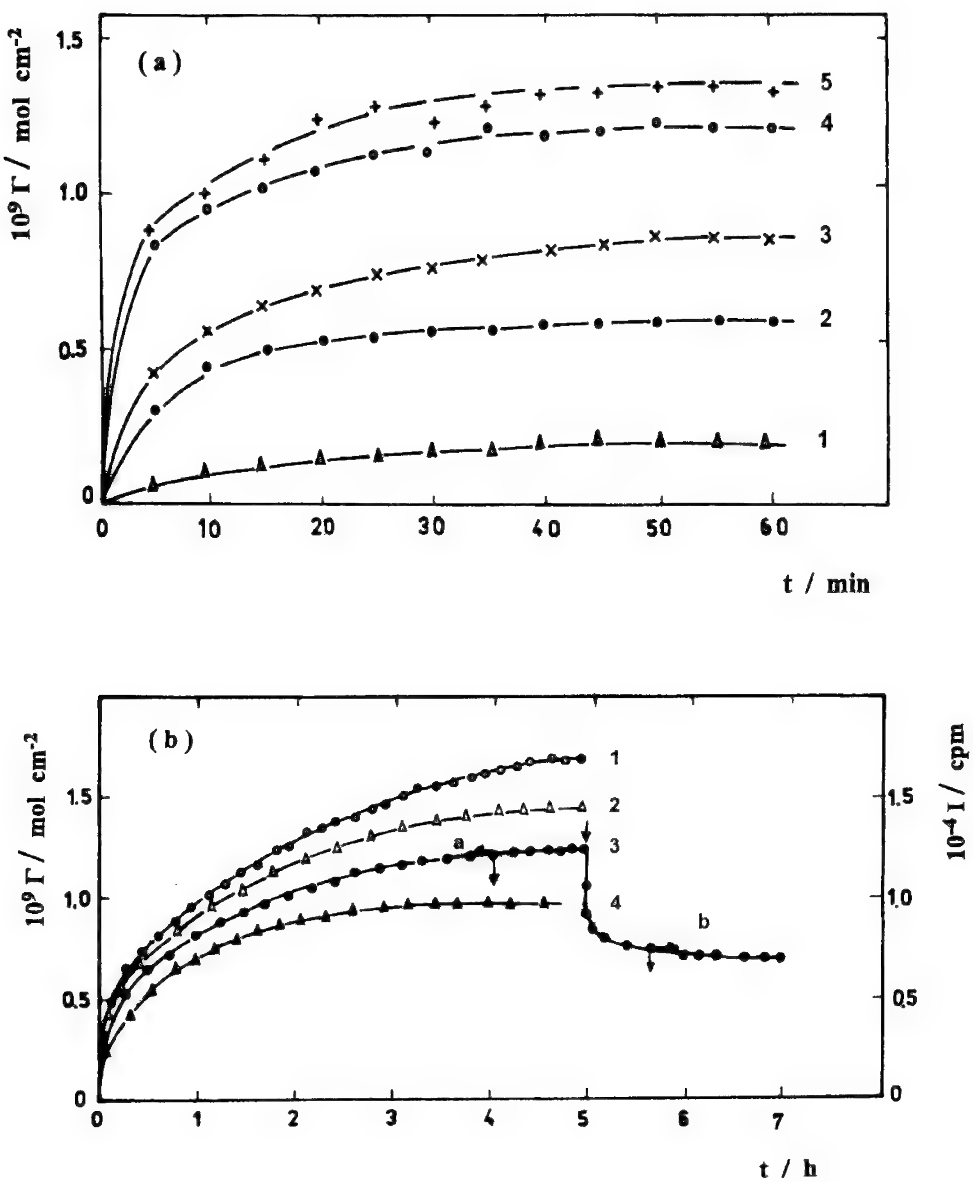

Fig.4. Γ vs. time curves of H_2SO_4 accumulation at open circuit potentials (E):
(a) on steel type 08x18H10T in 1 mol dm^{-3} $HClO_4$.
(1) 1x10^{-5} (E=500 mV); (2) 5x10^{-5} (E=450 mV); (3) 1x10^{-4} (E=320 mV);
(4) 5x10^{-4} (E=340 mV); (5) 1x10^{-3} (E=350 mV) mol dm^{-3} labelled H_2SO_4.
(b) on steel type AISI 316L+0.5% Ru in 0.1 mol dm^{-3} $HClO_4$.
(1) 2x10^{-5}; (2) 5x10^{-5}; (3.a.) 1x10^{-4}; (4) 1x10^{-3} mol dm^{-3} labelled H_2SO_4;
(3.b.) addition of 1x10^{-2} mol dm^{-3} non-labelled H_2SO_4.
(open circuit potentials were shifted in the range of -30 to 700 mV.).

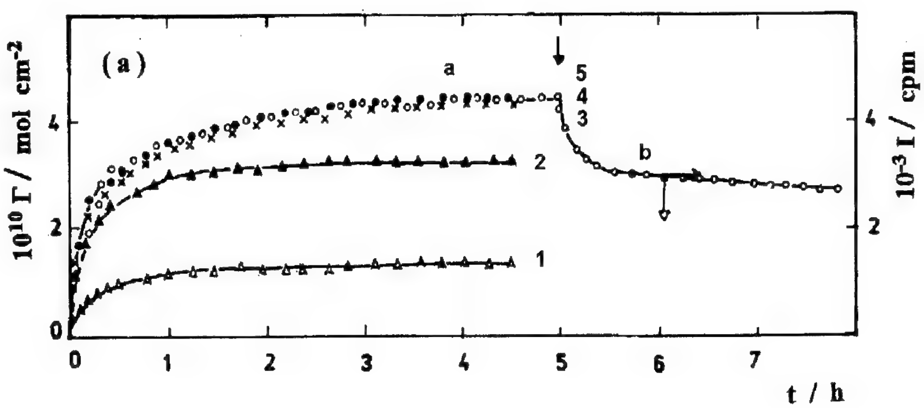

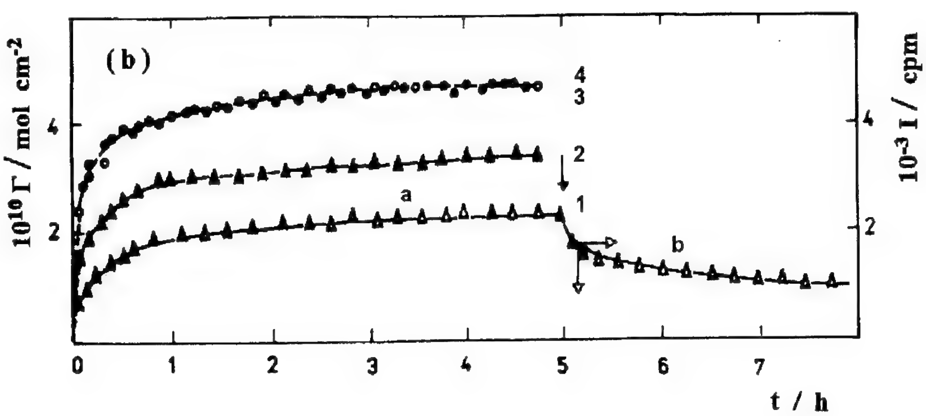

Fig.5. Γ vs. time curves of H_2SO_4 accumulation in 0.1 mol dm^{-3} $HClO_4$ at open circuit potentials:
(a) on duplex stainless steel No. 377.
(1) 5×10^{-6}; (2) 1×10^{-5}; (3.a.) 2×10^{-5}; (4) 1×10^{-4}; (5) 1×10^{-3} mol dm^{-3} labelled H_2SO_4;
(3.b.) addition of 1×10^{-2} mol dm^{-3} non-labelled H_2SO_4.
(open circuit potentials were shifted in the range of -50 to 700 mV)
(b) on duplex stainless steel No. 380.
(1.a.) 5×10^{-6};(2) 2×10^{-5}; (3) 1×10^{-4}; (4) 5×10^{-4} mol dm^{-3} labelled H_2SO_4;
(1.b.) addition of 1×10^{-2} mol dm^{-3} non-labelled H_2SO_4.
(open circuit potentials were shifted in the range of -80 to 720 mV)

As demonstrated in Fig.6, an increase in the bulk concentration of H_2SO_4 results in an increase in the rate of Fe dissolution from the steel surface undergoing structural transformation. Since the bisulfate/sulfate sorption is considered to be some specific interaction of anions with the active sites involved in the passive layer [10-11], the various phenomena observed give a strong indication that

- the presence of bisulfate/sulfate ions accelerates the spontaneous passivation of AISI 316L modified with 0.5% Ru leading to the formation of passive layers of enhanced corrosion resistance;
- the spontaneous passivation of steel studied causes the redistribution of such alloying components of the surface layer which are capable of interacting with bisulfate ions.

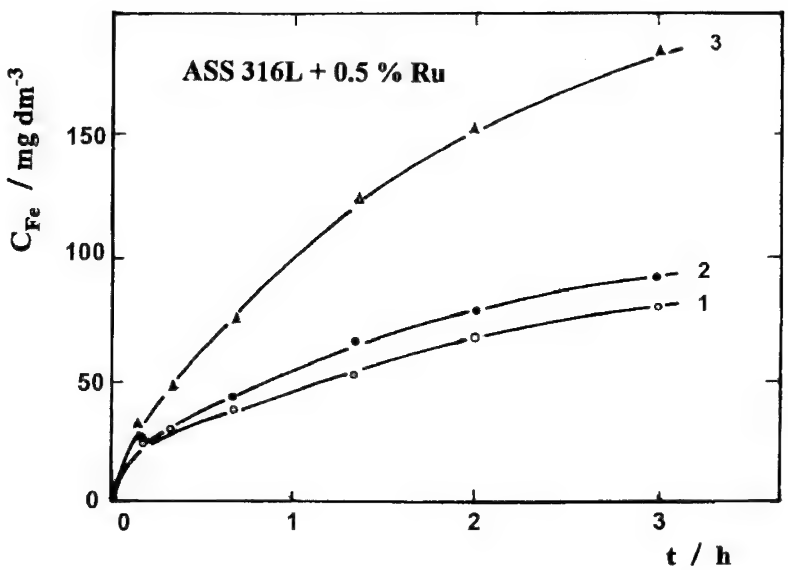

Fig.6. Time dependence of Fe dissolution measured by ICP Optical Emission Spectrometer upon spontaneous passivation of austenitic stainless steel type AISI 316L+0.5%Ru in solution consisting of (1) 0.1 mol dm^{-3} $HClO_4$; (2) 0.1 mol dm^{-3} $HClO_4$+2x10^{-5} mol dm^{-3} H_2SO_4; (3) 0.1 mol dm^{-3} $HClO_4$ + 1x10^{-3} mol dm^{-3} H_2SO_4.

Potential dependence of HSO_4^-/SO_4^{2-} and Cl^- sorption

The Γ vs. E curves obtained on the powdered samples of the duplex steels passivated spontaneously starting from the open circuit potential are shown in Fig.7. There is no considerable potential dependence of HSO_4^-/SO_4^{2-} accumulations on the steel surfaces in the potential range of 0 to 1200 mV, as depicted by curves 2-2' and 3-3' in Fig.7. This correlates well to the fact that both of the steels studied exhibit passive features in a wide potential region in 0.1 mol dm^{-3} $HClO_4$ in the absence and presence of H_2SO_4 up to concentration of 1x10^{-3} mol dm^{-3} (see Fig.8). The potential dependence of Cl^- sorption shown in curves 1-1' in Fig.7 does not differ significantly from that of bisulfate/sulfate ions. In this case, following the cathodic polarisation program a potential shift towards to more positive values (curve 1') results in a slight increase in the surface excess of Cl^- ions.

Similar observations were found on austenitic stainless steels with and without Ru as alloying component [10]. All these results give a further evidence that the extent of the accumulation of aggressive anions decisively depends on the structure and probable composition of the passive layer formed on the surface.

AES and XPS studies of passive layers formed on duplex steels

Comparative studies with surface analytical techniques such as AES and XPS were carried out in order to characterise the spontaneously formed passive films on duplex steels with and without Ru in HCl and H_2SO_4. The composition of the passive layers as a function of depth is given in Fig.9. The XPS spectra obtained for different elements and angles are the same, irrespective of whether the samples were passivated in HCl or H_2SO_4.

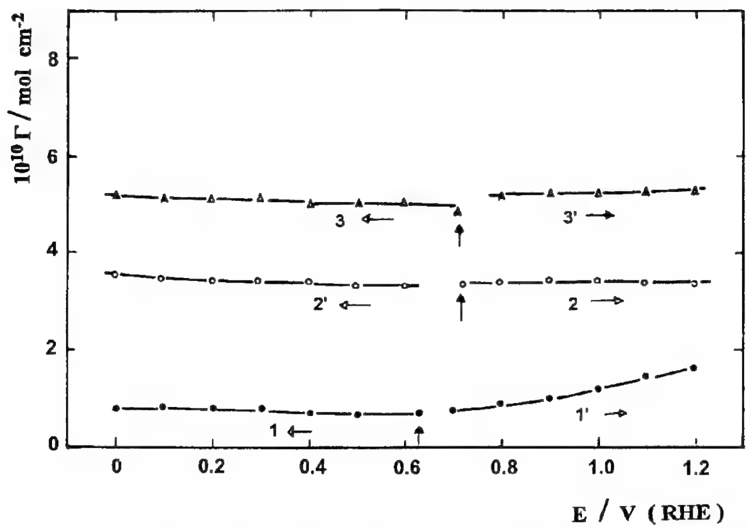

Fig.7. Potential dependence of HSO_4^-/SO_4^{2-} and Cl^- accumulation in 0.1 mol dm^{-3} $HClO_4$ under various experimental conditions:

(1-1') at Cl^- concentration of 1×10^{-4} mol dm^{-3} on duplex steel No. 380;
(2-2') at H_2SO_4 concentration of 2×10^{-5} mol dm^{-3} on duplex steel No. 380;
(3-3') at H_2SO_4 concentration of 1×10^{-4} mol dm^{-3} on duplex steel No. 377.
The open circuit potentials are indicated by arrows.

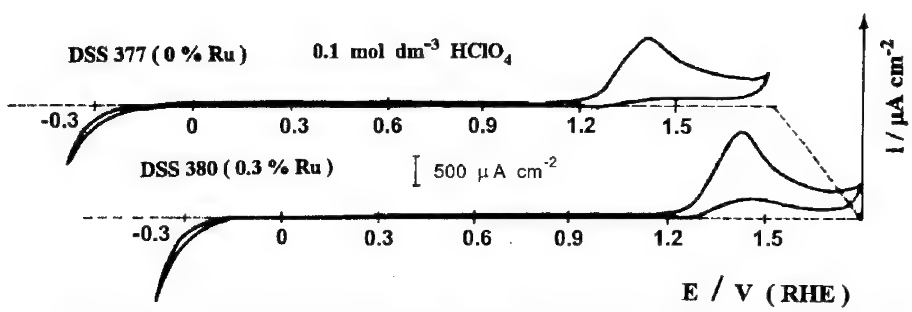

Fig.8. Cyclic voltammetric curves of duplex stainless steels in 0.1 mol dm^{-3} $HClO_4$. Scan rate: 20 mVs^{-1}.

AES and XPS results clearly show that Cr (mainly in Cr_2O_3 and $Cr(OH)_3$ forms) is moderately enriched in the passive layer, which is normally found for the most of stainless steels [4-5,12]. While at the outermost range of the passive film the relative amount of $Cr(OH)_3$ is prominent, in the deeper region the Cr_2O_3 is the predominant contributor to the Cr peak. Analysis by XPS on both steels indicates the existence of the various types of iron-oxides (Fe_3O_4, Fe_2O_3 and $FeO(OH)$). It should be noted that Fe_3O_4 and Cr_2O_3 contents are higher in the Ru containing samples. A very slight enrichment of the Ni (in metallic form) can also be observed in the sample surface region. In the case of duplex steel with 0.3% Ru spontaneously passivated in HCl a significant enrichment of Mo was detected.

All these results, in accordance with the data presented in [4], suggest that during selective dissolution of Fe the majority of the surface defect sites are initially occupied by Ni, Mo and Cr species. It is probable that the surface concentration of Ru also reaches a critical value which is found to be below the detection limit of the AES. Both the extent and the strong character of bisulfate/sulfate accumulation are most likely related to the redistribution of these alloying components.

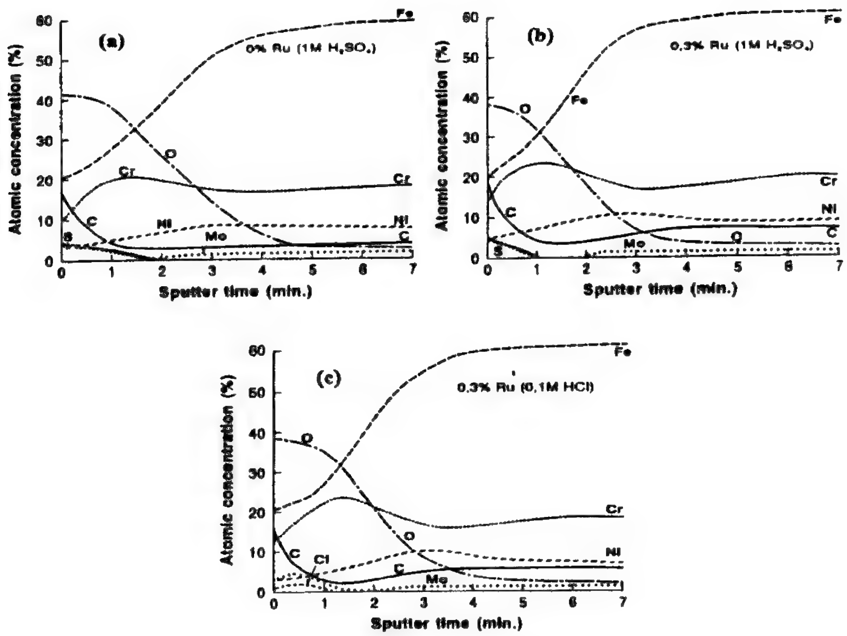

Fig.9. AES depth profiles for duplex stainless steels passivated spontaneously.
(a) DSS No. 377. passivated in 1 mol dm^{-3} H_2SO_4;
(b) DSS No. 380. passivated in 1 mol dm^{-3} H_2SO_4;
(c) DSS No. 380. passivated in 0.1 mol dm^{-3} HCl.

ACKNOWLEDGEMENT

This work was supported by the Hungarian Science Foundation (OTKA Grant No. F4002) and the Ministry of Education (MKM Grant No. 275/92; AMFK Grant No. 550/92). The authors are grateful to Prof. T. Lengyel (University of Veszprém, Hungary) for discussions and suggestions. One of the authors (WOB) is indebted to Prof. S.Hofmann (Max-Planck-Institut für Metallforschung, Stuttgart) for allowing him to conduct some of the experiments in his laboratories.

REFERENCES

[1] J.H. Potgieter, A.M. Heyns and W. Skinner, J. Appl. Electrochem. **20**, 711 (1990).
[2] J.H. Potgieter, J. Appl. Electrochem. **21**, 471 (1991).
[3] J.H. Potgieter, W. Skinner and A.M. Heyns, J. Appl. Electrochem. **23**, 11 (1993).
[4] S.C. Tjong, Applied Surf. Sci. **45**, 301 (1990).
[5] A. Higginson, R.C. Newman and R.P.M. Procter, Corros. Sci. **29**, 1293 (1989).
[6] S.C. Tjong, Applied Surf. Sci. **44**, 7 (1990) .
[7] S.C. Tjong, Werkstoffe und Korrosion **40**, 729 (1989) .
[8] J.H. Potgieter, W. Skinner and A.M. Heyns, INFACON 6. Proceedings of the 1st International Chromium Steel and Alloys Congress, Cape Town, Volume 2, Johannesburg, SAIMM, 1992. pp. 235-240.
[9] K. Varga, E. Maleczki, E. Házi and G. Horányi, Electrochim. Acta **35**, 817 (1990).
[10] K. Varga, E. Maleczki and G. Horányi, Electrochim. Acta **33**, 25 (1988).
[11] K. Varga, E. Maleczki and G. Horányi, Electrochim. Acta **33**, 1775 (1988).
M. Nagy, P. Baradlai, L. Tomcsányi and K. Varga, Acta Chim. Hung. (in press).
[12] N. Sato and G. Okamoto, In "Comprehensive Treatise of Electrochemistry" Eds. J.O'M. Bockris, B.E. Conway, Plenum Press, New York, Vol.4, p.193 (1981).

Materials Science Forum Vols. 185-188 (1995) pp. 769-778

Electrochemical study of passive films on stainless steel AISI 304 in carbonate aqueous solution at pH 8

M. Drogowska[1], L. Brossard[2] and H. Ménard[1]

[1] Dépt. de Chimie, Université de Sherbrooke, Sherbrooke, Québec, Canada J1K 2R1

[2] Institut de Recherche d'Hydro-Québec (IREQ), Varennes, Québec, Canada J3X 1S1

Keywords: Passive films, stainless steel, chromium, anodic coloration, carbonate

Abstract

The electrochemical behavior of stainless steel AISI 304 (SS304) has been investigated in deaerated 0.1M-1M $NaHCO_3$ solutions at pH 8, using a rotating disc electrode. The polarization curves are characterized by a lack of electrode activation at low potentials and an active-passive region between $0.4V_{SCE}$ and oxygen evolution. The carbonate/bicarbonate react as complexant ions enhancing the dissolution reaction but the passivation is due to an oxides/hydroxides film formation by solid-state reaction. The passive film formed on SS304 depended on the potential region: one at low potential and a second one at high potential, each with a different chemical composition. In the low potential range, the SS304 electrode behaves like a Cr-rich metallic phase, and the dissolution of Fe^{++} ions into the solution is unhindered by the formation of a Cr_2O_3 layer. As the potential reaches the critical value of 0.4V, chromium(III) in the passive layer oxidizes to chromate that dissolves into the solution and/or is retained in the stable mixed oxides. The dissolution of chromium, subsequent enrichment in iron (III) oxide and the increase of overall thickness of the film are time dependent. Aging has a great influence on the passive film, the longer the aging time the lower the anodic current related to the passive film.

A coloration of the SS304 surface was observed in the second passive region. A uniform gold color film was formed on SS304, mild steel 1024 and iron in carbonate and borate solutions of pH 8. The color of the electrode surface remained unchanged in air and in the solutions when under positive potential but was easily reduced in the first negative-going potential scan and even at open-circuit potential. Since the electrochemical and chemical reactions occur simultaneously, the oxidation time and oxidation charge have a considerable effect on the properties of the passive film. In high potential it is deduced that Fe(III) oxides (not the chromium compounds) plays a key role in SS304 passivity.

Introduction

The characterization of passive films on stainless steel remains far from clarified. The thermodynamical data are complex and the structural organization remains a difficult matter. The electronic structure of the passive layers on the stainless steel is not established.

The objective of this work is to investigate the electrochemical behavior of passive films formed on stainless steel AISI 304 in deaerated carbonate solutions of pH 8. The problem concerns the stainless steel that is used underground and exposed to aqueous carbonate and halide solutions. The voltammetric characteristics of SS304 were established and a special attention was also paid to chromium.

Experimental

The study was made using austenitic stainless steel AISI 304, with the following chemical composition (% in weight): *C 0.009, Mn 1.67, P 0.034, S 0.020, Si 0.51, Cu 0.35, Ni 8.2, Cr 19.4, V 0.07, Mo 0.30, Co 0.14, Sn 0.018, Al 0.006, Ti 0.006, Nb 0.033*. In order to compare the results, some measurements with the main components of SS304 were also performed. Specimens of SS304, iron (Johnson Matthey), nickel (Johnson Matthey) and chromium (99.99%, Omega) were machined in the shape of a cylinder and one of the tops of this cylinder (0.13 cm^2) was set in a Kel-F holder which constituted the working rotating-disc electrode. The electrodes were mechanically polished with an alumina suspension. The electrode was immersed in the solution with the potentiostat set at -0.9V. The auxiliary electrode was a platinum grid, which was separated from the main compartment by a Nafion membrane. A saturated calomel electrode (SCE) connected to the cell by a bridge with a Luggin capillary served as the reference electrode. All potentials quoted in the paper refer to this electrode.

Results and Discussion

The diagrams of corrosion potential vs time and voltammograms in Figs. 1 and 2 show the different electrochemical behavior of SS304, iron, chromium and nickel.

The potentiodynamic i-E curves illustrates that the typical activation current maximum that appears at negative potentials for Fe (Fig. 1b) is not present for SS304 (Fig. 1a) and for Cr (Fig. 1c) electrodes. At low potentials (-1V to 0.4V) the SS304 electrode appears to be in a passive state and the polarization curve is similar to that corresponding to Cr. The passivity current was found to be independent of carbonate/bicarbonate concentration. This would indicate that the passivation is due to the formation of oxides and/or hydroxides which are less soluble than the carbonates; the passive film is therefore thought to be composed of chromium (III) oxyhydroxides occupying mainly the inner layer as well as of iron (II/III) oxides in the outer layers /1-6/. At 0.4V the anodic depassivation occurs without any formation of visible pits and a second passive region is apparent before oxygen evolution.

For the four metals, the passive films formed on the electrodes have not been completely reduced regardless of the cathodic potential that was used but both the negative potential limit and the reduction time affected the anodic activity of electrode at negative potentials.

The corrosion potentials of -0.84V for Fe and -0.6V for Ni remained essentially unchanged over time but for SS304 and Cr electrodes the E_{corr} continuously increased along with the exposure time, at a faster rate for chromium. For example, after 9000s, E_{corr} equalled -0.55 V for Cr and -0.60 V for SS304 but no stable value was reached. E_{corr} values depended on the pretreatment of the electrode surface prior to the experiment but the trend remained the same for SS304 and Cr.

We have attributed the increase of E_{corr} of SS304 and Cr electrodes to the slow kinetics with which the films reach surface equilibrium; it is known that Cr^{3+} complexes react very slowly and thereby a film of Cr-hydroxide can be maintained /7/. The thinner oxide layers that were formed on chromium rather than on SS304 surface /8/ could explain the faster rate of Cr ennoblement. The similar characteristics for SS304 and Cr electrodes suggest that Cr(III) oxide/hydroxide is form on SS304 surface.

Chromium

In Fig. 1c, chromium electrode, rotated at 1000 rpm with a scan rate 0.02 V s^{-1}, in 1M $NaHCO_3$ solution, appears to be in a passive state in the potential range from -1V to +0.4V. At the latter potential, the anodic current increases with the applied potential without further passivation,

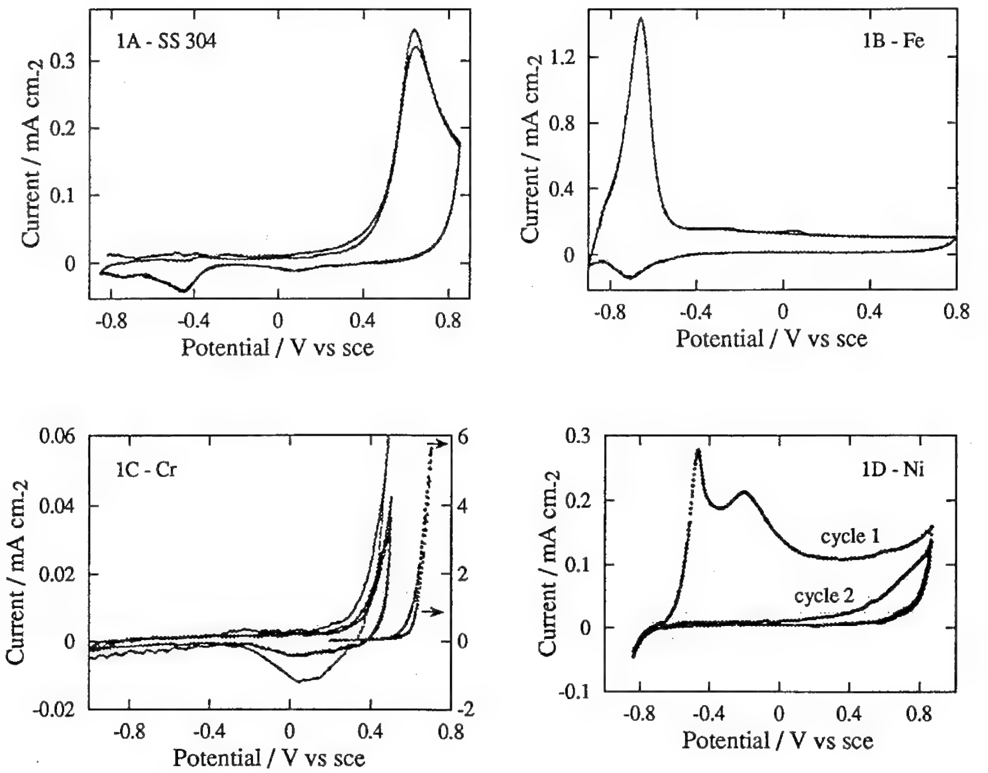

Fig. 1 Cyclic voltammograms for SS 304, iron, chromium and nickel electrodes rotated at 1000 rpm, dE/dt = 0.02 V s-1 in 1 M HaHCO3 solutions, pH8

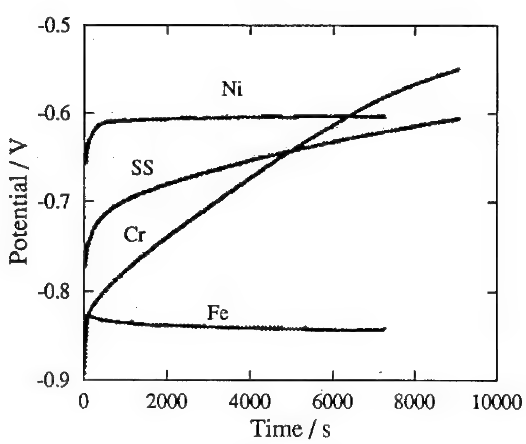

Fig. 2 Open circuit corrosion potential for SS 304, iron, chromium and nickel electrodes rotated at 1000 rpm in 1M $NaHCO_3$ solutions, pH 8

the oxidation of Cr(III) to Cr(VI) and oxygen evolution may proceed simultaneously in this potential range. Considering thermodynamical data in a neutral solution /9-11/, a sufficient overpotential exists to cause the dissolution of chromium oxide at potentials greater than +0.3V. In subsequent negative-going potential scan the cathodic current peak appeared at ~ +0.1V and slowly increased with the oxidation time at potentials ≥ 0.4V.

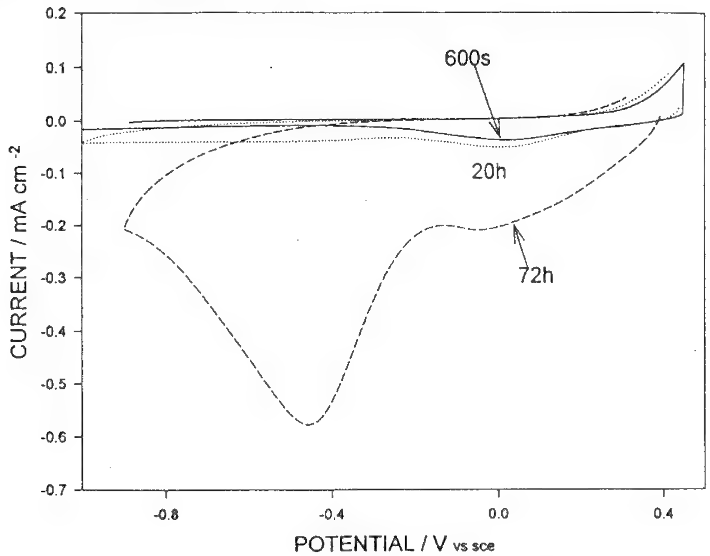

Fig. 3. Cyclic voltammograms for Cr-electrode oxidized at 0.45V for 600s, and at 0.4V for 20h and 72h; and subsequent cycling in negative direction with dE/dt = 0.05 V s^{-1}. Electrode rotated at 1000 rpm in 1M $NaHCO_3$ solution of pH 8.

A number of experiments was carried out with the Cr rotated electrode for various oxidation times in 1M $NaHCO_3$ solution and the formation of anodic film was estimated by reduction charges. Fig 3 shows the results for electrode oxidation at 0.45V for 600s, and at 0.4V for 20h and 72h, and subsequent cycling of the potential first in a negative then in a positive direction with a scan rate of 0.05 V s^{-1}. The surface film slowly grew during the first 20h but from 20h to 72h oxidation time, the reduction wave at 0.1V slightly increased but a new large current maximum dominated at -0.45V (Fig. 3). Some electrode passivation was evidenced by a decrease in the anodic current i_a to 3.3 μA cm^{-2} and by an increase in the reduction charge to Q_{red}=7.2 mC cm^{-2} for Q_{ox}=900 mC cm^{-2}. Under such circumstances the color of the electrode surface changed to bright gold. The oxidation product was easily reduced at a cathodic current peak located at -0.45V and the gold color disappeared after the first cathodic potential scan but once the electrode was removed from the solution and dried, the appearance of the surface remained unchanged in air.

The results suggested that Cr(VI) is dissolved into the solution and then precipitated as Cr(III) compounds. Some small amount of Cr(VI) species may be incorporated into the surface film and reduced at 0.1V cathodic wave. The reduction process of the surface film could be the transformation of Cr^{6+} to Cr^{3+}, Cr^{4+} to Cr^{3+} or Cr^{6+} to Cr^{4+}. The shape of the reduction current peak at -0.45V and the nature of the surface products combined with the lack of adhesion of the products suggest that the surface film is formed by a dissolution-precipitation mechanism.

Passivity of AISI 304 stainless steel at potentials above +0.4V

At the SS304 depassivation potential, 0.4V (Fig. 1a), the anodic current increases and a maximum is observed. This current peak was found to be independent of the rotation speed, ranging from 200 to 2000 rpm, revealing that the reaction rate is not limited by a diffusion to the solution process. The anodic current peak was found to be a linear function of $NaHCO_3$ concentration between 0.05M and 1M (Fig. 4), which means that the carbonate/bicarbonate react as complexant ions in the dissolution reaction of the low potential passive films. The potential of the anodic current peak at 0.6V remained constant, and it is deduced that the composition of the outer film is independent of the solution concentration. The measurements on SS304 in a borax solution at pH 8 show a similar shape of the polarization curves as in the carbonate/bicarbonate solution but the anodic and cathodic currents are smaller for the borate solution. The above considerations suggest that the second passivation is due to the formation of an oxide/hydroxide film, and the $CO_3^{=}/HCO_3^{-}$ ions are enhancing the dissolution rate without affecting on the passivation process.

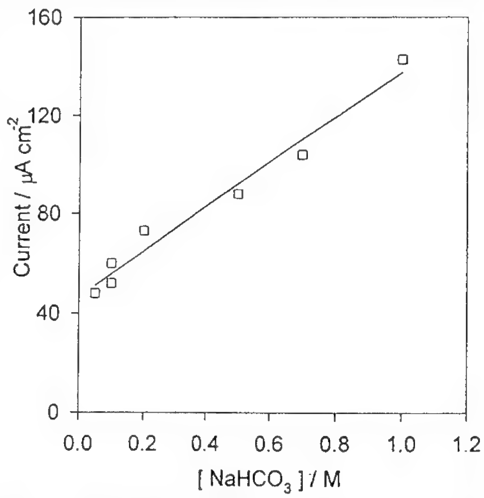

Fig. 4. Effect of $NaHCO_3$ concentration on anodic current maximum in positive potential region. SS304 electrode at 1000 rpm, dE/dt=0.005 V s^{-1}, pH=8.

The chemical composition of the surface films in two passive potential regions were different. The increase of anodic current above 0.4V corresponds to the solid-state oxidation of Cr(III) to Cr(VI) in the passive film. The formation of readily soluble chromium(VI) oxide and CrO_4^{2-} ions may explain the depassivation process at positive potentials.The Fe oxides which are an integral part of the passive film are still capable of surface passivation.

The occurrence of a critical potential at +0.4V in the properties of passive films on stainless steels containing chromium in neutral solutions have been reported in the literature /12-24/. The photoelectrochemical studies in 1M Na_2SO_4 solution /14,15,25/ demonstrate that passive film properties change with potential and strong changes occurred at +0.4V not only in the magnitude of the photocurrent but also in the shape of the photocurrent transients and capacitance values. Angular-dependent XPS examinations /6/ indicate an accumulation of Cr in the inner part of the films grown in alkaline solutions. Above +0.4V, the passive film is most probably composed of the chromium(III) oxide/hydroxide and the stable iron oxide γ-Fe_2O_3. Since Fe_2O_3 is isostructural with Cr_2O_3, Fe(III) may be easily substituted by Cr(III) in the lattice /25/ and subsequently Cr(III) oxidizes to Cr(VI). The presence of Cr(VI) in the oxides of the passive film on Fe-Cr alloys /4-6,16-19/ and on AlCr alloys /20,26/ at high positive potentials was demonstrated using x-ray absorption near edge spectroscopy (XANES) /16-18,20,26/ and XPS /4-6/ techniques. In passive film on SS304, CrO_4^{2-} was found to be formed and enriched in the solid state under the Fe-rich layer /4,6/. In the case of the Al-Cr alloy /25/, the stepping of the potential over a critical value resulted in Cr being incorporated into the Al oxide matrix in such a way that it was stable and could further oxidize to Cr(VI) without dissolving. According to the semiconductor model /24/, the oxidation of Cr(III) to Cr(VI) is expected to take place in the outer part of the film first. The CrO_4^{2-} species were not found in the extreme outer part of the film /5/ but appeared to populate the $Cr(OH)_3$ region below the outer

most surface. It is assumed that the CrO_4^{2-} ions are lost by selective dissolution. Aging has a beneficial effect on the stability of the passive layer and on the resistance to pitting /27/. The pitting resistance is directly related to changes in the chemistry of the passive film.

In the present investigation a series of experiments was performed to study the effect of the potential, charge and time of oxidation on passive film formation. The anodic film was formed on the rotating-disc electrodes by applying a potential step from -0.8V to high positive potential, and the nature and the quantity of the oxidation species were deduced from the reduction current waves using potentiodynamic and galvanostatic techniques. The high reduction current or long time needed for performing galvanostatic measurements had a detrimental effect on their sensitivity. The charges associated with the reduction waves increased with time for both the voltammetric and galvanostatic techniques, but poor reproducibility of data with the oxidation charge, time and potential allows led to only qualitative conclusions. The voltammetric technique seems to be more sensitive.

Figs. 5-7 show the effect of the oxidation time on the passive film formation. The potentiodynamic traces of Fig. 6 were recorded after 600s, 20h, 72h and 170h oxidation times, and the negative-going potential scan was 0.05 V s^{-1}. The amount of anodic products evaluated from the charge of the cathodic current waves increased with oxidation time. Simultaneously with the increase of the cathodic current peak(I) at ~0V, the current peak(II) at -0.6V becomes larger indicating that the product reduced at current peak(I) is at a higher oxidation state. Whereas the potential of current peak(II) remained unchanged, the potential of current peak(I) shifted in a positive direction indicating that the anodic product changed with the oxidation time; when a larger amount of product was accumulated, the corrosion product became easily to reduce.

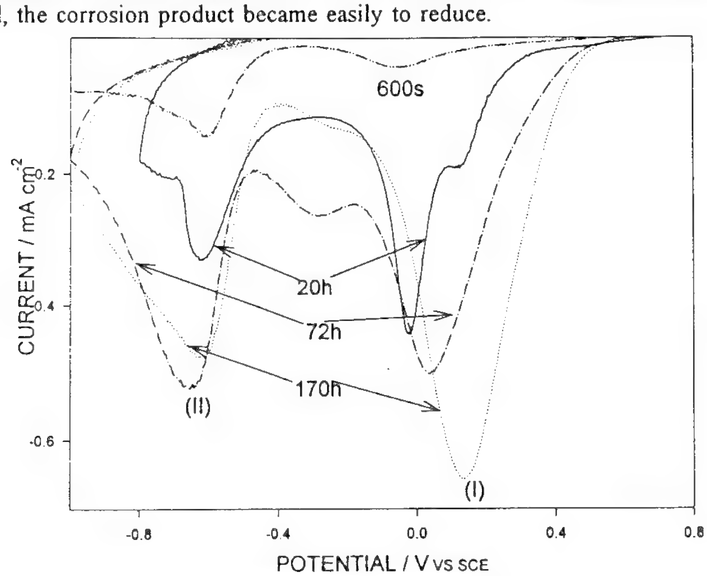

Fig. 5. Effect of the oxidation time of 600s, 20h, 72h and 170h at potential of 0.7V, illustrated by subsequent cycling of potential in negative direction with dE/dt = 0.05V s^{-1}. Electrode rotated at 1000 rpm in 1M $NaHCO_3$ solution of pH 8.

In order to compare the behavior of passive films formed on SS304 and Fe electrodes, the measurements were performed after a constant oxidation time and a comparable oxidation charge. The voltammograms after 20h oxidation time of SS304 in 1M $NaHCO_3$ and Fe in 0.5M $NaHCO_3$ solutions are presented in Fig. 6 and for an oxidation charge of 40mC cm^{-2} for both electrodes in 1M $NaHCO_3$ solution in Fig. 7. When an anodic potential step from -0.8V to +0.7V was applied

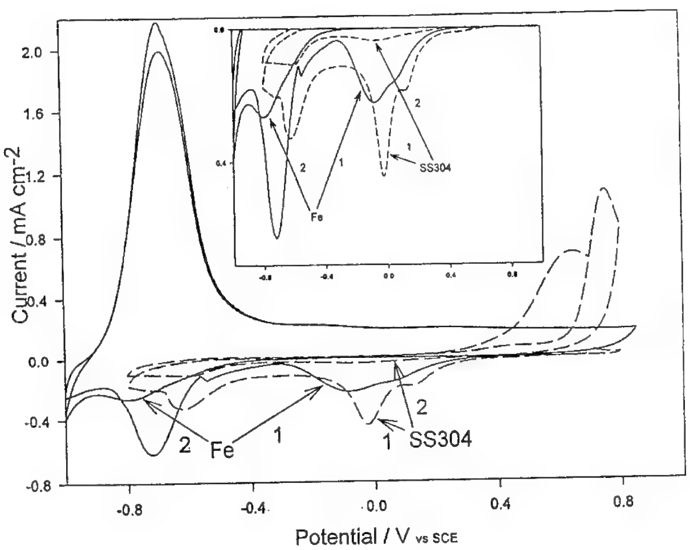

Fig. 6. Effect of 20h oxidation time on the passive film formation at potential of 0.7V on SS304 electrode in 1M $NaHCO_3$ solution and Fe electrode in 0.5M $NaHCO_3$ solution, illustrated by subsequent cycling of potential in negative direction with dE/dt = 0.05 V s^{-1}. Electrodes rotated at 1000 rpm.

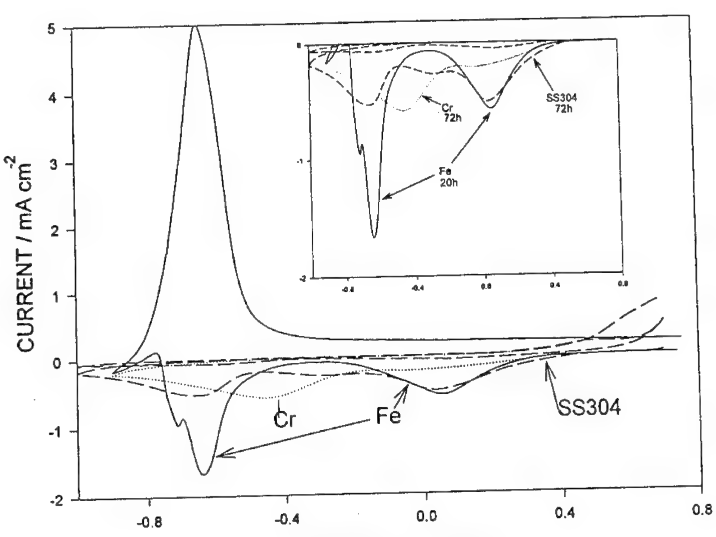

Fig. 7. Effect of an oxidation charge of 40 mC cm^{-2}, at potential 0.7V, on the passive film formation on SS304 and Fe electrodes. The amount of product was determined by subsequent cycling of potential in negative direction with dE/dt = 0.05 V s^{-1}. The results for Cr-electrode oxidized to 900 mC cm^{-2} (72h) are also shown for comparison purposes.

to the SS304 and Fe electrodes, the anodic current transient dropped (within several minutes) to a stable low value, less than 1μA cm^{-2} (although, the oxidation current remained much larger for the Cr-electrode, i.e., 15 μA cm^{-2} after 20h of oxidation). The shape of the cathodic sides of the voltammetric curves was similar for the SS304 and Fe electrodes. The largest increase of the cathodic charge was observed for the surface product reduced at 0.1V. This cathodic wave corresponds to the reduction of compounds in a high oxidation state, formed at a high positive potential, located in the second passivity region. The film thickens for a longer oxidation time, e.g. for the SS304-electrode the reduction charge increased from 0.3 mC cm^{-2} for 600s to 4.5 mC cm^{-2} for 72h. For the Fe-electrode, the quantity of the charge linked to the reduction of oxidation species grew faster than for the SS304-electrode. Under the experimental conditions of Fig. 7, the 40 mC cm^{-2} oxidation charge required an oxidation time of 72h for SS304 compared to 20h for iron to obtain a comparable reduction charge related to the current peak at 0.1V. Reduction current peak(II) at -0.6V, which increases as the cathodic current peak(I) becomes larger, is assigned to the reduction of Fe(II) products. It should be noted, that for the Cr-electrode in 1M $NaHCO_3$ solution after 72h oxidation time, a 900 mC cm^{-2} oxidation charge was measured and the cathodic characteristics were very different, as pointed above.

The surface of SS304, iron and 1024 mild steel rotating electrodes, anodically polarized for a sufficient duration of time or to have an oxidation charge >20 mC cm^{-2}, changed the color to a "brilliant gold", and an homogeneous surface layer with no traces of localized corrosion was observed under the optical microscope. The similar appearance of a gold color was noticed in the bicarbonate as well as in the borate solutions of pH 8. The film adhered well and after rinsing and drying the electrode surface remained unaffected in contact with air. In the solution, the gold color was stable only under the anodic potential above 0.4V; it was easily reduced at ~ 0.1V in the first negative-going potential scan or at open-circuit potential. The surface film was not uniform with the stationary electrode; rather, black spots were noticed on the surface, probably due to the precipitation of the dissolved species.

The overall results indicate that athigh potential passive region the electrochemical and chemical reactions occur simultaneously, and the oxidation time and charge are very impotant parameters. Since Fe_2O_3 is substantially less soluble than Cr(VI) species, the iron oxides should be an integral part of the passive film. The iron oxides may further oxidize to ferrate and by analogy with CrO_4^{2-}, a small amount of these anions may be incorporated into the passive film. The ferrate (VI) ion is relatively stable in basic solution, but in neutral and acidic solution it decomposes. It is an extremely potent oxidizing agent, even stronger than permanganate, and it can oxidize Cr(III) to chromate. The potassium ferrate has been shown to be isomorphous with potassium chromate. A part of the oxides film is most likely due to the dissolution and precipitation of ferric ions but for extended oxidation period the active dissolution is inhibited and oxidation via a direct growing passive layer becomes quite possible. The surface film is saturated with oxygen due to the oxidation of water molecules. Under such conditions, and since the composition of the passive films is potential dependent and the surface species may be stable only under the high positive potential or when dehydrated, the film of Fe(III) oxides has to be responsible for passivation SS304 electrode surface at potentials above 0.5V.

Conclusions

Two types of passive films on SS304 electrode surface with a different chemical composition are proposed. In the low potential range, the SS304 electrode behaves like a Cr-rich metallic phase, the dissolution of Fe^{++} ions was independent of carbonate solution concentration, and it was unhindered by the formation of Cr_2O_3 layer. This passive film was partially dissolved at 0.4V, and at higher potential a new passive film was formed. The dissolution reaction was dependent on

carbonate solution concentration. Since the electrochemical and chemical reactions occur simultaneously, the dissolution of chromium, subsequent enrichment in iron (III) oxides and increase of overall thickness of the film are potential and time dependent.

The coloration of stainless steel 304, mild steel 1024 and iron was observed at high positive potentials in carbonate/bicarbonate and borate solutions of pH 8. The uniform gold color surface film remains unchanged in air and in the solution when under potential above 0.4V but it disappeared at open-circuit potential or it was easy to reduce in negative-going potential scan.

Acknowledgments

This research was supported by Hydro-Quebec (IREQ) and Natural Sciences and Engineering Research Council of Canada.

REFERENCES

1. A.M.P. Simões, M.G.S. Ferreira, G. Lorang, M. da Cunha Belo, Electrochim. Acta, **36**, 315 (1991).
2. M.G.S. Ferreira, T. Moura e Silva, A.Catarino, M. Pankuch, C.A. Melendres, J. Electrochem. Soc., **139**, 3146 (1992).
3. M. Metikoš-Huković, M. Ceraj-Cerić, J. Electrochem. Soc., **134**, 2193 (1987).
4. A.R. Brooks, C.R. Clayton, K. Doss, Y.C. Lu, J. Electrochem. Soc., **133**, 2459 (1986).
5. C.R. Clayton, Y.C. Lu, J. Electrochem. Soc., **133**, 2465, (1986).
6. C. Calinski, H.-H. Strehblow, J. Electrochem. Soc., **136**, 1328 (1989).
7. I. Olefjord, L. Wegrelius, Corros. Sci., **31**, 89 (1990).
8. N. Hara, K. Sugimoto, J. Electrochem. Soc., **126**, 1328 (1979).
9. M. Pourbaix, Atlas of electrochemical equilibria in aqueous solutions, NACE, Texas, (1974).
10. K. Niki in A.J. Bard, R. Parsons and J. Jordan (Eds.), Standard Potentials in Aqueous Solutions, M. Dekker, New York (1985), p. 453.
11. G.H. Kelsall, C.I. House, F.P. Gudyanga, J. Electroanal. Chem., **244**, 179 (1988).
12. M. Drogowska, L. Brossard, H, Ménard, submited to J. Applied Electrochem.
13. M. Drogowska, L. Brossard, H. Ménard, submited to Corrosion Sci.
14. P. Schmuki, H. Böhni, J. Electrochem. Soc., **139**, 1908 (1992).
15. P. Schmuki, H. Böhni, in *Proc. of the Symposium on Oxide Films on Metals and Alloys,* The Electrochemical Society Meeting, Toronto 1992, p. 326.
16. J.A. Bardwell, G.I. Sproule, D.F. Mitchell, B. MacDougall, M.J. Graham, J. Chem. Soc. Faraday Trans., **87**, 1011 (1991).
17. J.A. Bardwell, G.I. Sproule, B. MacDougall, M.J. Graham, A.J. Davenport, H.S. Isaacs, J. Electrochem. Soc., **139**, 371 (1992).
18. A.J. Davenport, M. Sansone, J.A. Bardwell, A.J. Aldykiewicz, Jr., M. Taube, C.M. Vitus, J. Electrochem. Soc., **141**, L6 (1994).
19. G.G. Long, J. Kruger, D. Tanaka, J. Electrochem. Soc., **134**, 264 (1987).
20. J. Davenport, H.S. Isaacs, G.S. Frankel, A.G. Schrott, C.V. Jahnes, M.A. Russak, J. Electrochem. Soc., **138**, 337 (1991).
21. D. Landolt, in *Passivity of Metals,* R.P. Frankenthal, J. Kruger, eds., The Electrochem. Soc. Inc, Princeton, N.J., 1978, p. 484.
22. C.Y. Chao, L.F. Lin, D.D. Macdonald, J. Electrochem. Soc. **129**, 1874 (1982)
23. S. Silverman, G. Cragnolino, D.D. Macdonald, J. Electrochem. Soc. **129**, 2419 (1982)
24. P. Schmuki, H. Böhni, J. Electrochem. Soc., **141**, 362, (1994).
25. A.M.P. Simoes, M.G.S. Ferreira, B. Rondot, M. da Cunha Belo, J. Electrochem. Soc., **137**, 82

(1990).
26. G.S. Frankel, A.G. Schrott, A.J. Davenport, H.S. Issacs, C.V. Jahnes, M.A. Russak, J. Electrochem. Soc., **141**, 83 (1994).
27. W.P.Yang, D. Costa, P. Marcus, in *Proc. of the Symposium on Oxide Films on Metals and Alloys,* The Electrochemical Society Meeting, Toronto 1992, p. 516.

Materials Science Forum Vols. 185-188 (1995) pp. 779-788

Similarity and difference in roles of chromium and molybdenum in passivating amorphous alloys in concentrated acids

K. Hashimoto, P.-Y. Park, J.-H. Kim, E. Akiyama, H. Habazaki, A. Kawashima and K. Asami

Institute for Materials Research, Tohoku University, Sendai 980-77, Japan

Keywords: Role of Cr, role of Mo, role of valve metal, spontaneous passivation, passivity in concentrated HCl

Abstract

A variety of alloys including Cr-valve metal, Mo-valve metal and Cr-Mo-Ni alloys have been successfully prepared in a single amorphous phase. All these alloys have extremely high corrosion resistance. Because of the formation of a single phase solid solution these alloys are suitable for study of the role of alloying element in the alloy matrix in enhancing the corrosion resistance. Amorphous Cr-valve metal alloys are spontaneously passive in 6 M and 12 M HCl. Their corrosion rates are significantly lower than those of alloy constituents and decrease with increasing alloy chromium content. Amorphous Cr-Mo-Ni alloys with high chromium and molybdenum contents are spontaneously passive in 12 M HCl, and their corrosion resistance increases with alloy molybdenum content. Zr-Mo alloys are spontaneously passive showing lower corrosion rates in comparison with those of zirconium and molybdenum metals. The corrosion rate of Zr-Mo alloys is lower when the alloy molybdenum content is lower. Cr-valve metal alloys form spontaneously passivated double oxyhydroxide films containing both chromic ion and valve metal cation. Cr-Mo-Ni alloys form a passive hydrated chromium oxyhydroxide film. Zr-Mo alloys form a bi-layered passive film of zirconium and molybdenum oxyhydroxide. When the cathodic reaction is oxygen reduction, the passivity of chromium is stable while the tetravalent molybdenum passive film often suffers trans-passive dissolution. The difference in the stability of the passive film affects the corrosion resistance and passive film composition, particularly when the stability of the film is high and when the corrosion potential is high.

Introduction

Tailoring corrosion-resistant new alloys has recently been performed mostly by sputter deposition technique. This technique is particularly suitable to form a single phase solid solution even when the boiling point of a component is lower than the melting point of the rest of components and/or when a component is immiscible to another component in the liquid state. A variety of alloys including aluminum-refractory metal [1-3], chromium-valve metal [4-8] and molybdenum-valve metal [9] alloys have been successfully prepared in a single amorphous phase. All these alloys show extremely high corrosion resistance in hydrochloric acids. Besides the high corrosion resistance, these alloys are suited for study of the role of alloying element in the alloy matrix in enhancing the corrosion resistance because of the formation of a single phase solid solution.

Both chromium and molybdenum are effective elements in enhancing the corrosion resistance especially in acidic environments. It has been well known [10] that the beneficial effect of molybdenum contained in steels is enhanced by increasing the chromium content. There are a number of investigations on the role of molybdenum in enhancing the corrosion resistance of chromium-bearing iron base alloys [10-12]. Some of the present authors [13] in studying the effect of molybdenum in

a ferritic stainless steel have reported that the molybdenum addition results in a large decrease in the passive current density due to elimination of weak points in the chromium-enriched passive film. Later investigation for amorphous Fe-Cr-Mo-P-C alloys by some of the present authors [14] has clarified that when anodic polarization for passivation is carried out, molybdenum prevents dissolution of chromium from the air-formed film and leads to rapid formation of a stable passive film in which chromic ions are highly concentrated.

Since the beneficial effects of chromium and molybdenum are found separately in binary chromium-valve metal alloys and molybdenum-valve metal alloys, it becomes possible to identify their roles separately from each other.

In this paper the roles of chromium and molybdenum in enhancing the passivating ability and thereby enhancing the corrosion resistance of the alloys have been discussed on the basis of the data obtained recently for extremely corrosion-resistant alloys [4-9,16].

Experimental

DC magnetron sputter deposition was used for preparation of amorphous alloys [1,16]. Targets were composed of a metal disc of 100 mm diameter and 6 mm thickness, on the sputter-erosion region of which small discs of alloying elements were symmetrically placed. The alloy composition was controlled by changing the number of small discs placed on the large disc. The target was placed upward in the sputtering chamber, and three substrates were placed downward and symmetrically around a central axis of the sputtering chamber. Glass plates were used as the substrates. For the purpose of homogenization of the sputter-deposits, the water-cooled three substrates were revolved around the central axis of the chamber, along with revolution of the substrates themselves around a central axis of each substrate disc.

Cr-Ti [4], Cr-Zr [5], Cr-Nb [6], Cr-Ta [6], Mo-Zr [9], Cr-Mo [8] and Cr-Mo-Ni [15] alloys were prepared by sputter deposition. The composition of sputter deposits was determined by an electron probe-microanalysis and the structure of the deposits was identified by X-ray diffraction.

Corrosion rates of alloys were estimated from amounts dissolved in 6 M or 12 M HCl at 30°C for mostly 168 h. Amounts dissolved were analyzed by means of inductively coupled plasma emission spectrometry.

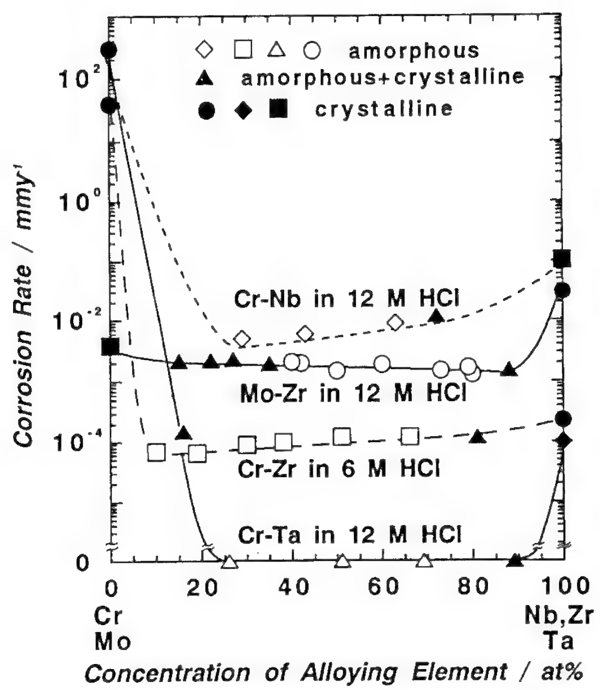

Fig. 1 Corrosion rates of Cr-Zr alloys in 6 M HCl at 30°C [5] and Cr-Nb [6], Cr-Ta [6] and Mo-Zr [8] alloys in 12 M HCl at 30°C.

Surfaces before and after immersion or polarization in solutions were characterized by X-ray photoelectron spectroscopy. Binding energies of electrons were calibrated by a method described elsewhere [17]; the binding energies of the Au $4f_{7/2}$ and $4f_{5/2}$ electrons of gold metal and the Cu $2p_{3/2}$ and $2p_{1/2}$ electrons of copper metal were taken as 84.07, 84.74, 932.53 and 952.35 eV, respectively, and the kinetic energy of the Cu $L_3M_{4,5}M_{4,5}$ Auger electron of copper metal as 918.65 eV. The composition and thickness of the surface film and the composition of the underlying alloy surface were determined by the previously proposed method [18,19] by using integrated intensities of photoelectrons under the assumption of three layered structure: the outermost contaminant hydrocarbon layer, the passive film and the substrate alloy with X-ray photoelectron spectroscopically infinite thickness, in each layer of which elements distribute homogeneously.

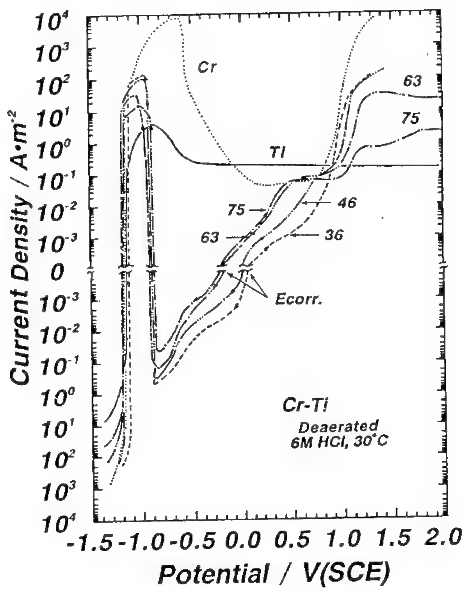

Fig. 2 Potentiodynamic polarization curves of Cr-Ti alloys measured in deaerated 6 M HCl at 30°C [5].

Results and Discussion

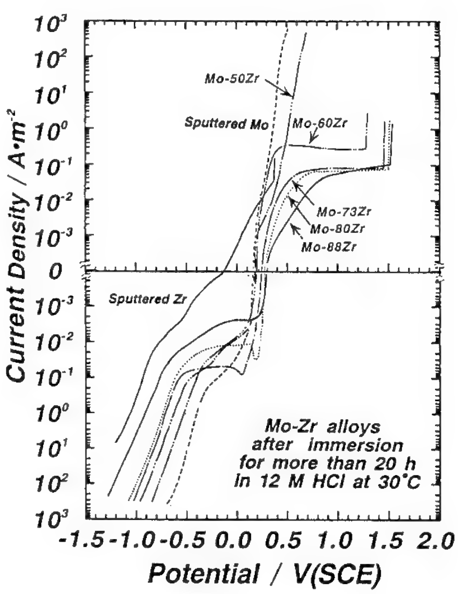

Fig. 3 Potentiodynamic polarization curves of molybdenum and zirconium metals and Mo-Zr alloys measured after immersion for more than 20 h in deaerated 6 M HCl at 30°C.

Figure 1 shows change in corrosion rates of Cr-Zr alloys in 6 M HCl [5] and Cr-Nb [6], Cr-Ta [6] and Mo-Zr [8] alloys in 12 M HCl at 30°C. Regardless of alloy structure all binary alloys have extremely high corrosion resistance that is higher than that of component metals. In particular, Cr-Ta alloys are immune to corrosion even in very aggressive 12 M HCl. The absolute value of the corrosion rate is determined by the valve metal contained in the alloy. Nevertheless, the corrosion resistance of chromium-valve metal alloys increases with increasing alloy chromium content. Accordingly, chromium is more effective in enhancing the corrosion resistance, although both chromium and valve metal act synergistically in improving the corrosion resistance. Mo-Zr alloys also have extremely high corrosion resistance, and increasing alloy zirconium content increases the corrosion resistance. Hence, zirconium is more effective in enhancing the corrosion resistance of Mo-Zr alloys. Consequently, roles of molybdenum and chromium in increasing the corrosion resistance are clearly different from each other because increasing chromium content is more effective in Cr-Zr alloys but increasing

molybdenum content is detrimental in Mo-Zr alloys even though the corrosion rate of zirconium metal in aggressive hydrochloric acid is more than one order of magnitude higher than that of Mo-Zr alloys.

On the other hand, it has been found [15] that when the ratio of chromium to nickel is fixed in chromium-rich Cr-Mo-Ni alloys, increasing molybdenum content decreases the corrosion rate in 12 M HCl at 30°C. Similarly, the corrosion resistance of binary Cr-Mo alloys in 12 M HCl at 30°C increases with increasing alloy molybdenum content, but cannot exceed the corrosion resistance of molybdenum metal [8]. We can, therefore, generally say that molybdenum is more effective than chromium in enhancing the corrosion resistance of alloys containing both chromium and molybdenum in less oxidizing strong acids.

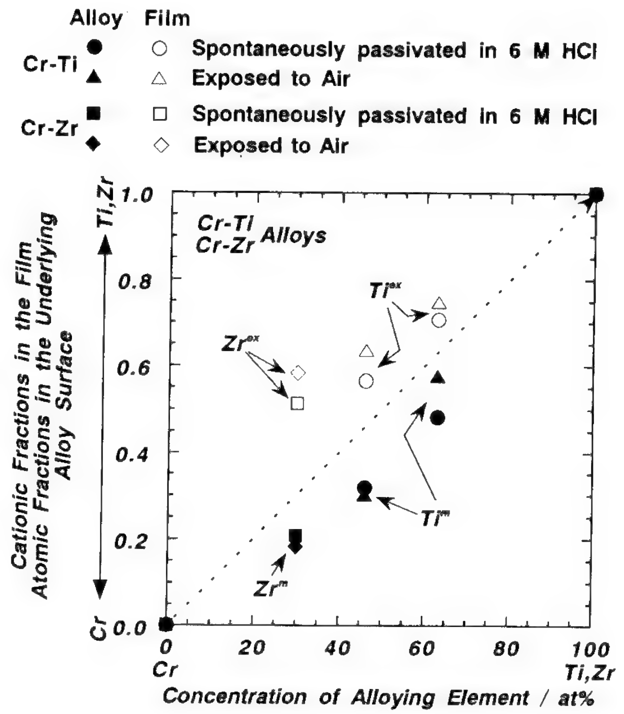

Polarization curves of these alloys are different from an alloy family to another alloy family. Figure 2 shows potentiodynamic polarization curves of Cr-Ti alloys measured in deaerated 6 M HCl at 30°C [5]. All these alloys are spontaneously passive in this aggressive acid. Decreasing alloy titanium content, that is, increasing alloy chromium content decreases anodic current density. Cathodic polarization results in depassivation in the active region of chromium and titanium. Because of poor deaeration, oxygen reduction occurs by slight cathodic polarization. The most interesting fact is that increasing alloy chromium content increases cathodic currents for oxygen reduction and hydrogen evolution. When potentiodynamic cathodic polarization is carried out, cathodic reactions take place before depassivation, and hence oxygen and proton reductions occur on the spontaneously passivated film. Accordingly, increasing film chromium content leads to an increase in activities for cathodic oxygen and proton reductions as well as decrease in the anodic current density. Almost the same behavior has been found for Cr-Zr alloys in 6 M HCl [5] and Cr-Nb and Cr-Ta alloys in 12 M HCl [6], although cathodic depassivation does not occur for further corrosion-resistant Cr-Ta alloys.

Fig. 4 Cationic fractions in the surface film and atomic fractions in the alloy surface just under the surface film for Cr-Ti and Cr-Zr alloys exposed to air after mechanical polishing in cyclohexane and spontaneously passivated in 6 M HCl at 30°C.

Figure 3 shows potentiodynamic polarization curves of Mo-Zr alloys in 12 M HCl at 30°C. All alloys are spontaneously passive in this aggressive acid. Zirconium metal is also passive and shows a relatively low activity for cathodic reactions. Anodic polarization leads to pitting corrosion of zirconium at potentials higher than 0.3 V(SCE). It has been known [20] that molybdenum in 6 M

HCl at 30°C is passive in the potential region from about -0.2 to about +0.2 V(SCE) forming a tetravalent molybdenum oxide film but suffers active dissolution in the potential region from about -0.45 to about -0.2 V(SCE) and transpassive dissolution at potentials higher than about +0.2 V(SCE). As can be seen in Figure 3, molybdenum is passive under the open circuit condition and shows significantly high cathodic activities for oxygen and proton reductions. Anodic polarization of molybdenum results in a sharp increase in the current due to transpassivation. The open circuit potential for Mo-Zr alloys is very close to that of molybdenum metal. Polarization curves of alloys with 50 at% or less zirconium are similar to the curve of molybdenum metal, although anodic and cathodic current densities of alloys are lower than those of molybdenum metal. Alloys with 60 at% or more zirconium exhibit a wide passive region, and hence the zirconium addition prevents transpassive dissolution of molybdenum. Further anodic polarization results in pitting at potentials higher than 1.3 V(SCE). It is noteworthy that the open circuit potential of zirconium-rich alloys exceeds that of molybdenum metal. This suggests that the top most surface of the passive film does not contain molybdenum because of transpassive dissolution of molybdenum.

XPS analysis gives a useful information on roles of various alloying elements. Figure 4 shows cationic fractions in the surface film and atomic fractions in the alloy surface just under the surface film for Cr-Ti [4] and Cr-Zr [5] alloys exposed to air after mechanical polishing in cyclohexane and passivated spontaneously in 6 M HCl at 30°C. Both air-formed films and spontaneously passivated films on Cr-Ti and Cr-Zr alloys are composed of valve metal cations and chromic ions, and valve metal cations are rather concentrated. They are formed by preferential oxidation of valve metals and hence valve metals are deficient in the underlying alloy surface.

Figure 5 shows cationic fractions in the surface film and atomic fractions in the alloy surface just under the surface film for Mo-Zr alloys exposed to air after mechanical polishing in cyclohexane and passivated spontaneously in 12 M HCl at 30°C [9]. Zirconium is rich in the air-formed film but deficient in the underlying alloy surface. The formation of the zirconium-enriched surface film is due to preferential oxidation of zirconium. After spontaneous passivation, the film composition is changed. The molybdenum-enriched passive film is formed on alloys with less than 40 at% zirconium, while the zirconium-enriched passive film is formed on alloys with more than 40 at% zirconium. When the zirconium-enriched passive film is formed, zirconium in the underlying alloy surface becomes significantly deficient. When

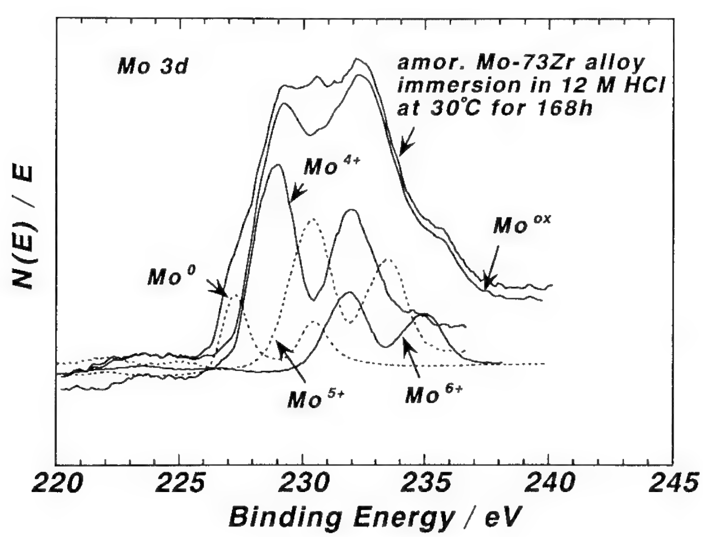

Fig. 5 Cationic fractions in the surface film and atomic fractions in the alloy surface just under the surface film for Mo-Zr alloys exposed to air after mechanical polishing in cyclohexane and spontaneously passivated in 12 M HCl at 30°C.

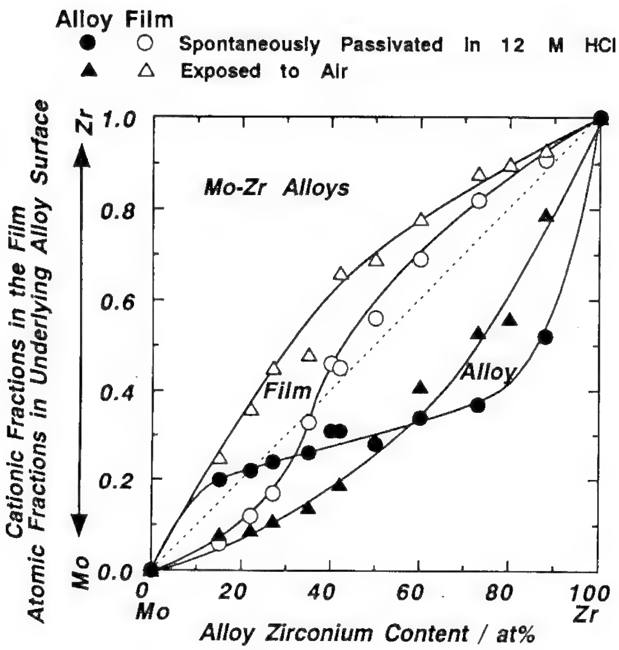

Fig. 6 Mo 3d spectrum measured from amorphous Mo-73Zr alloy after immersion in 12 M HCl at 30°C for 168 h. The spectrum consists of spectra corresponding to the metallic and oxidized states of molybdenum, and the spectrum of the oxidized state of molybdenum is further composed of molybdenum cations in the three kinds of oxidized states.

the molybdenum-enriched passive film is formed, zirconium is not appreciably enriched in the underlying alloy surface. Accordingly, all films are formed as a result of preferential dissolution and oxidation of zirconium.

An example of the Mo 3d spectrum is shown in Figure 6. Molybdenum in the surface film is composed of Mo^{4+}, Mo^{5+} and Mo^{6+} ions. The binding energies of the Mo $3d_{5/2}$ electrons in Mo^{6+}, Mo^{5+}, Mo^{4+} and Mo^{0} were taken as 232.2, 2230.5, 229.1 and 227.8 eV [21], respectively. The major molybdenum species in the passive film was Mo^{4+} ions, although Mo^{6+} ions were the major species in the air-formed film on molybdenum-rich alloys [9]. The relative amount of Mo^{4+} in the spontaneously passivated film decreased with alloy zirconium content [9]. Nevertheless, the major molybdenum species in the passive film was always Mo^{4+} [9], since molybdenum was in the passive state where molybdenum metal forms a tetravalent molybdenum oxide film [20, 22].

An important information on the structure of the surface film is obtained from the change in the binding energies of inner shell electrons of alloy components. In general, for chromium-valve metal alloys, the formation of alloys results in charge transfer from a valve metal atom to more electronegative chromium atom in the alloys. Accordingly, XPS measurements show that alloying leads to an increase in the binding energies of inner shell electrons of valve metals and to a decrease in the binding energy of Cr $2p_{3/2}$ electrons [4,5,7]. The situation is different in the passive film. Figure 7 shows binding energies of Cr $2p_{3/2}$ electrons in Cr^{3+} ions and Ti $2p_{3/2}$ electrons in Ti^{4+} ions in the spontaneously passivated film on Cr-Ti alloys [4]. In comparison with the binding energy of the Cr $2p_{3/2}$ electrons in the passive film formed on chromium metal, the peak binding energy of the Cr^{3+} $2p_{3/2}$ electrons in Cr^{3+} ions in the passive film on Cr-Ti alloys is higher, while that of the Ti^{4+} $2p_{3/2}$ electrons is lower than the binding energy of the Ti^{4+} $2p_{3/2}$ electrons in the passive film on titanium metal. This means that charge transfer occurs from chromic ion to titanium ion. Accordingly, these two kinds of cations locate very closely in the passive film to show the electronic interaction between them. It can, therefore, be said that the passive film formed on the binary Cr-Ti alloys does not consist of a simple mixture of chromium oxyhydroxide and titanium oxide but is composed

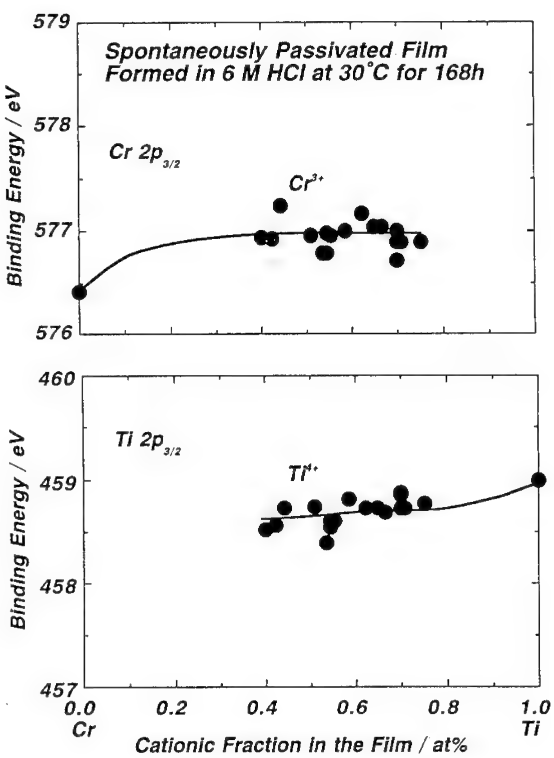

Fig. 7 Binding energies of Cr $2p_{3/2}$ electrons in Cr^{3+} ions and Ti $2p_{3/2}$ electrons in Ti4+ ions in the spontaneously passivated film on Cr-Ti alloys in 6 m HCl at 30°C.

of double oxyhydroxide of chromium and titanium. The charge transfer from chromic ions to valve metal cations has been fond similarly for Cr-Zr [5], Cr-Nb [7] and Cr-Ta [7] alloys. In this connection, although the binding energy of the Cr $2p_{3/2}$ electrons of chromium oxyhydroxide is higher than that of chromium oxide [17], this is not the case, since the ratio of $[O^{2-}]/[OH^-]$ in the spontaneously passivated film generally increases with the content of valve metal cations [4,5,7]. Accordingly, chromium and valve metal cations forms double oxyhydroxide film.

Consequently, formation of the passive double oxyhydroxide film seems responsible for better corrosion resistance of the alloys than alloy constituents. In addition, the composition of the air-formed film on chromium-valve metal alloys is not largely different from that of the passive film. Thus spontaneous passivation of these alloys occurs without considerable reconstruction of the air-formed film to the passive film even in aggressive concentrated hydrochloric acids. When the film chromium content is high, the anodic dissolution current is low and the cathodic currents for oxygen and proton reductions are high. For instance, the current density of chromium metal in the passive region in 6 M HCl is lower than passive current densities of titanium and zirconium. It can, therefore, be said that as far as the passive film is stable, the higher the film chromium content, the higher the protective quality of the passive film formed on the chromium-valve metal alloys. The formation of the passive film with a high concentration of chromium decreases the anodic current and increases the cathodic oxygen reduction current with a consequent increase in the open circuit potential.

Figure 8 shows binding energies of Mo $3d_{5/2}$ electrons in Mo^{4+} ions and Zr $3d_{5/2}$ electrons in Zr^{4+} ions in the surface film on Mo-Zr alloys exposed to air after mechanical polishing in cyclohexane and passivated spontaneously in 12 M HCl at 30°C [9]. There are Mo^{4+}, Mo^{5+} and Mo^{6+} ions in the film. Because the major molybdenum species in the passive film is Mo^{4+}, the comparison is made for the binding energy of Mo $3d_{5/2}$ electrons in Mo^{4+} ions. The peak binding energy of the Mo^{4+} $3d_{5/2}$ electrons in the air-formed film on the alloy decreases with increasing film zirconium content, while that of the Zr^{4+} $3d_{5/2}$ electrons in the air-formed film on the alloy increases the film molybdenum content. This means that charge transfer occurs from Zr^{4+} ion to Mo^{4+} ion in the air-formed film. Accordingly, these two kinds of cations locate very closely in the air-formed film to show the

electronic interaction between them. It can, therefore, be said that the air-formed film on the binary Mo-Zr alloys consists of a double oxyhydroxide of molybdenum and zirconium.

By contrast, the binding energies of Mo^{4+} and Zr^{4+} $3d_{5/2}$ electrons in the spontaneously passivated film are not affected by the film composition. XPS analysis reveals that, since the chloride content in the film is very low, the major anions in the passive film are oxyhydroxides. It is, therefore, likely that the passive film consists of bi-layered structure of zirconium oxyhydroxide and molybdenum oxyhydroxide. Molybdenum dissolves transpassively from the film surface on zirconium-rich alloys at the open circuit potential and metallic molybdenum is concentrated in the underlying alloy surface for zirconium-rich alloys. Molybdenum contributing to the passivity is Mo^{4+} species. Consequently, the passive film formed on Mo-Zr alloys seems consist of an outer zirconium oxyhydroxide and inner molybdenum oxyhydroxide. Depth profiling by argon ion sputter etching is not effective for this type of alloys. Sputter etching leads to reduction of molybdenum and zirconium to the metallic state and to formation of zirconium carbide.

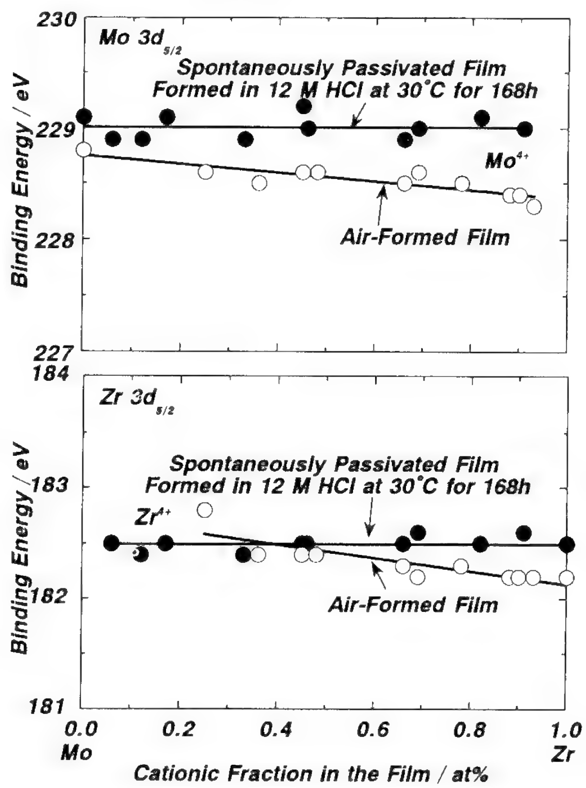

Fig. 8 Binding energies of Mo $3d_{5/2}$ electrons in Mo^{4+} ions and Zr $3d_{5/2}$ electrons in Zr^{4+} ions in the surface film on Mo-Zr alloys exposed to air after mechanical polishing in cyclohexane and passivated spontaneously in 12 M HCl at 30°C.

Some of the present authors [13] in investigating the beneficial effect of molybdenum addition to stainless steels have stated that more than two orders of magnitude decrease in the current in the passive region as a result of the addition of only 1 % of molybdenum to ferritic 30Cr steel is not due to the change in the diffusional transport of matters through the passive film but is based on a decrease in the activity of weak points in the passive film. In other words, the passive current for alloys in aggressive solutions is leakage currents through weak points of the passive film and the addition of a beneficial element decreases the activity of the weak points.

The significantly high corrosion resistance of Mo-Zr alloys in comparison with zirconium and molybdenum metals seems attributable to the fact that weak points in each layer are protected by another layer in the bi-layered passive film formed on the Mo-Zr alloys. The zirconium oxyhydroxide film protected by the underlying tetravalent molybdenum oxyhydroxide film has a very low activity of weak points, and hence the open circuit potential becomes very high. The open circuit potential for the zirconium-rich alloys is higher than the potential for transpassivation of molybdenum, and hence increasing alloy molybdenum content decreases the corrosion resistance of the alloys. Conse-

quently, Mo-Zr alloys have higher corrosion resistance in comparison to molybdenum and zirconium metals, but the lower the molybdenum content of the alloys the higher is the corrosion resistance in very aggressive hydrochloric acids.

On the other hand the spontaneously passivated film on Cr-Mo and Cr-Mo-Ni alloys in 12 M HCl are significantly rich in chromic ions [9.15]. The passive film consists of major hydrated chromium oxyhydroxide and minor tetravalent molybdenum oxide. The open circuit potential of these alloys is also significantly high but does not exceed that of molybdenum metal. As far as transpassivation of molybdenum does not occur, the alloy with a higher molybdenum content is more corrosion-resistant in concentrated hydrochloric acid. In particular, the angle resolved XPS analysis of the passive film formed on binary Mo-Cr alloys revealed that the passive film consists of bi-layered structure of outer chromium oxyhydroxide and inner molybdenum oxide. In this connection, the binding energies of inner shell electrons of chromium and molybdenum did not show the film composition dependence, similarly to Mo-Zr alloys.

In this manner, when oxygen reduction is the cathodic reaction, the passive film on chromium has a high stability but the passive tetravalent molybdenum film often suffers transpassive dissolution. Consequently, chromium in chromium-valve metal alloys is able to form a double oxyhydroxide film with valve metal element having a high passivating ability in strong acids, while for molybdenum containing alloys the formation of an extremely protective passive film with a sufficiently high activity for oxygen reduction results in ennoblement of the corrosion potential to the potential for transpassivation of molybdenum and prevents the formation of a double oxyhydroxide film containing tetravalent molybdenum ions.

Conclusions

Cr-Ti, Cr-Zr, Cr-Nb, Cr-Ta, Mo-Zr, Cr-Mo and Cr-Mo-Ni alloys prepared by sputter deposition method are spontaneously passive in 6 M and 12 M HCl at 30°C. Their corrosion resistance is higher than that of alloy components, except for latter two alloys. The corrosion resistance of Cr-Mo and Cr-Mo-Ni alloys increases with alloy molybdenum content and does not exceed that of molybdenum metal.

Spontaneous passivation of Cr-valve metal alloys occurs due to formation of a passive double oxyhydroxide film consisting of chromic ion and valve metal ion. The order of the corrosion rate is determined by the valve metal contained in the alloy. Nevertheless, the corrosion resistance of a binary alloy family increases with alloy chromium content, that is, the film chromium content, since the protective quality of the passive film of chromium is essentially better than that of valve metals.

Mo-Zr Alloys are spontaneously passive in 12 M HCl due to formation of bi-layered passive film consisting of zirconium and molybdenum oxyhydroxides. The higher corrosion resistance of the Mo-Zr alloys than that of molybdenum and zirconium metals is attributable to the fact that weak points of each layer are protected by another layer in the bi-layered passive film. The open circuit potential of alloys covered with zirconium oxyhydroxide with a low activity of weak points is higher than the potential where molybdenum suffers transpassive dissolution, and hence decreasing alloy molybdenum content increases the corrosion resistance.

The passive film formed spontaneously on alloys containing high concentrations of chromium and molybdenum mostly consists of hydrated chromium oxyhydroxide. The open circuit potential of these alloys is also significantly high but does not exceed that of molybdenum metal. Since no transpassivation of molybdenum occurs, the alloy with a higher molybdenum content has high corrosion resistance in concentrated hydrochloric acid.

When oxygen reduction is the cathodic reaction in strong acids, the passive film on chromium has a high stability but the passive tetravalent molybdenum film often suffers transpassive dissolution. Consequently, chromium is able to form a double oxyhydroxide film with another element having a high passivating ability in strong acids, and hence Cr-valve metal alloys show higher corrosion resistance in comparison with alloy constituting chromium and valve metals. On the other hand, the formation of an extremely protective passive film with a sufficiently high activity for oxygen reduction on molybdenum-containing alloys results in ennoblement of the corrosion potential to the potential for transpassivation of molybdenum and hence molybdenum cannot be contained in the top most surface of the protective passive film on extremely corrosion-resistant alloys with molybdenum in strong acids.

References

[1] H. Yoshioka, A. Kawashima, K. Asami and K. Hashimoto, in "Corrosion, Electrochemistry and Catalysis of Metallic Glasses, R. B. Diegle and K. Hashimoto, Eds., The Electrochemical Society, (1988) p.242.
[2] H. Yoshioka, A. Kawashima, K. Asami and K. Hashimoto, Proc. MRS International Meeting on Advanced Materials, Tokyo, Materials Research Society, Pittsburgh, (1988), Vol.3, p.429.
[3] H. Yoshioka, Q. Yan, H. Habazaki, A. Kawashima, K. Asami and K. Hashimoto, *Corros. Sci*. **31**, 349(1990).
[4] J. H. Kim, E. Akiyama, H. Yoshioka, H. Habazaki, A. Kawashima, K. Asami and K. Hashimoto, *Corros. Sci*. **34**, 975 (1993).
[5] J. H. Kim, E. Akiyama, H. Habazaki, A. Kawashima, K. Asami and K. Hashimoto, *Corros. Sci*. 34, 1817 (1993).
[6] J. H. Kim, E. Akiyama, H. Habazaki, A. Kawashima, K. Asami and K. Hashimoto, *Corros. Sci*. **34**, 1947 (1993).
[7] J. H. Kim, E. Akiyama, H. Habazaki, A. Kawashima, K. Asami and K. Hashimoto, *Corros. Sci*. **36**, 511 (1994).
[8] P. Y. Park, E. Akiyama, H. Habazaki, A. Kawashima, K. Asami and K. Hashimoto, *Corros. Sci*. Submitted.
[9] P. Y. Park, E. Akiyama, H. Habazaki, A. Kawashima, K. Asami and K. Hashimoto, *Corros. Sci*. **36**, (1994) in press.
[10] M. A. Streicher, *Corrosion* **30**, 77 (1974).
[11] J. Horvath and H. H. Uhlig, *J. Electrochem. Soc*. **115**, 791 (1968).
[12] A. P. Bond and E. A. Lizlovs, *J. Electrochem. Soc*. **115**, 1130 (1968).
[13] K. Hashimoto, K. Asami and K. Teramoto, *Corros. Sci*. **19**, 3 (1979).
[14] H. Habazaki, A. Kawashima, K. Asami and K. Hashimoto, *Mater. Sci. Eng*. **A134**, 1033 (1991).
[15] P. Y. Park, E. Akiyama, A. Kawashima, K. Asami and K. Hashimoto, *Corros. Sci*. **36**, 1395 (1994).
[16] K. Shimamura, K. Miura, A. Kawashima, K. Asami and K. Hashimoto, in "Corrosion, Electrochemistry and Catalysis of Metallic Glasses, R. B. Diegle and K. Hashimoto, Eds., The Electrochemical Society, (1988) p.232.
[17] K. Asami and K. Hashimoto, *Corros. Sci*. **17**, 559 (1977).
[18] K. Asami, K. Hashimoto and S. Shimodaira, *Corros. Sci*. **17**, 713 (1977).
[19] K. Asami and K. Hashimoto, *Corros. Sci*. **24**, 83 (1984).
[20] H. Habazaki, A. Kawashima, K. Asami and K. Hashimoto, Corros. Sci. 33, 225 (1992).
[21] K. S. Kim and N. Winograd, *Surf. Sci*. **43**, 625 (1974).
[22] M. Pourbaix, "*Atlass of Electrochemical Equilibria in Aqueous Solutions*", p. 272. Pergamon Press, Elmsford, NY (1966).

Materials Science Forum Vols. 185-188 (1995) pp. 789-798

In-door atmospheric corrosion behavior of rapidly quenched amorphous Zr-Cu alloys

K. Asami, E. Akiyama, Y. Murakami, H.M. Kimura, M. Kikuchi and K. Hashimoto

Institute for Materials Research, Tohoku University, Sendai 980-77, Japan

Keywords: Rapid quenching, amorphous alloy, Zr-Cu alloy, atmospheric corrosion, surface film, surface composition, ZrO_2, preferential oxidation, localized corrosion

Abstract

A series of amorphous Zr-Cu alloys prepared by means of rapid quenching were exposed to a laboratory air (RH = 60±10%, *i. e.* wet air) for 15 months and in a desiccator (RH ≤ 30%, *i. e.* dry air) for 23 months. The surface of alloys after exposure was examined by SEM/EDX, XRD and AES. The original surface film on the alloys consisted mainly of ZrO_2, and was protective. By exposure to the wet air, metallic copper and ZrO_2 were formed as corrosion products. The ZrO_2 formed on the Zr-Cu alloys was not in form of film and was not protective. The ZrO_2 formed was crystalline and mixture of monoclinic and tetragonal phases, the content of the latter phase increased with the increase in the alloy copper concentration. The surface film formed on the region in contact with the cooling wheel during quenching was rather unstable as compared with that formed on the freely solidified surface. Contaminants, such as $C\ell$ and S were often observed on the sites where corrosion started. The higher the copper content or the relative humidity, the larger was the corrosion rate.

Introduction

Since Naka *et al.* [1] discovered highly corrosion resistant amorphous alloys, some of the present authors have developed a variety of extremely corrosion resistant amorphous alloys. Not only from the viewpoint of corrosion resistance, but also from that of catalytic materials, amorphous alloys have been attracting much interest of many investigators. [2] Among copper alloys, Ti-Cu and Zr-Cu alloys are amorphizable by rapid quenching from the liquid state. [3] Together with their mechanical properties [4] and thermal stability, [5] corrosion behavior was also investigated. [6, 7] The corrosion behavior of amorphous Zr-Cu alloys was first studied by Naka *et al.* in various environments, [6] and found that $Zr_{50}Cu_{50}$ alloy was corrosion resistant in $C\ell^-$-free solutions, but was corroded easily in $HC\ell$ and $NaC\ell$ solutions. It was also reported that crystalline $Zr_{40}Cu_{60}$ alloy was easily dissolved in $HC\ell$ solution and left a deposit of copper particles, while crystalline $Zr_{50}Cu_{50}$ alloy did not dissolve in 1 N $HC\ell$. [8] Amorphous Zr-Cu alloys were also studied for catalytic use. [9, 10] Preliminary work by the present authors revealed the formation of copper particles on amorphous Zr-Cu alloys as the result of corrosion in air at room temperature. [11] Generally speaking, zirconium forms a stable barrier-type film by anodic oxidation in neutral solutions with the anodizing ratio 2.0-2.1 *nm/V* on passive zirconium in aqueous ammonium borate solution . [12] It was also observed that pure zirconium passivated spontaneously in a chloride-containing neutral solution at 25°C [13] and even in a 1 N $HC\ell$ solution at 30°C, although zirconium in both solutions suffered pitting corrosion by anodic polarization.[14] Alloying of Cu, however, seems quite detrimental for the passivity of zirconium. In this report, the atmospheric corrosion behavior of the amorphous Zr-Cu alloys was studied at room temperature in detail.

Experimental details

The alloys studied were binary $Zr_{40}Cu_{60}$, $Zr_{50}Cu_{50}$ and $Zr_{65}Cu_{35}$ alloys. The subscript number attached to each atomic symbol represents the atomic % of the respective constituent. Ribbon-shaped alloys were prepared by rapid quenching from a melt by using a rotating wheel method in an argon atmosphere to avoid oxidation of zirconium during melting. The amorphous structure of the alloy ribbons as-prepared was confirmed by X-ray diffraction (XRD) in the θ–2θ mode with the Cu $K\alpha$ radiation. The amorphous alloys were exposed to air for *ca.* 15 months in a laboratory atmosphere (relative humidity, RH = 60±10%, *i. e.* wet air) or for *ca.* 23 months in a desiccator (RH ≤ 30%, *i. e.* dry air), but not being well controlled). The laboratory located near the city center of Sendai, and the room was not air-conditioned. The specimens were left on a working desk with a cover which allowed aeration of the laboratory air. The relative humidity of the laboratory air changed from 50% to 70% depending on season (high in the rainy season and low in winter), and day and night. The maximum and minimum temperatures were around 30 and 5℃, respectively. The surface of specimens were examined by XRD after the atmospheric exposure. The corrosion products of the exposed specimens were determined by XRD using a Rigaku Rotaflex RU-200B equipped with a rotary Cu target and a bend crystal monochromator of pyrolytic graphite. The measurement conditions were as follows: The angle scanning mode was α–2θ mode where the X-ray incidence angle α was fixed to 1° or 15°, the angle scanning rate (2θ/min); 2°/min, and the sampling width; 0.02 deg. The analyzing depth for Zr-Cu alloys by XRD in α–2θ mode depends on α, It was estimated that the diffraction patterns at α = 1° are those mainly from the surface region less than the depth of *ca.* 0.3 μm, while those at α = 15° is analyzing the region up to the depth of *ca.* 3 μm.

The surface morphology and compositions of the alloy specimens after the air exposure were observed with a scanning electron microscope (Hitachi S800) equipped with a Kevex model 3200 energy dispersive X-ray analyzer (SEM/EDX). The EDX analysis was performed at the accelerating voltages 12 *kV* and 20 *kV* to obtain the depth distribution information. The topmost surface compositions of the samples exposed to the dry air were also analyzed by Auger electron spectroscopy (AES) (JEOL model JAMP 7100) at the differential mode. The accelerating voltage of electrons was 5 *kV*, and the modulation voltage was 5 *eV*(peak to peak). The surface compositions were calculated from the AES signal intensities by using the sensitivity factors of JEOL handbook; 0.176 for C *KLL* (270 *eV*), 0.296 for O *KLL* (508 *eV*), 0.426 for Cu *LVV* (912 *eV*) and 0.0292 for Zr *LVV* (1828 *eV*) Auger lines. Intensity attenuation by contaminant carbon was corrected in the same way as some of the present authors have proposed for XPS data analysis by assuming the contaminant carbon covering the top surface.[15, 16]

Results

The $Zr_{40}Cu_{60}$ specimen kept in a desiccator, *i. e.* in a dry air, showed change in color. When it was left in a wet air of the laboratory atmosphere, it lost completely its metallic luster and was severely corroded. The amorphous $Zr_{50}Cu_{50}$ and $Zr_{65}Cu_{35}$ alloys showed the same tendency although their extent of change in both airs was lower than that of $Zr_{40}Cu_{60}$ alloy. In both airs, the change was largest for the high-copper amorphous alloy, $Zr_{40}Cu_{60}$ and lowest for the low-copper $Zr_{65}Cu_{35}$ alloy. It can be said that the extent of the atmospheric corrosion is dependent on the copper content and the relative humidity.

In Fig. 1, the XRD patterns of specimens after exposure to the laboratory atmosphere were shown. The patterns of the same specimen measured at incidence angles both α = 1° and 15° are shown for comparison. In Fig. 1, "Cu" and "Cu_2O" denote the peaks corresponding to the metallic copper and the cuprous oxide, respectively. "m" and "T" are corresponding to the peaks of monoclinic and tetragonal ZrO_2, respectively. No peaks of metallic Zr, nor metallic Zr-Cu compounds are observed by X-ray diffraction.

In case of the diffraction pattern of $Zr_{65}Cu_{35}$ alloy at α = 15°, just small humps corresponding

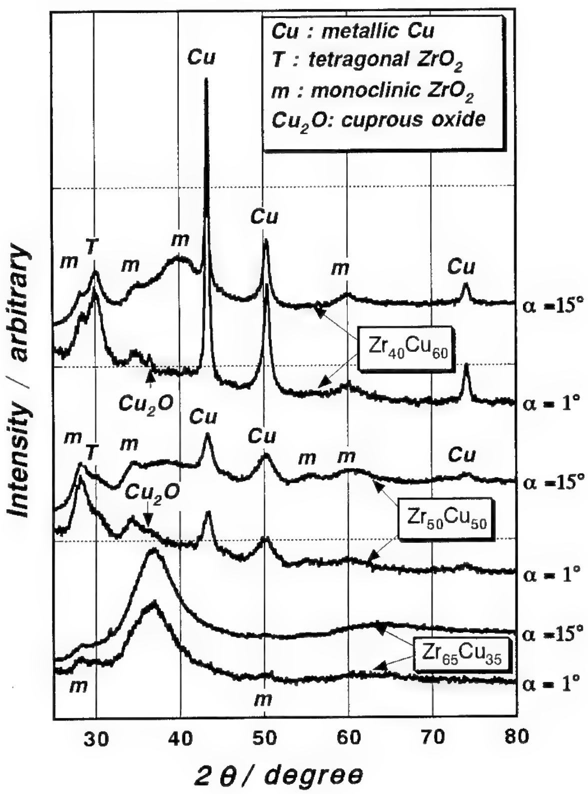

Fig. 1 X-ray diffraction patterns of amorphous Zr-Cu alloys after exposure to laboratory air.

to monoclinic ZrO_2 are observed on the top of a broad peaks of amorphous state which comes from the $Zr_{65}Cu_{35}$ alloy itself. It is apparent that the relative diffraction intensity of monoclinic ZrO_2 is higher when α is 1°. Any peaks of tetragonal ZrO_2 or metallic Cu are not apparent. Since the intensity of the substrate amorphous alloy in Fig. 1 for the $Zr_{65}Cu_{35}$ alloy is high even at $\alpha = 1°$, the thickness of the surface oxide would be much less than 0.3 μm.

On the diffraction patterns at $\alpha = 1°$ and 15° for the $Zr_{50}Cu_{50}$ alloy exposed to the wet air, peaks from the metallic Cu can clearly be seen. The width of the Cu peaks are broad suggesting very small particles. A small hump assignable to tetragonal ZrO_2 is also observed at 2θ = *ca.* 30°. Moreover, a small hump which can be assigned to Cu_2O also appears on the diffraction pattern measured at $\alpha = 1°$. The diffraction pattern observed at $\alpha = 15°$ shows an overlapped broad halo from the alloy itself although the intensity of the halo is much reduced. The amorphous $Zr_{40}Cu_{60}$ alloy exposed to the laboratory air shows very large diffraction peaks of the metallic copper. A peak assignable to Cu_2O is clearer than that on the $Zr_{50}Cu_{50}$ alloy.

On the amorphous $Zr_{40}Cu_{60}$ alloy, the tetragonal ZrO_2 peak at around $2\theta = 30°$ is taller than the monoclinic ZrO_2 peak although the former is shorter than the latter on $Zr_{50}Cu_{50}$ alloy, and even does not appear on $Zr_{65}Cu_{35}$ alloy. It is impossible to assign the substance by just a single peak at *ca.* 30°. However, some of the present authors studied the high temperature oxidation of a series of amorphous Zr-Ni alloys, and found a similar phenomenon for the ZrO_2 oxidation products, that is, tetragonal ZrO_2 phase in the oxidation products increased when the Ni content in the alloy increased. [17] From the analogy of the amorphous Zr-Ni alloy system and the peak position, the peak at 2θ = *ca.* 30° is assigned to the tetragonal ZrO_2. Usually, the monoclinic ZrO_2 is stable at temperatures under 1300 K, while the tetragonal ZrO_2 is a high temperature phase of zirconium oxide. The increase of relative quantity of the tetragonal ZrO_2 with increase of Cu content of the alloy suggests that the tetragonal ZrO_2 at low temperature can be stabilized by Cu addition similar to the Zr-Ni alloy system oxidized at high temperatures. It is also well known that tetragonal phase is stabilized at room temperature by addition of CaO, Y_2O_3, and so on. The quantity ratio of tetragonal ZrO_2 to monoclinic ZrO_2 produced during the corrosion can, therefore, be controlled by the alloy composition and oxidation conditions. It is, however, difficult to clarify if Cu is really

dissolved in ZrO_2 of the corrosion product. The relative diffraction intensities from metallic copper and cuprous oxide at $\alpha = 1°$ are higher than those at $\alpha = 15°$. It can, therefore, be said that copper distributes relatively in the surface region. The cuprous oxide would be the oxidation product of the copper appeared on the surface.

The surface morphology of the specimens were observed by SEM. Some of the typical photographs of $Zr_{40}Cu_{60}$ and $Zr_{50}Cu_{50}$ alloy surfaces after exposure to the laboratory air for 15 month are shown in Fig. 2. 'Top side' in the figure means the freely solidified side, and 'roll side' corresponds to the side which was in contact with the rotating wheel during quenching. It is clear

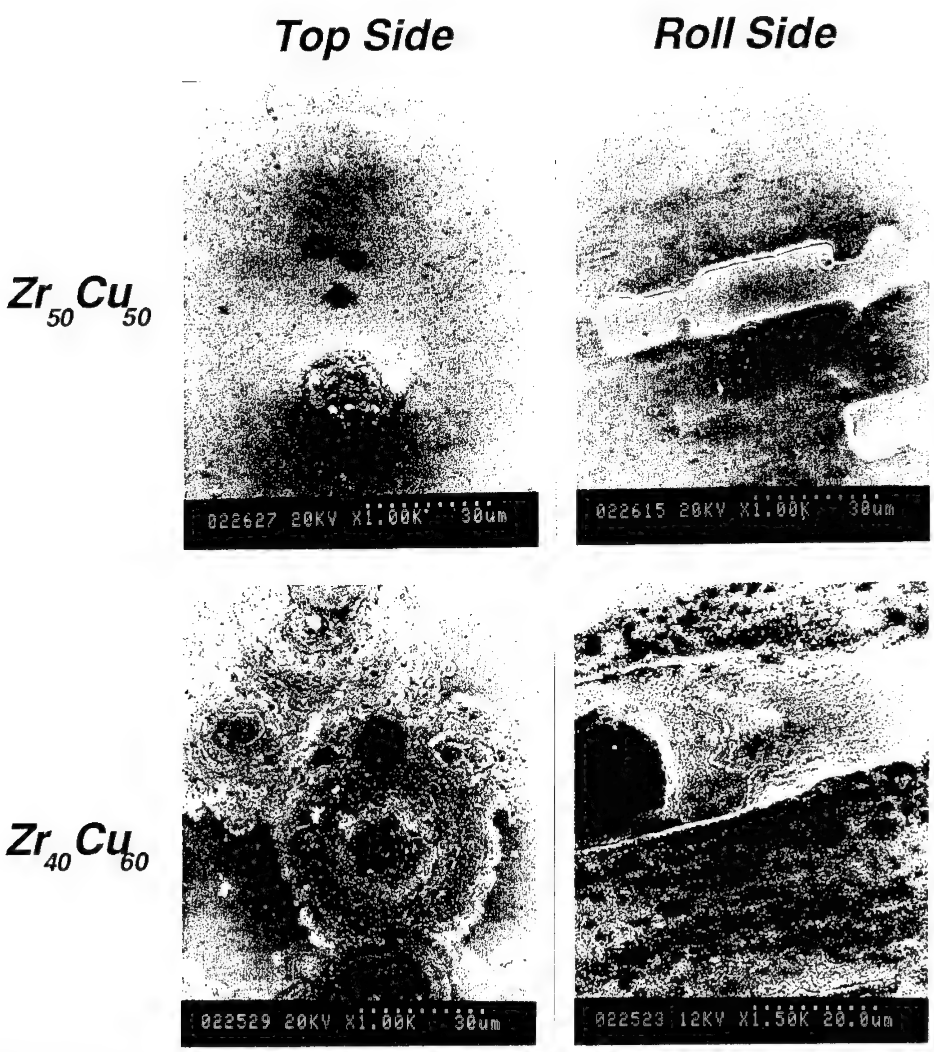

Fig. 2 Scanning electron micrographs of top side and roll side surfaces of amorphous Zr-Cu alloys exposed to a laboratory air for 15 month at room temperature. 'Top side' and 'roll side' refer the freely solidified side and the side in contact with the rotating wheel for quenching, respectively.

that morphology on the top side is quite different from that of the roll side. The troughs on roll side are cause by the gas bubbles which were enclosed between the wheel and the alloy melt when the alloy melt was impinged onto the wheel surface. It can be seen that $Zr_{40}Cu_{60}$ alloy is severely corroded in comparison with $Zr_{50}Cu_{50}$ alloy surface. The extent of corrosion was the least on $Zr_{65}Cu_{35}$ alloy among the alloys examined. On the top side of both alloys in Fig. 2, the corrosion is localized while that on the roll side looks rather like the general corrosion. The localized corrosion on the top side develops radially from the center. The original passive film may have been broken at the point corresponding to the center of the localized corrosion. From the results of XRD and SEM observation, it can be qualitatively said that the higher the copper content or the relative humidity, the larger is the corrosion rate.

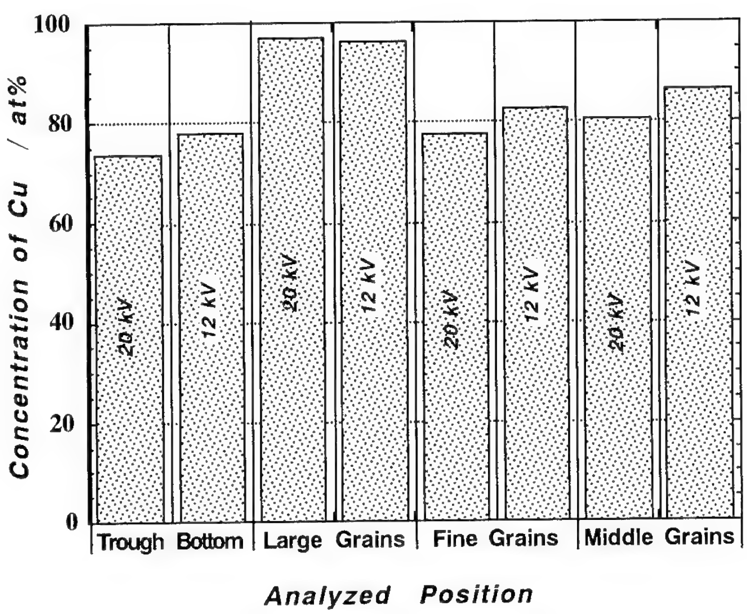

Fig. 3 EDX results of roll side of amorphous $Zr_{40}Cu_{60}$ alloys exposed to a laboratory air for 15 month at room temperature measured at accelerating voltages 20 kVand 12 kV.

The corroded surface of alloys were analyzed by EDX. Around the center region of the localized corrosion, $C\ell$ and S were detected. For example, *ca.* 9.5 at% $C\ell$ and 7.5 at%S were found from the region including the substance with bright contrast near the corrosion center on the top side of the $Zr_{50}Cu_{50}$ alloy in Fig. 2, and the contaminant at the corrosion center contained *ca.* 5 at% $C\ell$ and 21 at% S. On corrosion centers of top side of the $Zr_{40}Cu_{60}$ alloy, contaminants with a large amount of $C\ell$ and S were also found. On the roll side, contaminant with high content of $C\ell$ and S were also observed here and there. There were several regions different in grain size. Fig. 3 shows EDX results measured at trough bottom, and large grain, middle grain and fine grain regions on the roll side of $Zr_{40}Cu_{60}$ exposed to the wet air for 15 month at room temperature. In Fig. 3, the sum of concentrations of Cu and Zr is normalized to 100%. Generally speaking, it can be said that

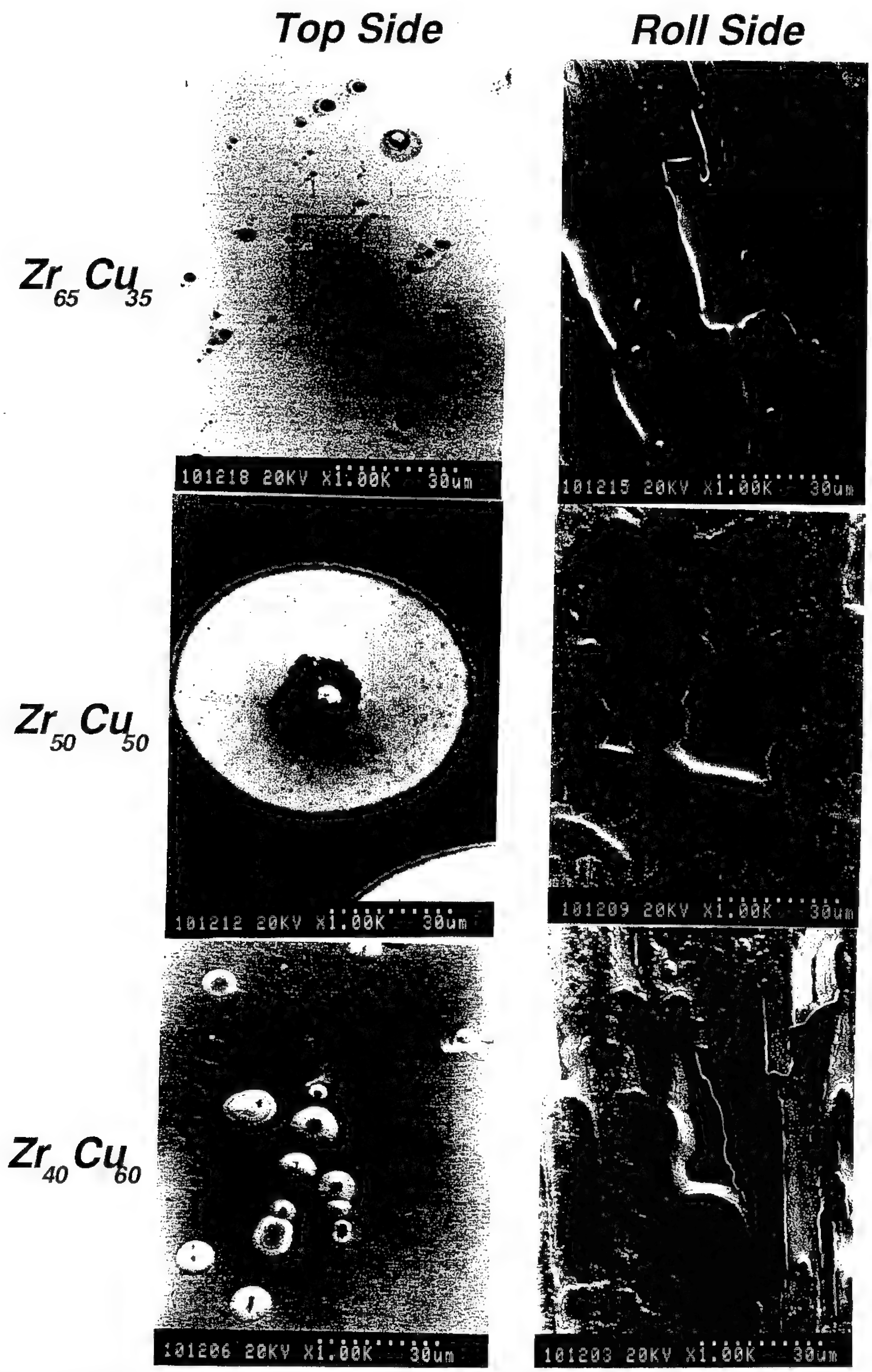

Fig. 4 Scanning electron micrographs of top side and roll side surfaces of amorphous Zr-Cu alloys kept in a desiccator for 23 month at room temperature.

Cu is concentrated in the corroded surface since the alloy composition is 60 at% Cu. In average, the Cu concentration is 75-85 at% except for a region with large grains where the Cu content is as high as *ca.* 95 at%. There is practically no difference in the values analyzed at accelerating voltages 20 *kV* and 12 *kV* for the large grain region. On the other hand, other regions show difference in concentration at different accelerating voltages, that is, the concentration at 12 *kV* is higher than that at 20 *kV*. Since the analyzing depths at accelerating voltages 12 *kV* and 20 *kV* are *ca.* 0.13 μm and 0.36 μm, respectively, [18] the results in Fig. 3 is suggesting the surface enrichment of Cu. The enrichment of Cu on the surface could occur if the oxidation of the alloy or Zr proceeds mainly by inward diffusion of oxygen. As ZrO_2 is a well known substance in which oxygen diffuses preferentially, above assumption would be reasonable. On $Zr_{50}Cu_{50}$ alloy, the same tendency was observed; copper is enriched in the surface although its extent was not high except some regions where the Cu concentration was as high as 90 at%. The lower enrichment of Cu on $Zr_{50}Cu_{50}$ compared with that on $Zr_{40}Cu_{60}$ can be explained by its lower degree of corrosion.

Scanning electron micrographs of top side and roll side of amorphous $Zr_{40}Cu_{60}$, $Zr_{50}Cu_{50}$ and $Zr_{65}Cu_{35}$ alloys kept in a desiccator for 23 month at room temperature are shown in Fig. 4. Since the atmosphere was not well controlled, the corrosion has already proceeded. However, it is clear that the extent of corrosion is much lower compared to those exposed to the laboratory wet air with much high humidity. The black squares on the top surface of $Zr_{65}Cu_{35}$ alloy are contrast caused by contamination during the observation at higher magnifications. Similar to the specimens exposed to the wet air, the corrosion starts at localized spots on top side. On the roll side, the corrosion seems to start mainly at regions where the alloy surface had contacted with the cooling wheel. It can be seen that the surface of the troughs caused by gas bubbles are rather corrosion resistant. The surface film in trough can be formed in the same way as that on top side, that is, the surface in troughs is freely solidified. The freely solidified surface may have reacted with the residual oxygen during the surface is still at relatively high temperature. The surface film thus formed is stable and protective. Once this film is broken down by corrosive ions such as chloride ions, the underlying alloy is quickly corroded and the stress produced by formation of corrosion products or evolved gas pressure causes more breakdown of the surface film.[19] The corrosion may thus propagate continuously thereupon. On the regions where the alloy melt was in contact with the rotating wheel, the surface film may not well develop in the low oxygen pressure atmosphere. Moreover, there is possibility that high residual stress exist around the roll side since the cooling rate can be different part to part, especially near the troughs. High mechanical stress in the surface region will assist the breakdown of the surface film.[19] In Fig. 4, it can be seen that the corrosion in trough starts from the boundary and proceeds to the central part.

Since the surface film on the specimens kept in the dry air is too thin to study by EPMA, the surface was examined by Auger electron spectroscopy (AES). The measurements on roll side were carried out at flat regions both in and out of the troughs. On all the specimen surfaces, carbon, oxygen and nitrogen were detected by AES in addition to the alloy constituents. The carbon will be from the contaminant, and the oxygen; from the surface film components such as oxide, oxyhydroxide or hydroxide, and also from the adsorbed oxygen species. The nitrogen may be nitride with zirconium or adsorbed nitrogen species although its chemical state was unable to be identified by AES. AES surface compositions of amorphous Zr-Cu alloys kept in a desiccator at room temperature for 23 months are shown in Fig. 5, where percentages among the main surface constituents, Zr, Cu and O are shown. 'Flat' in Fig. 5 corresponds to the region in contact with the roll surface during quenching. Generally speaking, Zr is much enriched compared to their bulk alloy compositions. The [Zr] / ([Zr] + [Cu]) in the surface film is 90 - 95 %, almost irrespective of alloy composition and specimen side, suggesting preferential ZrO_2 film formation on the top surface. Large difference in stability of passive film among different alloy compositions can not be explained simply by the surface compositions. Determination of chemical state of Cu in the surface would be important for clarification of difference in the stability of the passive films on

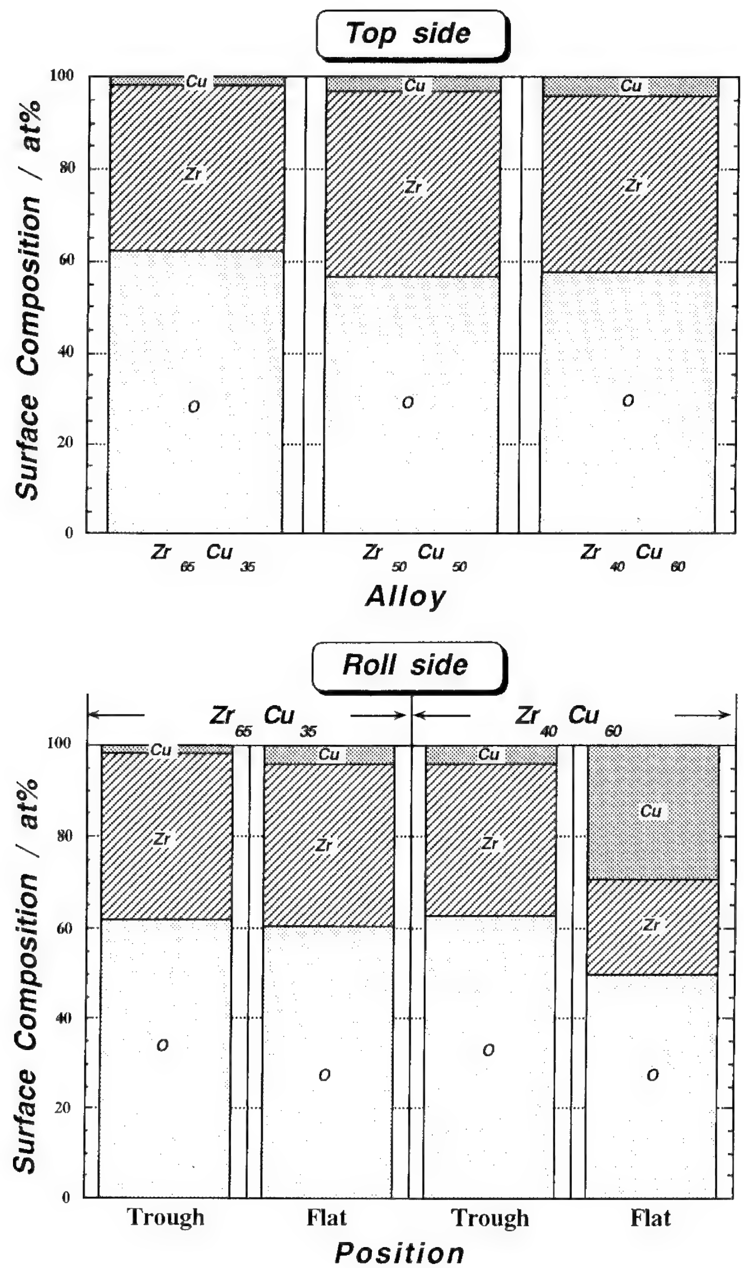

Fig. 5 Surface compositions among the main surface constituents, Zr, Cu and O, of amorphous Zr-Cu alloys kept in a desiccator at room temperature for 23 months.

Zr-Cu alloys. On the roll side surface of $Zr_{40}Cu_{60}$, the 'flat' region shows rather enrichment of Cu. This could be the result of the corrosion. It is in consistent with the EDX results of severely corroded surface shown in Fig. 3. However, the Cu enrichment by corrosion in the very surface region could not be explained by inward diffusion of oxygen because ZrO_2 film already exists on the top surface. Corrosion induced or chemically induced outward diffusion of copper must be assumed to explain the result.

Discussion

It is well known that zirconium itself is not easily corroded in an laboratory atmosphere because its surface is protected by an oxide film presumably of ZrO_2. In case of amorphous Zr-Cu alloys, the original surface film formed on the alloys just after the quenching consists mainly of ZrO_2 irrespective of alloy composition as shown in Fig. 5. It is likely to mean that ZrO_2 is formed when the bare surface is exposed to air, because the oxygen affinity of zirconium is higher than that of copper. Therefore, it could be assumed that the alloy can stay stable even if the passive film of ZrO_2 is broken. However, the passive film of ZrO_2 is likely never to be reconstructed once again under the atmospheric exposure when it is once destroyed by some reasons. From the broken point, the corrosion develops. In solutions, the passive film is usually considered to dissolve very slowly and to be reconstructed by the materials supplied from the bulk alloy. During the reconstruction, the alloy elements whose oxidized species are soluble to the solution and unable to be the main constituents of the passive film are removed from the surface film into the solution. In case of atmospheric condition, however, the reconstruction of the passive film would be difficult since the liquid phase on the surface film is very limited even under a highly humid atmosphere. Moreover, concentration of corrosive contaminants could be easily concentrated especially in-door condition while rain fall will wash away the contaminants in case of out-door corrosion. The specimens were left on a working desk with a cover which allowed aeration of the laboratory air. The relative humidity of the laboratory air ranged from 50% to 70% depending on season (high in the rainy season and low in winter), and day and night. The laboratory located in an urban region and the room was not air-conditioned. Consequently, the atmosphere might well be contaminated by Cl and S containing species in gaseous, liquid and solid phases. The corrosive species could be concentrated on the specimens during repetition of the dry and wet cycles. Those concentrated contaminants could cause break-down of the passive film of ZrO_2. Even the specimens kept in a desiccator, the surface is contaminated and corroded as shown in Fig. 4. Since the desiccator was not only for these specimens but rather general purpose, the humidity and contamination were not regulated even in the desiccator.

The corrodibility of the amorphous Zr-Cu alloy system depends on alloy composition. The results of AES analysis shown in Fig. 5 suggest that a small quantity of Cu is convoluted in the ZrO_2 film, and its content increases with the alloy Cu content. The convoluted Cu could give some effect on the properties of the ZrO_2 film. Actually, the tetragonal phase is stabilized on the Cu rich alloy.

Even on the same alloy composition, the passive film on the top-side surface is rather stable in comparison with that formed on the roll-side. These facts suggest that the stability of ZrO_2 is dependent on the conditions where and how the passive film is formed. The amorphous alloys were prepared in an argon atmosphere to avoid oxidation of zirconium during melting. The original surface film on the alloys could be formed by the reaction with the residual impurity species such as O_2 in the argon gas. On the freely solidified surface or the top-side, the supply of the oxidants should be larger as compared with that on the roll-side which is in contact with the quenching wheel. The difference between the top-side and the roll-side indicates that the ZrO_2 film is formed while the surface is still hot on the wheel. The cooling rate from the melt to the sold is of the order of 10^6-10^5 ℃/s. However, the cooling rate after solidification may be not high. Therefore, the surface film may be formed by the oxidation under low oxygen partial pressure. On

the top-side, relatively homogeneous and uniform ZrO_2 film will be formed. On the roll-side, the film will be nonuniform in thickness and composition because of gas convolution between the cooling wheel and the melt. The development of the oxide film will be incomplete on the region in direct contact with the wheel. Thus the higher corrodibility of the roll-side can be explained.

Conclusions

Amorphous $Zr_{40}Cu_{60}$ and $Zr_{50}Cu_{50}$ and $Zr_{65}Cu_{35}$ alloys prepared by a rapid quenching method were exposed to a laboratory air (RH = 60±10%, *i. e.* wet air) for 15 months and in a desiccator (RH ≤ 30%, *i. e.* dry air) for 23 months. The original surface film formed on the alloys just after quenching consisted mainly of ZrO_2, and was protective. By exposure to the wet air, metallic copper and ZrO_2 were formed as corrosion products. The ZrO_2 formed on the Zr-Cu alloys was not in form of film and was not protective. The ZrO_2 formed was crystalline and mixture of monoclinic and tetragonal phases. The content of the latter phase increased with the increase in the alloy copper concentration. The surface film formed on the region in contact with the wheel during quenching was rather unstable as compared with that formed on the freely solidified surface. Contaminants, such as $C\ell$ and S were often observed on the sites where corrosion started. The $Zr_{65}Cu_{35}$ alloy has relatively stable surface film, and only small amount of ZrO_2 is detectable by XRD. The extent of the atmospheric corrosion is dependent on the copper content and relative humidity; the corrosion rate increases with increasing Cu content in alloy and the relative humidity of the atmosphere.

References

[1] M. Naka, K. Hashimoto and T. Masumoto, *J. Jpn. Inst. Met.*, **38,** 835 (1974).
[2] for example, A. Yokoyama, H. Komiyama, H. Inoue, T. Masumoto and H. M. Kimura, *J. Catalysis*, **68,** (1981)355.
[3] R. Ray, B. C. Giessen and N. J. Grant, *Scr. Metall.*, **2,** 357 (1968).
[4] S. Tomozawa and T. Masumoto, *Sci. Rep. RITU*, **A26,** 263 (1977).
[5] L. E. Tunner and R. Ray, *Scr. Metall.,* **11,** 783 (1977).
[6] M. Naka, K. Hashimoto and T. Masumoto, J. Non-Cryst. Sol., **30,** 29 (1978).
[7] T. D. Burleigh and R. M. Latanision, *"Passivity of Metals and Semiconductors"* (ed. M. Froment), Elsevier, Amsterdam, 1983, p. 321.
[8] H. Bala and S. Szymura, *Appl. Surf. Sci.*, **35,** 41 (1988/89).
[9] M. Shibata, N. Kawata, T. Masumoto and H. M. Kimura, *J. Catalysis*, **108,** 263 (1987).
[10] T. Katona, Z. Hegedüs, Cs. Kopasz, Á. Molnár and M. Bartók, *Catal. Lett.*, **5,** 361 (1990).
[11] H. M. Kimura, K. Asami, A. Inoue and T. Masumoto, *Corros. Sci.*, **35,** 909 (1993).
[12] A. Charlesby, *Acta Met.*, **5,** 179 (1957).
[13] H. Yoshioka, H. Habazaki, A. Kawashima, K. Asami and K. Hashimoto, *Electrochim. Acta*, **36**, 1227 (1991).
[14] H. Yoshioka, H. Habazaki, A. Kawashima, K. Asami and K. Hashimoto, *Corros. Sci.,* **33,** 425 (1992).
[15] K. Asami, K. Hashimoto and S. Shimodaira, *Corros. Sci.*, **17,** 713 (1977).
[16] K. Asami and K. Hashimoto, *Corros. Sci.*, **24,** 83 (1984).
[17] K. Asami, H. M. Kimura, A. Inoue, K. Hashimoto and T. Masumoto, *"Proc. of Symp. on Corrosion, Electrochemistry, and Catalysis of Metastable Metals and Intermetallics"*, (1993, Hawaii, U.S.A.), (eds. C. R. Clayton and K. Hashimoto), The Electrochemical Society, Inc., Pennington, U.S.A., 1993, p.236.
[18] K. Asami, *Trans. JIM*, **21,** 302 (1980).
[19] K. Asami, H. Habazaki, A. Kawashima and K. Hashimoto, *Corros. Sci.*, **34,** 445 (1993).

Materials Science Forum Vols. 185-188 (1995) pp. 799-808

Nature of anodic dissolution of amorphous Ni-P alloys

A. Królikowski

Institute of Solid State Technology, Department of Chemistry, Warsaw University of Technology, Noakowskiego 3, PL-00-664 Warsaw, Poland

Keywords: Anodic dissolution, nickel-phosphorus, amorphous, crystalline, polarization, impedance

ABSTRACT

The anodic behaviour of amorphous and crystalline electrodeposited Ni-P alloys was studied in 0.1 N NaCl and 0.1 N H_2SO_4 solution by potentiodynamic/potentiostatic polarization and impedance spectroscopy. Crystalline alloys undergo intense active dissolution through the porous phosphate film. Instead, amorphous alloys show the suppression of anodic dissolution till about 0.25 V. This suppression can be related to an enrichment of the alloy surface with P rich amorphous phase having higher stability. The role of structural state and structure sensitive properties of Ni-P in the anodic behaviour was discussed.

INTRODUCTION

Nickel can be alloyed with P up to about 30 at.%. Increasing P content leads to transitions in the structural state of the alloy, and consequently, to interesting modifications of its properties. Ni-P alloys are widely used in practice because of their good corrosion and wear resistance as well as attractive magnetic and catalytic properties.

It is generally accepted that P rich Ni-P alloys exhibit a higher resistance to anodic dissolution than low P alloys. The alloys with high P content were proved to exhibit a peculiar anodic performance in acidic and neutral solutions: they show a marked suppression of dissolution in the potential range where unalloyed Ni dissolves actively [1-7]. Although several attempts have been made to explain this phenomenon, conclusions are conflicting and the issue is still under discussion. The retardation of Ni-P dissolution was associated with the generation of phosphates which inhibit anodic process as well as precipitate on the alloy surface [8]. A superficial formation of nickel phosphide showing high thermodynamic stability was also supposed [3]. Basing on results of XPS and AES analyses, Diegle at al. [4] proposed a model for chemical passivity of Ni-P through an adsorbed hypophosphite barrier layer which prevents the hydration of Ni atoms at the alloy surface. An alternative approach assumed that due to selective dissolution of Ni, a surface layer of elemental P is formed at the surface, acting as a diffusion barrier against active dissolution of the alloy [9].

All of these interpretations focused on the chemical function of alloying P itself. However, the amount of P present in Ni-P affects its structural state. With increasing P content the alloy structure evolves from crystalline to amorphous one. This transition occurs between 10 and 15 at.% P. Our earlier works [10-13] showed the essential role of structural state in relation to anodic dissolution of Ni-P in acidic and neutral media. Electrochemical investigation on electrodeposited alloys with P content varying in a wide range revealed that the inhibition of anodic dissolution typical of high P alloys is attributable to their amorphous structure. The contribution of amorphous structure of Ni-P to the inhibition of its anodic dissolution was also postulated by other authors [14-16].

The aim of this work is to gain a better understanding of the effect of structural state of Ni-P alloys on their anodic behaviour. It is a trial to give an explanation for the difference in anodic kinetics of crystalline and amorphous Ni-P. Understanding the main factors influencing the corrosion performance of this material is crucial issue in producing highly resistant protective Ni-P films.

EXPERIMENTAL

Ni-P alloys were produced by means of electrodeposition on 0.1 mm thick copper foil. Prior to the deposition, the substrate was mechanically polished with a series of emery papers, degreased in an alkaline solution, then etched with an acidic solution and partially masked with lacquer to have an effective plating area of 42 x 80 mm. Eventually it was coated with thin underlayer of a fine-grained copper. The electrodeposition of Ni-P alloys was carried out under galvanostatic control. The composition of the plating solution as well as operating conditions [17] are reported in Table 1. No surfactants were added. A shaped

anode of pure Ni wire was placed in a filter bag. Special care was taken to ensure the deposit uniformity (homogeneous distribution of P across the sample). During the deposition the substrate was mounted on an oscillatory holder to stir the solution at the cathode and prevent hydrogen bubbles adhering to the growing deposits. The pH value was monitored and corrected, if necessary, by an addition of sulphuric acid. Varying the ratio of concentrations of nickel sulphate and sodium hypophosphite, Ni-P alloys with P content between 6 and 29 at.% were obtained (the deposits composition was determined by classical wet analysis). The plating time was adjusted to obtain 30 - 40 μm thick deposits.

Table 1. Conditions of electrodeposition of Ni-P.

Solution composition:		Deposition parameters:	
$NiSO_4$	0.7 - 1 M	pH	1.6 - 2.0
NaH_2PO_2	0.02 - 0.3 M	temperature	70 ± 1°C
H_3BO_3	0.33 M	current density	1.7 - 2.8 A dm^{-2}
H_3PO4	0.5 M	plating time	45 - 150 min
NaCl	0.33 M		

The structure of the obtained alloys was proved by XRD measurements. Samples with less than 10% P were crystalline (supersaturated solid solution of P in fcc Ni) and samples containing above 15% P showed amorphous structure. For the transitional range: 10 - 15% P, alloys of the same composition were either crystalline or amorphous.

Anodic behaviour of Ni-P alloys of different structural states was studied by potentiodynamic and potentiostatic polarization as well as impedance spectroscopy. Electrochemical Measurement System Atlas 85 was applied. The experiments were performed mainly in 0.1 N NaCl and 0.1 N H_2SO_4 solutions, purged continuously with nitrogen. The solutions were prepared from p.a. grade chemicals and double distilled water. All measurements were performed at 20±2°C. Prior to electrochemical testing, samples were polished with a fine grade emery paper, rinsed in acetone and then in ethanol. They were mounted on a circular window in the side-wall of a Plexiglass cell. The area exposed to the solution (0.8 cm^2) was limited with a sealing O-ring. Pt netting counter electrode was placed in a compartment separated by a glass frit. A saturated calomel electrode served as the reference electrode. All potential readings are expressed with respect to this electrode.

Prior to start of measurements, the samples were kept in the solution for 30 min (if not stated otherwise) to reach a stationary state. Potentiodynamic tests were performed at potential scan of 1 mVs^{-1} . Cyclic polarization curves were also registered by reversing the potential scanning when the current density reached 0.6 $mAcm^{-2}$. Potentiostatic studies were employed by sweeping the potential from the open circuit conditions to selected anodic potentials. Changes of the dissolution current were monitored over 90 min. Impedance measurements were carried out at selected potentials, in the frequency range: 10 kHz to 40 mHz, using an A.C. voltage amplitude of 10 mV. Impedance data were interpreted in terms of equivalent circuits [18].

RESULTS

Figure 1 shows anodic polarization behaviour of electrodeposited Ni-P alloys of varying P content in neutral chloride solution. All the samples exhibit corrosion potentials lying within a quite narrow band (they are slightly shifted to more noble values with increasing P in the alloy). However, the course of the anodic curves depends markedly upon the structural state of Ni-P. The crystalline samples (6 and 9% P) show very sharp rise in anodic currents. Simultaneously a greyish-black film was formed on the alloy surface. In contrast with this, the amorphous samples (17% P and more) exhibit a suppression of anodic dissolution (an arrest on polarization curves) till approximately 0.25 V, followed by a rise in dissolution currents at higher potentials. The polarization curves for these samples are similar to each other. All the amorphous alloys maintained a metallic luster after completing the test. Samples of the P content within the range of the structural transition (11 and 14%) show intermediate polarization behaviour.

The striking difference in anodic performance of crystalline and amorphous Ni-P was proved by cyclic polarization runs. The observed behaviour was strongly related to the structural state of the alloy. Fig. 2 demonstrates two representative patterns. All the crystalline samples exhibit much higher dissolution currents and more active rest potentials during the reverse potential scan. These alloys remained covered with black film after completing of this test. After removal of this film the surface was found severely rough.

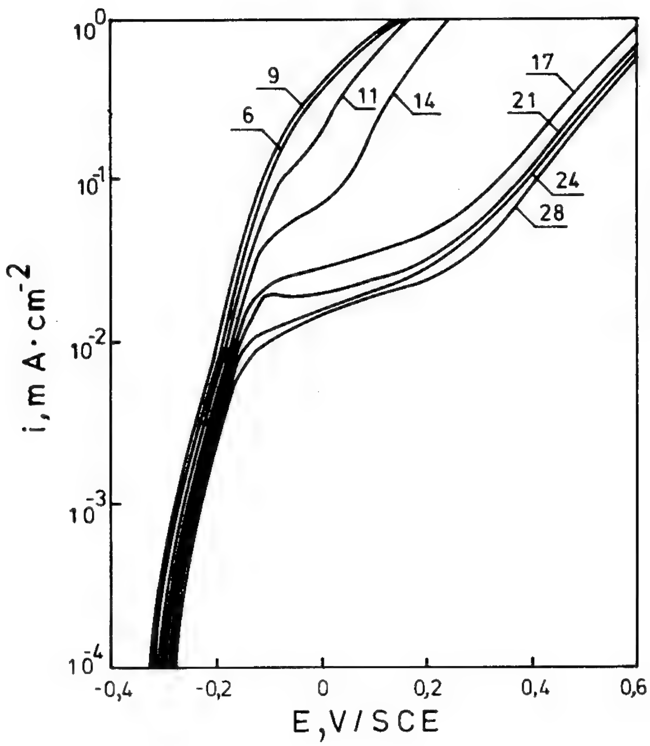

Fig. 1. Anodic polarization curves of electrodeposited Ni-P alloys in 0.1 N NaCl. The numbers denote P content in the alloy in at.%.

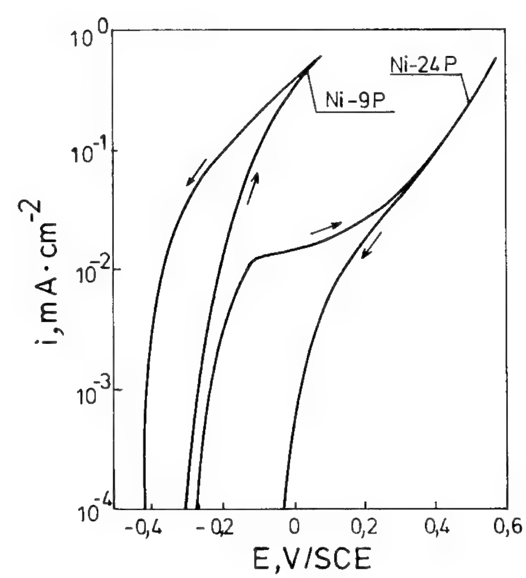

Fig. 2. Representative cyclic polarization curves for crystalline and amorphous Ni-P alloys in 0.1 N NaCl.

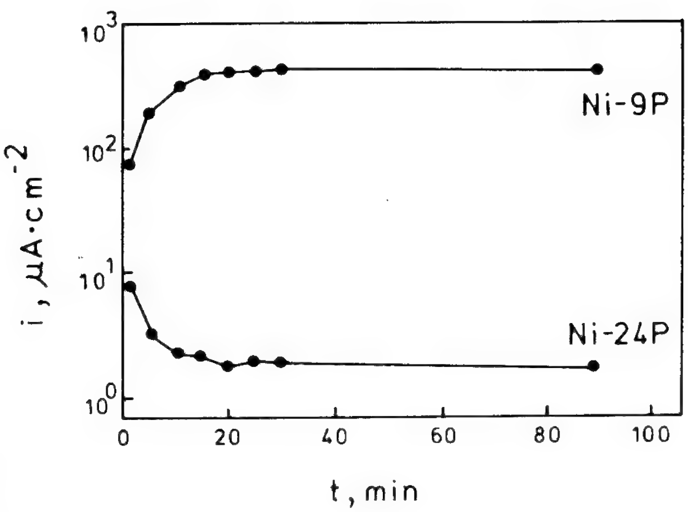

Fig. 3. Representative time dependences of anodic current density for crystalline and amorphous Ni-P alloys in 0.1 NaCl at -0.15 V.

By contrast, the backscanning curve for amorphous samples initially follows exactly the forward curve and diverges in the potential range corresponding to the current arrest, when much lower currents are recorded. Thus an opposite hysteresis loop appears and all the amorphous alloys exhibit more noble rest potentials after reverse scanning.

The results of cyclic polarization indicated that significant changes of observed anodic currents with time can be expected. Such an information was obtained from potentiostatic tests performed at selected potentials corresponding to the current arrest for amorphous Ni-P. Completely different patterns were found again for crystalline and amorphous alloys. Examples are given in Fig. 3. All the crystalline samples exhibit a sharp increase in dissolution currents at the start of anodic polarization. This fact was accompanied by the formation of a greyish-black film on the alloy surface. After few minutes, when the surface was completely covered with this film, the currents became stabilized on very high level. The adverse effect was observed for amorphous alloys. Dissolution currents decay continuously to some $mAcm^{-2}$, that is more than two orders of magnitude less than the steady state currents for crystalline samples. The surface appearance of amorphous samples remained intact after completing the test. Similar results were found from potentiostatic measurements performed at other potentials corresponding to the current arrest for amorphous Ni-P.

Impedance studies were carried out at the corrosion potential and at selected anodic potentials. Fig. 4 shows impedance spectra typical of amorphous Ni-P alloys. These samples exhibit quite similar impedance data taken at the corrosion potential and at the potential corresponding to the suppression of anodic dissolution. Both the spectra consist of one capacitive arc. Impedance values observed for amorphous Ni-P at the anodic potential are somewhat smaller. Impedance plot obtained for crystalline Ni-P at the corrosion potential (Fig 5a) is comparable in shape and size to those for amorphous samples. However,anodic polarization gives rise to drastic change in the impedance data of crystalline Ni-P (Fig. 5b and 5c). It is apparently linked with covering of the alloy surface with the black film. Impedance values drop markedly and an additional low frequency response appears. For measurement done in acidic medium an inductive loop is observed at low frequencies (Fig. 5c) Such a spectrum is typical of active dissolution of Ni in acidic media [19].

Figure 6 shows changes in the time constant for the charge transfer process derived from analysis of impedance spectra. It is interesting that under the open circuit conditions all Ni-P samples exhibit virtually similar values of this parameter, regardless of the alloy composition and structure. Instead, anodic polarization gives rise to a reduction of the time constant. The scale of this reduction is small for amorphous samples, but it is pronounced for crystalline ones. An evident differentiation in the time constant is noted in the range of the transition from crystalline to amorphous structure.

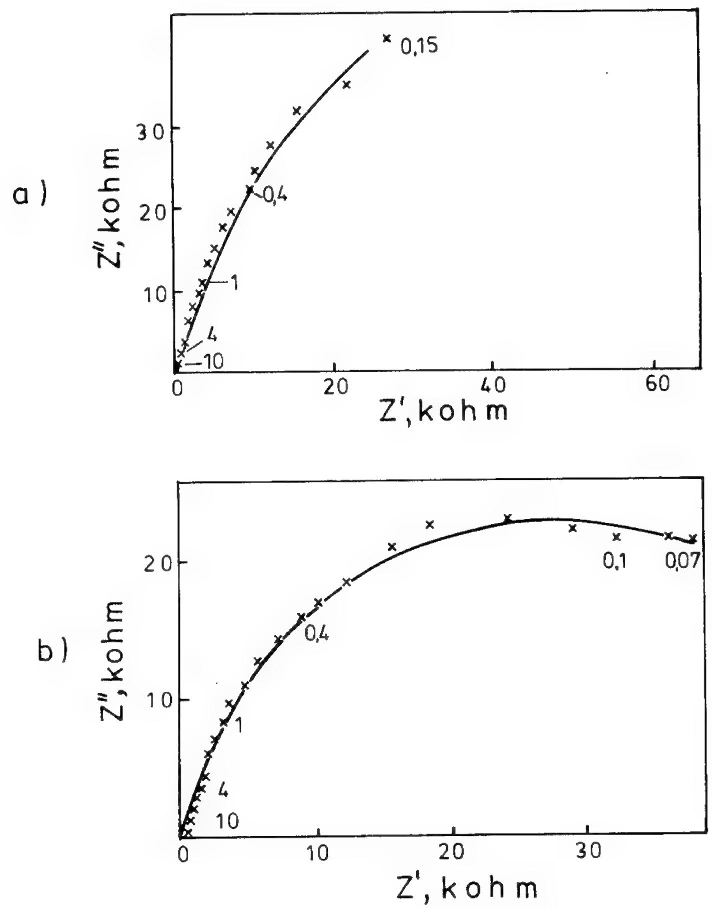

Fig. 4. Impedance spectra of amorphous Ni-P (23 % P) in 0.1 N NaCl at the corrosion potential (a) and at -0.15 V (b). Several values of frequency (in Hz) are marked.

DISCUSSION

It is apparent that Ni-P alloys show two different kinds of anodic behaviour, depending on their structural state. The suppression of anodic dissolution of P rich Ni-P alloys is evidently associated with their amorphous structure. The present results concern the anodic behaviour of electrodeposited alloys in NaCl solution. As has been reported previously, virtually similar relations were obtained for electrodeposited Ni-P samples in other neutral and acidic media [10,11,13]. Recently, quite similar findings have been found for electroless Ni-P deposits as well [20]. Polarization data for these samples in acidic solution are shown Fig. 7. These alloys of varying P content were produced from succinate based solution (with no surfactants) by adjusting pH value. As can be seen, only amorphous samples (> 16% P) show the suppression of anodic dissolution in the potential range corresponding to that of the current arrest in Fig. 1. Quite similar polarization behaviour was also observed for amorphous Ni-P alloys prepared by rapid quenching [2,4,9,21].

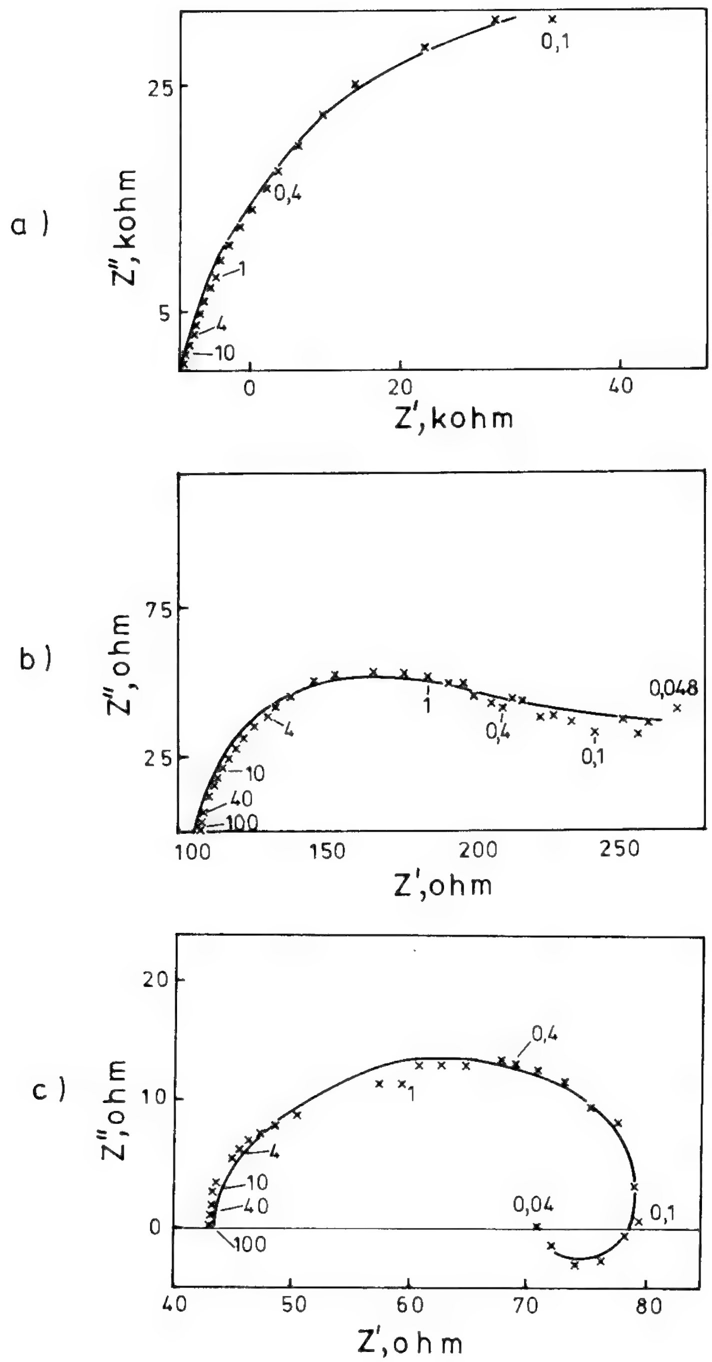

Fig. 5. Impedance spectra of crystalline Ni-P (9% P) taken under various conditions: in 0.1 N NaCl at the corrosion potential (a), in 0.1 N NaCl at -0.15 V (b) and in 0.1 H_2SO_4 at 0 V (c). Several values of frequency (in Hz) are marked.

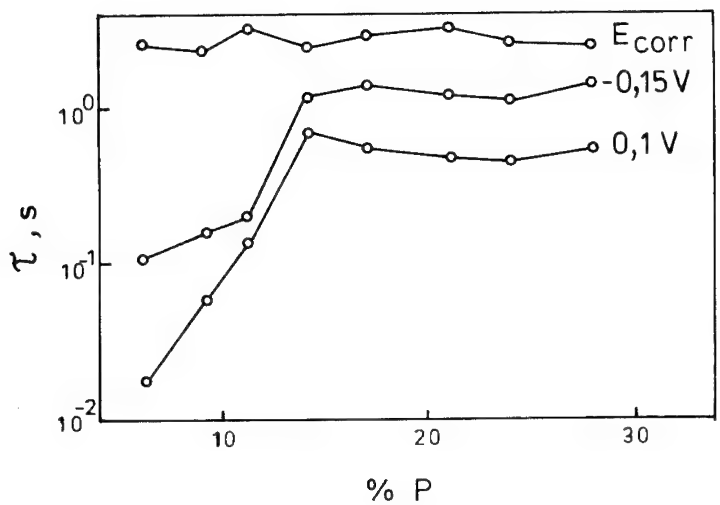

Fig. 6. Time constant for charge transfer process of Ni-P in 0.1 N NaCl (at various potentials) as a function of the alloy composition.

It therefore follows from the above, that the suppression of anodic dissolution of amorphous Ni-P in acidic and neutral media is well recognized phenomenon. However, this phenomenon is interpreted mainly in terms of function of alloying P and rather slight or no attention is given to links with structural state of Ni-P (see Introduction). One can argue that this suppression of dissolution is observed only for amorphous alloys because they have P content high enough to affect the anodic process. If so, more or less gradual changes in anodic behaviour with increasing P content should be expected. As a matter of fact, anodic characteristics show abrupt changes in the structural transition range and do not vary much in the ranges where either crystalline or amorphous structure occurs. This finding indicates the crucial role of structural factor. Differences in anodic behaviour of Ni-P samples of the same composition produced by various methods [9,21] confirm this point of view. According to Habazaki at al. [21], these differences are pronounced in the potential range of the suppression of anodic dissolution, but they are slight at higher potentials.

It is well recognized that anodic polarization of amorphous Ni-P alloys leads to preferential Ni dissolution and an enrichment of P on the alloy surface [3-5,9,22]. This behaviour can be interpreted in terms of different rates of active dissolution of the alloy components [23]. It is conceivable that an inhibition of P oxidation on amorphous Ni-P leads to the formation of P rich surface zone acting as a diffusion barrier against further dissolution of Ni [9,13]. The time dependence of the dissolution current for amorphous Ni-P (Fig. 3) follows the parabolic kinetics. This can be treated in terms of diffusion through the developing diffusion layer, according to Fick's second law [9]. Such an analysis (curve fitting) was performed for electrodeposited Ni-P alloys with P content ranging from 17 to 28% [13]. Values of Ni diffusivity were estimated to be of the order of 10^{-17} cm^2s^{-1}. Interdiffusivities measured in electrodeposited amorphous Ni-P (20% P) at 120°C were of the order of 10^{-18} cm^2s^{-1} [24].

The inhibition of P oxidation on amorphous Ni-P in comparison with crystalline Ni-P was confirmed by Hofmann and Weil [16]. The question arises as to the origin of this effect. It is well known, that the transition from crystalline to amorphous structure of Ni-P is associated with significant changes in electrical and magnetic properties of this material. Amorphous alloys exhibit evidently higher electrical resistivity [25] and are nonmagnetic whereas crystalline alloys are ferromagnetic [26]. The electrooxidation of P is strongly catalytic process and these modification of material properties may be of importance. In our opinion, however, contribution of particular electronic structure of amorphous Ni-P should be taken into consideration. It was suggested that in amorphous Ni-P chemical bonding between the alloy constituents exists [27,28]. Such an approach seems to be consistent with results of NMR investigation on electrodeposited amorphous Ni-P [29].

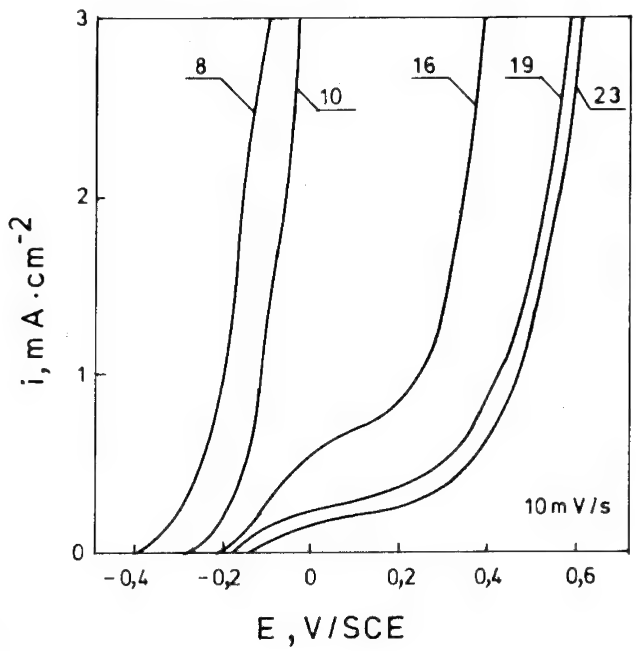

Fig. 7. Anodic polarization curves of electroless Ni-P alloys in 0.1 N H_2SO_4 [20]. The numbers denote P content in the alloy in at.%.

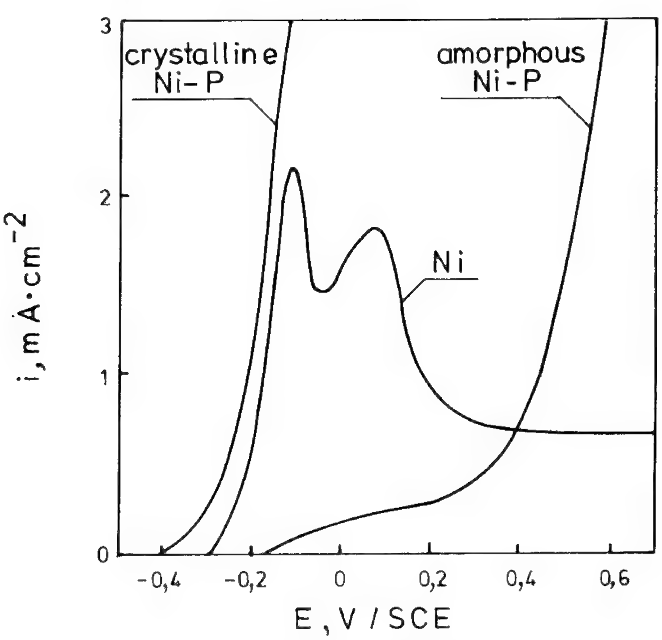

Fig. 8. Confrontation of anodic polarization curves for electroless Ni-P alloys: crystalline (8% P), amorphous (23% P) and electrodeposited pure Ni in 0.1 N H_2SO_4 [20].

Similarity in the local atomic environment of P atoms in these alloys and in crystalline Ni_3P was found.In Ni_3P, P atoms have only Ni nearest neighbors. This configuration contributes to the high stability of this compound. It was reported, that the formation of a continuous surface layer of Ni_3P on heat treated Ni-P alloys improves their corrosion resistance [30]. On the other hand, there are evidences that in amorphous Ni-P alloys at least two different amorphous phases of different stability exist [6,29]. Having these findings in the mind, we can conclude that the above mentioned P rich zone formed on the alloy surface during anodic dissolution consists of a stable amorphous Ni-P phase.

Another question concerns the anodic behaviour of crystalline Ni-P. Anodic polarization of this material leads to covering of the alloy surface with a greyish-black film. The formation of such a film on crystalline Ni-P was reported in [3,14,31,32]. According to XPS data [1], this film is composed of nickel phosphate. Phosphate conversion coating are known to be very porous. This is in agreement with nonprotectiveness of this film reported in the present work. Impedance data suggests that anodic process for crystalline Ni-P is similar to active dissolution of Ni. Conceivably the alloy dissolves readily through pores in the phosphate film. This point is confirmed by data presented in Fig 8. Anodic curves for crystalline Ni-P and for Ni in active state are quite similar. When Ni undergoes passivation, crystalline Ni-P remains still active because the phosphate film interferes with the growth of oxide passive layer [1,8]. It is worth noting that, in view of impedance data (Fig. 5 and 6), the above concept seems to be relevant for crystalline Ni-P exposed to anodic polarization but does not under open circuit conditions.

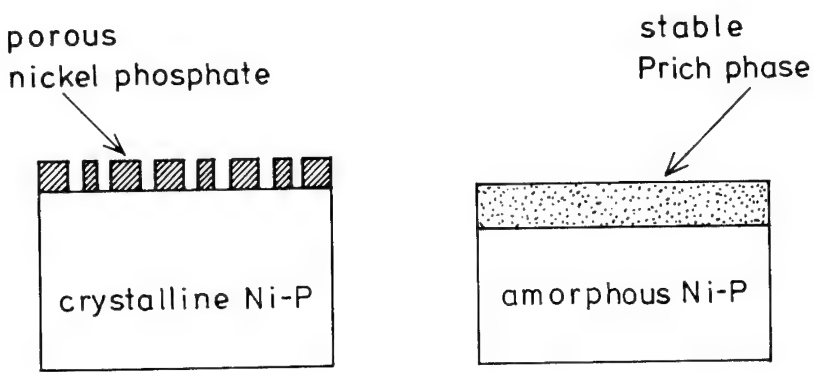

Fig. 9. Schematic presentation of the surface of crystalline and amorphous Ni-P upon anodic dissolution in acidic and neutral media. In the case of amorphous Ni-P this model is relevant only till about 0.25 V.

CONCLUSION

Crystalline and amorphous Ni-P alloys exhibit evidently different anodic behaviour in acidic and neutral solutions. Crystalline alloys undergo intense active dissolution through the porous phosphate film. Instead, amorphous alloys show the suppression of anodic dissolution till about 0.25 V. This is due to the inhibition of P electrooxidation on this material and consequent enrichment of the alloy surface with P rich amorphous phase having higher stability. This performance can be related to peculiar features of the amorphous state in this alloy. These approaches are schematically shown in Fig. 9.

ACKNOWLEDGEMENT

The financial support of the Rector of the Warsaw University of Technology under contract 504/488/1 is gratefully acknowledged.

REFERENCES

[1] A. Kawashima, K. Asami, K. Hashimoto, J. Non-Cryst. Solids **70**, 69 (1985),
[2] R.B. Diegle, N.R. Sorensen and G.C. Nelson, J. Electrochem. Soc. **133**, 1769 (1986),
[3] G. Salvago and G. Fumagalli, Met. Finish. **85**, 31 (1987),

[4] R.B. Diegle, N.R. Sorensen, C.R. Clayton, M.A. Helfand and Y.C. Yu, J. Electrochem. Soc. **135**, 1085 (1988),
[5] J.L. Carbajal and R.E. White, J. Electrochem. Soc. **135**, 2952 (1988),
[6] P.V. Nagarkar, P.C. Searson and R.M. Latanision, Proc. Symp. Corrosion Electrochemistry and Cataly sis of Metallic Glasses, Ed. R.B. Diegle and K. Hashimoto, Proc. Electrochem. Soc. 88-1, p.118 (1988),
[7] M. Gugau and H. Speckhardt, Werkstoffe Korrosion **42**, 296 (1991),
[8] J. Flis and D.J. Duquette, Corrosion **41**, 700 (1985),
[9] H. Habazaki, S.-Q. Ding, A. Kawashima, K. Asami, K. Hashimoto, A. Inoue and T. Masumoto, Corros. Sci. **29**, 1319 (1988),
[10] A. Królikowski, M. Pelowska and P. Butkiewicz, Proc. Eurocorr '91, Budapest 1991, Ed. I. Karl and M.Bod, p.199 (1991),
[11] A. Królikowski, M. Pelowska and P. Butkiewicz, Metallurgy and Foundry Engineering **18**, 189 (1992),
[12] A. Królikowski and P. Butkiewicz, Electrochim. Acta **38**, 1979 (1993),
[13] A. Królikowski, "Modifications of Passive Films", European Federation of Corrosion Publ. No 12, p.119 (1994),
[14] Z. Longfei, L. Shoufu and L. Pengxing, Surf. Coat. Technol. **36**, 455 (1988),
[15] M. Benje, U. Hofmann, U. Pittermann and K.G.Weil, Ber. Bunsenges. Phys. Chem. **92**, 1257 (1988),
[16] U. Hofmann and K.G. Weil, Corros. Sci. **34**, 423 (1993),
[17] R.S. Vakhidov, Elektrokhimiya **8**, 70 (1972),
[18] A. Królikowski and W. Stokarski, Abstr. Symp. Automatization in Corrosion and Electrochemical Research, Świdno 1989, Ed. Inst. Phys. Chemistry PAN, Warsaw 1989, p. 1 (1989),
[19] I. Epelboin and M. Keddam, Electrochim. Acta **17**, 177 (1972),
[20] J. Bieliński, A. Królikowski, I. Kędzierska and W. Stokarski, Acta Chim. Hung. in press,
[21] H. Habazaki, Y.-P. Lu, A. Kawashima, K. Asami, K. Hashimoto, Corros. Sci. **32**, 1227 (1991),
[22] B.-P. Zhang, H. Habazaki, A. Kawashima, K. Asami and K. Hashimoto, Corros. Sci **33**, 667 (1992),
[23] K.E. Heusler and D. Huerta, Proc. Symp. Corrosion Electrochemistry and Catalysis of Metallic Glasses, Ed. R.B. Diegle and K. Hashimoto, Proc. Electrochem. Soc. 88-1, p.1 (1988),
[24] C.A. Ross, D.T. Wu, L.M. Golgman and F. Speapen, J. Appl. Phys. **72**, 2773 (1992),
[25] W.H. Safranek, "Properties of Electrodeposited Metals and Alloys", 2nd Ed., Am. Electroplaters and Surface Finishers Soc., Orlando, pp. 345-348 and 497-529,
[26] R. Hasegawa, "Glassy Metals: Magnetic, Chemical and Structural Properties", CRC Press Inc., Boca Raton (1983),
[27] H.S. Chen and B.K. Park, Acta Metall. **21**, 395 (1973),
[28] W.Y. Ching, Phys. Rev. **B 34**, 2080 (1986),
[29] D.S. Lashmore, L.H. Bennett, H.E. Schone, P. Gustafson and R.E. Watson, Phys. Rev. Lett. **48**, 1760 (1982),
[30] H.G. Schenzel and H. Kreye, Plat. Surf. Fin. **77**(10), 50 (1990).
[31] L.V. Golovushkina, V.S. Epifanova, Yu.V. Prusov and V.N. Flerov, Elektrokhimiya **10**, 1526 (1974),
[32] J. Koevecses, Metalloberfläche **31**, 7 (1977),

Materials Science Forum Vols. 185-188 (1995) pp. 809-818

The corrosion behavior of sputter-deposited amorphous Al-Cr-Ti alloys in 1 M HCl

E. Akiyama, H. Habazaki, A. Kawashima, K. Asami and K. Hashimoto

Institute for Materials Research, Tohoku University, Sendai 980, Japan

Keywords: Sputter-deposition, amorphous metals, Al-Cr-Ti alloys, HCl

Abstract—Corrosion rate of the Al-Cr-Ti alloys with relatively high chromium content in 1 M HCl solution are almost one order of magnitude lower than those of Al-Cr alloys. The ternary alloys are passivated spontaneously, while the open circuit potentials of Al-Cr alloys are in the active region even if a large amount of chromium is added. The higher corrosion resistance of the Al-Cr-Ti alloys in comparison with Al-Cr and Al-Ti alloys can be explained in terms of the beneficial effects of titanium addition preventing the enrichment of aluminum in the surface film and chromium addition enhancing the passivity and cathodic reactions even in the chloride containing strong acid.

INTRODUCTION

In recent years, it has been found that alloying additions of corrosion-resistant metals, such as titanium [1, 2, 3, 4, 5], zirconium [1, 6, 7], niobium [1, 8, 9], tantalum [1, 8, 9], tungsten [1, 9, 10], molybdenum [1, 9], and chromium [11] to aluminum are effective in preparing amorphous aluminum-base alloys with a high corrosion resistance.

Corrosion rates of Al-Cr alloys are lower than that of aluminum in 1 M HCl and decrease with increasing alloy chromium content. However, the open circuit potential of the Al-Cr alloys containing less than 56 at% chromium is in the active region of chromium. Therefore, passivation does not occur and a chromium-concentrated passive film is not formed spontaneously on the high aluminum alloys [11].

On the other hand, sputter-deposited Al-Ti alloys containing 30-60 at% titanium consist of a single amorphous phase. Both aluminum and titanium are active in 1 M HCl, and hence the titanium addition is not effective in enhancing the corrosion resistance [1]. However, the titanium addition significantly ennobles the pitting potential in a neutral solution containing Cl^- ions [3]. Since the titanium addition to aluminum enhances the passivity, it is expected that the titanium addition to Al-Cr alloys increases the passivating ability.

Recently, it has been revealed that amorphous Ti-Cr alloys [12] are spontaneously passive showing significantly lower corrosion rates in comparison with those of titanium and chromium in 1 M and 6 M HCl solutions. According to XPS analysis the air-formed film and passive film on the Ti-Cr alloys are composed of a double oxyhydroxide of chromium and titanium rather than a mixture of chromium and titanium oxyhydroxides. The passive chromium-titanium oxyhydroxide film is more protective, stable and resistant in comparison with passive films on chromium and titanium metals. Accordingly, if alloying of aluminum with both of chromium and titanium results in formation of a single phase solid solution, this is a useful method for preparation of corrosion-resistant aluminum-base alloys, and the corrosion resistance of Al-Cr-Ti alloys is expected to be higher than that of amorphous Al-Ti and Al-Cr alloys. Formation of amorphous Al-Cr-Ti alloys can be expected

because Al-Ti, Al-Cr and Cr-Ti alloys are all amorphizable by sputter deposition.

The present work aims to prepare amorphous Al-Cr-Ti alloys by D.C. magnetron sputtering and to clarify the effect of alloying of aluminum with chromium and titanium on the corrosion resistance in 1 M HCl solution.

EXPERIMENTAL PROCEDURE

DC magnetron sputter-deposition was carried out for preparation of Al-Cr-Ti alloys tested. The target was composed of a 99.99 % pure aluminum disk of 100 mm diameter and 6 mm thickness, on the sputter erosion region of which 99.95 % pure titanium disks of 20 mm and 10 mm diameters and 99.99 % pure chromium disks of 20 mm and 10 mm diameters were placed. The composition of sputter deposits was changed by changing numbers of smaller disks placed on the aluminum disk. Glass plates were used as substrates which were rinsed by immersion in water containing a commercial detergent for cleaning of aluminum metal at about 75 °C. Sputtering apparatus and conditions used were the same as those described elsewhere [8, 13]. For the purpose of homogenization of the sputter deposit, water-cooled substrates were revolved around a central axis of the sputtering chamber, in addition to revolution of the substrates themselves around their own axes. After the target and substrates were installed in the sputtering machine the vacuum chamber was evacuated to about $1x10^{-6}$ torr. After pre-sputtering of the target for 5-10 minutes, sputtering was carried out at $3\text{-}6x10^{-4}$ torr of argon gas which was prepared by removal of oxygen, water and dust from high purity argon gas of 99.9995 % purity.

The composition of the alloys prepared was determined by electron probe microanalysis (Shimadzu EPMA C1). The structure was identified by X-ray diffraction method with Cu K_α radiation.

Corrosion tests were carried out in 1 M HCl solution open to air at 30 °C and the corrosion rate was estimated from the weight loss after immersion for 5 h. Open circuit potentials were measured in 1 M HCl open to air at 30 °C. In order to obtain reproducible results by removal of the oxide film on as-sputtered alloys, before immersion the specimens were polished mechanically with silicon carbide paper up to No. 1500 in cyclohexane and dried in air. A platinum electrode and a saturated calomel electrode (SCE) were used as counter and reference electrodes, respectively. Potentials hereafter are referred to the saturated calomel electrode.

After mechanical polishing in cyclohexane and open circuit immersion in 1 M HCl open to air at 30 °C, X-ray photoelectron spectra were measured by means of a Shimadzu 850 photoelectron spectrometer with Mg K_α excitation (hv=1253.6 eV). Binding energies of electrons were calibrated by a method described elsewhere [14, 15]; binding energies of the Au $4f_{7/2}$ and $4f_{5/2}$ electrons of gold metal and the Cu $2p_{3/2}$ and $2p_{1/2}$ electrons of copper metal were taken as 84.07, 87.74, 932.53 and 952.35 eV, respectively, and the kinetic energy of the Cu $L_3M_{4,5}M_{4,5}$ Auger electrons of copper metal as 918.65 eV [14].

The thickness and composition of the surface film and the composition of the alloy immediately under the surface film were quantitatively determined by a previously proposed method using integrated intensities of photoelectrons, assuming a three-layer model of the outer most contaminant hydrocarbon layer of uniform thickness, the surface film with uniform thickness and the underlying alloy with X-ray photoelectron spectroscopically infinite thickness [16]. It was also assumed that constituents of the layers distribute homogeneously in each layer. The photoionization cross-section of the Al 2p electrons relative to the O 1s electrons used was 0.1868 which was reported in a

previous paper [10]. The photoionization cross-section of the Ti $2p_{3/2}$ and Cr $2p_{3/2}$ electrons relative to the O 1s electrons used was 1.277 [17] and 1.71 [14], respectively. The photo-ionization cross-section of C 1s electrons relative to O 1s electrons was taken from the calculation by Scofield [18].

EXPERIMENTAL RESULTS

Figure 1 shows the composition-structure diagram of the Al-Cr-Ti alloy system. Alloy compositions hereafter are all denoted in at%. Since three kinds of binary alloys, that is, Al-Cr, Al-Ti and Cr-Ti alloys form the amorphous structure, amorphous Al-Cr-Ti alloys are obtained in an exceptionally wide composition range.

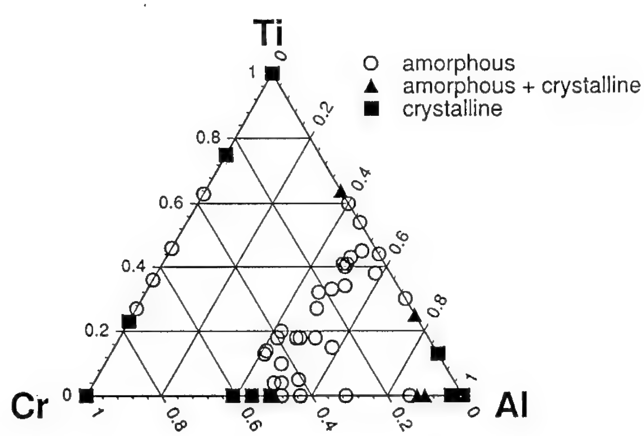

Fig. 1 A composition-structure diagram of sputter-deposited Al-Cr-Ti alloys.

Corrosion rates of Al-Cr-Ti alloys were measured in 1 M HCl open to air at 30 °C. Figure 2 shows the comparison of corrosion rates of the amorphous Al-Cr-Ti alloys with those for Al-Ti and Al-Cr binary alloys. The corrosion rate of Al-Ti alloys containing less than 60 at% of titanium is almost the same as the corrosion rate of aluminum [1]. On the other hand, the corrosion rate of Al-Cr alloys decreases with alloy chromium content [11]. Al-Cr-Ti alloys containing relatively low concentrations of chromium, such as, Al-11Cr-41Ti, Al-14Cr-34Ti alloys show lower corrosion rates than those of the Al-Ti alloys and the corrosion rates of these alloys are almost the same as that of the Al-Cr alloys containing the same concentration of aluminum. Accordingly, it can be said that substitution of chromium for titanium is effective in decreasing the corrosion rate of the Al-Ti alloys. Furthermore corrosion rates of Al-Cr-Ti alloys containing relatively high concentrations of chromium are almost one order of magnitude lower than those for the Al-Cr binary alloys. It can, therefore, be said that the simultaneous ad-

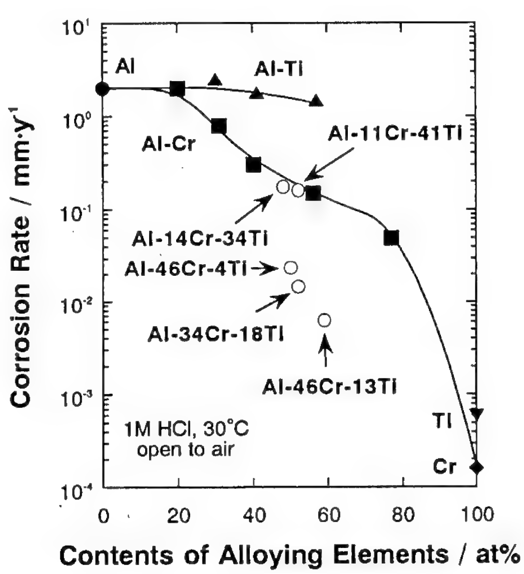

Fig. 2 Corrosion rates of Al-Cr-Ti, Al-Cr and Al-Ti alloys in 1 M HCl open to air at 30 °C as a function of contents of alloying element.

dition of a larger amount of chromium and titanium is more effective to improve the corrosion resistance rather than the single addition of chromium or titanium to aluminum.

Figure 3 shows corrosion rates of Al-Cr-Ti alloys as a function of the alloy chromium content. In these alloys alloy titanium and chromium contents are varied while the alloy aluminum content is almost constant at 47-52 at%. The corrosion rates of Al-Cr-Ti alloys are lower than that for the Al-54Ti alloy. Corrosion rates of the Al-Cr-Ti alloys containing 4-27 at% of chromium are almost the same as each other. However, corrosion rates of relatively high chromium alloys, such as Al-35Cr-18Ti and Al-43Cr-10Ti alloys, are apparently lower than those of relatively high titanium alloys. However, even if the chromium content is high, low titanium alloys, such as Al-46Cr-4Ti and Al-48Cr-4Ti alloys, show lower corrosion resistance than that of alloys with 34-35 at% chromium and 18-10 at% titanium. Consequently, it can be considered that the additions of relatively high chromium and a certain amount of titanium to aluminum are significantly effective to enhance the corrosion resistance.

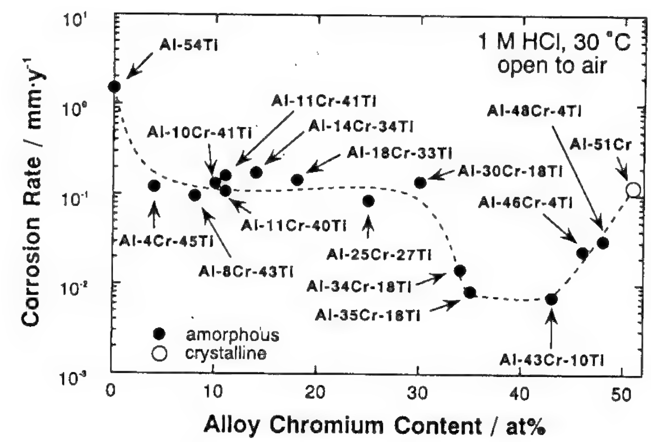

Fig. 3 Corrosion rates of the 47-52Al-Cr-Ti alloys in 1 M HCl open to air at 30 °C as a function of alloy chromium content.

All of Al-Cr-Ti alloys and Al-54Ti alloy shown in Fig. 3 are amorphous, while the Al-51Cr alloy is crystalline. It has been reported previously that amorphous alloys posses a high corrosion resistance and the high corrosion resistance of amorphous alloys is partly attributable to the chemically homogeneous single phase nature of amorphous alloys and to a low activity of micropores in the passive film formed [19, 20]. One explanation for the lower corrosion rate of the amorphous Al-Cr-Ti alloy with sufficiently high chromium content in comparison with the crystalline Al-51Cr alloy is that amorphization enhances the corrosion resistance. However, corrosion rates of the amorphous Al-Cr-Ti alloys containing larger amounts of titanium, such as the Al-43Cr-10Ti and Al-35Cr-18Ti alloys, are lower than that of the amorphous Al-46Cr-4Ti alloy. Therefore, the titanium addition to the

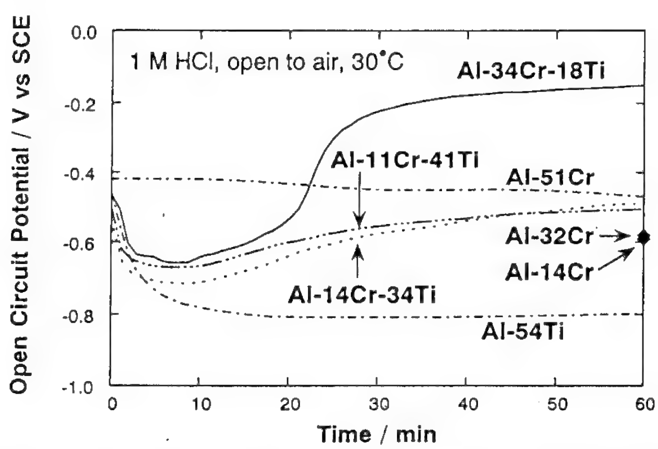

Fig. 4 A change in open circuit potential with time in 1 M HCl open to air at 30 °C.

Al-Cr alloy is assumed to play a beneficial role in promoting the passivity of chromium.

Figure 4 shows the change in open circuit potentials measured in 1 M HCl at 30 °C with time. The open circuit potential of the Al-54Ti alloy decreases in the beginning and later becomes almost constant. This steady potential is in the active state of titanium [21]. The open circuit potential of Al-Cr alloys is higher than that of Al-54Ti alloy. The open circuit potential is ennobled with alloy chromium content, but is still in the active region of chromium [11]. By contrast, the open circuit potential of the Al-34Cr-18Ti alloy is initially lowered by depassivation but then considerably ennobled to the passive region of chromium. On the other hand, the open circuit potentials of ternary alloys containing relatively low concentrations of chromium, such as Al-11Cr-41Ti and Al-14Cr-34Ti alloys, is not ennobled to the passive region of chromium.

Figure 5 shows the change in open circuit potentials of Al-Cr, Al-Ti and Al-Cr-Ti alloys measured after immersion for 2 h in 1 M HCl open to air at 30 °C as a function of the chromium content of alloys. Corrosion rates of these alloys are shown in Fig. 3. Al-Cr-Ti alloys containing relatively high concentrations of chromium and 10 at% or more titanium show remarkably high open circuit potentials in the passive region of chromium. On one hand, the open circuit potentials of Al-Cr-Ti alloys with relatively low concentration of chromium are in the active region of chromium. On the other hand, if the titanium content is low, the addition of high concentrations of chromium is not effective in passivating spontaneously.

These results are in agreement with the corrosion rates of these alloys as shown in Figs. 2 and 3. Alloys with low open circuit potentials are attacked with high corrosion rates, while those with high open circuit potentials are corrosion-resistant.

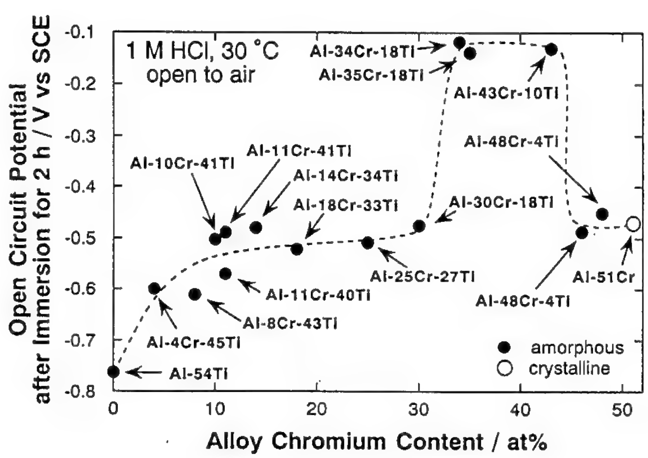

Fig. 5 Open circuit potentials of Al-Cr-Ti alloys measured after immersion for 2 h in 1 M HCl open to air at 30 °C as a function of alloy chromium content.

For a better understanding of the passivation of Al-Cr-Ti alloys, an XPS analysis for the amorphous Al-34Cr-18Ti alloy, whose open circuit potential is ennobled to the passive region of chromium, was performed after immersion. The X-ray photoelectron spectra consisted of peaks corresponding to Al, Cr, Ti, O and C. The photoelectron spectra of Cl from the solution was negligibly small. The thickness and composition of the surface film and the composition of the alloy surface immediately under the surface film were quantitatively determined using integrated intensities of photoelectrons [16].

Figures 6 and 7 show changes of cationic fractions in the surface film and atomic fractions in the underlying alloy surface, respectively, for the amorphous Al-34Cr-18Ti alloy after immersion in 1 M HCl open to air at 30 °C as a function of immersion time. Compositions of the surface film and alloy surface for the Al-51Cr alloy after immersion for 5 h under the same condition are added

for comparison. The open circuit potentials of the Al-34Cr-18Ti alloy are also shown. The composition of the film formed in air after mechanical polishing in cyclohexane and the atomic composition in the underlying alloy surface just below the air-formed film is also shown for comparison.

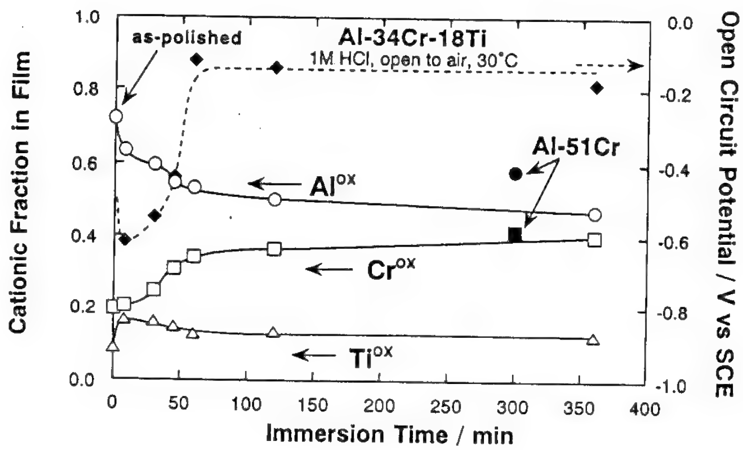

Fig. 6 Cationic fractions in the surface film formed on amorphous Al-34Cr-18Ti alloy as a function of immersion time in 1 M HCl open to air at 30 °C. The composition of the air-formed film after mechanical polishing in cyclohexane and that of film on Al-51Cr alloy measured after immersion for 300 min are also shown for comparison.

The aluminum content in the air-formed oxide film on the Al-34Cr-18Ti alloy is significantly higher than that of the bulk alloy, while aluminum in the underlying alloy surface is deficient. This fact indicates the preferential oxidation of aluminum in air after mechanical polishing in cyclohexane. The composition of the surface film gradually changes with immersion time. The cationic fraction of chromium increases and that of aluminum decreases, while the cationic fraction of titanium is almost constant. The cationic fraction of chromium becomes slightly higher than the fraction of chromium in the bulk alloy. Accordingly, the increase in the film chromium content occurs due to preferential dissolution of aluminum as well as dissolution of titanium. Because the chromium oxyhydroxide film is stable in 1 M HCl the increase of chromium cations in the film seems to decrease the anodic current density. Furthermore, it has been known [22] that the formation of the passive film with a high concentration of chromium has a high activity for cathodic oxygen reduction and ennobles the open circuit potential. Accordingly, the increase in the chromium content in the surface film seems to responsible for the ennoblement of the open circuit potential.

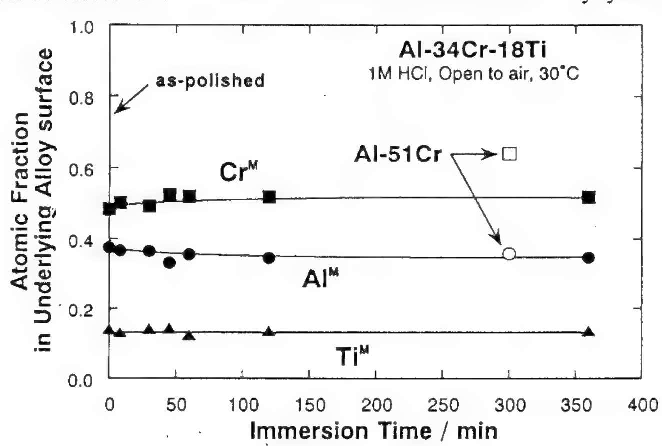

Fig. 7 Atomic fractions in the underlying alloy surface just below the surface film formed on the amorphous Al-34Cr-18Ti alloy as a function of the immersion time in 1 M HCl open to air at 30 °C. The underlying alloy composition just below the air-formed film after mechanical polishing in cyclohexane and that of film on Al-51Cr alloy measured after immersion for 300 min are also shown for comparison.

By contrast, the aluminum content of the film formed on the Al-51Cr alloy is higher than those of bulk

alloy and film formed on the Al-34Cr-18Ti alloy, though the alloy aluminum contents of Al-51Cr and Al-34Cr-18Ti alloys are almost the same as each other. Furthermore, the open circuit potential of the Al-51Cr alloy is in the active region of chromium, and the corrosion rate of the Al-51Cr alloy is one order of magnitude higher than that of the Al-34Cr-18Ti. Accordingly, the decrease in aluminum content with a consequent increase in chromium content in the film seems to enhance the corrosion resistance of the alloy.

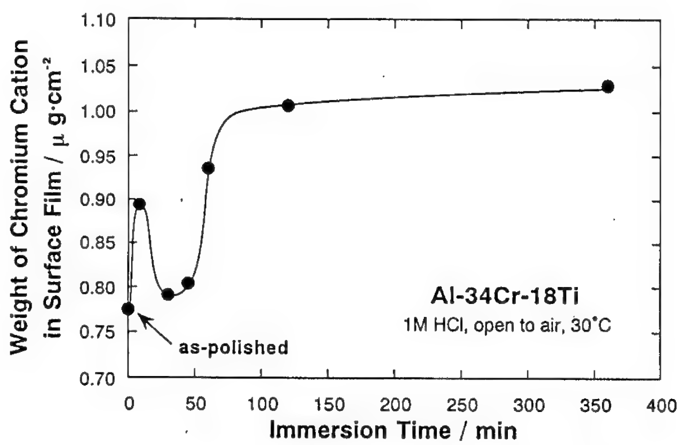

Fig. 8 Weight of chromium in the surface film formed on amorphous Al-34Cr-18Ti alloy as a function of immersion time in 1 M HCl open to air at 30 °C. The weight of chromium in the air-formed film after mechanical polishing in cyclohexane is also shown for comparison.

Figure 8 shows the change in the weight of chromium in the surface film formed on the amorphous Al-34Cr-18Ti alloy after open circuit immersion in 1 M HCl open to air at 30 °C. The weight of chromium in the air-formed film is also shown for comparison. The weight of chromium increases at 8 min in spite of no chromium enrichment in the film, and then decreases to almost the same weight of chromium in the air-formed film at 30 min. The initial increase in the weight of chromium corresponds to the appearance of the lowest open circuit potential where a thick corrosion product film is formed as a result of rapid initial corrosion. The weight of chromium starts to increase at about 30 min and reaches the steady state within 2 h. The increase in the weight of chromium corresponds to the ennoblement of the open circuit potential. Before the ennoblement of the open circuit potential, titanium is already deficient in the film. The formation of the film containing chromium seems to ennoble the open circuit potential and the ennoblement of the open circuit potential seems to enhance further the enrichment of chromium in the film.

Figures 9 and 10 show cationic fractions in the surface film and atomic fractions in the underlying alloy surface, respectively, for Al-Cr-Ti alloys measured after immersion for 2 h in 1 M HCl open to air at 30 °C as a function of chromium content of alloys. Corrosion rates and open circuit potentials of these alloys are shown in Figs. 3 and 5, respectively. The cationic fractions of chromium in the spontaneously passivated films on Al-Cr-Ti alloys with relatively high chromium and some titanium contents are slightly higher than or almost the same as concentrations of chromium in the bulk alloys. In the passive film on these alloys, aluminum is not concentrated, though aluminum is rich in the air-formed film after mechanical polishing in cyclohexane. In the underlying alloy surface for these alloys, atomic fractions of aluminum are lower than those of the bulk alloys. This is attributable to the preferential dissolution of aluminum.

By contrast, concentrations of chromium in the surface films on the alloys whose open circuit potentials are in the active region of chromium are lower than the alloy chromium content, and the film is rich in aluminum. Because aluminum oxyhydroxide is not stable in 1 M HCl, the surface film containing high concentration of aluminum cannot be protective against the aggressive chloride containing acid solution. Consequently, the prevention of enrichment of aluminum and the

increase in chromium in the surface film are responsible for high corrosion resistance of the Al-Cr-Ti alloys.

DISCUSSION

Even if aluminum is alloyed with titanium, the open circuit potential in 1 M HCl is not ennobled to that of titanium, because of the presence of aluminum with a low open circuit potential [1]. The open circuit potential of the Al-Ti alloy is in the active state of titanium where titanium readily dissolves as divalent titanium cations [21]. Accordingly, the corrosion rate of the Al-Ti alloys is almost the same as that of aluminum metal regardless of the titanium content. On the other hand, the corrosion rate of Al-Cr alloys in 1 M HCl is lower than that of aluminum, and their corrosion rates tend to decrease with increasing alloy chromium content [11]. However, the chromium addition to aluminum is not significantly effective in improving the corrosion resistance, since the surface film is rich in aluminum which is less noble than chromium. In other words, the concentration of chromium cannot increase to the level of the alloy chromium content, because preferential oxidation of aluminum prevents an increase in the concentration of chromium in the surface film.

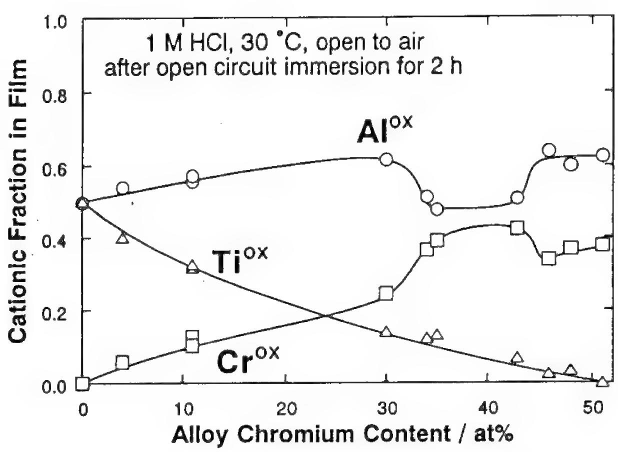

Fig. 9 Cationic fractions in the surface film formed on Al-Cr-Ti alloys measured after immersion for 2 h in 1 M HCl open to air at 30 °C as a function of alloy chromium content.

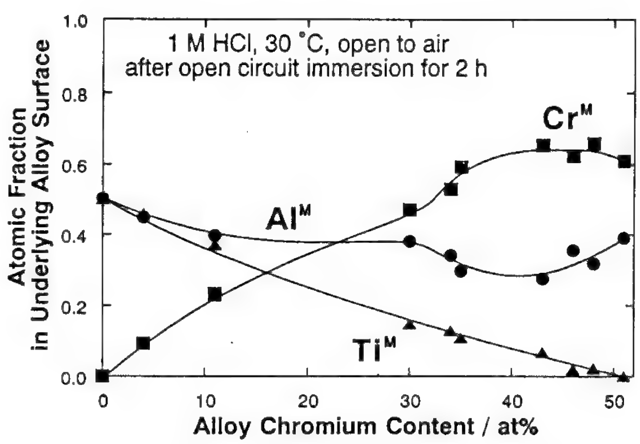

Fig. 10 Atomic fractions in the underlying alloy surface just below the surface film for Al-Cr-Ti alloys measured after immersion for 2 h in 1 M HCl open to air at 30 °C as a function of alloy chromium content.

By contrast, additions of a relatively high concentration of chromium along with a certain amount of titanium to aluminum result in considerable ennoblement of the open circuit potential in 1 M HCl to the passive region of chromium and titanium. Therefore, corrosion rates of these alloys are considerably lower than those of the Al-Ti or Al-Cr binary alloys containing the same concentration of aluminum.

XPS analysis showed that the cationic fraction of chromium in the surface film formed on Al-Cr-Ti alloys increases with time of immersion in 1 M HCl and becomes slightly higher than the concentration of chromium in the bulk alloy, as shown in Fig. 6. The increase in the cationic fraction of chromium is due to preferential dissolution of aluminum as well as titanium. It has been reported [23, 24] that the formation of passive films consisting mainly of hydrated chromium oxyhydroxide is one of the most important characteristics in ensuring the high corrosion resistance of alloys containing chromium. Furthermore, chromium has high activities for hydrogen evolution and oxygen reduction reactions. Therefore, the increase in chromium cations decreases the anodic current density and increases the cathodic current density. On the other hand, aluminum enrichment in the surface film on the Al-Cr binary alloys prevents chromium enrichment, and hence their open circuit potentials are not ennobled to the passive region of chromium.

It is suggested from the contrast between the properties of surface films on Al-Cr-Ti and Al-Cr alloys that titanium promotes preferential dissolution of aluminum with a consequent prevention of enrichment of aluminum in the passive film. It can, therefore, be said that simultaneous addition of chromium and titanium to aluminum is effective in improving the corrosion resistance of the alloy.

CONCLUSIONS

Corrosion rates of Al-Cr-Ti alloys with relatively low chromium contents are almost the same as those of Al-Cr alloys with the same aluminum content but lower than those of Al-Ti binary alloys containing the same amount of aluminum. Corrosion rates of the Al-Cr-Ti alloys with relatively high contents of chromium are almost one order of magnitude lower than those of the Al-Cr alloys. It can, therefore, be said that additions of chromium and titanium to aluminum are more effective in improving the corrosion resistance than the single-addition of chromium or titanium to aluminum.

Open circuit potentials of the Al-Cr-Ti alloys containing relatively high concentrations of chromium and some titanium are ennobled to the passive region of chromium, because of a decrease in the anodic current density along with an increase in the cathodic current density. The high cathodic current density is due to the high activities for oxygen reduction and hydrogen evolution reactions. By contrast, open circuit potentials of the Al-Cr alloys are not ennobled to the passive region of chromium.

The cationic fraction of aluminum in the spontaneously passivated film on Al-Cr-Ti alloy is lower than that in the film on alloys whose open circuit potential are in active region of chromium, because of the preferential dissolution of aluminum. It can be said that the prevention of enrichment of aluminum and the increase in chromium in the surface film are responsible for the high corrosion resistance of the Al-Cr-Ti alloys.

Acknowledgment - The present work is supported in part by Grant-in Aid for Scientific Research (A) No. 03403012 and Grant-in-Aid for Encouragement of Young Scientists No. 05750640 and No. 06750731 from the Ministry of Education, Science and Culture.

REFERENCES

1. H. Yoshioka, Q. Yan, H. Habazaki, A. Kawashima, K. Asami and K. Hashimoto, *Corros. Sci.* **31**, 349 (1990).
2. Q. Yan, H. Yoshioka, H. Habazaki, A. Kawashima, K. Asami and K. Hashimoto, *Corros. Sci.*

31, 401 (1990).
3. Q. Yan, H. Yoshioka, H. Habazaki, A. Kawashima, K. Asami and K. Hashimoto, *J. Non-Cryst.*, **125**, 25 (1990).
4. Q. Yan, H. Yoshioka, H. Habazaki, A. Kawashima, K. Asami and K. Hashimoto, *Corros. Sci.* **32**, 327 (1991).
5. H. Yoshioka, Q. Yan, K. Asami and K. Hashimoto, *Mater. Sci. Engng.* **A134**, 1054 (1991).
6. H. Yoshioka, H. Habazaki, A. Kawashima, K. Asami and K. Hashimoto, *Electrochimica Acta* **36**, 1227 (1991).
7. H. Yoshioka, H. Habazaki, A. Kawashima, K. Asami and K. Hashimoto, *Corros. Sci.* **33**, 425 (1992).
8. H. Yoshioka, A. Kawashima, K. Asami and K. Hashimoto, R. D. Diegle and K. Hashimotos, Eds., Proc. Corrosion, Electrochemistry and Catalysis of Metallic Glasses, The Electrochemical Society, Pennington, Honolulu, p. 242, (1988).
9. H. Yoshioka, A. Kawashima, K. Asami and K. Hashimoto, Eds., Proc. MRS Int. Meeting of Advanced Materials, Materials Research Society, Pittsburgh, vol. 3, p. 429, (1988).
10. H. Yoshioka, H. Habazaki, A. Kawashima, K. Asami and K. Hashimoto, *Corros. Sci.* **32**, 313 (1991).
11. J. H. Kim, E. Akiyama, H. Habazaki, H. Yoshioka, A. Kawashima, K. Asami and K. Hashimoto, K. Hashimoto and C. R. Claytons, Eds., Proc. Corrosion, Electrochemistry and Catalysis of Metastable Alloys and Intermetallics, The Electrochemical Society, Pennington, p. 48 (1993).
12. J. H. Kim, E. Akiyama, H. Yoshioka, H. Habazaki, A. Kawashima, K. Asami and K. Hashimoto, *Corros. Sci.* **34**, 975 (1993).
13. K. Shimamura, K. Miura, A. Kawashima, K. Asami and K. Hashimoto, R. D. Diegle and K. Hashimotos, Eds., Proc. Corrosion, Electrochemistry and Catalysis of Metallic Glasses, The Electrochemical Society, Pennington, New Jersey, p. 201, 232, (1988).
14. K. Asami, *J. Electron Spectrosc.* **9**, 469 (1976).
15. K. Asami and K. Hashimoto, *Corros. Sci.* **17**, 559 (1977).
16. K. Asami, K. Hashimoto and S. Shimodaira, *Corros. Sci.* **17**, 713 (1977).
17. K. Asami, S.-C. Chen, H. Habazaki, A. Kawashima and K. Hashimoto, *Corros. Sci.* **31**, 727 (1990).
18. J. H. Scofield, *Journal of Electron Spectroscopy and Related Phenomena* **8**, 129 (1976).
19. M. Naka, K. Hashimoto and K. Masumoto, *J. Japan Inst. Metals* **38**, 835 (1974).
20. K. Hashimoto, H. Habazaki, B. P. Zhang, A. Kawashima and K. Asami, *Metallurgy and Foundry Engineering* **18**, 165 (1992).
21. M. Pourbaix, *Atlas of electrochemical equilibria in aqueous solutions* (Pergamon Press, 1966).
22. J. H. Kim, E. Akiyama, H. Habazaki, A. Kawashima, K. Asami and K. Hashimoto, *Corros. Sci.* **36**, 511 (1994).
23. K. Asami, K. Hashimoto, T. Masumoto and S. Shimodaira, *Corros. Sci.* **16**, 909 (1976).
24. K. Hashimoto and K. Asami, in *Passivity of Metals* R. P. Frankenthal and J. Kruger, Eds. (The Electrochemical Society, Princeton, 1987) p. 749.

Materials Science Forum Vols. 185-188 (1995) pp. 819-828

Determination of the stability of the passive layer on Al-SiC composite material

M.A. Malik[1], H. Bala[1] and E. Maahn[2]

[1] Department of General Chemistry, Polytechnic of Czestochowa, PL-42-200 Czestochowa, Poland

[2] Institute of Metallurgy, The Technical University of Denmark, DK-2800 Lyngby, Denmark

Keywords: Metal matrix composite, aluminium alloy, SiC-particulates, stability of the passive layer, sulphate solutions, rotating disc electrode, limiting current of oxygen, polarization curves

Abstract: A new electrochemical method for evaluation of the coverage of Al-based metal matrix composite material with an oxide layer is presented. The comparison of oxygen reduction current densities on pure Al, Al-SiC composite and limiting O_2 current density on the surface of non-passivating metal at constant electrode potential and stirring rate allows to evaluate the degree of the coverage for the composite material. This coverage can be considered to be a measure of resistance of the Al-SiC composite material against corrosion.

Introduction

Metal matrix composites (MMC) fabricated with lightweight Al alloy matrices and high-modulus graphite or SiC reinforcements (10-40wt%) offer excellent structural properties. However, differences in electrochemical activity of Al-matrix and the particulates cause serious corrosion problems as a result of formation of the local Al/particulate galvanic couples [1, 2]. It is believed that the presence of a particle in the surface introduces a break in the passive film [3], facilitates the pitting attack in chloride solutions [1, 3] and increases the number of intermetallic precipitates in the material leading to the increase of effective cathodic area [2, 4]. Generally, the literature on the corrosion properties of metal matrix composites is comparatively small and there has been no systematic investigation of the effect of SiC and $C_{graphite}$ reinforcement on the electrochemical polarization characteristics of the aluminium-base alloys in a range of environmental conditions. Most of the papers dealing with Al-based metal matrix composites evaluate the stability of the passive layer on the basis of the values of pitting (E_p) and repassivation (E_{pp}) potentials. Materials with a low pitting potential value are considered to have a stronger tendency to suffer from locallized corrosion. Because of poor reproducibility of such measurements [2], it is difficult to evaluate the effect of SiC content in the composite material and the particles pre-treatment on the pitting potential values [3]. An interesting method based on electrochemical impedance spectroscopy (EIS), making it possible to determine the fraction of the passivated surface on which pitting occurs has been presented by Mansfeld *et al* [5]. For the analysis of the impedance data the low frequency region contains very important information since both the polarization resistance and/or the impedance elements which are due to pitting have to be extracted from these data. An analysis of the impedance spectra with a use of special fitting procedures for anodized Al-base alloy and Al/SiC composite material indicates that the mechanism of formation of anodic coatings in the two cases must be different due to SiC particulates [1]. Recently, many papers which deal with chemical surface modification of the Al alloys and its composites (anodizing in sulphate solutions [1], chromate conversion processes [6], alkaline lithium baths [6, 7], cerium and other lanthanides chloride baths [8, 9] etc.) have appeared but, at present, very little is still known about the mechanism by which these coatings are formed and obtain their superior corrosion resistance.

The present paper aims at the evaluation of the fraction of surface of the aluminium based MMC non covered by the passive layer. The method proposed to achieve this goal consists of determination of O_2 reduction currents for pure Al, for Al-composite material and for non-passivating metal (e.g. amalgamated copper) at a constant electrode disk rotation rate in O_2-saturated acid sulphate solution. The dependence of the measured currents of oxygen reduction on the stirring rate enables further conclusions concerning the mechanism of the composite material protection against corrosion.

Assumptions and description of the test method

(a) A simplified model of surface layers of Al-SiC composite material

The present knowledge concerning the morphology, mechanism of formation and corrosion behaviour of the surface oxide layers on the Al-based MMCs allows to assume a simplified model of the corroding surface of the material, presented in Fig.1.

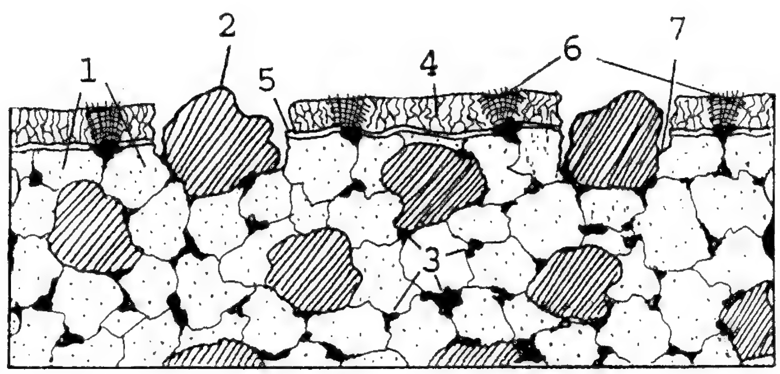

Fig 1. A simplified cross section model of the corroding Al-SiC composite material: 1 - grains of Al alloy matrix, 2 - particulates of SiC reinforcement, 3 - intermetallic precipitates, 4 - porous oxide layer, 5 - barrier oxide layer, 6 - cathodic spots over the precipitates, 7 - fragments of the "bare" metal

The idea of the existence of the "porous" and "barrier" layers on the surface of Al-SiC composites has been introduced by Lin *et al* [1] whereas the formation of "weak spots" in the oxide film, situated over the intermetallic heterogeneities (enriched in Cr, Ti, Fe and Si) has been shown by Griffiths and Turnbull [2]. The practical dimensions of the SiC particulates are mostly of the order of 10-20 μm in diameter [10], the grains of Al powder - 5 - 20 μm [11], the diameter of intermetallic precipitates < 3μm [2]. The thicknesses of the barrier and porous layers are evaluated to be ~10 nm and 10-50 μm, respectively [1].

On the surface of Al-SiC composite material there are at least three kinds of cathodic sites on which the reduction of dissolved O_2 can occur: (i) surface SiC particulates, (ii) cathodic spots over the intermetallic precipitates and (iii) narrow crevices of the "bare metal" neighbouring the surface particulates.

For sintered Al matrix alloy (without reinforcements) the sites (i) and (iii) do not exist, whereas for specpure Al, also the sites (ii) disappear. The cathodic currents of oxygen reduction measured for high purity Al are clearly smaller than for the Al-alloys and Al-SiC composites. In the case of continuos oxide layer, the oxygen reduction process is most likely strongly inhibited by slow

transport of O_2 molecules across the porous oxide layer. Prolonged anodic polarization increases the thickness of the passive layer on the Al and at adequately positive potentials (and for long anodic polarization time) the layer becomes practically nonpermeable for oxygen. The evidence for this statement is wide hysteresis loops on bidirectional potentiokinetic polarization curves for Al alloys in oxygenated solutions

(b) Determination of the coverage of Al-SiC composite with an oxide layer

Assuming that the partial electrode processes are independent of each other, the difference between potentiokinetic polarization curves measured in O_2- and Ar-saturated acid solutions of the same electrolyte should be equal to the oxygen reduction process rate (i_{O2})[1]. At constant electrode potential $\mathscr{E}$ and at constant stirring rate ω the current density of O_2 reduction is

$$i_{O2,\mathscr{E}} = [i_{(O2)} - i_{(Ar)}]_{\mathscr{E}} \tag{1}$$

If the oxide layer is compact and uniform as in the case of pure aluminium (the coverage of the surface with the oxide layer $\vartheta_{ox} = 1$) the oxygen dissolved in the test solution can diffuse towards the metal surface through two layers:

(i) diffusional layer in the solution (thickness "δ") and

(ii) solid oxide layer (thickness "δ_{ox}")

The thickness of the first layer decreases linearly with the increase of the square root of the angular velocity of the disk electrode ($\omega^{1/2}$) [12]. The thickness of the second layer depends on the anodic potential applied and on the exposure time of the electrode at this potential but does not depend on the stirring rate. The transport of O_2 molecules across this oxide layer most likely accomplishes mainly by pores, cracks and other discontinuities of the layer and its rate can be characterized by the apparent oxygen diffusion coefficient in this solid layer (D_{ox}). Densities of the oxygen current through these two layers are respectively

$$i_{O2,sol} = nFD(c_o - c_{ox})/\delta \tag{2}$$

and

$$i_{O2,ox} = nFD_{ox}c_{ox}/\delta_{ox} \tag{3}$$

where:

D, D_{ox} - diffusion coefficients of O_2 in the tested solution and in the oxide layer

δ, δ_{ox} - thickness of the diffusion layer in the solution and thickness of the oxide layer

c_o, c_{ox} - concentrations of O_2 in bulk solution and at the outer part of the oxide layer

In stationary conditions $i_{O2} = i_{O2,sol} = i_{O2,ox}$ which allows to eliminate c_{ox}:

$$i_{O2} = \frac{nFDD_{ox}\, c_o}{\delta\,\delta_{ox}(D/\delta + D_{ox}/\delta_{ox})} \tag{4}$$

A similar relationship has been obtained by Konyaev [13] for Ni-disk electrode in oxygenated acid solution covered with thin films of organic inhibitors.

---

[1] This statement is not correct for medium pH values (~3-8) when both depolarizers (O_2 and H^+) can reduce on the corroding surface because hydrogen ion is a common reagent for the both processes [14].

When the stirring rate is fast enough, $\delta \to 0$ and $D/\delta >> D_{ox}/\delta_{ox}$. This simplifies the Eq.(4):

$$i_{O2(\delta\to 0)} = nFD_{ox}c_o/\delta_{ox} \tag{5}$$

This way, for compact oxide layers (pure Al), the measured current of oxygen reduction should become constant at suitably great disk rotational velocities and should decrease with the increase of the oxide layer thickness. The absolute values of the $i_{O2(\delta\to 0)}$ will be much smaller compared to $i_{O2,lim}$ because it can be expected from the formal diffusion coefficient of oxygen "D_{ox}" (in the solid oxide layer) to take on considerably smaller values than the diffusion coefficient "D"in the aqueous solution. When the oxide film is not continuous and the coverage $\vartheta_{ox} < 1$ (the case of Al-based MMC material), the measured current of oxygen reduction consists of two terms:

$$i_{O2,MMC} = i_{O2(\delta\to 0)}\,\vartheta_{ox} + i_{O2,lim}\,(1-\vartheta_{ox}) \tag{6}$$

The second term in Eq.(6) describes the limiting current of O_2 on surface sites which are not covered with the oxide layer (compare Fig.1). Of course, the $i_{O2,lim}$ depends on the disk electrode rotational velocity and on the O_2 concentration in bulk solution according to the Levich equation [12, 14]:

$$i_{O2,lim} = 0.62\, D^{2/3} \nu^{-1/6} c_o \omega^{1/2} \tag{7}$$

where ν - kinematic viscosity of the solution

Because of $i_{O2(\delta\to 0)} << i_{O2,lim}$, for Al-SiC MMC, for which $\vartheta_{ox} < 1$, the cathodic current of O_2 reduction will always be greater than for specpure Al. Transformation of Eq.(6) allows to find the fraction of surface covered with the oxide layer:

$$\vartheta_{ox,MMC} = \frac{i_{O2,lim} - i_{O2,MMC}}{i_{O2,lim} - i_{O2,Al}} \tag{8}$$

In the last equation all the oxygen current densities have to be measured at the same, adequately fast, stirring rate and at the same O_2 concentration in the test solution. The $i_{O2,lim}$ does not depend on the electrode potential, however, owing to the dependence of the thickness of the oxide layer on the electrode potential, both the $i_{O2,MMC}$ and $i_{O2,Al}$ currents should be read from the polarization curves (measured at the same potential scanning) at the same electrode potential $\mathscr{E}$.

Experimental conditions

Three differently prepared commercial Al-10vol%SiC type alloys (A - ESK NF 12; mean SiC particulates size 11.5 μm, B - ESK F400; 21.7 μm and C - Norton E85 F500; 11.5 μm) were applied as test material. For comparison, Al-based alloy, MD 105, sintered (denoted as sample D) and specpure Al, IE-Ltd (sample E) were also used. The samples had the form of rotating disks with an operating surface area of 0.283 cm^2. Before each experiment the samples were polished using waterproof emery papers no 800, rinsed in distilled water and wet immersed into the measuring cell. All experiments were performed in Ar- and O_2-saturated 0.5 M H_2SO_4 solutions at a temperature of 25 ± 0.1°C.

The potentiokinetic polarization curves were measured in the following way: directly after immersion in the test solution, the sample was polarized cathodically, from $\mathscr{E}_{corr}$ towards -1.5 V vs SCE with the rate of potential scanning $25mVs^{-1}$. Then the direction of potential sweep was reversed and the sample was polarized in the anodic direction up to 1.0V vs SCE (so called "increasing

potential scanning"). After reaching $\mathscr{E}$ = 1.0 V the sample was polarized in the cathodic direction up to -1.5 V ("decreasing potential scanning"). Most of the polarization measurements were performed at a disk with a rotation rate of 15.0 rps. This rate ensured a laminar flow of the solution and eliminated screening of the surface by hydrogen bubbles at cathodic potentials. All electrochemical tests were made with the use of automatic measuring system consisting of an EP20 potentiostat (ELPAN), a scanner, logarithmic amplifier, data acquisition unit and computer compatible with IBM PC/AT.
All measurements of potentiokinetic polarization curves were repeated 4 times (each in fresh solution and after polishing of the electrode every time) and then the mean polarization curves were calculated. The error of cathodic current for the individual curves in the potential range of -0.8 to 0.0 V did generally not exceed 5%. For more negative potentials, because of hydrogen evolution, the experimental results showed much worse reproducibility.

Experimental results
In Fig.2 the mean potentiokinetic polarization curves of the tested samples in Ar- and O_2-saturated 0.5 M H_2SO_4 solution determined for both potential scan directions are presented. For "increasing potential scanning" (Fig.2a) the area of limiting current of oxygen reduction is clearly visible for all of the tested samples whereas for "decreasing potential scanning" the differences between curves measured in O_2 and Ar saturated solutions are considerably smaller. The main reason for this behaviour seems to be differences in the thickness of the passive layer. For "increasing potential scanning", at starting cathodic potential (-1.5 V vs SCE) the oxide film is reduced. Further polarization in the positive direction probably increases the thickness of the film, however, because of the fast production of H_2 it cannot be totally renewed. It can be assumed that in the cathodic range the surface film corresponds to the thin "barrier layer", permeable for oxygen molecules. For the "decreasing potential scanning" (Fig.2b) the oxide layer is considerably thicker, and, as a result, the anodic currents in the passive range are one order of magnitude smaller. Thick oxide layers are non permeable by oxygen and therefore differences between potentiokinetic polarization curves measured in Ar- and O_2-saturated solutions practically disappear. For strongly cathodic potentials (< -1.0 V vs SCE) the cathodic currents for Ar-saturated solutions are usually greater than for oxygenated solutions, which is discordant to the assumption of the independence of partial electrode processes. This phenomenon may be connected with (i) greater increase of pH at the surface of oxygenated solution (reduction of O_2 consumes H^+ ions), (ii) reaction of O_2 with adsorbed H atoms and (iii) oxidation of other catalysts for hydrogen evolution process, such as small quantities of product of reduction of sulphate ion [15].
In Fig.3 the corresponding subtractions between polarization curves for increasing potential scanning are presented[2]. In Fig.3a it is shown, as an example, the evaluation of measurement error (dashed line) for determination of the apparent current of O_2 reduction for the sample "C". Generally, the results for all of the tested samples showed the smallest error just in the range of these apparent limiting currents. In Fig.3b the subtractions between polarization curves measured in presence O_2 and Ar, respectively, in the potential range of the best reproducibility (-1.0 to -0.6 V vs SCE) for

[2]The results for increasing potential scanning showed much better reproducibility as compared with the decreasing one and the $i_{O2,\mathscr{E}}$ values found for the increasing scanning were independent of $\mathscr{E}$ in a comparatively wide potential range. They have a shape of "limiting currents". However, they do not increase linearly with $\omega^{1/2}$ and are distinctly smaller than $i_{O2,lim}$ values measured for amalgamated Cu-disk electrode. Therefore, the $i_{O2,\mathscr{E}}$ currents found for the tested Al-base materials are named here "apparent limiting currents of O_2 reduction". In contrary, $i_{O2,\mathscr{E}}$ currents measured at decreasing scanning increased with the increase of cathodic polarization

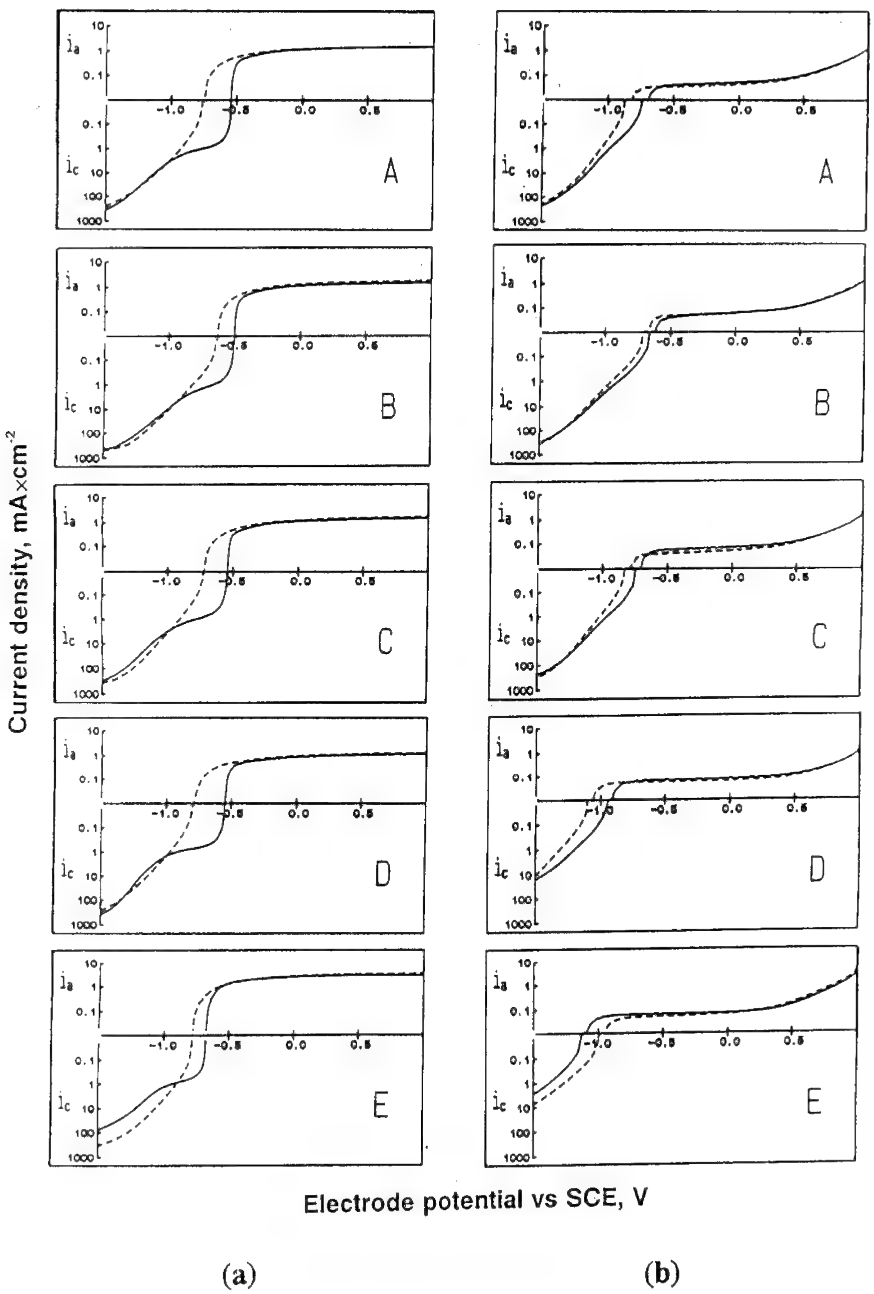

Fig.2. Potentiokinetic polarization curves of the tested samples A-E (mean values of 4 repetitions) in Ar (broken line) and in O_2-saturated 0.5 M H_2SO_4 solution (solid line) at an increasing (a) and a decreasing potential scanning (b). Experimental conditions: scanning rate 25 mVs^{-1}, stirring rate 15 rps, temperature 25^{o}C

the tested Al-base samples A-E are presented. As the representative $i_{O2,\mathscr{E}}$ values for the individual samples the values corresponding to their corrosion potentials in Ar-saturated solutions were arbitrary assumed. As it results from Fig.3b, the tested samples exhibit distinct differences in apparent values of the limiting oxygen reduction current. The smallest value of $i_{O2,\mathscr{E}}$ was found for specpure Al (sample "E"). It is worth noting that at potentials more noble than -0.55 V (SCE), apart from specpure Al, all the tested samples show cathodic differences $i_{(O2)}-i_{(Ar)}$, and these are on the order of magnitude smaller than the corresponding apparent currents of O_2. It is possible that for $\mathscr{E} > -0.55$ V the abrupt growth of the thickness of the porous layer begins.
The apparent values of $i_{O2,\mathscr{E}}$ of the tested samples read from Fig.3b vary between limits of 0.53 to 0.96 $mAcm^{-2}$ whereas the limiting current of oxygen in the tested solution at the applied stirring rate $\omega/2\pi$ = 15 rps is $i_{O2,lim}$ = 1.74 mA cm^{-2} [14]. The determined apparent values of i_{O2} and the ϑ_{ox} values calculated for the tested samples using the Eq.(8) are listed in Table 1.

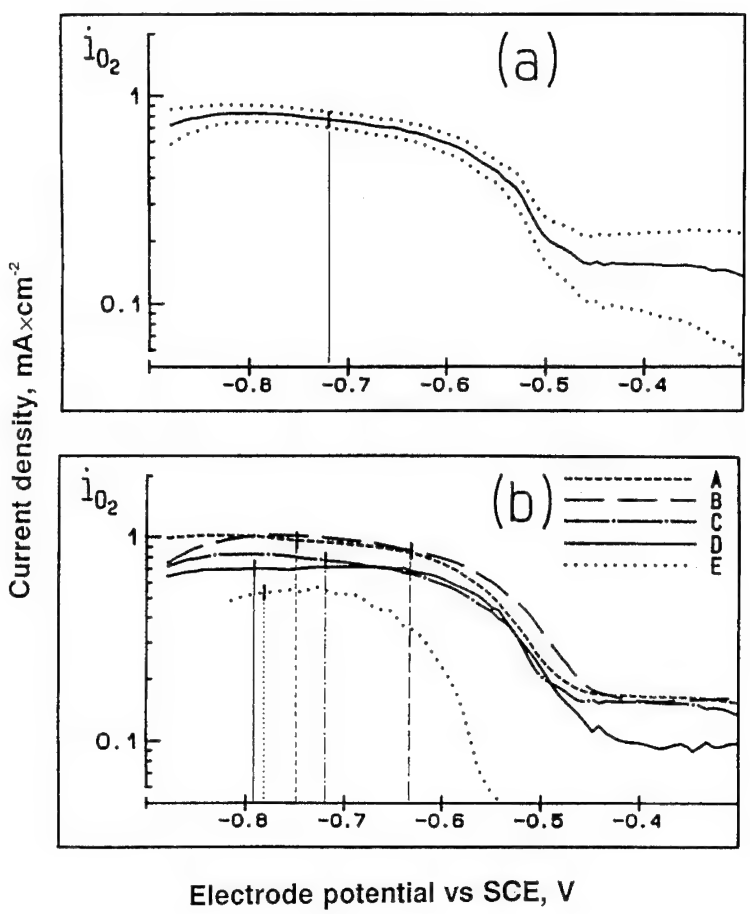

Fig.3. Differences between potentiokinetic polarization curves measured at increasing potential scanning $i_{O2,\mathscr{E}} = [i_{(O2)} - i_{(Ar)}]_{\mathscr{E}}$ for the tested samples in potential range -1.0 to -0.3 V (SCE). In Fig.(a) dashed lines represent the error bars for i_{O2} measured on sample "C". Vertical lines cross the potential axis for individual samples at their $\mathscr{E}_{corr,\ Ar}$

Table 1 Apparent limiting currents of oxygen reduction on the tested samples (i_{O2}, $mAcm^{-2}$) and calculated fractions of the surface coverage with the oxide film (ϑ_{ox})

Sample	i_{O2}	ϑ_{ox}
A	0.96	0.64
B	0.85	0.74
C	0.77	0.80
D	0.70	0.86
E	0.53	1.00

Discussion and concluding remarks

The proposed method of determination of the fraction of the surface coverage with the passive layer allows to arrange a number of passivating samples according to their increasing stability of the oxide film. The method exhibits a good reproducibility and requires only conventional electrochemical apparatus. In case of very thick and compact oxide layers the measured i_{O2} values are considerably smaller and the experimental error of their determination strongly increases. Because of the limited solubility of oxygen in aqueous solutions, the only way to increase the O_2 flux towards the surface is to increase the stirring rate, however, the flux has to be laminar (practically, the stirring rate should not be greater as 60-80 rps). As seen, the good isolating oxide layers need greater concentrations of depolarizers in the solution. As an alternative depolarizer, the hydrogen peroxide, having unlimited solubility in aqueous solutions, can be used. To apply of other possible oxidants we should have in mind the possibility of modification of the passive layers by these oxidants (e.g. Ce^{4+}, CrO_4^{2-} etc.). Finally, the thickness and the isolating properties of the oxide layers depend on the electrode potential and on the potential scanning rate. The i_{O2} currents determined in this paper are practically constant in a rather narrow range of the electrode potential (-0.9 to -0.6 V vs.SCE - compare Fig.2b); the values presented in Table 1 correspond to the corrosion potential each of the tested samples in deaerated (Ar-saturated) solution. This way, much better characterization of the passive layer it would be the dependence $\vartheta_{ox} = f(\mathscr{E})$, however, in wide potential range new limitations appear: in strong cathodic range the cathodic processes are not independent upon each other and for more noble potentials the reduction of oxygen enters the activactionally controlled range.

References

1. S.Lin, H.Greene, H.Shih and F.Mansfeld, Corrosion, **48**, 61 (1992)

2. A.J.Griffith and A.Turnbull, Corros.Sci., **36**, 23 (1994)

3. S.Roepstorff and E.Maahn, 12th Scandinavian Corrosion Congress & Eurocorr'92; Proceedings, vol.1, p.279, Dipoli, Espoo, 31.05-04.06.1992

4. P.P.Trzaskoma, Corrosion, **46**, 402 (1990) and P.P.Trzaskoma, E.McCafferty and C.R.Crowe, J.Electrochem.Soc., **130**, 1804 (1983)

5. F.Mansfeld, S.Lin, S.Kim and H.Shih, Electrochim.Acta, **34**, 1123 (1989)

6. R.G.Buchheit, M.D.Bode and G.E.Stoner, Corrosion, **50**, 205 (1994)
7. J.Gui and T.M.Devine, Script.Metal., **21**, 853 (1987)
8. B.R.W.Hinton, D.R.Arnott and N.E.Ryan, Metals Forum **7**, 211 (1984)
9. B.R.Hinton, D.R.Arnott and N.E.Ryan, Mater.Forum, **9**, 162 (1986)
10. Y.L.Liu and B.Kindl, Scripta Metall., *in press*
11. J.Narciso, C.Garcia-Cordovilla and E.Louis, Mater.Sci.Eng., **B15**, 148 (1992)
12. V.G.Levich, Fizikokhimicheskaya gidrodinamika, Fizmatgiz, Moskva 1959
13. B.Ya.Konyaev, Zashchita Met., **11**, 619 (1975)
14. H.Bala, Z.Phys.Chem.N.F., **141**, 91 (1984)
15. H.Bala, Electrochim.Acta, **29**, 119 (1984)

Materials Science Forum Vols. 185-188 (1995) pp. 829-842

Corrosion and stability of lead brass alloy in acid and neutral solutions - EIS investigation

W.A. Badawy[1], A.A. Mazhar[2], S.S. Elegamy[2] and A.S. El-Azabe[2]

[1] Author to whom all correspondence should be addressed.
present address: University of Kuwait, Department of Chemistry, Faculty of Science, PO Box 5969 Safat, 13060 Kuwait

[2] Department of Chemistry, Faculty of Science, University of Cairo, Giza, Egypt

Keywords: Impedance spectroscopy, lead brass, selective corrosion

Abstract

The corrosion and passivation behaviour of lead brass (58% Cu, 1.8% Pb and Zn = rest) was investigated in acid and neutral chloride and sulphate solutions under open–circuit and polarization conditions using the EIS techniques. The corrosion of the alloy is caused solely by the dissolved oxygen depolarizer. CuCl and Cu_2SO_4 together with some surface oxides are assumed to be corrosion products leading to passivation o the electrode surface. Impedance spectra in the form of Nyquist plots consist of depressed semicircles with different degrees of depression. The depression was attributed to surface inhomogeneity and roughness. At high cathodic potentials ideal semicircles with high polarization resistance values were obtained. This was attributed to the adsorption of anions and intermediates from oxygen reduction at the electrode surface. Potentiostatic polarization in the potential range $-0.6\ V \leq V \leq -0.2V$, leads to selective dissolution of zinc and accumulation of CuCl or Cu_2SO_4 films. At potentials $\geq -0.1V$ pitting corrosion was observed.

The electrochemical behaviour of brass alloys is an important subject that requires more effort to clarify the anomalous corrosion behaviour of these alloys which are widely used in industrial applications. In the field of non–ferrous alloys, the problem of

1. Introduction

Electrochemical impedance spectroscopy (EIS) is a popular and powerful technique and has been applied to all types of passivation and corrosion phenomena. The theoretical background of the EIS and the applications of this technique to different electrochemical processes have attracted the attention of many investigators /1–7/.

dealloying is of current interest. Dezincification is one of the well known dealloying processes occurring in brass–alloys which leads to the loss of the valuable physical and mechanical properties and then to total failure of the alloy. Many attempts have been made to understand and to solve this problem including electrochemical, radiometric and optical techniques /8–12/.

The dissolution of brass occurs either preferentially (selective dissolution) or simultaneously, i.e. all constituents dissolve at the same time. It was found that the dissolution mode is dependent of the zinc content in the alloy and the electrode potential /10,13 & 14/. Preferential dissolution occurs readily in the Zn–rich brasses and at less noble potentials. In Zn–arm brasses simultaneous corrosion is predominant and occurs at more noble potentials. It was shown that the dissolution of an alloy by the simultaneous mode should be preceded by an induction period of preferential dissolution of the less noble metal /15/.

The galvanic corrosion of Cu, Zn and three brasses in neutral solutions was investigated /16/. The steady state potentials for Cu and brasses were practically the same. The highest corrosion rates of the Cu–Zn systems were measured in chloride solutions. Potential scanning and galvanic current measurements did not show any galvanic corrosion between pairs involving Cu and any of the three brasses or between pairs of the Cu–Zn alloys themselves.

In this work the corrosion behaviour of one of the widely used alloys in industrial applications, the lead brass, [58% Cu, 1.8% Pb, remainder Zn), was investigated using the EIS technique under open–circuit and potentiostatic conditions. The impedance characteristics of the alloy/electrolyte interface with reference to the stability of the material against corrosion are discussed.

2. Experimental

The impedance measurements were carried out using the IM5d system which is based on the universal data acquisition and analysis system AMOS–ANDI (Zahner Elektrik GmbH & Co. KRONACH, Germany). An excitation amplitude of 10 mV peak to peak was used. Excitation wave forms of these amplitude cause only minimal perturbation of the electrochemical system, reducing the error caused by the measuring system. In principle, the method involves direct measurement of the impedance of the electrochemical system under investigation in the frequency domain 100 kHz to 0.1 Hz. The cell impedance, Z, the phase shift, θ, are presented as Bode and Nyquist plots. The different corrosion parameters can then be determined using a simulation program.

The electrochemical cell, working electrode preparation and electrode surface treatment were as described previously /17/. The working electrode area facing the test solution was 0.25 cm^2. The electrode potentials were measured against and referred to a saturated calomel electrode (SCE). The counter electrode was a large surface area platinum foil. Test solutions were prepared from analytical grade reagents by appropriate dilutions with triply distilled water. All measurements were carried out in a double–walled electrically controlled air thermostat at $30 \pm 0.1^{\circ}C$.

3. Results and Discussion

3.1– Corrosion phenomena in acid solutions:

In this series of experiments, the corrosion of lead brass was investigated in various HCl solutions. Before each experiment, the electrode was mechanically polished with emery papers of different grades down to 4/0, wrapped against smooth cloth using alcohol as lubricant, washed with distilled water, dried and then transferred quickly to the cell. The open circuit potential was recorded each minute from electrode immersion until it reached a more or less stable value (it took often 15 min. to reach steady state). Measurements of the cell impedance was then carried out at different time intervals. Fig. 1a, presents typical Bode diagrams measured after 160 min. of the electrode immersion in HCl solutions. The corresponding Nyquist plots are presented in Fig. 1b. The data represent simple impedance behaviour including one capacity contribution with no sign of diffusion. The electrochemical system in this case can be represented by the Randle's equivalent circuit (see Fig. 1c) /18/.

The polarization resistance, R_p, is of practical importance in determination of the instantaneous corrosion rate. It is given by the slope of the current–voltage characteristics of the corroding system at any polarization interval. The corrosion rate is inversely proportional to the value of R_p. In EIS, R_p, can be obtained from the values of the real part of admittance at the lowest frequency or from the Nyquist plots as the difference between the limiting values of impedance obtained at zero and infinite frequency limits /19/. A second important parameters in the characterization of the electrode/electrolyte interface is the capacitance, C_d, which can be obtained from the value of the absolute impedance /Z/ at the maximum phase shift, θ_{max}, using equation (1):

$$C_d = \frac{1}{\omega Z_{(\theta_{max})}} \qquad (1)$$

$$\omega = 2\pi f \qquad (2)$$

where f is the frequency.

The values of C_d and R_p calculated at different time intervals of electrode immersion in various HCl solutions are presented in Table 1. The results show that in dilute solutions ($\leq$ 0.1 M), the polarization resistance increases rapidly in the first 30 min. of electrode immersion reaching a maximum, followed by rapid decreased to a more or less constant value after about 2 h. In concentrated HCl ($\geq$ 0.5 M) on the other hand, a continuous decrease of R_p to a nearly constant value was observed. The variation of capacitance, C_d, is consistent with the results of R_p.

3.2. Behaviour of the alloy in H_2SO_4 solutions:

The behaviour of the lead brass alloy in sulphuric acid solutions is different from that in HCl. The impedance characteristics are affected markedly by the electrolyte concentration. For higher concentrations of H_2SO_4 ($\geq$ 0.05 M), two phase maxima in the Bode plot are present (cf. Fig. 2a). The Nyquist plot (Fig. 2b) shows one depressed semicircle instead of two, ie. the two semicircles are indistinct. Such a behaviour may be represented by the equivalent circuit model proposed by Michalovski et al /20/ for the painted metal/solution interface (Fig. 2c). The two phase maxima of Fig. 2a, merge toward each other. This behaviour is attributed to the close values of the paint and charge transfer resistances, with the extent that separation of the two resistance from each other is difficult.

Values of R_p and C_d (measured at $\theta_{\max(l)}$) for H_2SO_4 solutions are summarized in table (2). The increased values of the double layer capacity indicate that the lead brass alloy corrodes continuously in H_2SO_4 . This phenomenon becomes remarkable in dilute solutions ($\leq$ 0.1 M). As the concentration of H_2SO_4 increases the tendency to corrosion decreases and the value of C_d does not change with immersion time. The behaviour can be explained by a slight passivation of the electrode surface in concentrated sulphate solutions.

3.3. Corrosion phenomena in neutral solutions:

In this series of experiments, the behaviour of the alloy in NaCl and Na_2SO_4 solutions was investigated. Typical data for the electrode behaviour in NaCl or Na_2SO_4 solutions are presented in Fig. 3. In both solutions, a second phase maximum in the Bode diagram at the low frequency range could be observed. The Nyquist plot (Fig. 3c) consists of two arcs representing incomplete semicircles. Such a behaviour is attributed to the contribution of the Warburg diffusional impedance, which leads to the deviation from ideal semicircular behaviour at the low frequency end of the impedance spectrum /21/. This means that a diffusion controlled process is present for which the Warburg impedance, W, is given by:

$$W = \sigma \omega^{-1/2} (1-j) \quad (3)$$

where σ is the Warburg coefficient, ω is the angular frequency ($\omega = 2\pi f$) and $j = \sqrt{-1}$. This implies that the real and imaginary parts of the Warburg impedance are equal, and a slope of ≈ 1 on the Nyquist plot should be obtained. The phase shift, θ, tends to have a constant value of 45°C.

Fig. 3d shows expansion of the Nyquist plot in the low frequency region, whereas a typical example of the Randles plot of the real, Z', and imaginary Z'', components of the electrode impedance as functions of $\omega^{-1/2}$ in Na_2SO_4 solution is presented in Fig. 3e. The Warburg coefficient was obtained from the linear plots of Fig. 3e and a value of $2.75 \times 10^4\ \Omega$ was calculated.

The high frequency region of the Bode plot was used to evaluate the capacitance as described in part 1. The polarization resistance was also calculated from the real part of admittance at the lowest frequency /18/. The component elements of the electrode impedance calculated at different intervals in both NaCl and Na_2SO_4 solutions of different concentrations are summarized in table 3. The results reveal a general trend in neutral solutions which shows a gradual increase of R_p accompanied by a gradual decrease of C_d. This behaviour indicates that the alloy surface is passivated in neutral salt solutions and a decrease in the rate of corrosion can be identified.

3.4. Impedance measurements under potentiostatic control:

In this series of experiments, the electrochemical behaviour of the brass electrode was investigated at different potentials. Upon immersion of the electrode in the test solution, a constant potential was applied and the current was observed for a period of 15 min. after which the impedance spectrum was recorded. The results of these polarization measurements are presented in Figs. 4 and 5. At the most cathodic potentials (≤ -0.6V), the electrode impedance (measured at 0.1 Hz) is high. The most predominant reaction at this potential is the oxygen reduction according to:

$$O_2 + 4H^+ + 4e^- \longrightarrow 2H_2O \quad (4)$$

The ideal impedance behaviour of the electrode indicates that the process is under charge transfer control. The measured impedance values are comparatively high indicating passivation of the electrode surface. Passivation of the electrode on cathodic polarization is probably due to the formation of an inhibiting thin film on the electrode surface. Such film consists of adsorbed intermediates formed during oxygen reduction

(e.g. HO_2) and adsorbed anions. Since SO_4^{--} are more strongly adsorbed than Cl^-, higher impedance values will be recorded in sulphate media (compare Figs. 4 and 5).

At more cathodic potentials (<< –0.6V) the ideal semicircular behaviour of the impedance is maintained indicating the charge transfer control. The lower impedance values at the more cathodic potentials are due to increased rates of oxygen reduction.

Polarization at less negative potentials (> –0.5 V), is accompanied by a marked decrease of the electrode impedance, which can be attributed to selective dissolution of the zinc. Such dezincification process exists for a short period of time, since further removal of Zn needs extra energy for the Zn atoms to diffuse through the solid phase and reach the surface. After the induction period which depends on the potential and solution composition, copper begins to dissolve simultaneously with Zn with a subsequent redeposition of Cu as CuCl or Cu_2SO_4 on the alloy surface. The formed film acts as a passivating film. At more positive potentials (> –0.25 V) breakdown of the passivating film occurs with the initiation and growth of localized dissolution centers giving rise to the characteristic patchy appearance. The presence of zinc metal particles retards the formation of Cu(I) salts by preventing the diffusion of anions (Cl^- or SO_4^{--}) to the alloy surface. The film breakdown occurs through the formation of Cu(II) ions according to:

$$CuCl \longrightarrow Cu^{2+} + Cl^- + e^- \quad (5)$$

$$Cu_2SO_4 \longrightarrow 2Cu^{2+} + SO_4^{--} + 2e^- \quad (6)$$

$$CuCl + Cl^- \longrightarrow CuCl_2 + e^- \quad (7)$$

The film breakdown leads to the decrease of the electrode impedance (cf. Fig. 4 & 5) and oxygen evolution occur. At potentials > –0.1V, surface instability occurs with a profuse pitting type of attack. The remarkable decrease of impedance and the appearance of transmission line type in the impedance spectrum indicate the presence of pitting corrosion. Initially individual pits could be observed by the naked eye. Thereafter, pitting is more frequent in the immediate vicinity of other pits. These tendencies encourage clusters of dense pitting.

In neutral salt solutions, the behaviour is similar. The results of these investigations are presented in Figs. 6 and 7. At high cathodic potentials, oxygen reduction occurs according to:

$$O_2 + 2H_2O + 4e^- \longrightarrow 4OH^- \quad (8)$$

and water is reduced according to:

$$2H_2O + 2e^- \longrightarrow H_2 + 2OH^- \quad (9)$$

The impedance values measured in neutral solutions are relatively higher than those measured in acid solutions of the same anions (compare Fig. 4 with Fig. 7). This is due to the adsorption of reduction products and formation of thin surface oxides which are favoured in neutral solutions. At positive potentials, selective dissolution of Zn followed by simultaneous dissolution of Cu & Zn with the deposition of Cu(I) film takes place. At more anodic potentials film break down occurs and oxygen evolution predominates.

4. Discussion:

The corrosion of the brass sample under conditions of natural aeration occurs solely by the dissolved oxygen depolarizer. In acid medium the dissolution takes place according to:

$$Zn(Cu{-}Zn) \longrightarrow Zn^{2+} + 2e^- \quad (10)$$

$$Cu(Cu{-}Zn) \longrightarrow Cu^{2+} + 2e^- \quad (11)$$

$$O_2 + 4H^+ + 4e^- \longrightarrow 2H_2O \quad (12)$$

The overall reaction will be:

$$\text{Brass} + O_2 + 4H^+ \longrightarrow Cu^{2+} + Zn^{2+} + 2H_2O \quad (13)$$

In neutral solutions the conjugate cathodic reaction is reaction (8). The formation of Cu^+ ions is possible since they are rapidly formed as intermediates in the dissolution process /22/.

The observed variation in the kinetics of dissolution and the extent of dezincification in both chloride and sulphate media could be essentially due to the interaction between copper and the respective anions. During the corrosion process CuCl or Cu_2SO_4 together with some other surface oxides will be formed. The rapid formation of the Cu(I) compounds leads to the accumulation and adsorption of this compound (either CuCl or Cu_2SO_4) onto the corroding surface retarding the overall corrosion rate. This is in consistence with the increase of the polarization resistance R_p with time and passivation of the electrode. The decrease of R_p in dilute solution is due to the unstability of CuCl or Cu_2SO_4 as meta–stable compound in aqueous solutions /23/. The film decomposes resulting in the redeposition of Cu /24/ according to either scheme I or II:

Scheme I

$$2CuCl \longrightarrow Cu + CuCl_2 \quad (14)$$

or

$$Cu_2SO_4 \longrightarrow Cu + CuSO_4 \quad (15)$$

Scheme II

$$8CuCl + O_2 \longrightarrow 2Cu_2O + 4CuCl_2 \quad (16)$$

or

$$4Cu_2SO_4 + O_2 \longrightarrow 2Cu_2O + 4CuSO_4 \quad (17)$$

$$CuCl_2 + Cu \longrightarrow 2CuCl \quad (18)$$

$$CuCl_2 + Zn \longrightarrow Cu + ZnCl_2 \quad (19)$$

or

$$CuSO_4 + Cu \longrightarrow Cu_2SO_4 \quad (20)$$

$$CuSO_4 + Zn \longrightarrow Cu + ZnSO_4 \quad (21)$$

Detailed analysis of the experimental data shows that appreciable deviation from the ideal semicircular behaviour exists corresponding to rotation of the center of the capacitive semicircle by an angle ϕ below the real axis. The depression angle increases with the time of electrode immersion and electrolyte concentration (cf. Figs. 1b and 2b). Such deviation was termed as frequency dispersion and attributed to the presence of simultaneous charge transfer and mass transport steps in the electrode process beside electrode inhomogeneity /25/. Metal dissolution occurs where the surface is covered by corrosion products, whereas oxygen reduction occurs in the pores of the surface film. Inhomogeneities arise from sorption phenomena that lead to two dimensional partial blocking of the surface for certain reaction or from the formation of three dimensional surface layer of different structure, morphology, composition, etc. Other reasons for frequency dispersion include arrangement and size of the counter electrode, low concentration of the electrolyte, insufficient insulation of the working electrode and imperfect contacts /26–28/. It was also claimed that the frequency dispersion is due to surface roughness /29,30/.

Under polarization conditions the behaviour of the brass electrode in acid or in neutral solution is about the same. Under conditions of high cathodic polarization ($<$ -0.6 V) oxygen reduction occurs. At less cathodic potentials (> -0.5 V) dezincification starts followed by simultaneous dissolution of Cu and Zn. The corrosion rate decreases due to the formation of Cu(I) surface film which passivates the electrode. At more positive potentials (> -0.2 V) film breakdown occurs with the formation of localized corrosion centers. At extremely anodic potentials (> -0.1V) pitting corrosion and oxygen evolution occur at the same time.

Conclusion

The lead brass alloy was found to corrode continuously in acid chloride solutions especially at higher chloride ion concentrations ($\geq$ 0.5 M). The behaviour of the alloy can be represented by a simple model for a corroding metal/electrolyte interface. In acid sulphate solutions the alloy behaves like a painted metal surface. In neutral solutions the alloy surface passivates and deviation from ideal semicircular behaviour occurs. under polarization conditions the corrosion behaviour of the alloy is controlled by the applied potential.

Acknowledgement:

The authors are very grateful to the Alexander von Humboldt foundation (Bonn–Germany) for providing the impedance system.

References:

1. F. Mansfeld ; Corrosion, 37, 301 (1981).
2. F. Mansfeld, M.W. Kendig and S. Tsai; Corrosion, 38, 556 (1982).
3. F. Mansfeld ; Corrosion Science, 44, 856 (1988).
4. C. Gabrielli ; "Identification of Electrochemical Processes by Frequency Response Analysis"., Solartron Instrumentation Group, 1980.
5. M.W. Kendig, F. Mansfeld and S. Tsai; Corrosion Science, 23, 317 (1983).
6. F. Mansfeld, S. Lin, S. Kim and H. Shih ; Corrosion Science, 72, 997 (1987).
7. D.C. Silverman ; Corrosion, 45, 824 (1989).
8. G. Joseph and M.T. Arce–Corros. Sci. 7, 597 (1967).
9. E.E. Langeneggar and P.A. Robinson. Corrosion, 24, 411 (1968).
10. H. Sugawara and H. Ebike. Corros. Sci., 7, 513 (1967).
11. A.B. Si Tnikov, A.P. Pchepnekov, I.K. Marshakov and V.V. Losev, Z. Metallov., 14, 258 (19780).
12. J.E. Einnegar, R.E. Hummel and E.D. Verink. Corrosion 37, 256 (1981).
13. H.W. Pickering and P.J. Byrne, J. Electrochem. Soc. 116, 1492 (1969).
14. K. Balakrishnan and V.K. Venkatesan, Werkstoffe U. Kerros. 29, 113 (1978).
15. J.E. Holliday and H.W. Pickering., J. Electrochem. Soc. 120, 470 (1973).
16. A.M. Shams El–Din, J.M. Abd El–Kader and M.M. Badran, Br. Cros. J. 16, 132 (1981).
17. M.M. Hefny, W.A. Badawy, and S.S. Elegamy ; Electrochim. Acta; 35, 799 (1990).

18. J.E.B. Randles; Disc. Faraday Soc., 1, 11 (1947).
19. "Basics of Electrochemical Impedance Spectroscopy"., EG & G Princeton Applied Research, Application note AC–1, and references therein.
20. M.N. Mikhailovskii, V.V. Leonov, and N.D. Tomashov; Korr. Met., British Lending Library, Translation 202 (1965).
21. E. Warburg; Ann. Phys., 67, 493 (1899) and 6, 125 (1901).
22. R.K. Dinnappa and S.M. Mayanna., J. Appl. Electrochem. 11, 111 (1981).
23. J.W. Meller. Comprehensive Treatise on Inorganic and Theoretical Chemistry., Vol. 3, p. 160, Longmans, London (1952).
24. R.B. Abrams. Trans. Am. Electrochem. Soc. 42, 39, (1922).
25. K. Juttner. Electrochim. Acta, 35, 1501 (1990).
26. J.O'M. Bockris, E. Gileadi and K. Muller, J. Chem. Phys. 44, 1445 (1966).
27. C.K. Dyer and J.S.L. Leach, Electrochim. Acta 19, 695 (1974).
28. E.C. Dutoit, R.L. van Meirhaeghe and F. Cardon, Ber. Bunsenges. Phys. Chem. 79, 1206 (1975).
29. R.De Levie, Advances in Electrochemistry and Electrochemical Engineering, Vol. 6, pp. 329–397., Wiley Interscience, New York (1967).
30. M.J. Pryor and K.K. Giam, J. Electrochem. Soc. 129, 2157 (1982).

Table 1: Polarization resistance R_p, and capacitance C_d at different time intervals of electrode immersion in HCl solutions of various concentrations.

Time/Con.	1.0 M		0.5 M		0.1 M		0.05 M	
	R_p kΩ	C_d μFcm^{-2}	R_p kΩ	C_d μFcm^{-2}	R_p kΩ	C_d μFcm^{-2}	R_p kΩ	C_d μFcm^{-2}
15 min.	10.31	13.33	12.67	14.65	8.62	17.82	5.92	24.40
30 min.	10.68	13.30	12.12	14.30	14.56	16.10	13.60	18.10
60 min.	9.90	13.57	11.09	14.99	12.08	15.66	12.58	17.30
120 min	8.47	15.76	8.06	15.88	12.72	16.25	8.55	20.10
160 min	8.20	18.44	8.70	18.69	12.02	18.60	8.33	21.72

Table 2: Polarization resistance R_p, and capacitance C_d at different time intervals of electrode immersion in H_2SO_4 solutions of various concentrations.

Time/Con.	1.0 M		0.5 M		0.1 M		0.05 M	
	R_p kΩ	C_d μFcm^{-2}	R_p kΩ	C_d μFcm^{-2}	R_p kΩ	C_d μFcm^{-2}	R_p kΩ	C_d μFcm^{-2}
15 min.	8.62	19.90	8.55	14.18	10.75	9.22	2.00	6.59
30 min.	8.70	19.17	8.93	13.92	11.92	9.95	4.77	7.11
60 min.	10.28	18.27	11.24	14.82	11.56	10.15	8.55	9.39
120 min	11.33	18.35	12.24	14.68	9.90	9.92	8.55	12.70
160 min	12.32	18.44	12.26	16.10	8.62	9.86	8.33	14.30

Table 3: Polarization resistance R_p, and capacitance C_d at different time intervals of electrode immersion in neutral solutions of various concentrations.

Time/Con.	1.0 M R_p kΩ	1.0 M C_d μFcm^{-2}	0.5 M R_p kΩ	0.5 M C_d μFcm^{-2}	0.1 M R_p kΩ	0.1 M C_d μFcm^{-2}	0.05 M R_p kΩ	0.05 M C_d μFcm^{-2}
a) NaCl solutions:								
15 min.	4.36	3.97	14.23	1.30	31.88	0.98	32.15	0.94
30 min.	5.98	3.97	15.22	1.30	32.72	0.93	35.86	0.82
60 min.	6.84	5.06	13.40	1.42	38.84	0.98	38.20	0.63
120 min	9.85	6.78	16.24	1.13	49.93	0.76	46.18	0.44
160 min	11.82	10.34	18.83	1.66	49.68	0.74	50.39	0.35
b) Na_2SO_4 solutions:								
15 min.	49.25	1.46	58.81	1.15	67.07	1.93	68.88	1.78
30 min.	51.80	1.23	58.15	1.17	72.42	1.83	81.22	1.71
60 min.	56.82	1.45	66.65	1.24	79.96	1.79	95.16	1.56
120 min	60.12	1.50	72.47	1.07	90.86	1.52	109.57	1.43
160 min	64.51	1.50	73.51	1.03	95.19	1.48	107.56	1.45

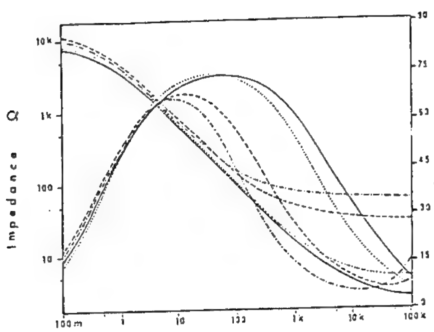

Fig. 1 a

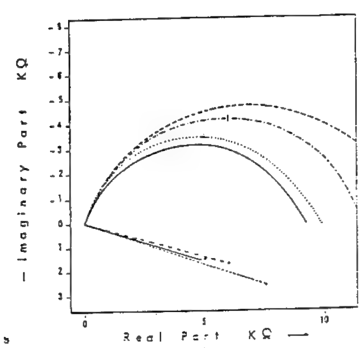

Fig. 1 b

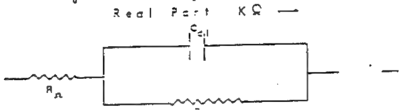

Fig. 1 c

Fig.1: a) Bode–diagram of the lead brass electrode after 180 min. immersion in HCl solutions of various concentrations. (–·–·–) 0.05 M, (– – –) 0.1 M, (....) 0.5 M and (___) 1.0 M HCl solution.

b) Nyquist–diagram of the same electrode in the same solutions.

c) Randles equivalent electronic circuit applied to corroding metal/solution interface.

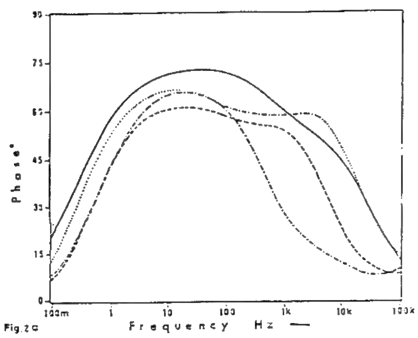

Fig. 2 a

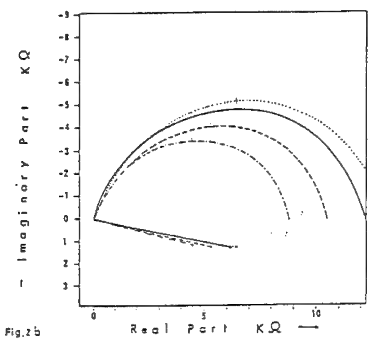

Fig. 2 b

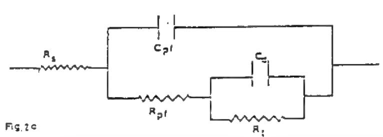

Fig. 2 c

Fig.2: a) Bode–diagram (phase angle, θ^0, vs. frequency Hz) of the lead brass electrode after 100 min. immersion in H_2SO_4 solutions of different concentrations (–·–·–) 0.05 M, (– – –) 0.1 M, (.....) 0.5 M and (___) 1.0 M H_2SO_4 solution.

b) Nyquist–diagram of the same electrode in the same solutions.

c) Painted metal/electrolyte interface equivalent circuit model in absence of diffusion.

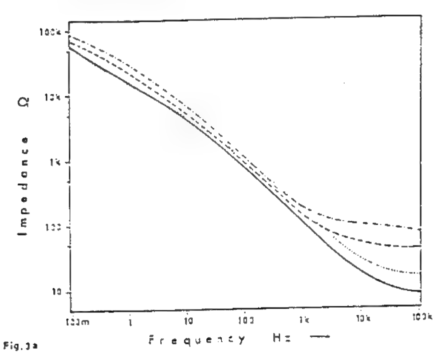

Fig. 3 a

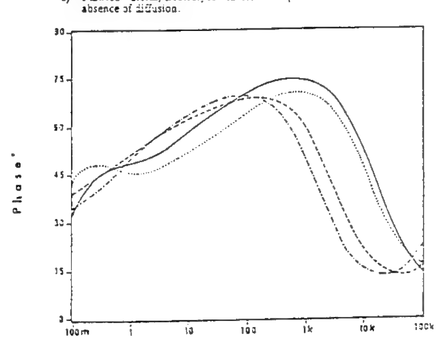

Fig. 3 b

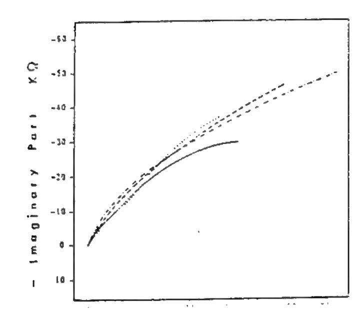

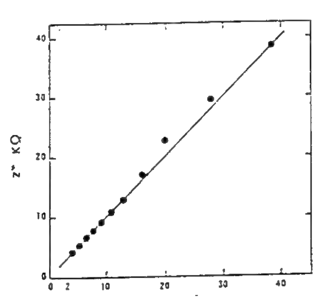

Fig.3: a) Bode–diagram (impedance, Ω, vs. frequency Hz) of the lead brass electrode after 120 min. immersion in Na_2SO_4 solutions of different concentrations (–.–.–) 0.05 M, (– – –) 0.1 M, (.....) 0.5 M and (___) 1.0 M Na_2SO_4 solution.

b) Bode–diagram (phase angle, $\theta°$, vs. frequency Hz) of the same electrode in the same solutions as (a).

c) Nyquist–diagram of the same electrode in the same solutions.

d) Expansion of the Nyquist plot (ie. Z" vs. Z') in the low frequency range.

e) Typical example of the Randels plot of the real, Z', and imaginary, Z", components of the lead brass electrode impedance as a function of $\omega^{-1/2}$ in Na_2SO_4 solution.

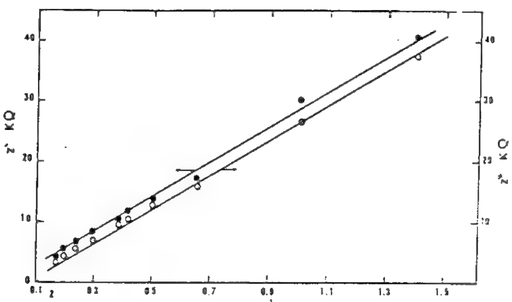

Fig 3 e

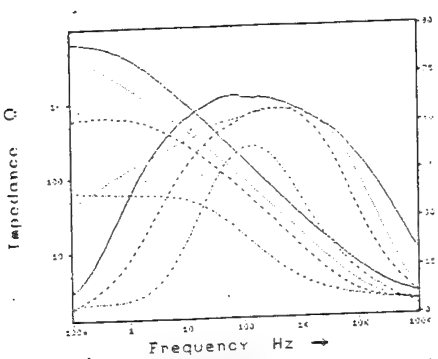

Fig.4: Bode–diagram of the lead brass electrode in 1 M HCl solution. (—) –0.5 V, (....) –0.5 V, (- - -) –0.3 V, and (–.–) –0.25 V.

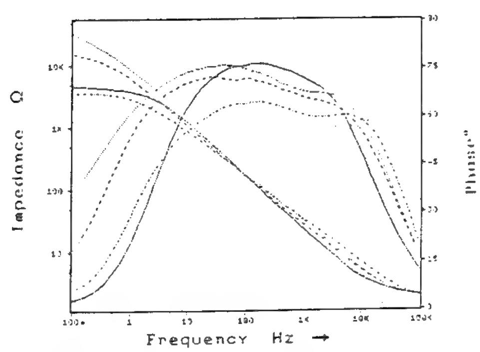

Fig.5: Bode–diagram of the lead brass electrode in 1 M H_2SO_4 solution. (—) –0.6 V, (....) –0.5 V, (- - -) –0.3 V, and (–.–) –0.25 V.

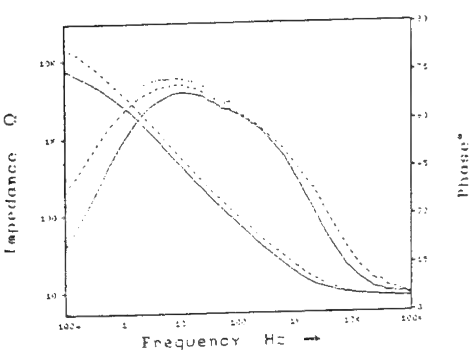

Fig. 6a Bode–diagram of the lead brass electrode in 1 M NaCl solution in the cathodic region. (___) –1.3 V, (- - -) –1.2 V, (...) –1.1 V

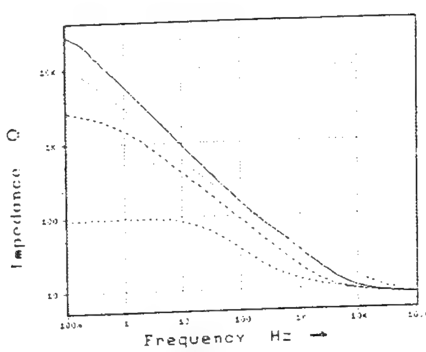

Fig.7a Bode (impedance) diagram for brass electrode in 1 M NaCl solution in the dezincification region. (___) –0.7 V, (....) –0.6 V, (- - -) –0.3 V, and (–.–) –0.25 V.

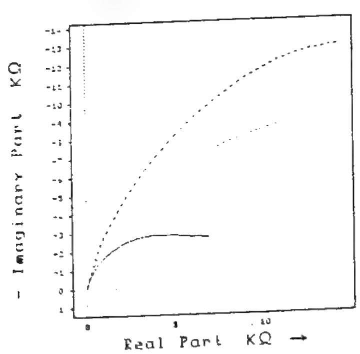

Fig. 6b complex plane impedance diagram for brass electrode in 1 M NaCl solution in the cathodic region. (___) –1.3 V, (- - -) –1.2 V, ( ) –1.1 V.

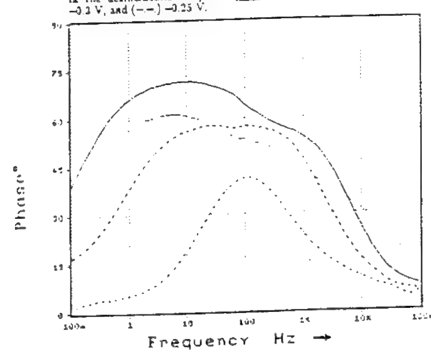

Fig.7b Bode (phase) diagram for brass electrode in 1 M NaCl solution in the dezincification region. (___) –0.7 V, (...) –0.5 V, (– – –) –0.3 V, and (–.–) –0.25 V.

Passivity in Nonaqueous Media

Materials Science Forum Vols. 185-188 (1995) pp. 845-852

Passivity of metals in anhydrous solutions of oxy-acids

J. Banas

University of Mining and Metallurgy, Faculty of Foundry Engineering,
ul. Reymonta 23, PL-30-059 Kraków, Poland

Keywords: Passivation, passivity, anodic films, anhydrous oxy-acids

Abstract

Oxide passivation of iron, nickel and chromium has been investigated in mixed aqueous-organic solutions of sulphuric, phosphoric,formic and acetic acids. The influence of electrolyte „structure" (acidity, activity of water, activity of undissociated acid molecules, and oxyanions) on anodic behaviour of these metals and on composition of anodic films is presented. The special attention is given to mechanism of passivation in anhydrous media.

Introduction

The passivation of metals leading to the formation of oxide film is a complicated anodic process between metal surface and surrounding medium. The process is strongly influenced by the electrolyte „structure", especially on the concentration of oxygen containing species. In aqueous electrolytes the oxide layer is formed in the reaction of metal atoms and water molecules:

$$Me + n/2H_2O = MeO_{n/2} + nH^+ + ne \qquad (1)$$

In this reaction the water molecules are a source of oxygen ions for the oxide formation. The participation of water in passivation process has been confirmed in experiments in mixed aqueous-organic solvents [1-10]. The dependence of passivation potential of some metals [1-6] on water activity in mixed aqueous-organic or concentrated electrolytes fulfills the Nernst equation for the reaction (1). The passivation of metals proceeds according to the reaction (1) in electrolytes with the ratio of H^+/H_2O lower than 1/4 [11-13]. At the higher ratio the water molecules are bound in hydration shell of hydrogen ions and do not take part in anodic reaction as a source of oxygen ions [14-16].

In anhydrous electrolytes the oxide passivation of metals is possible only at the presence of oxy-acids or oxyanions. The aim of the present lecture is to explain the mechanism of passivation in these environments.

Passivity of Iron, Nickel and Chromium in Anhydrous Sulphuric Acid Solutions

The influence of composition of H_2O-H_2SO_4 system on the anodic behaviour of iron, nickel, and chromium is presented in Fig.1 [12,13]. The H^+/H_2O ratio of 1/4 (8M/l H_2SO_4) corresponds to the borderline between concentrated and diluted solutions of acid. At higher ratio the water activity in the solution is very low. In the range of concentrations 6-14 M/l all of water molecules are linked in the hydration shell of hydrogen ions and sulphuric acid is nearly completely dissociated[14]. Passivity in such medium is very difficult. A thick unprotective salt or oxide-salt layer is formed on the metal surface and anodic dissolution is often controlled by the diffusion [17-20].

Concentrated solutions of sulphuric acid (> 14 M/l) contain undissociated acid molecules. These environments show oxidative properties, what can be seen in Fig.2, presenting the potential of platinized platinum electrode in the deaerated sulphuric acid solutions. The linear dependence of E_{Pt} on pH with the slope of -0.059 V in the range of concentration below 8 M/l indicates that the reduction of hydrogen is responsible for the potential of the platinum electrode. The sharp increase of potential for a higher concentration with the slope dE/dH^0 = - 0.117 V corresponds to the redox equilibria of undissociated acid

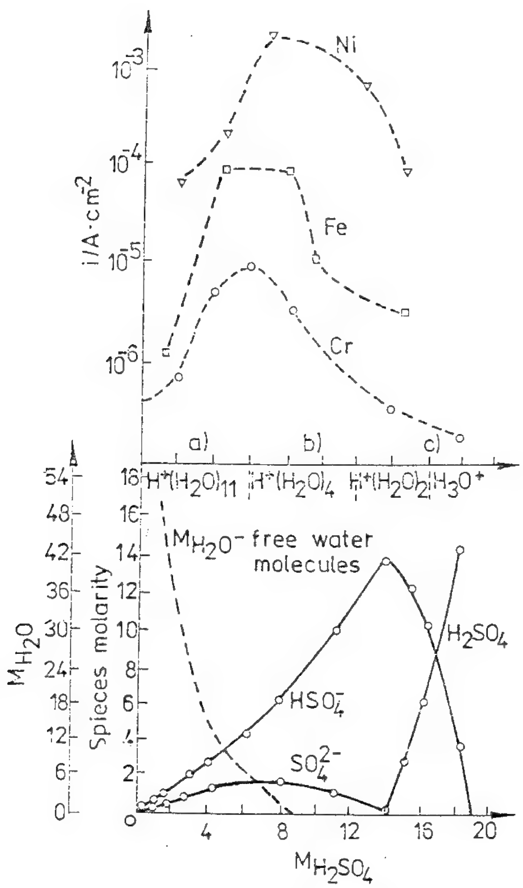

Fig. 1. Influence of the electrolyte structure on the anodic behaviour of iron, nickel , and chromium in the H_2SO_4-H_2O system [13]. The diagram at the top shows stationary values of current in the passive range (E_{SCE}=0.8V, t=30min).

molecules and HSO_4^- ions [21,22]. In these solutions the all investigated metals undergo oxide passivation (Fig.3-5). The XPS analysis of passive film performed on iron [23], nickel [24], and chromium [22,25] shows that oxide layer contains sulphur species of lower valences - S^0, S^{-2} in the inner part of the layer. The S^{-2} content in the passive film increases in-depth of the layer from oxide/electrolyte to metal/oxide interface (Fig.6). The presence of sulphur species in oxide films on iron and nickel anodic polarized in concentrated sulphuric acid solutions has been confirmed by other workers [18]. Our investigations demonstrate that sulphur dioxide can be determined in anolyte [22,23]. It is an evidence that sulphuric acid undergoes electrocatalytic reduction during anodic passivation of metals.

The passivation of metals in concentrated solutions of sulphuric acid proceeds with participation of undissociated acid molecules. The H_2SO_4 particles are a „source" of oxygen for oxide formation. For chromium we propose the following mechanism of passivation [22,25]:

$$Cr + H_2SO_4 = CrHSO_{4\,ad} + H^+ + e \qquad (2a)$$
$$CrHSO_{4\,ad} = CrOOH + SO_2 \qquad (2b)$$

The linear dependence of the passivation potential of chromium on H_2SO_4 content in concentrated solutions confirms the proposed mechanism (Fig.7).

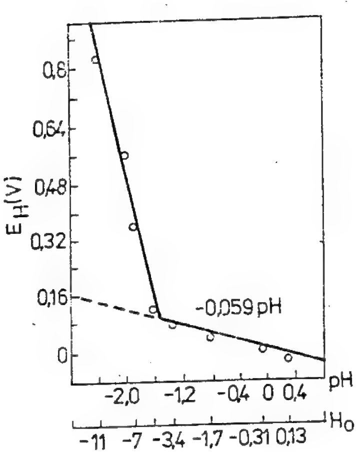

Fig. 2. Dependence of the plantium potential on pH in sulphuric acid solutions.

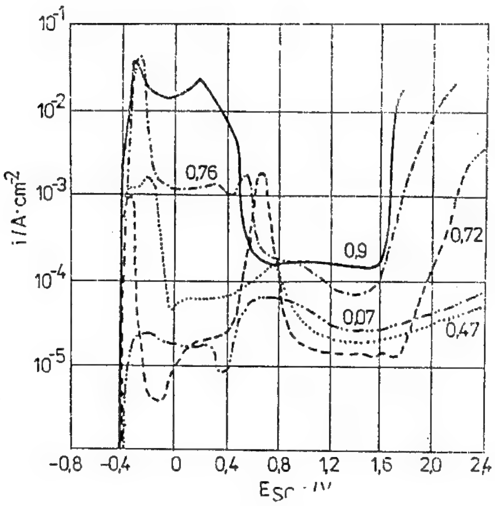

Fig. 3. Anodic polarization curves of iron in concentrated sulphuric acid solutions (the effect of molar fraction of water).

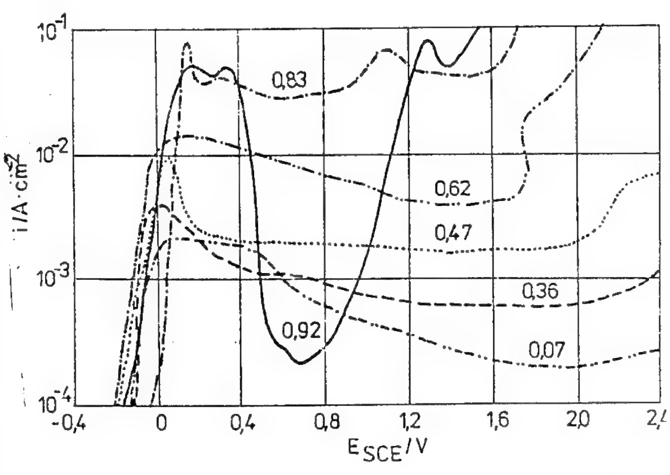

Fig. 4. Anodic polarization curves of nicel in concentrated sulphuric acid solutions (the effest of molar fraction of water).

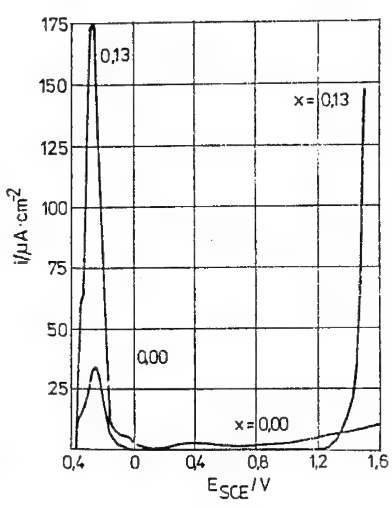

Fif. 5. Anodic polarization curves of chromium in concentrated sulphuric acid solutions (the effect of molar fraction of water)

Iron behaves in a similar way within the range of anodic potentials corresponding to the stability of Fe^{+3} ions (E > 0.6 V). At lower potentials iron is oxidized to Fe^{+2} ions and ferrous sulphate is precipitated on the metal surface [17-19].

In concentrated solutions of sulphuric acid the passive layer on nickel surface consists of oxide-hydroxide film with a significant amount of nickel sulphate [26]. The susceptibility of nickel to „salt passivation" is connected with the oxidation of this metal to Ni^{+2} ions. The affinity of Ni^{+2} and Fe^{+2} to oxygen is lower than the affinity of Fe^{+3} and Cr^{+3} ions (Table 1), and therefore the tendency to the formation of oxides can be presented by the following series: $Cr^{+3} > Fe^{+3} > Ni^{+2} > Fe^{+2}$. The investigated metals undergo oxide-passivation in the range of potentials corresponding to the stability of +3 ions, while sulphate-passivation prevails in the range of stability of +2 ions.

The passivating ability of sulphuric acid was observed also in anhydrous organic solvents. Fig.8 presents the anodic passivation of chromium in N-dimethylformamide - HCl solutions in the presence of water or anhydrous sulphuric acid [25]. The anhydrous acid passivates chromium and shows an analogous action as water. A similar behaviour of sulphuric acid can be observed in methanol solutions for nickel, iron and chromium [27,28]. The passivation ability of sulphuric acid depends on the dielectric permittivity of the solvent. In solvent with the low permittivity the acid dissociation is negligible. In these media iron, nickel and chromium can be passivated. Fig.9 presents the influence of solvent permittivity on anodic polarization of iron and nickel in formamide (ε = 109.5) and
N-dimethylformamide (ε = 36.71) solutions of sulphuric acid. In the solvent with the high permittivity, in which acid is nearly completely dissociated (formamide) iron and nickel form only sulphate layers. The oxide passivation occurs in the solvent with low permittivity (N-dimethylformamide) .

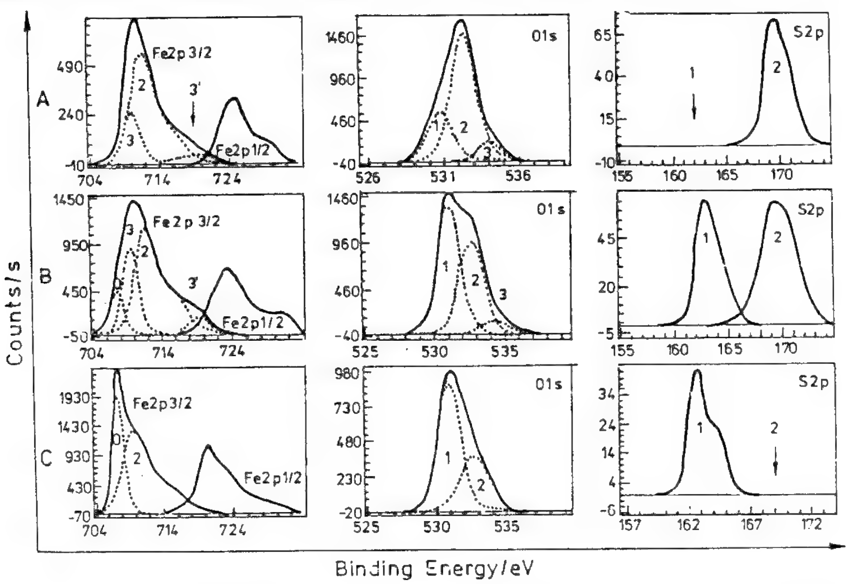

0-corresponds to Fe^0, 2-Fe^{+2}, 3-Fe^{+3} | 1-corresponds to O^{-2}, 2-OH^-, 3-H_2O | 1-corresponds to S^{-2}, 2-S^{+6}

Fig. 6. XPS analysis of anodic oxide film on iron polarized in 18 M H_2SO_4 at a potential 1.2 V_{SCE} A, B, C subsequant layers removed by sputtering with Ar-ions of 11.5 keV energy [23].

Table 1. The standard free enthalpy of oxide formation for the reactions:
1) $n\,Me + m/2\,O_2 = Me_nO_m$
2) $n\,Me + m\,H_2 = Me_nO_m + m\,H_2$

Oxide	ΔG^0_{298} (1), kJ/mol	ΔG^0_{298} (1), kJ/mol
FeO	-243.7	-6.7
Fe_2O_3	-741.1	-30.1
NiO	-214.8	+22.1
Cr_2O_3	-1047.5	-336.5

Fig. 10 and 11 present the influence of oxidative ability of alcohol-H_2SO_4 solutions on anodic behaviour of iron. As in Fig.2 the break point on the relationship the potential-acid concentration in Fig.10 corresponds to

the change from the „reductive" to the „oxidative" properties of the solutions. The increase of the permittivity of the solvent shifts the oxidative ability of the solution to the higher acid concentrations. Therefore the passivation of iron in 1M H_2SO_4 solutions is possible only in propanol, whereas in methanol iron does not form the passive film (Fig.11). In ethanol solutions an instable passive layer covers the iron surface. The passivation of iron and nickel in anhydrous methanol is possible only at high acid concentrations.

The XPS studies of anodic passive films on iron and chromium carried out in anhydrous organic solutions of sulphuric acid show that the composition of oxide layer is analogous to the composition of oxide film in concentrated sulphuric acid [25,29]. The presence of S^0 and S^{-2} in the oxide film shows that the acid molecules undergo reduction in the passivation process.

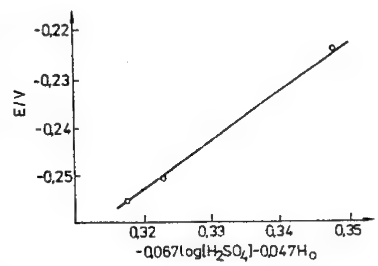

Fig. 7. Dependence of passivation potential of chromium on acidity (Ho) and log[H_2SO_4] in H_2O-H_2SO_4 system (the range c on Fig. 2, c>14 M H_2SO_4) [25].

Passivity of Iron and Nickel in Anhydrous Phosphoric Acid

The anodic behaviour of iron and nickel in concentrated phosphoric acid solutions is very similar to that in the concentrated sulphuric acid. Fig. 12 and 13 present the influence of water content on anodic polarization of both metals in phosphoric acid solutions. Two areas can be distinguished on the diagrams: the phosphating range and the range of oxide passivation. The increase of the ratio of acid to water diminishes the metal dissolution in the phosphating range. In completely anhydrous acid the continuous transition from phosphating range to passive range occurs (Fig.14). It seems that in the last environment the adsorption - solid state process dominates in anodic passivation, opposite to the aqueous solutions when precipitation of phosphate layer is observed.

The explanation of the mechanism of passivation of iron and nickel in anhydrous phosphoric acid is difficult. This medium shows very strong tendency to condensation according to the reaction [30,31]:

$$2H_3PO_4 = H_4P_2O_7 + H_2O \qquad K = 4{*}10^{-3} \qquad (3)$$

Experimentally it is found that 12.7% of the total P_2O_5 in 100% liquid H_3PO_4 is present in the form of pyrophosphoric acid [30]. It means, some amounts of „free water" are present in anhydrous phosphoric acid.

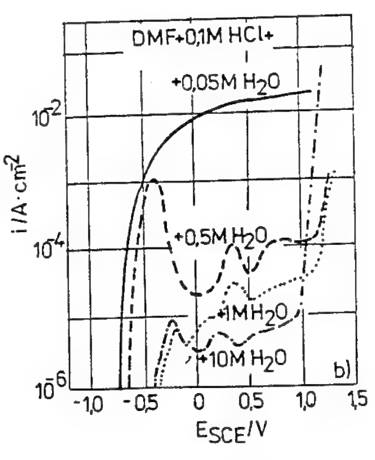

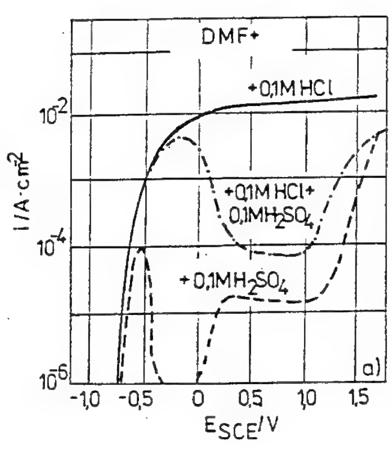

Fig. 8. Influence of water (a) and sulphuric acid (b) concentration on anodic polarization of chromium in HCl-N-dimethylformamide [25].

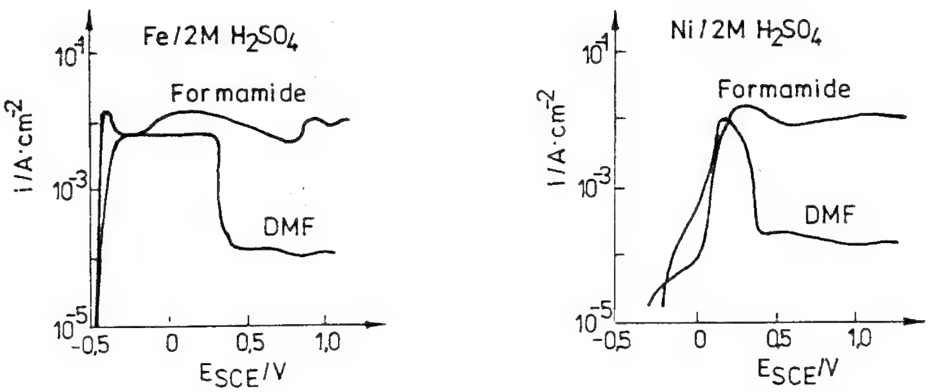

Fig. 9. Influence of organic solvent on the passivation of iron and nikiel in 2 M H_2SO_4

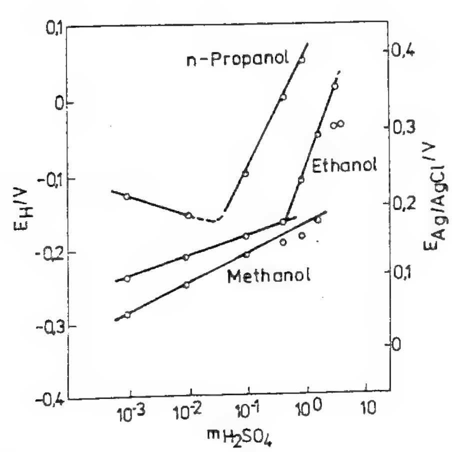

Fig.10. Potential of platinized plantium electrode in alcohol - H_2SO_4 0.001 M LiCL solutions.

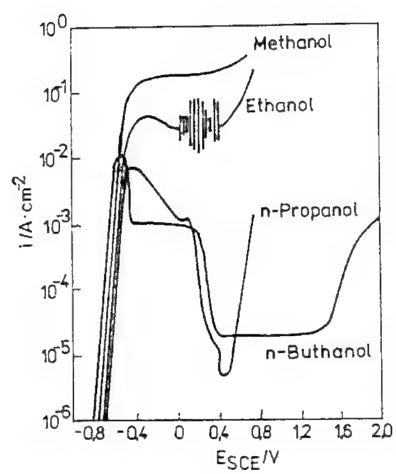

Fig. 11. Anodic polarization curves of iron in alcohol - 1M H_2SO_4 solutions.

Passivity of Iron and Nickel in Organic Carboxylic Acids

Our investigations of anodic behaviour of iron and nickel in concentrated formic and acetic acids show that the passivation of these metals is possible only in formic acid [32,33]. The formic acid molecule undergoes electrocatalytic decomposition during anodic passivation according to the equations:

$$Fe + 2HCOOH = FeOOH + 2CO + 3H^+ + 2e \qquad (4)$$
$$Ni + HCOOH = NiO + CO + 2H^+ + 2e \qquad (5)$$

The chemical analysis of anolyte by gas chromatography confirms the evolution of carbon monoxide on the anode during anodic etching both metals in the passive range [33].

The passivation of iron and nickel is possible only in concentrated solutions, when undissociated acid molecules are present in the environment. The increase of water content in the solution leading to the dissociation of acid diminishes the passivation ability of the medium .

In acetic acid solutions the oxide passivation of iron and nickel is not observed. The participation of acetic acid molecule in anodic passivation process is impossible.

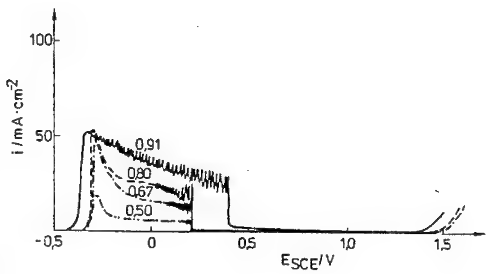

Fig. 12. Potentiodynamic polarization curves of iron in concentrated phosporic acid. Scan rate 0.1 V/min. The effect of molar fraction of water

Conclusions

The oxide passivation of metals is possible in anhydrous oxy-acids, but the mechanism of passivation is different than that in aqueous solutions. The undissociated acid molecules are a source of oxygen in anodic passivation process.

Anodic passivation of iron, nickel and chromium proceeds in anhydrous sulphuric and formic acids with electrocatalytic decomposition of acid particles. These metals show similar behaviour in anhydrous phosphoric acid.

Anhydrous acetic acid does not present oxidative properties. It undergoes Kolbe-type decomposition during anodic process and therefore the acetic acid particles can not be a source of oxygen during passivation.

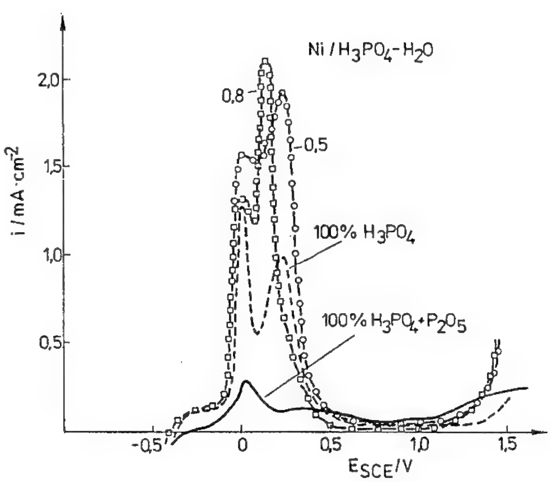

Fig. 13. Potentiodynamic polarization curves of nickiel concetrated phosporic acid. The effect of molar fraction of water. Scan rate 0.1 V/min

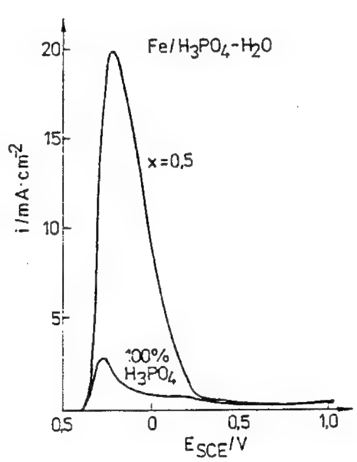

Fig. 14. The influence of molar fraction of water on the active - passive transition of iron in concentrated phosporic acid.

References

[1] Y. M. Kolotyrkin, G. G. Kosyj, Zashch. Metall. **1**, 252 (1965)

[2] K. Schwabe, S. Hermann, W. Oelssner, Passivity of Metals, Proceed. of the Fourth Intern. Symp. on Passivity, ed. R. F. Frankenthal and J. Kruger, N. Jersey 1977

[3] U. Ebersbach, J. Banaś, Electrochimica Acta, **27**, 177 (1982)

[4] K. Schwabe, Z. Phys. Chem. N. F. **108**, 61 (1977)

[5] K. Schwabe, W. Schmidt, Corr. Sci. **10**, 143 (1970)

[6] J. Banaś, Electrochimica Acta, **27**, 71 (1982)

[7] B. Elsener, H. Boehni, Proc. of the Fifth Int. Symp. on Passivity, Bombannes, France, ed. M. Froment, Elsevier 1983
[8] F. Mansfeld, J. Electrochem. Soc., **120**, 188 (1973)
[9] F. Belluci, G. Faita, C. A. Farina, F. Olivani, J. Appl. Electrochem.**11**, 781 (1981)
[10] F. Mazza, S. Torchio, N. Chialandi, Proc. 9th Int. Congr. Metallic Corrosion, Toronto 1984, p.102
[11] J. Banaś, Metallurgy and Foundry Engineering, **16**, 73 (1990)
[12] J. Banaś, Electrochimica Acta, **32**, 871 (1987)
[13] J. Banaś, B. Mazurkiewicz, B. Stypuła, Electrochimica Acta, **37**, 1069 (1992)
[14] J. W. Hamer, The Structure of Electrolytic Solutions, J. Wiley, N. York 1959
[15] E. Hoegfeld, Acta Chem. Scand., **14**, 1627 (1960)
[16] E. Hoegfeld, Acta Cientif. Venezolana, **17**, 13 (1966)
[17] G. Gilli, P. Borea, F. Zucchi, G. Trabanelli, Corr. Sci., **9**, 673 (1969)
[18] G. Blondeau, M. Frochlicher, M. Froment, A. Hugot-Le Golf and C. Vignaud, Proc. 4th Inern. Symp. on Passivity, ed. R. F. Frankenthal and J. Kruger, N. Jersey 1977
[19] G. Gilli, F. Zucchi, Corr. Sci., **8**, 801 (1968)
[20] R. Calson, M. Froment, C. R. Acad. Sci. Paris, **268**, C-1197 (1969)
[21] M. Pourbaix, Atlas of Electrochemical Equilibria, Pergamon Press 1966
[22] B. Stypuła, Metallurgy and Foundry Engineering,**18**, 301 (1992)
[23] B. Mazurkiewicz, Electrochimica Acta,**38**, 495 (1993)
[24] B. Mazurkiewicz, Werkst. und Korrosion, **43**, 565 (1992)
[25] B. Stypuła, J. Banaś, Modifications of Passive Films, ed. P. Marcus, B. Barroux, M. Keddam, The Inst. of Materials 1994, p.123
[26] J. Banaś, Passivity of Nickel in Aqueous and Organic Solutions of Sulphuric Acid, Report for Polish Academy of Science, Kraków 1985
[27] J. Banaś, B. Stypuła, B. Mazurkiewicz, Metallurgy and Foundry Engineering, **18**, 291 (1992)
[28] B. Mazurkiewicz, K. Banaś, J. Banaś, Materiały IV Krajowej Konferencji „Korozja 93" IChF PAN, Warszawa 1993, p.79
[29] B. Stypuła, J. Banaś, Electrochimica Acta **38**, 2309 (1993)
[30] J. R. van Wazer, Phosphorus and Its Compounds, Vol.1, Interscience Publ. Inc., N. York 1958
[31] F. G. R. Gimblett, Inorganic Polymer Chemistry, Butterworth, London 1963
[32] K. Banaś, B. Mazurkiewicz, J. Banaś, Materiały IV Krajowej Konferencji „Korozja 93" IChF PAN, Warszawa 1993, p.136
[33] J. Banaś, B. Mazurkiewicz, W. Solarski, K. Banaś, Passivity of Iron and Nickel in Concentrated Solutions of Sulphuric Acid, Seventh Int. Symp. on Passivity, Clausthal 1994

Materials Science Forum Vols. 185-188 (1995) pp. 853-860

Specific features of the metal passivation in organic and water-organic media

V.A. Safonov, E.V. Lapshina, T.H. Minh and S.Yu. Volosova

Department of Electrochemistry, Moscow State University, Moscow, 119899 Russia

Keywords: Water, organic solvents, iron, aluminum, thin-film electrodes, impedance, resistometry, ellipsometry, passivation, electric double layer, chemisorption

Abstract The effect is discussed of different factors on the peculiarities of metal passivation in a solution based on organic and water-organic solvents. Measurements of the double layer capacitance on Fe and Al electrodes in aprotic media testify that a chemisorption interaction exists between the metal surface and solvent molecules. It is shown that an oxide film of the same composition is formed independently of whether Fe is passivated in water or water-organic solutions. The thickness of the oxide film decreases with the growth of the organic component share in the solution; the kinetics of the oxide film formation changes as well. The influence of the electrolyte nature on the passivation of iron in water-organic media is considered.

Introduction

By now the main experimental and theoretical data on the corrosion behavior of metals and passivation processes are obtained for aqueous solutions. From the end of 60-s, apparently beginning with the paper of Kolotyrkin and Kossyi [1] devoted to studing the anodic behavior of Cr in water-methanol solutions of HCl, one can trace growing interest in investigations of passivation processes in the solutions based on organic and mixed water-organic solvents. It was suggested that by switching to new systems and varying the water molecule concentration one can get a substantial advance in understanding the passivation mechanism. It should be noted that up to 80-s these investigations were mostly qualitative. They were directed to determining the minimal water content necessary to observe an active — passive transition and also the effect of water concentration in mixed solvents on the passivation potential and currents in the passive region. For a number of metals these data were summarized by Schwabe *et al.* in the well-known review [2].

Considarable progress in these investigations has been achieved in 80-s and recent years. Firstly, it is due to the fact that during the last years a great number of new organic solvents promising for practice were introduced in the field of fundamental electrochemistry. These investigations have clearly shown that the character of the metal interaction with organic solvent molecules is of a great importance and in many cases determines the mechanism of electrochemical processes taking place in such systems [3 - 7]. It should be noted that data on the double layer structure of metal/organic solvent interface are necessary for a deep understanding of the mechanism of the passive state formation on metals in organic and water-organic media.

It should be also noted that by invoking new approaches and experimental methods, particularly *in situ* methods, one can achieve substantial progress in this field. The use of *in situ* methods makes it possible to obtain new qualitative results, to advance on the basis of a number of investigations from

the qualitative level to the quantitative one, and, thus, get valuble information about the composition, structure, and thickness of the surface films, the kinetic regularities of their formation and destruction on passive metals (see, e.g., [8 - 11]), etc.

One can notice that new data on the specific features of the interface between passive metals and solutions based on water-organic solvents were also obtained by means of non-traditional methods. Some of these results are yet to be unambiguously explained.

Consideration of the above-mentioned issues is the subject of this paper.

Specific features of the double layer structure on the corrosion-active metals in contact with the organic solutions.

To obtain reliable data on the interface structure of metal/organic solvent solution systems it is usually necessary to solve some serious experimental problems, i.e., the creation of a clear and well reproducible metal surface, special purification and preparation of solvents and electrolytes, etc. The experimental method is also very important. Now, we have come to the conclusion that compared to other methods the method of electrochemical measurements (impedance, potentiostatic) on the newly-generated metal surfaces is the most promising for our purposes. The electrode surface was renewed in the studied solutions by periodically cutting off a thin metal layer (*ca.* 10 μm) using a sapphire cutter. Experimental conditions were like those in [12], and the schematic representation of the apparatus unit for cutting is shown in Fig.1.

This method is also convenient for preliminarily analyzing metal/organic solution systems to determine their potential for future investigations. By measuring the time dependences of current (I vs. t curves) from the renewal moment at different potentials (E), it is easy to find the potential regions where the faradaic currents which complicate the study of interface properties are low. These potential regions for investigated systems may be considered as those of ideal polarizability.

Using this approach, it was established, e.g., that at the Fe/dimethylsulfoxide (DMSO) and Fe/acetonitrile (AN) solution interfaces the intensive faradaic processes take place after the electrode renewal at all studied potentials. These processes as was shown in detail in [13] point to the destructive character of DMSO molecule adsorption on a Fe electrode. As a result, in a short period (t ~ 0.02 - 0.1 s) an adsorption layer is formed on the newly-generated surface and levels the effect of potential on the double layer structure.

At the same time, there are many solvents, e.g., organic amide substances, which are much more stable in contact with a renewed Fe electrode surface. They are tetramethylurea (TMU), dimethylformamide (DMFA), dimethylacetamide (DMAA), N-methylpyrrolidine (N-MP), and hexamethylphosphortriamide (HMPTA). For example, initial currents after the cutting of a Fe electrode in TMU solutions of $LiClO_4$ at the potentials from 0.0 to -1.4 V (aq. sat. c. e.) do not exceed 30 $\mu A/cm^2$. The latter value is by *ca.* 1.5 -2 order of magnitude lower than that of in DMSO solutions. This only results in a slight time dependence of the electrode impedance components, i.e., the active (R) and reactive ($1/C\omega$) components of the electrode impedance change by not more than 3 - 5 % during the first minute after renewal. At the same conditions, the R and $1/C\omega$ dispersion in the frequency range 70 - 1000 Hz does not exeed 5 - 7 %. In other words, the newly-generated surface of a Fe electrode in TMU solutions of $LiClO_4$ can be considered ideally polarizable.

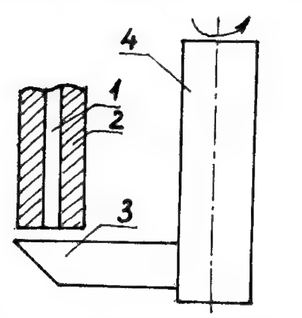

Fig.1. Scheme of apparatus unit for renewing the electrode surface. Following designations are used: (1) wire electrode, (2) teflon sleeve, (3) sapphire cutter, and (4) cutter holder.

Fig.2 shows C vs. E curves of a Fe electrode in $LiClO_4$ solutions of different concentrations in TMU. These curves have

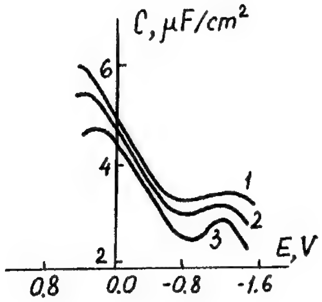

Fig.2. C vs. E dependences of Fe electrode in TMU solutions of x M $LiClO_4$, where x values: (1) 0.1, (2) 0.03, and (3) 0.003.

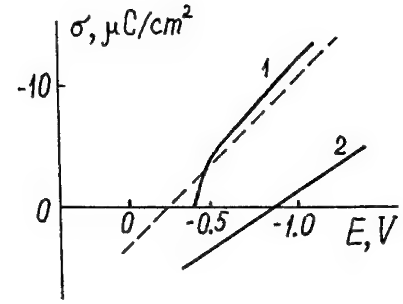

Fig.3. σ vs. E dependences of (1) Hg and (2) Fe electrodes in TMU solutions of 0.1 M $LiClO_4$. The dashed line is the hypothetical dependence for Fe.

a characteristic minimum which becomes deeper with the decrease in the salt concentration, and the potential of the minimum does not depend on the electrolyte concentration. A theoretical analysis of C vs. E curves of Fig.2 showed that these data are in a reasonable agreement with the Gouy-Chapman-Grahame model used for describing the double electric layer on the Fe electrode, and the potential of minimum at -0.8 V is the zero charge potential of Fe in this solvent.

When comparing Fe/TMU and Hg/TMU surfaces, it was shown that the capacitances at the Fe electrode are much lower than those at Hg and depend on the potential much weaker. Fig.3 shows calculated σ vs. E dependences for Hg and Fe electrodes (σ is the double layer charge). Here, the hypothetic line for Fe electrode is plotted under the assumption that the interaction of Fe with TMU molecules was absent (the work function of Fe was taken to be $W_e^{Fe} = 4.31$ eV). It is evident that the experimental curve for Fe shifts to the cathodic potential region with respect to the theoretical one. From these data, it is possible to estimate the potential drop produced by organic molecules adsorbed on an uncharged Fe surface. This value is -0.48 V, and it strongly differs from the analogous value for the Hg/TMU boundary (-0.17 V). All these results suggest that a strong interaction exists between the renewed Fe surface and solvent molecules in the studied potential region.

Above-mentioned distinctions between the Fe/TMU and Hg/TMU surfaces correlate with the known data comparing the properties of the Pt group and mercury-like boundaries with the solutions based on DMSO and AN [14,15]. This makes it possible to claim (as in the case of Pt group metals) that a strong chemisorption interaction of organic molecules with metal surfaces is the characteristic feature of the Fe/TMU system. Moreover, the same conclusion can be extended to the boundaries of Fe with some other solvents. These systems and some of their characteristics are summarized in the Table (the listed $E_{\sigma=0}$ values for Hg electrode were obtained by the flowing electrode method).

The problem concerning the effect of small water additions on C vs. E curves of metals in non-aqueous solutions is of great practical and theoretical interest. Special investigations have shown that the introduction of water up to 1 vol % in TMU, DMFA, and some other solvents has practically no effect on the C vs. E curves of Fe. Only when the water content reaches 5 or more vol % a substantial increase in the faradaic process intensity can be observed. The latter leads to a substantial pseudo-capacitance increase.

We used principally the same approach when studing contacts of an Al electrode with the solutions based on aprotic solvents. It was determined that on the renewed Al electrode surface in tetraalkyl-ammonium salt solutions in γ-butirolactone (γ-BL) in the potential range from -0.1 to -2.0 V and in DMSO and DMFA in the potential range from -0.5 to -2.2 V the faradaic process rates do not exeed

Table.

Ideal polarizability regions of a newly-generated Fe electrode in aprotic solvent solutions and zero-charge potentials of Fe and Hg electrodes in $LiClO_4$.

Solvent	Ideal polarizability region, V	$E_{\sigma=0}$, V	
		Fe	Hg
TMU	0.0 – -1.4	-0.80	-0.29
DMFA	-0.1 – -1.3	-0.65	-0.26
DMAA	-0.1 – -1.2	-0.55	-0.18
N-MP	-0.0 – -1.3	-0.85	-0.32
HMPTA	-0.4 – -1.4	~ -0.8	-0.34

30 - 50 $\mu A/cm^2$. In these conditions, we can assume that for a long period a clear Al surface is in contact with the studied solutions, and the measured capacitance is the double layer capacitance. Experimental results are shown in Fig.4. It can be seen that capacitances in concentrated solutions are practically independent of E, and, when the solutions are diluted, deep minima appear. The potentials of these minima do not depend on the salt concentration. These data have been shown to satisfactorily correlate with the Gouy-Chapman-Grahame model of double layer, and the potentials of the C vs. E curve minima in diluted solutions at -1.6 (γ-BL), -1.75 (DMSO), and -2.05 V (DMFA) are due to the maximal diffusness of the double layer at the zero-charge potentials in respective systems. It is interesting to note that by now Al is characterized by the most negative position of $E_{\sigma=0}$ of all systematically studied metals.

As an example, one can compare (Fig.5) σ vs. E curves calculated from experimental data for Al/DMSO and Hg/DMSO surfaces. Here, the hypothetic σ vs. E curve is also present. It was plotted

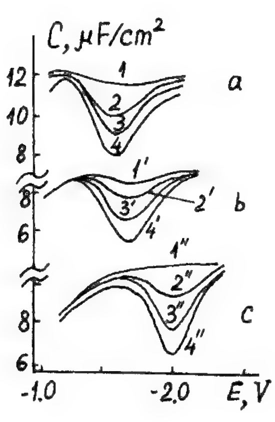

Fig.4. C vs. E curves of Al electrode in the solutions of (a) x M $TBABF_4$ in γ-BL; (b) y M $TMABF_4$ in DMSO; and z M $TBABF_4$ in DMFA. Here, x values: (1) 0.1, (2) 0.02, (3) 0.01, and (4) 0.005; y values: (1') 0.1, (2') 0.04, (3') 0.01, and (4') 0.005; z values: (1") 0.1, (2") 0.03, (3") 0.01, and (4") 0.005.

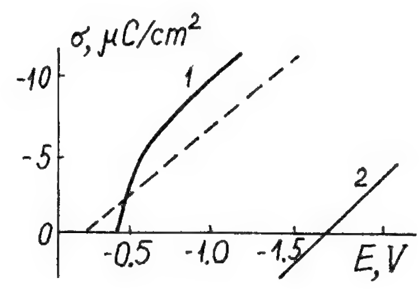

Fig.5. σ vs. E dependences of (1) Hg and (2) Al electrodes in DMSO solutions of 0.1 M $TMABF_4$. The dashed line is the hypothetic curve for Al.

under the assumption of the lack of interaction between Al surface and DMSO molecules (the work function of Al was taken to be $W_e^{Al} = 4.25$ eV). The experimental σ vs. E curve for Al is shifted cathodically with respect to the hypothetic one (by *ca.* 1.5 V). This suggests that Al like the above-mentioned corrosion and catalytically active metals is characterized by the strong chemisorption interaction with the studied organic solvent molecules in all available potential regions.

In [17] we offered a phenomenological model of two limiting states of solvent molecules which are in contact with the metal surface. This model can be used for describing the dense part of the double electric layer and the above-discussed C vs. E curves. Moreover, some new more rigorous approaches based on the model offered in [6,7] are now being developed.

Application of Fe thin-film electrodes for studing the passivation processes in water-organic media.

The data shown in the previous section indicate that the molecules of a number of organic solvents can be strongly chemisorbed on the iron electrode surface. Taking this into consideration, the issues connected with the effect of water-organic solvent composition on the metal surface state, the structure and thickness of films formed on the passive metals are of great interest.

We studied this problem using as an example the systems of Fe thin-film electrode — borate buffer in H_2O-DMFA mixtures (salt composition of buffer corresponded to pH 8.4 in aqueous solution). Application of Fe thin electrodes prepared by the vacuum evaporation of metal on a non-conductive substrate (devitrified glass such as Pyroceram) made it possible to obtain information on the electrode surface state using three independent methods, i.e., galvanostatic method, ellipsometry, and resistometry. Previous investigations have shown that the electrochemical behavior of film electrodes with the thickness of *ca.* 100 nm practically coincides with that of compact iron.

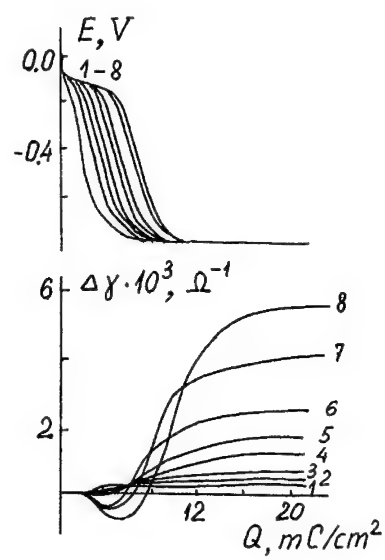

Fig.6. (a) E vs. Q and (b) $\Delta\gamma$ vs. Q dependences for the cathodic reduction of a thin-film Fe electrode preliminary passivated at E=0.72 V in H_2O-DMFA solutions of borate buffer. Water content, vol %: (1) 1, (2) 10, (3) 20, (4) 30, (5) 40, (6) 50, (7) 70, and (8) 100. i= 20 $\mu A/cm^2$.

E vs. Q and $\Delta\gamma$ vs. Q dependences obtained for the cathodic reduction of a Fe electrode which was passivated in H_2O-DMFA solutions are plotted in Fig.6 ($\Delta\gamma$ is the metal film electroconductance change). The electrode reduction was carried out in aqueous solutions of the same salt composition. The first plateau length of the E vs. Q curve at -0.1 V (n.h.e) decreases with the increase in the DMFA share in the solution. This decrease correlates with the decrease in $\Delta\gamma$ corresponding to the second (more negative) potential plateau. These data lead us to the conclusion that the surface-film thickness on a passive electrode decreases with the increase in the DMFA share in a mixed solvent.

An analysis of the effect of different factors on the conductance change of a thin-film electrode showed that the $\Delta\gamma$ increase during the cathodic reduction of passive iron corresponds to the transition of the surface oxide to the metal state. Under these conditions the following equation may be used for quantitative calculations

$$\Delta\gamma = k\, \kappa_m\, \Delta d_m\,, \qquad (1)$$

where k is the coefficient reflecting the geometry of a thin-film electrode used (in our case k=0.49), κ_m and Δd_m are the specific conductivity and the increment in the metal film thickness, respectively.

It should be noted that the processing of ellipsometric data obtained at three angles of incidence (these *in situ* results were obtained with galvanostatic and resistometric data simultaneously) allowed us within the frame of phenomenological microroughness model [19] to identify the surface film on a passive iron electrode in mixed solvents as the same oxide which is formed in aqueous solutions [20].

A quantitative comparison of the data plotted in Fig.6 with ellipsometric data was carried out under the assumption of different models of a surface layer structure on passive iron. The results of this analysis showed that the experimental data of three independent methods can be correlated under the following conditions: it should be assumed that practically only a three-valent metal oxide is present in the surface film on passive iron, and on the cathodic reduction this oxide transforms succesively to metal iron in accordance with the reactions

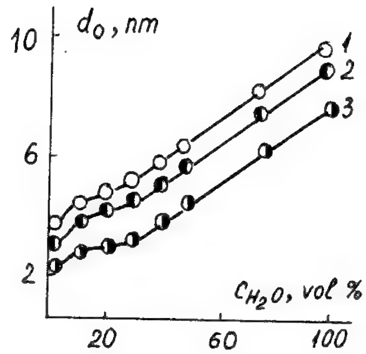

Fig.7. The effect of water content in H_2O-DMFA solutions of borate buffer on the oxide-film thickness on the passive iron. Calculations were based on (1) galvanostatic, (2) resistometric, and (3) ellipsometric data.

$$Fe(III) \rightarrow Fe(II), \tag{2}$$

$$Fe(II) \rightarrow Fe(0). \tag{3}$$

The calculated dependeces of the oxide film thickness on passive iron (d_o) on the volume composition of H_2O-DMFA (Fig.7) support our hypothesis. These calculations were based on: (i) the length of the first one-electrone arrest (Q_1) on the E vs. Q curve (Eq.2)

$$d_o = \frac{Q_1 M_o}{2 \rho_o F}, \tag{4}$$

(ii) the resistometric data (the increase of $\Delta\gamma$ at the second arrest; Eq.3)

$$d_o = \frac{\Delta\gamma \rho_m M_o}{2 k \rho_o M_m \kappa_m}, \tag{5}$$

and (iii) the ellipsometric data

$$d_o = q_o d_f. \tag{6}$$

In the Eqs. 4 - 6 the following values were used: M_o=159.6 and M_m=55.8 g/mol are the molecular masses of Fe_2O_3 and Fe; ρ_o=5.2 and ρ_m=7.8 g/cм^3 are the densities of Fe_2O_3 and Fe; d_f is the ellipsometric thickness of oxide film; and q_o is the share of oxide in the surface film.

From our standpoint, the most basic conclusion of this section is the independence of a composition of surface oxide on passive iron from the organic component content in a mixed solvent. At the same time, we should conclude that the organic component affects the thickness of the oxide layer and the kinetics of its formation on passive metals. Some aspects of this influence we discussed in [11].

Certain specific features of the effect of the electrolyte nature on the iron passivation in water-organic media.

Until recently the opinion that water molecules of water-organic solutions are always the main source of passivating oxygen was the generally accepted view. Obviously, precisely this idea formed the foundation of a large number of works directed at finding out the minimal water concentration necessary to observe the active-passive transition during anodic polarization of metals.At the same time, it is well-known [21,22] that oxidizers can cause passivation, i.e., they too can be the source of passivating oxygen.

Apparently, Banas *et. al.* first drew attention to the fact that non-dissociated sulfuric acid molecules can play the role of oxidizer and cause the metal passivation. Sulfuric acid molecules can exibit this

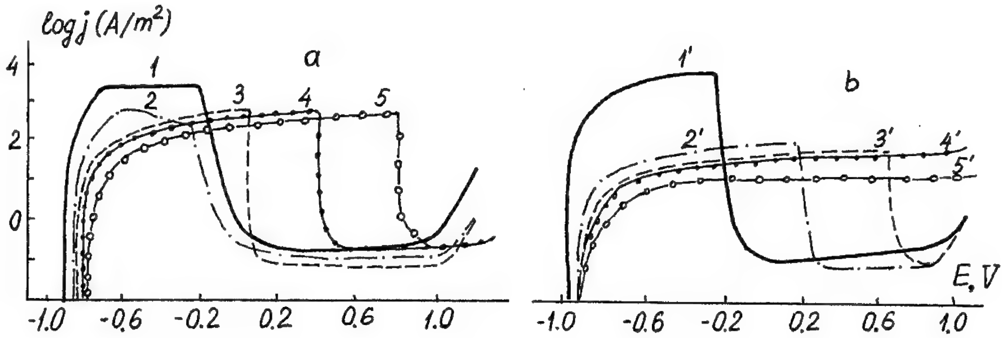

Fig.8. I vs. E curves of Fe electrode in H_2O-DMFA solutions of (a) 0.5 M H_2SO_4 and (b) 0.5 M H_3PO_4. Water content in the mixed solvent was, vol %: (1) 100, (2) 30, (3) 10, (4) 3, and (5) 0.2; (1') 100, (2') 30, (3') 25, (4') 20, and (5') 10.

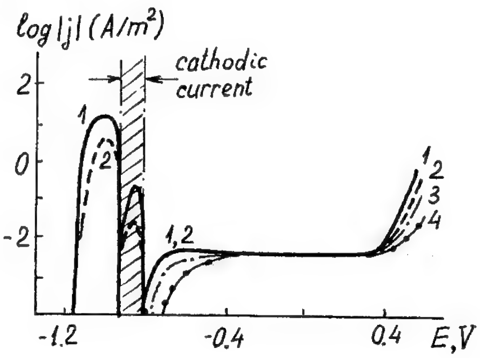

Fig.9. I vs. E curves of Cr in H_2O-DMFA solutions of 0.5 M H_2SO_4. Water content in the solvent was, vol %: (1) 100, (2) 30, (3) 10, and (4) 3.

property more distinctly in mixed solvent solutions, i.e., when their concentration increases due to the decrease of the dielectric permittivity of solvent.

Taking this into account, it was of interest to compare the effect of the composition of a water-organic solvent (H_2O-DMFA) on the Fe passivation in different electrolyte solutions, namely, in H_2SO_4 and H_3PO_4. Inasmach as the oxidizing ability of H_3PO_4 is lower than that of H_2SO_4, one may expect substantial distinctions in their influence on the anodic I vs. E curves. Respective dependences are shown in Fig.8, and the expected effects can be observed qualitatively. Namely, in aqueous media stationary I vs. E curves in H_2SO_4 and H_3PO_4 solutions almost coincide. However, the potential of the active-passive transition in the H_3PO_4 solutions shifts very quickly in the anodic direction with the increase in the DMFA share, and at $c_{DMFA} > 75$ vol % the passive region vanishes at all. At the same time, the current drop at the anodic polarization of Fe in sulfuric acid solutions is observed even at $c_{H_2O} \sim 0.1$ - 0.2 vol % [2]. Obviously, this indicates that H_2SO_4 molecules do participate in the formation of the passive state of iron.

Apparently, H_2SO_4 molecules play a substantial role (together with the composition of water-organic mixtures) in the specific features of Cr passivation in H_2O-DMFA solutions. It is seen in Fig.9 that the anodic I vs. E curve of Cr in an aqueous solution is characterized by three currentless potentials

and the potential region of cathodic currents. With an increase of DMFA content in a mixed solvent one may observe a sharp change in the shape of I vs. E curve. Moreover, at c_{DMFA} >70 vol % the corrosion potential of Cr drops down to the region of passivity and the cathodic current region vanishes [23]. Elucidation of the mechanism of Cr passivation in mixed solvent solutions and its specific features calls for further investigations.

Conclusion

Studies of the corrosion and the electrochemical behavior of metals in the solutions based on organic and water-organic solvents are a promising scientific direction. These investigations are of practical importance, they make it possible to find out new effects, provide additional insight into the mechanism of corrosion processes and passivation.

References

[1] Ya.M.Kolotyrkin, G.G.Kossyi, Zashch. Met. **1**, 272 (1965).
[2] K.Schwabe, S.Hermann, W.Oelssner, Passivity of Metals, R.P.Frankenthal, J.Kruger, Eds., The Electrochem. Soc., Princeton, New Jersy, p.413 (1978).
[3] T.R.Agladze, Itogi Nauki i Tekhniki, Korroziya i Zashchita ot Korrozii (Achievements of Science and Technology, Corrosion and Corrosion Protection), VINITI, Moscow. **9**, 3 (1982).
[4] V.A.Safonov, L.Yu.Komissarov, O.A.Petrii, V.M.Gerovoch, Elektrokhimiya. **23**, 1375 (1987).
[5] V.A.Safonov, S.A.Sokolov, Elektrokhimiya. **27**, 1317 (1991).
[6] S.Amokrane, J.P.Badiali, J. Electroanal. Chem. **266**, 21 (1991).
[7] I.A.Bagotskaya, B.B.Damaskin, V.E.Kazarinov, Elektrokhimiya. **30**, 293 (1994).
[8] V.A.Safonov, E.V.Lapshina, Zashch. Met. **26**, 531 (1990).
[9] J.Banas, B.Mazurkiewicz, B.Stypula, Electrochim. Acta. **37**, 1069 (1092).
[10] R.G.Kelly, P.J.Moran, Corros. Sci. **30**, 495 (1990).
[11] V.A.Safonov, T.G.Stepina, E.V.Lapshina, G.E.Vakhrushev, V.I.Shiryaev, Zashch. Met. **27**, 719 (1991).
[12] A.G.Zelinskii, R.Yu.Bek, Elektrokhimiya. **21**, 66 (1985).
[13] V.A.Safonov, L.Yu.Komissarov, O.A.Petrii, Zashch. Met. **22**, 212 (1986).
[14] O.A.Petrii, I.G.Khomchenko, J. Electroanal. Chem. **106**, 277 (1980).
[15] E.Yu.Alekseeva, V.A.Safonov, O.A.Petrii, Elektrokhimiya. **20**, 945 (1984).
[16] V.A.Safonov, S.A.Sokolov, V.M.Gerovich, Dokl. Akad. Nauk SSSR. **299**, 1438 (1988).
[17] B.B.Damaskin, V.A.Safonov, O.A.Petrii, J. Electroanal. Chem. **258**, 13 (1989).
[18] V.A.Safonov, E.V.Lapshina, Zashch. Met. **26**, 908 (1990).
[19] A.G.Borzenko, V.A.Safonov, V.F.Pikel'ni, Zashch. Met. **24**, 378 (1988).
[20] A.G.Borzenko, V.A.Safonov, Zashch. Met. **24**, 547 (1988).
[21] N.Ya.Bune, Ya.M.Kolotyrkin, Zh. Fiz. Khim. **15**, 1543 (1961).
[22] Ya.M.Kolotyrkin, N.Y.Bune, Z. phys. Chem. **214**, 274 (1960).
[23] Tran Hue Minh, V.A.Safonov, Zashch. Met. **29**, 324 (1993).

Materials Science Forum Vols. 185-188 (1995) pp. 861-870

Passivity of lithium in organic solvents

D. Rahner

Dresden University of Technology, Institute of Physical Chemistry and Electrochemistry,
Mommsenstrasse 13, D-01062 Dresden, Germany

Keywords: Lithium, passivity, organic solvents

Abstract

Since 1970 lithium has been intensively used as an anode material for high rate batteries. Starting from this time several kinds of lithium batteries have been developed. Serious scientific and technological research is still under development in order to advance existing types of batteries or to create new principles.

A short overview concerning the nature of lithium "passivity" and the use of in-situ techniques in lithium research will be given in order to emphasize the important role of the properties of the phase boundary metal / electrolyte. The electrochemical behaviour of lithium is strongly influenced by the formation of a surface layer, the reduction of the electrolyte, chemical side reactions and adsorption processes in the presence of some special additives used within the liquid or polymer solid electrolyte.

1. Lithium in contact with aprotic electrolyte systems

The passivity of a metal (e.g. Fe) in an aqueous solution is attributed to the formation of a dense oxide layer with a thickness of some unit cells. Under rest potential conditions the metal surface is in more or less free contact to the electrolyte solution. The rate determining step of the active dissolution is the charge transfer process which was formulated in the consecutive Heusler or Bockris mechanisms [1, 2]. An increase in anodic overpotential will increase the dissociation reaction of the solvent water at the metal surface under formation of the oxide layer. Now, the transition to the passive region is characterized by a sharp decrease in the anodic current density which is lower by some orders of magnitude in comparison to the active dissolution process. This process is schematically described in fig. 1.

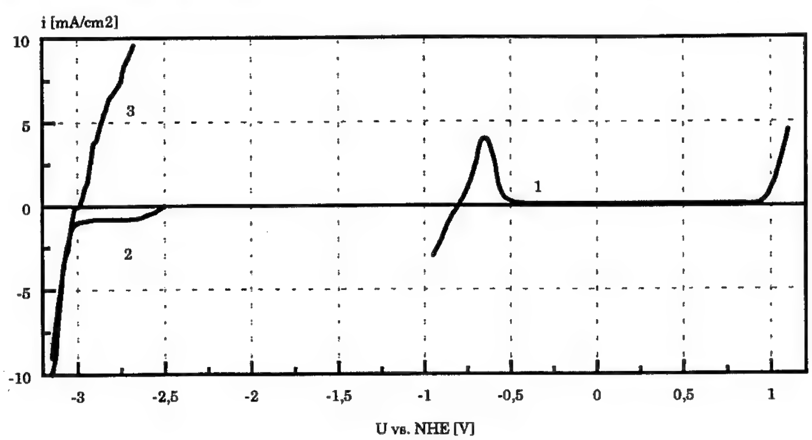

Fig. 1: Current-potential behaviour of metals in electrolyte solutions

1 - Fe in H_2O / Borate pH 7   2 - Ni in PC / 1 M $LiClO_4$ 3 - Li in PC / 1 M $LiClO_4$

·A completely other behaviour is observed in the case of lithium. Lithium is the most reactive metal. Its use is only possible in aprotic solvents. According to its negative standard electrode potential ($U_H^\circ = -3.04$ V) it reacts immediately and irreversible with a lot of organic and inorganic solvents and electrolytes under formation of a surface layer [3-10]. On air only lithium oxide, lithium carbonate or lithium nitride are formed.
In lithium batteries solid, inorganic and especially organic electrolytes are used [11]. A classical electrolyte solution is 1 M $LiClO_4$ in propylene carbonate (PC) or mixtures with other solvents like 1,2-dimethoxyethane (DME). The use of lithium in a battery depends on the stability range of the solvent and the electrolyte. Thus, the decomposition of PC starts at potentials less than 1 V (vs. Li/Li^+) or $U_H <$ -2.4 V in dependence on the electrode material [12]. In fig. 1 the decomposition process is shown at an inert nickel substrate forming the surface layer.
The electrochemical behaviour of lithium in aprotic media does not show the typical active-passive transition like iron in an aqueous solution. Under rest potential conditions the lithium surface is always covered by a protective layer. In electrolyte solutions it is generally recognized that the composition of the electrolyte solution determines the composition of the surface layer on the top of the lithium electrode [13-14]. This surface layer was found to be consist of a mixture of decomposition products of the solvent and the electrolyte used. The existence of this "passivating" layer is the prerequisit for the use of lithium in modern battery systems. Due to the formation of this layer lithium is kinetically stable with respect to many battery solvents. The layer is permeable for unsolvated lithium ions with a high velocity. Due to the small ionic radius of the lithium ion (78 pm) it can permeate through solid phases like metals or intercalate into open structures like oxides or sulphides.
The rate determining step of the lithium dissolution or deposition process is the migration of Li^+ ions through the surface layer. If we speak about the "passivity" of lithium we shall keep in mind that we speak about a kinetically hindered system. From a thermodynamically point of view the lithium system is not stable.

2. The "passive" layer on lithium

Models

Electrochemical in-situ techniques like impedance measurements or potentiostatic or galvanostatic transients combined with optical and surface analytical methods have been used to investigate the behaviour of the phase boundary lithium / electrolyte. It was found by FTIR, IR, XPS, SIMS, Raman and X-ray measurements [15-20] that lithium forms in contact with PC electrolytes a surface layer of decomposition products of the solvent and the anion of the electrolyte. As main component of the layer lithiumalkylcarbonates have been detected. In the presence of traces of water the alkylcarbonates react to lithiumcarbonate, alcohol and carbon dioxide. It was found by electrochemical in-situ techniques [21] that the surface layer is formed instantly upon contact of the metal with the solution. The thickness of the freshly formed layer is determined by the electron-tunneling range and changes by time. It acts as an interphase between the metal and the solution and has the properties of a solid electrolyte, with high electronic resistivity. There is no direct and free contact between the metal and the solution, either under rest potential conditions, or in metal dissolution or metal deposition.

The results of these investigations can be summarized in two models of the "passive" layer:

- ***SEI*** - model (solid electrolyte interface)
  According to Peled [21-23] the surface layer consists of a thin lithium ion conducting solid electrolyte of inorganic nature without electronic conductivity (Table 1).
- ***PEI*** - model (polymer electrolyte interface)
  In this model one takes into account the polymerization of organic solvent molecules induced by metallic lithium [24, 25]. The reaction products form an oligomeric and/or polymeric surface layer which is permeable for solvated lithium ions and its corresponding anions. This layer also contains small particles of inorganic decomposition products. The layer is gel-like and porous.

Table 1: Surface layers on lithium and other light metals according to [21]

metal	solvent	electrolyte	composition	spec. resistance Ωcm^2	thickness nm
Li	$SOCl_2$	$LiAlCl_4$	LiCl	10^7-10^9	2
Li	THF	$LiClO_4$	Li_2O	10^8	10
Li	PC	$LiClO_4$	Li_2CO_3	0.5-2.5*10^8	2.5
Mg	$SOCl_2$	$Mg(AlCl_4)_2$	$MgCl_2$	10^9-10^{10}	>2.5
Ca	$SOCl_2$	$Ca(AlCl_4)_2$	$CaCl_2$	10^{10}	2-4

Surface analytical investigations combined with optical methods have shown that the "passive" layer of metallic lithium should be described as a combination of the above discussed two models - an inner inorganic dense film and an outer porous organic layer [26, 27](Fig. 2).

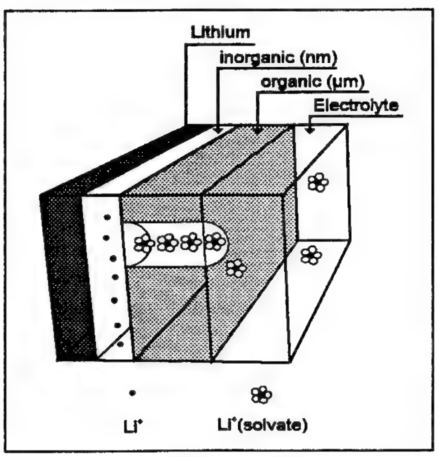

Fig. 2: Surface layer on lithium in organic electrolytes (model)

Current-potential behaviour

The protective surface layer of the lithium electrode posesses a high ionic conductivity. The composition of the layer, their thickness and kinetics of growth depends strongly on the composition of the electrolyte solution and the resting time in contact with the electrolyte solution. The kinetics of the lithium electrode has been described by Peled [21].

The rate determining step during the dissolution/deposition period is the migration of the Li^+ ion through the surface layer. At higher field strength the Ohm`s law is not longer valid. The current-potential curve can be expressed in terms of a field assisted migration process [28]:

$$i = 4\, z\, F\, a\, c\, \nu \exp\left(-\frac{W}{RT}\right) \sinh\left(\frac{a\, z\, F\, E}{R\, T}\right) \qquad \text{(Eq.1)}$$

with a - half jump distance, ν - vibration frequency of the ion in the crystal, c - concentration of lattice defects, z - valency of the mobile ion, W - barrier energy for jumping, E - electric field. In this case the applied overvoltage η is identical with the overvoltage η_{SEI} at the phase boundary of the solid

electrolyte interface (SEI) with a thickness d

$$\eta = \eta_{SEI} = E\, d \qquad \text{(Eq. 2).}$$

The exchange current density i_0 follows

$$i_o = 2\, z\, F\, a\, c\, \nu \exp\left(-\frac{W}{R\,T}\right) \qquad \text{(Eq. 3).}$$

For high field conditions (azFη > RTd) results a "*Tafel*"-like equation

$$i = i_o \exp\left(\frac{a\, z\, F\, \eta}{R\, T\, d}\right) \qquad \text{(Eq. 4)}$$

or

$$\eta = \frac{2.3\, R\, T\, d}{a\, z\, F} \lg i_o + \frac{2.3\, R\, T\, d}{a\, z\, F} \lg i = a_1 + b \lg i \qquad \text{(Eq. 5).}$$

At room temperature the slope b is expressed as

$$b \approx \frac{60\, d}{a\, z} \text{ [mV]} \qquad \text{(Eq. 6).}$$

With a typical assumption for the tunneling range of electrons (z=1 and a=0,3 nm) results the slope b from several hundred millivolts to several volts in dependence on the layer thickness. The time dependence of the current-potential curves (fig.3) gives informations on the dynamic growth of the surface layer. In general one observes a relative good coincidence of the estimated layer thickness d (Eq. 6) resulting from current-potential measurements and the estimated layer thickness by impedance spectroscopy (Eq. 11).

Under low field conditions Eq.1 reduces to Ohm`s law

$$i = \frac{4.6\, i_o\, \eta}{b} \qquad \text{(Eq. 7).}$$

The estimated resistance is the resistance of the surface layer R_{SEI}. Under the assumption of a homogeneous layer the specific resistivity ρ is given by

$$\rho = \frac{R_{SEI}}{d} = \frac{b}{4.6\, i_o\, d} \qquad \text{(Eq. 8).}$$

The results of the time dependence of the current-potential curve of lithium in different electrolytes (0.5 M $LiClO_4$ in PC/DME and 0.5 M $LiCF_3SO_3$ in PC/DME respectively) are shown in fig. 3 a,b. The process of layer formation is very dynamic. It can be observed that the presence of the ClO_4^--ion diminishes continously the exchange current density. In the presence of $CF_3SO_3^-$-ion the exchange current density is nearly constant within the error limit. At overvoltages of about 150...200 mV in all cases the surface layer will be partially broken and the dissolution process of lithium is enhanced. The estimated characteristic parameters of the surface layer (apparent thickness, exchange current density and resistivity) are tabulated in table 2. In the presence of ClO_4^--ions the layer thickness is increasing up to about 1.3 nm causing a decrease in the exchange current density. In the presence of $CF_3SO_3^-$-ions the layer thickness and the exchange current density is nearly constant (about 1 nm and 0.2 mA/cm^2.)

a)

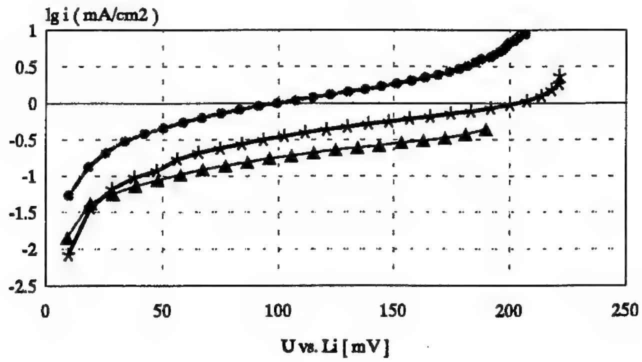

b)

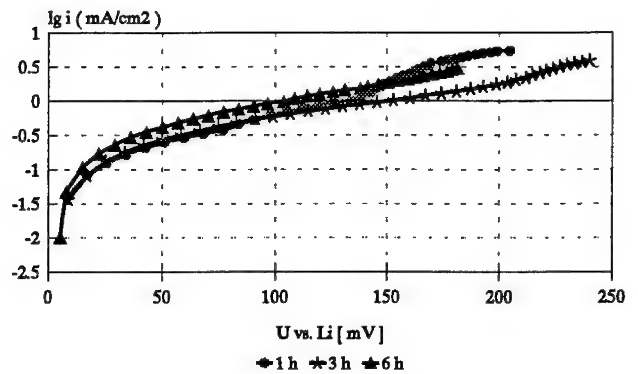

Fig. 3: Current-potential curve of lithium in dependence on the anion (dU/dt = 0.5 mV/s)
a) 0.5 M $LiClO_4$ in PC/DME b) 0.5 M $LiCF_3SO_3$ in PC/DME

Table 2:
Characteristic parameters of the surface layer on lithium in PC/DME in dependence on the anion

salt	time [h]	b [mV]	d [nm]	i_0 [mA/cm^2]	ρ [Ωcm]
$LiClO_4$	1	150	0.8	0.32	$1.4*10^9$
	3	200	1.0	0.10	$4.3*10^9$
	6	250	1.3	0.06	$7.2*10^9$
$LiCF_3SO_3$	1	200	1.0	0.25	$1.7*10^9$
	3	200	1.0	0.18	$2.4*10^9$
	6	200	1.0	0.18	$2.4*10^9$

Impedance behaviour

The protective surface layer at lithium immersed in aprotic organic media undergoes dynamic alterations during polarization or wet standing at the rest potential. Using *ac* impedance spectroscopy, it is often possible to divide an overall reaction into its partial reactions due to their different frequency responses. The "time-window" of this method is "open" from slow diffusion processes up to fast charge transfer or migration processes. The electrical equivalent is expressed in terms of different time constants R*C which contain informations related to rate constants, surface layer composition and thickness, diffusion parameters and transport numbers of moving charged species. Assuming, the discussed models will describe the electrochemical behaviour of the surface layer correctly, than the layer properties can be monitored.

A general treatment of the *ac* impedance behaviour of a binary dilute electrolyte placed between parallel non-blocking electrodes has been given by *MacDonald* [29,30] and was used to investigate the mass transport properties of lithium surface layers formed in several electrolytes [13, 31, 32]. Following the suggestions of *Sørensen* [32] and *Garreau* [13], three elementary processes related to the mass transport (migration process = arc < 1 >), the charge transfer process (arc < 2 >) and the diffusion process (arc < 3 >) should be expected (Fig. 4).

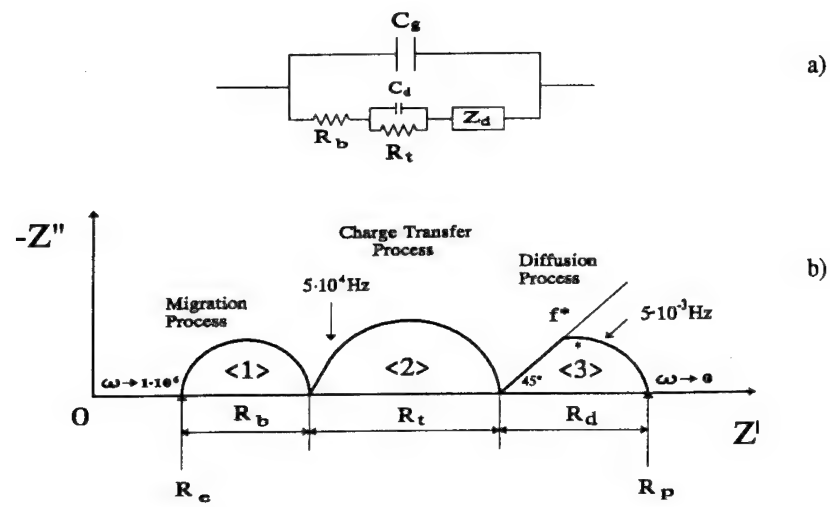

Fig. 4. Impedance behaviour of a surface layer according to [13]
(a) equivalent electrical circuit
(b) impedance diagram in the complex plane.

R_e: electrolyte resistance. R_p: polarization resistance. R_b: bulk resistance.
R_t: charge transfer resistance. C_d: double layer capacitance. Z_d: diffusion impedance.
R_d: diffusion resistance. f^*: frequency at the maximum of the imaginary part

The migration impedance is determined by the resistance of the surface layer R_b (or R_{SEI}) and the geometric capacitance C_g (normally some $\mu F/cm^2$). Knowing the layer thickness from independent methods (ellipsometry, SEM-pictures, current-potential curves) one can calculate the average specific resistivity ρ of the layer by

$$R_b = \rho \cdot \frac{d}{A} \qquad \text{(Eq. 10).}$$

Assuming, the model of the plate condensor is valid, the layer thickness is given by

$$d = \frac{\varepsilon\,\varepsilon_o\,A}{C_g} \qquad \text{(Eq. 11).}$$

$\varepsilon_0 = 8{,}86 \cdot 10^{-12} AsV^{-1}\,m^{-1}$, absolute dielectric constant; ε - relative dielectric constant (~12), A - area

In the case of a linear diffusion the diffusion impedance is the *Warburg* impedance Z_W

$$Z_w = (1-j)\,\sigma\,w^{-1/2} \qquad \text{(Eq. 12).}$$

For 1,1-valent electrolytes [13] the *Warburg* constant σ is given by

$$\sigma = \frac{2\sqrt{2}\cdot RT\cdot(1-t^+)^2}{F^2 c\cdot\sqrt{D_s}} \qquad \text{(Eq. 13)}$$

and is influenced by the diffusion coefficient of the mobile species D_s and the transfer number t^+.
The film formed on the lithium surface (cutted from a rod and foiled in the argon filled glove box) strongly depends on the solvent and electrolyte used (Fig. 5). The diagrams are composed of a semicircle in the high frequency region (maximum frequency f_2 ~ 200....2000 Hz) and a small arc in the low frequency region (maximum frequency f_3 ~ 1...200 mHz) on the complex plane.

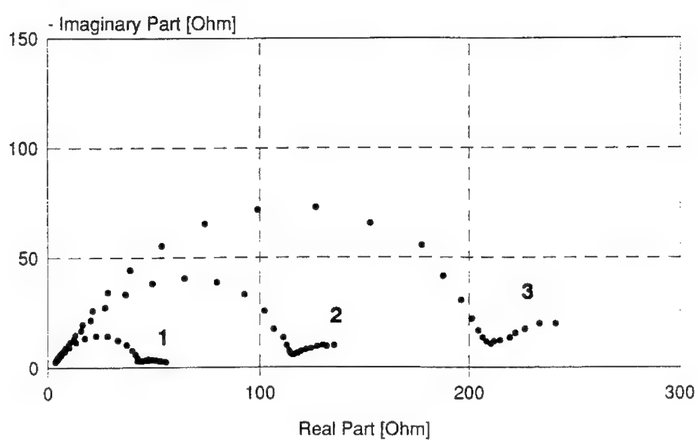

Fig. 5: Cole-Cole plot of lithium in PC / 1 M $LiClO_4$ in dependence on the immersion time
1 - 15 min 2 - 3 days 3 - 7 days

According to the discussed models the high frequency arc is considered to represent the charge transfer to a less conductive film at the lithium surface. The low frequency arc results from a slow diffusion process at the interface. Both arcs are time dependent, especially the maximum frequency is shifted to higher frequencies when the system is stored in the electrolyte solution. The expected migration process is not visible within the frequency range investigated (100kHz........1mHz).

During the measurements of the current-potential-curves in the mixed electrolyte PC/DME it was observed, that the solvent as well as the anion of the lithium salt strongly influence the properties of the surface layer (fig. 3a, b). Impedance measurements show in agreement with these findings that in the presence of $CF_3SO_3^-$-anions the surface layer is formed quickly. After one day wet standing in the solution no further change is observed in the impedance spectra. In the presence of ClO_4^--anions one day

immersion causes an increase of the charge transfer resistance from 1 Ωcm^2 (1 h immersion) to 25 Ωcm^2 (24 h immersion). Now the measured impedance spectra are similar to that measured in $LiCF_3SO_3$ solution. The difference in the charge transfer resistance is only slightly but very emphasized in the diffusion process (fig. 6).

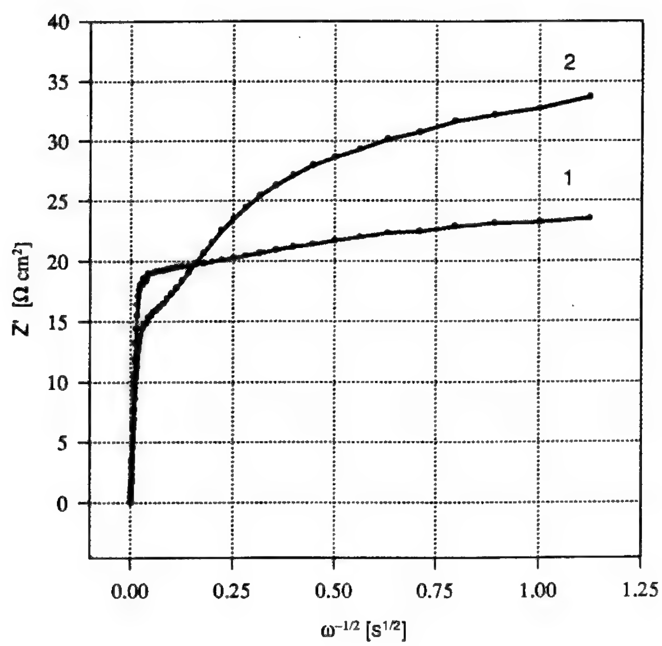

Fig. 6. Impedance of lithium (diffusion part) at OCV after 2 days immersion in
1 - 0,5 M $LiClO_4$ in PC/DME
2 - 0,5 M $LiCF_3SO_3$ in PC/DME

The *Warburg* constant σ was estimated in ClO_4^--media to $\sigma = 5.4\ \Omega cm^2 s^{-1/2}$ and in $CF_3SO_3^-$-media to $\sigma = 38.0$ and $8.8\ \Omega cm^2 s^{-1/2}$. The overall diffusion process seems to consist of two partial processes. The bigger $CF_3SO_3^-$-anion obviously causes a very "porous" structure on top of a dense surface layer. Experimental details are described in [11, 33].

3. Summary

It was shown by electrochemical methods that the protective surface layer at lithium immersed in liquid aprotic organic media undergoes dynamic alterations during polarization or wet standing at the rest potential. The solvent and the anion of the lithium salt have an influence on the properties of the formed surface layer. This influence is obvious in a change of the layer thickness, the exchange current density, the charge transfer resistance and the maximum frequency of the charge transfer arc.

Acknowledgments
Financial support from the Deutsche Forschungsgemeinschaft is gratefully acknowledged.
The author is endebted to Mrs. K. Siury, Mr. S. Machill and Dr. G. Ludwig for experimental assistance.

References

1 K. E. Heusler, Ber. Bunsenges. phys. Chem. **62**, 582 (1958)
2 J. O'M. Bockris, D. Drazic, A. R. Despic, Electrochim. Acta **4**, 325 (1961)
3 K. M. Abraham, J. S. Foos, J. L. Goldman, J. Electrochem. Soc. **131**, 2197 (1984)
4 K. M. Abraham, J. Power Sources **14**, 179 (1985)
5 J. O. Besenhard, J. Gürtler, P. Komenda, in DECHEMA Monographien, Vol.109, VCH Verlagsges., Weinheim, 1987, p. 315
6 Y. Matsuda, in Practical Lithium Batteries, JEC Press Inc., Cleveland, 1988, pp. 13-23
7 M. Morita, Y. Matsuda, in Practical Lithium Batteries, JEC Press Inc., Cleveland, 1988, pp. 87-92
8 D. Aurbach, M. L. Daroux, P. W. Faguy, E. Yeager, J. Electrochem. Soc. **134**, 1611 (1987)
9 R. D. Rauh, S. B. Brummer, Electrochim. Acta **22**, 75 (1977)
10 Y. Geronov, F. Schwager, R. H. Muller, J. Electrochem. Soc. **129**, 1422 (1989)
11 D. Rahner, G. Ludwig, H. Bischoff, I. Hauke, S. Machill, K. Siury, K. Wiesener, Wiss. Z. Techn. Univers. Dresden **41**, 48 (1992)
12 G. Eggert, J. Heitbaum, Electrochim. Acta **31**, 1443 (1986)
13 S. Fouache-Ayoub, M. Garreau, P. V. S. S. Prabhu, J. Thevenin, J. Electrochem. Soc. **137**, 1659 (1990)
14 M. Morita, S. Aoki, Y. Matsuda, Electrochim. Acta **37**, 119 (1992)
15 D. Aurbach, O. Chusid, J. Electrochem. Soc. **140**, L 155 (1993)
16 D. Aurbach, O. Chusid, J. Electrochem. Soc. **140**, L 1 (1993)
17 E. Goren, O. Chusid, D. Aurbach, J. Electrochem. Soc. **138**, L 6 (1991)
18 D. Aurbach, Y. Gofer, M. Ben-Zion, P. Aped, J. Electroanal. Chem. **339**, 451 (1992)
19 K. Kanamura, H. Tamura, Z. I. Takehara, J. Electroanal. Chem. **333**, 1217 (1992)
20 G. Nazri, R. H. Muller, J. Electrochem. Soc. **132**, 1385 (1985)
21 E. Peled, in Lithium Batteries, Ed. J.-P. Gabano, Academic Press, New York (1983), pp. 43-72
22 E. Peled, J. Power Sources **9**, 253 (1983)
23 E. Peled, J. Electrochem. Soc. **126**, 2047 (1979)
24 M. Garreau, 3rd International Meeting on Lithium Batteries, Kyoto (1986), Ext. Abstr. No. P4
25 J. Thevenin, J. Power Sources **14**, 45 (1985)
26 J.-O. Besenhard, J. Electroanal. Chem. **78**, 189 (1977)
27 M. Hess, Thesis, Westfälische Wilhelms-Universität Münster (1992)
28 L. Young, in Anodic Oxide Films, Academic Press, New York, London, (1961)
29 J. Ross MacDonald, J. Chem. Phys. **58**, 4982 (1973)
30 J. Ross MacDonald, J. Chem. Phys. **61**, 3977 (1974)
31 M. Morita, S. Aoki, Y. Matsuda, Electrochim. Acta **37**, 119 (1992)
32 P. R. Sorensen, T. Jacobsen, Electrochim. Acta **27**, 1671 (1982)
33 K. Wiesener, U. Eckoldt, D. Rahner, Electrochim. Acta **34**, 1277 (1989)

Materials Science Forum Vols. 185-188 (1995) pp. 871-876

Passivation of iron and nickel in concentrated solutions of formic and acetic acids

J. Banas, B. Mazurkiewicz, W. Solarski and K. Banas

University of Mining and Metallurgy, Faculty of Foundry Engineering, ul. Reymonta 23, PL-30-059 Kraków, Poland

Keywords: Passivity, passivity of iron, passivity of nickel, formic acid, acetic acid

Abstract

Anodic passivation of iron and nickel has been investigated in concentrated aqueous solutions of formic and acetic acids. In anhydrous formic acid both metals undergo oxide passivation. The passivation proceeds with the participation of undissociated acid molecules. The anodic oxidation of metals is coupled with the catalytic decomposition of acid. The chromatographic analysis of .the gaseous products during anodic passivation of metals confirms the presence of carbon monoxide. The evolution of carbon dioxide and hydrogen have been observed in the active range. The presence of CO_2 and H_2 can be interpreted as anodic oxidation of formic acid in accordance with Kolbe-type reaction. The evolution of CO is connected with the formation of oxide passive film.

The acetic acid is more stable and more resistant to electrochemical decomposition than formic acid. Therefore the passivation of iron and nickel in anhydrous acetic acid is not observed.

Introduction

Our investigations of passivation of metals in anhydrous solutions of sulphuric and phosphoric acids show that oxide passive film can be formed on the metal surface as a result of the decomposition of acid molecules [1-3]. The molecules of oxy-acids take part in anodic reaction and act as a source of oxygen in the passivation processes [4-7].

The investigations of corrosion and passivation of carbon and stainless steels in concentrated solutions of carboxylic acids (HCOOH, CH_3 COOH), performed by Sekine and co-workers, show that the influence of acidity and water activity on the dissolution and passivation in these environments is very similar to the effect of these factors in concentrated solutions of sulphuric acid [8-11]. The maximum of corrosion rate was observed at a definite water concentration. The authors observed the passivation of steels in anhydrous formic acid but they did not explain the mechanism of passivation .

The aim of the present work was to establish whether the passivation of metals in anhydrous carboxylic acids proceeds with the participation of acids molecules similarly to the passivation process in anhydrous solution of inorganic oxy-acids.

Experimental

The electrochemical measurements were performed on pure iron and nickel (99.99%) in de-aerated solutions of anhydrous (100%) formic and acetic acids. The influence of water concentration on passive behaviour of both metals has been also investigated. The anodic polarization measurements have been carried out by means of the potentiostat with an automatic IR compensation (an interruption technique). The saturated calomel electrode was used as a reference electrode.

The potentiostatic etching of metal surface for analytical measurements of anolyte was performed in a special vessel with the separated anode and cathode volumes (Fig. 1). The surface of the working electrode was equal 1.5 cm^2. The anodic etching of iron and nickel in anhydrous formic acid has

been performed at 0.1 V and 1.0 V during 10 hours. In acetic acid both metals were etched at 0.3 V during 20 hours. Conductivity of 100% acetic acid was very low and therefore the addition of 2% sodium acetate was used as a supporting electrolyte.

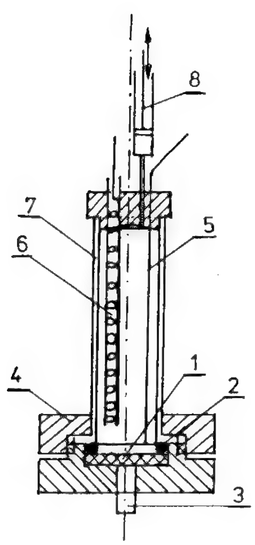

Fig. 1. Vessel for anodic etching of metal. 1 - sample, 2 - sample isolator, 3 - sample contact, 4 - PTFE holder, 5 - reference electrode, 6 - counter electrode (cathode), 7 - glass vessel, 8 - gas sampling syringe.

The gas chromatography of anolyte has been used for the qualitative product identification of formic and acetic acids electrochemical decomposition. The analysis of hydrogen was performed by katharometric detection using Chrom-5 gas chromatograph on a column filled with carbon (Merck's carbon, l = 1m, ϕ = 4 mm). The flow rate of carrier gas (nitrogen) was equal 30 ml/min. The limit of detectable of the method was 0.001 vol%. The analysis of carbon monoxide and carbon dioxide was performed by the same method, but with hydrogen as carrier gas. For CO determination a column filled with carbon was applied (Merck's carbon, l = 1 m, ϕ = 4 mm) and for CO_2 determination a column with a silica gel (Merck, l = 0.3 m, ϕ = 4 mm). The limit of detectable of CO was equal 0.05 vol% and that of CO_2 was equal 0.03 vol%. The analysis of other products of electrocatalytic decomposition of acids has been performed by gas chromatography with the flame ionization detector. The column was filled with a10% SP-2100 phase on 100/120 Supelcoport (Supelco, Inc.).

Results

Fig. 2 and 3 present the anodic polarization of iron and nickel in $HCOOH-H_2O$ system. The oxide passive layer can be formed only in anhydrous acid. The addition of water decreases passivation ability of the electrolyte. The analysis of anolyte during the anodic etching of iron (table 1) shows, that the CO_2 and H_2 evolution occurs on the metal surface in the active range (0.1 V). At more noble potential (1.0 V), in the passive range, the CO and H_2 evolution was observed. The presence of CO_2 was not confirmed by chromatographic analysis.

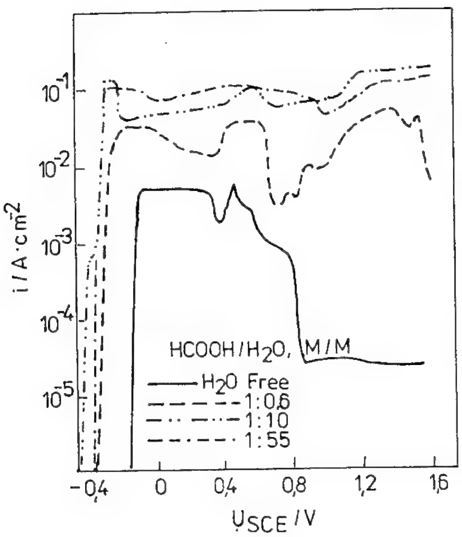

Fig. 2. Anodic polarization of iron in the HCOOH - H_2O system.

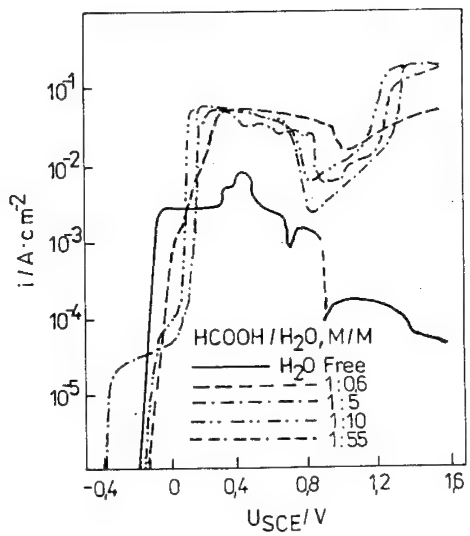

Fig. 3. Anodic polarization of nickel in the HCOOH - H_2O system.

Table 1. Analysis of anolyte for iron and nickel etched in formic and acetic acids.

Metal Solution	Potent. etching	H_2	CO	CO_2	CH_4	C_2H_6	CH_3CHO	unident.
Fe HCOOH	0.1 V	x		x				
	1.0 V	x	x					
Ni HCOOH	0.1 V	x		x				
	1.0 V	x	x					
Fe CH_3COOH	0.3 V			x	x	x	x	x
Ni CH_3COOH	0.3 V			x	x	x	x	x

Fig. 4 and 5 present the anodic polarization of iron and nickel in anhydrous acetic acid. Unlike the formic acid, the anhydrous acetic acid does not show distinct passivation ability.

The analysis of anolyte for iron etched at 0.3 V (during 19 hours) is presented in Table 1. The evolution of CO_2 was observed. The presence of CO and H_2 in anodic products was not confirmed. Gas evolved on the anode contains some amounts of CH_4 and C_2H_6. The anolyte contains also acetic aldehyde. Similar results have been obtained during anodic etching of nickel. For both metals small amount an unidentified product of acetic acid decomposition was observed.

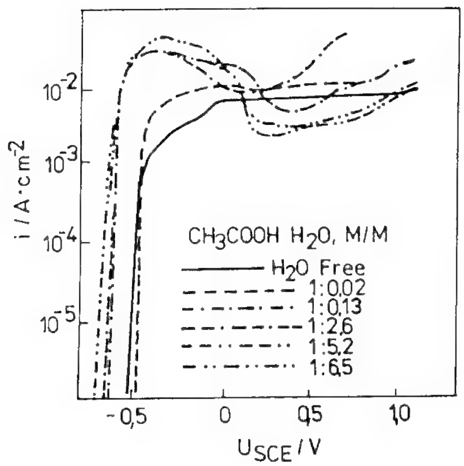

Fig. 4. Anodic polarization of iron in the CH_3COOH - H_2O system.

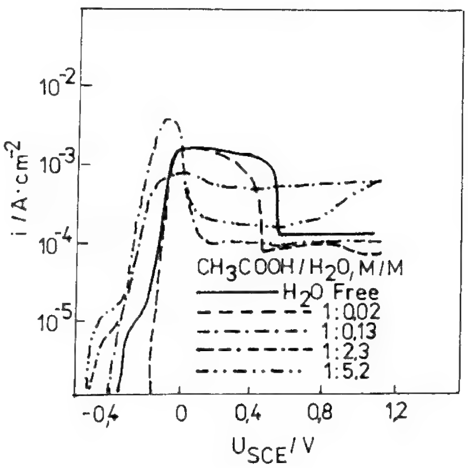

Fig. 5. Anodic polarization of nickel in the CH_3COOH - H_2O system.

Discussion

The mechanism of passivation of iron and nickel in anhydrous formic acid can be presented as an anodic reaction of metal surface with acid molecules, in accordance with the following equation:

$$2Fe + 3HCOOH = Fe_2O_3 + 3CO + 6H^+ + 6e \qquad \Delta G^0_{298} = -114.20 \text{ kJ/mol} \qquad (1)$$

$$Fe + 2HCOOH = FeOOH + 2CO + 3H^+ + 3e \qquad \Delta G^0_{298} = -192.08 \text{ kJ/mol} \qquad (2)$$

$$Ni + HCOOH = NiO + CO + 2H^+ + 2e \qquad \Delta G^0_{298} = -2.06 \text{ kJ/mol} \qquad (3)$$

The presence of carbon monoxide in anodic products is an evidence that formic acid molecules undergo electrocatalytic decomposition during the passivation process. In the active range, at low anodic polarization when metal dissolution dominates, the evolution of CO does not occur. In this potential range only CO_2 and H_2 are present in the gas evolved on the anode. The evolution of carbon dioxide and hydrogen is connected with the Kolbe reaction:

$$HCOOH = H_2 + CO_2 \qquad \Delta G^0_{298} = -10.37 \text{ kJ/mol} \qquad (4)$$

The evolution of carbon monoxide is directly connected with oxide formation on the surface of iron and nickel. The formic acid molecules are a source of oxygen during the anodic passivation process.

The participation of acetic acid molecules in anodic reactions similar to the reactions 1-3 is not very likely. In an anodic reaction a big acetic anhydride molecule should be formed. This is more difficult than the formation of carbon oxide molecule during the decomposition of formic acid:

$$2Fe + 6CH_3\,COOH = Fe_2\,O_3 + 3(CH_3CO)_2\,O + 6H^+ + 6e \qquad \Delta G^0_{298} = +90.72 \text{ kJ/mol} \qquad (5)$$
$$Ni + 2CH_3\,COOH = NiO + (CH_3\,CO)_2\,O + H^+ + 2e \qquad \Delta G^0_{298} = +65.64 \text{ kJ/mol} \qquad (6)$$

The electrochemical decomposition of anhydrous acetic acid during the anodic dissolution of iron and nickel proceeds probably according to the Kolbe reaction:

$$CH_3COOH = CH_4 + CO_2 \qquad \Delta G^0_{298} = -16.38 \text{ kJ/mol} \qquad (7)$$
$$2CH_3COOH = C_2H_6 + 2CO_2 + H_2 \qquad \Delta G^0_{298} = -16.33 \text{ kJ/mol} \qquad (8)$$

The carbon dioxide, methane and ethane have been identified in gaseous products of iron and nickel anodic etching. The acetic aldehyde presented in anolyte can be formed according to the following reactions:

$$2(CH_3COO)_2Fe + 3CH_3COOH = 2(CH_3COO)_3\,Fe + CH_3CHO + H_2O \qquad (9)$$

The unidentified product which was found in the chromatogram of anolyte during the etching of iron and nickel in anhydrous acetic acid is probably the product of trimerization or aldol condensation of acetaldehyde:

$$3CH_3CHO \rightarrow (CH_3CHO)_3 \qquad (10)$$
$$2CH_3CHO \rightarrow CH_3CH(OH)CH_2CHO \xrightarrow{-H2O} CH_3CH{=}CHCHO \qquad (11)$$

The analysis of the thick unprotective, anodic layer formed on the iron surface during the anodic etching shows that it is composed of Fe^{+3} acetate.

Conclusions

The oxide protective film can be formed on the iron and nickel surface during the passivation of these metals in anhydrous formic acid solutions. The passivation of metals proceeds with the participation of acid molecules. The molecules of formic acid undergo electrocatalytic decomposition and act as a source of oxygen for the formation of oxide film.

The passivation of iron and nickel in anhydrous acetic acid is difficult. Both metals dissolve strongly in this environment. Acetic acid shows very poor oxidative ability in comparison with the formic acid.

References

[1] J.Banaś, B.Mazurkiewicz, B.Stypuła, Electrochim. Acta **37**, 1069 (1992).
[2] J.Banaś, B.Mazurkiewicz, B.Stypuła, Metalurgia i Odlewnictwo **18**, 301 (1992).
[3] J.Banaś, "Passivity of Metals in anhydrous Solutions of Oxy-Acids", Seventh Internat. Symp. on Passivity, Clausthal, August 21 - 26, 1994.
[4] B.Mazurkiewicz, Electrochim. Acta **38**, 495 (1993).
[5] B.Stypuła, J.Banaś, Electrochim. Acta **38**, 2309 (1993).
[6] B.Stypuła, J.Banaś, Proceed. 15 Europ. Symp. on Modifications of Passive Films. Ed. P. Marcus, B. Baroux and M. Keddan, Paris 1993, p.123.
[7] B.Stypuła, "The Effect of Electrolyte Structure on the Passivation of Chromium", Seventh Internat. Symp. on Passivity, Clausthal, August 21 - 26, 1994.
[8] J. Sekine, K. Senoo, Corr. Sci., **24**, 439 (1984).
[9] J. Sekine, A. Chinda, Corrosion, **40**, 95 (1984).
[10] J. Sekine, S. Hatakeyama, Y. Nakazava, Electrochim. Acta **32**, 915 (1987).
[11] J. Sekine, S. Hatakeyama, Y. Nakazava, Corr. Sci. **27**, 275, (1987).

Materials Science Forum Vols. 185-188 (1995) pp. 877-886

Film formation on iron in methanol-water borate buffer solutions studied with the rotating split-ring disc electrode

J. Wilinski and J. Flis

Institute of Physical Chemistry of the Polish Academy of Sciences, PL-01-224 Warsaw, Poland

Keywords: Iron, borate, methanol/water, surface films, Fe(II), Fe(III), voltammograms, split-ring disc

Abstract

Formation of soluble Fe(II) and Fe(III) species on iron during anodic and cathodic scans in the borate/methanol-water solutions was studied with a rotating split-ring disc electrode (RSRDE).

The highest anodic currents for iron disc occurred in the solutions with 30 M and 35 M H_2O. In all the solutions a reduction peak appeared in the cathodic scans, indicating the formation of both Fe(II) and Fe(III) species, however, no soluble Fe(II) species were detected in the low water solutions (1.0 M H_2O and less), and no soluble Fe(III) species were detected in the medium-high water solutions (30 M and 35 M H_2O).

Four ranges of the water concentrations were distinguished with different passivation features. The main components of surface films in these ranges are suggested to be as follows:

(a) low water concentrations (1.0 M H_2O and less) - a Fe(III) salt and a low soluble Fe(II) salt;

(b) medium water concentrations (10 M and 20 M H_2O) - a mixture of Fe(III) salt and Fe(III) oxide or hydroxide;

(c) medium-high water concentrations (30 M and 35 M H_2O) - a large amount of a low protective Fe(III) salt of a low solubility, and a small amount of γ-FeOOH and Fe_3O_4;

(d) high water concentrations (45 M H_2O and more) - γ-FeOOH and Fe_3O_4.

Introduction

The state of the knowledge on corrosion and passivation of metals in organic solvents has been presented in the reviews by Heitz [1], Agladze [2], and Kelly and Moran [3]. In practical applications these solvents inevitably contain at least some trace contents of water, hence the effect of water on the corrosion and passivation in aqueous/non-aqueous systems has been extensively studied. These systems have also been studied to gain a better understanding of the role of water in the passivation of metals in aqueous solutions.

Kelly and Moran [3] conclude that the effect of small concentrations of water on the passivation in organic solvents strongly depends on pH of the solutions. In acidified solutions, usually with H_2SO_4, in anhydrous solutions a passivition does not occur, whereas additions of 0.5-5% wt.% H_2O result in the formation of an oxide-type passive film [4-6]. In the anhydrous solutions the active disssolution is usually mitigated by salt layers [4, 6, 7], however, an oxide-type passivation is also possible owing to the oxidation of metal by undissociated H_2SO_4 [8].

An opposite effect of water was found in neutral solutions, typically containing $LiClO_4$. Passivity was observed in anhydrous solutions, whereas additions of about 1 wt.% H_2O lead to the activation of metal [9-12]. The passivation in these solutions was ascribed to the chemisorption of solvent molecules, whereas the activation was explained by the competitive adsorption of water. Adsorbed water can decrease the protective ability of an air-formed film due to the acidification, and can interfere with the formation of a precipitated salt by increasing its solubility [3, 11, 12]. The detrimental effect of small concentrations of water on the passivity is a trend rather than a rule, since in some systems [3, 12] an opposite effect was observed.

The authors of papers [3, 11-13] explain the corrosion behaviour of metals in organic solvents and mixed water/non-aqueous solutions in terms of several passivation mechanisms, including (a) air-formed film, (b) salt film formation, (c) chemisorption of the solvent molecules, and (d) oxide-oxyhydroxide film; in some solvents electropolymerization is also possible [12]. These mechanisms can compete and be predominant depending on the metal, solvent, potential, and the electrolyte.

The oxide-oxyhydroxide films are essential for the metal passivation in aqueous solutions, and they can also be important for corrosion resistance of metals in mixed water/non-aqueous solutions.

The present work examines the effect of water on corrosion and film formation on iron in borate/methanol-water solutions. Rotating split-ring disc electrode (RSRDE) was used to determine the formation of Fe(II) and Fe(III) species and to assess their presence in surface films.

Methanol-water solutions are used in various chemical technologies, whereas buffered borate solutions have been widely applied in studies on passivation of iron in aqueous solutions [14-18]. Corrosion behaviour of iron in $LiClO_4$/methanol-H_2O solutions with 0.5 to 30 wt.% H_2O was studied by Farina *et al.* [19].

Experimental

Measurements were carried out on pure decarburized iron which was in form of a disc being 5.1 mm in diameter. The RSRDE was used [18, 20] with half-rings made of Type 316 SS [21]. The calculated collection efficiency for each of the half-rings was 15.5 %.

Measurements were performed at 25°C in deaerated methanol-water solutions of borate 0.15 M H_3BO_3 + 0.0375 M $Na_2B_4O_7$, prepared from bidistilled water and reagent grade chemicals. An aqueous solution of this composition has pH 8.4. The deaeration was made by purging with argon.

Potentials were measured with referenece to a saturated calomel electrode (SCE).

The electrodes in the RSRDE assembly were polished with 800 emery paper, rinsed with water and then with methanol. Prior to the measurements, iron disc was cathodically polarized at -1.3 V (SCE) for 15 min to reduce the air-formed films. The half-ring for the detection of Fe(II) species was kept at the potential of 0.4 V (SCE), and the half-ring for Fe(III) species was at -0.9 V (SCE). The rotation velocity of the disc assembly was 25 rps.

Cyclic voltammograms were measured at a potential sweep rate of 10 mV s^{-1}.

Results

A typical voltammogram for high water contents is presented in Fig. 1; it shows the iron disc current (i_D) and the current response on half-rings, $i_R Fe^{2+}$ and $i_R Fe^{3+}$, of soluble Fe(II) and Fe(III) species formed on the disc, respectively.

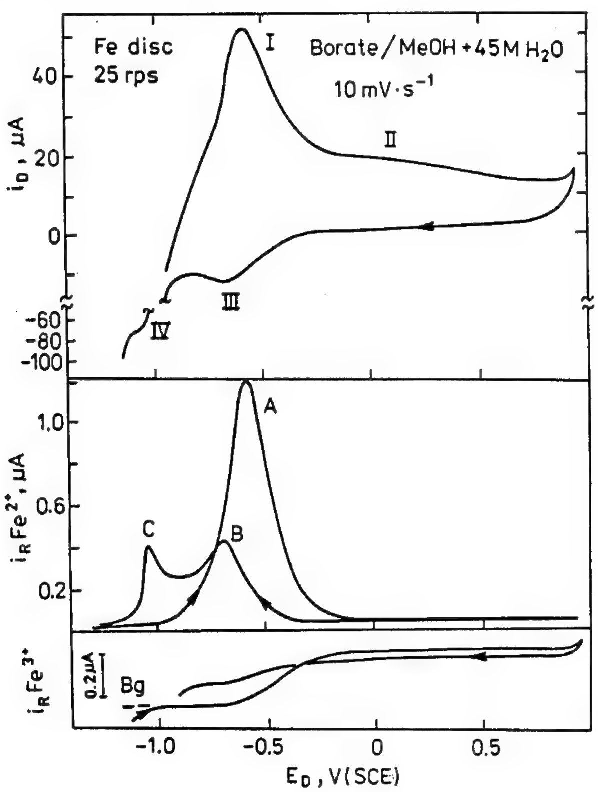

Fig. 1. Voltammogram for iron disc (i_d) and current response on half-rings ($i_R Fe^{2+}$ and $i_R Fe^{3+}$) in the methanol-45 M H_2O solution of borate.

Features of the voltammogram are similar to those for the aqueous borate solution [18]. Accordingly, they can be described as follows.

Active region and peak I:

- the measurements show the formation of Fe(II) and Fe(III) species;
- the equilibrium potentials suggest the formation of $Fe(OH)_2$, Fe_3O_4 and α-FeOOH;
- passivation (peak I) can be due mainly to the formation of FeOOH.

Active-passive transition region:

- a passive film forms whose composition can be described as a spectrum, with compounds ranging from $Fe(OH)_2$ through Fe_3O_4 to FeOOH;
- the film undergoes a transformation which is reflected in a shift of peak *C* to negative potentials.

Peaks II, III, and *B*:

these peaks can be related to the reaction:

$$Fe(OH)_2 \Leftrightarrow \gamma\text{-}FeOOH \qquad (1)$$

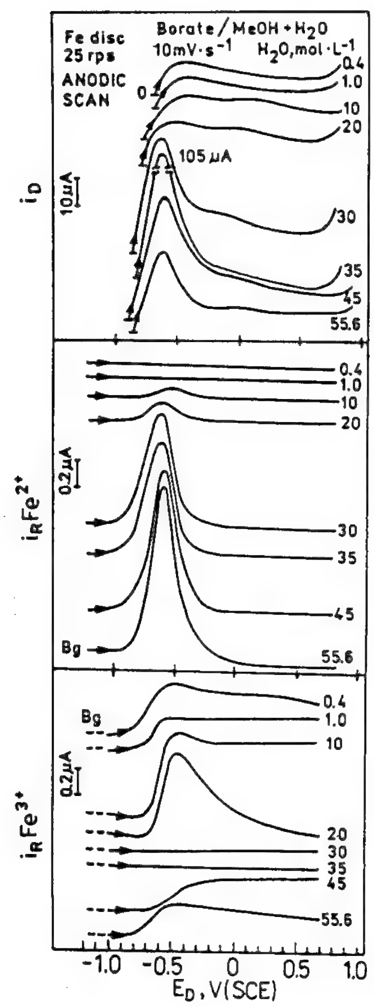

Fig. 2. Currents for iron disc (i_D), and of Fe(II) and Fe(III) species (i_RFe^{2+} and i_RFe^{3+}) in anodic scans measured in the borate/methanol-water solutions with varying water concentrations.

Peaks IV and C:

these peaks can be associated with the reduction of magnetite

$$Fe_3O_4 \Leftrightarrow Fe(OH)_2 \qquad (2)$$

Passive region:

- a passive film is formed which is reduced at peaks III and IV, giving Fe(II) species at peaks *B* and *C*, respectively;
- the reduction peaks suggest that the film is composed of Fe_3O_4 and γ-FeOOH.

Effect of the water content on the iron disc currents and on the formation of Fe(II) and Fe(III) in the anodic scans is shown in Fig. 2. The active-passive transition was observed only for the water concentrations above 20 M H_2O; for 20 M and lower water concentrations the open-circuit potential moved to the nobler direction, and the currents indicated the passivity.

In the solutions with the high water content (above 20 M), the currents in the active region initially increased with the decreasing water concentration, and attained the highest values for 35 M H_2O. In the solutions with 30 M and 35 M H_2O, the water decomposition began at the potentials by about 0.15 V lower than in the other solutions.

The formation of Fe(II) species varied with the water concentration similarly as did the disc current. In the active-passive transition region

this species was at maximum for 35 M H_2O, and then decreased with the decreasing water concentration down to nil for 1.0 M and 0.4M H_2O.

The currents of Fe(III) species appeared to be almost reversed to the Fe(II) currents. This species was not detected at 30 M and 35 M H_2O, at which the disc and Fe(II) currents attained maxima. Fe(III) was detected at all the other concentrations, exhibiting the maximum for 10 M and 20 M H_2O.

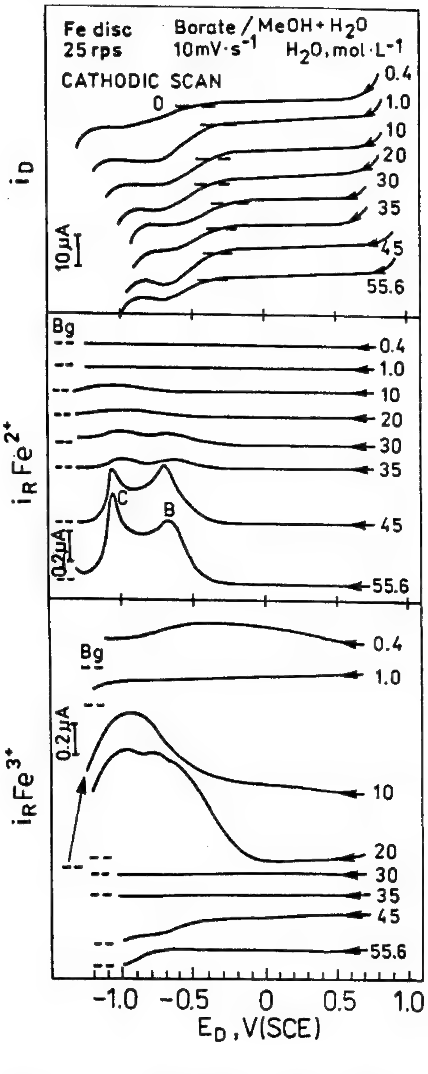

Fig. 3. Currents for iron disc (i_D) and for Fe(II) and Fe(III) species ($i_R Fe^{2+}$ and $i_R Fe^{3+}$) in cathodic scans.

Similar dependence of the Fe(II) and Fe(III) currents on the water concentration was also observed in the cathodic scans (Fig. 3). These scans were measured directly after the anodic scans, being the reversals of the latter.

The disc currents exhibited the reduction peak III in all the solutions, although the peak for 0.4 M H_2O was low and shifted to the negative potentials.

Fe(II) was not detected in the low water solutions; it appeared only in the solutions with 10 M H_2O and higher water concentrations. Peaks *B* and *C* of Fe(II) species were visible for 30 M and 35 M H_2O, and they were very distinct for 45 M H_2O and the aqueous solution (55.6 M H_2O).

Similarly as in the anodic scans, Fe(III) did not form in the solutions with 30 M and 35 M H_2O, but it formed in high amounts in 10 M and 20 M H_2O. In the latter solutions, Fe(III) attained a maximum at the potential by about 0.2 V more negative than the potential of the formation of this species.

The iron disc currents and true currents of soluble Fe(II) and Fe(III) species ($i_{Fe(II)}$ and $i_{Fe(III)}$) from Fig. 2 are presented at chosen potentials in Fig. 4 as a function of the water concentrations. The currents $i_{Fe(II)}$ and $i_{Fe(III)}$ were calculated after taking into account the collection efficiency. The potentials are related to the corrosion potential (E_c) and to the potential of peak I (E_I).

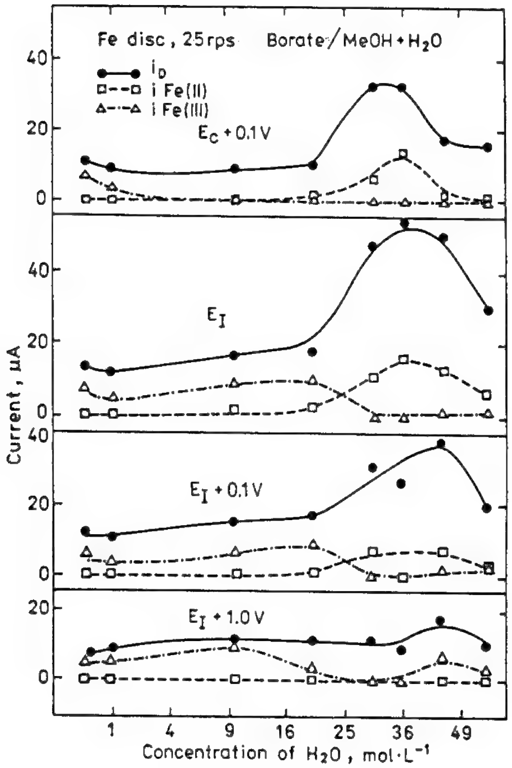

Fig. 4. Current for iron disc (i_D), and true currents of soluble Fe(II) and Fe(III) species ($i_{Fe(II)}$ and $i_{Fe(III)}$) at chosen potentials of anodic scans *vs.* water concentration.
E_c is the corrosion potential, E_I is the potential of peak I. Concentration of H_2O is on the square root scale.

At all the potentials the disc current was the highest for the water concentrations in the range of 35 M to 45 M H_2O. This indicates that these solutions can be the most aggressive to iron.

At this concentration was also formed soluble Fe(II) species at the highest amounts; this species formed in the active and active-passive transition region, but it was not detected in the passive region. In the low water solutions it was not detected at any potential.

Soluble Fe(III) species was not detected in the solutions with 30 M and 35 M H_2O, but it appeared in all the other solutions, also in the passive region.

Fig. 5 shows the i_F/i_D ratio in anodic scans for the different water concentrations; i_F is the current for the film formation determined as

$$i_F = i_T - i_{Fe(II)} - i_{Fe(III)} \qquad (3)$$

where i_T is the total current measured for the disc, $i_{Fe(II)}$ and $i_{Fe(III)}$ are the true currents for soluble Fe(II) and Fe(III) species, calculated after taking into account the collection efficiency.

The i_F/i_T ratio presents the fraction of the total current consumed for the film formation, including the formation of solid products and/or their anodic oxidation. It is possible that only some fraction of the total amount of the solid products can form a surface film, because a part of them can be precipitated in the solution.

In the aqueous solution (55.6 M H_2O) the segments of the i_F/i_D curve corresponded to the active, active-passive transition, peak II, and passive regions. In the active region over 70 % of the total current was used for the film formation. The i_F/i_T ratio was the lowest for the solution with 0.4 M H_2O, whereas the highest ratio appeared for the solution with 30 M H_2O. The high disc

current in the latter solution demonstrates that the solid products do not form a protective film.

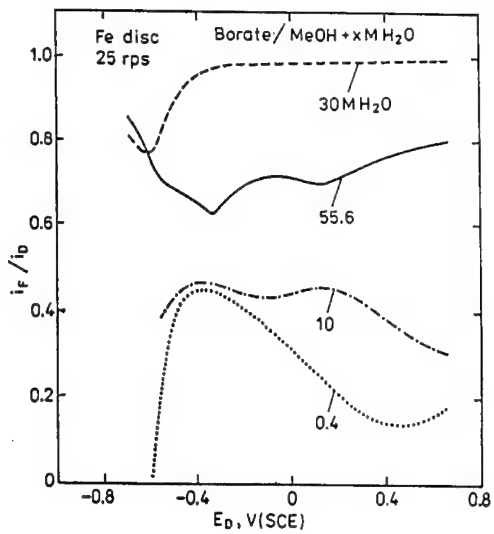

Fig. 5. Ratio of the current for the film formation (i_F) to the disc current (i_D) in borate/methanol-water solutions for chosen water concentrations.

Discussion

The results of this work (especially Figs. 2 and 3) suggest that the meachanism of passivatiom of iron in the borate/methanol-water solutions changes in irregular way with the water concentration. Roughly, four ranges of the water concentrations can be distinguished for which different passivation features have been observed.

(a) *Low water concentrations* (1.0 M H_2O and less)

In these solutions iron does not exhibit an active-passive transition; low i_F/i_D ratio indicates a small current contribution to the film formation and hence a small film thickness; there is formed soluble Fe(III), however, no soluble Fe(II) can be detected. The lack of soluble Fe(II) can be due to a low solubility of the Fe(II) products rather than to their absence, because an evidence for their formation is provided by the reduction peak III in the cathodic scans.

Is is supposed that the passivation in these solutions results from the formation of a salt film containing Fe(III) and particularly the Fe(II) species of low solubility. It is possible that also an adsorbed methanol film may be formed.

(b) *Medium water concentrations* (10 M and 20 M H_2O)

Similarly as in the low water solutions, iron does not show an active-passive transition, but the anodic currents are slightly higher. Soluble Fe(II) is formed in small amounts, whereas soluble Fe(III) forms in the largest amounts of all the solutions.

Particularly high amounts of soluble Fe(III) are formed in the cathodic scans; the Fe(III)-detecting current strongly rises almost simultaneously with the appearance of Fe(II), and reaches a maximum at the potential more negative than the potential of the Fe(III) formation in the anodic scans. Possibly, in the passive region the Fe(III) species is bound by an oxide-type Fe(III) film, e. g. FeOOH, and is released after reduction of the Fe(III) oxide or hydroxide. Probably, a complex or a mixture of Fe(III) salt with Fe(III) oxide is formed which can be designated as Fe(III) salt/oxide.

It is supposed that in these solutions the surface film is composed mainly of Fe(III) salt/oxide; it might also contain some Fe(II) salt and/or oxide.

(c) *Medium-high water concentrations* (30 M and 35 M H_2O)

Anodic oxidation of iron attains the maximum rate for the methanol-water solutions. Soluble Fe(II) species forms in large amounts in the anodic scans, and in small amounts at the cathodic peaks *B* and *C*; the latter peaks suggest that the passive film contains small amounts of γ-FeOOH and Fe_3O_4 [18].

The lack of soluble Fe(III) species and the high i_F/i_D ratio (Fig. 5) indicate that in the passive region the anodic products exhibit a very low solubility. Probably, this is a Fe(III) salt whose low solubility might be associated with a strong interaction of methanol and water molecules in these concentrations [22]. The occurrence of a relationship between minimum anodic currents, minimum solubility and maximum methanol-water interaction was earlier shown by Banas [7] for iron in H_2SO_4/methanol-water.

High disc currents demonstrate that despite the low solubility, the assumed Fe(III) salt does not render an adequate passivation.

It is supposed that the surface film contains a small amount of γ-FeOOH and Fe_3O_4, and a large amount of a low-protective Fe(III) salt.

(d) *High water concentrations* (45 M H_2O and more)

Soluble Fe(II) and Fe(III) species are formed in the anodic and cathodic scans similarly as in the aqueous solution, indicating the formation of iron oxides and oxyhydroxides. Peaks *B* and *C* in the cathodic scans suggest that the passive film is composed of γ-FeOOH and Fe_3O_4 [18].

Conclusions

A rotating split-ring disc electrode (RSRDE) was used to examine the formation of soluble Fe(II) and Fe(III) species during anodic and cathodic scans for iron in the borate/methanol-water solutions. The main conclusions are as follows.

1. The highest anodic currents for iron disc occurred in the solutions with 30 M and 35 M H_2O.

2. No soluble Fe(II) species were detected in the low water solutions (1.0 M H_2O and less), and no soluble Fe(III) species were detected in the medium-high water solutions (30 M and 35 M H_2O), however, the formation of these species was evidenced by the reduction peak III.

3. Four ranges of the water concentrations were distinguished with the passivation features as follows:

(a) Low water concentrations (1.0 M H_2O and less) - the formation of a salt film, containing Fe(III) and particularly the Fe(II) species of low solubility;

(b) Medium water concentrations (10 M and 20 M H_2O) - the surface film is composed mainly of Fe(III) salt/oxide; it might also contain some Fe(II) salt and/or oxide;

(c) Medium-high water concentrations (30 M and 35 M H_2O) - the surface film contains a small amount of γ-FeOOH and Fe_3O_4, and a large amount of a low-protective Fe(III) salt;

(d) High water concentrations (45 M H_2O and more) - the passive film is composed mainly of γ-FeOOH and Fe_3O_4.

References

[1] E. Heitz, in *Advances in Corrosion Science and Technology*, Vol. 4 (Eds. M. Fontana and R. Staehle), p. 149. Plenum Press, New York (1974).
[2] T. R. Agladze, in *Korroziya i zashchita ot korrozii*, Vol. 9 (Ed. Ya. M. Kolotyrkin), p. 3. VINITI, Moscow (1982).
[3] R. G. Kelly and P. J. Moran, Corros. Sci. **30**, 495 (1990).
[4] K. Schwabe, Zashchita Metallov **18**, 387 (1982).
[5] W. Schmidt, Prot. Metals **5**, 529 (1970).
[6] J. Banas, in *Passivity of Metals and Semiconductors* (Ed. M. Froment), p. 687. Elsevier, Amsterdam (1983).
[7] J. Banas, Z. Phys. Chemie **262**, 1105 (1981).
[8] J. Banas, B. Mazurkiewicz and B. Stypula, Electrochim. Acta **37**, 1069 (1992).
[9] T. R. Agladze, Ya. M. Kolotyrkin, T. G. Malysheva and O. O. Denisova, Zashchita Metallov **22**, 509 (1986).
[10] V. A. Safonov, L. Yu. Komissarov and O. A. Petrii, Prot. Metals **22**, 178 (1986).
[11] R. G. Kelly, P. J. Moran, E. Gileadi and J. Kruger, Electrochim. Acta **34**, 823 (1983).
[12] D. A. Shifler, P. J. Moran and J. Kruger, in *Proc. Congress on Corrosion of Metals*, Vol. **3B**, p. 2131. NACE, Houston (1993).
[13] D. A. Shifler, P. J. Moran and J. Kruger, Corros. Sci. **32**, 475 (1991).
[14] J. Kruger and J. Calvert, J. Electrochem. Soc. **114**, 403 (1967).
[15] Z. Szklarska-Smialowska and W. Kozlowski, J. Electrochem. Soc. **131**, 234, 499, 723 (1984).
[16] W. Kozlowski and J. Flis, Corros. Sci. **28**, 787 (1988).
[17] W. Kozlowski and J. Flis, Corros. Sci. **32**, 861 (1991).
[18] J. Flis and J. Wilinski, this volume.
[19] C. A. Farina, G. Faita and F. Olivani, Corros. Sci. **18**, 465 (1978).
[20] J. Wilinski, J. Flis and P. Kedzierzawski, Brit. Corros. J. **25**, 184 (1990).
[21] K. Heusler, Berichte Bunsengesell. **72**, 1197 (1968).
[22] H. H. Emons and B. Ponsold, Z. Chem. **10**, 471 (1970).

Materials Science Forum Vols. 185-188 (1995) pp. 887-896

Passivity of silicon-containing austenitic stainless steel in concentrated sulphuric acid

M.B. Ives, J.R. Kish and J.R. Rodda

Corrosion Laboratory, Department of Materials Science and Engineering,
McMaster University, Hamilton, Ontario, Canada

Keywords: Silicon stainless steels, concentrated sulphuric acid, anodic polarization, Auger electron spectroscopy

Abstract Preliminary experiments have been carried out to characterize the nature of passivity of silicon-containing stainless steels in 98.0 and 93.5% sulphuric acid at temperatures from 40°C to 200°C. Using immersion and electrochemical techniques, the corrosion behaviour of UNS S30601, a 5.3 wt.% silicon austenitic stainless steel, was compared with that of the more conventional alloy, UNS S31603.

It is found that the addition of silicon has a favourable influence on the corrosion resistance of these austenitic stainless steels. Lower corrosion rates were recorded for UNS S30601 and these are related to the suppression of the periodic cycling of the corrosion potential, which is typical of UNS S31603 at a wide range of temperatures and acid compositions. The mechanisms by which silicon stabilizes passivity are considered to relate to the manner in which the anodic and cathodic reactions compete for control of the corrosion process.

Introduction

The manufacture of sulphuric acid involves chemical reactions that produce large quantities of heat. Removal of this reaction heat is a process requirement. However useful recovery of the heat is a process challenge and is essential in the trend towards higher operating efficiencies [1],[2]. Since higher temperatures favour better utilization of the acid waste heat, more corrosion resistant alloys such as the silicon-containing "super" stainless steel and high nickel alloys are required for sulphuric acid service.

Normal sulphuric acid conditions encountered during manufacturing include 98 to 99 wt.% concentration up to 120°C, and 93 wt.% concentration up to 70°C. The temperature ceilings are governed by the performance of construction materials which often include anodically protected stainless steel. The 300 series austenitic stainless steels, especially alloys UNS S31600 and UNS S31603, find extensive use as the construction material for various components including piping, towers, tower internals and heat exchangers. Anodic protection is necessary to extend the useful range from ambient temperatures up to the forementioned temperature limits. It is well known that although unprotected stainless steel corrosion rates decrease with increasing concentration [3], a high level of resistance is achieved only at ambient temperatures. Despite the use of anodic protection further improvements in corrosion resistance are required to utilize the recovery of acid waste heat.

A stainless steel recently introduced to service concentrated sulphuric acid is UNS S30601, a silicon-containing, wrought austenitic steel. Corrosion data shows this alloy to have a marked improvement in the unprotected corrosion resistance to typical process acid environment conditions [4]. However the mechanism by which silicon improves the corrosion resistance still remains to be explained adequately.

This paper explores both the electrochemical and corrosion behaviour of alloys UNS S31603 and UNS S30601 in concentrated sulphuric acid environments in an attempt to understand the nature of passivity in these environments.

Experimental Details

MATERIALS

1.905 cm diameter tubes of alloy UNS S31603 and approximately 6 mm thick annealed plates of alloy UNS S31603 and UNS S30601 austenitic stainless steels were employed in this study. The nominal compositions of these alloys are shown in Table I.

Table I.
Nominal Composition of the Steels (wt.%)

Alloy	chromium	nickel	silicon	molybdenum	carbon
UNS S31603	18	12	- - -	2.5	0.03
UNS S30601	17.5	17.5	5.3	- - -	0.01

Tube samples were cut into 20 cm lengths which were then sealed at one end by an autogenous welded plate of the same material. These samples were then activated by wet-grinding with emery paper to 400 grit, cleaned in soap solution, rinsed with distilled water and then dried with absorbent paper immediately prior to immersion. The tube samples, used exclusively for testing in the 98 wt.% H_2SO_4 solutions, were immersed so as to expose an area of approximately 70 cm^2. Plate samples were cut into approximately 6 cm long x 3 cm wide coupons, which were cleaned and activated in an identical manner as the tube samples.

Corrosion tests were performed in concentrated 98.0 and 93.5 wt.% H_2SO_4 solutions which were prepared from reagent grade (97 wt.%) sulphuric acid, and fuming acid or distilled water. The strength of the prepared solutions was verified with a Model 6080 Nusonic Concentration Analyzer. Test solutions were initially spiked with 5 ppm by weight ferrous iron in the form $FeSO_4.7H_2O$ to mimic actual process conditions and to help stabilize the platinum reference electrode (required in the electrochemical tests). No attempt was made to aerate or deaerate the acid solutions. Solution temperatures were maintained to within ± 2°C in all experiments and continuously stirred.

ELECTROCHEMICAL MEASUREMENTS

Electrochemical measurements were performed in a conventional electrochemical cell. All potentials were measured against a bright platinum wire electrode. Rectangular coupons were mounted

according to the ASTM G-5 specification. Potentiodynamic anodic polarization scans were initiated after various exposure times within the first 2 hours. A computer controlled EG&G PARC Model 273 potentiostat polarized the specimens in the anodic direction at 0.1 Vhr^{-1}.

Behaviour of UNS S31603 in Concentrated Sulphuric Acid Solutions

ELECTROCHEMICAL BEHAVIOUR in 98.0 wt.% H_2SO_4

The open-circuit potential is shown as a function of time (immediately after immersion) and temperature in Fig. 1. An increase of temperature from 50 to 200°C changes the potential from a stable relatively noble value to a stable more active value. However the change is not progressive. At the intermediate temperatures the open-circuit potential oscillates over a range which is temperature dependent. Increasing temperature not only greatly increases the frequency of oscillation but it decreases the magnitude of oscillation as the maximum potential becomes progressively more electronegative. Such oscillations have been reported before on a number of occasions [5],[6],[7].

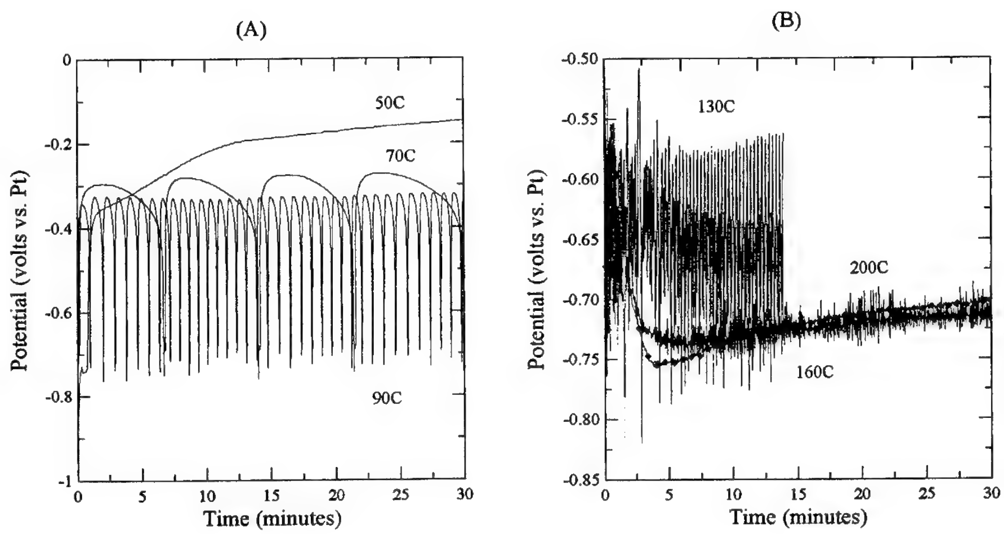

Figure 1 Effect of temperature on corrosion potential of UNS S31603 in 98.0 wt.% H_2SO_4

More information on the oscillating potentials was provided by making potentiodynamic anodic polarization scans at 130, 160 and 200°C, shown in Fig. 2(A). These measurements were made after the samples had been immersed for a 1 h period, with the scans initiated at a potential slightly more electronegative than the minimum observed during corrosion potential measurement. In each of the three curves a broad active/passive transition is noted. The transition is followed by an apparent region of passivity where the current density is relatively independent of potential. However, the passive current shows a complex temperature dependence. 160°C appears to be the least aggressive of the three temperatures tested.

The nature of the potential fluctuations of Fig. 1 can be understood by comparing the potential extremities with the corresponding anodic polarization curve, as is illustrated in Fig. 2(B). It seems reasonable that UNS S31603 may be cycling between an "active" and "passive" condition since the observed maximum and minimum corrosion potentials lie on either side of the apparent anodic nose.

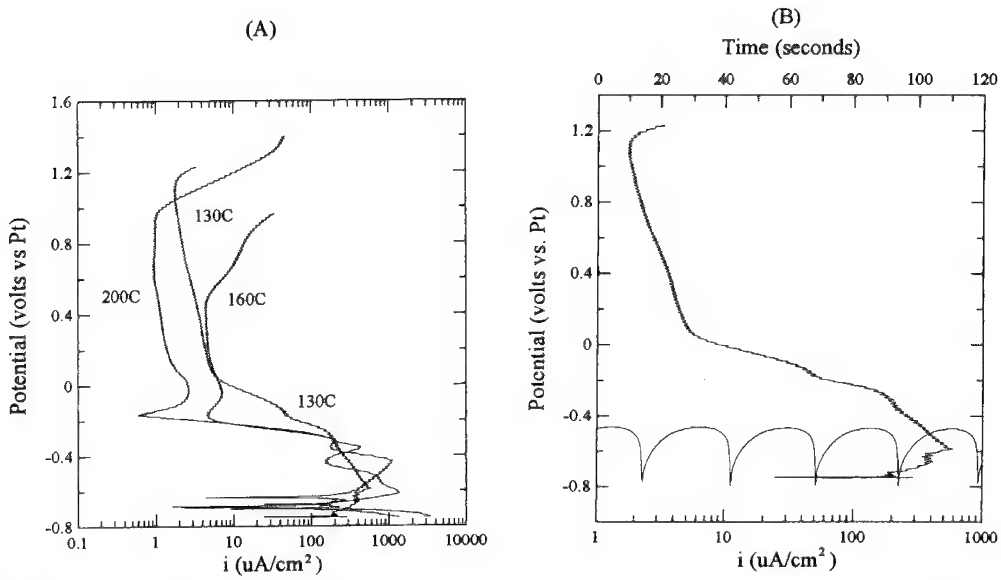

Figure 2 Potentiodynamic anodic polarization of UNS S31603 in 98 wt% H_2SO_4: (A) Effect of temperature, (B) Comparison between the open-circuit and polarization behaviour.

ELECTROCHEMICAL BEHAVIOUR IN 93.5 wt.% H_2SO_4

In the weaker 93.5 wt.% acid, the corrosion potential of UNS S31603 oscillates at an even lower temperature, as shown in Fig. 3(A). Stable passivity is only observed at 40°C, while increasing the temperature from 40 to 70°C results in changes similar to those found in the more concentrated 98.0 wt.% acid at higher temperatures. It is well known that these alloys exhibit less corrosion resistance at lower acid strengths [3]. At any given temperature the frequency of potential oscillation is greater in the weaker acid.

The anodic behaviour in 93.5 wt.% acid is somewhat similar to that observed for the 98 wt.% environment. Fig. 3(B) shows the potentiodynamic anodic polarization curve for UNS S31603 in 93.5 wt.% H_2SO_4 at 60°C to possess an anodic nose and an uneven current density in the apparent range of passivity. The anodic nose appears to be much narrower in this weaker acid environment. Furthermore the current density in the "passive" region is found to have a stronger dependence on potential. The "active/passive" open-circuit condition is more apparent in this acid environment when superimposing the potential behaviour on the anodic polarization curve.

CORROSION BEHAVIOUR

Instantaneous corrosion rates, obtained from polarization resistance measurement for UNS S31603 in the two acid strengths and at various temperatures are shown in Table II. It should be pointed out that the rates quoted are approximate values since the anodic polarization measurement were obtained during the more steady segments of the oscillating potential cycles. These data confirm two previous observations: (a) The 160°C environment appears to be the least aggressive for the 98.0 wt.% acid, and (b) lower temperatures are required in the weaker 93.5 wt.% acid to produce similar corrosion rates in the more concentratad 98 wt.% acid.

Table II.

Polarization Resistance Corrosion Rate of UNS S31603 in Concentrated H_2SO_4

wt.% H_2SO_4	Temperature (°C) / Rate (mpy)*		
98.0	130 / 227	160 / 82	200 / 480
93.5	60 / 4.5	70 / 230	

*Instantaneous rates by Polarization Resistance technique

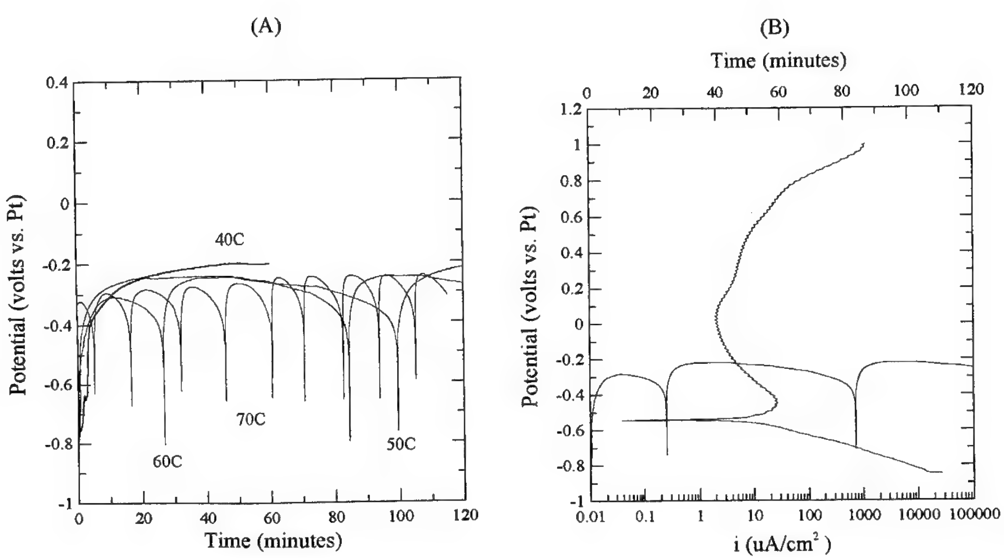

Figure 3 Behaviour of UNS S31603 in 93.5 wt.% H_2SO_4: (A) Temperature influence on corrosion potential vs. time; (B) anodic polarization and corrosion potential at 60°C.

Behaviour of Silicon-containing UNS S30601 in Concentrated Sulphuric Acid Solutions

HISTORY

The use of high silicon iron to improve the corrosion resistance to hot concentrated sulphuric acid solutions dates back to the early part of the century. The problem with these cast alloys is their lack of ductility which severely restricts their application. The beneficial effects of silicon on the corrosion resistance of stainless steel in oxidizing environments has been known for some time [8],[9]. Based on this knowledge, a 5.3 wt.% silicon containing austenitic stainless steel (UNS S30601) was developed to service hot concentrated nitric acid [10],[11]. However it was not until quite recently that the improved corrosion resistance of the alloy to hot concentrated sulphuric acid was realized [12],[4]. The cause of this beneficial effect of silicon in chromium containing steels in concentrated sulphuric acid environments remains to be explained adequately.

INFLUENCE OF SILICON ON THE ELECTROCHEMICAL BEHAVIOUR

The open-circuit potential for both UNS S30601 and UNS S31603 in 93.5 wt.% H_2SO_4 at 60°C is shown as a function of exposure time in Fig. 4. A marked difference in the time dependence of the corrosion potential is observed. The presence of 5.3 wt.% silicon appears to have suppressed the "active/passive" potential oscillations. The corrosion potential for UNS S30601 tends to stabilize at a relatively active potential, following which is a progressive drift towards more electropositive values. Even after 168 hours exposure the open-circuit condition for UNS S31603 remained unstable.

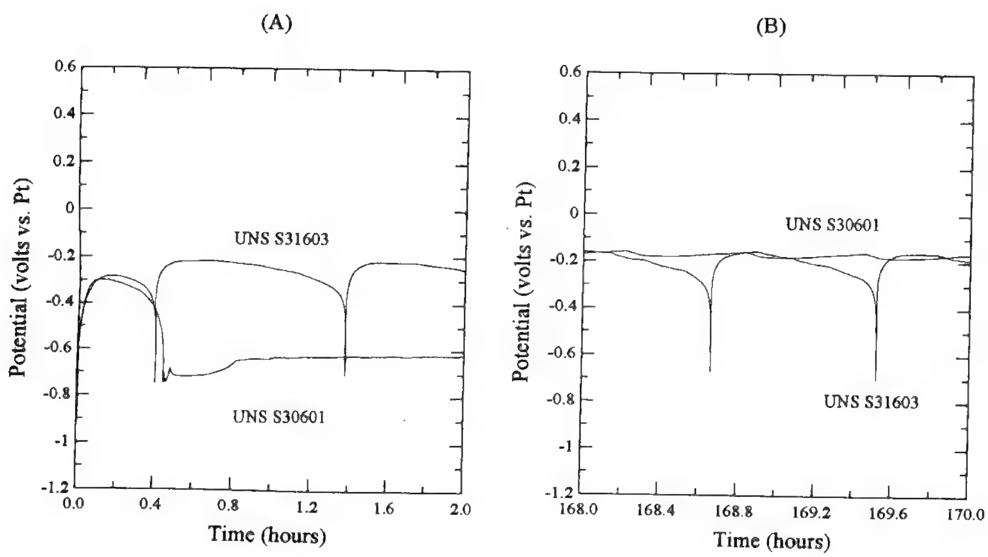

Figure 4 Open-circuit potential for two steels in 93.5 wt.% H_2SO_4 at 60°C, at two windows of time.

The potentiodynamic anodic polarization curves for the two stainless steels in 93.5 wt.% acid environment is displayed in Fig. 5. The silicon-containing stainless steel appears to have superior passivating ability in this environment. Both the anodic nose and the apparent passive region are characterized by lower current densities. Despite the marked differences in both current density and the open-circuit condition, the anodic polarization behaviour is quite similar.

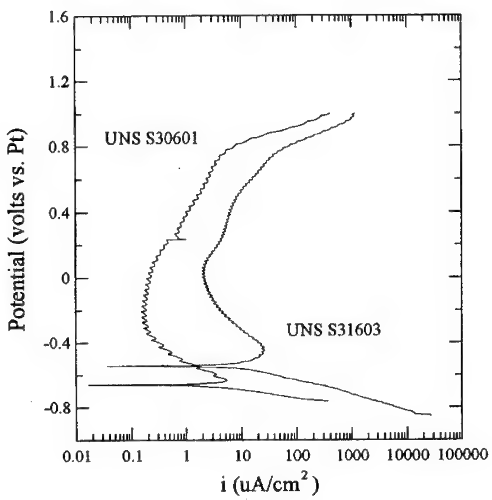

Figure 5 Potentiodynamic anodic polarization curves for two steels in 93.5 wt.% H_2SO_4 at 60°C.

INFLUENCE OF SILICON ON THE CORROSION BEHAVIOUR

Corrosion rates were determined by several techniques including weight-loss, solution iron analysis and polarization resistance. The dissolved iron content of the solution was analyzed spectrophotometrically using 1,10 phenanthroline according to the procedure of Harvey *et al.* [13]. The corrosion data in 93.5 wt.% H_2SO_4 at 60°C for the two alloys is shown in Table III. In all cases the corrosion rate measured for UNS S30601 in this acid environment was strikingly lower. It has been demonstrated that the majority of corrosion occurs during open-circuit potential cycling, when the potential decreases rapidly towards more electronegative potentials, i.e. during the potential "spike". Polarization resistance measurements show the corrosion rate to be 0.5 mpy at the top of the cycle and 4.5 mpy at an intermediate point, whereas the weight-loss data shows the average corrosion rate to be 29 mpy. The difference may certainly be accounted for by the dissolution occurring during the potential "spikes", as originally deduced by Chang [14].

Table III.

Corrosion Rates of Stainless Steel in 93.5 wt.% H_2SO_4 at 60°C (Test Duration: 168 hours).

Alloy	Weight-Loss average (mpy)	Iron Analysis steady state (mpy)	R_p passive state (mpy)	R_p active state[4] (mpy)
UNS S31603	29	32	0.5[2]	4.5
UNS S30601	0.2	---[1]	0.01[3]	2

[1] Rate below detectable level
[2] Rate measured at potential maximum during cycle after 168 hours exposure
[3] Rate measured after 168 hours exposure
[4] Rate measured from anodic polarization curve

Discussion

The cyclic nature of the open-circuit potential behaviour of stainless steel in concentrated sulphuric acid environments has been explained by Matsuhashi *et al.* [15]. The cathodic reaction occurring at the higher potential between the spikes is believed to be given by:

$$5H_2SO_4 + 2H^+ + 6e^- \rightarrow 4HSO_4^- + S + 4H_2O \tag{1}$$

The water produced by this reaction would tend to dissolve the protective film, ultimately returning the alloy to its "active" state. Once activated, the dissolving metal ions immediately reform the film and restore the "passive" state. This process occurs repeatedly, at a distinctive frequency. *In situ* laser Raman spectroscopy (LRS) identified the protective film to be a metal sulphate. This observation is consistant with an earlier study performed by Kuron *et al.* [7]. Auger electron spectroscopy (AES) showed the enrichment of oxygen and sulphur at the surface region and X-ray diffraction (XRD) suggested a film with the composition (Fe, Cr, Ni)$[HSO_4]_2.4H_2O$.

If the above mechanism is correct, it would seem that by moving the site of the cathodic reaction(s) from the stainless steel substrate, cycling could be avoided. Indeed, when UNS S31603 coupons were connected with an iridium wire in both 98.0 wt.% at 160°C and 93.5 wt.% at 60°C, the potential oscillations stopped.

The open-circuit potential behaviour for the silicon-containing UNS S30601 in 93.5 wt.% H_2SO_4 showed no tendency for oscillation at 60°C (see Fig.4) nor at other temperatures tested in the range

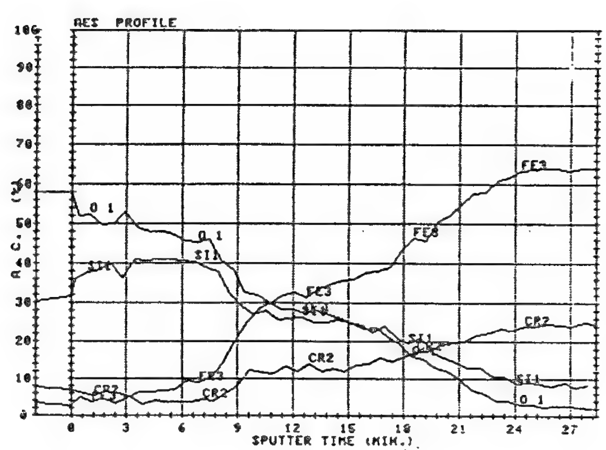

Figure 6 AES depth profile for UNS S30601 after immersion in 93.5 wt.% H_2SO_4 at 70°C for 264 hours.

from 40°C to 70°C. The significance of this stable potential behaviour is reflected in the weight-loss data, which show that the anodic dissolution rates are reduced by two orders of magnitude through silicon addition.

An Auger electron spectroscopic (AES) analysis was performed on a UNS S30601 coupon after exposure to explore the composition of its surface region. The analysis was performed using a Perkin-Elmer PHI 600 scanning Auger microprobe system with the electron gun voltage set at 5 kV. The results are shown in the sputter profile of Fig. 6, indicating that the surface film is rich in silicon and oxygen. Furthermore, no sulphur was detectable in the Auger spectrum. From the energy of the observed silicon peak, it is concluded that silicon is most likely present in the form of SiO_2. Surprisingly, chromium is clearly not accumulated in this surface layer, suggesting it is not playing a major role in the formation of a protective layer. The deleterious nature of the cathodic reaction(s) in concentrated sulphuric acid, which is so prominent with non-silicon containing stainless steel, appears to be minimized by the formation of a silicon-rich oxide film on the silicon containing stainless steel.

Acknowledgements

The financial support of the Natural Sciences and Engineering Research Council of Canada is gratefully appreciated, both in the provision of experimental supplies and in the provision of a student stipend (JRK). Samples were provided by Chemetics International Ltd. Special thanks are accorded to G.M. Cameron of Cecebe Technologies Ltd. for the permission to use some of the data.

References

[1] G.M. Cameron, Chem. Eng. Prog., **78**, 71 (1982).
[2] D.R. McAllister *et al.*, Chem. Eng. Prog., **77**, 34 (1986)
[3] M.G. Fontana, Ind. Eng. Chem., **44**, 89A (1952).
[4] M. Davies *et al.*, Sulphur 88, The British Sulphur Corporation Ltd., London, 1988
[5] R.M. Kain and P.E. Morris, Paper # 149, CORROSION 76, NACE, Houston.
[6] H.S. Tong, "Electrochemical Corrosion Testing", ASTM Special Technical Publication No. 727, 109 (1981).
[7] D. Kuron *et al.*, Werkst. Korros., **36**, 489 (1985).
[8] H. Coriou *et al.*, Revue Metall., **61**, 177 (1964).
[9] J.S. Armijo and B.E. Wilde, Corros. Sci., **8**, 649 (1968).
[10] E.-M. Horn and A. Kügler, Z. Werkstofftech.8, **11**, 362 (1977).
[11] E.-M. Horn and G. Hochörtler, ICMC Toronto, **2**, 444 (1984)
[12] F.W.S. Jones, US-Patent No. 4 543 244, 1985.
[13] A. E. Harvey *et al.*, Analytical Chemistry, **27**, 1 (1955).
[14] Y.-S. Chang, PhD Thesis, University of Cambridge, 1984.
[15] R. Matsuhashi *et al.*, Corros. Eng. **36**, 531 (1987).

Materials Science Forum Vols. 185-188 (1995) pp. 897-906

The effects of electrolyte structure on the passivation of chromium

B. Stypula

University of Mining and Metallurgy, ul. Reymonta 23, Kraków, Poland

Keywords: Chromium, anodic passivation, x-ray photoelectron spectroscopy

Abstract

The passivation of chromium has been studied by means of potentiostatic and chronopotentiostatic technique in aqueous and anhydrous sulphuric acid solutions. The X-ray photoelectron spectroscopy (XPS) were used to study the structure of passive films.

The composition of passive films and the dependence of passivation parameters on electrolyte structure allow us to propose the mechanism in concentrated and anhydrous solutions in which hydrosulphate ions and undissociated acid molecules are source of oxygen in the passivation process.

Introduction

The passivation of chromium in acid sulphate solutions has been a subject of numerous investigations, because of its practical importance in corrosion resistance of stainless steels and alloys [1-3]. Systematic studies seem to concern , however, the anodic passivation of chromium in dilute solutions only (with activity water equal to 1) where the passivation proceeds with the participation of water molecules [4-7]. The objective of this paper is the study of the passivity processes in the solutions with different activities of water and anhydrous solutions. We intend to explain the influence of physico-chemical properties of solutions on the mechanism of passivation process.

Experimental

The electrochemical investigation of chromium were performed by means of potentiostatic and chronoamperometric technique. The X-ray photoelectron spectroscopy (XPS) were used to study the structure of passive film [18]. The XPS spectra were recorded on a VG Scientific ESCA-3 photoelectron spectrometer. The indepth analysis was performed by removing outer layer (A) by sputtering with Ar^+ ions (inner layer B). An aqueous calomel electrode was used as reference electrode in aqueous solutions. In anhydrous organic environments the Ag/AgCl electrode in organic solvent was applied. The anhydrous solutions were prepared with anhydrous solvents - dimethylformamide, formamide, formamide containing non more than 0.02% water (the quantity of water was controlled by Karl-Fischer method) - and with anhydrous sulphuric acid.

The structure of aqueous sulphuric acid solutions.

The physical chemistry of sulphuric acid has been examined in great detail because of its importance in catalysis, electrochemical and galvanic processes [8-10].

Fig.1. presents the structure of aqueous solution of sulphuric acid. This diagram shows the changes of several quantities (the concentration of anions, of undissociated acid molecules, of free water molecules [11], the Hammett acidity H_0 and logarithm activity of water [12]) as a function of molar acid concentration. Fig. 2 according to Hoegfeldt [13] displays domains of various species of proton hydrated complexes that are determinated by the equilibrium:

$$H^+ + n\,H_2O = H(H_2O)_n^+ \qquad n = 1,2,3,....n$$

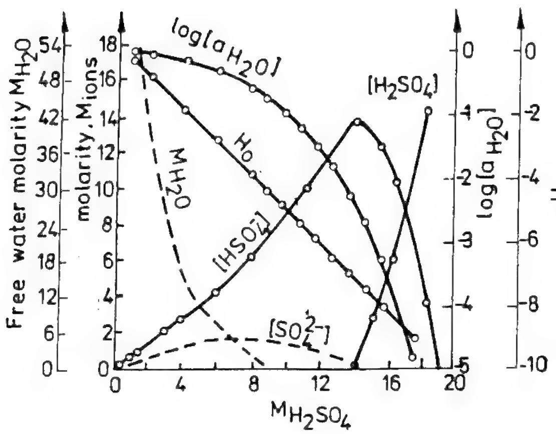

Fig. 1. The structure of sulphuric acid solutions, [11, 12]

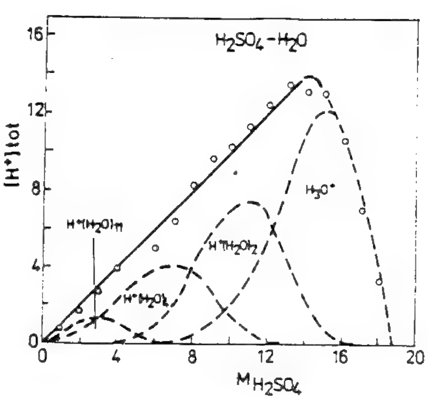

Fig. 2. The Hoegfeldt diagram, [13].

On the above diagrams can be distinguished three ranges:
- diluted solutions ($c<8$ M) where free water molecules (not bound in the coordinating shell of hydrogen ions) exist,
- middle concentrations ($8<c<14$ M) in which [HSO_4^-] ions predominate and water molucules are bound in the proton complexes $H^+ (H_2O)n$, where $1<n<4$,
- higher concentrations solutions ($c>14$M), where undissociated acid molecules appear and water molecules are bound in hydrogen ion complex H_3O^+.

Water molecules are bound most strongly in H_3O^+ ion. The standard Gibbs energy of formation of $H_3O^+_{(g)}$ (from $H^+_{(g)} + H_2O_{(g)}$) equals about - 170 kcal. [14]. The next three water molecules in the complex $H_9O_4^+$ are also relatively strongly bound. Their interaction energy is estimated to be about 45 kcal / bond. Water molecules in hydrated ions with $n > 4$ are known as free, because their binding energy is low. They appear in solutions having the molar ratio acid/water less than 1/4, which corresponds to concentration less than 8 M H_2SO_4.

The redox potential of aqueous solutions of sulphuric acid.

The passivation action of concentrated solutions of sulphuric acid with simultaneous reduction of the acid to SO_2 has been observed at the beginning of the 20th century. In much later studies of the corrosion alloys Fe-Si-Cu [15] and Hastelloy [16, 17] it has been demonstrated that the corrosion potential increase sharply with the increases of acid concentration (particularly above 53% H_2SO_4). This has been ascribed also to the reduction of the acid to SO_2 , S or H_2S.The mechanism of this process, however, has not been explained. Investigations of the stationary potential of the platinized platinum electrode in sulphuric acid solutions Fig. 3. [17, 18] show two domains of linear dependence of the potential on the acidity (pH,H_0).

The first sector appears for concentrations lower than 8 M with the slope $\partial E/\partial pH = -0.059$ (e.i. $\partial E/\partial H_0 = -0.022$) and it coincides with the slope of the hydrogen electrode H^+/H_2. The second zone is observed at higher concentrations ($c>8$ M) with the slope $\partial E/\partial H_0 = -0.117$ and is most likely related with reduction reactions of acid molecules and their anions to sulphur compounds (having valences

lower than 6). Figure 4 presents the potential - acidity (H_0) diagram for those redox equilibria of undissociated acid molecules and HSO_4^- -ions that are shown in Table 1.

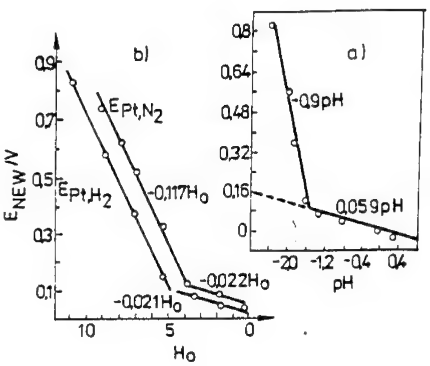

Fig. 3. Dependence of platinum potential on pH (a) [17] and H_0 (b) [18], E_{pt,H_2} - potential in hydrogen atmosphere, E_{pt,N_2} - in nitrogen atmosphere.

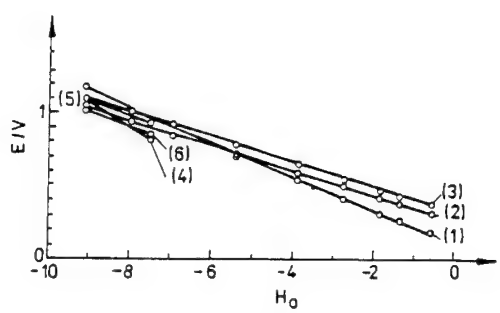

Fig. 4. The potential - acidity (H_0) for redox equilibria in H_2SO_4-H_2O system.

The experimental values of the slope ($\partial E/\partial H_0$) of the platinum potential (at c > 8 M) seem to correlate most likely with the reduction of HSO_4^- ions to SO_2 (Table 1, Eq. 1).

Table 1 The redox equilibria in H_2SO_4-H_2O system [19].

Eq. Number	Reactions	$\partial E/\partial H_0$, at p(SO_2, H_2S) =1atm
1	$HSO_4^- + 3H^+ + 2e = SO_2 + 2H_2O$	-0.124
2	$HSO_4^- + 7H^+ + 6e = S + 4H_2O$	-0.091
3	$HSO_4^- + 9H^+ + 8e = H_2S + 4H_2O$	-0.083
4	$H_2SO_4 + 2H^+ + 2e = SO_2 + 2H_2O$	-0.154
5	$H_2SO_4 + 6H^+ + 6e = S + 4H_2O$	-0.093
6	$H_2SO_4 + 8H^+ + 8e = H_2S + 4H_2O$	-0.103

In addition the presence of SO_2 in the electrolytic cell [18] suggests that among all thermodynamically possible reactions, a dominant role is played by the reaction with SO_2 evolution. In the case of higher concentrations (c > 14 M) when appear undissociated acid molecules, the redox potential is accepted to be determined by both the reduction of ions HSO_4^- and molecules H_2SO_4. The reductions of the SO_4^{-2} ions not taken into account because of their significant stability [20] and the complete lack of those ions in solutions above 14 M H_2SO_4.

Anodic behaviour of chromium in aqueous solutions - nature of passive films.
The chromium undergoes passivation in the whole range of the sulphuric acid concentration. The anodic polarization curves (Fig. 5,6,7) are characterized by sharp active passive transition, wide passivation area, clearly marked transpassive range.

In addition it has been observed (in chronoamperometric measurements) that the current density in the passivation range does not depend on the rotation of chromium electrode (Fig. 8). The shape of anodic curves and their independence on rotation of electrode indicate on the oxide nature of passive films. This has been supported by the Photoelectron Spectroscopy (XPS) analysis of passive layers.

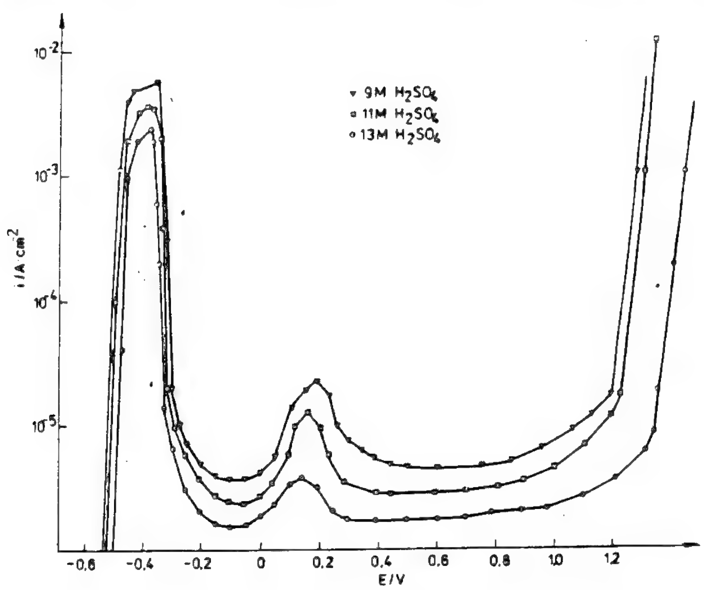

Fig. 5 The potentiostatic anodic polarization curves of chromium in aqueous sulphuric acid solutions.

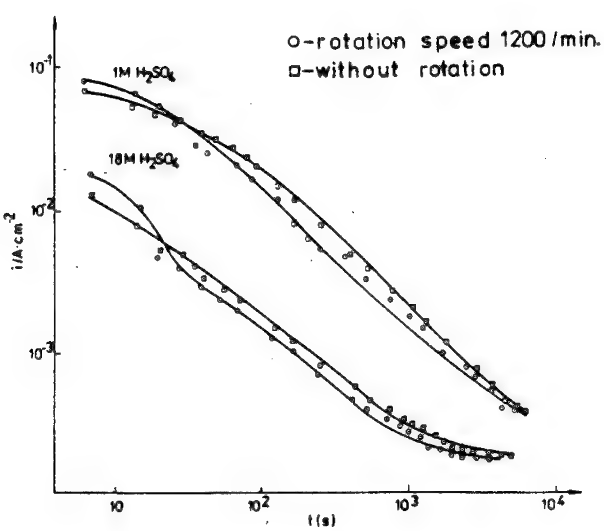

Fig. 6. Chronoamperometric curves of chromium in aqueous sulphuric acid solutions at E=0.8V.

The XPS spectra (Fig. 7, 8, 9) revealed the oxy-hydroxide chromium III in the passive films irrespective of the acid concentration. The only significant difference is the presence of sulphur species at valences lower than six in those passive films grown in higher concentrations of acid (c > 8 M).

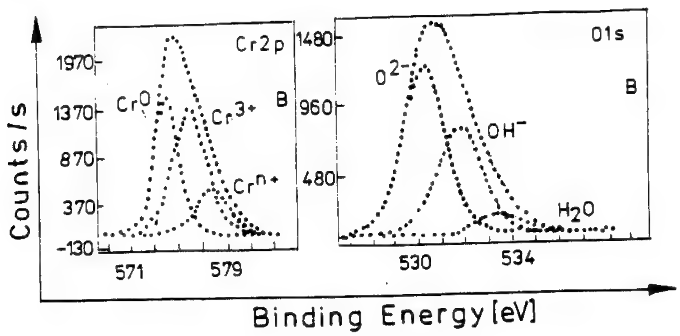

Fig. 7. XPS spectra from inner layer of chromium (B), formed in 1 M H_2SO_4 at E= 0.8V.

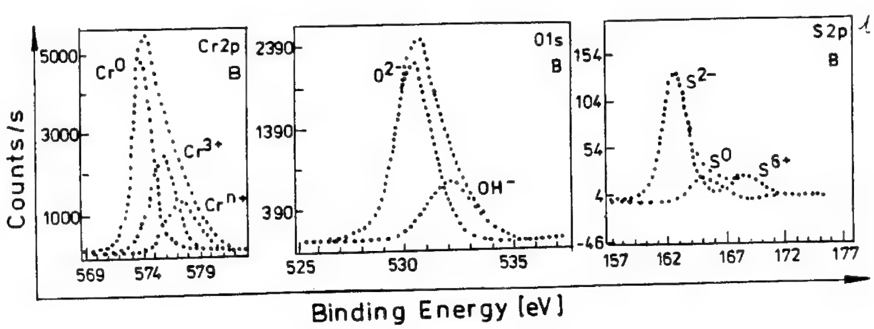

Fig. 8. XPS spectra from inner layer of chromium (B), formed in 8 M H_2SO_4 at E= 0.8V.

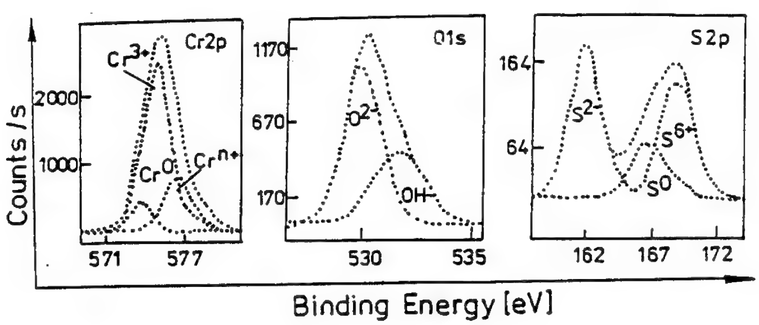

Fig. 9. XPS spectra from outer layer of chromium (A), formed in 18 M H_2SO_4 at E= 0.8V.

The presence of sulphur compounds on lower oxidation state in the passive layer is an evidence that acid molecules and/or its anion undergoes reduction in the passivation process.

The thermodynamically possible reactions of chromium in sulphuric acid environments.
As well know, the metalic chromium is thermodynamically unstable in contact with water. Water molecules can act as an oxidizing agent with respect to chromium surface. Standard Gibbs energy of chemical reactions (Eq. 7-9) is negative, Table 2.

Table 2. Standard Gibbs energy of chemical reactions of chromium in sulphuric acid environments.

Eq. Number	Reactions	ΔG^0[kcal]
7	$Cr + 3H_2O = Cr(OH)_3 + 3/2H_2$	-41.5
8	$2Cr + 3H_2O = Cr_2O_3 + 3H_2$	-80.3
9	$Cr + 3H_2O = CrOOH + 3H_2$	-46.9
10	$2Cr + 3H_2SO_4 = Cr_2O_3 + 3SO_2 + 3H_2O$	-113.8
11	$4Cr + 6H_2O = 4Cr(OH)_3 + 6SO_2$	-227.9
12	$Cr + HSO_4^- = CrOOH + SO_2$	-54.3

Sulphuric acid molecules and hydrogen sulphate ions may be compared relatively with water. The values of Gibbs energy of chemical reactions of chromium with above components (Eq. 10-12) are also negative. This indicate that acid molecules and HSO_4^- ions can be oxidizing agent too. It is likely that acid molecules and hydrogen sulphate ions similarly to water can be a donor of oxygen in the anodic passivation process.

The parameters of chromium passivation in aqueous solutions of sulphuric acid.
The dependences of passivation parameters, the passivation potential E_p (Fig. 10), and the critical anodic current density i_k, (Fig. 11), on acid concentrations marked three different ranges. Those ranges correspond to the three areas that appear on the diagram of sulphuric acid solutions (Fig. 1): diluted solutions (c<8M), middle concentrations (8<c<14) and higher concentrations c >14 M.

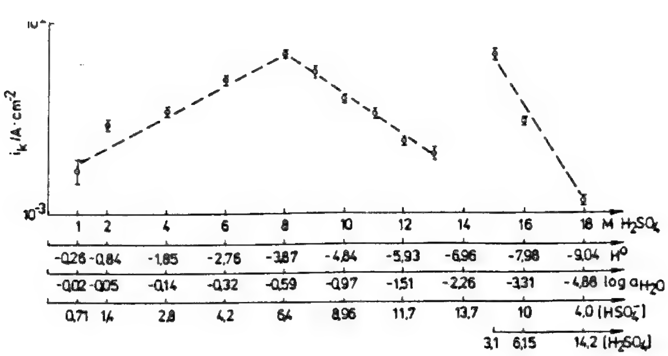

Fig. 10. The critical current density of chromium in sulphuric acid solutions.

The approximation by a linear dependence of passivation parameters on log a_{H2O}, H_0, $[HSO_4^-]$, $[H_2SO_4]$ in each of the three domains (using the least square method) allowed us to find a factor that determines the passivation processes.

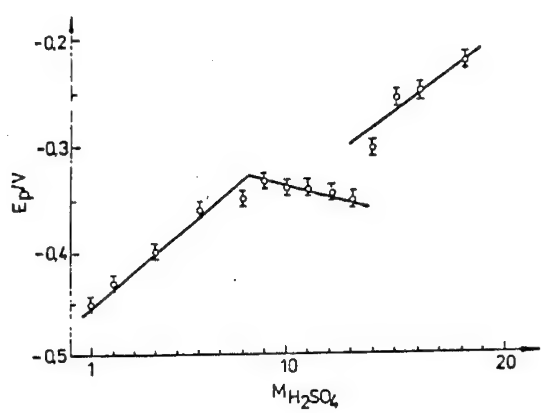

Fig. 11. The passivation potential of chromium in sulphuric acid solutions.

In diluted solutions, the passivation potential E_p and critical anodic current density (Fig. 12) depend linearly on log a_{H2O}. This confirms a dominant role of water molecules in the passivation process according to the total reaction:

$$Cr + 2H_2O \rightarrow CrOOH + H^+ + 3e \quad (13)$$

where CrOOH is produced (as shown by XPS analysiss). The mechanism of this process, involving water molecules proceeds (according to Okuyama) in two steps:

$$Cr + H_2O \rightarrow CrOH_{ad} + H^+ + e \quad (14)$$
$$CrOH_{ad} + H_2O \rightarrow CrOOH + 2H^+ + 2e \quad (15)$$

In the middle range of concentration, the passivation potential and the anodic current density (Fig. 13) linearly depend on the logarithm of HSO_4^- ions. The above dependences and the composition of the passive layer (CrOOH with sulphur species on the lower valencies S^{+4}, S^0, S^{-2}), Fig. 7, allow one to conclude that the passivation process in these range is related with HSO_4^- ions and their oxidative ability and it is described by the overall reaction:

$$Cr + HSO_4^- \rightarrow CrOOH + SO_2 + e \quad (16)$$

The above passivation process can proceed via analogy to the mechanism involving water molecules, with the one-electron transition (in the first step):

$$Cr + HSO_4^- \rightarrow Cr(HSO_4)_{ad} + e \quad (17)$$

and chemical reaction in the second step:

$$Cr(HSO_4)_{ad} \rightarrow CrOOH + SO_2 \qquad (18)$$

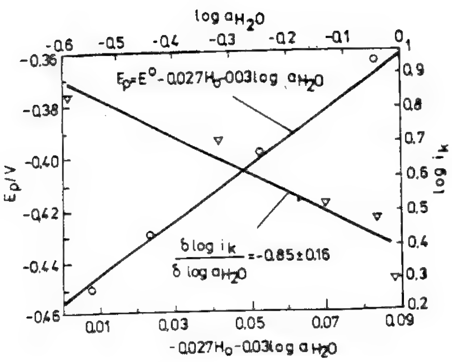

Fig. 12. Dependence of E_p and i_k on the logarithm a_{H2O} and H_0, c<8M

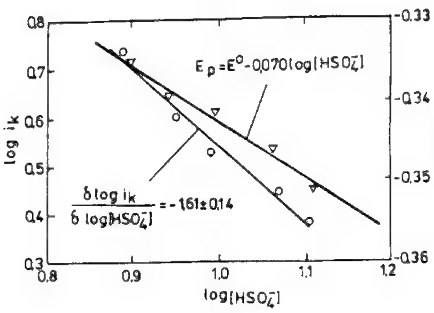

Fig. 13. Dependence of Ep and i_k on the logarithm $[HSO_4^-]$, 8M<c<14M.

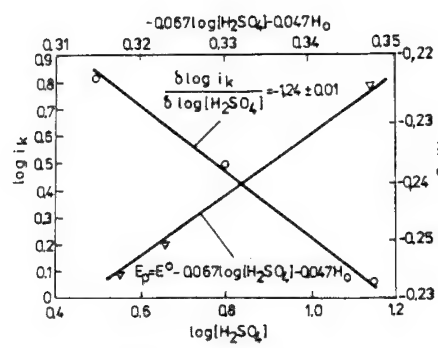

Fig. 14. Dependence of E_p and ik on the logarithm $[H_2SO_4^-]$ and H_0, c>14M

In higher concentration range, the passivation potential and the logarithm of the critical current density, (Fig. 14) are linear functions of the logarithm of undissociated acid molecules.

The above relations and the composition of passive film (CrOOH with S^{+4}, S^0, S^{-2}) are in agreement with the total reaction:

$$Cr + HSO_4^- \rightarrow CrOOH + SO_2 + H^+ + e \qquad (19)$$

Similarity to the hitherto discussed cause of the passivation with HSO_4^- ions suggests the following mechanism involving H_2SO_4 molecules:

$$Cr + H_2SO_4 \rightarrow Cr(HSO_4)_{ad} + H^+ + e \qquad (20)$$
$$Cr(HSO_4)_{ad} \rightarrow CrOOH + SO_2 \qquad (21)$$

Anodic behaviour of chromium in organic solutions of sulphuric acid.
In anhydrous organic solutions the sulphuric acid shows an oxidizing behaviour and the passivation action on chromium surface, Fig. 15.
This actions takes place in the solvent characterized by small dielectric constant, ε_{DMF}= 36.7 (where the sulphuric acid is not completely dissociated) and in a solvent with higher dielectric constant, $\varepsilon_{Formamid}$ = 109.5 (and completely dissociated acid). The above implies that both undissociated acid molecules and HSO_4^- ions are the passivation agents.

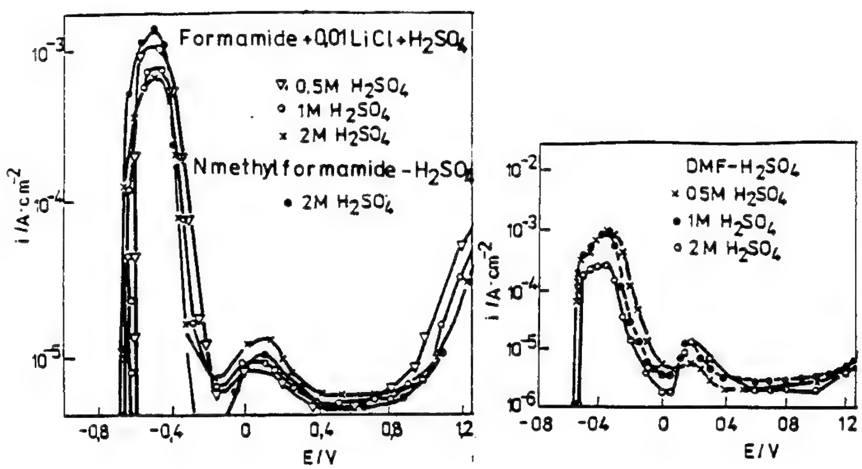

Fig. 15. Anodic polarization of chromium in anhydrous organic acid solutions.

The XPS analysis of the anodic passive layer, Fig. 16, shows that passive film consists of chromium III oxy-hydroxide with a small amount of S^{+4}..S^{-2}, analogous to the passive films in concentrated aqueous solutions. A similar composition of the anodic passive films in both systems alows one to conclude that the mechanism of the passivation process in these systems is similar and proceed with the participation of HSO_4^- ions or H_2SO_4 molecules according to the reactions (Eq. 16-18 or 19-21)

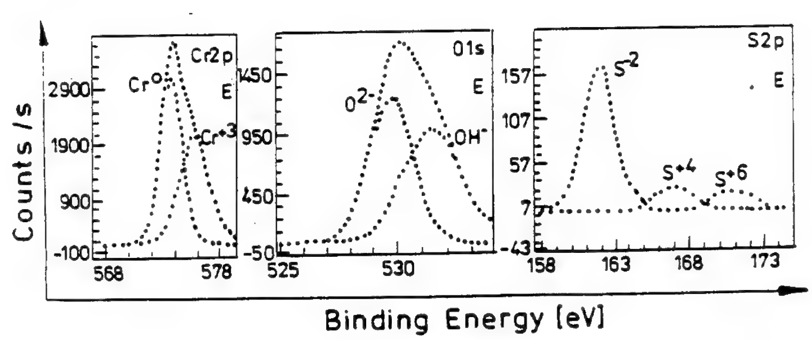

Fig. 16. XPS spectra from inner layer of chromium, formed in 1 M H_2SO_4 - formamide solution.

Conclusions

The chromium is subjected to the oxy-hydroxide passivation in the aqueous and anhydrous sulphuric acid solutionns. The role of donor of oxygen in the passivation process can be played not only by water molecules according to the established view but also by oxy-acid molecules and its oxy-anions (HSO_4^-).

The source of oxygen in the passivation process depends on the electrolyte structure and the thermodynamic stability (oxidizing ability) of acid.

References

1. K. Sugimoto, S. Matsuda, Mater. Sci. Eng. 42, 181, (1980).
2. N. Ramasubramanin, N. Preocanin, R.D. Davison, J. Electrochem. Soc. 132, 798, (1985).
3. R.L. Chance and S.W. Gaarenstroom, Corrosion 36, 94, (1980).
4. M.Okuyama, M. Kawakami, I. Ito, Electrochim. Acta 30, 757, (1985).
5. Bjonrnkwist, I. Olefiord, Corrosion 32, 231, (1992).
6. T.P. Moffat, R.M. Latanision, J. Electrochem. Soc 138, 1869, (1992).
7. J.A.L. Dobbelaar, E.C.M. Hernan, I.H.W. De Wit, Corros. Sci. 33, 765, (1992).
8. E.A. Long, M.A. Paul, Chem. Rev. 57, 935, (1957).
9. G. Siali, L.Giuffre, P.M. Spaziante, Trans Faraday Soc. 9, 2179, (1976).
10. H.S. Harned, W.J. Hamer, J. Amer. Chem. Soc. 57, 27, (1935).
11. W.J. Hamer, The Structure of Electrolytic Solutions, J. Wiley, New York (1956).
12. E. Hoegfeldt, Acta Chem. Scan. 14, 1643, (1960).
13. E. Hoegfeldt, Acta Cientif. Venezolana 17, 13, (1966).
14. B. E. Conway, Modern Aspect of Electrochem. 3, 43, London (1964).
15. T.E. Evans, A.C. Hart, Electrochim. Acta 16, 1955, (1971).
16. M.A.El. Zeky, Z. Szklarska-Smialowska, E. Lunarska, Corrosion 43, 656, (1987).
17. N.Sridhar, Proc. Conf. Sulphur 85, British Sulphur Corp. London (1985).
18. B. Stypula, J. Banas, Electrochim. Acta 38, 2309, (1993).
19. M. Pourbaix, Atlas of Electrochemical Equilibria in Aqueous Solutions, Houston (1974).
20. Ch.H. Paterson, R.P. Messmer, J. Amer. Chem. Soc. 112, 4138, (1990).

Materials Science Forum Vols. 185-188 (1995) pp. 907-916

A model for the passivation of bismuth in concentrated sulphuric acid solutions emphasizing the structure and properties of the anodic layer

M. Bojinov[1], Tz. Tzvetkoff[2] and A. Girginov[3]

[1] Central Laboratory of Electrochemical Power Sources, Bulgarian Academy of Sciences, BG-1113 Sofia, Bulgaria

[2] Elchem Engineering Laboratory, Sofia University of Technology, BG-1156 Sofia, Bulgaria

[3] Department of Physical Chemistry, Sofia University of Technology, BG-1156 Sofia, Bulgaria

Keywords: Passivation, photoelectrochemistry, AC impedance, kinetic model, space charge, bismuth electrode

ABSTRACT

The passivation of bismuth metal in concentrated H_2SO_4 solutions is investigated within the frames of a study of the initial stages of anodic film formation on metals and alloys. Voltammetric, AC impedance and photocurrent measurements combined with *ex-situ* surface analysis techniques are used to assess the passivation mechanism and to characterize anodic film properties.

It is established that at low overpotentials, active dissolution of bismuth to produce aquoions takes place. For overpotentials higher than 100 mV, owed to a saturation process, the precipitation of a porous salt layer of $Bi_2(SO_4)_3$ proceeds. As this layer covers most of the surface, alkalization in its pores leads to a formation of basic sulphates and finally bismuth oxide, Bi_2O_3, which is a semiconductor and has photoelectrochemical properties. A model for the passive state of bismuth is proposed reproducing successfully the impedance spectra in the region of passivity. It emphasizes a two-sublayer structure of the anodic film comprising a barrier sublayer at the metal side and a porous salt sublayer at the solution side.

INTRODUCTION

The investigations of the electrochemistry of bismuth were essentially limited to the determination of the conditions of anodic oxide films formation in various electrolytes using both galvanostatic and potentiostatic methods[1-6]. A high field migration mechanism was found to be consistent with the experimental results obtained.

On the other hand, investigations of the corrosion and the anodic behaviour of Bi in acid solutions are scarce [1,2]. No detailed mechanism of the corrosion and active dissolution processes was advanced in H_2SO_4 solutions, and no intensive studies of the active to passive transition were carried out.

The aim of the present study is to investigate the passivation, as well as the passive state of Bi in H_2SO_4 solutions. A model of the passive Bi electrode will be attempted.

EXPERIMENTAL

Electrodes and solutions

Disc shaped Bi electrodes were used prepared by inserting a high purity Bi rod (99,999%) into a teflon holder. The exposed area of the disc was 0.8 cm^2. The electrode pretreatment consisted of mechanical polishing with finer grade emery paper, degreasing with methanol and thorough washing with distilled water. A conventional three - electrode glass cell was used. A platinum plate with area of ca. 15 cm^2 served as a counterelectrode and a $Hg/Hg_2SO_4/K_2SO_4$ (sat.) reference electrode was employed (E_{ref} = 0.67 V vs. the SHE). The electrolyte (4.5 M H_2SO_4) was prepared from concentrated H_2SO_4 (p.a. Merck) and bidistilled water.

Apparatus and procedure

A computer driven Solartron 1286/1250 system was used for linear sweep voltammetry and ac impedance measurements in the frequency range 0,01 Hz - 65 KHz with a signal amplitude of 2 mV(rms).The photoelectrochemical measurements were accomplished with a setup consisting of a Bank POS 73 Potentioscan, a PAR 186A lock-in amplifier and a mechanical chopper. A 100 W halogen lamp served as a light source and monochromatic illumination was ensured via a 7300 grating monochromator (Applied Photophysics). This setup allowed the out-of-phase component of the photocurrent (modulation frequency 30 Hz) to be monitored as a function of potential and time using fast analog-to-digital converters (ProMicS). The *ex situ* CuK_α X-ray diffractograms (2θ range, 20 - 60^o) were obtained with a Philips APD 15 diffractometer .The samples were washed with distilled water and dried prior to surface analysis.

RESULTS

LSV and photoelectrochemical measurements

A linear sweep photovoltammogram of a Bi electrode in 4,5 M H_2SO_4 (scan rate 1 $mV.s^{-1}$, wavelength 380 nm) is presented in Fig.1.In the anodic sweep, a peak A_1 is observed at -0.2 V related to the nucleation and growth of a passive layer on the electrode surface. The current falls gradually to a value about two orders of magnitude smaller than the peak one. For potentials more positive than 0 V, a new rise in the current is observed and a further anodic peak A_2 is reached at 0.6 V, its intensity being far less than the intensity of the first peak. The current decreases slowly afterwards up to the end of the sweep(1.5 V). In the reverse sweep, the current remains almost constant down to 0.2 V, and after a slight decrease reproduces the A_1 peak. The onset of the photocurrent is situated at about 0.1 V, i.e. at the beginning of the second current rise, and increases in a quasi-linear fashion up to the anodic sweep limit. The photocurrent registered during the reverse scan is slightly higher than the forward photocurrent. The whole shape of Fig.1 suggests that a new phase is formed on the electrode at potentials higher than 0.1 V. This phase exhibits photoelectrochemical properties.

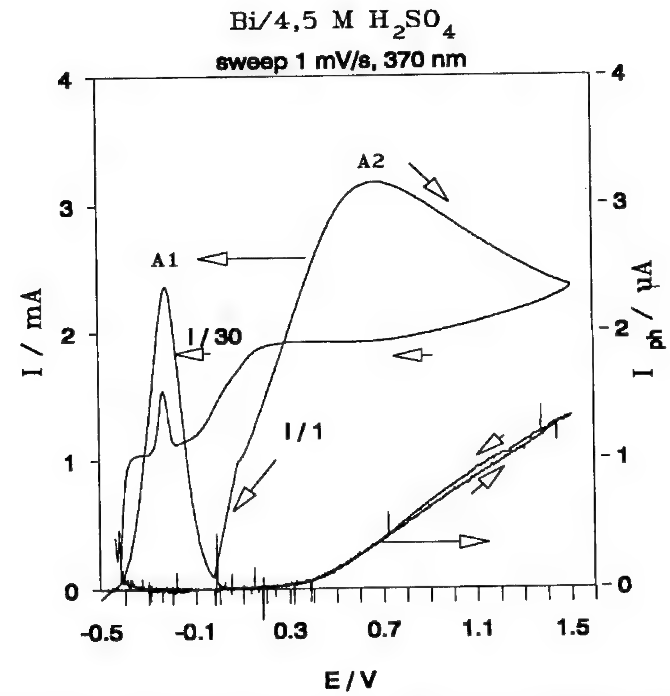

Fig.1. Photoelectrochemical linear sweep voltammogram of a Bi electrode in 4.5 M H_2SO_4 (scan rate 1 $mV.s^{-1}$).

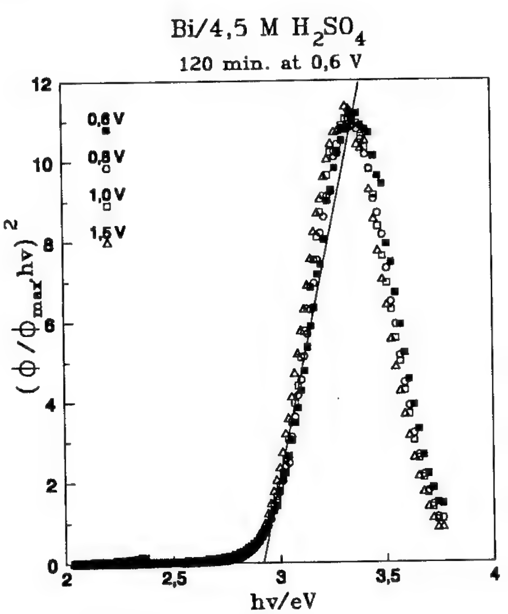

Fig.2. Photocurrent spectra of a Bi electrode at various anodic potentials in 4.5 M H_2SO_4.

Photocurrent spectra were registered after an oxidation of a Bi electrode in 4.5 M H_2SO_4 for 2 h at various potentials in the vicinity and after the A_2 maximum. A set of spectra are presented in Fig.2 in photocurrent efficiency coordinates. The photocurrent efficiency Φ was normalized to its maximum value (Φ_{max} = 10%) in order to allow better comparison of data at different potentials. The coincidence of the spectra suggests that no significant alteration of the properties of the photoactive phase takes place in the potential region studied.

For a direct allowed transition of electrons through the band gap(E_g), the following relation between efficiency and light energy is expected to hold

$$[(\Phi/\Phi_{max})h\nu]^2 = A(h\nu - E_g) \qquad (1)$$

Such plots are presented in Fig.2. From the intercepts of the obtained straight lines with the abscissa a mean value of E_g = 2.9±0.05 eV is obtained. This value is close to the one calculated by a number of workers [7-9] for anodic Bi_2O_3 films(2.8 eV). Thus it can be suggested that the photoactive layer formed on Bi in 4.5 M H_2SO_4 for potentials higher than 0 V is Bi_2O_3.

Ex-situ surface analysis of the anodic layer

An *ex-situ* X-ray diffractogram of the anodic layer formed on Bi after a 2 h oxidation in 4.5 M H_2SO_4 at 0 V is presented in Fig.3.

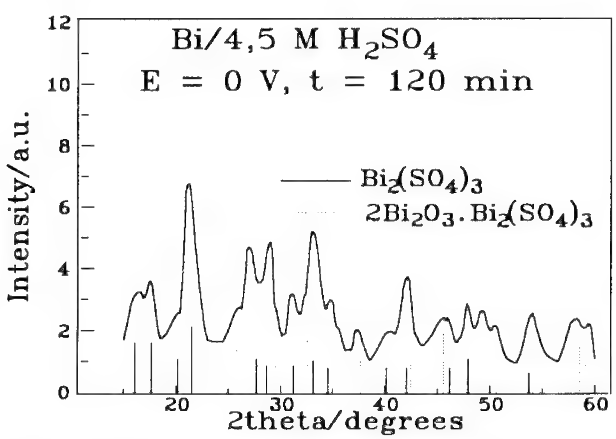

Fig.3. Cu-K_α X-ray diffractogram of a Bi electrode following a 120 min. oxidation at E = 0 V.

In all the potential range studied, similar diffraction patterns are observed. The main phase detected in the anodic layer is $Bi_2(SO_4)_3$. Its standard powder diffraction pattern (JCPDS 1987) is included in the figure with solid lines. It can be concluded that the electrochemically obtained $Bi_2(SO_4)_3$ does not differ substantially from the chemically produced one. The second crystalline phase which can be detected with X-ray diffraction in the investigated potential region is the bioxyde-sulphate-hydrate of bismuth $2Bi_2O_3.Bi_2(SO_4)_3.4H_2O$. Its standard diffraction pattern(JCPDS 1987) is also presented in Fig.3 with dashed lines. A conclusion can be drawn that

not all the lines of this compound are detected and that the relative intensities of the observed peaks diverge substantially from the standard ones, i.e. the electrochemically formed basic sulphate crystals diverge from the chemically obtained ones.

AC impedance measurements

Two series of impedance spectra of a Bi electrode in 4.5 M H_2SO_4 in the passivation region (-0.3 / 0. 1 V) and in the passivity region (above 0.1 V) are collected in Fig.4-5.

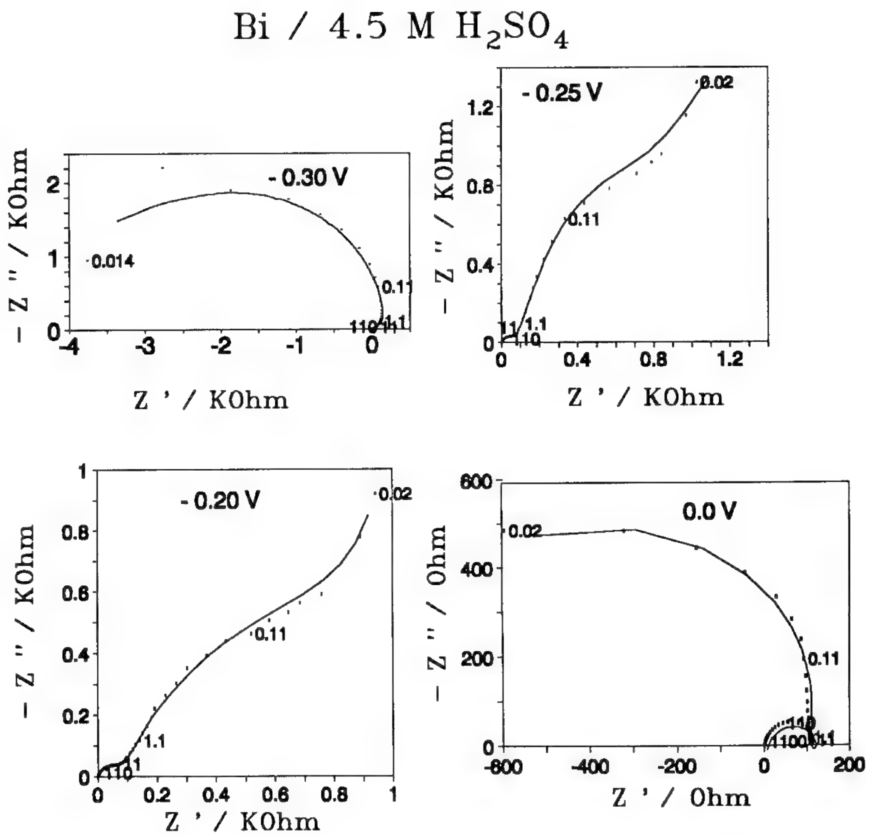

Fig.4. A series of AC impedance spectra of a Bi electrode in the passivation region (-0.3/0 V). Parameter is frequency in hertz. Solid lines are smoothing results.

At -0.3 V(first spectrum in Fig.4) a passivation process is evident by the real part of the impedance bending to the negative real axis. Spectra at -0.25 and -0.20 V exhibit features of metal dissolution limited by ion transport through a porous salt layer blocking most of the surface. At a potential of 0.0 V, a secondary passivation process takes place probably related with the formation of Bi_2O_3 (the real part of the impedance function bending again towards negative values, last

spectrum in Fig.4). A general conclusion is that the passivation process is at least a two step one. A mechanism of this process will be attempted in further studies.

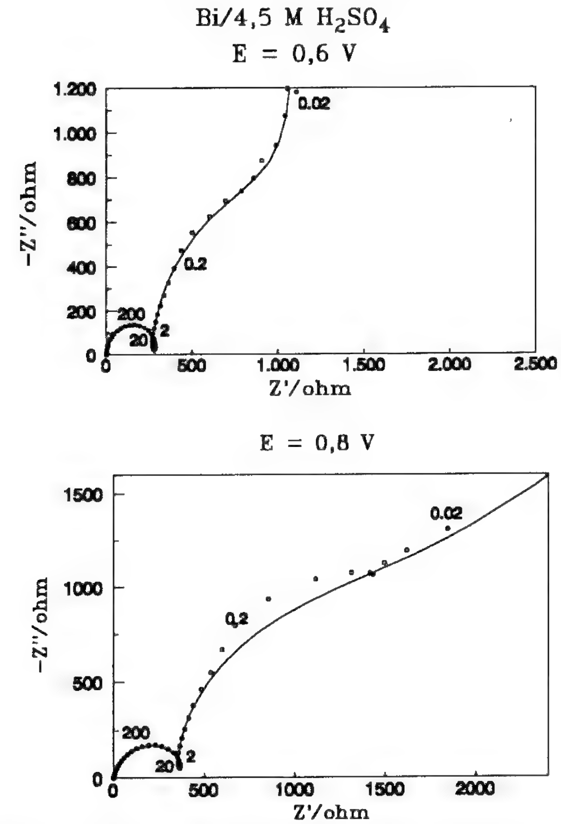

Fig.5.AC impedance spectra of a Bi electrode in 4.5 M H_2SO_4 in the passivity region(above 0 V). Solid lines are simulations according to the model outlined in the Discussion section.

In the passivity region, two capacitive semicircles are observed separated by an inductive-like loop(Fig.5). The low-frequency semicircle passes into a straight line with a slope close to 45^o. The high frequency semicircle is associated with ion migration through a barrier film including the resistance to charge carriers at constant thickness[10, 12,13]. Fig.6 shows the evolution of the high-frequency parameters C_b (film capacitance) and R_b (migration resistance) with the oxidation potential.

Both the ionic migration resistance R_b and the reciprocal inner layer capacitance C_b^{-1} increase with the potential in a linear fashion. These dependences can be expected for a high-field assisted film growth[10]. The following equations are valid

$$d(R_b i_{st})/dE = 1/B\mathcal{E} \quad (2)$$

$$d(C_b^{-1})/dE = 1/\varepsilon\varepsilon_o\mathcal{E} \quad (3)$$

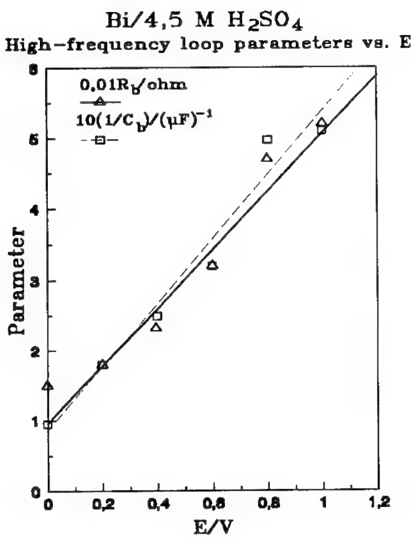

Fig.6. Dependence of the barrier layer capacitance C_b and migration resistance R_b on the anodic potential.

where i_{st} is the stationary current density after 2 h of oxidation (i_{st} = 1.2 mA.cm^{-2}), B = zF*a*/RT, z is the charge of the moving ion, *a* is the half-jump distance (assumed to be equal to 0.2 nm), ε is the dielectric constant of the barrier layer (for Bi_2O_3,ε = 18.1), ε_o is the permittivity of the free space and ***E*** is the field strength. Thus from the slopes of the dependences presented in Fig.6 the field intensity in the inner layer can be calculated. A value of 1.3±0.05 MV.cm^{-1} is obtained suggesting the validity of the high-field assisted growth mechanism. The identification of C_b with a dielectric film capacitance is not in contradiction with the Mott-Schottky treatment of the capacitive response of semiconductor films if it is assumed that the space charge layer thickness equals film thickness, which is usually correct for thin films.

DISCUSSION

When a Bi electrode is anodically polarized in 4.5 M H_2SO_4, active dissolution of the metal proceeds. With the potential increase, the solubility limit of bismuth sulphate is reached and a porous layer is most probably formed on the electrode surface. Within the pores of the $Bi_2(SO_4)_3$ layer, alkalization occurs and a new, barrier layer is formed on the electrode surface after a predefined pH is reached. Once this layer grows thick enough, the system exhibits photoactivity and the conductivity mechanism is changed involving high-field assisted migration. A implified scheme of the processes taking place in the electrode system Bi/barrier layer/sulphate layer/H_2SO_4 solution is presented in Fig.7.

At the metal/barrier layer boundary, positive defects (vacancies or interstitials) are generated. They migrate through the layer and reach the inner layer/sulphate layer interface. At this interface,

water is dissociated by the electric field and negative defects (vacancies or interstitials) are formed. The oxide phase network is obtained via the reaction of annihilation of defects. At the inner layer/H_2SO_4 solution interface (within the pores of the sulphate layer) dissolution of the inner layer occurs. The current is transported through the sulphate layer by hydrogen and/or bismuth ions diffusion. In order to transform this qualitative picture into kinetic equations, the following assumptions are made:

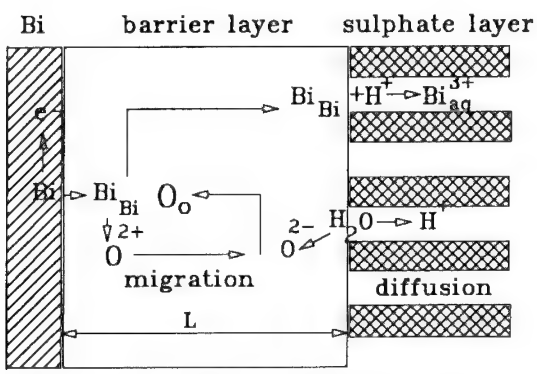

Fig.7. Simplified scheme of the processes taking place in the passive state of Bi in H_2SO_4 at high overpotentials.Bi_{Bi} and O_o represent bismuth and oxygen positions in the oxide network.

1) The interfacial potential drop at the metal/inner layer interface is neglected with respect to the potential drop within the film;

2) The migration is governed by a space - charge modified high field transport equation[11]

$i_b = i_{o,b}\exp[B(\phi_b/L + q/\varepsilon\varepsilon_o)]$ (4)

where $i_{o,b}$ is a constant depending on the mean defect concentration within the layer, ϕ_b is the potential drop in the layer, and q is the background space charge formed by the negative defects. The latter is assumed to vary with time according to De Wit *et al.* [11]:

$dq/dt = i_b A(B_r\phi_b/L-q)$

where A is a cross capture section for a charged defect, and B_r is a constant.

3) At the inner layer/solution interface, dissolution occurs followed by a sulphate formation. This reaction is assumed to obey a kinetics analogous to an electrochemical process (electrochemical dissolution [12])

$i_{b/s} = i_{o,b/s}\exp(b\phi_{b/s})$ (5)

where $\phi_{b/s}$ is the potential drop at the inner layer/sulphate layer boundary and b is a Tafel coefficient.

4) The thickness of the barrier inner layer increases with time following Faraday's law

$dL/dt = R(i_b - i_{b/s})$ (6)

where R is the molar volume per unit charge:$R = M/\rho nF$.

5) The current within the sulphate layer is controlled by linear semi-infinite diffusion of charge carriers:

$i_s = FD(dc_H/dx)_{x=L}$ (7)

6)The continuity equation imposes

$i = i_b = i_{b/s} = i_s = \text{const.}$ (8)

If an alternating component is superimposed on the electrode potential $E = \phi_b + \phi_{b/s}$:

$E = E_{dc} + |E|\exp(j\omega t)$

a corresponding change in the current follows

$i = i_{dc} + |i| \exp(j\omega t)$

It is assumed that the alternating component of the current does not imply additional film growth

$L_b = L_{b,dc}$

Following Clerc and Landolt [13] and Clerc and Alkire [14], one can assume that the total impedance of the electrode system is a sum of the impedance of the inner layer, the inner layer/sulphate layer boundary and the sulphate layer

$Z_{int} = Z_b + Z_{b/s} + Z_s$ (9)

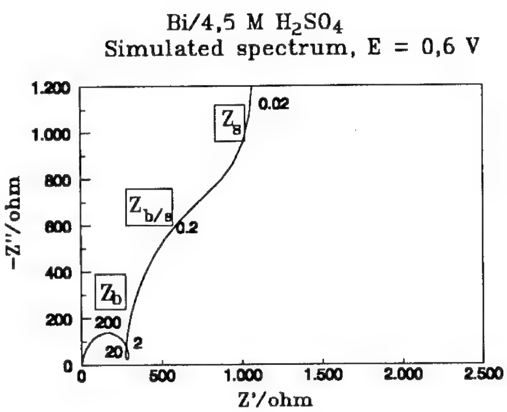

Fig.8. Simulated impedance spectrum for the anodic potential of 0,6 V obtained on the basis of the kinetic parameters listed in the Table.

Finally, transforming equations (5)-(8) to the frequency domain, after some algebra one can obtain for the components of the interfacial impedance

$Z_b = \{ j\omega\varepsilon\varepsilon_o/L_b + i_{dc}L_b[B + B_r i_{dc}A/(i_{dc}A + j\omega)]\}^{-1}$ (10)

$Z_{b/s} = [j\omega C_{b/s} + di/d\phi_{b/s}]^{-1}$ (11)

$Z_s = W\,(1-j)\omega^{-0,5}$ (12)

The overall impedance was calculated according to equations (9) - (12) for a potential of 0,6 V and a series ohmic resistance was added. The obtained impedance spectrum is presented in Fig.8

and the set of simulation parameters is listed in the Table. A conclusion can be drawn that the simulated spectrum reproduces the basic features of the experimental ones.

TABLE. Simulation parameters in the proposed kinetic model (equations (4) - (12)) used in obtaining the impedance spectrum in Fig.8.

$i_{o.b} = 1.10^{-8}$ A.cm^{-2}	$B_r = 1.10^{-5}$ F.cm^{-1}
$E = \phi_b/L = 1.3.10^{6}$ V.cm^{-1}	$i_{o,b/s} = 1.10^{-8}$ A.cm^{-2}
$B = 3.10^{-6}$ V^{-1}.cm	$b = 2.3(d\phi_{b/s}/dlgi) = 1.0$ V
$A = 1.10^{4}$ C^{-1}.cm^{2}	$i_{dc} = 1.10^{-3}$ A.cm^{-2}

CONCLUSIONS

The following main conclusions can be drawn from the results:

1) The anodic layer consists of an inner barrier photoactive layer and an outer porous sulphate layer. Photocurrent spectra reveal a band gap close to the one for Bi_2O_3. X-ray diffraction results suggest the identification of the inner layer as the basic sulphate $2Bi_2O_3.Bi_2(SO_4)_3.4H_2O$.

2) The growth of the inner layer proceeds via a high-field assisted migration mechanism. A background negative space charge is believed to enhance the transport of positive defects through the film.

3) At the inner layer/solution interface (within the pores of the sulphate layer) dissolution of the barrier film takes place. The current is transported through the sulphate layer most probably by diffusion.

REFERENCES

1. I.A.Ammar and M.W.Khalil, *Electrochim. Acta* 16, 1379(1971).
2. F.El-Taib Heakal, A.A.Mazhar and M.A.Ameer, *Br.Corros.J.* 23, 41(1988).
3. I.A.Ammar, S.Darwish and M.W.Khalil, *Corrosion*, 32, 173(1976).
4. S.Ikonopisov and Ts.Nikolov,*J.Electrochem.Soc.*119,1544(1972).
5. D.E. Williams and G.A. Wright, *Electrochim. Acta* 21,1009(1976).
6. D.E.Williams and G.A.Wright, *Ibid.* 22,505(1977).
7. S. Ikonopisov, L. Andreeva and Ts. Nikolov, *J. Electrochem. Soc.* 120,717(1972).
8. M. Metikos-Hukovic, *Electrochim. Acta* 26,989(1981)
9. L.M. Castillo and L.M. Peter, *J. Electroanal. Chem.* 146,377(1983).
10. M. Keddam, J.-F. Lizee, C. Pallotta and H. Takenouti, *J. Electrochem. Soc.* 131, 2016(1984).
11. H. J. De Wit, C. Wijenberg and C. Crevecoeur, *J. Electrochem. Soc.* 126, 779(1979).
12. V.P. Parkhutik, J.M. Albella and Jose Manuel Martinez-Duart, in *Modern Aspects of Electrochemistry,* No. 23, B.E. Conway, J. O'M. Bockris and R. E. White, Eds. Plenum Press, New York, 1992, p.325.
13. C. Clerc, D. Landolt, *Electrochim. Acta* 33,859(1988).
14. C. Clerc, R. Alkire, *J. Electrochem. Soc.* 138,25(1991).

Materials Science Forum Vols. 185-188 (1995) pp. 917-924

Passive oxide film growth and pitting corrosion of nickel in LiCl-KCl eutectic melt containing oxide ion

M. Tada and Y. Ito

Division of Energy Science and Engineering, Graduate School of Engineering, Kyoto University, Sakyo-ku, Kyoto 606-01, Japan

Keywords: Passive film growth, UPP, nickel oxide, pitting, molten chloride

Abstract

In LiCl-KCl eutectic melt containing oxide ion (O^{2-}), anodic current was observed in the potential region which was more negative than that of the conventional passivation. This anodic current was associated with oxide ion discharge on the nickel electrode. XPS analysis showed that this anodic reaction leads to the formation of thin non-stoichiometric oxide film. This reaction causes passivation, in the sense that the nickel surface is protected by a thin protective oxide film. This new type passivation behavior of nickel can be termed "Underpotential Passivation (UPP)", since it is observed at more negative potential than that of the conventional passivation. Passive oxide film growth during UPP has been thoroughly investigated. It was found that the growth kinetics and the phase state of passive oxide film were strongly influenced by the applied potential. Mechanism of passive oxide film growth is discussed from microscopic point of view. Moreover, pitting corrosion due to the breakdown of the thin oxide film by highly concentrated chloride ion was observed at the high potential limit of UPP. Electrochemical behavior of pitting corrosion was studied and critical pitting potential was determined by both electrochemical behavior and surface state observation.

Introduction

High temperature molten salts are interesting functional materials which are used for various engineering applications such as molten carbonate fuel cell (MCFC), molten salt batteries, electrochemical materials tailoring and electrolytic production of reactive metals. However, in all such practical applications, compatibility of constitution materials and electrode materials with molten salts should be guaranteed. Molten salt corrosion and its prevention are thus very important research subjects to be investigated. It is known that corrosion of metals in molten halide systems are often prevented by the formation of oxide film on the metal surface. For example, nickel metal shows high corrosion resistance in molten chloride as well as in molten fluoride, and this is believed to be due to the formation of thin oxide film on the nickel surface. However, the mechanism of the film formation and the role of this oxide film have not been studied from microscopic point of view so far. Microscopic studies are frequently done in the studies on passivation in aqueous solution systems. Some excellent microscopic models on passive film growth and pitting corrosion in aqueous solution systems have been developed [1] . But in molten chloride systems, the situation is rather different. For example, the temperature is high at around 500℃, and the molten chloride contains chloride ion with extremely high concentration and almost no water molecule or hydroxide ion.

The authors have found a new type formation of very thin oxide film on nickel in LiCl-KCl eutectic melt containing oxide ion at 450℃ by means of electrochemical measurement and surface analysis[2]. This oxide film formation occurs by the interdiffusion of adsorbed oxygen atoms formed by the discharge of oxide ion at the nickel surface and the nickel atoms. We have termed this phenomenon as "Underpotential Passivation (UPP)" since this film is formed at more negative potential than that of the conventional passivation. Unlike the coarse non-protective oxide film of micron-order thickness formed in the melt by the dissolution-precipitation mechanism of the

conventional passivation, the oxide film formed by UPP with its thickness ranging from several angstrom of one monolayer thickness to several hundreds of angstrom is dense and adherent. Consequently, the thin film is considered to have a role as a protective passive film against corrosion. Thus, the stability of this passive film in molten LiCl-KCl eutectic melt containing some amount of oxide ion, even at such a very high chloride concentration should be investigated further to understand the mechanisms involved in high temperature molten salt corrosion.

From these backgrounds, UPP oxide film formation, growth and also pitting corrosion in LiCl-KCl eutectic melt containing oxide ion at around 500℃ have been studied in detail by using both *in-situ* electrochemical method and *ex-situ* surface analyses.

Experimental

Electrodes were cut in rectangular form (0.2ᵗx8x15mm) from nickel sheet. They were polished with emery paper, then with aluminum powder to obtain mirror-like surface. Just before immersion, each specimen was washed with ethanol in a ultrasonic bath and dried carefully. After immersing the nickel specimen, ramp-wave multi potential sweep method was applied to remove the pre-formed oxide on nickel electrode. This pretreatment was necessary to obtain reproducibility of the data. Reagent grade LiCl and KCl (Wako Pure Chemical Industries Co., Ltd.) were mixed (LiCl:KCl= 59:41mol%) together and dried in vacuum for several days at 200°C to remove water. Salt was melted in an alumina crucible in a stainless steel holder filled with dry argon at 500℃. Then, dry argon gas was bubbled into the melt through an alumina tube for more than 12 hours to remove residual water Pure lithium oxide (99.9% : Rare Metallic Co., Ltd.) powdered in a drybox with very low water concentration (<0.5ppm) was used as an oxide ion source. Oxide ion concentration in the melt was estimated assuming that all added lithium oxide dissolves and produces oxide ion . Concentration is shown by mol%. Reference electrode was a Ag wire immersed in LiCl-KCl containing 1mol% AgCl, contained in a Pyrex glass tube with thinner bottom. A dynamic reference electrode using electrochemically deposited lithium [3] was used to correct the potential measured by Ag/AgCl reference electrode. In some cases, potentials are referred to this potential and expressed as [V (vs.Li^+/Li)]. Quasi-equilibrium potential (E_{QEP}) over which UPP oxide film begins to grow was also used as a reference potential and expressed as [V (vs. E_{QEP})].

Schematic drawing of the experimental cell is shown in Fig.1. Purging was conducted by flowing pure dry argon inside the holder Counter electrode was mounted at the center of the melt in the crucible. Working electrodes and reference electrode were mounted in the same distance from the counter electrode. A thermocouple was used as an indicator of temperature. The top of thermocouple covered by alumina tube was immersed at the same depth as the center of nickel specimen. Temperature was controlled by thermostat (Shimaden Co.,Ltd) monitoring temperature of an another thermocouple mounted near the furnace. Temperature

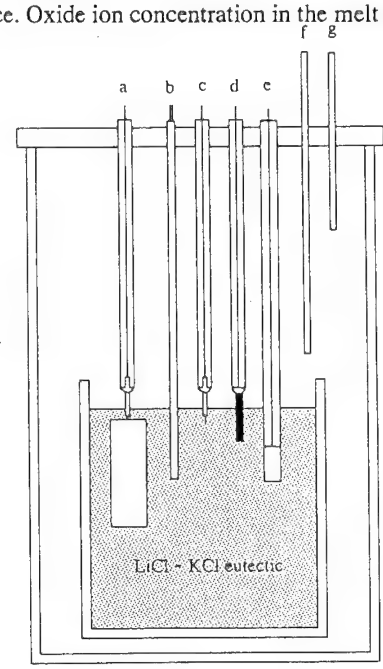

Fig.1 Experimental cell. ; (a) Ni plate working electrode. (b) thermocouple. (c) Li^+/ Li reference electrode. (d) glassy carbon electrode. (e) Ag^+/Ag reference electrode. (f) Ar inlet. (g) Ar outlet.

was controlled within 2℃.

A potential sweep reduction method was used to measure the growth behavior of thin UPP oxide film growth. The thickness range was from thinner than several angstrom to several hundreds of angstrom. Standard sweep rate was set at 100mV/s and potential range was usually set from -0.6V to 0V (vs. E_{QEP}). It takes only 6 seconds to measure the amount of the discharge. This fast sweep rate was adopted to avoid further oxidation during measurement. After performing oxidation at more positive potential than E_{QEP}, a ramp-wave potential sweeps was applied .

Potential sweep method was applied by a potentio/galvanostat (Hokuto Electric Co., Ltd.) combined with a function generator (Hokuto Electric Co., Ltd.). Cyclic voltammograms were recorded by using X-Y recorder (Rigaku co, Lid.). Surface analyses were conducted by XPS (Nihon Denshi .Co.,Ltd.) with argon sputtering beam (400V- 6mA). XPS signals of $Ni_{2p3/2}$ and those of O_{1s} were analyzed to measure the quantity of each element, respectively. Sputtering ratio was estimated to be 1-3 angstrom per second.

Results and Discussion

3.1 Underpotential passivation

Figure 2 shows the anodic polarization curve for nickel in molten LiCl-KCl eutectic melt after lithium oxide addition. Before lithium oxide addition, currents began to increase near 2.3V(vs.Li^+/Li), which is due to the occurrence of the anodic nickel dissolution. Whereas, after lithium oxide addition, anodic peak indicated as "a" appears at much more negative potential than that of the current increase. To investigate this "peak a" in more detail, cyclic voltammograms were measured as shown in Fig.3. Both peaks a and a' appeared immediately after 0.8mol% lithium oxide addition, which value increased with time and gradually approached to saturated ones. This indicates that oxide ion affects directly on the electrochemical behavior of nickel in this potential range. No peaks could be observed in the same potential range on Pt working electrode. Therefore, peaks a and a' apparently reflect the characteristic nature of Ni surface. Peak currents at a and a' increased as oxide ion concentration increased, as shown in Fig.4. Apparently, this behavior differs from the conventional passivation, because in case of the conventional passivation, peak current should decrease as oxide ion concentration increases. Potentials at i=0 in voltammograms and the rest potentials obtained after releasing the applied potential were in good agreement and these potentials could be considered as quasi-equilibrium potentials over which UPP oxide film begins to grow.

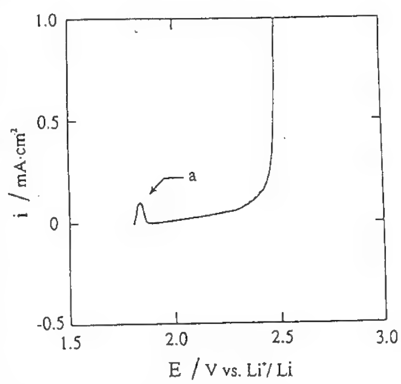

Fig.2 Polarization curve for nickel in molten LiCl-KCl eutectic after lithium oxide addition, oxide ion concentration 0.8mol%, scan rate 1mV·s^{-1}

Nickel surface gradually turned to golden during potentiostatic oxidation in the potential region more positive than the quasi-equilibrium potential. Whereas, by potentiostatic reduction in the potential region more negative than the quasi-equilibrium potential, nickel surface kept its original metallic surface for long period. XPS analysis was performed in order to investigate nickel surface change caused by the anodic oxidation. Figure 5 shows XPS spectra of nickel which color turned into gold after potentiostatic oxidation at 0.45V (vs. E_{QEP}) for 126 min at 450℃. It was found that higher value of $Ni_{2p3/2}$ peak binding energy at the outermost part of the surface and as sputtering time becomes longer, $Ni_{2p3/2}$ peak shifts towards Eb value indicating metallic nickel. This indicates that the oxide film is non-stoichiometric with its composition varying across the film. Thus, it is concluded that thin non-stoichiometric nickel oxide film is formed and grown on the surface of nickel specimen by the anodic reaction of peak a. Since nickel surface is protected by thin oxide film at more negative

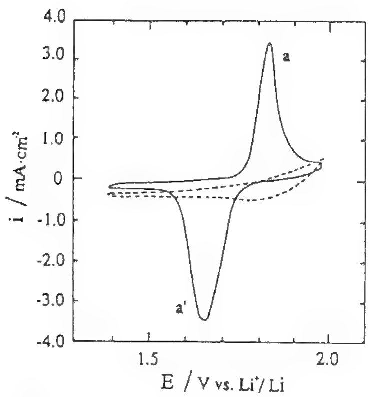

Fig.3 Cyclic voltammograms for nickel in molten LiCl-KCl eutectic; (--) before and (—) after lithium oxide addition, oxide ion concentration 0.8 mol%, scan rate $100 mV\cdot s^{-1}$

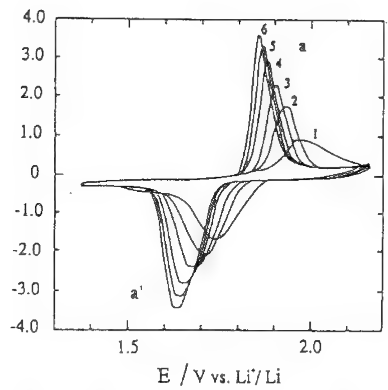

Fig.4 Cyclic voltammograms for nickel in molten LiCl-KCl eutectic; (1) 0.05 mol%, (2) 0.1 mol%, (3) 0.2 mol%, (4) 0.4 mol%, (5) 0.6 mol%, (6) 0.8 mol% oxide ion concentration, scan rate $100 mV\cdot s^{-1}$

potential than that of nickel dissolution, this behavior of nickel can be termed as "Underpotential Passivation (UPP)" to distinguish from the conventional passivation. This behavior rather resembles protective thin anodic oxide film formations of noble metals prior to oxygen evolution in aqueous solution systems.

From the experimental results and discussions described above, reaction scheme of UPP can be proposed as in the following: In the first step, chemisorbed oxide ion is discharged to form oxygen atom;

$$O^{2-} = O_{ad} + 2e- \qquad [1]$$

It should be stressed again that this discharge of oxide ion occurs at more negative potential than that of the conventional passivation. The second one is a surface reaction where chemical bonding between adsorbed oxygen atom and nickel atom on the surface is formed;

$$O_{ad} + Ni = Ni\text{-}O \qquad [2]$$

Oxygen atoms have the ability to pull electrons from nickel atom. That is why higher oxidation state of nickel oxide can be observed near surface region. The third one is a solid reaction involving interdiffusion of oxygen atoms and nickel atoms to form bulk nickel oxide :

$$Ni\text{-}O = Ni\text{-}O_{lattice} \qquad [3]$$

Schematic drawing of UPP oxide film formation was described in Fig.6.

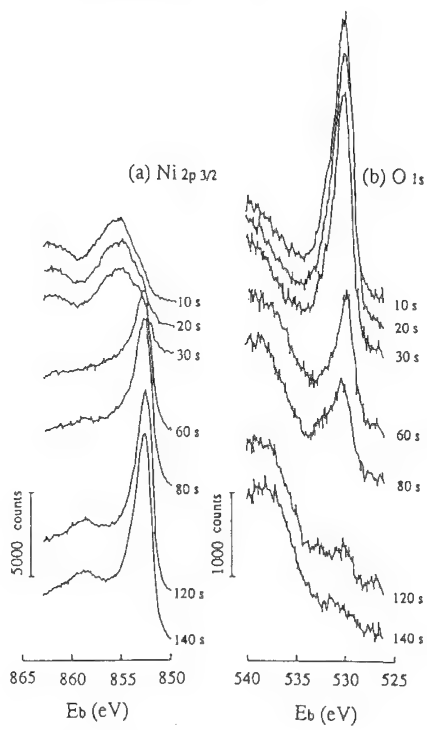

Fig.5 XPS spectra of nickel surface with various argon sputtering time; (a) Ni $2p_{3/2}$ spectrum and (b) O $1s$ spectrum after 126 min potentiostatic oxidation at 2.2V in LiCl-KCl eutectic containing 0.8 mol% oxide ion.

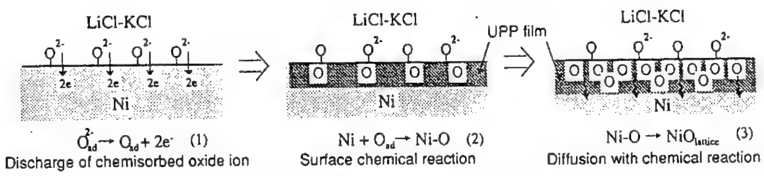

Fig.6 Shematic drawing of UPP

3.2 UPP Oxide Film Growth

Figure 7 shows voltammograms by the cathodic scan after potentiostatic oxide film growth at several potentials. Three kinds of cathodic peaks a',b'and c' were observed as summarized in Table 1. It was found that the spectrum of these peaks were strongly dependent on the applied potential. The growth of different cathodic peak implies a growth of oxide phase in different state. The dependence of quantity of electricity used for cathodic discharge of the oxide phase on the anodic potentiostatic holding time are plotted in Fig.8. The dependencies are summarized in the followings:

(i) At 0-0.2V(vs. E_{QEP}), peak a' first appeared, then b' gradually grew.

(ii) At 0.2-0.3V(vs. E_{QEP}), peak a' was mainly observed, and the growth of both b'and c' peaks was retarded.

(iii) At 0.3-0.6V(vs. E_{QEP}), peak a' was observed in an early stage and c' grew more conspicuously with the applied potential shifting to more positive direction.

In all cases it was found that the peak position for a' shifted gradually toward cathodic direction as potentiostatic holding time increased, which implies the stabilization of this oxide phase.

From XPS analysis it was found that peak a' resulted from the reduction of oxide phase with

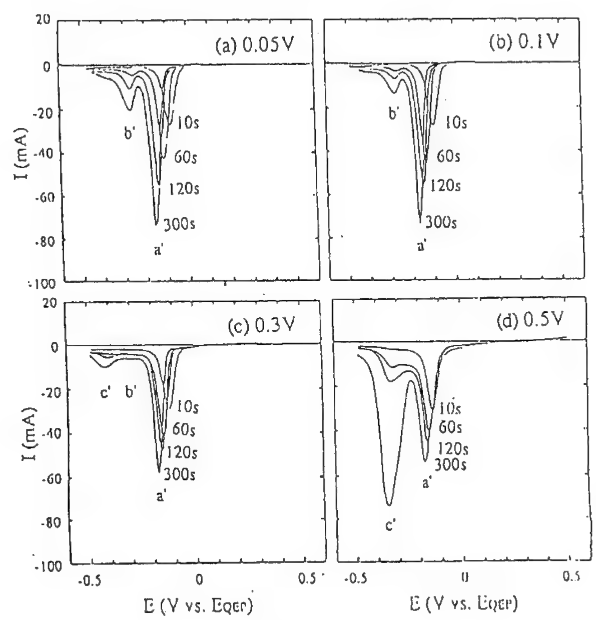

Fig.7 Voltammograms of nickel by the cathodic scan after potentiostatic oxide film growth at (a) 0.05V, (b) 0.1V, (c) 0.3V and (d) 0.5V [vs.E_{QEP}] in LiCl-KCl cutectic melt containing 0.8mol% oxide ion at 500℃, scan rate 100mV/s.

higher oxidation state at the outermost oxide film. While peak b' and c' resulted from the reduction of inner oxide phase with lower oxidation state. It is noted that by the same kind of experiment, the nickel oxide formed by high temperature oxidation in air, shows only peak b' and c'. That is, peak a' is related to the oxide phase peculiar to the oxidation in molten salt system. Hereafter those oxide phases giving cathodic peak a', b' and c' will be termed as phase a', b' and c', respectively.

From Fig.8, it can be seen that at early stages phase a' grows in every cases and at potentials more negative than 0.2-0.3V(vs. E_{QEP}) phase b' and at potentials more positive than 0.2-0.3V(vs. E_{QEP}) phase c' grows. The first step of UPP is the electrochemical formation of adsorbed oxygen by the discharge of oxide ion on nickel surface. Therefore a mechanism could be proposed that the first metastable oxide phase where adsorbed oxygen and nickel binds together to form higher oxide corresponds to phase a', while phase b' and c' corresponds to the stabilized phase.

Table 1 Reduction peaks observd in the voltammograms by cathodic scan.

peak	potential (V vs. E_{QEP})
a'	-0.18 ~ -0.05
b'	-0.28
c'	-0.42 ~ -0.32

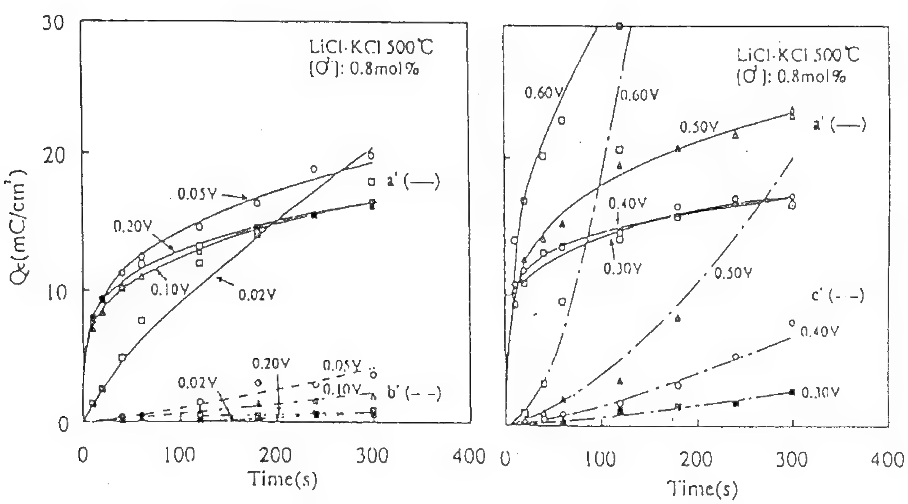

Fig.8 The dependence of quantity of electricity used for cathodic discharge of the oxide phase on the anodic potentiostatic holding time.

By considering the results of surface observation, those of RHEED analysis and the growth kinetic of each phase as shown in Fig.8, it was speculated that anodic peak a', b' and c' was considered to correspond to the reduction of amorphous, polycrystalline and non-stoichiometric oxide, respectively.

3.3 *Pitting Corrosion*

Figure 9 shows anodic polarization curves of nickel after subjected to potentiostatic passivation for 1min and 60min, respectively, in the UPP region. Currents began to increase with ripples during anodic scan in both curves. After anodic polarization experiments, pitting corrosion was observed on nickel which surface was covered with oxide film as shown in Fig.10. Therefore, current increases with ripples indicate the occurrence of pitting corrosion. Figure 9 also represents that the longer the passivation time is, at the more positive potential pitting corrosion begins. This

means that as passivation proceeds, i.e., thin oxide film grows, the time necessary for thin oxide filmbreakdown by chloride ion becomes longer as expected from the case of pitting corrosion in aqueous solution. Critical pitting potential was determined to be 0.57V(vs.E_{OEP}) in LiCl-KCl eutectic melt containing 0.8mol% oxide ion at 500℃ by both electrochemical behavior of pitting corrosion thus obtained and surface state observation.

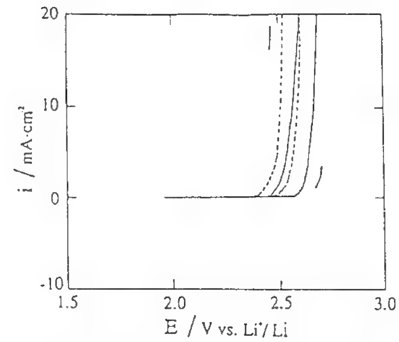

Fig.9 Polarization curves for nickel in molten LiCl-KCl eutectic after UPP at 1.94 V; for (--) 1 min and (—) 60 min , oxide ion concentration 0.8mol%, scan rate 10mV·s^{-1}

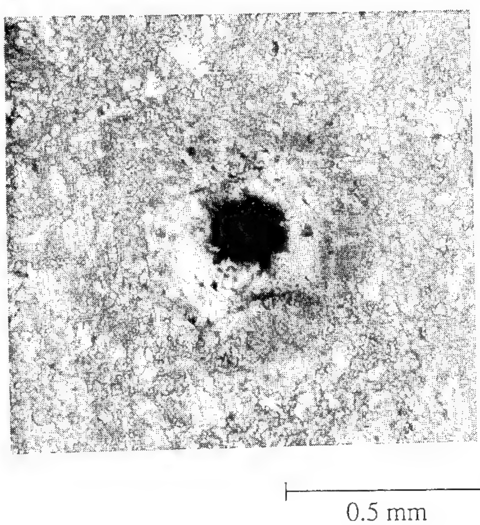

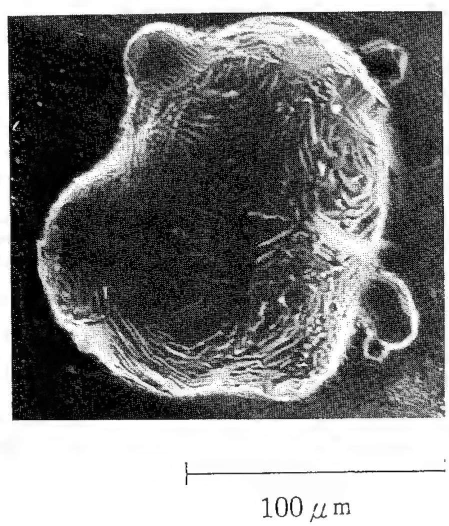

Fig.10 Microscopic photo and SEM image of typical pitting corrosion of nickel.

Conclusion

In molten LiCl-KCl containing oxide ion, anodic current peak associated with oxide ion discharge on nickel could be observed at more negative potential than that of the conventional passivation. Thin coherent non-stoichiometric oxide formation with its composition varying across oxide film is finally formed by this anodic reaction. Since nickel surface is protected by this thin oxide film at more negative potential than that of the conventional passivation, this new type behavior of nickel can be termed as "Underpotential Passivation (UPP)". Reaction scheme of UPP has been proposed; discharge of oxide ion to form oxygen atom is the first step. It is stressed that this discharge of oxide ion occurs at more negative potential than that of anodic dissolution of nickel into the melt. The second one is a surface reaction to form chemical bonding between adsorbed oxygen atom and nickel atom. The third one is a solid reaction involving interdiffusion of oxygen and nickel to form thin coherent non-stoichiometric oxide film.

Passive oxide film growth during UPP and pitting corrosion has been thoroughly investigated. The growth kinetics was strongly influenced by the applied potential and it was considered to be due to the existence of different types of oxide phase formed in the passive film. Electrochemical behavior of pitting corrosion was studied and critical pitting potential was estimated to be 0.57V(vs.E_{QEP}) in LiCl-KCl eutectic melt containing 0.8mol% oxide ion at 500℃.

The results described above will be helpful for a better understanding of the mechanisms involved in high temperature molten salt corrosion, as well as those involved in passive film growth and pitting corrosion in aqueous solution containing chloride ion.

Reference

[1] C.Y. Chao, L.F. Lin and D.D. Macdonald, J. Electrochem. Soc., 128, 1187 (1981), ibid 128, 1194 (1981), and ibid, 129, 1874 (1982)
[2] M. Tada and Y. Ito, Denki Kagaku (Journal of Electrochemical Soc., Japan), 60, 515 (1992)
[3] T. Takenaka, Y. Ito and J. Oishi, Denki Kagaku, 53, 476 (1985).

Pitting

Materials Science Forum Vols. 185-188 (1995) pp. 927-936

Concerning passivity breakdown on solid and liquid gallium and titanium in halide solutions

D.J. Ellerbrock and D.D. MacDonald

Center for Advanced Materials, The Pennsylvania State University, University Park, PA 16802, USA

Keywords: Blisters, gallium, passivity breakdown, point defect model, scanning electrochemical microscopy, titanium

ABSTRACT

The anodic polarization behaviors of solid vs. liquid gallium in borate-buffer + KCl solutions have been compared in order to test the cation vacancy condensation hypothesis of the point defect model (PDM) for the breakdown of passive films. Pits are found to nucleate on solid gallium in buffered chloride solutions, and we propose that the pits nucleate from blisters that form beneath the passive film on the metal substrate. Liquid gallium resists passivity breakdown much more readily than does the solid, which we attribute to the inhibition of cation vacancy condensation, and hence to the formation of blister precursors at the metal/film interface. The second thrust of this paper is to reinterpret recently reported Scanning Electrochemical Microscopy (SECM) data for passivity breakdown on titanium in 1M KBr + 0.05M H_2SO_4 at ambient temperature in terms of the PDM. We show that the experimental data obtained from the Ti/KBr system are consistent with passivity breakdown occurring in two stages; condensation of cation vacancies at the metal/film interface, followed by dissolution of the barrier layer cap at the film/solution interface to the point where mechanical instability occurs. Analysis of the data permits estimation of the heterogeneous rate constant for TiO_2 dissolution, $k_s = (1.1 \pm 0.2) \times 10^{-7}$ cm/s, which in turn yields a reasonable estimate of the passive current density of ~3.8 $\mu A/cm^2$, uncorrected for surface roughness.

INTRODUCTION

This paper presents recent advances in the study of passivity breakdown that have been made in this laboratory by exploring breakdown on liquid and solid gallium polarized in deaerated borate-buffer + KCl solutions, together with the reinterpretation of recently reported scanning electrochemical microscopy data for passivity breakdown on titanium in bromide-containing solutions.[1,2] Both studies will be discussed within the framework of the point defect model (PDM) for the growth and breakdown of passive films. This model[3-17] proposes that passivity breakdown is initiated via the condensation of cation vacancies at the metal/film interface, or possibly by destruction of the film at the film/solution interface via vacancy-pair coalescence.[4,15-17] As argued below, conditions may exist, particularly in the presence of an aggressive anion in an aqueous environment, that increase the flux of cation vacancies across the film. If the vacancies arriving at the metal/film interface cannot be annihilated by the oxidative injection of cations from the metal, the vacancies may coalesce resulting in the local decohesion of the barrier layer from the metal substrate. Vacancy coalescence or condensation at the inner interface of an oxide scale is a well-documented phenomenon in the high temperature oxidation of metals exposed, generally, to air or oxygen.[18] Here, we consider vacancy condensation at the metal/film interface as the precursor events in the breakdown of the passive films solid and liquid Ga in deaerated borate-buffer + KCl solutions. We contend that the experimental findings are in agreement with those predicted by the PDM, in that solid Ga exhibits blistering beneath the passive film as the precursor to the formation of pits. On the other hand, for low chloride concentrations, the liquid phase does not exhibit breakdown over the same voltage range, which we attribute to the fact that the liquid phase does not readily allow vacancy condensates to form. At higher [Cl^-], however, liquid Ga does experience general passivity breakdown in the form of dissolution/precipitation phenomena, but the morphology of the attack is fundamentally different than that observed on the solid.

Turning to the second subject, Casillas, Charlebois, Smyrl, and White[1,2] recently reported a detailed study of passivity breakdown on titanium foils in 1M KBr + 0.05M H_2SO_4 solutions using scanning electrochemical microscopy (SECM). The importance of this work is that it employed a scanning microscopy of sufficient resolution to permit the study of the dynamics of individual

breakdown sites. Accordingly, we have, for the first time, detailed information on the histories of individual pit nucleation sites. The authors[1] have interpreted their findings in terms of a breakdown mechanism that proposes a high electronic conductivity at the nucleation sites, and this mechanism gives a reasonable qualitative account of the findings. However, these same findings are also in excellent agreement with the predictions of the point defect model[3-17] for the growth and breakdown of passive films (which, apparently, was not considered by the authors) that we have developed over the past decade. Indeed, the sequence of events indicated by the experiments of Casillas, et al[1,2] is precisely that previously predicted by the PDM and, when interpreted in terms of the PDM, a detailed history of the breakdown phenomenon becomes evident. Accordingly, the second objective of this paper is to present reinterpreted findings of Casillas et al[1,2] in terms of the PDM.[19]

THE POINT DEFECT MODEL AND PASSIVITY BREAKDOWN

The five fundamental reactions that allow for film growth/dissolution are illustrated in Fig. 1 at their respective interfaces.[14] Details concerning growth and dissolution of the film may be found elsewhere.[3-17] But for now, it becomes apparent that if the cation vacancies, $V_M^{\chi'}$,arriving at the metal/film interface cannot be annihilated by the oxidative injection of cations into the passive film, the excess cation vacancies necessarily condense at this interface and result in localized detachment of the film. The three mechanisms for passivity breakdown, as provided for by the PDM[15] are diagrammed in Fig. 2. In one mechanism (Case I, Fig. 2), the loss of oxygen vacancies at the film/solution interface, due to the absorption of an "aggressive anion" (X^-), is compensated for by a Mott-Schottky pair reaction, which also generates cation vacancies. Note that this process is autocatalytic. Typically, chloride ion is the responsible anion, since it is prevalent in many environments and is particularly detrimental to stainless steels and aluminum alloys. Also, the combination of ion size and Gibbs energy of dehydration favors the absorption of chloride ion, compared with other anions, into surface oxygen vacancies of these alloys. (These latter ideas concerning Gibbs energy of hydration and ion size and how they determine which halides are damaging to a specific metal system are discussed elsewhere[19]) Desorption of the anion along with a neighboring surface cation may also occur to generate an anion vacancy/cation vacancy pair at the surface and a metal cation and the anion in solution (Case II, Fig. 2). If the cation vacancy diffusivity in the film is high, the cation vacancies of the vacancy pairs may submerge into the film leaving the oxygen vacancy to react with another halide ion, which makes this process autocatalytic as well. As noted above, if the additional cation vacancies created by these mechanisms are not annihilated at the metal/film interface, and hence are not absorbed (as metal vacancies) into the metal substrate, they may condense, resulting in the local detachment of the film from the base metal. Clearly, these events will tend to occur preferentially at those points in the film where the cation vacancy diffusivity is highest (i.e. at the so-called "weak spots", such as at the boundaries between the barrier layer and precipitates, and these points may ultimately be pit precursors sites. Once the film has become detached locally, growth of the barrier layer into the metal can no longer occur; however, the blister may grow laterally by continued cation vacancy condensation at its periphery. Concomitantly, dissolution of the detached film at the film/solution interface continues, thereby resulting in film thinning and eventual rupture, as depicted in Fig. 3 where a series of specific steps are outlined to occur prior to stable pit growth.[15-17] Thus, the cation vacancy condensation mechanism is characterized by the formation of blisters that eventually rupture to form pit initiation sites.

On the other hand, if the cation vacancy diffusivity is low, as may be the case for amorphous films or for films of high cation charge (e.g. WO_3 on W), where cation vacancy formation is energetically unfavorable, the vacancy pair created by ion desorption may persist at the film/solution interface. Case III of Fig. 2 illustrates this scenario, and we propose that the continued collection of vacancy pairs at the film/solution interface results in the destruction of the barrier layer at the film/solution interface.[15] In essence, Case III represents anion-assisted dissolution at the film/solution interface. However, this mechanism does not appear to be viable as a direct cause of passivity breakdown, because destruction of the barrier layer at the film/solution interface should result in concomitant growth of the barrier layer into the metal substrate. It is possible that this would eventually result in the formation of a local crevice, which may lead to passivity breakdown via an acidification mechanism. We term this mechanism "indirect". However, we hasten to add that localized thinning, alone, cannot be used to distinguish between Cases I and II (cation vacancy

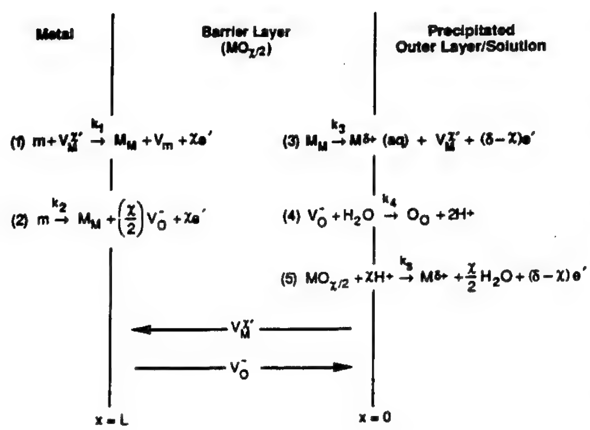

Fig. 1 Schematic of physicochemical processes that occur within a passive film according to the point defect model. m= metal atom, M_M = metal cation in cation site, O_O = oxygen ion in anion site, $V_M^{\chi'}$ = cation vacancy, $V_O^{\cdot\cdot}$ = anion vacancy, V_m = vacancy in metal phase. During film growth, cation vacancies are produced at the film/solution interface, but are consumed at the metal/film interface. Likewise, anion vacancies are formed at the metal/film interface, but are consumed at the film/solution interface. Consequently, the fluxes of cation vacancies and anion vacancies are in the directions indicated. Note that reaction 1, 3, and 4 are lattice conservative processes, whereas reactions 2 and 5 are not. Source: D. D. Macdonald, *J. Electrochem. Soc.*, 139, 3434 (1992)

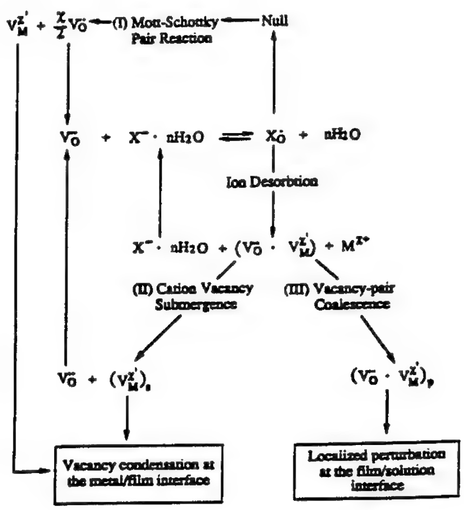

Fig. 2 Summary of proposed reactions leading to passivity breakdown. Source: D. D. Macdonald, *J. Electrochem. Soc.*, 139, 3434 (1992)

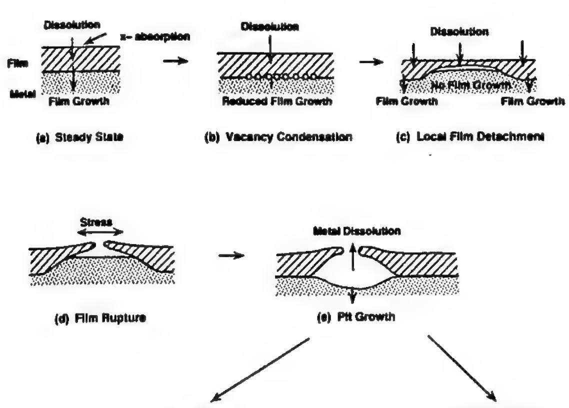

Fig. 3 Enhanced flux of cation vacancies through the passive film may occur upon anion absorption at the barrier layer/environment interface (a), which eventually leads to localized detachment of the film at the metal/film interface (b). Detachment of the film retards film growth (c) compared to the rest of the film. However, film dissolution still occurs above the detachment. film thinning continues until stresses in the film are sufficient to rupture the film and expose the bare metal substrate, (d). Growth of the blister is subsequently assisted by penetrateion of solution through fissures in the cap resulting in gas generation. Source: D. D. Macdonald, *J. Electrochem. Soc.*, 139, 3434 (1992)

condensation) and Case III (vacancy pair coalescence).

The prediction of blister formation as a precursor to pitting is entirely in accord with the observations of blisters by Bargeron and Givens[20,21] for the breakdown of passivity on aluminum in chloride-containing solutions. They also report the blister to be surrounded by a chloride-containing ring. Indeed, assuming that Cases I or II, Fig. 2, apply, one would predict that the absorption of the aggressive anion should occur most intensely at the periphery of the blister, because that is the location of the autocatalytic generation of oxygen vacancies. Bargeron and Givens[20,21] also speculated that the solution penetrated through the disbonded oxide, resulting in the generation of hydrogen, which may provide a hydrostatic pressure that accelerates blister growth. "Unbroken" blisters on aluminum were also found to evolve gases from a region approximately one radius width ahead of the advancing blister periphery. Furthermore, these researchers showed that the peripheries of the blisters are outlined by roughly circular rings of micropits, which form as the blisters grow laterally in incremental steps along the inner interface of pure aluminum specimens. Finally, the work of Bargeron and Givens has largely been supported by the subsequent studies of Natishan and McCafferty,[22] and McCafferty, Trzaskoma, and Natishan.[23]

Finally, we note that many other examples of blister or void formation could have been cited in support of the PDM. These include the observation of blisters and voids (and sometimes pits with ruptured caps) on aluminum,[24] stainless steels,[25-27] and zirconium.[28] Thus, it would appear that this mechanism is quite general although these few examples clearly do not demonstrate exclusivity.

PASSIVITY BREAKDOWN ON LIQUID AND SOLID GALLIUM

Since a liquid conforms to its container, vacancy condensation does not readily occur and we predict that the passive film on a liquid metal will resist localized breakdown more effectively than that on the solid substrate.[16,17] This prediction is most readily tested using Ga, which exhibits a melting temperature of 29.78°C, and which is a passive metal not unlike aluminum. Surprisingly, little systematic work has been reported on the growth and breakdown of passive films on this metal, even though it can be obtained in a very pure state and exhibits a number of advantageous properties for studies of this nature.

Anodic polarization curves for solid and liquid Ga in deaerated borate-buffer solutions containing 0.01 m KCl, and that of liquid Ga in 0.033 m KCl solution (*p*H=8), are shown in Figure 4. In the low $[Cl^-]$ solution, solid Ga clearly shows a well-defined passive region and a transition into pitting attack, as indicated by the sharp rise in current. Evidence of blister formation and detachment of the film around the perimeter of a pit is given in Fig. 5 for a solid Ga specimen. Note that the detached area (marked by the lower right arrow in Fig. 5a) is much larger than the pit observed (Fig. 5c) after ultrasonic removal of the film. These disbonded regions, only some of which were shown to cover geometrical pits (e.g.. arrow in lower right corner, Fig. 5a), were detected by using a high voltage electron beam (25-30kV) to penetrate the film during SEM examination, and by subsequent ultrasonic cleaning of the specimen to remove the film. An example of a detached area that was found not to cover a geometrical pit that could be resolved by SEM is indicated by the arrow in the center of Fig. 5a. Bargeron and Givens,[20] also used this SEM technique, in combination with ***in situ*** microscopic observation of blister formation. Hence, the blisters did not result from the vacuum applied to the specimen during SEM analysis, but in fact formed ***in situ*** during exposure to the solution.

As also shown in Fig. 4, liquid gallium (at 31°C) exhibits a passive region extending to $5V_{SCE}$ in 0.01 m KCl solution. Because the initial passive film on the liquid electrode was formed on the solid substrate (since the solid was melted *in situ*), and presumably contains the same impurities and structural defects, the lack of breakdown on the liquid substrate, in this case, argues strongly against the properties of the passive film as being the controlling factor. Rather, we propose that our observation is consistent with the point defect model, in that vacancy condensates do not readily form at the metal/film interface on a liquid substrate. We note that a similar result is obtained if the Ga is maintained in the liquid state throughout the entire experiment, so that the transition from the solid phase to the liquid phase in the experiment described above cannot account for the difference in polarization behavior between the solid and the liquid substrate shown in Fig. 4. Finally, at a sufficiently high chloride concentration (Fig. 4), passivity breakdown can be induced on liquid Ga, but the form of attack is quite different from that observed on the solid, being in the form of dissolution over large, but discontinuous, areas of surface and subsequent formation of visible

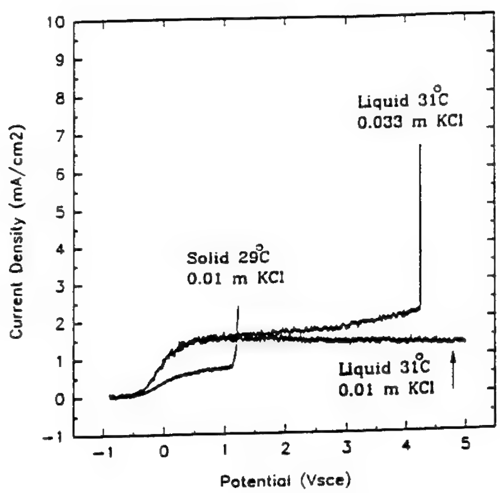

Fig. 4 Anodic polarization diagram of solid and liquid Ga in 0.01, and liquid Ga in 0.033 m KCl borate-buffer solutions (pH=8). Sweep rate = 0.5 mV/s.

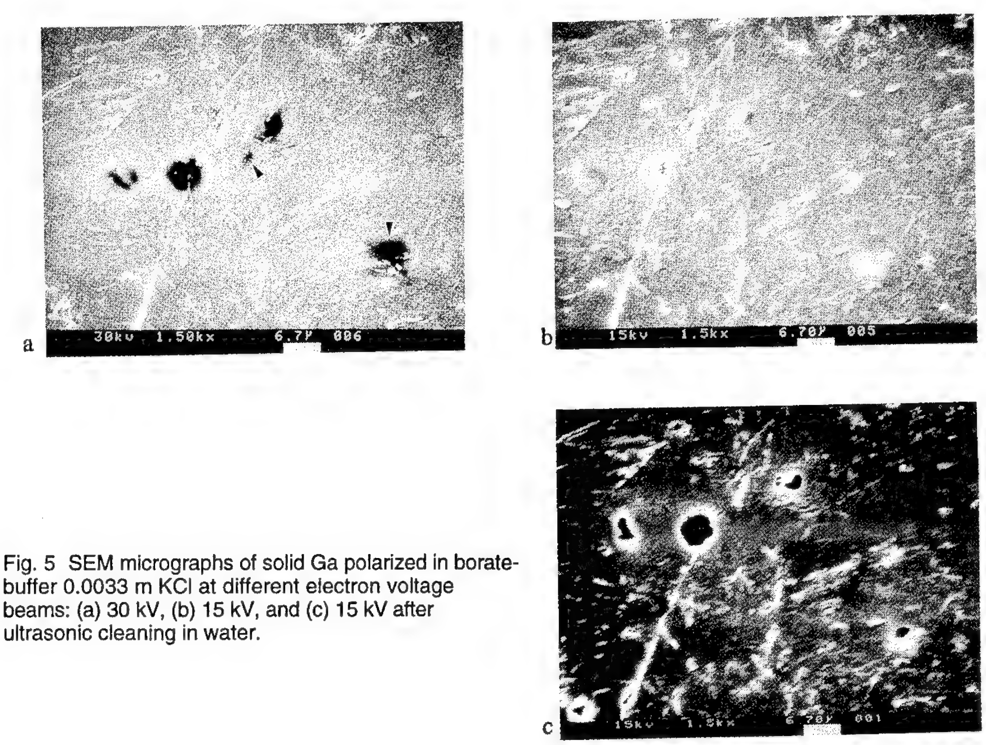

Fig. 5 SEM micrographs of solid Ga polarized in borate-buffer 0.0033 m KCl at different electron voltage beams: (a) 30 kV, (b) 15 kV, and (c) 15 kV after ultrasonic cleaning in water.

precipitates, rather than in the form of highly localized attack. This type of attack strongly resembles a transpassive dissolution phenomenon. The experiments described above have been repeated many times and are found to be quite reproducible.

Of course, a geometrical pit cannot form in a liquid, since the liquid would simply fill-in any protrusion, and the necessary conditions for pit growth (i.e. an IR drop and decreasing *p*H inside of the pit) cannot become established. Hence, "pitting" of liquid Ga cannot occur (by definition) and a rise in current is not seen. However, polarization of liquid Ga in a solution of sufficiently high chloride concentration does result in passivity breakdown as indicated by the current response shown in Fig. 4 for 0.033 m KCl. The argument which states that a rise in current is not seen because a geometrical pit cannot form in a liquid, fails to distinguish between a rise in current caused by pit growth and that caused by breakdown of the passive film, the latter being a necessary precursor to pit growth. In other words, an initial rise in current is the result of passivity breakdown regardless of a liquid or solid substrate, and in the case of the solid, the sudden increase in current immediately leads to growth of a pit. The current spikes on liquid Ga observed at a higher potential than that of the solid in the same[Cl^-] solution, or at sufficiently high [Cl^-], are indicative of passivity breakdown. It is for this reason that the term breakdown potential, V_c, is preferred in this work rather than pitting potential or pit nucleation potential.

The assertion that the current spike is the result of passivity breakdown may be tested experimentally by melting a solid Ga electrode that is experiencing pitting attack. Fig. 6 shows the polarization behavior of a solid Ga electrode melted (by raising the temperature of the water bath) once pitting attack had initiated. Pitting is clearly taking place, and upon melting the electrode, it repassivates, even though the potential is maintained at a value that is more positive than the breakdown potential on the solid. Thus, if the passive films on the solid and liquid substrates had the same propensities towards breakdown, one might have expected a continued high dissolution rate of the bare metal.

Further exploration into how the phase of the substrate effects its resistance to passivity breakdown may be accomplished by polarization of superheated solid Ga. Fig. 7 shows the anodic polarization behavior of solid, liquid, and superheated Ga in 0.0167 m KCl solution as a function of temperature. Solid Ga electrodes exhibited classical pitting attack as indicated by the sharp rise in current and subsequent microscopic examination. Liquid Ga is readily supercooled and does not exhibit passivity breakdown at 15, 29, and 35°C in this chloride concentration up to 5V, which is the limit of the potentiostat used in these experiments. However, a solid Ga electrode inserted into the cell and allowed to reach thermal equilibrium at 29.9°C, still retains a degree of crystallinity (or high viscosity) just above the melting point (Tm=29.78°C) and undergoes breakdown at ~2.4 V. Only solid electrodes raised no more than approximately 0.2°C above the melting temperature exhibited this superheated behavior, and visual observation revealed that the specimen did melt (but remained highly viscous). Thus, passivity breakdown occurs at a more positive potential than in the case of a solid, but nevertheless does occur in contrast with the liquid, since substitutional diffusion of metal vacancies away from the metal/film interface is expected to occur less readily in a superheated solid substrate, compared with the liquid, but more readily when compared with the solid. Clearly, the crystallinity (or viscosity), or lack thereof, of the substrate is an important factor in the passive film breakdown mechanism(s).

A predictable trend appears in the polarization behavior of solid and liquid Ga electrodes similar to that commonly observed for solid electrodes of any metal or alloy, in that V_c decreases as [Cl^-] increases. More specifically, the PDM expresses the critical breakdown potential as[3]

$$V_c = \frac{4.606RT}{\chi F \alpha}\log\left[\frac{J_m}{J^{\circ}u^{\frac{-\chi}{2}}}\right] - \frac{2.303RT}{\alpha F}\log\left(a_{X^-}\right) \qquad (1)$$

where there is a logarithmic dependence of V_c upon the halide activity (halide concentration). Plots of the breakdown potential vs. [Cl^-] for solid, superheated solid, and liquid Ga have been presented elsewhere[17] and show that there is a linear relationship in accord with Eqn. 1. Accordingly, α_{solid} is found to be 0.39 from the slope of the solid Ga data. This value of α is quite reasonable compared to values tabulated elsewhere,[13] but, because of the scatter in the experimental data and the substrate phase effects defined in this work, the value must be regarded with some caution.

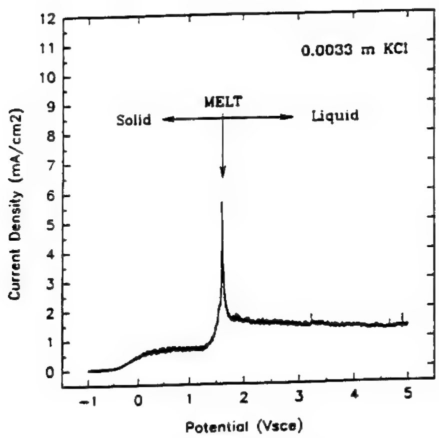

Fig. 6 Anodic polarization diagram of solid Ga that was melted by raising the water bath temperature once pitting ensued in 0.0033 m KCl borate-buffer solution (pH=8). Data is corrected for the different areas of solid and liquid Ga.

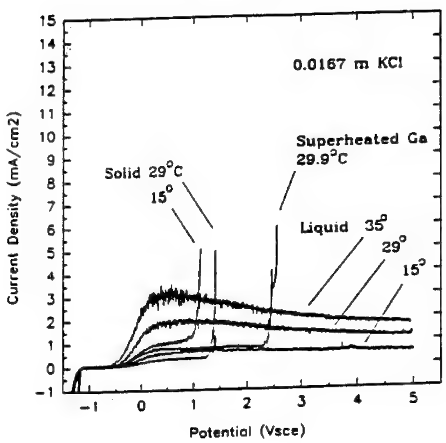

Fig. 7 Anodic polarization diagrams for solid, liquid, and superheated Ga at selected temperatures above and below Tm (29.78°C) in 0.0167 m KCl borate-buffer solution (pH=8). Note that Ga readily supercools.

Now that α_{sol} has been estimated, and noting that the breakdown potential for the liquid is at least 3.3 V more positive than that for the solid (Fig. 4), the relative diffusion rates of cation vacancies in the solid and liquid Ga substrates may be calculated. Rearranging Eqn. (1) yields

$$V_c^L - V_c^S = \frac{4.606RT}{\chi F\alpha}\log\frac{J_m^L}{J_m^S} = 3.3V \qquad (2)$$

where χ=3, α=0.39, and T=301K. J_m^L is calculated to be >2×10^{32} J_m^S (No. $cm^{-2}s^{-1}$), which is indeed an enormous change in the rate of metal vacancy submergence into the substrate or annihilation at the interface. From Fig. 7, calculation of J_m^L with superheated Ga gives a value that is about 6×10^{10} J_m^S, which is substantially less than with a crystalline Ga specimen. Nevertheless, liquid and superheated solid Ga have a far greater capacity to annihilate excess cation vacancies arriving at the metal/film interface than does solid Ga, in accord with the hypothesis of this work.

INTERPRETATION OF SECM DATA

We now return to consider the SECM studies of Casillas et al[1,2], and in doing so we reproduce Fig. 3 from their paper as Fig. 8 here. According to the PDM, the initial rise in the current as the potential of the substrate is swept past $1.2V_{SCE}$ in the positive direction is due to electronic conduction through the film due to the high local vacancy concentration (note that the current is due to the oxidation of Br^- to Br_2). However, simultaneously, cation vacancies begin to condense at the metal/film interface and, as this process proceeds, the current decreases because of the developing

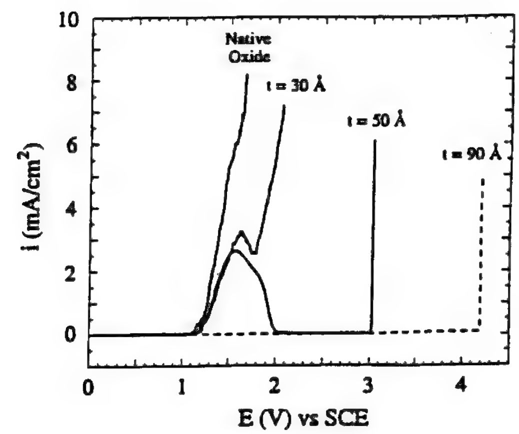

Fig. 8 Voltametric responses of Ti electrodes as a function of oxide thickness, t, in a 1 M KBr, 0.05 M H2SO4 (pH 1.05) solution. Scan rate = 1.0 mV/s. From Reference 1.)

decohesion of the film from the substrate at a number of localized sites. Ultimately, the condensates (or blisters) that form, shut off the local current and the observed current is reduced to the background value that is characteristic of the surrounding passive surface. Thus, as observed by Casillas et al[1,2], the surface becomes "passive" with respect to the oxidation of Br^- at potentials that are more positive than ca -1.6V (SCE). This is the expected response according to the PDM, because localized cation vacancy accumulation at the metal/film interface is a progressive and irreversible process.

According to the PDM,[4] the induction time for passivity breakdown is given by

$$t_{ind} = \xi'\left[\exp\left(\frac{\chi F\alpha\Delta V}{2RT}\right) - 1\right]^{-1} + \tau \qquad (3)$$

where χ is the oxide stoichiometry ($MO_{\chi/2}$), $\Delta V = V - V_c$, V_c is the critical potential (corresponding to the applied potential at which breakdown occurs in infinite time), V is the applied potential, and the other parameters are as defined in Ref. 3. Thus, the first term in Equation (3) corresponds to the time required for the accumulation of a critical (areal, mol/cm^2) concentration of cation vacancies per site at the metal/film interface, as previously discussed.[4,15] On the other hand, the parameter τ was previously identified as a "relaxation" time, and was found to be ~0 for thin barrier layers of the type that form on nickel (for example).[4] However, τ can also be identified with the time required for the film above the cation condensate to thin locally by dissolution, to the point where mechanical instability occurs.[19] Because mechanical rupture may occur before the film has completely dissolved, we may express τ by the inequality[19]

$$\tau \lesssim L_o/(dL^-/dt) = (L_o - L_c)/\Omega k_s C_{H+} \qquad (4)$$

where L_o is the thickness of the barrier layer at the initiation of the breakdown sequence, L_c is the thickness of the film at which rupture occurs, dL^-/dt is the rate of dissolution of the barrier layer at the film/solution interface (cm/s)[14], k_s is the heterogeneous rate constant for film dissolution (cm/s), and C_{H+} is the concentration (mol/cm^3) of hydrogen ion at the barrier layer/solution interface. Designating the potential at which vacancy condensation occurs as V_o and the apparent breakdown voltage as V_p (corresponding to E_p in Casillas et al's terminology) we may write[19]

$$\tau = (V_p - V_o)/v \qquad (5)$$

where v is the voltage sweep rate. Equating the right hand sides of equations (vi) and (vii) therefore yields

$$V_p = V_o + v\,(L_o - L_c)/k_s\Omega C_{H+} \qquad (6)$$

In deriving Equation (6) it is important to note that, because of decohesion of the barrier layer from the substrate at the breakdown site, film growth does not occur as the voltage is swept in the positive direction past the vacancy condensation potential. However, growth of the barrier layer into the metal can occur on surrounding areas, but it is not this film that determines the susceptibility of the site to breakdown. Equation (6) predicts that, for a given voltage sweep rate, and provided that k_s is independent of voltage (which is the case because film dissolution does not involve a change in oxidation state), the apparent breakdown voltage should vary linearly with L_o, which is precisely the relationship observed by Casillas et al.[1,2] However, this equation also demonstrates that the true breakdown potential, corresponding to the condition whence $\nu \rightarrow 0$, is the vacancy condensation voltage, V_o. That this is so is clearly demonstrated by the observation reported in Ref. 2 that breakdown eventually occurs even for $V_o < V < V_p$, if sufficient time is allowed to elapse. Thus, the relationship between the breakdown potential and the film thickness is, in essence, an artifact of Casillas et al's use of a voltage sweep to detect passivity breakdown.

We can extend the analysis further by rearranging Equation (viii) to yield[19]

$$k_s = \frac{\nu\,(L_o - L_c)}{(V_p - V_o)} / \Omega C_{H^+} \tag{7}$$

Selecting $\nu = 1$ mV/s, $C_{H^+} = 0.89\text{x}10^{-4}$ mol/cm^3 (pH = 1.05), and $\Omega = 18.76$ cm^3/mol (for TiO_2, rutile), and noting that $(V_p - V_o) / (L_o - L_c) = 4.3\text{x}10^6$, $6\text{x}10^6$, and $6\text{x}10^6$ V/cm for film thicknesses of 90, 50, and 30 Å (Figure 11), respectively, we obtain a value for k_s of $(1.1 \pm 0.2)\text{x}10^{-7}$ cm/s, independent of the film thickness and hence the growth voltage. In calculating this value for k_s, we have assumed that the dissolution reaction is first order in H^+ and that $L_c = 20$Å (i.e. the native oxide thickness), which is reasonable because the data given in Figure 8 indicate that $\tau \sim 0$ for breakdown of the native oxide at ambient temperature. The value of k_s is consistent with the dissolution of TiO_2 at the film/solution interface being activation (as opposed to mass-transport) controlled, which in turn is consistent with the large temperature effect on passivity breakdown observed by Casillas et al.[1,2]

The rate of dissolution TiO_2 at the barrier layer/solution interface in given by[13-15]

$$\frac{dL^-}{dt} = k_s\,\Omega C_{H^+} \tag{8}$$

Substituting values for the quantities on the right hand side we find that $dL^-/dt = 1.84\text{x}10^{-10}$ cm/s or 1.84Å every 100s. In the steady state, over non-defective regions of the surface, the current density due to penetration of the barrier layer into the substrate (i.e. due to the generation of oxygen vacancies via Reaction (2)) is given by[14]

$$I_{ss}^{a} = \delta F k_s C_{H^+} \sim 3{\cdot}8\mu A/cm^2 \tag{9}$$

where δ was taken as 4 and F = 96,487 C/equiv. This value is uncorrected for surface roughness. Because TiO_2 is predominantly an anion conductor, I_{ss}^{a} should be a good approximation of the passive current density. Although Casillas et al[1,2] do not report the steady state current for their experimental conditions, the value calculated above appears to be eminently reasonable.

CONCLUSIONS

Recent investigations of passivity breakdown on solid and liquid Ga[16,17] and Ti foil electrodes[1,2] polarized in Cl^- and B_r^- containing aqueous solutions, respectively, have been placed into the framework of the point defect model for the growth and breakdown of passive films, which readily accounts for the experimental behaviors of these separate systems. Based upon the results of anodic polarization experiments on solid and liquid Ga and scanning electron microscopy of solid Ga specimens, the following conclusions may be drawn:

- The passive film on liquid Ga exhibits a greater resistance to passivity breakdown compared to the passive film on the solid phase, for a given chloride concentration in borate-buffer, deaerated aqueous solutions.

- Using scanning electron microscopy, blisters at the metal/film interface on solid Ga have been found. Pits on solid Ga specimens have also been found to be covered by an oxide film, which is probably not intact.
- Additionally, we have calculated the rate of cation vacancy annihilation to be many orders of magnitude (~10^{32})greater for a liquid Ga substrate compared to the solid phase.

Concerning the Ti system, an analysis of data recently published[1,2] in the literature shows that:

- SECM data demonstrate the existence of two stages in passivity breakdown on titanium, as proposed previously by the PDM.
- The first stage is consistent with cation vacancy condensation at the metal/film interface beneath the breakdown sites, which are characterized by high cation vacancy diffusivities.
- The second stage corresponds to dissolution of the barrier layer that has become detached from the substrate due to cation vacancy condensation.
- Using the PDM, we derive a value for the heterogeneous rate constant for dissolution of the barrier layer [$k_s = (1.1 \pm 0.2) \times 10^{-7}$ cm/s] on Ti, which leads to a reasonable value for the passive current density (3.8 $\mu A/cm^2$, uncorrected for surface roughness) assuming that the predominant defects in the barrier layer are anion vacancies.

ACKNOWLEDGMENTS

The authors would like to thank the U. S. Department of Energy for the support of this work through Grant No. DE-DG03-84ER45164.

REFERENCES

1. N. Casillas, S. Charlebois, W.H. Smyrl, and H.S. White, J. Electrochem. Soc., **140**, L142 (1993)
2. N. Casillas, S. Charlebois, W.H. Smyrl, and H.S. White, ibid., **141**, 636 (1994)
3. C.-Y. Chao, L.-F. Lin, and D.D. Macdonald, ibid, **128**, 1187 (1981)
4. L.-F. Lin, C.-Y. Chao, and D.D. Macdonald, ibid, **128**, 1194 (1981)
5. C.-Y. Chao, L.-F. Lin, and D.D. Macdonald, ibid, **129**, 1874 (1982)
6. D.D. Macdonald and M. Urquidi-Macdonald, Electrochim. Acta., **31**, 1070 (1987)
7. D.D. Macdonald and S.I. Smedley, ibid., **35**, 1949 (1990)
8. M. Urquidi-Macdonald and D.D. Macdonald, J. Electrochem. Soc., **134**, 41 (1987)
9. D.D. Macdonald and S.I. Smedley, Corros. Sci., **31**, 667 (1990)
10. M. Urquidi-Macdonald and D.D. Macdonald, J. Electrochem. Soc., **136**, 961 (1991)
11. D.D. Macdonald and M. Urquidi, ibid, **132**, 555 (1985)
12. S. Lenhart, M. Urquidi-Macdonald, and D.D. Macdonald, Electrochim. Acta., **32**, 1739 (1987)
13. D.D. Macdonald and M. Urquidi-Macdonald, J. Electrochem. Soc., **137**, 2395 (1990)
14. D.D. Macdonald, S.R. Biaggio, and H. Song, ibid, **139**, 170 (1992)
15. D.D. Macdonald, ibid, **139**, 3434 (1992)
16. D. Ellerbrock and D.D. Macdonald, ibid, accepted for publication, J. Electrochem. Soc. (1994)
17. D. J. Ellerbrock, M. S. thesis, The Pennsylvania State University, (1994)
18. Shreir, L. L., *Corrosion, Metal/Environment Reactions* Vol.1, 243-248 Newnes-Butterworths (1976).
19. D.D. Macdonald, submitted, J. Electrochem. Soc. (1994).
20. C. B. Bargeron and R. B. Givens, ibid., **124**, 1845 (1977).
21. C. B. Bargeron and R. B. Givens, Corrosion, **36**, 618 (1980).
22. P. M. Natishan and E. McCafferty, J. Electrochem. Soc., **136**, 53 (1989)
23. E. McCafferty, P. P. Trzaskoma, and P. M. Natishan, in *Advances in Localized Corrosion*, (NACE-9), H. Isaacs, U. Bertocci, J. Kruger, and S. Smialowska, Editors (1990).
24. J. A. Richardson and G. C. Wood, Corros. Sci., **10**, 313 (1970).
25. G. S. Frankel, L. Stockert, F. Hunkeler, and H. Boehni, Corrosion, **43**, 429 (1987).
26. V. M. Novakovski and A. N. Sorokina, Corrosion Sci., **6**, 227 (1966).
27. J. Yahalom, L. K. Ives and J. Kruger, J. Electrochem. Soc., **120**, 384 (1973).
28. M. J. Chappell and J. S. L. Leach, in *Passivity of Metals*, R. P. Frankenthal and J. Kruger, Editors, The Electrochem. Soc., Pennington, N. J., 1978.

Materials Science Forum Vols. 185-188 (1995) pp. 937-944

Laser activation of passive electrodes

I. Efimov[1], M. Itagaki[1], M. Keddam[2], R. Oltra[1], H. Takenouti[2] and B. Vuillemin[1]

[1] Laboratoire „Réactivité des Solides", URA 23 CNRS, Université de Bourgogne, BP 138, F-21004 Dijon, France

[2] Laboratoire „Physique des Liquides et Electrochimie", UPR 15 CNRS, Université Paris VI, F-75252 Paris Cedex 05, France

Keywords: Depassivation, repassivation, channel flow double electrode, electrochemical quartz crystal microbalance, laser activation

Abstract

The techniques Channel Flow Double Electrode (CFDE) and Electrochemical Quartz Crystal Microbalance (EQCM) coupled to a laser activation of the working electrode are firstly used for studying repassivation kinetics under potentiostatic conditions. First experimental results concerning the behaviour of iron in an acidic solution are shown. Then, numerical simulations for the repassivation of iron based on a reaction model involving two adsorbed species are performed. Comparing the calculated to the experimental responses, the actual rate of repassivation is characterized by defining the time dependence of the fractional coverage with passivating species.Concerning the EQCM technique experimental results obtained for nickel repassivation in a neutral solution are presented. It is demonstrated that the air-formed passive film is about 20 nm thick, whereas its thickness varies only from 0.8 to 1.5 nm , depending on the time of polarization, if the film is formed electrochemically.

Introduction

The Channel Flow Double Electrode (CFDE) and the Electrochemical Quartz Crystal Microbalance (EQCM) are nowadays well-known in electrochemistry (1-2), but were not yet applied to depassivation or repassivation studies.

One of the main problem for studying passivation processes is that both metal dissolution and passivation processes involve charge transfer reaction and contribute to the current. Some additional assumptions should be made to separate their respective contributions to the overall repassivation current transient (3-4).

From an experimental point of view, one solution is to combine current measurements on a depassivated electrode with the above mentioned electrochemical analytical techniques in real-time. Furthermore, the passive film must break down under well defined conditions in spite of the thickness (around 0.5 mm) of the electrolyte in the case of CFDE or of the thickness of the electrode in the case of EQCM (few micrometers). In this study the pulsed laser activation of the passive electrode, perturbation without contact, was combined with the electrochemical techniques.

Laser activation of passive electrodes

The effects of an in-situ pulsed laser pertubation of the passive film interface was analysed in analogy with the mechanical effect generated by a confined medium and allows to define a critical stress for breakdown (5).

The external interface of the passive film, i.e. the passive film itself and the aqueous electrolyte can be assumed as transparent media for the laser radiation at $\lambda = 1.06\ \mu m$ as shown by some results reported in the literature about the absorption coefficient of the passive film (6).

A high temperature plasma is generated above 0.1 $GW.cm^{-2}$, whereas the laser experiments conducted to depassivate a passive electrode is in the power range of 10 $MW.cm^{-2}$. It is important to mention that in this range of laser energy there is no ablation of the metallic target itself (7).

The passive electrode was irradiated by the laser beam (pulsed Nd-YAG Laser wave length = 1.06 μm - pulse duration = 10 ns). A comprehensive understanding of the stress-wave environment is not the purpose of this paper, but it can be summarized by considering the following mechanical sequence induced by the laser pulse in this situation of confined ablation :

-compression of the metallic substrate due to the thermoelastic effect,

-generation of an opposite stress wave during the relaxation.

The momentum balance of the forces applied to the passive film interface is assumed to be disturbed by modifying the binding forces and producing spallation of the passive film (8).

Hydrodynamic techniques for determining the material balance of species involved in repassivation

Experimental device

CFDE is a hydrodynamic method to study electrodes kinetics based on the principles of the Rotating Ring Disc Electrode (9). Two electrodes are placed in the electrolyte stream separated by an insulating gap of 0.4 mm between them (Fig.1). A special home-made bi-potentiostat was used featuring the correction of the ohmic coupling between the two electrodes. After the laser depassivation of a 0.08 cm^2 rectangular section of the upstream passivated Fe electrode, corresponding to 40% of the working electrode area, a part of the Fe^{2+} ions emitted into solution is collected by oxidation at the downstream glassy carbon electrode with the area 0.08 cm^2. The reference electrode is a Saturated Sulfate Electrode (SSE).

The electrolyte is a $HClO_4$ solution, pH1. Its flow rate is fixed to 10^2 cm/s which corresponds to a laminar flow for the 0.5 mm thick channel.

Calibration

The CFDE cell is calibrated with a $Fe_2(SO_4)_3$ solution by superimposing to the potential of the emitting working electrode (-0.2 V/SSE corresponding to the reduction $Fe^{3+} + e^- = Fe^{2+}$) a 20 mV square pulse. The collecting electrode is polarized at 0.8 V/SSE which corresponds to Fe^{2+} oxidation.

In Fig.2 is shown the Nyquist plot of the transfer function $N_T(\omega)$ for various flow rates.

$$N_T(\omega) = (z_{col} \cdot \Delta i_{col}) / (z_{WE} \cdot \Delta i_{WE}) \\ = \Delta i_{col} / \Delta i_{WE}$$

where z_{col} and z_{WE} are the numbers of electrons involved in the collecting and working electrodes respectively ($z_{col} = z_{WE} = 1$). The value of the collection efficiency in the steady state, $N_T(0)$, is approximately 0.3 whatever the flow rate. The same coefficient can be obtained from the ratio of the charges or the integrated currents, i.e. the amount of material. From this diagram we can conclude that the detection system of the CFDE acts as a low pass filter whose cut-off frequency is about 10 Hz. Thus, if the input signal, i.e. the working electrode current, involves components with frequencies above 10 Hz, those will not be detected by the collecting electrode. In other words from a given experimental input signal i^{exp}_{WE}, it is always possible to obtain directly the transformed output signal i.e. :

$$i^{exp}_{WE} * N(\omega) \quad (\text{with } N(\omega) = N_T(\omega) * z_{col}/z_{WE})$$

which is identical to the experimental output signal i^{exp}_{col} (Fig.3b). However, from the latter, it is possible to calculate the input waveform with the following transformation :

$$i^{exp}_{col} * N^{-1}(\omega)$$

but all the high frequencies components (with f > 10 Hz) present in i^{exp}_{WE} disapear in the obtained transformed input signal (Fig.3a).

Results and discussion

Fig.4 represents the experimental currents at working and collecting electrode afetr laser depassivation and for two potentials in the passive range. The time delay due to the mass transport from the working to the collecting electrode is around 40 ms. We note that the more anodic the working electrode potential, (i) the shorter the period of i_{WE}, (ii) the higher the peak current of i_{WE}, (iii) the lower the peak current of i_{col}. From this set of curves we can calculate the charge flowing through each electrode as a function of the working electrode potential. If we assume that the working electrode current is equal to the sum of a dissolution current i_{diss}, and a passive film reformation current i_{film} then :

$$Q_{WE} = Q_{diss} + Q_{film}$$
$$Q_{film} = Q_{WE} - Q_{diss}$$

with

$$Qdiss = (Q_{col} / N_T(0)) * (z_{WE} / z_{col})$$

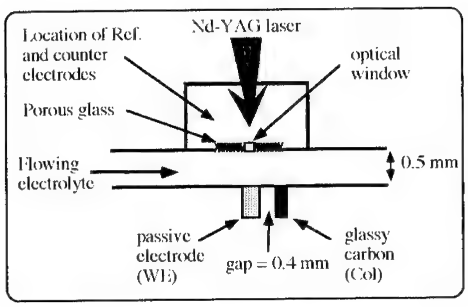

Figure 1 : Experimental device of the Channel Flow Double Electrode technique.

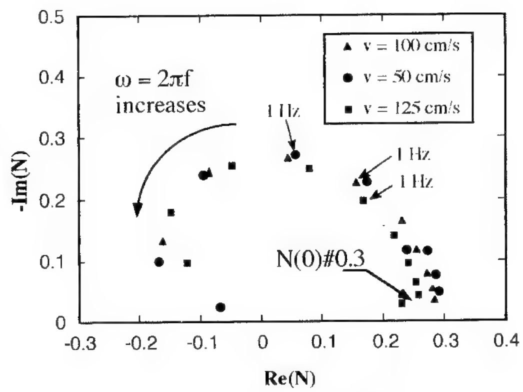

Figure 2 : Nyquist plot of the transfer function $N_T(\omega)$ obtained in a $Fe_2(SO_4)_3$ solution at various flow rates (E_{WE} = -200 ± 20 mV - E_{Col} = 0.8 V/SSE).

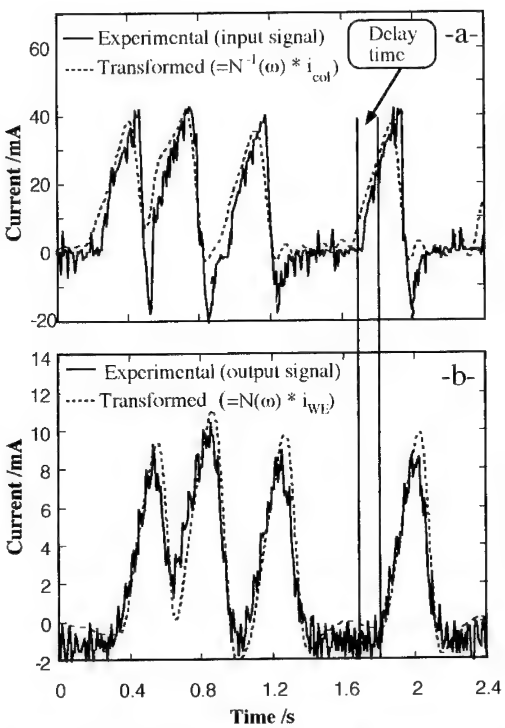

Figure 3 : Experimental and transformed currents obtained by a modulation of the working electrode potential in a $Fe_2(SO_4)_3$ solution (v = 100 cm/s) . Working electrode current (a) - collecting electrode current (b).

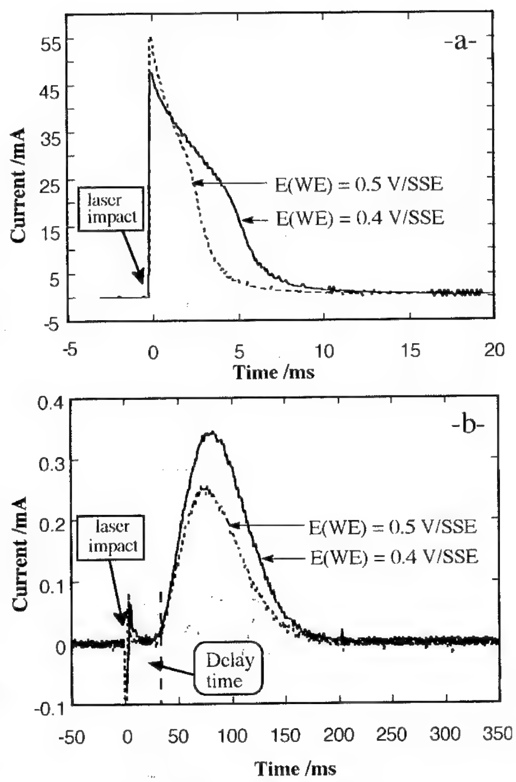

Figure 4 : Current transients of the working (a) and the collecting (b) electrodes obtained in a $HClO_4$, pH1, after a 60 mJ laser pulse (v = 100 cm/s - E_{Col} = 0.8 V/SSE).

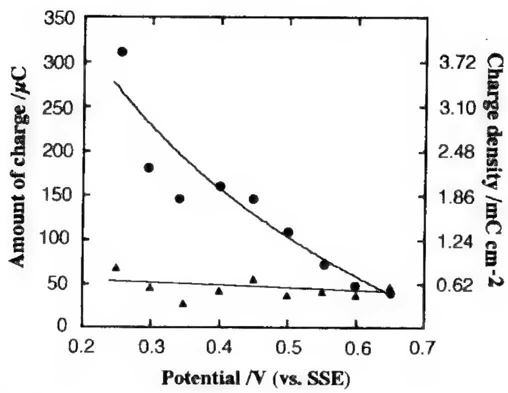

Figure 5 : Amount of charge used for dissolution (●) and film reconstruction (▲) vs. the potential of the working electrode.

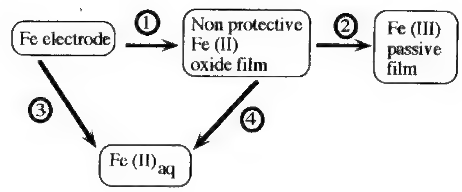

Figure 6 : Model proposed for iron repassivation

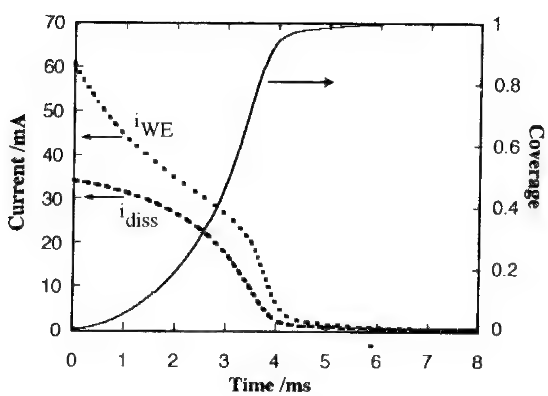

Figure 7 : Simulated dissolution and working electrode current transients and coverage in passive film vs. time (E_{WE} = 0.5 V/SSE).

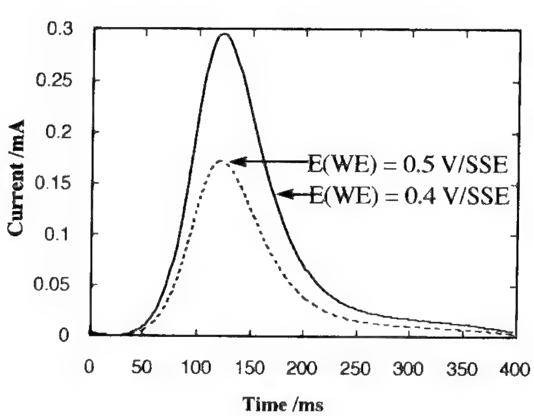

Figure 8 : Simulated collected current transients.

Here z_{WE} is the number of electrons involved in the dissolution reaction on the working electrode ($z_{WE} = 2$). We should note at this point that because of the too fast kinetic of dissolution of the Fe electrode, it is impossible to calculate i^{exp}_{diss} with the tranformation :

$$i^{exp}_{col} * N^{-1}(\omega)$$

In Fig.5 it can be noticed that $Q_{film} = Cst = 600\ \mu C\ cm^{-2}$ whatever the value of the working electrode potential. This value corresponds to the formation of a 2.10^{-9} mol cm^{-2} trivalent oxide film.

In order to check these experimental results, a model proposed by Benzekri et al. for the repassivation of iron has been tested (10). This model described in Fig.6 can be summarized as follow :

Reaction 1 : Formation of a monolayer of a divalent oxide film. This film is non-protective against dissolution of the metal (reaction 4).

Reaction 2 : Formation of a monolayer trivalent oxide film (= passive film)

Reaction 3 : Dissolution of the bare metal surface.

Reaction 4 : Dissolution of the metal through the non-protective Fe(II) film.

By using this model, theoretical transient currents relative to the working electrode are represented in Fig.7. It appears that they are in good agreement with the experimental ones. Such a simulation allows to plot the coverage with the passive film vs. time i.e. to represents the kinetics of the first stage of repassivation from a bare metal surface (coverage = 0) to a monolayer of passive film (coverage = 1) which corresponds to 2.10^{-9} mol cm^{-2} trivalent oxide film. From the theoretical current i^{th}_{WE} at the working electrode, it is possible to calculate the theoretical current i^{th}_{col} at the collecting electrode with the following transformation :

$$i^{th}_{col}(t) = N(\omega) * i^{th}_{WE}(t)$$

Here again there is a good fit between theoretical and experimental results (Fig.8).

Gravimetric techniques for determining the mass balance during repassivation

Experimental device

A quartz resonator operating with one face in contact with the solution acting simultaneously as working electrode is a sensitive tool for investigating electrochemical processes. A sketch of our experimental device is given in Fig.9. A 2 μm thick electrochemical deposit of nickel is made on one of the gold plated faces of the quartz (area = 1.33 cm^2). During the de-repassivation studies the Ni working electrode is held at the passive potential of 0 V/SSE in a pH 8.4 borate buffer solution.

The same central spot on the electrode surface is irradiated each time, with the first laser pulse being used to remove what we call the air-formed passive film. Actually this passive film had been formed partially in air and in the electrolyte just after the nickel plating. Passivation time is then measured from the previous pulse.

Calibration

When combining EQCM with laser depassivation the following points should be taken into account :

- the quartz resonance frequency is sensitive not only to the electrode mass changes themselves, but also to the stresses in the deposited film and to the motion of the solution. The last two factors are far from negligible when electrode surface is irradiated by the laser beam.
- laser depassivation is a local process, so the differential quartz sensitivity should be used in the interpretation of the frequency shift.

The differential sensitivity in the case of a local ablation of matter from a film covering the quartz was determined for the self propagating dissolution of a Ni-Cu film initiated by a 0.1 mm diameter laser spot (11). In the case of depassivation, i.e. ablation of passive film, the amount of matter which is removed from the electrode is very small and the conventional differential mass sensitivity of the EQCM can be applied to calculate the change of mass from the change in frequency. The differential mass sensitivity S in the centre of the 6 MHz quartz plates for a 1.5 mm diameter spot is equal to 138 kHz/mg (11).

Results and discussion

Fig.10 represents the frequency shift of the resonnance frequency and the current vs. time after the first laser depassivation for two separate samples. Note that the relaxation time of the current (≈ 150 ms) is slower than that of the resonance frequency (≈ 5 s). As mentioned above, the latter should correspond not only to a mass variation but also to the induced stresses in the film and the motion of the electrolyte near the surface after the laser pulse. Therefore the frequency response can be analysed in terms of mass variation only at the steady state i.e. t > 5 s. The initial mass of the working electrode is never recovered after the laser pulse. The frequency shift between the initial and the final resonnance frequency of the quartz gives the total mass loss Δm_t that we assume being the sum of both following components :

• Δm_q = mass of Ni dissolved before repassivation occurs.

$$\Delta m_q = (Q \,.\, M) / (2 \,.\, F)$$

where Q is the charge (integral of the current transient), M the atomic mass of Ni (58.7 g) and F the Faraday's constant.

• Δm_f = mass of Ni passive film removed by the laser pulse.

assuming that the mass increase due to the reconstruction of the passive film is negligible in this time domain.

$$\Delta m_f = \Delta m_T - \Delta m_q$$
$$= [-\Delta f / S] - [(Q \,.\, M) / (2 \,.\, F)]$$

If ρ, Δt and A are respectively the density (6.67 g cm^{-3}), the thickness and the area of removed matter then :

$$\Delta t = \Delta m_f / \rho A$$

Two sets of results obtained for the air-formed passive film (i.e. for the first laser pulse) are summarized in table 1. The total mass variation is to a large extent due to the film ablation. Its thickness is around 20 nm.

Table 1 : Results obtained for the air-formed passive film

Δf (Hz)	Q (mC)	Δm_T (ng)	Δm_q (ng)	Δm_f (ng)	t (nm)
35	6.7	254	2	252	21
41	9.6	297	3	294	25

Fig.11 represents the thickness of the passive film vs. time of passivation, each point corresponding to a laser pulse. Δt is around 0.7 nm for passivation times < 30 min and later increases up to about 1.5 nm. These results are in good agreement with those obtained by Sato in borate buffer for one hour polarisation (12). These authors obtained a value of Δt=0.8 nm by ellipsometry and 1.3 nm by coulometry.

Conclusion

The technique of laser pulse activation of passive electrode has proved to be a useful tool to obtain rapidly and without contact a depassivated surface. The kinetics of repassivation was been studied with the Channel Flow Double Electrode and the Quartz Crystal Microbalance techniques.

During the early stage, i.e. the first milliseconds, of iron repassivation the current transients obtained by the CFDE technique are in good agreement with a model of iron repassivation. The technique would be more appropriate for pitting corrosion studies (a single pit beeing initiated by a focused laser pulse) because in this case the current transients involve components of frequency below the 10 Hz cut-off frequency.

With the EQCM technique it is more difficult to work in real time because during the first seconds after the laser pulse the frequency variations of the nickel plated quartz are due not only to mass changes but also to stresses in the nickel film and/or to the motion of the electrolyte near its surface. Nevertheless it was possible to obtain mass balances and to calculate the thickness of the passive film which varies from 0.7 to 1.5 nm depending on the time of passivation

References
(1) T.Tsuru, Materials Science and Engineering, **A 1 4 6**, 1 (1991).
(2) D.A.Buttry, M.D.Ward, Chem. Rev., **9 2**, 1355 (1992).
(3) T.R. Beck , Electrochimica Acta, **1 8**, 807 (1973).
(4) J.R. Ambrose, Treatise on Materials Science and Technology, vol.23, p.175, Academic Press New York, (1983).
(5) R. Oltra, G.M. Indrianjafy, J.P. Boquillon, Journal de Physique IV, Colloque C7, p.769, suppl. Journal de Physique III, 12, 1991.
(6) G. Okamoto, Corrosion Sci. **1 3**, 471 (1971).
(7) D.A. Hutchins, R.J. Dewhurst, S.B. Palmer, **1 9**, 103 (1981).
(8) R.Oltra,Corrosion Deformation Interactions, Eds. T.MAGNIN et J.M. GRAS, Ed. de Physique, p.721, 1993.
(9) W.J.Albery and M.L.Hitchman, "Ring-Disc Electrodes", Oxford Univ.Press (1971), p.151.
(10) N. Benzekri, R. Carranza, M. Keddam, H. Takenouti, Corrosion Sci., **3 1** (1990) p627-635.
(11) I.Efimov and R.Oltra, J. Electrochem. Soc., **1 4 1**, 7 (1994) 1838-1842.
(12) N. Sato, K. Kudo, Electrochemica Acta, **1 9**, 461 (1974).

Acknowledgements: I. EFIMOV(Institute of Chemical Physics - Chernogolovka - Russia) and M. ITAGAKI (Institute of Technology - Tokyo - Japan) thank the "Conseil Régional de Bourgogne" for the financial support of their post-doctoral positions.

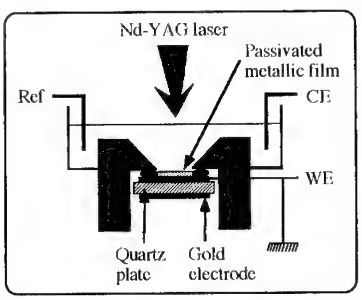

Figure 9 : Experimental device of the Electrochemical Quartz Crystal Microbalance.

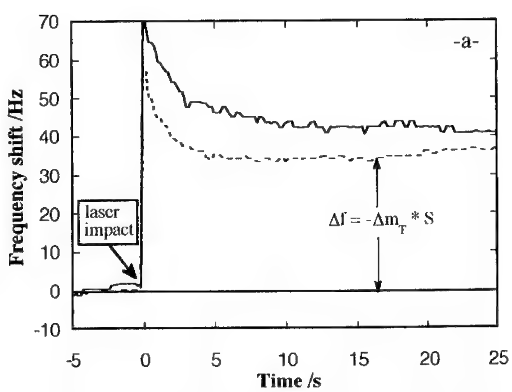

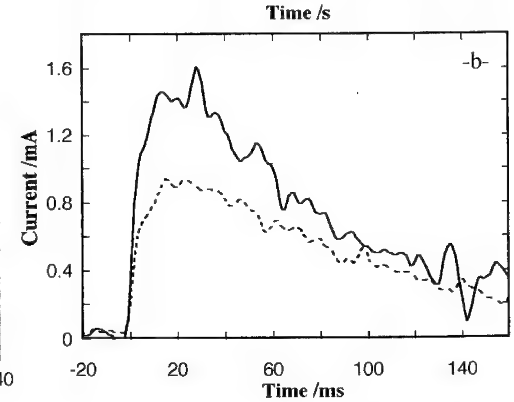

Figure 10 : Frequency shifts (a) and current transients (b) obtained for the air-formed passive film (V = 0 V/SSE - pH 8.4 borate buffer solution).

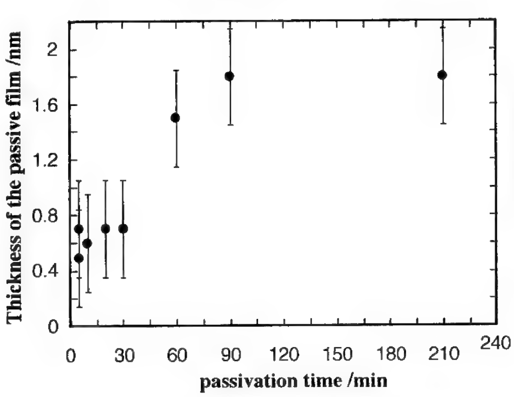

Figure 11 : Thickness of the pasive film vs. time of passivassion at 0 V/SSE in a pH8.4 borate buffer solution.

Materials Science Forum Vols. 185-188 (1995) pp. 945-954

Dissolution kinetics of model pits of stainless steels

L.I. Freiman

Academy of Municipal Economy, Volokolamskoe shosse 116, 123371 Moscow, Russia

Keywords: Pit dissolution kinetics, model pit, stainless steel, halide solutions

Abstract

Quasistationary dissolution rates (i_{mp}) of model pits (MPs)- disk electrodes made of austenitic Cr-Ni steels - were determined as a function of potential (E), neutral solution and steel compositions, temperature, and disk rotation frequency. It was shown that anodic polarization curves of MPs consisted of two main regions: Tafel lines close to the repassivation potential (E_{rp}) and anodic limiting current (ALC) at the higher current densities. In the Tafel region, the i_{mp} value is controlled simultaneously by surface and transport steps, with no IR drop in the closest vicinity of E_{rp}, and with growing IR contribution at the increasing potential. In the ALC region, the decisive role is played by the IR drop localized probably in capillary liquid of a capillary-porous layer of corrosion products.

In numerous works on pitting corrosion mechanism, the main characteristics studied were usually the pitting boundary potentials and/or the induction period of pit formation. Less attention was paid to dissolution kinetics of metal in pits, and most of the corresponding works considered mainly current-time curves for pit and development of its form in time (e.g.[1-5]).

Three main measuring methods were applied in the works on pitting kinetics: (1) on usual electrodes in solution imitating the real pit inner solution (e.g.[6]), (2) on real pits, with the microscopical determination of their sizes and forms (e.g. [7]) and (3) on model (artificial) pits: electrodes wich are completely activated by anodic polarization in halide solutions (e.g. [8, 9]). In our investigations on pit kinetics in stainless steels carried out mainly at the Karpov Institute of Physical Chemistry since 1981, the third method was used, which allows one to find with relative ease the dependencies of pit current densities upon experimental conditions. This method excludes the possible distinctions between real and imitated pit solutions, and complicated determination of

the true pit surfaces area as well. An essential limitation of this method for model pits (MPs) made of stainless steels is the difficulty in ensuring the necessary total anodic activation of the electrode surface. This narrows the interval of the solutions acceptable for the work. For this reason we used concentrated solutions of halides, especially aqueous and aqueous- methanolic solutions of 5 M LiCl at the temperature >30 C.

MP's in form of cylinders (diam. 3 - 5 mm) with the disk surface exposed to the solution were made of austenitic stainless steels, the compositions of which are given in Table 1*). Ohmic potential drop (IR) was excluded and/or determined by the known method of current interruption. Viscosity, density and conductivity of solutions were measured in a number of cases. Details of experiments are given elsewhere [10-15].

Table 1. Chemical composition of the steels studied.

Designation in the text	Elements content, w/o								
	C	Cr	Ni	Mo	S	Mn	Si	Ti	P
18-11(p)	0.025	18.27	12.33		0.002	0.41	0.50		
18-11(u)	0.024	18.42	12.04		0.013	1.35	0.50		
17-14(p)	0.028	17.0	13.9		0.002	0.17	0.68		
17-14(u)	0.012	16.9	14.2		0.014	1.46	0.61		
17-14-Mo(p)	0.025	17.0	13.9	2.56	0.003	0.12	0.71		
17-14-Mo(u)	0.024	17.93	14.0	2.88	0.013	1.55	0.74		
18-10-Ti	0.07	17.86	11.3		0.012	1.23	0.31	0.65	0.033

1) Pure in relation to MnS inclusions.
2) Usual quality (with MnS inclusions).

*) Iron electrodes were used in some experiments.

A typical quasistationary anodic curve of MP in a neutral halide solution shown schematically in Fig 1 includes two main regions: Tafel straight line with the slope b_α = 80-90 mV (except "u" steels, b_α= 60 mV) and anodic limiting current (ALC), with the transitional region between them. In the Tafel region, the MP surface is etched with formation of crystalline terrace structure showing influence of the surface-sensitive slow step. Inside the AIC region, the surface is smoothing in aqueous solutions and is polished in aqueous-methanolic solutions, i.e. the surface step has no effect on the MP dissolution rate i_{mp} here. The inflection point in the Tafel line at the side of less positive potentials (E), where repassivation begins at the reverse course of the polarization curve, is considered further as corresponding to repassivation potential (E_{rp}) and the MP critical current (i_{cr}, see Fig. 1). In a number of cases in the closest vicinity of E_{rp} there is a region (up to 100 mV wide, ab in Fig. 1), where the IR drop is absent. Evidently, under these conditions, the possibility of pit existence in passive metal is ensured by a non-ohmic factor. But at raising E, the role of IR drop increases, a mixed control (IR - no IR) is realized in the transition region (bc), and in the ALC region the MP dissolution proceeds with the IR-control completely. One can say that depending on E and solution conductivity, the pits in surface "use" various modes or survival.

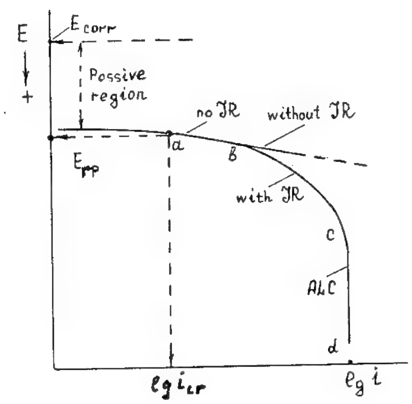

Fig. 1. Schematic anodic polarization curve of MP in a neutral concentrated halide solution

For understanding the MP's IR-free behavior in Tafel region, data are useful on the influence of disk rotation frequency (ω) upon i_{mp} in an aqueous 5 M LICl solution (Fig. 2a, [13]). It can be seen that at increasing ω the i_{cr} and E_{rp} values arise, and the Tafel line shifts to the more positive E values. i.e. stirring hinders the MP dissolution process. The E_{rp}-i_{cr} points in the curves can be com-bined with a certain approximation by a straight line with the slope

$$b'_{a}=(dE_{rp}/d\lg i_{cr})\approx 160\ \text{mV}\approx 2\ b_{a} \qquad (1)$$

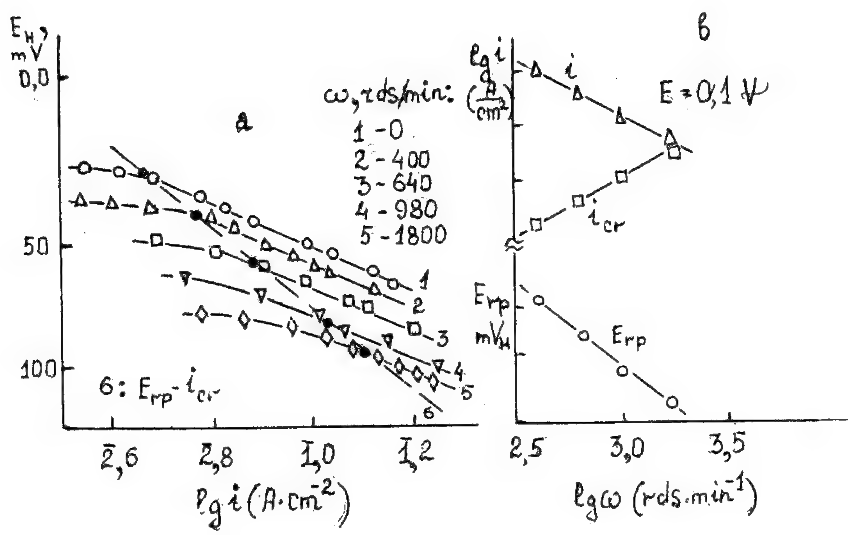

Fig. 2. Influence of the disk MP rotation frequency upon its anodic behavior in an aqueous 5 M LiCl solution at 30 C (steel 18-10-Ti): polarization curves (a) and the effect of ω on i_{cr}, E_{rp} and i at E=0.1 V (b).

Such effect of stirring can't be explained by a decrease of the near-surface concentration of activating Cl -ions as, in 5 M LiCl near E_{rp}, it can't exceed significantly the bulk concentration (not more than by 10 - 20%) [13]. According to [13,16], an enhanced removal of some second activator X must be decisive, most probably of hydrolytic H^{+} -ions (their role has long been recognized in a number of pitting theories, e.g. [17-20], and very low pH values (up to pH 0) were reported, e.g. [6, 21], for pits in stainless steels corroding in neutral chloride solutions). If the near surface concentrations of H^{+} (C_{H^+}) and ions of dissolving metals Me^{z+} (C) are related by the equation $C_{H^+}= k_1 \cdot C^{m}$ (m >0), and the same critical concentration of H^{+}, $C_{H^+}=C_{cr}$ corresponds to E_{rp} at all ω values, and removal of Me from MP proceeds mainly by stationary diffusion

processes, the formal equation (2) must be valid at a high concentration of halide in a neutral solution:

$$i_{mp} = k_2\, C_{H^+}^{n} \cdot \exp(2.3\ E/b'_{\alpha}). \qquad (2)$$

It can be shown that from eq. (2) follows:

$$i_{mp} = k_3 \cdot \delta \cdot D^{-1} \cdot \exp(2.3\ E/b_{\alpha}). \qquad (3)$$

Here D is mean diffusion coefficient of Me^{Z+}, n is the apparent reaction order with respect to H^+, δ is the thickness of diffusion layer. For the rotating disk ($\delta \sim \omega^{-0.5}$), eqs. (1) and (3) lead to the relations: $(dE_{pp}/d\lg\omega) = 0.5\ b'$; $(d\lg i_{cr}/d\lg\omega) = 0.5$, which agree well with the experimental values (Fig. 2b): 80 mV and 48 respectively.

The value of δ in (3) is associated with the characteristic real pit sizes by reported relations [22, 23]. Therefore, for usual electrodes with pits of regular geometrical shape, from the eq. (3) it follows that at the constant anodic current I during a definite time (t) interval, the relation $(dE/d\lg t) = -b$ should be valid, and the value of b should be close to the Tafel slope b_{α} for the MP [23]. This was experimentally confirmed for usual electrodes of steels 18-10-Ti, 18-11 (u), and 18-11 (p) for which the relation b/b_{α} in the aqueous 5 M LICI solution was equal to 0.64, 0.68 and 0.84, respectively [23].

The eq. (3) reflects the feedback between the MP dissolution rate and near-surface concentration of H^+ -ions : the C_{H^+} increases with an increase in δ, and activating action of H^+ lons leads to the acceleration of the dissolution process. This acceleration itself may be caused by hindering the formation of a quasipassive layer that lowers the share of the active surface *)(θ). If, in the slow quasistationary measurements, the i_{mp} decreases exponentially with θ, and θ grows linearly with E and decreases logarithmically with C_{H^+}, the observed relation $b'_{\alpha} > b_{\alpha}$ should be valid [13, 16]. An analysis of coefficients in the intermediate equations shows that real order of the MP dissolution reaction with respect to H^+ -ions

*)Some data point to the existence of similar layer on the surface of active iron in chloride solutions [24].

can be negative, in contrast to the apparent order n in eq. (2).

At fast changes of E, when θ and C_{H^+} values haven't enough time to vary, the Tafel slope b_f should be less than b_a. It was confirmed indirectly by potential-decay curves from Tafel region after switching off the current. When plotted as ΔE against lgt, these curves were straightened in a certain interval of time (t) $3 \cdot 10^{-4}$ - $3 \cdot 10^{-3}$ s. As it is known, the corresponding slope $b_d = d\Delta E/d\lg t$ should be equal to the true Tafel slope of the polarization curve not distorted by surface changes during the time of measurements. For the 18-10-Ti steel in aqueous-methanolic 5 M LiCl solutions, the b_d value is the same (like b_a) and equals $\approx$ 42 mV thus confirming the relation $b_f < b_a$. An analogy is evident with the data [25] for iron in the neutral chloride solution, according to which the ratio between Tafel slopes of the slow and fast anodic curves (80 and 40 mV) was equal to 2:1 like in our case for $b_a : b_d$.

In a number of works (e.q. [26,27]), the mechanism of metal dissolution in pits was identified presumably with that of active dissolution. Indeed, the data given above show doubtless similarty of these processes. But at the same time, the principal role of the slow transport step of pit dissolution and a number of other results point to serious differences between them. It can be demonstrated especially by comparison of MP anodic curves in neutral halide solutions and of "usual" active electrodes in acidic solutions (pH 0 and 1) with the same concentration of halide ions (5 M). It is seen in Fig. 3 [15] that the Tafel sections for the active steels both in chloride and bromide solutions are situated at essentially less positive potentials that those of the MP anodic curves. Moreover, the Tafel slope (at 45°C) in the active region is 40 mV for the steel without molybdenum (17-14(p)) and lowers up to 20 - 30 mV for Mo-containing steel (17-14-Mo(p)), while b_a values for MP given above are independent of alloying by Mo. It is especially interesting that in the bromide solution the curves in active region for two steels intersect in such a way that at E>0.1 V molybdenum accelerates the process. Nothing of the kind was observed for the MPs. It is useful also to compare the molybdenum influence upon conventional rate constants in the equation $i = k \cdot \exp(2.3 \cdot E/b)$, which is identical formally for both processes. Fig. 4 shows that the ratio between these constants for the steels without Mo and whith Mo in the case of active dissolution ($K_a/K_{a,Mo}$) is much higher

in both solutions than similar ratio for MPs ($K_{mp}/K_{mp,Mo}$). In so doing, in the bromide solution, with an increase in temperature the $K_{a}/K_{a,Mo}$ value raises significantly,

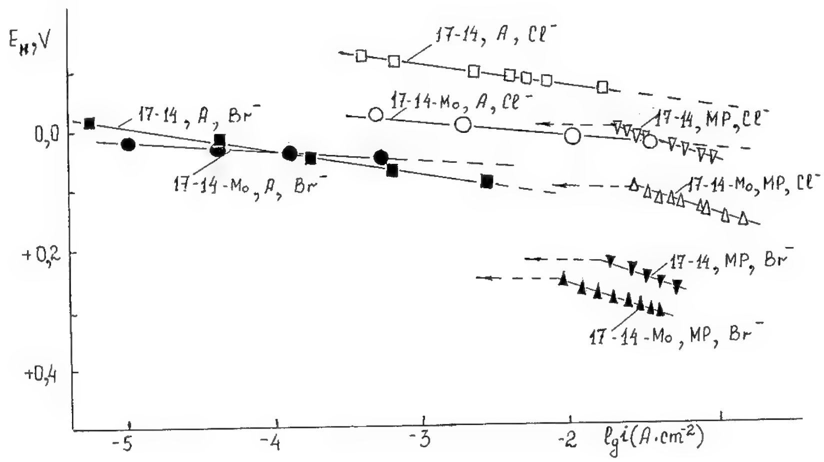

Fig. 3. Anodic polarization curves of active (A) electrodes in acidic (pH 0) solutions and MP's in neutral (pH 6) aqueous solutions of 5 M LiCl and 5 M NaBr at 45° C. Steels: 17-14 (p) and 17-14-Mo(p)

while the $K_{mp}/K_{mp,Mo}$ decreases slightly. Therefore, it seems reasonable to consider the dissolution of pits in Tafel region as a rather specific kind of active dissolution. Analysis of its steps is beyond the scope of this work.

For the ALC region, in accordance with a number of works (e.g. [28, 29]), the main part of the potential shift is localized as an IR drop in a certain surface layer of corrosion products, most likely in salt layer involving oxides. However,

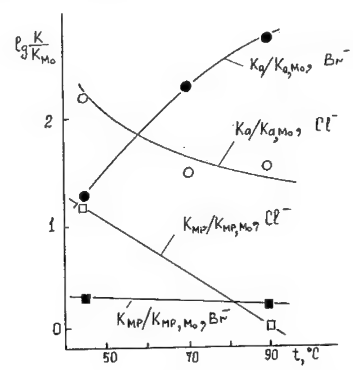

Fig. 4. Influence of temperature of 5 M LiCl and 5 M NaBr aqueous solutions upon the ratio between conventional constants of dissolution rate for the active electrode of steels 17-14(p) and 17-14Mo(p) at pH 0 ($K_{a}/K_{a,Mo}$) and for MP's of the same steels at pH 6 ($K_{mp}/K_{mp,Mo}$).

surprising was the absence of effect of disk rotation frequency on the ALC, though for iron disk such an effect was observed under the same experimental conditions, in agreement with [30]. On the other hand, a distinct correlation was found between the ALC and the properties of the 5 M LiCl aqueous-methanolic solutions like viscosity and especially conductivity ($\varkappa$), wich varied regulary with water content (C_{H_2O}), Fig. 5 [10, 14]. The apparent activation energy of the ALC (E_{ALC}) is low and decreases linearly with C_{H_2O} from 25 kJ/mole im methanolic solution up to 14,2 kJ/mole in the aqueous solution. This is difficult to explain assuming slow iron migration in the poreless salt layer. More probably, the limiting step is mass transfer (migration) through the liquid in pores of the capillary porous salt layer. Taking into account the data [31] for copper in phosphoric acid, one should assume that the E_{ALC} values are determined not only by activation energy of migration process, but also by the heat of salt dissolution Q_p:

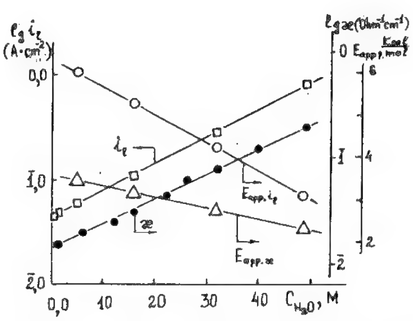

Fig. 5. The effect of water concentration in aqueous-methanolic solution of 5 M LiCl on ALC (i_ℓ) of the steel 18-10-Ti and solution conductivity ($\varkappa$) at 30 C (a), and on the apparent activation energies of the conductivity and of the ALC of the same steel (b).

$$ALC \sim \exp(-E_{\varkappa}/RT)\cdot\exp(-Q_p/RT)$$

i.e. $E_{ALC} = E_{\varkappa} + Q_p$. The Q_p value was determined from the solubilities of $FeCl_2$ salt in two solutions of 5 M LiCl at 30 and 70° C for each, assuming an exponential dependence of solubility on temperature. The calculated and experimental values of E_{ALC} (Table 2) agree satisfactorily confirming the proposal made.

Table 2. Energy values, kJ/mole

Characteristic	5 M LiCl in:	
	H_2O	$CH_3OH + 5\ M\ H_2O$
$E_{æ}$	8.5	14.6
$Q_p\ (FeCl_2)$	4.9	9.6
E_{ALC}, calc.	13.4	24.2
E_{ALC}, experim.	12.8	24.7

References

[1]. I.V. Harb and R.C. Alkire, J. Electrochem. Soc., V.138, 2594 (1991).
[2]. A.M. Riley, D.B. Wells and D.E. Williams, Corros. Sci., V. 32, 1307 (1991).
[3]. P.C. Pisrorius and G.T. Burstein, in "Progress in the Understanding and Prevention of Corrosion", publ. by Institute of Materials (London), 1993. V.1, p.1109.
[4]. R.Regada, F. Sagues and S.M. Costa, ibid, p.407.
[5]. Y.Xu, M. Wang and H.W. Pickering, J. Electrochem. Soc., V.140, 3448 (1993).
[6]. T. Suzuki, J. Minora, J. Kitamura, Corrosion (USA). V.29, 18 (1973).
[7]. H.-J. Engell, N.D. Stolica, Z. Phys. Chem, (N.F.). B.20, 113 (1959).
[8]. N.D. Green, M.G. Fontana, Corrosion (USA). V. 15, 32t (1959).
[9]. N.D. Tomashov, O.N. Markova , G.P. Chernova, Korroziya i Zashchita Konstruktsionnykh Splavov (Corrosion and Protection of Construction Alloys), Moscow: Nauka, 1966, p.3.
[10]. L.I.Freiman, I.I. Zamaletdinov, Zashch. Met. V. 18, 520 (1982).
[11]. I.I. Zamaletdinov, L.I. Freiman. Zashch. Met. V. 19, 556 (1983).
[12]. L.I. Freiman, I.I Zamaletdinov, Zashch. Met. V. 20, 373 (1984).

[13]. L. I. Freiman, I. I Zamaletdinov, Zashch. Met., V. 20, 586 (1984).
[14]. L. I. Freiman, I. I Zamaletdinov, Zashch. Met., V. 20, 890 (1984).
[15]. Ya. M. Kolotyrkin, L. I. Freiman, I. I. Reformatskaya, E. A. Pan'shin, Zashch. Met., V. 30, 453 (1994).
[16]. L. I. Freiman, Itogi Nauki i Tekniki. Korrosiya i Zashchita ot Korrozii. V. 11, Moscow: VINITI, 1985, p. 3.
[17]. T. P. Hoar, Trans Faraday Soc., V. 33, 1152 (1937).
[18]. Y. Hisamatsu, in "Passivity and its Breakdown on Iron-Base Alloys", USA-Japan Seminar, Houston, 1976, p. 99.
[19]. J. R. Galvele et al., in "Localized Corrosion", NACE, 1974, p. 580
[20]. N. Sato, J. Electrochem. Soc., V. 129, 260 (1982).
[21]. S. Szklarska-Smialowska, in "Localized Corrosion", publ. by NACE, 1974, p. 312.
[22]. L. I. Freiman, Zashch. Met., V. 20, 711 (1984).
[23]. L. I. Freiman, I. I. Reformatskaya, Zashch. Met., V. 21, 378 (1985).
[24]. F. M. Mikheeva, G. M. Florianovich, Zashch. Met., V. 23, 33 (1987).
[25]. S. Asakura, K. Nobe, J. Electrochem. Soc., V. 118, 19 (1971).
[26]. G. Herbsleb, H.-J. Engell, Z, Elektrochem. Ber. Bunsenges. Phys. Chem., B. 65, 881 (1961).
[27]. R. C. Newman, Corros. Sci., V. 24, 691 (1984).
[28]. K. J. Vetter, H. H. Streblow, in "Localized Corrosion", NACE, 1974, p. 240.
[29]. H. S. Isaacs, J. Electrochem. Soc., V. 120, 1456 (1973).
[30]. H. Kuo, D. Landolt, Electrochim. Acta, V. 20, 393 (1975).
[31]. R. Kirchheim, K. Maier, G. Tolg, J. Electrochem. Soc., V. 128, 1027 (1981).

Materials Science Forum Vols. 185-188 (1995) pp. 955-964

Effect of nonmetallic inclusions in steels on stability of their passive state

M. Janik-Czachor[1], A. Szummer[2] and S. Hofmann[3]

[1] Institute of Physical Chemistry, PAS, Warsaw, Poland

[2] Department of Materials Science and Engineering, Warsaw University of Technology, Warsaw, Poland

[3] Max-Planck Institut für Metallforschung, Stuttgart, Germany

Keywords: Passivity, nonmetallic inclusions, pitting corrosion, low Mn stainless steels

ABSTRACT

The stability of passive state of Cr-Ni stainless steels is often limited by their susceptibility to chloride attack (pitting) in chloride-containing media. Chemical inhomogeneities, notably non-metallic inclusions, within the metal matrix adversaly affect stability of the passive state. In this paper electrochemical, micoscopic, X-ray microprobe and surface analytical investigations of several series of steels are reported. The results of investigations aimed at showing a correlation between pitting resistance of steels, the composition of the non-metallic inclusions, and the composition of the passive film formed at the inclusions as compared to its composition at the adjacted metal matrix, are given. A tentative mechanism of pit initiation at various inclusions in neutral chloride solutions is proposed.

1. INTRODUCTION

Nonmetallic inclusions in steels follow consistent and reproducible patterns. Their character and composition are also features of steel composition. Indeed there is a strong relationship between the character of the inclusions and the mechanical and chemical properties of steels [1-6]. Since it is not always possible to eliminate inclusions entirely attempts are made to control their composition and shape.

On the basis of existing experimental evidence [4-22] it would appear that the sulphide inclusions are indeed the main source of pit initiation in stainless steels. There have, however, been sporadic reports about the effect of oxide inclusions on pitting [11,23]. In our early work oxide particles were sometimes found within the pits [11]. Careful electron microprobe investigations of the specimens before corrosion, revealed that the oxide particles were almost always associated with sulphides, sometimes as very tiny shells. An example of such a tiny sulphide associated with relatively large oxide is shown in Fig. 1. Our experience suggests, therefore, that the inclusions other than those of sulfide can play a role in pit nucleation, but only in the absence of sulphide inclusions. For more details see ref. [23].

The long term research on composition and morphology of sulfide inclusions has been summarized by Kiessling [1]. The composition of sulphide inclusions in steel depends on the content of elements exhibiting high chemical affinity to sulfur. Sulphides rich in manganese appear in steels containing Mn; however, in the presence of elements with higher affinity to S than Mn, sulphides of these elements, instead of MnS, appear. With a low Mn content in steel, mixed sulphides may

appear; for example in the case of Cr and Cr-Ni stainless steels the inclusions of the $(Cr,Mn)_xS$ - type form. When Ti is present in steel, titanium sulphides will dominate. It is difficult to lower the sulphur content sufficiently to eliminate completely sulphide inclusions since with an S content as low as 0.001% complex MnS - oxide inclusions still appear.

Jansen at all. [24], suggest that among the unstable inclusions (K, L, see Fig. 2) laying near the surface of the matrix, only (L) are possible initiation sites, because K will undergo an immediate dissolution and removal from the surface. However, the role of a given inclusion (K) seems to depend both on its composition and its ability to passivate in a given environment. A detailed information concerning passivity of the inclusions intersecting the surface are lacking. The surface analytical methods provide a possibility to obtain such an information.

The aim of this work was:

- to investigate (with SAM) the passive film formed at inclusions as compared to that at the adjacent matrix in neutral solutions in order to learn about the local composition of the film at these sites,
- to find a correlation between the anodic behaviour to the steels, the composition of their nonmetallic inclusions as well as the local composition of the passive film at the inclusions, as compared to that at the adjacent metal matrix.

2. EXPERIMENTAL

2.1. Materials

Considering the above discussed relationship between the steels composition and the composition of sulphide inclusions, formed within the matrix during the process of steel making, the 18Cr-14Ni stainless steels were used for the investigations. They could be divided into 3 groups:

- commercial steels with < 1.6% Mn and < 0.15% S and < 0.4% C
  - I - with 2.5% Mo and 0.22% Ti
  - II - with no additional alloying
- low Mn steels with < 0.3% Mn, < 0.015% S and < 0.04% C
  - E-1 additionally alloyed with 0.64% Ti
  - R-4 ---------
  - Z-7 additionally alloyed with 0.65% Ti and 0.7% Mo
- laboratory heats with 0.005% C and no Mo or Ti
  - A - with 0.15% Mn, 0.12% S
  - B - with 2.0% Mn, 0.24% S

The composition of the above materials was selected so that they contained different nonmetallic inclusions in their structure, see Table 1.

2.2. Electrochemical measurements

The electrochemical measurements were performed in deaerated solution of 0.5 M NaCl, buffered or not buffered, at 25^oC. The anode potential was measured vs "SCE". E_{np} - pit nucleation potential was determined, as described elsewhere [6].

For the surface analytical measurements the specimens were prepassivated in borate buffer of 0.11M H_3BO_3 + 0.027M $Na_2O_4B_7$, pH = 8.4, during 1h, at open circuit potential (aerated electrolyte), or at E = -250 mV_{SCE} in deaerated electrolyte. Both procedures resulted in the same passivation behaviour of the inclusions. The borate buffer was used for the prepassivation because

pit nucleation potential for a variety of steels in NaCl was equal in the buffered and not buffered solution [6]. Moreover, as it has been shown that chloride ions do not affect passive film composition, but rather its thickness [25], and, therefore, investigations of the film formed in the above nonagressive solution seemed reasonable.

2.3. Microscopic examinations

Microscopic examinations were carried out for all the specimens before and after the electrochemical measurements; optical microscopy, SEM and X-ray microprobe analysis were used. Non-metallic inclusions present within the steels under investigation were characterised. The X-ray microprobe analysis was carried out in a similar manner as before [6,11,20]. At least 5 specimens for each materials were taken for the analysis. Several areas for each sample were investigated and 5 - 10 typical sulphide inclusions were carefully analysed with X-ray microprobe. The quantitative "point" and "line" analyses of the inclusions have been performed at an accelerating voltage of 15 kV, by using JEOL JXA-3A Microprobe, equipped with two wavelength dispersive spectrometers (WDS). Analyses were performed for Mn, S, Cr, Fe, Ni and C and additionally for Ti and Mo depending on the type of inclusions. Pure metals, graphite or diamond, and pyrite for S, were used as standards in X-ray microanalysis. In the case of quantitative "point" analysis special correction program for "small particles" considering size and thickness of the inclusions was developed and applied .

2.4. SAM analysis

Specimens with large non-metallic inclusions were selected for AES-SAM. They were removed from the electrolyte after prepassivation, rinsed with pure ethanol, dried, and stored in small glass containers. The SAM analysis was performed with a Perkin-Elmer 600 SAM Spectrometer at 10^{-8} Pa, with 15nA raster electron beam. The lateral resolution was about 200nm. Depth profiling was carried out with 3kV Ar^+ ion beam and a sputtering rate of ca. 20A/min. based on Ta_2O_5 standard measurements. For the AES-SAM line scans the signal intensities for various elements were taken as the respective peak to background values of the normal N(E) spectra. For the analysis of the $(Cr,Mn)S_x$ inclusions the 529 eV Cr peak and the 589 eV Mn peak were considered. However, the 571 eV Cr peak partly overlapped with the 589 eV Mn peak. At the non-differentiated spectrum for the inclusions the 571 eV Cr peak usually appeared at the side of a large 589 eV Mn peak (or vice versa) and so the Mn signal could be deconvoluted for the purpose of a semiquantitative analysis.

3. RESULTS

3.1. Electrochemical investigations in neutral chloride solutions

Fig. 1 shows a diagram comparing E_{np} for various steels in 0.5M NaCl. The low Mn steels E-1, R-4 and Z-1 exhibit distincly higher E_{np} than the other steels, thus inferring that lowering the Mn content is an efficient strategy for increasing the resistance of the steels against Cl attack. It should be pointed out that even the steel R-4, with no Mo or Ti additions, exhibited higher E_{np} than the commercial steels. The special laboratory heats B and A, the latter with low Mn and C content, exhibited a more negative E_{np} than the novel low Mn steels. This points to the role of subtle interplay between various alloying elements in optimising the pitting resistance. Moreover, the effect

of the sulphur content and sulphide size (and probably its shape) plays a role here; steel A and B contained a high concentration of S, and rather large inclusions, what apparently increased pitting susceptibility of the material; the effect was pointed out by some other authors already [8,17].

3.2. X-ray microprobe and SAM results

X-ray microprobe investigations revealed that each steel contained sulphide and carbo-nitride inclusions containing Mn, Cr or Ti, depending on steel composition, as listed in Table 1.

MnS_X or $(Mn,Cr)S_X$ enriched with Mn inclusions

These inclusions occured in steels (II) and B.
Fig. 4 gives a typical example of results obtained with X-ray microprobe for steel (II). The line scanns show that the inclusion is enriched with Mn and S, as compared to their level within the matrix. On the contrary, Cr is depleted within the inclusion, although its level does not drop to zero because of the excitation of the adjacent matrix by X-ray fluoresecence (ϕ incl. < ϕ X-ray excitation zone). The absence of Cr signal within larger inclusions has been observed for steel B [19,26].

Surface analytical investigations with AES confirm the above findings, see Fig. 5. Mn and S signals are enchanced, but Cr and O signals are drastically reduced within the areas corresponding to the $(Mn,Cr)S_X$ inclusion in steel (II) as compared to their level at the matrix. This suggests that instead of a good protective chromium oxide passivating film at these sites, rather a very thin, poor protective iron/manganese oxide film is formed. One should mention here that, often O signal was zero in the area of pure MnS_X inclusions suggesting an absence of any passivating film at the inclusions there, as already reported [20,21,26].

$(Cr,Mn)S_X$ inclusions enriched with Cr

These inclusions ocurred in steels R-4 and A. Characteristic feature of these inclusions was an enrichment of S, Mn and notably Cr within the inclusion, as compared to their level within the matrix, see X-ray electron microprobe line scan in Fig. 6. Cr enrichment in these inclusions was in contrast to its depletion in the $(Mn,Cr)S_X$ inclusions, compare Fig. 4. Moreover, the Mn level within the matrix (Fig. 6) was much lower than that in steel II or steel B, compare Fig. 4.

Surface analytical investigations confirmed an enrichment of Cr within the passivation film formed at the $(Cr,Mn)S_X$ inclusions. A typical example of an AES-SAM line scan across such an inclusion is given in Fig. 7. Appearently inclusion was well passivated with a surface layer of chromium oxide as the oxygen signal there was quite high, in contrast to what has been found in steels II and B. One should point out, however, that the composition of the film at the inclusion clearly differed from that at the matrix (Fig. 7).

TiS_X and $TiS_XC_YN_Z$ inclusions

These inclusions ocurred in steels I, E-1 and Z-7. The TiS_X inclusions were often associated with some carbo-nitrides or nitrides, as reported in detail by Baroux et al. [18]. X-ray microprobe analysis revealed that Ti and S were strongly enriched within the inclusion, see Fig. 8. Surface analytical investigations revealed presence of oxygen at the surface of these inclusions, after passivation of the sample (Fig. 9). However, the oxygen signal was lower there as compared to its level at the adjacent matrix, suggesting a rather thin passivating titanium oxide film at the inclusion area.

TiC_xN_y inclusions

These inclusions occured in steels I, E-1 and Z-7. Surface analytical investigations revealed that after prepassivation of the sample, the oxygen signal was well measurable both at the matrix and at the inclusions of TiC_xN_y, suggesting presence of a titanium oxide type passivating film at the inclusions, also see Fig. 10.
Fig. 11 gives a typical example of a AES-SAM line scan across a carbo-nitride inclusion in steel Z-7, showing that oxygen signal does not drop down distincly at the inclusion area. This behavior is in contrast to the results found for steels I and B, where at the MnS_x inclusions oxygen signal dropped drastically down, sometimes even to zero, compare Fig. 5 or the results in Refs. [20, 21,26].

4. DISCUSSION

Summarising the above investigations and in particular the surface analytical results one can say that all the inclusions containing sufficient amount of Cr and/or Ti exhibited an ability to passivate. Only MnS_x inclusions seemed to be unable to passivate, thus producing discontinuities in the film or forming an iron/manganese oxide film, very thin and non protectiveat, at low anodic potentials in neutral solutions.

In order to understand the corrosion behaviour of steels the mechanism of pit nucleation there should be taken into account. The general opinion is that inclusions containing MnS_x or complex oxide/MnS_x are the most susceptible initiation sites. Our results infer that there may occur, as mentioned, a discontinuity of the passivating film at the matrix/MnS_x inclusion interface due to a lack of any passivation for the inclusion itself. This makes it quite clear why these materials are so prone to localised attack in chloride media [6-19]. The above result is in line with the mechanism of pit nucleation on voids within the passive film, suggested by Wood et al. [27].

Considering the problem of the chemical stability of individual non-metallic inclusions, as well as their ability to passivate, the following should be taken into account: in the low Mn steels where (Cr,Mn)S, TiS_x or $TiS_xC_yN_z$ inclusions, able to passivate, are occuring the mechanism of pit initiation may be different than at MnS_x and thus breakdown required higher anodic potentials. The most probable mechanism seems to be the localized aglomeration of chloride followed by film thinning [25] at the inclusion/matrix interface, as already proposed [26,28].

The following comment seems adequate to the discussion on the pit mchanism [29] in metals: the passive film at sulphide inclusions in steels in contact with neutral chloride solutions is distincly different from that at the matrix, and in certain cases even absent, which in various ways, may facilitate the chloride attack there.

The sulphur species derived from inclusions may additionaly contribute to the early stages of pitting on stainless steels. This problem is discussed in detail elsewhere [23,24,31].

5. CONCLUSIONS

1/. Electrochemical, microscopic, and surface analytical measurements revealed a correlation between the anodic behaviour of the steels, the composition of their non-metallic inclusions as well as the local composition of the passive film at the inclusions as compared to that at the adjacent metal matrix.

2/. X-ray microprobe analysis revealed that MnS, inclusions in steeels with a common Mn content (~ 2% Mn) are the most susceptible spots for pit nucleation. In the modifield low Mn steels the MnS_x inclusions have been eliminated. Instead some $(Cr,Mn)S_x$, TiS or TiC_xN_y were present. They appeared to be less susceptible to localised attack by chlorides, as shown by the corresponding electrochemical results (Fig. 3).

3/. SAM results suggest that the nonmetallic inclusions occurring within the steels under investigations do undergo a passivation. The oxide type film formed at the inclusions is in general different from that at the metal matrix. MnS_x inclusions occurring in commercial steels containing ~2% Mn, do not form a protective, chromium containing, oxide film during a process of anodic passivation. In low Mn steels the $(Cr,Mn)S_x$ inclusions occuring there do passivate forming a surface layer of chromium oxide. This explains the higher resistance of low Mn steels to localized attack as compared to the commercial ones. The same applies to steels supplementary alloyed with Ti, where TiS_x, TiC_xN_y or mixed sulphide-carbonitride inclusions appear, which undergo passivation in neutral electrolyte, forming a surface passivating layer of titanium oxide.

REFERENCES

[1] R. Kiessling et al.: "Sulphide Inclusions in Steels", proc. Symp. Prot Chester,USA,1974, Ed. R. Baboian, p. 104.
[2] H.J. Engell: Stahl und Eisen 94 (1974) 1085, and 93 (1973) 1203.
[3] P. Poyet, R. Leveque: Etude des Sulfures dans les Aciers, Influence de divers Elements d'Addition sur leur Composition; Rev. Met. 64 (1967) 653.
[4] L. Tronstad, J. Sejersted: J. Iron Steel Inst. 127 (1933) 425.
[5] M. Smialowski, Z. Smialowska, M. Rychcik, A. Szummer: Corr. Sci. 9 (1969) 123.
[6] M. Janik-Czachor: Bull. Sci. Acad. Polon. ser. sci. chim. 25 (1977) 561; M. Janik-Czachor, A. Szummer in "Passivity of Metals and Semiconductors", Ed. M. Froment, Elsevier 1983, p. 547.
[7] J.E. Castle, E. Ke: Corr. Sci. 30 (1990) 409.
[8] J. Steward, D.E. Williams: Corr. Sci. 33 (1992) 457.
[9] J. Degerbeck, K. Blom: Materials Performance, p. 53, July 1983.
[10] L.J. Freiman, J.J. Reformatskaya, Ya.M. Kolotyrkin, Yu.P. Kuonnov, A.E. Volkov: Proc. 10th ICMC, Madras 1987, p. 3919.
[11] Z. Szklarska-Smialowska, A. Szummer, M. Janik-Czachor: Brit. Corr. J. 5 (1970) 687.
[12] M.B. Ives, S.C. Srivastava: Corrosion 43 (1987) 687. M.B. Ives, S.C. Srivastava: Proc. Inter. Conf. on Localized Corrosion, Orlando 1987.
[13] M. Kesten: Corrosion 32 (1976) 94.
[14] G.S. Eklund: J. Electrochem. Soc. 121 (1974) 467.
[15] P. Forchhammer, H.J. Engell: Werkst. Korros. 20 (1969).
[16] J. Degerbeck, E. Wold: Werkst. Korros. 25 (1974) 172.
[17] V. Scotto, G. Ventura, E. Traverso: Corr. Sci. 19 (1979) 237.
[18] B. Baroux, D. Gorse: Proc. of the European Symp. on Modification of Passive Films, Ed. P. Marcus, B. Baroux, M Keddam. Paris 1993, The Institute of Materials, p. 300.
[19] A. Szummer, K. Lublińska, M. Janik-Czachor: Werkst. Korros. 14 (1990) 618; JSI International 31 (1991) 240.
[20] A. Szummer, M. Janik-Czachor: Corr. Sci. 35 (1993) 317.
[21] A. Szummer, M. Janik-Czachor, S. Hofmann: Mater. Chem. and Phys. 34 (1993) 181.

[22] M.A. Baker, J.E. Castle: Corr. Sci. 33 (1992) 1295.
[23] M.A. Baker, J..E. Castle: Corr. Sci. 34 (1993) 667.
[24] E.F.M. Jansen, W.G. Sloof, J.H.W. de Witt: as ref. 18, p. 290.
[25] K.E. Heusler, L. Fischer: Werkst. Korros. 27 (1976) 555.
[26] M. Janik-Czachor, A. Szummer: Corr. Reviews, Jerusalem, 11 (1994) 117.
[27] Abd. Rabbo, G.C. Wood, J.A. Richardson, C.K. Jackson: Corr. Sci. 14 (1974) 645 and 16 (1976) 677.
[28] M. Janik-Czachor: J. Electrochem. Sci. 128 (1981) 513C.
[29] H.J. Engell, R.A. Oriani: Corr. Sci. 29 (1989) 119.
[30] A. Wolowik: Master of Science Thesis, Dept. of Materials Science and Engineering, Warsaw University of Technology, Warsaw 1992.
[31] A. Szummer, M. Janik- Czachor, S. Hofmann: as ref. 18, p. 280.

Table 1. X-ray electron microprobe characterization of sulphide inclusions

Steel	Prevailing Inclusions x)
Commercial (I)	TiS_xN_y (~32%S, ~63%Ti, ~0.4%Mo, ~4.6%N)
Commercial (II)	$(Mn, Cr)S_x$ enriched with Mn
modified E–1	mostly $(Ti)S_xC_yN_z$ (~30%S)
modified R–4	$(Cr, Mn)S_x$(~48%S, ~32%Mn, ~20%Cr)
modified Z–7	$(Ti, Mn) S_xN_y$ (~30%S, ~64%Ti, ~0.4%Mo, ~5, 6%N)
lab. heat A	$(Cr, Mn)S_x$ (~14%Mn, ~38%Cr)
lab. heat B	MnS_x only (~46%S, ~54%Mn)

x)
The results have been normalised to 100%
The quantitative estimations have been performed by A. Wolowik, M. Sc. (30),see Experimental.

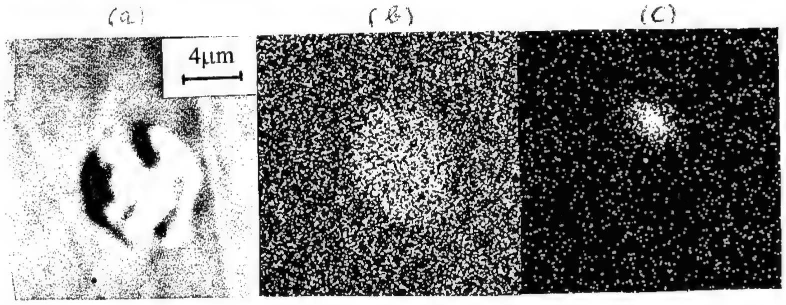

Fig. 1. Electron microprobe image of an oxide inclusion within Fe16Cr alloy associated with some small sulphide particles: a) backscattered electron image, composition, b) distribution of chromium (Kα), c) distribution of sulphur (Kα).

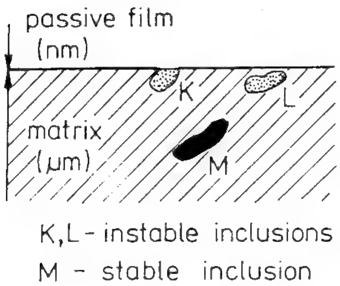

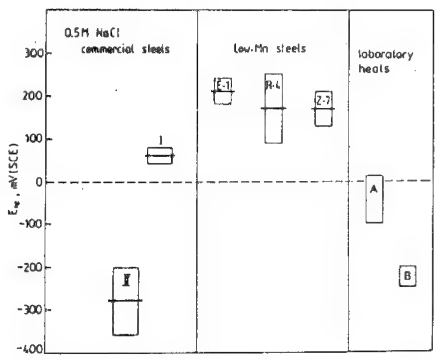

Fig. 2. Schematic representation of a stainless steel surface area.

Fig. 3. Diagram summarizing pitting resistance (E_{np} in 0.5M NaCl aq) of the commercial steels, novel low Mn modified steel and two special laboratory heats with a common (B) and low Mn content (A).

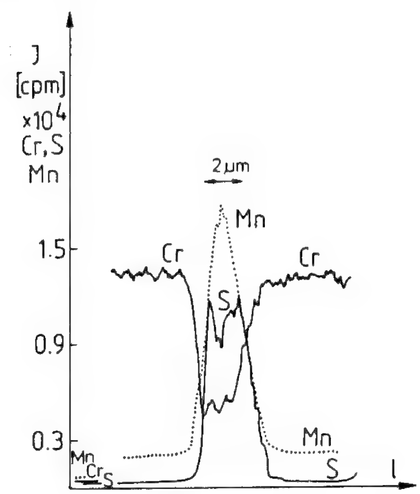

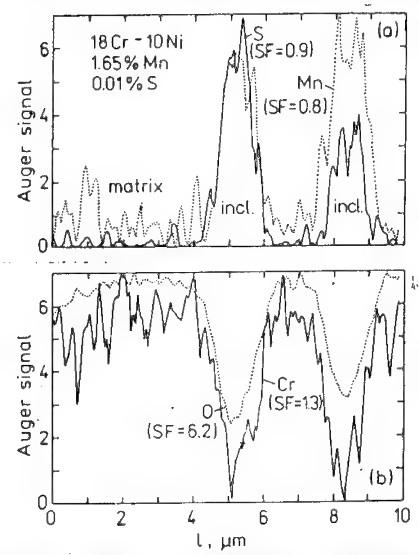

Fig. 4. X-ray microprobe analytical results for a typical $(Mn,Cr)S_x$ inclusion in commercial steel (II); line scan across the inclusion, as marked by an arrow, showeing distribution of Mn, Cr and S within the inclusion and outside, cpm - counts per minute.

Fig. 5. AES-SAM line scan across two inclusions of MnS_x and across the adjacent matrix (commercial steel II) passivated electrochemically in a borate buffer solution. Signals of both Cr and O are drastically reduced at the inclusions suggesting the presence of rather a very thin, poor protective iron/manganese passivating film but no a good protective chromium oxide film at these sites. SF - scaling factor.

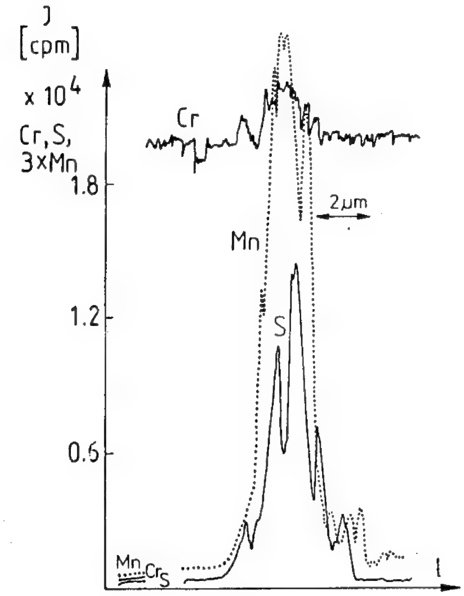

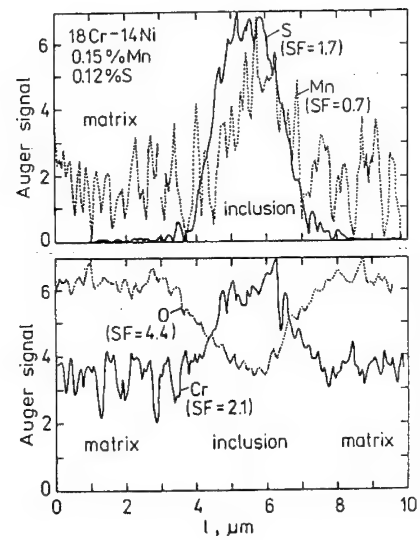

Fig. 6. Line scan across a typical $(Cr,Mn)S_X$ inclusion in the modified steel R-4, showing distribution of Mn, Cr and S within the inclusion and outside Mn(Kα) signal is 3x expanded for clarity.

Fig. 7. AES-SAM line scan across an inclusion of $(Cr,Mn)S_X$ and across the adjacent matrix (steel A passivated electrochemically in a borate buffer solution. The inclusion is covered with a passivating film (O level much above zero) enriched with Cr. Mn line scan is deformed by an overlap with Cr signal. SF - scaling factor

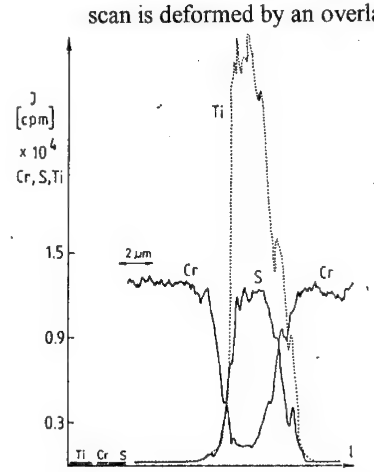

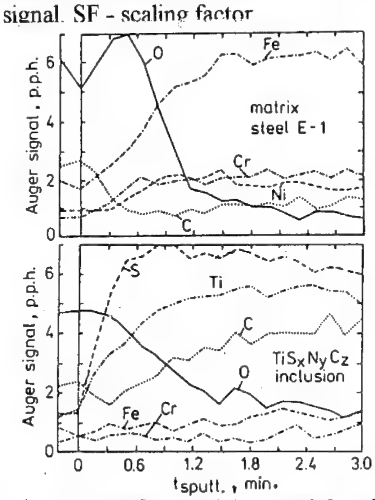

Fig. 8. Line scan across a typical TiS_X inclusion in the modified steel E-1, with low Mn content showing distribution of Ti, Cr and S within the inclusion and outside. X-ray microprobe analysis. cpm - counts per minute.

Fig. 9. Composition profile of the prepassivated surface of steel E-1 with low Mn content, supplementary alloyed with Ti; (a) metal matrix, (b) $TiS_XN_YC_Z$ inclusion.

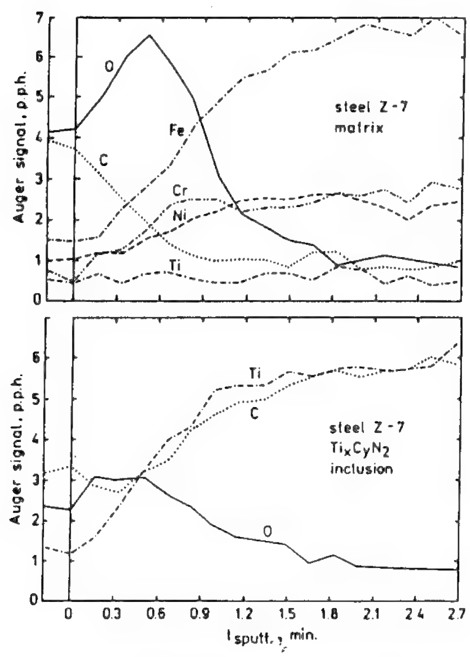

Fig. 10. Composition profile of the prepassivated surface of steel Z-7 with low Mn content, supplementary alloyed with Ti and Mo. (a) metal matrix; (b) titanium carbonitride inclusion. (N+Ti)p.p.h. signal at 383 eV is avoided here, as well as in Fig.9, for clarity. However, the N signal is detectable for these inclusions; the 383eV peak vs. 418eV Ti is larger here than the corresponding ratio for a pure Ti standard specimen.

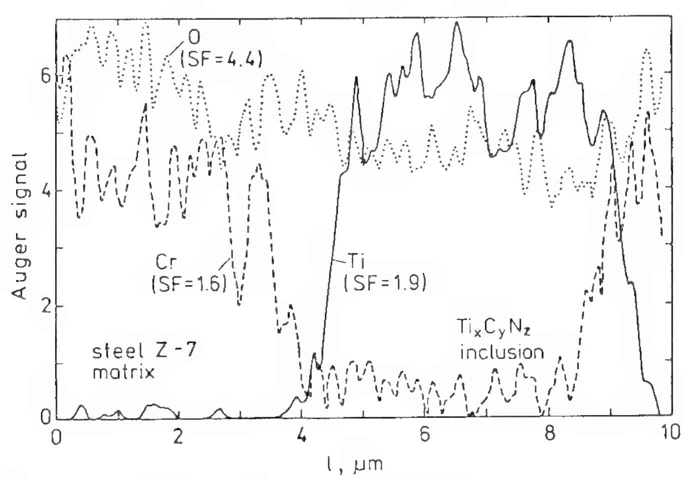

Fig. 11. AES-SAM line scan across an inclusion of TiC_xN_y and across the adjacent matrix (steel Z-7) passivated electrochemically in a borate buffer solution. Cr signal is drastically reduced to zero at the inclusion. Oxygen signal is only slightly reduced at the inclusion suggesting presence of a passivating titanium oxide film there. SF - scaling factor.

Materials Science Forum Vols. 185-188 (1995) pp. 965-974

On the stability of passive films on stainless steels

S. Virtanen and H. Böhni

Institute of Materials Chemistry and Corrosion, Swiss Federal Institute of Technology, ETH-Hönggerberg, CH-8093 Zürich, Switzerland

Keywords: Stainless steel, passivity, passive film, localized corrosion, open-circuit potential decay

Abstract

The pitting corrosion susceptibility and the stability against activation in acids of AISI 304 after various passivation treatments has been studied. The variable parameters during the passivation were the pH of the solution, time and potential of passivation. Further, in-situ photoelectrochemical measurements were carried out on differently passivated steel surfaces. Passivation in an acidic solution (H_2SO_4) leads generally to a more stable passive film than passivation in a neutral (Na_2SO_4) or alkaline solution ($NaOH + Na_2SO_4$). Photoelectrochemical measurements indicate that this is due to a higher chromium-oxide content in the film formed at lower pH values. The passive film's resistance against localized breakdown in Cl^--containing solutions is further strongly dependent on the passivation time - the pitting potential increases by a longer pre-passivation in Cl^--free solutions. This can result either from an increase of the Cr-content or decrease of "weak" sites of the passive film. A critical passivation potential was found to exist, above which the films formed show a remarkably higher resistance against pitting corrosion. This can be attributed to an oxidation of Cr(3+) species of the film into CrO_4^{2-}, which is incorporated in the film. The negative extra charge will repel the chlorides from the surface of the passive film. Generally, the experimental findings show that the properties of the passive film on stainless steel very strongly depend on its formation history - the film formation solution, time and potential of passivation. The increased pitting corrosion resistance after the passivation treatments disappears, if the passivated surface is cathodically pre-polarized before the pitting corrosion studies. Therefore the pitting corrosion susceptibility is strongly influenced by the properties of the passive film and not only by the presence of bulk heterogeneities.

Introduction

The properties of passive films on stainless steels depend on many passivation parameters. The chemical composition of passive films formed on stainless steels under various passivation conditions have been studied extensively by surface analytical ex-situ methods such as X-ray electron spectroscopy (XPS) and Auger-electron spectroscopy (AES) [e.g. 1-8]. Even though some controversial results on the composition of the passive films is existing it has been clearly shown that the thickness and the chemical composition of the passive film are strongly dependent on the pH of the solution, passivation potential and passivation time. Further it was found that the chemical composition of the passive film is influenced by surface pre-treatment [9}. Nevertheless, correlations between the thus studied chemical composition of the passive film and its corrosion properties have been investigated in a much lesser extent.

Shibata et al. have shown that resistance of stainless steel against pitting corrosion in Cl^--containing solutions is strongly dependent on the sample treatment, e.g. etching or passivation, prior to the pitting susceptibility measurements [10,11]. Yang et al. have similarly to these works found that a longer passivation time (aging) leads to better resistive properties of the passive film and to a higher pitting corrosion resistance [12]. Lately, Kwiatkowski and Mansfeld reported a strongly improved stability of passive films formed by an electrochemical AV-treatment [13]. The stability of the films was determined by open-circuit potential decay measurements in an acidic solution.

In this work the stability of passive films against chloride attack formed in various solutions for different times on AISI 304 stainless steel is studied by pitting potential measurements in 0.1M NaCl

and open-circuit potential decay studies in 1M H_2SO_4. In order to correlate the thus found behaviour of the passive films with the properties of passive films, the passive films formed under various conditions were characterized by photoelecrochemical methods.

Experimental

The material studied was a conventional AISI 304 stainless steel in form of a sheet. The samples were mechanically grinded (1000 grit), rinsed in ethanol and acetone and dried prior to the measurements. All samples were cathodically pre-polarized for 2 min at -1000 mV SCE before starting the experiments.
The electrochemical measurements were carried out in a conventional electrochemical cell with a 3-electrode configuration. The working electrode was pressed against an opening in the cell - an O-ring was used as a gasket. The reference electrode was a saturated calomel electrode. All solutions were deaerated with N_2. As passivation solutions 0.5M H_2SO_4 (pH 0.6), 0.5M Na_2SO_4 (pH 6.4) and 1M NaOH + 0.5M Na_2SO_4 (pH 12.4) were used. The pitting corrosion susceptibility was studied in 0.1M NaCl. Open circuit potential decay measurements were carried out in 1M H_2SO_4.
After passivating the sample for a given time in the passivation solution the solution was removed from the cell while letting the sample stay under a potentiostatic control. After this the cell and the sample surface were thoroughly rinsed with destilled water and dried with pressure air and subsequently the cell was filled with the new testing solution.
Prior to the potentiodynamic polarization curves the samples were let to stay 5 min at the open-circuit potential in the 0.1M NaCl solution. The sweep rate for the polarization curves was 1 mV / 5 s. Reference measurements were carried out on samples, which had not been electrochemically passivated prior to the measurements and on samples, which had been let to stay in the laboratory air various times after the mechanical surface treatment. All pitting potentials shown throughout this paper represent the medium values of at least 5 measurements.
For the open-circuit potential decay measurements the regulating current circuit was opened after filling the test solution (1M H_2SO_4) and the potential was recorded as a function of time.
Photoelectrochemical measurements were carried out with the experimental set-up described in [14,15] using the lock-in technique in order to separate the photocurrent from the passive current (chopper frequency 30 Hz). The photocurrents were generated by focusing chopped light of a 150 W Xe lamp onto the electrode which was held under potentiostatic control. In order to obtain photocurrent spectra a monochromator was placed in the light beam and the wavelength was scanned in the range of 800 - 250 nm. The photocurrent values presented are normalized to 1W output of the Xe-lamp at the corresponding wavelength.

Results

Fig. 1 shows the effect of passivation time on the breakdown potentials determined from the potentiodynamic polarization curves. The passivation potential for the measurements in different solutions was varied in order to keep the field strength in the passive film in the similar range with following assumptions:

$$F = (E-E_{fb}) / W \qquad (1)$$

F field strength
E potential
E_{fb} flat-band potential
W thickness of the space charge layer

$$E_{fb} \approx -59 \text{ mV / pH} \qquad (2)$$

Further, the potential value was fixed in the passive range below the transpassive dissolution in the potentiodynamic polarization curve in the corresponding solution. The passivation in 1M NaOH + 0.5M Na_2SO_4 (pH 12.4) was therefore carried out at a potential E =0 mV SCE, in 0.5M Na_2SO_4 (pH 6.4) at a potential E = +300 mV SCE and in 0.5M H_2SO_4 (pH 0.6) at a potential E = +500 mV SCE.

Typical i/E-curves in 0.1M NaCl after the different passivating treatments are shown in Figs. 2-4. Aging in air does not found to greatly affect the localized corrosion resistance. The passive current density was anyhow found to be dependent on the time of aging, becoming lower with increasing aging times. Passivation in solutions, on the other hand, influences the localized corrosion resistance, as can be seen from the increase in the values of the breakdown potential in Figs. 2-4. Especially passivation in the acidic solution seems to have a remarkable effect of the pitting corrosion behaviour.

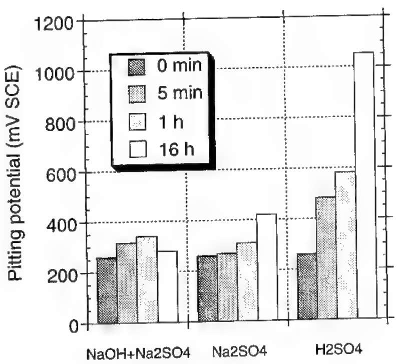

Fig. 1 Effect of passivation time on the pitting potential of AISI 304 measured in 0.1M NaCl after pre-passivation in solutions with different pH value

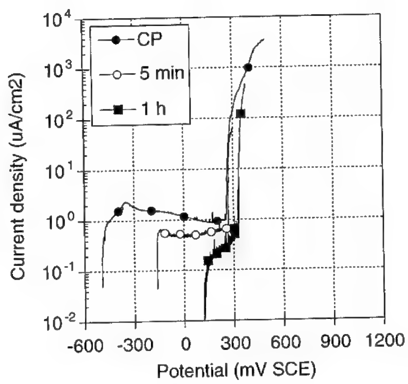

Fig. 2 Potentiodynamic polarization curves for AISI 304 in 0.1M NaCl after passivation for various times in 1M NaOH + 0.5M Na_2SO_4 at 0 mV SCE (CP = cathodic pre-polarization)

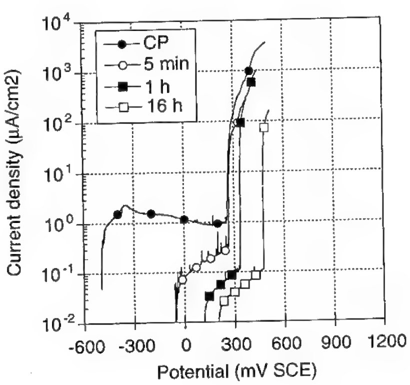

Fig. 3 Potentiodynamic polarization curves for AISI 304 in 0.1M NaCl after passivation for various times in 0.5M Na_2SO_4 at +300 mV SCE (CP = cathodic pre-polarization)

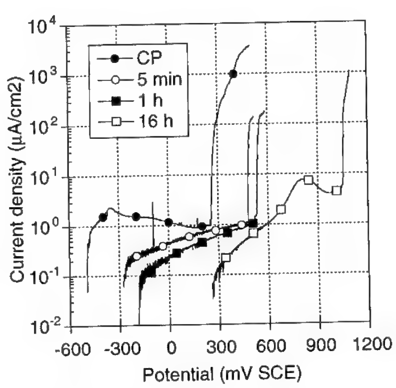

Fig. 4 Potentiodynamic polarization curves for AISI 304 in 0.1M NaCl after passivation for various times in 1N H_2SO_4 at +500 mV SCE (CP = cathodic pre-polarization)

The passivation potential also very strongly affects the pitting corrosion behaviour. Fig. 5 shows the pitting potential as a function of the potential, at which the sample was passivated in 0.5M Na_2SO_4 or in 0.5M H_2SO_4 prior to the potentiodynamic polarization curve measurement in 0.1M NaCl. It is

clear that above a passivation potential of about +300 mV SCE in Na_2SO_4 and +500 in H_2SO_4 the pitting potentials significantly increase as a function of the passivation potential up to a value of +700 mV SCE. Below these critical values the pitting potential depends on the passivation potential in a less straightforward manner.

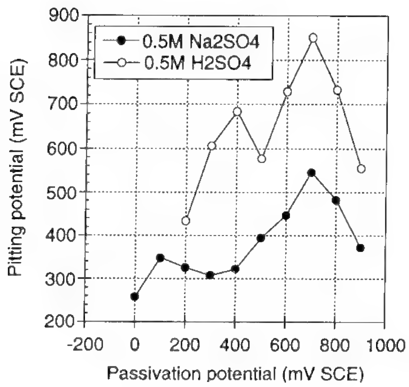

Fig. 5 Pitting potential in 0.1M NaCl determined from potentiodynamic polarization curves as a function of passivation potential in 0.5M Na_2SO_4 or in 0.5M H_2SO_4

The open-circuit potential decay measurements carried out in 1M H_2SO_4 after passivation in Na_2SO_4 or in H_2SO_4 further indicate that the stability against activation in acids is also strongly dependent on the passivation parameters. Pre-passivation for 1 h in 1N H_2SO_4 at +500 mV SCE leads to a formation of a stable film which is not activated in 1 M H_2SO_4 during 48 h, whereas the sample passivated in 0.5M Na_2SO_4 at +300 mV SCE for 1 h becomes active after a few minutes (Fig. 6). Fig. 7 shows the effect of passivation time in Na_2SO_4 on the stability in the acidic solution - here again the longer passivation time leads to formation of a more stable passive film.

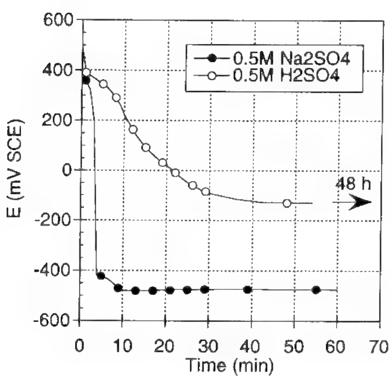

Fig. 6 Open-circuit potential decay curves in 1M H_2SO_4 after passivation for 1 h in in 0.5M Na_2SO_4 or in 0.5M H_2SO_4

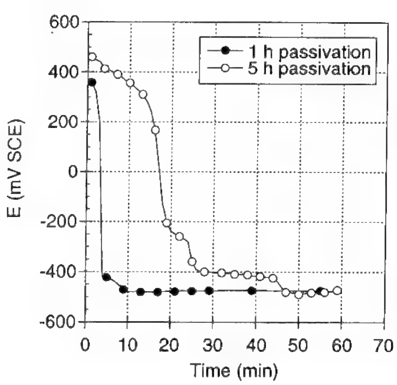

Fig. 7 Open-circuit potential decay curves in 1M H_2SO_4 after passivation in in 0.5M Na_2SO_4 for various times

The differently passivated samples were further characterized by photoelectrochemistry. Fig. 8 shows a comparison of the photocurrent spectra measured in 0.5M Na_2SO_4 at +300 mV SCE after

passivating the sample for 1 h in the solutions with different pH values at the fixed potentials. The sample passivated in the acidic solution shows significantly lower photocurrents than the samples passivated in the neutral or alkaline solutions. Also the onset wavelength of the photocurrent is shifted to smaller values for the sample passivated in the acidic solution. The potential-dependence of the photocurrents normalized to maximum photocurrent measured in Na_2SO_4 for the samples passivated for 1 h either in H_2SO_4 or in Na_2SO_4 is shown in Fig. 9. Further, Figs. 10, 11 show the photocurrent spectra as a function of the passivation time in the neutral or in the acidic solution - the photocurrent measurements were again carried out in Na_2SO_4. Increase of the passivation time in Na_2SO_4 leads to a slight increase of the photocurrents without changing the wavelength-dependence, whereas longer passivation in H_2SO_4 decreases the photocurrents and shifts the onset of the photocurrent towards smaller wavelengths. A further prolongment of the passivation time as shown in Figs. 10 and 11 does not lead to any measurable changes in the photocurrent behaviour.

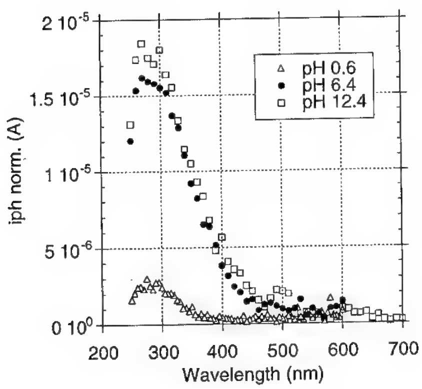

Fig. 8 Photocurrent spectra in 0.5M Na_2SO_4 at +300 mV SCE after passivation for 1 h in solutions with different pH values

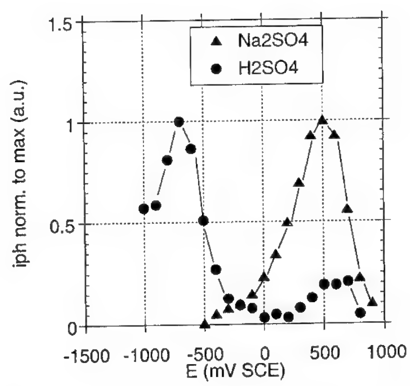

Fig. 9 Potential-dependence of the photocurrents in 0.5M Na_2SO_4 after passivation in H_2SO_4 or in Na_2SO_4

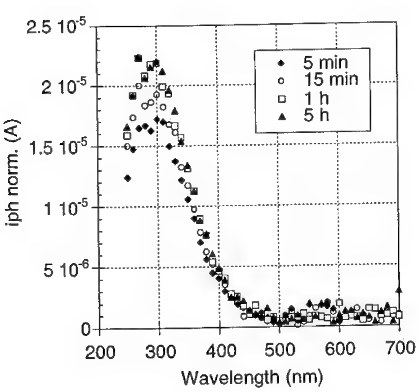

Fig. 10 Photocurrent spectra in 0.5M Na_2SO_4 at +300mV SCE after passivation in Na_2SO_4 for various times

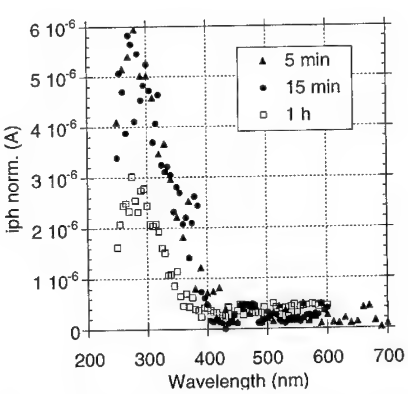

Fig. 11 Photocurrent spectra in 0.5M Na_2SO_4 at +300 mV SCE after passivation in H_2SO_4 for various times

From the photocurrent spectra the band-gap energies can be determined according to an indirect electron transition [16]. This leads to following values:

Passivation in 0.5M H_2SO_4, E = +500 mV SCE

Passivation time	5 min	$E_g = 2.6$ eV
	15 min	$E_g = 2.65$ eV
	1-24 h	$E_g = 2.9$ eV

Passivation in 0.5M Na_2SO_4, E = +300 mV SCE

Passivation time	5 min	$E_g = 2.4$ eV
	15 min	$E_g = 2.42$ eV
	1-24 h	$E_g = 2.45$ -2.5 eV

Passivation in 1 M NaOH + 0.5M Na_2SO_4, E = 0 mV SCE

Passivation time	5 min - 24 h	$E_g = 2.3$ eV

Discussion

The results clearly show that passivation of AISI 304 stainless steel in H_2SO_4 leads to a more stable passive film than passivation in Na_2SO_4 or in NaOH + Na_2SO_4. The reason for this may lie in the different chemical composition of the passive film depending on the solution pH.

Looking at the photocurrent behaviour of the passive films formed in the different solutions it is clear that the passive film formed in the acidic solution shows significantly smaller photocurrents and a higher band-gap energy than the passive films formed in the neutral and in the alkaline solutions. Studies on passivated pure iron and chromium [14] show generally much lower photocurrents on the passive film on chromium than on passive film of iron. Further, band-gap energy values of 2.45-3.1 eV for Cr passive film and 1.8-2.1 eV for Fe passive film were found [14]. In [17] an increase of Cr-content in Fe-Cr alloys was found to decrease the photocurrents. The results of the present work thus suggest that the film formed in the acidic solution contains more Cr-oxides than films formed in neutral or alkaline solutions. Since the band-gap energy and the photocurrent intensity are not only dependent on the chemical composition of the films but also on the structure and thickness of the film, it is not possible to determine the chemical composition of the passive film only by values of E_g and i_{ph}. Any how, the potential-dependence of the photocurrents of the differently treated passive films is a clear sign for differences in the chemical composition. The sample passivated in H_2SO_4 shows a very similar potential-dependence of the photocurrent as the passive film on Cr [14] and synthetic Cr-oxide thin films [18], whereas the potential-dependence of the sample passivated in Na_2SO_4 resembles the behaviour of the passive film on Fe [14].

Literature data on surface analytical studies on passive films on Fe-Cr alloys confirm the effect of pH on the chemical composition of the film. Haupt and Strehblow have shown by XPS [3,19] and Hara and Sugimoto by an in-situ potential-modulated UV-visible reflection spectroscopy [20] that the chromium content in the passive film of Fe-Cr alloys increases by decreasing pH of the solution. Therefore, the higher pitting corrosion resistance and the higher stability against activation in acids of the films formed in H_2SO_4 as compared to the films formed in neutral or alkaline solution is most probably due to a higher chromium enrichment in the films.

An indirect evidence for the higher chromium content in the passive film formed in the acidic solution can be found by measuring the polarization curves in 0.1M Na_2SO_4 after different passivation treatments. Fig. 12 shows a comparison of the polarization curves measured without pre-passivation and after passivation for 1 h either at +500 mV SCE in 1N H_2SO_4 or at +300 mV SCE in 0.5M Na_2SO_4. The current peak which occurs in all three curves at potentials between ≈ +400 and +850 mV SCE can be attributed to the transpassive dissolution of chromium oxides ($Cr^{3+} \rightarrow Cr^{6+}$). It is clear that in the case of the film formed in the acidic solution this Cr-oxidation peak is remarkably more pronounced than in the two other cases. This indicates that the film formed in H_2SO_4 contains a higher amount of Cr-oxides than the film formed in the neutral solution.

Since the pitting corrosion resistance of commercial stainless steels is very strongly influenced by their purity - especially the content of MnS-inclusions - the role of the purity in the results of this work has to be questioned. From literature it is known that the dissolution kinetics of pure MnS is much more rapid in acidic solutions than in neutral solutions [21]. Therefore, the increased resistance against pitting after passivation in H_2SO_4 could be at least partly due to the dissolution of MnS leading to a more homogeneous surface. In order to clarify if this is the case, a sample which had been passivated in H_2SO_4 at +300 mV SCE for 1 h was cathodically polarized in NaCl prior to the potentiodynamic measurement. As shown in Fig. 13 the pitting potential of the passivated and subsequently cathodically pre-polarized sample lies in the same range as the pitting potential of the sample without pre-passivation. Therefore it can be concluded that the large increase of the pitting potential by the pre-passivation cannot be merely due to dissolution of inclusions but the passive film itself plays a dominant role in the pitting resistance.

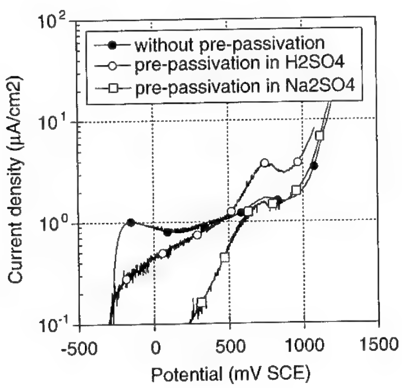

Fig. 12 Effect of pre-passivation on the potentiodynamic polarization curves in 0.5M Na_2SO_4

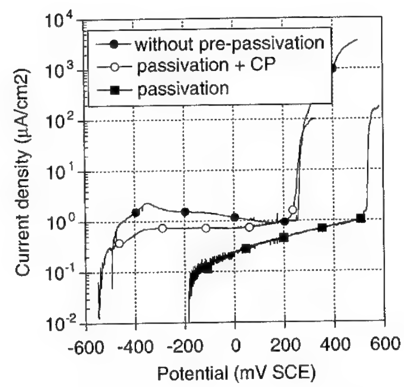

Fig. 13 Effect of different pre-treatment on the potentiodynamic polarization curves in 0.1M NaCl

The stability of the passive films was found to be clearly dependent on the time of passivation in the solutions. During the potentiostatic passivation treatment prior to the pitting potential measurements the current density is continuously decreasing. The decreasing current is a sign for a formation of a more protecting passive film as a function of time. Yang et al. attributed the increase in the protective properties of the passive film with increasing passivation time to an increase in the Cr-content of the films [12]. On the other hand other authors have found a positive effect of aging on the pitting resistance of pure iron, as well [22,23]. In this case the reason cannot be a change in the film composition. In these works the film thickness was found to be fairly constant during the pre-passivation time; therefore this effect was explained to be due to a change in film structure (decrease of defectiveness). According to Bardwell et al., on the other hand, the pit initiation on iron is associated with a particular critical thickness in the development of the passive film [24].

The effect of the passivation time on the photocurrent spectra (Figs. 10,11) suggest a different behaviour for passivation in Na_2SO_4 or in H_2SO_4. In case of Na_2SO_4 passivation the photocurrents slightly increase as a function of passivation time with practically no change in the band-gap energy - thus the chemical composition or the structure of the film is not significantly changing. The slight increase of the photocurrents can be due to a film thickening. A longer passivation in H_2SO_4 leads to a remarkable increase of the band-gap energy. This can be due to an increase of the Cr-content in the passive film. On the other hand, studies on thin Cr-oxide layers prepared by sputter deposition [18] have shown that the band-gap energy of Cr-oxides is depending on the stoichiometry. Thus the increase of the band-gap energy as a function of passivation time in H_2SO_4 can also be due to changes in film stoichiometry - more specifically to a formation of a less defective film. Thus it is

clear that with the present data it is not possible to attribute the increasing stability of the passive film after longer passivation times found in this work to one single changing property of the passive film.

The effect of passivation time on the pitting resistance is most pronounced in the case of the acidic solution. Passivation for even 48 h in the neutral solution does not lead to a higher resistance than passivation for 16 h. Therefore, the steady-state passive film formed in the neutral solution is inherently less resistant than the steady-state passive film formed in the acid. The higher Cr-content in the film formed in H_2SO_4 is due to a lower stability of iron-oxides in the acidic solution.

The potential-dependence of the stability of the passive film shows in Na_2SO_4 and in H_2SO_4 a critical potential, above which the pitting resistance is very strongly increased. The passivation potential affects the chemical composition and the thickness of the passive film. In literature it has been shown that the thickness of the passive film is continuously increased as a function of potential [19]. Therefore the abrupt increase of the pitting resistance at the critical potential cannot be explained by a sudden thickening of the film at this potential. Considering the chemical composition of the film - especially the Cr-content - it has been shown that the Cr/Fe-ratio decreases by increasing potentials and this again more or less continuously over a large potential range [20]. Thus the critical potential found in this work is most probably not due to a sudden change in the Cr/Fe-ratio of the film.

In earlier works it has been shown that the metastable pitting activity of AISI 304 steel, measured as current transients in potentiostatic experiments in 0.1M NaCl, shows a maximum at +400 mV SCE [25]. Schmuki and Böhni have found by photoelectrochemical methods and by Mott-Schottky measurements that this maximum in the metastable pitting rate coincides with changes in the electronic properties of the passive film formed in a neutral Na_2SO_4 solution [14,15,26,27]. They interpreted this finding to be due to an oxidation of Cr(3+) species in the passive film into CrO_4^{2-}, which is partly incorporated in the film. The extra negative charge of the incorporated CrO_4^{2-} anions would repel the chlorides from the solution and their adsorption would be hindered. Thus the pit initiation activity is decreased. This model is similar to the bipolar passivity model from Sakashita and Sato and from Clayton and Lu [28-30]. According to Schmuki and Böhni the CrO_4^{2-}-"inhibition" of the pitting corrosion will take place only above a critical potential (+400 mV SCE in a neutral solution), which corresponds to a potential at which chromium oxidation takes place at a sufficient rate. The potential of +400 mV SCE is in good agreement with thermodynamical data of chromium oxidation [31]. The presence of CrO_4^{2-} in the passive film of stainless steels has been verified by ex-situ (XPS) [29] and in-situ (XANES) [32,33] methods. As shown in [32,33], Cr(6+) in the passive film can be reduced to Cr(3+) during exposition in air. Further, it has been shown that the XPS-peak corresponding to Cr(6+) in the passive film disappears with time of exposure to the X-ray radiation [34]. These findings can explain some controversial results regarding the presence of CrO_4^{2-} in the passive film.

The finding of a critical passivation potential in this work can be explained by the Cr-oxidation in the passive film, as well. In the neutral solution the critical passivation potential is in good agreement with the critical potential found by Schmuki and Böhni. Taking into account the pH-dependence of the Cr-oxidation reaction a critical potential value of about +600 mV SCE in the acidic solution would result. Since the Cr(3+)-component in the passive film can be present either as CrOOH, $Cr(OH)_3$ or Cr_2O_3, and the amount of the different species can vary depending on the pH of the film formation solution, deviations from the -59 mV/pH-dependence of the Cr-oxidation potential can be expected. Anyhow the calculated critical potential in the acidic solution is in fairly good agreement with the findings in this work. Thus it can be concluded that most probably the strong increase of the resistance of the passive film against pitting corrosion at potentials above a critical potential is due to an incorporation of CrO_4^{2-} in the passive film.

At potentials lower than the critical potential the pitting potential depends less straightforwardly on the passivation potential. This can be due to the fact that at the same time two opposing effects are taking place: the film is becoming thinner [19] and the Cr/Fe-ratio is increasing by decreasing potentials [20]. The thinning of the film should lead to a lower resistance against localized attack whereas the increase in the chromium content should increase the stability of the film. After passivating at very high potentials the resistance of the passive film against localized corrosion is again decreasing. This

is probably due to the fact that at these potentials transpassive dissolution takes place and the films are becoming thinner. The CrO_4^{2-} species dissolve into the solution and the film loses its resistance.

The relevance of the pitting potential in characterizing the pitting corrosion resistance can of course be discussed. It is clear that pitting initiation takes place at potentials much lower than the potentiodynamically determined pitting potentials. Therefore the values of the pitting potentials should not be understood as a potential limit below which no localized corrosion takes place. Since the differences in the pitting potential values of differently pre-treated samples are very significant and beyond the scatter range (≈ 100 mV), the pitting potential can be used as a rough measure of the pitting susceptibility.

Conclusions

1. Passivation in an acidic solution (H_2SO_4) leads generally to a more stable passive film than passivation in a neutral (Na_2SO_4) or alkaline solution (NaOH + Na_2SO_4). This is most probably due to a higher chromium-oxide content in the film formed at low pH values.

2. The passive film's resistance against localized breakdown in Cl^--containing solutions as well as against activation in acids is strongly dependent on the passivation time - a longer pre-passivation increases the stability of the film. This can result either from an increase of the Cr-content or decrease of "weak" sites of the passive film.

3. A critical passivation potential exists, above which the films formed show a remarkably higher resistance against pitting corrosion. This can be attributed to an oxidation of Cr(3+) species of the film into CrO_4^{2-}, which is incorporated in the film. The negative extra charge will repel the chlorides from the surface of the passive film.

4. Generally, the properties of the passive film on stainless steel very strongly depend on its formation history - the film formation solution, time and potential of passivation. The increased pitting corrosion resistance after the passivation treatments disappears, if the passivated surface is cathodically pre-polarized before the pitting corrosion studies. Therefore the pitting corrosion susceptibility is strongly influenced by the properties of the passive film and not only by the presence of bulk heterogeneities.

References

1. K. Asami, K. Hashimoto, S. Shimodaira, Corr. Sci. **18**, 551 (1978)
2. P. Marcus, I. Olefjord: Corr. Sci. **28**, 589 (1988)
3. S. Haupt, H.-H. Strahblow: Corr. Sci. **29**, 163 (1989)
4. R. Kirchheim, B. Heine, H. Fischmeister, S. Hofmann, H. Knote, U. Stolz: Corr. Sci. **29**, 899 (1989)
5. J. E. Castle, J.H. Qiu: Corr. Sci. **29**, 591 (1989)
6. S. Mischler, A. Vogel, H.J. Mathieu, D. Landolt: Corr. Sci. **32**, 925 (1991)
7. I. Olefjord, L. Wegrelius: Corr. Sci. **31**, 89 (1990)
8. D. Landolt in Advances in Localized Corrosion, Eds. H. Isaacs, U. Bertocci, J. Kruger, S. Smialowska, NACE, Houston, p. 25 (1990)
9. K. Asami, K. Hashimoto: Corr. Sci. **19**, 1007 (1979)
10. H. Saito, T. Shibata, G. Okamoto: Corr. Sci. **19**, 693 (1979)
11. T. Shibata, H. Tonbe in Proc. 11th Int. Corr. Congr., Florence, Italy, Vol. 5, p. 5.279 (1990)
12. W.P. Yang, D. Costa, P. Marcus in Oxide Films in Metals and Alloys, Proc.-Vol. 92-22, B.R. MacDougall, R.S. Alwitt, T.A. Ramanarayanan Eds., The Electrochemical Society, Pennington NJ, p. 516 (1992)
13. L. Kwiatkowski, F. Mansfeld: J. Electrochem. Soc. **140**, L39 (1993)
14. P. Schmuki: Ph.D Thesis Nr. 9763, ETH-Zürich (1992)

15. P. Schmuki, H. Böhni: J. Electrochem. Soc. **139**, 1908 (1992)
16. E.J. Johnson, in Semiconductors and Semimetals, R.K. Willardson, Editor, Academic Press, NY (1967)
17. M. Kloppers, F. Bellucci, R.M. Latanision in Application of Surface Science Methods to Environmental / Materials Interactions, Proc.-Vol. 91-7, D.R. Baer, C.R. Clayton, G.D. Davis Eds., The Electrochemical Society, Pennington NJ, p. 287 (1991)
18. S. Virtanen, P. Schmuki, H. Böhni, P. Vuoristo, T.A: Mäntylä to be published in Proc. Symp. on Oxide Films on Metals and Alloys, The Electrochem. Soc. Meeting, Miami Beach, Oct., 1994
19. S. Haupt: PhD Thesis, University of Düsseldorf (1987)
20 N. Hara, K. Sugimoto: J. Electrochem. Soc. **138**, 1594 (1991)
21. H. Keller, H.J. Grabke, H.-P. Stoppa: Werkstoffe und Korrosion **32**, 275 (1981)
22 T. Zakroczymski, F. Chwei-Jer, S. Szklarska-Smialowska: J. Electrochem. Soc. **132**, 2868 (1985)
23. J.R. Ambrose, J. Kruger in Proc. 4th Int. Cong. on Met. Corr., NACE, Houston TX, p. 698 (1972)
24. J. A. Bardwell, J.W. Fraser, B. MacDougall, M.J. Graham in Critical Factors in Localized Corrosion, Proc.-Vol. 92-9, G.S. Frankel, R.C. Newman Eds., The Electrochemical Society, Pennington NJ, p. 109 (1992)
25. L. Stockert: PhD Thesis Nr. 8632, ETH-Zürich (1988)
26. P. Schmuki, H. Böhni: Werkstoffe und Korrosion **42**, 203 (1991)
27. P. Schmuki, H. Böhni in Oxide Films on Metals and Alloys, Proc.-Vol. 92-22, B.R. MacDougall, R.S. Alwitt, T.A. Ramanarayanan Eds., The Electrochemical Society, Pennington NJ, p. 326 (1992)
28. M. Sakashita, N. Sato in Passivity of Metals, Eds. R.P. Frankenthal, J. Kruger, The Electrochemical Society, Princeton, New Jersey, p. 479 (1978)
29. A.R. Brooks, C.R. Clayton, K. Doss, Y.C. Lu: J. Electrochem. Soc. **133**, 2459 (1986)
30. C.R. Clayton, Y.C. Lu: J. Electrochem. Soc. **133**, 2465 (1986)
31. M. Pourbaix: Atlas D'Equilibres Electrochimiques, Gauthier-Villars & Cie, Paris (1963)
32. J.A. Bardwell, A.J. Davenport; H.S. Isaacs, G.I. Sproule, B. MacDougall, M. Graham in X-ray Methods in Corrosion and Interfacial Electrochemistry, Proc.-Vol. 92-1, The Electrochemical Society, Pennington NJ, p. 254 (1992)
33. J.A. Bardwell, G.I. Sproule, B. MacDougall, M.J. Graham, A.J. Davenport, H.S. Isaacs: J. Electrochem. Soc. **139**, 371 (1992)
34. G.P. Halada, C.R. Clayton in Application of Surface Science Methods to Environmental / Materials Interactions, Proc.-Vol. 91-7, D.R. Baer, C.R. Clayton, G.D. Davis Eds., The Electrochemical Society, Pennington NJ, p. 99 (1991)

Materials Science Forum Vols. 185-188 (1995) pp. 975-984

A comprehensive electrochemical approach to the relation between pitting, passivity and inclusions in stainless steel

J.H.W. de Wit, E.F.M. Jansen and L.C. Jacobs

Materials Institute Delft, Delft University of Technology, Division of Corrosion Technology and Electrochemistry, Rotterdamseweg 137, NL-2628 AL Delft, The Netherlands

Keywords: Metastable pitting, MnS inclusions, current spikes, refractive index, stainless steel

Abstract
The meaning of current spikes, measured upon anodic polarisation of commercial AISI type 316, 304, 316L and 317L stainless steel specimens, has been investigated. The spikes could be related to visible pitting attack on the one hand and microscopically detectable dissolution of manganese sulphide inclusions on the other hand. It is shown that only the dissolution of the larger manganese sulphide inclusions can lead to attacks detectable through current spikes, for the experimental conditions considered (0.1 M NaCl, 250 or 350 mVSCE). Furthermore, the passive layer has a role in the propagation of localised attack, as is indicated by the results of measurements on a pickled specimen and on type 317L steel. New details on the passive layer thickness and composition as a function of the electrode potential, obtained with XPS and Ellipsometry, are incorporated in the discussion.

Introduction
Investigations on pitting corrosion are mostly performed by application of electrochemical techniques. The pitting potential, which can be defined as the potential above which pits nucleate and develop [1] is often used as a practical measure for the pitting susceptibility of stainless steels. However, the value of the pitting potential depends very much on the method of determination and the experimental circumstances like the scan rate, solution agitation, the composition of the electrolyte solution and the surface condition of the metal. Moreover, even pitting potentials measured under similar conditions on stainless steels cover a certain potential region. Therefore the usefulness of "the" pitting potential is still being discussed in literature [2-6].
In order to obtain mechanistic information on pitting corrosion different electrochemical techniques can be used such as current or potential noise measurements, current spike measurements or impedance spectroscopy, all sustained by surface analytical techniques. To study pitting of commercial, non homogeneous, stainless steels, potentiostatic measurements of current spikes occurring in the passive region can be appropriate. A number of studies on these spikes (also termed current fluctuations, noise, pulses, transients, events, peaks or transient spikes) has recently been published [7-17]. The current of the measured spikes varies from micro amperes down to pico amperes. The larger of these (nano- to micro amperes) are associated with film breakdown or pit initiation at inclusions, temporary pit growth and repassivation. The shape of the spikes is characterised by a gradual increase of the current followed by an abrupt drop to the level of the passive current. This phenomenon is now commonly called metastable pitting, as opposed to stable pitting which is characterised by an on-going increase of the current.
This paper deals with pitting corrosion of commercial stainless steels AISI type 304, 316(L) and 317L. Current spikes in the nano ampere regime are related to macroscopic pitting events on the one hand, and mainly MnS inclusions on the other hand. The initiation and propagation of pits are described and related with the composition, the size and the morphology of the manganese sulphide inclusions. The importance of the quality of the passive layer especially during pit growth is taken into consideration as well.
No experimental details are given in this paper. For this we refer to earlier published work [18-20]. All electrode potentials are given vs. the SCE, if not stated explicitly.

The relation between inclusions and spikes
A typical current-time profile and typical current spikes are shown in Fig. 1. The shape of the spikes, characterised by a gradual current increase followed by (often) a current peak and a fast current decrease, was similar for all the specimens. For 316, 316L and 317L the number of spikes and their

size and life time were determined at 350 mV over a period of 4 hours until their frequency had effectively become zero. The data are given in Table 1.

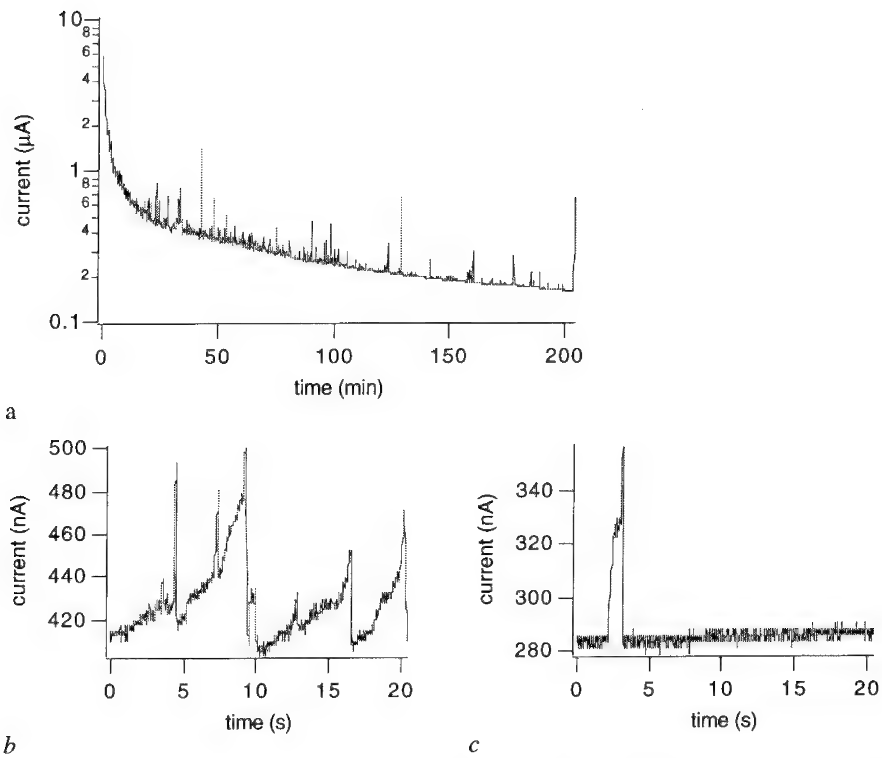

Figure 1: Typical current-time curve, type 316 steel, 350 mV, 0.1M NaCl, ambient temperature (a), examples of current spikes measured 2500 s (b) and 5530 s (c) after applying the potential.

Table 1: Current spikes measured on ground surfaces (SiC P1200) of type 316, 316L and 317L specimens at 350 mV, average of two measurements in 0.1M NaCl.

	number /78mm^2 *	average lifetime (s)	average height (nA)
316	1431	2.2	134
316L	2052	2.1	143
317L	719	3.2	79

* *The area of the specimen exposed to the solution.*

In order to investigate the possible relation between current spikes and manganese sulphide inclusions in the specimens, first an experiment was performed with a specimen on which these inclusions were removed by pickling [21-23]. The number of spikes measured on pickled specimens

should be lower. The current-time profile of a pickled type 316 specimen (immersed in 20% HNO_3/5%HF for 4 minutes at ambient temperature) is given in Fig. 2.

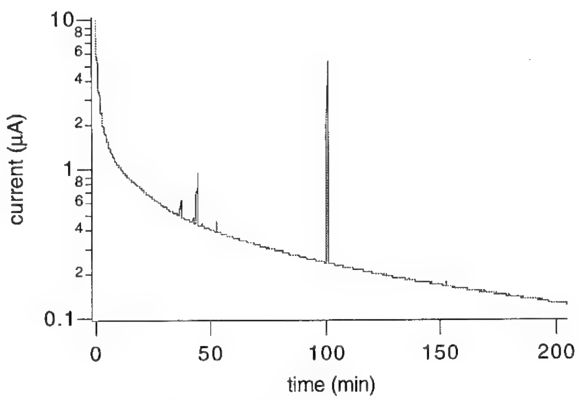

Figure 2: Current-time profile measured after pickling the surface, type 316 steel, 350 mV, 0.1 M NaCl, ambient temperature.

Indeed only a few spikes were detected, although they were relatively large showing an average lifetime of 8.8 s and an average height of 587 nA, compare with the data in Table 1.
The relation between the inclusions and the spikes was further studied by application of EPMA. The surfaces were polished down to 1 micron (diamond paste). Before current spikes were measured, the number, type and size of inclusions were determined. After the spikes' measurement the same surface analysis was performed again. The results of these surface analyses for alloy 316 are given in Table 2. Three types of inclusions were distinguished: discrete manganese sulphide inclusions, complex inclusions with various elements, and inclusions or spots with iron and chromium (oxide). The number of manganese sulphide inclusions measured after the exposure was markedly lower than the number determined before the exposure. The number of complex inclusions seemed to increase. A possible explanation for this apparent increase is that the surrounding of particles dissolved thereby uncovering insoluble (mainly titanium and silicon) compounds.
The results of the surface analyses on 316L and 317L were similar. The number of discrete manganese sulphide inclusions decreased, comparing the situation before and after exposure in 0.1M NaCl at 350 mV, from 291 to 21 and from 749 to 59 per mm^2 respectively. The number of the manganese sulphide inclusions in the type 304 steel exposed in 0.1M NaCl with an applied potential of 250 mV decreased also markedly, from 749 to 49 inclusions per mm^2. The sulphide inclusions obviously dissolve under these circumstances. Therefore "bare" metal gets exposed at these spots and the current increases, which can result in a detectable (nano ampere) spike.
The sulphide inclusions in 304 were found to be relatively large, the sulphide inclusions in 317L were comparable with the inclusions in 316. Only the number of large inclusions was slightly higher in 317L compared with 316. The lifetime of the spikes for 317L was, however, longer than for 316L and 316, see table 1.
Type 304 and type 316 specimens have been compared considering the charge associated with the current spikes measured at 250 mV (for type 304 steel spikes could not be measured at potentials higher than 250 mV.) At this potential more spikes were measured for 304 than for 316. However, the charge accompanying the spikes did not differ very much comparing 304 and 316, see Fig. 3.

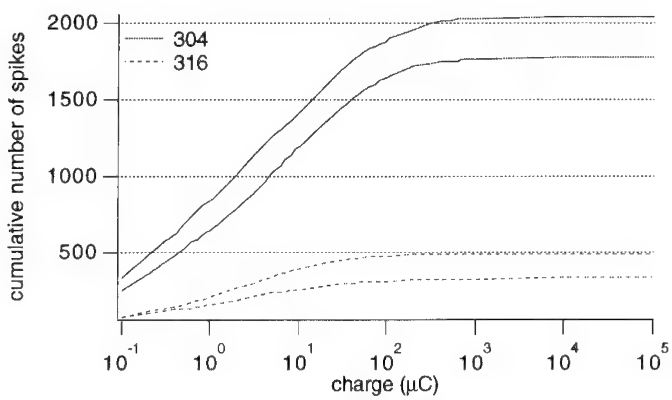

Figure 3: Cumulative number of spikes plotted as a function of the charge, comparison (duplicate measurements) of type 304 and 316 steel, ground (SiC grit P1200) surfaces, 250 mV, 0.1M NaCl.

Also in normal polarisation measurements the 304 alloy, containing the largest inclusions, showed more clearly the typical current increase at potentials cathodic from the transpassive region, typical for local attack, than the other alloys. Alloy 316L, containing larger inclusions than 316 was similarly somewhat more sensitive than 316.

From the experiments with pickled specimens and the combination of spikes measurements and surface analytical work it is obvious that a relation exists between manganese sulphide inclusions and current spikes. The relations between the charge of the spikes and the size of the inclusions and between the number of spikes and the number of inclusions will be discussed next.

The charge related with a spike can be as high as 10^4 μC. Simple oxidation of even the largest MnS inclusions observed according to $MnS \rightarrow Mn^{2+} + S + 2e$ would only account for 0.2μC. Therefore it must be concluded that the charge is mainly related to dissolution of the stainless steel matrix and possibly dissolution of more than one inclusion. When attack starts at one inclusion, other inclusions which are close to this spot are likely to dissolve subsequently. Stringers consisting of several manganese sulphide inclusions lying close together were common in the steels that were investigated.

Table 2: Number of inclusions in type 316 steel per mm², n, and average (cross) area at the specimen surface, A, distinguished to the main element(s) in the composition of the inclusions, numbers determined before and after exposure.

	before exposure		after exposure	
	N	A (μm^2)	N	A (μm^2)
MnS	587		94	
complex	543		1014	
Fe/Cr	2127		2981	
S	679	0.4	105	0.1
Mn	478	0.4	76	0.1
Si	226	1.5	336	0.9
Ca	226	1.7	287	1.0
Ti	446	0.7	636	0.4
Al	17	10 10	18	9 9

The number of manganese sulphide inclusions outnumbers the number of detected spikes, for example 9 spikes per mm^2 have been measured on the polished surface of the type 316 specimen while the difference in the number of inclusions before and after exposure is 493 per mm^2 (Table 2). A lot of inclusions dissolved without causing a detectable spike and certainly not any visible attack. The size of the sulphide inclusion and the extent to which an occluded cell will be formed are important aspects determining the eventual visible pitting.
The effect of inclusion size becomes clear when the measurements on the two types of 316 steel are compared. These steels contain manganese sulphide inclusions of a different size.

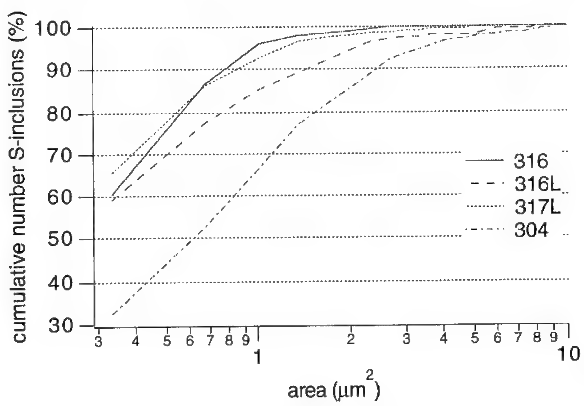

Figure 4: Cumulative number of sulphur containing inclusions per mm^2 plotted as a function of the area measured at the surface of the specimens, 100% = 679 (316), 335 (316L), 757 (317L) and 749 (304) inclusions per mm^2.

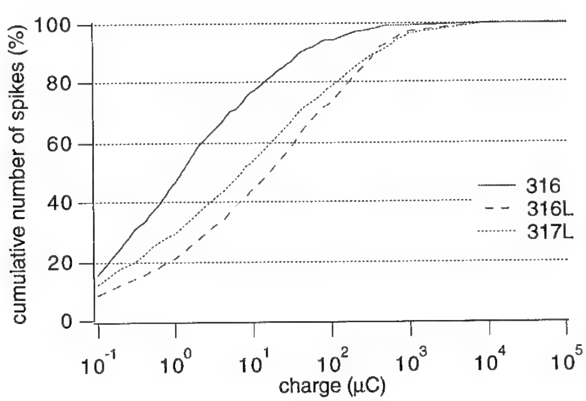

Figure 5: Cumulative number of spikes plotted as a function of the charge, measured during exposure of polished (1 micron diamond paste) surfaces, 0.1M NaCl, 350 mV, 100% = 702 (316), 1396 (316L) and 1108 (317L) spikes/78 mm^2, or 9, 17.9 and 14.2 spikes per mm^2 respectively.

In Fig. 4 the size distributions of sulphur containing inclusions in 316 and 316L are shown: for 316 steel 7 sulphur containing inclusions have an area greater than 2 µm^2, while for 316L steel 17

inclusions of similar size are present, despite the much lower overall number of inclusions. The results of the current spikes measurements are shown in Fig. 5. Many inclusions in 316 are small, obviously not leading to spikes, which leads to double the amount of spikes or 316L compared with 316 (18 vs. 9 per mm^2), in good relation to the number of sulphur containing inclusions in both materials sizing > 2 μm^2.
The results from the measurements for type 304 and type 316 steel at 250 mV, Fig. 3, which showed a large difference in the number of spikes, while the total number of sulphur-containing inclusions (749 for 304 and 679 for 316, see also Fig. 4.) did differ only slightly, can now be explained with the earlier expressed ideas on the importance of the size of the inclusions as follows. At a given potential (250 mV) only a certain number of sites is activated, starting with the dissolution of inclusions larger than a critical size (greater than 2 μm^2 at this lower potential, as we have seen there are only 7 per mm^2 of this size available) . So we may expect the number of spikes to be below 7 x 78 = 546, which is observed indeed in Fig. 3. At the same time it becomes clear why the charge per spike does not differ very much for the two materials. The spikes for both materials result from inclusions with similar critical or above critical size. Another difference between these two materials is the Mo content of the alloys. This will be discussed in the paragraph on the influence of the passive film on the life time of the growing pits.

The relation between spikes and macroscopically visible pits
In order to relate the spikes to pitting attack visible with the naked eye, a more anodic potential (850 mV) was applied to a polished (3 micron diamond paste) specimen of type 316. With a video camera, the nucleation and growth of pits was observed. A high initiation frequency (100-200 pits/cm^2 min) was seen shortly after polarisation. The frequency decreased during the experiment. The visible development of the pits took about 15 s, after which the pits stopped growing. The time of development corresponded with the lifetime of large current spikes which were measured simultaneously, not given here. These large spikes can also be characterised by a gradual current increase followed by a fast current decrease, a shape similar to the shape of the spikes measured at lower potentials as given in Fig. 1b. The corresponding physical events seem to scale up when the polarisation potential is shifted to more anodic values. At even more anodic potentials a limited amount of pits goes on growing. The current increase related with these pits is in the initial phase still gradual, showing resemblance with the real spike form at lower potential, but is soon followed by a fast not further detectable current increase: ongoing pitting attack.

The occluded cell and the passive film
The lifetime of the spikes and therefore the size of the resulting pits are believed to be related to the quality of the passive layer. Isaacs [24,25] proposed that the more stable the passive film is, the longer it will be able to keep a pit initially covered enabling local corrosion (acidification) to proceed in the occluded cell. Depending on the situation in the pit (pH, salt layer) at the moment of rupture of the cover, localised corrosion can proceed or the pit will die. The relatively long lifetime for spikes measured on 317L, and also the low average current peak height are therefore thought to be more likely caused by an improved ability of the passive layer of 317L, compared with 316, to keep occluded cell conditions, than by the small differences in the dimensions of inclusions. The chromium, nickel and molybdenum content of 317L are considerably higher than for 316, improving the passive film properties. However, as soon as the cover is ruptured, the same alloying elements will enable relatively fast repassivation of the pit.
Considering the huge influence of the potential on the number of spikes (e.g.: 702 at 350 mV vs. <500 at 250 mV for polished 316) we investigated the quality of the passive film as a function of potential with ellipsometry and XPS. Only a limited amount of the data gathered with these techniques can be given here. For more details we refer to some recent and future publications [27,28,29].
In Fig. 6 the stationary polarisation curve for a Fe17Cr model alloy is given which shows the wide potential range with constant passive current density. This model alloy does not contain any MnS inclusions. The potentials for which the values for the refractive index were determined are marked with letters. The passive region starts at about -925 mV and the passive film, which is formed, contains Cr^{2+} and will be present as an amorphous Cr(II)oxide/hydroxide [19,20] At this potential we find an increase of about 1.3° in Ψ and a decrease of about 6° in Δ compared with the bare substrate parameters. Hence we calculate a refractive index of 0.22-2.08i at a thickness of 1.5 nm

and 1.24-3.01i at a thickness of 2.5 nm. Going to more anodic potentials this passive film is further oxidised to Cr(III) oxide/hydroxide[19,20], while also some Fe is incorporated, i.e. the composition of the film has changed. The refractive index of the passive film will therefore also be different; we have calculated a refractive index of 0.26-3.05i at a thickness of 1.5 nm and 1.46-3.71i at 2.5 nm at a potential of -910 mV, see Fig. 7. It is possible that both the composition and the thickness of the passive film have changed

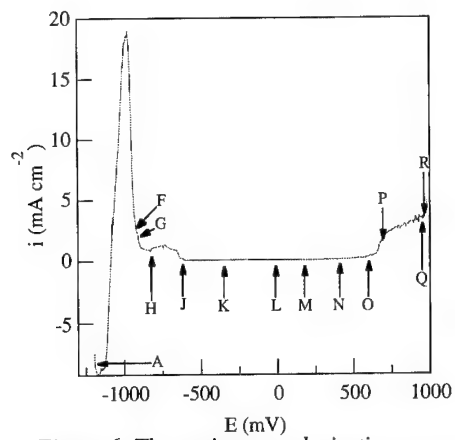

Figure 6.:The stationary polarisation curve for a Fe17Cr model alloy in 0.5 M sulphuric acid.

In the passive region (-800 mV to ± 600 mV) the changes in the ellipsometric parameters Δ and Ψ (relative phase retardation and relative amplitude diminution) are minimum [28].

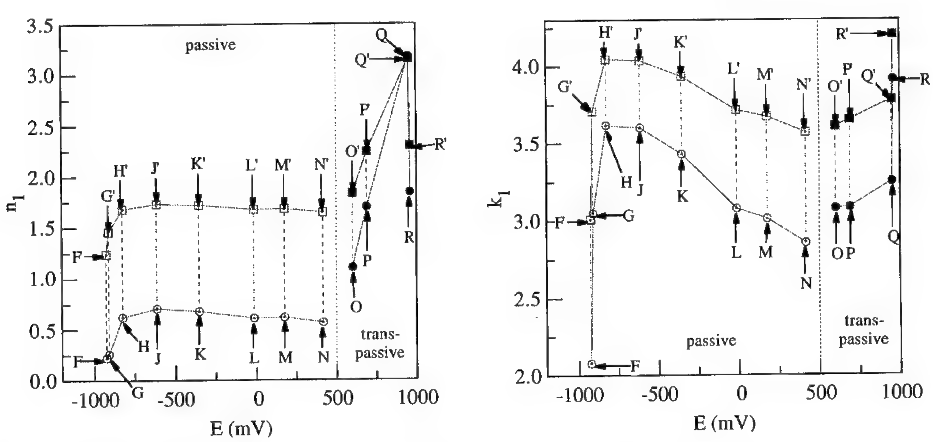

Fig. 7. The real (left) and imaginary (right) part of the refractive index of the film on Fe17Cr0 as a function of the potential. o: d=1.5 nm; □: d=2.5 nm; •: d=2.0 nm; ■: d=3.0 nm. The characters refer to points of the polarisation curve of Fig. 6.

Between -613 mV and +600 mV the film hardly changes in composition and thickness. The slight increase in n_1 (real part) and k_1 (imaginary part) (Δ↑ and Ψ↓) between -825 mV and -613 mV (figure

7) may result from a small composition change due to Fe incorporation or from hydrogen reoxidation, which is also reflected in i_{pass} in Fig. 6. Going to more anodic potentials in the passive region it can be seen that the real part of the refractive index shows a slight decrease from -600 mV to +450 mV independent of assumed thickness, see Fig. 7.
The imaginary part of the refractive index also decreases going from -613 mV to +416 mV. Because both the composition and the thickness of the layer are reflected in the ellipsometric data it is not possible to decide simply that the thickness is constant, while the composition is slightly changing, without using other information. However, from XPS-measurements we know that in this potential range the composition indeed slightly changes: the passive film contains less OH groups and obtains a more oxide-like character at increasing potentials and the Fe content also slightly changes, while the average valence of the metals gradually approaches 3+. So the slow decrease of the real part of the refractive index could be due to a slight decrease of the optical density due to these small changes in composition. The more clearly decreasing value of k_l can possibly be ascribed to the lower conductivity as a result of these small compositional changes the conductivity being very sensitive to this kind of compositional change. The relatively high values above 1.00 for k_l indicate that the passive film is highly conductive and not behaving like a true dielectric in accordance with the data of Marichev [26].
It can be seen from Table 3 that if a thickness of 1.5 nm is taken the real part of the refractive index (n_l) of the film is about 0.6-0.8 at -600 mV.

Table 3: Physically acceptable combinations of refractive indices of the film at thickness 1.5, 2.0, 2.5 and 3.0 nm for the passive region on Fe17Cr.

				PASSIVE REGION			
Point	E (mV)	Δ (deg)	Ψ (deg)	d=1.5 nm	d=2.0 nm	d=2.5 nm	d=3.0 nm
A	-1200	120.48	30.48	----	----	-----	-----
F	-925	114.97	31.65	0.22-2.08i	0.76-2.65i	1.24-3.01i	1.58-3.27i
G	-910	116.53	31.76	0.26-3.05i	1.01-3.47i	1.46-3.71i	1.75-3.88i
H	-825	117.40	31.70	0.62-3.62i	1.30-3.88i	1.68-4.05i	1.93-4.17i
J	-613	117.43	31.65	0.71-3.60i	1.36-3.87i	1.74-4.04i	1.98-4.16i
K	-352	117.21	31.62	0.68-3.43i	1.34-3.74i	1.72-3.93i	1.97-4.07i
L	-12	116.74	31.57	0.61-3.08i	1.28-3.47i	1.68-3.71i	1.94-3.89i
M	+177	116.66	31.55	0.62-3.01i	1.28-3.42i	1.68-3.67i	1.94-3.85i
N	+416	116.43	31.54	0.46-2.59i	1.23-3.30i	1.65-3.57i	1.91-3.77i

If the thickness is taken as 2.5 nm the real part is about 1.6-1.7. At the end of the passive region at about +450 mV n_l varies from about 0.5 to 0.8 at a thickness of 1.5 nm and from 1.3 to 1.65 at a thickness of 2.5 nm. In all cases the imaginary part of the film (k_l) decreases going from -600 mV to +450 mV. At -600 mV k_l is in the order of 2.2-3.6 in case of 1.5 nm, 2.5-4 in case of 2.5 nm and in the order of 1.7-3.6 at +450 mV in case of a thickness of 1.5 nm. At a thickness of 2.5 nm k_l is about 2.15-3.6.
Taking all these data it is reasonable to assume that also for alloys 304 and 316 the thickness of the passive film in acid solution is not changing very much in this potential region. Therefore we ascribe the huge influence of the potential on the pitting sensitivity rather to the small compositional changes than to the changes in thickness of the film. This is also in accordance qualitatively with the difference between 304 and 316 and 317 where the passive film is of similar thickness, but the composition of the film due to the Mo and the higher Ni content of 316 and 317, may be different, while at the same time the repassivation rate at break down of the porous pit cover has increased as we have shown before [29].

Film on top occlusions
The inclusions lying at the surface do not dissolve immediately after exposure, because if they would, the current-time profile of a pickled surface would not differ from the profile of a surface which was not pickled. The frequency of spikes decreases during a measurement, but does not become zero. As the passive layer is continuously renewed, new inclusions get exposed to the solution all the time. A rough estimate of the frequency with which new inclusions get exposed per hour can be made with the following formula: D.(I_p.k).3600/d; D = number of inclusions per unit surface area, I_p = passive current density, k = conversion from charge to volume (3.10^{-5} cm^3/C) and d = average diameter of the inclusions. With I_p = 0.4 µA/cm^2, d = 0.4 µm, D = 587/mm^2, the calculation results in 63 particles/cm^2h. As only the larger inclusions act as initiation sites, the frequency of spikes expected to be caused by the initially covered inclusions will only be a fraction of 63/cm^2h. After pickling the surface, 19 spikes were measured which corresponds to a frequency of 7/cm^2h which is therefore very reasonable. These spikes were, however, relatively large. This is understandable as the pits formed upon dissolution of large inclusions of which only a small part was initially exposed to the solution, will be very well shielded, so localised attack is promoted in these well occluded cells.

Summarising it can be concluded that spikes are only generated through dissolution of the larger manganese sulphide inclusions at the surface (B in Fig. 8), through weak spots in the passive film on top of the inclusions (pit cover), followed by dissolution of the pit walls. New inclusions get exposed during service life, representing possible new initiation sites for pitting as shown in Fig. 8. The pit walls are rather well shielded from the surroundings, providing occluded cell conditions, which can result in pit growth especially for the bigger inclusions. Pit growth is directly influenced by the quality of the pit cover and thus by the composition of the passive film. The different behaviour of 316 compared with 304 , including the potential dependence, can be explained by the quality of the passive film and the rate of repassivation due to the Mo in 316 in combination with the size of the inclusions.

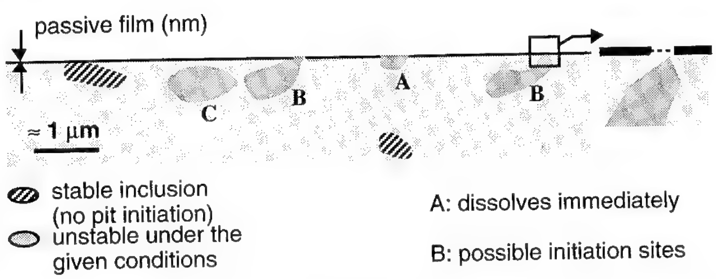

Figure 8: Schematic representation of pit initiation sites in a stainless steel surface. Attack start at particles B and can proceed to particles positioned like C (common in stringers of manganese sulphide inclusions). During exposure gradually inclusions which are positioned like C with respect to the surface will become activated like B.

References
[1] Z. Szklarska-Smialowska, Pitting Corrosion of Metals, NACE, Houston, USA (1986).
[2] B.E. Wilde, Corrosion **28** 283 (1972).
[3] F.L. Laque, Mater. Perform. **22** 34 (1983).
[4] N.G. Thompson and B.C. Syrett, Corrosion **48** 649 (1992).
[5] L. Soria and E.J. Herrera, La Metallurgia Italiana **83** 1017 (1991).
[6] P. Eskelinen, O. Forsén, H. Hänninen, J. Onnela and S. Yläsaari, Materials Science Forum **111-112** 515 (1992).
[7] H. Böhni and L. Stockert, Werkst. Korros. **40** 63 (1989).
[8] M. Keddam, M. Krarti and C. Pallotta, Corrosion **43** 454 (1987).
[9] W.M. Carroll and M.B. Howley, Corros. Sci. **30** 643 (1990).

[10] H. Ezuber, A.J. Betts and R.C. Newman, Materials Science Forum **44&45** 247 (1989).
[11] U. Bertocci, M. Koike, S. Leigh, F. Qiu and G. Yang, J. Electrochem. Soc. **133** 1782 (1986).
[12] Y. Miyata, T. Handa and H. Takazawa, Corros. Sci. **31** 465 (1990).
[13] D.E. Williams, J. Stewart and P.H. Balkwill, in Critical Factors in Localized Corrosion, ed. G.S. Frankel and R.C. Newman, The Electrochemical Society, Inc., Pennington, USA 36 (1992).
[14] A.M. Riley, D.B. Wells and D.E. Williams, Corros. Sci. **32** 307 (1991).
[15] T. Tsuru and M. Sakairi, Corros. Engineering **39** 401 (1990).
[16] G.T. Burstein and S.P. Mattin, Phil. Magazine Letters **66** 127 (1992).
[17] P.C. Pistorius and G.T. Burstein, Phil. Trans. R. Soc. Lond. A 341 531 (1992).
[18] E.F.M. Jansen, thesis Delft University of Technology (1993).
[19] J.H. Gerretsen and J.H.W. de Wit, Corrosion Sci. **30** (1990) 1075
[20] J.A.L. Dobbelaar, E.C.M Herman and J.H.W. de Wit, Corrosion Sci. **33** 765 (1992).
[21] W.M. Carroll and T.G. Walsh, Corros. Sci. **29** 1205 (1989).
[22] G. Hultquist, S. Zakipour and C. Leygraf, in Passivity of Metals and Semiconductors, ed. M. Froment, Elsevier Science Publ. B.V., Amsterdam, The Netherlands 399 (1983).
[23] M.A. Barbosa, A. Garrido, A. Campilho and I. Sutherland, Corros. Sci. **32** 179 (1991).
[24] H.S. Isaacs and G. Kissel, J. Electrochem. Soc. **119** 1628 (1972).
[25] H.S. Isaacs, Corros. Sci. **29** 313 (1989).
[26] V. A. Marichev, T. Saario and V.V. Molokanov, ICC 93, Houston Texas
[27] B.S. Norgren, M.A.J. Somers and J.H.W. de Wit, accepted for publication in Surf. Interface Anal. (1994).
[28] L.C. Jacobs, H.P. De Vogel, K. Hemmes, M.M. Wind and J.H.W. De Wit, submitted for publication in Corrosion Science.
[29] L.C. Jacobs, H.P. de Vogel, P.E. Habing, J.A.L. Dobbelaar, K. Hemmes and J.H.W. de Wit, Electrochimica Acta, Vol 38 **14** 1969 (1993).
[30] J.H. Gerretsen and J.H.W. de Wit, Electrochimica Acta,Vol 26 **9** 1465 (1991).

Materials Science Forum Vols. 185-188 (1995) pp. 985-990

Effect of nanometer size Cr-depleted Fe-rich region on passivity breakdown

Y. Ishikawa and T. Yoshimura

Mechanical Engineering Research Laboratory, Hitachi Ltd., 502 Kandatsu, Tsuchiura, 300 Japan

Keywords: Cr-depleted region, electrochemical potentiokinetic reactivation, atom probe, passivity breakdown, spinodal decomposition

Abstract

When ferrite containing stainless steels were aged at intermediate temperatures for as long as 10000h, phase separation occurs in ferrite phase by spinodal mechanism. This induces the formation of Cr-depleted Fe-rich and Cr-segregated Cr-rich regions. In the present study direct measurements of Cr depletion of the Cr depleted region by atom probe-field ion microscopy (AP-FIM) and position-sensitive atom probe (POSAP) are compared to measurements of the passivity breakdown characteristics using the electrochemical potentiokinetic reactivation (EPR) test. Correlations are presented between the Cr concentration, size and volume fraction of Cr depleted regions and reactivation ratio. As expected, the Cr concentration of 12at% is critical in inducing the passivity breakdown. However, with the Cr concentration of 11.2at%, no passivity breakdown occurs when the size of the Cr-depleted region is less than 2nm. Moreover when the volume fraction of the Cr-depleted region exceeds about 4%, a significant passivity breakdown occurs. Also in this case no breakdown occurs with the size of the Cr-depleted region being less than 2nm, even when the volume fraction is above 4%. The size of the Cr-depleted region appears to be the most critical parameter in inducing the passivity breakdown and the critical value exists somewhere between 2 and 5nm.

Introduction

Chromium is the most important alloying element of stainless steel which induces the formation of a good protective oxide film. When the amount of chromium is too low to cover the total surface with chromium containing oxide, passivation will not be complete. According to the literature [1], the steel must contain at least 11mass% chromium to form a stable passive film. Explanation of this critical amount of chromium has been attempted in a number of studies [2-4]. The distribution of chromium in the steel is also important in the formation of a good protective film. Localized areas sufficiently depleted in chromium will form less protective film than areas of high chromium. It is generally accepted that in sensitized stainless steels, the formation of chromium depleted zone occurs in the vicinity of grain boundaries because of carbide precipitation. In ferritic and ferritic/austenitic duplex stainless steels, nonuniform distribution of chromium occurs even in the grain owing to the phase separation of ferrite into Cr-rich and Cr-depleted regions during intermediate temperature ageing [5-7]. The presence of Cr-depleted region has been shown to induce the formation of less protective film [8-13]. Although the size of the Cr-depleted region is in the order of a few hundreds angstrom at most, much smaller than the Cr-depleted zone in grain boundaries, the degradation of passivity is significant. The aim of this work was to contribute to the understanding of the critical parameters in passivity breakdown. An attempt is made to correlate the passivity breakdown during the cathodic sweep after passivation to the chemical composition, volume fraction and size of the Cr-depleted Fe-rich region. The atom probe and the position-sensitive atom probe (POSAP) were used to directly measure those parameters and the electrochemical potentiokinetic reactivation (EPR) in potassium thiocyanate containing sulfuric acid, originally developed by Cihal [14], was used as a measure of passivity breakdown. Atom probe-field ion microscopy (AP-FIM) is unique among the family of surface analysis techniques that have been introduced in recent years in that in addition to its subnanometer order lateral resolution it examines only the outermost atomic layer of the surface atom by atom and depth profiling is possible by means of layer-by-layer evaporation without disturbing the structure underneath. In the EPR test, reactivation from the passive state leads to local film breakdown and attack of Cr-depleted regions.

Experimental

Test specimen

Materials examined were Fe-28Cr-5Ni ferritic, Fe-25Cr-6Ni-3Mo ferritic/austenitic duplex (α=65%) and 20Cr-10Ni-2.5Mo cast duplex (α=15 and 25%) stainless steels. The steels were aged at 350, 400 and 450°C for up to 10000h. The electrodes were prepared by spot-welding a lead onto one side of the samples and mounted them into epoxy resin. The surface of the electrodes was abraded down to 600 grit

silicon carbide paper and polished with 0.05μm alumina paste.

Electrochemical measurements

Electrochemical potentiokinetic reactivation (EPR) measurements, were carried out in 0.5M H_2SO_4+0.01M KSCN solution with a typical three-electrode cell. The solution was deaerated with pure nitrogen gas during the measurement. A platinum sheet (20mm×20mm) was used as the counter electrode and a saturated Ag/AgCl electrode as the reference electrode. Before the measurement, the electrode was cathodically polarized at -600mV (Ag/AgCl) for 5min to remove the air-formed oxide film. Then the potential was scanned from the open circuit to 200mV at a scan rate of 20mV/min and after holding 5min at 200mV, then the scan was reversed. A minimum of two EPR measurements were made on each specimen to determine the reactivation ratio.

Atom probe analysis

A pulsed laser atom probe and POSAP were used in this study. Since the details of the equipment were described elsewhere [15, 16], only a brief description will be given with regard to the POSAP [17]. Ions are removed from the specimen surface by field evaporation by the application to the sharp needlelike specimen of high voltage pulses superimposed to a standing voltage (5~15kV). The field evaporated ions are accelerated towards the POSAP detector which determines simultaneously, the impact position and the time of flight of the ions. Successive field evaporation of the surface atoms produced a 2-D elemental map with respect to time for a region of approximately 15nm in diameter. Then 3-D expansion of the time series data was performed based on the relation between the total voltage applied and the specimen radius. The bulk materials were mechanically cut into square rods of 0.2mm^2 and 20mm long. Electropolishing in (conc. HCl/HNO_3)=(1/3) solution with 3-4V ac, produces a sharp needle specimen with an end radius about 100nm suitable for atom probe analysis. The presence of ferrite at the tip apex was confirmed by scanning electron microscopic observation and electron probe microanalysis.

Results and Discussion

Figure 1 shows an example of the 2-D atom map from the ferrite phase of the Fe-25Cr-6Ni-3Mo duplex stainless steel as a function of ageing time at 450°C. This figure represents chromium (black spot) atoms contained in a sliced cross-section of 15nm in diameter and 1nm in thickness. In the unaged steel, chromium atoms are randomly distributed. Ageing for 100h shows the segregation of chromium atoms and further ageing shows enlargement of segregated areas and more concentration of chromium. This in turm gives rise to the formation of Cr-depleted regions, which are more clearly shown in the gray scale representation of the sliced section as shown in Fig.2. The black coloured area represents the area where the chromium concentration is less than 12at% and the white represents the chromium concentration 65at% or higher. Ageing for 100h causes the formation of the isolated Cr-depleted area of about 2nm wide and the prolonged ageing results in the expansion and interconnection of the Cr-depleted area. On the basis of these atom probe data, a quantitative determination of chromium concentration, size and volume fraction of the Cr-depleted area was performed through the auto-correlation analysis and simple averaging of chromium concentration in the Cr-depleted area (less than 20at%Cr) appeared in the

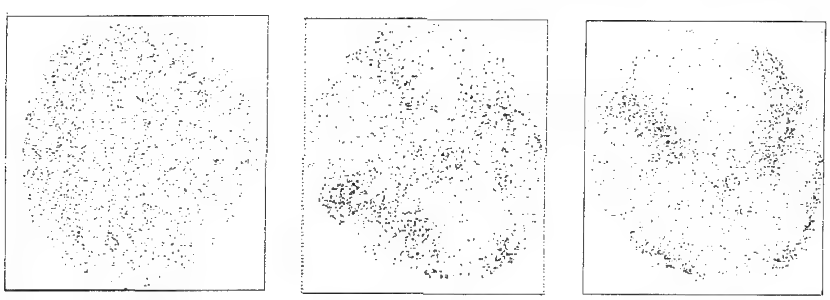

(a) unaged (b) 100h (c) 1000h

Fig.1 An example of 2-D chromium atom map obtained from ferrite phase of Fe-25Cr-6Ni-3Mo duplex stainless steel as a function of ageing time at 450°C (A sliced cross section of 15nm in diameter and 1nm in thickness)

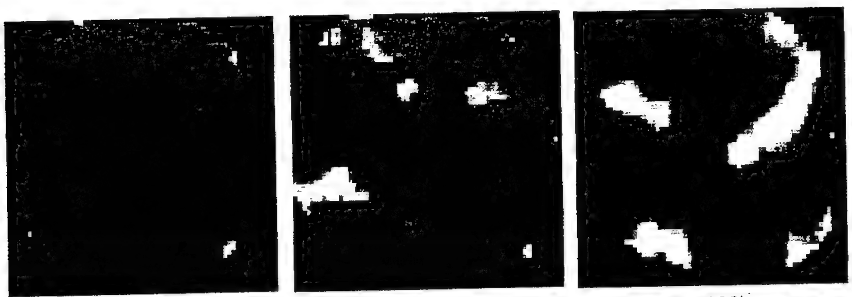

Fig.2 Gray scale representation of progressive formation of Cr-depleted region by ageing (A black coloured area represents Cr concentration less than 12at% and white, 65at% or higher)

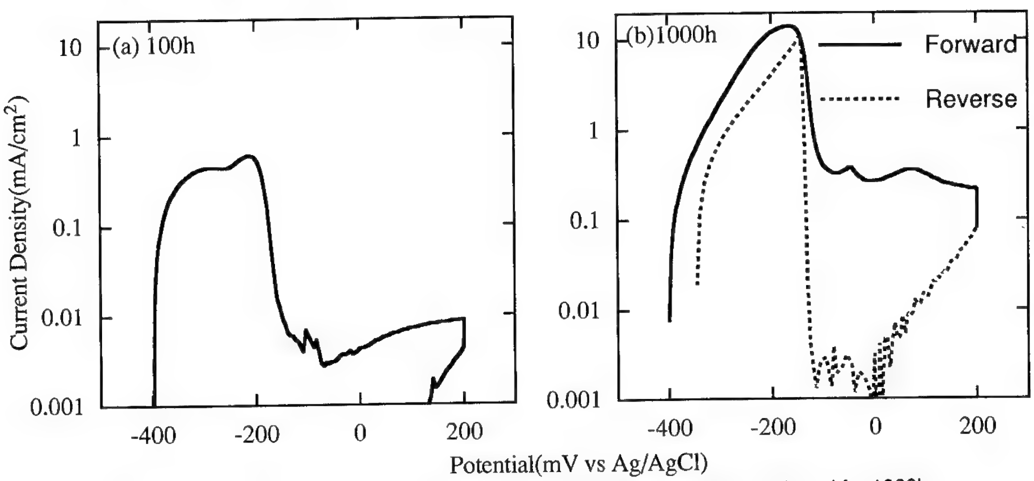

Fig.3 Comparison of cyclic polarization curves between the steel aged for 100h and for 1000h

gray scale representation of the tomographic sliced cross section. Figure 3 shows EPR results for the Fe-25Cr-6Ni-3Mo duplex stainless steel aged at 450°C for 100 and 1000h. Ageing the steel for 100h does not induce any reactivation during the cathodic sweep, while the reactivation current peak is observed for the 1000h aged steel. This indicates that for 100h aged steel, the passive film remains intact and suppress the large active peak observed during reactivation of the 1000h aged steel, though the steel possesses the Cr-depleted area similar to the 1000h aged steel as shown in Fig.2.

In the grain boundary chromium depletion a correlation has been examined between the Cr content, width and depth of the Cr-depleted zone and the degree of sensitization measured by EPR [18]. The results indicate that the EPR test attacks Cr-depleted regions containing less than about 12.5 to 13.5mass% chromium and that the amount of attack depends on the width and on the depth of the depleted region. In this study the ratio of the reactivation current (i_c) to the active dissolution current peak (i_a), i_r/i_a, was taken as a measure of passivity breakdown. Its applicability to the Cr-depletion in the ferrite phase of duplex stainless steel has been given in our previous work [12]. Figure 4 shows a comparison between Cr concentration in the Cr-depleted region and reactivation ratio. The Cr concentration in the Cr-depleted region is determined by simply averaging the Cr concentration in the Cr-depleted region of less than 20at%Cr. Significantly Cr-depleted regions, particularly those below 12at% produce high reactivation values. On the other hand, very low or no reactivation values were measured when Cr concentrations rise above 15at%. This is in a good agreement with the results obtained for Cr depletion at grain boundaries, suggesting, the critical Cr content below which attack occurs in the EPR test is about 13.5mass% [17]. However there is one data point which does not follow this. This is the Fe-25Cr-6Ni-3Mo duplex stainless steel aged at 450°C for 100h, which has the Cr-concentration of 11.3 at% in the Cr-

depleted region, but still maintains the passivity during the cathodic sweep in the EPR test, as shown in Fig.3a. No reactivation has been observed for this specimen even when the passivation time at 200mV was reduced to less than 1sec and the concentration of KSCN was increased to 0.02~0.05M. We also measured long term current changes at potentials lower than the reactivation potential of longer aged steels, -180~-220mV and we found no passivity breakdown. Passivity breakdown only occurred when the potential was lowered to the potential where the passivity of the austenitic phase was lost, that is, at -230~-240mV. The effect of Cr depletion size on reactivation is shown in Fig.5. The Cr depletion size is determined by auto-correlation analysis of the Cr-depleted region of less than 20at%Cr. When the size exceeds 5nm, a significant reactivation is observed. On the other hand no reactivation occurs, when the size is below 2nm. This is also in agreement with grain boundary Cr depletion width results [18].

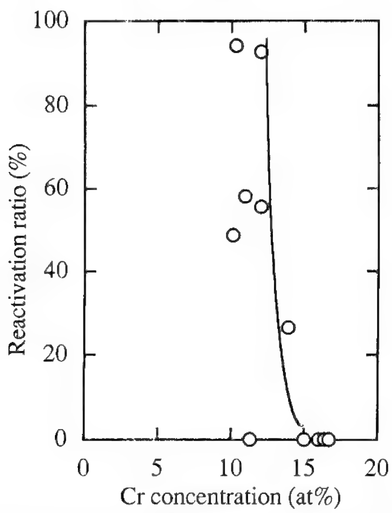

Fig. 4 Comparison between Cr concentration of Cr-depleted region and reactivation ratio

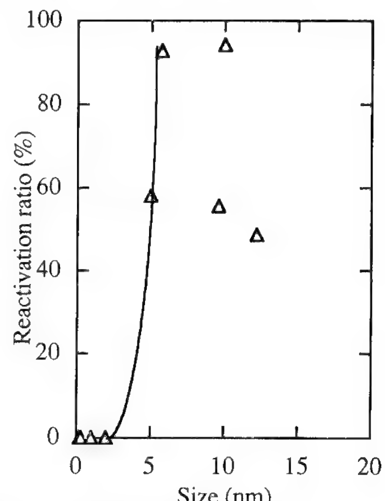

Fig. 5 Correlation between size of Cr-depleted region and reactivation ratio

Figure 6 shows a correlation between the volume fraction of the Cr-depleted region of less than 20at%Cr and reactivation. This also indicates the critical volume fraction above which reactivation becomes significant, that is, about 4%. However there are two data points which do not show any reactivation, even though their volume fraction are above 4%. The size of the Cr-depleted region of these specimens is 0.3 and 2nm respectively. This suggests that the size of the Cr-depleted region is more critical than the volume fraction. In the estimation of the minimum size of Cr-depleted zone measurable by EPR test [19], the value suggested is 5nm (2.5~6.5nm). This is in the range of value found in the present study. Since the Cr-depleted region must be large enough for species in the aqueous solution to penetrate, the size must be greater than the size of water molecules clustered by hydrogen bond, usually 50~100 molecules large and this is also in the range of value found. It may be premature to conclude the presence of the critical size of Cr-depleted region, because it is difficult to detect the charge flowing when the above mentioned Cr-depleted region (2nm in size and 4% in volume fraction) dissolves, which amounts to 10μC/cm^2.

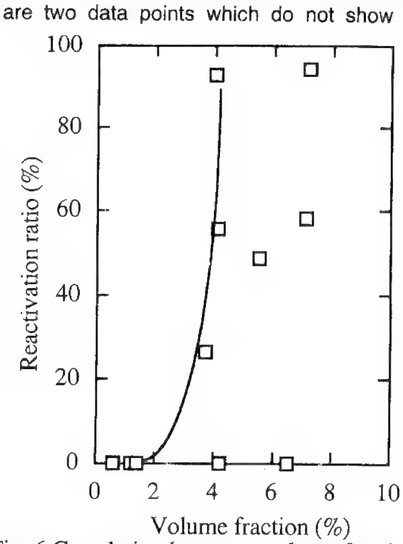

Fig. 6 Correlation betweem volume fraction of Cr-depleted region and reactivation ratio

Conclusions

The Cr depletion in the ferrite phase generated by phase separation was directly measured by AP-FIM and POSAP. A comparison was made between Cr depletion and passivity breakdown, as measured by the EPR test. The EPR test showed that a significant passivity breakdown occurs when the Cr concentration is less than 12at% and the size and volume fraction of the Cr-depleted region is above about 5nm and 4% respectively. Among the Cr depletion parameters, the size appears to be the most critical.

[1] P.Lacombe, B.Baroux and G.Beranger eds. : "Stainless Steels" Les Editions de Physique Les Ulis (1993) p171.

[2] H.Fischmeister and U.Roll : Z. Anal. Chem. **319**, 639 (1984).

[3] R.Kirchheim, B.Heine, H.Fischmeister, S.Hofmann, H.Knote and U.Stolz : Corros. Sci. **29**, 899 (1989).

[4] S.Qian, R.C.Newman, R.A.Cottis and K.Sieradzki : J. Electrochem. Soc. **137**, 435 (1990).

[5] T.Yoshimura and Y.Ishikawa : J. Japan Inst. Metals **56**, 873 (1992).

[6] H.Kuwano, Y.Ishikawa, T.Yoshimura and Y.Hamaguchi : J. Japan Inst. Metals **57**, 141 (1993).

[7] H.Kuwano, Y.Ishikawa, T.Yoshimura and Y.Hamaguchi : Nucl. Instrum. Methods in Phys. Res. **B76**, 290 (1993).

[8] J.A.L.Dobbelaar, E.C.M.Herman and J.H.W.de Wit : Corros. Sci. **33**, 779 (1992).

[9] Y.Ishikawa, X.C.Jiang, T.Yoshimura and T.Ozaki : Zairyo-to-Kankyo (Corrosion Engineering) **40**, 674 (1991).

[10] Y.Ishikawa, T.Yoshimura and T.Ozaki : *Mechanical Behaviour of Materials IV*, M.Jono and T.Inoue eds., ICM-6, Vol.2, Pergamon Press (1991) p607.

[11] S.Tsuchiya, Y.Ishikawa and M.Otaka : Trans. Jap. Soc. Mech. Engineers **59**, 1345 (1992).

[12] X.C.Jiang, T.Yoshimura, Y.Ishikawa, T.Shinohara and S.Tsujikawa : J. Electrochem. Soc. **139**, 1001 (1992).

[13] X.C.Jiang, T.Yoshimura, Y.Ishikawa : J. Japan Inst. Metals **56**, 1037 (1992).

[14] V.Cihal : Corros. Sci. **20**, 737 (1980).

[15] T.Yoshimura and Y.Ishikawa : Solid State Comm. Suppl. **33**, 321 (1990).

[16] T.Yoshimura and Y.Ishikawa : Proc. Asian Pacific Conf. on Fracture and Strength, JSME (1993) p745.

[17] A.Cerezo, T.J.Godfrey and G.D.W.Smith : Rev. Sci. Instrum. **59**, 862 (1988).

[18] S.M.Bruemmer, L.A.Charlot and B.W.Arey : Corrosion **44**, 328 (1988).

[19] J-S.Chen, V.Radmilovic and T.M.Devine : Corros. Sci. **30**, 477 (1990).

Materials Science Forum Vols. 185-188 (1995) pp. 991-1000

In situ ionic imaging for pitting corrosion sites on austenitic stainless steels with scanning electrochemical microscopy

H. Tanabe[1], Y. Yamamura[2] and T. Misawa[2]

[1] Department of Applied Chemistry, Muroran Institute of Technology, 27-1 Mizumoto, Muroran, Hokkaido 050, Japan

[2] Department of Materials Science and Engineering, Muroran Institute of Technology, 27-1 Mizumoto, Muroran, Hokkaido 050, Japan

Keywords: In situ observation, pitting corrosion, scanning electrochemical microscopy, precursor site, austenitic stainless steel

Abstract

We have successfully performed *in situ* observation of the localized distribution of reaction species of H^+ and Cl^- in microscopic region (1.0 μm x 1.0 μm) focused on the electrolyte solution side and identifying precursor sites for pitting on the substrate surface of austenitic stainless steels with different corrosion resistance by using the three modes of modified scanning electrochemical microscopy (SECM).

1. Introduction

Localized corrosion of various corrosion resisted metals and alloys, which is strongly influenced by solution environmental as well as metallurgical factors and conditions, causes serious materials problems for many technologies. One of the most frequently encountered varieties of localized corrosion is pitting. The effective prevention of pitting requires not only a knowledge of the factors and conditions which cause its occurrence at a given material/electrolyte interface but also a better understanding of the kinetics of precursor site formation and growth of pitting.

The considerable experimental studies in the last three decades have provided much valuable information on the pitting corrosion focused on stainless steel substrates. In addition, various techniques, such as a vibrating electrode technique[1)-3)], Kelvin probe method[4),5)] and scanning tunneling microscopy related techniques[6)-8)], have been developed previously to probe the physical and chemical structural information of substrate surface. Despite a huge research effort by means of these techniques, however, our knowledge in this field remains incomplete. In particular, it was usually not possible for these techniques to characterize the localized distribution of reaction species of H^+ and Cl^- at both precursor and pitting sites in microscopic space under corrosive solution environment. Challenge in this area is in progress in several laboratiries. A scanning reference electrode has also been used to map distributions of potential over corroding metals with a spacial resolution on the order of millimeters[9),10)]. An observation of one dimensional pH and chloride ion profiles in corrosion pits on metals has been reported[11),12)], but at much lower resolution. In situ imaging for these ionic concentration profiles is of much importance in the fundamental understanding of localized corrosion dynamics and the development of passivity technology. The experiment for in situ observation of interfacial concentration profiles has not been possible due to the lack of techniques with the necessary spacial and temporal resolution, while theories exist that describe interfacial average concentrations as a function of distance and time for a number of electroanalytical situations.

In order to achieve in situ measurement of the localized ionic concentration profiles of H^+ and Cl^-, we have been developed the scanning electrochemical microscopy (SECM) techniques[13)-17)]. Although the previously reported SECM results[13)-16)] should be available for measuring structural corrosion features at the electrode material, it is more difficult to obtain the kinetic effects of the local solution chemistry on the elementary steps of pit formation, and comparatively few studies focused on the solution side have therefore been reported.

The aim of this paper is to carry out *in situ* observation of localized distribution of ionic species of H^+ and Cl^- employing the new modes of SECM. We have successfully performed the in situ imaging of the localized distribution of reaction species of H^+ and Cl^- in a microscopic region (1.0 μm x 1.0 μm) focused on the electrolyte solution side and identifying precursor sites for pitting on the austenitic stainless steel surface by means of the new mode of SECM.

2. Experimental

In every mode of the SECM employed in situ imaging is produced by scanning ultramicroelectrode tip over the substrate surface using precision micropositioners. A particular advantage of the SECM developed in this study is that the tip current can detect direct chemical composition changes of the solution at the electrode/electrolyte interface. Furthermore, very few perturbation of the system under our investigation is introduced different from the previous works[13)-16)] with addition of a redox couple to the medium.

2.1. Substrate electrode

Three austenitic stainless steels of SUS304, SUS316L, and HR8C were used because of their different resistance to pitting. The chemical compositions of the steels tested are given in Table 1. After the substrate electrode material was annealed at 1050°C for 30 min and water quenched, it was mounted in a glass tube with epoxy, ground until smooth, and polished to a mirror finish with 0.05 μm alumina. Also, the edge of test electrode was sealed with epoxy except for the part of ϕ4 mm of surface. The finished electrode was stored in an air bath at 100°C for 8 h and then in a desiccator under the circumstance at room temperature and 30 % in relative humidity, to obtain stable reproducible surface condition.

Table 1. Chemical composition of stainless steels tested(mass%)

Steel	C	Si	Mn	P	S	Cr	Ni	N	Mo	Cu
SUS304	0.066	0.58	0.82	0.029	0.002	18.29	8.75	0.026	0.14	0.14
SUS316L	0.019	0.62	0.90	0.030	0.001	17.47	12.10	0.018	2.13	-
HR8C	0.005	0.23	1.56	0.004	0.001	19.67	24.17	0.052	4.46	1.45

2.2. Induced ac current mode

This is a new unique technique of SECM [17)], which is assembled from commercially available and home-built components. The block diagram is shown in Figure 1. The substrate potential is polarized with a very small amplitude sinusoidal potential signal (0.3 mV p-p, 1 kHz) superimposed on a dc potential. This ac potential modulation causes a significant small modulation

in the tip current, or the differential capacitance at tip end, at the same frequency. The induced ac current, which is detected by a lock-in amplifier through the potentiostat (4') in Fig.1, is then used as the imaging signal. Potentials of the tip and substrate electrode are controlled independently using two potentiostats, which are able to be operated under floating ground condition.

The cell was mounted on a X-Y nano positioner (Seiko Instrument Inc., SP4200), connected to the personal computer, and the tip position was controlled by a Z-axis piezoelectric device controlled by a high power speed amplifier as to a piezoelectric driver.

The tips of SECM were prepared from a Pt wire of 20 μm in diameter which was sealed in a glass micropipet (o.d. ϕ0.4 mm x i.d. ϕ0.2mm) by heating coil. Then, the end of tip was prepared by electrochemical etching in a flowing solution of KCN + NaOH against a carbon tube at a given ac voltage using a lock-in amplifier for the monitor of etching ac current, in oder to produce a slightly rounded smooth finish. After the etching, tips were ultrasonically cleaned in double distilled water followed by methanol, acetone, and metylenechloride. Pt tips were coated with Parylene C thin film of ca. 1μm in thickness prepared by the chemical vapor deposition (CVD) technique. These tips have been characterized by cyclic voltammetry and scanning electron microscopy (SEM) prior to measurements.

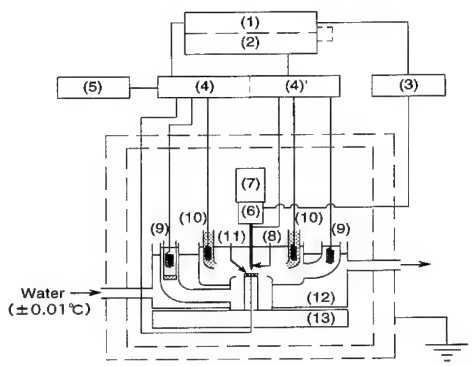

Fig.1. Block diagram of the SECM employed in this experiments
(1) Function generator (8) Tip
(2) Lock-in amprifier (9) Auxiliary electrode
(3) High speed power amprifier (10) Reference electrode (Ag/AgCl)
(4),(4)' Potentiostat
(5) Recorder (11) Target electrode
(6) Piezo positiner (12) Water bath
(7) Micropositioner (13) X-Ynanopositioner

Measurements were made in 0.6 mol dm^{-3} NaCl solution adjusted to pH 5.4 by Britton-Robinson buffer solution at 25 ± 0.01°C. All potentials were referred to a Ag/AgCl reference electrode. The auxiliary electrode was a platinum wire.

2.3. Ion-selective potentiometric mode

The tip electrode operates as an ion-selective potentiometric electrode. The basic instrument for this mode has been described in Fig.1. To allow potentiometric measurements, a high-impedance electrometer (Toho Technical Research Inc., Model 2000), which is introduced instead of a potentiostat (4') and a lock-in amplifier in Fig.1, was used to measure the potential to the ion-selective tip.

H^+ and Cl^- ion-selective potentiometric microelectrode tips have been used to measure local ion concentration over a pitting corrosion site. Before being used in localized corrosion measurements, the tip electrodes were calibrated in the various concentrations of H^+ and Cl^-.

(i) pH probe : The pH probe comprises a carbon fiber, with a diameter of 7 μm, mounted by epoxy resin in a glass capillary. The pH probe was conditioned for at least 3 h in the test solution before the measurements in order to establish a new stable surface situation.

(ii) chloride ion probe : The chloride ion probe was prepared by electrochemical deposition of Ag film around the end of a Pt tip employed in ac induced mode of SECM, followed by chloridization by anodic polarization in 1 mol dm^{-3} hydrochloric acid solution.

2.4. Tip oscillation mode

The instrument of the very small amplitude tip oscillation mode is similar to that in Fig.1. The Pt tip was oscillated by a piezoelectric device with a nominal displacement of 150 nm/V. The modulation voltage for the device was derived from the sinusoidal reference generator output of a two-phase lock-in amplifier (NF Circuit Design Block Co. Ltd., Model 5200B) and amplified to 20

mV by a high-speed power amplifier. The tip-oscillation frequency in this experiment was limited to 1 kHz. The measurement of ionic distribution within an active pit formed electrochemically was chosen as the subject of this SECM mode.

2.5. Chronoamperometric mode : Simultaneous detection SECM of H^+ and Cl^-

This SECM mode was designed as a new technique for the simultaneous measurement of pH and chloride ion profiles at a substrate electrode surface. The Pt tip used was prepared by the same method as that of ac induced mode of SECM. A potential step was applied to the microelectrode tip, which is composed of the first cathodic potential step for 50 μs to result in the reduction of H^+ to H_2, and then the second anodic potential step for 50 μs to result in the oxidation of Cl^- to Cl_2 after passing for 50 μs. The current was monitored through the Pt tip electrode as a function of time as soon as the tip potential was stepped by the potential pulse. To allow this measurement, a digital storage scope (Hewlett Packard Co. Ltd. : 54610A) was used, which is connected to a potentiostat (4') in Fig.1, instead of a lock-in amplifier. The use of this SECM mode has the advantage of providing directly both the local pH and the chloride ion concentration profiles within a very short time using only a simple tip without the ion-selective sensor tips described in session 2.3.

3. Results and Discussion

3.1. Current - potential curves and impedance spectra for substrate with passive oxide film

Figures 2 and 3 show the steady state current - potential curves and electrochemical impedance spectra at rest potential for three kind of stainless steel substrates, respectively, tested in a 0.6 mol· dm^{-3} NaCl solution at 25℃ under N_2 atmosphere. The obtained impedance spectra are characterized by the behavior of ideally polarizable interface between the rest potential and the potential before pitting potential. This suggests that the interface structure is represented in the equivalent circuit by the series combination of capacitance of surface oxide film and resistance. The sudden and large increase in current which is due to the onset of pitting corrosion appears, depending on substrate materials. The characteristic of these results indicates that corrosion resistance of the substrate electrodes tested is superior in the order, HR8C, SUS316L, and SUS304.

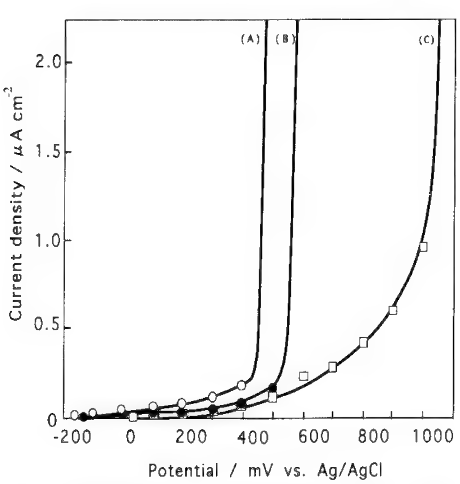

Fig.2. Steady state current-potential curves of stainless steel electrodes in 0.6 mol·dm^{-3} NaCl at 25℃ in N_2 atmosphere.
(A)SUS304, (B)SUS316L, (C)HR8C

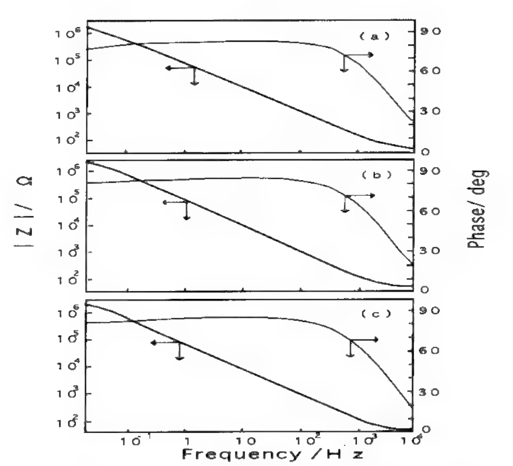

Fig.3. Impedance spectra at rest potential for (a)SUS304, (b)SUS316L, and (c)HR8C stainless steels in 0.6 mol·dm^{-3} NaCl at 25℃ under N_2 atmosphere.

3.2. Ionic profiles around a pitting site

(a) Induced ac current SECM image

AC induced SECM image of 500 μm x 250 μm region and the SEM images at the identical pitting site for the SUS304 substrate surface are shown in Fig.4(a) and (b), respectively. The SECM image was recorded by rastering the tip across the surface at a height of 20 μm ,while maintaining the tip potential at 0.0 V vs. Ag/AgCl and galvanostatically controlling the substrate current at ca. 1×10^{-2} mA after the active pit formation by the anodic polarization of ca. 2 mA for 10 s. The increase of induced ac current has been found to show the qualitative correspondence to pH decrease[17]. The brighter regions in Fig.4(a) represent higher tip current over a target pit and are due to the higher concentration of H^+ compared to the darker sites. It is found that a significant decrease of pH is observed over the center of the target pit on surface, and that the pH has fallen to ca. 1.6 compared to the pH value of 5.4 for the bulk solution of 0.6 mol·dm^{-3} NaCl /SUS304 system. The observed values of induced ac current have been estimated to those of pH by the combination measurement with the ion-selective potentiometric SECM, which uses a carbon fiber microelectrode sensor, mentioned in following (b). In addition, it is noteworthy that the pit diameter estimated from the SECM image has good agreement with that obtained by the SEM image.

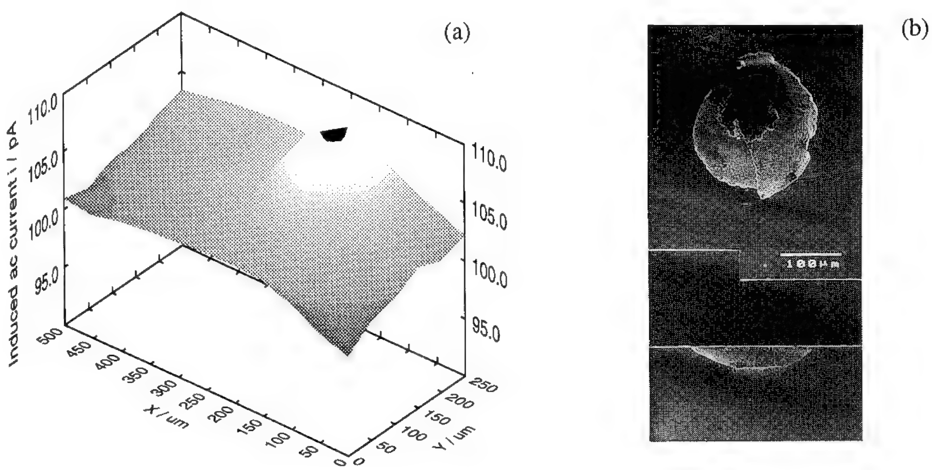

Fig.4. (a) Induced ac current SECM image of a 500 X 250 μm protion of SUS304 substrate with an active pit formed electrochemically and poised under the galvanostatic condition of ca. 10μA . The tip is a Pt microelectrode held at 0.0V vs. Ag/AgCl.(Z=20 μm).

(b) SEM images of the substrate surface with the identical pit imaged by SECM in part (a).

(Top view and cross section view)

(b) Ion - selective potentiometric SECM image

Figure 5 is the pH response curves of carbon fiber micro - pH probe, obtained by measuring the probe potential in the solution of a given chloride ion concentration with the pH in the range of ca.1 ~ 7. Although there are some scatter, the potential of the pH probe may be allowed to have a linear relationship with the pH. It is also found that there is almost no affect of chloride ion concentration in the range of 3.5 ~ 25 mass% on the potential of pH probe. The selectivity coefficient for pH in the various solutions may be estimated to be unity. Therefore, the probe electrodes could be used for imaging experiments with no further pretreatment.

Figure 6 is the calibration curves of the chloride ion probe, obtained by measuring the electrode potentials in a series of given pH solutions with chloride ion concentrations in the range from 3.5 to 25 mass%. The potential of the chloride ion probe has a very good linear relation with the chloride ion activities. No dependence of pH on the potential of the chloride ion probe was observed. The selectivity coefficients for chloride ion in the various pH solutions tested are estimated to be unity.

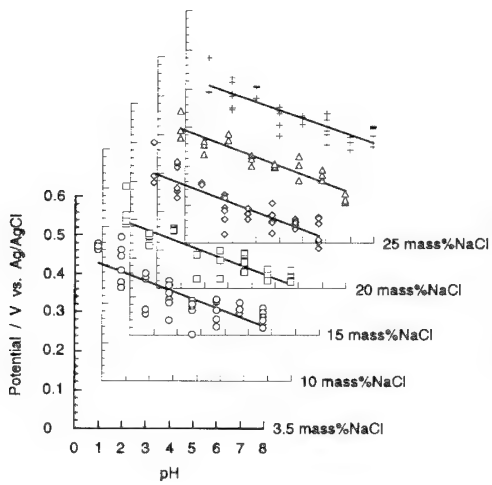

Fig.5. Potential-pH diagram of carbon fiber tip electrode in NaCl solution with a series of chloride ion concentrations adjusted to a desired pH.

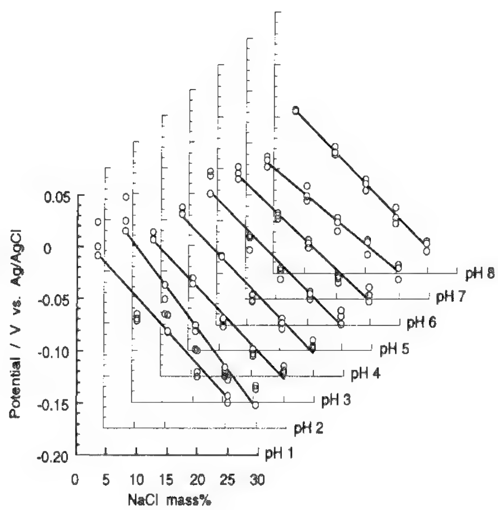

Fig.6. Potential-Cl⁻ concentration diagram of Ag tip electrode in a series of pH solution adjusted to a desired Cl⁻ concentration.

Figure 7 shows the SECM image for the concentration distribution of Cl^- around and over a target pit. It is found that the profile reflects significantly the size of pitting corrosion site and that the change of Cl^- concentration distribution extends even to the distance of 20 μm over the surface with an active pit. A significant increase of Cl^- concentration from 0.6 to ca. 0.9 $mol \cdot dm^{-3}$ was observed, in addition to tha decrease of pH from 5.4 to ca. 1.6 as shown in Fig.4(a). Although ion-selective potentiometric mode has the lower spacial resolution and response time of probe compared to ac induced mode, the quantitative evaluation of ionic concentration by this mode is superior to that of induced ac current mode.

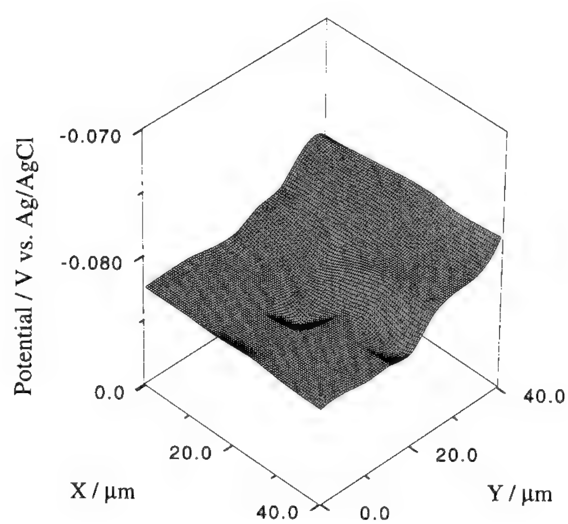

Fig.7. Chloride ion-selective SECM image of an active site for pitting corrosion on SUS304 substrate obtained electrochemically and poised under galvanostatic condition of ca. 10 μA.

(c) Tip position oscillating SECM image

The active pit is electrochemically grown until more than ca. 700 μm in diameter on SUS304 substrate and poised to be made active galvanostatically with constant current of ca. 500 μA. Figure 8 shows the image of tip-modulation current vs distance towards Z direction and SEM image of the target active pit. The modulated current increases gradually from the region of ca. 30 μm outer to ca. 20 μm within the active pit. The larger modulated current in an active pit suggests the higher concentration of H^+ than that of pit outside.

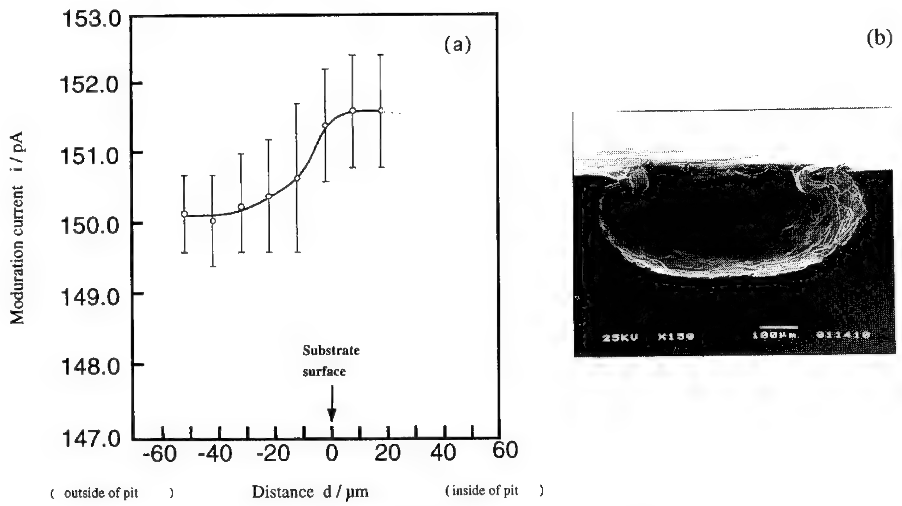

Fig.8. (a) Line scan of tip-moduiation current response for the tip location change from bulk solution to ca. 20 μm in depth of inside of pit. The active pit on SUS304 substrate is poised under the galvanostatic condition of 500 μA in 0.6mol·dm^{-3} NaCl at 25°C.
(b) Scanning electron micrograph of the cross section of identical active pit, after (a) measurement .

3.3. Ionic profiles at precursor sites

Chronoamperometric SECM image

This SECM mode is a very useful technique which should be able to carry out simultaneous measurement of pH and chloride ion profiles. At the potential region of passive state, the SECM images for HR8C substrate electrode tested show the more featureless distributions of pH and chloride ion than those of SUS304 and SUS316L substrates. As the potential of substrate electrode becomes more positive, the images of pH and chloride ion distribution for every substrate tested more essentially feature. In SUS316L and SUS304 systems, especially, images observed at the potentials near the pitting potential reveal a few microscopic electroactive sites, or precursor sites for pit formation.

Figure 9 shows a set of the SECM images of 1 μm x 1 μm region of the SUS 316L surface at a height of 10 μm, at 450 mV in passive region. These images give the important information on the pit nucleation. In the images of pH profile (a) and (a'), two clear localized large peaks of A and B with almost same size of ca. 0.1 μm can be found, and in chloride ion profile (b) and (b'), only a clear peak C. The peak of C is in close agreement with that of A. The agreement location with respect to peak B, however, is not able to be recognized in the image of Cl^- profile, namely the location B does not show the significant change of chloride ion concentration. This agreement on higher localized concentration between H^+ (site A) and Cl^- (site C) will grow a pit with life, on the

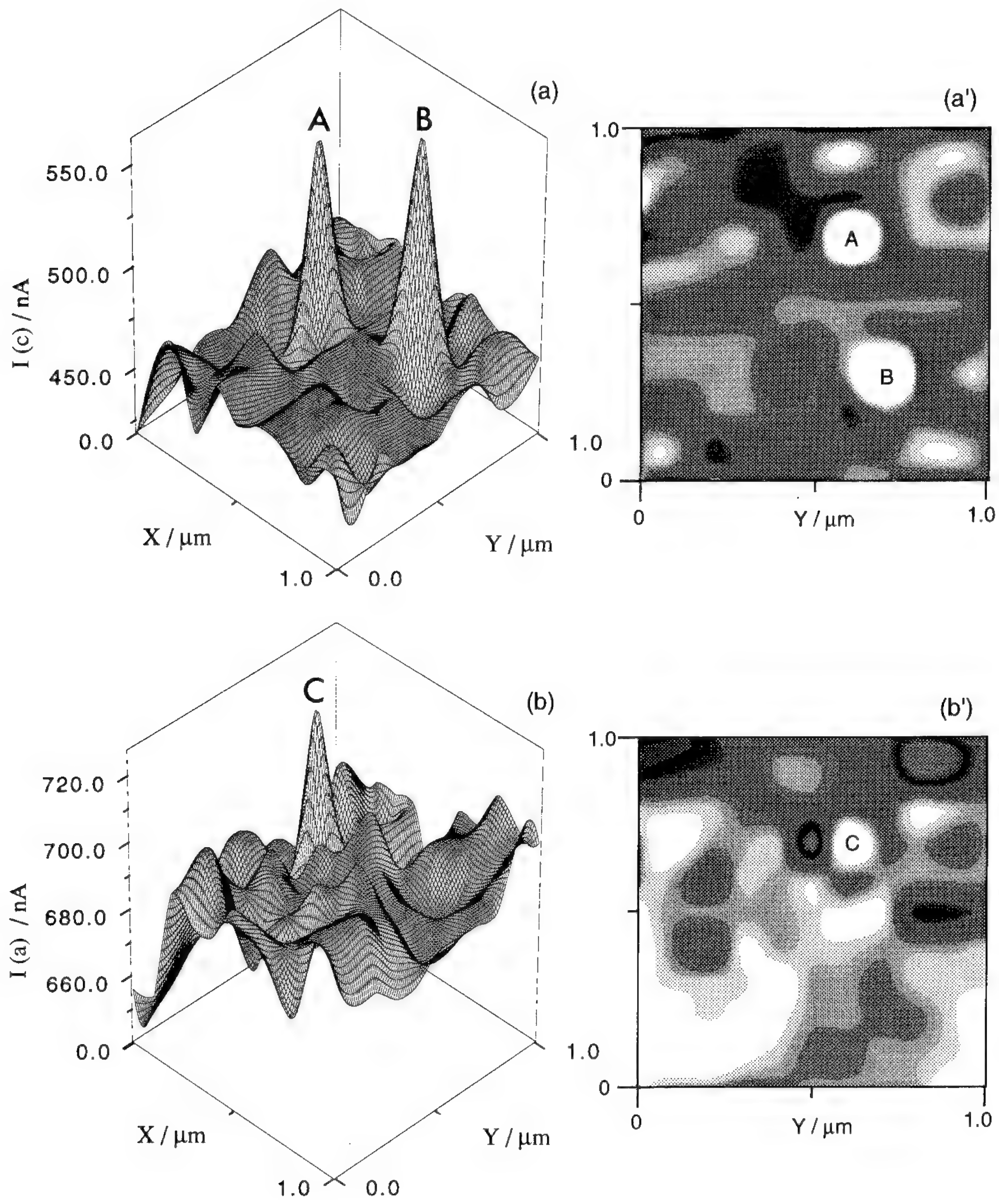

Fig.9. Chronoamperometry SECM images obtained by surface plots and contour plots of the 1 μm X 1 μm identical portions of a pair of (a) and (a') cathodic current distribution (hydrogen ion concentration), and a pair of (b) and (b') anodic current distribution (chloride ion concentration) profiles for SUS316L substrate at 450 mV in 0.6 mol·dm^{-3} NaCl adjusted to pH5.4 at 25°C. (Tip was located at 10 μm over the substrate surface.)

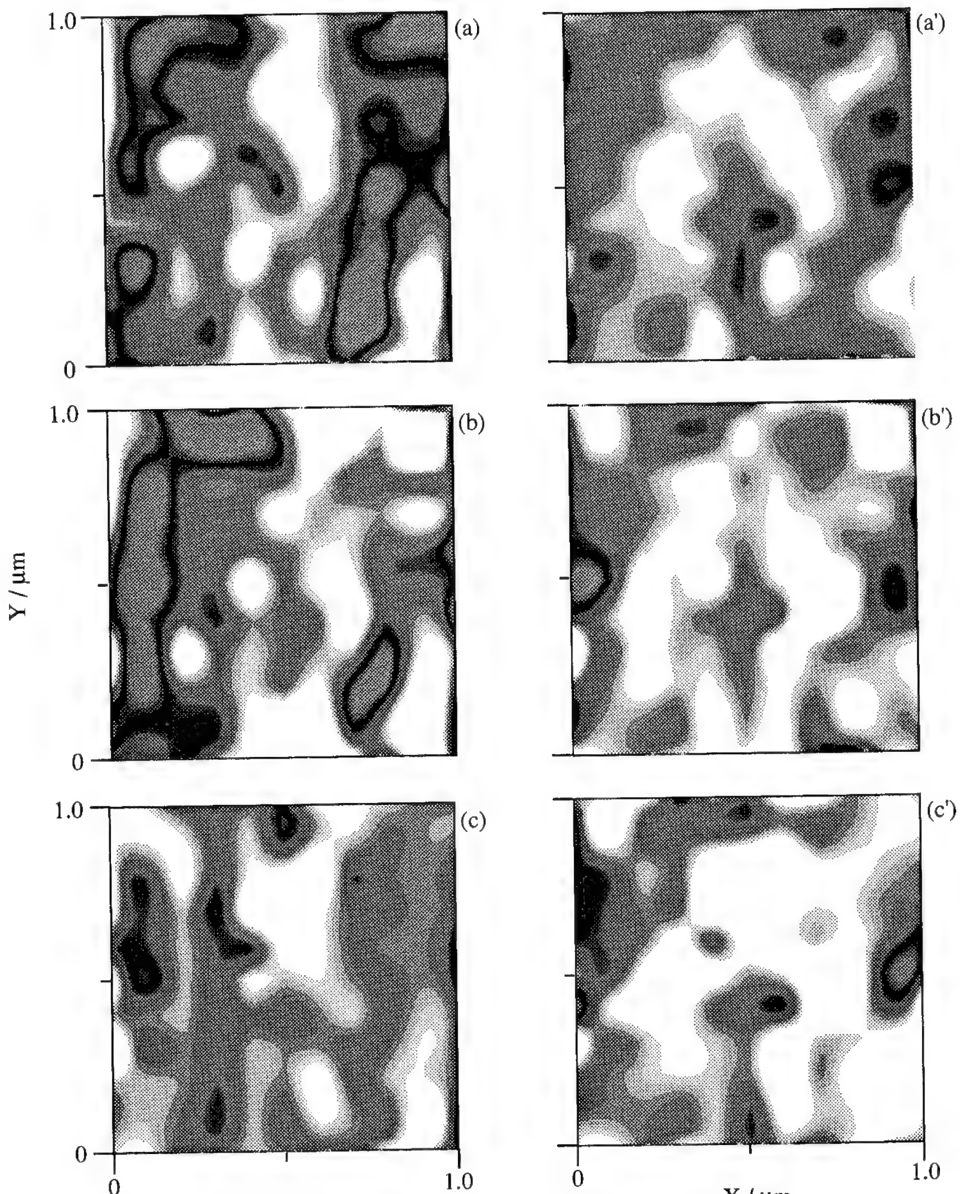

Fig.10. Chronoamperometry SECM images of 1µm X 1µm identical portion of cathodic current distribution ($i(c) / i_\infty (c)$: H^+ concentration) and anodic current distribution ($i(a) / i_\infty (a)$: Cl^- concentration) profiles for SUS304 substrate at given polarization potentials in 0.6 mol.dm^{-3} NaCl adjusted to pH 5.4 at 25°C.
(The tip was located at 10 µm over the substrate surface.)
$i(c) / i_\infty(c)$: (a) 250 mV, (b) 300 mV, (c) 350 mV
$i(a) / i_\infty(a)$: (a') 250 mV, (b') 300 mV, (c') 350 mV

other hand the disagreement will become to be in passive state as an inactive pit.

Figure 10 shows the SECM images of localized pH profiles ((a), (b), (c)) and chloride ion profiles ((a'), (b'), (c')) of the identical location, observed on a 1 μm x 1 μm portion of the SUS304 at various polarized potentials in Fig.2. The brighter region of images, where the value of i/i_{∞}(i_{∞} is a obtained current value at bulk solution region far from the substrate surface.) is larger than 3 percent(1.03 times), represents higher tip current and is due to higher concentrations of hydrogen ion and chloride ion compared to the darker regions. As can be easily seen in Fig.10, the images studded with the brighter, smaller regions with higher concentrations of H^+ and Cl^- are observed under smaller polarization potentials. As the applied potential becomes more positive, the region of higher concentrations of these ions becomes to be larger. Therefore, it is found that the location with both higher hydrogen and chloride ion concentrations becomes larger at the more positive potential, and that the effect together with both localized ions results in pit nucleation like the SUS316L system, as shown in Fig.9. However, the obtained anodic current probably contains a current of water oxidation reaction as well as that of chloride ion oxidation reaction and the extraction of current of chloride ion oxidation reaction brings with a lot of difficulties. Therefore, the detection current at a given time was taken as ionic imaging in this work.

4. Conclusions

This paper has demonstrated new techniques of SECM for *in situ* observation of localized distributions of ionic species of H^+ and Cl^- for pitting corrosion. The most important implication of our findings is that the precursor sites for pitting corrosion can be identified prior to passive oxide film breakdown and that active or inactive pitting precursor site can be recognized by the coincide of higher concentration region of both hydrogen and chloride ions. The imaging capabilities of the *in situ* SECM demonstrated should allow corrosion kinetics to be mapped on ionic distributions playing an important role in pit formation with micron or sub-micron resolution, and shed light on fundamental understanding of local solution chemistry in passive film breakdown.

Acknowledgement - Authors would like to thank the financial support of Iron and Steel Institute of Japan, as a Grant-in-Aid for steel reseach promotion.

References

1) H.S.Isaacs, *Corrosion*, **43**, 594(1987).
2) H.S.Isaacs, *J. Electrochem. Soc.*,**135**, 2180(1988).
3) L.F.Jaffe, R.Nuticelli, *J. Cell Biology*, **63**, 614(1974).
4) M.Stratmann, *Corros. Sci.*, **27**, 869(1987).
5) M.Stratmann, H.Streckel, *Ber. Bunsenges. Phys. Chem.*, **92**, 1244(1988).
6) G.Binning, H.Rohrer, *Helv. Phys. Acta*, **55**, 726(1982).
7) H.Masada, S.Matsuoka, and N.Nagashima, *Materials and Environment*, **40**, 754(1991).
8) B.Drake, R.Sonnenfeld, J.Schneir, and P.K.Hansma, *Surf. Sci.*, **181**, 92(1987).
9) H.S.Isaacs, G.Kissel, *J. Elecrochem. Soc.*, **119**, 1628(1972).
10) H.S.Isaacs, *Corros. Sci.*, **29**, 313(1989).
11) G.Denault, M.H.Troise-Frank, and L.M.Peter, *Faraday Discuss. Chem. Soc.*, 94(1992).
12) J.L.Luo, Y.C.Lu, and M.B.Ives, *J. Electroanal. Chem. Interfacial Electrochem.*, **326**, 51(1992).
13) A.J.Bard, F-R.Fan, D.T.Pierce, P.R.Unwin, D.O.Wipf, and F.Zhou, *Science*, **254**, 68(1991).
14) R.C.Engstrom and C.M.Pharr, *Anal. Chem.*, **61**, 1099A(1989).
15) A.J.Bard, F-R.Fan, J.Kwak, and O.Lev, *Anal. Chem.*, **61**, 132(1989).
16) B.R.Horrocks, M.V.Mirkin, D.T.Pierce, A.J.Bard, G.Nagy, and K.Toth, *Anal. Chem.*, **65**, 1213(1993).
17) (a) H.Tanabe, Y.Yamamura, and T.Misawa, *Proceeding of JSCE corrosion '94*, 89(1994).
(b) H.Tanabe and G.Maeda, Abstracts of the '92 Annual Meating of Hokkaido branch of Chemical Society of Japan, February 1992, p.19.

Materials Science Forum Vols. 185-188 (1995) pp. 1001-1010

Film breakdown and pit formation during cathodic polarization of aluminum covered with anodic oxide films: Effect of film preparation and structure

H. Takahashi, K. Fujiwara and M. Seo

Graduate School of Engineering, Hokkaido University, N-13, W-8, Kita-Ku, 060 Sapporo, Japan

Keywords: Film breakdown, pit formation, aluminum, cathodic polarization, anodic oxide film

ABSTRACT

Cathodic polarization behavior of aluminum covered with different types of barrier anodic oxide film has been investigated in a neutral borate solution to examine the effect of film structure on the film breakdown and pit formation during cathodic polarization.

Highly pure aluminum specimens were anodized in a neutral borate solution after a)electropolishing (BS-specimen), b)surface-roughening (BR-specimen), c)heat treatment (TA-specimen), or d)hydrothermal treatment(HA-specimen), and then polarized cathodically by scanning the potential at 2.9 V/s in the neutral borate solution.

Cathodic polarization curves for all specimens showed a very weak cathodic current, i_c, at potentials higher than E_c = -2 - -4 V, and below these i_c increased appreciably with lowering E_c. The i_c vs. E_c curve at the low potential region shifted in the anodic direction in the order of BS- < HA- < BR- < TA-specimens at 20 °C. The scanning electron microscopy showed evidence of pits after the cathodic polarization, and the number of pits, N_p, depended on the kind of preexisting oxide film. The value of N_p was between 10^7 and 10^{10} m^{-2}, increasing in the order of BS- < HA- < BR- < TA-specimens. The ratio of the corrosion rate of the metal substrate to the electrochemical reduction rate was between 0.02 - 0.8, increasing in the order of BS- < HA- < BR- <TA-specimens.

The cathodic polarization mechanism is discussed in terms of film breakdown initiating at the site of imperfections in the oxide films.

INTRODUCTION

Cathodic polarization behavior of aluminum has been investigated by many authors, in relation to rectification phenomena[1-5], cathodic corrosion[6-8], and tunnel etching[9-10]. The cathodic polarization of aluminum easily reduces protons to hydrogen at the surface, and this is understood to be responsible for rectification in aqueous solutions[2-4]. The hydrogen evolution causes the rise in pH of solution near the specimen surface, and this leads to dissolution of the metal substrate [6, 7], extraordinary hydrogen gas evolution[8], and the formation of hydroxide films[9-10].

In previous investigations [11, 12], the present authors reported that cathodic polarization of aluminum covered with anodic oxide films causes local film breakdown and pit formation in a neutral borate solution, and that the number of pits increases considerably when the specimen is subjected to immersion in an acid solution before cathodic polarization. This was concluded to be due to the increase in imperfections in the oxide films by local dissolution of oxide film during chemical sectioning.

In this investigation, aluminum specimens covered with different barrier-type anodic oxide films were polarized cathodically in a neutral borate solution

to examine the effect of film structure on the film breakdown pit formation during cathodic polarization.

EXPERIMENTAL

1)Specimen and pretreatment

Highly pure aluminum foil (99.99%) was cut to 10 x 30 mm with a handle and they were electropolished in an acetic acid/perchloric acid solution. After electropolishing, the specimens were immersed in a chromic acid/phosphoric acid solution to dissolve oxide films formed by the electropolishing, and then kept in a desiccator prior to the subsequent experiments.

2)Formation of barrier-type oxide films

To examine the effect of the structure of oxide films on the cathodic polarization behavior, the following specimens were prepared:

a)BS-specimen: The pretreated specimens were anodized in 0.5 kmol m^{-3}-H_3BO_3/0.05 kmol m^{-3}-$Na_2B_4O_7$ solution(pH = 7.4) at T_f = 20, 60, and 80 °C with a constant current of i_f = 10 A m^{-2} until the anode potential, E_f, reached 100 V(vs. Ag/AgCl, sat.-KCl) (BS-specimen, Fig. 1-a). At E_f = 20 °C, a barrier-type compact oxide films with about 170 nm of thickness is formed. At E_f = 60 and 80 °C, the oxide films are composed of two layers: a porous outer layer and a compact inner layer, and the thickness of the inner layer decreases with increasing T_f, while that of the outer layer increases[13].

b)BR-specimen: The pretreated specimens were anodized initially in 4%-H_3PO_4 solution at 100 V to form a porous-type anodic oxide film and then immersed in a 5 kmol m^{-3}-H_3PO_4/0.2 kmol m^{-3}-CrO_3 solution at 80 °C for 20 min to remove the anodic oxide film. After removing the oxide films, E_f = 100 V-barrier type anodic oxide films were formed in the neutral borate solution under the same condition as a)(BR-specimen, Fig. 1-b). The structure and thickness of the oxide films on the BR-specimen are essentially similar to those on the BS-specimen, and the metal/oxide interphase of the BR-specimen is scallop-shaped.

c)T- and TA-specimens: The pretreated specimens were kept in an electric furnace at 550 °C for 3 h to form 30 nm thick thermal oxide films (T-specimen, Fig. 1-c). The T-specimen was then anodized in the neutral borate solution under the same condition as a)(TA-specimen, Fig. 1-c). The film on the TA-specimen at T_f = 20 °C and 60 °C has a sandwich structure: an outer amorphous oxide layer, an intermediate crystalline oxide layer, and an inner amorphous oxide layer [14-16]. With increasing T_f, the thickness of the crystalline oxide layer increases while that of the amorphous oxide layers decrease. At T_f = 80 °C, the oxide film is composed of one layer of crystalline oxide. The total thickness of oxide films on the TA-specimens is 100 - 80 nm, decreasing with increasing T_f.

d)H-, HA-specimens: The pretreated specimens were immersed in boiling distilled water for 30 min to form hydrous oxide films(H-specimen, Fig. 1-d), and then anodized in the neutral borate solution to form E_f = 100 V composite oxide films under the same condition as a) (HA-specimen, Fig. 1-d). The H-specimen shows that the hydroxide film is composed of an outer porous layer and a relatively compact inner layer, and the thickness of each layer is 350 nm [17]. The composite oxide films formed on the HA-specimen shows two oxide layers underneath the hydrous oxide: an outer crystalline oxide layer and an inner amorphous oxide layer. With increasing T_f, the thickness of the outer oxide layer increases and that of the inner oxide layer decreases [17]. The total thickness of oxide layers underneath the hydroxide layer on the HA-specimens is 130 - 120 nm, decreasing with increasing T_f.

3)Cathodic polarization

The BS-, BR-, T-, TA-, H-, and HA-specimens were immersed in 0.5 kmol m^{-3}-H_3BO_3/0.05 kmol m^{-3}-$Na_2B_4O_7$ solution(pH = 7.4) at 20 °C and the potential of the specimens, E_c(vs. Ag/AgCl, sat.-KCl) was scanned from zero in the cathodic direction at 2.9 V min^{-1} to follow the change in the cathodic current, i_c, with E_c. After i_c reached -500 A m^{-2}, the current was cut, and specimens were removed from the solution. The amount of Al^{3+} ions dissolved into the solution during the cathodic polarization was determined by inductively coupled plasma atomic emission spectrometry(ICP-AES), and the surface of specimens was observed by scanning electron microscopy.

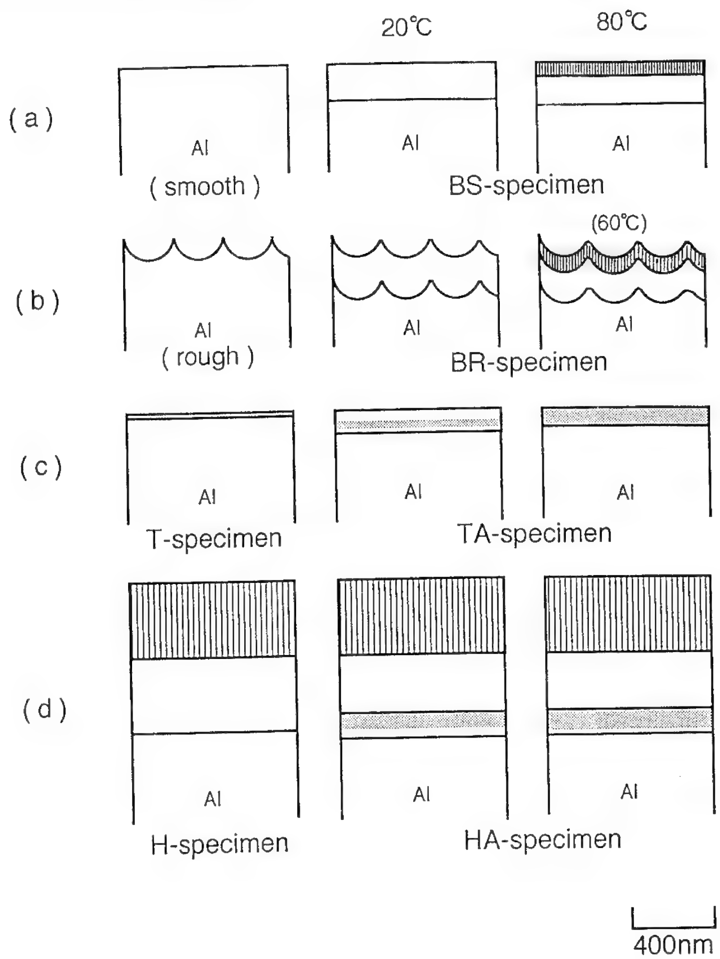

Fig. 1 Structure of oxide films of a)BS-, b)BR-, c)T-, TA-, d)H-, and HA-speciemens. Anodizing was carried out in 0.5 kmol $m^{-3}$$H_3BO_3$/0.05 kmol m^{-3}-$Na_2B_4O_7$ solution at different temperatures, T_f, with 10 A m^{-2} up to E_f = 100 V. The T- and H-specimens were prepared by thermal oxidation at 550 °C for 3 h, and by immersion in boiling distilled water for 30 min, respectively.

RESULTS

1)Cathodic polarization behavior

Fig. 2 shows the cathodic polarization curves obtained for a)BS- and b)BR-specimens with T_f = 20, 60, and 80 °C. The cathodic current, i_c, for the T_f = 20 °C BS-specimen shows a very small value at potentials higher than E_c = -4 V, and increases almost linearly as E_c is scanned in the cathodic direction beyond - 4 V. As T_f rises, the E_f vs.i_c curve shifts in the anodic direction, showing higher values of potential for the start of i_c increase. The i_c vs.E_c curves for the BR-specimens start to increase at about E_c = -3V, and the T_f = 20 °C BR-specimen shows a slope higher than the T_f = 60 °C specimen beyond E_c = -3 V.

A comparison of Fig. 2-a) with -b) shows that the i_c vs.E_c curves for BR-specimens locate in a potential region higher than those for BS-specimens, and that the direction of the curve shift with T_f change for BS-specimens is opposite to that for BR-specimens.

Fig. 3-a) shows the i_c vs.E_c curves for T- and TA-specimens. The curve for the T-specimen shows a very similar behavior to that of TA-specimens, showing a start of increase in i_c at a relatively higher potential and a relatively high slope of the i_c vs.E_c curve in the low potential region.

Fig. 3-b) shows the i_c vs.E_c curves for H- and HA-specimens. The curve for the H-specimen locates at a potential region much higher than those for TA-specimens, and the curve of HA-specimen with T_f = 60 °C shifts to the most negative potential region.

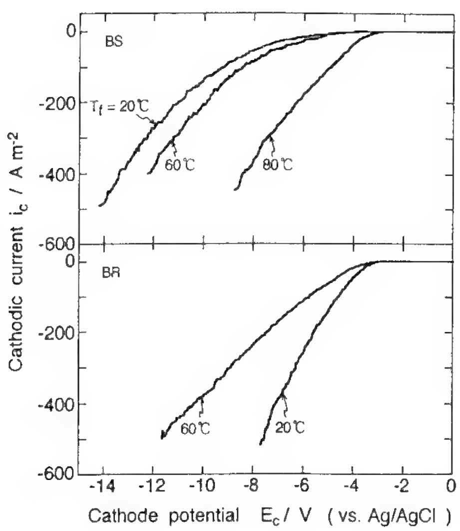

Fig. 2 Cathodic polarization curves obtained a) BS- and b) BR-specimens with different film formation temperatures, T_f. The cathodic polarization was carried out in 0.5 kmol m^{-3}-H_3BO_3 /0.05 kmol m^{-3}-$Na_2B_4O_7$ solution at 20 °C by potential scanning at 2.9 V min^{-1}.

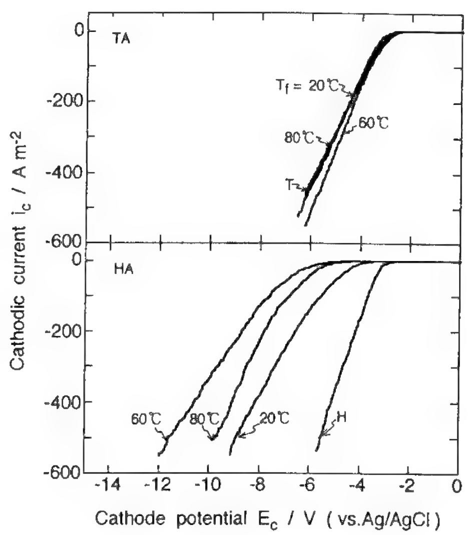

Fig. 3 Cathodic polarization curves obtained for a)T-, TA- b)H-, and HA-specimens with different film formation temperatures, T_f. The Cathodic polarization conditions are as in Fig. 2.

To compare the cathodic polarization curves for different specimens, the potentials, a)$E_{c(10)}$, at i_c = -10 A m^{-2}, and b)$E_{c(500)}$, at i_c = -500 A m^{-2} are plotted against the film formation temperature, T_f in Fig. 4. It can be seen that for all specimens the T_f dependence of $E_{c(10)}$ is similar to that of $E_{c(500)}$. $E_{c(500)}$ shifts more negative in the order of:

T- = H- = TA- > BR- > HA- > BS-specimens at T_f = 20 °C,
T- = H- = TA- > HA- = BR- > BS-specimens at T_f = 60 °C, and
T- = H- = TA- > HA- = BS-specimens at T_f = 80 °C.

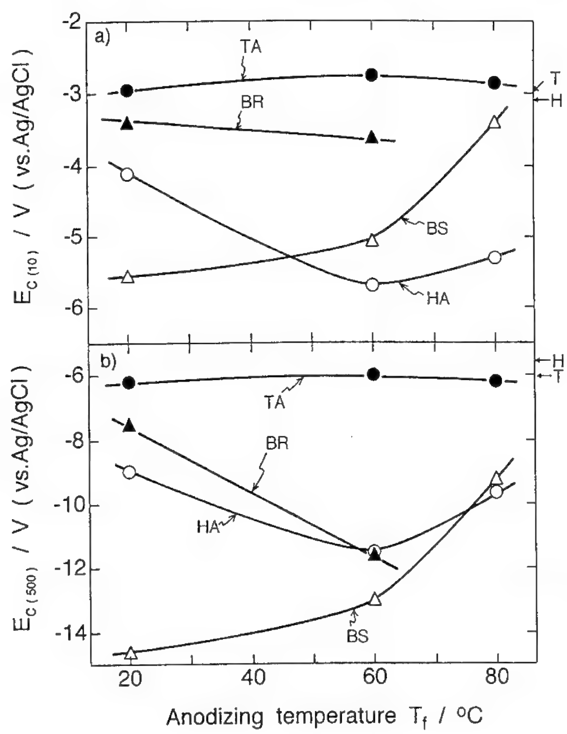

Fig. 4 Relationship between the film formation temperature, T_f, and a)E_c value at i_c = -10 Am^{-1}, $E_{c(10)}$, and b)E_c value at i_c= -500 A m^{-2}, $E_{c(500)}$, obtained for BS-, BR-, T-, TA, H-, and HA-specimens. The cathodic polarization conditions are as in Fig. 2.

2)Pit formation during cathodic polarization

Fig. 5 shows the scanning electron micrographs of the surface of a)BS-, b)BR-, c)T-, d)TA-, e)H-, and f)HA-specimens at T_f = 20 °C after cathodic polarization up to i_c = -500 A m^{-2}. All specimens show pits, of which the central part is open to the solution and the periphery is covered with anodic oxide film. The number and size of pits depend on the type of oxide films and T_f, since the formation of pits is the results of local film breakdown and dissolution of the metal substrate.

The number, N_p, and size, L_p, of pits and the amount of dissolved Al^{3+} ions, W_d, after the cathodic polarization up to i_c = -500 A m^{-2} are plotted against the film formation temperature, T_f, in Figs. 6 and 7. The number of pits, N_p, formed by cathodic polarization for BS-, and HA-specimens increase with increasing T_f, while that for BR-specimen decreases. The TA-specimen shows a minimum in N_p at T_f = 60 °C. The size of pits, L_p, for BS-, BR-, TA-, and HA-specimens is several to 10 μm, and changes only slightly with T_f; the L_p for T- and H-specimens show relatively small values. The amount of dissolved Al^{3+} ions, W_d, for BS-, TA-, and HA-specimens increases with increasing T_f, but that for the BR-specimen decreases.

The N_p value for BS-, BR-, T-,TA-, H-, and HA-specimens decreases in the order of:

T- > H- = TA- > BR- > HA- = BS-specimen at 20 °C,
T- > H- > TA- = BR- > HA- = BS-specimen at 60 °C, and
T- = TA- > H- > BS- > HA-specimen at 80 °C.

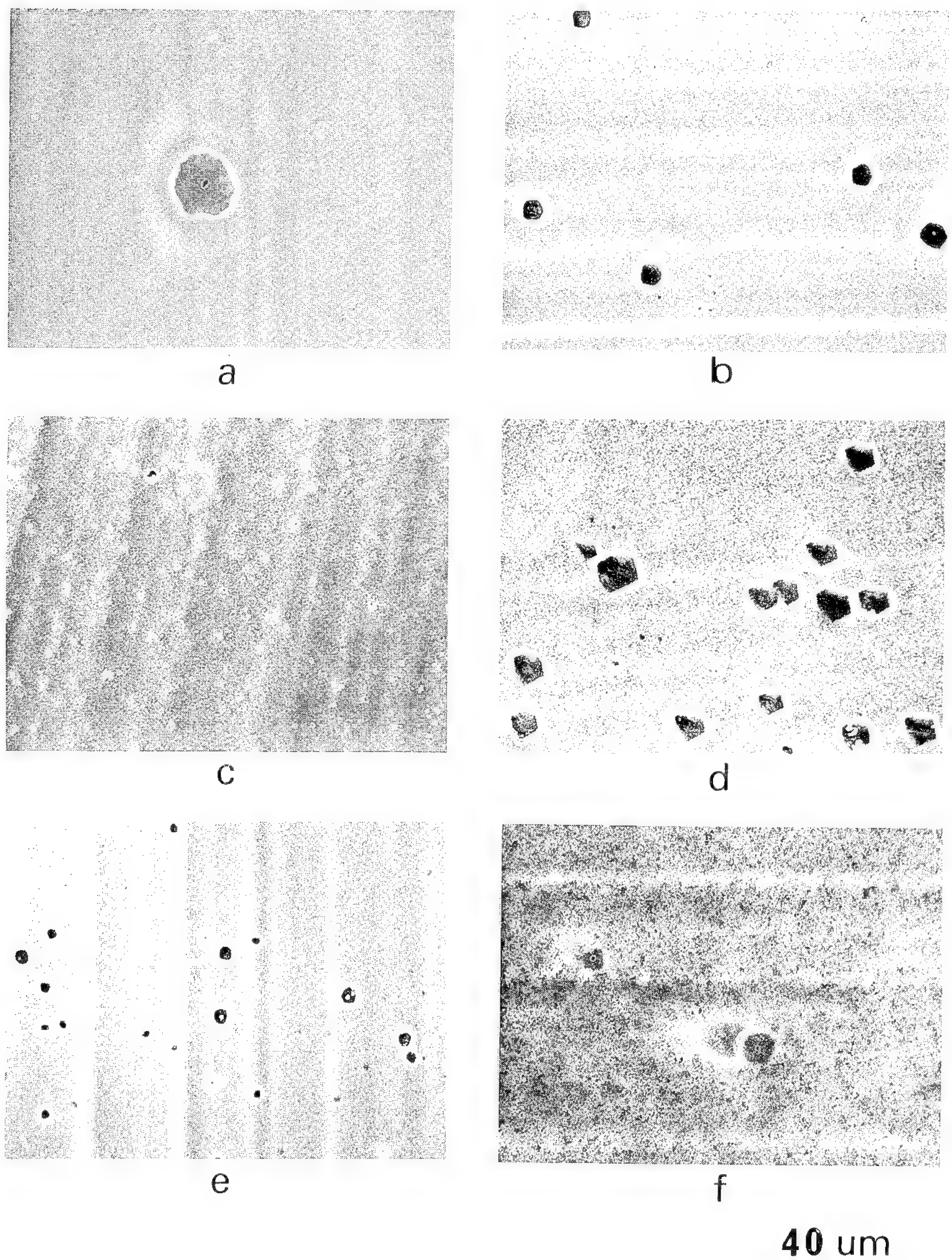

Fig. 5 Scanning electron micrographs of the surface of a)BS-, b)BR-, c)T-, d)TA-, e)H-, and f)HA-specimens after cathodic polarization up to $i_c = -500\ A\ m^{-2}$. The cathodic polarization conditions are as in Fig. 2.

It must be noted here that the order of N_p among the specimens at different temperatures is similar to the orders of $E_{c(10)}$ and $E_{c(500)}$.

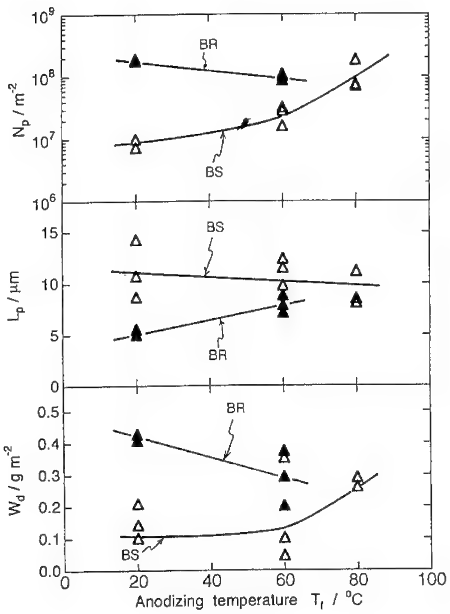

Fig. 6 Effect of the film formation temperature, T_f, on the pit number, N_p, pit size, L_p, and the amount of dissolved Al^{3+} ions, W_d, obtained for BS-, and BR-specimens cathodically polarized up to i_c = -500 A m^{-2}. The cathodic polarization conditions are as in Fig. 2.

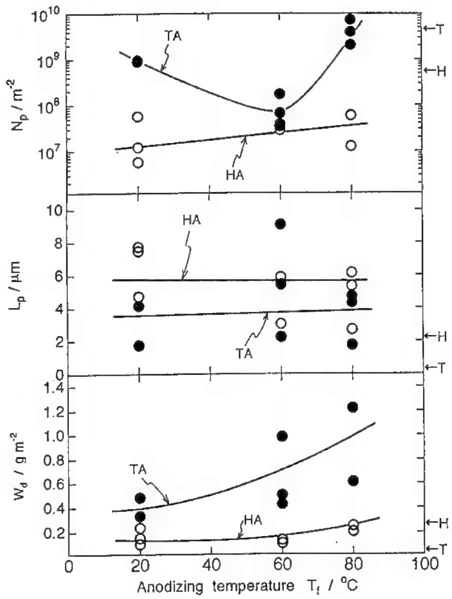

Fig. 7 Effect of the film formation temperature, T_f, on the pit number, N_p, pit size, L_p, and the amount of dissolved Al^{3+} ions, W_d, obtained for TA-, and HA-specimens cathodically polarized up to i_c =-500 A m^{-2}. The cathodic polarization conditions are as in Fig. 2.

DISCUSSION

1)Local film breakdown and pit formation during cathodic polarization

When aluminum covered with anodic oxide films is polarized in neutral borate solution, protons may move inwards across the oxide film at imperfections and are reduced to hydrogen at the oxide/metal interface by the following equation (Fig.8-a):

$$2H^+ + 2e^- = H_2 \quad (1)$$

The accumulation of H_2 at the oxide/metal interface may cause stresses in the oxide film, and the accumulation of OH^- ions at the oxide film surface may cause the local film dissolution at the imperfections (Fig.8-b). This eventually causes the local film breakdown (Fig.8-c), and the current concentration at the film breakdown positions leads to H_2O reduction to H_2 by the following equation:

$$2H_2O + 2e^- = H_2 + 2OH^- \quad (2)$$

The accumulation of OH^- ions at the film breakdown position causes the

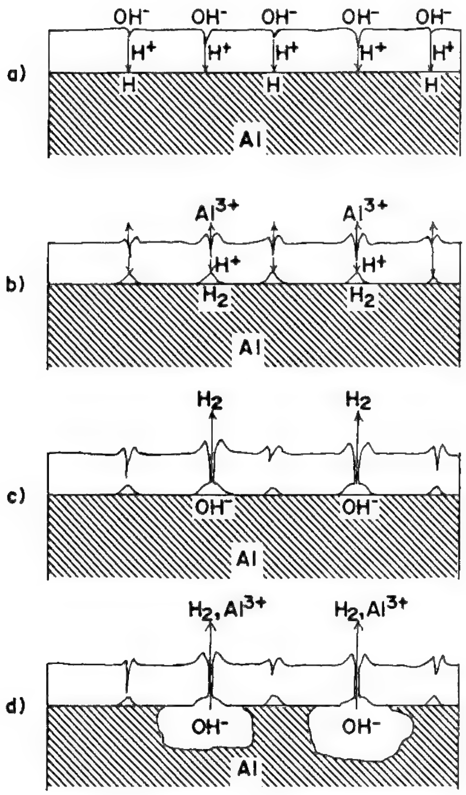

Fig. 8 Schematic presentation of local film breakdown and pit formation during cathodic polarization.

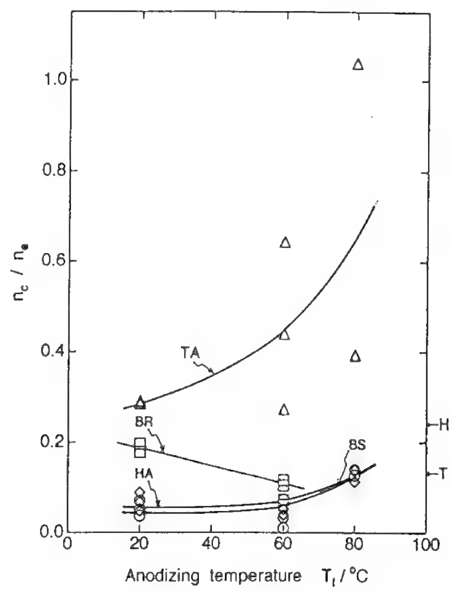

Fig. 9 Effect of the film formation temperature, T_f, on the mole ratio of hydrogen evolved by corrosion of the metal substrate against that evolved by electrochemical reduction, obtained for BS-, BR-, T-, TA-, H-, and HA-specimens cathodically polarized up to i_c = -500 A m^{-2}. The cathodic polarization conditions are as in Fig. 2.

dissolution of the metal substrate to form pits underneath the oxide film and the pit grows by undermining the metal substrate (Fig. 8-d). The dissolution of aluminum is accompanied by hydrogen evolution since this is the corrosion process expressed by the following equation:

$$Al + 6B(OH)_3 + 6OH^- = [Al[B(OH)_4]_6]^{3-} + 3e^- \quad (3)$$

$$3H_2O + 3e^- = (3/2)H_2 + 3OH^- \quad (4)$$

The amount of hydrogen evolved by electrochemical reduction (Eqs. 1 and 2) during cathodic polarization up to i_c = -500 A m^{-2} can be calculated by the following equation:

$$n_e = Q_c/2F \quad (5)$$

where Q_c is the amount of charge passed during cathodic polarization up to i_c = -500 A m^{-2}, and F is the Faraday constant. The amount of hydrogen evolved by the corrosion process (Eqs. 3 and 4) can be calculated by the following equation:

$$n_c = (3/2)(W_d/M_{Al}) \tag{6}$$

Here, M_{Al} is the atomic mass of aluminum. The ratio, n_c/n_e, is plotted against the film formation temperature,T_f, in Fig. 9. The value of n_c/n_e for BS-, HA-, and TA-specimens increases with increasing T_f, but The value for BR-specimen decreases. TA-specimens show relatively large values of n_c/n_e(0.3 - 0.8) at all T_fs.

The value of n_c/n_e decreases in the order of:

TA- > H- > BR- > T- > HA- >BS-specimen at 20 °C,
TA- > H- > T- > BR- > HA- > BS-specimen at 60 °C, and
TA- > H- > T- = HA- = BS-specimen at 80 °C.

The order of n_c/n_e is similar to that of $E_{c(100)}$, $E_{c(500)}$(Fig. 4) and N_p(Figs. 5 and 6), except for the T-specimen. This is because the value of L_p for the T-specimen is much smaller than that for the other specimens.

The anodic oxide films on aluminum include many imperfections, which are produced by impurities and surface irregularity in the metal substrate, and the crystallization of amorphous oxide films. The film breakdown and pit formation during cathodic polarization is strongly affected by the structure of the oxide films, and the number of pits after cathodic polarization can be assumed to be proportional to the number of original imperfections.

The findings that the N_p value for BS-specimen is much smaller than that for BR-specimen suggests that the surface irregularities cause many imperfections to form in the anodic oxide films. At higher T_f, anodic oxide films have a fine crystalline structure[18], and this may increase the N_p for BS- and HA-specimens with increasing T_f. The decrease in N_p for BR-specimens with increasing T_f can be understood as a result of the decrease in the roughness during anodizing by electrochemical dissolution of the oxide film. The TA-specimen includes many voids in the oxide films[16], and they may be precursors to the large number of pits formed during cathodic polarization.

In Figs. 10 and 11, the $E_{c(10)}$ and $E_{c(500)}$ are plotted against log N_p for BS-, BR-, T-, TA-, H-, HA-specimens. It is clear that the $E_{c(10)}$ and $E_{c(500)}$ can be correlated with N_p. By using these relationships, one can estimate semi-quantitatively the number of imperfections in the different types of oxide films on aluminum.

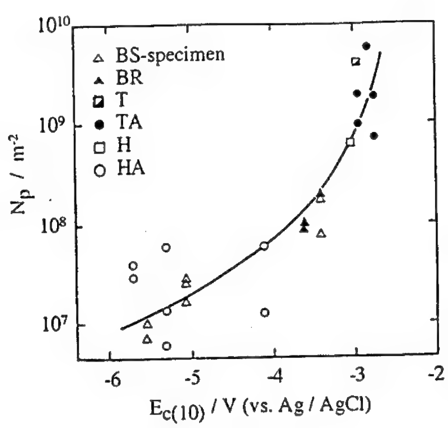

Fig. 10 Relationship between $E_{c(10)}$ and log N_p, obtained for BS-, BR-, T-, TA-, H-, and HA-specimens.

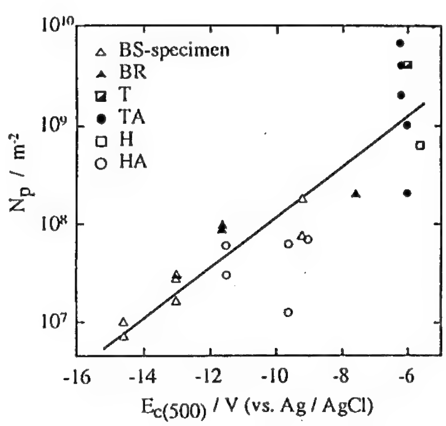

Fig. 11 Relationship between $E_{c(500)}$ and log N_p, obtained for BS-, BR-, T-, TA, H-, and HA-specimens.

CONCLUSION

Highly pure aluminum specimens were anodized in a neutral borate solution after a)electropolishing(BS-specimen), b)surface-roughening(BR-specimen), c)heat treatment(TA-specimen), or d)hydrothermal treatment(HA-specimen), and the cathodic polarization behavior of the specimens was investigated in a neutral borate solution to examine the effect of film structure on the film breakdown and pit formation during cathodic polarization. The following may be concluded.

1)Cathodic polarization curves for all specimens show a very small value of cathodic current, i_c, at potentials higher than -2 - -4 V, and below these i_c increases appreciably with lowering E_c.

2)The location of the i_c vs. E_c curve in the low potential region strongly depends on the kind of preexisting films and film formation temperature.

3)The film breakdown and pit formation take place by cathodic polarization, and the number of pits, N_p, is between 10^7 and 10^{10} m^{-2}, increasing in the order of BS- < HA- < BR- < TA-specimens.

4)The mole ratio of hydrogen evolved by the corrosion of the metal substrate to that by the electrochemical reduction is between 0.02 - 0.8, increasing in the order of BS- < HA- < BR- <TA-specimens.

5)The cathodic polarization curves can be correlated with the number of pits, which may be assumed to be originated from the imperfections in the oxide film.

6)The cathodic polarization curve can be used to estimate semi-quantitatively the number of imperfections in different types of anodic oxide film on aluminum.

REFERENCES

[1]W.Ch.van Geel, Physica 17, 761 (1951)
[2]A.Vermilyea, J. Appl. Phys., 27, 963 (1956)
[3]L.Young, Trans. Faraday Soc., 55, 842 (1959)
[4]A.Middelhoek, J. Elctrochem. Soc., 111, 379 (1964)
[5]T.Yamabe, Tech. Rep. of IEICE, R92-58, CPM92-175, p.7 (1993)
[6]K.J.Vetter, Electrochemical Kinetics, p.183, Academic press, New York (1967)
[7]K.Nisancioglu and H.Holtan, Corros. Sci., 19, 537 (1979)
[8]J.Radosevic, M.Kliskic, P.Dabic, R.Stevanovic, and A. Despic, J. Electroanal. Chem., 277, 105 (1990)
[9]C.F.Lin and K.R.Hebert, J. Electrochem. Soc., 137, 3723 (1990), 141, 104 (1994)
[10]C.F.Lin, M.D.Porter, and K.R.Hebert, ibid., 141, 96 (1994)
[11]H.Takahashi, K.Kasahara, K.Fujiwara, and M.Seo, Corros. Sci., 36, 677 (1994)
[12]H.Takahashi, K.Fujiwara, and M.Seo, Corros. Sci., 36, 689 (1994)
[13]H.Takahashi, M.Nagayama, Electrochim. Acta, 23, 279 (1978)
[14]H.Takahashi, C.Ikegami, M.Seo, and R.Furuichi, J. Electron Micros., 40, 101 (1991)
[15]H.Takahashi,C.Ikegami, and M.SEO, Proc.of Symp.on Oxide Films on Metals and Alloys, Edited by B.R.MacDougall, R.S.Alwitt, and T.A.Ramanarayanan, p.414 (1992)
[16]H.Takahashi, M.Dairaku, and M.Seo, J. Surface Finishing, Jpn.,45, No8 (1994) in press.
[17]H.Takahashi, Y.Umehara, T.Miyamoto, N.Fujimoto, and M.Nagayama, ibid., 38, 67 (1987)
[18]C.T.Chen and G.A.Hutchins, J. Electrochem. Soc., 132, 1567 (1985)

Materials Science Forum Vols. 185-188 (1995) pp. 1011-1020

Effect of Cr, W and Ta on the pitting potential of sputtered Ni-alloys

Z. Szklarska-Smialowska, S. Shademan and R. Inturi

Fontana Corrosion Center, The Ohio State University, 2041 College Rd., Columbus, OH 43210, USA

Keywords: Sputtered alloys, Ni-Cr, Ni-Ta, Ni-W, pitting, oxide solubility

Abstract: This investigation was conducted to determine the effect of alloying elements such as Cr, W, and Ta on the pitting potential of sputtered Ni-alloys films. The experimental results indicated that except for alloys containing high concentrations of Ta, and alloys with Cr, which exhibit high pitting potentials, the pitting potential of sputtered Ni alloy films containing 5at% W, and 5at% Ta increased with a decrease in the solubility of the alloying element oxide.

Several aluminum, iron, and nickel base films (Al-Ta, Al-Cr, Fe-Ta, Fe-W, Fe-Ta) prepared by sputtering were previously studied (1,2). Using TEM, it was found that all of the above elements were present in solid solution. A very good correlation was found between the pitting potentials and the experimentally determined solubility

of oxides (hydroxides) of alloying elements in solutions corresponding to those existing within pits.

The purpose of this work is to find if the pitting potential of nickel is dependent upon the alloying element oxide solubility similar to the case of aluminum and iron alloys.

Experimental procedure

The material used in this study are:

1) Bulk Ni, bulk Ni-Cr (3, 7, and 24 at%)
2) Sputter deposited Ni films
3) Sputter deposited Ni-Cr (7 and 18 at%), Ni-W (5 and 29 at%), Ni-Ta (5 and 10 at%) films.

The structural analysis of all the films were determined using an Analytical Electron Microscope from back thinned samples (1,2). The average grain size (taken from 100-200 grains) was evaluated from the micrographs by the Zeiss video plan systems. In order to prepare the films for polarization measurements, copper wires acting as the working electrode terminal were bonded to the films with silver epoxy. The electrical connections and the edges of the films were first covered with an acrylic cement coating and then covered with micro shield lacquer leaving an area of 0.30 to 1 cm^2 exposed to the electrolyte. For the auxiliary electrode a platinum sheet was used. All potentials are referred to a saturated calomel electrode (2). The polarization tests were conducted potentiodynamically at a scan rate of 0.5mv/s in deaerated 0.1M, and 1M NaCl solutions at 23^0c.

Results

As an example, the diffraction patterns of the Ni-7at% Cr, Ni-29at% W, and Ni-10at% Ta are shown in Figs 1. All the diffraction patterns can be indexed to a single phase fcc structures even though the solubility of Ta, and W has been extended beyond the equilibrium solid solubility limit of 5 and 9% respectively (3). The Ni-7at% Cr diffraction pattern also shows the presence of additional faint rings whose determined "d" (interplanar spacing) values agreed well with "d" values of the most intense diffracting planes of NiO. The NiO contamination was probably introduced in the films from the bulk material used in the sputtering targets. The weak intensity, as well

as the contrast of the dark field images obtained from the diffraction rings of the oxide phase indicated that its content is small and the oxide particles are very fine and uniformly distributed throughout the matrix. The

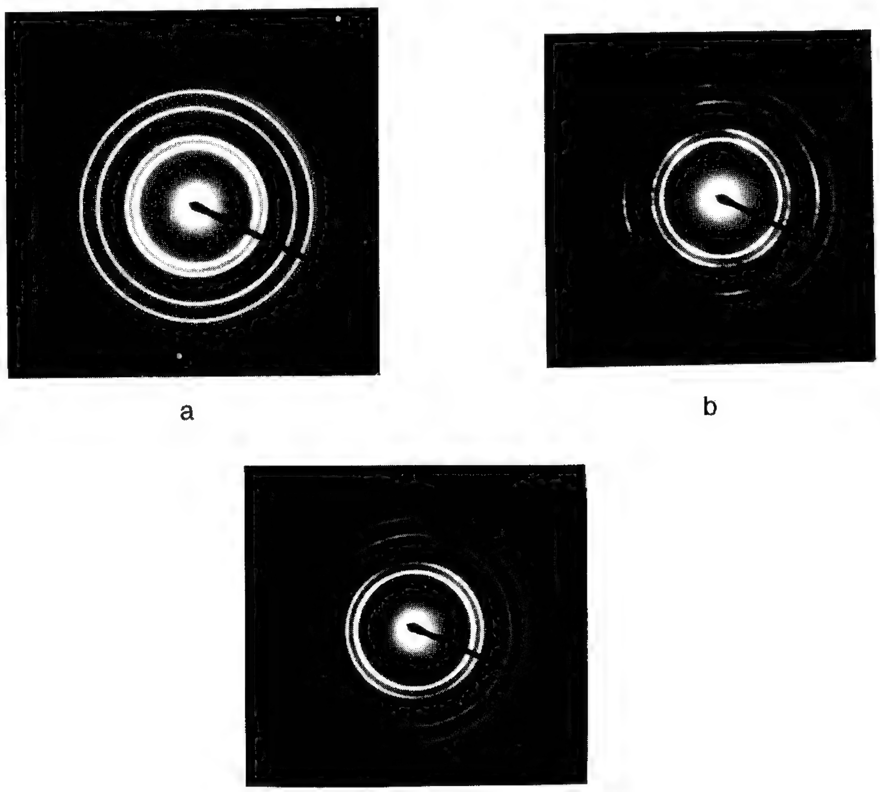

Fig. 1: Diffraction patterns of (a) Ni-7at% Cr, (b)Ni-10at% Ta, and (c) Ni-29at% W.

diffraction patterns of the Ni-29at% W, and Ni-10at% Ta films do not show the presence of additional faint rings.

Table 1 gives the grain size and pitting potentials of the bulk material and sputtered film of Ni and Ni-base alloys in 0.1M and 1M NaCl solutions. This table illustrates that the pitting potentials of

all sputtered films are higher than those of bulk samples of the same composition, while their grain size is much smaller.

Compositon	Grain size (μm) bulk	Pitting potential (bulk) V_{SCE} 0.1M NaCl	Pitting potential (bulk) V_{SCE} 1M NaCl	Grain size (nm) film	Pitting potential (film) V_{SCE} 0.1M NaCl	Pitting potential (film) V_{SCE} 1M NaCl
Ta	---	No pitting	---	---	---	---
Cr	---	---	---	---	0.700	---
Ni	25	0.350	0.130	22	0.570	0.470
Ni-7at% Cr	70	-0.100	---	5	0.660	---
Ni-18at% Cr	145	0.360	---	7	0.655	---
Ni-5at% Ta	---	---	---	---	0.500	0.265
Ni-10at% Ta	---	---	---	9	0.680	---
Ni-5at% W	---	---	---	---	0.450	0.185
Ni-29at% W	---	---	---	---	dissolution	---

Table. 1: Grain size and the pitting potentials of bulk nickel and sputtered Ni-film, Ni base alloy films in 0.1M and 1M NaCl.

Anodic polarization behavior

The polarization curve in Figure 2 shows that a slight decrease in purity can cause a significant drop in the pitting potential of bulk Ni. This Figure also indicates that the pitting potential of Ni film is much higher than that of bulk Ni of the same purity. Figure 3 as an example shows the polarization curves for Ni film, Ni-Ta films, and Ni-W films in 0.1M NaCl solution. The highest pitting potential is exhibited by the Ni-10at% Ta film while the Ni-29at% W film dissolves during polarization. The dissolution of the Ni-29at% W is due to the high solubility of WO_3 in neutral solutions. The pitting potential of the films containing 5at% W, and Ta is lower than that of the Ni film. The same trend was observed in 1M NaCl solution.

Solubility of alloying element oxides

Since the solubility of NiO in solutions of different pH values at room temperature were not available in the literature, the

solubilities were determined experimentally. Figure 4 shows the relationship between pH and the solubility of NiO. The solubility of alloying element oxides Cr, Ta, and W (4) in HCl solutions of pH 2 is given in Table 2.

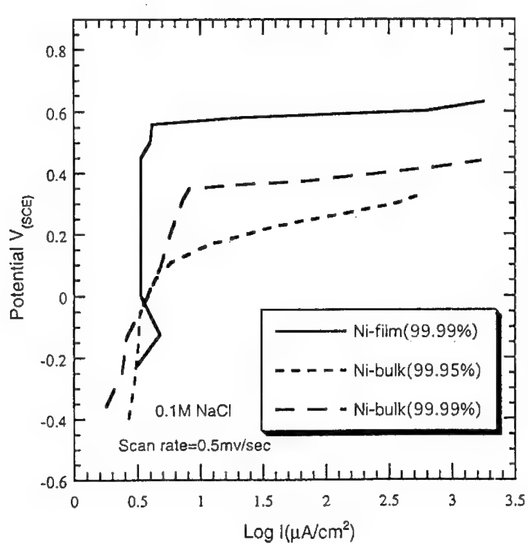

Fig. 2: Anodic polarization curves for Ni-film and bulk-Ni at two different purities.

Discussion

Figure 5 shows the dependence of the pitting potentials of nickel alloy films on the experimental solubility of studied alloying element oxides at pH=2. This pH value was measured within the nickel pits before the formation of a salt film by Luo and Ives (5). Figure 5 shows that except for the alloys containing high concentration of Ta, and alloys with Cr which exhibit very high pitting potentials in 0.1M NaCl, the pitting potentials of sputtered Ni alloy films increases with a decrease in the solubility of the alloying element oxide in the pit solution. Hence the proposed model describing the effect of alloying elements in Al, and Fe alloys (6,7) is also pertinent for Ni alloys containing 5at% Ta and 5at% W. This model assumes that the pitting potential of metastable Al and Fe

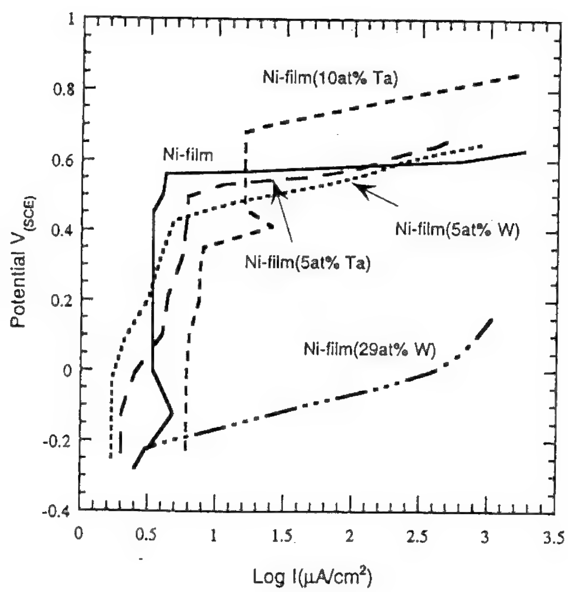

Fig. 3: Anodic polarization curves for Ni-film and Ni base alloy films in deaerated 0.1M NaCl.

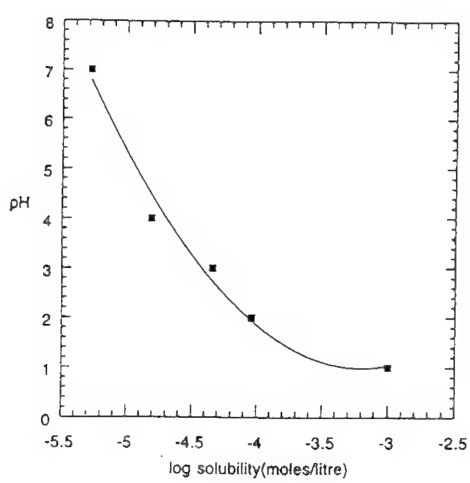

Fig. 4: Solubility of NiO in HCl solutions of various pH.

Alloying element	Oxide of alloying element	Log of solubility of alloying element oxide (mole/liter)
Ni	NiO	-4.036(*)
Cr	$Cr(OH)_3.nH_2O$	-3.619
Ta	Ta_2O_5	-3.270
W	WO_3	-2.869

* Evaluated in this study.

Table. 2: List of alloying element oxides of Ni alloy films for which experimental solubilities are found at pH=2. (4).

base alloys is determined by events occurring at the metal/oxide interface. The passive film contains different defects through which Cl^- ions and water migrate rather easily and reach the metal surface. Occluded cells are formed as a result of localized dissolution of the metal. Because of the hydrolysis of the cations, the pH of the pit solution decreases. Stable pits are formed when the pH becomes lower than the critical value. The effectiveness of the alloying elements in increasing the pitting potential is related to the stability and solubility of the oxidized species of the alloying element in the acidic solution present in the pit.

It has to be noted that the pitting potential of Cr is higher than that of Ni despite of a higher solubility of Cr oxides in the pit solutions. The reason for this discrepancy seems to be connected with the structure of the respective passive films. The oxide film on Cr is probably more dense and compact therefore, a higher potential is needed to accumulate Cl^- anions within the film. The presence of a more compact film and its effect in increasing the materials resistance to localized corrosion has been indicated by Marcus et al (8) after studying the effects of aging on the pitting resistance of Fe-17Cr alloys. From the XPS results of the passive film these

investigators have concluded that the enhanced pitting resistance after long periods of aging in the passive range is due to the formation of a thin enriched chromium oxide layer in the interior portion of the passive film. Studies of aging effects on pitting resistance of pure Fe (9) has shown that improved pitting properties are due to microscopic changes of the film structure which leads to the production of a higher density film. As result, taking into consideration the fact that improvement of the passivity can be obtained on a pure single phase metal, it seems that this

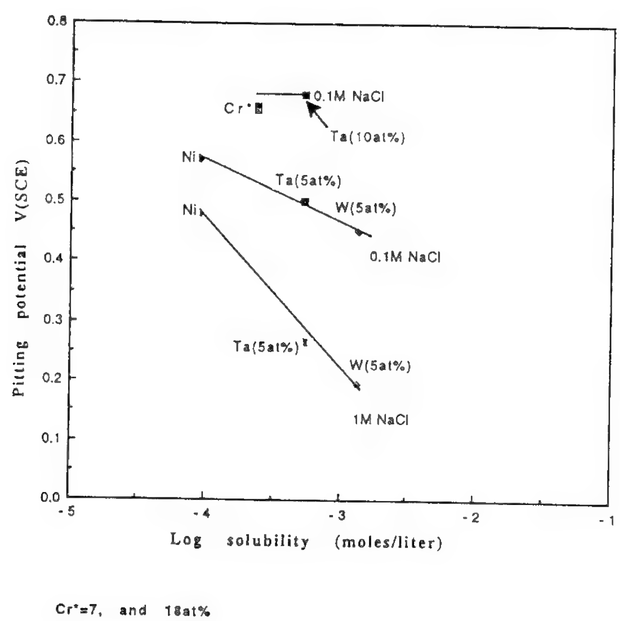

Fig. 5: Relationship between the pitting potential (measured in 0.1M, and 1M NaCl solutions) of the sputtered Ni alloy films and the experimental solubility of the alloying element oxide in acidic solutions of pH=2.

improvement is not necessarily connected with the change of chemistry of the oxide film but with the change in the structure (consolidation) of the oxide film.

Table 1 shows that the pitting potentials of Ni film, and Ni -Cr films are much higher than those corresponding to the same bulk

material. The difference seems to be first of all the result of higher concentration of impurities in the casting materials and the nature of the film formed on the surface. Figure 2 indicated that the pitting potential of bulk Ni (99.95% purity) is lower than that of bulk Ni with 99.99% purity. These pitting potentials were both lower than that of the Ni film (which was sputtered from a target made of Ni foil of 99.99% purity). This effect can not be explained by a higher amount of impurities in the bulk material. As indicated earlier, structural characteristics of the sputtered Ni-Cr films revealed the presence of NiO phase. This finely dispersed oxide phase is probably formed during sputtering in a chamber which was evacuated to a pressure of $6X10^{-6}$ torr. In order to find out whether these finely dispersed NiO phase are responsible in improving the pitting properties of Ni, an effort was made to produce a different NiO concentration by formation of films sputtered at a different partial gas pressure: $7X10^{-6}$ air, $2X10^{-5}$ pure oxygen, and $2X10^{-5}$ pure nitrogen. The pitting potentials obtained from the anodic polarization curves were identical. This indicated that either the presence of fine oxide particles is not the reason for higher pitting potentials or the level of oxygen needed to produce NiO which increases the pitting potential is very low.

It seems that the enhanced pitting resistance of sputtered Ni film can not be explained by their fine grain structure, as compared to the coarse grained bulk samples of the same composition. This conviction is based on the result obtained for sputtered Fe film and Fe bulk (2). It was observed that the pitting potentials of sputtered Fe film, and Fe bulk were identical (0.00VSCE) even though there was a large difference in their respective grain sizes (24nm and 100μm respectively). It is suggested that the high pitting resistance of the Ni film is due to a large number of uniformly distributed short (not deep) defects in the passive film. As a result, agglomeration of the chloride ions in such defects is more difficult in comparison to the material with deeper defects (bulk nickel). Preliminary observations of surface maps taken by scanning tunneling microscope support this suggestion. The low chloride concentration at each defect sites requires a greater driving force, or a higher anodic potential for stable pit growth. A higher roughness for the surface of Ni(lll) passivated in H_2SO_4 at different anodic potentials was reported by Marcus et al (10). Roughening with respect to the unpassivated surface was observed on the submicroscopic, and atomic scale. The roughness increased with the passivation potential. The observed roughness was attributed to the competition between metal dissolution and nucleation and growth of the passive film. Increase

in roughness (increase in number of defects) can decrease the resistance of metal to localized corrosion.

Conclusions

1) There is a good correlation between the solubility of Ta and Cr oxide in solution corresponding to the pH of the pit solution and the pitting potential of Ni-5at% Ta, Ni-5at% W alloys. The higher solubility of the alloying element oxide, the lower the pitting potential.
2) Pitting potential is determined by stable alloy dissolution within the pit, hence by the critical pH of the pit solution. At lower pH values than the critical pH, the pit is stable and grows.
3) It seems that accumulation of Cl^- ions is more difficult in shorter defects than deeper ones. As result, a higher potential is necessary to produce the critical pH for pitting.

References

(1) Rama Inturi and Z.Szklarska-Smialowska, Corr.Sci, **34**, 1201 (1993).
(2) Rama Inturi and Z.Szklarska-Smialowska, COrr.Sci, **34,** 1973 (1993).
(3) T.B.Massalski, Binary Alloy Phase Diagrams, Plenum Publishing Corporation, (1987) and W.G.Moffat, The Handbook of Binary Alloy Phase Diagrams, ASM (1986).
(4) Solubility of Inorganic and Organic Compounds, Edited by H.C.Silcock Vol.**3**, Ternary & Multiphase Systems of Inorganic Substances, part 1-3 (1963).
(5) J.L.Luo and M.B.Ives, in Critical Factors in Localized Corrosion, Edited by G.S.Frankel and R.C.Newman, The Electr.Soc.Inc (1992) p.134.
(6) Z.Szklarska-Smialowska, Corr.Sci, **33**, 1193 (1992).
(7) Rama Inturi and Szklarska-Smialowska, Corr.Sci, **34**, 705 (1993).
(8) W.P.Yang, D.Costa, P.Marcus, Proceedings of the Symposium on oxide Films on Metals and Alloys. Vol. 92-22. p. 516 (Pennington, NJ: Electrochemical Society, 1992).
(9) T.Zakroczymski, Chwei-Jer Fan and Z.Szklarska-Smialowska, J.Electrochem.Soc, **122**, 2868 (1985).
(1) P.Marcus, H.Talah, V.Maurice, Preceedings of 12th International Corrosion Congress, NACE (1993) p.2105.

Materials Science Forum Vols. 185-188 (1995) pp. 1021-1028

Studies on breakdown and repair of passivating films on iron and stainless steel

Á. Rauscher, Gy. Kutsán and Z. Lukács

Institute of Physical Chemistry, Attila József University, H-6701 Szeged, Hungary

Keywords: Iron, stainless steel, passivation, breakdown of passivity, hydrogen sulphide, chloride, intermittent galvanostatic polarization

Abstract

Intermittent galvanostatic and quasi-potentiostatic polarization measurements were carried out in Na_2SO_4 solution in the absence and presence of Cl^- ions and H_2S, using iron and stainless steel electrodes. With consideration to the potential-pH diagrams of Fe-H_2O binary and Fe-S-H_2O ternary systems, and also to the changes in the characteristics observed on galvanostatic potential vs. time diagrams when varying the experimental conditions, conclusions were drawn concerning the corrosion products anticipated under the given conditions, and also the breakdown and repair of the passive films. The differences in character of passive films on iron and stainless steel are reflected primarily in their degree of protectiveness and their susceptibility to breakdown.

Introduction

Anodic formation of passive films on iron and stainless steel has been investigated by a number of workers. The nature of the passivating film, and the factors controlling the establishment and maintenance of the passive state are as yet not cleared up.

In this investigation an intermittent galvanostatic polarization method was used with the aim of studying the differences in character and breakdown processes of passive films on iron and stainless steel.

The method of intermittent galvanostatic polarization was used first by Nagel, Ohse and Göhr [1,2] for the study of various metal-water binary systems. Theoretical aspects of the method have been discussed in detail by Lange and Göhr [2]. The method was also used by Horváth and Hackl [3] with some modifications for the study of metal-sulphur-water ternary systems.

Experimental

Cylindrical electrodes were made of high-purity iron (Johnson-Matthey Ltd.) and of stainless steel prepared from alloying components of spectroscopic purity (composition: Cr 15, Ni 13, Mo 2). The stainless steel electrodes were abraded with silicon-carbide paper to a 600-grit finish, degreased with acetone, then pickled in 15% HNO_3 and 5% HF solution at 353 K for 5 minutes, washed with a jet stream of tap water and rinsed in distilled water. The iron specimens were electropolished after mechanical polishing.

The stock solution was 0.25 mol dm^{-3} Na_2SO_4 the pH of which was adjusted to the required value by addition of H_2SO_4, or NaOH.

Deareation of the solutions was accomplished by bubbling purified N_2 gas through the solutions. Saturation with H_2S was carried out by bubbling H_2S gas through the solutions, previously deareated with nitrogen. In the experiments where the effect of NaCl and H_2S is examined, specimens were passivated in the Na_2SO_4 solution and then the solution was replaced by the solution containing these substances from a container through a three way stopcock connected to the cell.

Electrode potentials are given on the normal hydrogen scale.

The experimental technique, described in a previous paper [3] has been modified. The

control of measurements and data collection were performed by a PC. The advantage of this method is that different polarization and interruption periods can be easily and exactly adjusted. The measured potential data were plotted as a function of time on a compressed scale. In this way each of the curves in the polarization and interruption periods appear in the form of a simple line. In the period of current interruptions more or less sharp "steady-state" arrests can be obtained which are comparable to the equilibrium potentials of the various electrode reactions, calculated on the basis of thermodynamic data. Further, from the differences between the "steady-state" potential and the polarization potential, and from the changes of these potentials with time, conclusions can be drawn on the establishment, protectiveness, maintenance or breakdown of the passivating film.

Results and Discussion

For iron in strongly acidic solutions (pH<3) with the applied polarizing current densities (maximum 100 mA cm^{-2}) no passivation was observed in the course of intermittent galvanostatic anodic polarization. Experimental results indicate that the conditions are more favourable for the formation of iron oxides, i.e. for the passivation of iron, when either the polarizing current density or the pH of the solution is increased.

The shape of the potential vs. time diagram obtained with a 10 mA cm^{-2} polarizing current density at pH 6.5 (Fig. 1) is characteristic of the passivation behaviour of iron in Na_2SO_4 solutions at pH values between 4 and 10.

The progress of anodic passivation of iron is indicated in the potential vs. time diagram by a gradually increasing difference between the polarization potential and the "steady-state" potential observed in the period of current interruptions. Comparing Fig. 1 with the Pourbaix diagram of the Fe-H_2O binary system [4], it can be established that in the course of anodic polarization the value of the electrode potential of iron observed in the periods of current interruptions, passing through the range corresponding to the Fe/Fe_3O_4 equilibrium, shifts up to the equilibrium potential of the Fe_3O_4/Fe_2O_3 transformation, i.e. in the passive state it drops at most to the level corresponding to this transformation.

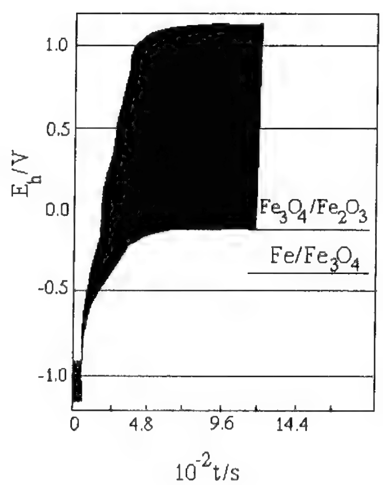

Fig. 1. Potential vs. time diagram for iron in 0.25 M Na_2SO_4 solution. pH = 6.5, current density 10 mA cm^{-2}.

The passivation behaviour of iron characterized by the potential vs. time diagram shown in Fig. 1 is not easily reproducible. In the course of anodic passivation, breakdown of the passive film occurred after various time intervals, even in cases where the conditions for the formation of oxide layers were apparently similar. The breakdown of the passive film is indicated by a sharp drop of the electrode potential in the negative direction. A typical example of this behaviour is to be seen in Fig. 2. It can be seen that, while the potential observed in the period of current interruptions shifted up to the equilibrium potential of the Fe_3O_4/Fe_2O_3 transformation, the polarization potential also increased towards more noble values. As soon as the potential of the electrode dropped from the value identified as that of the Fe_3O_4/Fe_2O_3 transformation to a lower arrest corresponding to the Fe/Fe_3O_4 equilibrium, a rapid drop of the polarization potential could also be observed, indicating the elimination of the passive properties of the oxide layer. When the electrode surfaces

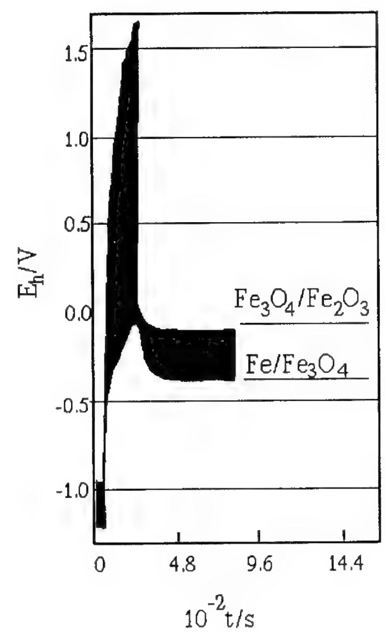

Fig. 2. Potential vs. time diagram characteristic of the breakdown of the passive film on iron. pH = 6.5, current density 16 mA cm^{-2}.

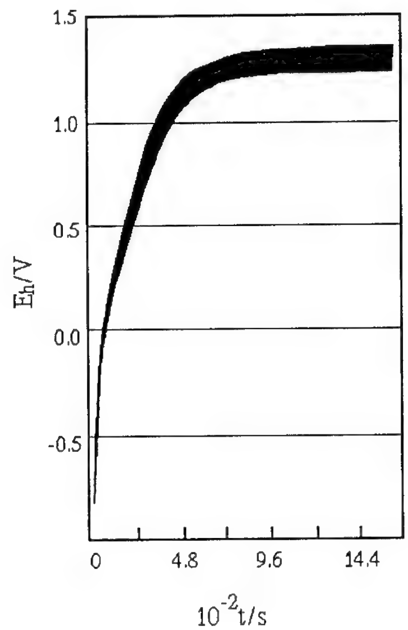

Fig. 3. Potential vs. time diagram obtained for a Cr 14, Ni 13, Mo 2 stainless steel electrode in 0.25 M Na_2SO_4 solution. pH = 6.5, current density 30 $\mu A\ cm^{-2}$.

were roughly abraded or etched without previous polishing, early breakdown of the passive layer occurred or no passivation could be observed.

In the case of stainless steel electrodes, even in slightly acidic or neutral solutions, at very low (3 ~ 30 $\mu A\ cm^{-2}$) anodic polarizing current densities the electrode potential shifts gradually towards a high noble value corresponding to the transpassive region. In the potential vs. time diagrams no potential arrest which could be correlated to the formation of metal oxides was observed (Fig. 3). For stainless steel electrodes, the time required to achieve perfect passivation was approximately inversely proportional to the applied current density.

The different character of the potential vs. time diagrams obtained for iron and stainless steel during anodic polarization is determined by their electrochemical behaviour which depends on several parameters e.g. on the rate by which the metal ions leave the metal lattice to enter the solution, the rate of oxygen chemisorption, and the relation of the strengths of the metal-metal bond and metal-oxygen chemisorption bond. Consequently, the processes leading to anodic dissolution or to passivation are rather complicated. Thus, a somewhat simplified picture is suggested to explain the observed phenomena.

On shifting the electrode potential towards more noble values, the quantity of adsorbed oxygen (H_2O, OH^- , OH) on the metal surface increases, as also does the strength of the chemisorptional interaction. At the same time, metal ions leave the metal lattice at a rate depending on the nature and quality of the metal, the hydration energy of the metal ions, the electrode potential and the pH. When, at a definite value of the electrode potential, the quantity of chemisorbed oxygen in the surface metal-oxygen chemisorption complex becomes nearly equal to

the quantity required for Fe_3O_4 formation, the formation of this oxide in stoichiometric proportions may start.

In strongly acidic solutions, the rate of iron dissolution and the rate of dissolution of the lower valency oxide are relatively high, and thus a further increase in the ratio of oxygen is not possible.

Increase in the pH of the solution results in a decrease of the dissolution of the oxide, and also makes the conditions more favourable for the chemisorption of oxygen from OH^- ions. This promotes the formation of Fe_2O_3 which, in the case of appropriate structure, may retard further anodic metal dissolution. However, if several factors affecting changes in the structure and solubility of the oxide layer and thus favour the formation of Fe_3O_4, or if the epitaxy of the oxide layer is not perfect, local breakdown of the passive film occurs. From this respect it has to be taken into consideration: the rate of thickening of the oxide layer, the decrease of the pH at the solid/electrolyte interface and the autoreductive oxide dissolution taking place in the presence of Fe^{2+} ions [5-7].

These considerations suggest that the passivation and depassivation phenomena in the case of iron can be attributed to various factors resulting in opposite effects. With consideration to the potential arrests observed in the potential vs. time diagrams, it can be concluded that Fe_3O_4 and Fe_2O_3 play the dominant role on the passivated iron surface between pH 4 and 10. Since only γ-Fe_2O_3 is in thermodynamic equilibrium with the Fe_3O_4 layer [2], passivation is due to the γ-Fe_2O_3 layer. The experimental evidence of numerous authors supports the above conclusion, but without excluding the possibility of oxygen chemisorption in the initial step of formation of the passive film on iron.

In the case of stainless steel the presence of alloying elements considerably retards the metal ions from leaving the metal lattice. Thus, oxides of definite stoichiometric composition do not form in the course of anodic passivation. It is assumed that the electrochemical behaviour observed in the case of stainless steel can be explained by the formation of a chemisorption film, in agreement with the hypotheses of Uhlig [8], Kolotyrkin [9], and other authors.

The iron electrode in 0.25 mol dm^{-3} Na_2SO_4 solutions, saturated with hydrogen sulphide indicated no sign of passivation when polarized anodically with max. cd. of 100 mA cm^{-2}. Considering the equilibrium potentials for Fe/FeS, FeS/FeS_2 and FeS/Fe_2O_3 transformations, calculated from thermodynamic data [3], it is reasonable to assume that iron sulphides may form on the metal surface during anodic polarization but the oxidation of iron sulphides to Fe_2O_3 does not occur. The presence of iron sulphides on the surface does not retard the iron dissolution, i.e. the hydrogen sulphide prevents the formation of passive film. It is seen from Fig. 4, that the potential of iron passivated in Na_2SO_4 solution changed rapidly towards the active potential range on introducing hydrogen sulphide. In accordance with this result, the appearance of pits covered by black sulphide deposits is observed, indicating the local breakdown of the passive layer.

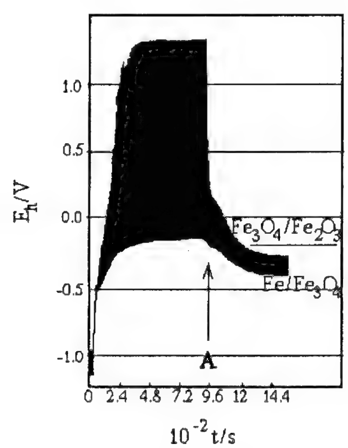

Fig. 4. Potential vs. time diagram for iron. Solution: 0.25 M Na_2SO_4 until the point of time marked with A; from this point the same solution, saturated with H_2S. Polarizing current density 10 mA cm^{-2}.

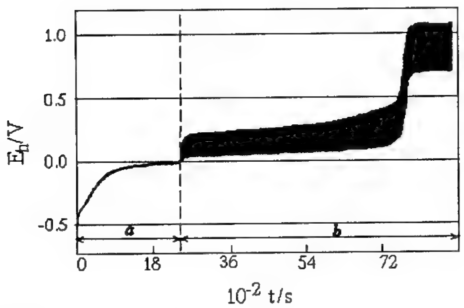

Fig. 5. Potential vs. time diagram for stainless steel in 0.25 M Na_2SO_4 solution saturated with H_2S.
Polarization current density:
a - 3 μA cm^{-2}; b - 75 μA cm^{-2}

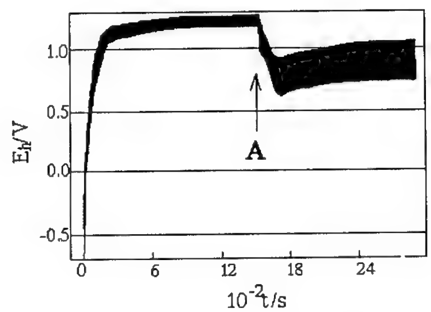

Fig. 6. Potential vs. time diagram for stainless steel in 0.25 M Na_2SO_4 solution. From the time marked with **A** the same solution, saturated with H_2S was introduced.
Polarization current density: 50 μA cm^{-2}

In contrast with iron, the electrode potential of stainless steel in the H_2S containing solution shifted to the passive potential range when applying a sufficiently high, but still a relatively low anodic current density such as 75 μA cm^{-2} (b range in Fig. 5). The first potential arrest may be correlated to the formation of sulphides of alloying elements, which increase the overvoltage of anodic process and thus the oxidation of metal sulphides occurs during anodic polarization. A potential arrest corresponding to second potential arrest (Fig. 5, b region) was also observed when hydrogen sulphide was introduced into the Na_2SO_4 solution in which the stainless steel electrode has been passivated at cd. of 50 μA cm^{-2} (Fig. 6). At this potential the electrode was passive without any indication of localized corrosion.

Considering these results and comparing the potential vs. time diagrams (Fig. 3. and Fig. 5.) obtained in the absence and presence of hydrogen sulphide, it can be concluded that the presence of H_2S considerably changes the passivation characteristics of stainless steel, i.e. the composition and structure of the passive film. It is supposed by the authors that, on the surface of the stainless steel electrode passivated in the presence of H_2S, the oxidation products of metal sulphides are also present. This layer, however, is less protective than that of the chemisorbed film formed primarily in the absence of H_2S.

For iron in solutions containing NaCl, no passivation took place during anodic polarization with intermittent galvanostatic method. Further, immediate breakdown of passivity was observed for iron previously passivated in Na_2SO_4 solution, after the introduction of chloride-containing electrolyte. These phenomena and the potential vs. time diagrams are similar to those observed with H_2S.

On stainless steel -in contrast to iron- periodic breakdown and repair of the passive film occurred during anodic polarization in NaCl solutions. A potential vs. time diagram, characteristic of this behaviour, is shown in Fig. 7. It can be seen, that the electrode potential shifts gradually

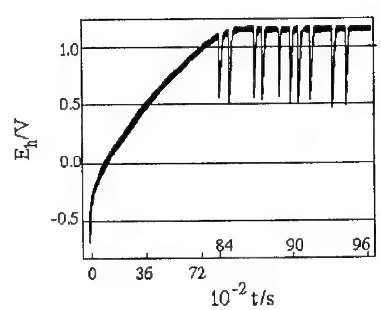

Fig. 7. Potential vs. time diagram obtained for stainless steel in 0.1 M NaCl solution. Polarizing current density: 3 μA cm^2.

towards the positive direction - like in Na_2SO_4 solutions - when, however, the electrode potential approaches the range,characteristic of the passive state, a sharp drop towards the negative direction will follow. This potential drop corresponds to the local breakdown of the passive film to start pitting corrosion. After falling down, the electrode potential rises relatively rapidly again to the previously attained positive value. This phenomenon occurs repeatedly. The minima of potential fluctuations provide a new range, which is characteristic of the susceptibility of stainless steel to pitting corrosion. The critical potential for pitting corrosion was also determined by galvanostatic method without current interruption and by quasi-potentiostatic polarization with a sweep rate of 20 mV/5 min. The critical potentials obtained by the three different methods as a function of Cl^- concentration are shown in Fig. 8.

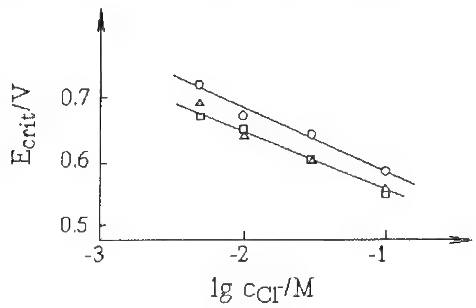

Fig. 8 Critical potentials obtained by intermittent galvanostatic polarization (Δ), galvanostatic polarization without current interruption (○) and quasi-potentiostatic method (□) as a function of Cl^- concentration

It is seen that the minima of potential fluctuations observed by intermittent galvanostatic method and considered as "repassivation potentials" are nearly equal to the "breakdown potentials" measured by quasi-potentiostatic polarization method. It can also be established that tenfold increase in chloride concentration renders the breakdown potential 0.095 V more negative. This shift is in good agreement with the results of Leckie and Uhlig [10] obtained for Cr-Ni stainless steels.

In galvanostatic experiments, without current interruptions, the mean value of the minima of potential fluctuations corresponding to the same chloride concentration is 30 mV more positive. The period of time measured from the start of anodic polarization till the first breakdown decreases slightly with increasing chloride concentration. Without current interruptions, however, this period is remarkably shorter (Fig. 9). The number of potential fluctuations per minute increases with increasing chloride concentration (Fig. 10). This increase, nevertheless, has a diminishing tendency and without current interruptions the number of fluctuations is almost twofold.

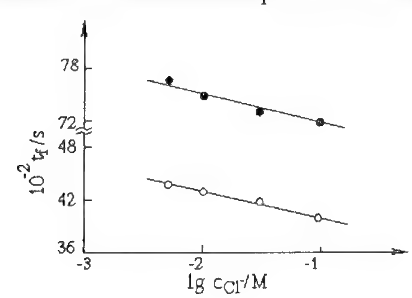

Fig. 9. Relation between the periods of time until the first breakdown and chloride concentration, observed by intermittent galvanostatic polarization (●) and galvanostatic polarization (○).

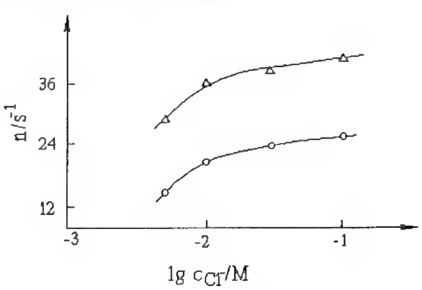

Fig. 10. Relation between the number of potential fluctuations per unit of time and Cl^- concentration determined from intermittent galvanostatic (○) and galvanostatic (Δ) potential time diagrams.

Experimental results obtained for stainless steel in chloride media can be interpreted on the basis of the chemisorption theory of passivity, considering the competitive adsorption of chloride ions and oxygen originating from water molecules and OH^-. Oxygen has normally higher affinity than Cl^- for adsorption sites on a stainless steel surface [10]. Since the shape of the initial section of potential vs. time diagrams obtained for Na_2SO_4 and NaCl solutions are quite similar; furthermore the time measured till the first breakdown decreases only slightly with increasing Cl^- concentration, it can be concluded that Cl^- ions initially do not disturb oxygen chemisorption leading to passivation. Shifting the electrode potential towards more noble values, the amount of adsorbed Cl^- ions increases [11] and the metal-chloride chemisorption bond is getting stronger [12]. If these parameters reach critical values at certain weak sites on the surface, pit nucleation and a subsequent local breakdown of the passive film may occur. In the course of anodic polarization without current interruption the electrode potential shifts more rapidly towards the transpassive region, thus the critical chloride concentration and bond strength are reached sooner and the period of time before the first breakdown is remarkably shorter. As a result of the intensive local dissolution of the steel, the electrode potential drops rapidly towards the negative direction with simultaneous desorption of Cl^- ions. However, the potential changes only to a definite, nearly constant value depending on the bulk concentration of Cl^- ions and the composition of the steel. Then, the oxygen chemisorption becomes prevailing again, resulting in repassivation. It may be supposed that at this potential a critical chloride/oxygen ratio and a nearly stationary state exist. This state can be attained using intermittent galvanostatic polarization or quasi-potentiostatic polarization, but cannot be attained without current interruption. In the latter case the critical potential is more positive. The variations in the experimentally determined parameters with Cl^- concentration can also be explained by means of the above assumption based on the competitive adsorption theory.

Conclusion

Considering the experimental results presented, the conclusion can be drawn that the possibility of the formation of a chemisorbed film or phase oxide depends on the experimental conditions.

From a comparison of the hypothesis concerning the formation of a passive state with the experimental evidence, it can be assumed that the higher the oxygen content of the surface layer, the smaller is its thickness and the higher its protection against metal dissolution. In the limiting case the retardation of metal dissolution is due to the presence of a chemisorption film. This conclusion is supported by the phenomena observed in the H_2S and/or Cl^- containing solutions.

On addition H_2S or chloride to a Na_2SO_4 solution, the passivity of iron previously established in the solution immediately breaks down. On stainless steel, however, corrosion induced by H_2S can be easily prevented with anodic polarization of the specimen to the potential range where metal sulphides are oxidized to oxides. The stainless steel surface passivated in the absence of H_2S are more protective than those contaminated with oxidation products of metal sulphides. In NaCl solution, stainless steel showed repeated breakdown and repair of the passive film during the intermittent galvanostatic polarization. This is explained as a result of the competitive adsorption of oxygen and Cl^- ions.

References

[1] K. Nagel, R. Ohse, E. Lange, Z. Electrochem **61**, 795 (1957).

[2] E. Lange, H. Göhr, Thermodynamische Elektrochemie, Dr.Alfred Huthig Verlag GmbH., Heidelberg 1962.

[3] J. Horváth, L. Hackl, Corr. Sci. **5**, 525 (1965).

[4] M. Pourbaix, Atlas of Electrochemical Equilibria, Pergamon Press 1966

[5] N. Hackerman, Z. Elektrochem. **62**, 632 (1958).

[6] M. Nagayama, M. Cohen, J. Electrochem. Soc. **109**, 781 (1962); **110**, 670 (1963).

[7] A. Pigeaud, H. B. Kirkpatrik, Corrosion **25**, 209 (1969).
[8] H. H. Uhlig, Corrosion and Corrosion Control, John Wiley and Sons, New York 1965.
[9] Ya. M. Kolotyrkin, J. Electrochem.Soc. **108**, 209 (1961).
[10] H. P. Leckie, H. H. Uhlig, J. Electrochem. Soc. **113**, 1262 (1966).
[11] I. L. Rosenfeld, P. Maximtsuk, Z. Phys. Chem. **215**, 25 (1960).
[12] B. N. Kabanov, Elektrokhimija metallov i adsorpcia, Nauka, Moskva 1966.

Materials Science Forum Vols. 185-188 (1995) pp. 1029-1040

Pitting corrosion resistance of high-alloyed stainless steels

V. Cíhal

Vysoká škola bánská, Technical University, Faculty of Metallurgy and Materials Engineering, 708 33 Ostrava, Czech Republic

Keywords: Pitting corrosion, stainless steels and alloys, potentiodynamic polarization, critical pitting temperature, breakdown and repassivation potential

ABSTRACT

In this work is determinated and evaluated the pitting resistance of traditional and new kinds of stainless steels and alloys by technics of potentiodynamic polarization curves for a few temperatures (from 5 - 95°C) in the one-molar water solution of Natrium Chloride. From temperature dependences of pitting potentials were determined or estimated critical temperature of pitting corrosion.

INTRODUCTION

The objective of this research is to compare the resistance of special high-alloyed steels and alloys to the pitting corrosion on the basis of the electrochemical polarization method. The single aim of this work is to determinate the temperature dependence of depassivation and repassivation potentials with the possibility to specify critical temperatures.

APPLICATED MATERIALS AND TECHNIQUES

For the testing of the disposition to the pitting corrosion there were chosen stainless steels and alloys (Table 1) for the use in chemical, energetic industry or paper-making and for ecological applications especially for corrosion-stressed parts in specific environments, for example by the desulphurization of the flue-gases.
Potentiodynamic polarization measurements were executed in the innovated corrosion cell according to Avestas design with the possibility to eliminate undiserable crevice corrosion by the addition of distilled water through filter rings around the surface of the sample about the area 1.0 cm^2 [1].
Following potentials were recorded for the conventional values of current density:
E_{CT} - critical potential by Truman for current density 10 $\mu A/cm^2$ connected with the initiation of first corrosion

microspots on detected areas of the passive layer [2],
E_{pr} - potential of breakdown for current density 100 $\mu A/cm^2$, which should show sensitivity for the initiation of macroscope pitting; this potential is conditional on the chamical composition of the material surface,
E_v - reversible potential for current density 5 $\mu A/cm^2$ connected with chemical composition in relatively bigger corrosion pits i.e. in the volume of material.
Except above named modes the depassivation potential E_D is possible to determine or to measure by other methods [2,3,4].
At the reversible polarization the repassivation potential was measured partly as the point of the intersection on the polarization curve (E_r) for the equality of current densities in possitive and negative directions of polarization, and partly as the potential (E_{pr}) during that the current density decreased to 10 $\mu A/cm^2$. These repassivation potentials are connected with the suppresion or stop of pitting and they are not connected with the origin of pitting, i.e. electrochemical dissolving or mechanical demage of the protected layer [3,5,6].

DESCRIPTION AND DISCUSSION OF RESULTS

Typical parts of potentiodynamic polarization curves in the area of pitting (loops), which were directly recorded on the plotter, are for some tested materials and temperatures rectifiered to Fig.1. There are also marked above named potentials of pitting (E_r, E_{pr},) at two curves for steels Cr19Ni9 and Cr23Ni6Mo3CuN.
On the basis of these measurements were constructed temperature dependences of pitting - potentials (Fig.2-6). The majority of finding temperature dependences of potentials shows the decreasing linear course in wide temperature intervals. Many of these dependences are practically parallel for different steels and potentials which is the advantage from the point of view of the quantitative description and electrochemical or physical reasons. It is possible to get together the sequence of the resistance of tested steels against the begining of pitting for the chosen temperature or in the specific temperature interval. For example: in the temperature interval 20-60°C is the sequence of the resistance against the macropitting following: Cr13, Cr19Ni9, Cr21Ni33, Cr17Ni13Mo3, Cr23Ni6Mo3CuN (Uranus 52N), and Cr24Ni24Mo6 (Uranus SB 8). But steels Cr20Ni18Mo6CuN (254 SMO) and Cr24Ni22Mo7CuN (654 SMO) are practically on the level of steels Uranus 52 N or Uranus SB 8 however steels 254 SMO and 654 SMO are more resistant for the higher temperatures 80-95°C. Similar sequences of the resistance could be used as the qualitative criterion for the choise of material for the specific use. The existence of pitting was not find on Ni-alloys Hasteloy C and C4 with very narrow reverse loops but in exposed areas of samples appeared corrosion products with the coloured (mostly brown) shade. For the development and the research of pitting on the above named alloys and similar nickel - alloys with the high content of Mo is necessary to use more convenient methods [7].
That is why the potentials for Hastelloy alloys have more formal sense and their relatively low values are conected with the transition to the transpassive area by the influence of the

high content of Mo.

CONCLUSION

On the basis of the measuring of depassivation and repassivation potentials there is possible to determine the sequence of the pitting resistance of chosen stainless materials, which is following for increased temperatures: Cr13, Cr19Ni9, Cr21Ni33, Cr17Ni13Mo3 (17353), Cr23Ni6Mo3CuN (Uranus 52N), Cr24Ni24Mo6 (Uranus SB 8), Cr20Ni18Mo6CuN (254 SMO) and Cr24Ni22Mo7CuN (654 SMO), Hastelloy C4 and Hastelloy C. From compiled sequences of resistances and temperature dependences of pitting potentials there was demonstrated, let us say, confirmation of the positive effect of Cr and Mo for the increase of the pitting resistance of steels and alloys. For the determination of the influence of other elements there is possible to use the convenient method of statistics.
Temperature linear dependences of measured potentials (except critical temperatures) make possible the prediction of potential values out of reach of testing temperatures. The number and size of pits were dependent on the temperature and on the content of molybdenum. The biggest pitting resistance achieved nickel alloys Hasteloy C4 and C where the pitting was not detected or observed at all.

REFERENCES

[1] E.Alfonson, R.Quarfort, An improved cell for electrochemical pitting corrosion testing, 11th Scandinavium Corrosion Congress, Stavanger, (1989).
[2] K.Tousek, Bodová koroze kovů. Studie ČSAV 16/83, Praha, Academia (1983).
[3] R.N.Parkins, Corrosion process Applied science publisher, Essex, (1982).
[4] N.Baugärtner, H.Kaesche, The pitting potential of aluminium in halide solutions. Materials and Corrosion, 4 (1991).
[5] K.E.Heusler, Werkst. Korros. 27, 555 (1976).
[6] M.Janik Czachor, J. Electrochem. Soc. 128, 513C (1981).
[7] P.Novák, Elektrochemické metody sledování koroze kovu, in. Sborník, Nové experimentální metody ve fyzikální metalurgii, Metodika studia a sledování korozních dějů, Praha, ČKD (1989).

Table 1: Chemical composition of stainless steels and alloys chosen for testing of pitting resistance

material	C	Mn	Si	Cr	Ni	Mo	additional
Cr13(17021) 1)	0.1	0.76	0.30	14.0	0.4	0.3	
Cr19Ni9(17246) 1)	0.1	1.1	0.24	19.5	9.2	0.4	+Ti
Cr17Ni13Mo3(17353) 1)	0.04			17.5	13.3	2.6	+Ti
Cr21Ni32(17358,AKRI7) 1)	0.06	1.0		21.0	32.5	–	Ti (17 358)
Cr15Ni54Mo16Fe5W3Co2(Hastelloy C) 2)	0.01	0.66	0.11	15.1	54	15.5	Fe5, W3, Co2
Cr16Ni69Mo14FeTi(Hastelloy C4) 2)	0.01	0.19	0.1	16	69	13.8	Fe0.5 Ti0.2
Cr23Ni6Mo3CuN(Uranus 52N) 3)	0.03	0.6	0.25	23.5	6.2	2.9	Cu1.2 N0.17
Cr24Ni24Mo6CuN(Uranus SB 8) 3)	0.01	0.62	0.27	23.7	23.6	5.7	Cu1.5 N0.21
Cr20Ni18Mo6CuN(SMO254) 4)	0.02			19.7	17.9	6.0	Cu0.7 N0.195
Cr24Ni22Mo7CuN(SMO 654) 4)	0.02	2.0		23.9	22.2	7.0	Cu0.4 N0.452

Trademarks:1 – POLDI, 2 – Haynes International Inc., 3 – Creusot-Loire Ind., 4 – AVESTA AB

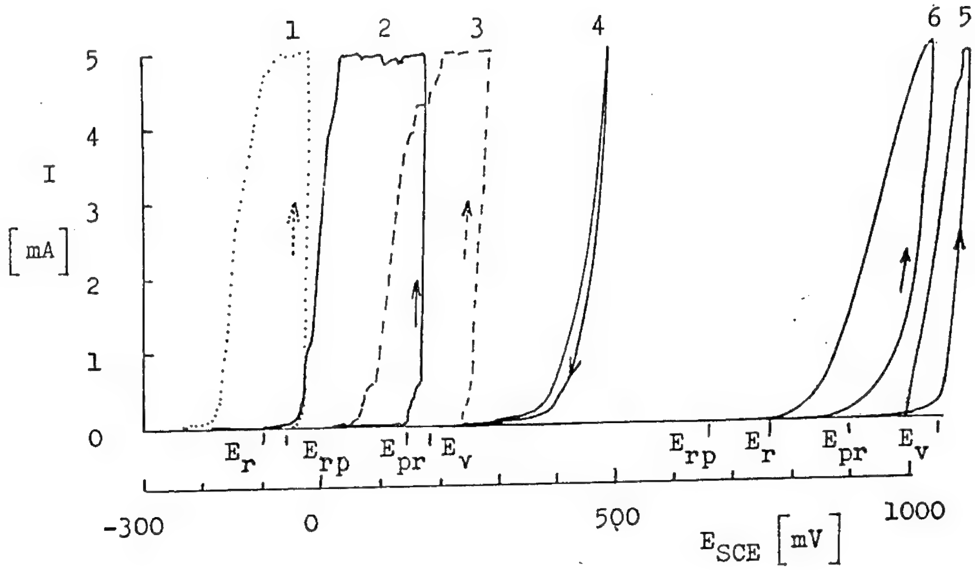

Fig.1: Parts of polarization curves of chosen materials for evaluation of pitting potentials.
1 - steel Cr13, 2 - Cr19Ni9, 3 - Cr17Ni13Mo3,
4 - Hastelloy C, 5 - Cr24Ni24Mo6,
6 - Cr23Ni6Mo3CuN,
Testing temperatures: steel 1,2,3 - 60^{o}C,
maaterial 4,5,6 - 20^{o}C
Mixed aerated water solution of 1.0 mol/l NaCl.
Pitting potentials are marked for steel 2 and 6.

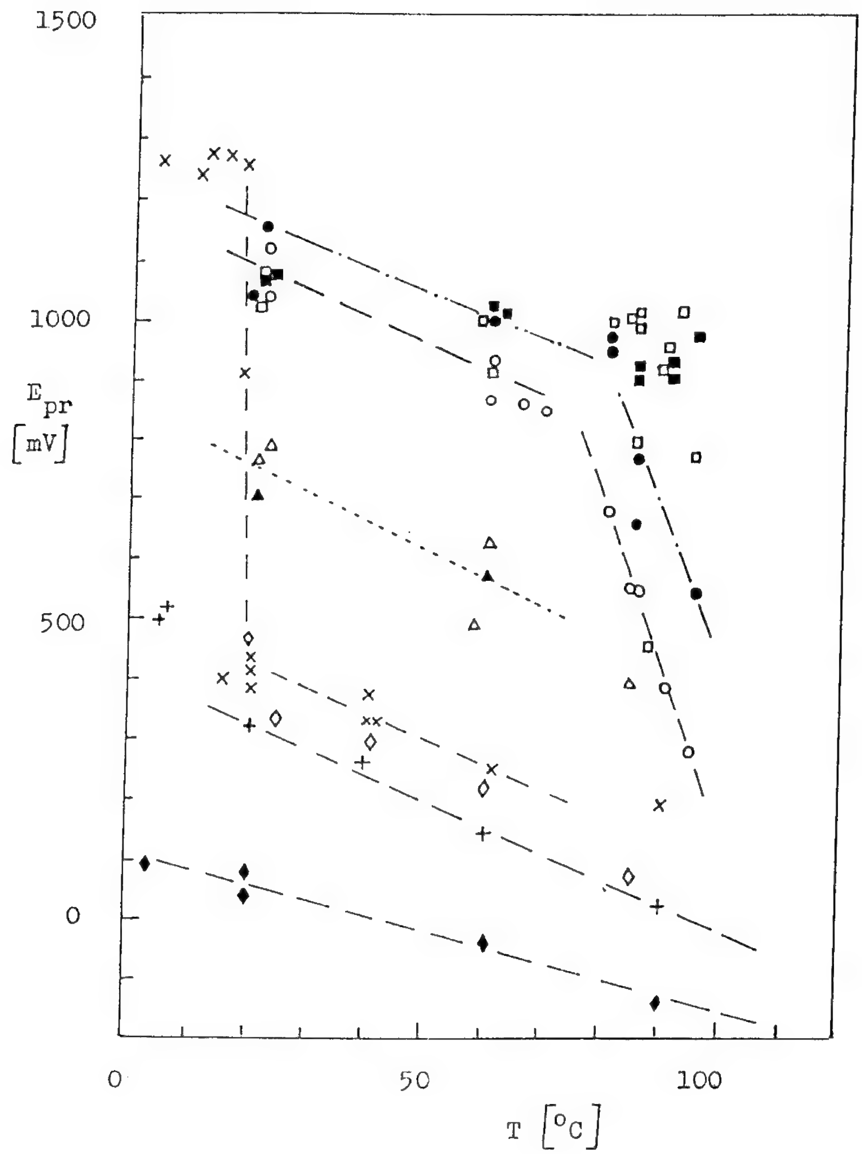

Fig.2a: Temperature dependences of potential of breakdown (E_{pr} for $J=100\ \mu A.cm^{-2}$) for selected stainless steels and alloys (Symbols see Fig.2b).

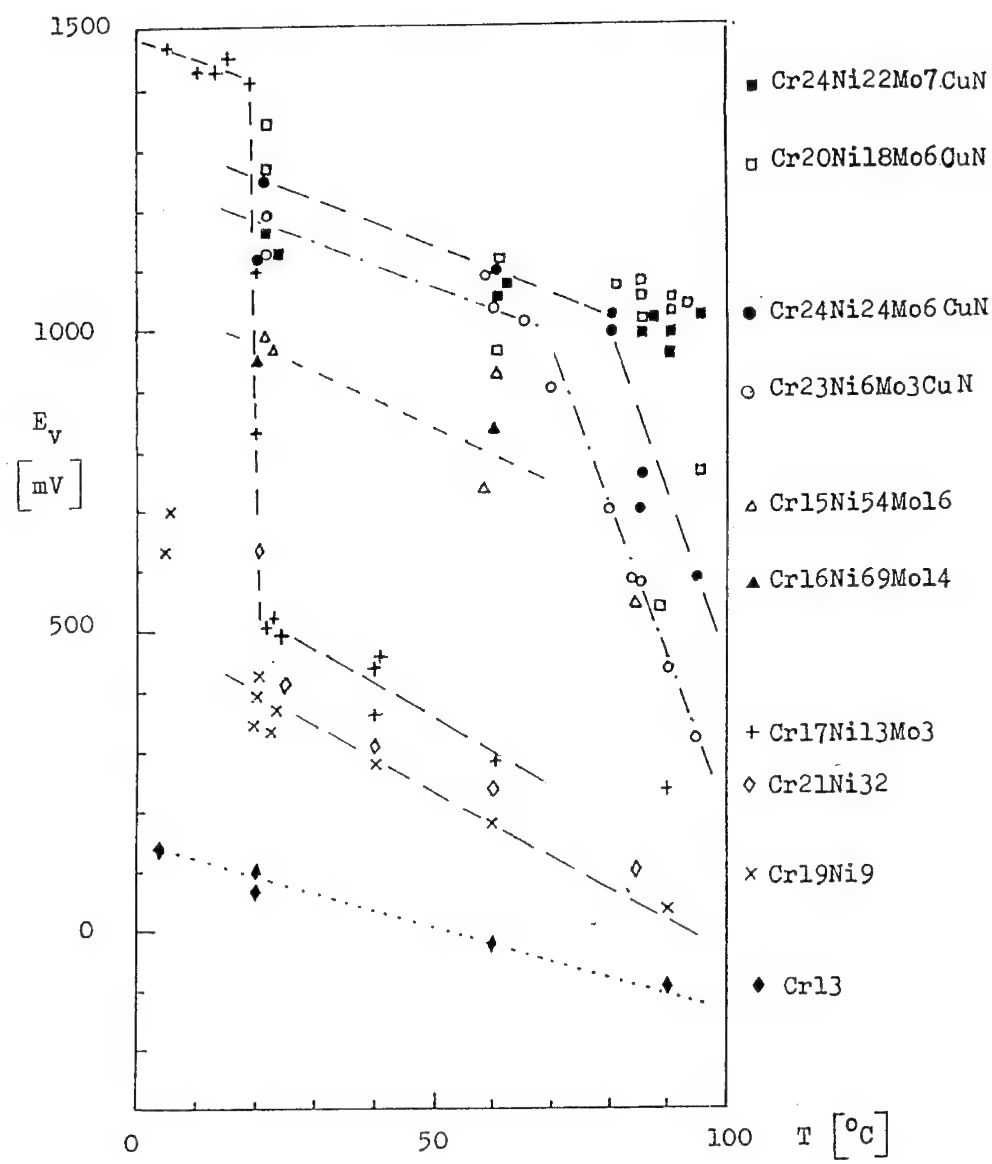

Fig.2b:Temperature dependences of reversible potential (E_V for J = 5 mA/cm^2) for selected stainless steels and alloys.

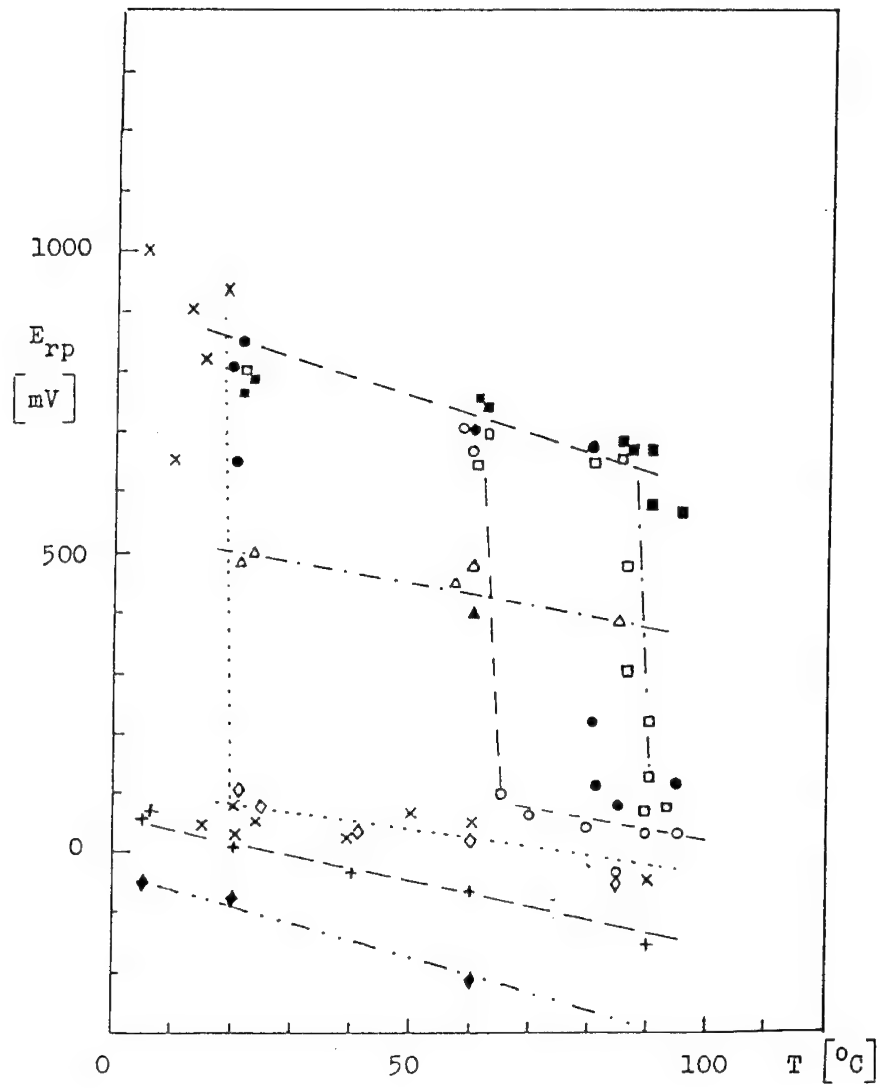

Fig.3a: Temperature dependences of repassivation potential (E_{rp}) for selected stainless steels and alloys.
(symbols see Fig.2b).

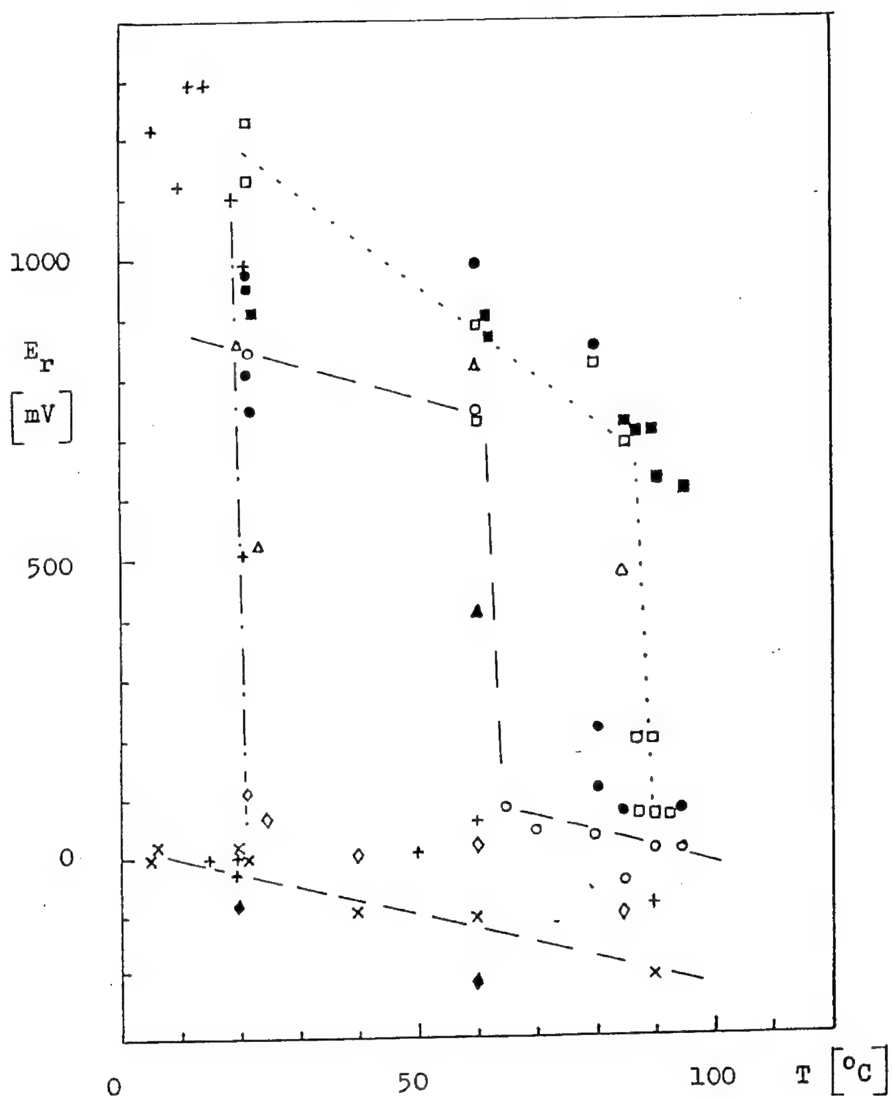

Fig.3b: Temperature dependences of repassivation potential (E_r) for selected stainless steels and alloys.
(symbols see Fig.2b).

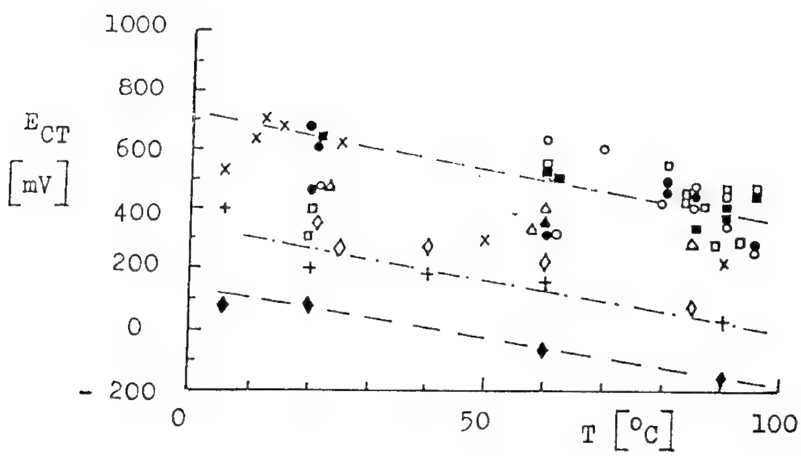

Fig.4: Temperature dependences of critical potential E_{CT}. (Symbols see Fig.2b).

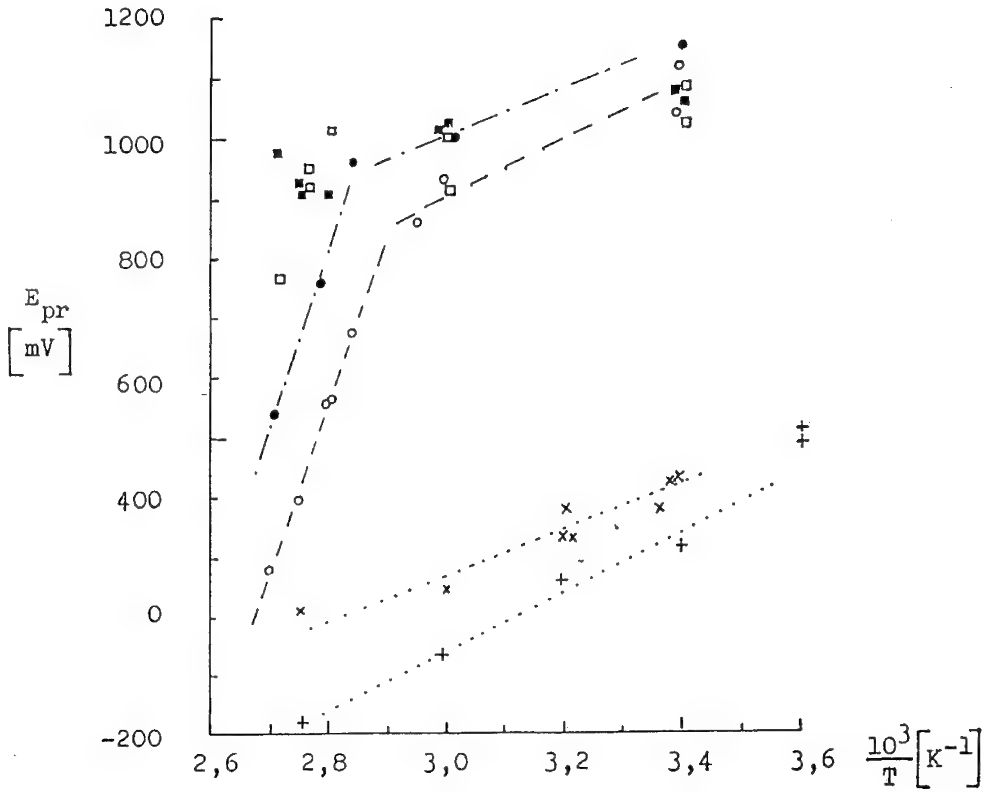

Fig.5: Dependences between potential of breakdown and reciprocal temperature for selected materials. (symbols for selected steels see Fig.2b).

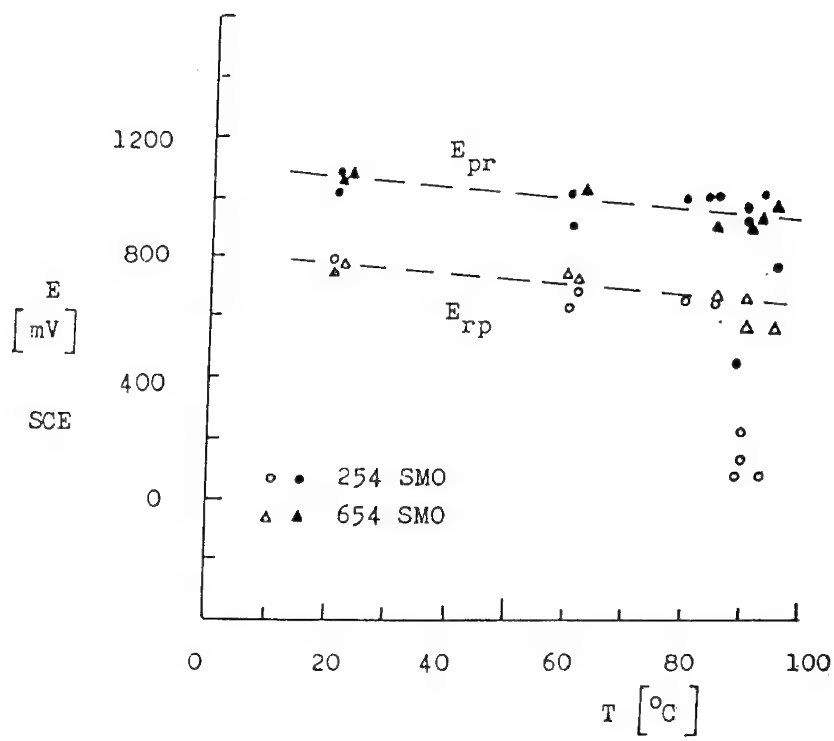

Fig.6: Potentials of breakdown (black symbols) and repassivation (white symbols) dependent on the temperature for selected steels. Neutral water solution NaCl (c_{NaCl}=1.0 mol/l).

Materials Science Forum Vols. 185-188 (1995) pp. 1041-1048

Pitting susceptibility of chromium modified passive films of a B2-FeAl intermetallic alloy

S. Frangini[1], J. Lascovich[1] and N. de Cristofaro[1,2]

[1] ENEA CRE Casaccia, Settore Nuovi Materiali, PO Box 2400, I-00100 Rome, Italy

[2] present address: CSM, Acciai e Materiali Speciali, Rome, Italy

Keywords: FeAl intermetallic alloy, cyclic voltammetry, XPS, modified passive films, pitting, chromium

ABSTRACT

The effect of chromium on the pitting corrosion resistance of an iron aluminide B2-FeAl alloy (40 at/o Al) has been evaluated in chloride borate solutions. Chromium was permanently incorporated into the passive film of FeAl by repetitive oxidation-reduction cycles from alkaline chromate solution. Although the Cr-modified passive FeAl surface was found to have a pitting behaviour comparable to that of stainless Fe-Cr steels containing Cr in the range 12-24 at/o, the XPS analysis showed that Cr enrichment within the passive film of FeAl was not as high suggesting that the protective properties of the film would be due to a synergistic effect between Cr and Al. The use of the Kirchheim model allowed to predict the ternary alloy composition in equilibrium with the Cr-modified passive film one.

INTRODUCTION

It is well known that chromium is one of the most effective alloying elements for improving the resistance of iron and iron-nickel alloys to general and localized corrosion, including pitting. The effect of chromium has been largely investigated in the past, making use of electrochemical as well as of surface analytical techniques. It has been reported that the composition of the passive film of Fe-Cr alloys is strongly enriched with Cr cations suggesting that the higher protective properties of such passive films are mainly due to the formation of a layer of hydrated chromium oxy-hydroxide [1-3]. Further, the chromium enrichment in these films has been explained by taking in account the different transport rates of Fe and Cr cations through the film as well as the preferential dissolution of Fe cations in the outer layers of the film adjacent to the solution [4,5]

Likewise, when the source of chromium is an electrolyte such as a chromate solution, a passive condition for iron and iron-based alloys is still established due to a surface uptake of Cr from the solution. Chromate solutions can represent, therefore, a viable method to provide a source of chromium in order to simulate the effect of chromium alloying on the corrosion resistance properties of iron passive films. Calvo et al. [6] performed cyclic voltammetric experiments in alkaline chromate solutions to incorporate permanently chromium into the passive films of iron. Such chromium modified passive iron electrodes were found to have relevant similarities with passive films formed on Fe-Cr alloys in terms of electrochemical behaviour.

In our previous work [7] the effect of aluminum alloying on the passivation properties of iron has been evaluated on iron aluminide specimens of B2 FeAl structure. A clear improvement of the protective properties of the FeAl passive films was found in sulphuric acid in comparison with pure iron. Although a strong enrichment of aluminum cations was measured within the film, the beneficial effect of Al was rather explained by suggesting that Al accelerates the onset of an amorphous iron oxy-hydroxide passive layer with enhanced passivating properties.

Little is known concerning the effects of Cr on Fe-Al alloys. Cho et al. [8] found that Cr in amorphous Fe-Cr-P-C alloys can be replaced for almost the 90% by Al without causing appreciable reduction in the corrosion resistance of the alloys. This finding may be interesting for the

development of iron aluminides for low temperature aqueous applications, because it seems to suggest a rather wide inter-changeability between Cr and Al in ferrous alloys.
The aim of this work was to evaluate the influence of Cr on the localized corrosion resistance of iron aluminides. To this purpose, chromium was incorporated into the passive film of a FeAl intermetallic compound by cyclic voltammetry from alkaline chromate solutions. The resulting chromium modified FeAl films were evaluated by X-ray photoelectron spectroscopy (XPS) and by electrochemical pitting tests in chloride-borate solutions.

EXPERIMENTALS

Disk specimens of $1cm^2$ surface area were obtained from a hot-extruded rod of B2 FeAl iron aluminide (40at/o Al) provided by Centro Sviluppo Materiali of Rome. Details concerning the chemical composition and the fabrication route of the rod have been given elsewhere [7].
The disk surfaces were abraded with emery paper to a 1000-grit finish, degreased with a mixture of acetone and toluene, and then rinsed with distilled water. For the electrochemical measurements two kinds of reference electrodes were employed depending on the pH of the solutions. In alkaline chromate solutions a Hg/HgO electrode immersed in 1M NaOH served as reference, whereas for the pitting experiments in chloride-borate solutions a satured calomel electrode (SCE) was used.
Cyclic voltammetry (CV) was recorded with a potential sweep rate of 100 mV/s at 30°C in deaerated 0.1M NaOH and 0.1M NaOH + 0.1M Na_2CrO_4 solutions. The measurements were performed between the limits of -0.8V and 0.9V and continued for 50 cycles. After the voltammetric treatment, the working electrodes were removed from the electrolyte, rinsed with distilled water and immediately inserted in the pitting test cell. For the XPS analysis the voltammetric measurements were carried out in glove box filled with purified nitrogen. The electrodes were subsequently transferred to the UHV chamber of the spectrometer using a transfer vessel. The pitting potentials of FeAl specimens were derived from the anodic polarization curves at 30°C in deaerated borate buffer solutions (pH 8.4) containing NaCl in the range 0.05-0.5M. The anodic curves were taken by sweeping linearly the potential at a rate of 1mV/s up to an abrupt increase of current was observed.
Details of the equipment and the procedures used for the XPS measurements can be found elsewhere [7]. A quantitative evaluation of the data was obtained recording the O 2s, Na 1s, Fe 2p, Al 2s, Cr 2p spectra with a 0.1 eV/step energy interval and a pass energy of 20 eV.

EXPERIMENTAL RESULTS

Cyclic voltammetry

Figure 1 shows the voltammetric curves of FeAl in 0.1M NaOH + 0.1M Na_2CrO_4 (Fig. 1a) and 0.1M NaOH (Fig. 1b), respectively.

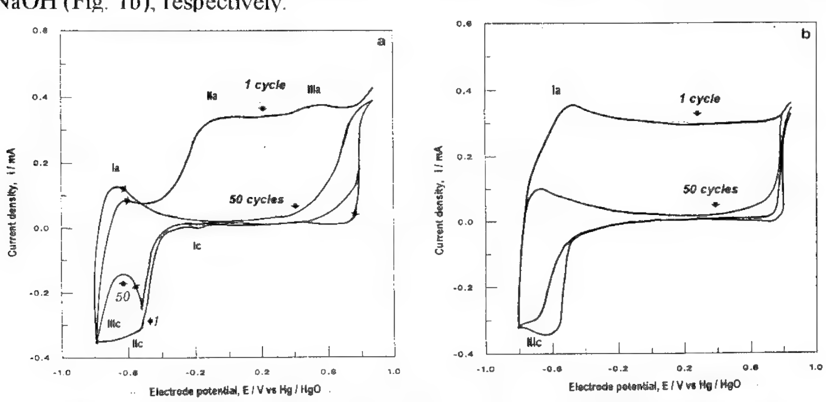

Figure 1 - Cyclic voltammograms for FeAl alloy in (a) 0.1M NaOH +0.1M Na_2CrO_4 and (b) 0.1M NaOH: scan rate 0.1V/s; T=30°C.

A remarkable difference in the E/I response is seen between the first and the stabilized profiles. In the chromate-containing solution (Fig. 1a) the first anodic scan exhibits three current peak maxima at about -0.6V, 0.0V and at nearly 0.5V. The first (peak Ia) is related to the formation of a pre-passive film. An additional peak (IIa) appears in a broad potential region where the Fe(II) cations incorporated in the passive film oxidize to Fe(III). The peak IIIa which is absent in Fig. 1b corresponds to the oxidation of Cr(III) ions present in the film to Cr(VI) soluble species that leads to an iron-rich passive film. After 50 cycles, only peak Ia is still observed, with the charge associated with the peak being increased probably because of the increase of the active area of the electrode during cycling.

On the cathodic side, the first cycle shows a slightly detectable peak at -0.2V (peak Ic) that is not lost in the following cycles. This is followed by a large peak (IIc) centered near the cathodic limit of the CV curve probably due a concomitant occurrence of reduction of passive film and hydrogen evolution. During the following cycles this peak was splitted in two giving raise to a further reduction peak at -0.8V (peak IIIc). On the other hand, both peaks Ic and IIc are almost completely absent in the case of CV performed in chromate-free solution (see Fig. 1b) indicating clearly that they are related to reduction processes of Cr.

In accordance to previous studies [6,9], these peaks can be attributed to two different forms of Cr(VI) species that reduce to Cr(III) cations. In particular, in Ref. [9] the authors relate the peak Ic to redox reactions between Cr(VI) - Cr(III) species entrapped into the passive film, whereas the peak IIc can be simply attributed to reduction of chromate to chromium hydroxide $Cr(OH)_3$ that precipitates on the top of the surface layer.

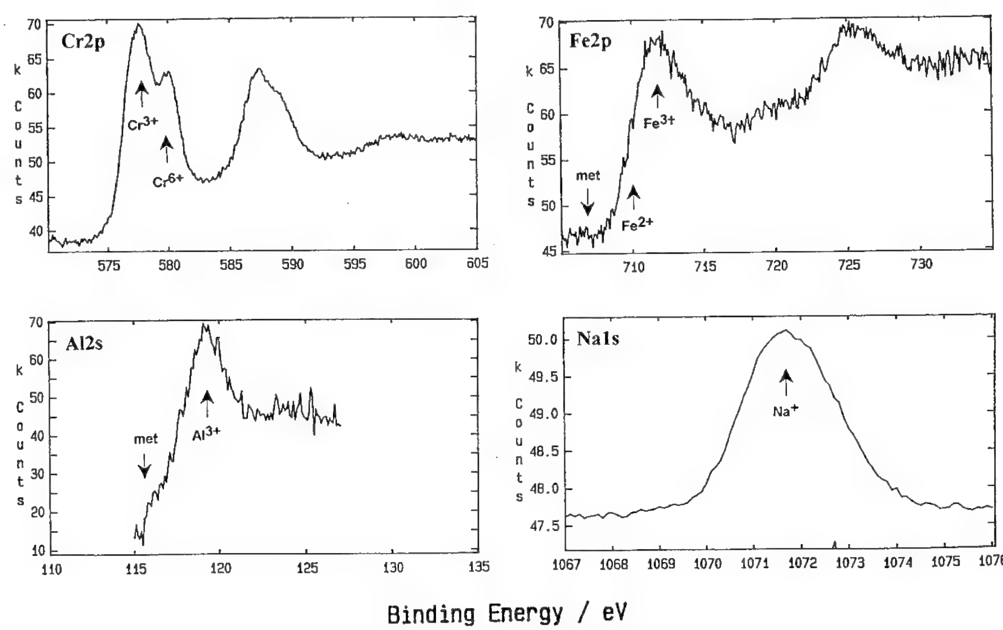

Figure 2 - XPS spectra for Cr 2p, Fe 2p, Al 2s and Na 1s electrons of passivated FeAl alloy after CV in chromate solution.

XPS data

Fig. 2 shows XPS spectra of the cations present in the chromium modified passive film of the FeAl alloy. The Fe 2p spectrum indicates that iron is prevalently present as Fe(III) cation. The peak position centered at about 711.5 eV suggests a major contribution of iron hydroxides with respect to oxides [16]. The Cr 2p spectrum shows a doublet due to Cr $2p_{3/2}$ and Cr $2p_{1/2}$ peaks. The Cr $2p_{3/2}$ signal permits to distinguish two different chromium species. Thus, the peaks at 577.5 and at 580 eV can be assigned to Cr(III) of Cr_2O_3 + $Cr(OH)_3$ and Cr(VI) of CrO_4^{--}, respectively. The positions of the two Al 2s peaks correspond to those assigned usually to metallic aluminum and to Al(III) of Al_2O_3. Finally, the Na 1s signal is obviously due to Na_2CrO_4.
A summary of the XPS quantitative analysis is reported in Table 1.

Table 1 - Chemical composition (at%) of the FeAl passive film formed after CV in chromate solution.

O^{2-}	71.6
Cr^{6+}	3.4
Cr^{3+}	6.1
Na^{+}	13.7
Fe^{3+}	1.9
Al^{3+}	3.3
Cr/(Fe+Cr+Al)	0.53
(Cr + Al)/(Fe + Cr + Al)	0.83

It is evident that Cr (as Cr(III)) is the predominant cation present in the passive film. Consequently, it can be said that cyclic voltammetry in chromate solution was effective for incorporating chromium into the passive film. The extent of Cr concentration expressed as atomic ratio Cr/(Fe+Cr+Al) is lower than that usually found on Fe-Cr alloys [4,15]. If we consider that Cr and Al are elements less noble than iron with a higher passivating ability than iron in slightly alkaline solutions, it seems more appropriate to discuss the protective characteristics of the passive film in terms of the sum (Cr + Al). The atomic ratio (Cr + Al)/(Cr + Fe + Al) is found to be approximately 0.83, which is very similar to the Cr/(Cr + Fe) values reported in the case of Fe-Cr steels with 24wt% of Cr [15].

Pitting corrosion tests
Pitting corrosion resistance of modified FeAl electrodes was evaluated from polarization curves. Comparative curves were run at 1mV/s in borate buffer + 0.05≤ NaCl ≤0.5M at 30 C on three types of electrode: (a) FeAl specimens polarized in absence of any pre-treatment: "blank specimens"; (b) FeAl after cycling in alkaline chromate solution and (c) FeAl after cycling in NaOH.
Fig. 3 shows the effects of the voltammetric cycling on the pitting nucleation potentials (E_{np}) in borate + 0.5M NaCl solution. It is evident that the potential cycling in NaOH exherts only a minor effect on the stabilization of the passive film with respect to the blank condition. The effect of cycling becomes remarkable after the chromate treatment indicating clearly that the incorporation of Cr in the passive film plays a greaterl role for improving the resistance to localized passivity breakdown of FeAl alloy.
The dependence of the E_{np} of FeAl on the Cl^- concentration is shown in Fig. 4. Each point represents the average of at least three measurements. The highest pitting resistance is displayed after the chromate treatment. Enp shifts in the negative direction as the Cl^- concentration increases from 0.05 to 0.5M, exception made for the electrodes stabilized in chromate where E_{np} does not show appreciable variations in the range 0.1-0.5M. It is possible that crevice corrosion may have occurred during the polarization tests as suggested by a continuous raise of the current observed in most experiments.

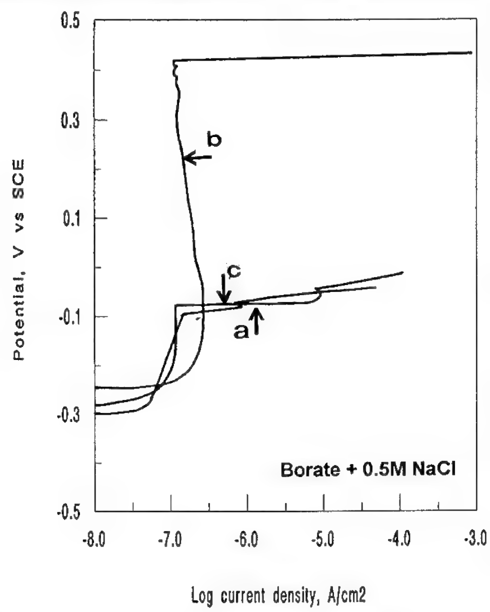

Figure 3 - Potentiodynamic polarization curves of FeAl specimens in borate + 0.5M NaCl: a) "blank"condition; b) after CV in chromate, c) after CV in NaOH. (scan rate 1mV/s, T=30°C).

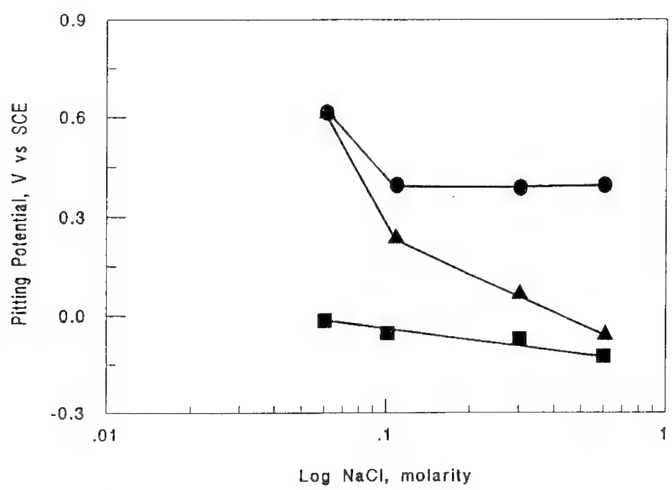

Figure 4 - Effect of Cl^- concentration on the pitting nucleation potentials (E_{np}) of FeAl (■ = "blank"; ● = after CV in chromate; ▲ = after CV in NaOH).

DISCUSSION

The results of this work indicate that incorporation of chromium into the passive film of a iron aluminide FeAl plays a beneficial role in improving the resistance to pitting breakdown.

The XPS analysis confirm that, during the running of cyclic voltammetry, chromate ions enter as Cr(III) in the mixed iron-aluminum oxide film of FeAl. Rather surprisingly, however, the XPS spectra indicate not only incorporation of Cr(III) into the passive film, but also presence of Cr(VI) as CrO_4^{2-}. It had been reported that only Cr(III) species are found in chromium modified films of iron and of stainless steels formed after cyclic voltammetry in chromate [6,14]. Calvo et al. [6] attribute the absence of Cr(VI) ions in the XPS spectra to a rapid redox reaction occurring between Fe(II) and Cr(VI) centers to form a mixed Fe(III)-Cr(III) oxide layer.

Our results, however, seem to find analogies with results observed for passivating films formed on aluminum in chromate solutions ([10]). In those cases, spectroscopic evidence of CrO_4^{2-} ions adsorbed on the top of oxide layers has been reported indicating that chromates are stable on the surface of aluminum oxides. Therefore, the explanation of the strong signal due to chromates in the XPS spectra of the passive film of FeAl may lie, in our opinion, in the fact that the amount of Fe ions in the modified FeAl passive film could be insufficient to reduce completely the chromate ions.

It has been shown in this work that pitting resistance of FeAl increases after incorporation of Cr in the passive film. It is interesting to note that pitting nucleation potentials of chromium-modified FeAl are similar to those reported in literature for binary Fe-Cr steels with a Cr content varying in the range 12-24 wt% [11]. However, the Cr content in the passive films of FeAl (expressed as ratio Cr / (Cr + Fe + Al) has been found to correspond only to that of a 10Cr ferritic steel [4]. But, if we consider the sum of Cr + Al we find a ratio (Cr + Al) / (Cr + Fe + Al) = 0.83 that is the same as reported for a 24Cr steel [15]. This means that a substantial part of Cr has been substituted by Al in the passive film composition without altering the pitting corrosion resistance of the alloy. From this result, it is argued that the pitting resistance of the intermetallic alloy FeAl is due to a combined effect of Cr and Al alloying elements in the structure and composition of the passive film.

With relevance to pitting breakdown, the results of the XPS analysis can be used also to predict the alloy composition with best pitting properties by using the Kirchheim model [4], which was

originally developed for explaining the Cr enrichment observed in the passive films of chromium steels. The model is based on the assumption that the composition of a passive layer is a direct consequence of the diffusivities of the cations present therein as well as of the composition of the base alloy. One of the theoretical implications of this model is that it allows to correlate the chemical composition of a passive film to the composition of the base alloy. In accordance to [4,5,12], it can be written:

$$(Al/Cr)_f=(Al/Cr)_a * D_{Cr}/D_{Al} \qquad (1)$$

where $(Al/Cr)_f$ indicates the atomic ratio experimentally determined in the passive film, $(Al/Cr)_a$ indicates the atomic ratio in the alloy and D_{Cr}/D_{Al} is the diffusivity ratio between Cr and Al cations in the film. By assuming for sake of simplicity that Al and Cr ions move in a matrix of iron oxide, the latter parameter may be roughly estimated using existing diffusion data of Cr and Al ions in a magnetite lattice at high temperatures [13]. It has been found that Al diffuses more rapidly than chromium resembling closely the behaviour of iron. The difference in the diffusion coefficients between Al and Cr were reported to be approximately one order of magnitude. This trend is consistent with our results in that we find a passive film in which Cr is the predominant cation. Hence, upon introduction of a reasonable value for $D_{Cr}/D_{Al} \sim 0.1$ in the eq. (1), an atomic ratio $(Al/Cr)_a$ of about 5 is found. With reference to a base composition Fe-40Al, this allows to predict that an alloy composition Fe-34Al-6Cr should have a comparable pitting resistance as chromium stainless steels.

CONCLUSIONS

Cyclic voltammetry in alkaline chromate solution provided an opportunity for simulating the effect of chromium alloying on the pitting behaviour of an iron aluminide FeAl alloy. The incorporation of chromium into the passive film gave values of pitting nucleation potentials comparable to those of Fe-Cr steels with a Cr content within the range 12-24%. On the other hand, the XPS results indicated that the enrichment with Cr corresponds only to that found in Fe-10Cr steels suggesting that the protective properties of the film are due to a synergistic action between Cr and Al. Based upon the use of the Kirchheim model, the bulk alloy composition in equilibrium with the composition of the chromium modified FeAl passive film has been predicted to be Fe-34Al-6Cr.

ACKNOWLEDGEMENTS

The authors wish to thank the Centro Sviluppo Materiali of Castel Romano (Rome) for the supply of iron aluminide material.

REFERENCES

[1] J. Olefjord, H. Fischmeister, Corros. Sci. 15, 697 (1975).

[2] K. Asami, K. Hashimoto, S. Shimoidaira, ibid. 18, 151 (1978).

[3] K. Hashimoto, K. Asami, K. Teramoto, ibid 19, 471 (1979).

[4] R. Kirchheim, B. Heine, H. Fischmeister, S. Hofmann, H. Knote and U. Stolz, ibid. 29, 899 (1989).

[5] A. Schneider, D. Kuron, S. Hoffman, R. Kircheim, ibid. 31, 191 (1990).

[6] E. J. Calvo, C. D. Pallotta, S. Hild, E. Garcia, J. Electrochem. Soc. 135, 314 (1988).

[7] S. Frangini, N. De Cristofaro, J. Lascovich, A. Mignone, Corros. Sci. 35, Nos.1-4, 153 (1993).

[8] K. Cho, C. H. Hwang, Y. S. Ryeom, C. S. Pak in "The Proceedings of the Fourth International Conference on Quenched Metals" (edited by T. Masumoto & K. Suzuki), The Japan Institute of Metals, Senday, Vol.II, 1479 (1982).

[9] E. J. Calvo, C. D. Pallotta, J. Electroanal. Chem. 198, 181 (1986).

[10] M. Koudelkova, J. Augustynski, H. Berthou, J. Electrochem. Soc. 124, 1165 (1977).

[11] J. Horvath, H. H. Uhlig, ibid. 115, 791 (1968).

[12] M. Janik-Czachor, Corros. Sci. 33, 1327 (1992).

[13] R. Dieckmann, T.O. Mason, J. D. Hodge, H. Schmalzried, Ber. Bunsenges. Phys. Chem. 82, 778 (1978).

[14] Z. Szlarska-Smialowska, R. W. Staehle, J. Electrochem. Soc. 121, 1146 (1974).

[15] S. Mischler, A. Vogel, H. J. Mathieu, D. Landolt, Corros. Sci. 32, 925 (1991).

[16] S Frangini, J. Lascovich, R. Giorgi, A. Mignone, Surf. Interf. Anal., 21, 435 (1994).

Materials Science Forum Vols. 185-188 (1995) pp. 1049-1056

Breakdown of passivity of Al-Mo glassy metals

M. Janik-Czachor[1], A. Wolowik[1] and Z. Werner[2]

[1] Institute of Physical Chemistry, Polish Academy of Sciences, Kasprzaka 44/52, PL-01-224 Warsaw, Poland

[2] Soltan Institute for Nuclear Studies, PL-05-400 Swierk, Poland

Keywords: Passivity, pitting, Al-Mo glassy metals, Al-base sputter deposited alloys, anodic behavior

Abstract

Anodic behavior of sputter deposited Al-Mo glassy alloys containing 15-45 at.% of Mo were investigated in 0.1-1M NaCl by using electrochemical, microscopic, and surface analytical methods. The alloys exhibited a stable passivity within a large potential region and eventually underwent breakdown at and above an anodic potential, which was about 1200mV higher than the corresponding pitting potential for Al metal. The pitting potential for Al-Mo glasses increased by ~200mV with a 10 at.% increase in Mo content and decreased by ~50mV with a tenfold increase of chloride concentration in the electrolyte. AES revealed the presence of oxidized Al, Mo and O within the passivating film. A tentative mechanism of pit nucleation in Al-Mo glasses is discussed.

Introduction

Mo is known for strongly enhancing pitting resistance of Al in chloride containing solutions [1-5]. Even small additions of Mo are extremely effective in Al because of the active nature of metallic Al. However, conventional methods of alloying are rather unsuitable here, as the melting point of Mo is above the boiling point of Al. Thus, two unconventional methods were used to form an alloy: ion implantation of Al with molybdenum ions and sputter deposition. Electrochemical investigations of Mo-implanted Al have revealed that Mo was incorporated into the passive film, resulting in a substantial increase in E_{np} [3,4] as compared with pure Al. The method of alloy formation by sputter deposition on a substrate appears suitable to form Al-Mo fine grained [5], or glassy alloys over a wide composition range [1,2]. This method is free of any deleterious effect of radiation damage caused by the ion bombardment during the implantation process. The corrosion resistance of the glassy alloys thus formed, as well as of a series of various Al-refractory metal alloys, were reported to depend strongly on composition and to be higher than that of pure Al metal [1,2]. The increased stability of the surface film on these alloys was ascribed to their homogeneous glassy structure, and in the case of Al-Mo glasses to the presence of Mo^{+4} species.

The aim of this work was to investigate anodic behavior of a series of sputter deposited Al-Mo glassy alloys in chloride containing electrolytes and to correlate the stability of their passive state with the composition of passivating films formed in these solutions.

Experimental

Materials used in the investigations were Al-Mo amorphous alloys obtained by a sputter deposition onto quartz glass substrates. The exposed surface area used was from $24 cm^2$ to $3.2 cm^2$. The alloys contained 15at.% to 45at.% Mo [*].

* *The materials were kindly donated by Prof. K. Hashimoto, Tohoku University*

Details concerning the fabrication procedure are given elsewhere [1]. The glassy nature of the samples was confirmed by X-ray diffraction. The samples before the electrochemical experiments were rinsed with methanol and subsequently with distilled water, and eventually dried in air. Optical and scanning electron microscopy were used to characterize the specimens before and after the experiments. Borate buffer solution with added chloride (from 0.05M up to 1M NaCl) were used for the electrochemical measurements. The electrolyte was de-aerated with pure argon. Potentiostatic and potentiodynamic (dE/dt=1V/h) experiments were performed to compare the anodic behaviour of various Al-Mo alloys. The potential was measured vs. SCE (saturated calomel electrode). Apparent pitting potential, E_{np}, was estimated from the anodic polarization curves. We are aware, however, that E_{np} may be some 100mV more positive than the true pitting potential [6-8], as discussed elsewhere[9].

Composition profiles of surface films on prepassivated Al-Mo alloys were measured with the aid of AES 500 Auger Electron Spectrometr (RIBER) [**] equipped with CI 50 (RIBER) Ar^{+} ion sputtering gun, at the following parameters: vacuum $<5\cdot10^{-10}$T, primary energy-2keV , modulation voltage 3V, electron current ~1μA at a beam spot of about ϕ30μm. Depth profiling was carried out with 4.5kV Ar^{+} ion beam.

Results

MICROSCOPIC EXAMINATIONS

As prepared samples were smooth and exhibited a metallic lustre. After the anodic polarization in a chloride containing solution, at sufficiently noble anodic potentials, localized activation/dissolution started. The pits thus formed were round, each with a characteristic tail of corrosion products (Fig.1), whereas the rest of the surface remained smooth and shiny.

ELECTROCHEMICAL MEASUREMENTS

a) Effect of alloy composition

E_{np} was up to ~1200mV more positive for the Al-Mo, depending upon alloy composition as compared to the corresponding value for Al metal [10-12].

The effect of Mo in the alloy was to increase E_{np} about 200mV per 10at.% increase in Mo content, as can be seen from Fig.2. The results are in a qualitative agreement with those reported by Frankel et al. [13] for supersaturated nanocrystalline alloys.

b) Effect of chloride concentration

Chloride concentration in solution did not affect E_{np} as much as it did for Al metal:

$\delta E_{np}/\delta lgCl_{Cl-}$ was about 50mV per decade for Al-Mo glasses, (Fig.3), whereas it was about 70mV per decade for Al metal [10-12].

c) Effect of anodization time

Fig.4 shows an example of i=f(t) curves during a series of subsequent anodizations (three times) of Al-Mo glassy alloy at E=const.<E_{np} in 1M NaCl. During the first anodization a steady state current was achieved quite soon. At the beginning of the second and third runs the current decreased due to film reconstruction/formation. However, after a certain time it increased, probably due to a corrosion/dissolution process, and eventually attained the steady state value. At lower chloride concentrations in the solution the first anodization started with a current decrease /film formation/reconstruction. After some time current increased, in a qualitative agreement with the curve shapes II and III in Fig.4. The subsequent anodizations resulted in a similar behavior, but the current was generally lower at any instant.

** *Kindly donated by Alexander von Humboldt Foundation (to MJC).*

SURFACE ANALYTICAL MEASUREMENTS

Fig.5 shows two typical examples of Auger spectra for a passivated Al-Mo sample before sputtering (a) and after a nearly complete sputtering away of the passivating film (45 min. sputtering,(b)). The following features can be distinguished in spectrum (a) : Al low energy doublet at ~35eV and ~56eV indicative of Al_2O_3-like configuration, Mo low energy peak at 28eV and three prominent Mo peaks at 161eV, 186eV and 221eV, as well as C (273eV) and O(510eV). Due to the overlap of 181eV Cl Auger signal with that of Mo one at 186eV, any definite conclusion concerning the presence of chloride could not be made at this point. In the spectrum (b) the C signal is absent, the O signal is quite small and Al and Mo signals are much larger than in the spectrum (a). Low energy Mo signal at 28eV is visible in both spectra; no distinct change in the peak shape or position could be detected here. On the other hand the shape of the low energy Al signals in spectrum (a), and (b) are quite different reflecting the chemical effect of transition from oxidized Al^{ox} within the passivating film (a) to metallic Al within the matrix (b); see detailed discussion in ref.[9].

Fig.6 shows depth composition profiles of a passivating film after passivation during 5 min. or 90 min. Aluminium is clearly enriched within the film, Fig.6a, whereas molybdenum content is at a lower concentration level than that within the matrix. This finding is in agreement with the results obtained for thick anodic films formed on Al-Mo glassy alloys sputter deposited on Al substrate [14]. The O signal in Fig.6 is also gradually diminishing and there seems to be a correlation between the O and Al^{ox} signals suggesting a chemical bonding of both elements within the film. It is unfortunately not possible to draw a similar conclusion concerning Mo as the chemical effects in the Auger spectra of Mo are too small to be detected. Therefore, one can only speculate that the mixed $(Al,Mo)O_x$ oxide is probably responsible for a higher resistance of Al-Mo alloys against pitting in chloride solutions and for an enhanced stability of the passivating film thus formed, in general. The effect of time is to increase film thickness and also the amount of oxygen with respect to that of the metallic components as can be seen from O/Al and O/Mo (186eV) depth profiles in Fig.6a and 6b.

Discussion

A question arises what is the mechanism of pit initiation in homogenous sputter deposited glassy alloy. Electrochemical investigations suggest a chemical breakdown of passivity, although $\delta Enp/\delta lgC_{Cl-}$ for Al-Mo glasses (Fig.3) is lower than for Al metal [10-12]. It is quite possible than some micro-inhomogeneities, both chemical and structural, exist within the sputter deposited glass [15] thus facilitating local chloride agglomeration and the subsequent film thinning and removal suggested by Heusler [16]. The present results infer that Mo strongly restrains pit formation by shifting E_{np} over 1V as compared to Al metal. The mixed $(Al,Mo)O_x$ oxide is probably responsible for a high resistance of Al-Mo alloys against pitting in chloride solutions and for an enhanced stability of the passivating film thus formed. Moreover, Mo in the alloy apparently makes the effect of chloride concentration less pronounced than it is for crystalline metals [17], see the results in Fig.5, where $\delta E_{np}/\delta lgC_{Cl-}$ is only about 50mV. As it is known, Mo compounds with chloride ions are insoluble [18]. It is possible that their precipitation at the surface during the anodic process reduces the aggressive activity of chloride ions for the local film thinning/dissolution; the mechanism already suggested for Fe-Cr base, Mo bearing alloys[18]. This process may also affect the pit growth; indeed "a tail" of corrosion products was observed at each pit (Fig.1) thus formed. The circular shape of pits, even when they are quite small ($\phi<1\mu m$) suggests that the mechanism of localization dissolution operative for crystalline Al [19,20] as well as for Fe and Fe alloys [21-23] is also valid here. However, true c.d. at the "active" pit area is extremely high for the sputter deposited alloys/metals. Frankel et al. [13]

measured values of 5-40A/cm² during pitting of Al or Al-base supersaturated alloys, which is much above the values measured for Fe [21] and its alloys [24]. Isotropic localized dissolution is apparently supported, for the above mentioned small pits, by the amorphous structure of the matrix, so that no "channels" or anisotropic pits are formed, in contrast to the observations made for crystalline metals [10,23] in the early stage of pitting. Frankel et al. [13] found that the E'_{np} of Al-Mo and many other sputter deposited nanocrystaline Al alloys were far higher than that for pure Al. However, they were only slightly higher than the repassivation potentials for the given alloys. The authors thus concluded that pit growth considerations played a much larger role than passive film effect in the pitting process for these alloys. They pointed out that:

- their measurements of repassivation potentials provided a direct causal link between the influence of alloying on pit growth considerations and the elevation of E_{np};
- their data suggested that changes in the passive film chemistry as a result of alloying were much less important .

While it is true that the addition of more noble elements to Al, which is extremely active, may ennoble dissolution process, resulting in the need for higher potentials to achieve a given current density [13], one should take into account that so called "stainless Al" was obtained by using a procedure including a chemical pretreatment involving molybdate ions in solution only [25,26]. Hence, in the latter case only modification of the surface passivating film did occur.

Conclusions

1. Electrochemical measurements showed that Al-Mo sputter deposited glassy alloys in NaCl containing solutions exhibited a stable passivity within a large potential range. AES investigations suggested presence of oxidized Al as well as Mo and O within the passivating film.

2. Pitting potential for these glasses decreased by some ~50mV with a tenfold increase of chloride concentration in the electrolyte,suggesting not only chemical but also structural effect in the breakdown process.

3. Pitting potential increased by ~200mV with a 10at.% increase of Mo content in the glass and was over 1200mV higher than a corresponding value for Al metal.
The pronounced beneficial effect of Mo was probably due to:
- its presence as the film's component thus increasing the films stability
- formation of some insoluble compounds with chloride which may reduce the effective amount of the aggressive Cl- species at the surface.

Acknowledgements

One of the authors (MJC) is most grateful to the Alexander von Humboldt Foundation for a generous gift, the Spectrometer AES 500 (RIBER), and to Professor K. Hashimoto for kindly donating a series of Al-Mo sputter deposited glassy metals.
This work has been supported by grants GW/XVI.1/93 and KBN 3 P407 041 06.

References

[1] H. Yoshioka, A. Kawashima, A. Asami, K. Hashimoto, in Proc International MRS Conference on Advanced Materials (Eds: S. Somiya, M. Doyama, R. P. Chang) vol.**3**, p.429. Materials Research Soc., Pittsburg 1989.
[2] H. Yoshioka, H. Habazaki, A. Kawashima, A. Asami, K. Hashimoto, Corr. Sci. **32**,313 and

327 (1991).
[3] P.M. Natishan, E. McCafferty, G. K. Hubler, J. Electrochem. Soc. **133**, 1061 (1986)
[4] A. H. Al-Saffar, V. Ashworth, A. K. O. Bairamow, D. J. Chivers, W. A. Grant, R. P. M. Procter, Corr. Sci. **20**, 127 (1980).
[5] W. C. Mosher, G. D. Davies, J. S. Ahearn, H. F. Hongh, J. Electrochem. Soc. **137**, 1063 (1986).
[6] M. Janik-Czachor, Corr. **49**,10 (1993).
[7] M. Janik-Czachor, Werkst. Korros. **31**,606 (1980).
[8] A. Broli, H. Holtan, M. Midjo, Brit. Corr. J. **8**, 173 (1973).
[9] M. Janik-Czachor, A. Wolowik, Z. Werner, Corros. Sci., submitted.
[10] H. Kaesche: in " Localized Corrosion", **NACE** -3 Ed. R. W. Stachle B. Brown, J. Kruger, A. Agrawal, Houston , (1974) p.516
[11] H. Bohni, H. H. Uhlig, Corros. Sci., **9**, 329 (1969).
[12] H. Kaesche, Z. phys. Chem. N. F., **34**, 87 (1962).
[13] G. S. Frankel, R. C. Newman, C. V. Jahnes and M. A. Russak, J. Electrochem. Soc., **140**, 2194 (1993).
[14] G. E. Thompson, G. C. Wood, P. Skeldon, H. Habazaki, private comunication.
[15] M. Dahlborg, paper presented at the International School "Physics for Materials Science", Jaszowiec 1993 published in Nucleonica **39**,47 (1994).
[16] K. E. Heusler, L. Fisher, Werkst. Korros. **27**, 550, 697 and 780 (1976).
[17] M. Janik-Czachor, J. Electrochem. Soc. **128**, 513C (1981).
[18] A. Schneider, S. Hofmann, R. Kirchheim, Werkst. Korros. **42**, 167 (1991).
[19] H. Kaeshe, in "Korrosion der Metalle" Springer Vlg., 264 (1991), p.264.
[20] H. Kaeshe, Z. phys. Chem. N. F. **26**, 138 (1960) and **34**, 264 (1962).
[21] H. J. Engell, N. D. Stolica, Z. phys. Chem. N. F. **20**, 113 (1959).
[22] H. J. Engell, G. Herbsleb, Z. phys. Chem. **215**,167 (1960).
[23] M. Janik-Czachor, Z. Szklarska-Smialowska, Corros. Sci. **8**, 215 (1968).
[24] M. Janik-Czachor, Z. Szklarska-Smialowska, Brit. Corr. J. **4**,138 (169).
[25] F. Mansfeld, Y. Wang, European Symposium "Modification of Passive Films", Paris 1993.
[26] F. Mansfeld, Y. Wang, H. Shih, Electrochim. Acta **73**, 2277 (1992).

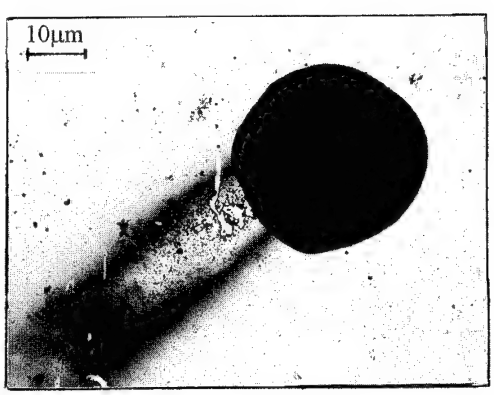

Fig. 1 Typical round shaped corrosion pit. formed in Al75-Mo25 glassy alloy during anodic polarization in 1M NaCl.

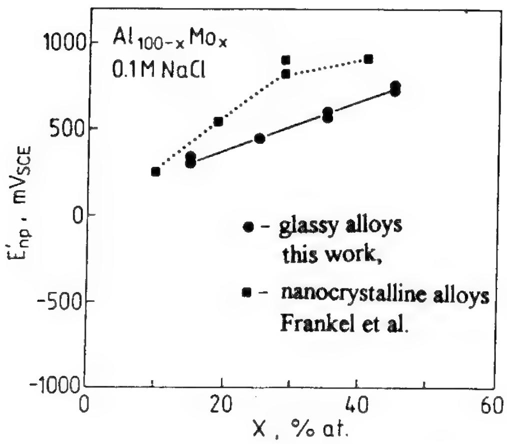

Fig.2 Effect of Mo content in Al-Mo sputter deposited glasses on apparent pit nucleation potential, E'_{np}
- this work, glassy alloys
- Frankel et al. [13], supersaturated nano-crystalline alloys.

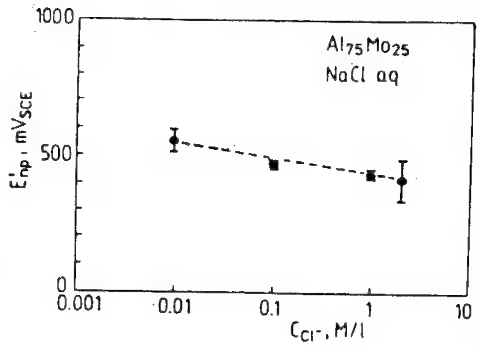

Fig.3 Effect of chloride concentration on apparent pit nucleation potential, E'_{np}, for Al75-Mo25 sputter deposited glassy alloy.

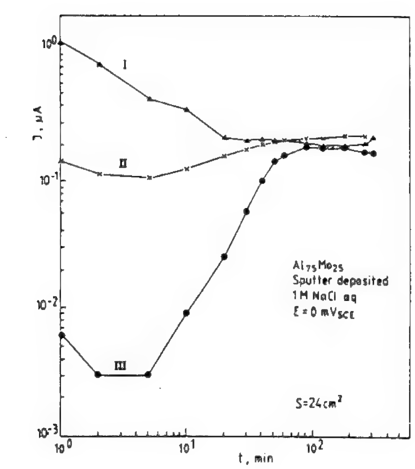

Fig.4 Effect of anodization time of Al-Mo glassy alloy on the anodic current at E=const., I-first anodization, II and III - subsequent anodizations at the specimen after rinsing with distilled water and drying.

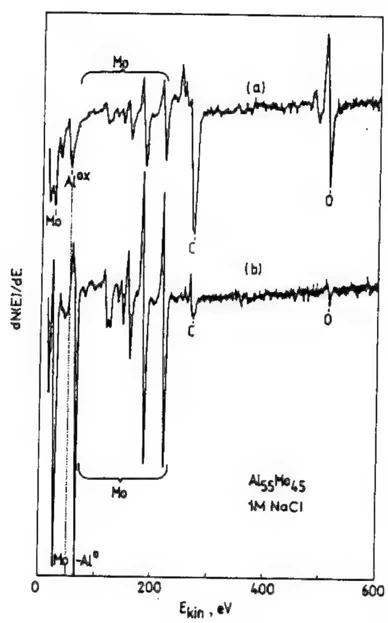

Fig.5 Typical Auger spectra Al55-Mo45 glassy alloy prepassivated 150 min. in 1M NaCl
(a) before sputtering
(b) at the termination of sputtering, 45min

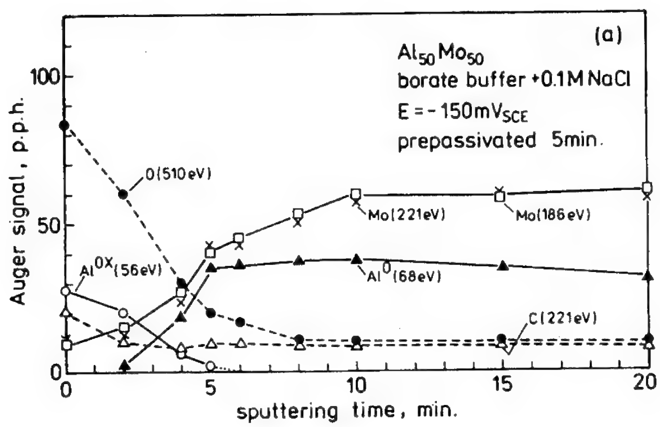

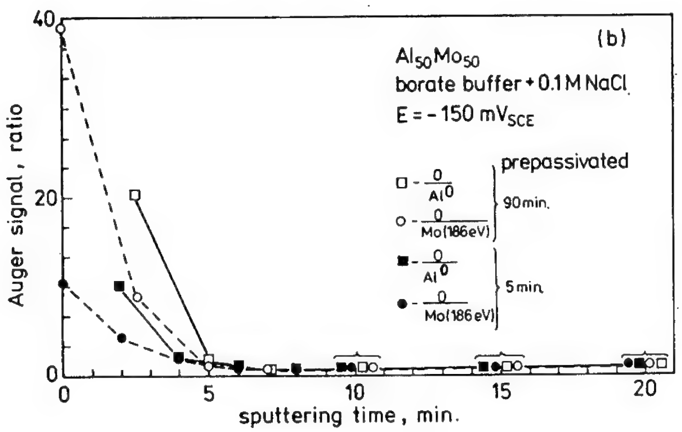

Fig.6 Effect of anodization time on the compositions profiles of passivating films formed at Al50-Mo50 glassy alloy in borate buffer + 0.1M NaCl, at E=-150mV

(a) after 5 min. prepassivation

(b) after 5 min .[from (a)], and 90 min. prepassivation. Relative O/Al^{O}, O/Mo^{O}, [p.p.h.] values vs. time are given for a clarity.

Materials Science Forum Vols. 185-188 (1995) pp. 1057-1064

Relationship between human perception and breakdown of passivity

I. Muto and H. Kihira

Steel Laboratories, Nippon Steel Corporation, 20-1, Shintomi Futtsu Chiba-ken, 293, Japan

Keywords: Breakdown of passivity, evaluation, staining, stainless steel, human perception

Abstract

By classifying hundreds of model rusted panels drawn by a computer into five dirtiness levels, it was found that relationship between human perception and passivity breakdown was characterized as a function of spot density and its area ratio. This method was applied to evaluate the evolution of rust on stained stainless steels, and the following became clarified:

1) At the initial stage of corrosion, number of small pits increases with exposure time.

2) In the middle stage, area of stained spots grows.

and, 3) At the last stage, expansion of rusty dots resulted in merging of the stains.

The behavior could be expressed on the spot density *vs.* area ratio chart in such a way that a point moves from the origin to upper right direction in a linear manner at the initial stage, horizontally right in the middle, and then down right at the last. Different typical trajectories were obtained for type 304 and 430 stainless steels in the same condition of cyclic corrosion test, which seemed to be originated from the nature of alloying elements.

Introduction

It is becoming popular to use stainless steels in architectural application. Roofs and walls of recently constructed buildings often consist of stainless steels with variety of compositions. Corrosion resistances of this type of alloys are due to the passive films mainly composed of chromium oxyhydroxides. Breakdown of passivity, by which staining of the surface may start, depends on corrosiveness of the atmosphere. In order not to fail in the selection of stainless steels, it is extremely important to match the materials to the environment, which could be more precise when proper evaluation method of rusting is established.

Conventionally, the weathering properties of stainless steels have been ranked based on so-called rating number methods, which is either the evaluation of area ratio of rusted portion over entire surface in logarithmic manner, or the comparison of their dirtiness with standard panels of different levels of rusting. The former, in which the rating is determined mostly based upon the following equation [1,2] with R rating number and A area ratio of rust;

$$R=3(2-\log_{10}A) \quad (1)$$

often mismatches sensually judged dirtiness, while the latter metod is not very quantitative, or sometimes too empirical. Thus it is necessary to clarify the relationship between human perception and rust evolution during passivity breakdown on the stainless steels exposed to the atmosphere with aid of sensual evaluation technique [3].

Experimental

<Classification of Dirtiness>

The model panels were prepared in such a way that closed circles of reddish brown with certain radius were plotted on a sheet of 100 x 100 mm^2 clean white paper by XY–Plotter (HP, ColorPro) so that stained area ratios and spot densities were varied from 0 to 1.8% and 0 to 100 per dm^2, respectively.Total of 108 different model panels were prepared. For simplicity, the same function to generate random number for determining positions of circles was used, and the same radius was applied to each model panel. Parameters for the random number generation were chosen to distribute the spots so that no enhanced segregation was observed. Note that the range of the presently designed area ratios corresponds to that between R = 5 and 10 according to ISO and JIS standards [1,2]. Samples of so drawn model panels were shown in Fig.1. The area of each circle was measured using microscope, which was added to calculate the area ratio.

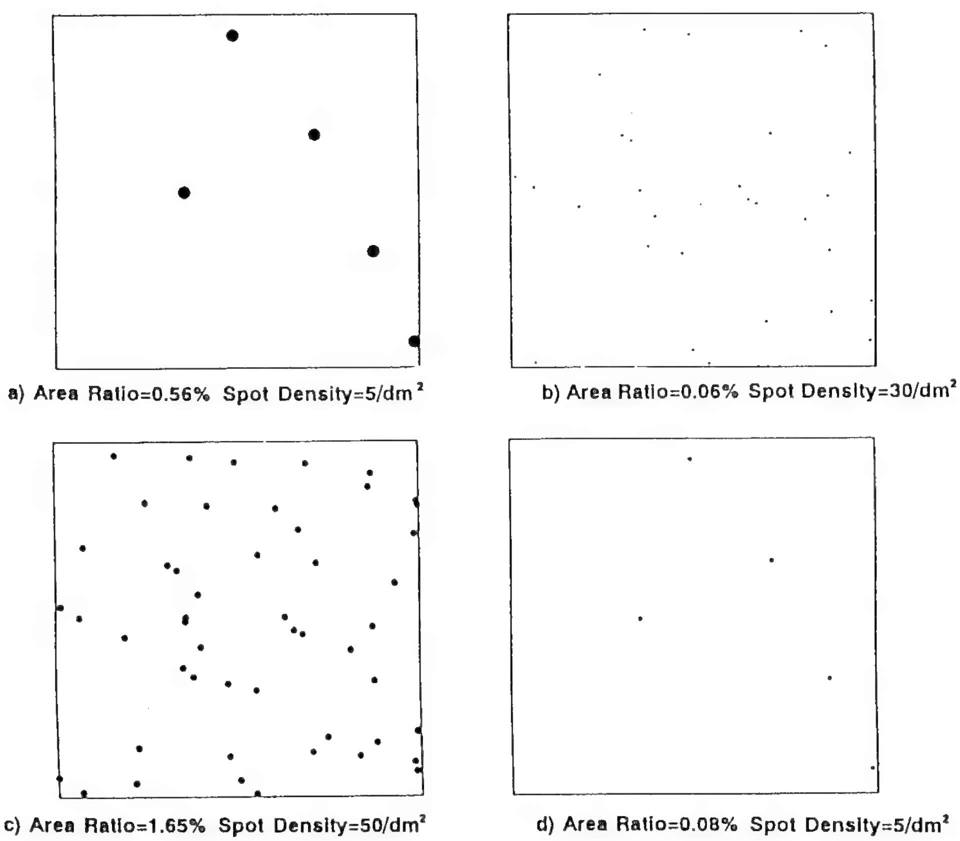

Figure 1. Examples of the model panels drawn by a computer. a) area ratio = 0.56% and spot density = 5/dm^2, b) 0.06%, 30/dm^2, c) 1.65%, 50/dm^2, d) 0.08%, 5/dm^2.

The model panels prepared were designated as open circles in Fig. 2, in which four standard rusting panels were chosen as shown by stars. Two persons, who were not relevant to this research project, classified these 108 panels into five dirtiness levels according to their perception within ten minutes.

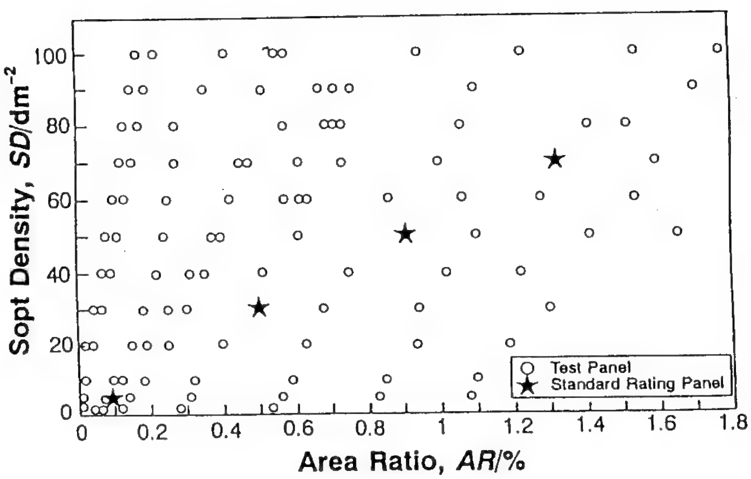

Figure. 2 Parameter map of prepared model panels as a function of spot density and area ratio.

<Image Analysis of Rusting on Stainless Steel>

Commercially available stainless steels of SUS304 and SUS430 were used for image analyses of rusting behavior. Surface of each specimen, which size is 75 x 75 mm^2, was wet polished by #1500 silicon carbide paper. In order to simulate a coastal environment, cyclic corrosion test were performed by use of the Suga ST–12L–CYH equipment in which the following sequence was repeated for 60 times: 1) Spraying synthetic sea water at 305 K for 4 h, 2) Drying at 333 K for 2 h, 3) Humidifying at 323 K with relative humidity more than 95% for 2 h.

Patterns of rusted surfaces were analyzed using black and white type of image analyzer (Mitani SUPER ASPECT ver.1.50L) combined with a CCD camera. The rust area ratios and the spot densities were measured within a central part of 50 x 50 mm^2 for each specimen surface. Resolution power of this instrument was 0.24 mm in length, which corresponded to 0.057 mm^2 as area.

Results and Discussion

< Relationship Between Human Perception and Rating >

Classification of the model panels into 5 dirtiness levels by two persons resulted in the same trend as in Fig. 3, which shows that each dirtiness level composes a diagonal band in the area ratio – spot density chart. This means that the case with

many small spots and that with a few large dots irritate human senses at the same intensity, and that the conventional rating method may have to be re-investigated.

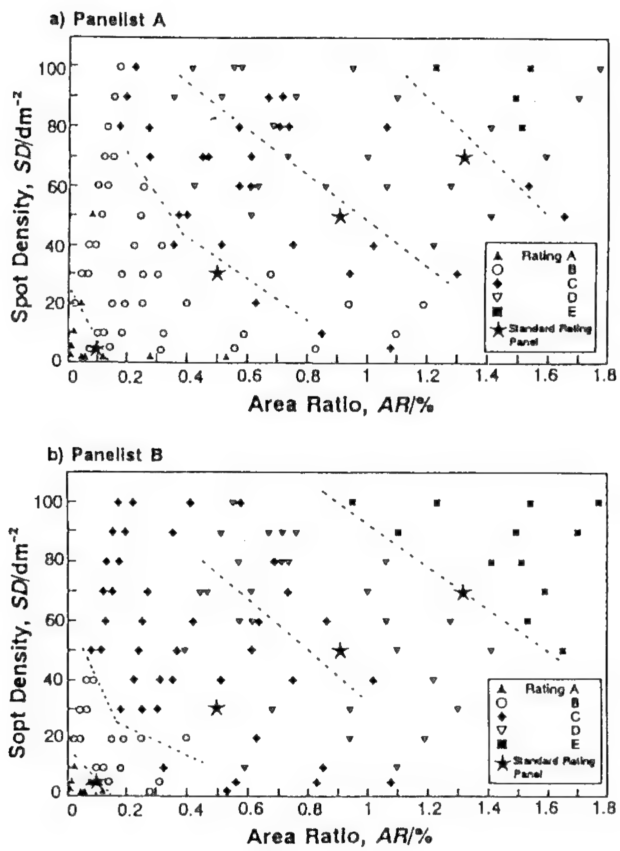

Figure 3. Sensual classification of model panels into five dirtiness levels. a) done by Panelist A with carrier in corrosion research for more than 10 years, and b) by B with less than a year.

< Evolution of Rust on Stainless Steel >

Sixteen samples of each kind of alloy were installed in the cyclic corrosion test equipment, and they were taken out one by one after designated cycles. Digitized pictures for rusted surfaces of SUS 304 and SUS 430 are shown in Fig. 4. The area ratio *v.s.* spot density charts for these steels were obtained by image analyses as shown in Figs. 5 and 6, respectively. Note that the slope of a line through origin of this diagram indicates average area of rusty spots: It is meaningful to mention that if number of dots increases without enlarging their sizes, the trajectory should follow a direct line through the origin, which is often observed at the initial stage of staining.

From both Figs.5 and 6, it is clear that the same trend is observed in such a way

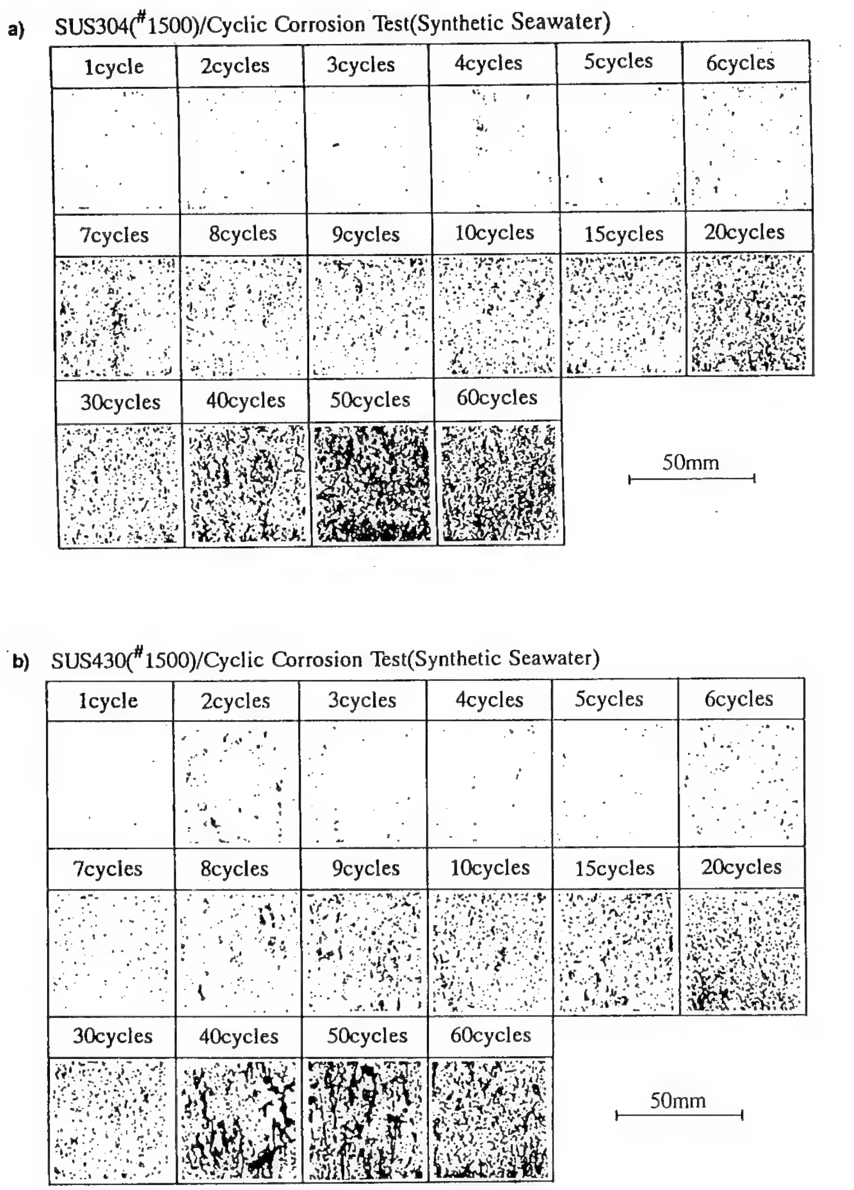

Figure 4. Digitized pictures for rust evolution of stainless steels during cyclic corrosion test. a) SUS 304, b) SUS 430.

that the trajectory moves from the origin toward up right direction, then horizontally right, and down right. This indicates the nature of passivity breakdown and evolution of rust in the following manner:

1) At the initial stage of corrosion, number of small pits increases with time.

2) In the middle stage, area of stained spots grows.

and, 3) At the last stage, expansion of rusty dots resulted in merging of the stains.

It is also interesting to notice that the peak points in Figs. 5 and 6 show characteristic feature of corrosion for austenitic and ferritic stainless steels, namely many small pits tend to occur on the former, and a few large on the latter.

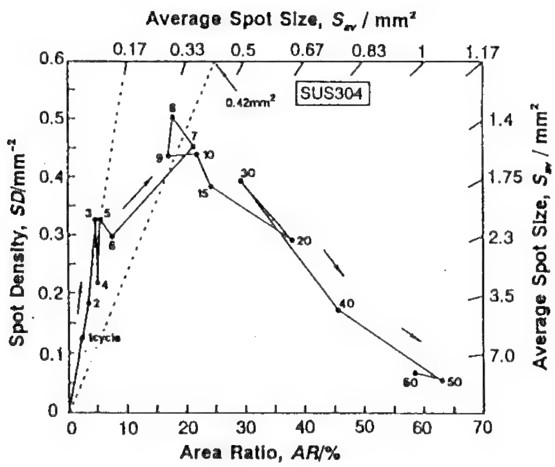

Figure 5. Area ratio *v.s.* spot density chart for SUS 304 stainless steel rusted by cyclic corrosion test.

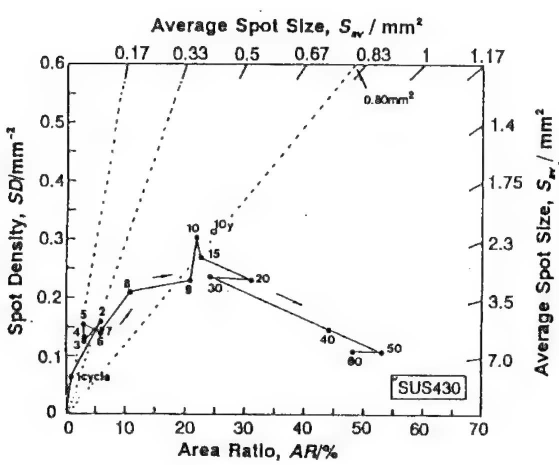

Figure 6. Area ratio *v.s.* spot density chart for SUS 430 stainless steel rusted by cyclic corrosion test.

Conclusion

It was indicated from model panel classification, that not only rust area ratio but also spot density must be taken into account in order to correlate human perception and breakdown of passivity.

The behavior of rust evolution on stainless steels could be characterized using the area ratio *v.s.* spot density chart by image analyses of stained surfaces.

References

[1] Metallic and other non–organic coatings, ISO Standard Handbook **20**, p100, p314(1984).

[2] JIS Hand Book, Surface Treatment, Japan Industrial Standard Association (1993).

[3] K. Noro, *Kan–nou Kensa Guid Book*, Japan Industrial Standard Association (1987).

Materials Science Forum Vols. 185-188 (1995) pp. 1065-1074

Light induced inhibition of local passivity breakdown

P. Schmuki and H. Böhni

Institute of Materials Chemistry and Corrosion, Swiss Federal Institute of Technology, ETH-Hönggerberg, CH-8093 Zürich, Switzerland

Keywords: photoelectrochemistry, passivity breakdown, pitting corrosion, light inhibition

Abstract

Light induced effects on passivity and the initiation of pitting corrosion on pure iron in borate buffer pH 8.4 is studied. By illuminating the sample with monochromatic (325nm) light a very strong increase in the pitting corrosion resistance - apparent from pitting potential and incubation time measurements in the chloride containing electrolyte - can be observed. This effect is strongly dependent on the light intensity. The cause for the decreased pitting susceptibility is not based on a change in the field distribution within the passive film, but is much more associated with light induced changes in the passive film properties during passivation. These changes cannot be attributed to a film thickening caused by illumination. The electronic properties of the passive films were studied by Mott-Schottky analysis, photocurrent transient and photoimpedance measurements. The results indicate that illumination during passivation leads to modifications of the film which are reflected in their electronic properties - specifically to an increase of the surface state density. Since surface states on passive films on iron can be associated with the adsorption of hydroxyl-ions, a possible reason for the improved pitting resistance might be - in terms of the competitive Cl^-/OH^- adsorption model - a suppression of Cl^- adsorption on the oxide surface.

Introduction

Passive films on most metals and alloys exhibit a semiconducting behaviour. Therefore in recent years a variety of experimental techniques have been applied for the study of the electronic properties of passive films. Apart from capacitance measurements of the Mott-Schottky type [1-9] most commonly photoelectrochemical methods were successfully used to determine important semiconductor parameters [9-13]. A number of models and concepts have been elaborated which correlate the semiconductive nature of passive films to their resistance against uniform and localized corrosion [9, 14-17].

In case of bulk semiconductors illumination not only can be used as a tool for characterization but it can have a significant influence on the chemical reactivity of semiconductor surfaces [1]. However, for passive films only little attention has been paid on the question if and how illumination can alter the film properties and hence can lead to changes in the corrosion resistance of the material. For copper it has been reported in literature that illumination can lead to a photoreduction of the oxide film [18]. For nickel a photo-inhibition of pitting corrosion has been found by Macdonald et. al. [19-22]. Within this work a series of experiments with pure iron in borate buffer solution pH 8.4 were carried out to evaluate light effects on the initiation of pitting corrosion. The Fe/borate system was selected because it forms passive films with a comparably high absorption coefficient for light with a energy higher than the band gap energy ($E_g \approx 1.9$ eV) [9-13] and because its electrochemical and corrosion behaviour is already relatively well known [23].

Experimental

All experiments were carried out on pure iron wires (>99.9%) with a diameter of 1mm. The wires were embedded in a three-component acrylic resin (Triofix, Struers) leaving an area of 0.785 mm^2 exposed to the environment. The samples were mechanically polished with SiC emery paper up to

grit 4000 and finally with diamond paste (1 μm), then rinsed and sonicated with distilled water and ethanol. After this procedure the samples were placed 2.00 mm from the quartz glass window (Suprasil II) of an electrochemical cell equipped with a platinum gauge as a counter electrode and a saturated calomel electrode (SCE) in a Haber-Luggin capillary. As electrolyte a borate buffer pH 8.4 (0.075 M $Na_2B_4O_7 \cdot 10\ H_2O$, 0.3 M H_3BO_3) was used to which in pitting experiments NaCl solution was added. The solutions were deaerated with N_2 during the measurements. Prior to all experiments the samples were cathodically polarized at -1000 mV SCE for 2min in order to remove the air formed oxide films.

As a light source for the illumination as well as for photoelectrochemical measurements a HeCd-LASER which provides a continuous 325 nm line and an output power of 5 mW was employed. The beam of the LASER is focused to a spot onto the sample surface. The electrochemical cell is mounted on an xyz stage and by a movement along the z direction it is possible to adjust the LASER spot size. In illumination experiments the spot size was set to 1.5mm to ensure an almost uniform intensity profile over the whole surface of the sample (sample diameter = 1 mm). This procedure led to a maximum applicable power density of 300mW/cm^2. A description of the measurement of the intensity distribution and the definition of the beam diameter is given elsewhere [17]. To vary the intensity of the laser irradiation neutral filters of different attenuation factors were placed in the beam. In photo impedance measurements a chopper is set in the light beam and using the lock-in technique it is possible to acquire the magnitude and the phase shift (relative to the chopper reference signal) of the photocurrent in dependence of the chopper frequency. If the photocurrent signal is large enough - compared to the passive current - the system response on a photopulse can directly be recorded e.g. by an oscilloscope. In such experiments no lock-in amplifier is needed and the chopper is replaced by an optical shutter system. These phototransient experiments were performed with a 450 μm diameter LASER spot, located in the center of the sample.
Potentiodynamic polarization curves were registered by superimposing the signal of a programmable voltage source to the compensation input of the potentiostat using a sweep rate of 1mV/5s. Galvanostatic and potentiodynamic reduction curves were recorded by the same equipment but in the potentiodynamic case with a sweep rate of 1 mV/s. Mott-Schottky type of AC Impedance investigations were performed with a Schlumberger Solartron ECI 1286 / FRA1250 set up controlled by a PC using a 1000Hz, +/- 10mV AC signal and a sweep rate of 20mV/30s.

Results and Discussion

1. Light effect on susceptibility to pitting corrosion

Fig. 1 shows the potentiodynamic polarisation curves of iron measured in borate buffer + 0.01 M NaCl with and without illumination of the sample. From the steep increase of the current densities the potential of stable pit growth - the pitting potential - can be determined. It is obvious that the pitting potential of iron is shifted by more than 700 mV in the positive direction when the measurement is carried out under illumination.

Further the effect of the LASER illumination on the incubation time of pitting corrosion was studied (Fig. 2). The samples were first passivated at 600 mV SCE in the borate buffer for 20 minutes and then NaCl was added to the solution to establish a 0.01 M chloride concentration. Within this study the incubation time was defined as the time period from chloride-addition until significant current transient activity could be detected - indicating the occurrence of metastable pitting (Fig. 2). This definition was chosen since the onset of metastable pitting is much more associated with the very early initiation stages of pitting corrosion than the occurrence of stable pit growth which is often affected and controlled by a number of factors [24,25].

From the experiment carried out in dark an incubation time of ≈9 minutes can be determined. Under the same conditions the illuminated sample does not show any breakdown event until the experiment was stopped after 12 h. Fig. 3 shows the results of a series of experiments in which the incubation

time as a function of the light intensity for two different chloride concentrations was studied. It can be seen that with higher light intensities a massive increase in the incubation time can be observed.

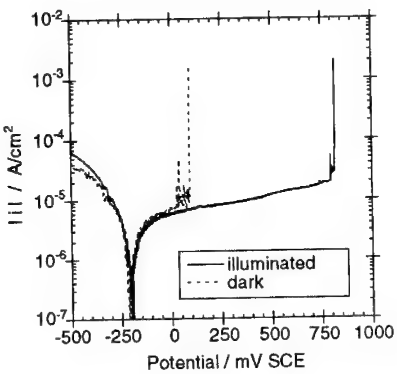

Fig.1 Potentiodynamic polarization curves of Fe in borate buffer (pH 8.4) + 0.01M NaCl with and without illumination of the sample (λ= 325nm; P=300 mW/cm^2)

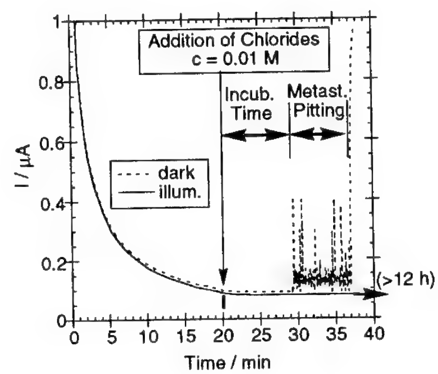

Fig. 2 Determination of the incubation time of pitting corrosion on iron in dark and under illumination.
Passivation in borate buffer, pH 8.4 for 20 min at U =+600 mV SCE followed by NaCl addition (0.01M)

A crucial point in the evaluation of possible causes for the light-inhibition of pitting corrosion is if illumination leads to changes of a permanent nature - meaning that the improved resistance still can be observed if the light is switched off - in this case illumination leads to a modification of the system properties. In the case of temporary changes - only effective during illumination - they can most likely be ascribed to light induced changes in the field distribution of the film. I.e. due to the semiconductive nature of the film illumination leads to the generation of electron/hole pairs, with the consequence that mainly the minority carrier concentration, that is in the case of an n-type semiconductor the hole concentration, is increased. Due to the non-crystalline film structure a high number of localized states is present in the band-gap which can act as traps for holes. This trapping of positive charge affects the band bending in the space charge region of the semiconductive layer and hence leads to a change in the field distribution [26] with the consequence that the field aided transport processes in the film are affected. According to all the Cl^- penetration models for pitting corrosion and particularly the point defect model a decrease in the field strength would lead to a retardation of migration effects as discussed in detail for the case of nickel [19,20].

Therefore, in order to evaluate if illumination causes system changes of a permanent or temporary nature, the incubation times were measured for different kind of light treatments (Fig. 4). In the first series of experiments the samples were kept under permanent illumination during the whole measurement sequence (as in Fig. 3). In the second series the samples were passivated for 20 minutes under illumination, then the light was switched off and the chlorides were added to the solution. In a third series of experiments the samples were passivated in dark for 20 minutes, then the light was switched on and chlorides were added. The results of Fig. 4 clearly show that for illuminated passivation followed by dark incubation the incubation times are identical to those observed for permanent illumination. On the other hand illumination only during the incubation period has no significant effect on the pitting corrosion resistance. Hence it is clear that illumination leads to permanent changes in the properties of the passive iron. An obvious explanation for such permanent changes would be a light supported film growth, which could be based on either a direct charge carrier participation in the growth mechanism or indirectly could be due to a change in the field distribution during film formation.

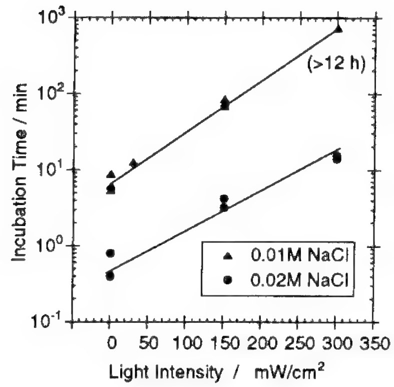

Fig. 3 Effect of the light intensity on the incubation time of pitting corrosion in borate buffer (pH 8.4) + 0.01 / 0.02M NaCl Passivation in borate buffer, pH 8.4 for 20min at U =+600 mV SCE followed by Cl^- addition

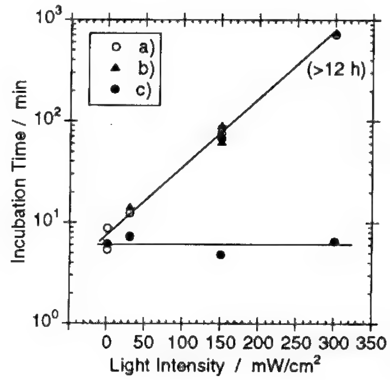

Fig. 4 Effect of light intensity on the incubation time with different kind of light treatments
a) permanent illumination (Fig. 3)
b) passivation under illumination dark incubation
c) passivation in dark incubation under illumination

2. Galvanostatic and potentiodynamic reduction curves

In order to clarify if the light-induced modification is due to changes in the film thickness galvanostatic and potentiodynamic reduction curves were measured on samples, which were passivated for 20 min. at 600mV SCE in dark and under illumination respectively - the reduction experiments were always performed in dark. For each reduction experiment 3-5 runs were performed - the standard deviation was in the range of +/- 0.1 mC/cm^2. With both methods almost identical charge values were obtained for the samples passsivate in dark or under illumination.

Particularly from the potentiodynamic curves it was obvious that the film reduction process occurs in two steps - as several times reported in literature [27,28] - which can be attributed to the Fe^{3+}/Fe^{2+} reduction in the outer γ-Fe_2O_3 and the inner Fe_3O_4 part of the film [5,7]. Although the explicit value of the film thickness depends on some assumptions it is known from several investigations [5,7,29,30] that in the case of passive iron the reduction charges are proportional to the thickness of the oxide film. Hence the almost identical reduction charges obtained for the passive films formed in dark and under illumination show that the film thickness is not significantly affected by illumination. Thus it can also be excluded that the increased corrosion resistance of the light-treated passive film is due to an increase in the film thickness. Further the almost identical shape of the reduction curves for the illuminated and dark case - especially regarding the two reduction steps - indicates that also the ratio of inner- to outer layer cannot be influenced by light and therefore is not the cause of the increased pitting corrosion resistance of films formed under illumination.

3. Mott-Schottky analysis

In order to gain information about the electronic properties of the passive films capacitance measurements of the Mott-Schottky type were performed. The samples were passivated for 20 minutes at 600 mV with and without illumination respectively, and subsequently in dark, the

imaginary part of the impedance (Z") at 1000 Hz was recorded as a function of the potential and the corresponding system capacitance (C) was obtained from C = -1/ωZ". This treatment was selected after a series of previous impedance spectra experiments had been carried out. In order to separate the electronic part of the ac response from ionic contributions a sufficiently high frequency has to be applied [1]. On the other hand the high frequency end is experimentally limited by the electrolyte resistance - which makes capacitance measurements at much higher frequencies erroneous.
According to the Mott-Schottky theory [1,31,32] the space charge capacitance of a semiconductor (C_{SC}) is given by Equation (1) :

$$\frac{1}{C_{sc}^2} = \frac{2}{\varepsilon\varepsilon_0 \, q \, N \, A^2}\left(U - U_{fb} - \frac{kT}{q}\right) \qquad (1)$$

where ε denotes the dielectric constant , ε_0 the vacuum permittivity, q the charge of the electron, A the area, N the donor concentration (for a n-type semiconductor), U the applied potential, U_{fb} the flatband potential and the term kT/q is at room temperature 25mV. Basically in series to C_{sc} also the capacitance of the Helmholtz layer (C_H) can become significant. In the present study it was assumed that $1/C_H$ can be neglected ($C=C_{sc}$) particularly since the introduction of an arbitrary value for C_H would only affect the absolute data evaluation but not have an effect on relative findings. Under this assumption the results of the impedance measurements can be plotted according to Equation (1) shown in Fig. 5. It is obvious that the passive film exposed to light during its formation differs significantly in its electronic properties from the passive film formed in dark.

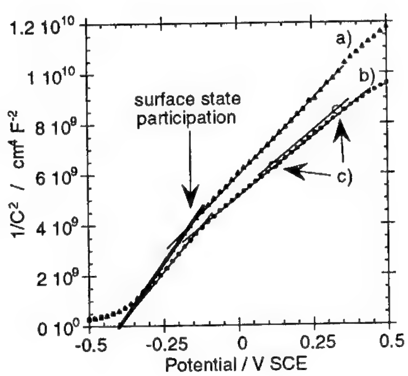

Fig. 5 Mott-Schottky plots of the passive film on iron formed in borate buffer, pH 8.4 for 20 min at U =+600 mV SCE
a) passivation without illumination, impedance measurement in dark
b) passivation under illumination, impedance measurement in dark
c) passivation under illumination, light switched on during the impedance measurement

In both cases the Mott-Schottky plots exhibit a break in the potential range of ≈ -170 mV SCE. A non-linear behaviour in Mott-Schottky plots can be due to several reasons such as an inhomogeneous doping profile [1]. or the presence of deep states e.g. [33 - 35]. A further explanation is the presence of surface states which become ionized as the Fermi level passes them and hence contribute to the measured charge for potentials positive to ≈ -170 mV SCE. By employing this approach the additional charge can be obtained by an integration of the excess capacitance due to surface states (C_{SS}) over the relevant potential range according to Equation (2) [36]:

$$N_{SS} = \frac{1}{q}\int_{U_0}^{U_1} C_{SS}\,dU \qquad (2)$$

This treatment assumes that the surface states lead to an additional capacitance, which is in terms of an equivalent circuit in parallel to the space charge capacitance [1]. Hence only for potentials cathodic to -170 mV SCE the application of the Mott-Schottky model is justified. With Equation (1) and using $\varepsilon=15.6$ [37] the doping concentration can be determined from the slope of the curve in the relevant potential range. In Table 1. the resulting bulk doping and the surface state density for the films formed in dark and under illumination are given.

Table 1:

	U_{fb} (mV SCE)	$N_{bulk} \cdot 10^{20}$ (cm^{-3})	$N_{SS} \cdot 10^{12}$ (cm^{-2})
dark	-400	5.4 ± 0.2	4.3 ± 0.5
illuminated	-400	6.2 ± 0.2	7.0 ± 0.5

These results show that illumination of the passive film during passivation leads to a slightly higher doping and a considerably higher surface state density.

In above experiments all the capacitance measurements were carried out in dark. In Fig. 5 two points (c) are shown which indicate the shift in the capacitance values when the light is switched on during the impedance measurements of a passive film formed under illumination. The only very slight increase in the $1/C^2$ values is a further evidence that the light effect on the field distribution can be neglected once the film has been formed - at least with the intensities used in this work.

4. Photocurrent transient and photoimpedance measurements

The electronic properties were further studied by photocurrent transient and photoimpedance measurements. Fig. 6 shows the shape of the photoresponse when a light pulse is applied 1min. after the samples were passivated for 20min. with and without illumination. For a further evaluation of the phototransient results following characteristic features are of interest: the initial magnitude of the photocurrent ($I_{ph}(t=0)$), the decay kinetics and the steady state value of the photocurrents ($I_{ph}.(t=\infty)$)

For ideal semiconductors often the Gärtner model [38] is applied to calculate the magnitude of the photocurrent Since the model does not consider recombination of photogenerated charge carries it can only be used to calculate the initial photocurrent of the phototransients and yields for the photocurrent in dependence of the doping concentration:

$$I_{ph} \propto I_{ph}(t=0) \propto N^{-0.5} \qquad (3)$$

According to equation (3) the initial photocurrent value should be proportional to $N^{-0.5}$ - i.e. the measured initial photocurrent is not very sensitive to changes in the bulk doping concentration. This is in agreement with Fig. 6 where the initial photocurrents for the illuminated and dark passivated sample show almost the same initial value.

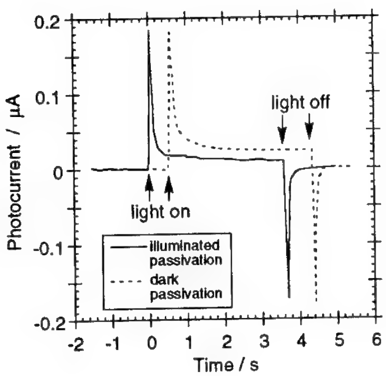

Fig. 6 Photocurrent transients for passive films formed in borate buffer, pH 8.4 for 20 min at U =+600 mV SCE with and without illumination

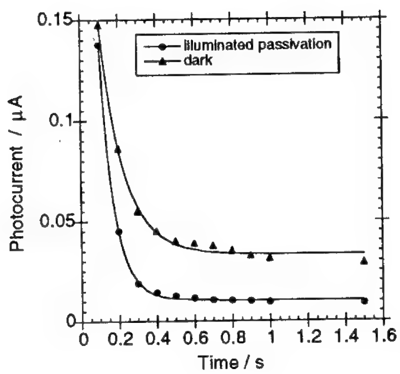

Fig. 7 Photocurrent transients from Fig.6 with a higher time resolution (symbols) and fit (solid line)

In Fig. 7 the first part of the photocurrent transients with a higher time resolution is shown. It can be assumed that the decay of the photocurrent is caused by a recombination of charge carriers at surface states. The most simple and common kinetic approach [39] is based on an exponential decay law [Equation (4)]:

$$Iph(t) = Iph(t{=}0) \cdot \exp(-k_r t) + Iph(t = \infty) \tag{4}$$

with $$k_r = N_{ss} \cdot \beta \cdot \exp(\Delta E / kT) \tag{5}$$

where k_r denotes the recombination rate constant , β the capture coefficient and ΔE the activation energy. This exponential decay approximation is in agreement with different other investigations [40, 41, 9].

By fitting Equation (4) to the data points of Fig. 7 the rate constants for the illuminated and dark case can be determined, yielding $k_r = 7.7\ s^{-1}$ for the dark and $k_r = 13\ s^{-1}$ for the illuminated experiment. Since k_r should be proportional to the surface states density [Equation (5)] the ratio of the rate constants for the illuminated case to the dark case should correspond to the ratio of the surface state densities. A comparison of the rate constants ratio {k_r (illuminated) / k_r (dark) = 1.69 } with the results from the Mott-Schottky analysis {N_{SS} (illuminated) / N_{SS} (dark) = 1.68 } yields almost identical values.

A second photoelectrochemical way to determine k_r are photoimpedance measurements. In Fig. 8 the magnitude and the phase shift of the photocurrent in dependence of the chopper frequency are plotted in a Bode diagram for samples passivated at 600mV SCE for 20 min in dark and under illumination.

Assuming a simple - one time constant - equivalent circuit (Fig. 9), which also corresponds to the exponential decay law from Equation (5), the complex photocurrent is given by Equation (6).

$$\frac{1}{I_{ph}} \propto Z = R_2 + \left(\frac{1}{R_1} + j\omega C\right)^{-1} \tag{6}$$

where Z represents the photoimpedance, R and C the resistive and capacitive elements of Fig. 9, and $\omega = 2\pi f$ (f = chopper frequency). By fitting Equation (6) to data of Fig. 8 it is possible to determine the values of R_1, R_2 and C and the rate constant of the system can be calculated [Equation (7)]

$$k_r = \frac{1}{R_1 C} \tag{7}$$

This leads to rate constants $k_r = 6.9\ s^{-1}$ for the dark and $k_r = 11.2\ s^{-1}$ for the illuminated passivation which are in the same range as the values determined from the photocurrent transient measurements and also the ratio of the rate constants $\{k_r \text{ (illuminated)} / k_r \text{ (dark)} = 1.62\}$ is in very good agreement with the values reported above.

The results of the Mott-Schottky analysis, phototransient and photoimpedance measurements indicate that the concept of surface and bulk states is reasonable and that illumination during passive film formation leads particularly to an increase in the surface state density. According to a model of Abrantes et. al. [40] surface states on passive films on iron are mainly associated with adsorbed OH^- -ions which are able to capture photogenerated holes. The formed radicals ($OH^{\cdot}$) are stabilized on the surface by a Fe^{3+}/Fe^{4+} equilibrium. Therefore it could speculatively be concluded that due to the illumination during passivation the adsorption properties at the outermost part of the oxide are changed. In most models of pit initiation the adsorption of Cl^- ions on the film surface is regarded to be the first step and hence such changes in the adsorption behaviour could be a reason for the increased pitting corrosion resistance.
However the illuminated films show also a higher density of bulk states which can be a sign of structural changes in the oxide and this may as well lead to an improved resistance against pitting corrosion.

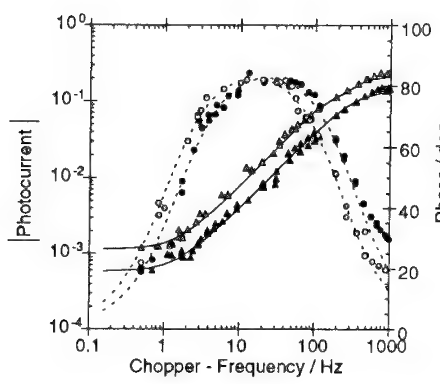

Fig. 8 Photoimpedance spectra in a Bode plot for samples passivated at 600 mV SCE for 20 min in dark (solid symbols) and under illumination (open symbols) - triangles represent /photocurrent/ and circles the phase. Solid lines show the result of fitting Eq. (9) to the data points.

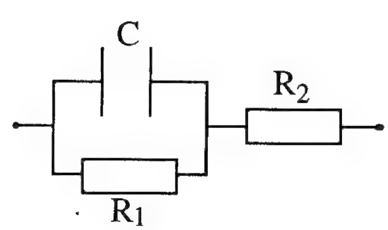

Fig. 9 Equivalent circuit applied for the interpretation of the photoimpedance measurements R denotes resistive and C capacitive elements

Summary and Conclusions

The results show that illumination strongly increases the resistance of passive iron against local breakdown in chloride-containing solutions. This effect is not based on a change in the field distribution within the passive film during illumination. Under the experimental conditions used in the present study illumination of a once formed passive film can influence the charge density in the film only very weakly and has no significant effect on the pitting corrosion susceptibility. The increased resistance against pitting corrosion can only be attained if the material is exposed to light during the formation of the passive film. Illumination leads to permanent changes in the film properties.

From galvanostatic and potentiodynamic reduction experiments it is evident that this permanent film modification is not a light-induced film thickening. The modification of the film becomes apparent in capacitance and photoelectrochemical measurements which indicate that the electronic properties of films formed under illumination are significantly different from films formed in dark. Specifically an increased surface state density is observed for light treated passive films. Since surface states on passive films on iron are likely to be associated with the adsorption of hydroxyl-ions, a possible reason for the improved pitting resistance might be - in terms of the competitive Cl^-/OH^- adsorption model - a suppression of Cl^- adsorption on the oxide surface.

Acknowledgements

The authors are pleased to acknowledge the Schweizerischer Nationalfonds zur Förderung der wissenschaftlichen Forschung for supporting this research within its national programme Nr. 24 (Chemie und Physik an Grenzflächen). Thank is also expressed to Mr. Lukas Eschbach for performing part of the experiments.

References

1 S. R. Morrison, Electrochemistry at semiconductor and oxidized metal electrodes, Plenum Press, New York, (1980).
2 B. D. Cahan and C. T. Chen, J. Electrochem. Soc. **129**, 474 (1982).
3 B. D. Cahan and C. T. Chen, J. Electrochem. Soc. **129**, 923 (1982).
4 U. Stimming and J. W. Schultze, Ber. Bunsenges. Phys. Chem. **80**, 1297 (1976).
5 U.Stimming, Ph.D Thesis, Freie Universität Berlin (1979).
6 U. Stimming and J. W. Schultze, Electrochim. Acta **24**, 859 (1979).
7 U. König, M. M. Lohrengel and J. W. Schultze, Ber. Bunsenges. phys. Chemie **91**, 426 (1987).
8 U. König, Ph.D Thesis, Heinrich-Heine-Universität Düsseldorf (1989).
9 P. Schmuki, Ph. D. Thesis Nr. 9763, ETH-Zürich, Switzerland (1992).
10 U. Stimming, Electrochimica Acta **31**, 415 (1986).
11 S.M. Wilhelm, K.S. Yun, L.W. Ballenger and N. Hackerman, J. Electrochem. Soc. **126**, 419 (1979).
12 S. M. Wilhelm and N. Hackerman, J. Electrochem. Soc. **128** ,1668 (1981).
13 P. C. Searson, R. M. Latanision and U. Stimming, J. Electrochem. Soc. **135**, 1358 (1988).
14 N. Sato, Corrosion-NACE, **45**, 354 (1989).
15 P. Schmuki and H. Böhni, Werkstoffe und Korrosion **42**, 203 (1991).
16 P. Schmuki and H. Böhni, J. Electrochem. Soc. **139**, 1908 (1992).
17 P. Schmuki and H. Böhni, J. Electrochem. Soc. **141**, 362 (1994).
18 U. Bertocci, J. Electrochem. Soc. **125**, 1598 (1978).
19 S. Lenhart, M. Urquidi-Macdonald and D.D. Macdonald, El. chim. Acta **32**, 1739 (1987).
20 D.D. Macdonald, M. Urquidi-Macdonald and S.J. Lenhart, in Surfaces, inhibition and passivation, Eds. E. McCafferty, R.J. Brodd, The Electrochemical Society, Pennington NJ, p. 402 (1986).
21 D.D. Macdonald, in Critical Factors in Localized Corrosion, Eds. G.S. Frankel, R. G. Newman, The Electrochemical Society, Pennington, NJ, 1 (1992).

22 D. D. Macdonald, J. Electrochem. Soc. **139**, 3434 (1992).
23 Z. Szklarska-Smialowska, Pitting Corrosion of Metals, NACE, Houston, (1986).
24 H. Böhni, Langmuir **3**, 924 (1987).
25 Critical Factors in Localized Corrosion, Eds. G.S. Frankel, R. G. Newman, The Electrochemical Society, Pennington, NJ (1992).
26 H. Gerischer, Corr. Sci. **29**, 257 (1989).
27 J.A. Bardwell and B. MacDougall, J. Electrochem. Soc. **135**, 2157 (1988).
28 J.A. Bardwell and B. MacDougall, Electrochim. Acta **34**, 229 (1989).
29 J. O'M. Bockris, M.A. Genshaw, V. Brusic and H. Wroblowa, Electrochim. Acta **16**,1859 (1971).
30 J. Kruger and J.P. Calvert, J. Electrochem. Soc. **114**, 43 (1967).
31 W. Schottky, Z. Phys. **113**, 367 (1939) , **118**, 539 (1942).
32 N. F. Mott, Proc. R. Soc. **A171**, 27 (1939).
33 M. Tomkiewicz, J. Electrochem. Soc. **126**, 1505, 2220 (1979).
34 M.H. Dean, U. Stimming, J. Electroanal. Chem. 228, 135 (1987)
35 J.F. Dewald, Bell Syst. Tech. J 39, 615 (1960)
36 U. König, P. Meisterjahn and J.W. Schultze , Werkstoffe und Korrosion, 42, 179 (1991)
37 A. M. P. Simoes, M.G.S. Ferreira, B. Rondot and M. da Cunha Belo, Proc. Electrochemical Methods in Corrosion Research, Ed. O. Forsen, Materials Science Forum, Vol. 111-112 (1992), p. 303.
38 W. W. Gärtner, Phys. Rev. **116**, 84 (1959).
39 R. H. Bube,"Photoelectronic Properties of Semiconductors", Oxford University press (1992).
40 L.M. Abrantes and L.M. Peter, J. Electroanal. Chem. **150**, 593 (1983).
41 A. R. Kucernak, R. Peat and D. E. Williams, J. Electrochem. Soc. **138**, 1645 (1991).

Materials Science Forum Vols. 185-188 (1995) pp. 1075-1082

Photo-protection of 304 stainless steel with TiO_2 coating

R. Fujisawa and S. Tsujikawa

The University of Tokyo, Faculty of Engineering, Department of Metallurgy,
7-3-1 Hongo, Bunkyo-ku, Tokyo, 113 Japan

Keywords: Stainless steel, TiO_2 coating, cathodic protection, photopotential

ABSTRACT

The photoelectrochemical behavior of Type 304 stainless steel coated with TiO_2 via sputtering was studied in NaCl solutions at ambient temperature under 300W Xenon lamp illumination. Photopotential of TiO_2-coated 304 shifted in less noble direction with increasing coating thickness up to 100nm. With enough light intensity to bring the photopotential toward its flatband potential, TiO_2-coated 304 could protect the substrate from crevice corrosion even in 20% NaCl solution. Finally, coating defect was found to give no significant damage on the protection performance when its area ratio is less than 1/10.

INTRODUCTION

The n-type TiO_2 semiconductor has been of great interest as a candidate material for solar energy conversion ever since Honda and Fujishima discovered its ability to electrolyze water with markedly reduced voltage under illumination [1]. The introduction of TiO_2 into corrosion science area fitted in its ability to shift electrode potential of photo-irradiated TiO_2 in less noble direction toward its flatband potential. The anodic decomposition potential of TiO_2 electrode is below that of water oxidation [2]. Thus, the photoelectrochemical reaction involved was not the decomposition of TiO_2 but the oxidation of H_2O by the photo-excited holes in valence band. These unique properties enable TiO_2 to protect some metallic materials from corrosion by having TiO_2 acting as a non-sacrificed anode.

This paper presents the experimental results for the cathodic protection of stainless steels via TiO_2 coating under illumination.

EXPERIMENTAL

(1)Specimen

Type 304 stainless steel sheet of 1mm thickness was cut to the size of 35 ×40 mm. The specimens are abbreviated as bare 304. Chemical composition in mass% of the Type 304 stainless steel is C:0.066, Si:0.58, Mn:0.82, P:0.029, S:0.002, Ni:8.75, Cr:18.29, Mo:0.14, Cu:0.14. The testing side of the specimen was polished to the mirror finish with 0.05 μm Al_2O_3 then rinsed with acetone before finally dried in the air.

The stainless steel substrates were polished to mirror finish with 0.05 μm Al_2O_3 before sputter-etched by about 200 nm to remove the air-formed oxide layer. TiO_2 films were reactively sputtered on the substrates in O_2/Ar mixtures using a Ti target. The vacuum system could achieve pump down pressures as low as 5.0 x 10^{-6} Torr. During sputtering, the chamber was held at 5.0 x 10^{-3} Torr, with a gas flow of 20 sccm for Ar and 10 sccm for O_2. The specimens were coated with TiO_2 film of thickness 1,3,10,30 and 100 nm, which are abbreviated as TiO_2-coated 304.

(2)Electrochemical measurement

The test solution used was mainly 0.3% NaCl solution at room temperature with an unadjusted pH value of about 6.5 prepared by using analytical grade reagent and de-ionized water. Polarization curves were recorded at a scanning rate of 25 mV/min.

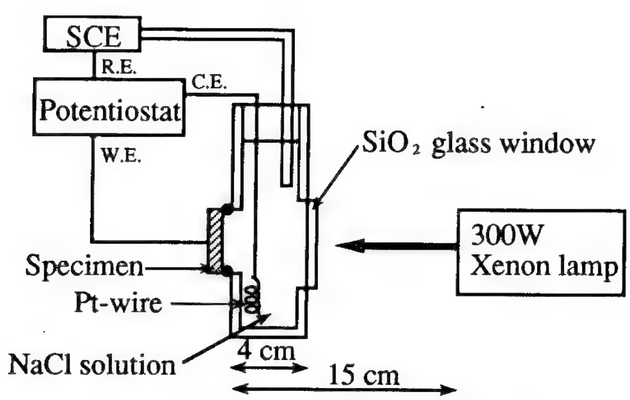

Fig.1 Schematic diagram of the cell for electrochemical measurements. Xenon lamp is normally located at a distance of 15cm from the specimen.

The photopotential measurement was conducted with a 300W Xenon lamp. The electrode potential was monitored for 30 min in dark before to be measured for two hours under illumination. The electrode potentials were measured with respect to saturated calomel electrode (SCE). Fig 1 shows the schematic diagram of cell.

RESULTS AND DISCUSSIONS

Fig.2 shows the polarization curves for Type 304 stainless steels with and without TiO_2 coating when illuminated under a 300W Xenon lamp. The anodic current of TiO_2-coated 304 showed marked increase under illumination because TiO_2 is a n-type semiconductor and the minority carrier concentration is greatly enhanced when light absorption generates photo-excited electrons and holes. The photocurrent of TiO_2-coated 304 observed is due to oxygen evolution by photoexcited holes in valence band [1]. Based on the polarization curves of bare 304 stainless steel, it is expected that TiO_2-coated 304 can protect Type 304 stainless steel cathodically under illumination. A galvanic couple of TiO_2-coated 304 and bare 304 was used to study its electrochemical behavior under illumination in 0.3% NaCl solution.

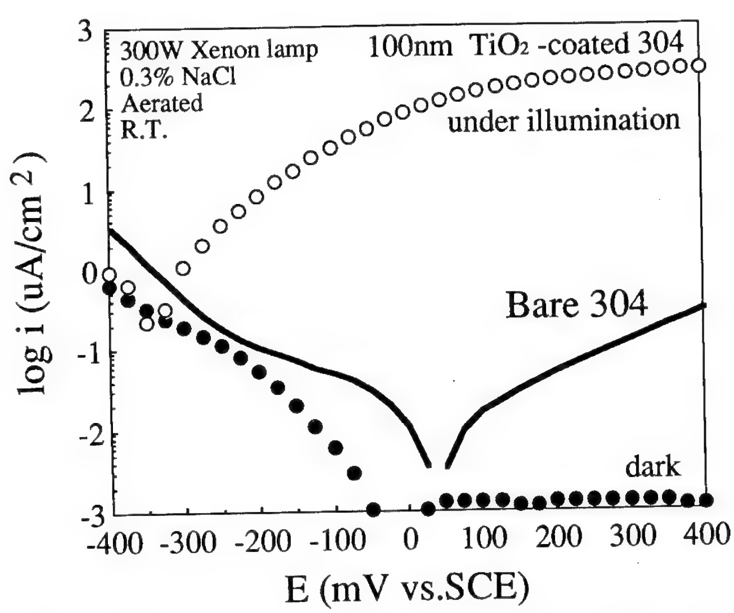

Fig.2 Polarization curves of type 304 steels with and without TiO_2 coating.

Fig.3 shows galvanic current and electrode potential of TiO_2-coated 304 coupled with bare 304 both having the same surface area. Under illumination large galvanic current to protect cathodically type 304 stainless steel was observed and a very low current was observed without illumination. The mixed potential was -300 mV vs. SCE as would be expected from Fig.2. The effect of coating defects on cathodic protection of TiO_2-coated 304 was studied by decreasing the area of bare 304 as shown in Fig.4. Area ratio of TiO_2-coated 304/bare 304 has no effect on electrode potential under illumination when its ratio is below 1/10. The protection performance is not hindered with coating defects less than 1/10 in the area ratio.

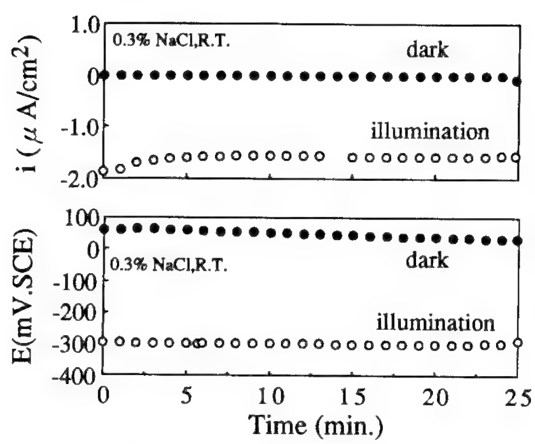

Fig.3 Effect of illumination on galvanic current and electrode potential (area ratio of bare 304/coated 304 = 1/1).

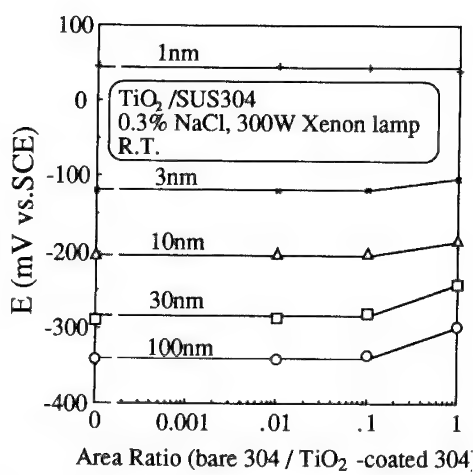

Fig.4 Effect of area ratio on electrode potential of coupled bare and TiO_2 (1~100nm) -coated 304 steels.

Fig.5 shows the effect of film thickness on photocurrent at 250 mV vs. SCE (a) and photopotential (b) of the TiO_2-coated 304. Photocurrent of TiO_2-coated 304 polarized at 250 mV vs. SCE increased drastically at 10 nm thickness and remained high in the range between 10 to 100 nm. Photopotential of TiO_2-coated 304 were shifted in less noble direction with increasing coating thickness in the range of 1 to 100 nm. The electrode potential of TiO_2 could approach its flatband potential under

intensified irradiation if its space-charge layer is thick enough. M.A.Butler and D.S.Ginley showed the flatband potential of TiO_2 to be -900 mV vs. SCE in solution at pH=13.3 [3]. Consequently, at pH 6.5, the flatband potential is calculated to be about -560 mV vs. SCE. As shown in the Fig.5, photopotential of TiO_2-coated 304 was about -370 mV vs. SCE for 100 nm coating thickness. When irradiated by a 500 W high pressure Hg lamp, the photopotential of TiO_2-coated 304 became -500 mV vs. SCE nearing its flatband potential.

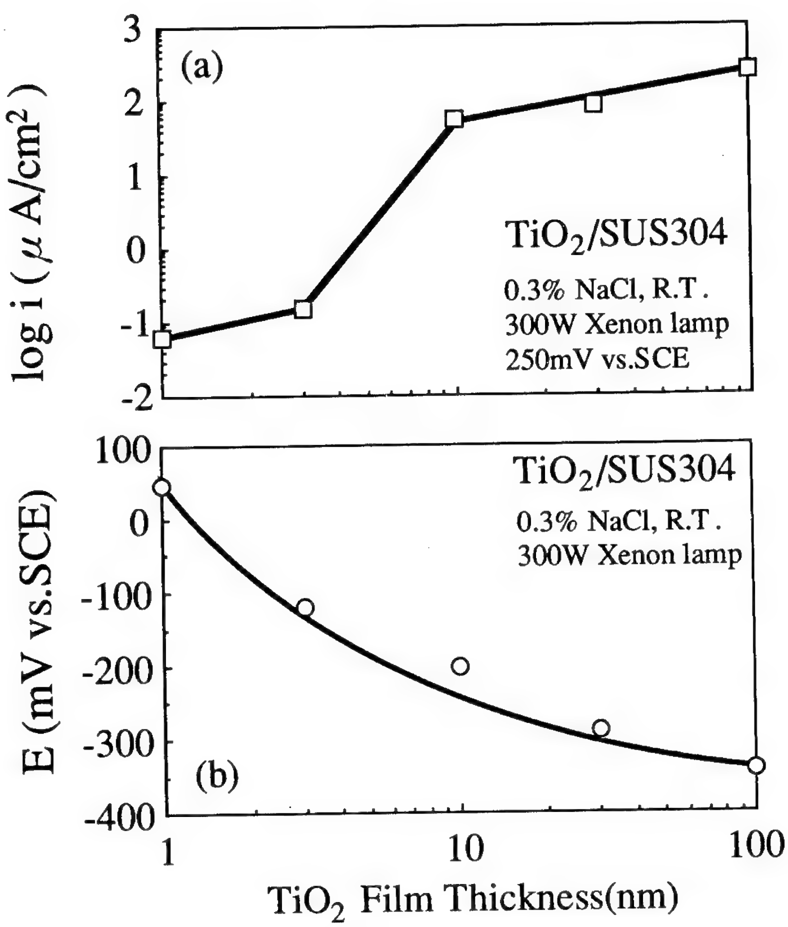

Fig.5 Effect of TiO_2 film thickness on (a) current density, i, a t 250mV vs.SCE and (b) photopotential,E, o f TiO_2 -coated 304 steel.

For stainless steels, crevice corrosion easily occurrs. Fig.6 shows the repassivation potential, $E_{R,CREV}$, for metal/metal-crevice of Type 304 stainless steel and photopotential of the TiO_2-coated 304 in various NaCl solutions. NaCl concentration have no effect on the photopotential of the TiO_2-coated 304. It is shown that photopotential of TiO_2-coated 304 is less noble than the $E_{R,CREV}$ in the range below 2%. But under illumination by 500 W Hg lamp, we can determin the photopotential of this specimen to be about -500 mV vs. SCE, which is located in the repassivation domain of the steel. This results could demonstrate and confirm the cathodic protection of Type 304 stainless steel against crevice corrosion by TiO_2 coating under illumination.

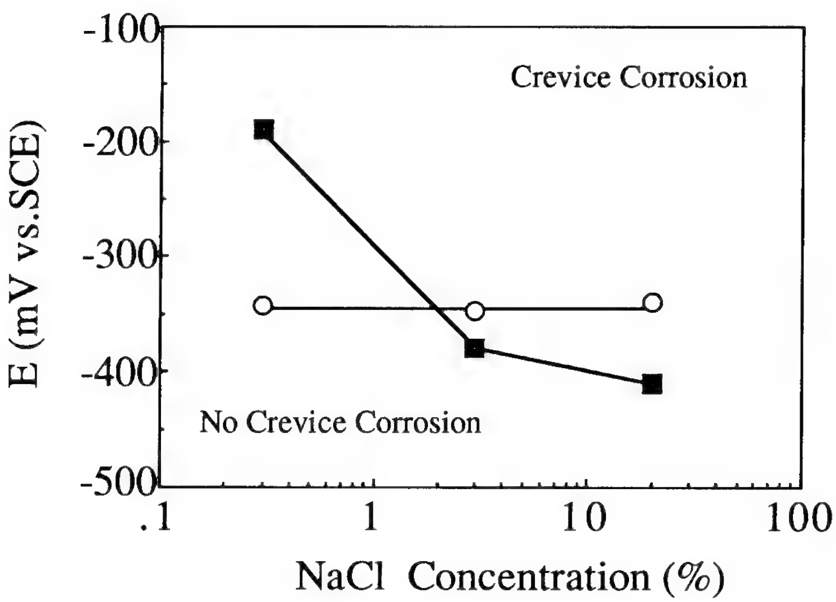

Fig.6 Photopotential of 100nm TiO_2 - coated 304 steel (○) with repassivation potential of crevice corrosion, $E_{R,CREV}$, for 304 steel (■) in various concentration of NaCl solutions.

CONCLUSIONS

The photoelectrochemical behaviors of 304 stainless steel coated with TiO_2 via sputtering were studied in NaCl solution. It was confirmed that TiO_2 coating can cathodically protect 304 substrate under illumination. The coating defect is found to give no significant damage on the protection performance when its area ratio is less than 1/10.

ACKNOWLEDGMENT

We thank Yuji Yamamoto of Nippon Sheet Glass Co. for his valuable assistance in making the specimens.

REFERENCES

[1]. A.Fujishima, K.Honda and S.Kikuchi, Kogyo-Kagaku Zasshi, 72, 108-13 (1969)

[2]. H.Gerischer, J.Electroanal.Chem., 82,133-143(1977)

[3]. M.A.Butler and D.S.Ginley, J.Electrochem.Soc.,125,228-231(1978)

AUTHOR INDEX

KEYWORD INDEX